Proceedings of the

# 10th ECCOMAS Thematic Conference on MULTIBODY DYNAMICS

December 12 - 15, 2021

https://eccomasmultibody2021.mm.bme.hu

Budapest University of Technology and Economics
Faculty of Mechanical Engineering

**Proceedings of the**
**$10^{\mathrm{th}}$ ECCOMAS Thematic Conference on MULTIBODY DYNAMICS**

**Edited by**

József Kövecses,
Gábor Stépán,
Ambrus Zelei

**Contact**

Department of Applied Mechanics,
Budapest University of Technology and Economics,
Műegyetem rkp 5., Budapest, H-1111, Hungary.

**Publisher**

Budapest University of Technology and Economics

ISBN 978-963-421-870-8

Budapest, Hungary, 2021.

## About the conference

### Organizing Committee

Gábor Stépán, Chair, Budapest University of Technology and Economics, Hungary
József Kövecses, Co-Chair, McGill University, Canada
Tamás Insperger, Budapest University of Technology and Economics, Hungary
László Bencsik, Secretary, Budapest University of Technology and Economics, Hungary
Ambrus Zelei, Budapest University of Technology and Economics, Hungary

### Scientific Committee of the review process

Ambrósio J. (Portugal)
Amirouche F. M. L. (USA)
Anderson K. (USA)
Arnold M. (Germany)
Bauchau O. (USA)
Bencsik L. (Hungary)
Berbyuk V. (Sweden)
Betsch P. (Germany)
Blajer W. (Poland)
Bottasso C. (Germany)
Brüls O. (Belgium)
Choi J. H. (Korea)
Cuadrado J. (Spain)
Eberhard P. (Germany)
Fisette P. (Belgium)
Font-Llagunes J. M. (Spain)
Flores P. (Portugal)
Frączek J. (Poland)
García Orden J. (Spain)
Gerstmayr J. (Austria)
Goicolea J. (Spain)
González Varela F. J. (Spain)
Ibrahimbegovic A. (France)
Jonker B. (Netherlands)
Kecskeméthy A. (Germany)
Kim S. (Korea)
Kövecses J. (Canada)
Lankarani H. (USA)
Liu C. (China)
McPhee J. (Canada)
Mikkola A. (Finland)
Müller A. (Austria)
Negrut D. (USA)
Nikravesh P. (USA)
Pennestrí E. (Italy)
Pfeiffer F. (Germany)
Pogorelov D. (Russia)
Polach P. (Czech Republic)
Raison M. (Canada)
Saha S. (India)
Schiehlen W. (Germany)
Schwab A. (Netherlands)
Seifried R. (Germany)
Shabana A. (USA)
Sharp R. S. (UK)
Sika Z. (Czech Republic)
da Silva M. M. (Brazil)
Silva M. T. (Portugal)
Sinatra R. (Italy)
Stépán G. (Hungary)
Suda Y. (Japan)
Terumichi Y. (Japan)
Terze Z. (Croatia)
Valásek M. (Czech Republic)
Verlinden O. (Belgium)
Woernle C. (Germany)
Wojtyra M. (Poland)
Zelei A. (Hungary)

### Supporting Organizations

Budapest University of Technology and Economics

Hungarian Academy of Sciences

The Academy of Europe, Budapest Knowledge Hub

### Industrial Support

Knorr-Bremse Hungary

## Preface

Welcome to the $10^{\text{th}}$ ECCOMAS Thematic Conference on Multibody Dynamics!

The conference series has a remarkable history. It is home to professionals specialized in different technologies and applications of multibody dynamics not only from Europe, but from all over the world. Our conference will be the 10th in a successful series of meetings held in Lisbon (2003), Madrid (2005), Milan (2007), Warsaw (2009), Brussels (2011), Zagreb (2013), Barcelona (2015), Prague (2017), Duisburg (2019). The organizers are grateful for the opportunity of organizing the ECCOMAS Thematic Conference on Multibody Dynamics in 2021 in Budapest. In spite of the difficulties caused by the pandemic, we managed to keep the biannual structure of the conference series.

Multibody dynamics plays a central role in the modeling, analysis, simulation and optimization of mechanical systems with a large variety of engineering applications. The conference serves as an excellent opportunity for researchers worldwide to exchange ideas in multibody dynamics concerning theoretical and application aspects such as multibody kinematics, formalisms and efficient numerical methods developed for multibody problems, dynamics of flexible multibody systems, slender structures, contact problems and impacts, mechatronics, robotics and control, vehicle dynamics, aerospace dynamics, system identification, optimization and sensitivity analysis, validation, software development, biomechanics, gait analysis and education. The conference also provides a platform for sharing novel ideas within the continuously growing multibody research community.

We faced major and unique challenges with the organization of the conference. As you know, the event was originally planned to take place in the summer of 2021 in Budapest. However, due to the unforeseen, special circumstances of the last two years imposed on us by the pandemic, we had to move the conference to the end of the year 2021, and eventually, we had to decide to go with a fully online event. Despite the online nature of the conference, the number of presentations, abstracts and papers received form 27 countries is still high, which shows the activity and enthusiasm of the researchers in the multibody community.

The organizers are especially thankful for the contribution of the members of the Scientific Committee during the thorough review process of the 40 full papers received from 15 countries.

Despite the challenges and the alternative form of the conference, we hope that you enjoy the event and find the Proceedings as a valuable professional material when studying in details the background of the lectures of your interest.

József Kövecses,
Gábor Stépán,
Ambrus Zelei,
editors

## Table of Contents

# Section
# BIOMECHANICS AND APPLICATIONS IN BIOMECHANICS

https://doi.org/10.3311/ECCOMASMBD2021-116



# An Efficient Discrete Model of a Simple Biped with a Torso

**Sarra A. Gismelseed** [1], **Amur S. Al Yahmedi** [2], **Riadh Zaier** [2], **Hassen M. Ouakad** [2], **Issam Bahadur** [2]

[1] Department of Mechanical & Industrial Engineering
Sultan Qaboos University
Al-Khoud, Muscat, 123, Oman
sarraabbasher@gmail.com

[2] Department of Mechanical & Industrial Engineering
Sultan Qaboos University
Al-Khoud, Muscat, 123, Oman
[amery, zaier, houakad, bahdoor@squ.edu.om]

**ABSTRACT**

Human locomotion involves a complex integration of muscles activity, central nervous system, and sensory information. Attempts to describe and understand the biomechanics of human locomotion have been made experimentally and mathematically (simulation). Mathematically, biped models with various complexities have been used to study human locomotion using different numerical methods and many features of human locomotion have been verified. In this paper, an optimization based prediction of human gait with its essential features using simple biped with torso is formulated. The biped can "qualitatively" mimic many features of human locomotion including the general behavior of human gait during running and walking.

**Keywords:** Discrete Mechanics, Optimization, Gait, Biped, Torso.

## 1. INTRODUCTION

Many researchers have studied human gait by modeling human body as a simple mechanical system represented mathematically as biped models that can describe the basics of human motion. Many studies in the literature on humanoid robots have focused in deriving the model using standard continuous-time mechanics. In [1], a gait trajectory of biped model in continuous time domain has been provided using simple technique that is based on the symmetric features in the dynamics of this compass-type model. The motion obtained by their technique resembles the phenomenon of a passive dynamic walking, since the motion contains swing phase and a foot collision taking place one after another. Srinivasan et. al., [2] have simulated human gait using an inverted pendulum model with the assumption of a rigid human body and massless legs. The model in [2] generated the energy-based optimal gait of three distinct types of human gait that are; i) walking, ii) inverted pendulum run, and iii) running. The discrete mechanics, on the other hand, have been recently applied to derive biped models. Compass-type biped model and discrete mechanics are used in [3] to formulate a gait generation problem. They have verified the generation of a stable gait by formulating a constrained nonlinear optimization problem in which the model minimizes the angular velocities using both impact and swing phases models. In 2015, Sun et. al. [4] have studied periodic gait optimization problem of the bipedal walking robot using discrete mechanics. The optimization problem was numerically solved using a class of global and feasible sequential quadratic programming algorithms [5][6]. Their study has shown that the algorithm can converge to a stable gait cycle by selecting a proper initial guess of the gait [4].

Biomedical researches have also focused on applying optimization techniques and algorithms to predict various types of human motion and dynamics. For a stable and a converging algorithm, several factors should be considered in the optimization routine such as the surrounded environment reaction forces and system inertia forces. Optimization algorithms can be applied for gait prediction, lifting, pushing, and pulling movements, to name a few. Prediction of these motions requires different optimization formulations and two or more tasks can be combined

https://doi.org/10.3311/ECCOMASMBD2021-116

together in a single optimization problem [7].

Numerical simulations are actively used today in different engineering and science fields to simulate the behavior of dynamic systems which was commonly involved to solve continuous models when simulating dynamical systems. However, when long-time simulation is required, it is frequently necessary to focus on preserving the qualitative behavior of the system such as transformation between velocity and momenta. The idea behind preserving energy in discrete mechanics is that, unlike other numerical methods, we discretize the basic principle of the mechanical system not the final differential equations. Therefore, symplectic methods [8] [9] (i.e., methods that are based on energy conservation) are becoming more widely used to simulate systems that have long-time simulation features such as humanoid robots. With these types of systems, it will be difficult to involve non-symplectic methods such as Runge-Kutta to simulate the behavior of those systems because it dissipates energy with time and hence increases the numerical error in the simulation [10]. To overcome the numerical errors with long- time simulation, discrete Lagrangian mechanics is introduced by considering a discrete Hamilton's principle [9][11]. In discrete mechanics, the Euler-Lagrange equations of the nonlinear mechanical systems are discretized. This way of formulating the equations of motion in mechanics has the capability of analysis with great compatibility with computers because of fewer errors in judgment with other similar numerical methods such as Euler method and Runge-Kutta method [7]. Furthermore, simulations can be performed for relatively large sampling times. Due to their symplectic nature, discrete mechanics are perfect for simulations that take long time. Therefore, the obtained discrete trajectories exhibit a good energy performance with time [12].

## 2. MATHEMATICAL MODEL

In this work, the developed model is based on the concept of the inverted pendulum model with the torso in order to generate more realistic information by mimicking human locomotion. The derivation of the model is based on the principle of discrete mechanics since it considers as a symplectic method that preserves momenta associated to symmetries of the system, and it also has perfect long-time energy compared to other numerical methods as discussed previously.

### 2.1. Discrete mechanics

In discrete Lagrangian, a path $q(t)$ for $t \in [0,T]$ is changed to a discrete path $q : \{t_0,...,t_k,...,t_N = T\}$, where $k \in \mathbb{N}$ and $N \in \mathbb{N}$. ($q_k$ is viewed as an estimation of $q(t_k)$). The Lagrangian $L(t)$ if estimated on each interval $[t_k, t_{k+1}]$ by a discrete Lagrangian $L_d(q_k, q_{k+1}, h)$; where, *h* is the time interval between two samples [9]:

$$h = t_{k+1} - t_k \,. \tag{1}$$

The formula of discrete Lagrangian is obtained by estimating the integral of the continuous-time Lagrangian over a small interval of time *h* using the midpoint rule [12].

$$q = \frac{q_{k+1} + q_k}{2}, \tag{2}$$

$$v = \frac{q_{k+1} - q_k}{h}, \tag{3}$$

$$L_d(q_{k+1}, q_k) = \int_{t_k}^{t_{k+1}} L(q, v)dt = hL\left(\frac{q_{k+1} + q_k}{2}, \frac{q_{k+1} - q_k}{h}\right). \tag{4}$$

Then we can approximate the discrete action $S_d$ as a sum of discrete Lagrangian and using Hamiltonian principle: if the path is slightly "varied", action is unchanged to the first order [13].

$$\delta S_d = \sum_{k=0}^{n-1} \delta L_d(q_{k+1}, q_k) = 0 \,. \tag{5}$$

Then, we minimize $S_d$ with respect to perturbations of trajectories. Using the boundary conditions for $\delta q$, we now have summation that must vanish for all values of $\delta q$ and one gets

https://doi.org/10.3311/ECCOMASMBD2021-116

the discrete Lagrangian formula [9]:

$$D_2L_d(q_{k-1},q_k)+f_d^+(q_{k-1},q_k)+D_1L_d(q_k,q_{k+1})+f_d^-(q_k,q_{k+1})=0. \quad (6)$$

Where, $f_d^-(q_k,q_{k+1})$ and $f_d^+(q_{k-1},q_k)$ left and right discrete forces, respectively, and:

$D_1L_d(q_k,q_{k+1})$: is the first derivative with respect to the first argument of $L_d$ (i.e., $q_k$ ).

$D_2L_d(q_{k-1},q_k)$: is the first derivative with respect to the second argument of $L_d$ (i.e., $q_k$ ).

And we have the discrete force related to the continuous force as the follows:

$$f_d^+(q_{k-1},q_k,t_{k-1},t_k)=f_d^-(q_k,q_{k+1},t_k,t_{k+1})=\frac{h}{2}f_c(\frac{q_{k+1}+q_k}{2},\frac{q_{k+1}-q_k}{h}\frac{t_{k+1}+t_k}{2}). \quad (7)$$

### 2.2. Biped model

Mechanical and mathematical biped models have been used to describe human basic motion. Although many studies have concentrated on the lower extremities in their models, there are two reasons that invite one to study the role of the torso in gait. First, most of the body weight is concentrated in the upper part of the body. The torso makes about 70% of total body weight. Second, the center of gravity of the whole body is in the upper body specifically in the torso, approximately 33 cm above the hip joint [14].

The proposed model shown in Fig. 1 has two point masses, one for the hip and the other for the rigid torso, and the two legs are considered to be massless. The hip mass $m_H$ has a position $(x_H,y_H)$ and the torso a position $(x_T,y_T)$ at time $t$. The motion of the torso is controlled via a torque $\tau(t)$ applied between the torso and the stance leg. A single telescopic axial actuator is used to combine flexion of the three joints in the leg: hip, knee, and ankle, which consequently cause variations of the leg length $q(t)$. This actuator transmits a compressive time-varying force $F(t)$ and both legs are assumed to have identical profiles of leg length and ground reaction force.

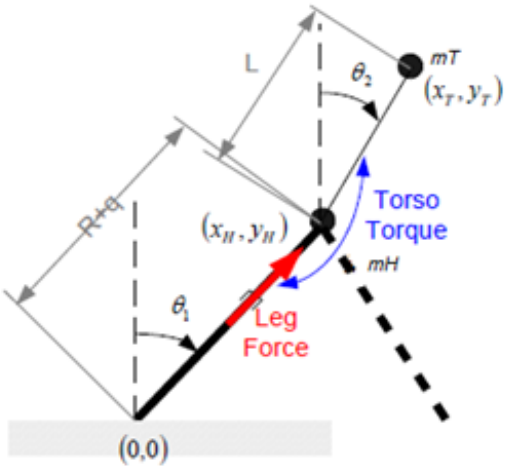


**Figure 1.** Biped model with a torso

The discrete Euler Lagrange equation of the biped is given by:

https://doi.org/10.3311/ECCOMASMBD2021-116

$$
\begin{aligned}
L_d(\theta_{1k},\theta_{1k+1},\theta_{2k},\theta_{2k+1},q_k,q_{k+1}) &= \frac{1}{2}h(m_H+m_T)(R+\frac{\Sigma q_k}{2})^2(\frac{\Delta\theta_{1k}}{h})^2 \\
&+\frac{1}{2}h(m_H+m_T)(\frac{\Delta q_{1k}}{h})^2+\frac{1}{2}hm_TL^2(R+\frac{\Sigma q_k}{2})^2(\frac{\Delta\theta_{2k}}{h})^2 \\
&+hm_TL(R+\frac{\Sigma q_k}{2})(\frac{\Delta\theta_{1k}}{h})(\frac{\Delta\theta_{2k}}{h})\cos(\frac{\Sigma\theta_{1k}}{2}-\frac{\Sigma\theta_{2k}}{2}) \\
&+hm_TL(\frac{\Delta\theta_{1k}}{h})(\frac{\Delta q_k}{h})\sin(\frac{\Sigma\theta_{1k}}{2}-\frac{\Sigma\theta_{2k}}{2}) \\
&-h(m_T+m_H)g(R+\frac{\Sigma q_k}{2})\cos(\frac{\Sigma\theta_{1k}}{2})-hm_TgL\cos(\frac{\Sigma\theta_{2k}}{2}).
\end{aligned} \tag{8}
$$

Note: $\Delta\theta_{1k}=\theta_{1k+1}-\theta_{1k}$, $\sum\theta_{1k}=\theta_{1k+1}+\theta_{1k}$, $\Delta\theta_{2k}=\theta_{2k+1}-\theta_{2k}$, $\sum\theta_{2k}=\theta_{2k+1}+\theta_{2k}$, $\Delta q_k=q_{k+1}-q_k$ and $\sum q_k=q_{k+1}+q_k$.

The Discrete Euler Lagrange formulation is used to find the equations of the biped by assuming only one-foot contacts the ground.

$$
\begin{aligned}
&D_2L_d(\theta_{1k-1},\theta_{1k},\theta_{2k-1},\theta_{2k},q_{k-1},q_k)+f_d{}^+(\theta_{1k-1},\theta_{1k},\theta_{2k-1},\theta_{2k},q_{k-1},q_k) \\
&+D_1L_d(\theta_{1k},\theta_{1k+1},\theta_{2k},\theta_{2k+1},q_k,q_{k+1})+f_d{}^-(\theta_{1k},\theta_{1k+1},\theta_{2k},\theta_{2k+1},q_k,q_{k+1})=0,
\end{aligned} \tag{9}
$$

Where,

$$
D_1L_d=\begin{bmatrix}
\frac{\partial L_d(\theta_{1k},\theta_{1k+1},\theta_{2k},\theta_{2k+1},q_k,q_{k+1})}{\partial\theta_{1k}} \\
\frac{\partial L_d(\theta_{1k},\theta_{1k+1},\theta_{2k},\theta_{2k+1},q_k,q_{k+1})}{\partial\theta_{2k}} \\
\frac{\partial L_d(\theta_{1k},\theta_{1k+1},\theta_{2k},\theta_{2k+1},q_k,q_{k+1})}{\partial q_k}
\end{bmatrix}, \tag{10}
$$

$$
D_2L_d=\begin{bmatrix}
\frac{\partial L_d(\theta_{1k-1},\theta_{1k},\theta_{2k-1},\theta_{2k},q_{k-1},q_k)}{\partial\theta_{1k}} \\
\frac{\partial L_d(\theta_{1k-1},\theta_{1k},\theta_{2k-1},\theta_{2k},q_{k-1},q_k)}{\partial\theta_{2k}} \\
\frac{\partial L_d(\theta_{1k-1},\theta_{1k},\theta_{2k-1},\theta_{2k},q_{k-1},q_k)}{\partial q_k}
\end{bmatrix}. \tag{11}
$$

The discrete forces are the Ground Reaction Force (GRF) and the torque acting on the leg and the torso.

$$
f_d{}^+(\theta_{1k-1},\theta_{1k},\theta_{2k-1},\theta_{2k},q_{k-1},q_k)=f_d{}^-(\theta_{1k},\theta_{1k+1},\theta_{2k},\theta_{2k+1},q_k,q_{k+1})=\frac{h}{2}\begin{bmatrix}\tau\\-\tau\\F\end{bmatrix}. \tag{12}
$$

The biped model has the dimensions descried in the following table.

**Table 1.** Dimensions of biped model with a torso

| Symbol | Description | Value |
|---|---|---|
| $m$ | Total body mass (Kg) | 10 |
| $m_T$ | Mass of the torso (Kg) | $\frac{2}{3}m$ |

https://doi.org/10.3311/ECCOMASMBD2021-116

| | | |
|---|---|---|
| $m_H$ | Mass of the hip (Kg) | $\frac{1}{3}m$ |
| $L$ | Distance from hip to the center of mass of the torso (m) | 0.46 |
| $R$ | Nominal Leg Length (m) | 1 |
| $g$ | Gravitational acceleration (m/s) | 9.81 |

## 3. OPTIMIZATION AND SIMULATION RESULTS

During human locomotion, the body consumes energy to perform work. Earlier studies tried to link the metabolic requirements of walking and running to the positive mechanical power required to raise and accelerate the body's center of mass and accelerate the limbs relative to the center of mass in animals and humans [15]. Metabolic cost of transport is the metabolic energy required to move a unit body weight or mass a unit distance. Given a specific step size *d* and if the biped starts its step with the nominal leg length *R+q (1) =R*; we search for the control approach that gives the minimum cost of transport that is

$$J=\sum_{k=1}^{N} h\frac{\left|F_k(t)(\frac{\Delta q_k}{h})\right|+\left|\tau_k(t)(\frac{\Delta\theta_{1k}}{h}-\frac{\Delta\theta_{2k}}{h})\right|}{2mgd}. \tag{13}$$

Subject to dynamics constraints of the biped and satisfying periodicity constraints of the gait:

- The torso starts and ends the step with the same position and velocity.

$$\theta_2(N+1)=\theta_2(1), \tag{14}$$

$$\frac{\theta_2(N+1)-\theta_2(N)}{h}=\frac{\theta_2(2)-\theta_2(1)}{h}. \tag{15}$$

- The hip starts and ends the step with the same velocity in both X and Y directions.

$$\begin{aligned}&(R+q(N+1))\cos(\theta_1(N+1))(\frac{\theta_1(N+1)-\theta_1(N)}{h})+(\frac{q(N+1)-q(N)}{h})\sin(\theta_1(N+1))\\&=(R+q(1))\cos(\theta_1(1))(\frac{\theta_1(2)-\theta_1(1)}{h})+(\frac{q(2)-q(1)}{h})\sin(\theta_1(1)),\end{aligned} \tag{16}$$

$$\begin{aligned}&-(R+q(N+1))\sin(\theta_1(N+1))(\frac{\theta_1(N+1)-\theta_1(N)}{h})+(\frac{q(N+1)-q(N)}{h})\cos(\theta_1(N+1))\\&=(R+q(1))\sin(\theta_1(1))(\frac{\theta_1(2)-\theta_1(1)}{h})+(\frac{q(2)-q(1)}{h})\cos(\theta_1(1)).\end{aligned} \tag{17}$$

- The hip starts and ends the step with the same position in Y direction.

$$(R+q(N+1))\cos(\theta_1(N+1))=(R+q(1))\cos(\theta_1(1)). \tag{18}$$

- The difference between the final and initial positions of the hip is the step length d.

$$d=(R+q(N+1))\sin(\theta_1(N+1))-(R+q(1))\sin(\theta_1(1)). \tag{19}$$

In addition to the pervious constraints, we represent the flexion and extension of knee and ankle joints with a maximum variation of 10% of the nominal length of the leg [16].

$$1-MaxExt<q<1+MaxExt. \tag{20}$$

Where, *MaxExt* is the maximum Extension of the length.

The optimization procedure was run with different initial conditions to search for the optimal solutions as we vary the desired step size *d* and biped speed *v*. For each set of these two parameters, the optimizer converges to a distinctive result (see sections 3.1 and 3.2) that

describes the optimal gait.

### 3.1. Walking

Humans tend to walk at low speed and the walking gait can be identified from the profile of GRF (Ground Reaction Force) of the gait. Fig. 2 shows the gait pattern for 0.6 m step size with velocity of 1.566 m/s. The optimal gait for these parameters, based on the minimum cost of transport, is walking. The profile of normal GRF has two symmetric peaks that represent two phases of gait cycle, the heel strike and push off. These two phases occur at the beginning and the end of gait cycle [17].

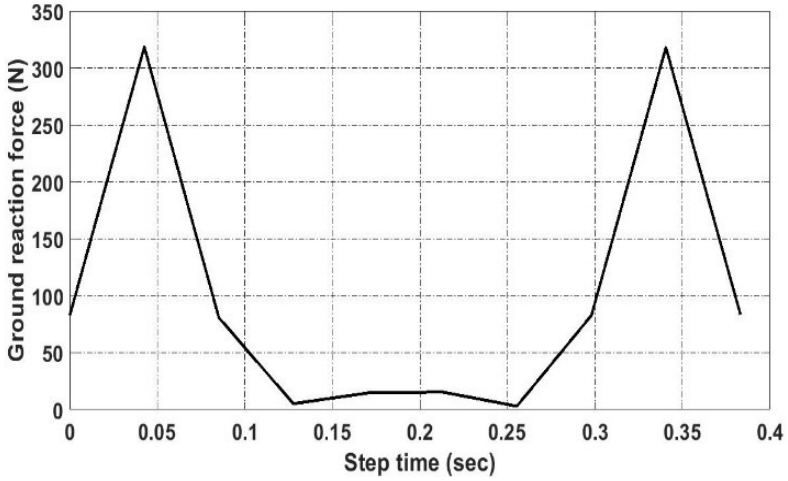


**Figure 2.** Ground Reaction Force (GRF) of walking

In walking, the torso movement in sagittal plane exhibited one full oscillation from backward to forward position, or the other way around, during a stance phase as shown in Fig. 3. At touch down of one foot, the torso moves in the direction of the same side and reached an extreme position during the period of a single support. Experimentally, this pattern of oscillation of torso angle is found to be approximately asymmetric [18]. Since the motion of the torso during walking is found to be very small, the oscillations are difficult to observe because of its small amplitudes [18].

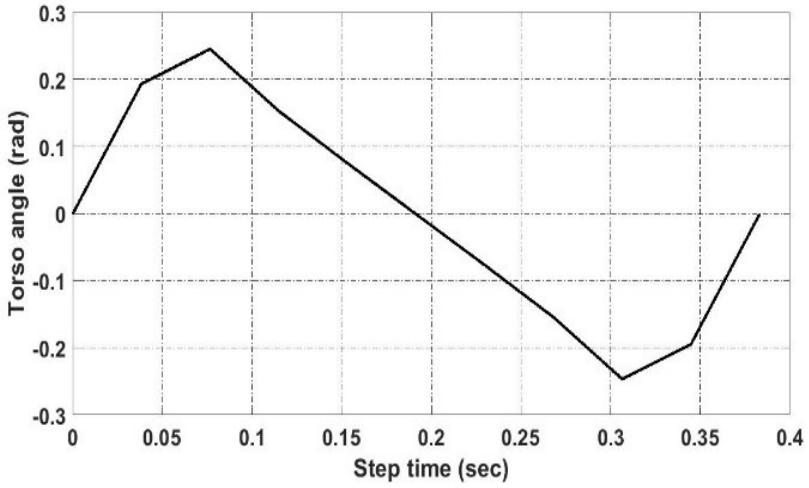


**Figure 3.** Torso angle during walking

Fig. 4 shows that as the step size increases, the angular displacement of the torso for the biped, peak-to-peak, also increases. For human as reported in [19], this increment in step size causes an

https://doi.org/10.3311/ECCOMASMBD2021-116

increment in the range of motion of body segments and joints, which include the torso as well.

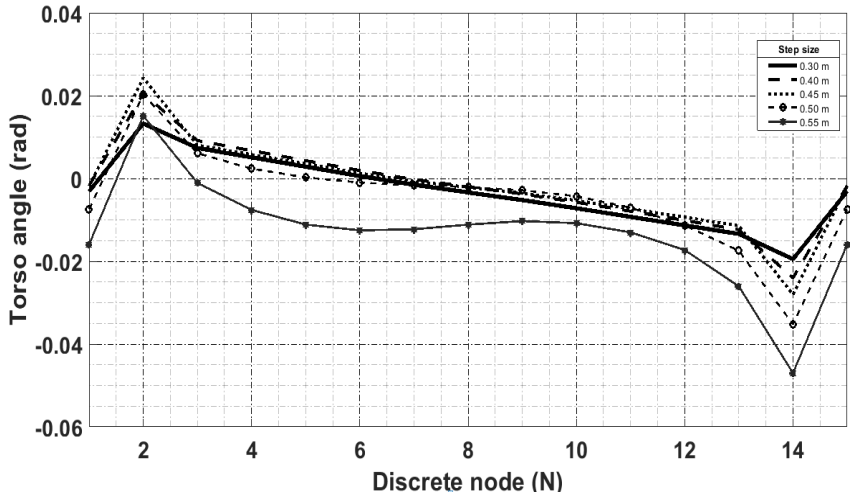


**Figure 4.** Oscillation of torso at different walking step sizes

Moreover, as the speed of walking increases, the amount of torso angular displacement decreases as shown in Fig. 5. This phenomenon is mainly attributed due to the walking speed, as it increases; it leads to an increase in the range of motion of the lower extremity joints to decrease the vertical shift in the body center of gravity, which is located in the torso [20]. The body behaves in this way in order to minimize the cost of transport by minimizing the movement of the center of gravity [15].

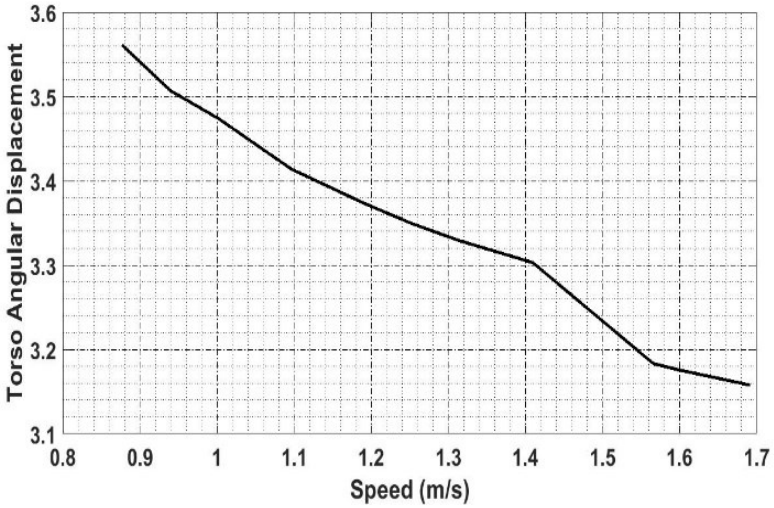


**Figure 5.** Angular Displacement of torso at different walking speed

### 3.2. Running

In legged locomotion, for a human to move with higher speed they must contract their muscles faster in order to move their limbs more quickly and reduce the amount of time that the feet are in contact with the ground. This process requires more metabolic energy. The optimal gait for high values of speed is impulsive run gait. In this gait, the biped express a high value and impulse of ground reaction force that represents the small stance phase with the start of the step. After this high impulse force, the profile of ground reaction force shows a zero force until the end of the step that represents the flight phase. This high impulse simulates the fast and strong interaction of the foot with the ground. Fig. 6 shows the GRF for impulsive run gait for the case of speed V = 7 m/s and step length D = 0.2 m.

https://doi.org/10.3311/ECCOMASMBD2021-116

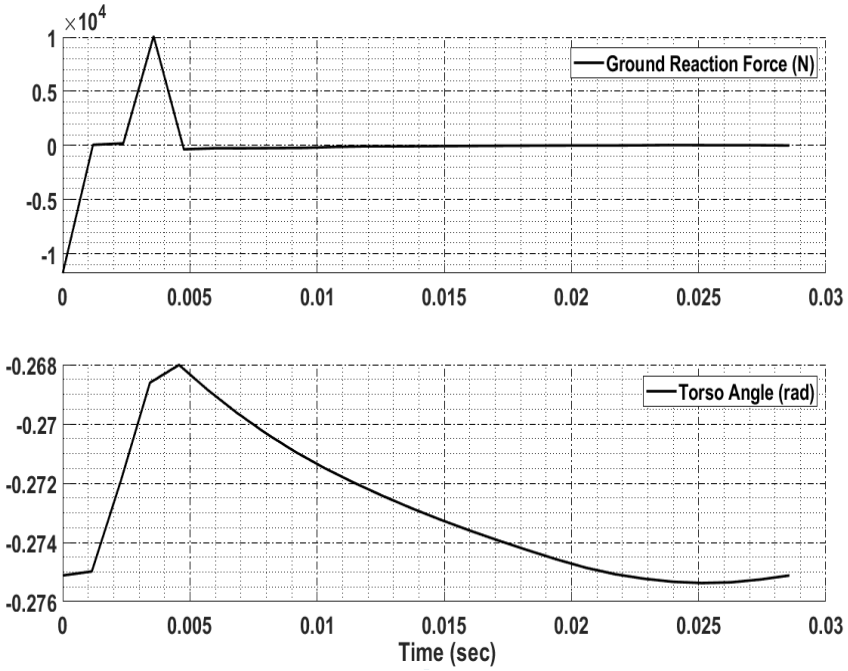


**Figure 6.** Ground reaction force and torso angle at high running speed (7 m/s)

Between every two impulsive stance phases, there is a flight phase. In this flight phase, the two legs are off the ground and the body flies in the air, so the ground reaction force is zero in this case [21]. During impulsive run, the body performs negative work to reduce the reaction force to zero in the flight phase and then performs positive work to increase the reaction force again in the next stance phase. In running with low speed, the foot contact with the ground is observed when the torso is almost at its most forward position. However, in running with high speed (e.g., 7 m/s), the touchdown of the foot occurred when the torso is in the peak of the backward position and it is just started to lean forward [18] as shown in Fig. 6.

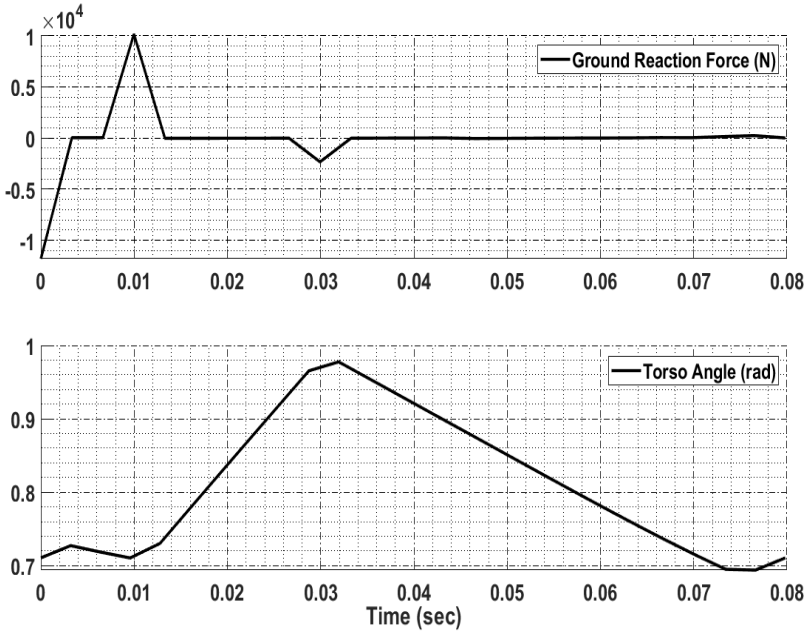


**Figure 7.** Ground reaction force and torso angle at low running speed (2.5 m/s)

Fig. 8 shows a reduction in the angular displacement of the torso as the speed increases for the

aim of minimizing the cost of transport by minimizing the movement of the center of gravity.

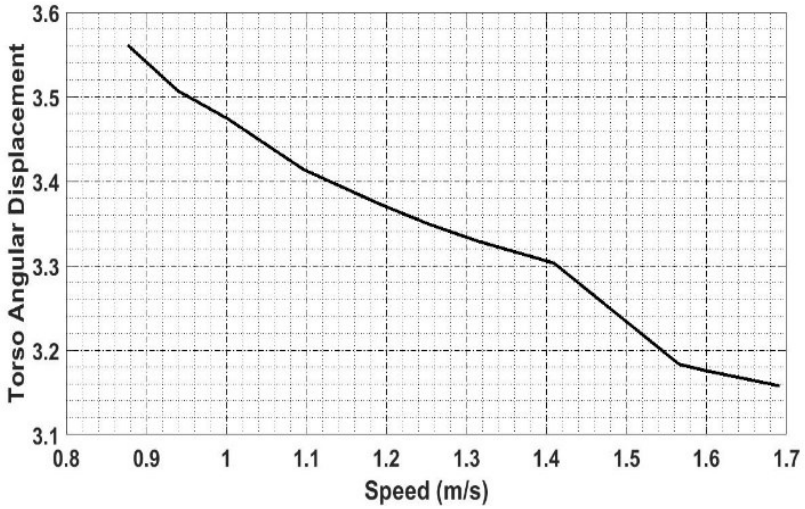


**Figure 8.** Angular displacement of torso at different running speed

## 4. CONCLUSIONS

Although the proposed model is simple in terms of the involved joints, however, both gait optimization and the biped were able to simulate various features of the human locomotion. The model was able to show the normal profile of the ground reaction force for both running and walking including the oscillation of the torso during both types of gaits. Moreover, the simulation results show that the movement of torso changes with changing the step size and walking speed. Increasing speed of either walking or running tends to reduce the total movement of the torso in the sagittal plane. Studies have shown that this reduction is a result of optimizing the energy required to walk or run. The simulation results showed that the initial position of the torso in running differs as the speed change and the trajectory of the torso changes.

## ACKNOWLEDGMENTS

The authors would like to thank Sultan Qaboos University for their financial support of this project.

## REFERENCES

[1] Morita S, Fujii H, Kobiki T, Minami S, Ohtsuka T. Gait generation method for a compass type walking machine using dynamical symmetry, 2004 IEEE/RSJ International Conference on Intelligent Robots and Systems (IROS)(IEEE Cat. No. 04CH37566) 2004 Oct (Vol. 3, pp. 2825-2830). IEEE.

[2] Srinivasan, M., 2006. Why Walk and Run: Energetic Costs and Energetic Optimality in Simple Mechanics-Based Models of a Bipedal Animal, New York: Cornell University.

[3] Kai T, Shintani T. A discrete mechanics approach to gait generation on periodically unlevel grounds for the compass-type biped robot. International Journal of Advanced Research in Artificial Intelligence. 2013 Sep;2(9):43-51.

[4] Sun, Z., Tian, Y., Li, H. and Wang, J., 2016. A superlinear convergence feasible sequential quadratic programming algorithm for bipedal dynamic walking robot via discrete mechanics and optimal control. Optimal Control Applications and Methods, 37(6), pp.1139-1161.

[5] Han, S.P., 1977. A globally convergent method for nonlinear programming. *Journal of optimization theory and applications*, *22*(3), pp.297-309.

[6] Izmailov, A.F. and Solodov, M.V., 2010. A truncated SQP method based on inexact interior-point solutions of subproblems. *SIAM Journal on Optimization*, *20*(5), pp.2584-2613.

[7] Abdel-Malek, K. & Arora, J. S., 2013. Human Motion Simulation Predictive Dynamics.

[8] Marrero, J.C., de Diego, D.M. and Martínez, E., 2006. Discrete Lagrangian and Hamiltonian mechanics on Lie groupoids. *Nonlinearity*, *19*(6), p.1313.

[9] West, M., 2004. Variational integrators (Doctoral dissertation, California Institute of Technology).

[10]Sharma, B.L., 2013. A Glimpse of Discrete Mechanics.

[11]Lew, A., Marsden, J.E., Ortiz, M. and West, M., 2004. An overview of variational integrators.

[12]Kraus, M. (2013). "Variational integrators in plasma physics." arXiv preprint arXiv:1307.5665.

[13]Schultz, J., et al. (2015). Trajectory optimization in discrete mechanics. Differential-Geometric Methods in Computational Multibody System Dynamics, Citeseer.

[14]Perry, J., 1992. *Gait Analysis: Normal Pathological Functions.* United States of America: SLACK Incorporated.

[15]Farris, D. J. & Sawicki, G., 2011. The Mechanics and Energetics of Human Walking and Running: a Joint Level Perspective. Journal of The Royal Society Interface, 25 May, pp. 110-118.

[16]AlYahmedi, A. & Sayari, M., 2014. Efficient Walking Of A Simple Biped With a Torso. Qatar, Middle East Conference on Biomedical Engineering (MECBME), pp. pp. 382-384.

[17]Whittle, M., 2007. Gait analysis, an introduction. USA: Oxford Orthopaedic Engineering Center, ELSEVIER.

[18]Thorstensson AL, Nilsson J, Carlson H, ZOMLEFER MR. Trunk movements in human locomotion. Acta Physiologica Scandinavica. 1984 May;121(1):9-22.

[19]Whitcome, K.K., Miller, E.E. and Burns, J.L., 2017. Pelvic rotation effect on human stride length: Releasing the constraint of obstetric selection. The Anatomical Record, 300(4), pp.752-763.

[20]Dugan, S.A. and Bhat, K.P., 2005. Biomechanics and analysis of running gait. Physical Medicine and Rehabilitation Clinics, 16(3), pp.603-621.

[21]Tongen, A. and Wunderlich, R.E., 2010. Biomechanics of running and walking. Mathematics and Sports, 43, pp.1-12.

https://doi.org/10.3311/ECCOMASMBD2021-245



# Kinematic Analysis of Planar Biomechanical Models using Mixed Coordinates

**Ivo Roupa**[1], **Sérgio Gonçalves**[1], **Miguel Tavares da Silva**[1]

[1]IDMEC - Instituto de Engenharia Mecânica
Instituto Superior Técnico, Universidade de Lisboa
Av. Rovisco Pais, Nº 1, 1049-001, Lisboa, Portugal
[ivo.roupa, sergio.goncalves, miguelsilva]@tecnico.ulisboa.pt

## ABSTRACT

Inverse Kinematics Analysis (IKA) is a powerful tool to study mechanical and biological systems, since it can be used to adjust the position and orientation of each segment of the model to the experimental data, enabling to achieve reliable and consistent model positions. Optimization-based methods have been successfully applied to perform IKA in intricate biomechanical systems. However, these methods tend to be more complex requiring more computational power and CPU times. This work presents an alternative methodology based on the use of Fully Cartesian Coordinates (FCC) and Mixed Coordinates (MC), alongside with a weighted least square approach to solve the IKA problem. The proposed methodology was applied in the study of a gait movement for a planar full body biomechanical model. The Root Mean Square Error (RMSE) between the experimental and computed positions was calculated both for the proposed method and for a forward kinematic analysis (FKA) carried out with pre-calculated angular drivers, resulting in smaller average differences in the former case (IKA: 0.018 m FKA: 0.019 m). Based on the obtained results it is possible to conclude that the proposed methodology is an accurate, efficient, and reliable approach to perform the IKA of biomechanical models, assuring the kinematic consistency between experimental data and the biomechanical model, and, at the same time, avoiding the usual drawbacks of the use of angular drivers or complex optimization techniques.

**Keywords:** Inverse Kinematics, Fully Cartesian Coordinates, Mixed Coordinates, Least Square Approach.

## 1. INTRODUCTION

Kinematic analysis (KA) is a powerful tool used in the study of biomechanical systems, since it allows for the computation of the orientation of the model segments, trajectory of specific points, angular displacement of joints, among other variables of interest. Two approaches can be used to perform the kinematic analysis of multibody systems, namely, forward kinematics (FK) or inverse kinematics (IK). In the first case, the model is guided using linear and angular drivers calculated in a previous step. Afterwards, the consistent generalized coordinates are obtained by imposing the kinematic constraints that define the model. On the other hand, in IK the position and orientation of each segment is computed by minimizing the difference between the experimental data and a set of points belonging to the model, namely the coordinates of the system or other points of interest. This procedure allows for the fitting of the computational model to the experimental data.

In biomechanical models, FK should be applied with caution due to experimental errors associated to the measurement, in particular soft tissue artifacts (STA) [1]. The STA refers to the motion of the markers on the surface of the body with respect to the underlying bones due to inertial effects, skin deformation and sliding, gravity and muscle contraction [2]. Moreover, STA is task- and subject- dependent, which makes standard filtering techniques ineffective [1]–[3].

https://doi.org/10.3311/ECCOMASMBD2021-245

Andersen et al. (2009) showed that the use of methodologies to minimize the errors between experimental markers and model points result in significant differences in the kinematic outcomes when compared with standard methods. On its turn, these differences can lead to large errors and inconsistencies during dynamic analysis [3]. Consequently, a method that enables to adjust the model to the output of the system in study is of particular interest for the biomechanics area, since it can minimize the errors associated to the experimental acquisition of anatomical points that constitute the biomechanical model. To address this issue, several methods have been proposed, being the most common based on optimization techniques [4].

In this work, a new approach, based exclusively on kinematic constraints and least-square minimization, is proposed to perform the KA of biomechanical systems. The methodology considers the use of angular coordinates to model the kinematic drivers of the system. These coordinates are referred to as 'mixed coordinates' and complement the set generalized coordinates used by the Fully Cartesian Coordinates (FCC) formulation adopted [5]. This method enables to perform an IK analysis and to determine simultaneously the angular drivers of the model. It allows also for the minimization of the error between experimental and computational points, ensuring a better fit of the model to the experimental data.

In order to assess its applicability and reliability, the MC method was applied in the KA of a gait movement for a planar biomechanical model. The results were posteriorly compared with the ones obtained using FK with angular drivers and with the experimental data.

## 2. METHODS

### 2.1. Fully Cartesian Coordinates

Fully Cartesian Coordinates are a development of Natural Coordinates [4] proposed in [4]–[7] They inherit their two major characteristics, i.e., multibody systems are still described using only the Cartesian coordinates of points and unit vectors, and the kinematic constraint equations are quadratic or linear, thus generating linear or constant contributions to the Jacobian matrix. However, in contrast to the Natural Coordinates formulation, where each rigid body might share points with its adjacent bodies, in FCC each rigid body is defined independently. As so, when applied in planar models, four generalized coordinates are required in its definition, namely the Cartesian coordinates of a point located at its center of mass (CoM) and the Cartesian coordinates of a unit vector representative of its orientation. A detailed description of the FCC formulation can be consulted in [5], [8].

### 2.2. Mixed Coordinates

Within the scope of the experimental analysis of human movement, the traditional KA resorts on the use of experimental trajectories/orientations measured using markers/sensors placed on specific points of the subject in analysis. Since these sensors can move with respect to the anatomical landmarks they refer, non-consistent positions can arise from the KA. MC methodology allows for the minimization of these errors, enabling to determine a position consistent with the defined model and experimental data.

The MC formulation is defined as a combination of FCC with generalized angular coordinates. These coordinates represent the angular degrees-of-freedom (DOFs) of the kinematic pairs of the model, being treated also as generalized coordinates of the system (**q**). For a general rigid body, the extended generalized coordinates' vector becomes:

$$\mathbf{q}_i = \{\mathbf{r}_{i_x} \quad \mathbf{r}_{i_y} \quad \mathbf{u}_{i_x} \quad \mathbf{u}_{i_y} \quad \theta_i\}^T \tag{1}$$

where $\mathbf{q}_i$ is the vector of generalized coordinates of body $i$, $\mathbf{r}$ is a vector that contains the cartesian coordinates of the center of mass of body $i$, $\mathbf{u}$ is a unit vector that defines body $i$ orientation and $\theta_i$ is the angular driver between vector $\mathbf{u}$ from body $i$ and a unit vector belonging to other rigid body (ground body included).

The introduction of MC coordinates leads to an augmented vector of generalized coordinates of the system, since a new angular coordinate is appended, per rigid body, to the already existent vector of generalized coordinates. Therefore, additional kinematic constraints need to be added to the MBS to solve the IK problem. These will be introduced in the form of trajectory

constraints that map the experimental coordinates of points of interest of the model, such are the markers coordinates, to the rigid body local reference frame, e.g., for a given point *P* belonging to rigid body *i*, one have:

$$\mathbf{\Phi} = \mathbf{C}_{P_i}\mathbf{q}_i - \mathbf{r}_P{}^*(t) = \mathbf{0} \tag{2}$$

where $\mathbf{C}_{\boldsymbol{P_i}}$ is a constant transformation matrix that relates the global coordinates of point *P*, obtained experimentally and denoted by $\mathbf{r}^*_{\boldsymbol{P}}(\boldsymbol{t})$, with the generalized coordinates of body *i* [5].

The inclusion of trajectory constraints is of particular relevance on the analysis of biomechanical MBS, since they can relate directly with position of the joints or the trajectory of the markers used in the subject. Moreover, the methodology enables to obtain directly the generalized coordinates of the system, needed to perform the dynamic analysis, and the kinematic angular drivers. This issue is particularly useful, since if the biomechanical model is defined according with the ISB recommendations [9], [10], the methodology provides directly the joints angles, which are one of the variables usually evaluated during the biomechanical analysis.

An important aspect of the MC methodology is that it only requires surgical changes in the structure of the angular driver constraint equations of the FCC formulation to become implemented. More precisely, instead of using angular drivers as inputs to control the DOFs of the system, the angular constraints will now explicitly depend on the newly added angular generalized coordinates. This action will result in an additional contribution to the Jacobian matrix per mix coordinate, i.e. the partial derivative of the angular driver constraint equation with respect to the mix coordinate $\boldsymbol{\theta}$, as well as an additional term in the contribution to the $\boldsymbol{\gamma}$ vector of these constraints (see Table 1).

**Table 1.** Constraint equations (line 1), contributions to Jacobian matrix (line 2) and to the RHS of the velocity and acceleration vectors (lines 3 and 4) for two angular constraints (dot and cross product) using MC formulation (note that $\tilde{\mathbf{u}}$ is a vector orthogonal to $\mathbf{u}$, such that $\mathbf{u} \times \mathbf{v} = \tilde{\mathbf{u}}^T\mathbf{v}$)

| **Angular Driver** | | |
|---|---|---|
| | ***Dot Product (DP)*** | ***Cross Product (CP)*** |
| $\Phi(\mathbf{q})$ | $\mathbf{u}^T\mathbf{v} - \cos(\theta)$ | $\tilde{\mathbf{u}}^T\mathbf{v} - \sin(\theta)$ |
| $\mathbf{\Phi_q}$ | $[\mathbf{v}^T \quad \mathbf{u}^T \quad \sin(\theta)]$ | $[-\tilde{\mathbf{v}}^T \quad \tilde{\mathbf{u}}^T \quad -\cos(\theta)\,]$ |
| $\nu$ | 0 | 0 |
| $\gamma$ | $-2\dot{\mathbf{u}}^T\dot{\mathbf{v}} - \cos(\theta)\dot{\theta}^2$ | $-2\dot{\tilde{\mathbf{u}}}^T\dot{\mathbf{v}} - sin(\theta)\dot{\theta}^2$ |

The addition of the trajectory constraints results in an overconstrained system, as each relation contributes with two equations to the kinematic constraints vector $\mathbf{\Phi}$. Different methods can be applied to solve the overconstrained system of equations. The one followed in this work considers the use of a weighted least squares approach (WLS) in tandem with the Newton-Raphson method (NRM). This approach has the main advantage of solving directly the IK problem, without requiring the use of optimization algorithms, such as the one presented in the work of Andersen et al. [11]:

$$\hat{\mathbf{q}}_{\text{WLS}} = (\mathbf{\Phi}_\mathbf{q}^T\mathbf{Z}\mathbf{\Phi}_\mathbf{q}\,)^{-1}\mathbf{\Phi}_\mathbf{q}^T\mathbf{Z}\,\mathbf{\Phi} \tag{3}$$

where $\mathbf{\Phi_q}$ is the Jacobian matrix of the system, $\mathbf{Z}$ is the weights matrix and $\mathbf{\Phi}$ is the vector of kinematic constraints.

The use of a weighted approach presents also the advantage of allowing for the definition of different weights for each kinematic constraint. When applied from a biomechanics perspective, the definition of different weights for the trajectory constraints can be used to tune the model to the experimental data, forcing the analysis to track the experimental markers with more relevance or those that are less prone to experimental errors. In a similar way, points characterized by higher levels of STA can be defined with lower weights, being the position of the model to these markers adjusted by the fulfillment of the remaining kinematic constraints which are related with the definition of the topology of the biomechanical model.

### 2.3. Implementation of the FCC Formulation with Mixed Coordinates

The FCC formulation was implemented in an in-house software [5] developed using Python language (v3.7.10) [12]. To solve the IK analysis, the iterative NRM alongside with the WLS routines implemented in the *numpy* library (*numpy.linalg.lstsq*) was used. To initially test the method, the nonzero elements of the positive-definite weighting diagonal matrix **W** were set to 1.0 as presented in the work of Aguiar et al [13].

The performance of the Mixed Coordinates formulation was evaluated by applying it in the KA of a planar full body biomechanical model. The RMSE between the cartesian coordinates of the experimental points, representing the anatomical joints and other distal points, and the KA outcomes was computed for each joint. In order to explore the computational differences between methods, the same analysis was performed for the results obtained using a FK analysis with angular drivers. Moreover, the time required to perform the analysis and the number of iterations of the NRM were also analyzed. Finally, the model joint angles were statistically compared with the values presented in Winter [14] by calculating the intraclass correlation coefficient (ICC).

### 2.4. Experimental Data Acquisition

The FCC formulation with Mixed Coordinates proposed previously was applied to the study of the gait patterns of one healthy volunteer to evaluate its performance. An informed consent with a detailed explanation of the experimental protocol was signed by the volunteer and the subject's participation on the study was dependent on the acceptance of such informed consent.

Kinematic data was acquired using an optoelectronic motion capture system composed by 14 Infrared ProReflex 1000 cameras (Qualisys©, Göteborg, Sweden), with an acquisition frame rate of 100 Hz. Prior to data acquisition, the subject performed an adaptation period to the experimental setup. Afterwards, a 15 seconds static trial was performed to collect the most relevant kinematical model parameters, followed by three gait cycles.

A biomechanical model with 12 segments, based on the one presented in Pamiés et al [15], was implemented. A marker set protocol composed by 68 markers was designed to allow for the driving of all the DOFs of the model. The elbow, wrist, knee, and ankle joint centers were computed as the midpoint of the retro reflective markers placed on lateral and medial bony landmarks of the respective joints. The hip joint center was computed using the regression method proposed by Davis et al. [16]. The trajectories of the elbow and knee markers were reconstructed using clusters of markers placed on the thigh and upper arm.

The coordinates of the markers were filtered using a $2^{nd}$ order low-pass Butterworth filter with a cut-off frequency of 6Hz. All necessary calculations were performed using in-house scripts developed in MATLAB (MathWorks©, Natick, MA) and Python 3.7 [12].

## 3. RESULTS

No problems were found, related with the modelling procedure and the convergence of the method, during the IKA of the planar biomechanical model. The average errors associated with the position of the joints were similar in the IK analysis with both formulations. On average, both methodologies present identical accuracy. However, the maximum error is higher when using FKA with angular drivers (FCC).

https://doi.org/10.3311/ECCOMASMBD2021-245

A propagation of errors along the gait cycle was observed when using the second method, in particular in the more distal points of the kinematic chains, while the method with MC coordinates presented a more consistent response with the experimental data (see Fig. 1).

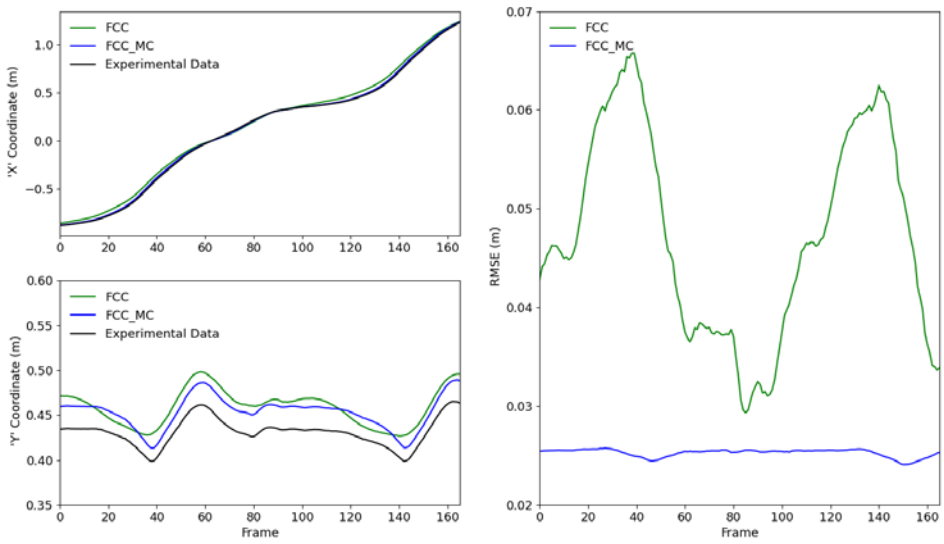


**Figure 1.** Representation of experimental and computed right knee joint center trajectory throughout the gait trial (upper and lower left figures) and respective Root Mean Square (RMSE) (right figure).

**Table 1.** Average Root Mean Square Error (RMSE) between the experimental coordinates of each joint center and its estimation based on the consistent generalized coordinates of the model

| | RMSE (m) | | | | | | | | | | | | |
|---|---|---|---|---|---|---|---|---|---|---|---|---|---|
| | Neck | Shoulder | | Elbow | | Hip | | Knee | | Ankle | | Average | Max |
| Formulation | - | R | L | R | L | R | L | R | L | R | L | | |
| FCC | 0.0 | 0.009 | 0.037 | 0.011 | 0.008 | 0.012 | 0.011 | 0.032 | 0.028 | 0.026 | 0.028 | 0.018 | 0.037 |
| FCC + MC | 0.0 | 0.015 | 0.023 | 0.017 | 0.016 | 0.026 | 0.026 | 0.025 | 0.024 | 0.021 | 0.023 | 0.019 | 0.026 |

**Table 2.** Maximum Root Mean Square Error (RMSE) between the experimental coordinates of each joint center and its estimation based on the consistent generalized coordinates of the model

| | RMSE (m) | | | | | | | | | | | | |
|---|---|---|---|---|---|---|---|---|---|---|---|---|---|
| | Neck | Shoulder | | Elbow | | Hip | | Knee | | Ankle | | Average | Max |
| Formulation | - | R | L | R | L | R | L | R | L | R | L | | |
| FCC | 0.0 | 0.013 | 0.042 | 0.027 | 0.023 | 0.034 | 0.030 | 0.066 | 0.053 | 0.059 | 0.052 | 0.036 | 0.066 |
| FCC + MC | 0.0 | 0.015 | 0.024 | 0.017 | 0.017 | 0.027 | 0.026 | 0.026 | 0.024 | 0.023 | 0.032 | 0.021 | 0.032 |

Regarding the CPU times, the FKA with FCC took 4.49s and approximately 4 iterations per time frame to obtain the solution using the NRM. On the other hand, the IKA with MC required 12.95s and an average of 8 iterations. Although both methods use a least square approach to obtain a solution to solve the problem, these differences could be explained by the higher dimension of the Jacobian matrix in the MC formulation (FK: $\mathbf{\Phi_{q[58x48]}}$, IK: $\mathbf{\Phi_{q[82x60]}}$) and the overconstrained nature of that methodology.

## 4. DISCUSSION

In this work, a methodology based only on kinematic constraints and least square minimization, is presented to compute the IKA of biomechanical systems. When compared to traditional IK techniques, the FCC + MC methodology presents some innovative aspects, such as the simultaneous computation of the generalized coordinates and angular drivers, while assuring the kinematic consistency of the model. This procedure can be achieve without the need of a preprocessing step to obtain a kinematic consistent model from inconsistent experimental data [17].

This feature results from the introduction of trajectory driver equations and angular coordinates in the vectors of kinematic constraints and generalized coordinates of the system. The trajectory driver equations map the experimental coordinates of the points of interest with the associated trajectories and orientations of the rigid segments of the biomechanical model. On its turn, the angular generalized coordinates will represent the angular DOFs of the kinematic pairs of the model, which will be calculated during the IKA. These modifications in the number of generalized coordinates of the system lead to an overdetermined system, which requires a least square approach to find a solution during the IKA. To this purpose an WLS approach was used following the works of Aguiar et al [13], Mantovani et al [18] and Lathrop-Lambach et al. [19]. This method enables to solve directly the linear kinematic constraints, while it simultaneously minimizes the trajectory equations, avoiding the need for complex optimization algorithms.

In the present study, one trajectory constraint was used per joint of the model. However, the method can be easily adapted to consider more points, enabling to fit the model to a cloud of points of interest. The points can also be defined such as the biomechanical model has a direct relation with acquisition protocol used during the experimental trials.

The accuracy of the kinematic reconstruction using the FCC with MC is similar however the RMSE value along the cycle is more stable than when only FCC are used. This is the direct result of the minimization of the distance between the model points and experimental data introduced by the method. These findings are confirmed by the lower RMSE values. A maximum error of 0.066 m was found for the knee joint, however, on average, all errors are inferior to the error values reported by Ausejo et al [20] as acceptable in motion reconstruction (5 to 25 mm).

From a computational point of view, the augmentation of the vector of generalized coordinates due to the inclusion of the angular coordinates and the increase of the number of kinematic constraints results in a complex problem to solve. On average an increase of the number of iterations and time spent per time step was observed in the IKA. However, it is important to note that the processing time spent to obtain the initial angular drivers in the FKA case was not included, while in the proposed IKA approach the reported time already considered all the required steps to perform the kinematic analysis and obtain the joint angles and generalized coordinates of the system. Moreover, despite this increase in the complexity of the problem to solve, the number of iterations per time frame is still reduced, attesting the computational efficiency of the method.

STA is one of the of the most common sources of errors in motion analysis [21], [22]. These inaccuracies can lead to significant errors and inconsistencies during the computation of the kinematic outcomes and, consequently, also on the dynamic results [23]–[25]. To overcome this problem, several methods have been proposed to reduce these experimental errors, being the most commons based on optimization techniques [26]. A different methodology is followed in this work, as only kinematic constraints and trajectory controls are applied. This approach enables to adjust the coordinates of the joints and other distal points simultaneously based on the minimization of distances between these and the equivalent experimental points and the kinematic constraints.

Besides reducing possible errors introduced by the STA, this adjustment of the experimental data to the biomechanical model enables to correct also errors introduced by the placement of markers on positions different from the ones defined in the begin of the analysis (e.g., fall of markers during the trial). Since the biomechanical model is defined using kinematic constraints based on measures acquired during the statical trial, errors in the placement of the markers will be partially corrected by the fulfilling of the kinematic constraints that define the rigid bodies and joints.

In addition, IKA avoids one of the main drawbacks of the typical FKA based on angular drivers, namely the propagation of errors along the kinematic chain, i.e., experimental errors will be passed continuously to the child bodies, resulting, in general, in higher distances between the experimental and model points in the distal joints.

From a modelling perspective, the use of the FCC with MC presents also other advantages, as the points used in the trajectory constraints can be defined such as they have direct relation with markers used on the common marker set protocols. Moreover, due to the simplicity of the FCC in the modelling of biomechanical models, the angular drivers can be defined to match the normal convention of the joint angles, computing them directly while solving the IKA. These characteristics are of particular relevance for the biomechanics community. By providing a methodology that computes simultaneously the joint angles and has a direct relation with the acquisition protocols, the pre-processing of the experimental data is simplified, facilitating its use.

Despite its promising results, the present study was based on a minimal dataset. Future studies with larger data samples should be carried out, as well as an extension to 3D models, to further validate the methodology.

## 5. CONCLUSIONS

This study presents a methodology to perform inverse kinematic analysis of multibody systems based on FCC with MC. This approach, based solely on kinematic constraints and a WLS method, allows for the determination of the consistent generalized coordinates, while simultaneously minimizing the error between the experimental and computed data.

In the presented case, the accuracy of the kinematic reconstruction using the FCC with MC is significantly higher than when only FCC are used, and therefore, it is possible to conclude that the proposed methodology provides an accurate, efficient, and reliable approach to perform kinematic analysis of human motion, avoiding the problems related with the use of kinematic drivers. Moreover, the IKA considering the FCC+MC formulation presents the advantage of computing the angular drivers that rule the system, without a pre-processing step.

## REFERENCES

[1] J. Fuller, L.-J. Liu, M. C. Murphy, and R. W. Mann, “A comparison of lower-extremity skeletal kinematics measured using skin- and pin-mounted markers,” *Hum. Mov. Sci.*, vol. 16, no. 2–3, pp. 219–242, Apr. 1997, doi: 10.1016/S0167-9457(96)00053-X.

[2] J. P. Holden, J. A. Orsini, K. L. Siegel, T. M. Kepple, L. H. Gerberc, and S. J. Stanhope, “Surface movement errors in shank kinematics and knee kinetics during gait ’,” vol. 5, pp. 217–227, 1997.

[3] M. S. Andersen, M. Damsgaard, B. MacWilliams, and J. Rasmussen, “A computationally efficient optimisation-based method for parameter identification of kinematically determinate and over-determinate biomechanical systems,” *Comput. Methods Biomech. Biomed. Engin.*, vol. 13, no. 2, pp. 171–83, Jan. 2010, doi: 10.1080/10255840903067080.

[4] G. Jalon and E. Bayo, *Kinematic and Dynamic Simulation of Multibody Systems: The Real-Time Challenge*. New York: Springer Verlag, 1993.

[5] I. Roupa, S. B. Gonçalves, and M. Tavares da Silva, “Dynamic Analysis of Planar Multibody Systems with Fully Cartesian Coordinates,” *Proceedings of International Conference on Multibody System Dynamics*. Lisbon, Portugal, June 24-28, 2018.

[6] M. T. Gameiro, P., Silva, “Modelação e Simulação Sistemática em Coordenadas Cartesianas Totais de Sistemas Multicorpo,” *Actas do Congresso de Métodos Numéricos em Engenharia*. Porto, Portugal, Junho 13-15, 2007.

[7] M. Silva and J. Ambrósio, “Nova Abordagem á Modelação de Sistemas de Corpos Múltiplos Utilizando Coordenadas Naturais,” *Actas do VII Congresso de Mecânica Aplicada e Computacional*. Évora, Portugal, Abril 14-16, 2003.

[8] P. Gameiro and M. Tavares da Silva, “A systematic approach to the simulation of multibody systems with natural coordinates,” *Actas da ECCOMAS Thematic Conference on Multibody Dynamics 2005*. Madrid, Spain, June 21–2. 2005.

[9] G. Wu *et al.*, “ISB recommendation on definitions of joint coordinate system of various joints for the reporting of human joint motion — Part I: Ankle, Hip, and Spine,” *J. Biomech.*, vol. 35, no. 4, pp. 543–548, Jun. 2002, doi: 10.1006/rtph.2002.1549.

[10] G. Wu *et al.*, “ISB recommendation on definitions of joint coordinate systems of various joints for the reporting of human joint motion - Part II: Shoulder, Elbow, Wrist and Hand,” *J. Biomech.*, vol. 38, no. 5, pp. 981–992, 2005, doi: 10.1016/j.jbiomech.2004.05.042.

[11] M. S. Andersen, M. Damsgaard, and J. Rasmussen, “Kinematic analysis of over-determinate biomechanical systems,” *Comput. Methods Biomech. Biomed. Engin.*, vol. 12, no. 4, pp. 371–384, 2009, doi: 10.1080/10255840802459412.

[12] G. Van Rossum and F. L. Drake, “Python & C API Reference Manual,” no. March, p. 151, 2006.

[13] L. Aguiar, C. Andrade, M. Branco, R. Santos-Rocha, F. Vieira, and A. Veloso, “Global optimization method applied to the kinematics of gait in pregnant women,” *J. Mech. Med. Biol.*, vol. 16, no. 6, 2016, doi: 10.1142/S0219519416500846.

[14] D. Winter, *The Biomechanics and Motor Control of Human Gait: Normal, Elderly and Pathological*, 2nd ed. Waterloo, Ontario, Canada: University of Waterloo, 1991.

[15] R. Pàmies-Vilà, J. M. Font-Llagunes, J. Cuadrado, and F. J. Alonso, “Analysis of different uncertainties in the inverse dynamic analysis of human gait,” *Mech. Mach. Theory*, vol. 58, no. January 2019, pp. 153–164, 2012, doi: 10.1016/j.mechmachtheory.2012.07.010.

[16] R. B. Davis, S. Ounpuu, D. Tyburski, and J. R. Gage, “A gait analysis data collection and reduction technique,” *Hum. Mov. Sci.*, vol. 10, no. 5, pp. 575–587, 1991, doi: 10.1016/0167-9457(91)90046-Z.

[17] M. Tavares da Silva, “Human Motion Analysis using Multibody Dynamics and Optimization Tools,” Universidade Técnica de Lisboa - Instituto Superior Técnico, 2003.

[18] G. Mantovani and M. Lamontagne, “How Different Marker Sets Affect Joint Angles in Inverse Kinematics Framework,” *J. Biomech. Eng.*, vol. 139, no. 4, 2017, doi: 10.1115/1.4034708.

[19] R. L. Lathrop-Lambach *et al.*, “Evidence for joint moment asymmetry in healthy populations during gait,” *Gait Posture*, vol. 40, no. 4, pp. 526–531, 2013, doi: 10.1016/j.gaitpost.2014.06.010.

[20] S. Ausejo, Á. Suescun, and J. Celigüeta, “An optimization method for overdetermined kinematic problems formulated with natural coordinates,” *Multibody Syst. Dyn.*, vol. 26, no. 4, pp. 397–410, 2011, doi: 10.1007/s11044-011-9263-x.

[21] A. Cappello, R. Stagni, S. Fantozzi, and A. Leardini, “Soft Tissue Artifact Compensation in Knee Kinematics by Double Anatomical Landmark Calibration : Performance of a Novel Method During Selected Motor Tasks,” vol. 52, no. 6, pp. 992–998, 2005.

[22] R. Stagni, S. Fantozzi, A. Cappello, and A. Leardini, “Quantification of soft tissue artefact in motion analysis by combining 3D fluoroscopy and stereophotogrammetry: a study on two subjects.,” *Clin. Biomech. (Bristol, Avon)*, vol. 20, no. 3, pp. 320–9, Mar. 2005, doi: 10.1016/j.clinbiomech.2004.11.012.

[23] V. Camomilla, A. Cereatti, A. G. Cutti, S. Fantozzi, R. Stagni, and G. Vannozzi, “Methodological factors affecting joint moments estimation in clinical gait analysis: A systematic review,” *Biomed. Eng. Online*, vol. 16, no. 1, pp. 1–27, 2017, doi: 10.1186/s12938-017-0396-x.

[24] M. P. T. Silva and J. A. C. Ambrósio, “Kinematic data consistency in the inverse dynamic analysis of biomechanical systems,” *Multibody Syst. Dyn.*, vol. 8, no. 2, pp. 219–239, 2002, doi: 10.1023/A:1019545530737.

[25] M. P. T. Silva and J. A. C. Ambrósio, “Sensitivity of the results produced by the inverse dynamic analysis of a human stride to perturbed input data,” *Gait Posture*, vol. 19, no. 1, pp. 35–49, 2004, doi: 10.1016/S0966-6362(03)00013-4.

[26] M. Begon, M. S. Andersen, and R. Dumas, “Multibody Kinematics Optimization for the Estimation of Upper and Lower Limb Human Joint Kinematics: A Systematized Methodological Review,” *J. Biomech. Eng.*, vol. 140, no. 3, 2018, doi: 10.1115/1.4038741.

https://doi.org/10.3311/ECCOMASMBD2021-235



# Optimization and Evaluation of Spinal Exoskeleton Design Concepts using Optimal Control

**Monika Harant**[1], **Matthias B. Näf**[2], **Katja Mombaur**[3]

[1] Mathematics for the Digital Factory
Fraunhofer Intitute for Industrial Mathematics
Fraunhofer-Platz 1, 67663 Kaiserslautern, Germany
monika.harant@itwm.fraunhofer.de

[2] Department of Mechanical Engineering
Vrije Universiteit Brussel
Pleinlaan 2, 1050 Brussels, Belgium
matthias.basil.naf@vub.be

[3] CERC Human-Centred Robotics and Machine Intelligence
University of Waterloo
200 University Avenue West, N2L 3G1 Waterloo, Canada
katja.mombaur@uwaterloo.ca

## ABSTRACT

Exoskeletons for the lower back are promising tools to support workers during heavy lifting tasks. Their development process faces several challenges. It is still not known which criteria the support must meet to prevent low-back pain and how users of different body stature and execution of lifting movements influence it. Thus, studying these factors needs an extensive testing on the human body and every considered design concept needs already a sophisticated prototype that subjects can wear for several hours. To overcome this issue, we propose a method using multibody dynamics and optimal control to optimize the design of an existing prototype (PO) as well as evaluate a new concept (DC) that incorporates motors at the hip joint. A dynamic model of the prototype with matching torque generation was developed, which also takes an approximation of possible misalignment into account. The human-robot interaction is simulated in an all-at-once approach that allows to calculate the muscle activity of the user required in addition to the exoskeleton support to reproduce recorded lifting motions. By minimizing the users' muscle activity, parameters describing the characteristics of the passive elements and, in case of DC, motor torque profiles are optimized. Compared to the initial setup, a significant improvement in exoskeletal support was achieved across all subjects in both cases while contact forces remained within prescribed limits to ensure a comfortable usage of the device. DC provides less support than PO but better control of the human-robot interaction.

**Keywords:** Optimal Control, Exoskeletons, Parameter Optimization, Multibody Dynamics, Biomechanics.

## 1 INTRODUCTION

Exoskeletons are receiving increasing attention not only in the medical field as a rehabilitation tool [1][2][3], but also in industry to improve working conditions [4][5][6]. Spinal exoskeletons are seen as a promising tool to assist workers with lifting tasks and reduce their muscle activity [5] [7], and thus their risk of low back pain. However, the development of wearable robots is challenging because the analysis of their effect on the human body as well as the assertion of a comfortable usage need an extensive testing of the device. This may take a long time and need a high number

https://doi.org/10.3311/ECCOMASMBD2021-235

of prototypes. Thus, it is desirable to use optimization techniques to accelerate and facilitate this process. In [8], a method is presented to optimize the support of a lower body exoskeleton while it is worn by subjects. This method is difficult to apply to spinal exoskeletons because the subjects would have to lift objects repeatedly over a long period of time while the robot applies high forces on them.

In this work, we illustrate an alternative approach by using multibody dynamics and optimal control to optimize the passive elements of an existing prototype [9] in simulation as well as evaluating a new design concept (DC) that incorporates motors at the hip joint. Both the human and the exoskeleton are simulated in an all-at-once approach that allows the calculation of forces applied by the exoskeleton and the muscle activity needed by the user to reproduce a recorded lifting motion. Previous work applied this method successfully to a simple generic exoskeleton [10][11]. In [12], preliminary results optimizing the passive elements of the same prototype are presented. In addition to the new design concept DC, which also includes motors, we extended the method of [12] by including an estimation of the exoskeleton's torque generation taking misalignment with respect to the user into account.

In Sec. 2, a brief overview of the experiments performed for the reference lifting motions and for the misalignment approximation of the state of the passive elements is given. Then the models of the user and the exoskeleton applied in the optimal control problem are described in Sec. 3. The optimal control problem itself is formulated in Sec. 4. The results of the optimization and a discussion in Sec. 5 and 6 conclude this paper.

## 2 EXPERIMENTS

Data of two different biomechanical experiments were used in this work. In the following, a short summary of both is presented.

### 2.1 Experiments for the Reference Lifting Motions

Lifting motions performed by 5 male subjects (age $21 - 36$ years, weight $60 - 82$ kg, height $1.70 - 1.82$ m) were recorded. For the optimization, we use stoop-lifts of a 10 kg box with handles that was picked up from a 0.3 m high pedestal placed directly in front of the subjects. Subjects were instructed on the general form of a stoop-lift but were advised to perform the motion in a way that is comfortable for them, i.e. bending the knees was allowed.

The kinematics (marker positions) were measured at 44 Hz by an active motion capture system with two cameras (Certus Northern Digital Inc., Canada). The position of the box was also recorded using two marker clusters. Ground reaction forces of the subject and of the box were recorded at 1000 Hz by two force plates (Kistler Instrumente GmbH, Suisse) and the forces between hands and box handles using uni-directional force sensors. During all trials, the muscle activity of the subjects was recorded using 12 EMG sensors.

For adjusting the models of the human actuation described in Sec. 3.1.3, it is useful to have an estimate of the maximum muscle activation observed during the recorded lifting motions. For this purpose, maximum voluntary contraction trials (MVC) were performed during the experiments with the aim to measure the EMG signal of the muscles when fully contracted. Two different MVC trials were used to measure the strength of the lumbar extensors and flexors as well as the hip extensors:

1. The subject stands on a force plate and performs a maximum effort deadlift against a fixed barbell.

2. The subject is restrained against an instrumented back rest using heavy Velcro straps and then having them extend, then flex their torso against the device.

For more information on this experiment, please refer to [11].

https://doi.org/10.3311/ECCOMASMBD2021-235

### 2.2 Experiments for the Alignment between User and Exoskeleton

Three young, healthy subjects (avg. age: 28 years, avg. height: 177 cm, avg. weight: 71.3 kg) performed a variety of tasks while wearing the prototype. We only consider the lifting tasks consisting of free lift, stoop lift, and squat lift. The tasks were performed with locked and unlocked misalignment mechanisms (three-revolute-joint-segment, and sliders, please refer to [9]). For our regression analysis described in Sec. 3.5, we only considered the recordings with unlocked configuration as this represents the standard behavior of the exoskeleton. Active markers were placed on the subject as well as the exoskeleton. Their positions were recorded using an active motion capture system with three cameras (Certus Optotrak, Northern Digital, Canada) at a frequency of 50 Hz. The markers for the exoskeleton were attached to the slider connected to the beams, the part of the pelvis module where the beams are connected to, the passive element at the hip joint and to the slider of the thigh interface. The state of the exoskeleton was additionally recorded using its on-board sensors at a frequency of 100 Hz. For further information, please refer to [13].

## 3 APPLIED MODELS

The recorded lifting motions used in the optimization are fairly symmetrical. This allows us to reduce the complexity of the system by modeling the human, exoskeleton, and box as symmetric rigid multibody systems in the sagittal plane (Fig. 1). First, a brief overview of the human model with muscle torque generators as joint actuators is given. Then the model of the exoskeleton prototype with its passive elements and the additional actuators for DC as well as the misalignment approximation is described.

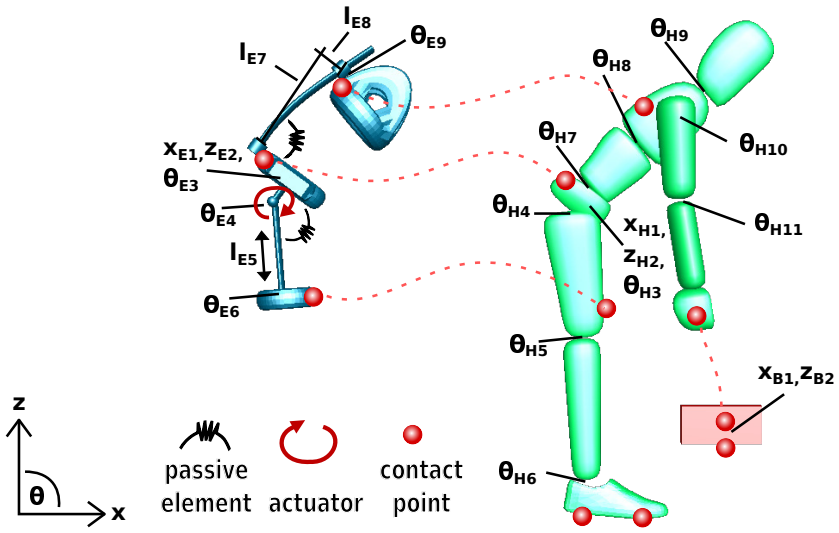


**Figure 1**. Modeled human, exoskeleton, and box with their respective degrees of freedom. The red dots show the locations where the box is connected to the ground and the human to the ground, the exoskeleton, and the box using contacts and loop closure constraints.

### 3.1 Modeling the Human with Box

The human model consists of 11 degrees of freedom (DoF) (Fig. 1). Both arms and legs are lumped together and the trunk is divided into three segments. Every human model was adjusted to represent the properties of each subject of the used motion capture recordings. The dynamic properties (segment mass, center of mass and inertia tensors) are estimated via regression equations proposed by de Leva [14] which are scaled by the height and weight of the person. In addition, the segment lengths of each subject were determined and the dynamic properties were linearly scaled accordingly.

https://doi.org/10.3311/ECCOMASMBD2021-235

### 3.1.1 Kinematic Fitting

For the optimization, the recorded motions have to be transferred onto the models to obtain the respective joint positions. Each model segment was equipped with multiple virtual markers, which were positioned with the aid of a static trial to match the real markers on the subjects. Because of the marker placement as clusters, the joint positions $q \in \mathbb{R}^{11}$ are obtained by minimizing a combination of the distance between certain virtual and motion capture markers and the difference in the orientation of the marker clusters and model segments for each frame separately:

$$\min_{q} \sum_{i \in N_p} a_i ||m_i^V(q) - m_i^C||_2^2 + \sum_{i \in N_r} b_i ||f_{angle\_axis}((R_i^V(q))^T R_i^C)||_2^2 \tag{1}$$

with $m_i^V(q)$ and $m_i^C \in \mathbb{R}^3$ the position of the virtual and motion capture markers. The matrices $R_i^V$ and $R_i^C \in \mathbb{R}^{3\times3}$ describe the orientation of the body segment and of the corresponding marker cluster in the global frame, respectively. $N_p$ and $N_r$ specify the set of marker indices whose position and whose orientation should be matched. The function $f_{angle\_axis}(R)$ calculates the angle-axis representation of rotation matrix $R$. Each term is weighted by the factors $a_i$ and $b_i \in \mathbb{R}$. In Tab. 1, the accuracy of the kinematic fitting in terms of position and angle error is given.

**Table 1**. Average angle and position error and standard deviation with respect to the sagittal plane of the recorded and fitted model clusters of the five subjects.

| Subject | avg. angle error | [std] | avg. position error | [std] |
|---|---|---|---|---|
| S1 | 2.20° | [0.92] | 0.62 cm | [0.40] |
| S2 | 1.89° | [0.89] | 0.28 cm | [0.22] |
| S3 | 2.82° | [1.31] | 0.74 cm | [0.35] |
| S4 | 2.73° | [1.50] | 1.00 cm | [0.82] |
| S5 | 2.67° | [1.01] | 0.66 cm | [0.41] |

### 3.1.2 Muscle Torque Generators

The human model is actuated by pairs of agonist and antagonist muscle torque generators (MTG) [15] with additional joint damping. One MTG summarizes the muscular properties for a joint in one direction (here: flexion and extension). Instead of having several line type muscles for bending a segment, only one MTG is needed, which greatly reduces the complexity of the problem without loosing much accuracy. The torque generated at the human joint $i$ is calculated by:

$$\tau_i^{HUMAN} = \tau_i^{FL} + \tau_i^{EX} + \beta_i \dot{q}_i \quad \text{with } \beta_i = \eta_i \frac{{}^i\tau_0^{FL} + {}^i\tau_0^{EX}}{{}^i\omega_{max}^{FL} + {}^i\omega_{max}^{EX}}. \tag{2}$$

The torque generated by the MTG for flexion and extension is denoted by $\tau^{FL}$ and $\tau^{EX}$, respectively. The joint velocities is given by $\dot{q}$. For each MTG, $\tau_0$ is the maximum isometric torque and $\omega_{max}$ the maximum angular velocity. The damping coefficient $\beta$ is scaled by factor $\eta$.

The amount of torque a muscle can produce depends on the level of activation, the joint position and the joint velocity. This dependency is modeled in the MTG by three curves: the active ($f^A$) and passive ($f^P$) torque - angle curve representing the active and passive forces generated by the muscles and the curve $f^V$ describing their torque - velocity relationship:

$$\tau^{MTG} = \tau_0^{MTG}[\alpha f^A(\theta) f^V(\omega) + s^P f^P(\theta - \theta_0^P)(1 - \beta^P \frac{\omega}{\omega_{max}^{MTG}})] \tag{3}$$

with muscle activation $\alpha \in [0,1]$ and nonlinear normalized damping term $\beta^P$. The parameters $s^P$ and $\theta_0^P$ scale and shift the passive torque-angle-curve. The MTG-specific angle $\theta$ and velocity $\omega$ are derived from the joint angle $q$ and velocity $\dot{q}$, respectively. It should be noted that only uniarticular muscles are currently supported by the MTG. Thus, the effect of biarticular muscles in the movement performance is neglected during simulation. Further information regarding the MTG can be found in [10] [15].

https://doi.org/10.3311/ECCOMASMBD2021-235

### 3.1.3 Muscle Torque Generator Fitting

The possible strength of a MTG at a given position and velocity can be adjusted by a set of parameters. For the optimization, it is vital that the muscle models can generate the torques necessary to perform the motion. This is not guaranteed when using the default properties derived from experimental data of the literature as every person differs in strength and flexibility.

A muscle-fitting-routine [15] was applied to adjust the MTG so that they can reproduce the motion with muscle activation not exceeding a given range $[0, \alpha_{max}]$. As the subject likely would not need their full strength to lift a 10 kg heavy box, an educated guess for the maximum activation level during the lifting motion would be helpful to get a more accurate representation of the muscle group properties for each joint. For this purpose, the available EMG data of the recorded lifting motions were normalized and its peak value was taken as activation limit $(\alpha_{max})$ of the MTG responsible for hip and lumbar extension during the muscle fitting process:

$$EMG_{trial}^{norm}(t) = \frac{EMG_{trial}(t) - \overline{EMG_{quiet}}}{EMG_{MVC}^{MAX} - \overline{EMG_{quiet}}} \tag{4}$$

with $EMG_{trial}$ the EMG data of the lifting trial, $\overline{EMG_{quiet}}$ the mean of the EMG data during quiet standing phase, and $EMG_{MVC}^{MAX}$ the peak value observed during a set of MVC trials explained in Sec. 2. In case no EMG data was available, 0.7 was taken as $\alpha_{max}$ which is a conservative guess for athletic subjects lifting a 10 kg heavy box.

## 3.2 Modeling the Exoskeleton

The exoskeleton model is reduced to the sagittal plane like the human model. It has 9 DoF (6 internal) and consists of several modules: pelvis module, thigh bar, thigh interface, torso bar (set of beams) and torso interface, which are illustrated in Fig. 1. Between pelvis module and torso interface and between thigh bar and thigh interface, there are prismatic joints representing the deflection of the beams and the sliders on the prototype, and there are rotational joints to align the exoskeleton with the human model at specific contact points. The dynamic parameters (mass, center of mass, and inertia) were derived from CAD models of the existing prototype. The total mass of the exoskeleton is 6.7 kg. It generates torques at the lower back by 3 carbon fiber beams and at the hip joint by passive elements with a nonlinear torque-angle relationship [16]. Mathematical models replicating their behavior are included in the optimization problem and are described in the next chapters. For DC, a motor is attached to the hip joint to evaluate their effect on the support and contact forces between user and exoskeleton which affects their alignment. The weight of the pelvis module is increased by 3 kg to account for the additional actuators.

## 3.3 Modeling the Passive Hip Element

The passive hip element [16] consists of a linear spring where a cable is attached to. The cable is guided through a system of rollers and attached to a heart-shaped profile at the center of a revolute joint. When the joint rotates, the cable is bend over the profile which leads to a nonlinear torque-angle relationship. The linear spring itself can be pretensioned. The following 6 parameters specify the shape of the torque profile:
$(S)$ linear spring stiffness, $(P)$ linear spring pretension, $(P_{max})$ maximum pretension of the spring, $(B)$ length of the lever arm, $(C)$ distance between rollers and cable attachment point at the joint, $(R)$ radius of the heart - shaped profile. Except for $(S)$ and $(P_{max})$, all parameters are later optimized. The torque $\tau$ generated at deflection angle $\alpha$ is derived as follows:

$$\tau = sign(\alpha)S(-C+B+D+E+PP_{max})J, \tag{5}$$

with

$$\begin{array}{llllll} D & = R\lambda, & E & = \sqrt{A^2-R^2}, & J & = Csin(\lambda - |\alpha|), \\ A & = \sqrt{I^2+H^2}, & I & = Ccos(\alpha) - B, & H & = R - Csin(|\alpha|), \\ \gamma & = arctan(\frac{H}{I}), & \theta & = arctan(\frac{E}{R}), & \lambda & = \frac{\pi}{2} - \gamma - \theta, \end{array} \tag{6}$$

Because of geometrical reasons, following constraint must hold so that the profile is fabricable:

$$E > 0 \tag{7}$$

The torque profile is non smooth for $\alpha = 0$, which is reflected in the absolute function. In order to obtain a smooth function, the absolute function was approximated with

$$|\alpha|_{approx} := 2\alpha \left( \frac{1}{1+e^{-100\alpha}} \right) - \alpha \tag{8}$$

### 3.4 Modeling the Carbon Fiber Beam

The beam is modeled as a long thin cantilever beam (Fig. 2) having a uniform circular cross section made of a linear elastic material which is homogeneous and isotropous. A force $F$ is applied at its free end in a direction specified by the angle $\alpha \in \mathbb{R}$. As the lifting movement is reduced to the sagittal plane, only sagittal deflections of the beam are considered as well.

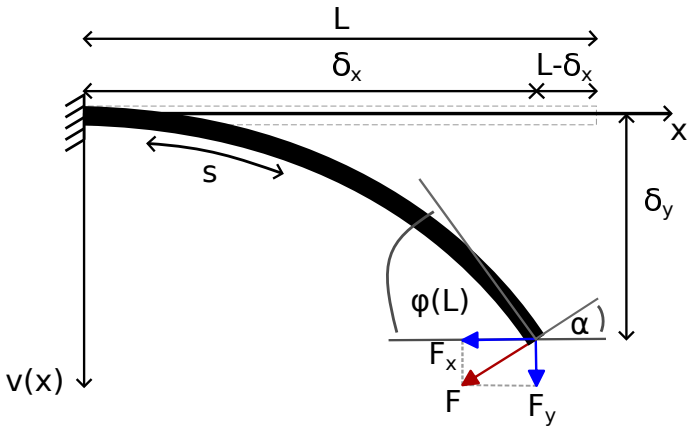


**Figure 2**. Cantilever beam

Assuming that the Bernoulli–Euler hypothesis is valid and applying the analysis proposed by [17] on the deflection of a cantilever beam, the Bernoulli–Euler bending moment–curvature relationship for this type of beam at a point $s$ along the beam with Cartesian coordinates $(x, y)$ (Fig. 2) can be formulated as follows:

$$EI\frac{d\phi}{ds} = M(s), \quad \text{with} \quad M(s) = F[sin(\alpha)(\delta_x - x) + cos(\alpha)(\delta_y - v(x))], \tag{9}$$

where $M$ and $\kappa = \frac{d\phi}{ds}$ are the bending moment and curvature, respectively. The moment of inertia of a beam with circular cross section specified by radius $r$ is denoted by $I = \frac{\pi}{4}r^4$. The horizontal and vertical displacement at the end of the beam are given by $\delta_x$ and $\delta_y$ and $\alpha$ is the angle between the direction of the force and the neutral position of the beam when no forces are applied. Between the curvature $\frac{d\phi}{ds}$ of the deformed beam and the transverse displacement $v(x)$ following relationship can be established:

$$\frac{d\phi}{ds} = \frac{\frac{d^2v}{dx^2}}{\left[1 + \left(\frac{dv}{dx}\right)^2\right]^{\frac{3}{2}}}. \tag{10}$$

By differentiating eq. 9 with respect to s and taking into account the relations $\frac{dx}{ds} = cos(\phi)$ and $\frac{dy}{ds} = sin(\phi)$, we obtain:

$$EI\frac{d^2\phi}{ds^2} + Fsin(\alpha + \phi) = 0. \tag{11}$$

This equation together with $\frac{dx}{ds} = cos(\phi)$ and $\frac{dy}{ds} = sin(\phi)$ can be integrated and solved for $F$ and $L$ when taking the following boundary conditions into account:

$$v(0) = 0, \quad v(\delta_x) = d_y, \quad \phi(0) = 0, \quad \frac{d\phi}{ds}(L) = 0, \tag{12}$$

with $L$ the beam length. Note that in our case, the horizontal and vertical displacement of the beam is known whereas the generated force and the length of the beam are unknown as the connector of the torso interface can move freely on the slider along the beam.

### 3.4.1 Polynomial Approximation of the Beam Deflection

The above described method includes solving a boundary value problem which is too complex to be included in the optimal control setup described in Sec. 4. To avoid the integration of the system, we approximate the deflection of the beam by a polynomial $v(x) \approx P(x) = \sum_{i=0}^{N} a_i x^i$ of order $N \in \mathbb{N}$. The coefficient of the polynomial can be reduced by applying the boundary conditions $v(0) = 0$ and $\frac{dv}{dx}(0) = 0$ yielding $a_0 = a_1 = 0$. The remaining coefficients and the force $F$ are computed by minimizing the distance to the deflection $\delta_y$ at the end and the deviation to the deflection-moment relationship (9) at equally spaced gridpoints $0 = x_0 < x_1 < \cdots < x_M = \delta_x$, $M \in \mathbb{N}$. By setting $M = N$ the problem reduces to solving following set of equations:

$$P(\delta_x) = \delta_y \tag{13}$$

$$P''(x_k) = \left[1 + P'(x_k)^2\right]^{\frac{3}{2}} M(x_k) \tag{14}$$

$$\text{with } M(x_k) = \frac{F}{EI}(sin(\alpha)(\delta_x - x_k) + cos(\alpha)(\delta_y - P(x_k)), \quad x_k = \frac{k}{N}\delta_x, \quad k = 0, \ldots, N-1 \tag{15}$$

Based on the results using different order $N$ (Tab. 2), $N = 7$ was used in the optimal control setup and the characteristics of the beam are optimized by adjusting the radius $r$ of the beam cross section.

**Table 2**. Deviation (mean [std]) of the force acting at the beam end calculated by the boundary value problem and the polynomial approximation of different order $N$ setting $\alpha = 90°$, $\delta_x = 0.4\,cos(x)$, $\delta_y = 0.4\,sin(x)$, $x = 0, \ldots, 50°$

| $N$ | 3 | 4 | 5 | 6 | 7 | 8 |
|---|---|---|---|---|---|---|
| Deviation (N) | 2.9 [4.1] | 1.1 [2.6] | 0.3 [0.7]] | 0.1 [0.2] | 0.03 [0.05] | 0.03 [0.06] |

### 3.5 Coupling of Human and Exoskeleton

In the simulation, a rigid coupling between human and exoskeleton model is assumed, which is realized over loop closure constraints. This assumption does not fully reflect reality as there is noticeable movement between user and exoskeleton. However, to model a realistic behavior of the interaction, adequate experimental data from the prototype is needed which was not available. In the experiment presented in Sec 2.2, the movement of the arms and head and the position of the box were not recorded, making the data unsuitable for contact model identification using full-body simulations.

However, they provide an analysis on how the deflection of the human torso and thigh is different from the deflection of the exoskeleton's torso and thigh interface. This data was used to approximate the state of the passive elements with a linear regression model. Parameter values $p_T^C$, $p_T^T$, $p_T^H$, $p_H^C$, $p_H^T$ and $p_H^H \in \mathbb{R}$ were identified so that the values for the deflection of the torso module connector (or the beams) $\hat{\theta}_T^E$ $(\equiv atan(l_{E8}/l_{E7}))$ and the exoskeleton hip joint angle $\hat{\theta}_H^E$ $(\equiv \theta_{E4})$ obtained by

$$\hat{\theta}_T^E = p_T^C + p_T^T \theta_T^H + p_T^H \theta_H^H \tag{16}$$

$$\hat{\theta}_H^E = p_H^C + p_H^T \theta_T^H + p_H^H \theta_H^H \tag{17}$$

https://doi.org/10.3311/ECCOMASMBD2021-235

match the experimental data best in the least-squares sense with $\theta_T^H$ ($\equiv \theta_{H7} + \theta_{H8}$) the human torso flexion angle and $\theta_H^H$ ($\equiv \theta_{H4}$) the human hip flexion angle (see Fig. 1). In Tab. 3, the optimized linear regression parameters can be obtained and the results show that a significant linear regression relationship exists between the human and exoskeleton deflection angles.

**Table 3**. Linear regression parameters for given angles in radian with an error variance of 0.0044 ($R^2$: 0.9616, p-value: 0.0) for $\hat{\theta}_T^E$ and 0.0043 ($R^2$: 0.9829, p-value: 0.0) for $\hat{\theta}_H^E$

| $p_T^C$ | $p_T^L$ | $p_T^H$ | $p_H^C$ | $p_H^T$ | $p_H^H$ |
|---|---|---|---|---|---|
| -0.0426 | 0.4082 | -0.3145 | -0.0017 | -0.2177 | 0.6912 |

Furthermore, several studies emphasized as an important requirement for exoskeletons to be comfortable to wear over hours even though they are tightly connected to the user with straps and plates and exert strong pushes and pullings [18] [4]. We address this issue by limiting the interaction forces between user and exoskeleton. These limits are based on [19] where several subjects were exposed to constant and repeating pressure and they graded in both cases at which level it was uncomfortable for them and at which level they felt pain. The average values for discomfort (Tab. 4) are used as limits in the optimization.

**Table 4**. Contact force limits based on the findings of [19] and a friction coefficient of 0.6

| Force Limit | Pelvis Contact | Thigh Contact | Torso Contact |
|---|---|---|---|
| Normal Force | 162.40 N | 333.40 N | 230.30 N |
| Shear Force | 97.44 N | 200.04 N | 138.18 N |

## 4 OPTIMAL CONTROL PROBLEM FORMULATION

The lifting motion of the human model wearing the exoskeleton is set up as a 3-phase optimal control problem (OCP). In the first phase, the user stands in an upright position, bends down and makes contact with the box. In the second phase, the user generates enough force to lift the box. The last phase starts when the box leaves the ground and ends when the user holds the box in an upright position. The OCP is formulated as follows:

$$\min_{q,\dot{q},z,\alpha,u,p} \Psi[q,\dot{q},z,\alpha,u,p] := \sum_{i=1}^{3} \left( \sum_{n=0}^{N_i} \|W_q(q(t_{i,n}) - q_{i,n}^{REF})\|^2 + \int_{t_i}^{t_{i+1}} \phi(q,\dot{q},z,\alpha,u,p)dt \right) \tag{18}$$

$$s.t. \qquad M(q)\ddot{q} + G_i(q)^T\lambda = \tau(q,\dot{q},z,\alpha,u,p) - C(q,\dot{q}) \tag{19}$$

$$\dot{\alpha} = ((u_m - \alpha_m)/T_m)_{m=1,\ldots,N_m} \tag{20}$$

$$f(q,z,p) = 0 \tag{21}$$

$$g_i(q,\dot{q},z,\alpha,u,p) \geq 0, \qquad i = 1,\ldots,3 \tag{22}$$

with $q$, $\dot{q}$, and $\ddot{q}$ the joint positions, velocities, and accelerations, respectively. The number of shooting nodes of phase $i$ is denoted by $N_i$. The motion to be tracked is given for time $t_{i,n}$ by the joint positions $q_{i,n}^{REF}$ and the fitting accuracy is specified by a weighting matrix $W_q$. The algebraic states $z$ and the system of equations (21) define the state of the beam. The parameters $p$ describe the design of the passive elements of the exoskeleton. The controls $u$ are the neural excitation of the MTG. In case of DC, the torque profile of the motors is a control as well. Eq.(20) are the MTG activation dynamics proposed by [20] with activation level $\alpha$ and (de-)activation time constant $T$. The number of MTG is given by $N_m$. The equation of motion of the constrained multibody system is given by (19) with mass matrix $M$, constraint jacobian $G_i$, and unknown force variables $\lambda$. The function $C$ contains the centrifugal, gravitational and Coriolis forces. The generalized forces are

https://doi.org/10.3311/ECCOMASMBD2021-235

denoted by $\tau$ consisting of the joint torques and forces generated by the MTG and the exoskeleton. The Constraints (22) include, among others, position constraints, constraints on hand-to-box, box-to-floor, and foot-to-floor contact forces, human/exoskeleton alignment regulations and limits on parameters, states and controls. The objective function (18) consists of a least squares term for tracking the recorded motion and a Lagrange term enforcing the reduction of human joint moments and pelvis contact moment. The OCP is discretized using direct multiple shooting and the resulting NLP is solved with SQP and active-set method provided by the toolbox MUSCOD-II [21]. For the rigid multibody dynamics calculations, the open-source library RBDL [22] was used.

## 5 RESULTS

The support of the exoskeleton was optimized for several recorded lifting motions. For the prototype optimization (PO), parameters describing the the behavior of the beam (beam cross section radius) and the passive elements (see Sec. 3.3) were optimized. For the new design concept (DC), motor torque profiles were optimized as well. The results are compared to the original configuration (O) of the prototype. The weighting of the cost function enforced a high fitting accuracy (avg. joint angle error across all subjects $0.17^\circ - 0.62^\circ$) with the same values for all simulation setups (O/PO/DC). This guarantees that the reduction in muscle activity comes solely from the support provided by the exoskeleton and not from an alteration of the motion.

In Tab. 5, the achieved support for each subject with respect to each setup is listed. Both optimized configurations, PO and DC, provide higher support than O across all subjects. However, PO increases the support by additional 2.5 - 4.1 % regarding the lumbar moment, 1.6 - 2.7 % regarding the hip moment, and 1.9 - 3.7 % regarding the peak lumbar moment compared to DC. The higher support of PO is based on torque profiles of the beams and PH with higher peaks than of DC during the motion (Fig. 3). Through the motors, a broader torque curve is achieved resulting in smaller loss of support at the hip joint than at the lumbar joint compared to PO. The fact that the limit on the normal contact force at the pelvis is reached for both PO and DC (Fig. 4) suggests that due to the higher weight of the pelvic module, a force/torque generation of the exoskeleton of DC at the same level as PO was not possible before the limit was reached.

The higher weight is also reflected in the shear forces acting at the pelvis contact point (Fig. 4), in particular at the beginning and end of the motion when the user is standing upright and the weight of the exoskeleton mainly contributes to them. The normal and shear forces of the thigh (max. 127 N and 7 N across subjects and PO/DC) and torso (max. 121 N and 16 N) contact point stayed far below the set limits. As intended, adding the motor to the prototype resulted in a high reduction of the moment acting at the pelvis contact compared to PO (Fig. 4), staying within [-4.9 Nm, 3.6 Nm] in contrast to [-11.4 Nm, 5.4 Nm] and yielding a very good alignment of exoskeleton and user. For comparison the contact moment of O lies in the range of [-8.1 Nm, 7.4 Nm] for all subjects.

**Table 5**. Reduction of hip and lumbar moment when using the exoskeleton of DC | PO | O with respect to the corresponding human-only-simulation

| Subject | lumbar moment reduction* | hip moment reduction* | peak lumbar moment reduc. |
|---|---|---|---|
| S1 | 15.5% \| 18.7% \| 14.1% | 12.1% \| 14.3% \| 11.2% | 19.9% \| 23.5% \| 17.5% |
| S2 | 13.5% \| 16.5% \| 11.9% | 12.4% \| 14.1% \| 10.1% | 13.4% \| 16.8% \| 12.0% |
| S3 | 12.0% \| 15.4% \| 10.7% | 7.7% \| 9.6% \| 6.5% | 12.0% \| 15.5% \| 10.6% |
| S4 | 14.3% \| 16.8% \| 9.5% | 10.0% \| 11.6% \| 4.9% | 12.2% \| 14.1% \| 7.6% |
| S5 | 18.6% \| 22.7% \| 17.3% | 12.2% \| 14.9% \| 11.3% | 16.3% \| 20.0% \| 14.9% |

* reduction in terms of the integrated area under the moment curve

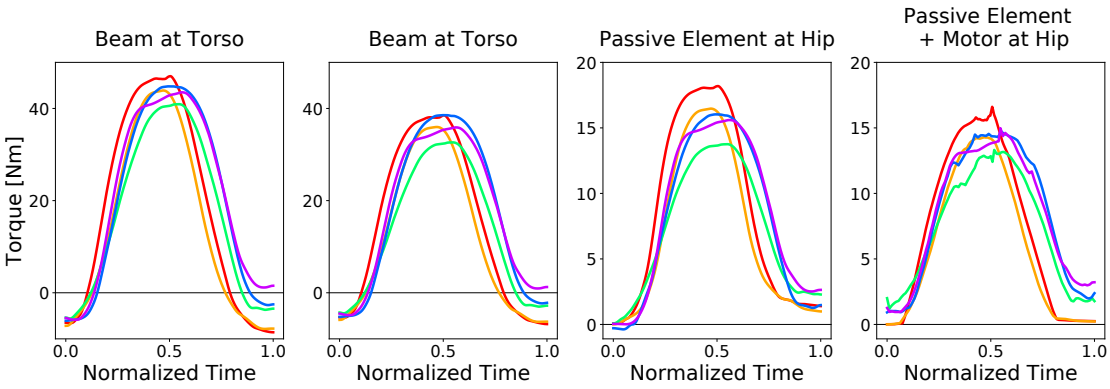


**Figure 3**. **From left to right:** The torques generated at the bottom of the beams (at lumbar joint level) during the motion of PO and of DC. The torques generated by PH during the motion using the exoskeleton configuration of PO and of DC. Please refer to Fig. 4 for the color legend regarding the subjects.

## 6 DISCUSSION AND CONCLUSIONS

In this work, we present a method to optimize and evaluate design concepts for exoskeletons in terms of contact forces between user and exoskeleton and load reduction using an optimal control formulation. It can be used to optimize the design of passive elements described by multiple parameters and motor torque profiles that serve as guidelines for the next prototype. The modular setup offers an easy switching between exoskeleton models. It can also be extended to perform optimization without reference data if the tracking term is left out, which was shown in [10]. Note that these calculations can also be done without having a real prototype and do not need biomechanical experiments involving long usages of the device as in [8].

It also provides an analysis of the actuation patterns of the user, which were not presented here but need to be considered during the optimization. Lifting motions involve going to the limits of the range of motion when also passive muscle forces are present. Thus, it is important to have an estimation of the distribution of active and passive muscle forces during simulation as the exoskeleton should only take over the active muscle part. Otherwise, the user may have to work against the exoskeleton while performing the same motion.

We analyzed the effect of including additional motors at the hip joint of an existing prototype having only passive elements and showed that this would lead to a decrease in the possible support while the contact moment acting at the pelvis can be much better controlled. One limitation is the assumption of rigid coupling between the user and the exoskeleton. In reality, movements occur with respect to each other. In context of the prototype evaluated, a movement or rotation of the exoskeleton segments with respect to the user may lead to a higher deflection of the beam resulting in a different, possible higher, support. We included an estimate of the effect the movement of the exoskeleton has on the passive elements using linear regression equations obtained by experimental data. A comparison to preliminary results presented in [12], showed that the simulated support in this work agrees better with the values observed in [5]. However, the regression equations only depend on the user's position and not on the generated torque distribution of the exoskeleton. In order to accurately model the human-robot interaction, additional experimental data is needed, which was not available for these calculations and is part of future work.

## ACKNOWLEDGMENTS

This work was funded by the European Commissions within the H2020 project SPEXOR (GA 687662).

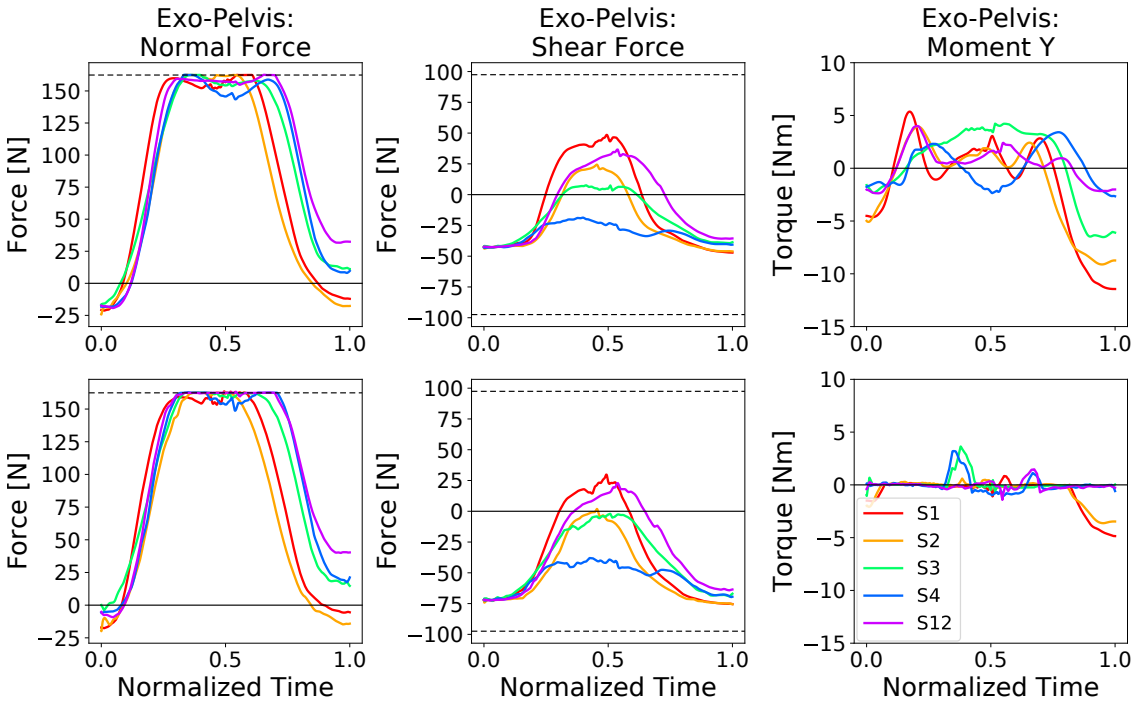


**Figure 4**. The calculated contact forces and moment acting at the pelvis contact point using the exoskeleton configuration of PO **(first row)** and of DC **(second row)**. The dashed lines indicate the prescribed limits on the forces during the optimization.

## REFERENCES

[1] Park, J.H., Stegall, P.R., Roye, D.P., Agrawal, S.K.: Robotic spine exoskeleton (rose): Characterizing the 3-d stiffness of the human torso in the treatment of spine deformity. IEEE Transactions on Neural Systems and Rehabilitation Engineering **26**(5) (2018) 1026–1035

[2] Jarrassé, N., Proietti, T., Crocher, V., Robertson, J., Sahbani, A., Morel, Guillaume andRoby-Brami, A.: Robotic exoskeletons: a perspective for the rehabilitation of arm coordination in stroke patients. Frontiers in human neuroscience **8**(947) (2014)

[3] Aach, M., Cruciger, O., Sczesny-Kaiser, M., Höffken, O., Meindl, R.C., Tegenthoff, M., Schwenkreis, P., Sankai, Y., Schildhauer, T.A.: Voluntary driven exoskeleton as a new tool for rehabilitation in chronic spinal cord injury: a pilot study. The Spine Journal **14**(12) (2014) 2847 – 2853

[4] Huysamen, K., de Looze, M., Bosch, T., Ortiz, J., Toxiri, S., O'Sullivan, L.W.: Assessment of an active industrial exoskeleton to aid dynamic lifting and lowering manual handling tasks. Applied Ergonomics **68** (2018) 125–131

[5] Koopman, A.S., Näf, M., Baltrusch, S.J., Kingma, I., Rodriguez-Guerrero, C., Babič, J., de Looze, M.P., van Dieën, J.H.: Biomechanical evaluation of a new passive back support exoskeleton. Journal of Biomechanics **105** (2020) 109795

[6] Luo, Z., Yu, Y.H.: Wearable stooping-assist device in reducing risk of low back disorders during stooped work. 2013 IEEE International Conference on Mechatronics and Automation (2013) 230–236

[7] de Looze, M.P., Bosch, T., Krause, F., Stadler, K.S., O?Sullivan, L.W.: Exoskeletons for industrial application and their potential effects on physical work load. Ergonomics **59**(5) (2016) 671–681 PMID: 26444053.

[8] Zhang, J., Fiers, P., Witte, K., Jackson, R., Poggensee, K., Atkeson, C., Collins, S.: Human-in-the-loop optimization of exoskeleton assistance during walking. Science **356**(6344) (2017) 1280–1284

[9] Näf, M.B., Koopman, A.S., Baltrusch, S., Rodriguez-Guerrero, C., Vanderborght, B., Lefeber, D.: Passive back support exoskeleton improves range of motion using flexible beams. Frontiers in Robotics and AI **5** (2018) 72

[10] Millard, M., Sreenivasa, M., Mombaur, K.: Predicting the motions and forces of wearable robotic systems using optimal control. Frontiers in Robotics & AI **4** (2017)

[11] Harant, M., Millard, M., Šarabon, N., Mombaur, K.: Cost function evaluation for optimizing design and actuation of an active exoskeleton to ergonomically assist lifting motions. In: IEEE/RAS International Conference on Humanoid Robots (Humanoids 2019). (2019)

[12] Harant, M., Näf, M.B., Mombaur, K.: Optimal control to facilitate the development process of exoskeletons. In: Progress in Industrial Mathematics at ECMI 2021. (2021) submitted

[13] Näf, M.B., Koopman, A.S., Rodriguez-Guerrero, C., Vanderborght, B., Lefeber, D.: Impact of the misalignment compensation mechanism on the relative motion of the spexor backsupport exoskeleton. submitted to IEEE Transactions on Medical Robotics and Bionics (2021)

[14] De Leva, P.: Adjustments to Zatsiorsky-Seluyanov's segment inertia parameters. Journal of Biomechanics **29**(9) (1996) 1223–1230

[15] Millard, M., Kleesattel, A.L., Harant, M., Mombaur, K.: A reduced muscle model and planar musculoskeletal model fit for synthesis of whole body movements. Journal of Biomechanics **89** (2019) 11–20

[16] Vanderborght, B., Tsagarakis, N.G., Semini, C., Van Ham, R., Caldwell, D.G.: Maccepa 2.0: Adjustable compliant actuator with stiffening characteristic for energy efficient hopping. In: 2009 IEEE International Conference on Robotics and Automation. (2009) 544–549

[17] Beléndez, T., Neipp, C., Beléndez, A.: Large and small deflections of a cantilever beam. European Journal of Physics **23**(3) (may 2002) 371–379

[18] Cho, K., Kim, Y., Yi, D., Jung, M., Lee, K.: Analysis and evaluation of a combined human – exoskeleton model under two different constraints condition. In: Int. Summit on Human Simulation. (05 2012)

[19] Kozinc, Ž., Babič, J., Šarabon, N.: Human pressure tolerance and effects of different padding materials with implications for development of exoskeletons and similar devices. Applied Ergonomics **93** (2021) 103379

[20] Winters, J.M., Stark, L.: Estimated mechanical properties of synergistic muscles involved in movements of a variety of human joints. Journal of Biomechanics **21**(12) (1988) 1027–1041

[21] Leineweber, D., Schäfer, A., Bock, H., Schlöder, J.: An efficient multiple shooting based reduced SQP strategy for large-scale dynamic process optimization: Part II: Software aspects and applications. Computers & Chemical Engineering **27**(2) (2003) 167–174

[22] Felis, M.L.: Rbdl: an efficient rigid-body dynamics library using recursive algorithms. Autonomous Robots **41** (2017) 495–511

# Section
# CONTACT, IMPACT AND CONSTRAINTS

https://doi.org/10.3311/ECCOMASMBD2021-113



# The Tippedisk: A Minimal Model For Friction-Induced Inversion

**Simon Sailer, Simon R. Eugster, Remco I. Leine**

Institute for Nonlinear Mechanics
University of Stuttgart
Pfaffenwaldring 9, 70569, Germany
[sailer, eugster, leine]@inm.uni-stuttgart.de

## ABSTRACT

The *tippedisk* is a new mechanical-mathematical archetype for friction induced instability phenomena, showing an inversion similar to the inversion of the tippetop. Unlike the tippetop, the tippedisk has no rotational symmetry, which greatly complicates its analysis. Since the system cannot be reduced to a planar one, one has to consider the full three-dimensional kinematics, being intrinsically nonlinear. In this work a new minimal model is derived that contains the main relevant physical effects so that the inversion phenomenon can be described qualitatively. The in-depth analysis leads to slow-fast systems with homoclinic connections and global bifurcations.

**Keywords:** gyroscopic system, friction-induced instability, dynamics, tippetop.

## 1 INTRODUCTION

Various gyroscopic systems which are interacting with a horizontal frictional support, such as the Euler disk [1, 2], the rattleback [3, 4] and the tippetop [5, 6, 7, 8], form a scientific playground for research in theoretical mechanics. The tippetop [5, 6], as well as the related dynamics of spinning eggs [9, 10], correspond to a subclass of gyroscopic systems which show inversion phenomena. The tippetop is a rotationally symmetric top, consisting of a spherical body and a stem attached to it. The center of gravity (COG) does not coincide with the geometric center, such that the stem remains pointing upwards as the top rotates slowly in its non-inverted orientation. If the top is spun fastly around its axis of symmetry, gravitational, normal and friction forces are acting on the top, such that the top starts to invert its orientation and balances on its stem. This phenomenon of inversion also occurs for other axisymmetric bodies with rotational symmetry in inertia and geometry, for example spinning eggs [9, 10, 11]. But what happens if this symmetry does not exist? In [12], we introduced the "tippedisk" as new archetype of a three-dimensional rigid body system with frictional contact. The tippedisk can be seen as a thin disk for which the COG does not coincide with the geometric center. If the tippedisk is spun rapidly around an in-plane axis, one can observe that the COG rises until the disk remains in an inverted configuration, see Fig. 1. The inversion phenomenon is therefore not restricted to axisymmetric rigid bodies and also takes place for the tippedisk. In this work, we derive a minimal model able to describe the inversion of the tippedisk. A suitable parametrization is introduced, which is able to describe the inversion phenomenon. The model developed in this work forms the basis for in-depth nonlinear analysis of the dynamics of the tippedisk, e.g., [13, 14].

## 2 MECHANICAL MODEL

The mechanical system depicted in Fig. 2 consists of an unbalanced rigid disk with mass $m$, radius $r$, eccentricity $e$, thickness $h$ and a flat frictional support. Since we are only interested in the essential physical phenomena, the contact kinematics is simplified by assuming the disk to be infinitely thin. According to this approximation, the contact point $C_1$, i.e., the point with minimal height, lies on a circle around the geometric center $G$, in the inclined $\Pi$-plane. The vertical projection of the contact point $C_1$ onto the horizontal support is denoted by $D_1$. Both the disk and the flat support are considered to be perfectly rigid, so that penetration is not possible. We introduce an orthonormal

https://doi.org/10.3311/ECCOMASMBD2021-113

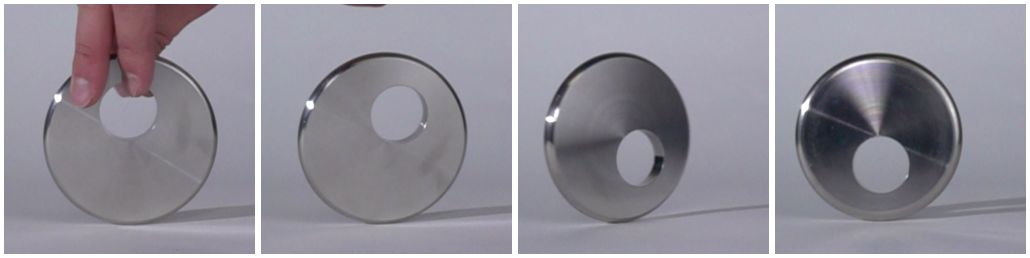

Figure 1: Stroboscopic image sequence showing the inversion phenomenon of the tippedisk. First Picture: Non-inverted configuration; Last Picture: Tippedisk spinning in its inverted configuration.

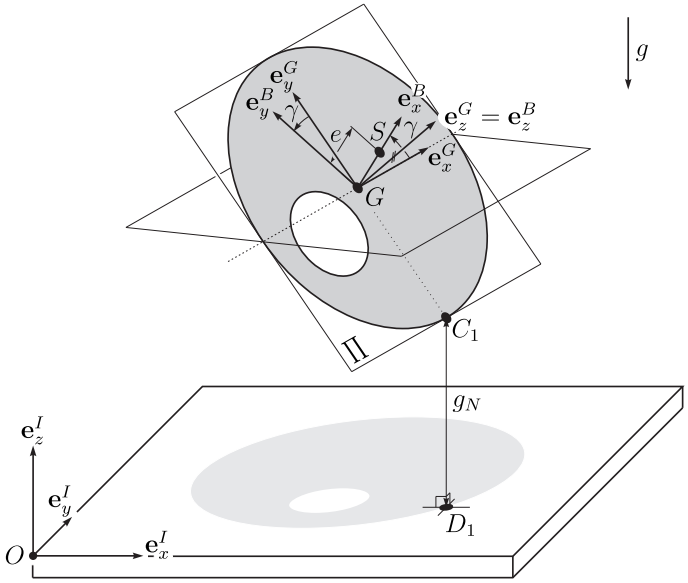


Figure 2: Mechanical model of the tippedisk, showing the definition of the floating $G$-frame and the contact points $C_1$ and $D_1$.

inertial frame $I = (O, \mathbf{e}_x^I, \mathbf{e}_y^I, \mathbf{e}_z^I)$ attached to the origin $O$, where $\mathbf{e}_z^I$ is normal to the flat support. The right-handed body-fixed $B$-frame $B = (G, \mathbf{e}_x^B, \mathbf{e}_y^B, \mathbf{e}_z^B)$ is attached to the geometric center $G$ of the disk, such that $\mathbf{e}_z^B$ is normal to the surface of the disk. The axis $\mathbf{e}_x^B$ is defined as the normalized vector of $\mathbf{r}_{GS}$, which points from the geometric center $G$ to the center of gravity $S$. The inertia tensor with respect to $G$ expressed in the body-fixed $B$-frame is given as ${}_B\boldsymbol{\Theta}_G = \mathrm{diag}(A,B,C)$, where $B < A < C$ holds. To describe the kinematics of the point $C_1$, we introduce analogue to [15] a floating coordinate system $G = (G, \mathbf{e}_x^G, \mathbf{e}_y^G, \mathbf{e}_z^G)$, which is attached to the geometric center $G$. Its unit vector $\mathbf{e}_z^G$ corresponds to $\mathbf{e}_z^B$. Since the cross product $\mathbf{e}_z^I \times \mathbf{e}_z^B$ is perpendicular to $\mathbf{e}_z^I$ and $\mathbf{e}_z^B$, we define the orthogonal vector

$$\mathbf{e}_x^G := \frac{\mathbf{e}_z^I \times \mathbf{e}_z^B}{||\mathbf{e}_z^I \times \mathbf{e}_z^B||} \quad \text{with} \quad \|\mathbf{e}_z^I \times \mathbf{e}_z^B\| = \sqrt{1 - R_{33}^2}, \tag{1}$$

as the horizontal unit vector of the floating coordinate system, where $R_{33}$ denoted the third diagonal element of the rotation matrix $\mathbf{R}$ given below. The symbol $||.||$ denotes the Euclidean norm. Definition (1) is only valid for non-horizontal configurations with $R_{33} \neq 1$. For horizontal configurations, note that $\mathbf{e}_x^G$ can not be determined uniquely. If $R_{33} \neq 1$, we can obtain with

$$\mathbf{e}_y^G := \mathbf{e}_z^B \times \mathbf{e}_x^G \tag{2}$$

a right handed orthonormal frame, such that the floating coordinate frame $G = (G, \mathbf{e}_x^G, \mathbf{e}_y^g, \mathbf{e}_z^G)$ is fully defined. The point $C_1$ with minimal height can be described with respect to the geometric

https://doi.org/10.3311/ECCOMASMBD2021-113

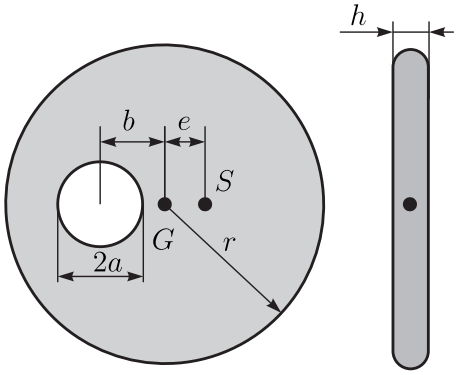


Figure 3: Dimensions of the tippedisk.

center $G$ as

$$\mathbf{r}_{GC_1} = -r\,\mathbf{e}_y^G. \tag{3}$$

The distance between the contact point $C_1$ and the flat support defines the signed gap $g_N$

$$g_N = \mathbf{r}_{OC_1} \cdot \mathbf{e}_z^I = (\mathbf{r}_{OG} + \mathbf{r}_{GC_1}) \cdot \mathbf{e}_z^I, \tag{4}$$

which is equal to the projection of $\mathbf{r}_{OC_1}$ onto the $\mathbf{e}_z^I$-axis.

## 3 DIMENSIONS

In the following we consider a stainless steel disk, which is depicted in Fig. 3. The dimensions and mass properties are given in Table 1, for a detailed derivation of the principal moments of inertia, we refer to [12].

Table 1: Dimensions and mass properties of the tippedisk.

| Property | Parameter | Magnitude | Unit |
|---|---|---|---|
| Disk radius | $r$ | 0.045 | m |
| Hole radius | $a$ | 0.015 | m |
| Distance | $b$ | 0.02 | m |
| Disk thickness | $h$ | 0.01 | m |
| Eccentricity | $e$ | $2.5 \cdot 10^{-3}$ | m |
| Mass | $m$ | 0.435 | kg |
| ${}_B\mathbf{\Theta}_G(1,1)$ | $A$ | $0.249 \cdot 10^{-3}$ | kg m$^2$ |
| ${}_B\mathbf{\Theta}_G(2,2)$ | $B$ | $0.227 \cdot 10^{-3}$ | kg m$^2$ |
| ${}_B\mathbf{\Theta}_G(3,3)$ | $C$ | $0.468 \cdot 10^{-3}$ | kg m$^2$ |

## 4 KINEMATICS

We parametrize the orientation of the tippedisk using Euler angles $\boldsymbol{\varphi} = [\alpha, \beta, \gamma]^{\mathrm{T}}$. Therefore, the rotating $R$-frame with $\mathbf{e}_z^R = \mathbf{e}_z^I$, $\mathbf{e}_x^R = \cos\alpha\,\mathbf{e}_x^I + \sin\alpha\,\mathbf{e}_y^I$ and $\mathbf{e}_y^R = \mathbf{e}_z^R \times \mathbf{e}_x^R$ is introduced. The sequence of rotation is then given as the first rotation with angle $\alpha$ around the $\mathbf{e}_z^I$-axis, the second rotation with angle $\beta$ around the $\mathbf{e}_x^R$-axis and the third rotation with angle $\gamma$ around the $\mathbf{e}_z^G$-axis

https://doi.org/10.3311/ECCOMASMBD2021-113

with corresponding elemental rotations

$$\mathbf{A}_{IR} = \begin{bmatrix} \mathrm{c}\alpha & -\mathrm{s}\alpha & 0 \\ \mathrm{s}\alpha & \mathrm{c}\alpha & 0 \\ 0 & 0 & 1 \end{bmatrix}, \mathbf{A}_{RG} = \begin{bmatrix} 1 & 0 & 0 \\ 0 & \mathrm{c}\beta & -\mathrm{s}\beta \\ 0 & \mathrm{s}\beta & \mathrm{c}\beta \end{bmatrix} \text{ and } \mathbf{A}_{GB} = \begin{bmatrix} \mathrm{c}\gamma & -\mathrm{s}\gamma & 0 \\ \mathrm{s}\gamma & \mathrm{c}\gamma & 0 \\ 0 & 0 & 1 \end{bmatrix}, \tag{5}$$

where the abbreviations $\mathrm{s}\alpha = \sin(\alpha)$, $\mathrm{c}\alpha = \cos(\alpha)$ etc. have been used. The rotation matrix

$$\mathbf{R}(\boldsymbol{\varphi}) = \begin{bmatrix} \mathrm{c}\alpha\mathrm{c}\gamma - \mathrm{s}\alpha\mathrm{c}\beta\mathrm{s}\gamma & -\mathrm{c}\alpha\mathrm{s}\gamma - \mathrm{s}\alpha\mathrm{c}\beta\mathrm{c}\gamma & \mathrm{s}\alpha\mathrm{s}\beta \\ \mathrm{s}\alpha\mathrm{c}\gamma + \mathrm{c}\alpha\mathrm{c}\beta\mathrm{s}\gamma & -\mathrm{s}\alpha\mathrm{s}\gamma + \mathrm{c}\alpha\mathrm{c}\beta\mathrm{c}\gamma & -\mathrm{c}\alpha\mathrm{s}\beta \\ \mathrm{s}\beta\mathrm{s}\gamma & \mathrm{s}\beta\mathrm{c}\gamma & \mathrm{c}\beta \end{bmatrix}, \tag{6}$$

which per se fulfills the orthogonality condition $\mathbf{R}^{\mathrm{T}}\mathbf{R} = \mathbf{I}$, then describes the relative orientation of the body-fixed $B$-frame with respect to the inertial $I$-frame.[1] The angular velocity $\boldsymbol{\Omega}$ of the tippedisk expressed in the body-fixed $B$-frame yields

$${}_B\boldsymbol{\Omega} = \dot{\alpha}\,\mathbf{A}_{RB}^{\mathrm{T}}\,{}_R\mathbf{e}_z^R + \dot{\beta}\,\mathbf{A}_{GB}^{\mathrm{T}}\,{}_G\mathbf{e}_x^G + \dot{\gamma}\,{}_B\mathbf{e}_z^B = \begin{bmatrix} \dot{\alpha}\mathrm{s}\beta\mathrm{s}\gamma + \dot{\beta}\mathrm{c}\gamma \\ \dot{\alpha}\mathrm{s}\beta\mathrm{c}\gamma - \dot{\beta}\mathrm{s}\gamma \\ \dot{\alpha}\mathrm{c}\beta + \dot{\gamma} \end{bmatrix}, \tag{7}$$

where the transformation matrix $\mathbf{A}_{RB} = \mathbf{A}_{RG}\mathbf{A}_{GB}$ has been used. The transformation

$${}_R\boldsymbol{\Omega} = \mathbf{A}_{RB}\,{}_B\boldsymbol{\Omega} = \begin{bmatrix} \dot{\beta} \\ -\dot{\gamma}\mathrm{s}\beta \\ \dot{\alpha} + \dot{\gamma}\mathrm{c}\beta \end{bmatrix} \tag{8}$$

yields the angular velocity of the tippedisk expressed in the rotating $R$-frame. The relative angular velocity of the $R$-frame is given with respect to the $I$-frame as ${}_R\boldsymbol{\omega}_{IR} = [0,\, 0,\, \dot{\alpha}]^{\mathrm{T}}$. Using coordinates $x$, $y$ and $z$, the position of the geometric center $G$ in the rotating $R$-frame is defined as

$${}_R\mathbf{r}_{OG} := \begin{bmatrix} x \\ y \\ z \end{bmatrix}. \tag{9}$$

The corresponding velocity

$${}_R\mathbf{v}_G = \begin{bmatrix} \dot{x} \\ \dot{y} \\ \dot{z} \end{bmatrix} + \begin{bmatrix} 0 \\ 0 \\ \dot{\alpha} \end{bmatrix} \times \begin{bmatrix} x \\ y \\ z \end{bmatrix} = \begin{bmatrix} \dot{x} - y\dot{\alpha} \\ \dot{y} + x\dot{\alpha} \\ \dot{z} \end{bmatrix} \tag{10}$$

is obtained, using Euler's rule of differentiation ${}_R\mathbf{v}_G = ({}_R\mathbf{r}_{OG})^{\cdot} + {}_R\boldsymbol{\omega}_{IR} \times {}_R\mathbf{r}_{OG}$. Introducing the set of coordinates $\mathbf{q} = [x, y, z, \alpha, \beta, \gamma]^{\mathrm{T}} \in \mathbb{R}^6$, the Jacobian matrices of rotation $\mathbf{J}_R$ and translation $\mathbf{J}_G$ are obtained with (7) and (10) as

$${}_B\mathbf{J}_R = \frac{\partial\,{}_B\boldsymbol{\Omega}}{\partial\dot{\mathbf{q}}} = \begin{bmatrix} 0 & 0 & 0 & \mathrm{s}\beta\mathrm{s}\gamma & \mathrm{c}\gamma & 0 \\ 0 & 0 & 0 & \mathrm{s}\beta\mathrm{c}\gamma & -\mathrm{s}\gamma & 0 \\ 0 & 0 & 0 & \mathrm{c}\beta & 0 & 1 \end{bmatrix}, {}_R\mathbf{J}_G = \frac{\partial\,{}_R\mathbf{v}_G}{\partial\dot{\mathbf{q}}} = \begin{bmatrix} 1 & 0 & 0 & -y & 0 & 0 \\ 0 & 1 & 0 & +x & 0 & 0 \\ 0 & 0 & 1 & 0 & 0 & 0 \end{bmatrix}. \tag{11}$$

The relative position of the center of gravity $S$ with respect to the geometric center $G$ is given as $\mathbf{r}_{GS} = e\,\mathbf{e}_x^B$, using the eccentric distance $e$. For reasons of notation, the bijective map

$$j: \quad \mathbb{R}^3 \to \mathbb{R}^{3\times 3}: \quad \mathbf{a} = \begin{bmatrix} a_1 \\ a_2 \\ a_3 \end{bmatrix} \mapsto \tilde{\mathbf{a}} = \begin{bmatrix} 0 & -a_3 & a_2 \\ a_3 & 0 & -a_1 \\ -a_2 & a_1 & 0 \end{bmatrix}, \tag{12}$$

is introduced, such that the cross product $\mathbf{a} \times \mathbf{b}$ can be written as matrix product of $\tilde{\mathbf{a}}\mathbf{b}$.

[1] The rotation matrix $\mathbf{R}$ becomes singular for $\beta = 0$ and $\beta = \pi$. However, the following simulation results show that the inversion of the tippedisk is far from singularity, which proves the validity of this parameterization.

https://doi.org/10.3311/ECCOMASMBD2021-113

## 5 KINETICS

The virtual work [16, 12] of a single rigid body is given coordinate free as

$$\delta W = \begin{bmatrix} \delta \mathbf{r}_G \\ \delta \boldsymbol{\varphi} \end{bmatrix} \cdot \left( \begin{bmatrix} m\,\mathbb{1} & m\tilde{\mathbf{r}}_{GS}^{\mathrm{T}} \\ m\,\tilde{\mathbf{r}}_{GS} & \boldsymbol{\Theta}_G \end{bmatrix} \begin{bmatrix} \mathbf{a}_G \\ \boldsymbol{\Psi} \end{bmatrix} - \begin{bmatrix} -m\boldsymbol{\Omega} \times (\boldsymbol{\Omega} \times \mathbf{r}_{GS}) \\ -\boldsymbol{\Omega} \times (\boldsymbol{\Theta}_G \boldsymbol{\Omega}) \end{bmatrix} - \begin{bmatrix} \mathbf{F}_G^{\mathrm{ext}} \\ \mathbf{M}_G^{\mathrm{ext}} \end{bmatrix} \right). \tag{13}$$

According to Eq. (9) the geometric center $G$ is parameterized with respect to the rotating $R$-frame[2]. Since the inertia tensor in the body-fixed $B$-frame ${}_B\boldsymbol{\Theta}_G$ is constant, it is convenient to express the angular velocity $\boldsymbol{\Omega}$ and the angular acceleration $\boldsymbol{\Psi}$ with respect to the body-fixed $B$-frame, so that the virtual work Eq. (13) expressed in mixed $R$- and $B$-coordinates reads as

$$\delta W = \begin{bmatrix} {}_R\delta \mathbf{r}_G \\ {}_B\delta \boldsymbol{\varphi} \end{bmatrix}^{\mathrm{T}} \left( \begin{bmatrix} m\mathbf{I} & m_R\tilde{\mathbf{r}}_{GS}^{\mathrm{T}}\mathbf{A}_{RB} \\ m\,{}_B\tilde{\mathbf{r}}_{GS}\mathbf{A}_{RB}^{\mathrm{T}} & {}_B\boldsymbol{\Theta}_G \end{bmatrix} \begin{bmatrix} {}_R\mathbf{a}_G \\ {}_B\boldsymbol{\Psi} \end{bmatrix} - \begin{bmatrix} -m\,{}_R\boldsymbol{\Omega} \times ({}_R\boldsymbol{\Omega} \times {}_R\mathbf{r}_{GS}) \\ -{}_B\boldsymbol{\Omega} \times ({}_B\boldsymbol{\Theta}_G\,{}_B\boldsymbol{\Omega}) \end{bmatrix} \right) - \delta W^{\mathrm{ext}}, \tag{14}$$

where

$$\delta W^{\mathrm{ext}} = \delta \mathbf{q}^{\mathrm{T}} \mathbf{f}^{\mathrm{ext}} = \begin{bmatrix} {}_R\delta \mathbf{r}_G \\ {}_B\delta \boldsymbol{\varphi} \end{bmatrix}^{\mathrm{T}} \begin{bmatrix} {}_R\mathbf{F}_G^{\mathrm{ext}} \\ {}_B\mathbf{M}_G^{\mathrm{ext}} \end{bmatrix} \tag{15}$$

denotes the virtual work of external forces an torques caused by force elements or contact forces. The introduced kinematics from Eq. (9), induces the variation of the geometric center as

$${}_R\delta \mathbf{r}_G = {}_R\mathbf{J}_G \delta \mathbf{q}. \tag{16}$$

Together with the $\delta\mathbf{q}$-induced variation of the orientation

$${}_B\delta \boldsymbol{\varphi} = {}_B\mathbf{J}_R \delta \mathbf{q}, \tag{17}$$

the virtual work (induced by the variation of coordinates $\delta\mathbf{q}$) yields

$$\delta W = \delta \mathbf{q}^{\mathrm{T}} \begin{bmatrix} {}_R\mathbf{J}_G \\ {}_B\mathbf{J}_R \end{bmatrix}^{\mathrm{T}} \cdot \left( \begin{bmatrix} m\mathbf{I} & m_R\tilde{\mathbf{r}}_{GS}^{\mathrm{T}}\mathbf{A}_{RB} \\ m\,{}_B\tilde{\mathbf{r}}_{GS}\mathbf{A}_{RB}^{\mathrm{T}} & {}_B\boldsymbol{\Theta}_G \end{bmatrix} \begin{bmatrix} {}_R\mathbf{a}_G \\ {}_B\boldsymbol{\Psi} \end{bmatrix} - \begin{bmatrix} -m\,{}_R\boldsymbol{\Omega} \times ({}_R\boldsymbol{\Omega} \times {}_R\mathbf{r}_{GS}) \\ -{}_B\boldsymbol{\Omega} \times ({}_B\boldsymbol{\Theta}_G\,{}_B\boldsymbol{\Omega}) \end{bmatrix} \right) - \delta W^{\mathrm{ext}}, \tag{18}$$

from which the equation of motion can be extracted as

$$\begin{bmatrix} {}_R\mathbf{J}_G \\ {}_B\mathbf{J}_R \end{bmatrix}^{\mathrm{T}} \cdot \left( \begin{bmatrix} m\mathbf{I} & m_R\tilde{\mathbf{r}}_{GS}^{\mathrm{T}}\mathbf{A}_{RB} \\ m\,{}_B\tilde{\mathbf{r}}_{GS}\mathbf{A}_{RB}^{\mathrm{T}} & {}_B\boldsymbol{\Theta}_G \end{bmatrix} \begin{bmatrix} {}_R\mathbf{a}_G \\ {}_B\boldsymbol{\Psi} \end{bmatrix} - \begin{bmatrix} -m\,{}_R\boldsymbol{\Omega} \times ({}_R\boldsymbol{\Omega} \times {}_R\mathbf{r}_{GS}) \\ -{}_B\boldsymbol{\Omega} \times ({}_B\boldsymbol{\Theta}_G\,{}_B\boldsymbol{\Omega}) \end{bmatrix} \right) = \mathbf{f}^{\mathrm{ext}}. \tag{19}$$

Inserting the introduced kinematics in Eq. (19) yields an equation of the form

$$\mathbf{M}(\mathbf{q})\ddot{\mathbf{q}} - \mathbf{h}(\mathbf{q}, \dot{\mathbf{q}}) = \mathbf{f}^{\mathrm{ext}} \tag{20}$$

with symmetric mass matrix

$$\mathbf{M}(\mathbf{q}) = \begin{bmatrix} \mathbf{M}_{11} & \mathbf{M}_{12} \\ \mathrm{sym.} & \mathbf{M}_{22} \end{bmatrix}, \tag{21}$$

$$\mathbf{M}_{11} = \begin{bmatrix} m & 0 & 0 \\ 0 & m & 0 \\ 0 & 0 & m \end{bmatrix}, \tag{22}$$

$$\mathbf{M}_{22} = \begin{bmatrix} M_{22,11} & \cdot & \mathrm{sym.} \\ M_{22,12} & Ac^2\gamma + Bs^2\gamma & \cdot \\ M_{22,13} & 0 & C \end{bmatrix}, \tag{23}$$

$$\mathbf{M}_{12} = \begin{bmatrix} -my - mec\beta s\gamma & 0 & -mes\gamma \\ mx + mec\gamma & -mes\beta s\gamma & mec\beta c\gamma \\ 0 & mec\beta s\gamma & mes\beta c\gamma \end{bmatrix}, \tag{24}$$

[2] In [12] there is a typo in Eq. (2.36), since with ${}_I\mathbf{a}_P$ the acceleration of the geometric center must correspond to ${}_I\mathbf{a}_G$.

https://doi.org/10.3311/ECCOMASMBD2021-113

$$M_{22,11} = m(x^2+y^2) + 2me(xc\gamma + yc\beta s\gamma) + (As^2\gamma + Bc^2\gamma)s^2\beta + Cc^2\beta, \tag{25}$$
$$M_{22,12} = (A-B)s\beta s\gamma c\gamma - mexs\beta s\gamma, \tag{26}$$
$$M_{22,13} = mexc\beta c\gamma + meys\gamma + Cc\beta, \tag{27}$$

and vector of gyroscopic forces

$$\mathbf{h}(\mathbf{q},\dot{\mathbf{q}}) := \begin{bmatrix} h_1 & h_2 & h_3 & h_4 & h_5 & h_6 \end{bmatrix}^{\mathrm{T}}, \tag{28}$$

$$h_1 = m\left[x\dot{\alpha}^2 + 2\dot{y}\dot{\alpha}\right] + me\left[(\dot{\alpha}^2+\dot{\gamma}^2)c\gamma - 2\dot{\alpha}\dot{\beta}s\beta s\gamma + 2\dot{\alpha}\dot{\gamma}c\beta c\gamma\right], \tag{29}$$
$$h_2 = m\left[y\dot{\alpha}^2 - 2\dot{x}\dot{\alpha}\right] + me\left[(\dot{\alpha}^2+\dot{\beta}^2+\dot{\gamma}^2)c\beta s\gamma + 2\dot{\alpha}\dot{\gamma}s\gamma + 2\dot{\beta}\dot{\gamma}s\beta c\gamma\right], \tag{30}$$
$$h_3 = me\left[\dot{\beta}^2 s\beta s\gamma + \dot{\gamma}^2 s\beta s\gamma - 2\dot{\beta}\dot{\gamma}c\beta c\gamma\right], \tag{31}$$
$$\begin{aligned} h_4 = &-2m\left[x\dot{x}\dot{\alpha} + y\dot{y}\dot{\alpha}\right] \\ &- me\left[2\dot{x}\dot{\alpha}c\gamma + (2\dot{y}\dot{\alpha} - x\dot{\beta}^2 - x\dot{\gamma}^2)c\beta s\gamma\right. \\ &- 2x\dot{\alpha}\dot{\gamma}s\gamma - 2x\dot{\beta}\dot{\gamma}s\beta c\gamma + y\dot{\gamma}^2 c\gamma - 2y\dot{\alpha}\dot{\beta}s\beta s\gamma + 2y\dot{\alpha}\dot{\gamma}c\beta c\gamma\left.\right] \\ &- (A-B)\left[\dot{\beta}^2 c\beta s\gamma c\gamma + 2\dot{\alpha}\dot{\gamma}s^2\beta s\gamma c\gamma + \dot{\beta}\dot{\gamma}s\beta(c^2\gamma - s^2\gamma)\right] \\ &- 2(As^2\gamma + Bc^2\gamma - C)\dot{\alpha}\dot{\beta}s\beta c\beta + C\dot{\beta}\dot{\gamma}s\beta, \end{aligned} \tag{32}$$
$$\begin{aligned} h_5 = &me\left[2\dot{x}\dot{\alpha} - y\dot{\alpha}^2\right]s\beta s\gamma + (A-B)\left[2\dot{\beta}\dot{\gamma}s\gamma c\gamma - \dot{\alpha}\dot{\gamma}s\beta(c^2\gamma - s^2\gamma)\right] \\ &+ (As^2\gamma + Bc^2\gamma)\dot{\alpha}^2 s\beta c\beta - C\left[\dot{\alpha}^2 s\beta c\beta + \dot{\alpha}\dot{\gamma}s\beta\right], \end{aligned} \tag{33}$$
$$\begin{aligned} h_6 = &-me\left[2\dot{y}\dot{\alpha} + x\dot{\alpha}^2\right]s\gamma - me\left[2\dot{x}\dot{\alpha} - y\dot{\alpha}^2\right]c\beta c\gamma \\ &+ (A-B)\left[(\dot{\alpha}^2 s^2\beta - \dot{\beta}^2)s\gamma c\gamma + \dot{\alpha}\dot{\beta}(c^2\gamma - s^2\gamma)s\beta\right] + C\dot{\alpha}\dot{\beta}s\beta. \end{aligned} \tag{34}$$

For a shorter notation, the abbreviations $c\gamma = \cos\gamma$ and $c^2\gamma = \cos^2\gamma$ are used. As the points $C_1$ and $S$ are not directly paramerterized, the rigid body formula ${}_R\mathbf{v}_P = {}_R\mathbf{v}_G + {}_R\boldsymbol{\Omega} \times {}_R\mathbf{r}_{GP}$ is used to obtain the Jacobian ${}_R\mathbf{J}_P = {}_R\mathbf{J}_G - {}_R\tilde{\mathbf{r}}_{GP}\,{}_R\mathbf{J}_R$ of an arbitrary body point $P$, where Jacobian ${}_R\mathbf{J}_R = \mathbf{A}_{RB}\,{}_B\mathbf{J}_R$ holds. The right hand side of Eq. (20) contains the generalized gravitational force

$$\begin{aligned} \mathbf{f}_G &= -mg\,{}_R\mathbf{J}_S{}^{\mathrm{T}}\,{}_R\mathbf{e}_z^I = -mg\,({}_R\mathbf{J}_G - {}_R\tilde{\mathbf{r}}_{GS}\,{}_R\mathbf{J}_R)^{\mathrm{T}}\,{}_R\mathbf{e}_z^R \\ &= -mg\begin{bmatrix} 0 & 0 & 1 & 0 & ec\beta s\gamma & es\beta c\gamma \end{bmatrix}^{\mathrm{T}}, \end{aligned} \tag{35}$$

the normal and tangential generalized contact forces $\mathbf{w}_N\lambda_N$ and $\mathbf{W}_T\boldsymbol{\lambda}_T$ with generalized force directions

$$\begin{aligned} \mathbf{w}_N &= {}_R\mathbf{J}_{C_1}{}^{\mathrm{T}}\,{}_R\mathbf{e}_z^R = ({}_R\mathbf{J}_G - {}_R\tilde{\mathbf{r}}_{GC_1}\,{}_R\mathbf{J}_R)^{\mathrm{T}}\,{}_R\mathbf{e}_z^R \\ &= \begin{bmatrix} 0 & 0 & 1 & 0 & -rc\beta & 0 \end{bmatrix}^{\mathrm{T}}, \end{aligned} \tag{36}$$
$$\begin{aligned} \mathbf{W}_T &= {}_R\mathbf{J}_{C_1}{}^{\mathrm{T}}\begin{bmatrix} {}_R\mathbf{e}_x^R & {}_R\mathbf{e}_y^R \end{bmatrix} = ({}_R\mathbf{J}_G - {}_R\tilde{\mathbf{r}}_{GC_1}\,{}_R\mathbf{J}_R)^{\mathrm{T}}\begin{bmatrix} {}_R\mathbf{e}_x^R & {}_R\mathbf{e}_y^R \end{bmatrix} \\ &= \begin{bmatrix} 1 & 0 & 0 & rc\beta - y & 0 & r \\ 0 & 1 & 0 & x & -rs\beta & 0 \end{bmatrix}^{\mathrm{T}} \end{aligned} \tag{37}$$

and writes as $\mathbf{f}^{\mathrm{ext}} = \mathbf{f}_G + \mathbf{w}_N\lambda_N + \mathbf{W}_T\boldsymbol{\lambda}_T$. The contact point $C_1$ does not detach during the inversion of the tippedisk, see [12]. This motivates the bilateral constraint $\mathbf{g}_N = 0$, which forces the gap from Eq. (4) to zero. The application of the bilateral constraint on position level leads to a system of differential algebraic equations (DAE) with index three. This index can be reduced by formulating the bilateral constraint on acceleration level

$$\text{for } t = 0 \quad \mathbf{g}_N(0) = \dot{\mathbf{g}}_N(0) = 0, \text{ for } t \geq 0 \quad \ddot{\mathbf{g}}_N = \mathbf{w}_N^{\mathrm{T}}\ddot{\mathbf{q}} + \dot{\mathbf{w}}_N^{\mathrm{T}}\dot{\mathbf{q}} = 0. \tag{38}$$

In this case the scalar normal force $\lambda_N$ takes the role of a Lagrange multiplier, which forces the constraint to be fulfilled. In [12] it is shown that smooth Coulomb friction

$$\boldsymbol{\lambda}_T = \mu\lambda_N\frac{\boldsymbol{\gamma}_T}{||\boldsymbol{\gamma}_T|| + \varepsilon}, \tag{39}$$

https://doi.org/10.3311/ECCOMASMBD2021-113

with the friction coefficient $\mu$ and the smoothing parameter $\varepsilon$ is sufficient to describe the inversion phenomenon qualitatively. The kinematic quantity $\boldsymbol{\gamma}_T$ describes the relative slip velocity between the associated contact points $C_1$ and $D_1$ with respect to the rotating $R$-frame and is defined as

$$\boldsymbol{\gamma}_T := \begin{bmatrix} \gamma_{Tx} \\ \gamma_{Ty} \end{bmatrix} = \begin{bmatrix} {}_R\mathbf{e}_x^R \cdot ({}_R\mathbf{J}_{C_1}\dot{\mathbf{q}}) \\ {}_R\mathbf{e}_y^R \cdot ({}_R\mathbf{J}_{C_1}\dot{\mathbf{q}}) \end{bmatrix}. \tag{40}$$

Moreover, we mention that the friction force $\boldsymbol{\lambda}_T$ here depends linearly on the normal contact force $\lambda_N$ and therefore directly on the Lagrange multiplier $\lambda_N$ of the bilateral constraint. The smoothing is hereby motivated, as set-valued Coulomb-Contensou friction couples drilling and tangential friction [17]. If the macroscopic contact point experiences a spinning velocity, then from a microscopic point of view the associated contact area is forced to be in slip state. As the tippedisk is always spinning during inversion, the contact point $C_1$ slips permanently, such that smooth Coulomb friction is justified.

## 6 SIMULATION

Introducing the trivial kinematic relation $\dot{\mathbf{q}} = \mathbf{u}$, which is combined with the equation of motion from Eq. (20) and the bilateral constraint on acceleration level $\ddot{\mathbf{g}}_N(t) = 0$, considering smooth coulomb friction, the system

$$\underbrace{\begin{bmatrix} \mathbf{I} & \mathbf{0} & \mathbf{0} \\ \mathbf{0} & \mathbf{M} & -\mathbf{W}_{NT} \\ \mathbf{0} & \mathbf{w}_N^{\mathrm{T}} & \mathbf{0} \end{bmatrix}}_{\mathbf{A}} \begin{bmatrix} \dot{\mathbf{q}} \\ \dot{\mathbf{u}} \\ \lambda_N \end{bmatrix} = \begin{bmatrix} \mathbf{u} \\ \mathbf{h} + \mathbf{f}_G \\ -\dot{\mathbf{w}}_N^{\mathrm{T}}\dot{\mathbf{q}} \end{bmatrix}, \tag{41}$$

with $\mathbf{W}_{NT} := \mathbf{w}_N - \mu \mathbf{W}_T \frac{\boldsymbol{\gamma}_T}{\|\boldsymbol{\gamma}_T\|+\varepsilon}$ is obtained. Equation (41) corresponds to an linear equation system (with invertible $\mathbf{A}$-matrix) such that it is possible to derive a first order ordinary differential equation (ODE) in generalized coordinates $\mathbf{q}$ and velocities $\mathbf{u}$. This ODE can be solved with any standard integrator, e.g., a four staged Runge-Kutta method. At this point we restrict us to the integrator *ode*15*s* from MATLAB. For a more detailed derivation, we refer to [12].

### 6.1 Initial conditions and model parameters

In this section, the results of numerical simulations using the derived minimal model are discussed. As shown in Figure 4, the tippedisk is called *not inverted* when $\beta = \frac{\pi}{2}$ and $\gamma = -\frac{\pi}{2}$ holds. In this configuration the center of gravity $S$ lies below the geometric center $G$. Vice versa, we call the disk *inverted* if $\beta = \frac{\pi}{2}$ and $\gamma = \frac{\pi}{2}$, i.e., the center of gravity $S$ lies above the geometric center $G$. Due to the periodicity of the trigonometric functions sine and cosine these definitions are not unique, since for $\beta = -\frac{\pi}{2}$ and $\gamma = \frac{\pi}{2}$ the tippedisk is also in a inverted configuration. However, the following numerical results show that $\beta$ is in the range of $(0, \pi)$ during the inversion, so this ambiguity does not matter.

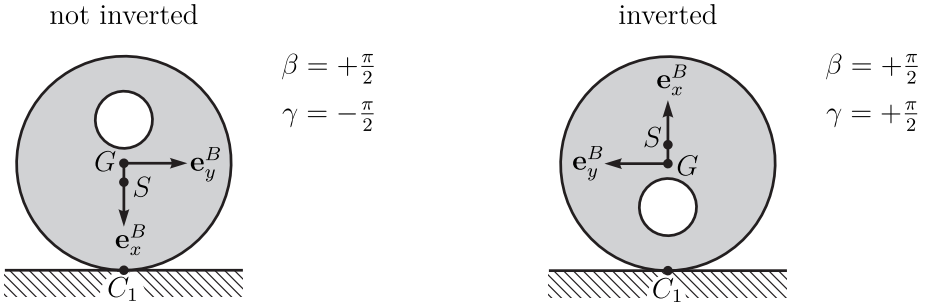


Figure 4: Non-inverted and inverted configuration of the tippedisk.

The initial conditions, at time $t_0 = 0\,\mathrm{s}$, are given in Table 2. The end time of the simulation is set to $t_1 = 5\,\mathrm{s}$. According to Table 2, the disk rotates initially with closed contact point in non-inverted orientation without slippage, i.e., $||\boldsymbol{\gamma}_T|| = 0$. For the following simulations, the friction coefficient $\mu = 0.3$ and smoothing parameter $\varepsilon = 0.1\frac{\mathrm{m}}{\mathrm{s}}$ are chosen.

Table 2: Initial condition: Perturbed non-inverted spinning with closed contact.

| Coordinate | Magnitude | Unit | Velocity | Magnitude | Unit |
|---|---|---|---|---|---|
| $x_0$ | 0 | m | $\dot{x}_0$ | 0 | m/s |
| $y_0$ | 0 | m | $\dot{y}_0$ | 0 | m/s |
| $z_0$ | 0.045 | m | $\dot{z}_0$ | 0 | m/s |
| $\alpha_0$ | 0 | rad | $\dot{\alpha}_0$ | 40 | rad/s |
| $\beta_0$ | $0.5\pi$ | rad | $\dot{\beta}_0$ | 0 | rad/s |
| $\gamma_0$ | $-0.5\pi + 0.1$ | rad | $\dot{\gamma}_0$ | $-\dot{\alpha}_0 \cos(\beta_0) = 0$ | rad/s |

### 6.2 Simulation results

The numerical results of the system from Eq. (41), assuming smooth Coulomb friction Eq. (39) and initial conditions from Table 2 are shown in color in Figure 5. For comparison, the results of the quaternion-based model from [12], which assumes unilateral contact and smooth Coulomb friction, are shown in black (dotted/dashed). At $t = 0\,\mathrm{s}$, the tippedisk is almost in the non-inverted configuration, as $\beta = +\frac{\pi}{2}$ and $\gamma = -\frac{\pi}{2} + 0.1$ holds. Starting from this, the angle $\gamma$ increases quickly from $-\frac{\pi}{2}$ and ends in an asymptotic oscillation around $+\frac{\pi}{2}$. During this first stage of motion the inclination angle $\beta$ does only change slightly, such that the inversion of the tippedisk can be directly related to the change of the angle $\gamma$. Both angles $\beta$ and $\gamma$ are increasingly superimposed by small oscillations with higher frequency. In the $z_S$-graph, the height of the center of gravity $S$ is shown, growing from $r - e$ to $r + e$, which also indicates that the disk ends up in an inverted configuration with closed contact. During this inversion process, the kinetic energy $E_{\mathrm{kin}}$ decreases while the potential energy $E_{\mathrm{pot}}$ increases, such that the total energy $E_{\mathrm{tot}}$ dissipates from $0.38\,\mathrm{Nm}$ to $0.36\,\mathrm{Nm}$ for $t < 0.5\,\mathrm{s}$. After this initial fast decay, the total energy slowly decreases as the tippedisk rotates near the inverted stationary solution. In the considered time interval, the rotation angle $\alpha$ increases almost linearly. The associated spinning velocity $\dot{\alpha}$ initially increases as the height $z_S$ of the center of gravity drops, followed by a saturating decrease on an 'intermediate' timescale. The long-term behavior is characterized by a slow decrease of the spinning velocity $\dot{\alpha}$.

https://doi.org/10.3311/ECCOMASMBD2021-113

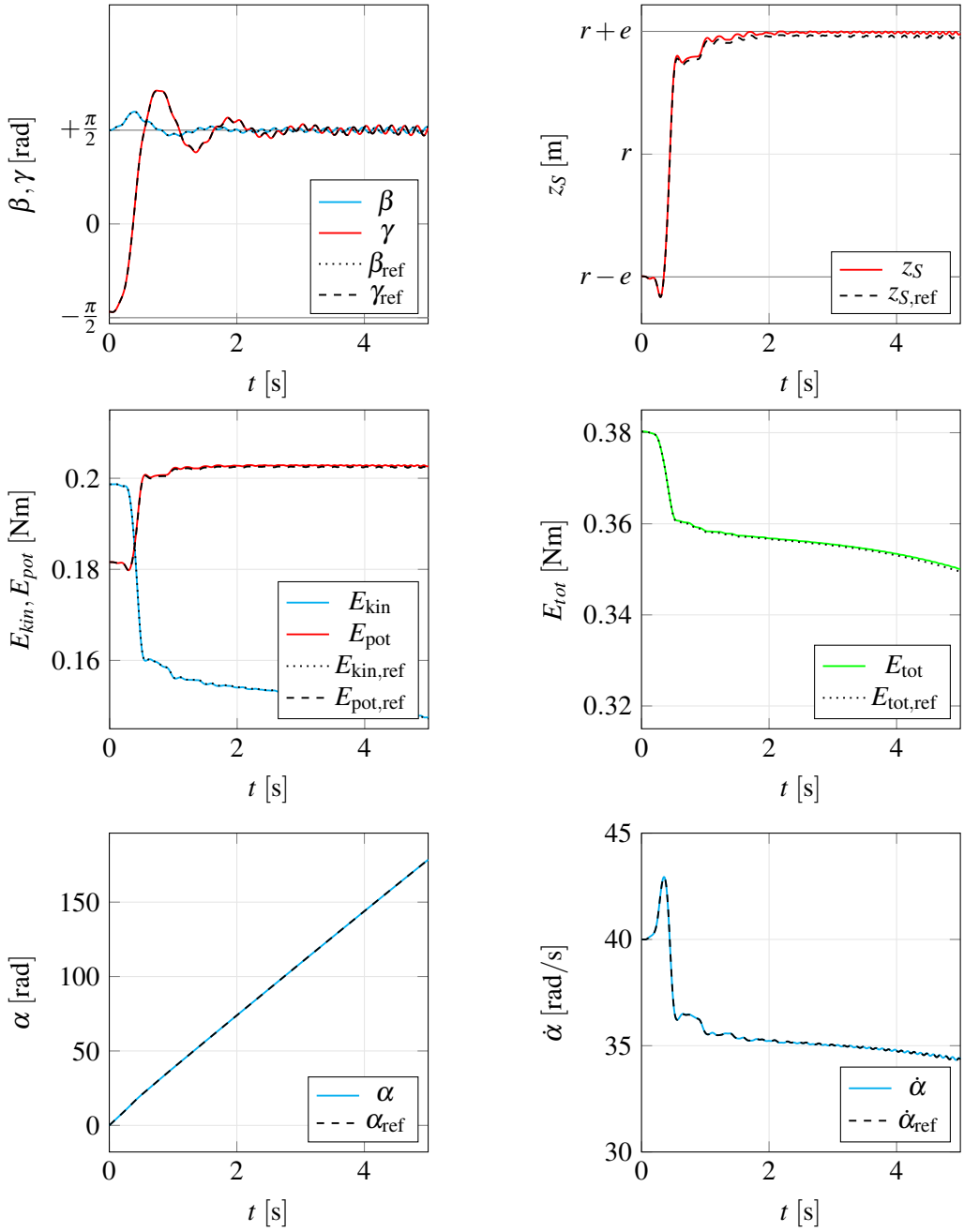


Figure 5: Simulation results showing the inversion of the tippedisk. The corresponding initial conditions are given in Table 2.

## 7 DISCUSSION

The simulation results from Fig. 5 show that the derived model with smooth Coulomb friction and a bilateral constrained contact point is able to describe the inversion behavior of the tippedisk. Comparison with the quaternion-based time stepping model proves that both models lead to the same results (with respect to numerical error), which shows the correctness of the new minimal model for the inversion phenomenon. As the Change of the spinning velocity $\dot{\alpha}$ is relatively small, the associated rotation angle $\alpha$ depends almost linearly on time $t$, i.e., $\alpha$ is approximately given as $\alpha(t) \approx \Omega t$ with constant spinning velocity $\Omega$. At this point, the derivation of the new minimal model seems artificial, since other models from [12] already describe the inversion phenomenon of the tippedisk correctly and even lead to the exactly same results, cf. Fig. 5. However, to characterize the stability of the inverted and non-inverted stationary solutions, it is convenient

to linearize the equations of motion around $\beta = +\frac{\pi}{2}$ and $\gamma = \pm\frac{\pi}{2}$. A given parametrization of the geometric center $G$ (or center of gravity $S$) with respect to the inertial frame $I$ yields system equations that depend explicitly on the angle $\alpha$, see [12]. As $\alpha(t)$ is a function in time $t$, the linearized system matrices are time dependent, therefore Lypunov's indirect method can not be applied and Floquet theory must be used, which greatly complicates the closed form analysis. In this work, we have introduced a new parametrization of the geometric center $G$ with respect to the rotating $R$-frame, which led to system equations that do not explicitly depend on $\alpha$ and thus do not depend on time $t$. This has the advantage that the linearized system matrices are constant and thus Lyapunov's indirect method can be applied to study the local stability behavior.

## 8 CONCLUSIONS

The tippedisk introduced in [12] serves as a link between analytical mechanics, theoretical mechanics and nonlinear dynamics. Our aim is to understand the nonlinear behavior behind the inversion phenomenon of the tippedisk. Therefore, a mathematical description is sought that will form the basis for future stability analyses of the nonlinear system. Depending on the parametrization, the system equations vary in their suitability for dynamic analysis. In this work, we have introduced a new minimal model of the tippedisk, which qualitatively describes the inversion phenomenon and has some advantages for future dynamical considerations, such as constant system matrices for the linearization around the inverted and non-inverted configurations. Based on the parametrization presented here, [13] applies Lyapunov's indirect method to obtain a closed-form expression for the critical spinning velocity $\Omega_{\text{crit}}$ above which the inverted spinning solution becomes stable. Moreover, the linear stability analysis indicates different timescales, suggesting slow-fast dynamical behavior. By analyzing this singularly perturbed structure, the complexity and order of the model can be reduced to obtain a lower dimensional dynamical system that describes the inversion phenomenon of the tippedisk, cf. [13, 14].

## ACKNOWLEDGMENTS

The authors declare that they have no conflicts of interest. This research received no specific grant from any funding agency in the public, commercial, or non-profit sectors.

## REFERENCES

[1] Moffatt, H.K.: Euler's disk and its finite-time singularity. Nature **404**(6780) (2000) 833–834

[2] Leine, R.I.: Experimental and theoretical investigation of the energy dissipation of a rolling disk during its final stage of motion. Arch Appl Mech **79**(11) (2009) 1063–1082

[3] Garcia, A., Hubbard, M.: Spin reversal of the rattleback: theory and experiment. Proc. R. Soc. Lond. A **418**(1854) (1988) 165–197

[4] Borisov, A.V., Mamaev, I.S.: Strange attractors in rattleback dynamics. Phys.-Usp. **46**(4) (2003) 393

[5] Magnus, K.: Kreisel. Springer, Berlin, Heidelberg, New York (1971)

[6] Cohen, R.J.: The tippe top revisited. American Journal of Physics **45**(1) (1977) 12–17

[7] Bou-Rabee, N.M., Marsden, J.E., Romero, L.A.: Tippe Top Inversion as a Dissipation-Induced Instability. SIAM J. Appl. Dyn. Syst. **3**(3) (2004) 352–377

[8] Rauch-Wojciechowski, S.: What does it mean to explain the rising of the tippe top? Regul. Chaot. Dyn. **13**(4) (2008) 316–331

[9] Moffatt, K., Shimomura, Y.: Spinning eggs — a paradox resolved. Nature **416**(6879) (2002) 385–386

[10] Branicki, M., Shimomura, Y.: Dynamics of an axisymmetric body spinning on a horizontal surface. IV. Stability of steady spin states and the 'rising egg' phenomenon for convex axisymmetric bodies. Proc. R. Soc. A. **462**(2075) (2006) 3253–3275

[11] Cross, R.: Why does a spinning egg rise? European Journal of Physics **39**(2) (2018) 025002

[12] Sailer, S., Eugster, S.R., Leine, R.I.: The Tippedisk: a Tippetop Without Rotational Symmetry. Regul. Chaot. Dyn. **25**(6) (2020) 553–580

[13] Sailer, S., Leine, R.I.: Model reduction of the tippedisk: a path to the full analysis. Nonlinear Dyn **105**(3) (2021) 1955–1975

[14] Sailer, S., Leine, R.I.: Singularly perturbed dynamics of the tippedisk. `arxiv:2109.02542 [physics.class-ph]` (2021)

[15] Le Saux, C., Leine, R.I., Glocker, C.: Dynamics of a Rolling Disk in the Presence of Dry Friction. J Nonlinear Sci **15**(1) (2005) 27–61

[16] Glocker, C.: Set-valued Force Laws: Dynamics of Non-smooth Systems. Volume 1 of Lecture Notes in Applied Mechanics. Springer Science & Business Media (2001)

[17] Leine, R.I., Glocker, C.: A set-valued force law for spatial Coulomb–Contensou friction. European Journal of Mechanics-A/Solids **22**(2) (2003) 193–216

https://doi.org/10.3311/ECCOMASMBD2021-140



# A Nonsmooth Dynamics Perspective on State Observer Design for Mechanical Systems with Unilateral Constraints

**Pascal V. Preiswerk, Remco I. Leine**

Institute for Nonlinear Mechanics
University of Stuttgart
Pfaffenwaldring 9, 70569 Stuttgart, Germany
[preiswerk, leine]@inm.uni-stuttgart.de

## ABSTRACT

One of the main difficulties in the state observer design for impulsive mechanical systems is the so-called peaking phenomenon: even for an arbitrarily small pre-impact estimation error, a slight mismatch between the impact time instants of the observer and the observed system can lead to large post-impact estimation error. Therefore, Lyapunov's stability theorems cannot be directly applied. For linear mechanical systems with unilateral constraints, we propose to take a Nonsmooth Dynamics perspective on the problem, which allows to sidestep the main difficulties by transforming and approximating the original continuous-time system by a discrete linear complementarity system through the use of the Schatzman-Paoli scheme. The discretization acts as a regularization, i.e. the impacts take place over two consecutive time steps. Furthermore, it involves force and impact laws on position-level with the favorable property of maximal monotonicity. Finally, a passivity-based observer design for discrete linear complementarity systems can be applied.

**Keywords:** Nonsmooth systems, linear complementarity systems, impacts, unilateral constraints, peaking phenomenon.

## 1 INTRODUCTION

An important aspect of the state observer design for impulsive mechanical systems is whether or not the impact time instants, where state jumps occur, are known. Most proposed observers assume that these impact time instants can directly be extracted from measurements, for example by measuring all relevant positions in a system where the impact time instants are position dependent [1, 2] or by directly measuring contact [3]. This allows for the design of a state observer that exhibits impacts (or state jumps) that occur at the same time instants as in the observed system. Under a maximal monotone impact law, it is then possible to construct a Lyapunov function which does not increase over impacts, and with which asymptotic stability of the error dynamics (i.e. the time evolution of the difference between the estimated state and the actual state) can be shown.
Only few attempts have been made to design state observers in the case of unknown impact time instants, such that the corresponding state jumps of the observed system and the state observer do not coincide. One of the main difficulties in that case is the peaking phenomenon: even for an arbitrarily small pre-impact estimation error, a slight mismatch in the impact time instants can lead to a large post-impact velocity error caused by velocity jumps. This makes it difficult to show asymptotic stability of the estimation error dynamics using Lyapunov's stability theory. In fact, due to the peaking phenomenon, the estimation error dynamics is not Lyapunov stable by definition. One approach for such systems is to find a state transformation from the original system into a new system without state jumps [4, 5], for which conventional state observer techniques can be applied. However, such a transformation does not always exist and is in general difficult to find.
In this paper, we aim at sidestepping the main difficulties in the observer design for impulsive mechanical systems by first discretizing the continuous-time problem using the Schatzman-Paoli scheme, in which force and impact laws are formulated on position level with the favorable property of maximal monotonicity.

https://doi.org/10.3311/ECCOMASMBD2021-140

## 2 CONTINUOUS-TIME PROBLEM

We consider a linear mechanical system which is subjected to unilateral constraints and a time-dependent external forcing. Let $\mathbf{q}(t)$ be the generalized coordinates and $\mathbf{u}(t)$ be the corresponding generalized velocities. In general, $\mathbf{u}(t)$ is assumed to be a function of bounded variation, leading to absolutely continuous $\mathbf{q}(t)$. The non-impulsive part of the dynamics is described by

$$\begin{aligned} \dot{\mathbf{q}} &= \mathbf{u}, \\ \mathbf{M}\dot{\mathbf{u}} + \mathbf{K}\mathbf{q} + \mathbf{D}\mathbf{u} &= \mathbf{W}\boldsymbol{\lambda} + \mathbf{f}(t), \end{aligned} \tag{1}$$

where the the mass matrix $\mathbf{M} = \mathbf{M}^\mathsf{T} \succ 0$, the stiffness matrix $\mathbf{K} = \mathbf{K}^\mathsf{T} \succ 0$ and the damping matrix $\mathbf{D} \succ 0$ are assumed to be constant and positive definite. The unilateral constraints are described by linear inequality conditions $\mathbf{g}(\mathbf{q}) = \mathbf{W}^\mathsf{T}\mathbf{q} \geq 0$, leading to the non-impulsive constraint forces $\boldsymbol{\lambda}$. The generalized force directions, given by the columns of $\mathbf{W} = \left(\frac{\partial \mathbf{g}}{\partial \mathbf{q}}\right)^\mathsf{T}$, are assumed to be constant and linearly independent (such that $\mathbf{W}$ has full rank). Furthermore, the system is excited by a bounded, time-dependent external forcing $\mathbf{f}(t)$. Note that the equations of motion (1) by themselves do not allow for discontinuities in the generalized velocities $\mathbf{u}$. In order to describe velocity jumps due to impacts, the impulsive part of the dynamics, i.e. the impact equations, are given by

$$\mathbf{M}(\mathbf{u}^+ - \mathbf{u}^-) = \mathbf{W}\boldsymbol{\Lambda}, \tag{2}$$

where $\mathbf{u}^+(t)$ and $\mathbf{u}^-(t)$ denote the left and right limit of $\mathbf{u}$ at time $t$ and $\boldsymbol{\Lambda}$ are the impulsive constraint forces. For the components of the constraint forces $\boldsymbol{\lambda}$ and $\boldsymbol{\Lambda}$ we assume Signorini's law on position level

$$0 \leq \mathbf{g} \perp \boldsymbol{\lambda} \geq 0, \tag{3a}$$

$$0 \leq \mathbf{g} \perp \boldsymbol{\Lambda} \geq 0, \tag{3b}$$

where we used the notation $\mathbf{g} \geq 0$ to express the non-negativity of every component $g_i \geq 0 \,\forall\, i$ and the notation $\mathbf{g} \perp \boldsymbol{\lambda}$ to express the orthogonality $\mathbf{g}^\mathsf{T}\boldsymbol{\lambda} = 0$. Hence, (3a) is equivalent to $g_i \geq 0, \lambda_i \geq 0, g_i\lambda_i = 0$ for all $i$ and is referred to as an inequality complementarity condition. The constraint forces can alternatively be formulated on position-switched velocity level [6]: with $\boldsymbol{\gamma} = \mathbf{W}^\mathsf{T}\mathbf{u}$, the laws (3) are equivalent to the component-wise law

$$\begin{aligned} g_i(\mathbf{q}) = 0 : 0 \leq \gamma_i \perp \lambda_i \geq 0\,, \quad g_i(\mathbf{q}) > 0 : \lambda_i = 0, \\ g_i(\mathbf{q}) = 0 : 0 \leq \gamma_i \perp \Lambda_i \geq 0\,, \quad g_i(\mathbf{q}) > 0 : \Lambda_i = 0. \end{aligned} \tag{4}$$

In addition to the force laws (4), an impact law has to be specified for a full description of the dynamics. Instantaneous impact laws directly relate post-impact relative velocities to pre-impact relative velocities and, in consistency with (4), are formulated on velocity level. Here, we will make use of a generalized Newtonian impact law [7], which is written component-wise as

$$g_i(\mathbf{q}) = 0 :\ 0 \leq \xi_i \perp \Lambda_i \geq 0\,, \quad g_i(\mathbf{q}) > 0 :\ \Lambda_i = 0, \tag{5}$$

with the kinematic variables $\xi_i := \gamma_i^+ + \varepsilon_i\gamma_i^-$ and given coefficients of restitution $\varepsilon_i \in [0,1]$.

In view of the time discretization, it is convenient to merge (1) and (2) in a compact formulation containing both the non-impulsive and the impulsive dynamics. This leads to an equality of measures of the form [8, 9]

$$\begin{aligned} \mathrm{d}\mathbf{q} &= \mathbf{u}\mathrm{d}t, \\ \mathbf{M}\mathrm{d}\mathbf{u} + (\mathbf{K}\mathbf{q} + \mathbf{D}\mathbf{u} - \mathbf{f}(t))\mathrm{d}t &= \mathbf{W}\mathrm{d}\mathbf{P}, \end{aligned} \tag{6}$$

where $\mathrm{d}\mathbf{q}$ is the so-called differential measure of the generalized coordinates $\mathbf{q}$. Similarly, $\mathrm{d}\mathbf{u} = \dot{\mathbf{u}}\mathrm{d}t + (\mathbf{u}^+ - \mathbf{u}^-)\mathrm{d}\eta$ is the differential measure of the generalized velocities, allowing for discontinuities in the generalized velocities $\mathbf{u}$. Herein, $\mathrm{d}\eta$ is an atomic measure, being the sum of Dirac point measures [8]. Furthermore, $\mathrm{d}\mathbf{P} = \boldsymbol{\lambda}\mathrm{d}t + \boldsymbol{\Lambda}\mathrm{d}\eta$ is the differential contact effort measure.

https://doi.org/10.3311/ECCOMASMBD2021-140

The force laws (4) and the impact law (5) can be gathered in a description of measures

$$g_i(\mathbf{q}) = 0 : \ 0 \leq \xi_i \perp \int_{\mathscr{I}} \mathrm{d}P_i \geq 0 \ , \quad g_i(\mathbf{q}) > 0 : \ \int_{\mathscr{I}} \mathrm{d}P_i = 0, \tag{7}$$

where the sign (or nullity) of $g_i$ and $\xi_i$ is assumed to be constant during the interval $\mathscr{I}$ (e.g. a short time step as used in a time discretization). For brevity, (7) is usually written as

$$g_i(\mathbf{q}) = 0 : \ 0 \leq \xi_i \perp \mathrm{d}P_i \geq 0 \ , \quad g_i(\mathbf{q}) > 0 : \ \mathrm{d}P_i = 0, \tag{8}$$

refraining from referring to the assumption on $\mathscr{I}$.

### 2.1 DISCRETE-TIME PROBLEM

In the following we pursue an approach, where we first discretize the dynamics and then design a state observer for the discrete (and therefore approximate) system. As explained in the Introduction, this alleviates the problem of state jumps in the observer design.
Here, we will make use of the scheme of Schatzman and Paoli [10, 11]. This scheme involves an impact law on position level, and was originally motivated by the fact that it allows for a rigorous convergence proof (which is not given for other, more widely used schemes such as the Moreau scheme [9]). The reason for choosing this scheme is the fact that its direct formulation of the contact/impact law on position level gives access to the maximal monotonicity property. However, the practical application of this scheme is restricted to mechanical systems with frictionless unilateral constraints which are decoupled such that $\mathbf{w}_i^\mathsf{T}\mathbf{M}^{-1}\mathbf{w}_j = 0$ for $i \neq j$, where $\mathbf{w}_i = \frac{\partial g_i}{\partial \mathbf{q}}$. For system (6), the Schatzman-Paoli discretization scheme can be written as

$$\begin{aligned} &\mathbf{q}_{k+1} = \mathbf{q}_k + \Delta t \mathbf{u}_{k+1}, \\ &\mathbf{M}(\mathbf{u}_{k+1} - \mathbf{u}_k) + (\mathbf{K}\mathbf{q}_k + \mathbf{D}\mathbf{u}_k - \mathbf{f}_k)\Delta t = \mathbf{W}\mathbf{P}_k, \end{aligned} \tag{9}$$

together with

$$\begin{aligned} \boldsymbol{\xi}_k &:= \mathbf{g}_{k+1} + \varepsilon \mathbf{g}_{k-1}, \\ 0 \leq \boldsymbol{\xi}_k &\perp \mathbf{P}_k \geq 0. \end{aligned} \tag{10}$$

Therein, $\Delta t$ is the (constant) time step and variables being evaluated (or approximated) at the discrete times $t = t_k := k\Delta t$ are referred to with an index $k$, e.g. $\mathbf{q}_k := \mathbf{q}(t_k)$. Likewise, the discrete contact distance is $\mathbf{g}_k = \mathbf{W}^\mathsf{T}\mathbf{q}_k$ and the corresponding discrete contact velocity is $\boldsymbol{\gamma}_k = \mathbf{W}^\mathsf{T}\mathbf{u}_k$. To keep it simple, we will assume all coefficients of restitution $\varepsilon_i = \varepsilon$ to be equal. An important aspect of the Schatzman-Paoli scheme that the discrete impact law (10), i.e. $0 \leq \mathbf{g}_{k+1} + \varepsilon \mathbf{g}_{k-1} \perp \mathbf{P}_k \geq 0$, is formulated on position level. Other discretization schemes, which directly discretize the combined contact/impact law (8) on velocity level, require the introduction of an index set, indicating which contacts are closed at a given time instant. This is not the case for the Schatzman-Paoli scheme, since the discrete impact law (10) is not a direct discretization of (8). To understand its meaning, let $\boldsymbol{\xi}_k$ vanish over two consecutive time steps, i.e. $\boldsymbol{\xi}_{k-1} = \boldsymbol{\xi}_k = \mathbf{0}$. It then follows from the definition of $\boldsymbol{\xi}_k$ in (10) that

$$\begin{aligned} \frac{\boldsymbol{\xi}_k - \boldsymbol{\xi}_{k-1}}{\Delta t} &= \frac{\mathbf{g}_{k+1} - \mathbf{g}_k}{\Delta t} + \varepsilon \frac{\mathbf{g}_{k-1} - \mathbf{g}_{k-2}}{\Delta t} = \mathbf{W}^\mathsf{T} \left( \frac{\mathbf{q}_{k+1} - \mathbf{q}_k}{\Delta t} + \varepsilon \frac{\mathbf{q}_{k-1} - \mathbf{q}_{k-2}}{\Delta t} \right) \\ &= \mathbf{W}^\mathsf{T}(\mathbf{u}_{k+1} + \varepsilon \mathbf{u}_{k-1}) = \boldsymbol{\gamma}_{k+1} + \varepsilon \boldsymbol{\gamma}_{k-1} = \mathbf{0}. \end{aligned} \tag{11}$$

The last equality, $\boldsymbol{\gamma}_{k+1} + \varepsilon \boldsymbol{\gamma}_{k-1} = \mathbf{0}$, shows that Newton's impact law is fulfilled in a discretized sense over two time steps. Velocity jumps that occur instantaneously in continuous time take place over an interval of two time steps in the discretization, which can be seen as a regularization. Interestingly, the discretized system (9), (10) can be rewritten as what is known as a discrete

https://doi.org/10.3311/ECCOMASMBD2021-140

linear complementarity system (LCS, as introduced in [12, 13]). Indeed, by introducing the state $\mathsf{x}_k := \begin{pmatrix}\mathbf{q}_k^\mathsf{T} & \mathbf{u}_k^\mathsf{T}\end{pmatrix}^\mathsf{T}$, equations (9) can be written as

$$\begin{pmatrix}\mathbf{I} & -\Delta t\mathbf{I}\\ \mathbf{0} & \mathbf{M}\end{pmatrix}\mathsf{x}_{k+1} = \begin{pmatrix}\mathbf{I} & \mathbf{0}\\ -\Delta t\mathbf{K} & \mathbf{M}-\Delta t\mathbf{D}\end{pmatrix}\mathsf{x}_k + \begin{pmatrix}\mathbf{0}\\ \mathbf{W}\end{pmatrix}\mathbf{P}_k + \begin{pmatrix}\mathbf{0}\\ \Delta t\mathbf{I}\end{pmatrix}\mathbf{f}_k. \tag{12}$$

Note that we are writing variables and matrices related to the state-space description without serifs, whereas in our original description of the mechanical system we are using serifs (therefore, variables denoted by the same letter, are assigned a different meaning depending on whether they are written with or without serifs). After inverting the matrix on the left hand side, an update rule for the state is obtained as

$$\mathsf{x}_{k+1} = \begin{pmatrix}\mathbf{I} & \Delta t\mathbf{M}^{-1}\\ \mathbf{0} & \mathbf{M}^{-1}\end{pmatrix}\left[\begin{pmatrix}\mathbf{I} & \mathbf{0}\\ -\Delta t\mathbf{K} & \mathbf{M}-\Delta t\mathbf{D}\end{pmatrix}\mathsf{x}_k + \begin{pmatrix}\mathbf{0}\\ \mathbf{W}\end{pmatrix}\mathbf{P}_k + \begin{pmatrix}\mathbf{0}\\ \Delta t\mathbf{I}\end{pmatrix}\mathbf{f}_k\right], \tag{13}$$

where $\mathbf{0}$ denotes a zero matrix of appropriate dimensions. Finally, after simple matrix multiplications we arrive at

$$\mathsf{x}_{k+1} = \mathsf{A}\mathsf{x}_k + \mathsf{B}\mathbf{P}_k + \mathsf{E}\mathbf{f}_k, \tag{14}$$

with the corresponding system matrices $\mathsf{A}, \mathsf{B}$ and $\mathsf{E}$ given by

$$\mathsf{A} = \begin{pmatrix}\mathbf{I}-\Delta t^2\mathbf{M}^{-1}\mathbf{K} & \Delta t(\mathbf{I}-\Delta t\mathbf{M}^{-1}\mathbf{D})\\ -\Delta t\mathbf{M}^{-1}\mathbf{K} & \mathbf{I}-\Delta t\mathbf{M}^{-1}\mathbf{D}\end{pmatrix}, \quad \mathsf{B} = \begin{pmatrix}\Delta t\mathbf{M}^{-1}\mathbf{W}\\ \mathbf{M}^{-1}\mathbf{W}\end{pmatrix}, \quad \mathsf{E} = \begin{pmatrix}\Delta t^2\mathbf{M}^{-1}\\ \Delta t\mathbf{M}^{-1}\end{pmatrix}. \tag{15}$$

The discrete contact/impact law (10) can also be written in the state variables. By using the contact distance $\mathbf{g}_k = \mathbf{W}^\mathsf{T}\mathbf{q}_k$ and the first equation of (9) in (10) we have

$$\begin{aligned}\boldsymbol{\xi}_k &= \mathbf{W}^\mathsf{T}(\mathbf{q}_{k+1} + \varepsilon\mathbf{q}_{k-1}) = \mathbf{W}^\mathsf{T}(\mathbf{q}_{k+1} + \varepsilon(\mathbf{q}_k - \Delta t\mathbf{u}_k))\\ &= \begin{pmatrix}\mathbf{W}^\mathsf{T} & \mathbf{0}\end{pmatrix}\mathsf{x}_{k+1} + \varepsilon\begin{pmatrix}\mathbf{W}^\mathsf{T} & -\Delta t\mathbf{W}^\mathsf{T}\end{pmatrix}\mathsf{x}_k\\ &= \begin{pmatrix}\mathbf{W}^\mathsf{T} & \mathbf{0}\end{pmatrix}[\mathsf{A}\mathsf{x}_k + \mathsf{B}\mathbf{P}_k + \mathsf{E}\mathbf{f}_k] + \varepsilon\begin{pmatrix}\mathbf{W}^\mathsf{T} & -\Delta t\mathbf{W}^\mathsf{T}\end{pmatrix}\mathsf{x}_k,\end{aligned} \tag{16}$$

which can compactly be written as

$$\boldsymbol{\xi}_k = \mathsf{C}\mathsf{x}_k + \mathsf{D}\mathbf{P}_k + \mathsf{F}\mathbf{f}_k, \tag{17}$$

with the corresponding matrices

$$\mathsf{C} = \begin{pmatrix}[(1+\varepsilon)\mathbf{I}-\Delta t^2\mathbf{M}^{-1}\mathbf{K}]^\mathsf{T}\mathbf{W}\\ \Delta t[(1-\varepsilon)\mathbf{I}-\Delta t\mathbf{M}^{-1}\mathbf{D}]^\mathsf{T}\mathbf{W}\end{pmatrix}^\mathsf{T}, \quad \mathsf{D} = \Delta t\mathbf{W}^\mathsf{T}\mathbf{M}^{-1}\mathbf{W}, \quad \mathsf{F} = \Delta t^2\mathbf{W}^\mathsf{T}\mathbf{M}^{-1}. \tag{18}$$

The matrix $\mathsf{D}$ in (18) is a scaled version of the so-called Delassus matrix $\mathbf{W}^\mathsf{T}\mathbf{M}^{-1}\mathbf{W}$ [14], which is symmetric and positive definite as we assume $\mathbf{W}$ to have full column rank. In summary, the discrete system dynamics (14), (16) and (10) together with an output equation $\mathsf{y}_k = \mathsf{G}\mathsf{x}_k$ (i.e. the available measurements) we have a discrete **linear complementarity system** of the form

$$\mathsf{x}_{k+1} = \mathsf{A}\mathsf{x}_k + \mathsf{B}\mathbf{P}_k + \mathsf{E}\mathbf{f}_k, \tag{19a}$$

$$\boldsymbol{\xi}_k = \mathsf{C}\mathsf{x}_k + \mathsf{D}\mathbf{P}_k + \mathsf{F}\mathbf{f}_k, \tag{19b}$$

$$0 \le \boldsymbol{\xi}_k \perp \mathbf{P}_k \ge 0, \tag{19c}$$

$$\mathsf{y}_k = \mathsf{G}\mathsf{x}_k, \tag{19d}$$

For a given $\mathsf{x}_k$ and $\mathbf{f}_k$, the equations (19b) and (19c) form together a **linear complementarity problem** (LCP) [15, 16], which has to be solved for $\boldsymbol{\xi}_k$ and $\mathbf{P}_k$ in each time step.

*Remark* 1. As noted in [11], the time-stepping scheme above admits a unique solution if the set $\mathscr{A} := \{\mathbf{q} \in \mathbb{R}^f \mid \mathbf{g}(\mathbf{q}) \ge 0\}$ of admissible positions is convex and the excitation fulfills some regularity conditions. Here, we restrict ourselves to linear inequality constraints $\mathbf{g}(\mathbf{q}) = \mathbf{W}^\mathsf{T}\mathbf{q}$. It is therefore straightforward to verify that $\mathscr{A}$ is always convex in our setting. Also, the LCP (19b), (19c) has a unique solution if all principal minors of the matrix $\mathsf{D}$ are strictly positive (i.e. it is a so-called $\mathscr{P}$-matrix, see [15]), which is fulfilled since $\mathsf{D}$ is symmetric and positive definite.

https://doi.org/10.3311/ECCOMASMBD2021-140

## 3 PASSIVITY-BASED OBSERVER

For continuous-time linear complementarity systems, Heemels et al. [17] suggest a Luenberger-type state observer, where the observer gains are determined based on a linear matrix inequality. In the following, we show that an equivalent procedure is applicable for a discrete linear complementarity system of the form

$$\begin{aligned} \mathbf{x}_{k+1} &= \mathbf{A}\mathbf{x}_k + \mathbf{B}\mathbf{w}_k + \mathbf{E}\mathbf{v}_k, \\ \mathbf{z}_k &= \mathbf{C}\mathbf{x}_k + \mathbf{D}\mathbf{w}_k + \mathbf{F}\mathbf{v}_k, \\ 0 \le \mathbf{z}_k &\perp \mathbf{w}_k \ge 0, \\ \mathbf{y}_k &= \mathbf{G}\mathbf{x}_k. \end{aligned} \tag{20}$$

For a more standard notation, we denote the state by $\mathbf{x}_k$, the input by $\mathbf{v}_k$, the output by $\mathbf{y}_k$ and the complementary variables by $\mathbf{z}_k$ and $\mathbf{w}_k$, playing the role of the kinematic variable $\boldsymbol{\xi}_k$ and the discrete impulse $\mathbf{P}_k$ in (19).

The proposed Luenberger-type state observer for the discrete LCS (20) is in analogy to [17]

$$\begin{aligned} \hat{\mathbf{x}}_{k+1} &= \mathbf{A}\hat{\mathbf{x}}_k + \mathbf{B}\hat{\mathbf{w}}_k + \mathbf{E}\mathbf{v}_k + \mathbf{L}_1(\mathbf{y}_k - \hat{\mathbf{y}}_k), \\ \hat{\mathbf{z}}_k &= \mathbf{C}\hat{\mathbf{x}}_k + \mathbf{D}\hat{\mathbf{w}}_k + \mathbf{F}\mathbf{v}_k + \mathbf{L}_2(\mathbf{y}_k - \hat{\mathbf{y}}_k), \\ 0 \le \hat{\mathbf{z}}_k &\perp \hat{\mathbf{w}}_k \ge 0, \\ \hat{\mathbf{y}}_k &= \mathbf{G}\hat{\mathbf{x}}_k, \end{aligned} \tag{21}$$

where all observer related variables are written with a circumflex (ˆ). The state observer contains two correction terms, both linear in the output difference (which is known through measurements). Defining the estimation errors as $\tilde{\mathbf{x}}_k := \mathbf{x}_k - \hat{\mathbf{x}}_k$, $\tilde{\mathbf{z}}_k := \mathbf{z}_k - \hat{\mathbf{z}}_k$ and $\tilde{\mathbf{w}}_k := \mathbf{w}_k - \hat{\mathbf{w}}_k$, it follows that

$$\begin{aligned} \tilde{\mathbf{x}}_{k+1} &= (\mathbf{A} - \mathbf{L}_1\mathbf{G})\tilde{\mathbf{x}}_k + \mathbf{B}\tilde{\mathbf{w}}_k, \\ \tilde{\mathbf{z}}_k &= (\mathbf{C} - \mathbf{L}_2\mathbf{G})\tilde{\mathbf{x}}_k + \mathbf{D}\tilde{\mathbf{w}}_k, \\ \tilde{\mathbf{z}}_k^{\mathsf{T}}\tilde{\mathbf{w}}_k &\le 0. \end{aligned} \tag{22}$$

The last inequality in (22) expresses the maximal monotonicity of the discrete contact/impact law. It is easily checked by expanding

$$\tilde{\mathbf{z}}_k^{\mathsf{T}}\tilde{\mathbf{w}}_k = (\mathbf{z}_k - \hat{\mathbf{z}}_k)^{\mathsf{T}}(\mathbf{w}_k - \hat{\mathbf{w}}_k) = \mathbf{z}_k^{\mathsf{T}}\mathbf{w}_k - \mathbf{z}_k^{\mathsf{T}}\hat{\mathbf{w}}_k - \hat{\mathbf{z}}_k^{\mathsf{T}}\mathbf{w}_k + \hat{\mathbf{z}}_k^{\mathsf{T}}\hat{\mathbf{w}}_k. \tag{23}$$

Therein, the first and the last term vanish and the two other terms are non-positive due to the inequality complementarities in (20) and (21). The inequality $\tilde{\mathbf{z}}_k^{\mathsf{T}}\tilde{\mathbf{w}}_k \le 0$ is however not an inequality complementarity. The equations (22) do therefore not form a full description of the error dynamics, because $\tilde{\mathbf{w}}_k$ cannot be expressed as a function of the estimation error $\tilde{\mathbf{x}}_k$. We rather have to use the last three lines of (20) and (21). As a consequence, $\tilde{\mathbf{w}}_k$ depends on $\mathbf{x}_k, \hat{\mathbf{x}}_k$ and $\mathbf{v}_k$, where $\hat{\mathbf{x}}_k$ can be replaced by $\mathbf{x}_k - \tilde{\mathbf{x}}_k$ (or the other way around). As pointed out in [17] for the continuous-time case, the error dynamics is therefore non-autonomous and has two states, $\tilde{\mathbf{x}}_k$ and $\mathbf{x}_k$ (or alternatively $\tilde{\mathbf{x}}_k$ and $\hat{\mathbf{x}}_k$). However, only the estimation error $\tilde{\mathbf{x}}_k$ has to tend to zero as $k$ increases.

Now, even though (22) is not a full description of the estimation error dynamics, it contains sufficient information for a Lyapunov stability analysis. Indeed, we can select a quadratic Lyapunov function candidate $V(\tilde{\mathbf{x}}_k) = \tilde{\mathbf{x}}_k^{\mathsf{T}}\mathbf{P}\tilde{\mathbf{x}}_k$ with $\mathbf{P} = \mathbf{P}^{\mathsf{T}} > 0$ and calculate

$$\begin{aligned} V(\tilde{\mathbf{x}}_{k+1}) - V(\tilde{\mathbf{x}}_k) &= \tilde{\mathbf{x}}_{k+1}^{\mathsf{T}}\mathbf{P}\tilde{\mathbf{x}}_{k+1} - \tilde{\mathbf{x}}_k^{\mathsf{T}}\mathbf{P}\tilde{\mathbf{x}}_k \\ &= (\tilde{\mathbf{x}}_{k+1} + \tilde{\mathbf{x}}_k)^{\mathsf{T}}\mathbf{P}(\tilde{\mathbf{x}}_{k+1} - \tilde{\mathbf{x}}_k) \\ &= ((\mathbf{A} - \mathbf{L}_1\mathbf{G})\tilde{\mathbf{x}}_k + \mathbf{B}\tilde{\mathbf{w}}_k + \tilde{\mathbf{x}}_k)^{\mathsf{T}}\mathbf{P}((\mathbf{A} - \mathbf{L}_1\mathbf{G})\tilde{\mathbf{x}}_k + \mathbf{B}\tilde{\mathbf{w}}_k - \tilde{\mathbf{x}}_k), \end{aligned} \tag{24}$$

which only contains the observer gains $\mathbf{L}_1$. After first subtracting and then again adding the term

https://doi.org/10.3311/ECCOMASMBD2021-140

$2\tilde{\mathbf{z}}_k^\mathsf{T}\tilde{\mathbf{w}}_k$, (24) can be written as

$$V(\tilde{\mathbf{x}}_{k+1}) - V(\tilde{\mathbf{x}}_k) = \begin{pmatrix}\tilde{\mathbf{x}}_k\\ \tilde{\mathbf{w}}_k\end{pmatrix}^\mathsf{T}\begin{pmatrix}(\mathbf{A}-\mathbf{L}_1\mathbf{G})^\mathsf{T}\mathbf{P}(\mathbf{A}-\mathbf{L}_1\mathbf{G})-\mathbf{P} & (\mathbf{A}-\mathbf{L}_1\mathbf{G})^\mathsf{T}\mathbf{P}\mathbf{B}-(\mathbf{C}-\mathbf{L}_2\mathbf{G})^\mathsf{T}\\ \mathbf{B}^\mathsf{T}\mathbf{P}(\mathbf{A}-\mathbf{L}_1\mathbf{G})-(\mathbf{C}-\mathbf{L}_2\mathbf{G}) & \mathbf{B}^\mathsf{T}\mathbf{P}\mathbf{B}-(\mathbf{D}+\mathbf{D}^\mathsf{T})\end{pmatrix}\begin{pmatrix}\tilde{\mathbf{x}}_k\\ \tilde{\mathbf{w}}_k\end{pmatrix} + 2\tilde{\mathbf{z}}_k^\mathsf{T}\tilde{\mathbf{w}}_k, \tag{25}$$

which now contains both observer gains $\mathbf{L}_1$ and $\mathbf{L}_2$. Because $\tilde{\mathbf{z}}_k^\mathsf{T}\tilde{\mathbf{w}}_k \leq 0$, it follows that we have $V(\tilde{\mathbf{x}}_{k+1}) - V(\tilde{\mathbf{x}}_k) \leq -\mu V(\tilde{\mathbf{x}}_k)$ if the matrix inequality

$$\begin{pmatrix}(\mathbf{A}-\mathbf{L}_1\mathbf{G})^\mathsf{T}\mathbf{P}(\mathbf{A}-\mathbf{L}_1\mathbf{G})-\mathbf{P}+\mu\mathbf{P} & (\mathbf{A}-\mathbf{L}_1\mathbf{G})^\mathsf{T}\mathbf{P}\mathbf{B}-(\mathbf{C}-\mathbf{L}_2\mathbf{G})^\mathsf{T}\\ \mathbf{B}^\mathsf{T}\mathbf{P}(\mathbf{A}-\mathbf{L}_1\mathbf{G})-(\mathbf{C}-\mathbf{L}_2\mathbf{G}) & \mathbf{B}^\mathsf{T}\mathbf{P}\mathbf{B}-(\mathbf{D}+\mathbf{D}^\mathsf{T})\end{pmatrix} \leq 0, \tag{26}$$

holds. This matrix inequality is nonlinear in the unknowns $\mathbf{L}_1, \mathbf{L}_2$ and $\mathbf{P}$. However, by introducing $\mathbf{S} := \mathbf{P}\mathbf{L}_1$ and applying the Schur complement lemma, it can be checked that (26) is equivalent to the linear matrix inequality (LMI)

$$\begin{pmatrix}-\mathbf{P}+\mu\mathbf{P} & -(\mathbf{C}-\mathbf{L}_2\mathbf{G})^\mathsf{T} & \mathbf{A}^\mathsf{T}\mathbf{P}-\mathbf{G}^\mathsf{T}\mathbf{S}^\mathsf{T}\\ -(\mathbf{C}-\mathbf{L}_2\mathbf{G}) & -(\mathbf{D}+\mathbf{D}^\mathsf{T}) & \mathbf{B}^\mathsf{T}\mathbf{P}\\ \mathbf{P}\mathbf{A}-\mathbf{S}\mathbf{G} & \mathbf{P}\mathbf{B} & -\mathbf{P}\end{pmatrix} \leq 0. \tag{27}$$

Since $\mathbf{P}$ is invertible, $\mathbf{L}_1$ can be recovered in a second step as $\mathbf{L}_1 = \mathbf{P}^{-1}\mathbf{S}$.

*Remark* 2. The matrix inequality (26) is linked to a passivity condition: A linear time-invariant discrete-time system of the form

$$\begin{aligned}\mathbf{x}_{k+1} &= \mathbf{A}\mathbf{x}_k + \mathbf{B}\mathbf{w}_k,\\ \mathbf{y}_k &= \mathbf{C}\mathbf{x}_k + \mathbf{D}\mathbf{w}_k,\end{aligned} \tag{28}$$

written in short as system $(\mathbf{A},\mathbf{B},\mathbf{C},\mathbf{D})$, is said to be **passive** if there exists a nonnegative function $V : \mathbb{R}^n \to \mathbb{R}$ (called the storage function) with $V(\mathbf{0}) = 0$ such that

$$V(\mathbf{x}_{k+1}) - V(\mathbf{x}_k) \leq \mathbf{y}_k^\mathsf{T}\mathbf{w}_k \tag{29}$$

$\forall\, \mathbf{w}_k$ and $\forall\, k$.
It can be shown, that system (28) is passive if and only if if there exists a matrix $\mathbf{P} = \mathbf{P}^\mathsf{T} \geq 0$ such that the matrix inequality

$$\begin{pmatrix}\mathbf{A}^\mathsf{T}\mathbf{P}\mathbf{A}-\mathbf{P}+\mu\mathbf{P} & \mathbf{A}^\mathsf{T}\mathbf{P}\mathbf{B}-\mathbf{C}^\mathsf{T}\\ \mathbf{B}^\mathsf{T}\mathbf{P}\mathbf{A}-\mathbf{C} & \mathbf{B}^\mathsf{T}\mathbf{P}\mathbf{B}-(\mathbf{D}+\mathbf{D}^\mathsf{T})\end{pmatrix} \leq 0 \tag{30}$$

is fulfilled with $\mu = 0$. As a stronger condition we call system (28) strictly passive, if there exists a matrix $\mathbf{P} = \mathbf{P}^\mathsf{T} \geq 0$ such that (30) holds for any $\mu > 0$. In that case, it can be shown that the inequality (29) holds strictly.

## CONCLUSION

In this work, we proposed to attack the state observer problem for linear mechanical systems subjected to unilateral constraints from a Nonsmooth Dynamics perspective. After approximating the continuous-time problem using the Schatzman-Paoli scheme, we have shown that the discrete-time system forms a discrete linear complementarity system for which, in principle, the discrete adaptation of an existing passivity-based state observer can be applied. Thereby we achieved a first step towards a state observer design for unknown impact time instants. A next step would be to investigate under which conditions the linear matrix inequality, which is a sufficient condition for the asymptotic stability of the estimation error dynamics, admits a solution. Furthermore, it is necessary to analyze the behavior of the resulting observer gains as the time step $\Delta t$ tends to zero.

https://doi.org/10.3311/ECCOMASMBD2021-140

## REFERENCES


[1] Tanwani, A., Brogliato, B., Prieur, C.: Observer design for unilaterally constrained Lagrangian systems: A passivity-based approach. IEEE Transactions on Automatic Control **61**(9) (2016) 2386–2401

[2] Menini, L., Tornambè, A.: Velocity observers for non-linear mechanical systems subject to non-smooth impacts. Automatica **38**(12) (2002) 2169–2175

[3] Baumann, M., Leine, R.I.: A synchronization-based state observer for impact oscillators using only collision time information. International Journal of Robust and Nonlinear Control **26**(12) (2016) 2542–2563

[4] Menini, L., Tornambè, A.: State immersion observers for mechanical systems with impacts. In: 2016 IEEE 55th Conference on Decision and Control (CDC). (Dec 2016) 7117–7122

[5] Kim, J., Cho, H., Shamsuarov, A., Shim, H., Seo, J.H.: State estimation strategy without jump detection for hybrid systems using gluing function. In: 53rd IEEE Conference on Decision and Control. (Dec 2014) 139–144

[6] Glocker, Ch.: Set-valued Force Laws, Dynamics of Non-smooth Systems. Volume 1 of Lecture Notes in Applied Mechanics. Springer-Verlag (2001)

[7] Glocker, Ch.: Energetic consistency conditions for standard impacts. Part I: Newton-type inequality impact laws and Kane's example. Multibody System Dynamics **29**(1) (2013) 77–117

[8] Leine, R.I., van de Wouw, N.: Stability and Convergence of Mechanical Systems with Unilateral Constraints. Lecture Notes in Applied and Computational Mechanics. Springer, Germany (2008)

[9] Moreau, J.J.: Unilateral contact and dry friction in finite freedom dynamics. In: Non-Smooth Mechanics and Applications. Springer-Verlag (1988) 1–82

[10] Paoli, L., Schatzman, M.: A Numerical Scheme for Impact Problems I: The One-Dimensional Case. SIAM Journal on Numerical Analysis **40**(2) (January 2002) 702 – 733

[11] Paoli, L.: Mathematical aspects of vibro-impact problems. In Leine, R.I., Acary, V., Brüls, O., eds.: Advanced Topics in Nonsmooth Dynamics: Transactions of the European Network for Nonsmooth Dynamics. Springer International Publishing, Cham (2018) 135–189

[12] Heemels, W., Schumacher, J., Weiland, S.: Linear complementarity systems. SIAM J. Appl. Math **60** (1997) 2000

[13] Heemels, W.P.M.H., Brogliato, B.: The complementarity class of hybrid dynamical systems. European Journal of Control **9**(2-3) (2003) 322–360

[14] Brogliato, B.: Nonsmooth Mechanics. Models, Dynamics and Control. 3 edn. Communications and Control Engineering. Springer-Verlag, International Publishing (2016)

[15] Cottle, R.W., Pang, J.S., Stone, R.E.: The Linear Complementarity Problem. Classics in Applied Mathematics. Society for Industrial and Applied Mathematics (SIAM) (1992)

[16] Murty, K.: Linear Complementarity, Linear and Nonlinear Programming. Sigma Series in Applied Mathematics. Heldermann (1988)

[17] Heemels, W.P.M.H., Camlibel, M.K., Schumacher, J.M., Brogliato, B.: Observer-based control of linear complementarity systems. International Journal of Robust and Nonlinear Control **21**(10) (2011) 1193–1218

https://doi.org/10.3311/ECCOMASMBD2021-114



# Synchronous Contact/Impact Events Modelling With A Smooth-Based Approach

**Raúl Gismeros Moreno, Eduardo Corral Abad, Jesús Meneses Alonso, María Jesús Gómez García, Cristina Castejón Sisamón**

MAQLAB Research Group, Department of Mechanical Engineering
Universidad Carlos III de Madrid
Avenida de la Universidad 30, 28911 Leganés, Spain
[rgismero, ecorral, meneses, mjggarci, castejon]@ing.uc3m.es

## ABSTRACT

This work focuses its scope on the smooth contact approach and its management of multiple contact events, proposing several models developed under this methodology and discussing the main issues that have arisen when designing, modelling, and verifying them. The main purpose of this paper is to provide a reference to those researchers that work with smooth methods in the context of multibody dynamics of how to deal with them. Among the models presented, there are some engineering-focused ones, whereas the readers can also find some more practical, day-to-day examples.

**Keywords:** Contact phenomena, Contact detection, Smooth approaches, Multiple-simultaneous impact systems, Multibody System dynamics, Error containment methods.

## 1. INTRODUCTION

Contact forces and impact events, which are present in almost all fields of engineering [1]–[3], provokes the appearance of harmful phenomena in mechanical systems (vibrations [4], wave propagation [5], fatigue [6], wear [7], crack [8] and so on). In impact events, sudden changes take place, in which the conditions of the mechanical system vary in very short times. This causes the appearance of great magnitude forces, energy dissipation processes and both velocities and accelerations discontinuities, among other issues. Contact/impact events are difficult to model and pose a challenge for the engineers due to the large number of variables that must be taken into account: contacting surfaces geometry, material properties, inclusion of friction phenomena, multiple-simultaneous impacts, …

There are two main approaches when modelling contact events: the non-smooth approach and the models based on contact forces. Each one has a distinct set of advantages and limitations [9]: non-smooth methods are known for considering bodies as rigids solids and their computational efficiency. However, some of these methods pose several issues when dealing with friction phenomena or multiple-simultaneous impact scenarios. On the other hand, models based on contact forces are continuous functions of the relative penetration (and its temporal derivative) of the contacting bodies, which are supposed to be deformable. Their main benefit is that there is no need to define unilateral restrictions. Nonetheless, the proper, accurate choice of the parameters of the definitions of the forces, as well as the right detection of the initial instant of contact [10], that makes the computing time to increase dramatically on certain occasions, are their most distinctive drawbacks.

This paper focuses on the latter, collecting the expertise of several previous works based on this approach. Some of the most typical issues related to these methods are commented through a set of simple, day-to-day models. Then, different alternatives to overcome them are proposed.

The manuscript is structured as follows: in Section 2 the main contact detection algorithms

https://doi.org/10.3311/ECCOMASMBD2021-114

associated to the described models are presented, along with some of the most used contact force models. In Sections 3, 4 and 5 the three models are introduced and outlined, underlining their most distinctive features along with some of the results obtained and the issues arisen during the tests. The main conclusions are drawn in Section 6.

## 2. CONTACT DETECTION ALGORITHMS AND CONTACT FORCE MODELS

In this section, some detection algorithms for the most basis contact interactions are presented and developed. Subsequently, the contact force models used in the models later described are introduced and detailed.

### 2.1. Contact detection algorithms

#### 2.1.1. Sphere-sphere interaction

A system consisting of two spheres *u* and *v* with radii $R_u$ and $R_v$, respectively, coming into contact is presented in Figure 1. Two different interactions can take place, according to the arrangement of the bodies: an external contact (Figure 1 (a)) or an internal one (Figure 1 (b)).

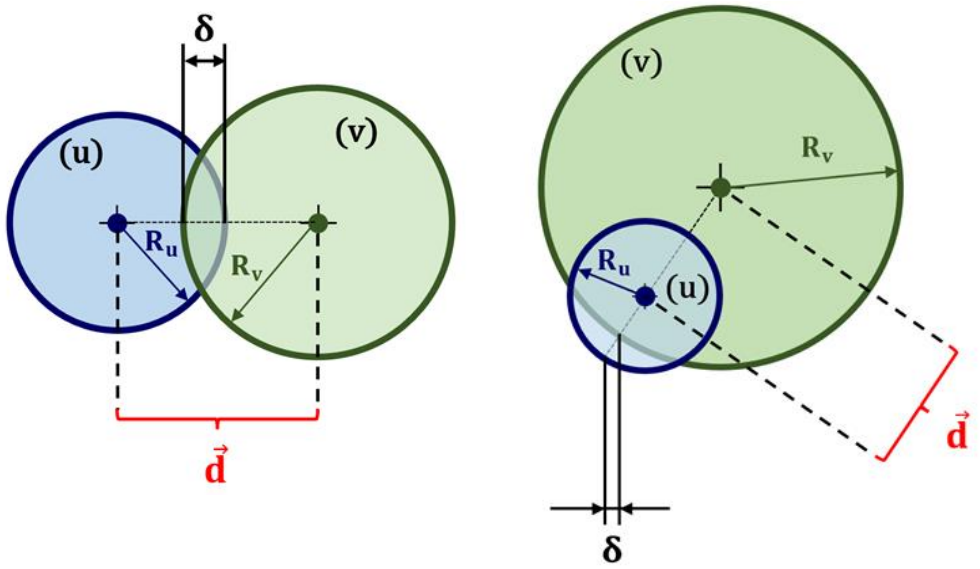


(a) (b)

**Figure 1.** Sphere-sphere contact interaction.

The algorithm for calculating the relative penetration between the bodies varies minimally between both cases. For an external contact, the expression that defines penetration, δ, is

$$\delta = R_u + R_v - \|\vec{d}\| \tag{1}$$

Whereas the value of the indentation in an internal interaction is given by the following equation

$$\delta = R_u + R_v + \|\vec{d}\| \tag{2}$$

However, in this last case, the value of the largest radius is introduced with negative sign. For both interactions, if δ is negative, no contact will be happening, being the initial instant of contact when δ = 0.

#### 2.1.2. Sphere-plane interaction

Given the system shown in Figure 2 formed by a sphere *u* (its centre being on point C, with radius R) and an infinite plane *v* (its mass centre being on P), the implicit function or general equation is defined

$$a \cdot x + b \cdot y + c \cdot z + d = 0 \tag{3}$$

https://doi.org/10.3311/ECCOMASMBD2021-114

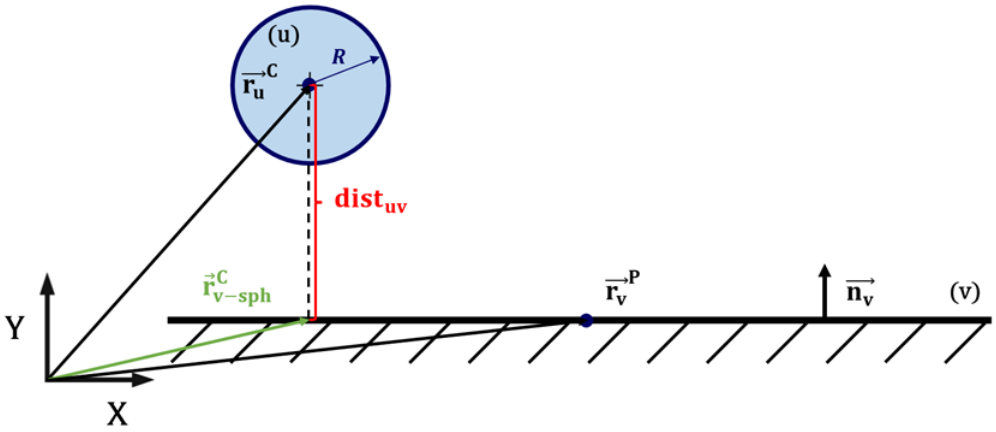


**Figure 2.** Sphere-plane contact interaction.

where *a*, *b* and *c* denote the components of the vector normal to the plane in the XYZ global frame, respectively. Using the coordinates of the plane mass centre, the value of parameter *d* is obtained

$$d = -a \cdot r_x^P - b \cdot r_y^P - c \cdot r_z^P \tag{4}$$

With $d$ the distance from the centre of the sphere to the plane, $dist_{uv}$, can be calculated

$$dist_{uv} = \vec{n}_v \cdot \vec{r}_u^C + d \tag{5}$$

The projection of the mass centre of the sphere on plane *v*, $\vec{r}_{v-sph}^C$ is then defined

$$\vec{r}_{v-sph}^C = \vec{r}_u^C - dist_{uv} \cdot \vec{n}_v \tag{6}$$

This projection must be changed into local-frame plane coordinates when obtaining the value of the relative contact velocity

$$\vec{s}_{v-sph}^C = A_v^{-1} \cdot (\vec{r}_{v-sph}^C - \vec{r}_v^P) \tag{7}$$

Once the $dist_{uv}$ is calculated, $\delta$ can be derived

$$\delta = R - dist_{uv} \tag{8}$$

Negative values of penetration indicate that there is no contact happening between the sphere and the plane. The initial instant of contact takes place when $\delta = 0$.

A set of more complex interaction can be derived from these simple algorithms, as shown in Figure 3 [11].

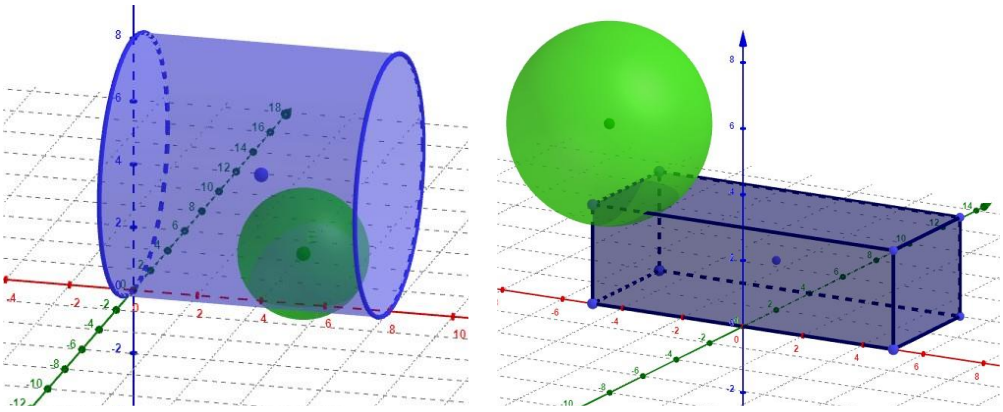

(a) (b)

**Figure 3.** Complex contact interactions derived from the ones introduced above [11]: (a) Sphere-cylinder; (b) Sphere-parallelepiped.

https://doi.org/10.3311/ECCOMASMBD2021-114

### 2.2. Contact forces models

Once the contact condition is met, a suitable constitutive law is required to obtain the value of the contact force. The interested reader can find a wide variety of works that collect a reasonably large number of contact force models [9], [12], [13], most of them proposed in the last decades. The models developed in this work make use of some of the most widely used and well-known contact laws.

The overall integrity of the model and an accurate contact detection are pursued during the early stages of the design and development of a model. For this purpose, Hertzian contact model proves to be the right choice, which defines force as a function of the relative penetration between the contacting bodies:

$$F_N = K \cdot \delta^n \tag{9}$$

where K is the contact stiffness parameter and n is an exponent that quantifies the degree of nonlinearity of the force-indentation relation [9]. The definition of the K varies depending on the geometries of the bodies involved in the contact process. Exponent n usually takes a value of 3/2, according to the work by Hertz, who assumed a parabolic distribution of the stresses in the contact area.

The Hertzian model allows a simple definition of the contact force with a fairly good performance, for any contact interaction. However, it doesn't consider any energy dissipation phenomena, which is inconsistent from a physical point of view. For this reason, a great number of models that deal with this issue have been developed.

One of the most used constitutive laws is the one proposed by Lankarani and Nikravesh, with multiple applications [9]

$$F_N = K \cdot \delta^{3/2} + \chi \cdot \delta^{3/2} \cdot \dot{\delta} = K \cdot \delta^{3/2} \cdot \left(1 + \frac{3 \cdot (1 - c_r^2)}{4} \cdot \frac{\dot{\delta}}{\dot{\delta}^{(-)}}\right) \tag{10}$$

where $\chi$ denotes the hysteresis damping factor, a measure of the energy dissipated throughout the contact process. $c_r$ is the coefficient of restitution, whereas $\dot{\delta}^{(-)}$ is the initial normal velocity and $\dot{\delta}$ represents the normal contact velocity. This model has proved to work well with contact events in which the value of $c_r$ is close to unity and the impact velocities are low. Impacts at velocities higher than the wave propagation velocity have an energy dissipation mechanism not considered in this model, mainly in form of permanent deformation.

Another, more recent model is the one described by Flores et al., who considered the relation between the energy dissipated and the coefficient of restitution through the kinetic energy balance and the principle of conservation of momentum, the elastic strain energy stored due to the normal-force work and the energy dissipated due to internal damping to develop a constitutive law that can be applied to the entire range of values of $c_r$

$$F_N = K \cdot \delta^{3/2} + \chi \cdot \delta^{3/2} \cdot \dot{\delta} = K \cdot \delta^{3/2} \cdot \left(1 + \frac{8 \cdot (1 - c_r)}{5 \cdot c_r} \cdot \frac{\dot{\delta}}{\dot{\delta}^{(-)}}\right) \tag{11}$$

These two last models include in their definitions the relative contact velocities and the coefficient of restitution. However, the main problem is that they only consider two bodies in their conception, so, when dealing with contact events in which more bodies are involved, some unexpected and/or inconsistent results can be obtained. For example, in some cases, the value of the normal impact velocity could lead to attractive forces if three bodies collide successively, something that is possible. Some of these issues and are presented in the following sections.

## 3. FIRST MODEL: A BALL BEARING

The first model presented is a classical ball bearing, as shown in Figure 4(a). One of the most typical causes of failure in rotary machine is the appearance of defects in bearings [14]. According to some reports, almost half of the failures of electric motors have their origin in bearing-related breakdowns [15]. This kind of failure can lead to more severe problems in other parts of the engine, increasing dramatically the financial losses. Traditional maintenance methods consist of replacing the bearing periodically once a certain operation time expires. Two issues are associated to these methods: this way of proceeding is experience-based, which cannot consider factors such

https://doi.org/10.3311/ECCOMASMBD2021-114

as a wrong assembling, poor lubrication, etc.; and the location of the machines, which may be not easily accessible (for example, offshore turbines). For these reasons, predictive maintenance techniques are quite useful to analyse these components with frequency-based studies, allowing engineers to determine accurately the condition of the bearing without a periodic replacement.

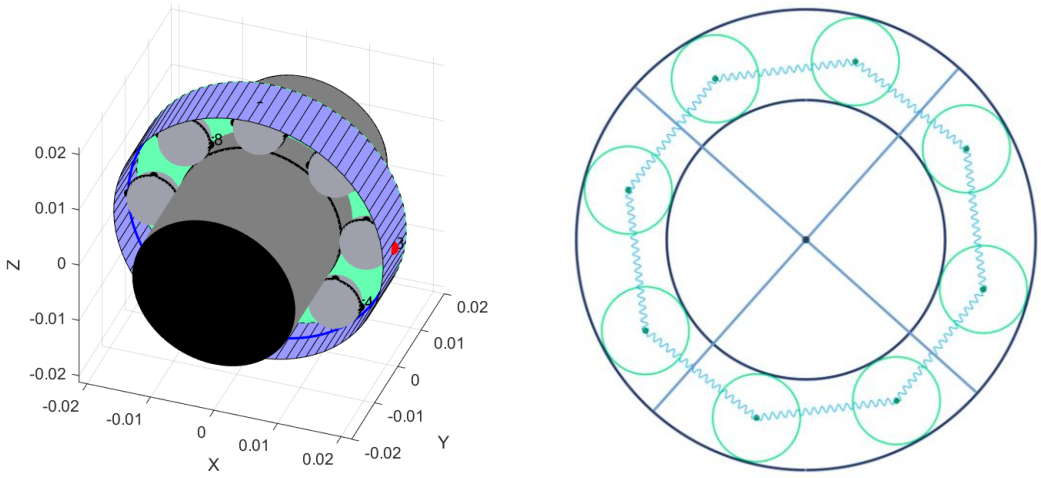


(a) (b)

**Figure 4.** Ball bearing model: (a) Matlab-generated animation of the first model; (b) Design of the bearing model, considering spring point-to-point elements to simulate the cage.

In this primitive model, the cage was modelled by a set of spring elements between the centres of the balls, as shown in Figure 4(b). The stiffness parameter of these spring elements was quite high, in order to keep the stability of the system but, at the same time, allowing them to vibrate properly. The inner race is a fixed body, so the model resembles to a real bearing tested in a machine bench, where the bearing is fixed to the shaft. The driving force is applied to the outer race, transmitting the motion through friction forces to the balls.

Two models were developed regarding contact interactions: the first one, based on the sphere-sphere contact interaction described above, neglecting any kind of axial loads, and the latter, more advanced, considering axial loads through a sphere-cylinder contact interaction. During the development of this contact algorithm, the main issue faced was the proper detection of the initial instant of contact. For the test model shown in Figure 5, in which a ball bounces along Z axis, for an elastic impact, the initial position should be reached after each impact.

Two Matlab integrators widely used were tested and compared. ODE45, which is based on the Runge-Kutta method developed by Dormand and Prince [16], stands out for being the most versatile Matlab integrator and being able to work reasonably well with almost all type of Initial Value Problems, thanks to its variable time step which allows an efficient computation. "45" makes reference to the order of formulas ($4^{th}$ and $5^{th}$) used by the algorithms. As can be seen in Figure 6, the values of the tolerances had a decisive impact on the results. *Abstol* denotes the absolute tolerance, a threshold value below which the value of the solution becomes unimportant. It determines the accuracy when the solution approaches zero. *Reltol*, and acronym for relative tolerance, is a measure of the error relative to the size of each solution component. It controls the number of correct digits in all solution components, except those smaller than threshold *AbsTol*. The main values for these two magnitudes are $1 \cdot 10^{-6}$ and $1 \cdot 10^{-3}$, respectively. For these, the results were a bit inconsistent, as the sphere gained energy after each rebound and surpassed the initial position at one point of the simulation. This issue was solved reducing these tolerances, first with an extreme value ($1 \cdot 10^{-12}$) and then looking for a balance between the accuracy of the results and the computational efficiency. The optimal values obtained for this model were $Abstol = 1 \cdot 10^{-6}$ and $Reltol = 1 \cdot 10^{-8}$, respectively. These provided consistent results, as the ball didn't surpass the initial Z-axis position or lose energy after each impact either.

However, ODE45 integrator is not the Holy Grail and experiences some issues when dealing with stringent expensive tolerances, which arose when an inelastic impact was tested instead. In the case shown in Figure 7, the contact event was modelled with a coefficient of restitution of 0.7, using the Lankarani and Nikravesh model introduced earlier. As can be seen, the simulation collapses with ODE45, even for really small tolerance values.

https://doi.org/10.3311/ECCOMASMBD2021-114

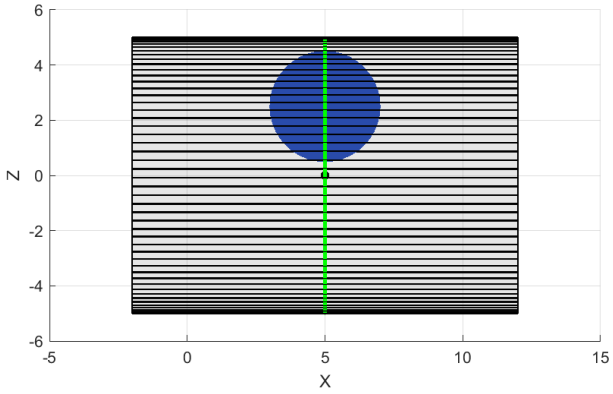


**Figure 5.** Matlab-generated animation of the sphere-cylinder interaction test model.

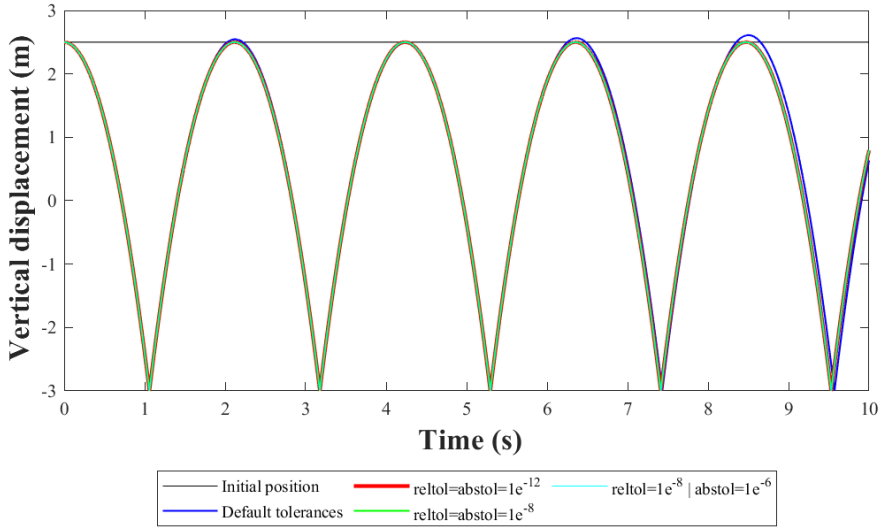


**Figure 6.** Variation in the results given by ODE45 Matlab integrator when changing the values of the tolerances associated to it.

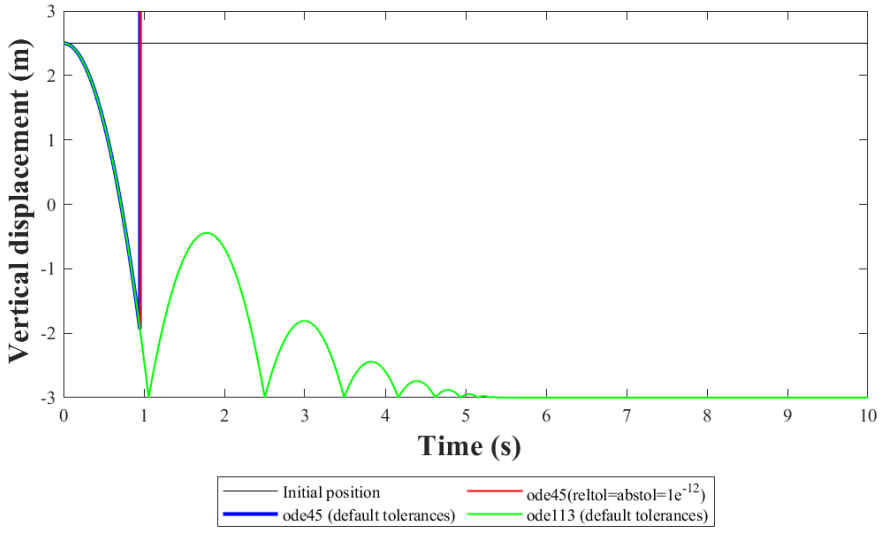


**Figure 7.** Evolution of the Z-axis position of the bouncing ball, for different values of time step, for a impact defined by a $c_r = 0.7$.

In contrast with this integrator, ODE113, which is a PECE implementation of Adams-Bashforth-Moulton methods [16], proved to give better results than ODE45, for a non-fully elastic impact. “113” makes reference to the fact that it is a variable order solver, from 1 to 13. PECE means Predict-Evaluate-Correct-Evaluate, where this second evaluation improves the accuracy of the method, as improved function values are used in the set of backpoints in the subsequent steps [17]. However, when testing the elastic impact (Hertzian model), this integrator led to a subsequent slight energy loss, preventing the ball from reaching the initial position.

https://doi.org/10.3311/ECCOMASMBD2021-114

Regarding the verification phase, the material properties of a ball bearing ER10K, presented in Table 1, were used. The PSD (Power Spectral Density) of the acceleration of the balls, for a healthy bearing, is shown in Figure 8. It can be observed a consistent behaviour of the model, as there is only a peak at low frequencies, caused by the own system, and there are no traces of defects.

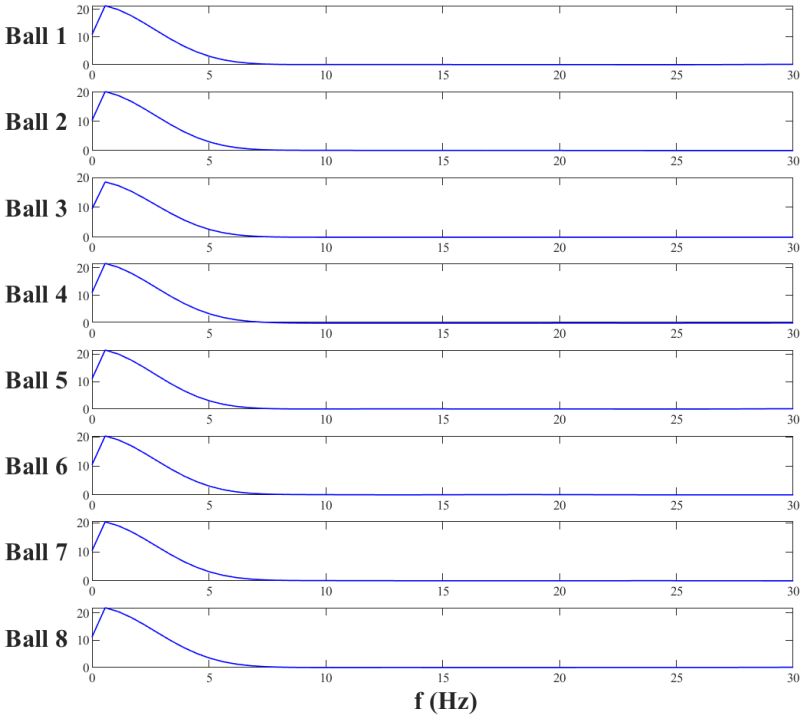


**Figure 8.** PSD of the acceleration of the balls generated by Matlab.

**Table 1.** Properties of the reference bearing (obtained from REXNORD catalog and experimental measures)

| Property | Value |
|---|---|
| Shaft diameter / bore | 15.875 mm |
| Outside diameter | 47.000 mm |
| Mean diameter | 31.438 mm |
| Number of balls | 8 |
| Ball diameter | 7.938 mm |
| Contact angle | 0º |

## 4. SECOND MODEL: POOL/BILLIARD TABLE

The second model proposed was presented in a previous work [18] and has been now further developed, as can be seen in Figure 9. Pocket algorithm has been defined and implemented, so the balls fall when they get to them. Starting from the sphere-regular parallelepiped interaction introduced earlier, a sphere-triangular prism contact detection algorithm was developed for the ball-cushion interaction around the pockets. Each cushion was then divided into three bodies, as shown in Figure 10. The rounded area of the cushion in the cushions is at the moment being developed from the sphere-cylinder interaction presented above.

In this model, in which the balls can move freely in all directions, two different scenarios were considered: a permanent contact (between the balls and the cloth, as long as the ball is not hit so that it is lifted off the ground) and an intermittent one (between the balls themselves and these and the cushions). When calculating the value of both friction and contact forces, the peculiarities of each interaction had to be taken into account. The values of the parameters for each contact event were taken from experimental works [19]. Considering this, a Hertzian contact force was

https://doi.org/10.3311/ECCOMASMBD2021-114

chosen to calculate the value of normal force for the permanent contact, being the model proposed by Ambrósio the best choice to account for the friction force. On the other hand, for the ball-cushion interaction, which are not-fully elastic, the model defined by Lankarani and Nikravesh was the optimal option to obtain the value of the normal force, with Ambrósio's model characterising again the friction phenomena. Lastly, the contact events between the balls were modelled using again Lankarani and Nikravesh's model for the normal force and two different models for the friction force: Threlfall's approximation and a tangential velocity-dependent model developed by Alciatore [19]. The different values considered are shown in Table 2.

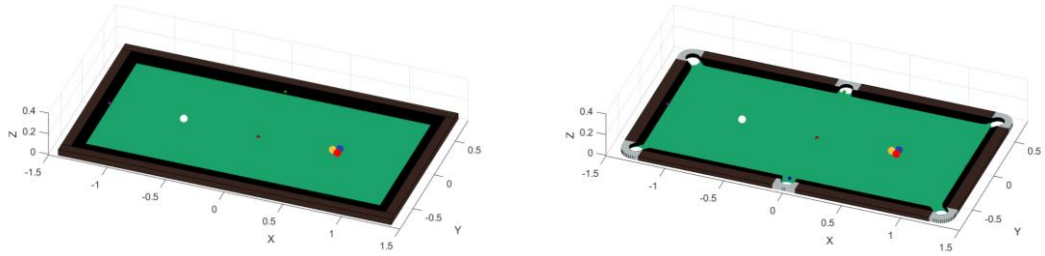

(a) (b)

**Figure 9.** Matlab-generated animation of the second model: (a) Previous version; (b) Current version.

**Table 2.** Restitution and friction coefficients used to model the different interactions of the system [19], [20].

| Interaction | Contact force model | Friction force model | Friction coefficient | Restitution coefficient |
|---|---|---|---|---|
| Ball-ball | Lankarani and Nikravesh | Threlfall | 0.06 | 0.93 |
| | | Alciatore | $9.951 \cdot 10^{-3} + 0.108 \cdot e^{-1.088 \cdot v}$ | 0.93 |
| Ball-cloth | Hertz | Ambrósio | 0.2 | - |
| Ball-cushion | Lankarani and Nikravesh | - | - | 0.85 |
| | | Ambrósio | 0.14 | 0.98 |

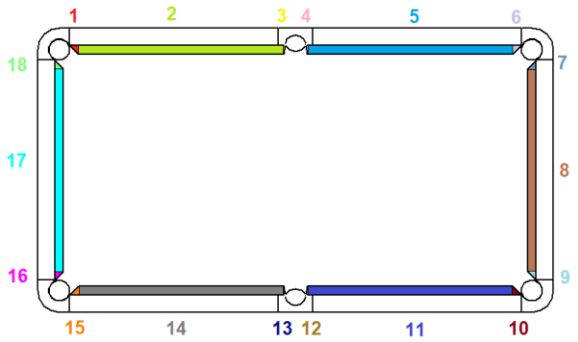


**Figure 10.** Arrangement of the bodies that form the cushions of the pool/billiard table.

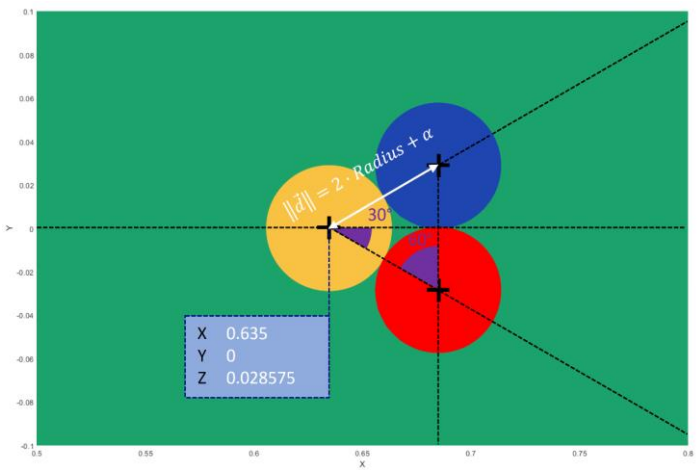


**Figure 11.** Arrangement of the balls as a function of α.

https://doi.org/10.3311/ECCOMASMBD2021-114

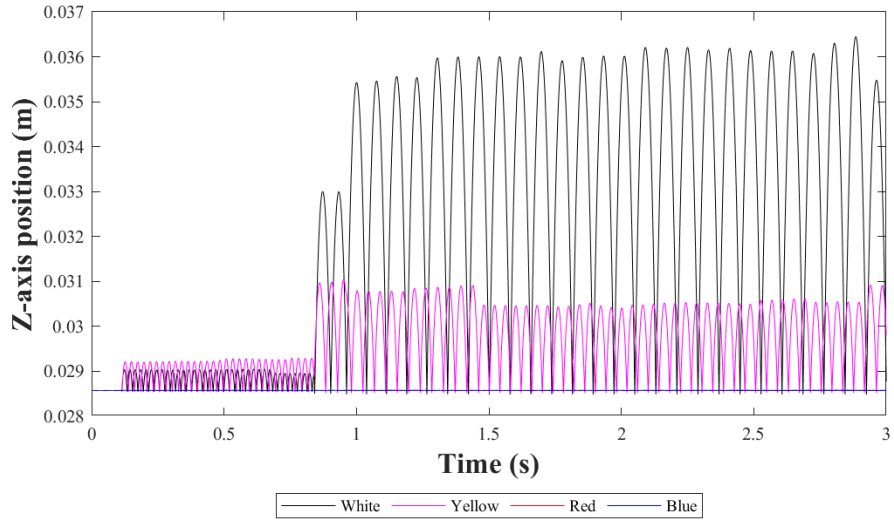


(a) $\alpha = 10^{-9}$ m

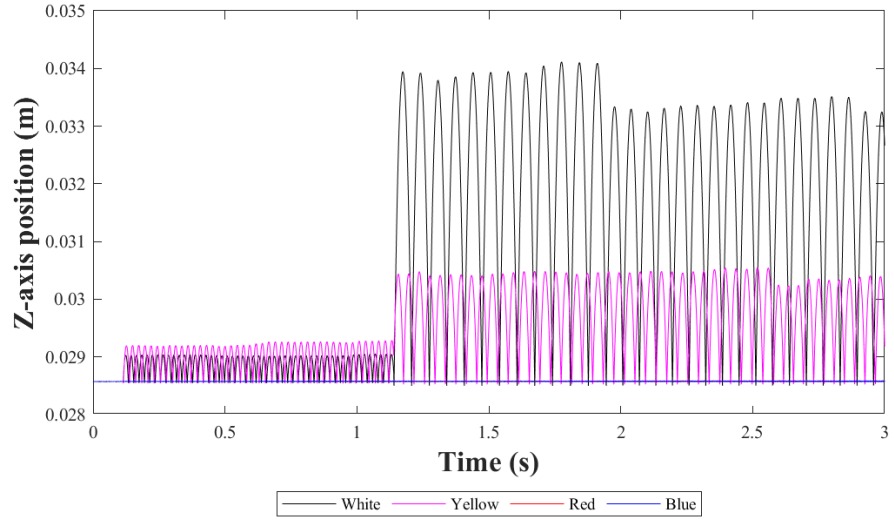


(b) $\alpha = 10^{-6}$ m

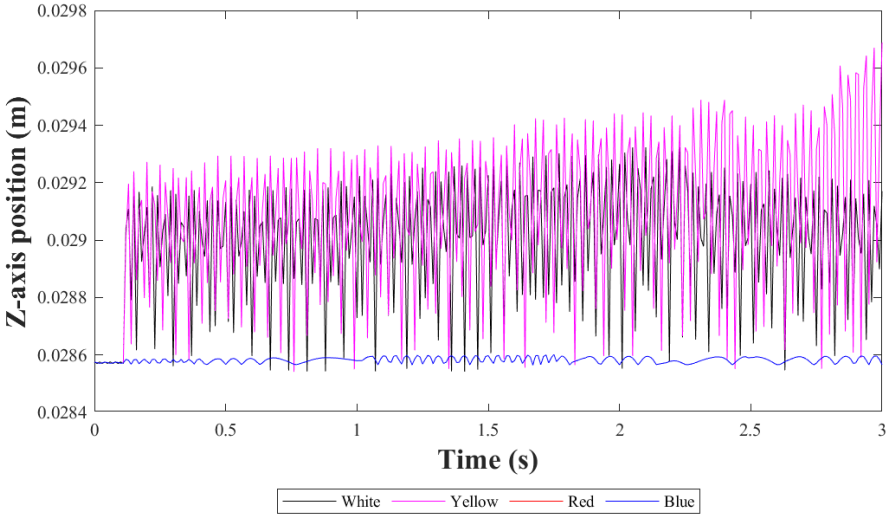


(c) $\alpha = 2.1325735 \cdot 10^{-4}$ m

**Figure 12.** Evolution of the Z-axis position components of the balls, depending on the value of α chosen.

In the early stages of the development of the model, balls static at the outset (coloured spheres in Figure 9) were arranged with a certain distance between their surfaces, avoiding the system to stall in excessively early times of the simulation due to the own definition of the forces. The coloured balls were always arranged so their mass centres formed an equilateral triangle. The distance between the mass centres of the coloured balls were defined by the expression $d = 2 \cdot \text{Radius} + \alpha$, being α a value set by the user, as shown in Figure 11. Several values were tested,

from the order of $10^{-9}$ to $10^{-4}$. These proved to have a decisive impact on the results obtained. For instance, with lower values of α, some of the balls (mainly the cue and the yellow ones) tended to increase their position in global Z-axis as the analysis progressed and they rolled on the cloth (see Figure 12). As α was increased, the maximum values reached by these balls reduced, providing a more reasonable behaviour of the model, i.e., balls did not tend to gain energy and increase their Z-axis position. For the random value set of order $10^{-4}$, the cue and yellow balls hardly moved in Z axis.

This is also an example of how a certain configuration of one of the contact interactions affects to the rest of contact events that happen simultaneously. For this reason, in the first simulations performed with this model during the tuning phase, both normal force in the ball-cloth contact and gravity force were neglected, therefore keeping constant Z-axis position. This resulted in a substantial reduction of the computing time, from an average of 15500 s for the lower values of α and 7700 s for the random value, to clearly lower values of 1730 s and 440 s, respectively. This modification of the model had some consequences: friction forces normal to the cloth had to be neglected to avoid the balls to either fly over the cloth or to sink into it.

## 5. THIRD MODEL: NEWTON'S CRADLE

The third model presented is a device widely used in educational contexts: Newton's cradle. This object is usually used to demonstrate the principles of conservation of momentum and conservation of energy through a set of swinging spheres (with the same size and mass) that collides elastically [21]. When a ball in one end of the chain is held at a certain height and released, so it collides with the remaining balls, the ball at the opposing end is kicked off and reaches about the same dropping height.

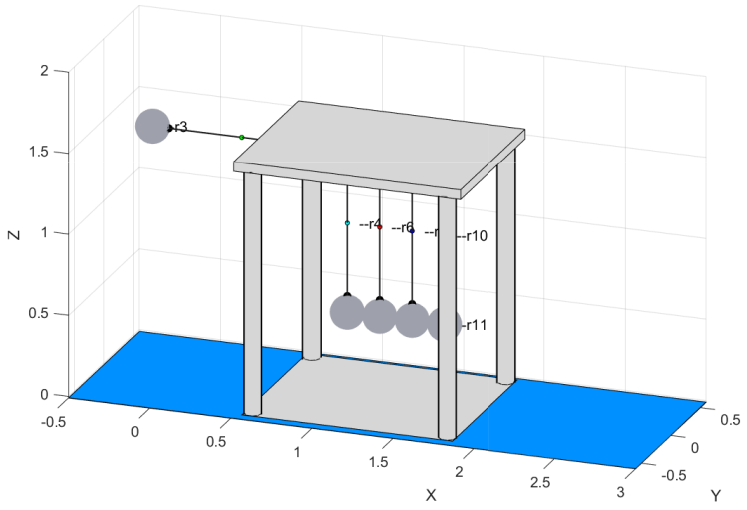


**Figure 13.** Matlab-generated animation of the third model.

The main assumptions in this model are usually to neglect friction phenomena and consider fully elastic contacts between the balls. In this case, the main issue that arose was the stall of the system when an inelastic contact (and, therefore, a contact model that considers explicitly normal relative velocity) was considered. Most dissipative contact force models, including the ones described above, include a ratio between the normal velocity at any given time and the value of the same magnitude at the initial instant of impact. If the bodies are together at that moment, which is the case of the static balls in Figure 13, these values will be the form of a 0/0 indeterminate form. A possible solution to this problem could be to consider a ratio of 1/1, but this is still under study.

Some data can be extracted from the graphs from Figure 14. The method based on standard Lagrange multipliers led to a failure of the system and, therefore, inconsistent results. Both Matlab integrators introduced earlier, ODE45 and ODE113, made the ball gain energy after each impact and reach a higher position, which is also incoherent. As in the previous model, reducing the default tolerances values improved the results, but also made the system lose some energy. Again, ODE113 provided better results at a lower computational cost, as the tolerance values were reduced to $1 \cdot 10^{-7}$, whereas ODE45 gave lower Z-axis positions for even lower tolerance values ($1 \cdot 10^{-10}$).

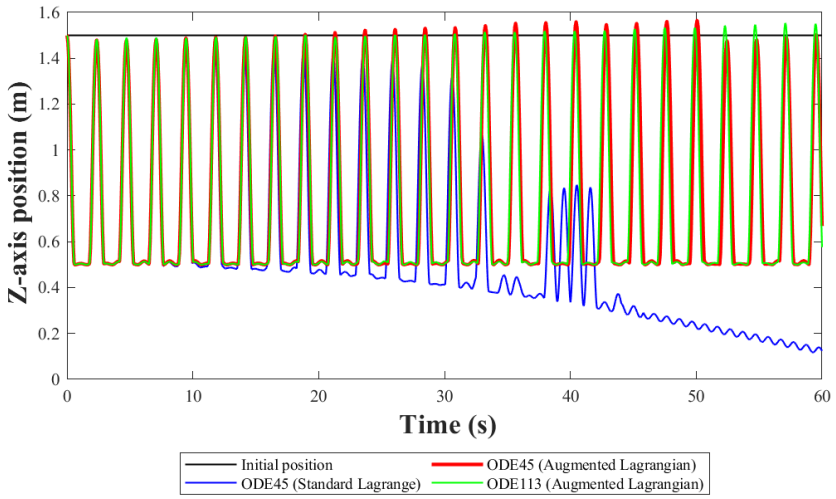


(a) Comparison between ODE45 and ODE113 Matlab integrators.

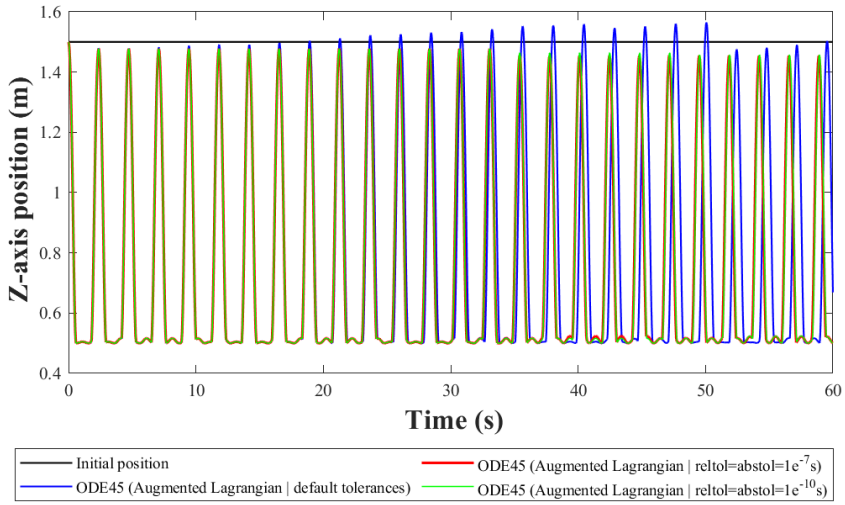


(b) Comparison for different tolerance values, for ODE45 integrator.

**Figure 14.** Evolution of Z-axis position of the ball released, throughout the simulation, for different settings of the integrators and constraint violation control methods.

## 6. CONCLUSIONS

Throughout this work, the main contact detection algorithms in the context of smooth multibody dynamics have been introduced and described. Some evolutions of these have been presented and applied to day-to-day systems and engineering applications, obtaining some promising results from each one of them, and facing some issues related to contact detection when performing dynamic analysis with Matlab software. Matlab default integrators proved to fall back when dealing with complex systems, specially when multiple contact/impact events take place simultaneously. Adjusting some parameters of these integrators improved considerably the results, but these settings involved a significant increase of the computational cost. However, there is still work to be made and some options that could be implemented, for example, a penetration-dependent integration scheme like the one some authors developed previously or to limit the number of iterations during each step.

## ACKNOWLEDGMENTS

The authors would also like to acknowledge the support received by the Community of Madrid through its multi-year agreement with University Carlos III focused on its policy "Excelencia para el Profesorado Universitario".

## REFERENCES

[1] J. Pagaimo, H. Magalhães, J. N. Costa, and J. Ambrósio, 'Derailment study of railway cargo vehicles

using a response surface methodology', *Veh. Syst. Dyn.*, 2020, doi: 10.1080/00423114.2020.1815810.

[2] M. Machado *et al.*, 'Development of a planar multibody model of the human knee joint', *Nonlinear Dyn.*, 2010, doi: 10.1007/s11071-009-9608-7.

[3] E. Corral, M. J. G. García, C. Castejon, J. Meneses, and R. Gismeros, 'Dynamic modeling of the dissipative contact and friction forces of a passive biped-walking robot', *Appl. Sci.*, 2020, doi: 10.3390/app10072342.

[4] G. Peláez, H. Rubio, E. Souto, and J. C. García-Prada, 'Optimal Model Reference Command Shaping for vibration reduction of Multibody-Multimode flexible systems: Initial Study.', in *Mechanisms and Machine Science*, 2019.

[5] R. Zander, M. Förg, and H. Ulbrich, 'Impacts on beam structures: Interactions of wave propagation and global dynamics', *Solid Mech. its Appl.*, vol. 1, pp. 327–338, 2007, doi: 10.1007/978-1-4020-5981-0_29.

[6] M. Filippini, M. Luke, I. Varfolomeev, D. Regazzi, and S. Beretta, 'Fatigue strength assessment of railway axles considering small-scale tests and damage calculations', *Procedia Struct. Integr.*, vol. 4, pp. 11–18, Jan. 2017, doi: 10.1016/J.PROSTR.2017.07.013.

[7] D. Infante-García, M. Marco, A. Zabala, F. Abbasi, E. Giner, and I. Llavori, 'On the role of contact and system stiffness in the measurement of principal variables in fretting wear testing', *Sensors (Switzerland)*, vol. 20, no. 15, pp. 1–20, Aug. 2020, doi: 10.3390/S20154152.

[8] M. Zamorano, M. J. Gómez Garcia, and C. Castejón, 'Selection of a mother wavelet as identification pattern for the detection of cracks in shafts', *J. Vib. Control*, p. 107754632110260, Jun. 2021, doi: 10.1177/10775463211026033.

[9] E. Corral, R. Gismeros Moreno, M. J. Gómez García, and C. Castejón, 'Nonlinear phenomena of contact in multibody systems dynamics: a review', *Nonlinear Dynamics*. Springer Science and Business Media B.V., pp. 1–27, Mar. 14, 2021, doi: 10.1007/s11071-021-06344-z.

[10] P. Flores and J. Ambrósio, 'On the contact detection for contact-impact analysis in multibody systems', *Multibody Syst. Dyn.*, 2010, doi: 10.1007/s11044-010-9209-8.

[11] E. Corral, R. Gismeros Moreno, J. Meneses, M. J. Gómez García, and C. Castejón, 'Spatial algorithms for geometric contact detection in multibody system dynamics', *Mathematics*, vol. 9, no. 12, Jun. 2021, doi: 10.3390/MATH9121359.

[12] M. Machado, P. Moreira, P. Flores, and H. M. Lankarani, 'Compliant contact force models in multibody dynamics: Evolution of the Hertz contact theory', *Mech. Mach. Theory*, 2012, doi: 10.1016/j.mechmachtheory.2012.02.010.

[13] M. Rodrigues da Silva, F. Marques, M. Tavares da Silva, and P. Flores, 'A compendium of contact force models inspired by Hunt and Crossley's cornerstone work', *Mech. Mach. Theory*, vol. 167, Jan. 2022, doi: 10.1016/J.MECHMACHTHEORY.2021.104501.

[14] J. E. Quiroga, G. Trujillo, and S. Quintero, 'Study on incipient fault bearing detection based on enveloping and cepstrum techniques', *Ingeniare*, vol. 20, no. 3, pp. 350–359, 2012, doi: 10.4067/S0718-33052012000300009.

[15] P. F. Albrecht, J. C. Appiarius, R. M. McCoy, E. L. Owen, and D. K. Sharma, 'Assessment of the reliability of motors in utility applications — updated', *IEEE Trans. Energy Convers.*, vol. EC-1, no. 1, pp. 39–46, 1986, doi: 10.1109/TEC.1986.4765668.

[16] L. F. Shampine and M. W. Reichelt, 'The MATLAB ode suite', *SIAM J. Sci. Comput.*, 1997, doi: 10.1137/S1064827594276424.

[17] M. M. Berry, 'A Variable-Step Double-Integration Multi-Step Integrator', Virginia Polytechnic Institute and State University, Blacksburg, Virginia, 2004.

[18] E. Corral, R. Gismeros, F. Marques, P. Flores, M. J. Gómez García, and C. Castejon, 'Dynamic Modeling and Analysis of Pool Balls Interaction', in *Computational Methods in Applied Sciences*, vol. 53, Springer, 2020, pp. 79–86.

[19] D. G. Alciatore, *The Illustrated Principles of Pool and Billiards*. Sterling Pub., 2004.

[20] S. Mathavan, M. R. Jackson, and R. M. Parkin, 'A theoretical analysis of billiard ball dynamics under cushion impacts', *Proc. Inst. Mech. Eng. Part C J. Mech. Eng. Sci.*, vol. 224, no. 9, pp. 1863–1873, Jan. 2010, doi: 10.1243/09544062JMES1964.

[21] N. A. De Sá Teixeira, A. M. Oliveira, and A. D. Silva, 'An information integration study on the intuitive physics of the Newton's cradle', *Psicologica*, vol. 35, no. 3, pp. 479–502, 2014.

# Section
# FLEXIBLE MULTIBODY DYNAMICS

https://doi.org/10.3311/ECCOMASMBD2021-218



# Computation of internal stress resultants in beam elements with constrained torsional warping

**Koen Dwarshuis, Marijn Nijenhuis, Ronald Aarts, Marcel Ellenbroek, Dannis Brouwer**

Faculty of Engineering Technology
University of Twente
P.O. Box 217, 7500 AE Enschede, The Netherlands
[k.s.dwarshuis, m.nijenhuis, r.g.k.m.aarts, m.h.m.ellenbroek, d.m.brouwer]@utwente.nl

**ABSTRACT**

The computation of stress in beam elements requires the internal stress resultants like axial force and bending moments. For displacement-based beam elements, these resultants can be obtained 1) based on equilibrium, 2) consistent to the constitutive law or 3) based on load interpolation functions. Although the methods give similar results in case of small deformation, the discrepancies in case of large deformation are significant. This paper shows that the method based on equilibrium gives the most accurate results.

Torsion of beam elements causes warping of the cross section. This warping is constrained at clamped ends of beam elements, causing extra stress. This paper shows a method to accurately obtain the corresponding internal stress resultants, i.e. the Saint-Venant torsion moment and bimoment.

**Keywords:** Beam, stress, internal stress resultants, Vlasov beam theory, flexures.

## 1. INTRODUCTION

Structures are often analyzed using beam-elements. This paper is motivated by flexure mechanisms in particular, where each leaf spring can be modelled by multiple serial connected beam elements [1-5]. Fig. 1 shows an example. Stress in mechanisms that are modelled by beam-elements can be computed in three steps, see Fig. 1:

1. The displacements, deformations and reaction forces on each beam element are computed based on the stiffness relations;
2. For each beam-element the internal stress resultants are computed at a finite number of points along the beam axis. These stress resultants are quantities like the axial force and bending moments.
3. The stress-distribution on the cross section is computed based on the internal stress resultants. Formulas for this can be found in standard text books [6].

This paper focusses on step 2, the computation of internal stress resultants for three-dimensional beams undergoing large deformation. Firstly by comparing 3 different methods to compute five of the internal stress resultants and secondly by proposing an accurate method to interpolate the internal stress resultants related to torsion.

The internal stress resultants can be determined from equilibrium equations or be computed consistent with the constitutive law. These two methods give a different result. For small planar elastic deformations though, it was concluded that the discrepancies between these methods are small [7-9].

However, the deformation in a beam element can be large. Moreover, by using beam elements that are accurate for larger deformation, less serial connected beam elements are required to model a single leafspring accurately, and this increases the computational efficiency. A significant

https://doi.org/10.3311/ECCOMASMBD2021-218

amount of literature is published on the modelling of stiffness of beam elements for large deformation. An overview can be found in [10]. The use of these beam models urges for an accurate method to obtain internal stress resultants in case of large deformation.

Two specific beam formulations are used in this paper, a 2nd order formulation [11] and a 3rd order formulation [12]. The 3rd order formulation is based on the Hellinger-Reissner principle, which implies that interpolation functions for both load and displacement fields are used. The load interpolation functions can be used to obtain the internal stress resultants. This is the third method that is used in this paper for comparison.

Torsion of a beam generally causes warping of the cross section. This warping however is constrained at the clamped ends of the beam element and this can cause significantly extra stiffness and stress [13, 14]. This effect can be included in a beam element by two extra deformation modes for the torsion, which is also applied in the used formulations [11, 12]. The correct computation of the corresponding stress requires two internal stress resultants, namely the bimoment and the Saint-Venant torsion. These stress resultants however cannot be derived very accurately by the three previously mentioned methods. This paper presents a more suitable method to obtain the bimoment and Saint-Venant torsion moment.

The results in this paper are derived for the case of flexure mechanisms, using beam elements with thin rectangular cross section, in which the torsional warping is explicitly modelled. However, the results also apply to most other applications, beam formulations and different cross sectional shapes.

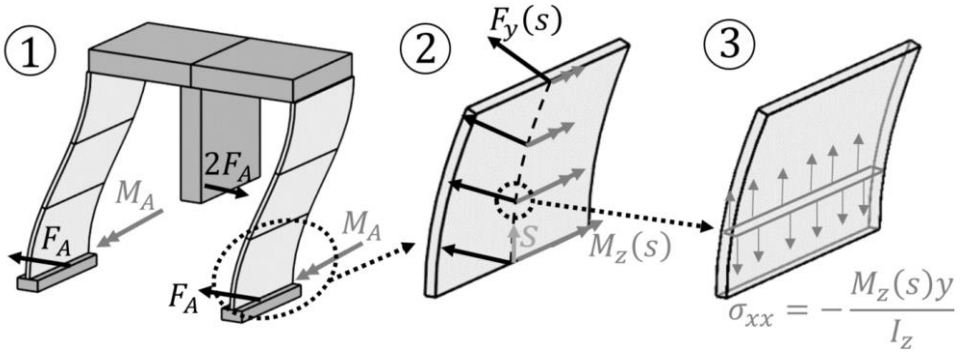


**Figure 1.** Steps to obtain stress, shown for a parallel flexure guidance consisting of two flexures (each modelled by three beam elements) and a connecting rigid part, 1) compute forces and displacements of a mechanism, 2) compute for each beam element the internal stress resultants 3) compute the stress distribution on the cross section

## 2. METHOD

This section shows how the internal stress resultants can be obtained based on the results of step 1 of Fig. 1. These results are visualized in Fig. 2: the positions ($\boldsymbol{r}_p$ $\boldsymbol{r}_q$) and orientations ($\boldsymbol{R}_p$, $\boldsymbol{R}_q$) of both nodes of the beam-element, and the forces ($\boldsymbol{F}_p, \boldsymbol{F}_q$), moments, ($\boldsymbol{M}_p$, $\boldsymbol{M}_q$) and bimoments ($B_p$, $B_q$) at both nodes. Based on the nodal positions, orientations and the mode-shapes of the element, the local displacements, ($u_x(s)$, $u_y(s)$, $u_z(s)$) and local rotations ($\phi_x(s)$, $\phi_y(s)$, $\phi_z(s)$) can be obtained. Here $s$ is the axial coordinate from 0 to the undeformed length $L_0$. Using these local displacements, the global positions ($\boldsymbol{r}(s)$) and orientations ($\boldsymbol{R}(s)$) inside the element can also be found.

Seven internal stress resultants should be obtained: section 2.1 presents three methods to obtain the axial force, shear forces in the local $y$-direction and $z$-direction and the bending moment around the local $y$-axis and $z$-axis. Section 2.2 explains three methods to obtain the Saint-Venant torsion moment and the bimoment.

https://doi.org/10.3311/ECCOMASMBD2021-218

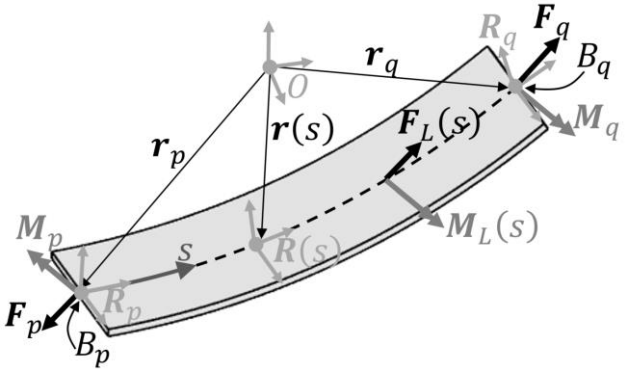


**Figure 2.** Beam-element, showing the forces, positions and orientations for both nodes and internally. Reference frame $O$ is the global reference frame.

### 2.1. Internal stress resultants for extension, shear and bending

**Method A1 – Equilibrium**. The internal stress resultants can be found based on equilibrium, using the values at both nodes:

$$\boldsymbol{F}_L(s) = \boldsymbol{R}^T(s)\boldsymbol{F}_q,\ \boldsymbol{M}_L(s) = \boldsymbol{R}^T(s)\big(\boldsymbol{M}_q + \big(\boldsymbol{r}(s) - \boldsymbol{r}_q\big) \times \boldsymbol{F}_q\big) \tag{1}$$

where the subscript $L$ emphasizes that it is expressed in the local reference frame $\boldsymbol{R}(s)$. The local force is composed of the axial force and the 2 shear forces and the moment is composed of the total torsion moment and the 2 bending moments:

$$\boldsymbol{F}_L(s) = \begin{Bmatrix} F_x(s) \\ F_y(s) \\ F_z(s) \end{Bmatrix},\ \boldsymbol{M}_L(s) = \begin{Bmatrix} M_x(s) \\ M_y(s) \\ M_z(s) \end{Bmatrix}. \tag{2}$$

**Method A2 – Constitutive law**. The internal stress resultants are directly related to the derivatives of the local displacements:

$$\begin{aligned} F_x(s) &= EAu_x'(s) \\ F_y(s) &= GA\kappa_y\left(u_y'(s) - \phi_z(s)\right), \qquad M_y(s) = EI_y\phi_y'(s), \\ F_z(s) &= GA\kappa_z\left(u_z'(s) + \phi_y(s)\right), \qquad M_z(s) = EI_z\phi_z'(s), \end{aligned} \tag{3}$$

where $(\,)'$ defines a derivative to coordinate $s$. $E$ is the elasticity modulus of the material and $G$ the shear modulus, $A$ is the cross sectional area, $\kappa$ the shear correction factor according to Cowper [15] and $I_y$ and $I_z$ are the second moments of area.

**Method A3 – Load interpolation functions.** The third order beam element is derived based on the Hellinger-Reissner principle. This implies that it is derived based on a combination of load interpolation functions and displacement interpolation functions of which the corresponding coordinates are computed in step 1 of Fig 1. These load interpolation functions (see eq. 24 of ref. [12]) give a direct estimation for the required internal stress resultants.

### 2.2. Saint-venant torsion moment and bimoment

Torsion causes warping of the cross section. At the clamped ends of a beam this warping is constrained, resulting in additional strain energy storage, which causes extra stiffness and stress. The internal stress resultant related to warping is the bimoment, $B$. The shear stress is related to the Saint-Venant torsion moment, $T_x$. According to Vlasov torsion theory [14] the total torsion moment is composed of the Saint-Venant torsion moment and the derivative of the bimoment:

$$T_x(s) + B'(s) = M_x(s), \tag{4}$$

Below, three methods are given to compute the Saint-Venant torsion moment and the bimoment.

https://doi.org/10.3311/ECCOMASMBD2021-218

**Method B1 – Interpolation.** The bimoment is available at both nodes such that the bimoment can be obtained by a linear interpolation between these two values:

$$B(s) = -B_p \frac{L-s}{L} + B_q \frac{s}{L} \tag{5}$$

The Saint-Venant torsion moment is not available at the nodes so it cannot be obtained by interpolation. The Saint-Venant torsion moment can however be approximated by the total torsion moment $T_x(s) \approx M_x(s)$, which is a good approximation far from the clamped ends. This total torsion moment $M_x(s)$ can be computed based on equilibrium, see method A1, eq. (2).

**Method B2 – Constitutive law.** The Saint-Venant torsion moment and bimoment are directly related to derivatives of the torsion angle:

$$T_x(s) = GI_t \phi_x'(s), \qquad B(s) = -EI_\omega \phi_x''(s) \tag{6}$$

where $I_t$ is Saint-Venant's torsion constant and $I_\omega$ is Vlasov's warping constant [14].

**Method B3 – ODE.** The Saint-Venant torsion moment and the bimoment can be solved based on the differential equation in eq. (4). According to eq. (6) the Saint-Venant torsion moment and bimoment are related like:

$$B(s) = -\frac{EI_\omega}{GI_t} T_x'(s) \tag{7}$$

Substituting this result into eq. (4) gives the ordinary differential equation (ODE):

$$T_x - \frac{EI_\omega}{GI_t} T_x'' = M_x(s) \tag{8}$$

To solve for $T_x$ a homogeneous and a particular solution have to be obtained.

For the particular solution $M_x(s)$ is approximated by a 4th order polynomial. This is done by first approximating the internal forces on the undeformed element (the orange, dotted line in Fig. 3a). The torsion $M_x^*(s)$ and the shear force $F_z^*(s)$ are linearly interpolated between their values on the nodes. The bending moment $M_y^*(s)$ is approximated by a second order polynomial that corresponds to the moments on the nodes and satisfies $M_y^{*\prime\prime}(s) = F_z^{*\prime}(s)$. Then, using equilibrium considerations, the total torsion moment at the deformed line (black dotted line in Fig. 3a) is computed by:

$$M_x^{(4th)}(s) = M_x^*(s) + M_y^*(s) \cdot \phi_z(s) - F_z^*(s) \cdot u_y(s) \tag{9}$$

The resulting relation is fourth order, assuming the displacement $u_y(s)$ to be a third order polynomial which is common in beam elements. Note that this equation neglects displacements in the z-direction as the shown beam element is very stiff in this direction. However, displacements in the z-direction could be accounted for in similar way as for the $y$-direction by including the term $-M_z^*(s) \cdot \phi_y(s) + F_y^*(s) \cdot u_z(s)$. Having a polynomial expression for $M_x(s)$, the particular solution $T_x^{(P)}$ of the ODE is easily obtained. The corresponding bimoment can be obtained by using eq. (7). For a constant total torsion moment, the solution is $T_x^{(P)}(s) = M_x$, $B^{(P)}(s) = 0$. This indicates that the particular solution describes the bimoment due to a variation of the total torsion moment over the axial coordinate.

The homogeneous solution describes the effects at the boundaries of a leafspring where the warping is usually fully constrained or completely released. The homogeneous solution of the ODE is:

$$T_x^{(HG)}(s_{LF}) = C_1 \cosh(\lambda s_{LF}) + C_2 \sinh(\lambda s_{LF}), \ \lambda = \sqrt{GI_t/EI_\omega} \tag{10}$$

where $s_{LF}$ is the axial coordinate for a whole leaf spring, from 0 to the undformed length $L_{LF}$. The corresponding bimoment is, according to eq. (7):

$$B^{(HG)}(s_{LF}) = -\sqrt{\frac{EI_\omega}{GI_t}} (C_1 \sinh(\lambda s_{LF}) + C_2 \cosh(\lambda s_{LF}))$$

The constants $C_i$ are computed based on the end-conditions of a full leafspring. For a clamped

https://doi.org/10.3311/ECCOMASMBD2021-218

end we have the boundary condition $T_x = 0$ and for a free end we have the condition $B = 0$ (see Fig. 3b). So the particular solution was computed for each beam element individually, where the homogeneous solution is computed for a whole leafspring at once.

Note that as this method does not use the bimoment at the nodes that was computed in step 1 of Fig 1, it can also be used with beam elements that do not have warping modes.

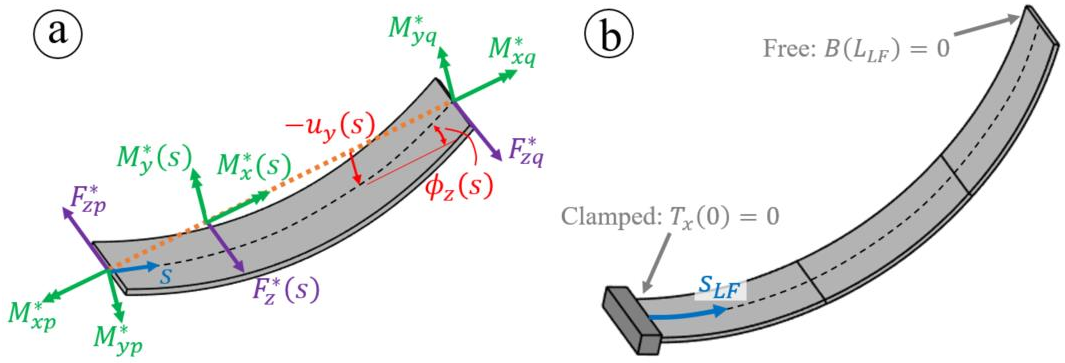


**Figure 3.** a) The particular solution is obtained using an estimation of the total torsion moment, which is derived based on an approximation of the forces on the undeformed line $M^*_x(s)$, $M^*_y(s)$ and $F^*_z(s)$, and its deflection, $u_y(s)$, $\phi_z(s)$. b) The homogeneous solution is based on the end-points of a whole leafspring

## 3. RESULTS

This section applies the methods to investigate which method is most accurate. A 2nd order beam model [11] and a 3rd order model [12] are used, with slightly different deformation modes as derived in appendix A of [16]. A rectangular beam with the following dimensions and material properties is used: length: $L = 100$ mm, width: $w = 10$ mm, thickness: $t = 0.3$ mm, material elasticity: $E = 200$ GPa, Poisson ratio: $\nu = 0.3$. Vlasov's warping constant is computed as $I_\omega = w^3t^3/144$, see [17, 18]. The left side of the beam is fixed to the ground, the torsional warping at both sides is constrained and the right side is subjected to six different loading conditions, visualized in Fig. 4.

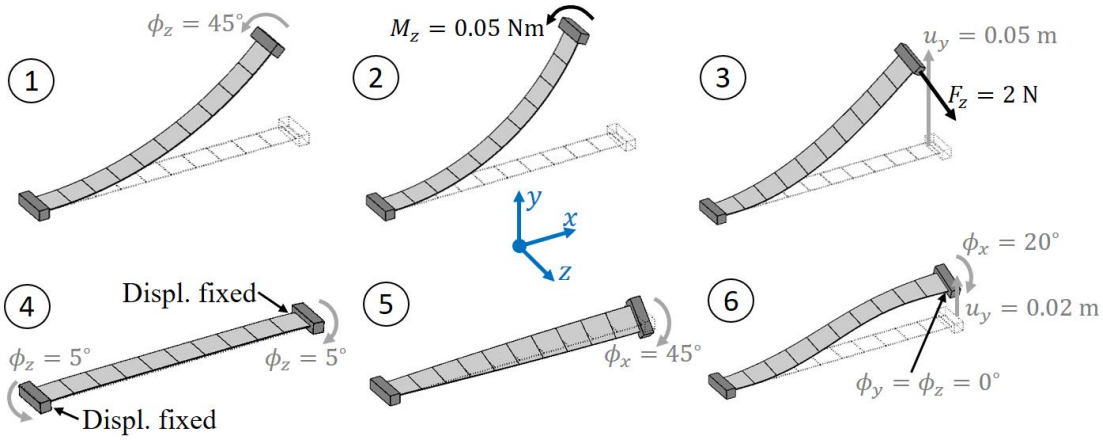


**Figure 4.** Load cases of the leaf spring, modelled by 10 beam elements. The left side is always completely fixed, except for case 4. 1) bending rotation, 2) applied bending moment, 3) bending displacement in combination with a shear force, 4) the displacement of both ends is fixed and both ends are rotated to create a coupling between the axial and bending direction, 5) torsion, 6) torsion in combination with bending to create a significantly varying torsion over the axial coordinate.

https://doi.org/10.3311/ECCOMASMBD2021-218

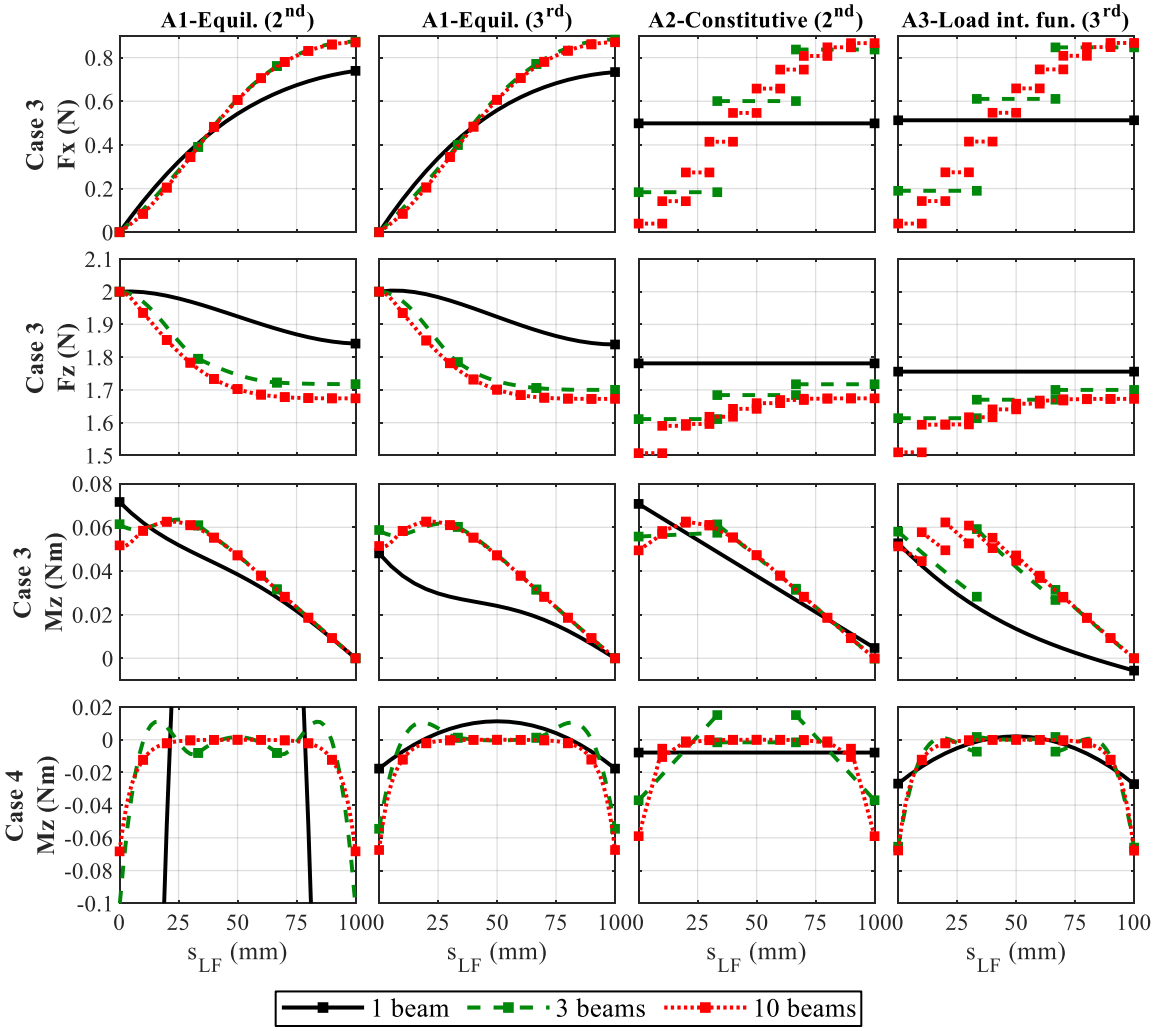


**Figure 5.** Resulting internal stress resultants as function of the axial coordinate $s_{LF}$ for two loading cases shown in Fig. 4. The leaf spring is modelled with 1, 3 and 10 beam elements. Method A1 is applied with the 2nd order and with the 3rd order beam element. Method A2 is only applied with the 2nd order beam element (the results with the 3rd order element were worse in general). Method A3 can only be applied with the 3rd order element.

Case 1 and 2 are simple, the only nonzero internal stress resultant is the bending moment around the z-axis which is constant. For these two cases all methods give the exact result. Fig. 5 shows results for case 3 and 4 to compare methods A1, A2 and A3. Some observations are:

- The differences between the results of the three methods are significant if few beam elements are used.
- The results show that all methods converge to the same result if many beam elements are used in series, indicating that all methods converge to the exact solution. One exception on this observation is in the shear force $F_z$ where method A2 and A3 give fundamentally wrong results. Appendix A explains this and shows that the resulting relative error in the final stress is small.
- Method A1 converges the most rapidely to the exact solution when using more beam elements. The most imporantant reason for this is that this method accounts for local rotations of the cross section, i.e. the vector with internal foces $\boldsymbol{F}_L(s)$ and the vector with internal moments $\boldsymbol{M}_L(s)$ is rotated according to the orientation of the cross section $\boldsymbol{R}(s)$, see eq. (1).
- The internal stress resultants obtained by method A1 are continuous between the elements, where this is not the case for the methods A2 and A3.

https://doi.org/10.3311/ECCOMASMBD2021-218

- The 3rd order beam element gives generally better results than the 2nd order beam element, especially in case 4.

Fig. 6 shows results of torsion (method B1-B3). The following observations are made:

- The bimoment on the beam nodes of case 5 is perfectly computed by the 3rd order beam element, but method B1 still gives a quite bad estimation inside the elements because of the linear interpolation. Method B2 also gives significant errors, even with 10 beam elements the bimoment at both ends is 40% off. Method B3 gives a perfect result for case 5, even with only one beam element.
- In case 6 the total torsion moment varies over the axial coordinate and therefore the bimoment at the nodes is not accurately approximated by the 2nd order and 3rd order beam element if only 1 or 3 beam elements are used. Therefore method B1 gives a bad estimation of the internal bimoment. Method B3 gives a relatively accurate result, even with only 1 beam element.
- The Saint-Venant torsion moment in case 6 is in method B1 approximated by the total torsion moment. Internally this approximation is quite good (for 3 or more beam elements) but not at both ends of the leaf spring. In method B2 clearly a lot of beam elements are required for an accurate estimation of the Saint-Venant torsion moment. Method B3 gives an accurate result with 3 or more beam elements.

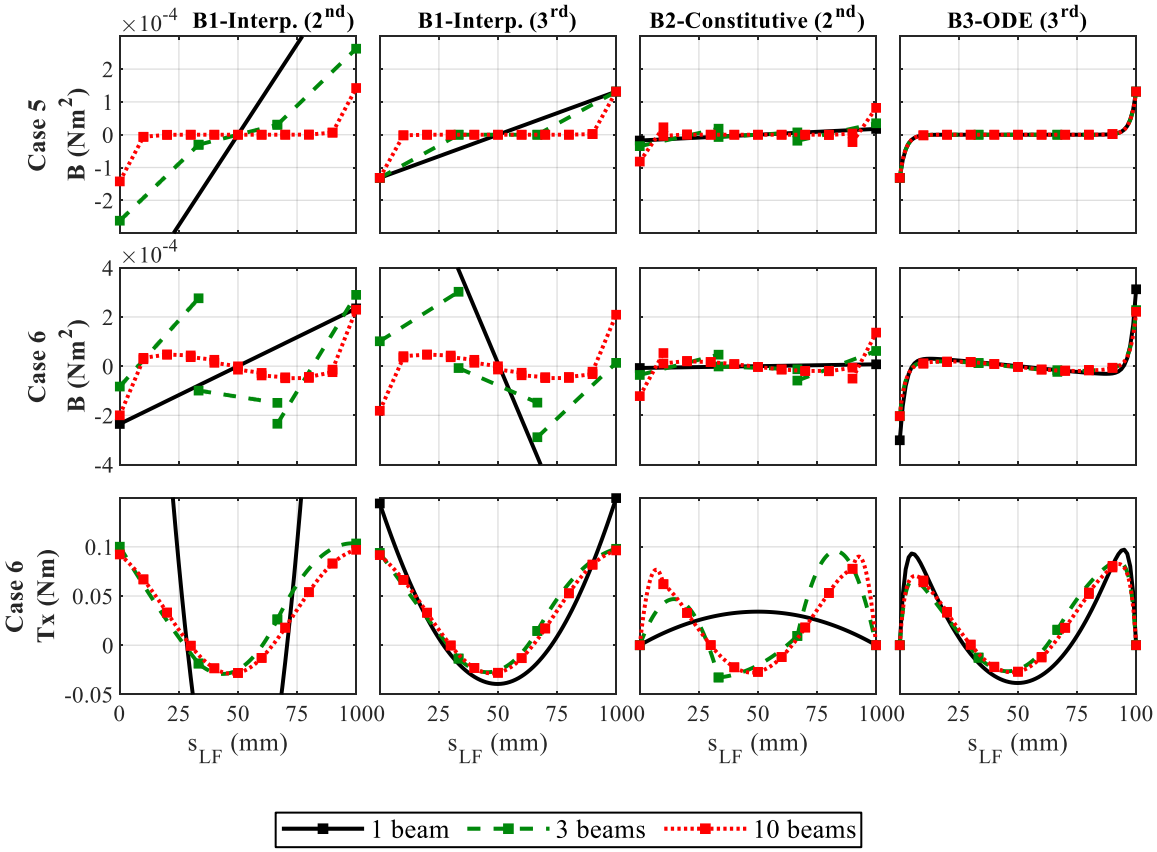


**Figure 6.** Resulting internal bimoment and Saint-Venant torsion moment as function of the axial coordinate $s_{LF}$. The leaf spring is modelled with 1, 3 and 10 beam elements. Results are given for methods B1-B3 based on results of the 2nd order or 3rd order beam element.

In summary, method A1 gives more accurate results than method A2 and A3. The most important reason is that it is easy to evaluate the nonlinear equilibrium-equation (see eq. (1)), therefore method A1 accounts for the effect of local displacements and rotations of the cross sections on the equilibrium. Method A2 and A3 use interpolation functions that are based on equilibrium in the undeformed state.

Method B3 gives the most accurate results for torsion. Similar to method A1, this method obtains an accurate estimation of the total torsion moment based on equilibrium and the local displacements of the beam. Based on this estimation the Saint-Venant torsion moment and the bimoment can be obtained accurately.

As this reasoning is not limited to the used beam dimensions and loading conditions, method A1 and B3 will be the most accurate for displacement based elements in general.

## 4. CONCLUSIONS

The computation of stress in beam elements requires the internal stress resultants to be obtained. These resultants can be obtained by different methods, which result in significant different results in case of large deformation. Three methods were compared to obtain the internal stress resultants for extension, shear and bending. The method based on equilibrium equations gives the most accurate results.

Three other methods are proposed to obtain the internal stress resultants related to torsion, i.e. the Saint-Venant torsion moment and the bimoment. It was found that these resultants can be obtained accurately based on the solution of the differential equation that relates the total torsion moment, the Saint-Venant torsion moment and the bimoment.

The results indicate that a right choice of the method to obtain the internal stress resultants is highly relevant for an accurate computation of the stress in beam elements undergoing large deformation.

## ACKNOWLEDGMENTS

This work is part of the research programme HTSM 2017 with project number 16210, which is partly financed by the Netherlands Organisation for Scientific Research (NWO).

## REFERENCES

[1] Wiersma, D., Boer, S., Aarts, R.G., Brouwer, D.M., Design and performance optimization of large stroke spatial flexures, Journal of computational and nonlinear dynamics, 9(1) (2014) 011016. doi: 10.1115/1.4025669.

[2] Naves, M., Brouwer, D.M., Aarts, R.G., Building Block-Based Spatial Topology Synthesis Method for Large-Stroke Flexure Hinges, Journal of mechanisms and robotics, 9(4) (2017) 041006. doi: 10.1115/1.4036223.

[3] Boer, S.E., Aarts, R., Brouwer, D.M., Jonker, J.B., Multibody modelling and optimization of a curved hinge flexure, In: The 1st joint international conference on multibody system dynamics, Lappeenranta, (2010)

[4] Naves, M., Aarts, R., Brouwer, D., Large stroke high off-axis stiffness three degree of freedom spherical flexure joint, Precision engineering, 56 (2019) 422-431. doi: 10.1016/j.precisioneng.2019.01.011.

[5] Brouwer, D.M., Meijaard, J.P., Jonker, J.B., Large deflection stiffness analysis of parallel prismatic leaf-spring flexures, Precision engineering, 37(3) (2013) 505-521.

[6] Ugural, A.C., Stresses in beams, plates, and shells. CRC press (2009)

[7] Saje, M., Turk, G., Kalagasidu, A., Vratanar, B., A kinematically exact finite element formulation of elastic–plastic curved beams, Computers & structures, 67(4) (1998) 197-214.

[8] Vratanar, B., Saje, M., A consistent equilibrium in a cross-section of an elastic–plastic beam, International Journal of Solids and Structures, 36(2) (1999) 311-337.

[9] Zupan, D., Saje, M., Finite-element formulation of geometrically exact three-dimensional beam theories based on interpolation of strain measures, Computer Methods in Applied Mechanics and Engineering, 192(49-50) (2003) 5209-5248.

[10] Sen, S., Beam Constraint Model: Generalized Nonlinear Closed-form Modeling of Beam Flexures for Flexure Mechanism Design. (2013).

[11] Jonker, J., Implementation of shear deformable thin-walled beam element for flexible multibody dynamics, In: Proceedings of the 8th ECCOMAS thematic conference on multibody dynamics 2017, Prague, Czech Republic, (2017)

[12] Nijenhuis, M., Meijaard, J., Brouwer, D., A spatial closed-form nonlinear stiffness model for sheet flexures based on a mixed variational principle including third-order effects, Precision Engineering, 66 (2020) 429-444. doi: 10.1016/j.precisioneng.2020.08.003.

[13] Nijenhuis, M., Jonker, B., Brouwer, D., Importance of warping in beams with narrow rectangular cross-sections: an analytical, numerical and experimental flexible cross-hinge case study, In: European Congress on Computational Methods in Applied Sciences and Engineering: Springer (2019)

[14] Vlasov, V.Z., Thin-walled elastic beams. Jerusalem: Israel program for scientific translations (1961)

[15] Cowper, G., The shear coefficient in Timoshenko's beam theory, Journal of applied mechanics, 33(2) (1966) 335-340.

[16] Dwarshuis, K., Aarts, R., Ellenbroek, M., Brouwer, D., Kinematically started efficient position analysis of deformed compliant mechanisms utilizing data of standard joints, Mechanism and Machine Theory, 152 (2020) 103911. doi: 10.1016/j.mechmachtheory.2020.103911.

[17] Trahair, N.S., Flexural-torsional buckling of structures. CRC press (2017)

[18] Timoschenko, S., On the torsion of a prism, one of the cross-sections of which remains plane, Proceedings of the london mathematical society, 2(1) (1922) 389-397.

## APPENDIX A – INCONSISTENCY INTERNAL SHEAR FORCE

This appendix explains why an inconsistency is found between the shear force that is obtained based on the equilibrium-method and the shear force obtained by the constitutive law, even for short beams. The inconsistency occurs in generalized strain beam elements. First the relations of these elements are summarized. Then two causes of the inconsistencies are derived. Finally, it is shown why the error in the final stress is small in engineering practice.

The derivations in this appendix use the formulation of the 2nd order element [11], but also hold for the used 3rd order element, which are both generalized strain elements.

### Summary generalized strain beam formulation

In a generalized strain beam element deformation modes are defined, which are related to the nodal coordinates

$$\boldsymbol{\varepsilon} = \boldsymbol{\mathcal{D}}(\boldsymbol{x}) \tag{11}$$

The used beam elements have 8 deformation modes (eq. 7 of [11]), but only the first 6 are relevant. They are visualized in Fig. 7.

https://doi.org/10.3311/ECCOMASMBD2021-218

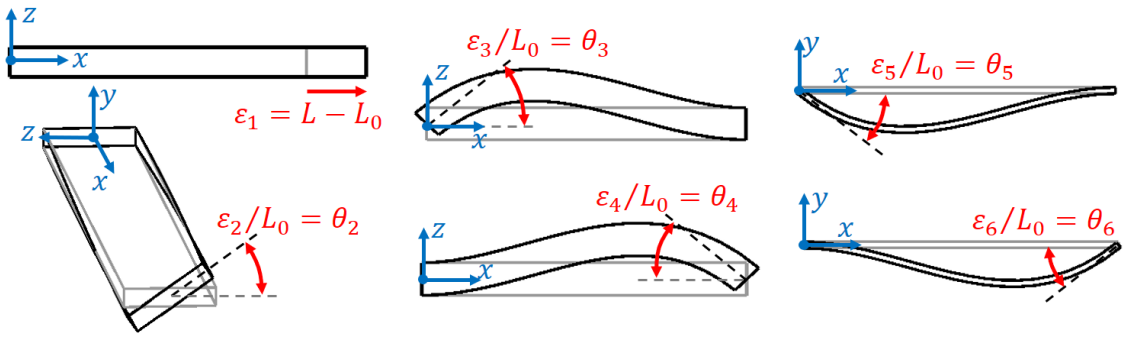


**Figure 7**. Six deformation modes of the beam element

The generalized forces of these deformation modes are called generalized external stresses, $\boldsymbol{\sigma}$. They are related to the generalized strains by a constant stiffness matrix: $\boldsymbol{\sigma} = \boldsymbol{S\varepsilon}$. The exact expression for the stiffness matrix is given in eq. 40 of [11], but not relevant for the current derivation. According to the principle of virtual work the nodal forces are related to the generalized stresses (eq. 15 of [11])

$$\boldsymbol{F} = \boldsymbol{\mathcal{D}}_{,\boldsymbol{u}}^{T}\boldsymbol{\sigma} \tag{12}$$

in which $\boldsymbol{F}$ consist of 12 terms, i.e. the forces and moments at both nodes. $\boldsymbol{\mathcal{D}}_{,\boldsymbol{u}}^{T}$ is the derivative of $\boldsymbol{\mathcal{D}}(\boldsymbol{x})$ to the nodal displacements and rotations, $\boldsymbol{u}$. The exact relations given in eq. 10-15 of [11]. The relevant results (eq. 16 of [11]) are:

$$\begin{aligned}
&\sigma_1 = -F_x^p = F_x^q && \text{(normal force)}\\
&L\sigma_2 = -M_x^p = M_x^q && \text{(torsion moment)}\\
&L\sigma_3 = -M_y^p, \quad L\sigma_4 = M_y^q \\
&L\sigma_5 = -M_z^p, \quad L\sigma_6 = M_z^q && \text{(bending moments)}
\end{aligned} \tag{13}$$

These reaction forces are also visualized in Fig. 8.

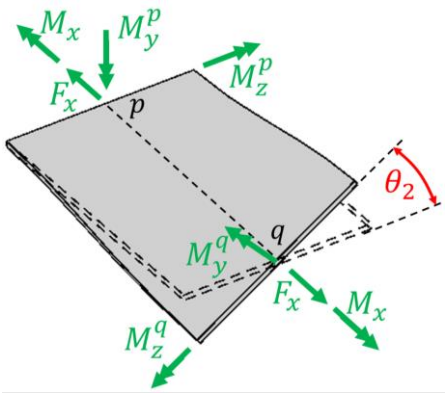


**Figure 8**. Reaction forces on a beam element with torsion

### Cause 1 – Different coordinate-axes

In short the first reason for inconsistency is that the relations between the deformation modes and coordinates are defined using different coordinate axes such that also the relations between $\boldsymbol{\sigma}$ and reaction forces are defined in different axes. Fig. 8 shows for example that $M_z^p$ and $M_y^p$ have a different orientation.

It can be easily seen from Fig. 8 that based on method A1 (equilibrium), the shear force at node p should be:

$$F_z^p = -\frac{M_y^p}{L} + \frac{M_y^q}{L}\cos(\theta_2) - \frac{M_z^q}{L}\sin(\theta_2) \tag{14}$$

The same result is obtained by substituting eq. (13) into the full expression of eq. (12). By assuming a short beam element, such that also the deformations become small, we can linearize this result and substitute $\theta_2 = \phi_x' L$:

$$F_z^p = -\frac{M_y^p}{L} + \frac{M_y^q}{L} - \frac{M_z^q}{L}\phi_x' L = -\frac{M_y^p}{L} + \frac{M_y^q}{L} - M_z^q \phi_x' \tag{15}$$

which is the internal shear stress at node p that is found from equilibrium.

The resulting shear force at node $p$ based on method A2 (constitutive law) is intuitively only related to the moments around the $y$-axis:

$$F_z^p = -\frac{M_y^p}{L} + \frac{M_y^q}{L} \tag{16}$$

This result can also be obtained by a more detailed derivation: First substituting the mode shapes (eq. 38 of [11]) into eq. (3) of this paper:

$$F_z^p = EA\kappa_z \cdot \left(u_z'(s) + \phi_y(s)\right) = \frac{EA\kappa_z}{L} \cdot \frac{\Phi_z}{2(1+\Phi_z)}(\varepsilon_4 - \varepsilon_3) \tag{17}$$

where $\Phi_z = 12EI_y/GA\kappa_y L^2$. Then the inverse of the stiffness relation (eq. 40 of [11]) and eq. (13) can be used to obtain:

$$F_z^p = \frac{1}{L}(-\sigma_3 + \sigma_4) = -\frac{M_y^p}{L} + \frac{M_y^q}{L} \tag{18}$$

The difference in result between the equilibrium method and the constitutive-law-method is the term $-M_z^q \phi_x'$. This term can be nonzero, even for very short beams. As the bending moment in a very short beam is almost constant we will write this as $-M_z \phi_x'$

**Cause 2 – Second order term in the deformation modes**

In the 2nd order beam element a second order term is included which correct for the fact that the local rotation matrices are not linear in the virtual rotations around the $x$, $y$ and $z$ axis (eq. 45 of [11] gives the full expression of the rotation matrix). This causes a coupling term between the torsional deformation ($\varepsilon_2$) and the bending deformation ($\varepsilon_3$ till $\varepsilon_6$). This effect is included by modifying the strain definitions (see eq. 54 of [11]). The modification that causes an inconsistency is in the torsional mode:

$$\hat{\varepsilon}_2 = \varepsilon_2 + \frac{1}{L}(-\varepsilon_3\varepsilon_6 + \varepsilon_4\varepsilon_5) \tag{19}$$

where $\hat{\varepsilon}_2$ is the second order generalized strain definition and the other generalized strains are the linear definitions as visualized in Fig. 7. For short elements, all the generalized strains become small, meaning that this second order term with squared generalized strains becomes negligible.

The reason for the inconsistency is that the extra term in the derivative $\widehat{\mathcal{D}}_{,\boldsymbol{u}}^{(2)} = d\hat{\varepsilon}_2/d\boldsymbol{u}$ does not become zero for short beams. This causes an extra term in eq. (12), which causes an inconsistency as derived in more detail below.

Eq. (12) can be evaluated for $F_z^p$. Note that $F_z^p$ is a term in $\boldsymbol{F}$ such that only the derivative of $\boldsymbol{\mathcal{D}}$ to the corresponding displacement, $z_p$, is required:

$$F_z^p = \widehat{\boldsymbol{D}}_{,z_p}^T \boldsymbol{\sigma} = \left(\frac{\partial \hat{\boldsymbol{\varepsilon}}}{\partial z_p}\right)^T \boldsymbol{\sigma} = \frac{\partial \varepsilon_1}{\partial z_p}\sigma_1 + \frac{\partial \hat{\varepsilon}_2}{\partial z_p}\sigma_2 + \frac{\partial \varepsilon_3}{\partial z_p}\sigma_3 + \frac{\partial \varepsilon_4}{\partial z_p}\sigma_4 + \frac{\partial \varepsilon_5}{\partial z_p}\sigma_5 + \frac{\partial \varepsilon_6}{\partial z_p}\sigma_6, \tag{20}$$

in which the nonzero terms in the derivative of $\hat{\varepsilon}_2$ are, see eq. (19):

https://doi.org/10.3311/ECCOMASMBD2021-218

$$\frac{\partial \hat{\varepsilon}_2}{\partial z_p} = \frac{\partial \varepsilon_2}{\partial z_p} - \frac{\varepsilon_6}{L}\frac{\partial \varepsilon_3}{\partial z_p} - \frac{\varepsilon_3}{L}\frac{\partial \varepsilon_6}{\partial z_p} + \frac{\varepsilon_5}{L}\frac{\partial \varepsilon_4}{\partial z_p} + \frac{\varepsilon_4}{L}\frac{\partial \varepsilon_5}{\partial z_p} \tag{21}$$

In a beam element that is only deformed in bending around the $z$-axis, eq. (20) reduces to:

$$F_z^p = -\left(\frac{\varepsilon_6}{L} + \frac{\varepsilon_5}{L}\right)\sigma_2 - \sigma_3 + \sigma_4 = (\theta_6 + \theta_5)\frac{M_x}{L} + \frac{M_y^p}{L} + \frac{M_y^q}{L} \tag{22}$$

For short beam elements the resulting terms are:

$$F_z^p = \frac{\theta_6+\theta_5}{L} M_x + \frac{M_y^p}{L} + \frac{M_y^q}{L} = \phi_z' M_x + \frac{M_y^p}{L} + \frac{M_y^q}{L} \tag{23}$$

This is the internal stress resultant found by method A1 (equilibrium). The internal stress resultant obtained by method A2 (Constitutive law) is given in eq. (16). So the inconsistent term is $\phi_z' M_x$. This is a nonzero error, even for very short beam elements.

**Influence of the inconsistencies on the total stress**

The inconsistent terms in the shear stress are: $-M_z\phi_x'$ and $\phi_z' M_x$ as derived above. The resulting stress terms can be shown to be negligible for initially straight beams of common materials, based on classical beam theory, see e.g. [6]. For common materials we can assume that the maximum strain is limited to 1% and the maximum shear strain to 0.5%, this limits the curvatures $\phi_x'$ and $\phi_z'$. For bending of a beam with rectangular cross section of thickness $t$ and width $w$ (Fig. 9) the relation between the highest strain and the bending curvature is:

$$\varepsilon_{xx\,max}^{(bend)} = \frac{t}{2}\phi_z' \le 0.01 \Rightarrow \phi_z' \le \frac{1}{50t} \tag{24}$$

For torsion, the relation between the highest shear stress and the curvature is approximately:

$$\gamma_{xz\,max}^{(tor)} = \phi_x' t \le 0.005 \Rightarrow \phi_x' \le \frac{1}{20t} \tag{25}$$

The following relations exist between the highest stress and the internal stress resultants of shear, bending and torsion:

$$\tau_{xz\,max}^{(shear)} = \frac{3}{2wt}\cdot F_z(s), \qquad \sigma_{xx\,max}^{(bend)} = \frac{6}{wt^2}M_z(s), \qquad \tau_{xz\,max}^{(tor)} = \frac{6}{wt^3}T_x(s) \tag{26}$$

Using these formulas we can relate the inconsistency in shear stress because of the terms $-M_z\phi_x'$ and $\phi_z' M_x$ to the existing stress of bending and torsion, accounting for the constraints in eqs. (24,25):

$$\tau_{xz\,max}^{(shear,inconsis)} = \frac{3}{2wt}|\phi_z' M_x - M_z\phi_x'| \le \frac{3}{2wt}\left|\frac{\tau_{xz\,max}^{(tor)} wt^2}{6}\cdot\frac{1}{50t} - \frac{\sigma_{xx\,max}^{(bend)} wt^2}{6}\cdot\frac{1}{20t}\right| \tag{27}$$

By simplifying this equation we obtain the maximum extra shear stress:

$$\tau_{xz\,max}^{(shear,inconsis)} \le \left|\frac{\tau_{xz\,max}^{(tor)}}{100} - \frac{\sigma_{xx\,max}^{(bend)}}{80}\right| \tag{28}$$

Which indicates that the error in shear stress is below 1/80 of the total stress. Moreover, both terms in these equation are likely to partly cancel each other, which further reduces the error.

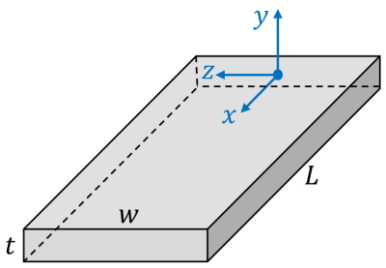


**Figure 9**. Rectangular cross section with thickness $t$ and width $w$

https://doi.org/10.3311/ECCOMASMBD2021-274



# Sloshing Dynamics Estimation for Liquid-filled Containers under 2-Dimensional Excitation

**Roberto Di Leva**[1], **Marco Carricato**[1], **Hubert Gattringer**[2], **Andreas Müller**[2]

[1] Department of Industrial Engineering
University of Bologna
Viale del Risorgimento 2, 40136 Bologna, Italy
[roberto.dileva, marco.carricato]@unibo.it

[2] Institute of Robotics
Johannes Kepler University Linz
Altenberger Straße 69, 4040 Linz, Austria
[hubert.gattringer, a.mueller]@jku.at

**ABSTRACT**

Many industrial applications require the displacement of liquid-filled containers on planar paths, by means of linear transport systems or serial robots. The movement of the liquid inside the container, known as *sloshing*, is usually undesired, so there is the necessity to keep under control the peaks that the liquid free surface exhibits during motion. This paper aims at validating a model for estimating the liquid sloshing height, taking into account 2-dimensional planar motions of a cylindrical container, with accelerations up to 9.5 m/s$^2$. This model can be exploited for assessment or optimization purposes.
Experiments performed with a robot following three paths, each one of them with different motion profiles, are described. Comparisons between experimental results and model predictions are provided and discussed.

**Keywords:** Sloshing, Prediction model, Validation, Experiments, 2-Dimensional motion.

## 1 INTRODUCTION

The transport of containers filled with liquids finds application in several industrial contexts, e.g. in food&beverage or pharmaceutical production and packaging lines. Typically, the manipulation of such containers is assigned to linear transport systems or industrial serial robots; in many cases the required motion follows planar curves. The prediction of the liquid movement inside the container, known as *sloshing*, is important to prevent the liquid from overflowing. Additionally, a reliable sloshing prediction model can be exploited to limit the stirring of the liquid during task execution.
For this purpose, machine-learning methodologies are presented in [1] and [2], where, starting from data collection, predictive algorithms are built to inspect the behavior of discrete liquid particles inside a cylindrical container. This technique, though very powerful, requires experiments to be run in advance, together with a not negligible computational effort.
In [3] the coefficients of the nonlinear sloshing dynamics model presented in [4] are provided to evaluate the sloshing height for 3-dimensional motions, leading to a complex formulation, which may be difficult to use.
A ready-to-use alternative is represented by the development of equivalent discrete mechanical models. The literature considers two main discrete approaches for the modelling of sloshing dynamics inside a container subject to 2-dimensional planar motion [5]: a spherical pendulum and a 2-dof mass-spring-damper system. In the former case, the generalized coordinates describing the system are the angles defining the position of the pendulum mass, whereas, in the latter one, they are the mass displacements from the reference position. Although being intuitive, the use of the angular coordinates of the pendulum mass to assess the sloshing behavior of the liquid (see [6, 7]) lacks physical meaning, above all when the knowledge of the liquid peak height is important. For this reason, in the spherical pendulum model used in [8], [9] and [10], the sloshing height is estimated by means of the tangent functions of the spherical coordinates. However, estimating the

https://doi.org/10.3311/ECCOMASMBD2021-274

sloshing height by means of the tangent of the pendulum angles may lead to singularity conditions, when the container acceleration is high, since in this case these angles can approach 90° and the tangent tend to assume unrealistic high values.
To overcome this drawback, a novel approach, based on the mass-spring-damper model [11], is proposed in [12] for the sloshing-height estimation. This model is validated for 1-dimensional motions and the authors propose the possible extension to planar motions, but no experimental validation is provided. The latter is the objective of this paper, particularly referring to 2-dimensional planar motions of a cylindrical container.
The paper is structured as follows. Section 2 presents the model parameters and the equations of motion (EOMs) of the corresponding generalized coordinates. Section 3 provides the formulation of the sloshing-height estimation. In Section 4, the results from an experimental campaign are described and discussed. Lastly, in Section 5 conclusions are drawn and suggestions for future developments are given.

## 2 SLOSHING MODEL

### 2.1 Model Parameters

We will consider a cylindrical container of radius $R$, filled with a liquid of height $h$ and mass $m_F$. A simplified discrete mechanical model can be used to reproduce the liquid-sloshing dynamics. In particular, the mass-spring-damper model comprises a rigid mass $m_0$ (whose signed vertical distance from the liquid's center of gravity $G$ is $h_0$) that moves rigidly with the container, and a series of moving masses $m_n$, with each one of them representing the equivalent mass of a sloshing mode (Fig. 1a). Each modal mass $m_n$ is restrained by a spring $k_n$ and a damper $c_n$, and its signed vertical distance from $G$ is $h_n$. The model parameters can be determined by imposing a number of equivalence conditions with the original system [5]:

- the overall mass must be the same:

$$m_F = m_0 + \sum_{n=1}^{\infty} m_n \tag{1}$$

- the height of the center of gravity $G$ must remain the same for small oscillations of the liquid:

$$m_0 h_0 + \sum_{n=1}^{\infty} m_n h_n = 0 \tag{2}$$

- the natural frequency associated with the $n$-th mode must coincide with the one that can be obtained from the continuum model:

$$\omega_n^2 = \frac{k_n}{m_n} = g\frac{\xi_{1n}}{R}\tanh\left(\xi_{1n}\frac{h}{R}\right) \tag{3}$$

- the sloshing force acting on the container wall must be the same as the one calculated from the continuum model:

$$m_n = m_F \frac{2R}{\xi_{1n} h(\xi_{1n}^2 - 1)}\tanh\left(\xi_{1n}\frac{h}{R}\right). \tag{4}$$

In Equations (3) and (4), $\xi_{1n}$ is the root of the derivative of the Bessel function of the first kind with respect to the radial coordinate $r$, for the $1^{st}$ circumferential mode and the $n$-th radial mode [13], while $g$ is the gravity acceleration. The damping ratio $\zeta_n = \frac{c_n}{2\sqrt{k_n m_n}}$ can be determined by using empirical formulas [5].
For a container under 2-dimensional motion on the horizontal $xy$ plane, the excitation is provided by the container accelerations along the $x$ and $y$ directions, i.e. $\ddot{\mathbf{S}}_0 = [\ddot{x}_0 \;\; \ddot{y}_0]^T$. The motion of the $n$-th sloshing mass is described by the generalized coordinates $(x_n, y_n)$, whose definition is illustrated in Fig. 1b. The latter are then used to compute the liquid sloshing height.

https://doi.org/10.3311/ECCOMASMBD2021-274

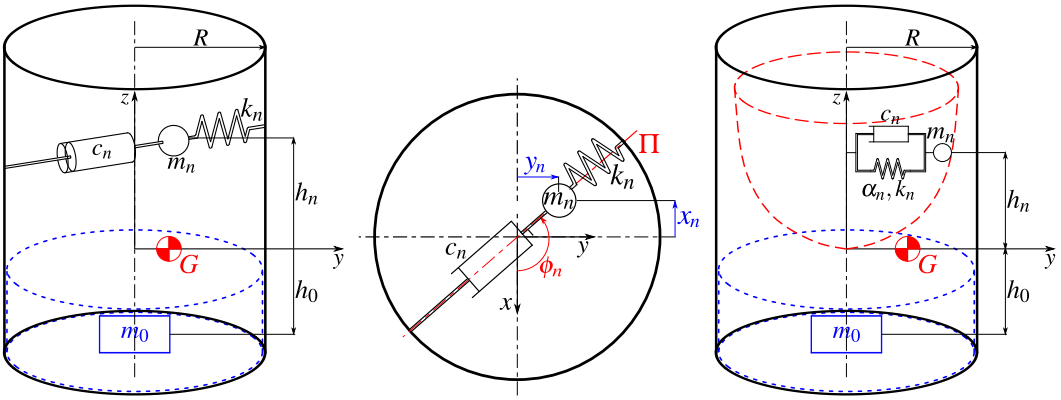


(a) Model Parameters. (b) Top view showing the $n$-th generalized coordinates. (c) Sloshing mass sliding on a parabolic surface.

Figure 1: Mass-spring-damper model.

### 2.2 Equations of Motion

In general, three dynamic regimes are possible [5]:

- small oscillations in which the liquid free surface remains planar (Fig. 2a);
- relatively-large-amplitude oscillations in which the liquid free surface is no longer planar (Fig. 2b);
- strongly nonlinear motion, where the liquid free surface exhibits instantaneous peaks characterized by swirling shapes.

While the third motion regime will not be object of the present study, the first and second cases can be analyzed by means of a linear mass-spring-damper model (L model) and a nonlinear mass-spring-damper model (NL model), respectively.

The NL model considers the sloshing mass $m_n$ as sliding on a parabolic surface, with an attached nonlinear spring of order $w$ (Fig. 1c) [11]. The analytical expression of the parabolic surface allows the writing of the vertical coordinate $z_n$ as a function of $x_n$ and $y_n$, namely:

$$z_n = \frac{C_n}{2R}(x_n^2 + y_n^2) \tag{5}$$

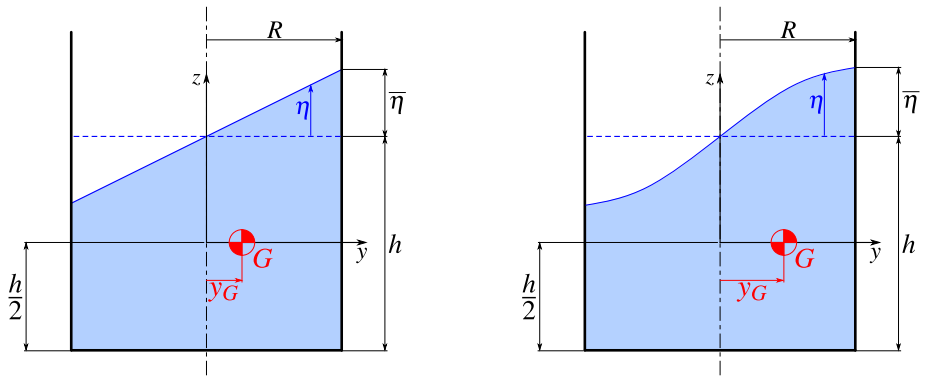


(a) Assumption of planar free surface. (b) Assumption of nonplanar free surface.

Figure 2: Liquid free-surface shapes.

https://doi.org/10.3311/ECCOMASMBD2021-274

where $C_n = \omega_n^2 \frac{R}{g}$. The time derivative of Equation (5) yields:

$$\dot{z}_n = \frac{C_n}{R}(\dot{x}_n x_n + \dot{y}_n y_n) \tag{6}$$

The nonlinear spring exerts the forces $\alpha_n k_n x_n^{2w-1}$ and $\alpha_n k_n y_n^{2w-1}$, along the $x$ and $y$ direction respectively. In this paper, we choose $w = 2$ and $\alpha_n = 0.58$ [11]. If the radial generalized coordinate $r_n = \sqrt{x_n^2 + y_n^2}$ is introduced, the nonlinear-spring force in the radial direction can be written as $\alpha_n k_n r_n^{2w-1}$.
The equations of motion (EOMs), describing the time evolution of the generalized coordinates $(x_n, y_n)$, can be obtained by means of the Lagrange Equations:

$$\begin{cases} \dfrac{d}{dt}\left(\dfrac{\partial T}{\partial \dot{x}_n}\right) - \dfrac{\partial T}{\partial x_n} + \dfrac{\partial V}{\partial x_n} = -\dfrac{\partial D}{\partial \dot{x}_n} \\ \dfrac{d}{dt}\left(\dfrac{\partial T}{\partial \dot{y}_n}\right) - \dfrac{\partial T}{\partial y_n} + \dfrac{\partial V}{\partial y_n} = -\dfrac{\partial D}{\partial \dot{y}_n} \end{cases} \tag{7}$$

where:

- the kinetic energy $T$ of the $n$-th sloshing mass can be computed by taking into account its velocity $\dot{\mathbf{s}}_n = [\dot{x}_n \ \dot{y}_n \ \dot{z}_n]^T$, the container velocity $\dot{\mathbf{S}}_0 = [\dot{x}_0 \ \dot{y}_0]^T$ and by exploiting the Equation (6):

$$T = \frac{1}{2} m_n [(\dot{x}_0 + \dot{x}_n)^2 + (\dot{y}_0 + \dot{y}_n)^2 + \dot{z}_n^2] = \frac{1}{2} m_n \left[ (\dot{x}_0 + \dot{x}_n)^2 + (\dot{y}_0 + \dot{y}_n)^2 + \frac{C_n^2}{R^2}(\dot{x}_n x_n + \dot{y}_n y_n)^2 \right] \tag{8}$$

- the potential energy $V$ considers the contribution of gravity and nonlinear-spring forces, namely:

$$V = m_n g z_n + \int_0^{r_n} \alpha_n k_n r_n^{2w-1} dr_n = m_n g \frac{C_n}{2R}(x_n^2 + y_n^2) + \frac{\alpha_n k_n}{2w}(x_n^2 + y_n^2)^w \tag{9}$$

- the Rayleigh function $D$ accounts for energy dissipation:

$$D = \frac{1}{2} c_n (\dot{x}_n^2 + \dot{y}_n^2 + \dot{z}_n^2) = m_n \zeta_n \omega_n \left[ \dot{x}_n^2 + \dot{y}_n^2 + \frac{C_n^2}{R^2}(\dot{x}_n x_n + \dot{y}_n y_n)^2 \right]. \tag{10}$$

The substitution of Equations (8), (9) and (10) in the system (7) leads to the formulation of two coupled EOMs for the NL model:

$$\begin{cases} \ddot{\bar{x}}_n + 2\omega_n \zeta_n [\dot{\bar{x}}_n + C_n^2(\bar{x}_n^2 \dot{\bar{x}}_n + \bar{y}_n \dot{\bar{y}}_n \bar{x}_n)] + C_n^2(\bar{x}_n \dot{\bar{x}}_n^2 + \bar{x}_n^2 \ddot{\bar{x}}_n + \bar{x}_n \dot{\bar{y}}_n^2 + \bar{x}_n \ddot{\bar{y}}_n \bar{y}_n) + \\ \qquad \omega_n^2 \bar{x}_n [1 + \alpha_n (\bar{x}_n^2 + \bar{y}_n^2)^{w-1}] + \dfrac{\ddot{x}_0}{R} = 0 \\ \ddot{\bar{y}}_n + 2\omega_n \zeta_n [\dot{\bar{y}}_n + C_n^2(\bar{y}_n^2 \dot{\bar{y}}_n + \bar{x}_n \dot{\bar{x}}_n \bar{y}_n)] + C_n^2(\bar{y}_n \dot{\bar{y}}_n^2 + \bar{y}_n^2 \ddot{\bar{y}}_n + \bar{y}_n \dot{\bar{x}}_n^2 + \bar{y}_n \ddot{\bar{x}}_n \bar{x}_n) + \\ \qquad \omega_n^2 \bar{y}_n [1 + \alpha_n (\bar{x}_n^2 + \bar{y}_n^2)^{w-1}] + \dfrac{\ddot{y}_0}{R} = 0 \end{cases} \tag{11}$$

where $\bar{x}_n = x_n/R$, $\bar{y}_n = y_n/R$. As far as the L model is concerned, the linearization of the EOMs in Equation (11) provides two decoupled EOMs in the generalized coordinates $(x_n, y_n)$ of the $n$-th mode:

$$\begin{cases} \ddot{x}_n + 2\zeta_n \omega_n \dot{x}_n + \omega_n^2 x_n = -\ddot{x}_0 \\ \ddot{y}_n + 2\zeta_n \omega_n \dot{y}_n + \omega_n^2 y_n = -\ddot{y}_0 \end{cases} \tag{12}$$

https://doi.org/10.3311/ECCOMASMBD2021-274

Table 1: SH estimation for a 1-dimensional planar motion.

| | | |
|---|---|---|
| **L model** | $\overline{\eta}_n = \frac{4hm_n}{m_F R} y_n$ | (19) |
| **NL model** | $\overline{\eta}_n = \frac{\xi_{1n}^2 hm_n}{m_F R} y_n$ | (20) |

## 3 SLOSHING-HEIGHT ESTIMATION

### 3.1 1-Dimensional Motion

If only a 1-dimensional excitation in the $y$ direction is provided and the phenomenon of rotary sloshing is neglected [5], solely the generalized coordinate $y_n$ is different from zero. In such a case, the conservation of the center of gravity $y$-coordinate, between the continuum model and the equivalent model, yields:

$$y_G m_F = \sum_{n=1}^{\infty} y_n m_n + y_0 m_0 = \sum_{n=1}^{\infty} y_n m_n \tag{13}$$

Considering a cylindrical container of section $S = \pi R^2$, filled with a liquid of height $h$, $y_G$ can be computed as:

$$y_G = \frac{1}{Sh} \iint_S \int_{-\frac{h}{2}}^{\frac{h}{2}+\eta(r,\theta,\overline{\eta}_n)} y \, dz dS = \frac{1}{\pi R^2 h} \int_0^R \int_0^{2\pi} \int_{-\frac{h}{2}}^{\frac{h}{2}+\eta(r,\theta,\overline{\eta}_n)} r^2 \sin\theta \, dz d\theta dr, \tag{14}$$

where the function $\eta(r,\theta,\overline{\eta}_n)$ describes the liquid free-surface shape, $\overline{\eta}_n$ is the sloshing height of the $n$-th mode, $(r,\theta)$ are the polar coordinates, with $x = r\cos\theta$, $y = r\sin\theta$, $dS = r\, d\theta dr$. As for the L model, the function $\eta(r,\theta,\overline{\eta}_n)$ describes a plane (Fig. 2a):

$$\eta(r,\theta,\overline{\eta}_n) = \sum_{n=1}^{\infty} \overline{\eta}_n \frac{r}{R} \sin\theta, \tag{15}$$

whereas, for the NL model, the nonplanar free surface can be described by means of the first-kind Bessel function (Fig. 2b), namely:

$$\eta(r,\theta,\overline{\eta}_n) = \sum_{n=1}^{\infty} \overline{\eta}_n \frac{J_1(\xi_{1n}\frac{r}{R})}{J_1(\xi_{1n})} \sin\theta. \tag{16}$$

Independently from the adopted function $\eta$, the expression of $y_G$ from Equation (14) can be used in Equation (13) to express $\overline{\eta}_n$ as a function of the model parameters and the generalized coordinates $(x_n, y_n)$, with the latter being obtained by solving the EOMs (see Section 2.2). The L-model assumption of planar surface leads to:

$$y_G = \frac{1}{\pi R^2 h} \int_0^R \int_0^{2\pi} \int_{-\frac{h}{2}}^{\frac{h}{2}+\sum \overline{\eta}_n \frac{r}{R}\sin\theta} r^2 \sin\theta \, dz d\theta dr = \frac{R}{4h} \sum_{n=1}^{\infty} \overline{\eta}_n \tag{17}$$

Regarding the NL model, by exploiting one of the Bessel function properties, i.e. $\int_0^R r^2 J_1(\xi_{1n}\frac{r}{R})\, dr = R^3 \frac{J_1(\xi_{1n})}{\xi_{1n}^2}$, $y_G$ can be evaluated as:

$$y_G = \frac{1}{\pi R^2 h} \int_0^R \int_0^{2\pi} \int_{-\frac{h}{2}}^{\frac{h}{2}+\sum \overline{\eta}_n \frac{J_1(\xi_{1n}\frac{r}{R})}{J_1(\xi_{1n})}\sin\theta} r^2 \sin\theta \, dz d\theta dr = \frac{R}{h} \sum_{n=1}^{\infty} \frac{\overline{\eta}_n}{\xi_{1n}^2} \tag{18}$$

Inserting the results from Equations (17) and (18) in Equation (13) allows the formulation of the $n$-th sloshing height (SH) for the L and NL models, respectively, as shown in Table 1.

https://doi.org/10.3311/ECCOMASMBD2021-274

### 3.2 2-Dimensional Motion

When accounting for a 2-dimensional excitation, the plane $\Pi$, on which the maximum sloshing height (MSH) occurs, changes its orientation instantaneously, according to a rotation about the $z$-axis by the angle (Fig. 1b):

$$\phi_n = \arctan\left(\frac{y_n}{x_n}\right) \tag{21}$$

If the liquid behavior is analyzed on the plane $\Pi$ at every instant, Equation (13) can be extended to the radial coordinate of $G$, remembering that $r_n = \sqrt{x_n^2 + y_n^2}$:

$$r_G m_F = \sum_{n=1}^{\infty} r_n m_n = \sum_{n=1}^{\infty} m_n \sqrt{x_n^2 + y_n^2} \tag{22}$$

Equations (17) and (18) can be used to express $r_G$ in terms of $\overline{\eta}_n$, depending on the adopted model. The approach seen in Section 3.1 allows to write the formulas for the $n$-th maximum sloshing height (MSH) evaluation, both for the L model and the NL model, considering a 2-dimensional motion of the container (Table 2).

### 3.3 Remarks

By looking at Tables 1 and 2, one can point out that, for equal values of the generalized coordinates $(x_n, y_n)$, the ratio between $\overline{\eta}_n$ obtained from the L model in Equations (19, 23) and $\overline{\eta}_n$ from the NL model in Equations (20, 24) is always $4/\xi_{1n}^2$. If only the $1^{st}$ mode is considered, this ratio is equal to $4/\xi_{11}^2 \approx 1.18$ and shows that the assumption of planar free surface always overestimates the sloshing height compared to the assumption of a nonplanar free surface. Furthermore, while in Equations (19, 20), $\overline{\eta}_n$ has the same sign of $y_n$, in Equations (23, 24) $\overline{\eta}_n$ is always positive. This means that Equations (19, 20) express the trend of the sloshing height on only one side of the container (on the other side, the sloshing height is estimated as the opposite of $\overline{\eta}_n$): in this case, we will simply talk about *sloshing height* (SH). Conversely, in Equations (23, 24), $\overline{\eta}_n$ indicates the maximum peak that occurs on the container wall (on a plane oriented as described in Equation (21)): in this case, we will use the expression *maximum sloshing height* (MSH).

## 4 EXPERIMENTAL RESULTS

The experimental setup considers a cylindrical container with radius $R = 50$ mm and a liquid static height $h = 70$ mm. The employed liquid is water, which is colored by adding dark brown powder, in order to obtain a better contrast for the image processing analysis. Motions are performed by an industrial robot (Stäubli RX130L) and recorded by a GoPro Hero3 camera. The trajectories are planned so that the robot follows three geometrical paths (Fig. 3), each one of them with different motion profiles, characterized by increasing container accelerations:

- a back-and-forth linear path (indicated as *l-motion*);
- an eight-shaped path (*e-motion*);
- a circular path, performed twice in succession (*c-motion*).

Table 2: MSH estimation for a 2-dimensional planar motion.

| | | |
|---|---|---|
| **L model** | $\overline{\eta}_n = \frac{4hm_n}{m_F R}\sqrt{x_n^2 + y_n^2}$ | (23) |
| **NL model** | $\overline{\eta}_n = \frac{\xi_{1n}^2 hm_n}{m_F R}\sqrt{x_n^2 + y_n^2}$ | (24) |

https://doi.org/10.3311/ECCOMASMBD2021-274

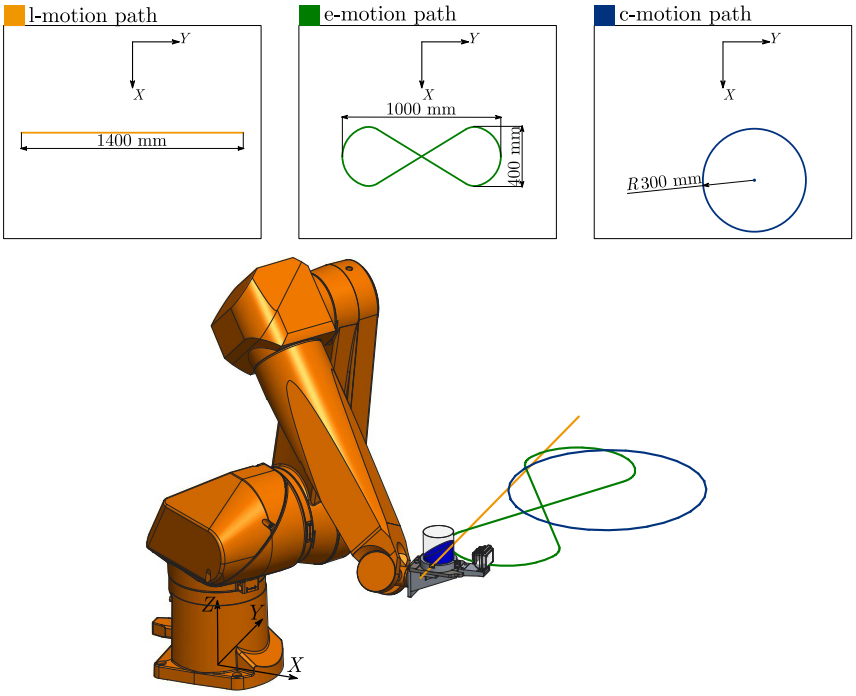


Figure 3: The three paths followed by the robot during experimental validation.

In Fig. 4, the trends of the path parameter second time derivative[1] $\ddot{\sigma}$ are illustrated: for every path, all three motion profiles are showed. Note that the legend refers to the maximum of the container acceleration norm $||\ddot{\mathbf{S}}_0||_{max}$ reached during the corresponding motion.

In Fig. 5, the L and NL model predictions are compared with the results from the experimental motions, only considering the $1^{st}$ sloshing mode. A good adherence between the experiments and the models can be appreciated for the 1-dimensional motions (Fig. 5a, 5b, 5c), and the tracking remains reliable also for 2-dimensional motions, especially when considering lower values of $||\ddot{\mathbf{S}}_0||_{max}$ (Fig. 5d, 5g). As the value of the 2-dimensional excitation $\ddot{\mathbf{S}}_0$ is increased, the model predictions still capture the trend of the real liquid MSH, although they seem to lose accuracy in correspondence of the peaks reached by the liquid (Fig. 5e, 5f, 5h, 5i). This can be eventually attributable to two reasons:

- the high dynamics given to the container causes a regime of strongly nonlinear motions,

[1]Remember that the acceleration $\ddot{\mathbf{S}}_0$ can be written as $\ddot{\mathbf{S}}_0(\sigma,\dot{\sigma},\ddot{\sigma}) = \mathbf{S}_0''(\sigma)\dot{\sigma}^2 + \mathbf{S}_0'(\sigma)\ddot{\sigma}$, where $()' = \partial()/\partial\sigma$ denotes the derivative with respect to the path parameter $\sigma$.

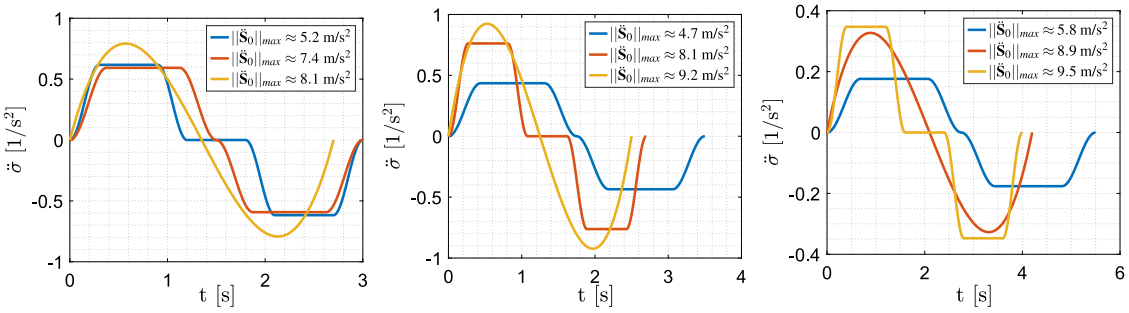


(a) l-motion. (b) e-motion. (c) c-motion.

Figure 4: The three motion profiles performed per each path.

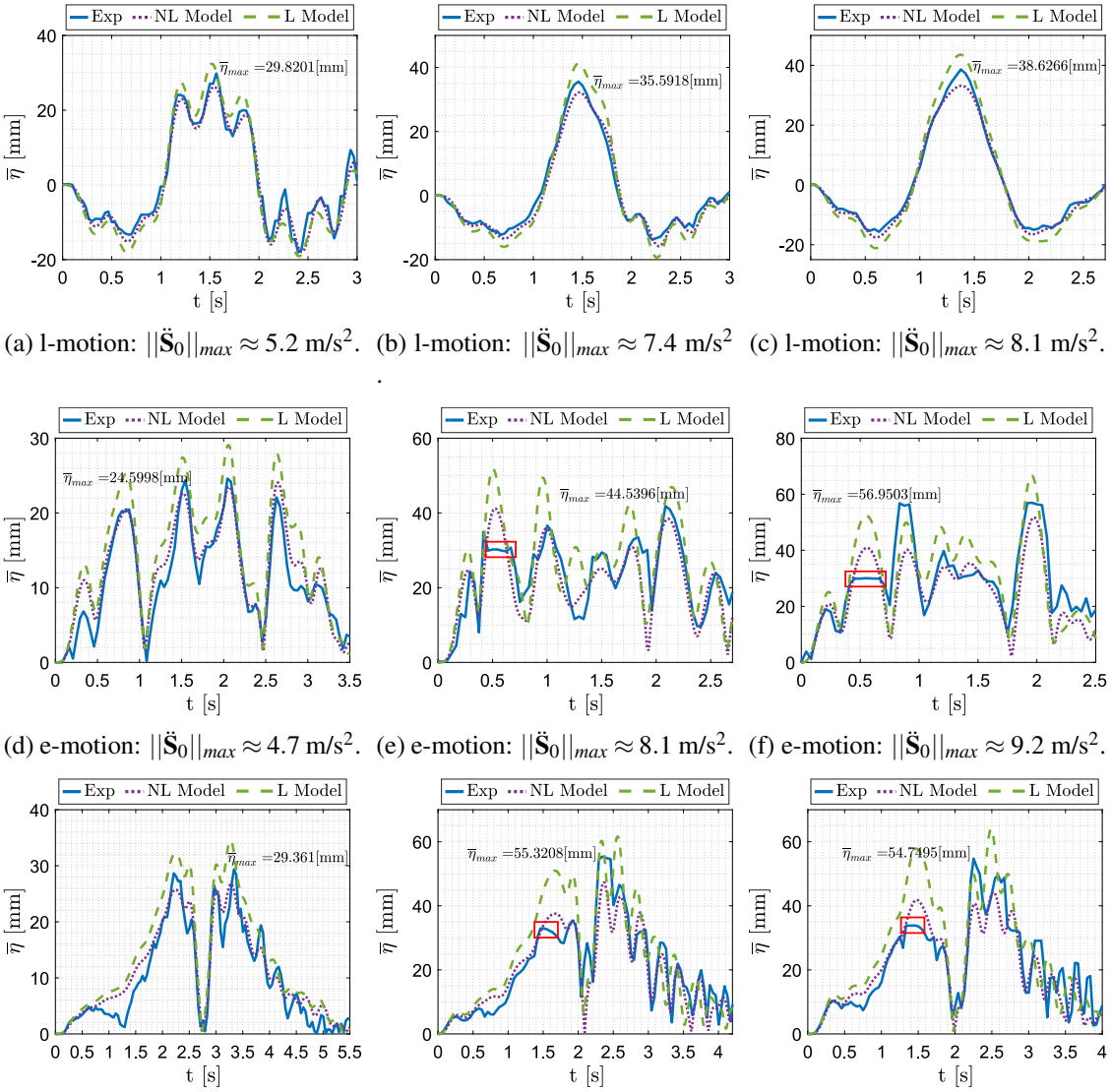


(a) l-motion: $||\ddot{\mathbf{S}}_0||_{max} \approx 5.2$ m/s$^2$. (b) l-motion: $||\ddot{\mathbf{S}}_0||_{max} \approx 7.4$ m/s$^2$ (c) l-motion: $||\ddot{\mathbf{S}}_0||_{max} \approx 8.1$ m/s$^2$.

.

(d) e-motion: $||\ddot{\mathbf{S}}_0||_{max} \approx 4.7$ m/s$^2$. (e) e-motion: $||\ddot{\mathbf{S}}_0||_{max} \approx 8.1$ m/s$^2$. (f) e-motion: $||\ddot{\mathbf{S}}_0||_{max} \approx 9.2$ m/s$^2$.

(g) c-motion: $||\ddot{\mathbf{S}}_0||_{max} \approx 5.8$ m/s$^2$. (h) c-motion: $||\ddot{\mathbf{S}}_0||_{max} \approx 8.9$ m/s$^2$. (i) c-motion: $||\ddot{\mathbf{S}}_0||_{max} \approx 9.5$ m/s$^2$.

Figure 5: Comparison between the proposed models and the experimental results.

where the liquid free surface loses the assumed shape and shows instantaneous swirly peaks, as illustrated in Fig. 6a;

- the height of the frames that are employed for the image processing analysis, grants a greater field of view when the liquid peak occurs on the rear wall of the container (Fig. 6b), whereas, for a peak on the front wall (Fig. 6c), the value of the real MSH is saturated by the frame upper limit.

For instance, the latter reason explains the discrepancy between the experiments and the prediction models in the red areas that are highlighted in Fig. 5e, 5f, 5h, 5i.
Table 3 summarizes the obtained results by reporting the accuracy index

$$\%\varepsilon_{mod} = \frac{\overline{\eta}_{max,mod} - \overline{\eta}_{max,exp}}{\overline{\eta}_{max,exp}} \times 100 \tag{25}$$

where *mod* and *exp* denote the adopted model (L or NL) and the experimental results, respectively. For all motions, $|\%\varepsilon_L|$ is always below the 18%, and $|\%\varepsilon_{NL}|$ never exceeds 19%, with the NL model granting a better tracking during the whole time period. Furthermore, the positive sign of

https://doi.org/10.3311/ECCOMASMBD2021-274

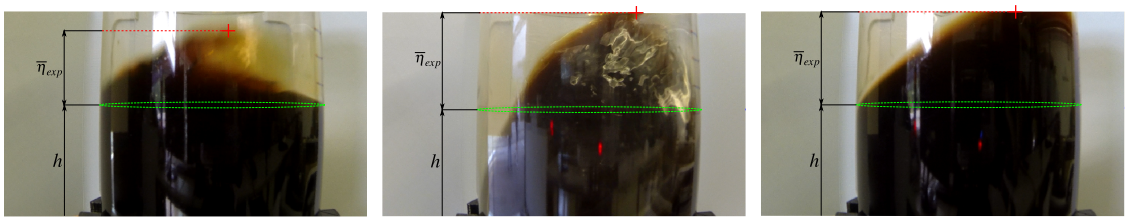


(a) Swirly peak. (b) Back peak. (c) Front peak.

Figure 6: Snapshots from the recorded videos, showing the different peaks reached by the liquid.

Table 3: Accuracy index both for the L model and the NL model.

| | | | |
|---|---|---|---|
| l-motion | $\|\|\ddot{\mathbf{S}}_0\|\|_{max} \approx 5.2$ m/s$^2$ | $\|\|\ddot{\mathbf{S}}_0\|\|_{max} \approx 7.4$ m/s$^2$ | $\|\|\ddot{\mathbf{S}}_0\|\|_{max} \approx 8.1$ m/s$^2$ |
| | $\%\varepsilon_{NL} = -11.9\%$ | $\%\varepsilon_{NL} = -9.5\%$ | $\%\varepsilon_{NL} = -14.1\%$ |
| | $\%\varepsilon_{L} = 8.8\%$ | $\%\varepsilon_{L} = 15.8\%$ | $\%\varepsilon_{L} = 12.8\%$ |
| e-motion | $\|\|\ddot{\mathbf{S}}_0\|\|_{max} \approx 4.7$ m/s$^2$ | $\|\|\ddot{\mathbf{S}}_0\|\|_{max} \approx 8.1$ m/s$^2$ | $\|\|\ddot{\mathbf{S}}_0\|\|_{max} \approx 9.2$ m/s$^2$ |
| | $\%\varepsilon_{NL} = -2.1\%$ | $\%\varepsilon_{NL} = -7.5\%$ | $\%\varepsilon_{NL} = -9.2\%$ |
| | $\%\varepsilon_{L} = 18.3\%$ | $\%\varepsilon_{L} = 16.2\%$ | $\%\varepsilon_{L} = 17.1\%$ |
| c-motion | $\|\|\ddot{\mathbf{S}}_0\|\|_{max} \approx 5.8$ m/s$^2$ | $\|\|\ddot{\mathbf{S}}_0\|\|_{max} \approx 8.9$ m/s$^2$ | $\|\|\ddot{\mathbf{S}}_0\|\|_{max} \approx 9.5$ m/s$^2$ |
| | $\%\varepsilon_{NL} = -8.7\%$ | $\%\varepsilon_{NL} = -14.3\%$ | $\%\varepsilon_{NL} = -19\%$ |
| | $\%\varepsilon_{L} = 17.6\%$ | $\%\varepsilon_{L} = 11.6\%$ | $\%\varepsilon_{L} = 16.9\%$ |

$\%\varepsilon_L$ proves that the L model always overestimates the real SH and MSH peaks, as expected (see Section 3.3), hence providing a more conservative estimation.

## 5 CONCLUSIONS AND FUTURE WORK

A novel technique for the sloshing-height estimation of a liquid inside a cylindrical container subject to 2-dimensional planar motions was proposed, extending what was presented in [12]. The technique is based on simple discrete mechanical models, rather than machine-learning or complex fluidodynamical methodologies, thus granting a reliable and easy-to-compute estimation.
Experiments, considering three container paths performed by an industrial robot with different motion profiles, were presented and the relative results were discussed. An accuracy index was used to prove the effectiveness of the estimation, even for high values of the container acceleration (up to 9.5 m/s$^2$).
Future work will address the use of the proposed sloshing-height estimation for square-section containers, adapting the formulation that was presented in Section 3. Moreover, the extension of the technique to 3-dimensional motions will be investigated. In [6, 7] the additional term $\ddot{z}_0$ is treated as a quantity only affecting the $n$-th natural frequency $\omega_n$. This approach will be transferred to the L and NL models and verified by experimental tests.

## REFERENCES

[1] B. Moya, D. Gonzalez, I. Alfaro, F. Chinesta and E. Cueto. Learning Slosh Dynamics by Means of Data. *Computational Mechanics*, 64(2):511–523, 2019.

[2] B. Moya, I. Alfaro, D. Gonzalez, F. Chinesta and E. Cueto. Physically Sound, Self-learning Digital Twins for Sloshing Fluids. *PLOS ONE*, 15(6):1–16, 2020.

[3] J. Huang and X. Zhao. Control of Three-Dimensional Nonlinear Slosh in Moving Rectangular Containers. *Journal of Dynamic Systems, Measurement, and Control*, 140(8), 2018.

[4] Odd M. Faltinsen, Olav F. Rognebakke and Alexander N. Timokha. Resonant three-dimensional nonlinear sloshing in a square-base basin. *Journal of Fluid Mechanics*, 487:1–42, 2003.

[5] Raouf A. Ibrahim. *Liquid Sloshing Dynamics: Theory and Applications*. Cambridge University Press, 2005.

[6] W. Aribowo, T. Yamashita, and K. Terashima. Integrated Trajectory Planning and Sloshing Suppression for Three-dimensional Motion of Liquid Container Transfer Robot Arm. *Journal of Robotics*, 2015.

[7] J. Reinhold, M. Amersdorfer, and T. Meurer. A Dynamic Optimization Approach for Sloshing Free Transport of Liquid Filled Containers using an Industrial Robot. In *2019 IEEE/RSJ International Conference on Intelligent Robots and Systems (IROS)*, pages 2336–2341, 2019.

[8] L. Moriello, L. Biagiotti, C. Melchiorri, and A. Paoli. Control of Liquid Handling Robotic Systems: A Feed-forward Approach to Suppress Sloshing. In *2017 IEEE International Conference on Robotics and Automation (ICRA)*, pages 4286–4291, 2017.

[9] L. Moriello, L. Biagiotti, C. Melchiorri, and A. Paoli. Manipulating Liquids with Robots: A Sloshing-free Solution. *Control Engineering Practice*, 78:129–141, 2018.

[10] L. Biagiotti, D. Chiaravalli, L. Moriello, and C. Melchiorri. A Plug-In Feed-Forward Control for Sloshing Suppression in Robotic Teleoperation Tasks. In *2018 IEEE/RSJ International Conference on Intelligent Robots and Systems (IROS)*, pages 5855–5860, 2018.

[11] H. Bauer. Nonlinear Mechanical Model for the Description of Propellant Sloshing. *AIAA Journal*, 4:1662–1668, 1966.

[12] L. Guagliumi, A. Berti, E. Monti, and M. Carricato. A Simple Model-based Method for Sloshing Estimation in Liquid Transfer in Automatic Machines. *IEEE Access*, 9:129347–129357, 2021.

[13] H. Bauer. Tables of Zeros of Cross Product Bessel Functions. *Mathematics of Computation*, 18(85):128–135, 1964.

https://doi.org/10.3311/ECCOMASMBD2021-203



# Flexible Multibody Dynamics and Sensitivity Analysis in the Design of a Morphing Leading Edge for High-Performance Sailplanes

**Veit Gufler**[1], **Erich Wehrle**[1], **Johannes Achleitner**[1,2], **Renato Vidoni**[1]

[1] Faculty of Science and Technology
Free University of Bozen-Bolzano
Universitätsplatz - Piazza Università 1
39100 Bozen-Bolzano, South Tyrol, Italy
{Veit.Gufler, Erich.Wehrle, Renato.Vidoni}@unibz.it

[2] Institute of Aircraft Design
Technical University of Munich
Boltzmannstr. 15
85748 Garching, Germany
Johannes.Achleitner@tum.de

## ABSTRACT

High-performance sailplanes have a wide speed range. Form-variable wings with a morphing leading edge in combination with a trailing flap for a high-speed and a low-speed configuration have shown to increase the performance. In the present work, a morphing wing leading edge modeled as a system constituted of a flexible external wing skin and an actuation mechanism with rigid bodies is investigated. Flexible multibody dynamics with the floating frame of reference formulation is applied to analyze the behavior of the system during the motion from the high-speed configuration to the low-speed configuration. The methodology includes generalized-$\alpha$ time integration with Newton–Raphson iterations and efficient design sensitivity analysis. The design sensitivities are calculated with a semi-analytical approach based on direct differentiation. Of particular interest in the simulation are the deviations of the wing profile from the target shape in morphed configuration and the stresses in the external wing skin. The design variables used in the sensitivity analysis include geometric parameters, material parameters and loading parameters. The introduced methods show high efficiency and provides reliable results. The sensitivities are visualized giving an easy interpretation of the sensitivity values and in understanding how the design variables can be changed to improve the design. The sensitivity computations enable further investigations such as uncertainty analysis or gradient-based design optimization of the system.

**Keywords:** flexible multibody dynamics, sensitivity analysis, generalized-$\alpha$ method, morphing wing, morphing leading edge

## 1 INTRODUCTION

High-performance sailplanes have a large envelope of operating speeds. Fixed-geometry aircraft are designed to be a compromise for this wide speed range. Form-variable – or morphing – wings have shown to increase performance particularly when the leading edge of the wing is morphed in combination with a conventional trailing-edge flap [1, 2, 3]. Morphing leading edges have been modeled with traditional "hinged" mechanisms [2, 4] and with compliant mechanisms [3, 5]. Here, flexible multibody dynamics including rigid and flexible bodies is applied to a hinged mechanism. Flexible multibody simulation is a valuable tool to simulate and optimize flexible deformations and large displacements and rotations of such a mechanism. This enables the dynamic analysis during the motion of the mechanism in contrast to previous works in which the system was considered to be quasi-static [2, 3, 4, 5]. In this work, we extend an in-house flexible multibody simulation code SIMULI to accommodate the simulation and sensitivity analysis of a morphing leading edge to be integrated in a future work in a design optimization framework.

The flexible multibody simulation approach of this work was developed and introduced in the application to cleaning mechanisms of Tyrolean weirs, intake systems of small Alpine hydroelectric plants [6, 7, 8]. The developed methodology includes efficient sensitivity analysis with the goal of

https://doi.org/10.3311/ECCOMASMBD2021-203

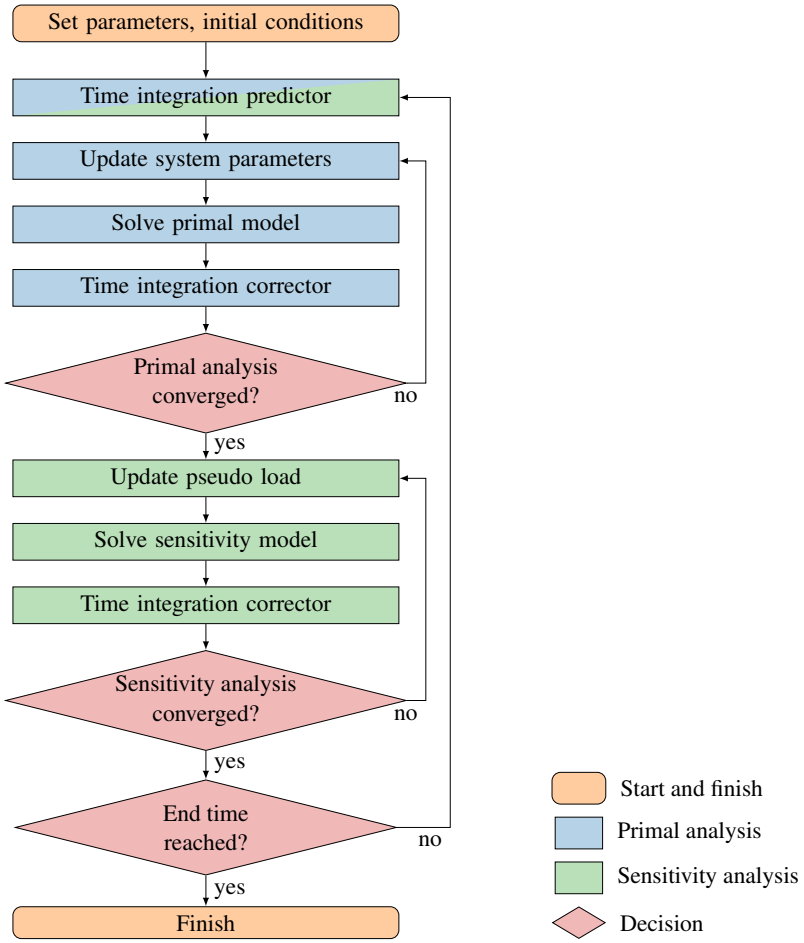


Figure 1: Flow chart for solving routine for flexible multibody dynamics and integrated sensitivity analysis

use in gradient-based design optimization of flexible mechanisms. This is developed for the simulation of a morphing leading edge concept using a flexible wing structure and a mechanism with rigid bodies driving the deformation from the high-speed profile configuration to the low-speed profile configuration. Special attention is paid to the computation, analysis and interpretation of design sensitivities. Therefore, the sensitivities of both stress and geometric deviation from the target geometry with respect to the design variables are investigated. The design variables considered here include geometric parameters, material parameters and loading parameters.

## 2 FLEXIBLE MULTIBODY DYNAMICS

The simulation of flexible multibody dynamics is categorized in three components as described in [8]: governing equation, time integration and nonlinear solver. The simulation is referred as primal analysis to differentiate from the sensitivity analysis. Fig. 1 shows the flow chart of the method and the components are introduced here in § 2 for the primal analysis and in § 3 for the sensitivity analysis.

### 2.1 Governing equation

The governing equations are given by index-1 differential–algebraic equations for the motion of flexible multibody systems and the constraint equations of kinematic joints,

$$\underline{R} = \begin{bmatrix} \underline{\underline{m}} & \underline{\underline{\mathrm{J}}}_{\Phi}^{T} \\ \underline{\underline{\mathrm{J}}}_{\Phi} & \underline{\underline{0}} \end{bmatrix} \begin{bmatrix} \ddot{\underline{q}} \\ \underline{\lambda} \end{bmatrix} - \begin{bmatrix} \underline{F}_{\mathrm{ext}} + \underline{F}_{v} - \underline{\underline{d}}\,\dot{\underline{q}} - \underline{\underline{k}}\,\underline{q} \\ \underline{F}_{c} \end{bmatrix} = \underline{0}, \tag{1}$$

https://doi.org/10.3311/ECCOMASMBD2021-203

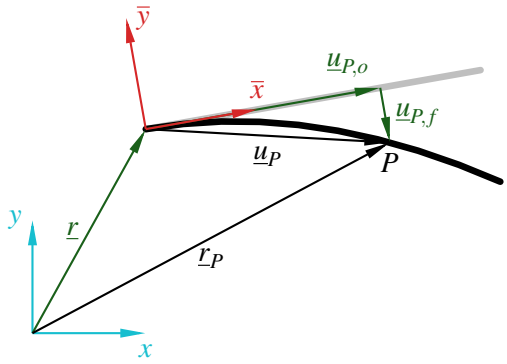


Figure 2: Floating frame of reference formulation (FFRF)

where $R$ is the residual, $q$ is the generalized position, $\lambda$ are Lagrangian multipliers of the kinematic constraints, $m$ is the mass, $d$ is the damping, $k$ is the stiffness, $\Phi$ are kinematic constraints, J is the Jacobian (i.e. the partial derivative with respect to position), $F_{\text{ext}}$ is the external force, $F_c$ is the right hand side of acceleration constraints, $F_v$ is the quadratic velocity force and overdots represent the first $\dot{\star}$ and second $\ddot{\star}$ differentiation with respect to time. Single underlined symbols $\underline{\star}$ represent vectors, double underlined symbols $\underline{\underline{\star}}$ are two-dimensional matrices, triple underlined symbols are three-dimensional and quadruple underlined symbols are four-dimensional, those without underlines are scalars and symbols with an overline $\overline{\star}$ are expressed in local coordinates. Specifically, the floating frame of reference formulation (FFRF) is used to represent flexibility [9, 10]. The generalized positions of a flexible body with FFRF is given by the position $\underline{r}$ and orientation $\underline{\theta}$ of the reference frame and flexible deformations $\overline{\underline{q}}_f$, see fig. 2,

$$\underline{q} = \begin{bmatrix} \underline{r}^T & \underline{\theta}^T & \overline{\underline{q}}_f^T \end{bmatrix}^T. \tag{2}$$

The continuous position of a material point on a flexible body is

$$\underline{r}_P = \underline{r} + \underline{\underline{A}}\,\overline{\underline{u}}_P = \underline{r} + \underline{\underline{A}}\left(\overline{\underline{u}}_{P,o} + \overline{\underline{\underline{S}}}\,\overline{\underline{q}}_f\right), \tag{3}$$

where $\underline{\underline{A}}$ is the transformation matrix and $\overline{\underline{u}}_P$ is the local position vector decomposed by the undeformed term $\overline{\underline{u}}_{P,o}$ and the deformed term $\overline{\underline{u}}_{P,f}$ given by the local matrix of shape functions $\overline{\underline{\underline{S}}}$ and the nodal deformations $\overline{\underline{q}}_f$. In this implementation of FFRF, a linear-elastic material model is used, which leads to a linear stiffness matrix,

$$\underline{\underline{k}} = \begin{bmatrix} \underline{\underline{0}} & \underline{\underline{0}} & \underline{\underline{0}} \\ \underline{\underline{0}} & \underline{\underline{0}} & \underline{\underline{0}} \\ \underline{\underline{0}} & \underline{\underline{0}} & \underline{\underline{k}}_{ff} \end{bmatrix}, \tag{4}$$

with the finite-element stiffness matrix $\underline{\underline{k}}_{ff}$. In contrast, the mass matrix is highly nonlinear

$$\begin{aligned} \underline{\underline{m}} &= \begin{bmatrix} \underline{\underline{m}}_{tt} & \underline{\underline{m}}_{tr} & \underline{\underline{m}}_{tf} \\ & \underline{\underline{m}}_{rr} & \underline{\underline{m}}_{rf} \\ \text{sym.} & & \underline{\underline{m}}_{ff} \end{bmatrix}, \\ &= \int_V \rho \begin{bmatrix} \underline{\underline{e}} & \underline{\underline{B}} & \underline{\underline{A}}\,\overline{\underline{\underline{S}}} \\ & \underline{\underline{B}}^T\underline{\underline{B}} & \underline{\underline{B}}^T\underline{\underline{A}}\,\overline{\underline{\underline{S}}} \\ \text{sym.} & & \overline{\underline{\underline{S}}}^T\overline{\underline{\underline{S}}} \end{bmatrix} \mathrm{d}V, \end{aligned} \tag{5}$$

with the finite-element mass matrix $\underline{\underline{m}}_{ff}$, the volume $V$, the density $\rho$, the identity matrix $\underline{\underline{e}}$ and the matrix $\underline{\underline{B}}$. The lattermost term is defined by

$$\underline{\underline{B}} = -\underline{\underline{A}}\,\tilde{\overline{\underline{u}}}_P\,\overline{\underline{\underline{G}}}, \tag{6}$$

https://doi.org/10.3311/ECCOMASMBD2021-203

with the skew-symmetric matrix of local coordinates $\tilde{\underline{\underline{\bar{u}}}}_P$ and the matrix $\underline{\underline{\bar{G}}}$ that relates the local angular velocity vector $\underline{\bar{\omega}}$ and the velocity terms of the orientation parameters $\underline{\dot{\beta}}$,

$$\underline{\bar{\omega}} = \underline{\underline{\bar{G}}}\,\underline{\dot{\beta}}. \tag{7}$$

Moreover, the quadratic velocity vector is also highly nonlinear

$$\underline{F}_v = \begin{bmatrix} \underline{F}_{v,t} \\ \underline{F}_{v,r} \\ \underline{F}_{v,f} \end{bmatrix} = \int_V \rho \begin{bmatrix} -\underline{\underline{A}}\left(\tilde{\underline{\underline{\bar{\omega}}}}^2 \underline{\bar{u}}_P + 2\tilde{\underline{\underline{\bar{\omega}}}}\,\underline{\underline{\bar{S}}}\,\underline{\dot{\bar{q}}}_f - \tilde{\underline{\underline{\bar{u}}}}_P \underline{\underline{\dot{\bar{G}}}}\,\underline{\dot{\beta}}\right) \\ \underline{\underline{\bar{G}}}^T \tilde{\underline{\underline{\bar{u}}}}_P^T \left(\tilde{\underline{\underline{\bar{\omega}}}}^2 \underline{\bar{u}}_P + 2\tilde{\underline{\underline{\bar{\omega}}}}\,\underline{\underline{\bar{S}}}\,\underline{\dot{\bar{q}}}_f - \tilde{\underline{\underline{\bar{u}}}}_P \underline{\underline{\dot{\bar{G}}}}\,\underline{\dot{\beta}}\right) \\ -\underline{\underline{\bar{S}}}^T \left(\tilde{\underline{\underline{\bar{\omega}}}}^2 \underline{\bar{u}}_P + 2\tilde{\underline{\underline{\bar{\omega}}}}\,\underline{\underline{\bar{S}}}\,\underline{\dot{\bar{q}}}_f - \tilde{\underline{\underline{\bar{u}}}}_P \underline{\underline{\dot{\bar{G}}}}\,\underline{\dot{\beta}}\right) \end{bmatrix} \mathrm{d}V. \tag{8}$$

The vector of external forces in FFRF is

$$\underline{F}_{\mathrm{ext}} = \begin{bmatrix} \underline{\underline{e}} \\ \underline{\underline{\bar{B}}}^T \\ \underline{\underline{\bar{S}}}^T \underline{\underline{A}}^T \end{bmatrix} \underline{F}_{\mathrm{ext}}. \tag{9}$$

The introduced governing equation must be fulfilled at any time and needs to be solved for every time step of the flexible multibody simulation.

### 2.2 Time integration

Numerical time integration is carried out with the generalized-α method originally introduced by [11] and implemented as a predictor–corrector scheme, as described in [8, 12]. The method is based on Newmark's equations,

$$\underline{q}_{n+1} = \underbrace{\underline{q}_n + \Delta t\,\underline{\dot{q}}_n + \left(\frac{1}{2} - \beta\right)\Delta t^2 \underline{\ddot{q}}_n}_{\text{predictor } \underline{q}_{\mathrm{pred}}} + \underbrace{\beta \Delta t^2 \underline{\ddot{q}}_{n+1}}_{\text{corrector}}, \tag{10}$$

$$\underline{\dot{q}}_{n+1} = \underbrace{\underline{\dot{q}}_n + (1-\gamma)\,\Delta t\,\underline{\ddot{q}}_n}_{\text{predictor } \underline{\dot{q}}_{\mathrm{pred}}} + \underbrace{\gamma \Delta t \underline{\ddot{q}}_{n+1}}_{\text{corrector}}, \tag{11}$$

and intermediate approximations for all force terms,

$$\underline{\underline{m}}\,\underline{\ddot{q}} = (1-\alpha_m)\,\underline{\underline{m}}_{n+1}\underline{\ddot{q}}_{n+1} + \alpha_m \underline{\underline{m}}_n \underline{\ddot{q}}_n, \tag{12}$$

$$\underline{\underline{d}}\,\underline{\dot{q}} = (1-\alpha_f)\,\underline{\underline{d}}_{n+1}\underline{\dot{q}}_{n+1} + \alpha_f \underline{\underline{d}}_n \underline{\dot{q}}_n, \tag{13}$$

$$\underline{\underline{k}}\,\underline{q} = (1-\alpha_f)\,\underline{\underline{k}}_{n+1}\underline{q}_{n+1} + \alpha_f \underline{\underline{k}}_n \underline{q}_n, \tag{14}$$

$$\underline{\underline{\mathrm{J}}}_{\Phi}^T \underline{\lambda} = (1-\alpha_m)\,\underline{\underline{\mathrm{J}}}_{\Phi,n+1}^T \underline{\lambda}_{n+1} + \alpha_m \underline{\underline{\mathrm{J}}}_{\Phi,n}^T \underline{\lambda}_n, \tag{15}$$

$$\underline{\underline{\mathrm{J}}}_{\Phi}\,\underline{\ddot{q}} = (1-\alpha_m)\,\underline{\underline{\mathrm{J}}}_{\Phi,n+1}\underline{\ddot{q}}_{n+1} + \alpha_m \underline{\underline{\mathrm{J}}}_{\Phi,n}\underline{\ddot{q}}_n, \tag{16}$$

$$\underline{F}_{\mathrm{ext}} = (1-\alpha_f)\,\underline{F}_{\mathrm{ext},n+1} + \alpha_f \underline{F}_{\mathrm{ext},n}, \tag{17}$$

$$\underline{F}_v = (1-\alpha_f)\,\underline{F}_{v,n+1} + \alpha_f \underline{F}_{v,n}, \tag{18}$$

$$\underline{F}_c = (1-\alpha_f)\,\underline{F}_{c,n+1} + \alpha_f \underline{F}_{c,n}. \tag{19}$$

These lead to the effective system of equations of flexible multibody dynamics,

$$\begin{bmatrix} \underline{\underline{m}}_{\mathrm{eff}} & \underline{\underline{\mathrm{J}}}_{\Phi,\mathrm{eff}}^T \\ \underline{\underline{\mathrm{J}}}_{\Phi,\mathrm{eff}} & \underline{\underline{0}} \end{bmatrix} \begin{bmatrix} \underline{\ddot{q}}_{n+1} \\ \underline{\lambda}_{n+1} \end{bmatrix} = \begin{bmatrix} \underline{F}_{a,\mathrm{eff}} \\ \underline{F}_{c,\mathrm{eff}} \end{bmatrix}, \tag{20}$$

https://doi.org/10.3311/ECCOMASMBD2021-203

where

$$\underline{\underline{m}}_{\text{eff}} = (1-\alpha_m)\,\underline{\underline{m}}_{n+1} + (1-\alpha_f)\,\gamma\Delta t\,\underline{\underline{d}}_{n+1} + (1-\alpha_f)\,\beta\Delta t^2\,\underline{\underline{k}}_{n+1}, \tag{21}$$

$$\underline{\underline{\mathrm{J}}}_{\Phi,\text{eff}} = (1-\alpha_m)\,\underline{\underline{\mathrm{J}}}_{\Phi,n+1}, \tag{22}$$

$$\begin{aligned}\underline{F}_{a,\text{eff}} = {} & (1-\alpha_f)\,\underline{F}_{\text{ext},n+1} + \alpha_f\underline{F}_{\text{ext},n} + (1-\alpha_f)\,\underline{F}_{v,n+1} + \alpha_f\underline{F}_{v,n} - \alpha_m\underline{\underline{m}}_n\,\ddot{\underline{q}}_n + \\ & - (1-\alpha_f)\,\underline{\underline{d}}_{n+1}\dot{\underline{q}}_{\text{pred}} - \alpha_f\underline{\underline{d}}_n\dot{\underline{q}}_n - (1-\alpha_f)\,\underline{\underline{k}}_{n+1}\underline{q}_{\text{pred}} - \alpha_f\underline{\underline{k}}_n\underline{q}_n - \alpha_m\underline{\underline{\mathrm{J}}}^T_{\Phi,n}\underline{\lambda}_n,\end{aligned} \tag{23}$$

$$\underline{F}_{c,\text{eff}} = (1-\alpha_f)\,\underline{F}_{c,n+1} + \alpha_f\underline{F}_{c,n} - \alpha_m\underline{\underline{\mathrm{J}}}_{\Phi,n}\ddot{\underline{q}}_n. \tag{24}$$

With the new acceleration values, the updates for the position and velocity values can be performed and the simulation continues to the next time step.

### 2.3 Nonlinear solver

With generalized-$\alpha$ time integration, the residual equations are

$$\begin{aligned}\underline{R}_{1,n+1-\alpha_f} = {} & (1-\alpha_m)\,\underline{\underline{m}}_{n+1}\ddot{\underline{q}}_{n+1} + \alpha_m\underline{\underline{m}}_n\ddot{\underline{q}}_n + (1-\alpha_f)\,\underline{\underline{d}}_{n+1}\dot{\underline{q}}_{n+1} + \alpha_f\underline{\underline{d}}_n\dot{\underline{q}}_n + \\ & + (1-\alpha_f)\,\underline{\underline{k}}_{n+1}\underline{q}_{n+1} + \alpha_f\underline{\underline{k}}_n\underline{q}_n + (1-\alpha_m)\,\underline{\underline{\mathrm{J}}}^T_{\Phi,n+1}\underline{\lambda}_{n+1} + \alpha_m\underline{\underline{\mathrm{J}}}^T_{\Phi,n}\underline{\lambda}_n + \\ & - (1-\alpha_f)\,\underline{F}_{\text{ext},n+1} - \alpha_f\underline{F}_{\text{ext},n} - (1-\alpha_f)\,\underline{F}_{v,n+1} - \alpha_f\underline{F}_{v,n},\end{aligned} \tag{25}$$

$$\underline{R}_{2,n+1-\alpha_f} = (1-\alpha_m)\,\underline{\underline{\mathrm{J}}}_{\Phi,n+1}\ddot{\underline{q}}_{n+1} + \alpha_m\underline{\underline{\mathrm{J}}}_{\Phi,n}\ddot{\underline{q}}_n - (1-\alpha_f)\,\underline{F}_{c,n+1} - \alpha_f\underline{F}_{c,n}. \tag{26}$$

To consider the nonlinearities of the system, Newton–Raphson iterations are used here with the following equation

$$\begin{bmatrix} \ddot{\underline{\underline{\mathrm{J}}}}_R & \overset{\lambda}{\underline{\underline{\mathrm{J}}}}_R \end{bmatrix} \begin{bmatrix} \Delta\ddot{\underline{q}} \\ \Delta\underline{\lambda} \end{bmatrix} + \underline{R} = \underline{0}, \tag{27}$$

where $\ddot{\mathrm{J}}$ and $\overset{\lambda}{\mathrm{J}}$ are the Jacobians with respect to acceleration and Lagrangian multipliers,

$$\ddot{\underline{\underline{\mathrm{J}}}}_R = \frac{\partial\underline{R}}{\partial\ddot{\underline{q}}}, \tag{28}$$

$$\overset{\lambda}{\underline{\underline{\mathrm{J}}}}_R = \frac{\partial\underline{R}}{\partial\underline{\lambda}}. \tag{29}$$

The terms of the Jacobian matrix are

$$\begin{aligned}\ddot{\underline{\underline{\mathrm{J}}}}_{R_1} = {} & (1-\alpha_m)\,\beta\Delta t^2\,\underline{\underline{\mathrm{J}}}_{m,n+1}\,\ddot{\underline{q}}_{n+1} + (1-\alpha_m)\,\underline{\underline{m}}_{n+1} + \\ & + (1-\alpha_f)\,\beta\Delta t^2\,\underline{\underline{\mathrm{J}}}_{d,n+1}\,\dot{\underline{q}}_{n+1} + (1-\alpha_f)\,\gamma\Delta t\,\underline{\underline{d}}_{n+1} + \\ & + (1-\alpha_f)\,\beta\Delta t^2\,\underline{\underline{\mathrm{J}}}_{k,n+1}\,\underline{q}_{n+1} + (1-\alpha_f)\,\beta\Delta t^2\,\underline{\underline{k}}_{n+1} + \\ & + (1-\alpha_m)\,\beta\Delta t^2\,\underline{\underline{\mathrm{J}}}^T_{\Phi,n+1}\,\underline{\lambda}_{n+1} + \\ & - (1-\alpha_f)\left(\beta\Delta t^2\,\underline{\underline{\mathrm{J}}}_{F_{\text{ext}},n+1} + \gamma\Delta t\,\underline{\underline{\mathrm{J}}}_{F_{\text{ext}},n+1}\right) + \\ & - (1-\alpha_f)\left(\beta\Delta t^2\,\underline{\underline{\mathrm{J}}}_{F_v,n+1} + \gamma\Delta t\underline{\underline{\mathrm{J}}}_{F_v,n+1}\right),\end{aligned} \tag{30}$$

$$\begin{aligned}\ddot{\underline{\underline{\mathrm{J}}}}_{R_2} = {} & (1-\alpha_m)\,\beta\Delta t^2\,\underline{\underline{\mathrm{J}}}^T_{\Phi,n+1}\,\ddot{\underline{q}}_{n+1} + (1-\alpha_m)\,\underline{\underline{\mathrm{J}}}_{\Phi,n} + \\ & - (1-\alpha_f)\left(\beta\Delta t^2\,\underline{\underline{\mathrm{J}}}_{F_c,n+1} + \gamma\Delta t\,\underline{\underline{\mathrm{J}}}_{F_c,n+1}\right),\end{aligned} \tag{31}$$

$$\overset{\lambda}{\underline{\underline{\mathrm{J}}}}_{R_1} = (1-\alpha_m)\,\underline{\underline{\mathrm{J}}}^T_{\Phi,n+1}, \tag{32}$$

$$\overset{\lambda}{\underline{\underline{\mathrm{J}}}}_{R_2} = \underline{\underline{0}}. \tag{33}$$

A complete derivation of the terms for the effective system and the nonlinear solver including the design sensitivities is found in [12].

https://doi.org/10.3311/ECCOMASMBD2021-203

## 3 DESIGN SENSITIVITY ANALYSIS

The sensitivities of the system responses with respect to certain parameters are useful in design optimization, uncertainty analysis as well as the direct use of the sensitivities. In this work, the design sensitivity analysis is carried out with a semi-analytical approach using direct differentiation. The differentiation must be carried through all three steps of the calculation routine: governing equation, sensitivity analysis and nonlinear solver.

### 3.1 Governing equation

The direct differentiation of the primal equations results in the governing equations for the sensitivity analysis,

$$\underline{\underline{\nabla R}} = \begin{bmatrix} \underline{\underline{m}} & \underline{\underline{\mathrm{J}}}_{\Phi}^{T} \\ \underline{\underline{\mathrm{J}}}_{\Phi} & \underline{\underline{0}} \end{bmatrix} \begin{bmatrix} \underline{\underline{\nabla \ddot{q}}} \\ \underline{\underline{\nabla \lambda}} \end{bmatrix} - \underline{\underline{F}}_{\text{pseudo}}, \tag{34}$$

where the pseudo load $\underline{\underline{F}}_{\text{pseudo}}$ contains the partial derivatives of the system parameters with respect to the design variables,

$$\underline{\underline{F}}_{\text{pseudo}} = \begin{bmatrix} \underline{\underline{\nabla F}}_{\text{ext}} + \underline{\underline{\nabla F}}_{v} - \underline{\underline{\nabla m}}\,\underline{\ddot{q}} - \underline{\underline{\nabla d}}\,\underline{\dot{q}} - \underline{\underline{d}}\,\underline{\underline{\nabla \dot{q}}} - \underline{\underline{\nabla k}}\,\underline{q} - \underline{\underline{k}}\,\underline{\underline{\nabla q}} - \underline{\underline{\nabla \mathrm{J}}}_{\Phi}^{\mathrm{T}}\,\underline{\lambda} \\ \underline{\underline{\nabla F}}_{c} - \underline{\underline{\nabla \mathrm{J}}}_{\Phi}\,\underline{\lambda} \end{bmatrix}. \tag{35}$$

To limit the implementation effort in the simulation code, the partial derivatives are evaluated with numerical forward differences, thus resulting in a semi-analytical approach.

### 3.2 Time integration

The time integration for the sensitivities is analogous to the time integration of the primary analysis as a predictor–corrector scheme with Newmark's equations and intermediate approximations [8, 12]. Therefore, the effective system of equations of the sensitivity analysis is

$$\begin{bmatrix} \underline{\underline{m}}_{\text{eff}} & \underline{\underline{\mathrm{J}}}_{\Phi,\text{eff}}^{\mathrm{T}} \\ \underline{\underline{\mathrm{J}}}_{\Phi,\text{eff}} & \underline{\underline{0}} \end{bmatrix} \begin{bmatrix} \underline{\underline{\nabla \ddot{q}}}_{n+1} \\ \underline{\underline{\nabla \lambda}}_{n+1} \end{bmatrix} = \begin{bmatrix} \underline{\underline{F}}_{a,\text{pseudo}} \\ \underline{\underline{F}}_{c,\text{pseudo}} \end{bmatrix}, \tag{36}$$

where the pseudo load case is

$$\begin{aligned} \underline{\underline{F}}_{a,\text{pseudo}} = {} & (1-\alpha_f)\,\underline{\underline{\nabla F}}_{\text{ext},n+1} + \alpha_f\,\underline{\underline{\nabla F}}_{\text{ext},n} + (1-\alpha_f)\,\underline{\underline{\nabla F}}_{v,n+1} + \alpha_f\,\underline{\underline{\nabla F}}_{v,n} + \\ & - (1-\alpha_m)\,\underline{\underline{\nabla m}}_{n+1}\,\underline{\ddot{q}}_{n+1} - \alpha_m\,\underline{\underline{\nabla m}}_{n}\,\underline{\ddot{q}}_{n} - \alpha_m\,\underline{\underline{m}}_{n}\,\underline{\underline{\nabla \ddot{q}}}_{n} + \\ & - (1-\alpha_f)\,\underline{\underline{\nabla d}}_{n+1}\,\underline{\dot{q}}_{n+1} - \alpha_f\,\underline{\underline{\nabla d}}_{n}\,\underline{\dot{q}}_{n} - (1-\alpha_f)\,\underline{\underline{d}}_{n+1}\,\underline{\underline{\nabla \dot{q}}}_{\text{pred}} - \alpha_f\,\underline{\underline{d}}_{n}\,\underline{\underline{\nabla \dot{q}}}_{n} + \\ & - (1-\alpha_f)\,\underline{\underline{\nabla k}}_{n+1}\,\underline{q}_{n+1} - \alpha_f\,\underline{\underline{\nabla k}}_{n}\,\underline{q}_{n} - (1-\alpha_f)\,\underline{\underline{k}}_{n+1}\,\underline{\underline{\nabla q}}_{\text{pred}} - \alpha_f\,\underline{\underline{k}}_{n}\,\underline{\underline{\nabla q}}_{n} + \\ & - (1-\alpha_m)\,\underline{\underline{\nabla \mathrm{J}}}_{\Phi,n+1}^{T}\,\underline{\lambda}_{n+1} - \alpha_m\,\underline{\underline{\nabla \mathrm{J}}}_{\Phi,n}^{T}\,\underline{\lambda}_{n} - \alpha_m\,\underline{\underline{\mathrm{J}}}_{\Phi,n}^{T}\,\underline{\underline{\nabla \lambda}}_{n}, \end{aligned} \tag{37}$$

$$\underline{\underline{F}}_{c,\text{pseudo}} = (1-\alpha_f)\,\underline{\underline{\nabla F}}_{c,n+1} + \alpha_f\,\underline{\underline{\nabla F}}_{c,n} - (1-\alpha_m)\,\underline{\underline{\nabla \mathrm{J}}}_{\Phi,n+1}\,\underline{\ddot{q}}_{n+1} - \alpha_m\,\underline{\underline{\nabla \mathrm{J}}}_{\Phi,n}\,\underline{\ddot{q}}_{n} - \alpha_m\,\underline{\underline{\mathrm{J}}}_{\Phi,n}\,\underline{\underline{\nabla \ddot{q}}}_{n}. \tag{38}$$

The updates from the acceleration values to the position and velocity values are performed analogously to the primal analysis.

### 3.3 Nonlinear solver

The Jacobian of the sensitivity analysis is that of the primary analysis [8, 12], allowing for an efficient calculation method of the gradients,

$$\overbrace{\begin{bmatrix} \underline{\underline{\ddot{\mathrm{J}}}}_{\nabla R} & \underline{\underline{\overset{\lambda}{\mathrm{J}}}}_{R} \\ \underline{\underline{\nabla \ddot{\mathrm{J}}}}_{\nabla R} & \underline{\underline{\nabla \overset{\lambda}{\mathrm{J}}}}_{\nabla R} \end{bmatrix}}^{:=\begin{bmatrix} \ddot{\mathrm{J}}_R & \overset{\lambda}{\mathrm{J}}_R \end{bmatrix}} \begin{bmatrix} \Delta \underline{\underline{\nabla \ddot{q}}} \\ \Delta \underline{\underline{\nabla \lambda}} \end{bmatrix} + \underline{\underline{\nabla R}} = \underline{\underline{0}}, \tag{39}$$

https://doi.org/10.3311/ECCOMASMBD2021-203

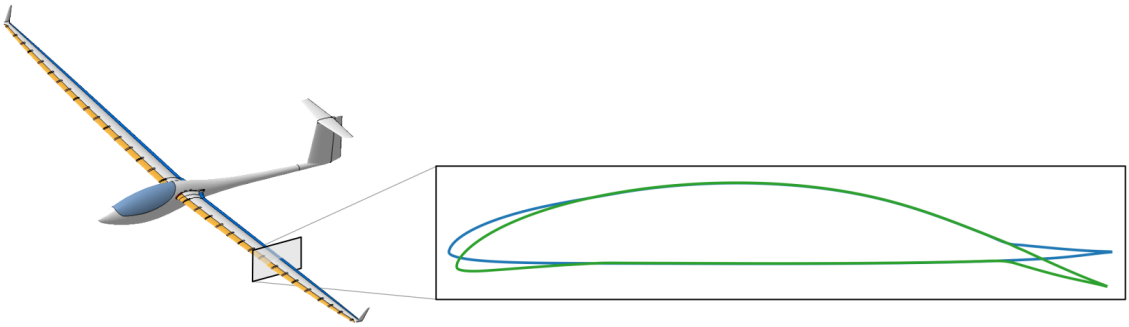

Figure 3: Demonstration example for a morphing wing with airfoil shapes for — high-speed and — low-speed configurations.

Figure 4: Morphing wing demonstrator based on topology optimization results in undeformed and morphed configuration [5]

where $\nabla\ddot{\mathbf{J}}$ and $\nabla\overset{\lambda}{\mathbf{J}}$ are the Jacobians with respect to acceleration sensitivity and Lagrangian multipliers sensitivity, respectively. This is the key to efficient sensitivity analysis of multibody dynamics. Without this simplification, the Jacobian of the sensitivity analysis is four-dimensional, requiring excessive memory usage. This is avoided by recognizing that these Jacobians are equivalent to those from the primary analysis and therefore avoiding any further calculation.

## 4 MORPHING WING MODEL

The design of the target geometry of the morphing wing sailplane in undeformed and morphed configuration is presented in [1, 13] and shown in fig. 3. Airfoil shapes are designed using a numerical optimization approach considering aerodynamic lift and drag [14, 15]. A morphing concept shows a significant performance advantage over conventional sailplanes with a camber changing flap. In earlier work [5], the morphing actuation is achieved using compliant mechanisms. A concept with a stack of six individual compliant mechanisms is shown in fig. 4.

Flexible multibody dynamics with FFRF is applied to the planar model of the system shown in fig. 5a. A conventional hinged mechanism is investigated for actuation. The flexible outer shell, i.e. wing skin, (body 1) is modeled with planar Euler–Bernoulli beams considering a section of the wing profile with the length of 1000 mm and a wall thickness of 2 mm. The mesh consists of 31 nodes and 30 elements. The upper end of the leading edge wing profile (point F) is fixed in all three degrees of freedom, i.e. $x$, $y$ and $\theta$. The lower end of the leading edge wing profile (point G) is fixed in $y$ and $\theta$, allowing for free motion in $x$. The actuation mechanism consists of four rigid bodies 2, 3, 4 and 5. These are connected by five revolute joints in A, B, C, D and E and a rigid joint between the bodies 2 and 4 in B. The mechanism is actuated by a torque starting from zero and going to a maximum value of 10 Nm that is applied to body 2 on point A. Aluminum is used as material with a density of $2.7 \times 10^{-9}\,\mathrm{t/mm^3}$, a Young modulus of 70 000 MPa and a Poisson ratio of $0.35\,[-]$. Fig. 5b shows the motion of the multibody system from the high-speed configuration (undeformed) to the low-speed configuration (morphed).

The key element for a proper function of the morphing leading edge is the design of the actuation mechanism considering the interaction with the flexible wing skin. It is important to approximate the target wing profile in morphed configuration as closely as possible. Another important aspect is to consider the material limits. A simulation with flexible multibody dynamics is performed

https://doi.org/10.3311/ECCOMASMBD2021-203

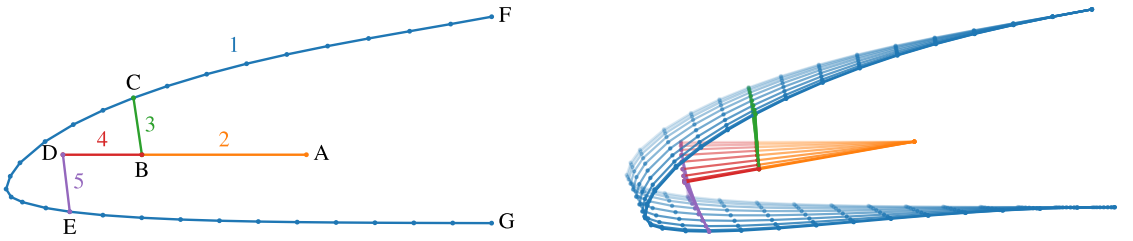


(a) Model of mechanism and wing skin

(b) Motion of rigid mechanism and deformable wing skin

Figure 5: Flexible multibody system of the morphing wing leading edge

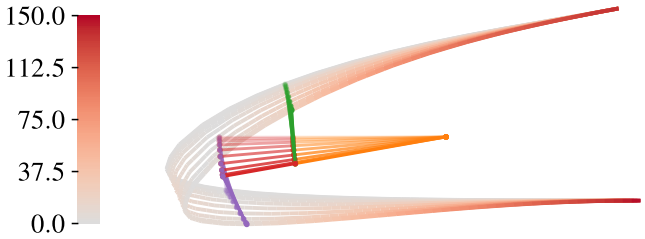


Figure 6: Stress $\sigma$ [MPa] during the motion of the mechanism

to assess both deformed shape as well as the stresses. Fig. 6 shows the stress distribution in the wing skin during the motion of the mechanism from the undeformed configuration to the morphed configuration. The highest values are found in morphed configuration and near to the constraints of the wing skin (points F and G). The maximum stress of all elements and all time steps is approximated with the Kreisselmeier–Steinhauser function [16] to obtain a differentiable function

$$\sigma_{\max} = \mathscr{F}_{KS}\left(\sigma^{i,j}\right), \qquad i = 1,\ldots,n_t,\ j = 1,\ldots,n_e, \tag{40}$$

where $\mathscr{F}_{KS}$ is the Kreisselmeier–Steinhauser function, $\sigma$ is the stress, $n_t$ is the number of time steps and $n_e$ is the number of elements. Here, the approximated maximum stress is given by 149.96 MPa.

Fig. 7a shows the external wing profile in the undeformed configuration, the target morphed configuration and the simulated morphed configuration. It is possible to observe an error between the simulated morphed configuration and the target morphed configuration. This error is given by the distance between the simulated node positions and the target profile in morphed configuration,

$$e_k = \sqrt{\left(x_s^k - x_t^k\right)^2 + \left(y_s^k - y_t^k\right)^2}, \qquad k = 1,\ldots,n_N, \tag{41}$$

where $x_s^k$ and $y_s^k$ are the simulated node coordinates, $x_t^k$ and $y_t^k$ are the target node coordinates and $n_N$ is the number of nodes. Fig. 7b shows the error value of the morphed configuration. The largest error is 1.185 mm and is located behind the tip on the lower side of the wing profile.

The deviation from the target shape as a global consideration is expressed via root-mean-square error,

$$e_{\text{rms}} = \sqrt{\frac{1}{n_N}\sum_{k=1}^{n_N} e_k^2}, \tag{42}$$

and is given by 0.6348 mm. The deviations from the target wing profile with a maximum value of 1.185 mm and a root-mean-square error of 0.6348 mm are to acceptable accuracy, especially considering the wing width of 550 mm, the wing height of 67.5 mm and the width of the leading edge of 137.5 mm. Nevertheless, it is important to analyze and minimize the deviations, since the shape of the wing profile is crucial for the aerodynamics and the performance of sailplanes.

https://doi.org/10.3311/ECCOMASMBD2021-203

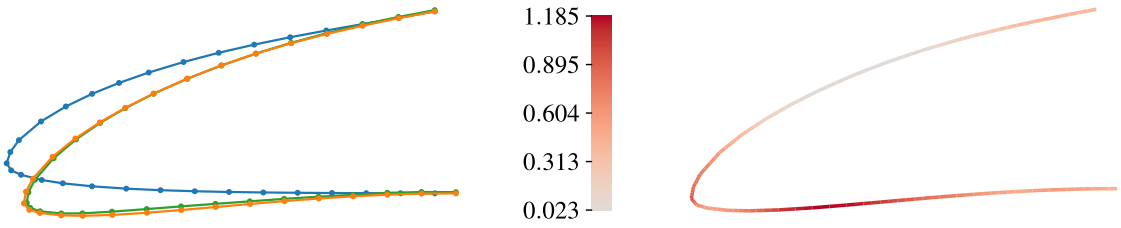


(a) — undeformed configuration — target configuration — simulated configuration

(b) Error in morphed configuration $e$ [mm]

Figure 7: Shape of the external wing profile

To understand how the stress distribution and the deviation from the target profile are affected by the design variables, a sensitivity analysis is performed. The sensitivity analysis is performed with respect to the design variables, which include the thickness of the external wing skin $t_w$, the value of the torque that is applied to actuate the mechanism $M_t$, the coordinates $x_A$ and $y_A$ of the point where the torque is applied (point A) and the Young's modulus $E$. The sensitivities are computed as shown in § 3 and the chain rule is applied to all operations.

Fig. 8 shows the stress sensitivities during the motion of the system[1]. In terms of simulation time, the highest sensitivity values are always found at the end of the motion in morphed configuration of the wing profile. In terms of position on the wing profile, the highest sensitivity values with respect to the $x$-coordinate $x_A$ of the application point of the torque are found on the tip of the wing profile and on the upper connection point between the actuation mechanism and the external wing profile (point C), while for all other design variables, the highest sensitivity values are found near to the constraints of the wing profile (points F and G). In contrast to the primal analysis, where the highest stress values are found on the lower constraint (point $G$), the highest values of the stress sensitivities are on the upper constraint (point $F$). A comparison between fig. 6 and fig. 8 allows to conclude that the stress $\sigma$ can be reduced by increasing the thickness of the external wing skin $t_w$, the $x$-coordinate $x_A$ of the application point of the torque and the Young's modulus $E$ or by reducing the actuation torque $M_t$ and the $y$-coordinate $y_A$ of the application point of the torque.

Fig. 8 shows the sensitivities of the error in morphed configuration. Here it is possible to observe that especially in the nose of the leading edge, the sensitivities on the lower side have the opposite sign from the sensitivities on the upper side of the wing profile. Comparing the error values on fig. 7b with the error sensitivities on fig. 9 allows to predict in which direction the design variables should be modified in order to reduce the error. Since the highest values of the error are on the lower side of the wing skin, these can be reduced by increasing the thickness of the external wing skin $t_w$, the $x$-coordinate $x_A$ of the application point of the torque and the Young's modulus $E$ or by reducing the actuation torque $M_t$ and the $y$-coordinate $y_A$ of the application point of the torque.

Tab. 1 gives the sensitivity values of the maximum stress and the root-mean-square error. These have been computed by the differentiation of the Kreisselmeier–Steinhauser function and the function of the root-mean-square error. Comparing the values from tab. 1 with the values on fig. 8 and fig. 9, the results show great consistency. In the case of the maximum stress, the maximum value is found on the lower end of the wing profile leading edge (point G). The sensitivity on this position of fig. 8 corresponds exactly to the approximated values reported in tab. 1. The same comparison is not possible for the root-mean-square error because all nodes are considered by the function, but the values from fig. 9 and tab. 1 show the same order of magnitude.

The results from the semi-analytical sensitivity analysis are validated with numerical sensitivity analysis and the values coincide. Table 2 shows the computation time for both methods[2]. This

[1] Units of sensitivity results are not reduced to demonstrate the physical and engineering meaning of these values.
[2] Computations are performed on a PC with Intel Core i7-8700 CPU @ 3.20GHz × 12 and 32 GB RAM.

https://doi.org/10.3311/ECCOMASMBD2021-203

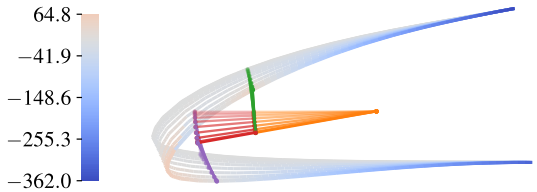


(a) Sensitivity w.r.t. thickness $\frac{\partial \sigma}{\partial t_w}$ [MPa/mm]

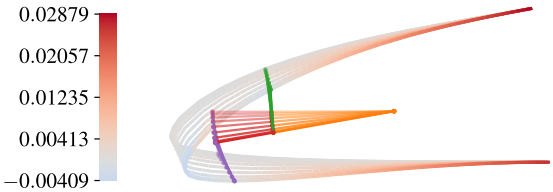


(b) Sensitivity w.r.t. torque $\frac{\partial \sigma}{\partial M_t}$ [MPa/N·mm]

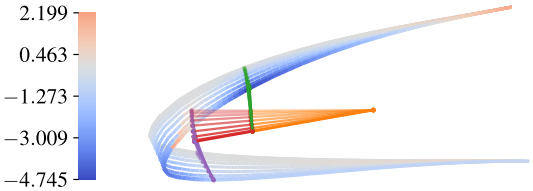


(c) Sensitivity w.r.t. actuation point in $x$ $\frac{\partial \sigma}{\partial x_a}$ [MPa/mm]

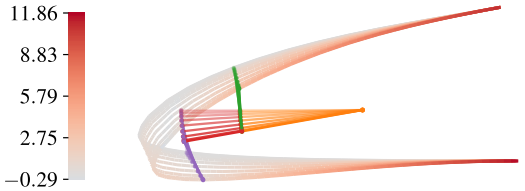


(d) Sensitivity w.r.t. actuation point in $y$ $\frac{\partial \sigma}{\partial y_a}$ [MPa/mm]

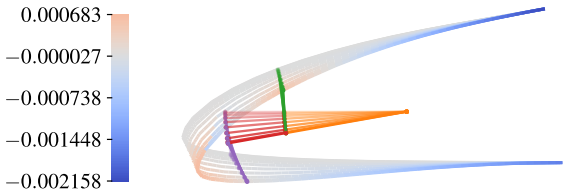


(e) Sensitivity w.r.t. Young's modulus $\frac{\partial \sigma}{\partial E}$ [MPa/MPa]

Figure 8: Design sensitivities of the stress $\sigma$

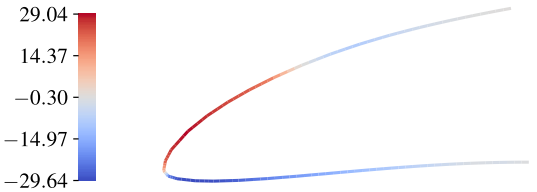


(a) Sensitivity w.r.t. thickness $\frac{\partial e}{\partial t_w}$ [mm/mm]

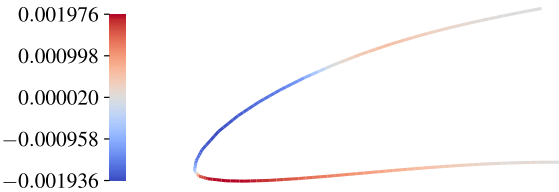


(b) Sensitivity w.r.t. torque $\frac{\partial e}{\partial M_t}$ [mm/N·mm]

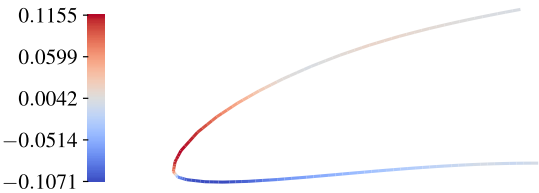


(c) Sensitivity w.r.t. actuation point in $x$ $\frac{\partial e}{\partial x_a}$ [mm/mm]

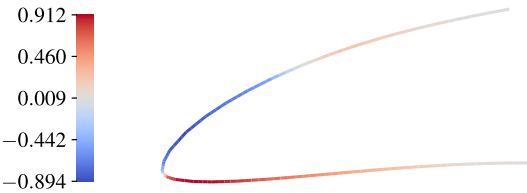


(d) Sensitivity w.r.t. actuation point in $y$ $\frac{\partial e}{\partial y_a}$ [mm/mm]

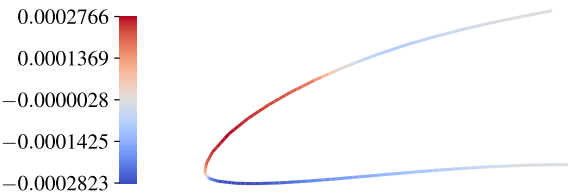


(e) Sensitivity w.r.t. Young's modulus $\frac{\partial e}{\partial E}$ [mm/MPa]

Figure 9: Design sensitivities of the error $e$ in morphed configuration

https://doi.org/10.3311/ECCOMASMBD2021-203

Table 1: Design sensitivities of the maximum stress $\sigma_{\max}$ and the root-mean-square error $e_{\mathrm{rms}}$

| | | w.r.t. to design variables | | | | |
|---|---|---|---|---|---|---|
| | | $\cdot/\partial t_w\,[\cdot/\mathrm{mm}]$ | $\cdot/\partial M_t\,[\cdot/\mathrm{N{\cdot}mm}]$ | $\cdot/\partial x_A\,[\cdot/\mathrm{mm}]$ | $/\partial y_A\,[\cdot/\mathrm{mm}]$ | $\cdot/\partial E\,[\cdot/\mathrm{MPa}]$ |
| response | $\partial\sigma_{\max}/.\,[\mathrm{MPa}/.]$ | $-324.64$ | $0.02664$ | $-0.7800$ | $11.86$ | $-0.001664$ |
| | $\partial e_{\mathrm{rms}}/.\,[\mathrm{mm}/.]$ | $-5.544$ | $3.695\cdot10^{-4}$ | $-0.01440$ | $0.1668$ | $-5.280\cdot10^{-5}$ |

Table 2: Computational effort of semi-analytical and numerical sensitivity analysis

| method | computation time [min : s] |
|---|---|
| semi-analytical sensitivity analysis | 03 : 32 |
| numerical sensitivity analysis | 14 : 48 |

comparison shows the high efficiency of the implemented semi-analytical sensitivity approach. The computational effort of the numerical sensitivity analysis is given by the sum of $n_{\mathrm{x}}+1$ primal evaluations and is given here by 6 evaluations with a mean evaluation time of $02:28\,[\mathrm{min}:\mathrm{s}]$. The computational effort of a system evaluation with the semi-analytical sensitivity analysis is less then twice ($1.43\times$) the computational effort of one primal evaluation due to the simplification shown in § 3.3.

## 5 CONCLUSION

The present work introduces an efficient sensitivity analysis of flexible multibody dynamics with a semi-analytic direct differentiation approach of generalized-α time integration with Newton–Raphson iterations for a morphing wing concept. This concept for a morphing wing leading edge with a trailing flap for a high-speed and a low-speed configuration increases the performance in the wide speed range of a high-performance sailplane. The morphing wing leading edge models the external wing skin with flexible elements, while the actuation mechanism is modeled with rigid bodies. Special interest was devoted to the deviation error from the target shape in morphed configuration and the stress values in the wing skin in addition to both of these sensitivities. Semi-analytical sensitivity analysis is utilized for its computational efficiency and accuracy. The calculated design sensitivities include those with respect to geometric properties, material properties and the position and torque of the actuator. This sensitivity analysis is the basis for future uncertainty analysis and gradient-based design optimization of the morphing wing and its actuation mechanism. The maximum stress is considered as material limit, though the consideration of the fatigue (including sensitivities) would be of great practical use. This work is an integral part of the integration of a design optimization framework to optimally design the actuation mechanism and geometry of a morphing wing leading edge.

## ACKNOWLEDGMENTS

This work is supported by the project CRC 2017 TN2091 doloMULTI *Design of Lightweight Optimized structures and systems under MULTIdisciplinary considerations through integration of MULTIbody dynamics in a MULTIphysics framework* funded by the Free University of Bozen-Bolzano. Further support was provided in the framework MILAN – Morphing wIngs for saiLplANes, funded by the German Federal Ministry for Economic Affairs and Energy under the grant of the German Federal Aviation Research Program (Luftfahrtforschungsprogramm, LuFo) V-3.

## REFERENCES


[1] Achleitner, J., Rohde-Brandenburger, K., Rogalla von Bieberstein, P., Sturm, F., Hornung, M.: Aerodynamic design of a morphing wing sailplane. In: AIAA Aviation 2019 Forum, Reston, Virginia, American Institute of Aeronautics and Astronautics (2019)

[2] Sinapius, M., Monner, H.P., Kintscher, M., Riemenschneider, J.: DLR's morphing wing activities within the European network. Procedia IUTAM **10** (2014) 416–426

[3] Sturm, F., Achleitner, J., Jocham, K., Hornung, M.: Studies of anisotropic wing shell concepts for a sailplane with a morphing forward wing section. In: AIAA Aviation 2019 Forum, Reston, Virginia, American Institute of Aeronautics and Astronautics (2019)

[4] Rudenko, A., Hannig, A., Monner, H.P., Horst, P.: Extremely deformable morphing leading edge: Optimization, design and structural testing. Journal of Intelligent Material Systems and Structures **29**(5) (2017) 764–773

[5] Reinisch, J., Wehrle, E., Achleitner, J.: Multiresolution topology optimization of large-deformation path-generation compliant mechanisms with stress constraints. Applied Sciences **11(6)**(2479) (2021)

[6] Gufler, V.: Multibody dynamics and optimal design of a Tyrolean weir cleaning mechanism. Master thesis, Free University of Bozen-Bolzano (2019) Advisors: E. J. Wehrle, R. Vidoni.

[7] Gufler, V., Wehrle, E., Vidoni, R.: Multiphysical design optimization of multibody systems: Application to a Tyrolean weir cleaning mechanism. In: Advances in Italian Mechanism Science. Springer International Publishing (2021) 459–467

[8] Wehrle, E., Gufler, V.: Lightweight engineering design of nonlinear dynamic systems with gradient-based structural design optimization. In: Proceedings of the Munich Symposium on Lightweight Design 2020. Springer Berlin Heidelberg (2021) 44–57

[9] Gufler, V., Wehrle, E., Zwölfer, A.: A review of flexible multibody dynamics for gradient-based design optimization. (submitted)

[10] Shabana, A.A.: Dynamics of multibody systems. 5 edn. Cambridge University Press (2020)

[11] Chung, J., Hulbert, G.: A time integration algorithm for structural dynamics with improved numerical dissipation: The generalized-$\alpha$ method. Journal of Applied Mechanics **60** (1993) 371–375

[12] Wehrle, E., Gufler, V.: Analytical sensitivity analysis of dynamic problems with direct differentiation of generalized-$\alpha$ time integration. (submitted)

[13] Achleitner, J., Rohde-Brandenburger, K., Hornung, M.: Airfoil optimization with CST parameterization for (un-)conventional demands. In: XXXIV OSTIV Congress. (2018) 117–120

[14] Bongers, J.: Implementation of a new transition prediction method in XFOIL. Masters thesis, TU Delft, Netherlands (2008)

[15] Drela, M.: XFOIL: An analysis and design system for low Reynolds number airfoils. In: Low Reynolds Number Aerodynamics, Lecture Notes in Engineering. Springer Berlin Heidelberg (1989) 1–12

[16] Kreisselmeier, G., Steinhauser, R.: Systematic control design by optimizing a vector performance index. In: International Federation of Active Controls Symposium on Computer-Aided Design of Control Systems. Volume 12. Elsevier (1979) 113–117

https://doi.org/10.3311/ECCOMASMBD2021-153



# Simultaneous Space-Time Discretization for Controlling the Motion of Rigid Bodies Actuated Through Elastic Ropes

**Timo Ströhle and Peter Betsch**

Institute of Mechanics
Karlsruhe Institute of Technology (KIT)
Otto-Ammann-Platz 9, 76131 Karlsruhe, Germany
timo.stroehle@kit.edu, peter.betsch@kit.edu

## ABSTRACT

This contribution deals with the feedforward control of rigid bodies actuated through elastic ropes. After introducing a method which enables a stable inversion process of the dynamics of a geometrically exact rope, a strategy to solve the cooperative control of a rigid body through multiple ropes is presented.

**Keywords:** Flexible multibody system, Cooperative control, Inverse dynamics

## 1 INTRODUCTION

The inverse dynamics of flexible mechanical systems is concerned with searching forces acting on this system such that a finite number of selected points of this system follow a prescribed motion. One subclass of such systems are ropes for large elastic deformations which can be seen as a one-dimensional continuum. Here the aim is to find a force which acts at one end of the rope, such that the other end follows a prescribed trajectory (see Fig. 2). In this connection, the end of the rope might be attached to a mass point or connected to a rigid body.

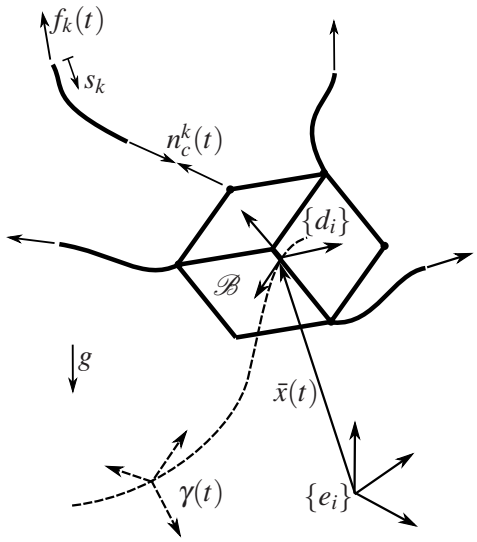


**Figure 1**. Cooperative transport of a rigid body through $k \in \mathbb{N}$ elastic ropes only actuated through the forces $f_k(t)$ at $s_k = 0$ such that the prescribed motion of the rigid body is realized

After introducing a geometrically exact model for ropes in Section 2, a space-time finite element method based on a simultaneous space-time discretization of the problem at hand is established which solves the inverse dynamics problem (see [1, 2]). In Section 3, first the rigid body is introduced as a Cosserat point subjected to geometric constraints. Subsequently, after the inverse dynamics of the rigid body has been discussed, a strategy to solve the cooperative control problem consisting of the rigid body controlled through several elastic ropes undergoing large deformations

https://doi.org/10.3311/ECCOMASMBD2021-153

is presented (see Fig. 1). In particular, the cascade-like solution strategy of the inverse multibody system is addressed. The structure of the equations of motion of a multibody system comprised of geometrically exact ropes and rigid bodies is outlined in Section 4. A representative numerical example of the inverse dynamics problem under consideration is presented in Section 5. Eventually, conclusions are drawn in Section 6.

## 2 GEOMETRICALLY EXACT ROPES

The motion of elastic ropes with mass-density $\rho$, length $L$, cross sectional area $A$ and Young's modulus $E$ (see Fig. 2) undergoing large deformations can be described in terms of the arc-length $s \in S = [0,L] \subset \mathbb{R}$ by quasi-linear hyperbolic partial differential equations. For simplicity and without loss of generality, in a stress-free reference configuration, the length of the rope and the cross sectional area is set to $L_0 = 1$ and $A_0 = 1$ respectively. For this, an arbitrary configuration of the rope can be described by the function $r(s,t) : S \times T = \Omega \subset \mathbb{R}^2 \mapsto \mathbb{R}^\alpha$ for all $\alpha \in \{1,2,3\}$ and $t \in T = [0,\infty)$. Following [3] the governing equations of motion can be established as follows. With the normal force in the rope $n(s,t) : \Omega \mapsto \mathbb{R}^\alpha$ and the body-forces $b(s,t) : \Omega \mapsto \mathbb{R}^\alpha$, balance of linear momentum of an infinitely small piece of rope yields:

$$\partial_s n(s,t) + b(s,t) = \rho \partial_t^2 r \tag{1}$$

Strings are per definition perfectly flexible e.g. normal forces are strictly tangential to the line of centroids

$$\partial_s r(s,t) \times n(s,t) = 0 \tag{2}$$

Introducing the stretch

$$\nu(s,t) = \|\partial_s r(s,t)\| \tag{3}$$

then there exists a $N(s,t) : \Omega \mapsto \mathbb{R}$ such that

$$n(s,t) = N(s,t)\nu^{-1}\partial_s r \tag{4}$$

After assuming the following constitutive relation

$$N(s,t) = \frac{E}{2}(\nu - \nu^{-1}) \tag{5}$$

and introducing the coefficients

$$A = \rho, \qquad B = N(s,t)\nu^{-1}, \qquad C = b(s,t)$$

the motion of elastic ropes can be described by the following partial differential equation:

$$A(r,s,t)\partial_t^2 r(s,t) - \partial_s(B(r,s,t)\partial_s r(s,t)) = C(r,s,t) \quad \forall \quad (s,t) \in \Omega \tag{6}$$

Note, that due to the quasi-linearity of the problem at hand, the coefficients $A \in \mathbb{R}, B \in \mathbb{R}$ and $C \in \mathbb{R}^\alpha$ may depend on the space and time variables as well as on the solution $r(s,t) : S \times T = \Omega \subset \mathbb{R}^2 \mapsto \mathbb{R}^\alpha$ for time $t \in T = [0,\infty)$. To solve the PDE at hand uniquely the following initial

$$r(s,0) = r_0(s),\ \partial_t r(s,0) = v_0(s) \quad \forall \quad s \in S \tag{7}$$

and boundary conditions

$$B\partial_s r(0,t) = f(t),\ B\partial_s r(1,t) = n_c(t),\ r(1,t) = \gamma(t) \quad \forall \quad t \in T \tag{8}$$

need to be defined. Herein $f(t) : T \mapsto \mathbb{R}^\alpha$ is the searched actuating force at $s = 0$ such that the rope at $s = 1$ follows the prescribed trajectory ($r(1,t) = \gamma(t)$. And $n_c(t) : T \mapsto \mathbb{R}^\alpha$ is the contact

https://doi.org/10.3311/ECCOMASMBD2021-153

force at $s = 1$. If a mass point $m_T$ is attached to the rope at $s = 1$, the contact force can be directly computed from the prescribed trajectory of the rope at $s = 1$, which coincides with the trajectory of the mass point, via

$$n_c(t) = m_T(\partial_t^2 \gamma(t) + g e_z) \tag{9}$$

Now, the initial boundary value problem constituting the control problem at hand can be solved by applying appropriate numerical procedures. After addressing issues arising from the common semi-discrete approach, where the initial boundary problem at hand is solved by applying the finite element method and subsequently integrating the resulting ordinary differential equation subjected to the given servo-constraint in time by appropriate time-stepping schemes, a space-time finite element method based on a simultaneous space-time discretization is proposed.

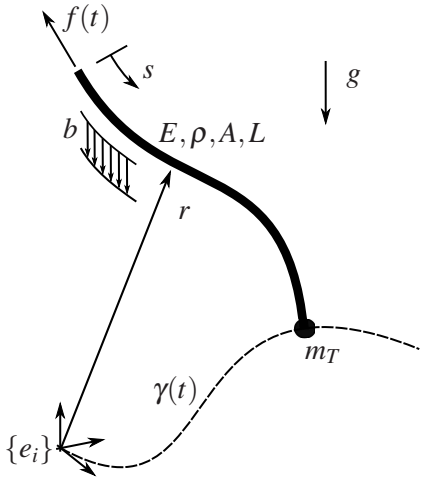


**Figure 2**. Illustration of the elastic rope for large deformations only actuated by $f(t)$ at $s = 0$ such that the rope at $s = 1$ follows the prescribed trajectory $\gamma(t)$

### 2.1 Semi-discrete equations of motion

As mentioned above, one common way of solving mechanical problems which are leading to hyperbolic problems is to transform the partial differential equation at hand into a system of ordinary differential equations. Therefore, equation (6) is multiplied with a sufficiently smooth test function and integrated over the spatial domain $s$:

$$\int_S w \cdot \partial_s (B \partial_s r)\, ds + \int_S w \cdot C\, ds = \int_S w \cdot A \partial_t^2 r\, ds$$

Integrating the first integral on the left side by parts

$$\int_S w \cdot \partial_s (B \partial_s r)\, ds = [w \cdot (B \partial_s r)]_S - \int_S \partial_s w B \partial_s r\, ds$$

leads together with the boundary conditions

$$B \partial_s r(s = 0) = f(t), \qquad B \partial_s r(s = 1) = 0$$

to a weak formulation of the problem at hand:

$$\int_S w \cdot A \partial_t^2 r\, ds + \int_S \partial_s w B \partial_s r\, ds = \int_S w \cdot C\, ds + [w \cdot (B \partial_s r)]_S$$

https://doi.org/10.3311/ECCOMASMBD2021-153

Approximation of the test and trial functions with piecewise continuous Lagrangian polynomials $L_i$:

$$r^h(s) = \sum_{j=1}^{p+1} L_j(s) r_j\,; \qquad w^h(s) = \sum_{i=1}^{p+1} L_i(s) w_i$$

yields with the unknown variables

$$\hat{q} = \begin{bmatrix} r_1 \\ \vdots \\ r_{p+1} \end{bmatrix} \tag{10}$$

the following semi-discrete equations of motion:

$$\hat{M}\hat{q} + \hat{F}^{int} = \hat{N}^1 - \hat{N}^0 + \hat{G} \tag{11}$$

with the components of the quantities given in (11)

$$\hat{M}_{ij} = \int_S L_i(s) A^h L_j(s)\, ds \tag{12}$$

$$\hat{F}_i^{int} = \int_S \partial_s L_i(s) B^h \partial_s L_j(s)\, ds \partial_s r_j \tag{13}$$

$$\hat{G}_i = \int_S L_i(s) C^h\, ds \tag{14}$$

$$\hat{N}_i^1 = \delta_{i,p+1} n_c(t) \tag{15}$$

$$\hat{N}_i^0 = \delta_{i,1} f(t) \tag{16}$$

By introducing the control condition $r(s=1,t) - \gamma(t) = 0$, the control problem can be formulated in terms of the resulting differential algebraic system of equations (DAE). Unfortunately, the differentiation index of the DAE at hand as well as the demands on the differentiability of the given trajectory depend on the spatial discretisation (cf. [4] and [5]). This significantly restricts the applicability of the semi-discrete approach. Therefore a method based on the characteristics of the PDE and a space-time finite element method has been established. Both methods are searching for the solution of the control problem at hand in space and time simultaneously (see [1] and [2] for more details). In this contribution, the space time finite element method is used for computing the inverse dynamics of the problem at hand.

### 2.2 Space-time finite element method

Due to the highly restrictive applicability of solving the control problem at hand sequentially in time, the problem will now be solved simultaneously in space and time. Therefore a space-time finite element method will be presented in the following (cf.[6],[7],[8]). By introducing the velocity $v(s,t) = \partial_t r(s,t)$ the underlying partial differential equation at hand (6) can be transformed into the following system of equations:

$$\begin{aligned} \partial_t r - v &= 0 \\ A\partial_t v - \partial_s(B\partial_s r) &= C \end{aligned} \tag{17}$$

Multiplying each equation in (17) with sufficiently smooth test functions $w_1(s,t)$ and $w_2(s,t)$ and integrating over the space-time domain $\Omega = S \times T$ yields the following weak formulation:

$$\int_\Omega w_1 \cdot (\partial_t r - v)\, d\Omega = 0 \tag{18}$$

$$\int_\Omega w_2 \cdot (A\partial_t v - \partial_s(B\partial_s r))\, d\Omega = \int_\Omega w_2 \cdot C\, d\Omega \tag{19}$$

https://doi.org/10.3311/ECCOMASMBD2021-153

Integrating the second term in (19) by parts

$$\int_\Omega w_2 \cdot \partial_s (B \partial_s r)\, d\Omega = \int_T [w_2 \cdot B \partial_s r]_{s=0}^1 \, dt - \int_\Omega \partial_s w_2 \cdot B \partial_s r \, d\Omega \tag{20}$$

the following equation for (19) can be established:

$$\int_\Omega w_2 \cdot A \partial_t v \, d\Omega - \int_T [w_2 \cdot B \partial_s r]_{s=0}^1 \, \mathrm{d}t + \int_\Omega \partial_s w_2 \cdot B \partial_s r \, d\Omega = \int_\Omega w_2 \cdot C \, d\Omega \tag{21}$$

Additionally the servo-constraint $r(s=1,t) = \gamma(t)$ can be demanded weakly on the boundary $\partial\Omega_\gamma = \{1\} \times T$

$$\int_{\partial\Omega_\gamma} w_3(t) \cdot (r(1,t) - \gamma(t)) \, dt = 0 \tag{22}$$

The task is now to find the unknown functions

$$\begin{gathered} r(s,t) \in V_1 = \{ r : \Omega \mapsto \mathbb{R}^\alpha \,|\, r(\partial\Omega_0) = r_0 \} \\ v(s,t) \in V_2 = \{ v : \Omega \mapsto \mathbb{R}^\alpha \,|\, v(\partial\Omega_0) = v_0 \} \\ f(t) \in V_3 = \left\{ f : \partial\Omega_f \mapsto \mathbb{R}^\alpha \,|\, f(\partial\Omega_\gamma \cap \partial\Omega_0) = f_0 \right\} \end{gathered}$$

such that for arbitrary but sufficiently smooth test functions

$$\begin{gathered} w_1(s,t), w_2(s,t) \in W_1 = \{ w_1, w_2 : \Omega \mapsto \mathbb{R}^\alpha \,|\, w_1(\partial\Omega_0) = 0, w_2(\partial\Omega_0) = 0 \} \\ w_3(t) \in W_2 = \left\{ w_3 : \partial\Omega_\gamma \mapsto \mathbb{R}^\alpha \,|\, w_3(\partial\Omega_\gamma \cap \partial\Omega_0) = 0 \right\} \end{gathered}$$

the equations (18), (21) and (22) are satisfied together with the Neumann boundary conditions

$$B \partial_s r(\partial\Omega_f) = f(t) \quad \text{and} \quad B \partial_s r(\partial\Omega_\gamma) = n_c(t) \quad t \in T$$

and the Dirichlet boundary conditions

$$r(\partial\Omega_0) = r_0(s) \quad \text{and} \quad \partial_t r(\partial\Omega_0) = v_0(s) \quad s \in S$$

The weak formulation consisting of (18), (21) and (22) subjected to the given Neumann and Dirichlet boundary conditions can then be solved numerically using the finite element method based on a piecewise continuous approximation.

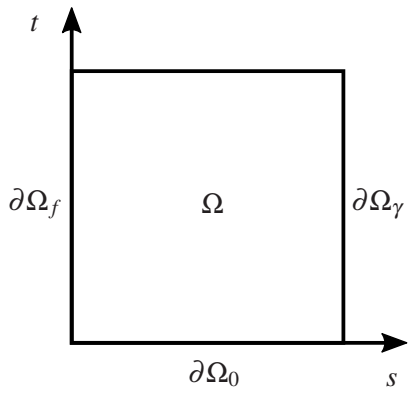


**Figure 3**. Space-Time domain $\Omega = S \times T$ with the boundaries $\partial\Omega_0 = S \times \{0\}$, $\partial\Omega_f = \{0\} \times T$ and $\partial\Omega_\gamma = \{1\} \times T$

https://doi.org/10.3311/ECCOMASMBD2021-153

## 3 RIGID BODY

When considering general rigid bodies, in principle the same strategy as for the attached mass point can be applied. The actuating forces needed to achieve the desired motion of the rigid body can be calculated directly from the governing equations of motion. These forces can then be inserted into the Neumann boundary condition of the control problem (8). In this contribution a Cosserat point subjected to geometric constraints is used to describe the motion of a rigid body with density $\rho_0 : \mathscr{B}_0 \mapsto \mathbb{R}$ and total mass $\bar{M} = \int_{\mathscr{B}_0} \rho_0 \, \mathrm{dV}$ (see [9] for more details). Accordingly, the equations of motion can be written as

$$\begin{aligned} \bar{M}\partial_t^2 \bar{x} - f_{ext} - G &= 0 \\ E_{ij}\partial_t^2 d_j - f_{ext}^i + \Lambda_{ij} d_j &= 0 \\ g_c(d_i) = d_i \cdot d_j - \delta_{ij} &= 0 \end{aligned} \tag{23}$$

Herein $G = \bar{M} g e_z$ is the gravitational force and $E_{ij}$ are the components of the referential Euler tensor which is closely related to the classical inertia tensor of rigid body dynamics. Furthermore, $f_{ext}$ is the resultant external force and

$$f_{ext}^i = X_i^k n_c^k \tag{24}$$

are the external director forces (Fig. 4). This holds for a discrete actuation of the rigid body. Note that by introducing the matrix

$$H_{jk} = \begin{bmatrix} I \\ X_1^k I \\ X_2^k I \\ X_3^k I \end{bmatrix} \tag{25}$$

containing the information of the geometric position of the contact points the following linear relation between the external (director) forces $\bar{f}(t) = \begin{bmatrix} f_{ext} & f_{ext}^i \end{bmatrix}^T$ and the contact forces $n_c^k$

$$\bar{f}(t) = H n_c^k(t) \tag{26}$$

holds. The geometric constraints $(23)_3$ are enforced by the Lagrange multipliers $\Lambda_{ij}$. To force the rigid body at hand to follow a prescribed motion $\gamma(t) = \begin{bmatrix} \gamma_{\bar{x}} & \gamma_{d_i} \end{bmatrix}^T$ additionally to the holonomic constraints $(23)_3$, the following control constraints

$$g_s = \bar{q} - \gamma(t) = 0 \tag{27}$$

are introduced. In (27) the motion of the rigid body, which is fully described by the directors $d_i : T \mapsto \mathbb{R}^3$ and the position of the centre of gravity $\bar{x} : T \mapsto \mathbb{R}^3$ is contained in $\bar{q} = \begin{bmatrix} \bar{x} & d_i \end{bmatrix}^T$. The servo-constraints (27) of course must not violate the holonomic constraints $(23)_3$. The differential part of the DAE at hand, consisting of $(23)_1$ and $(23)_2$, together with the control constraint (27) yield an algebraic equation for the external (director) force $\bar{f}(t)$ conjugate to $q$ given by

$$\bar{f}(t) = D\partial_t^2 \gamma(t) + F\gamma(t) - \bar{G} \tag{28}$$

with

$$D = \begin{bmatrix} M & 0 \\ 0 & E_{ij} \end{bmatrix} \quad , \quad F = \begin{bmatrix} 0 & 0 \\ 0 & \Lambda_{ij} \end{bmatrix} \quad , \quad \bar{G} = \begin{bmatrix} G \\ 0 \end{bmatrix} \tag{29}$$

where $G$ is the gravitational force. After $\bar{f}(t)$ has been computed, the $k \in \mathbb{N}$ contact forces $n_c^k(t)$ for the $k$ ropes at $s_k = 1$ can be easily computed by knowing the position of the contact point of the rope at the rigid body through the following linear relation:

$$n_c^k(t) = Q_{kl} \bar{f}_l(t) \tag{30}$$

https://doi.org/10.3311/ECCOMASMBD2021-153

Herein $Q_{kl}$ are the components of the inverse of the positive definite matrix $H \in \mathbb{R}^{4\alpha,4\alpha}$ introduced in (25). Once the forces $n_k(t)$ have been calculated, each rope can be solved separately by inserting the forces into the corresponding boundary condition of the quasi-linear hyperbolic partial differential equation established in Section 2. Before the cascade-like approach outlined above is investigated numerically in Section 5, the multibody system at hand consisting of a rigid body attached to a geometrically exact rope is developed in the next Section. The numerical results of the inverse calculation can then be verified using this model.

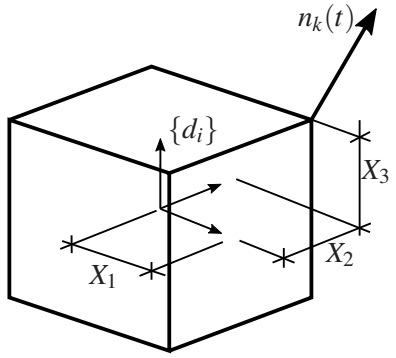


**Figure 4**. Force $n_k$ acting on a rigid body at point $P = \bar{x} + X_i d_i$

**Remark 3.1** (Lagrange multipliers)**.** *The actuating forces depend on the Lagrange multipliers $\Lambda_{ij}$ and hence a unique solution for the actuation of the rigid body requires the six independent components $\bar{\lambda}_k$ for $k \in \{1,\cdots,6\} \subset \mathbb{N}$ of $\Lambda_{ij}$ to be partly specified.*

$$\bar{\lambda}_k = \gamma_{\lambda_k}$$

*In essence, this amounts to partly specifying the stresses within the rigid body (cf.[10]).*

## 4 MULTIBODY SYSTEM

When considering flexible multibody systems consisting of a rigid body connected to a rope, the motion can be described by the semi-discrete equation of motion of the rope (11) together with the differential algebraic equation (23) governing the motion of the rigid body depending on the unknown spatial discrete variables $q = \begin{bmatrix}\hat{q}^T & \bar{q}^T\end{bmatrix}^T$.

$$R(\partial_t^2 q, q, \bar{\lambda}, t) = \begin{bmatrix}\hat{M}\partial_t^2\hat{q} + f_i^{int} - \hat{G} \\ D\partial_t^2\bar{q} + F\bar{q} - \bar{G}\end{bmatrix}$$

subjected to the following geometric contact constraint

$$g_k = r_{p+1} - (\bar{x} + X_i d_i) = 0 \tag{31}$$

by the following semi-explicit differential algebraic equation:

$$\begin{aligned} R(\partial_t^2 q, q, t) - (\partial_q g_k(q))^T \lambda &= 0 \\ g_c &= 0 \\ g_k &= 0 \end{aligned}$$

Note that the Lagrange multipliers $\lambda : T \mapsto \mathbb{R}^\alpha$ can be identified with the contact force acting

https://doi.org/10.3311/ECCOMASMBD2021-153

between the rope and the rigid body. Compare therefore (11) and (23) with

$$\lambda \partial_q g(q) = \begin{bmatrix} 0 \\ \vdots \\ \lambda \\ -\lambda \\ -\lambda X_1 \\ -\lambda X_2 \\ -\lambda X_3 \end{bmatrix} \tag{32}$$

To verify the numerical implementation of the procedure outlined in this section, an example for the forward dynamics of a rigid body suspended by a flexible rope is considered. In particular, snapshots of a free oscillation of a rigid cube with edge length $a$ and total mass $\bar{M}$, which is attached to a flexible rope, are shown in Figure 5. For the time $t = 0.0\ s$ the initial translational velocity $v_0 = \begin{bmatrix} 2 & -5 & 0 \end{bmatrix}^T$ is presupposed.

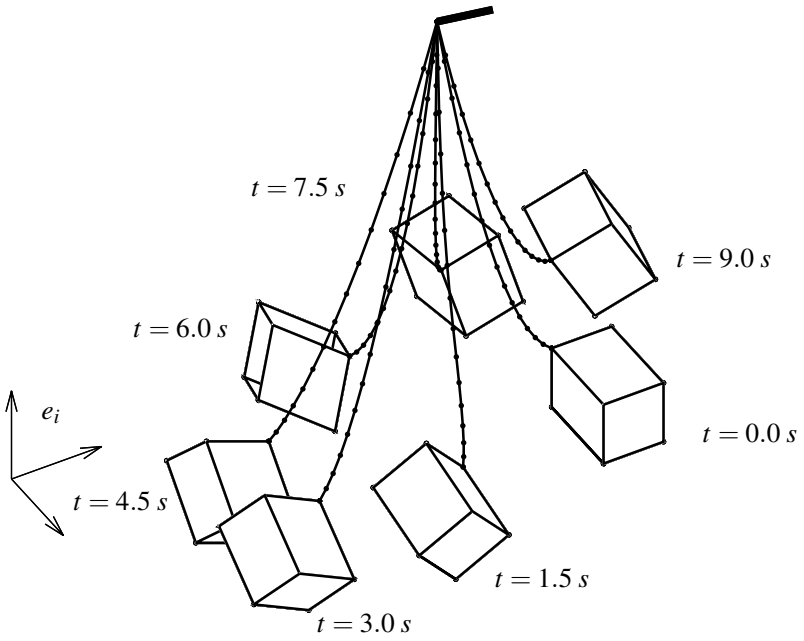


**Figure 5**. Free oscillation of a rigid cube with edge lenth $a = 2$ and total mass $\bar{M} = 0.1$ connected to a flexible rope with $\rho = 1$ and $E = 2$

## 5 NUMERICAL EXAMPLE

To verify the presented approach to the inverse dynamics problem under consideration, the following scenario is given. A rigid cube with edge length $a = 2$ and mass $\bar{M} = 1$ is supposed to accomplish a rest-to-rest maneuver. For this a translation of the cube from point $P_0 = (0,0,0)$ to point $P_f = (2,2,2)$ along a straight line together with a simultaneous rotation of $\pi$ around the z-axis is planned. The maneuver is intended to start at $t_0 = 1.0\ s$ and end at $t_f = 9.0\ s$. The motion of the rigid body described in terms of a Cosserat point subjected to geometric constraints can then be prescribed together with

$$\varphi = -\frac{\pi}{2}(\cos(\frac{\pi}{2}(\sin\theta + 1)) - 1) \quad , \quad \theta = \pi(\frac{t - t_0}{t_0 - t_f} - \frac{1}{2}) \tag{33}$$

https://doi.org/10.3311/ECCOMASMBD2021-153

through the following trajectory:

$$\gamma_{rb} = \begin{bmatrix} 0 \\ 0 \\ 0 \\ 1 \\ 0 \\ 0 \\ 0 \\ 1 \\ 0 \\ 0 \\ 0 \\ 1 \end{bmatrix} \quad \forall\, t < t_0, \quad \gamma_{rb} = \begin{bmatrix} -\cos\varphi + 1 \\ -\cos\varphi + 1 \\ -\cos\varphi + 1 \\ \cos\varphi \\ \sin\varphi \\ 0 \\ -\sin\varphi \\ \cos\varphi \\ 0 \\ 0 \\ 0 \\ 1 \end{bmatrix} \quad \forall\, t \in T_m = [t_0, t_f], \quad \gamma_{rb} = \begin{bmatrix} 2 \\ 2 \\ 2 \\ -1 \\ 0 \\ 0 \\ 0 \\ -1 \\ 0 \\ 0 \\ 0 \\ 1 \end{bmatrix} \quad \forall\, t > t_f \quad (34)$$

Thereby, four elastic ropes with mass density $\rho = 1$ and Young's modulus $E = 1$, are used to actuate the rigid body for which the motion is prescribed.

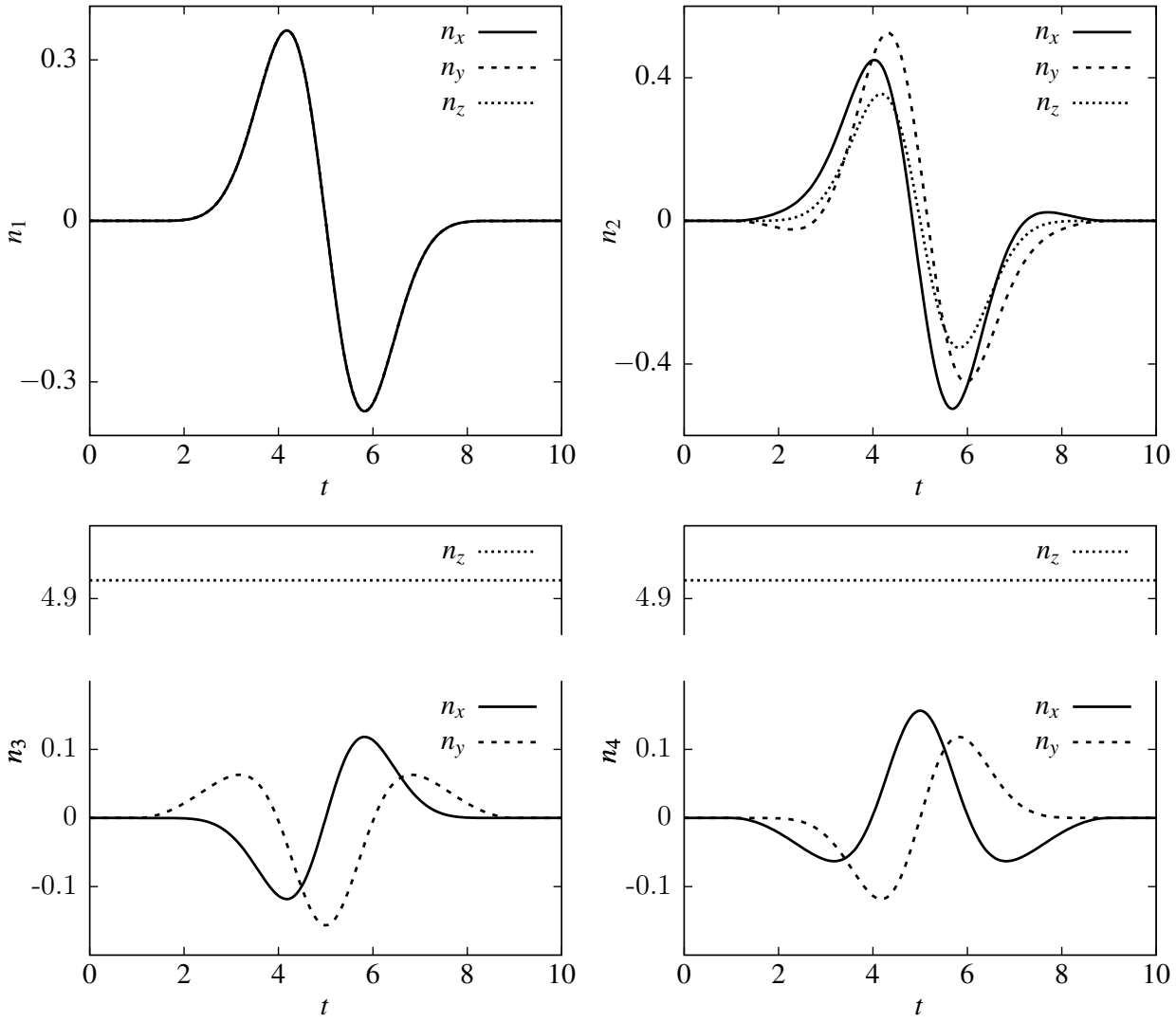


**Figure 6**. Components of the contact forces $n_k(t)$ such that the rigid body follows the prescribed translation of the rigid body from point $P_0 = (0,0,0)$ to point $P_f = (2,2,2)$ accompanied by a simultaneous rotation $\pi$

https://doi.org/10.3311/ECCOMASMBD2021-153

Regarding the $k$ predefined contact points for $i \in \{1,2,3\}$

$$P_k = \bar{x} + X_i^k d_i$$

and following Section 3 the contact forces needed to achieve the desired motion can then be computed using (30) with

$$H = \begin{bmatrix} I & I & I & I \\ I & -I & I & -I \\ I & -I & -I & I \\ -I & I & I & I \end{bmatrix}$$

where $I \in \mathbb{R}^{\alpha,\alpha}$ is the identity matrix. Note that, following Remark 3.1, the Lagrange multipliers cannot be left undefined. For the given maneuver, a uniaxial tension within the rigid body is choosen:

$$\bar{\lambda} = \begin{bmatrix} 0 & 0 & \bar{M}g & 0 & 0 & 0 \end{bmatrix}^T \tag{35}$$

In Figure 6 components of the $k$ contact forces are shown. Subsequently, using the methods presented in Section 2 and Section 3, the forces acting on the upper end of the $k$ ropes at $s_k = 0$ such that the rigid body at hand follows the prescribed trajectory, can be calculated. The numerical solution is shown in Figure 7.

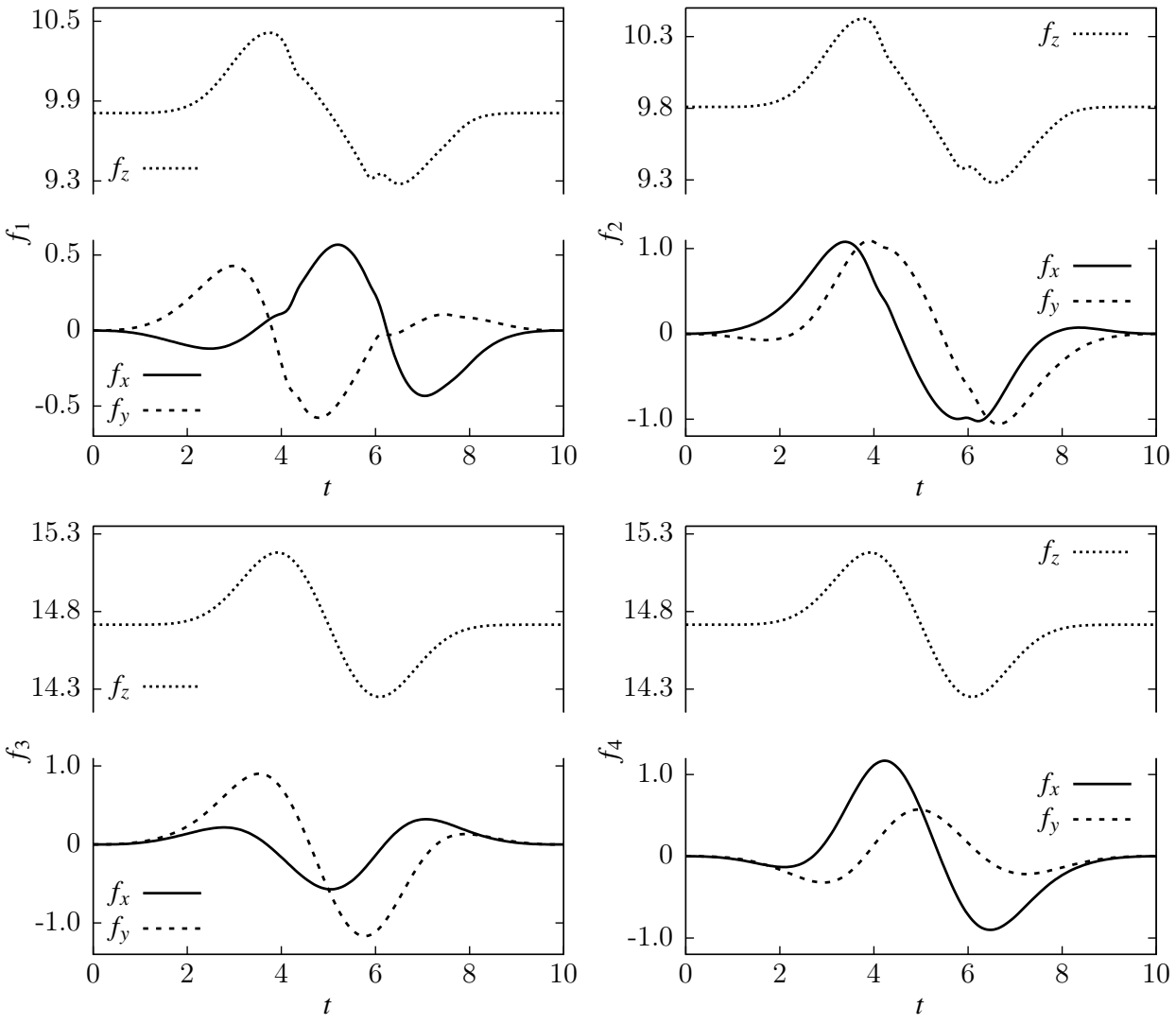


**Figure 7**. Components of the actuating forces $f_k$ acting on the upper end of the ropes at $s_k = 0$

https://doi.org/10.3311/ECCOMASMBD2021-153

To verify the outlined method, the forces $f_k(t)$ can be inserted into the flexible multibody system presented in Section 4. In Figure 8 snapshots of a forward simulation of the flexible multibody system at hand actuated with the forces $f_k(t)$ acting at the upper ends of the $k$ ropes computed numerically using the approach presented above are shown.

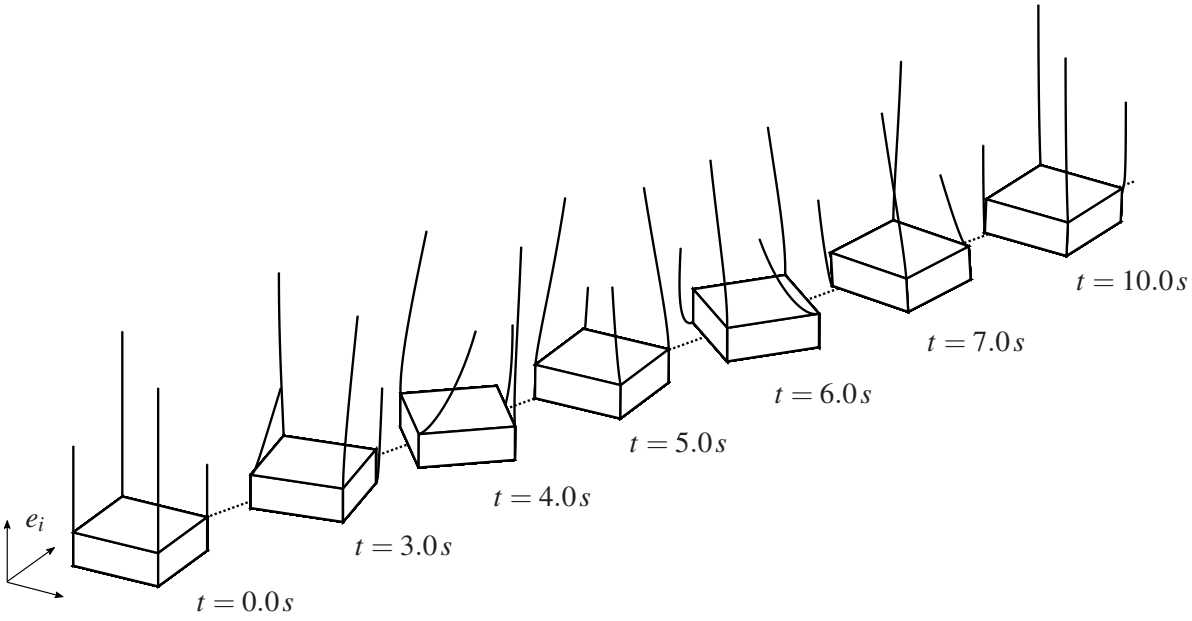


**Figure 8**. Snapshots of a rigid cube with edge length $a = 2$ and total mass $\bar{M} = 1$ actuated through four flexible ropes with $\rho = 1$ and $E = 2$ following a straight line from $P_0 = (0,0,0)$ to $P_f = (2,2,2)$ while rotating simultaneously by the prescribed angle $\pi$

## 6 CONCLUSIONS

In this contribution the focus is laid on the cooperative control of a rigid body through flexible ropes. For this, the rigid body is supposed to follow any prescribed motion and an actuation is only achieved through flexible ropes attached to the rigid body at hand. Due to the differential flatness of the rope and the rigid body, the determination of the searched actuating forces, which are only allowed to act upon the upper ends of the attached ropes, can be carried out in a cascade-like manner. For this purpose, the rigid body is modelled as a Cosserat point under geometric constraints. By knowing the given motion of the body, the contact forces acting between the ropes and the rigid body can then be calculated directly from the resulting differential algebraic equation describing the motion of the body without integration. Now the task is to find the actuating force at the upper end of each rope, such that the geometric and static boundary conditions together with the partial differential equation governing the motion of the rope are fulfilled. The geometric and static boundary conditions are given by the prescribed motion of the lower end of the rope and the contact force, respectively. Common approaches, like the semi-discrete approach in which the underlying initial boundary value problem is discretised in space by applying appropriate methods and subsequently integrated in time, are not feasible for the control problem of flexible structures considered here. Therefore, a space-time finite element method is proposed in this contribution. This novel approach solves the control problem simultaneously in space and time and yields the actuating forces at the upper end of the ropes. Due to the cascade-like approach, the inverse computations of the rope-dynamics can be solved in parallel. The results of the inverse calculation of the actuating forces can then be verified by a forward simulation of a model of the considered flexible multibody system excited through the computed actuating forces. For this a direct model of

the considered flexible multibody system is established in this contribution. This paper concludes by presenting a represenative numerical example.

## ACKNOWLEDGMENTS

This work was supported by the Deutsche Forschungsgemeinschaft (DFG) under Grant BE 2285/12-1. This support is gratefully acknowledged.

## REFERENCES

[1] Ströhle, T., Betsch, P.: Solution techniques for problems of inverse dynamics of flexible underactuated systems. In Kecskeméthy, A., Geu Flores, F., eds.: Multibody Dynamics 2019, Cham, Springer International Publishing (2020) 131–138

[2] Ströhle, T., Betsch, P.: Controlling nonlinear elastic systems in structural dynamics. In: WCCM-ECCOMAS2020, Paris, Virtual Congress, 14th World Congress on Computational Mechanics (WCCM) and ECCOMAS Congress (11-15 January 2021)

[3] Antman, S.S.: Nonlinear Problems of Elasticity. Volume 2. Springer (2005)

[4] Murray, R.M.: Trajectory generation for a towed cable system using differential flatness. IFAC Proceedings Volumes **29**(1) (1996) 2792–2797 13th World Congress of IFAC, 1996, San Francisco USA, 30 June - 5 July.

[5] Altmann, R., Heiland, J.: Simulation of multibody systems with servo constraints through optimal control. Multibody System Dynamics **40** (2017) 75–98

[6] Argyris, J.H., Scharpf, D.W.: Finite elements in time and space. Nuclear Engineering and Design **10** (1969) 456–464

[7] Hughes, T.J.R., Hulbert, G.M.: Space-time finite element methods for elastodynamics: Formulations and error estimates. Computer Methods in Applied Mechanics and Engineering **66** (1988) 339–363

[8] Hesch, C., Schuß, S., Dittmann, M., Eugster, S.R., Favino, M., Krause, R.: Variational space-time elements for large systems. Computer Methods in Applied Mechanics and Engineering **326** (2017) 541–572

[9] Betsch, P.: Energy-momentum integrators for elastic Cosserat points, rigid bodies, and multibody systems. In Betsch, P., ed.: Structure-preserving Integrators in Nonlinear Structural Dynamics and Flexible Multibody Dynamics, Cham, Springer International Publishing (2016) 31–89

[10] Irscheid, A., Konz, M., Rudolph, J.: A flatness-based approach to the control of distributed parameter systems applied to load transportation with heavy ropes. In Kondratenko, Y.P., Chikrii, A.A., Gubarev, V.F., Kacprzyk, J., eds.: Advanced Control Techniques in Complex Engineering Systems: Theory and Applications: Dedicated to Professor Vsevolod M. Kuntsevich, Cham, Springer International Publishing (2019) 279–294

https://doi.org/10.3311/ECCOMASMBD2021-131



# Flexible Multibody Impact Simulations Using Hierarchically Refined Isogeometric Models

**Tobias Rückwald, Alexander Held, Robert Seifried**

Institute of Mechanics and Ocean Engineering
Hamburg University of Technology
Eißendorfer Straße 42, 21073 Hamburg, Germany
{tobias.rueckwald, alexander.held, robert.seifried}@tuhh.de

## ABSTRACT

Detailed impact simulations in flexible multibody systems can be simulated based on reduced isogeometric analysis (IGA) models. A precise simulation of an impact requires a high element resolution in the contact area. Usually, global refinement methods are used, which are easy to implement. However, the literature proposes the use of hierarchical refinement to refine locally. The local refinement generates fewer countable degrees of freedom compared to an equivalent global refinement. Numerous application areas can be found in the literature, such as contact simulations, where the computational effort is reduced by local refinement. This work tests the hierarchical refinement in the context of an impact simulation with the floating frame of reference formulation. In the application example, the impact of two elastic spheres is simulated and compared to an analytic solution. The focus is set on calculation time and accuracy compared to globally refined reference models.

**Keywords:** impact simulation, IGA, floating frame of reference formulation.

## 1 INTRODUCTION

In impact problems within flexible multibody systems, the rigid body motions before and after impact are often large while only small elastic deformations occur during impact. This is the case for relatively stiff materials. Flexible bodies made of steel or aluminum are considered stiff, which allows the application of the floating frame of reference formulation [1] in this work. The use of the floating frame of reference formulation requires global shape functions $\boldsymbol{\Phi}$ of the flexible bodies to model the body flexibility. The global shape functions can be obtained with the finite element method [2] and a reduction method, such as the Craig-Bampton method [3]. When simulating flexible multibody systems and impacts, the bodies are usually meshed with isoparametric elements. A major drawback of isoparametric elements is the discretization of the geometry. Since the calculation of the contact force is based on the geometry of the finite element model, errors can occur. An alternative to isoparametric elements is the IGA, whose use is motivated by two advantages. First, the use of non-uniform rational basis splines (NURBS) as local shape functions of the elements allows an exact representation of the body geometry. Second, high modes of flexible bodies are represented more accurately compared to isoparametric elements [4]. The latter advantage is useful for the floating frame of reference formulation introduced in the later course of this work. These advantages are bought by increased computational costs in the evaluation of the nonlinear local shape functions compared to linear shape functions of isoparametric elements.

An accurate impact simulation, which captures the local deformation, requires a high element resolution in the contact area, as this is where the largest elastic deformations and stresses occur. However, the refinement methods usually used in IGA only allow global refinement. When the number of elements is increased in the contact area, additional elements and control points are created over the entire body, as exemplified on the left hand side in Fig. 1. The control points represent the degrees of freedom in the IGA, thus the global refinement greatly increases the number of equations in the finite element model. One method for local refinement is a hierarchical approach,

https://doi.org/10.3311/ECCOMASMBD2021-131

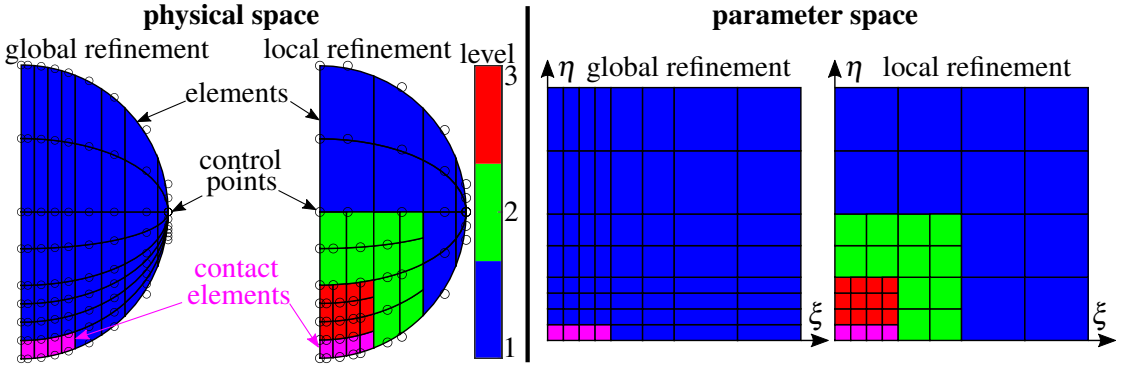


Figure 1: Example of a semicircle that should be refined in the contact area.

where subordinate levels are introduced, as displayed in Fig. 1. The hierarchical refinement is widely used in the literature. It is applied in elementary fluid and structural analysis [5], heat conduction problems [6], topology optimization [7] and contact simulations [8]. The aforementioned literature summarizes that the computational effort can be reduced due to the smaller number of degrees of freedom compared to a global refinement. These examples are mostly from statics, in this work hierarchical refinement is applied in a dynamic problem. The aim of this work is to show whether the computational effort is reduced when simulating the impact of hierarchically refined bodies in the context of the floating frame of reference formulation.

This work is organized in the following way. Initially, the concept of the floating frame of reference formulation is briefly summarized in Section 2. Section 3 introduces the concepts of the IGA, the hierarchical refinement, and the extraction of the global shape functions. The contact algorithm is briefly explained in Section 4. The following Section 5 is a detailed discussion of an application example, and the results are summarized in Section 6.

## 2 FLOATING FRAME OF REFERENCE FORMULATION

When simulating flexible multibody systems, the floating frame of reference formulation is a well-established approach [1]. Large nonlinear rigid body motion of the body frame $\mathrm{K_R}$ can be described within the inertial frame $\mathrm{K_I}$. In this work, a Buckens-frame [1] is utilized as floating frame. Provided that the body deformations remain small and linear elastic, they can be described in the body frame $\mathrm{K_R}$. Using the global shape functions $\boldsymbol{\Phi}$ and the $n_\mathrm{q}$ elastic coordinates $\boldsymbol{q}_\mathrm{e}$, the elastic deformation can be approximated. The equations of motion of a single flexible body are given by

$$\underbrace{\begin{bmatrix} m\mathbf{E} & \mathbf{0} & \boldsymbol{C}_\mathrm{t}^\mathsf{T} \\ \mathbf{0} & \boldsymbol{I} & \boldsymbol{C}_\mathrm{r}^\mathsf{T} \\ \boldsymbol{C}_\mathrm{t} & \boldsymbol{C}_\mathrm{r} & \overline{\boldsymbol{M}}_\mathrm{e} \end{bmatrix}}_{\boldsymbol{M}} \underbrace{\begin{bmatrix} {}^\mathrm{R}\dot{\boldsymbol{v}}_\mathrm{IR} \\ {}^\mathrm{R}\dot{\boldsymbol{\omega}}_\mathrm{IR} \\ \ddot{\boldsymbol{q}}_\mathrm{e} \end{bmatrix}}_{\dot{\boldsymbol{z}}_\mathrm{II}} = \underbrace{\boldsymbol{h}_\mathrm{p} + \boldsymbol{h}_\mathrm{d} + \boldsymbol{h}_\mathrm{b} - \boldsymbol{h}_\omega - \boldsymbol{h}_\mathrm{e}}_{\boldsymbol{h}_\mathrm{a}}, \tag{1}$$

where ${}^\mathrm{R}\boldsymbol{v}_\mathrm{IR}$ is the velocity of the rigid body motion from the inertial frame to the reference frame and ${}^\mathrm{R}\boldsymbol{\omega}_\mathrm{IR}$ is the angular velocity. In Eq. (1), the mass of the body is denoted by $m$, the translational coupling matrix by $\boldsymbol{C}_\mathrm{t}$, the rotational coupling matrix by $\boldsymbol{C}_\mathrm{r}$ and the mass moment of inertia by $\boldsymbol{I}$. The right hand side vector $\boldsymbol{h}_\mathrm{a}$ is composed of the vector of surface forces $\boldsymbol{h}_\mathrm{p}$, the discrete forces $\boldsymbol{h}_\mathrm{d}$, the body forces $\boldsymbol{h}_\mathrm{b}$, and the inertial forces $\boldsymbol{h}_\omega$. The mass matrix $\overline{\boldsymbol{M}}_\mathrm{e}$ of a linear elastic body as well as the stiffness $\overline{\boldsymbol{K}}_\mathrm{e}$ and damping matrix $\overline{\boldsymbol{D}}_\mathrm{e}$ needed to compute the inner forces $\boldsymbol{h}_\mathrm{e}$ are introduced in a later section. Contact forces are considered in the discrete forces $\boldsymbol{h}_\mathrm{d}$. The standard input data (SID), a well-known standard in providing elastic data in the context of the floating frame of reference formulation [1], is used to assemble the equations of motion (1). For the formulation of the equations of motion and the transient analysis, the MATLAB toolbox DYNMANTO [9] is

used. The resulting equations of motion are solved by the `ode15s` MATLAB solver with numerical differentiation formulas (NDF).

## 3 GLOBAL SHAPE FUNCTIONS FROM IGA

Determining the global shape functions $\boldsymbol{\Phi}$ is a key issue in using the floating frame of reference formulation. A general way to determine the global shape functions is to generate a finite element model of the flexible body and then identify the global shape functions from the finite element model using model reduction techniques. This section briefly presents the idea of the IGA and the procedure to obtain the global shape functions from an IGA model. A more detailed introduction to the IGA can be found in [4]. Additionally, the concept of hierarchical refinement and a methodology to locally refine isogeometric models are introduced.

### 3.1 Basis Splines

The IGA consists of three spaces: The physical space, the parameter space, and the index space. The first two spaces are essential for understanding the IGA. The shape functions of isogeometric elements are defined in the parameter space, which can be seen for a 2D example on the left hand side in Fig. 2. The parameter space is divided into elements and spanned by the knot vectors $\boldsymbol{\Xi} = \begin{bmatrix}\xi_1 & \xi_2 & \dots & \xi_{\mathrm{n+p+1}}\end{bmatrix}$ and $\boldsymbol{\mathcal{H}} = \begin{bmatrix}\eta_1 & \eta_2 & \dots & \eta_{\mathrm{m+q+1}}\end{bmatrix}$.

Thereby, $p$ and $q$ are the order of the basis functions and $n$ and $m$ are the numbers of the basis functions $N_{i,\mathrm{p}}$ and $M_{j,\mathrm{q}}$. The order of the basis functions can be subsequently increased with the algorithm in [10]. In IGA, the local shape functions are based on B-splines, which can be computed recursively with the Cox-de Boor algorithm [4]. In $\xi$-direction, the B-splines are computed as

$$p = 0: \quad N_{i,0}(\xi) = \begin{cases} 1 & \text{if } \xi_i \leq \xi < \xi_{i+1}, \\ 0 & \text{otherwise.} \end{cases} \tag{2}$$

$$p > 1: \quad N_{i,\mathrm{p}}(\xi) = \frac{\xi - \xi_i}{\xi_{i+\mathrm{p}} - \xi_i} N_{i,\mathrm{p-1}}(\xi) + \frac{\xi_{i+\mathrm{p+1}} - \xi}{\xi_{i+\mathrm{p+1}} - \xi_{i+1}} N_{i+1,\mathrm{p-1}}(\xi). \tag{3}$$

The calculation rule given by Eq. (2) and Eq. (3) is identical in $\eta$-direction. In practice, recursive functions are numerically inefficient. Therefore, a non-recursive algorithm suggested in [10] is used.

### 3.2 Non-Uniform Rational Basis Splines

Besides the parameter space there is the physical space, which can be seen on the right hand side in Fig. 2. In the physical space, the control points $\boldsymbol{P}_{i,j}$ are defined, which are arranged by the control net. The task of the control points is to span the geometry in the physical space. The dimension

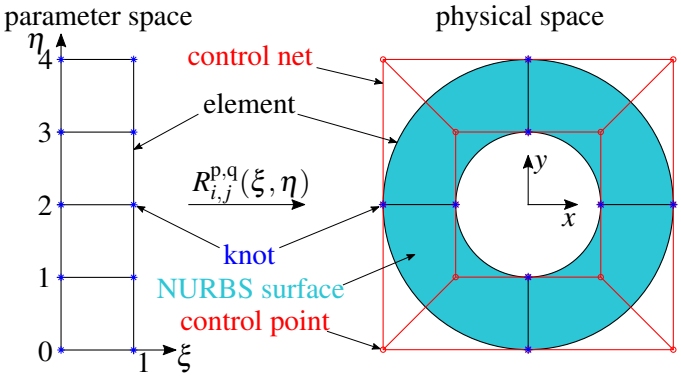


Figure 2: Parameter space and physical space in the IGA.

https://doi.org/10.3311/ECCOMASMBD2021-131

of the control points corresponds to the numbers of B-splines $n$ and $m$ in the parameter space. In addition to the physical position, each control point has a weight $w_{i,j}$. The transformation from the parameter space into the physical space requires the NURBS basis $R_{i,j}^{\mathrm{p,q}}$ given by

$$R_{i,j}^{\mathrm{p,q}}(\xi,\eta) = \frac{N_{i,\mathrm{p}}(\xi) M_{j,\mathrm{q}}(\eta) w_{i,j}}{\sum_{\hat{i}=1}^{\mathrm{n}} \sum_{\hat{j}=1}^{\mathrm{m}} N_{\hat{i},\mathrm{p}}(\xi) M_{\hat{j},\mathrm{q}}(\eta) w_{\hat{i},\hat{j}}}. \tag{4}$$

The NURBS basis $R_{i,j}^{\mathrm{p,q}}$ and the control points $\boldsymbol{P}_{i,j}$ then lead to the NURBS surface

$$\boldsymbol{S} = \sum_{i=1}^{\mathrm{n}} \sum_{j=1}^{\mathrm{m}} R_{i,j}^{\mathrm{p,q}}(\xi,\eta) \boldsymbol{P}_{i,j}, \tag{5}$$

in the physical space. The degrees of freedom in the IGA correspond to the displacements of the control points

$$\boldsymbol{u}_{i,j} = \boldsymbol{P}_{i,j} - \boldsymbol{P}_{i,j}^{0}, \tag{6}$$

whereby $\boldsymbol{P}_{i,j}^{0}$ represents the position of the control points in the undeformed and $\boldsymbol{P}_{i,j}$ in the deformed configuration. The deformation $\boldsymbol{d}$ of the NURBS surface can be written in matrix-vector notation as

$$\boldsymbol{d} = \underbrace{\begin{bmatrix} R_{1,1}^{\mathrm{p,q}} & 0 & R_{1,2}^{\mathrm{p,q}} & 0 & \dots & 0 \\ 0 & R_{1,1}^{\mathrm{p,q}} & 0 & R_{1,2}^{\mathrm{p,q}} & \dots & R_{\mathrm{p+1,q+1}}^{\mathrm{p,q}} \end{bmatrix}}_{\boldsymbol{N}} \underbrace{\begin{bmatrix} u_{1,1,\mathrm{x}} \\ u_{1,1,\mathrm{y}} \\ u_{1,2,\mathrm{x}} \\ u_{1,2,\mathrm{y}} \\ \vdots \\ u_{\mathrm{p+1,q+1,y}} \end{bmatrix}}_{\boldsymbol{u}}, \tag{7}$$

where the basis functions of the corresponding element are summarized in matrix $\boldsymbol{N}$.

### 3.3 Hierarchical Refinement

The concept of the hierarchical refinement relies on the property of B-splines to be represented by a linear combination of finer B-splines defined on smaller knot-intervals. With the calculation rule

$$a_j = 2^{-p} \binom{p+1}{j} = 2^{-p} \frac{(p+1)!}{j!\,(p+1-j)!} \tag{8}$$

linear coefficients can be determined to represent a B-spline in a higher level with B-splines of lower level. It should be noted that Eq. (8) is only valid for uniform knot vectors. As an example, a quadratic B-spline with the high-level knot vector

$$\boldsymbol{\Xi}^{1} = \begin{bmatrix} 0 & 1 & 2 & 3 \end{bmatrix} \tag{9}$$

should be represented by a number of lower level B-splines with the corresponding low-level knot vector

$$\boldsymbol{\Xi}^{2} = \begin{bmatrix} 0 & \underline{0.5} & 1 & \underline{1.5} & 2 & \underline{2.5} & 3 \end{bmatrix}. \tag{10}$$

The inserted knots in Eq. (10) are underlined. By applying Eq. (8) the concept of the hierarchical refinement can be visualized in Fig. 3. The procedure, which is implemented and used in this work, is briefly summarized in the following. For a detailed introduction to the hierarchical refinement, see [5].

Initially, the parameter space is divided into the different hierarchy levels. Recapturing the motivation example in Fig. 1, the corresponding parameter space is displayed on the right hand side. This division is made up by intervals in knot coordinates. The concept of hierarchical refinement is that a finer mesh resolution can be defined section by section. Therefore, the levels are initialized using

https://doi.org/10.3311/ECCOMASMBD2021-131

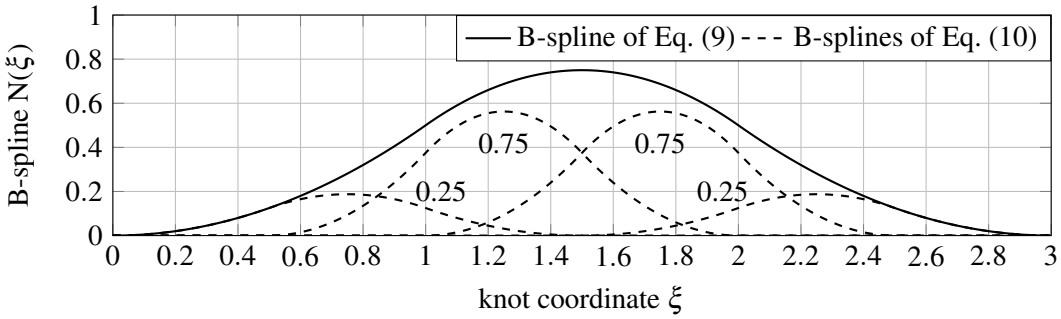


Figure 3: Concept of the hierarchical refinement in the IGA.

the global knot insertion algorithm described in [4]. With this algorithm, the position of the control points and their weights can be determined for the finer mesh. The number of hierarchy levels is denoted as $n_{\mathrm{lvl}}$.

In hierarchical refinement, B-splines of higher level are based on B-splines of lower level. For the construction of higher level B-splines, the linear combination coefficient matrix $\boldsymbol{A}$ is determined by solving

$$N^{\ell}_{i,\mathrm{p}} = \boldsymbol{A}^{\ell}_{i,j} N^{\ell+1}_{j,\mathrm{p}} \qquad \ell = 1 \ldots n_{\mathrm{lvl}} - 1 \tag{11}$$

between all $n_{\mathrm{lvl}}$ hierarchy levels. A detailed description of this procedure can be found in [11].

In the next step, the elements are defined with the knot vectors of the different levels and the intervals, which defined the hierarchy level with respect to the knot coordinates. The previous step allows certain B-splines to be identified as inactive. Thus, the associated control points of each element can be determined. Thereby, the control points can be located in different hierarchy levels. The control points that are not part of an element are identified as inactive.

The hierarchical B-splines of the example introduced at the beginning in Fig. 1 are depicted in Fig. 4. It can be seen that B-splines of different hierarchy levels can be active, e.g. at the knot coordinate $\xi = 0.2$ in Fig. 1. This overlap becomes relevant when calculating the NURBS basis from Eq. (4). The B-splines of the different dimensions of the parameter space need to be multiplied out. These intersections of the B-splines lead to the fact that for the computation of the NURBS any level can interact with any level of the other dimensions in the parameter space. The more hierarchical levels that are created, the more combinations of possible intersections of the B-splines can occur. This may increase the calculation time of the hierarchical NURBS basis compared to a globally refined model. In addition to the more complex calculation of the NURBS, the B-splines from the different hierarchy levels must be constructed, which takes additional computation time.

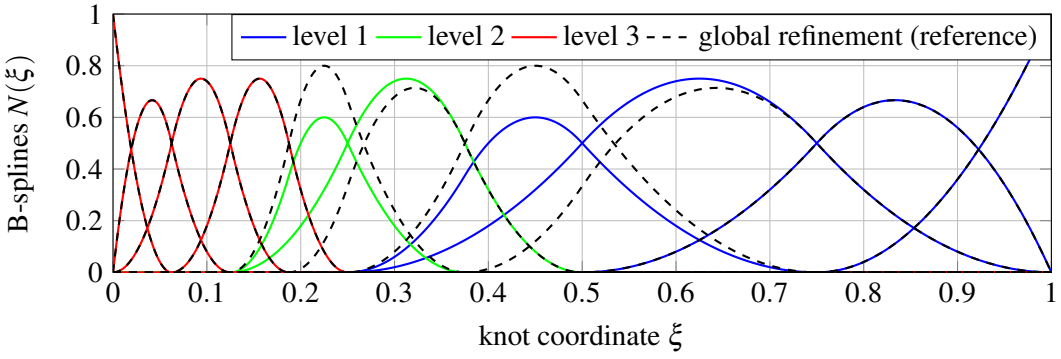


Figure 4: Concept of the hierarchical refinement in the IGA.

https://doi.org/10.3311/ECCOMASMBD2021-131

### 3.4 IGA Equations of Motion

As with the floating frame of reference formulation, it is assumed that only small elastic deformations occur in a relatively stiff material. Therefore, linear elasticity is assumed and the weak Galerkin method is applied as for isoparametric elements [2]. The local mass and stiffness matrix of an element is therefore given by

$$\boldsymbol{K}_{\mathrm{e},j} = \int_{\Omega_{\mathrm{e},j}} \boldsymbol{B}^{\mathsf{T}} \boldsymbol{C} \boldsymbol{B} \, \mathrm{d}\Omega_{\mathrm{e},j} \qquad j = 1...n_{\mathrm{e}}, \tag{12}$$

$$\boldsymbol{M}_{\mathrm{e},j} = \rho \int_{\Omega_{\mathrm{e},j}} \boldsymbol{N}^{\mathsf{T}} \boldsymbol{N} \, \mathrm{d}\Omega_{\mathrm{e},j} \qquad j = 1...n_{\mathrm{e}}, \tag{13}$$

where $\boldsymbol{C}$ is the material elasticity matrix and $n_{\mathrm{e}}$ the number of elements. The strain displacement matrix $\boldsymbol{B}$ is obtained by differentiating the NURBS basis $R_{i,j}^{\mathrm{p,q}}$ and using the Jacobian transformation [2]. The integration over each element $\Omega_{\mathrm{e},j}$ is performed by Gauss quadrature in the parameter space. The basis functions $\boldsymbol{N}$ and the strain displacement matrix $\boldsymbol{B}$ are evaluated at each Gauss point. As stated in [4], the same Gauss rule for a polynomial of the order $p$ can be applied to a $p$-th order B-spline. Therefore, the Gauss order $p+1$ is chosen in $\xi$-direction and $q+1$ in $\eta$-direction. The global system matrices $\boldsymbol{K}_{\mathrm{e}}$ and $\boldsymbol{M}_{\mathrm{e}}$ are assembled from the corresponding element matrices $\boldsymbol{K}_{\mathrm{e},j}$ and $\boldsymbol{M}_{\mathrm{e},j}$. The equations of motion of the complete finite element model are then given by

$$\boldsymbol{M}_{\mathrm{e}} \ddot{\boldsymbol{u}}_{\mathrm{e}} + \boldsymbol{K}_{\mathrm{e}} \boldsymbol{u}_{\mathrm{e}} = \boldsymbol{f}_{\mathrm{e}}, \tag{14}$$

where the displacements of the control points are represented by $\boldsymbol{u}_{\mathrm{e}}$ and the external forces by $\boldsymbol{f}_{\mathrm{e}}$.

### 3.5 Model Order Reduction

For the incorporation of the isogeometric model into the flexible multibody simulation, the global shape functions $\boldsymbol{\Phi}$ are required. The global shape functions $\boldsymbol{\Phi}$ for Eq. (1) can be determined from the linear system equations (14) with a model order reduction method. The straightforward approach for reducing the equations of motion (14) is modal reduction. However, as shown in [12], modal reduction leads to inaccurate results in case of impact problems, since the local deformation in the contact region is not included in the reduced model. Alternatively, the Craig-Bampton method [3] is used, which has already been successfully applied to impact problems with isoparametric elements [12]. The key idea of the Craig-Bampton method is to combine fixed-interface normal modes and constraint modes. The normal modes represent the overall flexibility and the constraint modes allow a relatively accurate representation of the deformation in a specific area of the flexible body, e.g. the contact area. For the constraint modes, predefined interface control points on the exterior surface can be selected. The procedure results in the global shape functions $\boldsymbol{\Phi}$, which are normalized to the mass matrix. The reduced mass and stiffness matrix are then given by

$$\overline{\boldsymbol{M}}_{\mathrm{e}} = \boldsymbol{\Phi}^{\mathsf{T}} \boldsymbol{M}_{\mathrm{e}} \boldsymbol{\Phi} = \mathbf{E} \qquad \text{and} \qquad \overline{\boldsymbol{K}}_{\mathrm{e}} = \boldsymbol{\Phi}^{\mathsf{T}} \boldsymbol{K}_{\mathrm{e}} \boldsymbol{\Phi} = \mathrm{diag}(\omega_i^2) \tag{15}$$

respectively, where $\mathbf{E}$ is the identity matrix and $\omega_i$ are the natural frequencies. Since the normal modes tend to be low and the constrained modes high, the equations of motion (1) become numerically stiff. Damping the high modes with the method of [13] and the parameters of [14] increases the numerical performance.

## 4 CONTACT HANDLING IN IGA

There exist several methods for discretizing the contact of two isogeometric bodies. Two frequently used types of methods are the integral description of the contact and the node-to-segment methods. In the integral description of the contact, Gauss points of preselected elements are checked [14]. The number of evaluation points depends on the number of elements in the contact area and on the order of the B-splines due to the Gauss integral. For node-to-segment methods, the number of evaluation

points depends only on the number of elements in the contact area. Since node-to-segment methods require fewer points to be checked for contact and the accuracy is still comparable to that of an integral description [15], a node-to-segment method is chosen for this work.

For node-to-segment methods, different collocation methods, e.g. Botella points can be used [15]. The following section briefly summarizes the contact algorithm described in [14]. This collocation method is combined with the penalty method for contact treatment. The corresponding penalty factor $c_\mathrm{p}$ is chosen heuristically. Thereby, the penalty factor should be chosen large enough such that the results become independent of the chosen parameter [16]. When the penalty factor is increased beyond its converging value, the differential equation (1) becomes stiffer and the simulation time is unnecessarily increased or the simulation might even terminate unsuccessfully.

At each time step, the individual bodies must be checked for contact. To this end, the position of the deformed control points $\boldsymbol{P}_{i,j}$ is determined. First, the control points displacements are recovered

$$\boldsymbol{u}_\mathrm{e} = \boldsymbol{\Phi}\boldsymbol{q}_\mathrm{e} \tag{16}$$

with the global shape functions $\boldsymbol{\Phi}$ and the elastic coordinates $\boldsymbol{q}_\mathrm{e}$. After that, the position of the control points is computed from Eq. (6). In case of contact between two bodies, one body is defined as the contact body and the other as the target body, as depicted in Fig. 5. The Botella points, which are located on the outer surface of the contact body and in the contact area, are tested for contact with the exterior surface of the target body. The contact check is achieved by solving

$$\left(\frac{\partial \boldsymbol{x}_\mathrm{T}(\xi)}{\partial \xi}\right)^\mathsf{T} (\boldsymbol{x}_\mathrm{C} - \boldsymbol{x}_\mathrm{T}(\xi)) = 0 \tag{17}$$

with the Newton–Raphson method for the respective knot coordinate, e.g. $\xi$. This knot coordinate $\xi$ corresponds to the target point $\boldsymbol{x}_\mathrm{T}(\xi)$, which is closest to the current Bottela point $\boldsymbol{x}_\mathrm{C}$ of the contact body. The distance $g_\mathrm{n}$ between the contact and target point is determined by

$$g_\mathrm{n} = \boldsymbol{n}^\mathsf{T}(\boldsymbol{x}_\mathrm{C} - \boldsymbol{x}_\mathrm{T}(\xi)), \tag{18}$$

where the normal vector $\boldsymbol{n}$ is orthogonal to the surface of the target body. If the normal gap $g_n$ is greater than zero, there is no contact. Otherwise, the contact force for the current sampling point is determined by

$$\boldsymbol{f}_\mathrm{c} = c_\mathrm{p} g_\mathrm{n} \boldsymbol{N}^\mathsf{T} \boldsymbol{n} \hat{\omega}_i, \tag{19}$$

where $c_\mathrm{p}$ is the penalty factor, $\boldsymbol{N}$ the local shape functions and $\hat{\omega}_i$ the collocation weight of the current collocation point. See [15] for the derivation of the collocation weight. To eliminate the distinction between contact and target body, they are switched and the contact force is averaged. After the contact search, the discrete forces can be calculated with

$$\boldsymbol{h}_\mathrm{d} = \sum_{i=1}^{\mathrm{n}} \sum_{j=1}^{\mathrm{m}} \begin{bmatrix} \mathbf{E} \\ \tilde{\boldsymbol{P}}_{i,j} \\ \boldsymbol{\Phi}_{i,j}^\mathsf{T} \end{bmatrix} \boldsymbol{f}_{\mathrm{c},i,j} \tag{20}$$

and inserted into Eq. (1). The contact algorithm described above is implemented in MATLAB. However, for the sake of computational efficiency, the algorithm is compiled into C-code using the MATLAB-MEX toolbox. The contact search can be parallelized with respect to the contact evaluation points.

## 5 APPLICATION EXAMPLE: IMPACT OF TWO SPHERES

The aim of this application example is to compare globally and locally refined isogeometric models in the context of an impact simulation in a flexible multibody system. It is investigated whether a locally refined model has the same accuracy as an equivalent globally refined model and how locally and globally refined models differ in computation time.

https://doi.org/10.3311/ECCOMASMBD2021-131

In this application example, the impact of two spheres is simulated. This simple example is well-suited as a benchmark because an analytical solution exists [17]. For the sake of simplicity, the spheres are identical and, therefore, the problem is symmetric. Despite the symmetry, both spheres are modeled. However, the axisymmetric property of a sphere is exploited by a semicircle. The simulation setup is visualized in Fig. 6. The radii of the spheres are $r = 1\,\mathrm{cm}$ and the selected

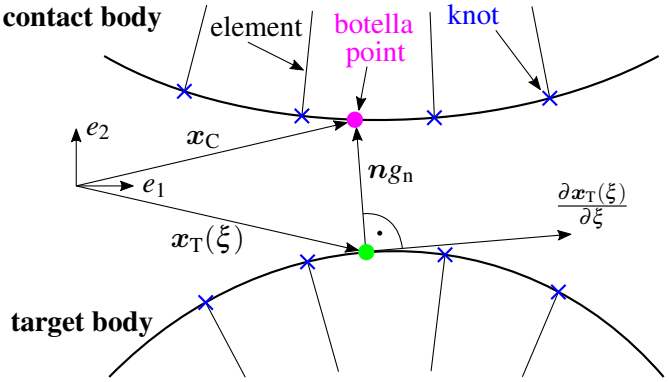


Figure 5: Contact detection between two bodies.

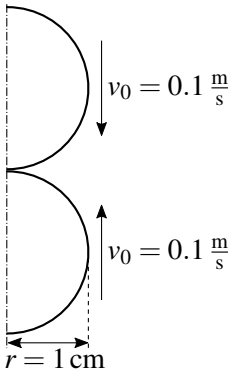


Figure 6: Impact of two spheres.

material is steel. Therefore, the Young's modulus is chosen as $E = 2.11 \times 10^{11}\,\mathrm{Pa}$, the density as $\rho = 7850\,\frac{\mathrm{kg}}{\mathrm{m}^3}$ and the Poisson's ratio as $\nu = 0.3$. Both spheres have an initial velocity of $v_0 = 0.1\,\frac{\mathrm{m}}{\mathrm{s}}$ and gravity is ignored. For the initialization of the geometry the knot vectors of the semicircle are defined as $\boldsymbol{\Xi} = \begin{bmatrix}0 & 0 & 0 & 1 & 1 & 1\end{bmatrix}$ and $\boldsymbol{\mathcal{H}} = \begin{bmatrix}0 & 0 & 1 & 1\end{bmatrix}$. The initial order of the B-splines is given by $p = 2$ and $q = 1$. The control points and weights in the physical space are

$$\boldsymbol{P}^0_{i,j,1} = \begin{bmatrix} 0 & 0 \\ r & r \\ r & r \end{bmatrix}, \qquad \boldsymbol{P}^0_{i,j,2} = \begin{bmatrix} -r & r \\ -r & r \\ 0 & 0 \end{bmatrix}, \qquad \text{and} \qquad \boldsymbol{w}_{i,j} = \begin{bmatrix} 1 & 1 \\ \frac{1}{\sqrt{2}} & \frac{1}{\sqrt{2}} \\ 1 & 1 \end{bmatrix}. \tag{21}$$

After defining the geometry, the model is globally refined to represent the overall elastic deformation better. In this, the order of the B-splines is increased by two resulting in the order $p = 2+2 = 4$ and $q = 1+2 = 3$. Adding 15 knots in $\xi$- and 24 knots in $\eta$-direction increases the number of elements from one to 400. This refined model serves as a starting point for various benchmark models. It is worth noting, that all tested models have an element edge length of $10\,\mu\mathrm{m}$ in the contact area. The models are reduced with the Craig-Bampton method, using ten normal modes, and the exterior control points in the contact area are used for the constrained modes.

Four locally refined models are compared for the following studies. The number of hierarchy levels $n_\mathrm{lvl}$ is varied between three and six. Each of these four locally refined models has an equivalent globally refined reference model. The equivalence is that the knot vectors of the globally refined models are identical to the knot vectors in the lowest level of the locally refined models. The investigated models are listed in Table 1 and visualized in Fig. 7. The number of interface control points is nearly identical for all models. Accordingly, the number of elastic coordinates $n_\mathrm{q}$ after the model reduction is almost identical regardless of whether the model was globally or locally refined. In addition, it should be emphasized that in this example, the number of degrees of freedom $n_\mathrm{dof}$ decreases as the number of hierarchy levels $n_\mathrm{lvl}$ increases. The dimensions on the left side of the four IGA models in Fig. 7a-7d represent the height of the lowest hierarchy level, which becomes relevant in the further course of the analysis. The model with five hierarchy levels in Fig. 7c represents the most uniform distribution of elements. Since the goal in this application example is to create an element length of $10\,\mu\mathrm{m}$ in the contact area, models with more than six hierarchy levels are not necessary, as shown in Fig. 7d.

The impacts in this work are simulated with a penalty method. As mentioned before, the penalty factor $c_\mathrm{p}$ is increased until the results become independent of the penalty factor. In Fig. 8, the

https://doi.org/10.3311/ECCOMASMBD2021-131

Table 1: Globally and locally refined benchmark models of an axisymmetric sphere.

| **locally refined** | $n_{\mathrm{lvl}} = 3$ | $n_{\mathrm{lvl}} = 4$ | $n_{\mathrm{lvl}} = 5$ | $n_{\mathrm{lvl}} = 6$ |
|---|---|---|---|---|
| degrees of freedom $n_{\mathrm{dofs}}$ | 3856 | 2884 | 2728 | 1708 |
| number of elastic coordinates $n_{\mathrm{q}}$ | 10+82 | 10+80 | 10+84 | 10+82 |
| **globally refined** | | | | |
| degrees of freedom $n_{\mathrm{dofs}}$ | 9216 | 7440 | 6726 | 5368 |
| number of elastic coordinates $n_{\mathrm{q}}$ | 10+82 | 10+80 | 10+80 | 10+78 |

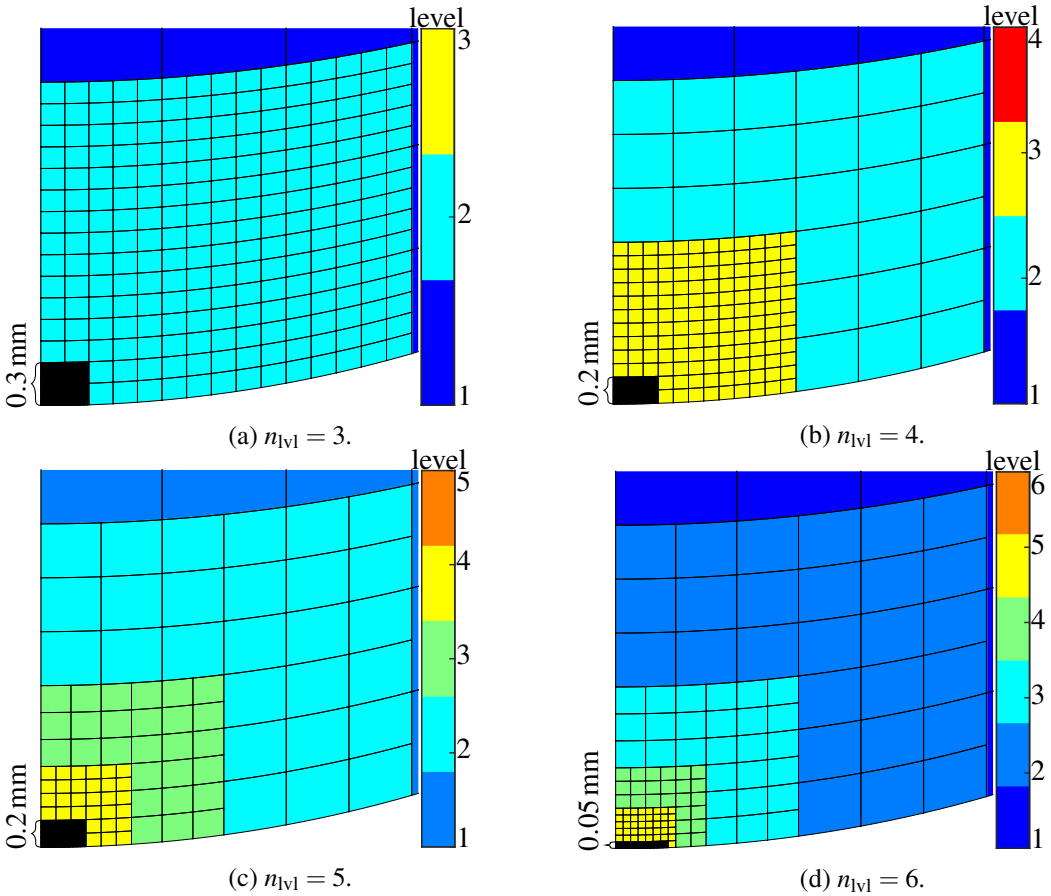


(a) $n_{\mathrm{lvl}} = 3$. (b) $n_{\mathrm{lvl}} = 4$.

(c) $n_{\mathrm{lvl}} = 5$. (d) $n_{\mathrm{lvl}} = 6$.

Figure 7: Detail plot of contact area of the hierarchical models of the axisymmetric sphere.

maximum relative error of the contact force for the analytic solution [17] is visualized. Two observations can be made from Fig. 8. First, it is observed in Fig. 8a that the penalty factor is independent of the number of hierarchy levels. Second, a globally and locally refined model behaves almost identically here, as seen in Fig. 8b. Figure 8 shows that for the penalty factors $c_{\mathrm{p}}$ greater than $5 \times 10^{18}\,\mathrm{N/m}$ the error of the contact force remains constant at approximately $2\,\%$. Therefore, this factor is used for the following simulations. It is noted that the calculation time also increases with increasing penalty factor, since the equations of motion to be solved become stiffer.

Next, the influence of the number of hierarchy levels $n_{\mathrm{lvl}}$ on the computation time of the impact simulation shown in Fig. 9 is discussed. Although the contact search can be parallelized with respect to the evaluation points, sequentially executed simulations are more independent of the architecture of the computer, the MATLAB-MEX implementation of parallel for-loops, the code quality, and the used operating system WINDOWS. Therefore, the sequential computation allows a better relative comparison of the individual models. The processor used is the Intel W-2295 model

https://doi.org/10.3311/ECCOMASMBD2021-131

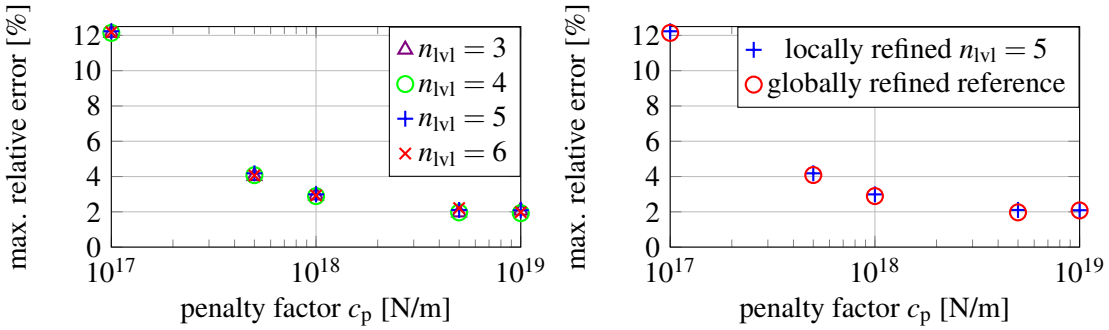


(a) All locally refined models.

(b) Local $n_{lvl} = 5$ model and its global reference.

Figure 8: Contact force error with respect to the analytic solution by Hertz [17].

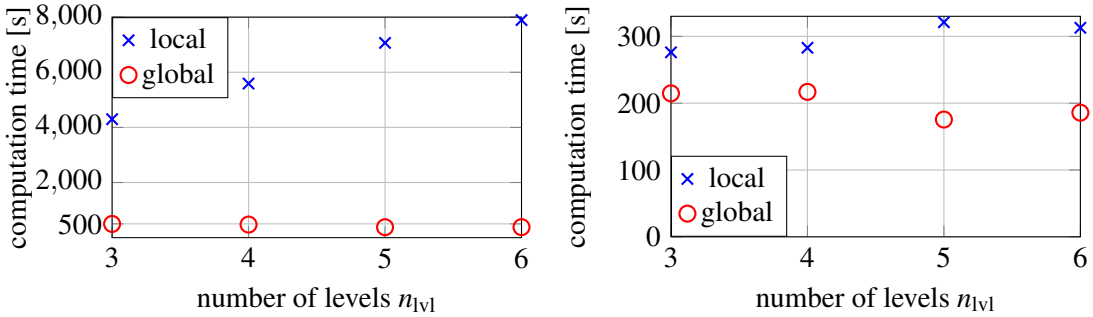


(a) Sequential computing.

(b) Parallelized computing.

Figure 9: Comparison of computation times.

with 18 cores. It should be noted that the following qualitative observations may depend on the particular application example.

Observing the computation time of the sequential simulation in Fig. 9a, it can be seen that the computation time increases, in this case linearly, as the number of hierarchy levels increases. In contrast, the computation time of the globally refined reference models decreases. The latter observation can be attributed to the fact that the number of degrees of freedom $n_{dof}$ decreases, see Table 1. Since the globally refined models have only one level in the parameter space, it is likely that the number of degrees of freedom $n_{dof}$ directly influences the computation time. If the number of degrees of freedom $n_{dof}$ is smaller, the matrix of global shape functions $\boldsymbol{\Phi}$ is also smaller, and the calculation of Eq. (16) and Eq. (20) is faster.

Although, the degrees of freedom of the locally refined models decrease as the number of hierarchy levels increases, the aforementioned effect does not seem to be dominant here. In the literature [5, 6, 7, 8], the degrees of freedom saved by local refinement are listed as an advantage. This advantage does not apply in this work since the models are reduced with the Craig-Bampton method and the reduction of the number of elastic coordinates $n_q$ is almost identical regardless of the type of refinement, see Table 1. In applying the floating frame of reference formulation, the reduced mass and stiffness matrix are used for calculation. The full mass matrix does not have to be inverted in each time step. Only the global shape functions $\boldsymbol{\Phi}$ have to be transposed in Eq. (20) for the contact algorithm, which is much more time-saving than a matrix inversion. Since the number and position of contact evaluation points are also identical for the respective globally and locally refined models, the evaluation of the NURBS in the course of the contact evaluation remains the last possible cause for the difference in computation time. The additional computational effort in computing hierarchical NURBS described in Section 3.3 is responsible for the higher computational time in Fig. 9a.

In the parallel computation in Fig. 9b, the globally refined models are likewise faster. However, the difference between the globally and locally refined models is smaller compared to the sequential computation. In this case, the locally refined models seem to benefit more from the parallel computation than the globally refined models, whereby the MATLAB-MEX implementation could be responsible for this.

In the last analysis of this application example, the von Mises stresses are observed when they are maximum. The time of maximum occurrence of the von Mises stresses is when the contact force is maximum [17]. With the analytical solution by Hertz [17], the von Mises stresses along the symmetry axis of the sphere are displayed in Fig. 10. Initially, it can be observed that all locally

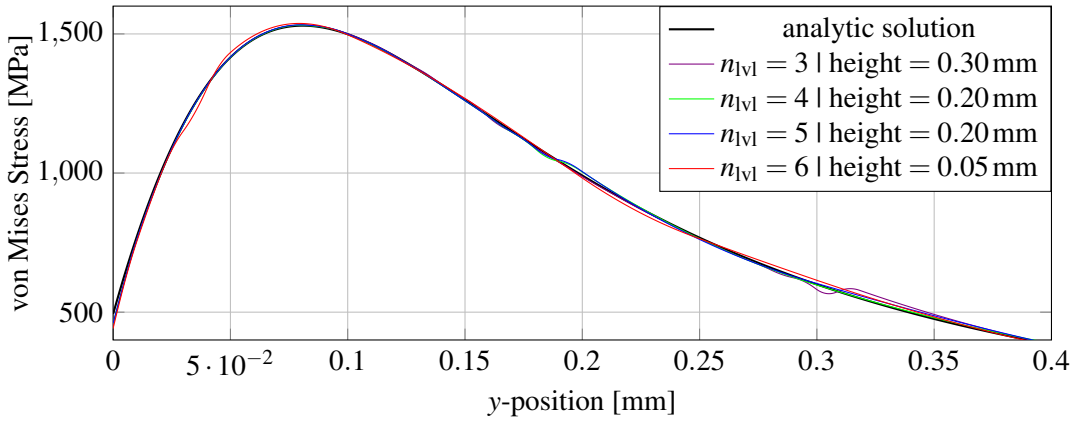


Figure 10: Maximum von Mises stresses along the symmetry axis of the locally refined models.

refined models can represent the stresses well. However, it is noticeable that a small oscillation can be seen at the $y$-position, where a switch of the hierarchy level takes place. The height of the lowest hierarchical level from Fig. 7 can be reflected in the stress analysis in Fig. 10. For comparison, a full hierarchical IGA model is tested. In order to include it in the same framework, the full IGA model is modally transformed using all modes. The oscillations still occur and thus are independent of the model reduction. In the globally refined models, which are not shown here, these small oscillations do not occur.

## 6 CONCLUSIONS

Overall, it can be concluded that it is feasible to obtain global shape functions for flexible multibody systems from hierarchically refined isogeometric finite element models. A model reduction with the Craig-Bampton method can be performed, and the global shape functions of the IGA can be smoothly included in the floating frame of reference formulation. Subsequently, an impact simulation can be performed using the penalty formulation. The penalty factor converges for hierarchically refined models, and the differences in the accuracy between the locally and globally refined models are minor. Since the locally and globally refined models are approximated with the same number of elastic coordinates and the evaluation of hierarchical NURBS in the contact routine is more complex, the overall computation time using the locally refined models is higher than the globally refined models. The computational savings achieved in the literature [5, 6, 7, 8] cannot be achieved with transient contact simulations in flexible multibody systems. However, it remains an open question whether a more efficient hierarchical NURBS algorithm can outperform a globally refined model. Adjustments to the contact algorithm are also feasible, whereby the NURBS basis of the contact body is determined in preprocessing.

## REFERENCES


[1] Schwertassek, R., Wallrapp, O.: Dynamik flexibler Mehrkörpersysteme (in German). Teubner B.G. GmbH (2014)

[2] Bathe, K.J.: Finite Element Procedures. Klaus-Jürgen Bathe, United States Watertown, MA (2014)

[3] Craig, R.R., Bampton, M.C.C.: Coupling of substructures for dynamic analyses. AIAA Journal **6**(7) (jul 1968) 1313–1319

[4] Cottrell, J.A., Hughes, T.J.R., Bazilevs, Y.: Isogeometric Analysis. John Wiley & Sons, Ltd (aug 2009)

[5] Schillinger, D., Dedè, L., Scott, M.A., Evans, J.A., Borden, M.J., Rank, E., Hughes, T.J.: An isogeometric design-through-analysis methodology based on adaptive hierarchical refinement of NURBS, immersed boundary methods, and t-spline CAD surfaces. Computer Methods in Applied Mechanics and Engineering **249-252** (dec 2012) 116–150

[6] D'Angella, D., Kollmannsberger, S., Rank, E., Reali, A.: Multi-level bézier extraction for hierarchical local refinement of isogeometric analysis. Computer Methods in Applied Mechanics and Engineering **328** (jan 2018) 147–174

[7] Noël, L., Schmidt, M., Messe, C., Evans, J., Maute, K.: Adaptive level set topology optimization using hierarchical b-splines. Structural and Multidisciplinary Optimization **62**(4) (jul 2020) 1669–1699

[8] Zimmermann, C., Sauer, R.A.: Adaptive local surface refinement based on LR NURBS and its application to contact. Computational Mechanics **60**(6) (aug 2017) 1011–1031

[9] Held, A., Moghadasi, A., Seifried, R.: DynManto: A matlab toolbox for the simulation and analysis of multibody systems. In: Volume 2: 16th International Conference on Multibody Systems, Nonlinear Dynamics, and Control (MSNDC), American Society of Mechanical Engineers (aug 2020)

[10] Les Piegl, W.T.: The NURBS Book. Springer-Verlag GmbH (1997)

[11] Matzen, M.E.: Isogeometrische Modellierung und Diskretisierung von Kontaktproblemen (in German). PhD thesis, University of Stuttgart, Institute of Structural Mechanics (2015)

[12] Tschigg, S.: Effiziente Kontaktberechnung in Fexiblen Mehrkörpersystemen (in German). PhD thesis, Hamburg University of Technology (2020)

[13] Stelzmann, U., Groth, C., Müller, G.: FEM für Praktiker 2. Strukturdynamik: Basiswissen und Arbeitsbeispiele zu FEM-Anwendungen der Strukturdynamik - Lösungen mit dem FE-Programm ANSYS (in German). Expert-Verlag (2008)

[14] Rückwald, T., Held, A., Seifried, R.: Reduced isogeometric analysis models for impact simulations. In: 17th International Conference on Multibody Systems, Nonlinear Dynamics, and Control. (2021)

[15] Matzen, M., Bischoff, M.: A weighted point-based formulation for isogeometric contact. Computer Methods in Applied Mechanics and Engineering **308** (aug 2016) 73–95

[16] Seifried, R., Hu, B., Eberhard, P.: Numerical and experimental investigation of radial impacts on a half-circular plate. Multibody System Dynamics **9**(3) (2003) 265–281

[17] Johnson, K.L.: Contact Mechanics. Cambridge University Press (2004)

https://doi.org/10.3311/ECCOMASMBD2021-222



# Dynamic Analysis of an Internal Turning Tool with Elastic Foundation (Winkler Model)
# ECCOMAS Thematic Conference on Multibody Dynamics 2021

**Rouben Rostamian [1], Wallyson Thomas [2], Attila Szilagyi [3]**

[1] Department of Mathematics and Statistics
University of Maryland
Baltimore County
Baltimore, MD 21250, USA
rostamian@umbc.edu

[2] Faculty of Mechanical Engineering and Informatics
University of Miskolc
Miskolc, 3515, Hungary
szmwally@uni-miskolc.hu

[3] Faculty of Mechanical Engineering and Informatics
University of Miskolc
Miskolc, 3515, Hungary
szilagyi.attila@uni-miskolc.hu

**ABSTRACT**

This paper focuses on the clamping properties influence on the dynamic properties of clamped boring bars. The boring bar is modeled as a cantilever Euler–Bernoulli beam and a three span configuration in a Winkler foundation, in this way, this theory is applied to derive the transcendental equation for a general case applicable to the system with span beam at an arbitrary location. Eigenvalue plots of the first three modes are presented along with their respective mode shapes. The corresponding natural frequency equations are given and obtained by numerical calculation. The theoretical calculations are validated and discussed. These results confirm that within reason, the theory matches the literature and have relatively approach with the experimental values.

**Keywords:** boring bar, Euler–Bernoulli beam, Winkler foundation, Eigenvalue, natural frequency.

## 1. INTRODUCTION

Consider the transverse displacements *y(x, t)* at time *t* of a beam of length *L* aligned with the interval $0 < x < L$ in the Cartesian *xy* plane. There are several mathematical models of varying complexities that describe the motion *y(x, t)*, the simplest of which is due to Euler and is known as *the Euler beam model*:

$$EI\frac{\partial^4 y}{\partial x^4} + \rho A\frac{\partial^2 y}{\partial t^2} = f(x,t) \tag{1}$$

Here, *A* is the beam's cross-sectional area, *I* is the cross-sectional moment of inertia, $\rho$ is the density (i.e., mass per unit volume of the beam), *E* is the material's Young's modulus, and *f(x, t)* is the load per unit length applied to the beam.

Each of the derivatives $\partial^n y/\partial^n x$, n = 1; 2; 3, has a physical interpretation and significance:

$\partial y/\partial x$ is the beam's slope,

EI $\partial^2 y/\partial^2 x$ is the bending moment at the cross-section *x*,

EI $\partial^3 y/\partial^3 x$ is the vertical shear force at the cross-section *x*,

https://doi.org/10.3311/ECCOMASMBD2021-222

as illustrated in Fig. 1. Boundary conditions associated with the PDE (1) are determined by translating the physics of the setting through these observations; see Fig. 2.

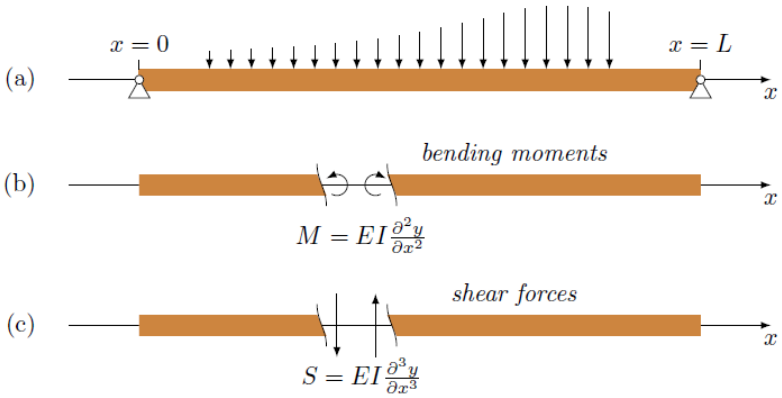


**Figure 1.** (a) A beam with pinned supports at the ends and a distributed load applied to a part of it. The bending of the beam results in an internal moment M (Figure (b)) and a transverse shear S at each cross section (Figure (c)).

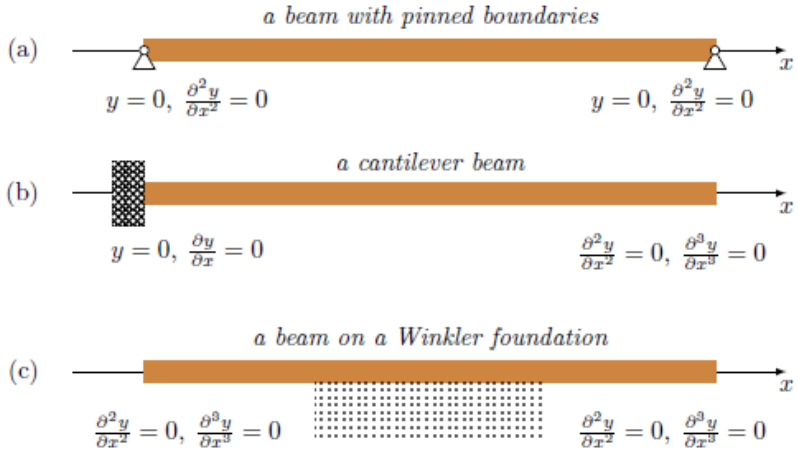


**Figure 2.** The diagrams show the boundary conditions associated with (a) a beam with pinned supports at the ends; (b) a cantilever beam; (c) a beam partially supported on a Winkler foundation and free otherwise.

## 2. WINKLER FOUNDATION

The earliest formulation of the foundation model was due to Winkler, who assumed the foundation model to consist of closely spaced independent linear springs, as shown in Fig.3. If such a foundation is subjected to a partially distributed surface loading, $q$, the springs will not be affected beyond the loaded region. For such a situation, an actual foundation is observed to have the surface deformation as shown in Fig. 4. Hence by comparing the behavior of theoretical model and actual foundation, it can be seen that this model essentially suffers from a complete lack of continuity in the supporting medium. The load deflection equation for this case can be written as

$$q = kw \tag{2}$$

where $k$ is the spring constant and is often referred to as the foundation modulus, and $w$ is the vertical deflection of the contact surface. It can be observed that Equation 2 is exactly satisfied by an elastic plate floating on the surface of a liquid and carrying some load which causes it to deflect. The pressure distribution under such a plate will be equivalent to the force of buoyancy, $k$ being the specific weight of the liquid. With this analogy in view, the first solution for the bending of plates on a Winkler-type foundation was presented by Hertz (1884).

https://doi.org/10.3311/ECCOMASMBD2021-222

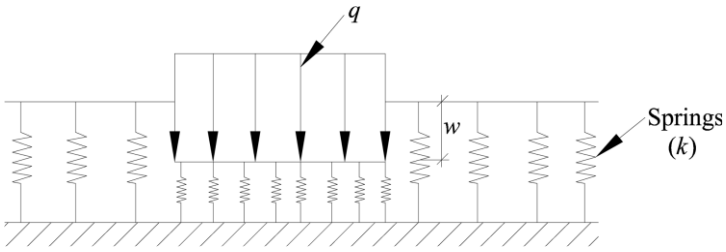


**Figure 3.** Load on Winkler's foundation

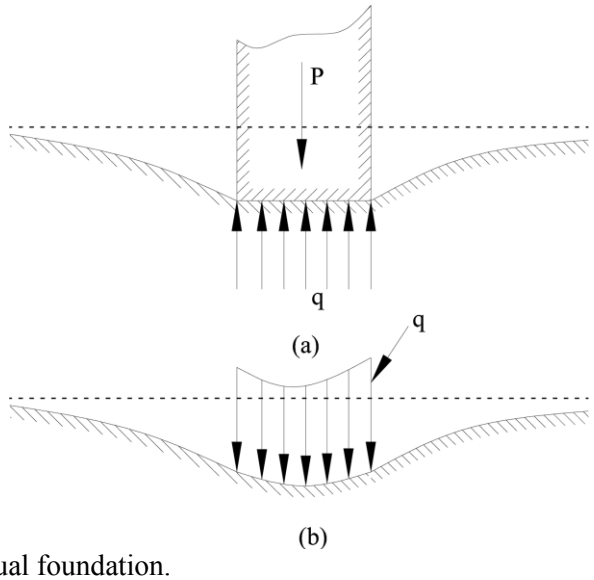


**Figure 4.** Deformation of actual foundation.

A Winkler foundation is a distributed springy support, similar to a mattress, that restrains the beam's motion. The Winkler foundation may extend to the entire beam, from end to end, or be limited to a subset of the beam as in Fig. 2(c). We write *K(x)* for stiffness of the foundation, allowing for the stiffness to vary with *x*. The force exerted by the foundation per unit length of the beam is *-K(x) y(x, t)*, where *y(x, t)* is the beam's transverse displacement. This leads to the modified form of Euler's equation.

$$EI\frac{\partial^4 y}{\partial x^4}+\rho A\frac{\partial^2 y}{\partial t^2}=f(x,t)-K(x)y \tag{3}$$

In the study of a beam's natural frequencies of vibration which is our concern in these notes, the applied load is immaterial. Therefore we let *f(x, t) = 0* from this point onward and focus on the equation:

$$EI\frac{\partial^4 y}{\partial x^4}+\rho A\frac{\partial^2 y}{\partial t^2}+K(x)y=0 \tag{4}$$

## 3. NATURAL FREQUENCY OF VIBRATIONS

We wish to investigate the natural frequencies of vibrations of an Euler beam of length L supported on a Winkler foundation. We reduce the equation of motion to a nondimensional form by introducing $\xi = x/L$ as the dimensionless length variable, and write $Y(\xi, t) = y(x, t)$. Then the equation of motion (3) changes to

$$\rho A\frac{\partial^2 Y}{\partial t^2}+\frac{EI}{L^4}\frac{\partial^4 Y}{\partial \xi^4}+K(\xi L)=0,\qquad 0<\xi<1,\qquad t>0. \tag{5}$$

We seek harmonic oscillations of the form $Y(\xi, t) = e^{i\Omega t}u(\xi)$, where *i* is the unit imaginary number and the angular frequency is to be determined. We substitute this form into Equation (4) and simplify to arrive at

$$u''''(\xi)-\frac{\rho AL^4}{EI}\Omega^2 u(\xi)+\frac{K(\xi L)L^4}{EI}u(\xi)=0,\qquad 0<\xi<1. \tag{6}$$

https://doi.org/10.3311/ECCOMASMBD2021-222

This leads to the introduction of the dimensionless frequency $\omega$ and dimensionless stiffness $\kappa$ through

$$\omega^2 = \frac{\rho A L^4}{EI}\Omega^2, \qquad \kappa(\xi) = \frac{K(\xi L)L^4}{EI}, \tag{7}$$

Where upon Equation (4) takes the form

$$u''''(\xi) - \omega^2 u(\xi) + \kappa(\xi)u(\xi) = 0, \qquad 0 < \xi < 1. \tag{8}$$

## 4. A CANTILEVER BEAM

As an exercise, and also to motivate the next section's calculations, let us determine the natural frequencies of vibrations of a cantilever beam in the absence of a Winkler foundation, that is, $\kappa(\xi) = 0$ in Equation (8). Thus, referring to Fig. 2(b), we are faced with the boundary value problem

$$u''''(\xi) - \omega^2 u(\xi) = 0, \qquad 0 < \xi < 1, \tag{9}$$

$$u(0) = 0, \qquad u'(0) = 0, \qquad u''(1) = 0, \qquad u'''(1) = 0. \tag{10}$$

The characteristic equation of the differential Equation (9) is $r^4 - \omega^2 = 0$. Therefore $r^2 = \pm\omega$ (we assume $\omega > 0$ without a loss of generality) and conclude that the characteristic roots are $r = \pm\omega^{1/2}$ and $r = \pm i\omega^{1/2}$, or, letting $\lambda = \omega^{1/2}$ to simplify the notation, $r = \pm\lambda$, and $r = \pm i\lambda$. We conclude that the general solution of the differential equation is

$$u(\xi) = c_1 \cos\lambda\xi + c_2 \sin\lambda\xi + c_3 \cosh\lambda\xi + c_4 \sinh\lambda\xi \tag{11}$$

Applying the boundary conditions leads to the equations

$$\begin{aligned} c_1 + c_3 &= 0 \\ c_2 + c_4 &= 0 \\ -c_1\cos\lambda - c_2\sin\lambda + c_3\cosh\lambda + c_4\sinh\lambda &= 0 \\ c_1\sin\lambda - c_2\cos\lambda + c_3\sinh\lambda + c_4\cosh\lambda &= 0 \end{aligned} \tag{12}$$

which we express in the matrix form as

$$\begin{bmatrix} 1 & 0 & 1 & 0 \\ 0 & 1 & 0 & 1 \\ -\cos\lambda & -\sin\lambda & \cosh\lambda & \sinh\lambda \\ \sin\lambda & -\cos\lambda & \sinh\lambda & \cosh\lambda \end{bmatrix} \begin{bmatrix} c_1 \\ c_2 \\ c_3 \\ c_4 \end{bmatrix} = \begin{bmatrix} 0 \\ 0 \\ 0 \\ 0 \end{bmatrix} \tag{13}$$

Let us write $M(\lambda)$ for the 4x4 coefficient matrix in (13). This system of four linear homogeneous equation in the four unknowns $c_1$, $c_2$, $c_3$, $c_4$ will have a nontrivial

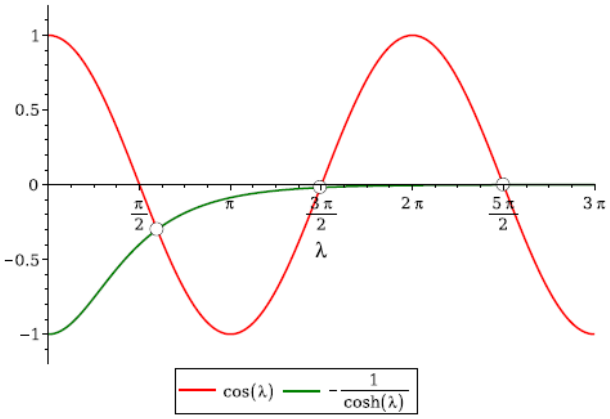


**Figure 5.** The circles mark the first three roots of the Equation (14). Except for the first, the roots

essentially agree with those of the cosine function.

solution provided that *det M(λ) = 0*. Expanding and simplifying the determinant, leads to the equation

$$\cos(\lambda) = -\frac{1}{\cosh(\lambda)} \tag{14}$$

whose roots are depicted graphically in Fig. 5. The first three roots are

$$\lambda_1 \approx 1.875104068 \qquad \lambda_2 \approx 4.694091132 \qquad \lambda_3 \approx 7.854757438 \tag{15}$$

Corresponding to each root $\lambda_i$, i = 1, 2, …, the system (13) has a nontrivial solution lying within the one-dimensional null space of $M(\lambda_i)$. A numerically robust way of calculating the basis vector of that one-dimensional null space is through the singular value decomposition of $M(\lambda_i)$, that is,

$$M(\lambda_i) = USV^T \tag{16}$$

where $U$ and $V$ are orthogonal matrices, and $S$ is the diagonal matrix of $M(\lambda_i)$'s singular values. See, for instance [3, 4, 5, 6]. It turns out, see, e.g., Theorem 5.2 in [5], that the rightmost column of the matrix $V$ is the basis of the null space. Thus, we calculate the null spaces of $M(\lambda)$ corresponding to the first three roots $\lambda_i$ and obtain

$$\begin{bmatrix} c_1 \\ c_2 \\ c_3 \\ c_4 \end{bmatrix}_1 = \begin{bmatrix} -0.5000 \\ 0.3670 \\ 0.5000 \\ -0.3670 \end{bmatrix} \quad \begin{bmatrix} c_1 \\ c_2 \\ c_3 \\ c_4 \end{bmatrix}_2 = \begin{bmatrix} 0.5000 \\ -0.5092 \\ -0.5000 \\ 0.5092 \end{bmatrix} \quad \begin{bmatrix} c_1 \\ c_2 \\ c_3 \\ c_4 \end{bmatrix}_3 = \begin{bmatrix} -0.5000 \\ 0.4996 \\ 0.5000 \\ -0.4996 \end{bmatrix} \tag{17}$$

and therefore, according to (11), the mode shapes are

$$\begin{aligned} u_1(\xi) &= -0.5\cos\lambda_i\xi + 0.3670\sin\lambda_i\xi + 0.5\cosh\lambda_i\xi - 0.3670\sinh\lambda_i\xi, && (\lambda_1 = 1.8751) \\ u_1(\xi) &= -0.5\cos\lambda_i\xi - 0.5092\sin\lambda_i\xi - 0.5\cosh\lambda_i\xi + 0.5092\sinh\lambda_i\xi, && (\lambda_2 = 4.6941) \\ u_1(\xi) &= -0.5\cos\lambda_i\xi + 0.4996\sin\lambda_i\xi + 0.5\cosh\lambda_i\xi - 0.4996\sinh\lambda_i\xi, && (\lambda_3 = 7.8548) \end{aligned} \tag{18}$$

We have normalized the modes so that $u_i(1) = 1$ for each mode. That $c_1$ and $c_3$ are ±1/2 is not a coincidence. It can be shown that $c_1$ and $c_3$ are ±1/2 for all normalized modes for all frequencies. The mode shapes are shown in Fig. 6.

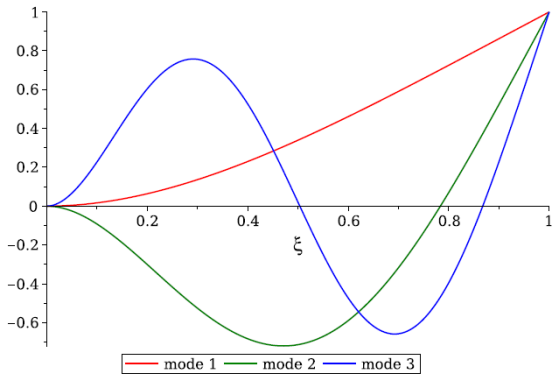


**Figure 6.** The first three mode shapes of the natural vibrations of a cantilever beam.

## 5. A NUMERICAL EXAMPLE – CANTILEVER BEAM

For this illustration, we consider a cantilever beam with parameter values taken from [1] which is somewhat extended pre-print manuscript corresponding to the published article [2]. (Some of the parameter values have been omitted in the latter.) Specifically, from page 13 of [1] we have

$$\begin{aligned} A &= 1.1933\times10^{-3}\,m^2, & I &= 1.138\times10^{-7}\,m^4, \\ \rho &= 7850\,kg/m^3 & E &= 205\times10^9\,N/m^2 \end{aligned} \tag{19}$$

https://doi.org/10.3311/ECCOMASMBD2021-222

and from Section 3.2.1 of [1] we have $L = 0.200m$

Let us calculate beam's three lowest natural frequencies. From Equation (14) and referring to Fig. 5, the three smallest roots are

$$\lambda_1 \approx 1.875104068 \qquad \lambda_2 \approx 4.694091132 \qquad \lambda_3 \approx 7.854757438 \tag{20}$$

and therefore

$$\omega_1 = \lambda_1^2 = 3.516015266 \qquad \omega_2 = \lambda_2^2 = 22.03449156 \qquad \omega_3 = \lambda_3^2 = 61.69721441 \tag{21}$$

From (5) we have

$$\Omega = \sqrt{\frac{EI}{\rho A L^4}}\omega \tag{22}$$

Plugging in the data into the above, we conclude that circular frequencies are

$$\Omega_1 = 4386.611508 s^{-1} \qquad \Omega_2 = 27490.42508 s^{-1} \qquad \Omega_1 = 76973.98625 s^{-1} \tag{23}$$

Then we calculate the (ordinary) frequency (oscillations per second) from $f = \Omega/(2\pi)$:

$$f_1 = 698.1509048 \text{ Hz} \qquad f_2 = 4375.237039 \text{ Hz} \qquad f_2 = 12250.79040 \text{ Hz} \tag{24}$$

which agree with the data given in Table 3.11 of [1] (and Table 5 of [2]), as expected.

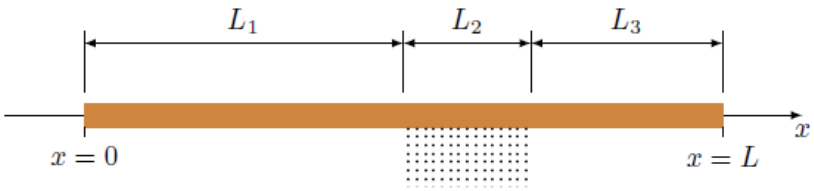


**Figure 7.** A beam of length L partially supported on a Winkler foundation. The resulting three spans are of lengths $L_1$, $L_2$, and $L_3$, from left to right. We let $\alpha = L1/L$, $\beta = (L1 + L2)/L$.

## 6. A NUMERICAL EXAMPLE – 3 SPAN BEAM

Fig. 7 depicts a beam of length L supported on a Winkler foundation for a part of its length. We write $L_1$, $L_2$, and $L_3$ for the lengths of the beam's three segments. As in the previous sections, we introduce the nondimensional length variable $\xi = x/L$, and write $\alpha = L_1/L$ and $\beta = (L1+L2)/L$ for the (nondimensional) coordinates of the interfaces of the three segments.

We assume that foundation's nondimensional stiffness (see (7)) is a constant $k$ on the supported part, that is, the coefficient $\kappa(\xi)$ of Equation (8) is of the form

$$\kappa(\xi) = \begin{cases} k & \text{if} \quad \alpha < \xi < \beta \\ 0 & \text{otherwise} \end{cases} \tag{25}$$

Consequently, we express the deflection, $u(\xi)$, as a piecewise defined function

$$u(\xi) = \begin{cases} u_1(\xi) & \text{if} \quad 0 < \xi < \alpha \\ u_2(\xi) & \text{if} \quad \alpha < \xi < \beta \\ u_3(\xi) & \text{if} \quad \beta < \xi < 1 \end{cases} \tag{26}$$

The functions $u_1$, $u_2$, and $u_3$ are solutions of the equations

$$\begin{cases} u_1''''(\xi) - \omega^2 u_1(\xi) = 0 & \text{if} \quad 0 < \xi < \alpha \\ u_2''''(\xi) - (\omega^2 - k) u_2(\xi) = 0 & \text{if} \quad \alpha < \xi < \beta \\ u_3''''(\xi) - \omega^2 u_3(\xi) = 0 & \text{if} \quad \beta < \xi < 1 \end{cases} \tag{27}$$

The general solution of each of these fourth order equations comes with four undefined coefficients. Therefore, the solution of the overall system involves 12 unknown coefficients. The

physics of the problem supplies 12 boundary and continuity conditions which may be applied to determine the 12 unknowns. Those conditions are

$$u_1''(0) = 0, \quad u_1'''(0) = 0, \tag{28}$$

$$u_1(\alpha) = u_2(\alpha), \quad u_1'(\alpha) = u_2'(\alpha), \quad u_1''(\alpha) = u_2''(\alpha), \quad u_1'''(\alpha) = u_2'''(\alpha), \tag{29}$$

$$u_1(\beta) = u_2(\beta), \quad u_1'(\beta) = u_2'(\beta), \quad u_1''(\beta) = u_2''(\beta), \quad u_1'''(\beta) = u_2'''(\beta), \tag{30}$$

$$u_1''(1) = 0, \quad u_1'''(1) = 0, \tag{31}$$

The boundary conditions (28) set the moment and shear at the endpoint $\xi = 0$ to zero, implying that end moves freely. The boundary conditions (31) do the same for the endpoint $\xi = 1$. The boundary conditions (30) indicate that the displacement, slope, moment, and shear are continuous at $\xi = \alpha$, and thus, the interface at $\xi = \alpha$ moves free of constraints. The boundary conditions (30) assert the same thing about the interface at $\xi = \beta$.

Equations $(27)_1$ and $(27)_3$ are the same as (9), and therefore their solutions are as given in (11), that is

$$u_1(\xi) = A_1\cos(\sqrt{\omega}\xi) + A_2\sin(\sqrt{\omega}\xi) + A_3\cosh(\sqrt{\omega}\xi) + A_4\sinh(\sqrt{\omega}\xi) \tag{32}$$

$$u_3(\xi) = C_1\cos(\sqrt{\omega}\xi) + C_2\sin(\sqrt{\omega}\xi) + C_3\cosh(\sqrt{\omega}\xi) + C_4\sinh(\sqrt{\omega}\xi) \tag{33}$$

Solving $(27)_2$ requires more e ort since the expression for the general solution depends on the sign of $\omega^2$-k. For that reason, the analysis branches out into three cases.

Case 1: $\omega^2 > k$. In this case, equation $(27)_2$ is qualitatively the same as the two other equations in (27). It is a matter of replacing $\omega^2$ by $\omega^2$-k. Therefore, we obtain

$$u_2(\xi) = B_1\cos(\sqrt[4]{\omega^2 - k}\xi) + B_2\sin(\sqrt[4]{\omega^2 - k}\xi) + B_3\cosh(\sqrt[4]{\omega^2 - k}\xi) + B_4\sinh(\sqrt{\omega}\xi), \quad \text{(assuming } \omega^2 > k\text{)} \tag{34}$$

We apply the 12 boundary conditions (28) to (31) to the solution fragments (32), (33), and (34) and obtain a homogeneous linear system of 12 equations in the 12 unknowns $A_1$, $A_2$, $A_3$, $A_4$, $B_1$, $B_2$, $B_3$, $B_4$, $C_1$, $C_2$, $C_3$, $C_4$. The system will have a nontrivial solution provided that the determinant of its 12x12 coefficient matrix is zero. The symbolic calculation of that determinant is quite a demanding task. We computed that in Maple but we do not show the result here since it will fill several printed pages. What needs to be noted here is that the determinant involves the non-dimensionalized frequency ω and stiffness k. By setting the determinant to zero, we may solve for the natural frequencies ω for any given k.

Having calculated the natural frequencies, the modal shapes are determined as in the case of the cantilever beam in Section 5 by applying the singular value decomposition to the system's 12 x 12 coefficient matrix.

Case 2: $\omega^2 = k$. In this case, equation $(27)_2$ reduces to $u''''(\xi) = 0$ which has a cubic polynomial as its general solution:

$$u_2(\xi) = B_1 + B_2\xi + B_3\xi^3 + B_4\xi^4 \tag{35}$$

We apply the boundary and interface conditions (13) and obtain a homogeneous linear system of 12 equations in 12 unknowns $A_1$, $A_2$, $A_3$, $A_4$, $B_1$, $B_2$, $B_3$, $B_4$, $C_1$, $C_2$, $C_3$, $C_4$. We set the determinant of the coefficient matrix to zero in order to obtain nontrivial solutions. The determinant involves the foundation stiffness k. Therefore, Case 2 occurs only for special choices of the foundation stiffness. The special values of k and the corresponding mode shapes may be obtained by a calculation similar to that of Case 1.

Case 3: $\omega^2 < k$. Recall that equation $(27)_2$ reads

$$u_2''''(\xi) - (\omega^2 - k)u_2(\xi) = 0 \tag{36}$$

https://doi.org/10.3311/ECCOMASMBD2021-222

Since $\omega^2 < k$, we rewrite it as

$$u_2''''(\xi) + \left(k - \omega^2\right) u_2(\xi) = 0 \tag{37}$$

The sign change of the parenthesized coefficient has a profound effect on the form of the equation's general solution. Let us write $\lambda^4 = k\text{-}\omega^2$. The equation reads $u_2'''' + \lambda^4 u_2 = 0$. The characteristic equation is $r^4 + \lambda^4 = 0$, which has roots $\lambda = [1/(2)^{1/2}](\pm 1 \pm i)$. It follows that the differential equation's general solution is

$$\begin{aligned} u_2(\xi) = {} & B_1 \cosh\frac{\lambda}{\sqrt{2}}\xi \cos\frac{\lambda}{\sqrt{2}}\xi + B_2 \sinh\frac{\lambda}{\sqrt{2}}\xi \cos\frac{\lambda}{\sqrt{2}}\xi + \\ & B_3 \cosh\frac{\lambda}{\sqrt{2}}\xi \sin\frac{\lambda}{\sqrt{2}}\xi + B_4 \sinh\frac{\lambda}{\sqrt{2}}\xi \sin\frac{\lambda}{\sqrt{2}}\xi \end{aligned} \tag{38}$$

where $\lambda = (k\text{-}\omega^2)^{1/4}$. The calculation of the eigenfrequencies $\omega$ proceeds as in in previous cases.

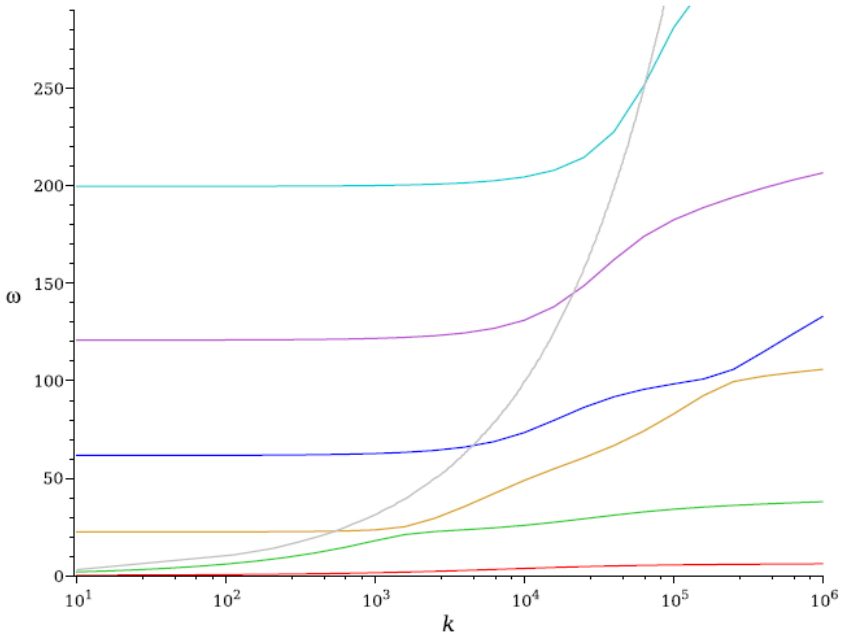


**Figure 8.** The frequencies $\omega$ plotted against the foundation stiffness k for the Winkler-supported beam of Figure 7. The gray curve is the graph of $\omega^2 = k$ that separates the three cases considered in Section 6.

## 7. NUMERICAL CALCULATIONS OF A THREE-SPAN WINKLER-SUPPORTED BEAM

We apply an appropriately modified version of Section 5's numerical data to the Winkler-supported beam. Following [1] and [2], we take

$$\begin{aligned} & L_1 = 0.215m, \quad L_2 = 0.050m, \quad L_3 = 0.035m \\ & A = 1.1933\times10^{-3} m^2, \quad I = 1.138\times10^{-7} m^4, \\ & \rho = 7850 kg/m^3, \quad E = 205\times10^9 N/m^2, \end{aligned} \tag{39}$$

whence $L = L1 + L2 + L3 = 0.300\ m$, and $\alpha = 215/300$, $\beta = 265/300$. We allow for a wide range of the (non-dimensionalized) foundation stiffness by letting $k$ range from $10^1$ to $10^6$. For $k$ in that range we calculate the beam's natural frequencies $\omega$. Fig. 8 shows the results for the first six vibration modes.

The calculation that produces that diagram is quite nontrivial due to the fact that the determinant of the coefficient matrix is not only an exceedingly large transcendental expression, but that is oscillates wildly as a function of k, taking values in the range $10^{-80}$ to $10^{-80}$. As a result, calculating

https://doi.org/10.3311/ECCOMASMBD2021-222

the roots of the determinant is not feasible in the usual *hardware floating point arithmetic* of a typical computer which handles roughly 16 to 17 significant digits. Attempting to calculate the roots in hardware floating point either produces no result (no convergence) or produces junk. We performed the calculations in Maple's software floating point arithmetic with 70 significant digits and verified that a further increase of the number of significant digits does not affect the results in an appreciable way.

The specific beam analyzed in [1, 2] is just like the beam considered above, but instead of a Winkler foundation, the beam is held in place with three pairs of torqued screws. The screws are elastic and therefore allow for some transverse displacement of the beam, somewhat similar to our Winkler foundation. The spring constants kT of the screws are given in Table 2.6 of [1] (Table 3 of [2]) as kT =4.881 x $10^9$ N/m and kT = 7.732 x $10^9$ N/m, depending on the type of the screw. For the present calculations, we take an intermediate value of kT = 6 x $10^9$ N/m. There are three pairs of such retaining screws acting along the length $L_2 = 0.050\ m$. If we distribute the force exerted by the screws uniformly along the length $L_2$, we obtain the Winkler foundation's stiffness as

$$K = \frac{3\times\left(6\times10^{9}\right)}{0.05} = 3.6\times10^{11}\,N/m^2 = 3.6\times10^{11}\,Pa \tag{40}$$

and then, according to (5), the dimensionless stiffness is

$$\kappa = \frac{KL^4}{EI} = \frac{(3.6\times10^{11})\times0.3^4}{(205\times10^{9})\times(1.138\times10^{-7})} = 124994.64 \approx 1.25\times10^{5} \tag{41}$$

The non-dimensional natural frequencies ω of such a beam may be read off of the graphs in Fig. 8, or for greater accuracy, calculated directly. We find the first three frequencies to be

$$\omega_1 = 5.569355, \quad \omega_2 = 34.655339, \quad \omega_3 = 87.598947, \tag{42}$$

and then calculate the actual circular frequencies from (11) as:

$$\Omega_1 = 3088.167304\mathrm{s}^{-1}, \quad \Omega_2 = 19216.13583\mathrm{s}^{-1}, \quad \Omega_3 = 48572.98441\mathrm{s}^{-1}, \tag{43}$$

Finally, we calculate the (ordinary) frequency (oscillations per second) from f = Ω/2π:

$$f_1 = 491.497, \quad f_2 = 3058.343, \quad f_3 = 7730.630, \tag{44}$$

These frequencies are somewhat lower than those presented in Table 3.13 of [1] (Table 5 of [2]), which is expected, since a Winkler foundation allows greater flexibility compared to clamping screws.

Fig. 7 depicts the mode shapes corresponding to these frequencies.

## 8. CONCLUSION

It was possible to model a fixation of the tooling system by applying Euler Bernoulli beam model with Winkler Foundation. Furthermore, costly and time-consuming experiments could be replaced by even analytical modelling with manual calculations, which enables us to judge the influence of the geometrical dimensions, the material properties, the possible overhangs and the fixation dimensions of the tool-holder system.

## ACKNOWLEDGMENTS

This research was supported by the European Union and the Hungarian State, co-financed by the European Regional Development Fund in the framework of the GINOP-2.3.4-15-2016-00004 project, aimed to promote the cooperation between the higher education and the industry.

## REFERENCES

[1] Henrik _Akesson, Tatiana Smirnova, and Lars H_akansson. Analysis of dynamic properties of boring bars concerning different clamping conditions. Preprint manuscript, 2007.

[2] Henrik Akesson, Tatiana Smirnova, and Lars Hakansson. Analysis of dynamic properties of boring bars concerning di erent clamping conditions. Mechanical Systems and Signal Process-ing, 23:2629{2647, 2009.

[3] Kendall E. Atkinson. An Introduction to Numerical Analysis. Wiley, New York, 2 edition, 1989.

[4] David Kincaid and Ward Cheney. Numerical Analysis: Mathematics of Scienti_c Computing. American Mathematical Society, Providence, RI, 3 edition, 2002.

[5] Carl Meyer. Matrix analysis and applied linear algebra. Society for Industrial and Applied Mathematics (SIAM), Philadelphia, PA, 2000.

[6] Lloyd N. Trefethen and David Bau, III. Numerical linear algebra. Society for Industrial and Applied Mathematics (SIAM), Philadelphia, 1997.

https://doi.org/10.3311/ECCOMASMBD2021-181



# Non-Linear Beam Formulation with NURBS Interpolation for the Simulation of Sliding Contacts

**Paul Wasmer, Peter Betsch**

Institute of Mechanics
Karlsruhe Institute of Technology (KIT)
Otto-Ammann-Platz 9, 76131 Karlsruhe, Germany
paul.wasmer@kit.edu, peter.betsch@kit.edu

## ABSTRACT

The simulation of beams with sliding joints is of interest for many different applications such as aerial runways or pantograph-catenary systems. However, classical discretization with Lagrangian finite elements cannot represent the geometry smoothly over element boundaries, which leads to impacts at element boundaries. Therefore, the isogeometric framework is applied to a director based formulation of the geometrically exact beam formulation using non-rational B-Splines (NURBS) for the discretization as NURBS can be used to represent many geometries smoothly and exactly. An energy-momentum scheme is used for the time integration to obtain a stable algorithm. Two methods are proposed to realize the sliding contact condition: a classical approach using Lagrange multipliers and an approach based on the master-slave concept applied in the framework of the discrete null space method.

**Keywords:** geometrically exact beams, sliding contact, null space method, energy-momentum schemes

## 1 Introduction

The simulation of sliding contacts of two (or more) slender structures is of interest for many different applications such as aerial runways or pantograph-catenary systems. Slender structures can be simulated very efficiently using beam models. One of the most important beam models in the non-linear analysis is the geometrically exact beam formulation (or Reissner-Simo beam theory) [1, 2, 3]. The geometrically exact beam formulation allows arbitrarily large deformations with finite strains, while the cross-section of the beam remains planar. The orientation of the beam's cross-section is often described using rotational variables. However, without additional effort, the discretization of the rotations with finite elements is not frame-indifferent [4]. Thus, we use a formulation based on directors, three orthonormal vectors, which describe the orientation of the beam's cross-section [5, 6, 7, 8].

Hamiltonian mechanical systems, such as beams, are based on the balance laws for linear and angular momentum as well as the balance of energy in case of conservative loadings. However, these conservation properties might not carry over to the discretized time domain. Especially, in the case of nonlinear configuration manifolds, this might lead to physical impossible solutions or numerical instabilities [9]. A remedy for this problem is the use of conserving integrators, which preserve some of the structure of the continuous problem. A general approach on how to construct such energy-momentum conserving integrators was shown by Gonzalez [9]. The conserving time integration scheme, which preserves momentum and energy, for elastodynamics was first proposed in [10]. In [11] Simo *et. al* showed the advantage of the energy-momentum scheme over the conventional midpoint and trapezoidal rule when used for the geometrically exact beam. Therefore, the energy-momentum scheme is applied to simulate the dynamic behavior of the beam.

For the simulation of a sliding contact, it is essential to represent the geometry without any non-physical kinks, which may arise due to the discretization. Otherwise, this leads to impacts at the

https://doi.org/10.3311/ECCOMASMBD2021-181

kinks, which are not present in the continuous problem. A smooth representation of the geometry is not possible if the classical isoparametric finite element method (FEM) in combination with Lagrangian shape functions is used, as here no smooth representation over element boundaries is possible. The isogeometric analysis (IGA) [12] can present a remedy for this problem. The IGA can be used for an exact, smooth representation of the whole geometry. In the IGA framework the functions, which are used to exactly display the geometry in computer graphics, are also used as basis functions for the FEM discretization. Often non-uniform rational B-Splines (NURBS) are applied for this purpose. NURBS are $C^{p-1}$ continues over element boundaries, where $p$ is the polynomial order of the shape functions.

It is the goal of the present work to achieve a contact algorithm, which adopts the conserving property of the energy-momentum scheme. For this purpose, two methods to enforce the contact condition are investigated: First, the more classical approach using Lagrange multipliers is stated. The second approach relies on the master-slave concept [13, 14, 15, 16] which is applied within the discrete null space method [17, 18, 19].

An outline of the rest of the paper is as follows. In Section 2 we give a very short summary on the used NURBS basis functions. It follows a detailed description of the geometrically beam formulation relying on directors in Section 3, along with an outline of the applied energy-momentum scheme. The sliding contact condition is addressed in Section 4. Eventually, some conclusions are drawn in Section 5.

## 2 Isogeometric Analysis

First introduced by Hughes *et al.* [20] in 2005, the IGA using NURBS was applied to a variety of problems since then and has become it's own field of research. The origin of NURBS basis functions lies in computer graphics. A comprehensive introduction to the topic of NURBS can be found in [21]. A NURBS curve is built from B-Splines. Each B-Spline function is defined through a knot vector

$$\Xi_p = [\underbrace{0,\dots 0}_{p+1}, \underbrace{\xi_{p+2},\dots,\xi_{n_{\text{ele}}+p+1}}_{n_{\text{ele}}-1}, \underbrace{1,\dots 1}_{p+1}] \tag{1}$$

where the index $p$ denotes the polynomial degree of the shape function and $n_{\text{ele}}$ the number of curve segments, which is equivalent to the number of elements in a FEM sense. Eq. (1) defines an open knot vector, which is classically used in IGA. An open knot vector defines functions, where the basis functions are interpolatory at the beginning ($\xi = 0$) and the end ($\xi = 1$). Using the knot vector a B-Spline basis can be computed with the help of the Cox-de-Boor recursive algorithm [21, 12]

$$\begin{aligned} N_{i,0}(\xi) &= \begin{cases} 1 & \text{if } \xi_i \leq \xi < \xi_{i+1} \\ 0 & \text{otherwise} \end{cases} \\ N_{i,p}(\xi) &= \frac{\xi - \xi_i}{\xi_{i+p} - \xi_i} N_{i,p-1}(\xi) + \frac{\xi_{i+p+1} - \xi}{\xi_{i+p+1} - \xi_{i+1}} N_{i+1,p-1}(\xi) \end{aligned} \tag{2}$$

where division by zero is defined as zero ($\frac{(\bullet)}{0} := 0$). The NURBS basis is constructed form

$$R_i^p(\xi) = \frac{N_{i,p}(\xi) w_i}{W(\xi)} = \frac{N_{i,p}(\xi) w_i}{\sum_{\hat{i}}^{n_{\text{CP}}} N_{\hat{i},p}(\xi) w_{\hat{i}}} \tag{3}$$

where $w_i$ is the $i$-th weight. If all weights are set to one ($w_i = 1$) the NURBS basis coincides with the B-Spline basis defined above. With the control points $\mathbf{B}_i$, where $\mathbf{B}_i \in \mathbb{R}^d$ is the $i$-th control point, a NURBS curve can be constructed

$$\mathbf{C}(\xi) = \sum_{i=1}^{n_{\text{CP}}} R_i^p(\xi) \mathbf{B}_i \tag{4}$$

https://doi.org/10.3311/ECCOMASMBD2021-181

where $n_{\mathrm{CP}} = n_{\mathrm{ele}} + p$ is the number of control points. NURBS curves can be used to display many common geometries exactly and smoothly.

## 3 Geometrically Exact Beam Formulation

Many different formulations for non-linear beams exist in the literature. The here presented formulation follows closely the following publications [5, 6, 7, 8].

### 3.1 Beam Kinematics

The position of any point on the beam can be described by

$$\mathbf{x}(s,t,\theta^1,\theta^2) = \boldsymbol{\varphi}(s,t) + \boldsymbol{\theta}(s,t) = \boldsymbol{\varphi}(s,t) + \theta^\alpha \mathbf{d}_\alpha(s,t) \tag{5}$$

where $s \in [s_1, s_2]$, with $s_1, s_2 \in \mathbb{R}$, is referred to as the arc-length in the reference configuration. $\theta^i \in \mathbb{R}$ are convective coordinates ($\theta^1$, $\theta^2$, $\theta^3 = s$). $\boldsymbol{\varphi} \in \mathbb{R}^3$ points to the centerline of the beam and $\theta^\alpha$ gives the position on the cross-section. The Einstein notation for double indices is used. Note that from now on indices with Greek letters run from one to two ($\alpha, \beta = 1,2$), whereas indices with Roman letters run from one to three ($i, j, k = 1,2,3$).

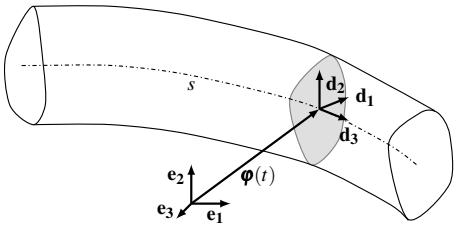


**Figure 1**. Configuration of the beam

Three directors $\mathbf{d}_i \in \mathbb{R}^3$ are defined, where $\mathbf{d}_1$ and $\mathbf{d}_2$ span the cross-section area of the beam, and $\mathbf{d}_3$ is defined by

$$\mathbf{d}_3(s,t) = \mathbf{d}_1(s,t) \times \mathbf{d}_2(s,t) \tag{6}$$

In the reference configuration at time $t = 0$ the director $\mathbf{d}_3(s,0)$ is equivalent to the tangent of the centerline $\mathbf{d}_3(s,0) = \boldsymbol{\varphi}_{,s}(s,0)$. Here the abbreviation of the partial derivative $\frac{\partial(\bullet)}{\partial s}$ is introduced. The directors are mutually orthonormal for all $t \in \mathbb{R}$, that is

$$\mathbf{d}_i(t) \otimes \mathbf{d}_i(t) = \mathbf{I} \tag{7}$$

where $\mathbf{I}$ is the unit tensor. The relation between the orthonormal, Cartesian basis $\mathbf{e}_i$ and the directors $\mathbf{d}_i$ can be expressed by

$$\mathbf{d}_i = \mathbf{R}(s,t) \cdot \mathbf{e}_i \tag{8}$$

where

$$\mathbf{R}(s,t) = \mathbf{d}_i(s,t) \otimes \mathbf{e}_i \tag{9}$$

$\mathbf{R} \in \mathrm{SO}(3)$ is an orthogonal tensor belonging to the special Euclidean group $\mathrm{SO}(3)$.

### 3.2 Constitutive Equations

We introduce two strain measures $\boldsymbol{\Gamma}$ and $\mathbf{K}$

$$\boldsymbol{\Gamma} = \Gamma_i \mathbf{e}_i \text{ with } \Gamma_i = \mathbf{d}_i \cdot \boldsymbol{\varphi}_{,s} - \delta_{i3} \tag{10}$$

$$\mathbf{K} = K_i \mathbf{e}_i \text{ with } K_i = \frac{1}{2} \varepsilon_{ijk} \left[ \mathbf{d}_k \cdot \mathbf{d}_{j,s} - (\mathbf{d}_k \cdot \mathbf{d}_{j,s}) \big|_{t=0} \right] \tag{11}$$

where $\varepsilon_{ijk}$ is the Levi-Civita symbol. Both strain measures are invariant under rigid body movements, which also carries over to the discretized measures as shown in [5]. We assume a Saint

https://doi.org/10.3311/ECCOMASMBD2021-181

Vernant-Kirchhoff type material model, where the stored energy is given by the function $w(\mathbf{\Gamma},\mathbf{K})$. We obtain the constitutive equations from

$$\bar{\mathbf{N}} = \frac{\partial w(\mathbf{\Gamma},\mathbf{K})}{\partial \mathbf{\Gamma}} \quad \text{and} \quad \bar{\mathbf{M}} = \frac{\partial w(\mathbf{\Gamma},\mathbf{K})}{\partial \mathbf{K}} \tag{12}$$

The total strain energy follows from

$$W = \frac{1}{2}\int_0^L \mathbf{\Gamma}\cdot\mathbf{D_1}\cdot\mathbf{\Gamma} + \mathbf{K}\cdot\mathbf{D_2}\cdot\mathbf{K}\,\mathrm{d}s \tag{13}$$

with

$$\mathbf{D_1} = \begin{bmatrix} GA_1 & 0 & 0 \\ 0 & GA_2 & 0 \\ 0 & 0 & EA \end{bmatrix} \mathbf{e}_i \otimes \mathbf{e}_j \qquad \mathbf{D_2} = \begin{bmatrix} EI_1 & 0 & 0 \\ 0 & EI_2 & 0 \\ 0 & 0 & GJ \end{bmatrix} \mathbf{e}_i \otimes \mathbf{e}_j \tag{14}$$

### 3.3 Kinetic Energy

The kinetic energy of the beam is given by

$$\begin{aligned} E^{\mathrm{kin}} &= \frac{1}{2}\int_0^L \rho_0(\boldsymbol{\theta},s)\dot{\mathbf{x}}(s,t)\cdot\dot{\mathbf{x}}(s,t)\mathrm{d}V \\ &= \frac{1}{2}\int_0^L \left[A_\rho \dot{\boldsymbol{\varphi}}(s,t)\cdot\dot{\boldsymbol{\varphi}}(s,t) + 2\dot{\boldsymbol{\varphi}}(s,t)\cdot\dot{\mathbf{d}}_\alpha S^\alpha + M_\rho^{\alpha\beta}\dot{\mathbf{d}}_\alpha\cdot\dot{\mathbf{d}}_\beta\right]\mathrm{d}s \end{aligned} \tag{15}$$

where $A_\rho(s)$ it the mass density per unit reference length

$$A_\rho(s) = \int_{A_s} \rho_0(\boldsymbol{\theta},s)\,\mathrm{d}A \tag{16}$$

with the density function $\rho_0(s)$. $A_s(s)$ is the beam cross-section at $s$. The first moment of area is computed from

$$\mathbf{S}_\rho(s) = \int_{A_s} \rho_0(\boldsymbol{\theta},s)\boldsymbol{\theta}\,\mathrm{d}A \tag{17}$$

with the components $S_\rho^\alpha = \mathbf{S}_\rho\cdot\mathbf{e}_\alpha$ and the mass-moment of inertia of the cross-section is given by

$$\mathbf{M}_\rho(s) = \int_{A_s} \rho_0(\boldsymbol{\theta},s)\boldsymbol{\theta}\otimes\boldsymbol{\theta}\,\mathrm{d}A \tag{18}$$

with the components $M_\rho^{\alpha\beta} = \mathbf{M}_\rho : (\mathbf{e}_\alpha\otimes\mathbf{e}_\beta)$

### 3.4 Constraints

Lagrange multipliers $\boldsymbol{\lambda}$ are introduced to enforce the orthonormality of the directors

$$\boldsymbol{\lambda}(s,t) : [\mathbf{d}_i\otimes\mathbf{d}_i - \mathbf{I}] = \boldsymbol{\lambda}(s,t) : \mathbf{\Phi}_{\mathrm{in}} = 0 \tag{19}$$

where the constraints $\mathbf{\Phi}_{\mathrm{in}}$ are given by

$$\mathbf{\Phi}_{\mathrm{in}} = \mathbf{d}_i\otimes\mathbf{d}_i - \mathbf{I} \tag{20}$$

### 3.5 Virtual Work

Using the variations of the variables we obtain the variations of the strain measures as

$$\delta\mathbf{\Gamma} = \delta\Gamma_i\,\mathbf{e}_i \qquad \text{with } \delta\Gamma_i = \delta\mathbf{d}_i\cdot\boldsymbol{\varphi}_{,s} + \mathbf{d}_i\cdot\delta\boldsymbol{\varphi}_{,s} \tag{21}$$

$$\delta\mathbf{K} = \delta K_i\,\mathbf{e}_i \qquad \text{with } \delta K_i = \frac{1}{2}\varepsilon_{ijk}\left[\delta\mathbf{d}_k\cdot\mathbf{d}_{j,s} + \mathbf{d}_k\cdot\delta\mathbf{d}_{j,s}\big|_{t=0}\right] \tag{22}$$

https://doi.org/10.3311/ECCOMASMBD2021-181

It follows, that the internal virtual work can be computed from

$$G^{\text{int}}(\mathbf{x}, \delta\mathbf{x}) = \int_0^L \delta\boldsymbol{\Gamma} \cdot \mathbf{D_1} \cdot \boldsymbol{\Gamma} + \delta\mathbf{K} \cdot \mathbf{D_2} \cdot \mathbf{K} \, \mathrm{d}s \tag{23}$$

and the virtual work of the inertia terms is given by

$$G^{\text{kin}}(\mathbf{x}, \delta\mathbf{x}) = \int_0^L A_\rho \left( \ddot{\boldsymbol{\varphi}}(s,t) + \ddot{\mathbf{d}}_\alpha S_\alpha \right) \cdot \delta\boldsymbol{\varphi}(s,t) + \left( S^\alpha \ddot{\boldsymbol{\varphi}}(s,t) + M_\rho^{\alpha\beta} \cdot \ddot{\mathbf{d}}_\beta \right) \cdot \delta\mathbf{d}_\alpha \, \mathrm{d}s \tag{24}$$

The external loads, external forces and moments, result in the following virtual work expression

$$G^{\text{ext}}(\mathbf{x}, \delta\mathbf{x}) = \int_0^L \delta\boldsymbol{\Gamma} \cdot \bar{\mathbf{N}}_{\text{ext}} + \delta\mathbf{K} \cdot \bar{\mathbf{M}}_{\text{ext}} \, \mathrm{d}s \tag{25}$$

and the variation of the constraints leads to

$$G^{\text{con}}(\mathbf{d}_i, \boldsymbol{\lambda}, \delta\mathbf{d}_i, \delta\boldsymbol{\lambda}) = \int_0^L \boldsymbol{\lambda} : \mathbf{G} \cdot \delta\mathbf{d}_i + \delta\boldsymbol{\lambda} : \boldsymbol{\Phi}_{\text{in}} \, \mathrm{d}s \tag{26}$$

where

$$\mathbf{G}_{\text{in}} = \text{Grad}(\boldsymbol{\Phi}_{\text{in}}) \tag{27}$$

From the principle of virtual work follows

$$G^{\text{int}} + G^{\text{kin}} - G^{\text{ext}} + G^{\text{con}} = 0 \tag{28}$$

### 3.6 Finite Element Discretization

The displacements and directors are discretized in a finite element sense with NURBS shape functions. In classical FEM the shape function chosen for the discretization of the Lagrange multipliers coincide with Dirac deltas associated with the nodes [5, 7]. As the NURBS shape functions are not interpolatory, this method can no longer be applied directly. Instead one can chose to discretize the Lagrange multipliers with the NURBS shape functions. In [8] it is argued that the linear theory indicates that different orders of shape functions for displacements as for directors and Lagrange multipliers should be applied. They propose to use shape functions of the order $p_\varphi - 1$ for the directors and Lagrange multipliers, where $p_\varphi$ is the order of the shape functions applied to discretize the displacements. However, a proof for the optimal discretization is not given.
Under the assumption of the arbitrariness of the test functions we obtain the following time-continuous system of differential algebraic equations (DAE's)

$$\mathbf{M}\ddot{\mathbf{q}} + \boldsymbol{\nabla} V(\mathbf{q}) + {\mathbf{G}_{\text{in}}}^\top \boldsymbol{\lambda} = \mathbf{f}_{\text{ext}} \tag{29}$$

$$\boldsymbol{\Phi}_{\mathbf{in}}(\mathbf{q}) = \mathbf{0} \tag{30}$$

where $\mathbf{q}$ contains the values of the control points of the displacements and directors and $\boldsymbol{\lambda}$ contains the values of the Lagrange multipliers.

#### 3.6.1 Initialization of Directors

In the IGA the control points, which correspond to the degrees of freedom, in general do not lie inside the physical domain. The quantities inside the physical domain are given by the linear combination of the values on the control points multiplied with the shape functions. The non-interpolatory nature of the shape functions has to be taken into account in the definition of the directors in a preprocessing step. An algorithm, where the directors in every integration point are used to compute the directors on the control points is introduced in [22]. We use the proposed algorithm. The directors of the beam at the Gauss points are given by

$$\mathbf{d^h}_i(s_{\text{GP}}) = \sum_{j=1}^{n_{\text{CP}}} N_i(s_{\text{GP}}) \mathbf{d}^j_{i,\text{CP}} \tag{31}$$

https://doi.org/10.3311/ECCOMASMBD2021-181

where $\mathbf{d}_i^h(s_{\mathrm{GP}})$ are the discretized directors on the Gauss points and $\mathbf{d}_{i,\mathrm{CP}}^A$ the directors on the control points. Note that $s$ can be used interchangeably with $\xi$. Eq. (31) can be written in matrix notation

$$\mathbf{d}_i^{\mathrm{GP}} = \mathbf{N}\,\mathbf{d}_i^{\mathrm{CP}} \tag{32}$$

where $\mathbf{N}$ has the dimension of $(n_{\mathrm{GP}} \cdot n_{el} \times n_{\mathrm{CP}})$. $n_{\mathrm{GP}}$ is the number of Gauss points per element and $n_{el}$ the number of elements. By multiplying with $\mathbf{N}^\top$ we obtain the following normal equations

$$\mathbf{N}^\top \mathbf{d}_i^{\mathrm{GP}} = \mathbf{N}^\top \mathbf{N}\,\mathbf{d}_i^{\mathrm{CP}} \tag{33}$$

The matrices $\mathbf{N}^\top \mathbf{d}_i^{\mathrm{GP}}$ and $\mathbf{N}^\top \mathbf{N}$ can be assembled element wise. The values of the director vectors on the control points follow than from

$$(\mathbf{N}^\top \mathbf{N})^{-1} \mathbf{N}^\top \mathbf{d}_i^{\mathrm{GP}} = \mathbf{d}_i^{\mathrm{CP}} \tag{34}$$

### 3.7 Numerical Objectivity Test

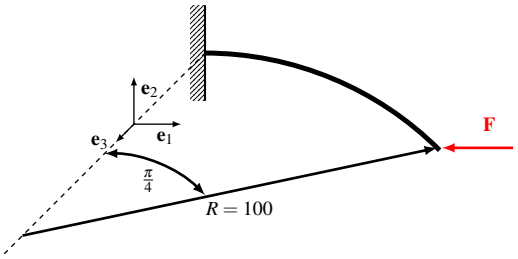


**Figure 2**. 3D cantilever bend

Geometrically exact beam formulations based on a discretization of rotations may suffer from a lack of objectivity, if the discretization is not performed with great care [4]. To show that the presented formulation does not suffer from this problem the following example from [5] is simulated. A 3D cantilever bend as shown in Fig. 2 is investigated. The stiffness properties of the beam are $GA_1 = GA_2 = 5 \cdot 10^6$, $EA = 10^7$ and $EI_1 = EI_2 = GJ = \frac{1}{12} \cdot 10^7$. As shown the cantilever is fixed at one end. On the other end of the beam the force $\mathbf{F} = \begin{bmatrix} F_1, & F_2, & F_3 \end{bmatrix} \mathbf{e}_i$ acts. The force is applied in increments of $\|\Delta F_i\| = 25$. In Table 1 the load cycle is shown in detail. The Newton-Raphson solver is considered converged for a Euclidean norm of $\|\mathbf{g}\| \leq \varepsilon = 10^{-7}$ of the residual $\mathbf{g}$. In Table

**Table 1**. Load cycle and tip displacement $\boldsymbol{\varphi} \cdot \mathbf{e_2}$ of the 3D cantilever bend

| Load levels | polynomial order | | |
|---|---|---|---|
| $\begin{bmatrix} F_1, & F_2, & F_3 \end{bmatrix}$ | $p = 1$ | $p = 2$ | $p = 3$ |
| $\begin{bmatrix} 0 & 0 & 0 \end{bmatrix}$ | 0 | 0 | 0 |
| $\begin{bmatrix} -600 & 0 & 0 \end{bmatrix}$ | 0 | 0 | 0 |
| $\begin{bmatrix} -600 & 600 & 0 \end{bmatrix}$ | 61.9106 | 59.9274 | 58.9219 |
| $\begin{bmatrix} -600 & 600 & 600 \end{bmatrix}$ | 40.1867 | 38.2493 | 37.7772 |
| $\begin{bmatrix} 0 & 600 & 600 \end{bmatrix}$ | 37.9928 | 36.2738 | 36.7271 |
| $\begin{bmatrix} 0 & 0 & 600 \end{bmatrix}$ | $\ll \varepsilon$ | $\ll \varepsilon$ | $\ll \varepsilon$ |
| $\begin{bmatrix} 0 & 0 & 0 \end{bmatrix}$ | $\ll \varepsilon$ | $\ll \varepsilon$ | $\ll \varepsilon$ |

1 the displacement of the tip in the direction of $\mathbf{e}_2$ is presented. After the whole load cycle is completed the configuration has to coincide with the initial configuration again. The cantilever bend is discretized with 8 beam elements. The simulations are conducted for polynomial orders from $p = 1$ to $p = 3$. All results are in good agreement with [5]. It can be seen that the displacement in direction of $\mathbf{e}_2$ is zero in a numerical sense at the end of the load cycle and, thus, coincides with the initial configuration as expected.

### 3.8 Time Discretization

As described in Sec. 1 it is of great advantage to use an energy-momentum scheme in combination with geometrically exact beams. Using the energy-momentum scheme described in [19] the fully discretized DAE for the geometrically exact beam reads as

$$\mathbf{M}\mathbf{a}_{n+\frac{1}{2}} + \bar{\nabla} V\left(\mathbf{q}_n, \mathbf{q}_{n+1}\right) + \mathbf{G}_{\text{in}}{}^{\top}\left(\mathbf{q}_{n+\frac{1}{2}}\right)\boldsymbol{\lambda}_{n+1} = 0 \tag{35}$$

$$\boldsymbol{\Phi}(\mathbf{q}_{n+1}) = 0 \tag{36}$$

where

$$\mathbf{q}_{n+\frac{1}{2}} = \frac{1}{2}\left(\mathbf{q}_n + \mathbf{q}_{n+1}\right) \tag{37}$$

$$\mathbf{v}_n = \frac{2}{\Delta t}\left(\mathbf{q}_n - \mathbf{q}_{n-1}\right) - \mathbf{v}_{n-1} \tag{38}$$

$$\mathbf{a}_{n+\frac{1}{2}} = \frac{2}{\Delta t^2}\left(\mathbf{q}_{n+1} - \mathbf{q}_n\right) - \frac{2}{\Delta t}\mathbf{v}_n \tag{39}$$

$\Delta t$ is the time step and $\mathbf{q}_n$ the nodal values at time $n\Delta t$, and $\mathbf{q}_{n+1}$ the nodal values at time $(n+1)\Delta t$ respectively (analogous for $\boldsymbol{\lambda}_{\mathbf{n+1}}$). $\bar{\nabla}\mathbf{f}$ is called the discrete gradient of a function $\mathbf{f}$. According to Gonzalez [9] it has to fulfill the following properties to inherit the symmetry properties (concerning linear and angular momentum and energy) from the continuous problem

- directionality condition

$$\bar{\nabla}\mathbf{f}\left(\mathbf{q}_n, \mathbf{q}_{n+1}\right)\left(\mathbf{q}_{n+1} - \mathbf{q}_n\right) = \mathbf{f}(\mathbf{q}_{n+1}) - \mathbf{f}(\mathbf{q}_n) \tag{40}$$

- consistency condition

$$\bar{\nabla}\mathbf{f}\left(\mathbf{q}_n, \mathbf{q}_{n+1}\right) = \bar{\nabla}\mathbf{f}\left(\frac{\mathbf{q}_n + \mathbf{q}_{n+1}}{2}\right) + \mathscr{O}\left(\|\mathbf{q}_{n+1} - \mathbf{q}_n\|\right) \tag{41}$$

In case of a quadratic strain energy function the discrete gradient uses the average of the strains and not the average of the configurations such as with the midpoint rule [10].

#### 3.8.1 Beam with Concentrated Masses

In Fig. 3 the initial configuration of a beam with concentrated masses is shown. This problem is taken from [6]. The beam has a length of $2L$, where $L = 1\,\text{m}$. At both ends as well as in the middle of the beam concentrated masses are added with $M = 10\,\text{kg}$ and $m = 1\,\text{kg}$. The beam itself has a mass density per unit length of $A_\rho = 0.27\,\frac{\text{kg}}{\text{m}}$ and a mass-moment of inertia of the cross-section of $M_\rho = 9 \cdot 10^{-8}\,\frac{\text{kg}}{\text{m}}$. The beam stiffness parameters are given as $EI = 2.43\,\text{Nm}^2$, $GJ = 586\,\text{Nm}^2$, $GA = 2.43 \cdot 10^6\,\text{N}$ and $EA = 7.3 \cdot 10^6\text{N}$.

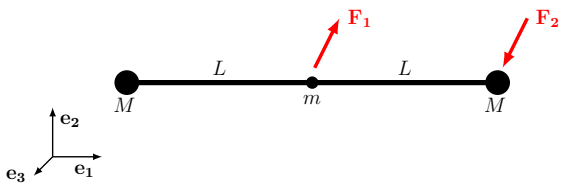


**Figure 3**. Initial configuration of the beam with concentrated masses.

The system is exited by two time-dependent external dead loads $\mathbf{F_1}$ and $\mathbf{F_2}$

$$\mathbf{F}_\alpha = \mathbf{P}_\alpha f(t) \qquad \begin{aligned} \mathbf{P}_1 &= -1\,\text{N}\,\mathbf{e_1} - 3\,\text{N}\,\mathbf{e_3} \\ \mathbf{P}_2 &= 2\,\text{N}\,\mathbf{e_1} + 4\,\text{N}\,\mathbf{e_3} \end{aligned}$$

https://doi.org/10.3311/ECCOMASMBD2021-181

The time-dependent function $f(t)$ is given by

$$f(t) = \begin{cases} \frac{1}{2}\left(1-\cos\left(\frac{2\pi t}{T}\right)\right) & \text{for} \quad t \leq T \\ 0 & \text{for} \quad t \geq T \end{cases}$$

where $T = 3\,\mathrm{s}$. The simulation results for the angular momentum $\mathbf{L} = \begin{bmatrix} L_1, & L_2, & L_3 \end{bmatrix} \mathbf{e}_i$ and the

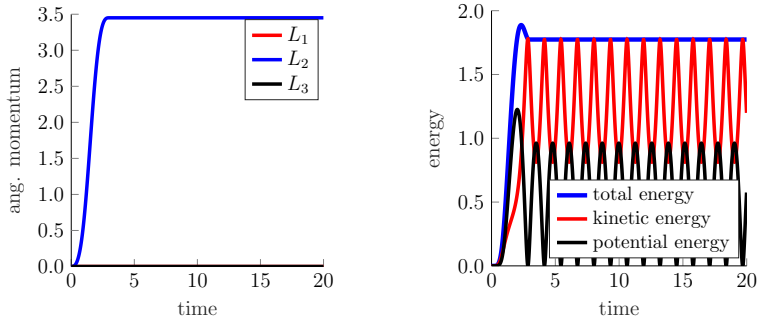


**Figure 4**. Angular momentum and energy over time for the beam with concentrated masses.

energy of the system are shown in Fig. 4. A constant time steps size of $\Delta t = 1 \cdot 10^{-2}\,\mathrm{s}$ is used and the beam is discretized with 22 linear elements. All results are in very good agreement with [6]. It can be seen very easily, that for $t > T$ the component $L_2$ in $\mathbf{e_2}$-direction of the angular momentum is constant (both other components are zero for all $t$). The same effect can be found when considering the total energy of the system. It is constant, after all external loads are set to zero.

## 4 Sliding Joint

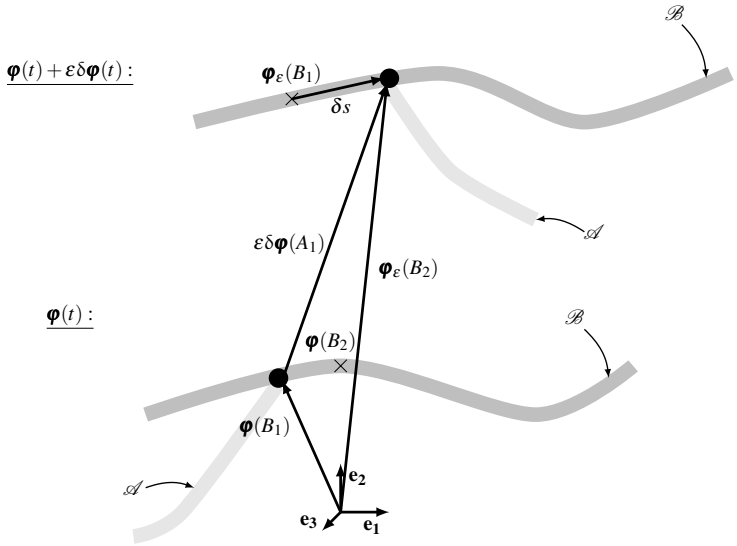


**Figure 5**. Sketch of two beams with sliding contact without and with pertubation.

We assume that two beams, $\mathscr{A}$ and $\mathscr{B}$, are in contact at one point in the deformed configuration $\boldsymbol{\varphi}(t)$ as shown in Fig. 5. We make the following assumptions describing the physical system

1. The material point $A_1$ on beam $\mathscr{A}$ is always in contact with beam $\mathscr{B}$, whereas the contact point on beam $\mathscr{B}$ may change over time. Beam $\mathscr{A}$, therefore, slides along beam $\mathscr{B}$

https://doi.org/10.3311/ECCOMASMBD2021-181

2. The assumption of a frictionless contact is made. Thus, the contact forces act only in normal direction

$$\mathbf{N}_I = \mathbf{n}_I \|\mathbf{N}_I\| \qquad \text{where } I = A_1, B_1 \tag{42}$$

where the subscribed $A$ denotes that the variable belongs to beam $\mathscr{A}$ and the subscribed $B$ denotes that the variable belongs to beam $\mathscr{B}$. From those assumptions the constraints for a spherical sliding joint follow as

$$\mathbf{\Phi}_{\text{ex}}(\mathbf{q}_\mathbf{n}) = \begin{bmatrix} (\boldsymbol{\varphi}_A(A_1) - \boldsymbol{\varphi}_B(B_1)) \cdot \mathbf{n}_1 \\ (\boldsymbol{\varphi}_A(A_1) - \boldsymbol{\varphi}_B(B_1)) \cdot \mathbf{n}_2 \end{bmatrix} \tag{43}$$

The local normal vectors $\mathbf{n}_\alpha$ are given by

$$\mathbf{t} = \frac{\boldsymbol{\varphi}_{B,s}|_{s=s_\text{c}}}{\|\boldsymbol{\varphi}_{B,s}|_{s=s_\text{c}}\|} \tag{44}$$

$$\mathbf{n}_1 = \frac{\boldsymbol{\varphi}_{B,ss}|_{s=s_\text{c}}}{\|\boldsymbol{\varphi}_{B,ss}|_{s=s_\text{c}}\|} \tag{45}$$

$$\mathbf{n}_2 = \mathbf{n}_1 \times \mathbf{t}_3 \tag{46}$$

where $s_\text{c}$ is the arc-length of beam $\mathscr{B}$, which is closest to the point of contact of beam $\mathscr{A}$. Here the assumption is made that beam $\mathscr{A}$ is in contact at the last control point at $s_A = 1$. $s_\text{c}$ has to be determined in each time step. An efficient algorithm for this task can be found in [21].

### 4.1 Null Space Method

A transformation of a system of DAE's to a system of ordinary differential equations (ODE's) can be achieved using the so-called null space projection [17]. A general constrained mechanical system is governed by a system of equations of the following form

$$\begin{aligned} \mathbf{M}\ddot{\mathbf{q}} + \nabla V(\mathbf{q}) + \mathbf{G}^\top(\mathbf{q})\boldsymbol{\lambda} &= 0 \\ \mathbf{\Phi}(\mathbf{q}) &= 0 \end{aligned} \tag{47}$$

where $\mathbf{q} \in \mathbb{R}^u$ are the redundant coordinates and $\boldsymbol{\lambda} \in \mathbb{R}^v$ are the Lagrange multipliers. By multiplication with a null space matrix $\mathbf{P}$, from the null space of the gradient $\mathbf{G}$, the constraint forces $(\mathbf{G}^\top(\mathbf{q})\boldsymbol{\lambda})$ can be can be eliminated from Eq. (47), as $\mathbf{GP} = \mathbf{0}$. When additionally a mapping $\mathbf{F}(\mathbf{u}) = \mathbf{q}$ from $U \in \mathbb{R}^{u-v}$ to $Q \in \mathbb{R}^u$ is introduced, the DEA can be rewritten into an ODE

$$\mathbf{P}^\top [\mathbf{M}\ddot{\mathbf{q}} + \nabla V(\mathbf{q})] = 0 \tag{48}$$

An approach similar to the null space projection, called master-slave approach, was developed to simulate various joints between beams [13, 14, 15, 16]. Here, the null space matrix is constructed through geometrical reasoning without the introduction of constraints. The contact condition for a sliding spherical joint in a perturbed configuration (see Fig. 5) is given by

$$\boldsymbol{\varphi}_\varepsilon(A_1) = \boldsymbol{\varphi}_\varepsilon(B_2) \tag{49}$$

Thus, the virtual displacement $\delta\boldsymbol{\varphi}(A_1)$ can be expressed as

$$\delta\boldsymbol{\varphi}(A_1) = \frac{\mathrm{d}}{\mathrm{d}\varepsilon}\Big|_{\varepsilon=0} \boldsymbol{\varphi}_\varepsilon(A_1) = \frac{\mathrm{d}}{\mathrm{d}\varepsilon}\Big|_{\varepsilon=0} \boldsymbol{\varphi}_\varepsilon(B_2) = \boldsymbol{\varphi}_{,s}(B_1)\delta s + \delta\boldsymbol{\varphi}(B_1) \tag{50}$$

where $\delta s$ is the variation of the arc-length. After discretizing the displacements and directors in a finite element sense, the virtual displacements can be written as

$$\delta\mathbf{q}_n = \mathbf{P}_{\text{ex}}\delta\mathbf{q}_\mathbf{h} \tag{51}$$

https://doi.org/10.3311/ECCOMASMBD2021-181

where the virtual displacements $\delta\mathbf{q}_\mathbf{h} \in \mathbb{R}^{12(a+b)-2}$ are given by

$$\delta\mathbf{q}_\mathbf{h} = \left[\delta\mathbf{q}_A^1, \quad \ldots, \quad \delta\mathbf{q}_A^{a-1}, \quad \delta s, \quad \delta\mathbf{d}_A^n, \quad \delta\mathbf{q}_B^1, \quad \ldots, \quad \delta\mathbf{q}_B^b\right]^\top \tag{52}$$

$a$ is the number of control points of beam $\mathscr{A}$, respectively, $b$ is the number of control points of beam $\mathscr{B}$. The null space matrix $\mathbf{P}_{\text{ex}} \in \mathbb{R}^{(12(a+b))\times(12(a+b)-2)}$ is thus given by

$$\mathbf{P}_{\text{ex}} = \begin{bmatrix} \mathbf{I}_{12} & & & & & & & & \\ & \ddots & & & & & & & \\ & & \mathbf{I}_{12} & & & & & & \\ & & & \hat{\mathbf{F}}_{B_1} & & \mathbf{I}_3 N_{m_{\text{cp}}}(s_{\text{c}}) & \cdots & \mathbf{I}_3 N_{m_{\text{cp}}+p+1}(s_{\text{c}}) \\ & & & & \mathbf{I}_9 & & & \\ & & & & & \mathbf{I}_{12} & & \\ & & & & & & \ddots & \\ & & & & & & & \mathbf{I}_{12} \end{bmatrix} \tag{53}$$

where

$$\hat{\mathbf{F}}_{B_1} = \sum_{i=m_{\text{cp}}}^{m_{\text{cp}}+p+1} N_{i,s}(s_{\text{c}})\boldsymbol{\varphi}^i \tag{54}$$

and $\mathbf{I}_{12} \in \mathbb{R}^{12\times12}$ is the identity matrix ($\mathbf{I}_9 \in \mathbb{R}^{9\times9}$ and $\mathbf{I}_3 \in \mathbb{R}^{3\times3}$, respectively). The index $i$ runs from $m_{\text{cp}}$ to $m_{\text{cp}+p+1}$, thus including all relevant shape functions and control points of beam $\mathscr{B}$ to display the displacement $\boldsymbol{\varphi}_B(B_1)$ at $s_{\text{c}}$.
The reparametrization of the sliding joint contact is given by

$$\mathbf{F}(\mathbf{u}) = \begin{bmatrix} \mathbf{q}_{nA}^1 + \mathbf{u}_A^1 \\ \vdots \\ \mathbf{q}_{nA}^{n-1} + \mathbf{u}_A^{a-1} \\ \sum_{i=m_{\text{cp}}}^{m_{\text{cp}}+p+1} N_i(s_{\text{c}n+1})\left(\boldsymbol{\varphi}_{nB}^i + \mathbf{u}_{\varphi_B^i}\right) \\ \mathbf{d}_{nA}^n + \mathbf{u}_\mathbf{d} A^a \\ \mathbf{q}_{nB}^1 + \mathbf{u}_B^1 \\ \vdots \\ \mathbf{q}_{nB}^m + \mathbf{u}_B^b \end{bmatrix} \tag{55}$$

where $\mathbf{u}_{\square\bigcirc}^{(\bullet)}$ is the incremental displacement of control point $(\bullet)$, variable $\square$ and beam $\bigcirc$.
So far the null space matrix $\mathbf{P}_{\text{ex}}$ is time continuous. Two conditions for the discretized null space matrix are given in [18]

1. For time steps $\Delta t \to 0$ the discrete matrix has to coincide with the continuous one

$$\mathbf{P}(\mathbf{q}_n, \mathbf{q}_{n+1}) \to \mathbf{P}(\mathbf{q}_n) \quad \text{as} \quad \mathbf{q}_{n+1} \to \mathbf{q}_n \tag{56}$$

2. It is further required that

$$\mathbf{G}(\mathbf{q}_n, \mathbf{q}_{n+1})\mathbf{P}(\mathbf{q}_n, \mathbf{q}_{n+1}) = \mathbf{0} \tag{57}$$

Taking into account the above conditions the discrete null space matrix $\mathbf{P}_{\text{ex}}(\mathbf{q}_n, \mathbf{q}_{n+1})$ pertaining to the (external) sliding constraints can now be devised as discrete version of (53).

Note that the internal constraints associated with the orthonormality of the directors still need to be taken into account to complete the discrete null space method. To this end, an additional null space matrix $\mathbf{P}_{\text{in}}$ can be applied. Furthermore, the reparametrization $\mathbf{F}(\mathbf{u})$ needs be adjusted appropriately. These additional steps required to complete the discrete null space method can be found in [19] for the geometrically exact beam based on a director formulation.

## 5 Conclusion / Outlook

A short introduction of the used NURBS shape functions is given in Sec. 2. The shape functions are implemented into the well-known geometrically exact beam theory. A description based on directors is hereby used as described in Sec. 3. The orthonormality of the directors is only enforced in a weak sense. The objectivity of the implemented formulation is shown in the 3D cantilever bend example. For the time discretization an energy-momentum scheme is employed. The conervation properties of the scheme are shown in the example of the beam with concentrated masses.
Two algorithms for the sliding spherical joint are introduced. Both are expected to be energy and momentum-conserving. The accuracy of both algorithms and their conserving properties has still to be proven on numerical examples.

## REFERENCES

[1] Simo, J.C.: A finite strain beam formulation. The three-dimensional dynamic problem. Part I. Computer Methods in Applied Mechanics and Engineering **49**(1) (1985) 55–70 doi:10.1016/0045-7825(85)90050-7.

[2] Simo, J.C., Vu-Quoc, L.: A three-dimensional finite-strain rod model. part II: Computational aspects. Computer Methods in Applied Mechanics and Engineering **58**(1) (1986) 79–116 doi:10.1016/0045-7825(86)90079-4.

[3] Simo, J.C., Vu-Quoc, L.: On the dynamics of flexible beams under large overall motions-the plane case: Part I. Journal of Applied Mechanics **53**(4) (1986) 849–854 doi:10.1115/1.3171871.

[4] Crisfield, M.A., Jelenic, G.: Objectivity of strain measures in the geometrically exact three-dimensional beam theory and its finite-element implementation. Proceedings of the Royal Society A Mathematical, Physical and Engineering Sciences **455** (1998) 1125–1147 doi:10.1098/rspa.1999.0352.

[5] Betsch, P., Steinmann, P.: Frame-indifferent beam finite elements based upon the geometrically exact beam theory. International Journal for Numerical Methods in Engineering **54**(12) (2002) 1775–1788 doi:10.1002/nme.487.

[6] Betsch, P., Steinmann, P.: Constrained dynamics of geometrically exact beams. Computational Mechanics **31** (2003) 49–59 doi:10.1007/s00466-002-0392-1.

[7] Romero, I., Armero, F.: An objective finite element approximation of the kinematics of geometrically exact rods and its use in the formulation of an energy-momentum conserving scheme in dynamics. International Journal for Numerical Methods in Engineering **54**(12) (2002) 1683–1716 doi:10.1002/nme.486.

[8] Harsch, J., Capobianco, G., Eugster, S.R.: Finite element formulations for constrained spatial nonlinear beam theories. Mathematics and Mechanics of Solids (2021) doi:10.1177/10812865211000790.

[9] Gonzalez, O.: Time Integration and Discrete Hamiltonian Systems. Journal of Nonlinear Science **6**(5) (1996) 449–467 doi:10.1007/BF02440162.

[10] Simo, J.C., Tarnow, N.: The discrete energy-momentum method. Conserving algorithms for nonlinear elastodynamics. ZAMP Zeitschrift für angewandte Mathematik und Physik **43**(5) (1992) 757–792 doi:10.1007/BF00913408.

[11] Simo, J.C., Tarnow, N., Doblare, M.: Non-linear dynamics of three-dimensional rods: Exact energy and momentum conserving algorithms. International Journal for Numerical Methods in Engineering **38**(9) (1995) 1431–1473 doi:10.1002/nme.1620380903.

[12] Cottrell, J.A., Hughes, T.J., Bazilevs, Y.: Isogeometric Analysis - Toward Integration of CAD and FEA. John Wiley and Sons, Ltd, West Sussex (2009) ISBN:9780470748732.

[13] Jelenić, G., Crisfield, M.A.: Non-linear 'master-slave' relationships for joints in 3-D beams with large rotations. Computer Methods in Applied Mechanics Engineering **135**(3-4) (1996) 211–228 doi:10.1016/0045-7825(96)01017-1.

[14] Muñoz, J.J., Jelenić, G.: Sliding contact conditions using the master-slave approach with application on geometrically non-linear beams. International Journal of Solids and Structures **41**(24–25) (2004) 6963–6992 doi:10.1016/j.ijsolstr.2004.05.032.

[15] Muñoz, J.J.: Modelling unilateral frictionless contact using the null-space method and cubic B-Spline interpolation. Computer Methods in Applied Mechanics and Engineering **197**(9-12) (2008) 979–993 doi:10.1016/j.cma.2007.09.022.

[16] Sibilieau, A., Muñoz, J.J.: Conserving time-integration of beams under contact constrains using B-Spline interpolation. In: MULTIBODY DYNAMICS 2011, ECCOMAS Thematic Conference, Brussels, Belgium (July 2011)

[17] Betsch, P.: The discrete null space method for the energy consistent integration of constrained mechanical systems. Part I: Holonomic constraints. Computer Methods in Applied Mechanics and Engineering **194**(50-52) (2005) 5159–5190 doi:10.1016/j.cma.2005.01.004.

[18] Betsch, P., Leyendecker, S.: The discrete null space method for the energy consistent integration of constrained mechanical systems. Part II: Multibody dynamics. International Journal for Numerical Methods in Engineering **67**(4) (2006) 499–552 doi:10.1002/nme.1639.

[19] Leyendecker, S., Betsch, P., Steinmann, P.: The discrete null space method for the energy-consistent integration of constrained mechanical systems. Part III: Flexible multibody dynamics. Multibody System Dynamics **19**(1-2) (2008) 45–72 doi:10.1007/s11044-007-9056-4.

[20] Hughes, T., Cottrell, J., Bazilevs, Y.: Isogeometric analysis: CAD, finite elements, NURBS, exact geometry and mesh refinement. Computer Methods in Applied Mechanics and Engineering **194**(39) (2005) 4135–4195 doi:10.1016/j.cma.2004.10.008.

[21] Piegl, L., Tiller, W.: The NURBS Book. Springer-Verlag Berlin Heidelberg GmbH, Berlin (1997) ISBN:978354061545-3.

[22] Dornisch, W., Klinkel, S., Simeon, B.: Isogeometric Reissner-Mindlin shell analysis with exactly calculated director vectors. Computer Methods in Applied Mechanics and Engineering **253** (2013) 491–504 doi:10.1016/j.cma.2012.09.010.

https://doi.org/10.3311/ECCOMASMBD2021-139



# Coupled Multibody Model Of Industrial Robot With Milling Simulator For Trajectory Compensation

**V. Dambly[1], H.N. Huynh[2], O. Verlinden[1], É. Rivière-Lorphèvre[1]**

[1] Faculty of Engineering
University of Mons
20 place du Parc, 7000 Mons, Belgium
[valentin.dambly,olivier.verlinden,
edouard.rivierelorphevre]@umons.ac.be

[2] Department of Mechanical Engineering
University of British Columbia
Vancouver BC V6T 1Z4, Canada
hoainam.huynh@ubc.ca

## ABSTRACT

Robotic machining is a fast-growing technology in the field of mechanical manufacturing. Indeed, it is generally accepted that for the same working space, a fully equipped robotic machining cell can cost 30 to 50 % less than a conventional machine tool. However, inaccuracies resulting either from vibrations or deflections occur while the robot is subjected to cutting forces, inherent to its flexible structure. As an order of magnitude, the stiffness at the tool-tip is about $1N/\mu m$ for industrial robots against more than $50N/\mu m$ for CNC machine tools. The flexibility source has been investigated and appears to be caused by the robot articulations in a proportion of 80% while the remaining flexibility issues from the structural elasticity. In order to improve the accuracy of robotic machining operations, several approaches have been carried out such as the study of stable cutting conditions and the online/offline compensation of the tool trajectory.

Two aspects of the operation must be modeled, on the one hand the model of the cutting machine, being an industrial robot in robotic machining, and on the other hand, the machining model including the resulting geometry of the workpiece. A coupled model is then proposed with the multi-body model of the robot subjected to machining forces. The multi-body model includes the flexibility induced by the structure and the articulations. In order to compensate the deviations, a solution is proposed where the trajectory is discretized in nodes with a compensation taking the system dynamics into account by successive simulations of the operation. The algorithm involves two steps, firstly it aims to detect critical locations of the path and add or reposition nodes to reduce the deviation and secondly an optimization layer modifies nodes positions and velocities for a finer reduction. The method is deployed for three systems of increasing complexity for a face milling operation, showing a machining error reduction.

**Keywords:** Robotics, dynamic simulation, trajectory optimization, coupled models.

## 1 INTRODUCTION

Robotic machining is a fast-growing technology in the field of mechanical manufacturing. Indeed, it is generally accepted that for the same working space, a fully equipped robotic machining cell can cost 30 to 50% less than a conventional machine tool. Furthermore, robotic machining enables an interesting agility in the cutter motion to deal with complex workpieces geometry. However, inaccuracies resulting either from vibrations or deflections occur while the robot is subjected to cutting forces. As an order of magnitude, the stiffness at the tool-tip is about $1N/\mu m$ for industrial robots against more than $50N/\mu m$ for CNC machine tools [1].

The causes of these issues are numerous and have been identified then classified according to their nature [2]. Among the deviations sources, a major contribution appears to be the flexibility of the

https://doi.org/10.3311/ECCOMASMBD2021-139

robot, caused by its articulations in a proportion of 80% while the remaining flexibility issues from the structural elasticity of the links [3].

In order to improve the accuracy of robotic machining operations, several approaches have been carried out such as the study of stable cutting conditions and the online/offline compensation of the tool trajectory [2]. Within the frame of industry 4.0 and the concept of virtual twin, offline models can be developed in order to predict instabilities and compensate deviations. However, for the offline compensation, it is necessary to model both aspects of the operation, on the one hand the model of the cutting machine, being an industrial robot in robotic machining, and on the other hand, the machining model including the resulting geometry of the workpiece [4]. Offline compensation methods are closely related to modeling of the robot flexibility. The static deflection is directly computed from the identified stiffness matrix and the estimation of the milling forces.

The existing models mostly locate the flexibility at the articulations (precisely in the gearbox and bearings) and at links (presenting significant bending depending on their shape). Several offline compensation approaches are developed in the literature depending on the parameters chosen for the flexibility modeling [2]. These approaches propose to determine an equivalent torsional stiffness value at the articulation and to use it to calculate the corresponding deflection of the tool center point [5, 6].

The more sophisticated the flexibility modeling the better the static deflection evaluation, with for example a complete identification at the articulation level [5] or with simpler torsional model such as the virtual joint modeling approach [7]. In each case, an equivalent stiffness value is computed (with for example the Conservative Congruence Transformation [8]) and used to calculate the corresponding static deflection of the tool center point [1]. This deflection is used to shift the initial trajectory, also called the mirroring method [9].

Even though the stiffness-based deviation estimation presents a important error reduction, the dynamic deflection has not been addressed [4] and may cause non-negligible deviations. The dynamical behavior is significant at different moments of the operation for example when the tool enters or leaves the matter or even while performing small amplitude back and forth movements (changing the direction of motors torques) [10].

The optimal trajectory generation for underactuated flexible robots is an active research topic where optimal trajectory generation and control are central issues [11]. However, the perturbations generated by machining forces make these algorithms complex to apply in our context. An other reason requiring dynamic models is the presence of damping. It has indeed been shown that the articular flexibility modeling is improved by adding a damping contribution [3].

A robot performing a machining operation can be considered as a multibody chain with perturbation forces applied on the tool center point (TCP). In order to be able to simulate 5-axis operations, it is necessary to include a machining force module that can compute these forces from the tool motion. Concerning the modeling of machining operation, several approaches exist depending on the expected inputs of the simulation [12]. The most appropriate candidates for time-based simulation of 5-axis operations where the cutting forces and workpiece geometry are needed at each time-step are the voxel and the dexel approaches [12]. Models based on voxels have been developed for model-based compensation [6]. However, the complexity of voxel model is up to $O(n^3)$ against $O(n^2)$ for dexel. Besides, for 2.5D operations, the stack of slices approach is faster and reliable [13].

This paper first describes the flexibility model of the robot. Afterwards, the repositioning algorithm is presented and applied on several multibody systems. Three models of increasing complexity are addressed. In the first place, a minimal case, being the tool-mass body fixed with linear spring/damper to a support whose motion is prescribed, is studied. Afterwards, non-linear robots

https://doi.org/10.3311/ECCOMASMBD2021-139

are a two-degree-of-freedom robot and the machining robot Stäubli TX200, with the introduction of torsional spring/damper pairs at the articulations to model the flexibility. The repositioning of the trajectory nodes is improved with an optimization layer considering nodes positions and velocities as design variables. Perspectives are discussed for the development, refinement and extension for 5-axis operations of the proposed method.

## 2 MULTIBODY DYNAMIC MODEL

The equations of motions for a multiple-degree-of-freedom mechanical system are expressed as follows

$$\mathbf{M_q}(\mathrm{q})\ddot{\mathrm{q}}(\mathbf{t}) + \mathbf{h_q}(\mathrm{q},\dot{\mathrm{q}}) = \mathbf{F}(\mathbf{t}) \tag{1}$$

where $\mathbf{M_q}(\mathrm{q})$, $\mathbf{h_q}(\mathrm{q},\dot{\mathrm{q}})$ and $\mathbf{F}(\mathbf{t})$ are defined in generalized coordinates, according to the virtual power theorem, with equations (2,3,4), where $\mathbf{M_q}(\mathrm{q})$ the mass matrix, $\mathbf{h_q}(\mathrm{q},\dot{\mathrm{q}})$ the vector gathering the Coriolis, gyroscopic and centrifugal forces and $\mathbf{F}(\mathbf{t})$ the vector of external forces applied on the system are expressed in terms of the generalized coordinates $q$ according to equations (2) to (4). The vector q regroups the actuated degrees-of-freedom $\mathrm{q}_a$ and the unactuated degrees-of-freedom $\mathrm{q}_u$.

$$\mathbf{M}_{\mathrm{q}}(\mathrm{q}) = \sum_{i=1}^{n_\mathrm{B}} \left( m_i [\mathbf{J}_{S,i}]_{\mathrm{Base}}^T \cdot [\mathbf{J}_{S,i}]_{\mathrm{Base}} + [\mathbf{J}_{\omega,i}]_{\mathrm{Base}}^T \cdot \mathbf{R}_{\mathrm{Base},i} \cdot [\Phi_{G,i}]_i \cdot \mathbf{R}_{\mathrm{Base},i}^T \cdot [\mathbf{J}_{\omega,i}]_{\mathrm{Base}} \right). \tag{2}$$

$$\begin{aligned} \mathbf{h}_{\mathrm{q}}(\mathrm{q},\dot{\mathrm{q}}) = \sum_{i=1}^{n_\mathrm{B}} & \left( m_i [\mathbf{J}_{S,i}]_{\mathrm{Base}}^T \cdot [\dot{\mathbf{J}}_{S,i}]_{\mathrm{Base}} + [\mathbf{J}_{\omega,i}]_{\mathrm{Base}}^T \cdot \mathbf{R}_{\mathrm{Base},i} \cdot [\Phi_{G,i}]_i \cdot \mathbf{R}_{\mathrm{Base},i}^T \cdot [\dot{\mathbf{J}}_{\omega,i}]_{\mathrm{Base}} \right) \dot{\mathrm{q}} \\ & + [\mathbf{J}_{\omega,i}]_{\mathrm{Base}}^T \cdot \left( \{\omega_i\}_{\mathrm{Base}} \times \mathbf{R}_{\mathrm{Base},i} \cdot [\Phi_{G,i}]_i \cdot \mathbf{R}_{\mathrm{Base},i}^T \cdot \{\omega_i\}_{\mathrm{Base}} \right). \end{aligned} \tag{3}$$

$$\mathbf{F}_{\mathrm{q}} = \sum_{i=1}^{n_\mathrm{B}} \left( [\mathbf{J}_{S,i}]_{\mathrm{Base}}^T \cdot \{\mathrm{R}_i\}_{\mathrm{Base}} + [\mathbf{J}_{\omega,i}]_{\mathrm{Base}}^T \cdot \{\mathrm{M}_{G,i}\}_{\mathrm{Base}} \right), \tag{4}$$

where the subscript *Base* refers to the base frame, $[\mathbf{J}_{S,i}]_{\mathrm{Base}}$ and $[\mathbf{J}_{\omega,i}]_{\mathrm{Base}}$ are the translational and rotational Jacobian matrices of body $i$ expressed in the base frame.

To model the gearbox flexibility, unactuated degrees-of-freedom are introduced at the articulation, allowing a deflection introducing elastic and damping action/reaction torques on the bodies on either side of the articulation. The torques between body $i$ and $j$ are expressed by

$$\begin{aligned} \{\mathrm{M}_{G,i}\}_{\mathrm{Base}} &= -\left( k_{q_{u,l}} \cdot q_{u,l} + d_{q_{u,l}} \cdot \dot{q}_{u,l} \right) \cdot \mathbf{R}_{\mathrm{Base},i} \cdot \mathrm{u}_l \quad \text{(action)}, \\ \{\mathrm{M}_{G,j}\}_{\mathrm{Base}} &= \left( k_{q_{u,l}} \cdot q_{u,l} + d_{q_{u,l}} \cdot \dot{q}_{u,l} \right) \cdot \mathbf{R}_{\mathrm{Base},i} \cdot \mathrm{u}_l \quad \text{(reaction)} \end{aligned} \tag{5}$$

where $k_{q_{u,l}}$ and $d_{q_{u,l}}$ are respectively the torsional stiffness and damping of the articulation along local axis $l$.

The machining forces are computed considering the mechanistic approach [14]. Theses forces are computed as the sum of elementary contributions along the tool axis as follows:

$$\mathrm{F}_\alpha = \sum_{k=1}^{n_s} K_{\alpha,c}.h.dz + K_{\alpha,e}.ds \tag{6}$$

with $h$ the uncut chip thickness, $dz$ the height of the elementary slice, $n_s$ the number of tool slices [14], $\alpha = t,r,a$ the tangential, radial and axial directions respectively, $K_{\alpha,c}$ and $K_{\alpha,e}$ the cutting coefficients and $ds$ the local cutter edge length. The forces are then applied on the TCP. Their computation is the result of the coupling of two simulators, on the one hand EasyDyn, an in-house multi-body solver and on the other hand DyStaMill, an in-house solver as well, dedicated to the simulation of machining operations [13].

https://doi.org/10.3311/ECCOMASMBD2021-139

The global block diagram of the correction is shown in Fig. 1. The system is controlled with an inverse dynamic controller [15] in which $\mathbf{M_q}(\mathbf{q}), \mathbf{h_q}(\mathbf{q}, \dot{\mathbf{q}}), \mathbf{F_q}$ are computed with the rigid model of the robot in order to provide the assumption that the robot controller is not aware of the flexibility. The Cartesian trajectory $[p_t \ \dot{p}_t \ \ddot{p}_t]^T$ is first transposed in the joint space $[q_t \ \dot{q}_t \ \ddot{q}_t]^T$ with second order inverse dynamics, also based on a hypothetical perfectly rigid robot, and tracked with the controller generating the motor torques $[u_{1,t} \dots u_{n_{dof},t}]^T$. The aim of this architecture is to reproduce the conditions where the inner controller of the robot is not accessible and the input is the trajectory sent to the system.

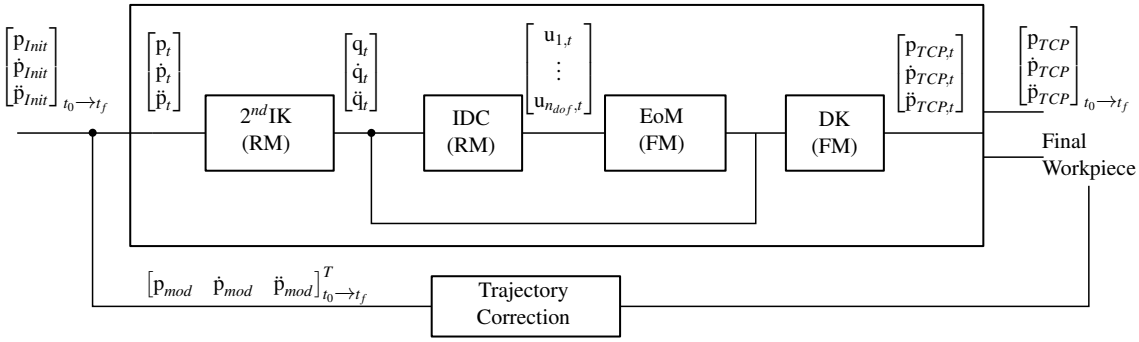


Figure 1: Block diagram of the off-line operational trajectory correction. With IK: Inverse Kinematics, IDC: Inverse Dynamics Controller, EoM: Equations of Motion, DK: Direct Kinematics, RM: Rigid model, FM: Flexible Model. The initial trajectory based on the G-code is $[p_{Init} \ \dot{p}_{Init} \ \ddot{p}_{Init}]^T_{t_0 \to t_f}$. The simulated TCP position is $[p_{TCP} \ \dot{p}_{TCP} \ \ddot{p}_{TCP}]^T_{t_0 \to t_f}$ and the corrected trajectory $[p_{mod} \ \dot{p}_{mod} \ \ddot{p}_{mod}]^T_{t_0 \to t_f}$.

## 3 DEVIATIONS COMPENSATION

The trajectory is discretized by nodes $H_i$ between which an Hermite interpolation is carried out. Each node includes a homogeneous transformation matrix and velocity requirements for the TCP.

$$H_i = \begin{bmatrix} R_{n,i} & p_{n,i} \\ 0 & 1 \end{bmatrix}, \quad \dot{H}_i = \begin{bmatrix} \omega_{n,i} & v_{n,i} \end{bmatrix} \tag{7}$$

where $R_{n,i}$ the rotation matrix of node $i$ whose $z$ axis correspond to the tool orientation, $p_{n,i}$ the TCP position, $\omega_{n,i}$ and $v_{n,i}$ the rotational and translational velocities respectively.

The aim is to model the trajectory using a minimal number of nodes. The first step of the compensation method is to detect the areas where the deviation is problematic in order to act on the existing nodes position to reduce the machining error and possibly place additional nodes. A first correction is carried out using the mirroring approach for each node, which consists in applying at the trajectory nodes the error between the actual TCP position and the node position. This correction intends to compensate mainly the deviations from static forces, such as the impact of gravity on the structure.

Afterwards, the operation is simulated to determine the deviation at each time step. A correction is then applied on the nodes having an impact on the machining, i.e. the nodes surrounding trajectory sections where the robot is milling. The updated trajectory is the input for the following simulation. This correction is computed as the mean machining error caused for the upcoming path section, meaning that the node $i$ is replaced depending on the machining error accumulated in path section $i \to i+1$. The deviations of a dynamical nature are thus taken into account since this error is computed with the system response from the integration in time of the equation of motions. The trajectory $\mathbf{H}$ is updated at each iteration $k$ with the modified position of the nodes $\mathbf{H_{mod}}$. It allows to anticipate the deviation, in particular for the entry, and accept to deviate from the ideal trajectory while the TCP is outside the matter if it is in the interest of reducing the machining error.

https://doi.org/10.3311/ECCOMASMBD2021-139

Once the nodes have been repositioned at best, the global machining error is compared to a threshold and if the gap is still too important, a node is added in the critical position, being the location presenting the highest deviation. Finally, when the error is under the threshold, the trajectory is sent to the optimization layer where, in addition to the position, the velocity at each of the nodes will be considered as a design variable. The node-repositioning algorithm is presented in Fig. 2.

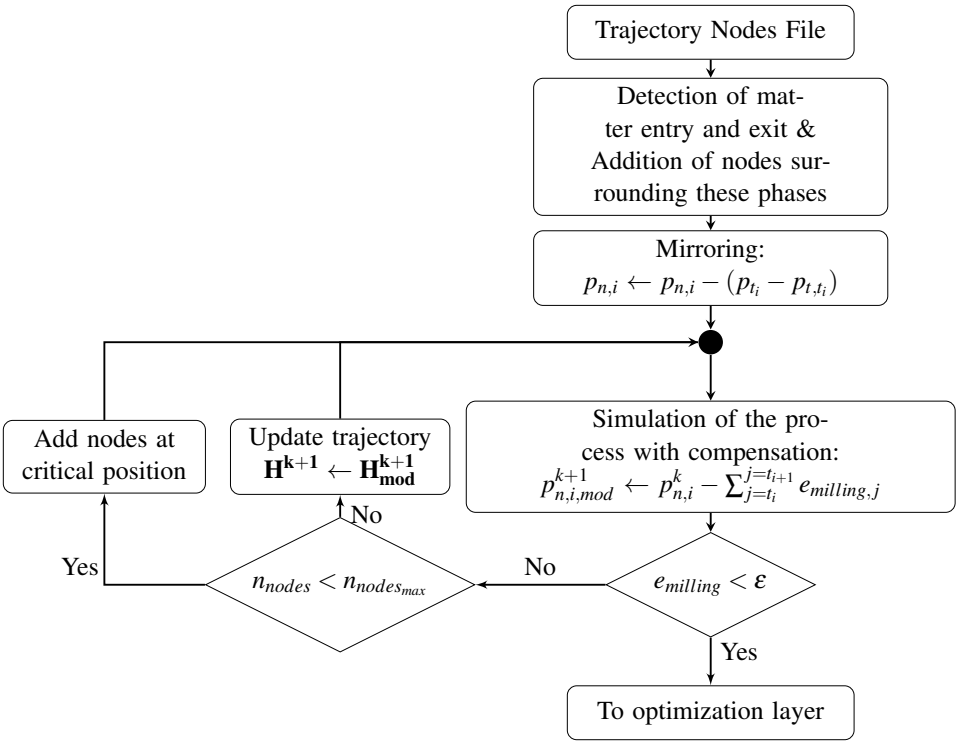


Figure 2: Trajectory nodes repositioning algorithm.

## 4 TRAJECTORY NODES OPTIMIZATION

Once the nodes have been replaced based on successive simulations of the dynamical system, a finer result can be obtained by acting on the velocity $v_{n,i}$ as well as the position $p_{n,i}$ of the nodes linked to the machining. The optimization problem is given in the following equation:

$$\min_{\mathrm{p}_{n,i},\mathrm{v}_{n,i},\mathrm{p}_{n,i+1},\mathrm{v}_{n,i+1}} cost = \sum_{k=0}^{N} \|\mathrm{p}_{TCP} - \mathrm{p}_t\|_2^2 \cdot \gamma_k \tag{8}$$

where the parameters are successive nodes $(n_i, n_{i+1})$ positions and velocities, $p_{TCP}$ is the tool center point position, $p_t$ the ideal path and $\gamma_k$ is a weighting factor equal to 1 while machining and 0 else where and $N$ is the number of observation points, i.e. the number of time steps to simulate the process from $t_0$ to $t_f$. In order to reduce the design variables research horizon and remain in feasible areas, boundaries $[x_l\,;x_u]$ are imposed by logarithmic barrier transformation $tr(x)$ as presented in Eq. 9. As stated before, a deterministic method is preferred, hence quasi-Newtonian l-BFGS is selected.

$$\begin{aligned} tr(x) &= \ln(x - x_l) - \ln(x_u - x) \\ tr^{-1}(y) &= \frac{e^y x_u + x_l}{1 + e^y} \end{aligned} \tag{9}$$

For the sake of readability, the legend of the curves used in Figs. 4a,5,7a,8 and 9b is detailed and kept along the paper. The red dashed line with circles (- -●- -) represents the trajectory sent to the system and the without symbol one (- - -) gives the system response. The blue dashed line with triangles (- -▲- -) shows the trajectory after the node repositioning algorithm and the corresponding

tool motion without symbols (- - -) .The final compensated trajectory sent to system is presented with the green dashed line with squares (- ■ -) and the full line (——) represent the final tool motion. Finally, the dotted line (·····) line shows the moments the tool enters and leaves the matter.

The machining operation performed by the aforementioned systems is the face milling of a Al6060 block with a flat-end mill of diameter $D_{tool} = 10$ mm with 2 teeth presenting a 30° helix angle in half-immersion over a cutting dept of 2 mm. The spindle rotation speed is 11250 RPM for a feed per tooth of 0.13 mm/tooth. The trajectory is limited to a single pass along the $y$ axis. The nodes added are then the ones surrounding the entry and exit and one at the middle of the part (since the section with the highest error is between entry and exit).

### 4.1 Tool mass system

In the first instance, the node replacement with optimization layer has been carried out for the simplified tool-mass model represented in Fig. 3. This system is composed of a mass connected to a support with a pair of spring/damper along the $x$ and $y$ directions. The motion of the support is imposed by the trajectory. The inertia parameters as well as stiffness and damping values were chosen such as the tool-mass exhibits a rather similar deflection behavior than the TX200 for this kind of machining operations which results in $M = 200kg$, $k = 100kN/m$ and $c = 4kN.s/m$.

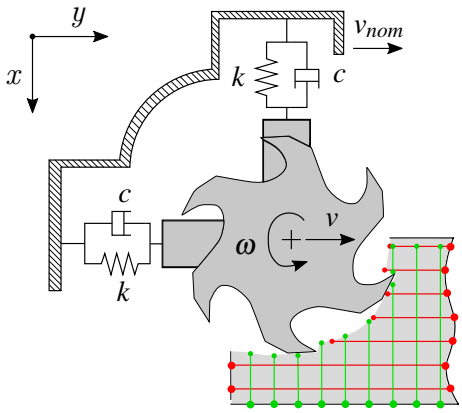


Figure 3: Simplified system, consisting of a tool attached, through spring-damper pairs, to a support moving along $y$ direction and machining a workpiece in half-immersion.

The result of the repositioning algorithm and the optimization of the nodes positions and velocities is presented in Fig. 4a, where the amplitude of the error is already strongly reduced in the milling area with the first compensation stage (- - -). The optimization layer managed to reduce the amplitude of the gap at the entry and exit as shown in Fig. 5. The evolution of the cost function along the corrections is displayed in Fig. 4b. The optimization layer does not bring strong improvement since its contribution is mainly located around the entry and exit.

### 4.2 Two degree of freedom flexible system

The second system implemented is a two-degree-of-freedom system with additional flexibility at the articulations presented in Fig. 6. This model introduces coupling between $q_1$ and $q_2$ and non-linearity between the task space and the operational space since the actuated degrees of freedom are the joints angular positions. The first body ($s_1$) is linked to the ground through the motor where the gearbox flexibility is modeled by a torsional spring-damper pair (Eq. 5). The motor actuating the second link $s_2$ is located at the tip of $s_1$, with the gearbox flexibility modeled in the same way. The unactuated degrees-of-freedom representing the articular deflection are gathered in $\mathrm{q}_u = \begin{bmatrix} q_3 & q_4 \end{bmatrix}^T$. An additional mass $s_3$ is placed at the tip of the body $s_2$ in order to represent the equivalent charge of the spindle. Just as the tool-mass model, the machining operation is the

https://doi.org/10.3311/ECCOMASMBD2021-139

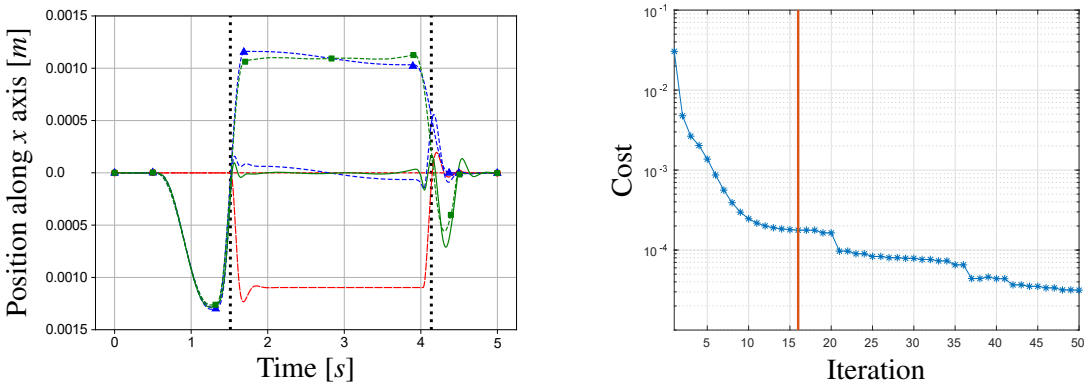


(a) (b)

Figure 4: (a) Evolution of the tool trajectories along $x$ direction throughout the correction procedure for the tool-mass system. Legend is given in Sec. 4. (b) Evolution of the cost function. The line (—) symbolize the demarcation between the node repositioning and the optimization layer.

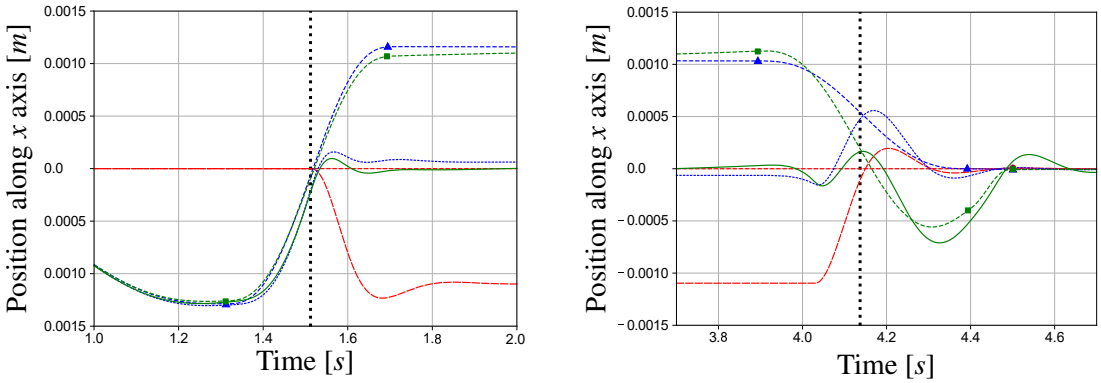


(a) (b)

Figure 5: Close-up views of the trajectories for the tool-mass system presented in Fig. 4a for entry (a) and exit (b) of matter.

surface milling in half-immersion of the tool along the $y$ axis. The inertia properties are chosen to behave the same way as the machining robot does.

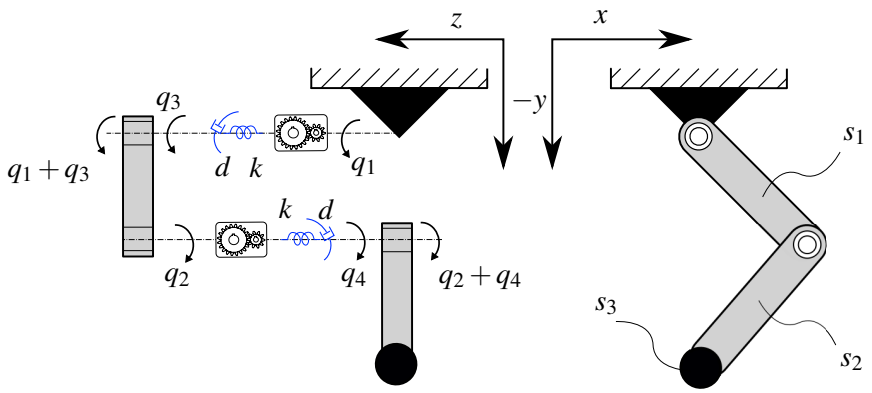


Figure 6: Two actuated degrees-of-freedom system with articular flexibility. Solids $s_1$ and $s_2$ are the robot links and $s_3$ is a mass supporting the tool. The articular flexibility is represented by the deflections $q_3$ and $q_4$ with the torsional springs and dampers $k$ and $d$.

https://doi.org/10.3311/ECCOMASMBD2021-139

Similarly to the tool-mass model, the tracking error is reduced within the machining part of the trajectory. The compensated and final trajectories are shown in Fig. 7a and the evolution of the cost value in Fig. 7b. The anticipation of the deviation at the entry and exit resulting from the optimization layer is emphasized in Fig. 8.

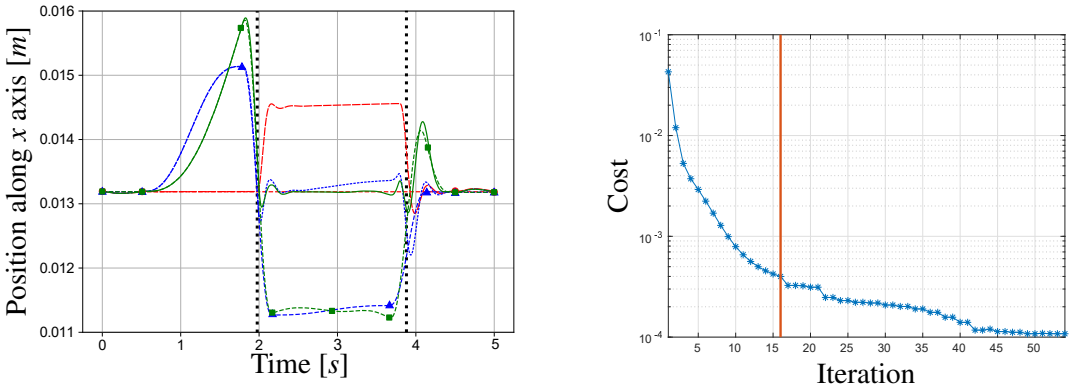


(a) (b)

Figure 7: (a) Evolution of the tool trajectories along $x$ direction throughout the correction procedure for the two-degree-of-freedom system. Legend is given in Sec. 4. (b) Evolution of the cost function for the trajectory correction of the two-degree-of-freedom system. The line (—) symbolize the demarcation between the node repositioning and the optimization layer.

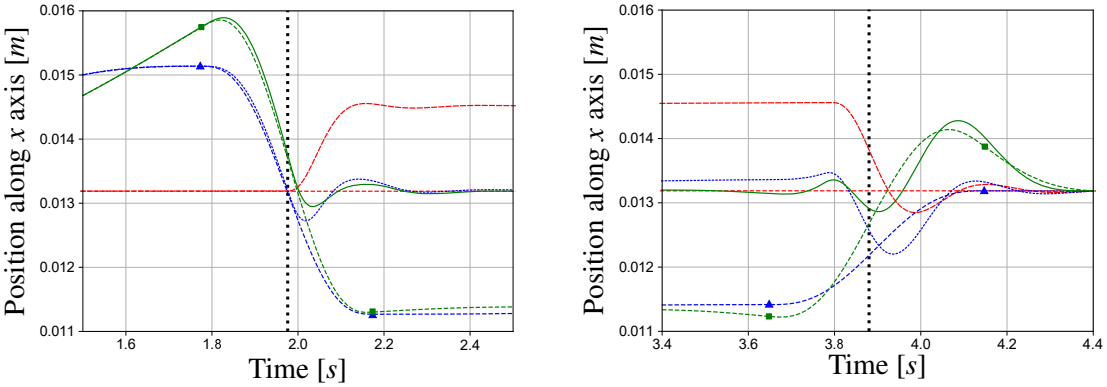


(a) (b)

Figure 8: Close-up views of the trajectories presented in Fig. 4a for entry and exit of matter.

### 4.3 Anthropomorphic Robot

The anthropomorphic robot studied in this work is the TX200 from Stäubli illustrated in Fig.9a. The multibody system includes is the result of the complete identification of the flexibility, with the tri-axial torsional flexibility model [3]. Additional degrees of freedom are then induced at the articulations and links, leading to a multiple-degrees-of-freedom system composed of six actuated degrees-of-freedom $\mathrm{q}_a = \left[q_{a,1} \ldots q_{a,6}\right]$ and 34 others $q_u$, modeling the deflections [16]. The tri-axial method consists in three torsional spring/damper pairs consecutively connected after the gearbox and oriented along each of the three local frame directions. The unactuated degrees-of-freedom at the second joint $q_{u,2}$ ($q_{x,2}$, $q_{y,2}$, $q_{z,2}$) thus represent the joint deflections and lead to the following formulation of the Body 2 center of mass ($G_{\text{Body 2}}$) location with respect to the base

https://doi.org/10.3311/ECCOMASMBD2021-139

($O_{\text{Base}}$) on which the robot is mounted

$$\begin{aligned}\mathbf{H}_{O_{\text{Base}},G_{\text{Body 2}}} =& \mathbf{H}_{O_{\text{Base}},O_{\text{Body 2}}} \cdot \mathbf{H}_{\text{rotz}}(q_{a,2}) \cdot \mathbf{H}_{\text{rotz}}(q_{z,2}) \cdot \\ & \mathbf{H}_{\text{rotx}}(q_{x,2}) \cdot \mathbf{H}_{\text{roty}}(q_{y,2}) \cdot \mathbf{H}_{O_{\text{Body 2}},G_{\text{Body 2}}} .\end{aligned} \tag{10}$$

Similarly to the two-degree-of-freedom planar robot detailed in Section 4.2, the rigid model of the robot is used for the inverse dynamics controller as well as the second order inverse kinematics (Fig. 1). As well as the previous systems, the robot is machining along the $y$ direction, maintaining the $x$ position constant. The evolution of trajectories along the $x$ direction is presented in Fig. 9b. At the exit, the dynamic deflection is well compensated however the contribution of the optimization for the entry is rather small. It can be improved by changing the weighting of the entry section in the definition of the cost function.

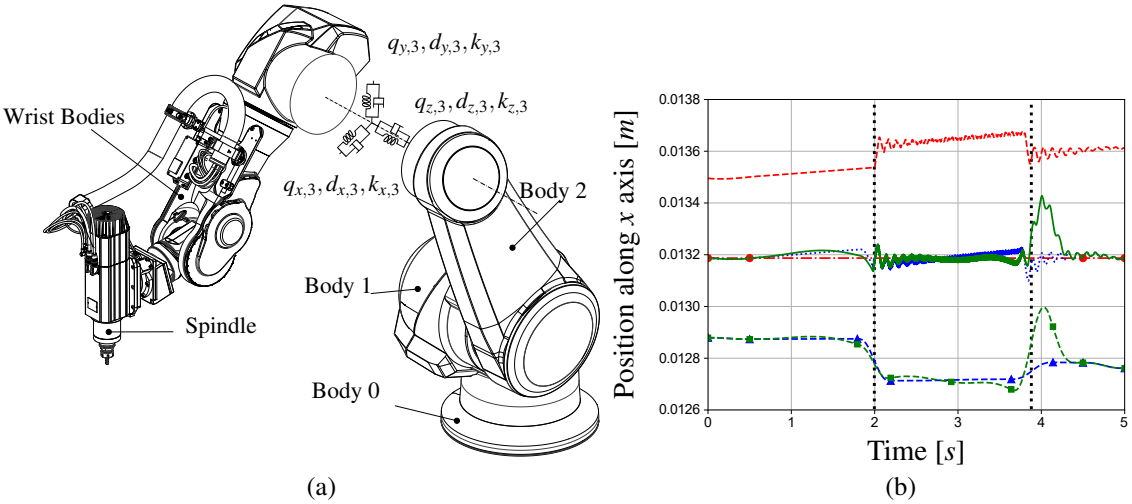


Figure 9: (a) Representation of the multibody modeling of a Stäubli TX200 robot dedicated to machining. For readability reasons, the articular flexibility is only explicitly shown for the third joint. (b) Evolution of the tool trajectories along $x$ direction throughout the correction procedure for the TX200 robot model. Legend is given in Sec. 4.

## 5 PERSPECTIVES

As a perspective of development, a stronger contribution can be given to the optimization part. A refinement of the cost function is to be considered, where, instead of using the accumulated positioning error obtained by the comparison of trajectories, the difference between the ideal workpiece (in a dexel form) and the workpiece resulting from the simulation is proposed. The importance is centered on the realization of the expected workpiece and no longer on the accomplishment of a trajectory. Since the machining is preferred at constant velocity for stability and surface quality reasons, a penalty in the norm of the TCP velocity may be added. The improved cost function is presented as follows :

$$J = \sum_{i=0}^{N_x} d_{\Delta,x,i} + \sum_{j=0}^{N_y} d_{\Delta,y,j} + \sum_{k=0}^{N_z} d_{\Delta,z,k} + \sum_{l=0}^{N_t} \gamma_l \cdot \| \mathrm{v}_{TCP,s_l} - \mathrm{v}_{TCP,t_l} \| \cdot dt \tag{11}$$

where $d_{\Delta,x,i}$ represents the difference between the dexel $i$ along the $x$ axis obtained from the simulation with the corresponding one from the ideal workpiece. The illustration of the difference between dexels workpiece in given in Figure 10. The time code of the trajectory nodes can be included in the design variables set in order to enable the nodes to be more moving.

Furthermore, a balance between the two correction layers (node-repositioning/introduction and optimization) to define an optimal amount of nodes to be added for a sufficient pre-compensation.

https://doi.org/10.3311/ECCOMASMBD2021-139

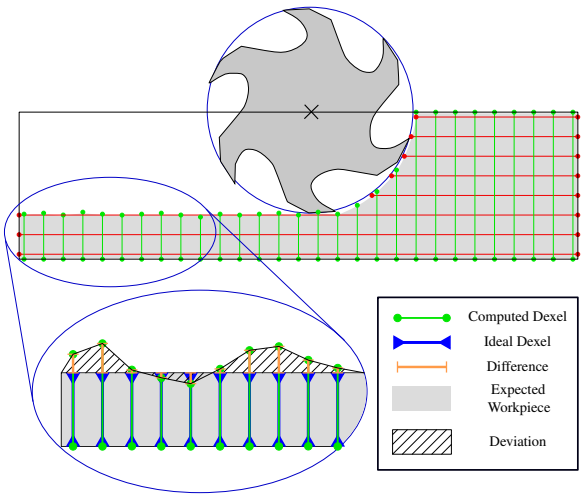


Figure 10: Determination of difference between the ideal workpiece and the resulting workpiece from the dynamic simulation.

Finally, further investigation and tests are being considered for complex multibody systems, such as the TX200 robot model, to challenge the proposed method. For such applied case, experimental validation is planned. The dexel approach opens the perspective of more complex trajectories to be simulated [17], the deployment of the method is intended for 5-axis operations.

## 6 CONCLUSIONS

Robotic machining is a growing technology but suffers from the lack of accuracy for hard-material machining, mainly caused by the overall structure flexibility. An in-dept studies of the phenomena allowed to model the flexibilities. Using these models, it is then possible to estimate, up to a certain accuracy, the deflections at the tool-tip caused by the machining forces. Within the frame of Industry 4.0, these models are virtual twins of the operation, and can be used to predict the behavior of the robot as well as the result. The machine models can be expressed as under-actuated multibody systems, where some degrees-of-freedom are the articulations and others represents deflections.

This article presents a method taking advantage of such models to build a tool trajectory, expressed in the operational space, anticipating the deviations from static and dynamic nature while subjected to machining forces. The method is employed on under-actuated multibody systems of increasing complexity with flexibility. The reduction of the deviation can be improved by varying the cost function as well as the amount of added nodes. For more complex systems as the one presented, the simulation time becomes a constraint since the optimization layer requires several iterates to propose improvements.

## ACKNOWLEDGMENTS

The authors would like to acknowledge the Belgian National Fund for Scientific Research (FNRS-FRS) for the grant allotted to V. Dambly.

## REFERENCES

[1] Kim, S.H., Nam, E., Ha, T., Hwang, S.H., Lee, J., Park, S.h., Min, B.K.: Robotic machining: A review of recent progress. International Journal of Precision Engineering and Manufacturing **20** (08 2019)

[2] Verl, A., Valente, A., Melkote, S., Brecher, C., Ozturk, E., Tunc, T.: Robots in machining. CIRP Annals (06 2019)

[3] Huynh, H.N., Assadi, H., Dambly, V., Rivière-Lorphèvre, E., Verlinden, O.: Direct method for updating flexible multibody systems applied to a milling robot. Robotics and Computer-Integrated Manufacturing **68** (04 2021)

[4] Reinl, C., Friedmann, M., Bauer, J., Pischan, M., Abele, E., Von Stryk, O.: Model-based off-line compensation of path deviation for industrial robots in milling applications. IEEE/ASME International Conference on Advanced Intelligent Mechatronics, AIM (07 2011) 367–372

[5] Klimchik, A., Bondarenko, D., Pashkevich, A., Briot, S., Furet, B.: Compliance error compensation in robotic-based milling. Informatics in Control, Automation and Robotics **283** (09 2014)

[6] Zaeh, M., Schnoes, F., Obst, B., Hartmann, D.: Combined offline simulation and online adaptation approach for the accuracy improvement of milling robots. CIRP Annals **69** (05 2020)

[7] Mamedov, S., Popov, D., Mikhel, S., Klimchik, A.: Compliance error compensation based on reduced model for industrial robots. 15th International Conference on Informatics in Control, Automation and Robotics (01 2018) 180–191

[8] Kaldestad, K., Hovland, G.: Off-line path correction of robotic face milling using static tool force and robot stiffness. (09 2015) 5506–5511

[9] Schnoes, F., Zaeh, M.: Model-based planning of machining operations for industrial robots. Procedia CIRP **82** (01 2019) 497–502

[10] Cordes, M., Hintze, W.: Offline simulation of path deviation due to joint compliance and hysteresis for robot machining. The International Journal of Advanced Manufacturing Technology **90** (04 2017)

[11] Brüls, O., Bastos, G.J., Seifried, R.: A Stable Inversion Method for Feedforward Control of Constrained Flexible Multibody Systems. Journal of Computational and Nonlinear Dynamics **9**(1) (10 2013) 011014.

[12] Altintas, Y., Kersting, P., Biermann, D., Budak, E., Denkena, B., Lazoglu, I.: Virtual process systems for part machining operations. CIRP Annals - Manufacturing Technology **63** (12 2014)

[13] Huynh, H.N., Rivière-Lorphèvre, E., Ducobu, F., Ozcan, A., Verlinden, O.: Dystamill: a framework dedicated to the dynamic simulation of milling operations for stability assessment. The International Journal of Advanced Manufacturing Technology **98**(5) (2018) 2109–2126

[14] Altintas, Y., Engin, S.: Generalized modeling of mechanics and dynamics of milling cutters. Cirp Annals-manufacturing Technology - CIRP ANN-MANUF TECHNOL **50** (12 2001) 25–30

[15] Siciliano, B., Sciavicco, L., Luigi, V., Oriolo, G.: Robotics: Modelling, Planning and Control. (01 2009)

[16] Hoai Nam, H.: Robotic machining: Development and validation of a numerical model of robotic milling to optimise the cutting parameters. PhD thesis, University of Mons (09 2019)

[17] Dambly, V., Huynh, H.N., Verlinden, O., Rivière-Lorphèvre, E.: Development of tri-dexel based cutting simulator for cutter-workpiece engagement and cutting forces determination. (06 2021) 399–402

https://doi.org/10.3311/ECCOMASMBD2021-206



# Analytical Port Inversion For A Flexible Model In The Two-Input Two-Output Port Approach

**A. Finozzi**[1], **F. Sanfedino**[1], **D. Alazard**[1]

[1] Institut Supérieur de l'Aéronautique
et de l'Espace (ISAE-SUPAERO)
Université de Toulouse
31055 Toulouse, FRANCE
[antonio.finozzi, daniel.alazard, francesco.sanfedino]@isae-supaero.fr

**ABSTRACT**

In the context of multi-body modeling techniques, this paper introduces a new analytical approach to build a Two-Input-Two-Output Port (TITOP) model for a *clamped-clamped* flexible appendage. By expanding the previous work found in literature, which relied on numerical procedures, this model represents a fundamental block for the construction of parametric multi-body systems in a sub-structuring approach, such as closed-loop kinematic mechanisms. Specifically, this new procedure allows to assemble a linear state-space system by analytically inversing the input-output channels of the original *clamped-free* TITOP model. This analytical method presents the advantage of avoiding non-physical behaviors introduced by numerical inversions as well as removing the need to reduce the quasi-zero poles associated with the non-analytical model. This paper presents the mathematical formulation of the system, as well as the formalism behind the method, and an illustrative case study to showcase the advantages of this approach.

**Keywords:** Multibody dynamics, Analytical Inversion, Linear System, Closed-Loop Kinematics.

## 1 INTRODUCTION

In the past decades, structural and control co-design has attracted a lot of attention due to its ability of merging multiple multidisciplinary requirements in a single design flow. Moreover, the increasing use of large structures and appendages for Space applications has rendered flexible modal analysis mandatory for the design of proper spacecraft control laws.

In order to tackle the non-trivial modeling and analysis of these large and complex space systems, a sub-structuring technique using a multi-body approach is often considered to conceptually simplify the model. Seeing the overall structure as an assembly of multiple simpler sub-systems with increasing complexity has also the advantage of handling different types of boundary conditions at block assemblage level and easy sub-system validation.

The wide use of this approach for space applications has raised a significant interest in the development of proper modeling techniques that can prove to be versatile enough to account for multiple multi-body configurations, ranging from open-loop chains to closed-loops mechanisms.

Many sub-structuring techniques can be found in literature. A common approach relies on approximations linked to the Finite Element Method (FEM) or the Assumed Modes Method (AMM) [1]. However, these methods are heavily influenced by the set of predetermined boundary conditions assigned to the model, which may be drastically variable,

https://doi.org/10.3311/ECCOMASMBD2021-206

for example by time-varying mass changes in the system. Another approach often used is the Transfer Matrix Method (TMM) [2], which creates a transfer matrix that links up the state vectors (generalized accelerations and forces) of the two extremities of the flexible body. This has also been linked with the Finite Element Method in order to reduce computational times in solving the eigenvalue problem (FE-TMM). These methods are particularly well suited for serially connected bodies and open-chain structures. Their major drawback is the inversion problems of the model, whose matrices may be non-square or non-invertible depending on the boundary conditions. Moreover, these approaches are not optimal for a multi-body tree-like structures, where multiple appendages are connected to a single central parent body: in this case the interest is finding the dynamic relation between state vectors in the same root point for each sub-structure. Methods based on effective mass/inertia of the appendages [3] represent a viable option to solve this last problem, but they lose the complete vibrational behavior description, as they aim at delivering only the dynamic relation of state variable at the appendage root point with a simplified model of the body.

The Two-Input-Two-Output Port (TITOP) Model, a direct dynamic approach initially proposed in [4], overcomes these issues. The structure is conceived as a minimal state-space transfer between the accelerations and wrenches at the extremity points of the appendage and embeds both the direct and inverse dynamics: the IN/OUT channels are easily numerically invertible to account for multiple boundary conditions. Moreover, as seen in [5], this approach in a block-diagram model permits the design of closed-chain multi-body systems for any boundary conditions by creating feedback loops and inverting IN/OUT channels. These models, already implemented in a toolbox developed at ISAE-Supaero - the Satellite Dynamics Toolbox (SDT) [6]- represent the basis of this research.

Nevertheless, the application of the numerical channel inversion proposed in [5] shows some critical aspects, specifically in obtaining the *clamped-clamped* boundary conditions. For this boundary condition configuration twelve rigid modes are expected to be at exactly zero frequency. However, because of numerical issues in the channel inversion, these modes present a quasi-null value instead. This issue, which may seem trivial at single beam level, can have a huge impact in the context of sub-structuring models: it may introduce numerical issues due to block repetitions as well as increasing the effort for model reduction at global structure level.

This research therefore proposes a new approach to obtain a TITOP *clamped-clamped* model, introducing a novel analytical procedure to invert the TITOP channels to obtain a model which does not present the previously discussed numerical issues. This was achieved by relying on a modal transformation of the state variables, distinguishing from flexible and junction modes, as introduced in [3] and later on applied by [7].

In the first section, the general formalism used to define flexible and junction modes is detailed, as well as how these concepts were applied to the formulation of the TITOP model. This will outline the basis for the mathematical formulation of the analytically inverted TITOP model presented in section 3. A simple example finally proves the increased accuracy of the proposed framework.

https://doi.org/10.3311/ECCOMASMBD2021-206

## 2 ANALYTICAL BEAM MODEL

### 2.1 Formalism Adopted

Let us consider a generic flexible appendage. A common approach used to characterize its vibrational response is to use modal analysis to find normal modes whose superposition describes the flexible behavior of the body.

The formalism adopted in this paper slightly varies from this classic approach. The vector of Degrees of Freedom (DOFs) $\mathbf{u}$ is divided into two sub-vectors, using the formalism proposed in [3]: internal DOFs $\mathbf{u}_i$ and junction DOFs $\mathbf{u}_j$. The latter are generally associated to boundary conditions or interfaces with other bodies. They are mostly reserved for parts of the structure where a generic imposed motion is applied. While the internal DOFs respond with a motion $\mathbf{u_i}, \dot{\mathbf{u}}_\mathbf{i}, \ddot{\mathbf{u}}_\mathbf{i}$ to a force/torque forcing term $\mathbf{F_i}$, the junction DOFs respond with a reaction force/torque $\mathbf{F_j}$ to an imposed motion-type excitation $\mathbf{u_j}, \dot{\mathbf{u}}_\mathbf{j}, \ddot{\mathbf{u}}_\mathbf{j}$. The equations of motion for a dynamic system may be written according to the following subdivision of the DOFs:

$$\begin{bmatrix} \mathbf{M}_{ii} & \mathbf{M}_{ij} \\ \mathbf{M}_{ij}^T & \mathbf{M}_{jj} \end{bmatrix} \begin{bmatrix} \ddot{\mathbf{u}}_i \\ \ddot{\mathbf{u}}_j \end{bmatrix} + \begin{bmatrix} \mathbf{C}_{ii} & \mathbf{C}_{ij} \\ \mathbf{C}_{ij}^T & \mathbf{C}_{jj} \end{bmatrix} \begin{bmatrix} \dot{\mathbf{u}}_i \\ \dot{\mathbf{u}}_j \end{bmatrix} + \begin{bmatrix} \mathbf{K}_{ii} & \mathbf{K}_{ij} \\ \mathbf{K}_{ij}^T & \mathbf{K}_{jj} \end{bmatrix} \begin{bmatrix} \mathbf{u}_i \\ \mathbf{u}_j \end{bmatrix} = \begin{bmatrix} \mathbf{F}_i \\ \mathbf{F}_j \end{bmatrix} \tag{1}$$

where we can identify the three fundamental symmetrical matrices: the mass matrix $\mathbf{M}$, the damping matrix $\mathbf{C}$ and the stiffness matrix $\mathbf{K}$, each one composed of sub-matrices associated with both types of DOFs (internal and junction). The modes are obtained by analyzing the homogeneous undamped harmonic equations of motion. To obtain the homogeneous system, the forcing terms $\mathbf{F}_i$ and $\mathbf{u}_j$ are suppressed from the previous equation. Additionally, the undamped equations are considered by setting the whole damping matrix $\mathbf{C} = \mathbf{0}$. This approach leads to two sets of equations: the first one allows for the definition of the normal modes.

$$\mathbf{M}_{ii}\ddot{\mathbf{u}}_\mathbf{i} + \mathbf{K}_{ii}\mathbf{u}_i = \mathbf{0} \tag{2}$$

The normal modes of the system, denoted with $\mathbf{\Phi}_{ik}$, can be derived by imposing the harmonic solution $\mathbf{u_i} = \mathbf{U}_i e^{j\omega t}$:

$$(-\omega^2 \mathbf{M}_{ii} + \mathbf{K}_{ii})\mathbf{U}_i = 0 \tag{3}$$

By solution of the corresponding eigenvalue problem, the eigenvalues $\omega_k$ are obtained, as well as the normal eigenmodes $\mathbf{\Phi}_{ik}$ where $k$ denotes the association with the $k$-eigenvalue frequency $f_k = \frac{\omega_k}{2\pi}$. These modes have diagonalizing properties on both $\mathbf{M}_{ii}$ and $\mathbf{K}_{ii}$.

Furthermore, it is possible to define static modes denoted as junction modes $\mathbf{\Psi}$ by imposing a unit displacement $\mathbf{u}_j = 1$ on the second homogeneous undamped equation derived from Eq. 1. These modes verify:

$$\begin{aligned} &\mathbf{\Psi}_{jj} = \mathbf{I}_{jj}, \quad \mathbf{K}_{ii}\mathbf{\Psi}_{ij} + \mathbf{K}_{ij} = 0 \\ &\implies \mathbf{\Psi}_{ij} = -\mathbf{K}_{ii}^{-1}\mathbf{K}_{ij} \end{aligned} \tag{4}$$

An important remark is that the static modes can be interpreted as static transmissibility in displacements between the DOFs $i$ and $j$. The two sets of modes can be exploited to perform a modal superposition in order to describe the displacement vector $\mathbf{u} = [\mathbf{u}_i, \mathbf{u}_j]^T$ as described as follows:

$$\begin{bmatrix} \mathbf{u}_i \\ \mathbf{u}_j \end{bmatrix} = \begin{bmatrix} \mathbf{\Phi}_{ik} & \mathbf{\Psi}_{ij} \\ \mathbf{0} & \mathbf{I}_{jj} \end{bmatrix} \begin{bmatrix} \boldsymbol{\eta}_k \\ \mathbf{u}_j \end{bmatrix} \tag{5}$$

https://doi.org/10.3311/ECCOMASMBD2021-206

The first row expresses the absolute displacement $\mathbf{u}_i$ as composed by an interpolation of internal relative DOFs, given by modal coordinates $\boldsymbol{\eta}_k$, and junction displacements $\mathbf{u}_j$. The second row states that the junction displacements are conserved. By performing this superposition, a new set of equations of motion can be derived from Eq. 1:

$$\begin{bmatrix} \mathbf{m}_{kk} & \mathbf{L}_{kj} \\ \mathbf{L}_{kj}^T & \overline{\mathbf{M}}_{jj} \end{bmatrix} \begin{bmatrix} \ddot{\boldsymbol{\eta}}_k \\ \ddot{\mathbf{u}}_j \end{bmatrix} + \begin{bmatrix} \mathbf{c}_{kk} & \mathbf{0}_{jk}^T \\ \mathbf{0}_{jk} & \mathbf{0}_{jj} \end{bmatrix} \begin{bmatrix} \dot{\boldsymbol{\eta}}_k \\ \dot{\mathbf{u}}_j \end{bmatrix} + \begin{bmatrix} \mathbf{k}_{kk} & \mathbf{0}_{jk}^T \\ \mathbf{0}_{jk} & \overline{\mathbf{K}}_{jj} \end{bmatrix} \begin{bmatrix} \boldsymbol{\eta}_k \\ \mathbf{u}_j \end{bmatrix} = \begin{bmatrix} \boldsymbol{\Phi}_{ik}^T \mathbf{F}_i \\ \boldsymbol{\Psi}_{ij}^T \mathbf{F}_i + \mathbf{F}_j \end{bmatrix} \tag{6}$$

Where:

- $\mathbf{m}_{kk} = \boldsymbol{\Phi}_{ik}^T \mathbf{M}_{ii} \boldsymbol{\Phi}_{ik}$: diagonal matrix of generalized masses $m_k$. By selecting a normalized set of $\boldsymbol{\Phi}_{ik}$, it corresponds to the identity matrix $\mathbf{I}_{kk}$;
- $\mathbf{c}_{kk} = \boldsymbol{\Phi}_{ik}^T \mathbf{C}_{ii} \boldsymbol{\Phi}_{ik}$: matrix of generalized damping. *A priori* this matrix is fully populated but under hypothesis of proportional damping w.r.t mass and stiffness or lightly damped structure the matrix can be considered diagonal with $\mathbf{c}_{kk} = diag(2\omega_k \xi m_k)$, where $\xi$ is the damping coefficient for the appendix;
- $\mathbf{k}_{kk} = \boldsymbol{\Phi}_{ik}^T \mathbf{K}_{ii} \boldsymbol{\Phi}_{ik}$: diagonal mass of generalized stiffness $k_k = m_k \omega_k^2$;
- $\mathbf{L}_{kj} = \boldsymbol{\Phi}_{ik}^T [\mathbf{M}_{ii} \mathbf{M}_{ij}] \begin{bmatrix} \boldsymbol{\Psi}_{ij} \\ \mathbf{I}_{jj} \end{bmatrix} = \boldsymbol{\Phi}_{ik}^T (\mathbf{M}_{ii} \boldsymbol{\Psi}_{ij} + \mathbf{M}_{ij})$: matrix of participation factors. It expresses the coupling between the normal and junction modes.
- $\overline{\mathbf{M}}_{jj} = \boldsymbol{\Psi}_{ij}^T \mathbf{M}_{ii} \boldsymbol{\Psi}_{ij} + \boldsymbol{\Psi}_{ij}^T \mathbf{M}_{ij} + \mathbf{M}_{ij}^T \boldsymbol{\Psi}_{ij} + \mathbf{M}_{jj}$: condensed mass matrix. In the case of a rigid statically determined junction $j = r$, it is equal to structure rigid body mass matrix which includes its properties on mass, center of mass and inertia relative to the unique node reference frame.
- $\overline{\mathbf{K}}_{jj} = \mathbf{K}_{jj} - \mathbf{K}_{ij}^T \mathbf{K}_{ii} \mathbf{K}_{ij}$: condensed stiffness matrix. In the case of a rigid statically determined junction, it is equal to zero.

The formalism introduced here has been applied directly to TITOP models to perform modal analysis in [7]. In the following section the same procedure will be applied specifically for the TITOP beam model and it will provide the fundamental basics for the analytical inversion described in section 3.

### 2.2 Application to TITOP Model

#### 2.2.1 TITOP Model Presentation

Let us consider a uniform flexible appendage $\mathcal{L}_i$ as in Fig. 1, defined by means of two points: point $P$, the point to which the flexible appendage is linked to a parent structure $\mathcal{L}_{i-1}$, and point $C$, where a child body $\mathcal{L}_{i+1}$ is linked to the beam.

In the beam model of the appendage $\mathcal{L}_i$, *clamped-free* boundary conditions are considered: the joint at point $P$ is considered rigid and statically determinate, with the parent body $\mathcal{L}_{i-1}$ imposing a motion on $\mathcal{L}_i$, while point $C$ is internal and unconstrained and the action of $\mathcal{L}_{i+1}$ is by mean of a transmitted effort. This can be done without any loss of generality as seen in [5].

The flexible appendix is modeled using a beam model, taken from [6], which describes the 3D vibrational behavior of $\mathcal{L}_i$ by considering its bending in planes $(x, z)$ and $(x, y)$, torsion around the $x$-axis and traction along the $x$-axis in the local frame $\mathcal{R}_0$. The resulting TITOP model $\mathbf{D}_{PC}^{\mathcal{L}_i}(s)$, displayed in Fig. 1, is a $\{12 \times 12\}$ linear dynamic model function of the Laplace variable $s$. Its inputs are:

https://doi.org/10.3311/ECCOMASMBD2021-206

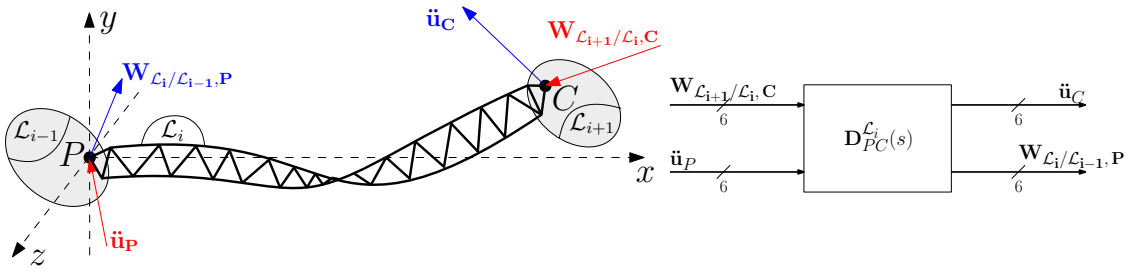


**Figure 1**. TITOP model and nomenclature for a generic flexible appendage $\mathcal{L}_i$

- $\mathbf{W}_{\mathcal{L}_{i+1}/\mathcal{L}_i,C}$: The $\{6\times1\}$ Wrench (Forces and Torques) exerted by the body $\mathcal{L}_{i+1}$ to $\mathcal{L}_i$ at point C;
- $\ddot{\mathbf{u}}_P$: The $\{6\times1\}$ accelerations (linear and angular) imposed by the parent body $\mathcal{L}_{i-1}$ at point $P$ to $\mathcal{L}_i$;

while the outputs are:

- $\ddot{\mathbf{u}}_C$: The $\{6\times1\}$ components of the accelerations of point $C$;
- $\mathbf{W}_{\mathcal{L}_i/\mathcal{L}_{i-1},P}$: The $\{6\times1\}$ Wrench (Forces and Torques) transferred by $\mathcal{L}_i$ to the parent structure $\mathcal{L}_{i-1}$ at point P.

### 2.2.2 Mathematical Formulation

The vector of DOFs used in the description of the vibrational behaviors is assembled in order to contain two distinct entities: the kinematic parameters of point $P$ and the relative deformation at point $C$ with respect to point $P$. The beam is defined by the main direction of vector $\overline{PC}$, which defines the x-axis of the local frame of reference. This mathematical formulation stems from the one proposed in [5], where a full description of the DOFs and the corresponding structural matrices can be found.

For the two bending models, the first 4 modes are considered and the DOFs adopted are reported in Eq. 7 and Eq. 8.

$$\widetilde{\mathbf{q}} = \left[y_P,\, \Phi^z_P,\, \frac{T_{bPz}}{EI_z},\, y_C - l\Phi^z_P - y_P,\, \Phi^z_C - \Phi^z_P,\, \frac{T^z_{bC}}{EI_z}\right]^T \tag{7}$$

$$\widetilde{\mathbf{p}} = \left[z_P,\, \Phi^y_P,\, \frac{T^y_{bP}}{EI_y},\, z_C - l\Phi^y_P - z_P,\, \Phi^y_C - \Phi^y_P,\, \frac{T^y_{bC}}{EI_y}\right]^T \tag{8}$$

Here we denote with $(y_P,\, z_P)$ and $(y_C,\, z_C)$ the displacement components of $\mathbf{u}_P$ and $\mathbf{u}_C$ along the corresponding axis. In the same manner, $(\Phi^z_P,\, \Phi^y_P)$ and $(\Phi^z_C,\, \Phi^y_C)$ are the angular slopes of the deflection on the indicated axis. Finally, $(T^y_{b,C},\, T^z_{b,C})$ and $(T^y_{b,P},\, T^z_{b,P})$ are the bending moments at the two endpoints.

By means of the DOFs introduced in Eq. 7 and Eq. 8, both mass and stiffness matrices may be derived, which are denoted with $\widetilde{\mathbf{M}}_\mathbf{y}$, $\widetilde{\mathbf{K}}_\mathbf{y}$ for $(x,y)$ bending and $\widetilde{\mathbf{M}}_\mathbf{z}$, $\widetilde{\mathbf{K}}_\mathbf{z}$ for $(x,z)$ bending.

The same approach may be applied for torsion and axial deformations, by taking into account the DOFs vector of Eq. 9-10, originally proposed by [5]:

$$\widetilde{\boldsymbol{\theta}} = \left[\theta_P,\, \theta_C - \theta_P\right]^T = \left[\theta_P,\, \delta_\theta\right]^T \tag{9}$$

$$\widetilde{\mathbf{u}}_x = \left[x_P,\, x_C - x_P\right]^T = \left[x_P,\, \delta_u\right]^T \tag{10}$$

https://doi.org/10.3311/ECCOMASMBD2021-206

In this case only their fundamental mode is taken into account. From these vectors the mass and stiffness matrices $\widetilde{\mathbf{M}}_\theta$, $\widetilde{\mathbf{K}}_\theta$ and $\widetilde{\mathbf{M}}_\mathbf{u}$, $\widetilde{\mathbf{K}}_\mathbf{u}$ are obtained.

In order to obtain the *global* mass and stiffness matrices ($\widetilde{\mathbf{M}}_\mathbf{gl}$, $\widetilde{\mathbf{K}}_\mathbf{gl}$) for the whole beam, the sub-matrices corresponding to each vibrational behavior may be assembled in a block diagonal fashion, so that it corresponds to the global DOFs vector $\widetilde{\mathbf{d}}_{gl}$.

$$\widetilde{\mathbf{d}}_{gl} = \left[\widetilde{\mathbf{q}},\, \widetilde{\mathbf{p}},\, \widetilde{\boldsymbol{\theta}},\, \widetilde{\mathbf{u_x}}\right]^T \tag{11}$$

$$\widetilde{\mathbf{M}}_\mathbf{gl} = \begin{bmatrix} \widetilde{\mathbf{M}}_\mathbf{y} & \mathbf{0} & \mathbf{0} & \mathbf{0} \\ \mathbf{0} & \widetilde{\mathbf{M}}_\mathbf{z} & \mathbf{0} & \mathbf{0} \\ \mathbf{0} & \mathbf{0} & \widetilde{\mathbf{M}}_\theta & \mathbf{0} \\ \mathbf{0} & \mathbf{0} & \mathbf{0} & \widetilde{\mathbf{M}}_\mathbf{u} \end{bmatrix}, \qquad \widetilde{\mathbf{K}}_\mathbf{gl} = \begin{bmatrix} \widetilde{\mathbf{K}}_\mathbf{y} & \mathbf{0} & \mathbf{0} & \mathbf{0} \\ \mathbf{0} & \widetilde{\mathbf{K}}_\mathbf{z} & \mathbf{0} & \mathbf{0} \\ \mathbf{0} & \mathbf{0} & \widetilde{\mathbf{K}}_\theta & \mathbf{0} \\ \mathbf{0} & \mathbf{0} & \mathbf{0} & \widetilde{\mathbf{K}}_\mathbf{u} \end{bmatrix} \tag{12}$$

A permutation on these matrices can be performed in order to obtain a DOFs division as seen in Eq. 1, through the use of a permutation matrix $\mathbf{P}$. The resulting global mass and stiffness matrices, as well as the vector of DOFs $\mathbf{d}_\mathbf{gl}$ is shown in Eq. 13 and Eq. 14. The point $P$ is a junction node, therefore we can substitute the subscript $j$ with $P$.

$$\mathbf{d}_\mathbf{gl} = \left[\mathbf{u}_P,\, \mathbf{u}_f\right]^T = \mathbf{P}\widetilde{\mathbf{d}}_{gl} \tag{13}$$

$$\mathbf{M}_{gl} = \mathbf{P}\widetilde{\mathbf{M}}_\mathbf{gl}\mathbf{P}^T = \begin{bmatrix} \mathbf{M}_{rr} & \mathbf{M}_{rf} \\ \mathbf{M}_{fr} & \mathbf{M}_{ff} \end{bmatrix}, \qquad \mathbf{K}_{gl} = \mathbf{P}\widetilde{\mathbf{K}}_\mathbf{gl}\mathbf{P}^T = \begin{bmatrix} \mathbf{0}_{rr} & \mathbf{0}_{rf} \\ \mathbf{0}_{fr} & \mathbf{K}_{ff} \end{bmatrix} \tag{14}$$

The matrix $\mathbf{M}_{rr}$ represents the mass matrix of the *rigid* body at point $P$, while $\mathbf{M}_{fr}$ and $\mathbf{M}_{rf}$ are the coupling terms between the displacement of point $P$ and the internal *flexible* DOFs of vector $\mathbf{u}_f$. The vectors $\mathbf{u}_P$ and $\mathbf{u}_f$ are given by:

$$\begin{aligned} \mathbf{u}_P &= \left[x_P,\quad y_P,\quad z_P,\quad \theta_P,\quad \Phi_P^y,\quad \Phi_P^z\right]^T \\ \mathbf{u}_f &= \Big[x_C - x_P, y_C - y_P - l\Phi_P^z, z_C - z_P - l\Phi_P^y, \theta_C - \theta_P, \\ &\qquad \Phi_C^y - \Phi_P^y, \Phi_C^z - \Phi_P^z, \frac{T_{bP}^y}{EI_y}, \frac{T_{bP}^z}{EI_z}, \frac{T_{bC}^y}{EI_y}, \frac{T_{bC}^z}{EI_z}\Big]^T \end{aligned}$$

We introduce $\boldsymbol{\tau}_{CP}$ as the kinematic link between the internal node $C$ and the junction node $P$:

$$\boldsymbol{\tau}_{CP} = \begin{bmatrix} \mathbf{I}_{3\times3}, & {}^*\mathbf{CP} \\ \mathbf{0}_{3\times3} & \mathbf{I}_{3\times3} \end{bmatrix} \tag{15}$$

Where ${}^*\mathbf{CP}$ is the skew-symmetric matrix obtained from the vector from point $C$ to point $P$. It can be verified that matrix $\boldsymbol{\tau}_{CP}$ corresponds exactly to the junction modes matrix $\boldsymbol{\Psi}_{ij}$ introduced in section 2. By performing modal analysis on this system, remarking that by imposing Eq. 4 we get $\boldsymbol{\Psi}_{ij} = 0$, the following expression can be found:

$$\begin{bmatrix} \mathbf{M}_{rr} & \mathbf{L}_{kP}^T \\ \mathbf{L}_{kP} & \mathbf{I}_{kk} \end{bmatrix} \begin{bmatrix} \ddot{\mathbf{u}}_P \\ \ddot{\boldsymbol{\eta}}_k \end{bmatrix} + \begin{bmatrix} \mathbf{0}_{PP} & \mathbf{0}_{kP} \\ \mathbf{0}_{kP}^T & \mathbf{c}_{kk} \end{bmatrix} \begin{bmatrix} \dot{\mathbf{u}}_P \\ \dot{\boldsymbol{\eta}}_k \end{bmatrix} + \begin{bmatrix} \mathbf{0}_{PP} & \mathbf{0}_{kP} \\ \mathbf{0}_{kP}^T & \mathbf{k}_{kk} \end{bmatrix} \begin{bmatrix} \mathbf{u}_P \\ \boldsymbol{\eta}_k \end{bmatrix} = \begin{bmatrix} \boldsymbol{\Phi}_{Ck}^T \mathbf{W}_{\mathcal{L}_{i+1}/\mathcal{L}_i, C} \\ \boldsymbol{\tau}_{CP}^T \mathbf{W}_{\mathcal{L}_{i+1}/\mathcal{L}_i, C} - \mathbf{W}_{\mathcal{L}_i/\mathcal{L}_{i-1}, P} \end{bmatrix} \tag{16}$$

Where:

- $\mathbf{L}_{kP} = \boldsymbol{\Phi}_{ik}^T \mathbf{M}_{fr}$
- $\mathbf{c}_{kk} = diag(2\xi_k\omega_k)$
- $\mathbf{k}_{kk} = diag(\omega_k^2)$

The state space system can be directly obtained from this formulation, thanks to the relation:

$$\ddot{\mathbf{u}}_C = \boldsymbol{\Phi}_{Ck}\ddot{\boldsymbol{\eta}}_k + \boldsymbol{\tau}_{CP}\ddot{\mathbf{u}}_P \tag{17}$$

https://doi.org/10.3311/ECCOMASMBD2021-206

The resulting system is therefore showcased in Eq. 18, where the state-space system $\mathbf{D}_{PC}^{\mathcal{L}_i}(s)$ is the TITOP model corresponding to the one of Fig. 1.

$$\begin{bmatrix} \dot{\boldsymbol{\eta}}_k \\ \ddot{\boldsymbol{\eta}}_k \\ \hline \ddot{\mathbf{u}}_C \\ \mathbf{W}_{\mathcal{L}_i/\mathcal{L}_{i-1},P} \end{bmatrix} = \underbrace{\left[\begin{array}{cc|cc} \mathbf{0}_{kk} & \mathbf{I}_{kk} & \mathbf{0}_{kC} & \mathbf{0}_{kP} \\ -\mathbf{k}_{kk} & -\mathbf{c}_{kk} & \boldsymbol{\Phi}_{Ck}^T & -\mathbf{L}_{kP} \\ \hline -\boldsymbol{\Phi}_{Ck}\mathbf{k}_{kk} & -\boldsymbol{\Phi}_{Ck}\mathbf{c}_{kk} & \boldsymbol{\Phi}_{Ck}\boldsymbol{\Phi}_{Ck}^T & (\boldsymbol{\tau}_{CP}-\boldsymbol{\Phi}_{Ck}\mathbf{L}_{kP}) \\ \mathbf{L}_{kP}^T\mathbf{k}_{kk} & \mathbf{L}_{kP}^T\mathbf{c}_{kk} & (\boldsymbol{\tau}_{CP}-\boldsymbol{\Phi}_{Ck}\mathbf{L}_{kP})^T & \mathbf{L}_{kP}^T\mathbf{L}_{kP}-\mathbf{M}_{rr} \end{array}\right]}_{\mathbf{D}_{PC}^{\mathcal{L}_i}(s)} \begin{bmatrix} \boldsymbol{\eta}_k \\ \dot{\boldsymbol{\eta}}_k \\ \hline \mathbf{W}_{\mathcal{L}_{i+1}/\mathcal{L}_i,C} \\ \ddot{\mathbf{u}}_P \end{bmatrix} \tag{18}$$

## 3 ANALYTICALLY INVERTED TITOP MODEL

### 3.1 TITOP Beam Models and Closed-Loop Kinematics

The TITOP beam model detailed in section 2.2 presents a specific set of boundary conditions. Despite this, the importance of handling different boundary conditions plays a fundamental role in the correct modeling of complex systems, specifically in closed-loop kinematics.

For instance, let us consider a basic closed-loop mechanism, such as a triangle, which can be used as a building block to assembly more complex structures using a sub-structuring approach.
This mechanism, composed by three flexible bodies and represented in Fig. 2a, can be imagined clamped to a parent body $\mathcal{L}_0$ at point $A$ and being submitted to efforts coming from two external bodies $\mathcal{L}_4$ and $\mathcal{L}_5$ attached at points $B$ and $C$ respectively.

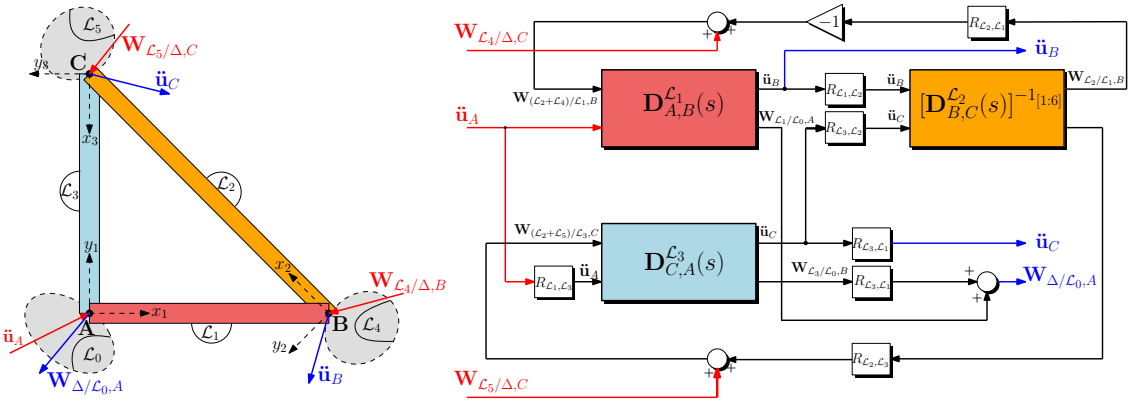


**Figure 2.** Block diagram of the Δ mechanism, showcased in 2a and modeled in 2b in the TITOP framework. Note that the blocks $R_{i,j}$ represent the rotation matrices between the $i$–th and $j$–th frames of references.

The triangular structure, which can be denoted as Δ, can be modeled as a dynamic system whose inputs are the accelerations $\ddot{\mathbf{u}}_\mathbf{A}$ imposed at point $A$ by $\mathcal{L}_0$ and the external efforts $\mathbf{W}_{\mathcal{L}_4/\Delta,B}$, $\mathbf{W}_{\mathcal{L}_5/\Delta,C}$ applied by the bodies $\mathcal{L}_4$ and $\mathcal{L}_5$ to the triangle mechanism Δ.

In the context of a sub-structuring approach, the triangular structure Δ can be conceived as an assembly of multiple TITOP models, as seen in Fig. 2b. These blocks have to be properly connected in order to impose the correct input-output configuration and to close the kinematic loop.

The only way to achieve this result is to use not only *clamped-free* models, but a *clamped-clamped* TITOP model as well. In fact, at sub-structure level, the two beams $\mathcal{L}_1$ and $\mathcal{L}_3$

https://doi.org/10.3311/ECCOMASMBD2021-206

can be considered *clamped-free* using the two direct TITOP models $\mathbf{D}^{\mathcal{L}_1}_{A,B}(s)$ and $\mathbf{D}^{\mathcal{L}_3}_{A,C}(s)$, as they have an acceleration imposed by a parent body at point $A$ and are submitted to an effort by external bodies at points $B$ and $C$. The assembly of the closed-loop is then achieved by imposing force/moment balance at each node of the structure. Since the distribution of the external efforts on the different beams is unknown, the third beam $\mathcal{L}_2$ is considered with accelerations imposed at both ends: the accelerations outputted by the TITOP models of $\mathcal{L}_1$ and $\mathcal{L}_3$ are the inputs of the TITOP block of $\mathcal{L}_2$, as this allows for the retrieval of the reaction forces exerted by $\mathcal{L}_2$ to the other bodies, namely $\mathbf{W}_{\mathcal{L}_2/\mathcal{L}_1,B}$ and $\mathbf{W}_{\mathcal{L}_2/\mathcal{L}_3,C}$. This means considering a TITOP model with the first six channels inverted, $\left[\mathbf{D}^{\mathcal{L}_2}_{B,C}(s)\right]^{-1_{[1:6]}}$, that represents a *clamped-clamped* beam.

A numerical procedure to invert the channels of a TITOP model has been introduced in [5]. The following section provides a new analytical formulation for the *clamped-clamped* beam that solves the numerical issues found in the current TITOP model channel inversion.

### 3.2 Mathematical Formulation

An analytical inversion is here proposed for the first six channels of the original TITOP beam model introduced in section 2.2, which correspond to the free node $C$.

The inversion process aims at obtaining the analytically inversed model $\left[\mathbf{D}^{\mathcal{A}}_{PC}(s)\right]^{-1_{(1:6)}}_{ana}$ whose input-output configuration reflects a *clamped-clamped* boundary condition applied to the beam. As depicted in Fig. 3, the inputs of the system are the endpoint accelerations $\ddot{\mathbf{u}}_P$ and $\ddot{\mathbf{u}}_C$, while the corresponding outputs are the efforts on those points, which are still maintaining the same formalism of the original TITOP model.

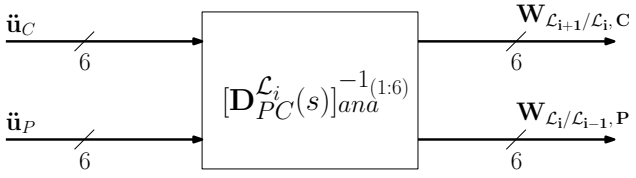


**Figure 3**. Input-output configuration for the analytically inverted *clamped-clamped* TITOP beam model

A change of variables is applied to the system in Eq. 16. We introduce vector $\boldsymbol{\epsilon}_k$, partitioned in two sub-vectors: $\boldsymbol{\epsilon}_{k_1}$ and $\boldsymbol{\epsilon}_{k_2}$. The first one, of size $\{6\times 1\}$, corresponds to the twelve poles at exactly zero frequency of the system. This is done to enforce the *clamped-clamped* boundary condition. The second vector, on the other hand, has a size of $\{4\times 1\}$ and determines the internal vibrational response of the system. The modal coordinates can be rewritten as:

$$\boldsymbol{\eta}_k = \mathbf{F}\boldsymbol{\epsilon}_k = \begin{bmatrix}\boldsymbol{\Phi}^{+}_{Ck} & null(\boldsymbol{\Phi}_{Ck})\end{bmatrix}\begin{bmatrix}\boldsymbol{\epsilon}_{k_1}\\ \boldsymbol{\epsilon}_{k_2}\end{bmatrix} \tag{19}$$

where the $(\cdot)^{+}$ operator denotes the generalized inverse (or pseudo-inverse) of the non-square matrix and $null(\cdot)$ the null space operator (or kernel). The use of this last operator allows the creation of a model whose modes corresponding to $\boldsymbol{\epsilon}_{k_1}$ are intrinsically set to zero, while the modes associated to $\boldsymbol{\epsilon}_{k_2}$ do not get simplified.

The first state equation for the new system can be directly derived from Eq. 19. By substituting this equation into Eq. 17, an explicit expression for $\boldsymbol{\epsilon}_{k_1}$ may be obtained as

https://doi.org/10.3311/ECCOMASMBD2021-206

function of the two inputs $\ddot{\mathbf{u}}_P$ and $\ddot{\mathbf{u}}_C$.

$$\ddot{\boldsymbol{\epsilon}}_{k_1} = \boldsymbol{\Phi}_{Ck}\mathbf{F}\ddot{\boldsymbol{\epsilon}}_k = \begin{bmatrix}\mathbf{I} & \mathbf{0}\end{bmatrix}\ddot{\boldsymbol{\epsilon}}_k = \ddot{\mathbf{u}}_C - \boldsymbol{\tau}_{CP}\ddot{\mathbf{u}}_P \tag{20}$$

The change of variables may be performed on the modal equations of motion in Eq. 18:

$$\ddot{\boldsymbol{\epsilon}}_k = \begin{bmatrix}\ddot{\boldsymbol{\epsilon}}_{k_1} & \ddot{\boldsymbol{\epsilon}}_{k_2}\end{bmatrix}^T = -\overline{\mathbf{k}}_{kk}\boldsymbol{\epsilon}_k - \overline{\mathbf{c}}_{kk}\dot{\boldsymbol{\epsilon}}_k - \mathbf{F}^{-1}\mathbf{L}_{kP}\ddot{\mathbf{u}}_P + \mathbf{F}^{-1}\boldsymbol{\Phi}_{Ck}^T\mathbf{W}_{\mathcal{L}_{i+1}/\mathcal{L}_i,C} \tag{21}$$

where $\overline{\mathbf{k}}_{kk} = \mathbf{F}^{-1}\mathbf{k}_{kk}\mathbf{F}$ and $\overline{\mathbf{c}}_{kk} = \mathbf{F}^{-1}\mathbf{c}_{kk}\mathbf{F}$. Moreover, this expression may be rewritten in order to explicit the two sub-vectors which compose vector $\boldsymbol{\epsilon}_k$, therefore obtaining a set of two equations. The following notation is hereby introduced, which defines the partition of matrices $\overline{\mathbf{k}}_{kk}$ and $\overline{\mathbf{c}}_{kk}$: $\overline{\mathbf{X}} = \begin{bmatrix}\overline{\mathbf{X}}_{11} & \overline{\mathbf{X}}_{12}\\ \overline{\mathbf{X}}_{21} & \overline{\mathbf{X}}_{22}\end{bmatrix}$.
The first of the two equations obtained from Eq. 21, expressing $\ddot{\boldsymbol{\epsilon}}_{k_1}$, is:

$$\ddot{\boldsymbol{\epsilon}}_{k_1} = -\overline{\mathbf{k}}_{kk_{11}}\boldsymbol{\epsilon}_{k_1} - \overline{\mathbf{k}}_{kk_{12}}\boldsymbol{\epsilon}_{k_2} - \overline{\mathbf{c}}_{kk_{11}}\dot{\boldsymbol{\epsilon}}_{k_1} - \overline{\mathbf{c}}_{kk_{12}}\dot{\boldsymbol{\epsilon}}_{k_2} + \boldsymbol{\Phi}_{Ck}\boldsymbol{\Phi}_{Ck}^T\mathbf{W}_{\mathcal{L}_{i+1}/\mathcal{L}_i,C} - \boldsymbol{\Phi}_{Ck}\mathbf{L}_{kP}\ddot{\mathbf{u}}_P \tag{22}$$

An explicit expression for $\mathbf{W}_{\mathcal{L}_{i+1}/\mathcal{L}_i,C}$ can be derived from this equation, substituting $\ddot{\boldsymbol{\epsilon}}_{k_1}$ by inverting Eq. 20. This represents the first output equation for the new state-space system:

$$\begin{aligned}\mathbf{W}_{\mathcal{L}_{i+1}/\mathcal{L}_i,C} = (\boldsymbol{\Phi}_{Ck}^T)^{+}\boldsymbol{\Phi}_{Ck}^{+}\Big(&\overline{\mathbf{k}}_{kk_{11}}\boldsymbol{\epsilon}_{k_1} + \overline{\mathbf{k}}_{kk_{12}}\boldsymbol{\epsilon}_{k_2} + \overline{\mathbf{c}}_{kk_{11}}\dot{\boldsymbol{\epsilon}}_{k_1}\\ &+ \overline{\mathbf{c}}_{kk_{12}}\dot{\boldsymbol{\epsilon}}_{k_2} + \ddot{\mathbf{u}}_C + (\boldsymbol{\Phi}_{Ck}\mathbf{L}_{kP} - \boldsymbol{\tau}_{CP})\ddot{\mathbf{u}}_P\Big)\end{aligned} \tag{23}$$

which can be rewritten in the form:

$$\mathbf{W}_{\mathcal{L}_{i+1}/\mathcal{L}_i,C} = \mathbf{C}_{11}\boldsymbol{\epsilon}_{k_1} + \mathbf{C}_{12}\boldsymbol{\epsilon}_{k_2} + \mathbf{C}_{13}\dot{\boldsymbol{\epsilon}}_{k_1} + \mathbf{C}_{14}\dot{\boldsymbol{\epsilon}}_{k_2} + \mathbf{D}_{11}\ddot{\mathbf{u}}_C + \mathbf{D}_{12}\ddot{\mathbf{u}}_P \tag{24}$$

Where:

- $\mathbf{C}_{11} = (\boldsymbol{\Phi}_{Ck}^T)^{+}\boldsymbol{\Phi}_{Ck}^{+}\overline{\mathbf{k}}_{kk_{11}}$;
- $\mathbf{C}_{12} = (\boldsymbol{\Phi}_{Ck}^T)^{+}\boldsymbol{\Phi}_{Ck}^{+}\overline{\mathbf{k}}_{kk_{12}}$;
- $\mathbf{C}_{13} = (\boldsymbol{\Phi}_{Ck}^T)^{+}\boldsymbol{\Phi}_{Ck}^{+}\overline{\mathbf{c}}_{kk_{11}}$;
- $\mathbf{C}_{14} = (\boldsymbol{\Phi}_{Ck}^T)^{+}\boldsymbol{\Phi}_{Ck}^{+}\overline{\mathbf{c}}_{kk_{12}}$;
- $\mathbf{D}_{11} = (\boldsymbol{\Phi}_{Ck}^T)^{+}\boldsymbol{\Phi}_{Ck}^{+}$;
- $\mathbf{D}_{12} = (\boldsymbol{\Phi}_{Ck}^T)^{+}\boldsymbol{\Phi}_{Ck}^{+}(\boldsymbol{\Phi}_{Ck}\mathbf{L}_{kP} - \boldsymbol{\tau}_{CP})$

The second equation in Eq. 21 describes the behavior of $\ddot{\boldsymbol{\epsilon}}_{k_2}$:

$$\begin{aligned}\ddot{\boldsymbol{\epsilon}}_{k_2} = &-\overline{\mathbf{k}}_{kk_{21}}\boldsymbol{\epsilon}_{k_1} - \overline{\mathbf{k}}_{kk_{22}}\boldsymbol{\epsilon}_{k_2} - \overline{\mathbf{c}}_{kk_{21}}\dot{\boldsymbol{\epsilon}}_{k_1} - \overline{\mathbf{c}}_{kk_2}\dot{\boldsymbol{\epsilon}}_{k_2}\\ &- null(\boldsymbol{\Phi}_{Ck})^T\boldsymbol{\Phi}_{Ck}^T\mathbf{W}_{\mathcal{L}_{i+1}/\mathcal{L}_i,C} - null(\boldsymbol{\Phi}_{Ck})^T\mathbf{L}_{kP}\ddot{\mathbf{u}}_P\end{aligned} \tag{25}$$

Note that by definition of the kernel operator, $\boldsymbol{\Phi}_{Ck}\cdot null(\boldsymbol{\Phi}_{Ck}) = \mathbf{0}$. Therefore also $null(\boldsymbol{\Phi}_{Ck})^T\boldsymbol{\Phi}_{Ck}^T = \mathbf{0}$. This property has the effect of canceling the contribution of

https://doi.org/10.3311/ECCOMASMBD2021-206

**Table 1**. Parameters of TITOP Beams used for the case study

| $l[m]$ | $S[m^2]$ | $\rho[kg/m^2]$ | $E[GPa]$ | $\nu$ | $I_y[m^{-4}]$ | $I_z[m^{-4}]$ | $\xi$ |
|---|---|---|---|---|---|---|---|
| 20 | 0.0004 | 2700 | 70 | 0.35 | 6.7e-7 | 6.7e-7 | 0.001 |

$\mathbf{W}_{\mathcal{L}_{i+1}/\mathcal{L}_i,C}$ to the second order dynamics of $\boldsymbol{\epsilon}_{k_2}$, allowing for an explicit expression of $\ddot{\boldsymbol{\epsilon}}_{k_2}$ as function of state variables and inputs only.

The final expression needed to complete the TITOP model is the output equation for $\mathbf{W}_{\mathcal{L}_i/\mathcal{L}_{i-1},P}$. This can be easily obtained from the outputs of Eq. 18, to which the change of state variables is applied. The resulting equation is:

$$\mathbf{W}_{\mathcal{L}_i/\mathcal{L}_{i-1},P} = \mathbf{C}_{21}\boldsymbol{\epsilon}_{k_1} + \mathbf{C}_{22}\dot{\boldsymbol{\epsilon}}_{k_1} + \mathbf{C}_{23}\boldsymbol{\epsilon}_{k_2} + \mathbf{C}_{24}\dot{\boldsymbol{\epsilon}}_{k_2} + \mathbf{D}_{21}\ddot{\mathbf{u}}_C + \mathbf{D}_{22}\ddot{\mathbf{u}}_P \tag{26}$$

Where:

- $\mathbf{LKF} = \mathbf{L}_{kP}^T\mathbf{k}_{kk}\mathbf{F}$;
- $\mathbf{LCF} = \mathbf{L}_{kP}^T\mathbf{c}_{kk}\mathbf{F}$;
- $\mathbf{TPL} = (\boldsymbol{\tau}_{CP} - \boldsymbol{\Phi}_{Ck}\mathbf{L}_{kP})$;
- $\mathbf{C}_{21} = \mathbf{LKF}(:, 1:6) + \mathbf{TPL}^T(\boldsymbol{\Phi}_{Ck}^T)^+\boldsymbol{\Phi}_{Ck}^+\overline{\mathbf{k}}_{kk_{11}}$;
- $\mathbf{C}_{22} = \mathbf{LKF}(:, 1:6) + \mathbf{TPL}^T(\boldsymbol{\Phi}_{Ck}^T)^+\boldsymbol{\Phi}_{Ck}^+\overline{\mathbf{c}}_{kk_{11}}$;
- $\mathbf{C}_{23} = \mathbf{LKF}(:, 7:10) + \mathbf{TPL}^T(\boldsymbol{\Phi}_{Ck}^T)^+\boldsymbol{\Phi}_{Ck}^+\overline{\mathbf{k}}_{kk_{12}}$;
- $\mathbf{C}_{24} = \mathbf{LKF}(:, 7:10) + \mathbf{TPL}^T(\boldsymbol{\Phi}_{Ck}^T)^+\boldsymbol{\Phi}_{Ck}^+\overline{\mathbf{c}}_{kk_{12}}$;
- $\mathbf{D}_{22} = \mathbf{TPL}^T(\boldsymbol{\Phi}_{Ck}^T)^+\boldsymbol{\Phi}_{Ck}^+$;
- $\mathbf{D}_{22} = \mathbf{L}_{kP}^T\mathbf{L}_{kP} - \mathbf{M}_{rr} + \mathbf{TPL}^T(\boldsymbol{\Phi}_{Ck}^T)^+\boldsymbol{\Phi}_{Ck}^+\mathbf{TPL}$

These results can be used to obtain a TITOP Model for the inversed *clamped-clamped* beam. By using the results of Eq.s 20,24,25,26, the final system can be assembled as follows

$$\begin{bmatrix} \dot{\boldsymbol{\epsilon}}_{k_1} \\ \ddot{\boldsymbol{\epsilon}}_{k_1} \\ \dot{\boldsymbol{\epsilon}}_{k_2} \\ \ddot{\boldsymbol{\epsilon}}_{k_2} \\ \hline \mathbf{W}_{\mathcal{L}_{i+1}/\mathcal{L}_i,C} \\ \mathbf{W}_{\mathcal{L}_i/\mathcal{L}_{i-1},P} \end{bmatrix} = \underbrace{\left[\begin{array}{cccc|cc} \mathbf{0}_{k_1k_1} & \mathbf{I}_{k_1k_1} & \mathbf{0}_{k_1k_2} & \mathbf{0}_{k_1k_2} & \mathbf{0}_{k_1C} & \mathbf{0}_{k_1P} \\ \mathbf{0}_{k_1k_1} & \mathbf{0}_{k_1k_1} & \mathbf{0}_{k_1k_2} & \mathbf{0}_{k_1k_2} & \mathbf{I}_{k_1C} & -\boldsymbol{\tau}_{CP} \\ \mathbf{0}_{k_2k_1} & \mathbf{0}_{k_2k_1} & \mathbf{0}_{k_2k_2} & \mathbf{I}_{k_2k_2} & \mathbf{0}_{k_2C} & \mathbf{0}_{k_2P} \\ -\overline{\mathbf{k}}_{kk_{21}} & -\overline{\mathbf{c}}_{kk_1} & -\overline{\mathbf{k}}_{kk_{22}} & -\overline{\mathbf{c}}_{kk_2} & \mathbf{0}_{k_2C} & -null(\boldsymbol{\Phi}_{Ck})^T\mathbf{L}_{kP} \\ \hline \mathbf{C}_{11} & \mathbf{C}_{12} & \mathbf{C}_{13} & \mathbf{C}_{14} & \mathbf{D}_{11} & \mathbf{D}_{12} \\ \mathbf{C}_{21} & \mathbf{C}_{22} & \mathbf{C}_{23} & \mathbf{C}_{24} & \mathbf{D}_{21} & \mathbf{D}_{22} \end{array}\right]}_{\left[\mathbf{D}_{PC}^{\mathcal{L}_i}(s)\right]_{ana}^{-1_{[1:6]}}} \begin{bmatrix} \boldsymbol{\epsilon}_{k_1} \\ \dot{\boldsymbol{\epsilon}}_{k_1} \\ \boldsymbol{\epsilon}_{k_2} \\ \dot{\boldsymbol{\epsilon}}_{k_2} \\ \hline \ddot{\mathbf{u}}_C \\ \ddot{\mathbf{u}}_P \end{bmatrix} \tag{27}$$

The $\left[\mathbf{D}_{PC}^{\mathcal{L}_i}(s)\right]_{ana}^{-1_{[1:6]}}$ model in Eq. 27 is the analytically inverted *clamped-clamped* TITOP model showcased in Fig. 3.

https://doi.org/10.3311/ECCOMASMBD2021-206

## 4 MODEL APPLICATION AND VALIDATION

In order to validate the accuracy of the newly derived model, the system has been verified by comparison to a reference theoretical beam model [3] as well as the numerically inverted TITOP beam of [5].

Given a homogeneous beam of lenght $l$, section $S$, density $\rho$, Young modulus $E$, Poisson's ratio $\nu$, second moments of inertia $I_y$, $I_z$ along y and z axes and damping coefficient $\xi$, the parameters presented in Table 1 were used to obtain the singular value plots seen in Fig.4.

This plot describes the transfers between $\ddot{\mathbf{u}}_P$ and $\mathbf{W}_{\mathcal{L}_i/\mathcal{L}_{i-1},P}$ for both analytically and numerically inverted models. In particular we define:

$$\mathbf{G}^{ana}_{\mathbf{W}_P,\ddot{\mathbf{u}}_P}(s) = \left(\left[\mathbf{D}^{\mathcal{L}_i}_{PC}(s)\right]^{-1[1:6]}_{ana}\right)_{\ddot{\mathbf{u}}_P \to \mathbf{W}_P}, \qquad \mathbf{G}^{num}_{\mathbf{W}_P,\ddot{\mathbf{u}}_P}(s) = \left(\left[\mathbf{D}^{\mathcal{L}_i}_{PC}(s)\right]^{-1[1:6]}_{num}\right)_{\ddot{\mathbf{u}}_P \to \mathbf{W}_P} \tag{28}$$

as the multiple-input-multiple-output transfers between $\ddot{\mathbf{u}}_P$ and $\mathbf{W}_{\mathcal{L}_i/\mathcal{L}_{i-1},P}$ for the analytically inverted $\left[\mathbf{D}^{\mathcal{L}_i}_{PC}(s)\right]^{-1[1:6]}_{ana}$ and the numerically inverted $\left[\mathbf{D}^{\mathcal{L}_i}_{PC}(s)\right]^{-1[1:6]}_{num}$ models.

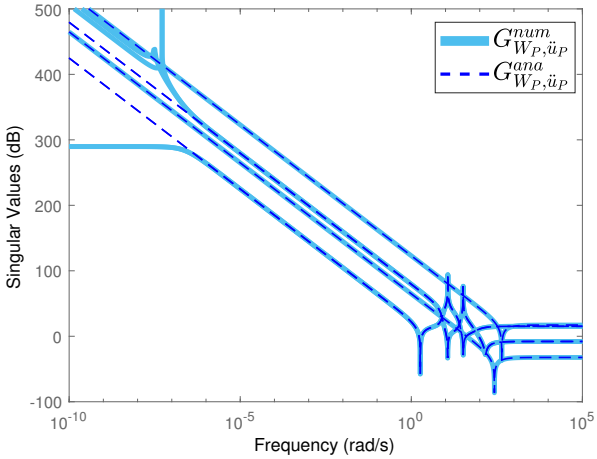


**Figure 4**. Singular values for the analytically $\mathbf{G}^{ana}_{\mathbf{W}_P,\ddot{\mathbf{u}}_P}(s)$ and numerically $\mathbf{G}^{num}_{\mathbf{W}_P,\ddot{\mathbf{u}}_P}(s)$ inverted TITOP models

The two responses match exactly except for near-to-zero frequency values: in this range the numerical inversion produces artificial behaviors like non-physical zeros and poles. The proposed analytical system overcomes these issues, granting an infinite gain at zero frequency with a correct $1/s^2$ dynamics at low frequency. This is in fact the expected behavior of the system, where the imposition of non-compatible accelerations at the two extremities of the rigid beam produces infinite efforts.

These results are furthermore corroborated by comparing the modes of the two models: Table 2 shows the normalized natural frequencies of the two *clamped-clamped* models - analytical and numerical. The frequencies, normalized by $\sqrt{\frac{EI}{\rho S l^4}}$, are also compared to the reference theoretical values expected for each mode.

A study of Table 2 shows how the introduction of the analytical model solved the non-zero poles issues found in the numerically inverted TITOP model, while granting the same level of accuracy in the description of the vibrational phenomena. The last four

https://doi.org/10.3311/ECCOMASMBD2021-206

**Table 2**. Comparison of the natural frequencies, normalized by $\sqrt{\frac{EI}{\rho S l^4}}$, of the numerically inverted TITOP model ($\omega_{k,num}$) and the new analytically inverted model ($\omega_{k,ana}$) to the reference theoretical value $\omega_{ref}$

| $Mode\ k$ | $\omega_{k,ref}$ | $\omega_{k,num}$ | $\omega_{k,ana}$ | $Mode\ k$ | $\omega_{k,ref}$ | $\omega_{k,num}$ | $\omega_{k,ana}$ |
|---|---|---|---|---|---|---|---|
| 1 | 0 | 0.00 | 0.00 | 6 | 0 | 9.15e-08 | 0.00 |
| 2 | 0 | 0.00 | 0.00 | 7 | 22.373 | 22.450 | 22.450 |
| 3 | 0 | 6.04e-17 | 0.00 | 8 | 22.373 | 22.450 | 22.450 |
| 4 | 0 | 2.28e-14 | 0.00 | 9 | 61.673 | 62.929 | 62.929 |
| 5 | 0 | 9.15e-08 | 0.00 | 10 | 61.673 | 62.929 | 62.929 |

flexible modes are in fact corresponding exactly to the modes found in [5] for the bending of a *clamped-clamped* beam, and represent a good approximation of the reference frequency value.

## 5 CONCLUSIONS

An analytical model of a *clamped-clamped* TITOP beam was derived in order to overcome the limits of the numerical inversion of the *clamped-free* TITOP model.
The proposed model has been validated by theoretical results and it represents a building block for modeling more complex multi-body flexible structures in closed-loop configurations.

## REFERENCES

[1] Theodore, R.J., Ghosal, A.: Comparison of the assumed modes and finite element models for flexible multilink manipulators. The International Journal of Robotics Research **14**(2) (1995) 91–111

[2] Leckie, F., Pestel, E.: Transfer-matrix fundamentals. International Journal of Mechanical Sciences **2**(3) (1960) 137 – 167

[3] Girard, A., Roy, N.: Structural Dynamics in Industry. Wiley (2008)

[4] Alazard, D., Perez, J.A., Cumer, C., Loquen, T.: Two-input two-output port model for mechanical systems. In: AIAA Guidance, Navigation, and Control Conference. (2015) 1778

[5] Chebbi, J., Dubanchet, V., Perez Gonzalez, J.A.: Linear dynamics of flexible multibody systems: A system-based approach. Multibody System Dynamics **41** (11 2016)

[6] Alazard, D., Cumer, C.: Satellite Dynamics Toolbox. (2014)

[7] Sanfedino, F., Alazard, D., Pommier-Budinger, V., Falcoz, A., Boquet, F.: Finite element based n-port model for preliminary design of multibody systems. Journal of Sound and Vibration **415** (2018) 128 – 146

# Section
# FORMALISMS, NUMERICAL METHODS AND REAL-TIME ALGORITHMS

https://doi.org/10.3311/ECCOMASMBD2021-196

ECCOMAS Thematic Conference on Multibody Dynamics
December 12 - 15, 2021, Budapest, Hungary

# Efficient Earthquake Simulation Of Stiff And High DOF Bridge Expansion Joint Models With Python

**Michael Tahedl**[1], **Fredrik Borchsenius**[2], **Andreas Taras**[3]

[1] MAURER Engineering GmbH
Frankfurter Ring 193, 80807 Munich, Germany
m.tahedl@maurer.eu

[2] Faculty of Mechanical Engineering
OTH Regensburg
Galgenbergstr. 13, 93053 Regensburg, Germany
fredrik.borchsenius@oth-regensburg.de

[3]Dept. of Civil, Environmental
and Geomatic Engineering
ETH Zürich
Stefano-Franscini-Platz 5, 8093 Zurich,
Switzerland
taras@ibk.baug.ethz.ch

## ABSTRACT

Various types of seismic protection devices has been developed to protect structures like bridges from collapse during an earthquake event, such as hydraulic or metallic hysteresis dampers and spherical pendulum bearings. The expansion joints however, which are already included in most large-span bridges, are not considered as an earthquake protection device regardless of the significant friction forces they produce. These friction forces can be seen as damping forces between the shaking environment and the oscillating bridge. To investigate the effect of those damping forces during different earthquake loads, a multibody dynamics simulation model of the expansion joints will be created. This model should be accurate enough to represent the generation of the damping forces and effects of the geometric setup of the expansion joints. Because large expansion joints for large-span bridges are of special interest, the number of degrees of freedom (DOF) becomes very high. Because this models include stiff bushings, implicit solvers need to be used to gain a stable simulation. Expansion joints are almost unique constructions for every specific bridge, which requires a automated model generation. Because of its excellent modules for numerical mathematics, the scripting language Python is used. To create an efficient simulation model, several optimization techniques such as Just-In-Time (JIT) compilation and parallelization are implemented and tested.

**Keywords:** Parallelization, Optimization, Python, Earthquake Engineering.

## 1 INTRODUCTION

Earthquakes are one of the most dangerous hazards to our civilization. Protecting buildings is of special interest in earthquake engineering to save life during an earthquake as well as to maintain critical infrastructure for rescue operations after such an event. To achieve this, so called seismic protection devices are developed. They can be roughly grouped into ground isolation and energy dissipation devices. The former acting as a decoupling between the shaking ground and the construction to reduce the movement which is brought into the structure. They also have the task of recentering the building to its initial position. An example for those devices are sliding pendulum isolation bearings with spherical sliding surfaces. The second category are the energy dissipation devices, which should transform as much movement energy into thermal energy. This is typically done by hydraulic dampers, which are using the friction of a fluid to dissipate energy. Depending on their dimension, hydraulic dampers are capable of large displacements. Steel hysteresis

https://doi.org/10.3311/ECCOMASMBD2021-196

dampers on the other hand are using the energy dissipation from plastic deformation of steel, which is highly economical and effective, but their movement capacity is very limited compared to hydraulic dampers.

Another device, which is included in most medium to large-span bridges and is initially not considered as an earthquake protection device, are the expansion joints. Their task is to cover gaps between several bridge sections and between the bridge and the respective abutment. These gaps are included to compensate relative movements between those segments due to heat expansion of the bridge. Larger bridges generating larger expansion movements, so those gaps become larger, too. To divide those large gaps into smaller gaps, modular expansion joints come into consideration. They are consisting of steel center beams which are placed perpendicular to the roadway and subdivide the gap into sub-gaps. To distribute the change of the gap over all sub-gaps, a control mechanism must be included. A modern approach for this task, which is suitable for almost all sizes of expansion joints, is the swivel joist control mechanism. The support beams, which are fulfilling the task of the swivel joist, are rotating in consequence of a changing gap. The rubber bearings, which are connected to the support beams and can only rotate around the vertical axis, transmitting the swivel motion to the overlying center beams. The complete control mechanism follows the intercept theorem and guarantees that the gap is distributed equally over all sub-gaps at any time. A schematic representation of this mechanism is displayed in figure 1.

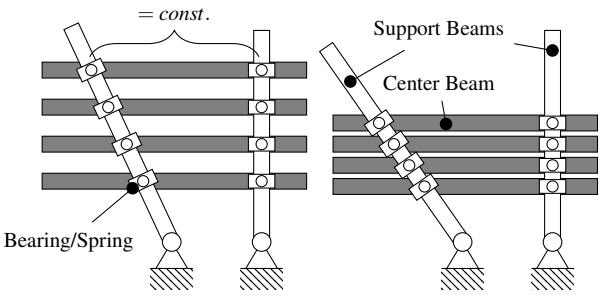


Figure 1: Schematic representation of the kinematic control mechanism of a swivel joist expansion joint

Modular expansion joints are not considered as seismic protection device yet. But they include some interesting properties as they generate high friction forces due to many sliding contacts in large expansion joints. Those friction forces acting in opposite direction of the relative movement and can be therefore seen as damping forces as they are generated by dissipation devices. Those forces are acting at strategically advantageous locations as they are able to reduce the movement of the bridge superstructure. Another outstanding benefit of the modular expansion joint, especially for larger devices, is their enormous movement capacity. Those possibilities are very promising and should be investigated to further enhance the seismic performance of those devices.

Other works like [1] investigated the seismic response of bridges with models which represent the pounding on finger expansion joints. In this work however, a multibody dynamics model of more complex modular expansion joints will be built. Therefore, a simulation model of the dynamic response of modular bridge expansion joints and the connected bridge under earthquake loads is developed. The mechanical control mechanism of modular expansion joints can, depending on the bridge size, consist of several hundred bodies and therefore around thousand degrees of freedom (DOF). This combined with the stiff differential equations arising from stiff force elements requires several optimization steps.

## 2 MODELING

Large expansion joints are of special interest, because the hazard potential and economical damage on large span bridges with such expansion joints is very high. In this work, the expansion joint

https://doi.org/10.3311/ECCOMASMBD2021-196

displayed in figure 2b will be modeled and simulated.

(a) MAURER Swivel Joist Expansion Joint

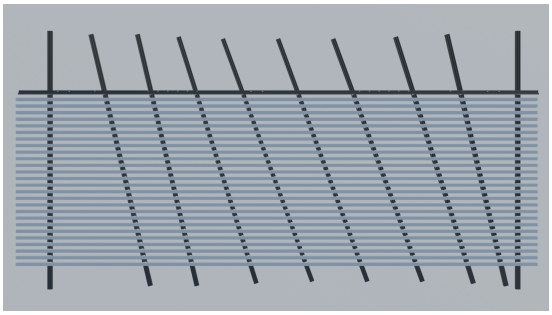

(b) Reduced simulation model

Figure 2: Expansion joint, modeled with 307 rigid bodies, 270 bushings, 270 friction force elements and 270 prismatic sliding joints

This expansion joint is of type swivel joist expansion joint with 10 support beams and 27 center beams. The support beam on the left hand side is fixed on both ends and acts as a guide for the center beams. All other support beams are translationally fixed on the bottom side an can therefore only rotate around the vertical axis of the drawing plane. The support beams have angles of 0°, 13°, 17° and 20° relative to the roadway direction and are 7.5 m long. The center beams are 15 m long. Each center beam is connected to the support beams via one rubber bearing, which leads to a total of 270 bearings.

The complete modeling and simulation will be implemented with the scripting language Python and mainly with the numerical module Numpy [2]. Python offers an easy and efficient way to create such simulation models and connect to other development environments with its broad range of modules. Furthermore, Python has great interfaces and frameworks to display, analyze and interactively publish results via notebooks or even as web applications. Numpy comes with many functions for numerical computing and it is mostly written in C for better performance. For optimization purposes, which are described in the next section, the complete calculation parts for the simulation are structured into Python functions. In the end, there will be one function called `qdot(t,q,...)` which computes the time derivative of the global state vector. This function calls the other functions for computing forces, constraint reactions, Lagrange multipliers, solving the equation system and much more.

### 2.1 Bodies

The presented model consists of 307 rigid bodies. In order to describe them as 3D bodies, Euler angles could be used. This leads to 6 DOF for each body, respectively, and to an overall DOF count of 1842. Because implicit integration schemes must be used as described in section 2.4, the time expensive calculation of a Jacobian matrix is required, which has the shape $[2 \cdot \mathrm{DOF}, 2 \cdot \mathrm{DOF}]$. Because the Jacobian will be computed numerically by finite differences, each extra DOF will increase the effort for each function evaluation as well as the required number of those function evaluations. Because of this, the computation effort for the Jacobian matrix increases exponentially as displayed in figure 3. Using 2D bodies for the simulation, the number of DOF is halved compared to 3D bodies and the computation time for the Jacobian reduces to about one fifth.

The used rigid 2D bodies can translationally move in a plane defined by the $x$- and $y$-axis and

https://doi.org/10.3311/ECCOMASMBD2021-196

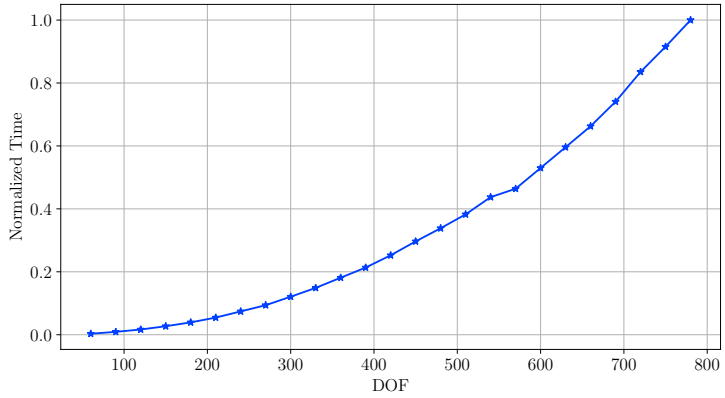


Figure 3: Normalized computation time for the calculation of the Jacobian matrix by finite differences depending on the DOF

rotate around the perpendicular $z$-axis. The state vector of one body is defined as follows

$$q = \left[x, y, \phi, \dot{x}, \dot{y}, \dot{\phi}\right]^T \tag{1}$$

## 2.2 Forces

### 2.2.1 Bushings

The main parts, of which a swivel joist expansion joint consists, is displayed in figure 4.

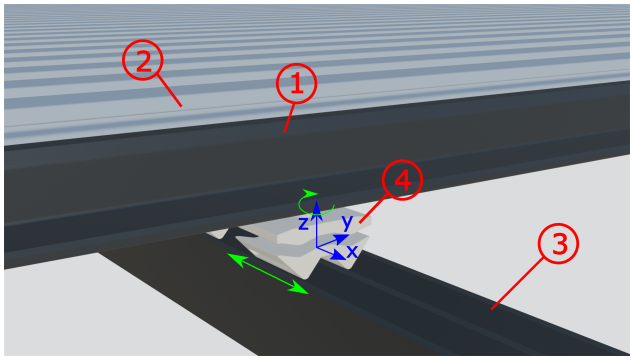


Figure 4: Parts of the swivel joist control mechanism. 1: Edge Beam, 2: Center Beam, 3: Support Beam, 4: Bearing

The bearing is connected to the overlying center or edge beam by a bushing, which has translational stiffness but can rotate freely. The translational stiffness is defined to match the corresponding shear stiffness of the rubber inlets of the bearing. The force gets calculated by a Python function with the displacement $\Delta x$ in respective to the starting displacement $u_0$ at $t = 0$

$$\Delta x = (r_{01,0} + A_{01} \cdot r_{SP,1} - r_{02,0} - A_{02} \cdot r_{SP,2}) - u_0 \tag{2}$$

where $r_{0n,0}$ is the global position vector, $A_{0n}$ the rotation matrix and $r_{SP,n}$ is the body-fixed vector from the center of mass to the actual connection point, all in respective to the connected bodies $n \in [1,2]$ and in the global coordinate system 0 or the local, body-fixed coordinate system of the corresponding bodies. The resulting bushing force is then obtained by

$$F_{B,0} = k_B \cdot \Delta x \tag{3}$$

https://doi.org/10.3311/ECCOMASMBD2021-196

with the stiffness vector $k_B$ including the stiffness in $x$- and $y$-direction. If $r_{SP,n} \neq 0$, then the resulting moment

$$M_{Bn,0} = (A_{0n} \cdot r_{SP,n}) \times F_{B,0} \tag{4}$$

is also evaluated.

### 2.2.2 Friction

The bearings are able to slide along the support beams. To ensure that those components are always in contact, a pre-loading mechanism is included which is not displayed in figure 4. The resulting normal force produces friction forces in the sliding plane. The newest generation of sliding bearings consists of sliding surface made out of ultra high molecular weight polyethylene (UHMWPE) with excellent sliding properties. Although friction coefficients are initially relatively low, it is expected that this coefficient increases over time due to dirt and other particles. With this long term effects in mind, a friction coefficient of 5 % is used for all upcoming simulations. In reality, there is another sliding component at the bottom sliding surface of the support beam included by the aforementioned pre-loading mechanism. Because this component does not affect the control mechanism, it gets ignored for the simulation model and only its friction force, which is similar to the friction force of the bearing, is considered.

The friction forces are calculated by the regularized friction model [3] displayed in figure 5. This model represents the singularity of the Coulomb friction model at $v_t = 0$ with a linear approximation. Friction tests have shown, that the friction force of the UHMWPE sliding bearing is nearly constant at higher velocities, so the assumption of constant friction is acceptable.

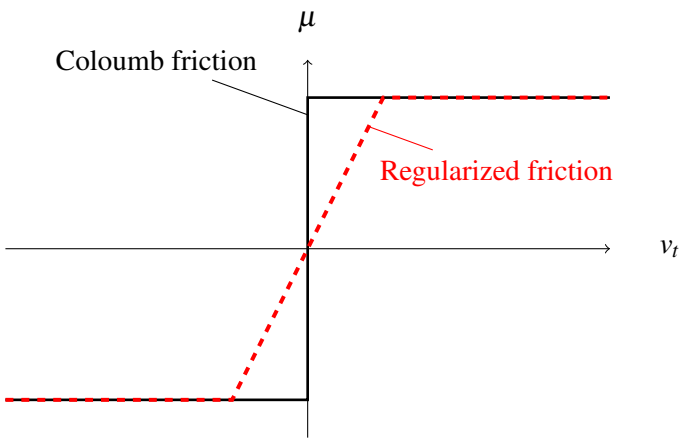


Figure 5: Schematic representation of the regularized friction model

The velocity between the two sliding bodies gets determined as

$$\Delta\dot{x} = \dot{r}_{01,0} + \dot{A}_{01} \cdot r_{SP,1} - \dot{r}_{02,0} - \dot{A}_{02} \cdot r_{SP,2} \tag{5}$$

The absolute tangential velocity is then calculated by the Frobenius norm

$$v_t = |\Delta\dot{x}|_F \tag{6}$$

With the friction coefficient, obtained by the tangential velocity, the Friction force can be calculated as follows

$$F_{fric} = \mu F_N \frac{\Delta x}{v_t} \tag{7}$$

## 2.3 Constraints

The bearings are considered to slide along the corresponding support beam without any significant gaps on the either side. This means, the support beam and bearing can be considered as a sliding

https://doi.org/10.3311/ECCOMASMBD2021-196

joint where the bearing can only slide along an axis defined by the support beam. All other DOF of the bearing are eliminated by the kinematic constraint. Because this system will be described by a index reduced differential algebraic equation system (DAE), a constraint equation for this kinematic joint is defined. The example below defines that the $x$-axis of body 1 defines the sliding axis

$$g(y) = \begin{bmatrix} (A_{01} \cdot e_x)^T (A_{02} \cdot e_y) \\ (A_{01} \cdot e_x)^T r_{12,0} \end{bmatrix} = 0 \tag{8}$$

where $e_x$ and $e_y$ are unity vectors in each direction and $y$ is the location vector. This equation system implies in the first equation that the local coordinate systems of each body must be equally oriented and in the second equation that the connecting array must be perpendicular to the sliding direction [4].

### 2.4 Differential-Algebraic-Equations

As mentioned in the section before, the system is described by DAE of the form

$$\dot{y} = z \tag{9}$$

$$M\dot{z} = F^e + J_g^T \lambda \tag{10}$$

$$0 = g(y) \tag{11}$$

where $y$ is the location vector, $z$ is the velocity vector, $M$ is the mass matrix, $F^e$ are the external forces, $J_g$ is the Jacobian matrix of the constraint equations, $\lambda$ are the Lagrange multipliers and $g(y)$ are the constraint equations [5]. In order to solve this equation system, the index need to be reduced from 3 to 1, which could be done with to consecutive time derivations of $g(y)$, so that equation 11 becomes

$$0 = J_g \dot{z} + \dot{J}_g z \tag{12}$$

and the DAE can be solved with any ordinary numerical integrator. To reduce the drift in the constraint equation resulting from the index reduction, a stabilization according to Gear, Gupta and Leimkuhler [6] is implemented, which adds another Lagrange multiplier

$$\mu = -\left(J_g J_g^T\right)^{-1} J_g z \tag{13}$$

so that equation 9 becomes

$$\dot{y} = z + J_g^T \mu \tag{14}$$

This stabilizes the equation system on the velocity level and reduces the drift in the constraint equations.

## 3 OPTIMIZATION

When running a simulation with the described Python and Numpy implementation of the model displayed in figure 2b, the overall computation time even for simple and steady movements is extremely high. For example, the so called service case, where the joint opens and closes with a velocity of $0.2\,\mathrm{m\,s^{-1}}$, takes several days to complete, even on virtual machines with up to 64 processor cores and optimized vector processing capabilities. Numpy is able to us multithreading for several vector workloads, but increasing the core count does not make any noticeable difference and the maximum number of used threads is limited to 32 anyway. This means, the roots of all heavily time consuming calculations has to be identified and specifically treated.

### 3.1 Just-in-Time Compiling

To identify the bottlenecks inside the simulaiton, a line-by-line profiler for the function $\dot{q} = f(t,q)$ is used. With this techniques, the specific time consumed by a single line in a function can be identified. The main evaluation times for $f(t,q)$ are displayed in table 1.

https://doi.org/10.3311/ECCOMASMBD2021-196

| Task | Time/Hit | % Time |
|---|---|---|
| Computaion bushing/friction forces | 0.25 s | 55.7 % |
| Computaion constraints | 0.2 s | 44.3 % |

Table 1: Evaluation times of specific parts of the function $f(t,q)$

Almost the complete effort of one function call goes into the determination of bushing, friction and constraint forces. All other tasks, like the solution of the linear equation system from equation 10, are not affecting the computation time by much. The following chart shows the included functions and how often they are called in this setup.

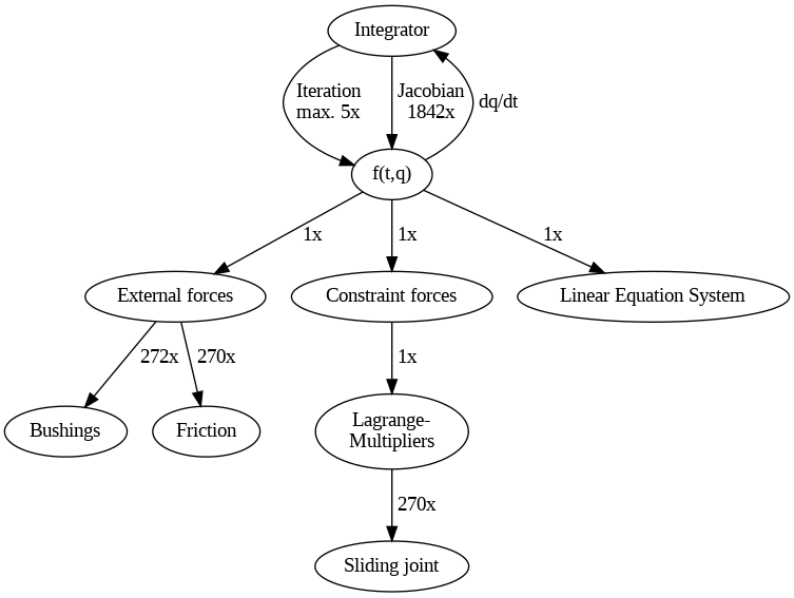


Figure 6: Relationship between different function calls and how often these functions are called

It can be seen, that the function $f(t,q)$ is calling each function about 270 times for this model. The function itself is called 1-5 times, depending on the convergence, by the used BDF integrator described in [7]. The integrator needs the Jacobian matrix

$$J \approx \frac{\partial f(t,q)}{\partial q} \tag{15}$$

to solve the nonlinear equation system, as described in [8]. Although the evaluation of the Jacobian matrix is not done at each time step, overall it introduces a lot of function calls. This shows the importance of efficient function evaluations.

Python is generally a relatively low performing programming language when it comes to computation time because it is interpreted. Even with the optimized Numpy calculations, many loops and other pure Python operations need to be done. To gain more efficiency, a compiled code is preferred. One solution would be to re-write the functions with C/C++, compile them as shared libraries and wrap them via ctypes. A similar performance with less re-programming effort can be reached with compiling the Python functions with the just-in-time compiler Numba [9]. Numba is designed to be used with Numpy arrays. After adding Numba to the functions called by $f(t,q)$, the overall evaluation time of this function gets reduced by 60 %. Because the overall simulation time linearly depends on the function evaluation time, it is reduced by approximately two thirds as well.

https://doi.org/10.3311/ECCOMASMBD2021-196

### 3.2 Sparse Jacobian Matrix

When profiling the solver, it can be seen that the evaluation of the Jacobian is by far the most time consuming part. Obtaining the Jacobian with the default dense finite difference approach takes about 90 s. The used integrator `scipy.integrate.BDF` offers the possibility to use a sparse Jacobian. When using this option, the sparsity pattern must provided in a form, which tells the integrator at which locations the Jacobian is nonzero. For the expansion joint from figure 2b, the sparsity pattern is as displayed in figure 7.

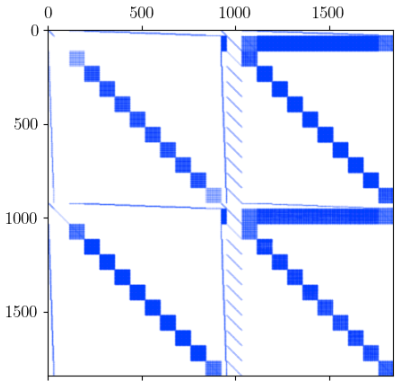


Figure 7: The sparsity pattern of the Jacobian matrix. Blue dots indicate where the matrix entry is not zero.

A count of the nonzero element results in 334747 nonzero element which represent about 10 % of the complete matrix. When providing this sparsity pattern, only those elements are getting calculated when the Jacobian is re-evaluated [10]. This lowers the evaluation time for the Jacobian matrix to about 47 s, which is almost twice as fast as the dense computation. But overall, the whole simulation takes still several days to finish, which is not convenient when aiming for parameter studies.

### 3.3 Parallel Jacobian Matrix

Another option is parallelization of heavy workloads such as the computation of the Jacobian matrix, which is by far the most demanding part when integrating a time step. Modern computing architectures are offering (virtual) machines with a wide range of hardware capabilities for such tasks. Instead of successively computing parts of the Jacobian matrix, it would be highly beneficial if those tasks could be done simultaneously at different cores of the CPU. The computation of the approximation of the Jacobian matrix, which should be parallelized, can be achieve with finite differences

$$J_i = \frac{f(t, q_{q[i]+\varepsilon}) - f(t,q)}{\varepsilon} \tag{16}$$

where $i \in [1, 1842]$, $J_i$ is the $i$-th column of $J$ and $\varepsilon$ is a small value of typically $1 \times 10^{-8}$. This shows, that the columns of $J$ could be calculated independently from each other, which means that multiple columns could be calculated in parallel and getting joined afterwards.

One of the core concept of Python is the global interpreter lock (GIL). This means that every Python code needs the single GIL to be executed and could not be multithreaded, which guarantees a thread-safe memory management. On the other hand, one Python interpreter could only run one thread at a time. This might be beneficial when using multithreading for Input/Output (I/O) bound tasks, but could result in a decreased performance of CPU bound tasks, which the computation of the Jacobian matrix is.

A solution for this problem is multiprocessing. Instead of one Python process using multiple threads, multiple Python processes are spawned where each process is completely isolated from the others. This is well suited for the computation of the Jacobian matrix because the calculation of each column is independent of the other columns. Each of those processes have their own Python interpreter, are therefore not affected by the GIL and can run truly in parallel. The overhead introduced by creating multiple processes and joining the results together is more than compensated by the achieved parallelism at CPU bound tasks.

Multiprocessing in Python could be achieved with the `multiprocessing` module, which is in the standard library of Python. When testing the performance of the multiprocessed computation of the Jacobian matrix, the evaluation time surprisingly increased when using more processes, as displayed in figure 8.

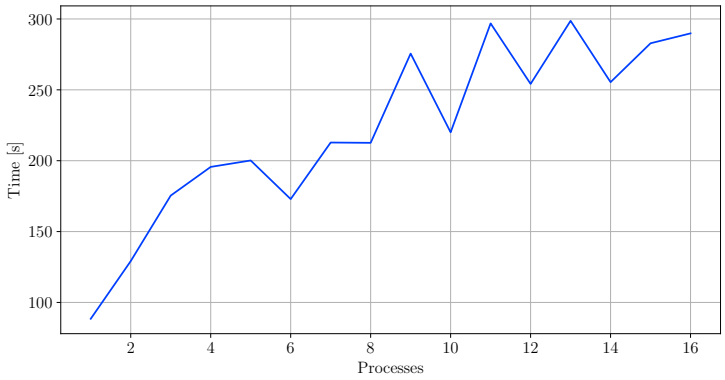


Figure 8: Increasing evaluation time of the Jacobian when using more processes

In consequence of this, the overhead of the multiprocessing steps are investigated. It was suspected, that more processes are leading to more overhead in splitting the workloads and joining the results so that the advantage of parallelism is neglected. But it was observed, that the overhead for each process is very small compared to the evaluation time of the function inside the computation of the corresponding Jacobian matrix column. This indicates that there must be other overhead, which throttles the performance of this processes.

When further investigating the Numpy processes, it was noticed, that Numpy is using true multithreading without a GIL, which is possible because they are written in C. What happens when using more processes, is that each of those processes wants to use multiple threads, which results in additional overhead managing the threads because many workloads demanding a limited amount of CPU threads. Luckily, it is possible to limit the number of threads which Numpy is using for it's functions. Adding the thread count as another dimension to the parameter study from image 8, the graph from image 9 is obtained.

This result shows, that the parallelization through multiprocessing becomes more effective when the maximum number of threads used by Numpy is limited to 1. It can be seen also, that more processes result in an exponential decay. To identify the saturation, at which increasing the process count does not have a noticeable effect, the Python simulation is executed with 1-64 processes on a machine with 64 cores. The result is displayed in figure 10.

This indicates that a higher core count of more than 32 cores does not increase the performance of the Jacobian matrix evaluation any further.

Because the parallel computation of the Jacobian matrix is the most efficient with about 3 s, the future computations will use this method. Therefore, a wrapper function is implemented to create an interface which the solver can use for the re-evaluation of this matrix.

https://doi.org/10.3311/ECCOMASMBD2021-196

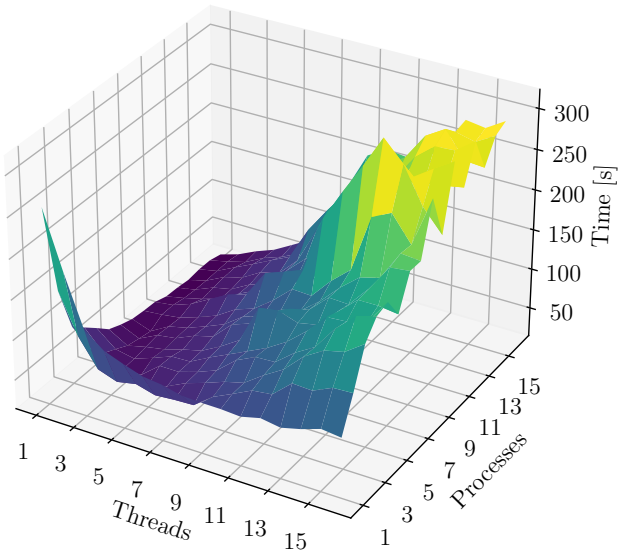


Figure 9: Jacobi matrix evaluation time depending on processes and allowed thread usage by Numpy

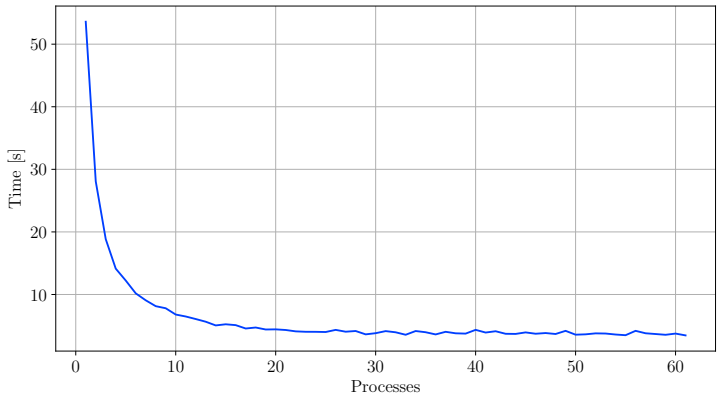


Figure 10: Jacobi matrix evaluation time depending on processes with clear saturation at about 32 processes

## 4 ASSESSMENT OF SEISMIC PROTECTION POTENTIAL

### 4.1 Environment Setup

The initial purpose of this model development was to investigate the seismic protection potential of an expansion joint like displayed in figure 2b. The suggested method to obtain this potential is by creating a response spectrum of a single DOF model which represents the bridge building. A response spectrum displays the maximum acceleration, also called spectral acceleration, in dependence of the period of the single DOF model. These accelerations can be obtained by making several time step simulations with different natural frequencies of the single DOF model and using the maximum acceleration response of those simulations. In order to generate a spectral acceleration, the complete simulation system displayed in figure 11.

The mass gets exposed to an earthquake ground acceleration and oscillates according to its natural frequency. The expansion joint is connected to this mass and experiences a earthquake acceleration from the abutment, too. The parameters from table 2 are used for the simulation.

The ground acceleration from the 1989 Loma Prieta earthquake [11] is used as the earthquake

https://doi.org/10.3311/ECCOMASMBD2021-196

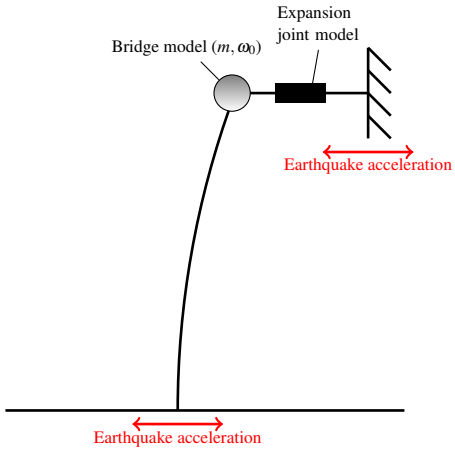


Figure 11: Earthquake system setup

| | | |
|---|---|---|
| Mass | $m$ | $1 \times 10^8$ kg |
| Natural frequency | $\omega_0$ | $6.3\,\mathrm{s}^{-1}$ |
| Friction | $\mu$ | 0.05 |

Table 2: Parameters used for the earthquake simulation

acceleration.

### 4.2 Simulation Results

When considering, that larger bridges containing more than one expansion joint, the used mass for the single DOF model is realistic when computing with one expansion joint only. To see the damping effect, which the expansion joint generates on the oscillating mass, the acceleration of the mass with and without the expansion joint model is displayed in figure 12.

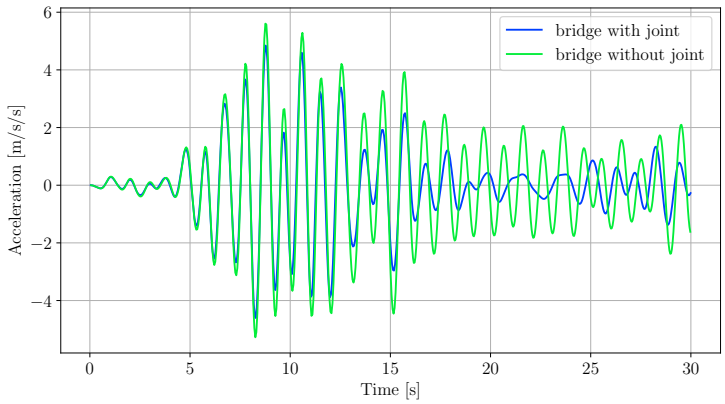


Figure 12: Bridge response acceleration with and without the expansion joint model

This result gives a first impression, on how expansion joints can influence the dynamic response of a bridge caused by an earthquake. The spectral acceleration from this step by step time integration would be $5.6\,\mathrm{m\,s}^{-2}$ without and $4.8\,\mathrm{m\,s}^{-2}$ with the expansion joint. Overall, this is a reduction of over 14 %.

## 5 CONCLUSIONS

It has been shown, how to achieve an efficient simulation for very large expansion joints. The Python model was structured in a way, that heavy and often called workloads are compiled into efficient functions. The fact, that many stiff force elements are present, an implicit solver was necessary to gain a stable result. This however introduced the need for the calculation of a Jacobian matrix, which is very time consuming when using the standard methods of the given Python solvers. A study on multiprocessing and limiting the number of threads used by the code showed that the most efficient method is using multiprocessing and deactivate multithreading within Numpy. This way, the Jacobi matrix evaluation time could be reduced from 90 s to 3 s, which is a significant speedup. The overall simulation time for such a model is now reduced to few hours instead of several days. The first results with a single DOF model representing a bridge showed very promising damping capabilities of the expansion joint. To investigate this behavior more deeply, several parameter studies will be done in order to identify the dependency of geometry, bridge model, friction parameters, ground motion and much more. The model is now efficient enough to deliver fast and stable results.

## ACKNOWLEDGMENTS

I would like to express my very great appreciation the company MAURER SE for the financial support to make this project possible.

## REFERENCES

[1] Quan, G., Kawashima, K.: Effect of finger expansion joints on seismic response of bridge. Doboku Gakkai Ronbunshuu A **65** (2009) 243–254

[2] Harris, C.R., Millman, K.J., van der Walt, S.J., Gommers, R., Virtanen, P., Cournapeau, D., Wieser, E., Taylor, J., Berg, S., Smith, N.J., Kern, R., Picus, M., Hoyer, S., van Kerkwijk, M.H., Brett, M., Haldane, A., del Río, J.F., Wiebe, M., Peterson, P., Gérard-Marchant, P., Sheppard, K., Reddy, T., Weckesser, W., Abbasi, H., Gohlke, C., Oliphant, T.E.: Array programming with NumPy. Nature **585**(7825) (September 2020) 357–362

[3] Oden, J., Martins, J.: Models and computational methods for dynamic friction phenomena. Computer Methods in Applied Mechanics and Engineering **52**(1) (1985) 527–634

[4] Flores, P.: Concepts and Formulations for Spatial Multibody Dynamics. (01 2015)

[5] Rill, G., Schaeffer, T., Borchsenius, F.: Grundlagen und computergerechte Methodik der Mehrkörpersimulation – Vertieft in Matlab-Beispielen, Übungen und Anwendungen. (02 2020)

[6] Gear, C., Leimkuhler, B., Gupta, G.: Automatic integration of Euler-Lagrange equations with constraints. Journal of Computational and Applied Mathematics **12-13** (1985) 77–90

[7] Byrne, G.D., Hindmarsh, A.C.: A Polyalgorithm for the Numerical Solution of Ordinary Differential Equations. ACM Trans. Math. Softw. **1**(1) (1975) 71–96

[8] Hairer, E., Wanner, G.: Solving Ordinary Differential Equations II. Volume 14. (2010)

[9] Lam, S., Pitrou, A., Seibert, S.: Numba: a LLVM-based Python JIT compiler. (2015) 1–6

[10] Curtis, A.R., Powell, M.J.D., Reid, J.K.: On the Estimation of Sparse Jacobian Matrices. IMA Journal of Applied Mathematics **13**(1) (1974) 117–119

[11] Pollitz, F., Biirgmann, R., Segall, P.: Joint estimation of afterslip rate and postseismic relaxation following the 1989 Loma Prieta earthquake. Journal of Geophysical Research: Solid Earth **103992** (11 1998) 975–26

https://doi.org/10.3311/ECCOMASMBD2021-166

ECCOMAS Thematic Conference on Multibody Dynamics
December 12 - 15, 2021, Budapest, Hungary

# Projection Continuation for Minimal Coordinate Set Dynamics of Constrained Systems

**Ping Zhou**[1], **Andrea Zanoni**[2], **Pierangelo Masarati**[2]

[1] School of Astronautics
Harbin Institute of Technology
Harbin, China
ping.zhou@polimi.it

[2] Department of Aerospace Science and Technology
Politecnico di Milano
via La Masa 34, 20156, Milano, Italy
{andrea.zanoni,pierangelo.masarati}@polimi.it

## ABSTRACT

The formulation of constrained system dynamics using coordinate projection onto a subspace locally tangent to the constraint manifold is revisited using the QR factorization of the constraint Jacobian matrix to extract a suitable subspace, and integrating the evolution of the QR factorization along with that of the constraint Jacobian matrix, as the solution evolves. A true continuation algorithm is thus proposed for the subspace of independent coordinates, which does not visibly affect the quality of the solution, but avoids the artificial algorithmic discontinuities in the generalized velocities that would result from arbitrary reparameterization of the coordinate set. This property is exemplified by solving simple multi-degree-of-freedom problems with and without the proposed continuation.

**Keywords:** Minimal Coordinate Set, Coordinate Projection, Automatic Coordinate Reduction, QR Factorization.

## 1 INTRODUCTION

In mechanical system dynamics, unconstrained dynamics problems are usually formulated as a set of second-order ordinary differential equations (ODE) that depend on a corresponding set of coordinates. A convenient approximation to describe the interaction between the parts of the system is often their idealization at a purely kinematic level, in form of algebraic relationships between the coordinates of the parts. The addition of these algebraic equations turns the problem into a system of differential-algebraic equations (DAE). The original coordinates are no longer independent; the actual number of independent coordinates reduces to that of the truly independent degrees of freedom. The enforcement of the constraints results in constraint reaction generalized forces, usually formulated as Lagrange multipliers. They represent the (unknown) internal forces whose value is whatever is required to guarantee the enforcement of the constraints. For a review of the possible approaches, see for example [1].

The constrained dynamics problem can be solved either directly, in form of a system of DAEs, where the original coordinates, augmented by the Lagrange multipliers, represent the unknowns in the so-called redundant coordinate set (RCS) formulation or, through manipulations that will be detailed in a later section, it can be transformed into the corresponding underlying ODE problem, reducing the set of coordinates to the truly independent (Lagrangian) ones, following the so-called minimal coordinate set (MCS) formulation. For a review of the possible approaches, see for example [2]. This paper focuses on this latter approach.

It is worth noticing that third approach is possible, i.e. to somehow embed the constraints in the unconstrained problem, formally preserving the original structure and unknowns. See for example the so-called Augmented Lagrangian approach [3] or the force projection method [4]. Also in this case, the problem formally reduces to ODE, with all the related implications, opportunities

[1] Ping Zhou is currently a visiting PhD student at Politecnico di Milano.

https://doi.org/10.3311/ECCOMASMBD2021-166

and limitations in terms of approaches for its numerical integration: explicit methods can be used, subjected to conditional stability limitations.

It is recognized that the reduction of the original coordinates into the MCS may be a challenging task, and that their nature is *local*, i.e. there may not exist a generally valid choice, which works for all configurations of the system [5]. Being such choice local, when the coordinates need to be redefined with respect to a new configuration discontinuities in the generalized coordinates (specifically in their derivatives) are expected, although not related to any physical discontinuity in the kinematics or dynamics of the system. Indeed, the motion with respect to the original coordinates is not expected to show any discontinuity, the latter being mere artifacts of a redefinition of the local coordinates. This work presents a well-known and effective method for selecting a subspace of independent coordinates that is intrinsically tangent to the constraint manifold at a specific configuration, based on the QR factorization of the constraint Jacobian matrix, and discusses how to operate the redefinition of the coordinates' subspace in a continuous manner, to eliminate those unnecessary, formal discontinuities.

## 2 PROBLEM DESCRIPTION

### 2.1 Constrained Dynamics Problem Formulation

A generic constrained system dynamics problem is formulated by adding $m$ (holonomic, in the present case, and ideal) kinematic constraints, in form of the set of algebraic equations

$$\mathbf{c}(\mathbf{x},t) = \mathbf{0} \tag{1}$$

with $\mathbf{c} \in \mathbb{R}^m$, to a set of $n$ ordinary differential equations ($n \geq m$, but usually $n > m$) that express the dynamics of an unconstrained system of $n$ coordinates $\mathbf{x} \in \mathbb{R}^n$,

$$\mathbf{M}\ddot{\mathbf{x}} = \mathbf{f} \tag{2}$$

subjected to a set of generalized forces $\mathbf{f} \in \mathbb{R}^n$, energetically conjugated to a virtual perturbation of the coordinates, $\delta\mathbf{x}$. These equations are modified by the addition of the constraint reactions $\mathbf{f}_c = -\mathbf{c}_{/\mathbf{x}}^T \boldsymbol{\lambda}$, as

$$\mathbf{M}\ddot{\mathbf{x}} + \mathbf{c}_{/\mathbf{x}}^T \boldsymbol{\lambda} = \mathbf{f} \tag{3}$$

where $\mathbf{c}_{/\mathbf{x}} = \mathbf{A} \in \mathbb{R}^{m \times n}$ is the partial derivative of the constraint equations $\mathbf{c}$ with respect to the coordinates $\mathbf{x}$, namely the constraint Jacobian matrix, and $\boldsymbol{\lambda} \in \mathbb{R}^m$ are the corresponding Lagrange multipliers.

### 2.2 Minimal Coordinate Set Approach

The Minimal Coordinate Set approach consists in defining a suitable subspace $\mathbf{T} \in \mathbb{R}^{n \times (n-m)}$ of the space spanned by the coordinates $\mathbf{x}$ which is tangent to the constraint manifold, namely $\mathbf{T}^T\mathbf{A}^T \equiv \mathbf{0} \in \mathbb{R}^{(n-m)\times m}$, such that

$$\dot{\mathbf{x}} = \mathbf{T}\dot{\mathbf{q}} + \boldsymbol{\beta}' \tag{4a}$$

$$\ddot{\mathbf{x}} = \mathbf{T}\ddot{\mathbf{q}} + \boldsymbol{\beta}'' \tag{4b}$$

where $\mathbf{q} \in \mathbb{R}^{n-m}$ are local, truly independent coordinates, with $\boldsymbol{\beta}'$ and $\boldsymbol{\beta}''$ defined accordingly, the former being non-zero only in case of rheonomous constraints, such that

$$\mathbf{c}_{/\mathbf{x}}\dot{\mathbf{x}} + \mathbf{c}_{/t} = \mathbf{0} \qquad \rightarrow \qquad \mathbf{c}_{/\mathbf{x}}\left(\mathbf{T}\dot{\mathbf{q}} + \boldsymbol{\beta}'\right) + \mathbf{c}_{/t} = \mathbf{0} \qquad \rightarrow \qquad \mathbf{c}_{/\mathbf{x}}\boldsymbol{\beta}' = -\mathbf{c}_{/t} \tag{5}$$

being $\mathbf{c}_{/\mathbf{x}}\mathbf{T} = \mathbf{A}\mathbf{T} \equiv \mathbf{0}$, and analogously

$$\mathbf{c}_{/\mathbf{x}}\ddot{\mathbf{x}} + (\dot{\mathbf{c}})_{/\mathbf{x}}\dot{\mathbf{x}} + (\dot{\mathbf{c}})_{/t} = \mathbf{0} \qquad \rightarrow \qquad \mathbf{c}_{/\mathbf{x}}\boldsymbol{\beta}'' = -(\dot{\mathbf{c}})_{/\mathbf{x}}\dot{\mathbf{x}} - (\dot{\mathbf{c}})_{/t} \tag{6}$$

https://doi.org/10.3311/ECCOMASMBD2021-166

The constrained dynamics problem, projected in such subspace, yields

$$\mathbf{T}^T\mathbf{M}\mathbf{T}\ddot{\mathbf{q}} + \cancel{\mathbf{T}^T\mathbf{A}^T\boldsymbol{\lambda}} = \mathbf{T}^T\left(\mathbf{f} - \mathbf{M}\boldsymbol{\beta}''\right) \tag{7}$$

The solution is sought by first integrating Eq. (7) to obtain the generalized velocities $\dot{\mathbf{q}}$; then, Eq. (4a) is integrated to obtain an estimate of $\mathbf{x}$, which needs to be subsequently refined by enforcing the constraint at the position level, Eq. (1).

### 2.3 QR Factorization for Optimal Minimal Coordinate Set Selection

Among the several approaches proposed in the literature [6], a suitable choice for $\mathbf{T}$ is obtained through the QR factorization [7] of the transpose of the constraint Jacobian matrix,

$$\mathbf{A}^T = \mathbf{Q}\mathbf{R} = \begin{bmatrix} \mathbf{Q}_1 & \mathbf{Q}_2 \end{bmatrix} \begin{bmatrix} \mathbf{R}_1 \\ \mathbf{0} \end{bmatrix} = \mathbf{Q}_1\mathbf{R}_1 \tag{8}$$

where matrix $\mathbf{Q} \in \mathbb{R}^{n\times n}$ is orthogonal and submatrix $\mathbf{R}_1 \in \mathbb{R}^{m\times m}$ is upper triangular. Submatrix $\mathbf{Q}_2 \in \mathbb{R}^{n\times(n-m)}$ represents an optimal choice for $\mathbf{T}$.

Velocities are then expressed as

$$\dot{\mathbf{x}} = \mathbf{Q}_2\dot{\mathbf{q}} + \mathbf{Q}_1\mathbf{p}' \tag{9}$$

with $\mathbf{Q}_1\mathbf{p}' = \boldsymbol{\beta}'$, such that

$$\mathbf{0} = \mathbf{A}\dot{\mathbf{x}} + \mathbf{c}_{/t} = \mathbf{R}_1^T\mathbf{Q}_1^T\left(\mathbf{Q}_2\dot{\mathbf{q}} + \mathbf{Q}_1\mathbf{p}'\right) + \mathbf{c}_{/t} = \mathbf{R}_1^T\mathbf{p}' + \mathbf{c}_{/t} \qquad \rightarrow \qquad \mathbf{p}' = -\mathbf{R}_1^{-T}\mathbf{c}_{/t} \tag{10}$$

whereas accelerations are expressed as

$$\ddot{\mathbf{x}} = \mathbf{Q}_2\ddot{\mathbf{q}} + \mathbf{Q}_1\mathbf{p}'' \tag{11}$$

with $\mathbf{Q}_1\mathbf{p}'' = \boldsymbol{\beta}''$, such that

$$\begin{aligned} &\mathbf{0} = \mathbf{A}\ddot{\mathbf{x}} + \left(\dot{\mathbf{c}}\right)_{/\mathbf{x}}\dot{\mathbf{x}} + \left(\dot{\mathbf{c}}\right)_{/t} = \mathbf{R}_1^T\mathbf{Q}_1^T\left(\mathbf{Q}_2\ddot{\mathbf{q}} + \mathbf{Q}_1\mathbf{p}''\right) + \left(\dot{\mathbf{c}}\right)_{/\mathbf{x}}\dot{\mathbf{x}} + \left(\dot{\mathbf{c}}\right)_{/t} = \mathbf{R}_1^T\mathbf{p}'' + \left(\dot{\mathbf{c}}\right)_{/\mathbf{x}}\dot{\mathbf{x}} + \left(\dot{\mathbf{c}}\right)_{/t} \\ &\rightarrow \ \mathbf{p}'' = -\mathbf{R}_1^{-T}\left[\left(\dot{\mathbf{c}}\right)_{/\mathbf{x}}\dot{\mathbf{x}} + \left(\dot{\mathbf{c}}\right)_{/t}\right] \end{aligned} \tag{12}$$

According to Eqs. (7) and (9), the problem becomes

$$\mathbf{Q}_2^T\mathbf{M}\mathbf{Q}_2\ddot{\mathbf{q}} = \mathbf{Q}_2^T\left(\mathbf{f} - \mathbf{M}\boldsymbol{\beta}''\right) \tag{13a}$$

$$\dot{\mathbf{x}} = \mathbf{Q}_2\dot{\mathbf{q}} + \mathbf{Q}_1\mathbf{p}' \tag{13b}$$

Its integration from time $t_k$ to $t_{k+1}$ yields

$$\mathbf{x}_{k+1}^{(0)} = \mathbf{Q}_{2_k}\mathbf{q}_{k+1} + \mathbf{Q}_{1_k}\mathbf{p}^{(0)} \tag{14}$$

where the subscript $(\cdot)^{(0)}$ indicates an estimate of the final value, pending verification that it complies with the constraint of Eq. (1). The final value of the unknown $\mathbf{p}$ results from the iterative solution of

$$\mathbf{c}(\mathbf{x}_{k+1}, t_{k+1}) = \mathbf{0} \tag{15}$$

namely

$$\mathbf{c}\left(\mathbf{x}_{k+1}^{(i)}, t_{k+1}\right) + \left(\mathbf{c}_{/\mathbf{x}}\right)_{k+1}^{(i)}\mathbf{Q}_{1_k}\Delta\mathbf{p} = \mathbf{0} \tag{16}$$

i.e.

$$\Delta\mathbf{p} = -\left(\left(\mathbf{c}_{/\mathbf{x}}\right)_{k+1}^{(i)}\mathbf{Q}_{1_k}\right)^{-1}\mathbf{c}\left(\mathbf{x}_{k+1}^{(i)}, t_{k+1}\right) \tag{17}$$

$$\mathbf{p} \mathrel{+}= \Delta\mathbf{p} \tag{18}$$

where $\left(\mathbf{c}_{/\mathbf{x}}\right)_{k+1}^{(i)}$ is the constraint Jacobian matrix at time $t_{k+1}$ during the $i$th constraint enforcement iteration, evaluated as a function of $\mathbf{x}_{k+1}^{(i)}$.

https://doi.org/10.3311/ECCOMASMBD2021-166

### 2.4 Tangent Subspace Selection and Continuation

Submatrices $\mathbf{Q}_1$ and $\mathbf{R}_1$ are uniquely determined[1], once $\mathbf{A}$ is known. Submatrix $\mathbf{Q}_2$, instead, is only subjected to matrix $\mathbf{Q}$'s general constraint of being orthogonal, namely $\mathbf{Q}_2^T\mathbf{Q}_2 \equiv \mathbf{I} \in \mathbb{R}^{(n-m)\times(n-m)}$ and $\mathbf{Q}_2^T\mathbf{Q}_1 \equiv \mathbf{0} \in \mathbb{R}^{(n-m)\times m}$, but otherwise undefined. Specifically, it is defined in excess of post-multiplication by an arbitrary orthogonal matrix, $\mathbf{P} \in \mathbb{R}^{(n-m)\times(n-m)}$: $\tilde{\mathbf{Q}}_2 = \mathbf{Q}_2\mathbf{P}$ also complies with the orthogonality requirement, since $\tilde{\mathbf{Q}}_2^T\tilde{\mathbf{Q}}_2 = \mathbf{P}^T\mathbf{Q}_2^T\mathbf{Q}_2\mathbf{P} = \mathbf{P}^T\mathbf{P} \equiv \mathbf{I}$ and $\tilde{\mathbf{Q}}_2^T\mathbf{Q}_1 = \mathbf{P}^T\mathbf{Q}_2^T\mathbf{Q}_1 = \mathbf{P}^T\mathbf{0} = \mathbf{0}$.

In fact, the QR factorization produces a "local" representation of the constraint Jacobian matrix; as such, the generalized coordinates associated with the subspace $\mathbf{T} = \mathbf{Q}_2$, which do not have any specific physical meaning, represent a local reparameterization of the subspace of the coordinates that is tangent to the constraint manifold. When the QR factorization is computed at different time steps $t_k$, if $n-m > 1$ the columns of the resulting $\mathbf{Q}_{2_k}$ are completely unrelated, their resulting value being solely dictated by the internal intricacies of the QR factorization algorithm.

The aim of the present work is to propose a simple and intuitive algorithm that tracks the evolution of the subspace spanned by $\mathbf{Q}_2$ using a form of differential "continuation," to preserve some sort of spatial continuity of the generalized coordinates, $\mathbf{q}$, by minimizing the amount of deviation of the subspace that is intrinsically required to maintain $\mathbf{Q}_2$ tangent to the constraint manifold across time steps, without altering the quality of the solution.

Consider the time derivative of the transpose of the constraint Jacobian matrix in its QR factorized form,

$$\dot{\mathbf{A}}^T = \dot{\mathbf{Q}}\mathbf{R} + \mathbf{Q}\dot{\mathbf{R}} \tag{19}$$

The derivative of matrix $\mathbf{Q}$ may be expressed as $\dot{\mathbf{Q}} = \mathbf{Q}\boldsymbol{\Omega}$, where the skew-symmetric nature of matrix $\boldsymbol{\Omega} \in \mathbb{R}^{n\times n}$ descends from the orthogonality of matrix $\mathbf{Q}$:

$$\frac{\mathrm{d}}{\mathrm{d}t}\left(\mathbf{Q}^T\mathbf{Q}\right) = \dot{\mathbf{Q}}^T\mathbf{Q} + \mathbf{Q}^T\dot{\mathbf{Q}} = \left(\mathbf{Q}^T\dot{\mathbf{Q}}\right)^T + \mathbf{Q}^T\dot{\mathbf{Q}} = \mathbf{0} \qquad \rightarrow \qquad \mathbf{Q}^T\dot{\mathbf{Q}} = \boldsymbol{\Omega} \tag{20}$$

When the problem is integrated numerically, the solution from time step $t_k$ to time step $t_{k+1}$ is computed. The QR factorization at time $t_k$ yields submatrices $\mathbf{Q}_{1_k}$ and $\mathbf{R}_{1_k}$. The generalized velocities at time $t_k$ are computed with reference to the subspace spanned by $\mathbf{Q}_{2_k}$. After computing the solution at the new time step, the Jacobian matrix at time $t_{k+1}$, $\mathbf{A}_{k+1}$, is known. As such, through the economy QR factorization of its transpose, submatrices $\mathbf{Q}_{1_{k+1}}$ and $\mathbf{R}_{1_{k+1}}$ are determined. Instead of computing also submatrix $\mathbf{Q}_{2_{k+1}}$ through the full QR factorization, the proposed continuation algorithm is used as illustrated in the following. Consider

$$\mathbf{Q}_1^T\dot{\mathbf{A}}^T\mathbf{R}_1^{-1} = \mathbf{Q}_1^T\dot{\mathbf{Q}}_1 + \dot{\mathbf{R}}_1\mathbf{R}_1^{-1} \tag{21}$$

Matrix $\dot{\mathbf{R}}_1\mathbf{R}_1^{-1}$ is the product of two upper triangular matrices, thus it is itself an upper triangular matrix. Matrix $\mathbf{Q}_1^T\dot{\mathbf{Q}}_1 = \boldsymbol{\Omega}_1 \in \mathbb{R}^{m\times m}$ is skew-symmetric by construction; it can be seen as $\boldsymbol{\Omega}_1 = \boldsymbol{\Omega}_{1_L} - \boldsymbol{\Omega}_{1_L}^T$, where $\boldsymbol{\Omega}_{1_L} = \mathrm{stril}(\boldsymbol{\Omega}_1)$ is the strictly lower triangular part of matrix $\boldsymbol{\Omega}_1$, which can be obtained as

$$\boldsymbol{\Omega}_{1_L} = \mathrm{stril}\left(\mathbf{Q}_1^T\dot{\mathbf{A}}^T\mathbf{R}_1^{-1}\right) \tag{22}$$

since $\mathrm{stril}\left(\dot{\mathbf{R}}_1\mathbf{R}_1^{-1}\right) \equiv \mathbf{0}$ by construction, being $\dot{\mathbf{R}}_1\mathbf{R}_1^{-1}$ upper triangular. From Eq. (20), one can show that the derivative of matrix $\mathbf{Q}$,

$$\begin{aligned}\dot{\mathbf{Q}} = \begin{bmatrix} \dot{\mathbf{Q}}_1 & \dot{\mathbf{Q}}_2 \end{bmatrix} &= \begin{bmatrix} \mathbf{Q}_1 & \mathbf{Q}_2 \end{bmatrix} \begin{bmatrix} \boldsymbol{\Omega}_1 & -\mathbf{R}_1^{-T}\dot{\mathbf{A}}\mathbf{Q}_2 \\ \mathbf{Q}_2^T\dot{\mathbf{A}}^T\mathbf{R}_1^{-1} & \cancel{\boldsymbol{\Omega}_2} \end{bmatrix} \\ &= \begin{bmatrix} \mathbf{Q}_1 & \mathbf{Q}_2 \end{bmatrix} \begin{bmatrix} \boldsymbol{\Omega}_1 & -\boldsymbol{\Omega}_{21}^T \\ \boldsymbol{\Omega}_{21} & \mathbf{0} \end{bmatrix} = \mathbf{Q}\boldsymbol{\Omega}\end{aligned} \tag{23}$$

[1] To this end, we choose the diagonal elements of $\mathbf{R}_1$ to be non-negative, a zero value indicating indetermination.

https://doi.org/10.3311/ECCOMASMBD2021-166

is entirely known, where the bottom right block of the rightmost matrix, $\mathbf{\Omega}$, should contain an unknown skew-symmetric contribution $\mathbf{\Omega}_2 \in \mathbb{R}^{(n-m)\times(n-m)}$, that is arbitrarily set to zero to modify as little as possible the subspace $\mathbf{Q}_2$; specifically,

$$\dot{\mathbf{Q}}_2 = -\mathbf{Q}_1\mathbf{\Omega}_{21}^T = -\mathbf{A}^+\dot{\mathbf{A}}\mathbf{Q}_2 \tag{24}$$

In fact, $\mathbf{\Omega}_2$ may be interpreted as the *angular velocity* of subspace $\mathbf{Q}_2$, the rate of reorientation with respect to itself, whereas $\mathbf{\Omega}_{12}$ expresses the rate of reorientation with respect to $\mathbf{Q}_1$, in order to remain orthogonal to it.

Thus, the subspace $\mathbf{Q}_2$ can be integrated, taking appropriate measures (e.g. using Munthe-Kaas' method [8]) to guarantee that the resulting matrix $\mathbf{Q}$ preserves orthogonality, and submatrix $\mathbf{Q}_1$ matches that resulting from the decomposition of the transpose of the constraint Jacobian matrix. For example, for $\mathbf{\Omega}$ constant across a time step of duration $t_{k+1} - t_k = h$,

$$\mathbf{Q}_{k+1} = \mathbf{Q}_k \mathrm{e}^{\mathbf{\Omega}h} \tag{25}$$

or

$$\mathbf{Q}_{2_{k+1}} = \mathrm{e}^{-\mathbf{A}^+\dot{\mathbf{A}}h}\mathbf{Q}_{2_k} \tag{26}$$

the latter being only a first-order approximation of the former, since the intrinsic skew-symmetric structure of the exponent matrix $\mathbf{\Omega}$ is lost.

Submatrix $\mathbf{Q}_{2_{k+1}}$ resulting from the proposed integration may need to be corrected to guarantee orthogonality with respect to submatrix $\mathbf{Q}_{1_{k+1}}$ obtained from the economy QR factorization of $\mathbf{A}_{k+1}^T$.

## 3 RESULTS

Two simple examples, a spatial (3D) pendulum and a spin top, are analyzed to illustrate how the proposed method produces a more regular and intuitive choice of the projection subspace during the integration of the solution.

**Spatial Pendulum** Consider a simple point mass spherical pendulum of mass $M$ and length $\ell$, subjected to a uniform gravity field $g = 9.81$ m/s$^2$, directed along the negative $z$ axis. Its equations of motion are

$$\begin{bmatrix} M & 0 & 0 \\ 0 & M & 0 \\ 0 & 0 & M \end{bmatrix} \begin{Bmatrix} \ddot{x} \\ \ddot{y} \\ \ddot{z} \end{Bmatrix} + \begin{bmatrix} 2x \\ 2y \\ 2z \end{bmatrix} \lambda = \begin{Bmatrix} 0 \\ 0 \\ -Mg \end{Bmatrix} \tag{27a}$$

$$x^2 + y^2 + z^2 - \ell^2 = 0 \tag{27b}$$

The unconstrained problem has 3 degrees of freedom, $x$, $y$ and $z$, and 1 constraint, Eq. (27a); thus, the constrained problem has 2 degrees of freedom. Consequently, $\mathbf{Q}_1 \in \mathbb{R}^{3\times1}$ and $\mathbf{Q}_2 \in \mathbb{R}^{3\times2}$. The constraint Jacobian matrix and its time derivative are

$$\mathbf{A} = \begin{bmatrix} 2x & 2y & 2z \end{bmatrix} \tag{28}$$

$$\dot{\mathbf{A}} = \begin{bmatrix} 2\dot{x} & 2\dot{y} & 2\dot{z} \end{bmatrix} \tag{29}$$

The QR factorization of $\mathbf{A}^T$ in a given initial configuration $(x,y,z) = (x_0,y_0,z_0)$ yields

$$\mathbf{A}^T = \begin{bmatrix} 2x_0 \\ 2y_0 \\ 2z_0 \end{bmatrix} = \left[\begin{array}{c|cc} x_0/\ell & q_{12} & q_{13} \\ y_0/\ell & q_{22} & q_{23} \\ z_0/\ell & q_{32} & q_{33} \end{array}\right] \left[\begin{array}{c} 2\ell \\ \hline 0 \\ 0 \end{array}\right] = \mathbf{QR} \tag{30}$$

https://doi.org/10.3311/ECCOMASMBD2021-166

where the 6 coefficients $q_{ij}$, $i = 1,2,3,\ j = 2,3$ are related by 5 orthogonality conditions, leaving only one undetermined parameter.

Without loss of generality, let us assume that $(x_0, y_0, z_0) = (\ell, 0, 0)$, which complies with the constraint equation; this yields

$$\mathbf{A}^T = \left[\begin{array}{c} 2\ell \\ 0 \\ 0 \end{array}\right] = \left[\begin{array}{c|cc} 1 & 0 & 0 \\ 0 & \cos\alpha_0 & -\sin\alpha_0 \\ 0 & \sin\alpha_0 & \cos\alpha_0 \end{array}\right] \left[\begin{array}{c} 2\ell \\ \hline 0 \\ 0 \end{array}\right] = \mathbf{QR} \tag{31}$$

where $\alpha_0$ is an arbitrary parameter. Clearly, when $\alpha_0 = 0$, the two vectors that span the subspace of $\mathbf{Q}_2$ are the coordinate axes $y$ and $z$.

The projected equations of motion in the initial configuration are:

$$\left[\begin{array}{cc} M & 0 \\ 0 & M \end{array}\right] \left\{\begin{array}{c} \ddot{q}_1 \\ \ddot{q}_2 \end{array}\right\} = \left\{\begin{array}{c} -\sin\alpha_0 \\ -\cos\alpha_0 \end{array}\right\} Mg \tag{32}$$

Without loss of generality, it is assumed that $(\dot{x}_0, \dot{y}_0, \dot{z}_0) = (0, v_0, 0)$, which complies with the derivative of the constraint equation in the initial configuration,

$$0 = \mathbf{A}\dot{\mathbf{x}} = \left[\begin{array}{ccc} 2\ell & 0 & 0 \end{array}\right] \left\{\begin{array}{c} 0 \\ v_0 \\ 0 \end{array}\right\} \tag{33}$$

in this case, one obtains

$$\mathbf{\Omega}_{1_L} = 0 \text{ [as one would expect for a diagonal element of a skew-symmetric matrix]} \tag{34}$$

$$\mathbf{\Omega}_{21} = \left[\begin{array}{ccc} 0 & \cos\alpha_0 & \sin\alpha_0 \\ 0 & -\sin\alpha_0 & \cos\alpha_0 \end{array}\right] \left[\begin{array}{c} 0 \\ 2v_0 \\ 0 \end{array}\right] \frac{1}{2\ell} = \left[\begin{array}{c} \cos\alpha_0 \\ -\sin\alpha_0 \end{array}\right] \frac{v_0}{\ell} \tag{35}$$

thus

$$\mathbf{\Omega} = \frac{v_0}{\ell} \left[\begin{array}{ccc} 0 & -\cos\alpha_0 & \sin\alpha_0 \\ \cos\alpha_0 & 0 & 0 \\ -\sin\alpha_0 & 0 & 0 \end{array}\right] \tag{36}$$

and

$$\Delta\mathbf{Q} = \left[\begin{array}{ccc} \cos\Delta\theta & -\sin\Delta\theta\cos\alpha_0 & \sin\Delta\theta\sin\alpha_0 \\ \sin\Delta\theta\cos\alpha_0 & \cos\Delta\theta\cos\alpha_0^2 - \cos\alpha_0^2 + 1 & -\sin(2\alpha_0)\left(\cos\Delta\theta - 1\right)/2 \\ -\sin\Delta\theta\sin\alpha_0 & -\sin(2\alpha_0)\left(\cos\Delta\theta - 1\right)/2 & \cos\Delta\theta + \cos\alpha_0^2 - \cos\Delta\theta\cos\alpha_0^2 \end{array}\right] \tag{37}$$

with $\Delta\theta = v_0 h/\ell$ which, for $\alpha_0 = 0$, reduces to

$$\Delta\mathbf{Q} = \left[\begin{array}{ccc} \cos\Delta\theta & -\sin\Delta\theta & 0 \\ \sin\Delta\theta & \cos\Delta\theta & 0 \\ 0 & 0 & 1 \end{array}\right] \tag{38}$$

namely, a finite rotation about the $z$ axis by an angle $\Delta\theta$.

In the present example, the mass of the pendulum is $M = 1.0$ kg, and its length is $\ell = 0.16$ m. The initial position of the mass center is $\mathbf{r}_0 = [0.08, 0, 0]^T$ m, and the initial condition is set as $v_0 = 0.7895$ m/s.

https://doi.org/10.3311/ECCOMASMBD2021-166

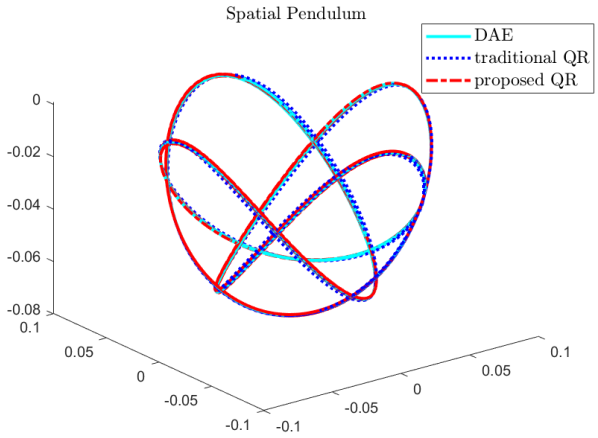


**Figure 1**. Trajectory of the spatial pendulum's center of mass: traditional and proposed QR approach results are compared to those obtained from DAE integration using MBDyn.

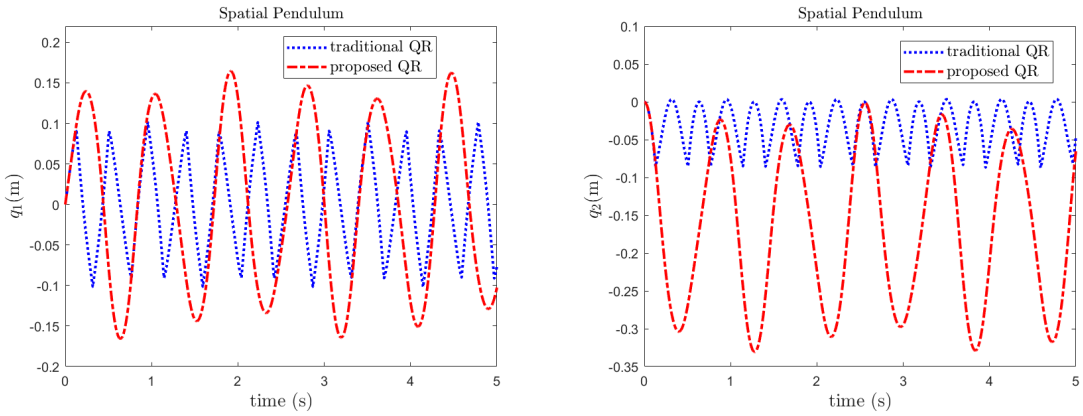


**Figure 2**. Minimal coordinates $q_i$, $(i = 1,2)$: comparison of traditional and proposed QR factorization method.

The trajectory of its center of mass resulting from the simulation using ode45 in Matlab with $h = 0.001$ s is compared to that resulting from the integration of the original DAE governing equations using the free general-purpose multibody solver MBDyn[2] [9], using a second-order accurate implicit linear multistep integration method with algorithmic dissipation (asymptotic spectral radius $\rho_\infty = 0.6$) [10], and a projection method based on the QR factorization of the transpose of the Jacobian matrix performed at each time step, without any knowledge of its evolution, using ode45 with a time step $h = 0.000005$ s to act as a reference solution, as shown in Fig. 1. The resulting minimal set generalized coordinates $q_1$ and $q_2$ and the projected generalized velocities $\dot{q}_1$ and $\dot{q}_2$ ($\dot{q}_i = \mathbf{Q}_2(:,i)^T \dot{\mathbf{x}}$) are compared to the results obtained from what is here termed "traditional QR method", as shown in Fig. 2 and Fig. 3, respectively. One may observe that the coordinates $q_i$ resulting from the proposed method are much more regular than those resulting from the traditional QR factorization. Specifically, those resulting from the proposed method appear to be continuous and differentiable, whereas those resulting from the traditional QR factorization show discontinuities in their first derivatives, $\dot{q}_i$.

This is well explained by the continuity and regularity of the evolution of each column of matrix

[2] `https://www.mbdyn.org/`.

https://doi.org/10.3311/ECCOMASMBD2021-166

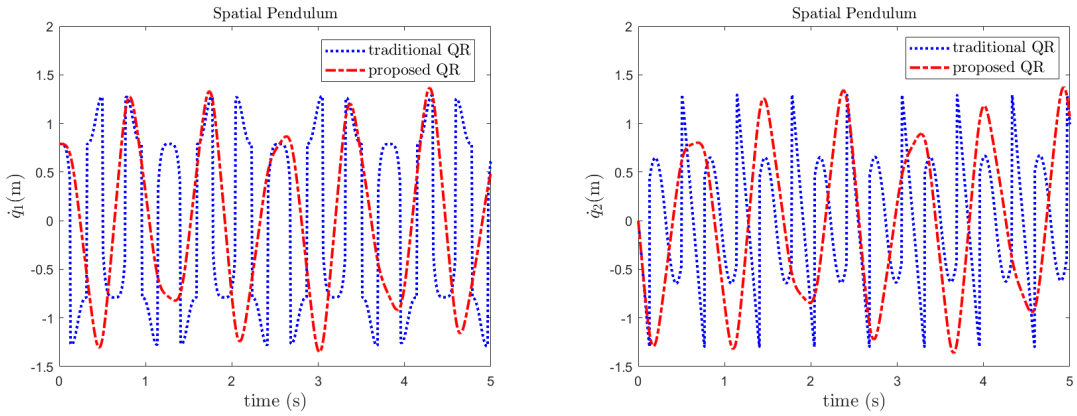


**Figure 3**. Projected velocities $\dot{q}_i$ $(i = 1,2)$: comparison of traditional and proposed QR factorization method.

$\mathbf{Q}_2$ for the proposed method, compared to the discontinuity of those resulting from the traditional QR factorization, as depicted in Fig. 4.

Furthermore, from Fig. 4 one can observe that for $t = 0$, the first column of matrix $\mathbf{Q}_2$ corresponds to $[0,1,0]^T$, i.e. the unit vector along the $y$ axis, whereas the second column of matrix $\mathbf{Q}_2$ corresponds to $[0,0,1]^T$, i.e. the unit vector along the $z$ axis, i.e. the QR algorithm chose $\alpha_0 = 0$ in Eq. (31) when initializing the subspace $\mathbf{Q}_2$. Indeed, considering the initial velocity of the spin top, one can observe that $\dot{q}_1(0) \equiv v_0$ and $\dot{q}_2(0) \equiv 0$, which is consistent with the given initial conditions. At time $t = 0$, $\dot{q}_1$ corresponds to $v$, and $\dot{q}_2$ to $w$.

**Spin Top** Consider a symmetric spin top, whose tip is constrained to be at unit distance from the origin of the global coordinate system, i.e. lying on a sphere of unit radius centered in the origin. The tip of the spin top is 1 m far away from its center of mass. The problem is sketched in Fig. 5. The inertia properties of the spin top are $m = 30$ kg and $\mathbf{J} = \text{diag}(90,90,30)$ kg·m$^2$. The initial position of the spin top is $\mathbf{r}_0 = [0,-1,0]^T$ m. The local coordinate system $x'$-$y'$-$z'$ is initially coincident with the global coordinate system $x$-$y$-$z$. A uniform gravity field of magnitude 9.81 m/s$^2$ is assumed in the negative $z$ direction. In this model, the Euler parameters $\mathbf{e}$ are used to describe the rotation of the spin top; their initial value is $\mathbf{e}_0 = [1,0,0,0]^T$. The initial velocity is $\dot{\mathbf{r}}_0 = \mathbf{0}$ m/s and the initial angular velocity is $\omega_0 = [0.1,0.1,0.3]^T$ rad/s. The initial derivative of the Euler parameters $\dot{\mathbf{e}}_0$ is computed from $1/2 \cdot \mathbf{E}(\mathbf{e}_0)\omega_0$. The constrained equations of motion of the spin top are

$$m\ddot{\mathbf{r}} + c_{\mathbf{r}}^T \lambda = \mathbf{f} \tag{39a}$$

$$4\mathbf{E}^T\mathbf{J}\mathbf{E}\ddot{\mathbf{e}} + 8\dot{\mathbf{E}}^T\mathbf{J}\mathbf{E}\omega + c_{\mathbf{e}}^T\lambda + 2\mathbf{e}^T\mu = 2\mathbf{E}^T\mathbf{t} \tag{39b}$$

$$c(t,\mathbf{r},\mathbf{e}) = 0 \tag{39c}$$

$$\mathbf{e}^T\mathbf{e} - 1 = 0 \tag{39d}$$

where $\mathbf{f}$ and $\mathbf{t}$ are the applied force and torque at the mass center, respectively. Since only gravity is applied, $\mathbf{f} = (0,0,-9.81m)$ and $\mathbf{t} = \mathbf{0}$, with

$$\mathbf{E} = \begin{pmatrix} -e_1 & e_0 & e_3 & -e_2 \\ -e_2 & -e_3 & e_0 & e_1 \\ -e_3 & e_2 & -e_1 & e_0 \end{pmatrix}$$

$c$ denotes the constraint equation, $\lambda$ and $\mu$ are the Lagrange multipliers corresponding to the constraint equation $c$, Eq. (39c), and the Euler parameter normalization, Eq. (39d), respectively.

https://doi.org/10.3311/ECCOMASMBD2021-166

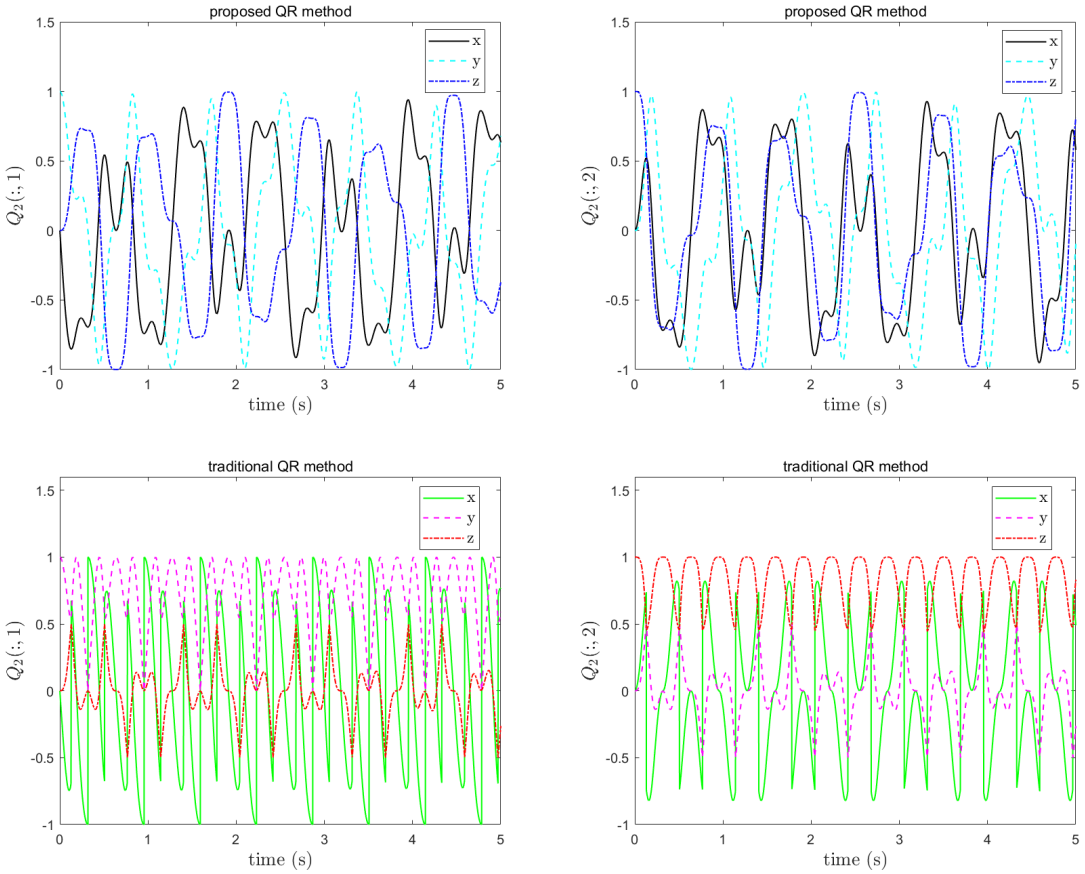


**Figure 4**. $\mathbf{Q}_2(:,i)$ $(i=1,2)$ from the proposed (top) and the traditional QR method (bottom).

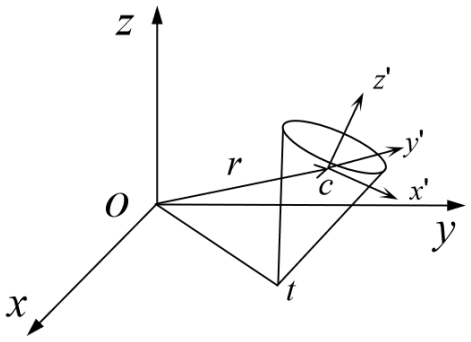


**Figure 5**. Spin top.

https://doi.org/10.3311/ECCOMASMBD2021-166

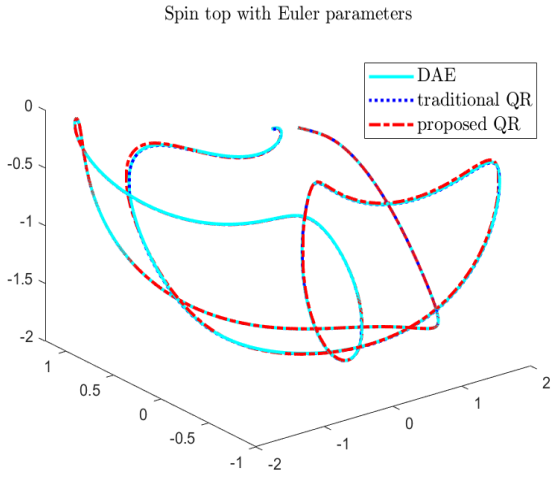


**Figure 6**. Trajectory of the spin top's center of mass: traditional and proposed QR approach results are compared to those obtained from DAE integration using MBDyn.

The absolute position of the tip is $\mathbf{r}_t = \mathbf{r} + \mathbf{A}\mathbf{u}_0$, where $\mathbf{u}_0 = [0,0,-1]^T$ m and $\mathbf{A} = \bar{\mathbf{E}}\mathbf{E}^T$ is the orientation matrix, with

$$\bar{\mathbf{E}} = \begin{pmatrix} -e_1 & e_0 & -e_3 & e_2 \\ -e_2 & e_3 & e_0 & -e_1 \\ -e_3 & -e_2 & e_1 & e_0 \end{pmatrix}$$

Therefore, the constraint equation can be expressed as

$$c = \mathbf{r}_t^T \mathbf{r}_t - 1 = \mathbf{r}^T \mathbf{r} + 2\mathbf{r}^T \mathbf{A}\mathbf{u}_0 \tag{40}$$

since $\mathbf{u}_0^T \mathbf{u}_0 \equiv 1$. The problem is described by 7 coordinates, $\mathbf{r} \in \mathbb{R}^3$ and $\mathbf{e} \in \mathbb{R}^4$, and 2 constraint equations, Eqs. (40) and (39d), thus possesses 5 degrees of freedom, $q_i$ $(i = 1,\ldots,5)$.

The trajectory of the centroid resulting from the simulation using the previously mentioned method with $h = 0.0001$ s is compared in Fig. 6 to those obtained by integrating the original DAE system using MBDyn and by using the traditional QR method, with $h = 0.0001$ s. The projection motion of $q_i$ $(i = 1,\ldots,5)$ is compared to the results of the traditional QR method without any projection in Fig. 7, whereas that of $\dot{q}_i$ $(i = 1,\ldots,5)$ is compared to the results of the traditional QR method without any projection in Fig. 8. Again, one can notice the much greater regularity of the coordinates and their derivatives as they result from the proposed method.

## 4 CONCLUSIONS

This paper presented a continuation algorithm for the redefinition of the subspace of minimal coordinates that is tangent to the constraint manifold. It is based on the full QR factorization of the constraint Jacobian matrix to initialize the subspace through the portion of the space defined by the orthogonal matrix Q that is orthogonal to the constraint Jacobian matrix. The economy QR factorization is then used to exactly factor the subspace in which the constraint Jacobian lies, while evolution of the tangent subspace is tracked by integrating the time derivative of matrix Q, eventually re-orthogonalizing the result to eliminate possible drift from the integrated tangent subspace. Numerical examples show that the result of the analysis is unchanged, but the generalized velocities do not show the discontinuities that characterize them when the tangent subspace is recomputed without considering its previous value.

https://doi.org/10.3311/ECCOMASMBD2021-166

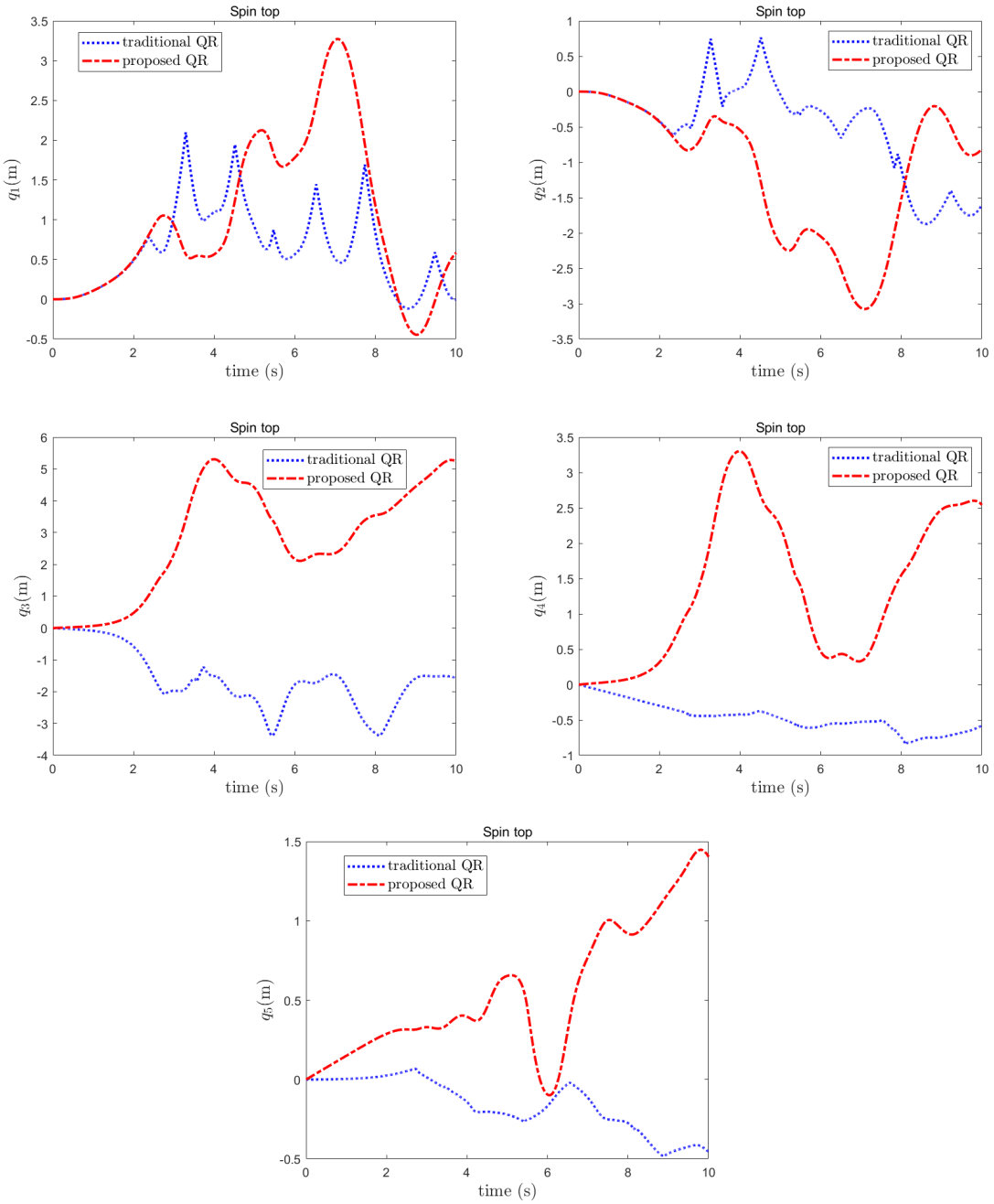


**Figure 7**. Minimal coordinates $q_i$ $(i = 1, \ldots, 5)$: comparison of traditional and proposed QR factorization method.

https://doi.org/10.3311/ECCOMASMBD2021-166

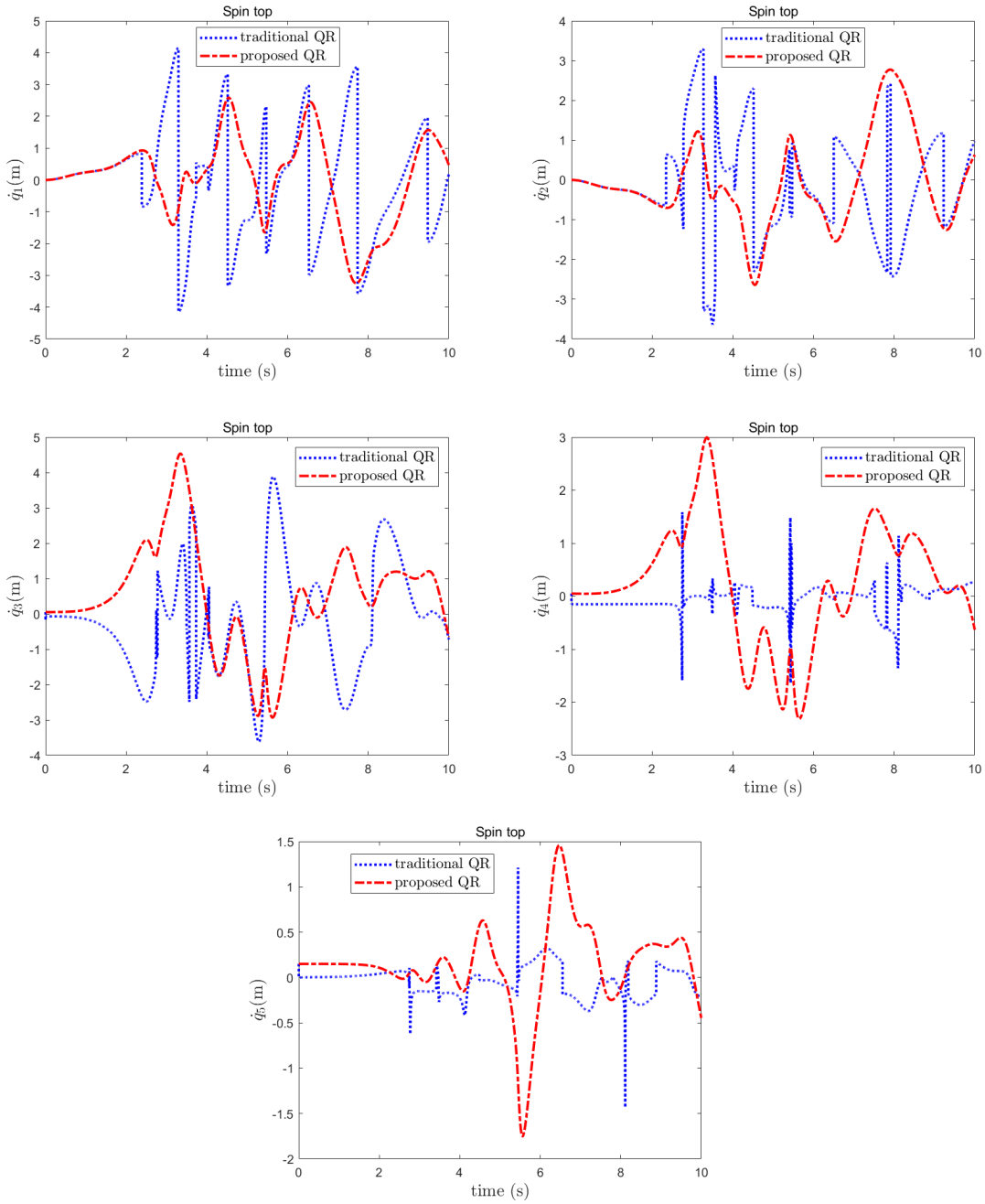


**Figure 8**. Projected velocities $\dot{q}_i$ $(i = 1, \ldots, 5)$: comparison of traditional and proposed QR factorization method.

## ACKNOWLEDGMENTS

The first author acknowledges support from the China Scholarship Council.

## REFERENCES

[1] Bauchau, O.A., Laulusa, A.: Review of contemporary approaches for constraint enforcement in multibody systems. J. of Computational and Nonlinear Dynamics **3**(1) (January 2008) doi:10.1115/1.2803258.

[2] Laulusa, A., Bauchau, O.A.: Review of classical approaches for constraint enforcement in multibody systems. J. of Computational and Nonlinear Dynamics **3**(1) (January 2008) doi:10.1115/1.2803257.

[3] Bayo, E., de Jalón, J.G., Serna, M.A.: A modified Lagrangian formulation for the dynamic analysis of constrained mechanical systems. Comput. Meth. Appl. Mech. Engng. **71**(2) (1988) 183–195 doi:10.1016/0045-7825(88)90085-0.

[4] Masarati, P.: Adding kinematic constraints to purely differential dynamics. Computational Mechanics **47**(2) (2011) 187–203 doi:10.1007/s00466-010-0539-4.

[5] Haug, E.J.: Multibody Dynamics on Differentiable Manifolds. J. of Computational and Nonlinear Dynamics **16**(4) (02 2021) 041003 doi:10.1115/1.4049995.

[6] Mariti, L., Belfiore, N.P., Pennestrì, E., Valentini, P.P.: Comparison of solution strategies for multibody dynamics equations. Intl. J. Num. Meth. Engng. (2011) doi:10.1002/nme.3190.

[7] Golub, G.H., Van Loan, C.F.: Matrix Computations. 3rd edn. The Johns Hopkins University Press, Baltimore and London (1996)

[8] Munthe-Kaas, H.: High order Runge-Kutta methods on manifolds. Applied Numerical Mathematics **29**(1) (1999) 115–127 doi:10.1016/S0168-9274(98)00030-0.

[9] Masarati, P., Morandini, M., Mantegazza, P.: An efficient formulation for general-purpose multibody/multiphysics analysis. J. of Computational and Nonlinear Dynamics **9**(4) (2014) 041001 doi:10.1115/1.4025628.

[10] Zhang, H., Zhang, R., Masarati, P.: Improved second-order unconditionally stable schemes of linear multi-step and equivalent single-step integration methods. Computational Mechanics (2021) doi:10.1007/s00466-020-01933-y.

https://doi.org/10.3311/ECCOMASMBD2021-125

ECCOMAS Thematic Conference on Multibody Dynamics
December 12 - 15, 2021, Budapest, Hungary

# The GGL Variational Principle for Constrained Mechanical Systems

**P. L. Kinon, P. Betsch**

Institute of Mechanics
Karlsruhe Institute of Technology (KIT)
Otto-Ammann-Platz 9, 76131 Karlsruhe, Germany
peter.betsch@kit.edu

## ABSTRACT

We present an extension of the Livens variational principle (sometimes also referred to as Hamilton-Pontryagin principle) to mechanical systems subject to holonomic constraints. The newly proposed principle embodies an index reduction in the spirit of the often-applied GGL stabilization and thus may be termed "GGL principle". The Euler-Lagrange equations of the GGL principle assume the form of differential-algebraic equations (DAEs) with differentiation index two. In contrast to the original GGL-DAEs, the present formulation fits into the Hamiltonian framework of mechanics. Therefore, the GGL principle facilitates the design of symplectic integrators. In particular, it offers the possibility to construct variational integrators. This is illustrated with the development of a new first-order scheme which is symplectic by design. The numerical properties of the newly devised scheme are investigated in a representative example of a constrained mechanical system.

**Keywords:** Livens principle, Constrained dynamics, Gear-Gupta-Leimkuhler stabilization, Index reduction, Variational integrators.

## 1 INTRODUCTION

Dynamical systems may be formulated in various ways. The well-known Lagrangian and Hamiltonian formalisms both consider descriptive energetic scalars and deploy certain operations on them to generate the system's *equations of motion*. Another formulation, which unifies both above-mentioned formalisms by means of independent position, velocity and momentum quantities has been proposed by Livens [1]. This *Livens principle* has been recently taken up by Bou-Rabee [2], Yoshimura & Marsden [3] and Holm [4] under the name of *Hamilton-Pontryagin principle* due to its close relation to the *Pontryagin principle* from the field of optimal control [5]. Livens principle allows for an advantageous universal description due to its mixed character.

A large variety of dynamical systems are subject to *constraints*, which reduce the degrees of freedom of the system and impose some constraint function to be satisfied. When describing the system with redundant coordinates, the equations of motion emerge as a set of *differential-algebraic equations* (DAEs), which combine both differential equations and algebraic constraint equations. It is to mention that the numerical treatment of DAEs requires some additional effort compared to purely differential equations (cf. Kunkel & Mehrmann [6]). As the constraints have to hold at every point in time (*consistency condition*), so-called *secondary constraints* for the position and velocity quantities are induced.

In a vast majority of dynamical problems, one cannot find an analytical solution. Thus, in recent times, the focus of scientific research has become to derive *numerical integration* methods, which are capable of solving the equations of motion approximately. Therefore, the class of *structure-preserving integrators* seeks to inherit the conservation principles of dynamical systems in a discrete sense (cf. monographs such as Hairer et al. [7] or Leimkuhler & Reich [8]). The first contributions can be traced back to symplectic methods (see e.g. de Vogelaere [9]). In the field of mechanics, structure-preserving integration schemes can be mainly divided into two different groups: *variational integrators* and *energy-momentum integrators*.

https://doi.org/10.3311/ECCOMASMBD2021-125

Variational integrators approximate the action integral and are typically able to conserve the symplectic structure as well as the system's momentum maps in a discrete sense (cf. Lew & Mata [10]). These are consequences of the variational procedure of derivation (cf. Marsden & West [11]). The main idea to find discrete counterparts of the variational principles goes back to Maeda [12]. Based on this concept, Marsden & West [11] provided a framework of discrete Lagrangian and Hamiltonian mechanics. Until now, variational integrators have been developed for various applications, e.g. for constrained dynamical systems (see e.g. Leyendecker et al. [13]).

Integration schemes for constrained dynamics typically only account for the constraints on configuration level (*primary constraint*) but not for the secondary constraints and thus have a *differentiation index* of 3. This may lead to numerical instabilities, especially when singular points exist (cf. Yoshimura [14]). By replacing the primary constraints on position level with the secondary velocity-level constraints, DAEs with index 2 are obtained. Thus, the numerical problems can be avoided but violations of the primary constraints are induced (cf. Yoshimura [14]). However, this issue can be alleviated by extending the system of unknowns and coupling the secondary constraints into the equations. The most famous technique, the *Gear-Gupta-Leimkuhler (GGL) stabilization*, traces back to Gear et al. [15] in 1985 and is widely used until today. This classical GGL formulation relies on the direct modification of the equations of motion. Yet, this procedure leads to a destruction of the Hamiltonian structure such that most GGL stabilized integration schemes are not symplectic.

To the best of the author's knowledge, numerical integration schemes for constrained dynamics have been formulated either in a Hamiltonian or in a Lagrangian way. Moreover, variational integration schemes have not been yet constructed such that primary and secondary constraints are considered at once. Thus, this work tries to fill both gaps by introducing a novel Livens-based variational framework for the integration of dynamical systems accounting for both primary and secondary constraints. In particular, the new framework makes possible to justify the commonly used GGL formulation in a variational sense. Contrary to the original version, the newly proposed formalism provides index 2 DAEs with a Hamiltonian structure. Moreover, the novel variational principle opens up the possibility to develop new variational integration schemes with a GGL-type stabilization.

## 2 FUNDAMENTALS

### 2.1 Livens principle

Consider a dynamical system with $d$ degrees of freedom and positions $\boldsymbol{q} \in \mathbb{R}^d$. From Hamilton's principle of least action one can proceed by allowing the velocities to be independent variables $\boldsymbol{v} \in \mathbb{R}^d$. Thus, the kinematic relation $\dot{\boldsymbol{q}} = \boldsymbol{v}$ has to be enforced by means of a Lagrange multiplier $\boldsymbol{p} \in \mathbb{R}^d$. The corresponding augmented functional reads

$$\tilde{S}(\boldsymbol{q},\boldsymbol{v},\boldsymbol{p}) = \int_0^T \left[L(\boldsymbol{q},\boldsymbol{v}) + \boldsymbol{p}\cdot(\dot{\boldsymbol{q}}-\boldsymbol{v})\right] \mathrm{d}t \,, \tag{1}$$

where $L(\boldsymbol{q},\boldsymbol{v})$ is the Lagrangian. The functional (1) was firstly termed *Livens principle* (cf. Sect. 26.2 in Pars [16]) after G.H. Livens who proposed this functional for the first time (cf. Livens [1]). More recently, Marsden and co-workers [2, 3] coined the name *Hamilton-Pontryagin principle* for this functional due to its close relation to the classical *Pontryagin principle* from the field of optimal control [5]. Due to its mixed character with three independent fields $(\boldsymbol{q},\boldsymbol{v},\boldsymbol{p})$, it resembles the *Hu-Washizu principle* from the area of elasticity theory (cf. Washizu [17]). Livens principle unifies both Lagrangian and Hamiltonian viewpoints on mechanics and automatically accounts for the Legendre transformation.

By stating the stationarity condition $\delta\tilde{S}(\boldsymbol{q},\boldsymbol{v},\boldsymbol{p}) = 0$ and executing the variations with respect to

https://doi.org/10.3311/ECCOMASMBD2021-125

every independent variable, one obtains the equations of motion in the form

$$\dot{\boldsymbol{q}} = \boldsymbol{v} \,, \tag{2a}$$
$$\dot{\boldsymbol{p}} = \mathrm{D}_1 L(\boldsymbol{q}, \boldsymbol{v}) \,, \tag{2b}$$
$$\boldsymbol{p} = \mathrm{D}_2 L(\boldsymbol{q}, \boldsymbol{v}) \,. \tag{2c}$$

With regard to (2c) the multiplier $\boldsymbol{p}$ can be identified as the conjugate momentum, which thus directly emanates from the principle. Within the framework of Hamiltonian dynamics momentum variables have to be defined a priori or emerge from the Legendre transformation as a fiber derivative of $L(\boldsymbol{q}, \dot{\boldsymbol{q}})$. Note that after reinserting (2c) into (2b) and making use of (2a), Livens principle traces back to the Lagrangian equations of the second kind.

For natural mechanical systems the Lagrangian takes the form

$$L(\boldsymbol{q}, \boldsymbol{v}) = \frac{1}{2} \boldsymbol{v} \cdot \boldsymbol{M} \boldsymbol{v} - V(\boldsymbol{q}) \tag{3}$$

where $\boldsymbol{M}$ is the mass matrix and $V(\boldsymbol{q})$ is a potential function. Now (2c) yields $\boldsymbol{p} = \boldsymbol{M}\boldsymbol{v}$, so that (2a) and (2b) can be rewritten as

$$\dot{\boldsymbol{q}} = \boldsymbol{M}^{-1} \boldsymbol{p} \,, \tag{4a}$$
$$\dot{\boldsymbol{p}} = -\mathrm{D}V(\boldsymbol{q}) \,. \tag{4b}$$

These equations correspond to the Hamiltonian form of the equations of motion. Making use of the phase space vector $\boldsymbol{z} = [\boldsymbol{q}^{\mathrm{T}}, \boldsymbol{p}^{\mathrm{T}}]^{\mathrm{T}}$ and the symplectic structure matrix

$$\mathbb{J} = \begin{bmatrix} \boldsymbol{0}_{d\times d} & \boldsymbol{I}_{d\times d} \\ -\boldsymbol{I}_{d\times d} & \boldsymbol{0}_{d\times d} \end{bmatrix} \,, \tag{5}$$

where $\boldsymbol{I}_{d\times d} \in \mathbb{R}^{d\times d}$ denotes the $d \times d$ identity matrix, the Hamiltonian equations of motion read

$$\dot{\boldsymbol{z}} = \mathbb{J}\,\mathrm{D}H(\boldsymbol{z}) \tag{6}$$

where the standard Hamiltonian function corresponding to (3) is given by

$$H = \frac{1}{2} \boldsymbol{p} \cdot \boldsymbol{M}^{-1} \boldsymbol{p} + V(\boldsymbol{q}) \,. \tag{7}$$

### 2.2 Symplectic structure of dynamics

Let us firstly introduce a bilinear and skew-symmetric function $\Omega : \mathbb{R}^{2d} \times \mathbb{R}^{2d} \to \mathbb{R}$ acting on two elements $\boldsymbol{\xi}, \boldsymbol{\eta} \in \mathbb{R}^{2d}$ which assume an ordering of components as in the phase space vector, such that exemplarily

$$\boldsymbol{\xi} = \begin{bmatrix} \xi_1^{(1)} & \xi_1^{(2)} & \dots & \xi_1^{(d)} & \xi_2^{(1)} & \xi_2^{(2)} & \dots & \xi_2^{(d)} \end{bmatrix}^{\mathrm{T}} \,. \tag{8}$$

Bilinearity refers to the fact that $\Omega$ is linear in both arguments. Skew-symmetry implies that $\Omega(\boldsymbol{\xi}, \boldsymbol{\eta}) = -\Omega(\boldsymbol{\eta}, \boldsymbol{\xi})$. The canonical structure matrix introduced in (5) gives rise to the symplectic two-form

$$\Omega(\boldsymbol{\xi}, \boldsymbol{\eta}) = \boldsymbol{\xi} \cdot \mathbb{J}^{-1} \boldsymbol{\eta} \,. \tag{9}$$

A map $\boldsymbol{\Psi} : \mathbb{R}^{2\mathrm{d}} \to \mathbb{R}^{2\mathrm{d}}$ is called *symplectic* if it leaves the symplectic two-form $\Omega$ invariant in the sense that

$$\Omega(\mathrm{D}\boldsymbol{\Psi}(\boldsymbol{z})\boldsymbol{\xi}, \mathrm{D}\boldsymbol{\Psi}(\boldsymbol{z})\boldsymbol{\eta}) = \Omega(\boldsymbol{\xi}, \boldsymbol{\eta}) \,, \tag{10}$$

https://doi.org/10.3311/ECCOMASMBD2021-125

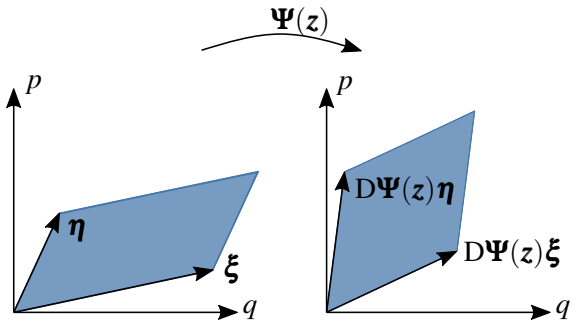


**Figure 1**. Symplectic area preservation for $d = 1$ (inspired by Hairer et al. [7])

where the original two-form is equal to the two-form of the transports of $\boldsymbol{\xi}$ and $\boldsymbol{\eta}$ under the linearization of $\boldsymbol{\Psi}$. Fig. 1 displays the mapping of elements $\boldsymbol{\xi}$ and $\boldsymbol{\eta}$ by $\boldsymbol{\Psi}$ and the preservation of the symplectic two-form, representing the oriented area for $d = 1$. Making use of the definition (9), the last equation leads to a symplecticness condition that reads

$$\mathrm{D}\boldsymbol{\Psi}(\boldsymbol{z})^{\mathrm{T}}\mathbb{J}^{-1}\mathrm{D}\boldsymbol{\Psi}(\boldsymbol{z}) = \mathbb{J}^{-1} \,. \tag{11}$$

The wedge product of two differential one-forms $\mathrm{d}\boldsymbol{a} \in \mathbb{R}^d$ and $\mathrm{d}\boldsymbol{b} \in \mathbb{R}^d$ acting on any two vectors $\boldsymbol{\xi}, \boldsymbol{\eta} \in \mathbb{R}^{2d}$ is given by (cf. Leimkuhler & Reich [8])

$$(\mathrm{d}\boldsymbol{a} \wedge \mathrm{d}\boldsymbol{b})(\boldsymbol{\xi}, \boldsymbol{\eta}) = \sum_{i=1}^{d} (\mathrm{d}a_i \wedge \mathrm{d}b_i)(\boldsymbol{\xi}, \boldsymbol{\eta}) = \sum_{i=1}^{d} (\mathrm{d}b_i(\boldsymbol{\xi})\,\mathrm{d}a_i(\boldsymbol{\eta}) - \mathrm{d}a_i(\boldsymbol{\xi})\,\mathrm{d}b_i(\boldsymbol{\eta})) \,. \tag{12}$$

Thus, the symplectic two form (9) can be rewritten in terms of the wedge product as

$$\Omega(\boldsymbol{\xi}, \boldsymbol{\eta}) = \sum_{i=1}^{d} \mathrm{d}q_i \wedge \mathrm{d}p_i\,(\boldsymbol{\xi}, \boldsymbol{\eta}) \,, \tag{13}$$

where the differential one-forms $\mathrm{d}q_i, \mathrm{d}p_i$ extract the $i$-th coordinate or momentum component, respectively, such that

$$\mathrm{d}q_i(\boldsymbol{\xi}) = \xi_1^{(i)} \,, \quad \mathrm{d}p_i(\boldsymbol{\xi}) = \xi_2^{(i)} \,. \tag{14a}$$

Omitting the arguments, the symplectic two-form can be rewritten more briefly in vector notation as

$$\Omega = \mathrm{d}\boldsymbol{q} \wedge \mathrm{d}\boldsymbol{p} \,. \tag{15}$$

Note that this representation is only a briefer notation of (13) that still accounts for the summation of the wedge product of scalar one-forms. One can show that Hamiltonian flow maps are symplectic. Thus, it is equivalent to say that the symplectic two-form (15) is conserved along solutions of the Hamiltonian equations of motions (6), viz.

$$\frac{\mathrm{d}}{\mathrm{d}t}\Omega = \frac{\mathrm{d}}{\mathrm{d}t}(\mathrm{d}\boldsymbol{q} \wedge \mathrm{d}\boldsymbol{p}) = 0 \,. \tag{16}$$

For differential one-forms, given in vector notation as $\mathrm{d}\boldsymbol{a}, \mathrm{d}\boldsymbol{b}$ and $\mathrm{d}\boldsymbol{c} \in \mathbb{R}^d$, any scalar valued quantities $\alpha, \beta \in \mathbb{R}$, any matrix $\boldsymbol{A} \in \mathbb{R}^{d\times d}$ and any symmetric matrix $\boldsymbol{B} = \boldsymbol{B}^{\mathrm{T}} \in \mathbb{R}^{d\times d}$ the wedge product defined in (12) has the following properties (see, for example, Leimkuhler & Reich [8]):

$$\mathrm{d}\boldsymbol{a} \wedge \mathrm{d}\boldsymbol{b} = -\,\mathrm{d}\boldsymbol{b} \wedge \mathrm{d}\boldsymbol{a} \,, \tag{17a}$$

$$\mathrm{d}\boldsymbol{a} \wedge (\alpha\,\mathrm{d}\boldsymbol{b} + \beta\,\mathrm{d}\boldsymbol{c}) = \alpha\,\mathrm{d}\boldsymbol{a} \wedge \mathrm{d}\boldsymbol{b} + \beta\,\mathrm{d}\boldsymbol{a} \wedge \mathrm{d}\boldsymbol{c} \,, \tag{17b}$$

$$\mathrm{d}\boldsymbol{a} \wedge (\boldsymbol{A}\,\mathrm{d}\boldsymbol{b}) = (\boldsymbol{A}^{\mathrm{T}}\,\mathrm{d}\boldsymbol{a}) \wedge \mathrm{d}\boldsymbol{b} \,, \tag{17c}$$

$$\mathrm{d}\boldsymbol{a} \wedge (\boldsymbol{B}\,\mathrm{d}\boldsymbol{a}) = 0 \,. \tag{17d}$$

https://doi.org/10.3311/ECCOMASMBD2021-125

### 2.3 GGL method for constrained mechanical systems

Assume that the coordinates $\boldsymbol{q}$ are redundant due to the presence of $m$ independent scleronomic, holonomic constraints $g_k : \mathbb{R}^d \to \mathbb{R}$ ($k = 1, \ldots, m$). The constraints can be comprised in a column vector $\boldsymbol{g} \in \mathbb{R}^m$, such that

$$\boldsymbol{g}(\boldsymbol{q}) = \boldsymbol{0} \,. \tag{18}$$

Since all constraint functions shall be independent, the constraint Jacobian $\boldsymbol{G}(\boldsymbol{q}) = \mathrm{D}\boldsymbol{g}(\boldsymbol{q})$ is of rank $m$. As (18) is true for any point in time, the time derivative has to vanish accordingly (*consistency condition*). Thus, the constraints *on velocity level* or *secondary constraints*

$$\frac{\mathrm{d}}{\mathrm{d}t}\boldsymbol{g}(\boldsymbol{q}) = \boldsymbol{G}(\boldsymbol{q})\dot{\boldsymbol{q}} = \boldsymbol{0} \tag{19}$$

are induced. It is well-known that the motion of the constrained mechanical systems under consideration is governed by differential-algebraic equations (DAEs) which have differentiation index $\nu = 3$. These equations of motion can be derived with a variational approach, which augments Livens principle (1). Accordingly, introducing $\hat{S}(\boldsymbol{q}, \boldsymbol{v}, \boldsymbol{p}, \boldsymbol{\lambda}) = \tilde{S}(\boldsymbol{q}, \boldsymbol{v}, \boldsymbol{p}) + \int_0^T \boldsymbol{\lambda} \cdot \boldsymbol{g}(\boldsymbol{q})\,\mathrm{d}t$, stating the stationary condition $\delta\hat{S}(\boldsymbol{q}, \boldsymbol{v}, \boldsymbol{p}, \boldsymbol{\lambda}) = 0$ and eliminating the velocities as above leads to an extension of the Hamiltonian equations (4) for constrained systems, such that the index-3 DAEs are obtained as

$$\dot{\boldsymbol{q}} = \boldsymbol{M}^{-1}\boldsymbol{p} \,, \tag{20a}$$

$$\dot{\boldsymbol{p}} = -\mathrm{D}V(\boldsymbol{q}) - \boldsymbol{G}(\boldsymbol{q})^{\mathrm{T}}\boldsymbol{\lambda} \,, \tag{20b}$$

$$\boldsymbol{0} = \boldsymbol{g}(\boldsymbol{q}) \,. \tag{20c}$$

The classical GGL stabilization, which traces back to Gear et al. [15], represents an index reduction technique by minimal extension (see Kunkel & Mehrmann [6]). The main idea of the GGL stabilization is to couple the secondary constraints into the dynamics by making use of additional variables $\boldsymbol{\gamma} \in \mathbb{R}^m$, such that the system of equations of motion is extended and the differentiation index drops to $\nu = 2$. Correspondingly, the numerical ill-conditioning of index-3 DAEs are alleviated without having the drawback of drift phenomena. The resulting index-2 DAEs can be written in the form

$$\dot{\boldsymbol{q}} = \boldsymbol{M}^{-1}\boldsymbol{p} + \boldsymbol{G}(\boldsymbol{q})^{\mathrm{T}}\boldsymbol{\gamma} \,, \tag{21a}$$

$$\dot{\boldsymbol{p}} = -\mathrm{D}V(\boldsymbol{q}) - \boldsymbol{G}(\boldsymbol{q})^{\mathrm{T}}\boldsymbol{\lambda} \,, \tag{21b}$$

$$\boldsymbol{0} = \boldsymbol{g}(\boldsymbol{q}) \,, \tag{21c}$$

$$\boldsymbol{0} = \boldsymbol{G}(\boldsymbol{q})\boldsymbol{M}^{-1}\boldsymbol{p} \,. \tag{21d}$$

Ever since, the GGL stabilization has been widely used and is thus of great importance. Numerical methods can be constructed directly by discretizing the DAEs (21). Note, however, that due to the GGL modification of the kinematic equation (21a), the system (21) loses its Hamiltonian structure. For the time-continuous case, some algebra leads to $\boldsymbol{\gamma} = \boldsymbol{0}$. Consequently, the GGL-DAEs boil down to the standard formulation (20).

## 3 GGL PRINCIPLE

### 3.1 Governing equations

The newly proposed GGL principle relies on a generalization of Livens principle (1) by considering Lagrange multipliers $\boldsymbol{\lambda}, \boldsymbol{\gamma} \in \mathbb{R}^m$ to enforce the primary constraints (18) and secondary constraints (19), respectively. Imposing stationarity on a corresponding augmented action integral

$$\delta S_{\mathrm{GGL}}(\boldsymbol{q}, \boldsymbol{v}, \boldsymbol{p}, \boldsymbol{\lambda}, \boldsymbol{\gamma}) = 0 \tag{22}$$

https://doi.org/10.3311/ECCOMASMBD2021-125

with

$$S_{\mathrm{GGL}} = \int_0^T \left[ L(\boldsymbol{q},\boldsymbol{v}) - \boldsymbol{\lambda}\cdot\boldsymbol{g}(\boldsymbol{q}) + \boldsymbol{p}\cdot(\dot{\boldsymbol{q}} - \boldsymbol{v} - \boldsymbol{M}^{-1}\boldsymbol{G}(\boldsymbol{q})^{\mathrm{T}}\boldsymbol{\gamma}) \right] \mathrm{d}t \,, \tag{23}$$

yields the stationarity conditions

$$\int_0^T \delta\boldsymbol{p}\cdot\left(\dot{\boldsymbol{q}} - \boldsymbol{v} - \boldsymbol{M}^{-1}\boldsymbol{G}(\boldsymbol{q})^{\mathrm{T}}\boldsymbol{\gamma}\right) \mathrm{d}t = 0 \,, \tag{24a}$$

$$\int_0^T \left( \mathrm{D}_1 L(\boldsymbol{q},\boldsymbol{v})\cdot\delta\boldsymbol{q} - \boldsymbol{G}(\boldsymbol{q})^{\mathrm{T}}\boldsymbol{\lambda}\cdot\delta\boldsymbol{q} + \boldsymbol{p}\cdot\delta\dot{\boldsymbol{q}} - \boldsymbol{p}\cdot\boldsymbol{M}^{-1}\delta\boldsymbol{G}(\boldsymbol{q})^{\mathrm{T}}\boldsymbol{\gamma} \right) \mathrm{d}t = 0 \,, \tag{24b}$$

$$\int_0^T \delta\boldsymbol{v}\cdot(\mathrm{D}_2 L(\boldsymbol{q},\boldsymbol{v}) - \boldsymbol{p})\,\mathrm{d}t = 0 \,, \tag{24c}$$

$$\int_0^T \delta\boldsymbol{\lambda}\cdot\boldsymbol{g}(\boldsymbol{q})\,\mathrm{d}t = 0 \,, \tag{24d}$$

$$\int_0^T \boldsymbol{p}\cdot\boldsymbol{M}^{-1}\boldsymbol{G}(\boldsymbol{q})^{\mathrm{T}}\,\delta\boldsymbol{\gamma}\mathrm{d}t = 0 \,. \tag{24e}$$

As one can see, relation (24b) requires some more effort in order to achieve the final Euler-Langrange equation. Therefore, $\delta\dot{\boldsymbol{q}}$ can be replaced through integration by parts such that

$$\int_0^T \boldsymbol{p}\cdot\delta\dot{\boldsymbol{q}}\,\mathrm{d}t = -\int_0^T \delta\boldsymbol{q}\cdot\dot{\boldsymbol{p}}\,\mathrm{d}t + \delta\boldsymbol{q}(T)\cdot\boldsymbol{p}(T) - \delta\boldsymbol{q}(0)\cdot\boldsymbol{p}(0) \,. \tag{25}$$

The endpoint conditions on admissible variations $\delta\boldsymbol{q}(0) = \delta\boldsymbol{q}(T) = 0$ make the latter two terms vanish. Furthermore, the variation of the gradient of the constraint functions can be executed as

$$\delta\boldsymbol{G}(\boldsymbol{q}) = \mathrm{D}\boldsymbol{G}(\boldsymbol{q})\delta\boldsymbol{q} = \mathrm{D}^2\boldsymbol{g}(\boldsymbol{q})\delta\boldsymbol{q} \,. \tag{26}$$

In order to avoid the third order expression $\mathrm{D}^2\boldsymbol{g}(\boldsymbol{q})$, the stationary condition (24b) can be written in terms of the individual constraint functions $g_{\mathrm{k}}(\boldsymbol{q})$ for $k = 1,\ldots,m$. Thus, the variation of the constraint gradients is given by

$$\delta(\mathrm{D}g_k(\boldsymbol{q})) = \mathrm{D}^2 g_k(\boldsymbol{q})\delta\boldsymbol{q} \,, \tag{27}$$

where the constraint Hessian $\mathrm{D}^2 g_k(\boldsymbol{q}) \in \mathbb{R}^{d\times d}$. Consequently, the arbitrariness of the variations $\delta\boldsymbol{q}$, $\delta\boldsymbol{v}$, $\delta\boldsymbol{p}$, $\delta\boldsymbol{\lambda}$ and $\delta\boldsymbol{\gamma}$ can be taken into account such that the governing DAEs are deduced as

$$\dot{\boldsymbol{q}} = \boldsymbol{v} + \boldsymbol{M}^{-1}\boldsymbol{G}(\boldsymbol{q})^{\mathrm{T}}\boldsymbol{\gamma} \,, \tag{28a}$$

$$\dot{\boldsymbol{p}} = \mathrm{D}_1 L(\boldsymbol{q},\boldsymbol{v}) - \boldsymbol{G}(\boldsymbol{q})^{\mathrm{T}}\boldsymbol{\lambda} - \sum_{k=1}^{m} \gamma_k \mathrm{D}^2 g_k(\boldsymbol{q})\boldsymbol{M}^{-1}\boldsymbol{p} \,, \tag{28b}$$

$$\boldsymbol{p} = \mathrm{D}_2 L(\boldsymbol{q},\boldsymbol{v}) \,, \tag{28c}$$

$$\boldsymbol{0} = \boldsymbol{g}(\boldsymbol{q}) \,, \tag{28d}$$

$$\boldsymbol{0} = \boldsymbol{G}(\boldsymbol{q})\boldsymbol{M}^{-1}\boldsymbol{p} \,. \tag{28e}$$

Thus equations in the fashion of the standard GGL stabilization (21) are obtained with an additional term in the momentum equation. Note that (28c) represents the fiber derivative of the newly proposed variational principle, such that the Lagrange multiplier $\boldsymbol{p}$ denotes the conjugate momenta. By introducing the secondary constraints to the functional, the resulting Euler-Lagrange equations are DAEs with index $\nu = 2$, similarly to the GGL stabilized equations of motion, whereas the standard DAEs of constrained dynamics have index $\nu = 3$. Thus, the newly established DAEs (28) can be regarded as an extension to the classical GGL stabilization. Similar to the classical GGL stabilization one obtains $\boldsymbol{\gamma} = \boldsymbol{0}$ for the time-continuous case. However, the third term on the right-hand side of (28b) is of crucial importance as it maintains the Hamiltonian structure of the equations of motion, in contrast to the classical GGL method.

https://doi.org/10.3311/ECCOMASMBD2021-125

### 3.2 Hamiltonian structure

The equations of motion induced by the GGL principle have Hamiltonian structure, viz.

$$\dot{\boldsymbol{q}} = +\mathrm{D}_2 H_{\mathrm{GGL}}(\boldsymbol{q},\boldsymbol{p},\boldsymbol{\lambda},\boldsymbol{\gamma}) \,, \tag{29a}$$

$$\dot{\boldsymbol{p}} = -\mathrm{D}_1 H_{\mathrm{GGL}}(\boldsymbol{q},\boldsymbol{p},\boldsymbol{\lambda},\boldsymbol{\gamma}) \,, \tag{29b}$$

$$\boldsymbol{0} = +\mathrm{D}_3 H_{\mathrm{GGL}}(\boldsymbol{q},\boldsymbol{p},\boldsymbol{\lambda},\boldsymbol{\gamma}) \,, \tag{29c}$$

$$\boldsymbol{0} = +\mathrm{D}_4 H_{\mathrm{GGL}}(\boldsymbol{q},\boldsymbol{p},\boldsymbol{\lambda},\boldsymbol{\gamma}) \,, \tag{29d}$$

with a corresponding augmented Hamiltonian

$$H_{\mathrm{GGL}}(\boldsymbol{q},\boldsymbol{p},\boldsymbol{\lambda},\boldsymbol{\gamma}) = \frac{1}{2}\boldsymbol{p}\cdot\boldsymbol{M}^{-1}\boldsymbol{p} + V(\boldsymbol{q}) + \boldsymbol{\lambda}\cdot\boldsymbol{g}(\boldsymbol{q}) + \boldsymbol{\gamma}\cdot\boldsymbol{G}(\boldsymbol{q})\boldsymbol{M}^{-1}\boldsymbol{p} \,. \tag{30}$$

The above equations can be related to the Euler-Lagrange equations (28) of the GGL functional after elimination of the velocities by employing the Legendre transformation (28c). Next, we show that the equations of motion of the novel framework conserve the Hamiltonian exactly. For that purpose, we compute the time derivative of the augmented Hamiltonian (30) such that

$$\begin{aligned}\frac{\mathrm{d}}{\mathrm{d}t}H_{\mathrm{GGL}} &= \mathrm{D}_1 H_{\mathrm{GGL}}\cdot\dot{\boldsymbol{q}} + \mathrm{D}_2 H_{\mathrm{GGL}}\cdot\dot{\boldsymbol{p}} + \mathrm{D}_3 H_{\mathrm{GGL}}\cdot\dot{\boldsymbol{\lambda}} + \mathrm{D}_4 H_{\mathrm{GGL}}\cdot\dot{\boldsymbol{\gamma}} \\ &= \mathrm{D}_1 H_{\mathrm{GGL}}\cdot\mathrm{D}_2 H_{\mathrm{GGL}} - \mathrm{D}_2 H_{\mathrm{GGL}}\cdot\mathrm{D}_1 H_{\mathrm{GGL}} + \boldsymbol{0}\cdot\dot{\boldsymbol{\lambda}} + \boldsymbol{0}\cdot\dot{\boldsymbol{\gamma}} = 0 \,,\end{aligned} \tag{31}$$

where the Hamiltonian equations of motion (29) have been considered. As the augmented Hamiltonian (30) is conserved along solutions of the equations of motion, also the Hamiltonian $H$ itself is conserved since both constraints on configuration level and momentum level are identically zero such that $\dot{H} = 0$. In contrast to the originial GGL formulation (cf. Sect. 2.3), this conservation law holds regardless of the actual value of the Lagrange multipliers $\boldsymbol{\gamma}$.

### 3.3 Symplectic structure

We show that the GGL functional inherits the symplectic structure of Hamiltonian systems and thus the symplectic two-form is conserved along solutions of (28) or (29), respectively. We begin by deriving the total differentials based on the equations of motion as

$$\mathrm{d}\dot{\boldsymbol{q}} = \mathrm{D}^2_{21}H(\boldsymbol{q},\boldsymbol{p})\,\mathrm{d}\boldsymbol{q} + \mathrm{D}^2_{22}H(\boldsymbol{q},\boldsymbol{p})\,\mathrm{d}\boldsymbol{p} + \mathrm{d}\left(\mathrm{D}_2\boldsymbol{g}^{\mathrm{v}}(\boldsymbol{q},\boldsymbol{p})^{\mathrm{T}}\boldsymbol{\gamma}\right) \,, \tag{32a}$$

$$\mathrm{d}\dot{\boldsymbol{p}} = -\mathrm{D}^2_{11}H(\boldsymbol{q},\boldsymbol{p})\,\mathrm{d}\boldsymbol{q} - \mathrm{D}^2_{12}H(\boldsymbol{q},\boldsymbol{p})\,\mathrm{d}\boldsymbol{p} - \mathrm{d}\left(\mathrm{D}\boldsymbol{g}^{\mathrm{q}}(\boldsymbol{q})^{\mathrm{T}}\boldsymbol{\lambda}\right) - \mathrm{d}\left(\mathrm{D}_1\boldsymbol{g}^{\mathrm{v}}(\boldsymbol{q},\boldsymbol{p})^{\mathrm{T}}\boldsymbol{\gamma}\right) \,, \tag{32b}$$

$$\boldsymbol{0} = \mathrm{D}\boldsymbol{g}^{\mathrm{q}}(\boldsymbol{q})\,\mathrm{d}\boldsymbol{q} \,, \tag{32c}$$

$$\boldsymbol{0} = \mathrm{D}_1\boldsymbol{g}^{\mathrm{v}}(\boldsymbol{q},\boldsymbol{p})\,\mathrm{d}\boldsymbol{q} + \mathrm{D}_2\boldsymbol{g}^{\mathrm{v}}(\boldsymbol{q},\boldsymbol{p})\,\mathrm{d}\boldsymbol{p} \,, \tag{32d}$$

where we have introduced the distinct functions $\boldsymbol{g}^{\mathrm{q}}(\boldsymbol{q}) = \boldsymbol{g}(\boldsymbol{q})$ for the holonomic constraint on configuration level and $\boldsymbol{g}^{\mathrm{v}}(\boldsymbol{q},\boldsymbol{p}) = \mathrm{D}\boldsymbol{g}(\boldsymbol{q})\boldsymbol{M}^{-1}\boldsymbol{p}$ for the corresponding constraint on momentum level. It is straightforward to compute the temporal evolution of $\Omega$ by means of the product rule such that

$$\frac{\mathrm{d}}{\mathrm{d}t}\Omega = \mathrm{d}\dot{\boldsymbol{q}}\wedge\mathrm{d}\boldsymbol{p} + \mathrm{d}\boldsymbol{q}\wedge\mathrm{d}\dot{\boldsymbol{p}} \,, \tag{33}$$

into which the above differential equations (32a) and (32b) can be inserted. One can consider the symmetry of the Hessian of $H$ and make use of the properties of the wedge product. Note that $\mathrm{D}^2_{11}H$ and $\mathrm{D}^2_{22}H$ both are symmetric matrices, such that

$$\mathrm{D}^2_{22}H(\boldsymbol{q},\boldsymbol{p})\,\mathrm{d}\boldsymbol{p}\wedge\mathrm{d}\boldsymbol{p} = 0 \,, \tag{34}$$

$$-\mathrm{d}\boldsymbol{q}\wedge\mathrm{D}^2_{11}H(\boldsymbol{q},\boldsymbol{p})\,\mathrm{d}\boldsymbol{q} = 0 \,, \tag{35}$$

https://doi.org/10.3311/ECCOMASMBD2021-125

due to property (17d). Moreover, the two terms with the off-diagonal entries of the Hessian of $H$ cancel each other out, because

$$\mathrm{D}^2_{21}H(\boldsymbol{q},\boldsymbol{p})\,\mathrm{d}\boldsymbol{q}\wedge\mathrm{d}\boldsymbol{p} = (\mathrm{D}^2_{12}H(\boldsymbol{q},\boldsymbol{p}))^{\mathrm{T}}\,\mathrm{d}\boldsymbol{q}\wedge\mathrm{d}\boldsymbol{p} = \mathrm{d}\boldsymbol{q}\wedge\mathrm{D}^2_{12}H(\boldsymbol{q},\boldsymbol{p})\,\mathrm{d}\boldsymbol{p}\,, \tag{36}$$

where in the last equation property (17c) has been used. The term stemming from the primary constraints can be written as

$$\mathrm{d}\left(\mathrm{D}\boldsymbol{g}^{\mathbf{q}}(\boldsymbol{q})^{\mathrm{T}}\boldsymbol{\lambda}\right)\wedge\mathrm{d}\boldsymbol{q} = \mathrm{D}\boldsymbol{g}^{\mathbf{q}}(\boldsymbol{q})^{\mathrm{T}}\,\mathrm{d}\boldsymbol{\lambda}\wedge\mathrm{d}\boldsymbol{q} + \sum_{\mathrm{k}=1}^{\mathrm{m}}\lambda_{\mathrm{k}}\mathrm{D}^2 g_{\mathrm{k}}(\boldsymbol{q})\,\mathrm{d}\boldsymbol{q}\wedge\mathrm{d}\boldsymbol{q} = \mathrm{d}\boldsymbol{\lambda}\wedge\mathrm{D}\boldsymbol{g}^{\mathbf{q}}(\boldsymbol{q})\,\mathrm{d}\boldsymbol{q} = 0\,, \tag{37}$$

where again (17c) and (17d) have been used along with (32c). Therefore, all terms emerging from the right-hand side of (33) cancel out except for those containing the constraint on momentum level $\boldsymbol{g}^{\mathbf{v}}(\boldsymbol{q},\boldsymbol{p})$. We therefore obtain

$$\begin{aligned}\frac{\mathrm{d}}{\mathrm{d}t}\Omega &= \mathrm{d}\left(\mathrm{D}_2\boldsymbol{g}^{\mathbf{v}}(\boldsymbol{q},\boldsymbol{p})^{\mathrm{T}}\boldsymbol{\gamma}\right)\wedge\mathrm{d}\boldsymbol{p} - \mathrm{d}\boldsymbol{q}\wedge\mathrm{d}\left(\mathrm{D}_1\boldsymbol{g}^{\mathbf{v}}(\boldsymbol{q},\boldsymbol{p})^{\mathrm{T}}\boldsymbol{\gamma}\right) \\ &= \mathrm{D}_2\boldsymbol{g}^{\mathbf{v}\mathrm{T}}\,\mathrm{d}\boldsymbol{\gamma}\wedge\mathrm{d}\boldsymbol{p} + \mathrm{D}_1\boldsymbol{g}^{\mathbf{v}\mathrm{T}}\,\mathrm{d}\boldsymbol{\gamma}\wedge\mathrm{d}\boldsymbol{q} + \sum_{k=1}^{m}\gamma_k\mathrm{D}^2_{12}g^{\mathbf{v}}_k\,\mathrm{d}\boldsymbol{q}\wedge\mathrm{d}\boldsymbol{p} + \sum_{k=1}^{m}\gamma_k\mathrm{D}^2_{21}g^{\mathbf{v}}_k\,\mathrm{d}\boldsymbol{p}\wedge\mathrm{d}\boldsymbol{q} \\ &= \mathrm{d}\boldsymbol{\gamma}\wedge(\mathrm{D}_1\boldsymbol{g}^{\mathbf{v}}(\boldsymbol{q},\boldsymbol{p})\,\mathrm{d}\boldsymbol{q} + \mathrm{D}_2\boldsymbol{g}^{\mathbf{v}}(\boldsymbol{q},\boldsymbol{p})\,\mathrm{d}\boldsymbol{p}) + \sum_{k=1}^{m}\gamma_k\left(\mathrm{D}^2_{12}g^{\mathbf{v}}_k - (\mathrm{D}^2_{21}g^{\mathbf{v}}_k)^{\mathrm{T}}\right)\mathrm{d}\boldsymbol{q}\wedge\mathrm{d}\boldsymbol{p} = 0\,,\end{aligned} \tag{38}$$

where the first term vanishes in view of the total differential of the secondary constraint (32d) and the second one cancels due to the symmetry of the Hessian of $g^{\mathbf{v}}_k$. Note that it has been taken into account that terms including $\mathrm{D}^2_{11}g^{\mathbf{v}}_k$ and $\mathrm{D}^2_{22}g^{\mathbf{v}}_k$, respectively, cancel due to their symmetry. This proofs the symplecticness of the equations of motion emanating from the GGL functional. Again this property does not depend on the Lagrange multiplier $\boldsymbol{\gamma}$, which is an advantage over the original GGL method by Gear et al. [15], for which $\boldsymbol{\gamma}=\mathbf{0}$ is required in order to conserve $\Omega$.

## 4 GGL VARIATIONAL INTEGRATOR

We next illustrate how the GGL principle introduced in Section 3 can be employed to derive a variational integrator. Subsequently, structure-preserving properties of the newly devised variational integrator will be considered.

### 4.1 Governing Equations

Let us construct a time-stepping scheme by means of a direct discretization of the GGL functional (23). Enforcing the constraint on configuration level in the endpoint and the constraint on momentum level in an intermediate state and discretizing the velocity by means of an explicit Euler method, we obtain the discrete action integral

$$S_{\mathrm{d}} = \sum_{n=0}^{N-1}\left[hL(\boldsymbol{q}^n,\boldsymbol{v}^n) - h\boldsymbol{\lambda}^{n+1}\cdot\boldsymbol{g}(\boldsymbol{q}^{n+1}) + \boldsymbol{p}^{n+1}\cdot\left(\boldsymbol{q}^{n+1} - \boldsymbol{q}^n - h\boldsymbol{v}^n - h\boldsymbol{M}^{-1}\boldsymbol{G}(\bar{\boldsymbol{q}})^{\mathrm{T}}\boldsymbol{\gamma}^{n+1}\right)\right]\,, \tag{39}$$

where the configuration variable $\bar{\boldsymbol{q}} = \boldsymbol{q}^n + h\boldsymbol{v}^n$ has been introduced. Stationarity conditions can be applied directly to the discrete functional, yielding

$$\sum_{n=0}^{N-1}\delta\boldsymbol{p}^{n+1}\cdot\left(\boldsymbol{q}^{n+1} - \boldsymbol{q}^n - h\boldsymbol{v}^n - h\boldsymbol{M}^{-1}\boldsymbol{G}(\bar{\boldsymbol{q}})^{\mathrm{T}}\boldsymbol{\gamma}^{n+1}\right) = 0\,, \tag{40a}$$

$$\sum_{n=0}^{N-1}\delta\boldsymbol{q}^{n}\cdot\left(h\mathrm{D}_1L(\boldsymbol{q}^n,\boldsymbol{v}^n) - \boldsymbol{p}^{n+1} - h\sum_{k=1}^{m}\gamma_k^{n+1}\mathrm{D}^2 g_k(\bar{\boldsymbol{q}})\boldsymbol{M}^{-1}\boldsymbol{p}^{n+1}\right) \tag{40b}$$

$$+\sum_{n=0}^{N-1}\delta\boldsymbol{q}^{n+1}\cdot\left(-h\boldsymbol{G}(\boldsymbol{q}^{n+1})^{\mathrm{T}}\boldsymbol{\lambda}^{n+1} + \boldsymbol{p}^{n+1}\right) = 0\,,$$

$$\sum_{n=0}^{N-1}\delta\boldsymbol{v}^{n}\cdot\left(h\mathrm{D}_2L(\boldsymbol{q}^n,\boldsymbol{v}^n) - h\boldsymbol{p}^{n+1} - h^2\sum_{k=1}^{m}\gamma_k^{n+1}\mathrm{D}^2 g_k(\bar{\boldsymbol{q}})\boldsymbol{M}^{-1}\boldsymbol{p}^{n+1}\right) = 0\,, \tag{40c}$$

https://doi.org/10.3311/ECCOMASMBD2021-125

along with

$$\sum_{n=0}^{N-1} \delta\boldsymbol{\lambda}^{n+1} \cdot \boldsymbol{g}(\boldsymbol{q}^{n+1}) = 0 \,, \tag{40d}$$

$$\sum_{n=0}^{N-1} \delta\boldsymbol{\gamma}^{n+1} \cdot \boldsymbol{G}(\bar{\boldsymbol{q}})\boldsymbol{M}^{-1}\boldsymbol{p}^{n+1} = 0 \,. \tag{40e}$$

Applying an index shift in the second part of (40b) from $n+1$ to $n$ and taking into account the arbitrariness of all variations, we obtain the discrete EL equations

$$\boldsymbol{q}^{n+1} - \boldsymbol{q}^n = h\,\boldsymbol{v}^n + h\boldsymbol{M}^{-1}\boldsymbol{G}(\bar{\boldsymbol{q}})^{\mathrm{T}}\boldsymbol{\gamma}^{n+1} \,, \tag{41a}$$

$$\boldsymbol{p}^{n+1} - \boldsymbol{p}^n = h\,\mathrm{D}_1 L(\boldsymbol{q}^n, \boldsymbol{v}^n) - h\,\boldsymbol{G}(\boldsymbol{q}^n)^{\mathrm{T}}\boldsymbol{\lambda}^n - h\sum_{k=1}^{m} \gamma_k^{n+1}\mathrm{D}^2 g_k(\bar{\boldsymbol{q}})\boldsymbol{M}^{-1}\boldsymbol{p}^n \,, \tag{41b}$$

$$\mathrm{D}_2 L(\boldsymbol{q}^n, \boldsymbol{v}^n) = \left(\boldsymbol{I}_{d\times d} + h\sum_{k=1}^{m} \gamma_k^{n+1}\mathrm{D}^2 g_k(\bar{\boldsymbol{q}})\boldsymbol{M}^{-1}\right)\boldsymbol{p}^{n+1} \,, \tag{41c}$$

$$\boldsymbol{g}(\boldsymbol{q}^{n+1}) = \boldsymbol{0} \,, \tag{41d}$$

$$\boldsymbol{G}(\bar{\boldsymbol{q}})\boldsymbol{M}^{-1}\boldsymbol{p}^{n+1} = \boldsymbol{0} \,, \tag{41e}$$

for $n = 0, \ldots, N-1$. In total we have obtained a set of $(3d+2m)$ equations for the unknowns $(\boldsymbol{q}^{n+1}, \boldsymbol{p}^{n+1}, \boldsymbol{v}^n, \boldsymbol{\lambda}^n, \boldsymbol{\gamma}^{n+1})$ in every time step. These are discrete counterparts of the continuous EL equations given in (28). It is advantageous that, due to the enhancement of the discrete action integral, the secondary constraints are now taken into account as well (cf. relation (41e)). Note that relation (41c) can be interpreted as the discrete fiber derivative of the Legendre transformation, which links velocity and momentum quantities. It is worth mentioning that scheme (41) can be regarded as generalization to constrained mechanical systems of the symplectic Euler method (see Hairer et al. [7] and Euler-B in Leimkuhler & Reich [8]).

### 4.2 Conservation Properties

It is clear that the primary constraints are correctly captured in every time step by design (see relation (41d)). The secondary constraints are enforced in an intermediate sense (cf. (41e)).

Moreover, we can show that the integrator governed by (41) is symplectic. In order to demonstrate this, we calculate the differentials of (41a) to (41c). This yields

$$\mathrm{d}\boldsymbol{q}^{n+1} - \mathrm{d}\boldsymbol{q}^n = h\,\mathrm{d}\boldsymbol{v}^n + h\,\mathrm{d}\left(\mathrm{D}_2\boldsymbol{g}^{\mathrm{v}}(\bar{\boldsymbol{q}}, \boldsymbol{p}^{n+1})^{\mathrm{T}}\boldsymbol{\gamma}^{n+1}\right) \,, \tag{42a}$$

$$\mathrm{d}\boldsymbol{p}^{n+1} - \mathrm{d}\boldsymbol{p}^n = h\,\mathrm{D}_{11}^2 L(\boldsymbol{q}^n, \boldsymbol{v}^n)\,\mathrm{d}\boldsymbol{q}^n - h\,\mathrm{d}\left(\boldsymbol{G}(\boldsymbol{q}^n)^{\mathrm{T}}\boldsymbol{\lambda}^n\right) - h\,\mathrm{d}\left(\mathrm{D}_1\boldsymbol{g}^{\mathrm{v}}(\bar{\boldsymbol{q}}, \boldsymbol{p}^{n+1})^{\mathrm{T}}\boldsymbol{\gamma}^{n+1}\right) \tag{42b}$$

$$\mathrm{D}_{22}^2 L(\boldsymbol{q}^n, \boldsymbol{v}^n)\,\mathrm{d}\boldsymbol{v}^n = \mathrm{d}\boldsymbol{p}^{n+1} + h\,\mathrm{d}\left(\mathrm{D}_1\boldsymbol{g}^{\mathrm{v}}(\bar{\boldsymbol{q}}, \boldsymbol{p}^{n+1})^{\mathrm{T}}\boldsymbol{\gamma}^{n+1}\right) \,. \tag{42c}$$

where $\boldsymbol{g}^{\mathrm{v}}(\bar{\boldsymbol{q}}, \boldsymbol{p}^{n+1}) = \boldsymbol{G}(\bar{\boldsymbol{q}})\boldsymbol{M}^{-1}\boldsymbol{p}^{n+1}$ has been introduced in analogy to the continuous case. Moreover, $\mathrm{D}_{12}^2 L(\boldsymbol{q}^n, \boldsymbol{v}^n) = \mathrm{D}_{21}^2 L(\boldsymbol{q}^n, \boldsymbol{v}^n)^{\mathrm{T}} = \boldsymbol{0}$ as been taken into account which is valid for Lagrangians of the form (3). The differential forms of the constraint equations (41d) and (41e) read

$$\mathrm{d}\boldsymbol{g}(\boldsymbol{q}^{n+1}) = \boldsymbol{G}(\boldsymbol{q}^{n+1})\,\mathrm{d}\boldsymbol{q}^{n+1} = \boldsymbol{0} \,, \tag{43a}$$

$$\mathrm{d}\boldsymbol{g}^{\mathrm{v}}(\bar{\boldsymbol{q}}, \boldsymbol{p}^{n+1}) = \mathrm{D}_1\boldsymbol{g}^{\mathrm{v}}(\bar{\boldsymbol{q}}, \boldsymbol{p}^{n+1})\,\mathrm{d}\bar{\boldsymbol{q}} + \mathrm{D}_2\boldsymbol{g}^{\mathrm{v}}(\bar{\boldsymbol{q}}, \boldsymbol{p}^{n+1})\,\mathrm{d}\boldsymbol{p}^{n+1} = \boldsymbol{0} \,. \tag{43b}$$

Now, making use of the skew-symmetry of the wedge product, property (17a), one can deduce that

$$\mathrm{d}\boldsymbol{p}^{n+1} \wedge (\,\mathrm{d}\boldsymbol{q}^{n+1} - \mathrm{d}\boldsymbol{q}^n) + (\,\mathrm{d}\boldsymbol{p}^{n+1} - \mathrm{d}\boldsymbol{p}^n) \wedge \mathrm{d}\boldsymbol{q}^n = \mathrm{d}\boldsymbol{q}^n \wedge \mathrm{d}\boldsymbol{p}^n - \mathrm{d}\boldsymbol{q}^{n+1} \wedge \mathrm{d}\boldsymbol{p}^{n+1} \,. \tag{44}$$

Substituting from (42a) and (42b) into the last equation, we obtain

$$\begin{aligned}\mathrm{d}\boldsymbol{q}^n \wedge \mathrm{d}\boldsymbol{p}^n - \mathrm{d}\boldsymbol{q}^{n+1} \wedge \mathrm{d}\boldsymbol{p}^{n+1} &= \mathrm{d}\boldsymbol{p}^{n+1} \wedge h\,\mathrm{d}\boldsymbol{v}^n + h\,\mathrm{d}\boldsymbol{p}^{n+1} \wedge \mathrm{d}\left(\mathrm{D}_2\boldsymbol{g}^{\mathrm{v}}(\bar{\boldsymbol{q}}, \boldsymbol{p}^{n+1})^{\mathrm{T}}\boldsymbol{\gamma}^{n+1}\right) \\ &+ h\,\mathrm{D}_{11}^2 L(\boldsymbol{q}^n, \boldsymbol{v}^n)\,\mathrm{d}\boldsymbol{q}^n \wedge \mathrm{d}\boldsymbol{q}^n - h\,\mathrm{d}\left(\boldsymbol{G}(\boldsymbol{q}^n)^{\mathrm{T}}\boldsymbol{\lambda}^n\right) \wedge \mathrm{d}\boldsymbol{q}^n - h\,\mathrm{d}\Big(\sum_{k=1}^{m} \gamma_k^{n+1}\mathrm{D}_1\boldsymbol{g}_k^{\mathrm{v}}(\bar{\boldsymbol{q}}, \boldsymbol{p}^{n+1})\Big) \wedge \mathrm{d}\boldsymbol{q}^n \,.\end{aligned} \tag{45}$$

https://doi.org/10.3311/ECCOMASMBD2021-125

We next insert $\mathrm{d}\boldsymbol{p}^{n+1}$ from (42c) into the first term on the right-hand side of (45). Moreover, the third term on the right-hand side of (45) vanishes due to property (17d) of the wedge product. The fourth one vanishes in analogy to relation (37). Consequently, we obtain

$$\begin{aligned}\mathrm{d}\boldsymbol{q}^n \wedge \mathrm{d}\boldsymbol{p}^n - \mathrm{d}\boldsymbol{q}^{n+1} \wedge \mathrm{d}\boldsymbol{p}^{n+1} &= \Big(\mathrm{D}^2_{22} L(\boldsymbol{q}^n \boldsymbol{v}^n)\,\mathrm{d}\boldsymbol{v}^n - h\,\mathrm{d}\big(\sum_{k=1}^{m} \gamma_k^{n+1} \mathrm{D}_1 \boldsymbol{g}_k^{\mathrm{v}}(\bar{\boldsymbol{q}}, \boldsymbol{p}^{n+1})\big)\Big) \wedge h\,\mathrm{d}\boldsymbol{v}^n \\ &+ h\,\mathrm{d}\boldsymbol{p}^{n+1} \wedge \mathrm{d}\left(\mathrm{D}_2 \boldsymbol{g}^{\mathrm{v}}(\bar{\boldsymbol{q}}, \boldsymbol{p}^{n+1})^{\mathrm{T}} \boldsymbol{\gamma}^{n+1}\right) - h\,\mathrm{d}\big(\sum_{k=1}^{m} \gamma_k^{n+1} \mathrm{D}_1 \boldsymbol{g}_k^{\mathrm{v}}(\bar{\boldsymbol{q}}, \boldsymbol{p}^{n+1})\big) \wedge \mathrm{d}\boldsymbol{q}^n \end{aligned} \tag{46}$$

The symmetric matrix multiplication property of the wedge product (17d) can be used once more to cancel the first term on the right-hand side of (46). Moreover, it is possible to collect the second and fourth term, yielding

$$\begin{aligned}&\mathrm{d}\boldsymbol{q}^n \wedge \mathrm{d}\boldsymbol{p}^n - \mathrm{d}\boldsymbol{q}^{n+1} \wedge \mathrm{d}\boldsymbol{p}^{n+1} = \\ &\quad - h\,\mathrm{d}\big(\sum_{k=1}^{m} \gamma_k^{n+1} \mathrm{D}_1 \boldsymbol{g}_k^{\mathrm{v}}(\bar{\boldsymbol{q}}, \boldsymbol{p}^{n+1})\big) \wedge \mathrm{d}\bar{\boldsymbol{q}} + h\,\mathrm{d}\boldsymbol{p}^{n+1} \wedge \mathrm{d}\left(\mathrm{D}_2 \boldsymbol{g}^{\mathrm{v}}(\bar{\boldsymbol{q}}, \boldsymbol{p}^{n+1})^{\mathrm{T}} \boldsymbol{\gamma}^{n+1}\right)\end{aligned} \tag{47}$$

Executing the remaining differentials leads to the expression

$$\begin{aligned}&\mathrm{d}\boldsymbol{q}^n \wedge \mathrm{d}\boldsymbol{p}^n - \mathrm{d}\boldsymbol{q}^{n+1} \wedge \mathrm{d}\boldsymbol{p}^{n+1} = \\ &\quad \left(\mathrm{D}_1 \boldsymbol{g}^{\mathrm{v}}(\bar{\boldsymbol{q}}, \boldsymbol{p}^{n+1})\,\mathrm{d}\bar{\boldsymbol{q}}\right) \wedge h\,\mathrm{d}\boldsymbol{\gamma}^{n+1} + \left(\mathrm{D}_2 \boldsymbol{g}^{\mathrm{v}}(\bar{\boldsymbol{q}}, \boldsymbol{p}^{n+1})\,\mathrm{d}\boldsymbol{p}^{n+1}\right) \wedge h\,\mathrm{d}\boldsymbol{\gamma}^{n+1} \\ &\quad - h \sum_{k=1}^{m} \gamma_k^{n+1} \mathrm{D}^2_{12} g_k^{\mathrm{v}}(\bar{\boldsymbol{q}}, \boldsymbol{p}^{n+1})\,\mathrm{d}\boldsymbol{p}^{n+1} \wedge \mathrm{d}\bar{\boldsymbol{q}} + h\,\mathrm{d}\boldsymbol{p}^{n+1} \wedge \sum_{k=1}^{m} \gamma_k^{n+1} \mathrm{D}^2_{21} g_k^{\mathrm{v}}(\bar{\boldsymbol{q}}, \boldsymbol{p}^{n+1})\,\mathrm{d}\bar{\boldsymbol{q}}\end{aligned} \tag{48}$$

In analogy to the proof given in Sect. 3.3, terms including $\mathrm{D}^2_{11} g_k^{\mathrm{v}}$ and $\mathrm{D}^2_{22} g_k^{\mathrm{v}}$, respectively, cancel due to their symmetry. It becomes obvious that the last two terms on the right-hand side of (48) cancel each other out due to (17c) since $(\mathrm{D}^2_{12} g_k^{\mathrm{v}})^{\mathrm{T}} = \mathrm{D}^2_{12} g_k^{\mathrm{v}}$. The first two terms on the right-hand side of (48) can be collected such that (43b) can be taken into account. Eventually, the whole expression on the right-hand side of (48) vanishes and we obtain

$$\mathrm{d}\boldsymbol{q}^n \wedge \mathrm{d}\boldsymbol{p}^n = \mathrm{d}\boldsymbol{q}^{n+1} \wedge \mathrm{d}\boldsymbol{p}^{n+1}\,, \tag{49}$$

which shows that the present scheme is indeed symplectic.

## 5 NUMERICAL EXAMPLE

The objective of this subsection is to analyze the behavior of the previously derived symplectic method by means of a numerical example. We investigate the motion of a rigid body according to a director framework which has already been used by Betsch & Steinmann [18], Krenk & Nielsen [19] and many others. This formulation describes rigidity using the orthonormality condition of three directors $\{\boldsymbol{d}_i\}$ positioned in the center of mass $\boldsymbol{\varphi}$. Consequently, every point is uniquely defined by its material coordinates $X_i$ with respect to the director frame's origin such that we are able to express the spatial placement as a function of the material coordinates and time such that

$$\boldsymbol{x}(\boldsymbol{X}, t) = \boldsymbol{\varphi}(t) + X_i \boldsymbol{d}_i(t)\,, \tag{50}$$

where the summation convention applies. Eventually, it is possible to describe the motion of the rigid body by $n = 3 + 9 = 12$ redundant coordinates accumulated in the coordinate vector

$$\boldsymbol{q} = \begin{bmatrix} \boldsymbol{\varphi} \\ \boldsymbol{d}_1 \\ \boldsymbol{d}_2 \\ \boldsymbol{d}_3 \end{bmatrix}\,. \tag{51}$$

https://doi.org/10.3311/ECCOMASMBD2021-125

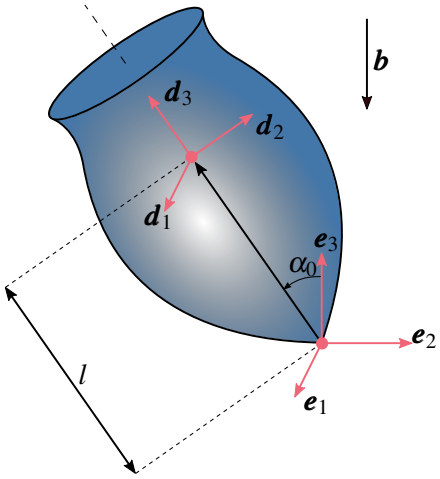


**Figure 2**. Initial configuration of the gyroscopic top

This framework consequently allows for a representation of the system's Lagrangian in the standard fashion (3) with the constant and diagonal mass matrix

$$\boldsymbol{M} = \begin{bmatrix} m\boldsymbol{I} & \boldsymbol{0} & \boldsymbol{0} & \boldsymbol{0} \\ \boldsymbol{0} & E_1\boldsymbol{I} & \boldsymbol{0} & \boldsymbol{0} \\ \boldsymbol{0} & \boldsymbol{0} & E_2\boldsymbol{I} & \boldsymbol{0} \\ \boldsymbol{0} & \boldsymbol{0} & \boldsymbol{0} & E_3\boldsymbol{I} \end{bmatrix} , \tag{52}$$

where principle values of the Euler tensor can be computed with the principal moments of inertia as $E_i = 1/2\,(J_j + J_k - J_i)$ for even permutations of the indices $(i, j, k)$. The primary constraints enforce the directors to stay orthonormal for all times due to the rigidity of the body, viz.

$$\boldsymbol{g}(\boldsymbol{q}) = \tilde{\boldsymbol{g}}(\{\boldsymbol{d}_\mathrm{i}\}) = \begin{bmatrix} \frac{1}{2}(\boldsymbol{d}_1 \cdot \boldsymbol{d}_1 - 1) \\ \frac{1}{2}(\boldsymbol{d}_2 \cdot \boldsymbol{d}_2 - 1) \\ \frac{1}{2}(\boldsymbol{d}_3 \cdot \boldsymbol{d}_3 - 1) \\ \boldsymbol{d}_1 \cdot \boldsymbol{d}_2 \\ \boldsymbol{d}_1 \cdot \boldsymbol{d}_3 \\ \boldsymbol{d}_2 \cdot \boldsymbol{d}_3 \end{bmatrix} = \boldsymbol{0} . \tag{53}$$

Specifically in this example, a gyroscopic top, as depicted in Fig. 2, has been investigated for a total simulation time of $T = 2\,\mathrm{s}$ with a time step size of $h = 0.002\,\mathrm{s}$ computed with the symplectic variational integrator from Sect. 4.

The total mass of the top amounts to $m = 0.7069\,\mathrm{kg}$ and the momenta of inertia read $J_1 = J_2 = J_3 = 5.3014 \cdot 10^{-4}\,\mathrm{kg\,m^2}$ which corresponds to a cylinder with mass density $\rho = 2700\,\mathrm{kg/m^3}$, height $a = 0.1\mathrm{m}$, top radius $r = a/2$ and a location of the center of mass along the symmetry axis $l = 3/4\,a$. In this case, the momenta of inertia can be computed via

$$J_1 = J_2 = \frac{3}{80} m(4r^2 + a^2) , \quad J_3 = \frac{3}{10} m r^2 , \tag{54a}$$

and the total mass is given by $m = \frac{1}{3}\rho\pi r^2 a$. Gravitation acts in the negative $\boldsymbol{e}_3$-direction with $\boldsymbol{b} = [0\,,0\,,-9.81\mathrm{m/s^2}]^\mathrm{T}$ such that the potential energy of the system only depends on the position of the center of mass $\boldsymbol{\varphi}$, viz.

$$V(\boldsymbol{q}) = \hat{V}(\boldsymbol{\varphi}) = -m\,\boldsymbol{b} \cdot \boldsymbol{\varphi} . \tag{55}$$

It is crucially important that the top is subject to an additional constraint

$$g_\mathrm{cm}(\boldsymbol{q}) = \boldsymbol{\varphi} - l\boldsymbol{d}_3 = 0 , \tag{56}$$

which fixes the tip of the gyroscopic top to the origin of $\{\boldsymbol{e}_i\}$ by enforcing that the center of mass is located on the axis of symmetry with a distance of $l$ to the origin. The initial nutation angle is $\alpha_0 = \pi/3$ and the gyroscopic top is subject to an initial angular velocity vector

$$\boldsymbol{\omega}_0 = \omega_\mathrm{p}\,\boldsymbol{e}_3 + \omega_\mathrm{s}\,\boldsymbol{d}_3\,, \tag{57}$$

where the initial precession rate is chosen as $\omega_p = 10\,\mathrm{s}^{-1}$ and the initial spin rate for the case of steady precession can be computed via the relation

$$\omega_\mathrm{s} = \frac{m\,g\,l}{J_3\,\omega_\mathrm{p}} + \frac{J_1 + m l^2 - J_3}{J_3}\,\omega_p\cos(\alpha_0) \tag{58}$$

(cf. p. 221 in Goldstein [20]), which amounts to $\omega_\mathrm{s} = 135.6\,\mathrm{s}^{-1}$ for the present case. Note that $g = 9.81\,\mathrm{m/s}^2$ denotes the magnitude of gravitational acceleration here. The transformation from the global $\boldsymbol{e}_i$ coordinate system to the initially inclined system can easily be done by the use of a rotation matrix $\boldsymbol{R}_0 \in SO(3)$ with the well-known property $\boldsymbol{R}_0^\mathrm{T} = \boldsymbol{R}_0^{-1}$. For the present case this reads

$$\boldsymbol{R}_0 = \begin{bmatrix} 1 & 0 & 0 \\ 0 & \cos(\alpha_0) & -\sin(\alpha_0) \\ 0 & \sin(\alpha_0) & \cos(\alpha_0) \end{bmatrix}\,, \tag{59}$$

which prescribes a rotation about the $\boldsymbol{e}_1$-axis with the angle $\alpha_0$ as can be seen in Fig. 2. Thus, the initial velocities of the center of mass and the directors can be computed by taking the cross product with the initial configuration

$$\dot{\boldsymbol{\varphi}}(t=0) = \boldsymbol{\omega}_0 \times \boldsymbol{\varphi}(t=0)\,, \qquad \dot{\boldsymbol{d}}_\mathrm{i}(t=0) = \boldsymbol{\omega}_0 \times \boldsymbol{d}_\mathrm{i}(t=0)\,, \tag{60a}$$

where $\boldsymbol{\omega}_0$ can be transformed to the global coordinate system first with the aid of $\boldsymbol{R}_0$ to simplify the computation. The Newton's method's tolerance has been set to $\varepsilon_\mathrm{tol} = 10^{-9}$. The computation has been performed using the *metis* code, which is available at [21].

By ensuring the condition for a steady precession (58) the center of mass is rotating on a constant height $\varphi_3$ around the vertical axis since gravitational forces and restabilizing effects due to the rotation are in an equilibrium. The horizontal coordinate of the center of mass $\varphi_3$ can thus be regarded as an analytical reference to the solutions. The results given by the symplectic integration scheme oscillates around this analytical solution, as can be seen in Fig. 10.

The evolution of the energetic quantities $T, V$, and $H$ is shown in Fig. 3. The total energy of the system is not conserved identically along the solutions of this integration scheme as it can be seen in Fig. 5 which displays the increments in $H$ from one time step to another. However, as it is typical for symplectic methods (cf. Fig. 16 in Lew & Mata [10]), $H(t)$ oscillates around its true value and the energy error remains stable. Furthermore, as the gyroscopic top is subject to external forces acting in the $\boldsymbol{e}_3$-direction, the symmetry of the system reduces to a conservation of the angular

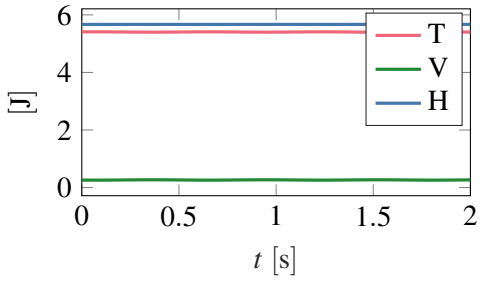


**Figure 3**. Energy quantities

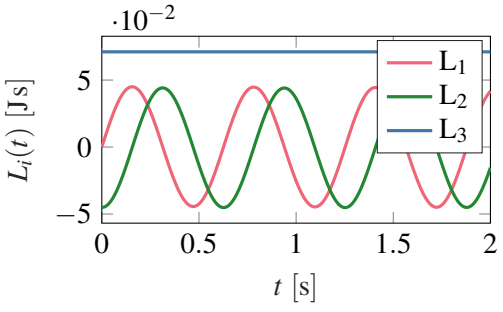


**Figure 4**. Angular momentum

https://doi.org/10.3311/ECCOMASMBD2021-125

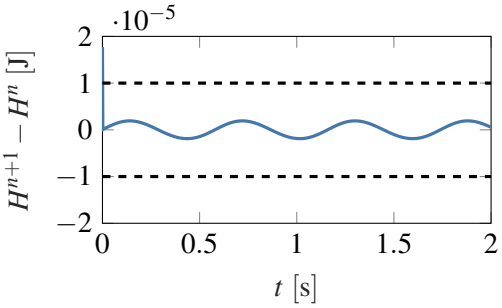


**Figure 5**. Hamiltonian difference

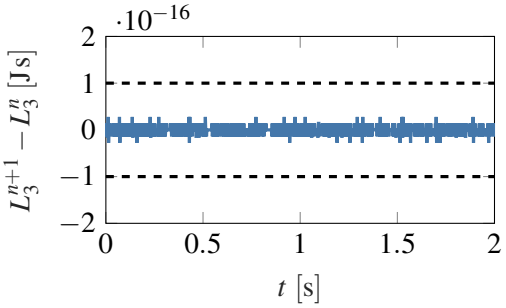


**Figure 6**. Angular momentum difference

momentum about the $\boldsymbol{e}_3$-axis such that $L_3 = \text{constant}$. This is correctly captured by the symplectic method and can be seen in Fig. 4. Differences in $L_3$ from one point in time to another are close to computer precision (cf. Fig. 6).

By design, the constraints on configuration level are identically fulfilled which can be observed in Fig. 7. In contrast to that, in each time step the secondary constraints are merely enforced in an intermediate configuration leading to the results depicted in Fig. 8.

We can moreover analyze the h-convergence of the symplectic variational integrator. Therefore we have investigated the relative error in the vertical coordinate of the center of mass, which is supposed to remain constantly $\phi_{3,\text{ana}} = 0.0375\,\text{m}$, after a total simulation time of $t = 0.001\,\text{s}$ for various time step sizes. In Fig. 9 we display the relative error

$$e = \frac{|\varphi_3(t = 0.001\,\text{s}) - \varphi_{3,\text{ana}}|}{\varphi_{3,\text{ana}}} \tag{61}$$

for the different time step sizes $h$. It becomes visible that the present method is first order accurate.

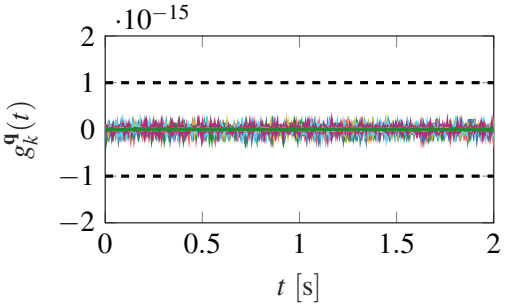


**Figure 7**. Constraints on configuration level

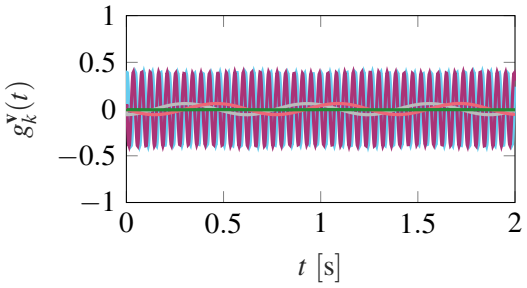


**Figure 8**. Constraints on velocity level

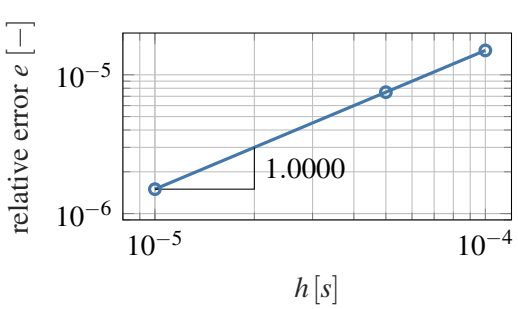


**Figure 9**. h-convergence of relative error in $\boldsymbol{q}$

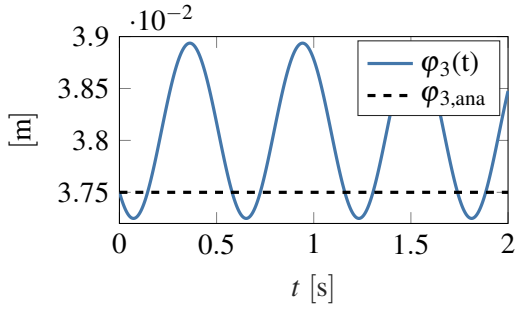


**Figure 10**. Vertical coordinate of center of mass

https://doi.org/10.3311/ECCOMASMBD2021-125

## 6 CONCLUSION AND OUTLOOK

In this work, a new variational principle for the analysis of constrained dynamics has been proposed. The underlying functional takes account of both primary and secondary constraints. Due to its mixed character with independent position, velocity and momentum quantities, it generalizes Livens principle [1] and thus unites Lagrangian and Hamiltonian viewpoints. By coupling constraints on position and velocity level into the equations we have obtained a set of DAEs which can be regarded as an extension of the well-known GGL stabilization [15]. Contrary to the original formulation, however, the emanating equations of motion have Hamiltonian structure.

The novel GGL functional gives rise to DAEs with differentiation index 2 and thus circumvents the numerical problems of the standard index-3 DAEs pertaining to mechanical systems subject to holonomic constraints. We could show, that the formulation is symplectic and has Hamiltonian structure. The conservation principles of constrained dynamics can be carried over to the novel augmented formulation. We have demonstrated that, in analogy to the classical GGL formulation [15], in the time-continuous case the additional Lagrange multipliers need to vanish. However, in contrast to the original GGL formulation, this property is not required to retain the conservation of the Hamiltonian and the symplectic structure.

Based on the newly proposed variational principle, we have succesfully derived a new first-order variational integrator. This integrator satisfies the primary constraints and is capable to conserve the angular momentum of the system. We could show that the method is symplectic which is a typical property of variational integrators (cf. Marsden & West [11]). The secondary constraints have been taken into account in an intermediate sense.

The novel variational framework represents a promising basis for the construction of structure-preserving integration schemes. The method which has been deduced throughout this work can thus be seen as a starting point for further developments. In particular, due to the close relationship of the GGL principle to optimal control, previously developed direct methods based on the philosophy “first discretize then optimize” (see, for example, Betsch & Becker [22]) can be used to obtain higher-order variational integrators for constrained mechanical systems. These integrators are symplectic by design. Furthermore, slight modifications can be applied to obtain energy-momentum consistent integrators which represent another important class of structure-preserving time-stepping schemes.

## ACKNOWLEDGEMENTS

This work was funded by the Deutsche Forschungsgemeinschaft (DFG, German Research Foundation) – project number 227928419 (BE 2285/9-3). This support is gratefully acknowledged.

## REFERENCES

[1] Livens, G.H.: On Hamilton’s principle and the modified function in analytical dynamics. Proceedings of the Royal Society Edinburgh **39**(IX) (1919) 113–119

[2] Bou-Rabee, N., Marsden, J.E.: Hamilton–Pontryagin Integrators on Lie Groups Part I: Introduction and Structure-Preserving Properties. Foundations of Computational Mathematics **9**(2) (2009) 197–219

[3] Yoshimura, H., Marsden, J.E.: Dirac structures in Lagrangian mechanics Part II: Variational structures. Journal of Geometry and Physics **57**(1) (2006) 209–250

[4] Holm, D.D.: Geometric Mechanics: Part II: Rotating, Translating and Rolling. 2 edn. Imperial College Press (2011)

[5] Pontryagin, L., Boltayanskii, V., Gamkrelidze, R., Mishchenko, E.: The mathematical theory of optimal processes. Wiley (1962)

[6] Kunkel, P., Mehrmann, V.: Differential-algebraic equations: analysis and numerical solution. EMS textbooks in mathematics. European Mathematical Society (2006)

[7] Hairer, E., Lubich, C., Wanner, G.: Geometric numerical integration: structure-preserving algorithms for ordinary differential equations. Springer (2006)

[8] Leimkuhler, B., Reich, S.: Simulating Hamiltonian Dynamics. Cambridge Monographs on Applied and Computational Mathematics. Cambridge University Press (2005)

[9] De Vogelaere, R.: Methods of Integration which Preserve the Contact Transformation Property of the Hamilton Equations. Technical report (University of Notre Dame. Dept. of Mathematics) (1956)

[10] Lew, A.J., Mata, P.: A Brief Introduction to Variational Integrators. In Betsch, P., ed.: Structure-preserving Integrators in Nonlinear Structural Dynamics and Flexible Multibody Dynamics. Volume 565. Springer (2016) 201–291

[11] Marsden, J.E., West, M.: Discrete mechanics and variational integrators. Acta Numerica **10** (2001) 357–514

[12] Maeda, S.: Lagrangian formulation of discrete systems and concept of difference space. Math. Japon **27** (1982) 345–356

[13] Leyendecker, S., Marsden, J., Ortiz, M.: Variational integrators for constrained dynamical systems. ZAMM - Journal of Applied Mathematics and Mechanics / Zeitschrift für Angewandte Mathematik und Mechanik **88**(9) (2008) 677–708

[14] Yoshimura, H.: A Geometric Method of Constraint Stabilization for Holonomic Mechanical Systems. Proceedings of ACMD06 **A00712** (2006)

[15] Gear, C., Leimkuhler, B., Gupta, G.: Automatic integration of Euler-Lagrange equations with constraints. Journal of Computational and Applied Mathematics **12-13** (1985) 77–90

[16] Pars, L.A.: A Treatise on Analytical Dynamics. The Mathematical Gazette **50**(372) (1966) 226–227

[17] Washizu, K.: Variational Methods in Elasticity and Plasticity. Pergamon Press (1975)

[18] Betsch, P., Steinmann, P.: Constrained integration of rigid body dynamics. Computer Methods in Applied Mechanics and Engineering **191**(3-5) (2001) 467–488

[19] Krenk, S., Nielsen, M.B.: Conservative rigid body dynamics by convected base vectors with implicit constraints. Computer Methods in Applied Mechanics and Engineering **269** (2014) 437–453

[20] Goldstein, H.: Classical mechanics. 2 edn. Addison-Wesley Pub. Co. (1980)

[21] Kinon, P.L.: metis: computing constrained dynamical systems (github repository). `https://github.com/philipplk/metis` (2021)

[22] Betsch, P., Becker, C.: Conservation of generalized momentum maps in mechanical optimal control problems with symmetry. International Journal for Numerical Methods in Engineering **111**(2) (2017) 144–175

https://doi.org/10.3311/ECCOMASMBD2021-171



# Kane's Equations for Nonholonomic Systems in Bond-Graph-Compatible Velocity and Momentum Forms

**James R. Phillips**[1], **Farid Amirouche**[2]

[1] Senior Applications Engineer
Applied Dynamics International
Ann Arbor, MI, USA
phillips@adi.com

[2] Department of Orthopaedic Surgery
University of Illinois at Chicago
Chicago, IL, USA
amirouch@uic.edu

## ABSTRACT

The authors' previously published results on a nonholonomic momentum form of Kane's equations are extended from scleronomic to rheonomic systems. The momentum form is found to be partially Hamiltonian, and a new velocity form is found that is partially Lagrangian. The results are derived for general particle systems, and then specialized to rigid-body systems. Except for externally constrained velocities, all system matrices are independent of time, making the results power-conserving, and suitable for use with bond graphs. A new nonholonomic IC (NIC) bond-graph element is defined, and bond graphs for the new results are exhibited using this element.

**Keywords:** Kane's equations, bond graph, NIC element, partially Hamiltonian, partially Lagrangian.

## 1 INTRODUCTION

Bond graphs are a widely used graphical formalism for representing dynamic systems, which may encompass multiple energy domains, in a uniform fashion, using a small set of ideal elements [1, 2]. Prior to the appearance of our 2018 paper [3], the most advanced methods for representing multibody systems in a concise bond-graph form were based on generalized momentum, using the IC-field bond-graph element, and these were limited to holonomic systems. In [3] we introduced a bond-graph-compatible momentum method for nonholonomic systems, based on Kane's equations [4, 5, 6], but it was limited to scleronomic systems. In this paper we further extend our momentum method to incorporate systems with external time-varying constraints, and we find that this momentum method is partially Hamiltonian (to be defined below). We also introduce a velocity-based method that is partially Lagrangian (also to be defined below). Finally, we introduce a generalization of the IC bond-graph element, the nonholonomic, or NIC bond-graph element, and exhibit bond graphs for our nonholonomic methods.

Kane's formulation is used in the development, because it can provide concise, matrix-based descriptions of multibody systems [7]. The methodology here differs from [7] however, in that it makes no assumptions about the kinematic formulation, other than that a set of partial velocity vectors describing the system is available. For the greatest generality, we begin with particle systems, and then specialize the results to systems of rigid bodies.

## 2 SCOPE, ASSUMPTIONS AND APPROACH

### 2.1 Degrees of freedom, generalized coordinates, generalized velocities

We consider a simple nonholonomic system [6, 8] in an inertial frame, with all rheonomic constraints initially relaxed, making it scleronomic. Therefore assume $R$ generalized coordinates $q_r$ completely determine the positions of all particles in the frame, and $S$ generalized velocities $f_s$ completely determine the coordinate derivatives $\dot{q}_r$; $S$ is the number of scleronomic degrees of freedom for the system, and the number of nonholonomic constraints is $R - S$. The coordinate derivatives and generalized velocities are related through the matrix equation

$$\dot{\mathbf{q}} = \mathbf{Q}\mathbf{f}\,, \tag{1}$$

https://doi.org/10.3311/ECCOMASMBD2021-171

where $\mathbf{q}$ and $\dot{\mathbf{q}}$ are length $R$ column matrices of coordinates and coordinate derivatives, $\mathbf{f}$ is a length $S$ column matrix of generalized velocities, and $\mathbf{Q}$ is an $R \times S$ matrix of rank $S$, a function only of the generalized coordinates $\mathbf{q}$. After finding equations of motion for the scleronomic degrees of freedom $\mathbf{f}$, we will then apply $S_\mathrm{c}$ rheonomic constraints, so that the final number of unconstrained degrees of freedom for the system is $S - S_\mathrm{c}$. Without loss of generality, we assume the rheonomic constraints are directly known functions of time. Thus when the rheonomic constraints are applied, we will partition the $\mathbf{f}$ matrix as

$$\mathbf{f} = \begin{bmatrix} {}^{\mathrm{u}}\mathbf{f} \\ {}^{\mathrm{c}}\mathbf{f} \end{bmatrix}, \tag{2}$$

where ${}^{\mathrm{c}}\mathbf{f}$ is a length $S_\mathrm{c}$ column matrix of known constrained generalized velocities, and ${}^{\mathrm{u}}\mathbf{f}$ is a length $S - S_\mathrm{c}$ column matrix of unconstrained generalized velocities.

*Remark.* Although the precise technical meaning of holonomicity is that $S = R$, we shall describe the system equations of motion as being in holonomic form only when $\mathbf{f} = \dot{\mathbf{q}}$. This is the case for classical dynamics methodologies such as Lagrange's and Hamilton's equations. The introduction of the $\mathbf{Q}$ matrix allows the use of so-called nonholonomic velocities as elements of the generalized velocity vector $\mathbf{f}$, which for multibody systems is a vital convenience in formulating the equations of motion. Selection of generalized velocities $f_s$ to minimize the complexity of the equations of motion is treated in [9, 10].

### 2.2 Particle velocities and partial velocities

By assumption, the velocity $\boldsymbol{v}$ of every particle in the system can be expressed as

$$\boldsymbol{v} = \left( \frac{\partial \boldsymbol{v}}{\partial \mathbf{f}^{\mathsf{T}}} \right) \mathbf{f}\,, \tag{3}$$

where $\partial \boldsymbol{v} / \partial \mathbf{f}^{\mathsf{T}}$ is a row matrix of partial derivatives, each of which is a function only of the generalized coordinates $\mathbf{q}$. These are nonholonomic partial velocities, in Kane's terminology [6, 11]. The particle notation will be extended to model rigid bodies in Section 4.

For the purpose of formulating correct equations of motion, we require knowledge of these partial velocity vectors. Any competent method for formulating the system kinematics could be used for this purpose, e.g. the use of lower-body arrays [7] ; however, we need not account here for the lower-level details of the kinematic formulation.

## 3 DEVELOPMENT OF GENERAL PARTICLE-BASED FORMS OF THE EQUATIONS

### 3.1 Impressed and Constraint Forces

We assume that every particle, having differential mass $\mathrm{d}m$, is subject to a differential force resultant $\mathrm{d}\boldsymbol{R}$, given by

$$\mathrm{d}\boldsymbol{R} = \mathrm{d}\boldsymbol{F} + \mathrm{d}^{\mathrm{c}}\boldsymbol{F}\ , \tag{4}$$

where $\mathrm{d}\boldsymbol{F}$ is the total impressed force, and $\mathrm{d}^{\mathrm{c}}\boldsymbol{F}$ is the total constraint force. The constraint force $\mathrm{d}^{\mathrm{c}}\boldsymbol{F}$ is that force, and only that force, required to enforce the motion constraints implied by the partial velocity vectors defined above. The impressed force $\mathrm{d}\boldsymbol{F}$ represents all other forces acting on the particle, which may be specified by constitutive laws, or may be unspecified functions of time. All dissipative or friction effects are accounted for in the impressed forces, as well as all conservative or otherwise unspecified actuation forces not considered to be constraint reactions.

*Remark.* This is standard analytical dynamics terminology for impressed and constraint forces, as expounded in e.g. [12]. However Kane's terminology for $\mathrm{d}\boldsymbol{F}$, as used in [6], is "active force", while his preferred terminology for $\mathrm{d}^{\mathrm{c}}\boldsymbol{F}$ is "noncontributing force". In [11], which is a revised and updated edition of [6], both "noncontributing force" and "constraint force" are used to describe $\mathrm{d}^{\mathrm{c}}\boldsymbol{F}$.

https://doi.org/10.3311/ECCOMASMBD2021-171

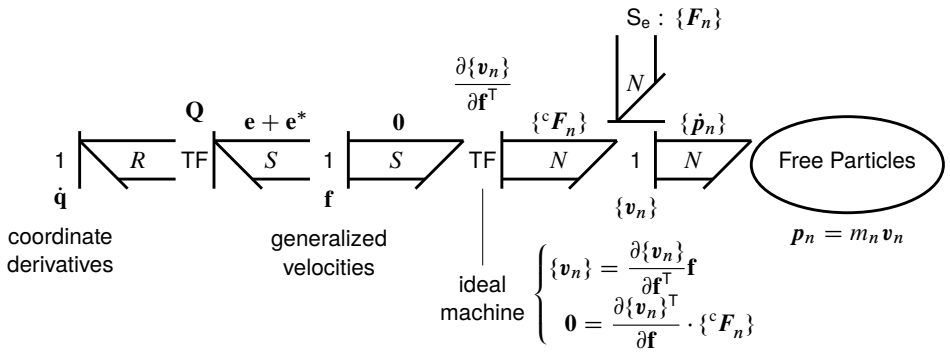


**Figure 1**. Multibond graph of unreduced Kane's equations

### 3.2 Kane's Equations in Unreduced Form

Defining the differential linear momentum of each particle as

$$\mathrm{d}\boldsymbol{p} = \boldsymbol{v}\mathrm{d}m\,, \tag{5}$$

we may write Newton's second law as

$$\mathrm{d}\dot{\boldsymbol{p}} = \mathrm{d}\boldsymbol{R}\,. \tag{6}$$

Kane's equations in unreduced form for the particle system are (using Stieltjes integration over the particle system):

$$\int \left(\frac{\partial \boldsymbol{v}}{\partial \mathbf{f}}\right) \cdot (\mathrm{d}\dot{\boldsymbol{p}} - \mathrm{d}\boldsymbol{F}) = \mathbf{0}\,, \tag{7}$$

where $\mathbf{0}$ is a length $S$ column matrix of zeros; in view of (4) this is equivalent to saying

$$\int \left(\frac{\partial \boldsymbol{v}}{\partial \mathbf{f}}\right) \cdot \left(\mathrm{d}^{\mathrm{c}}\boldsymbol{F}\right) = \mathbf{0}\,. \tag{8}$$

Eq. (8) is a consequence of the principle of virtual power, which is a generalization of the more well known principle of virtual work, that is applicable to nonholonomic systems [13].

We define the total generalized impressed (or "active") force matrix $\mathbf{e}$ as

$$\mathbf{e} \equiv \int \left(\frac{\partial \boldsymbol{v}}{\partial \mathbf{f}}\right) \cdot \mathrm{d}\boldsymbol{F}\,, \tag{9}$$

so that we have

$$\int \left(\frac{\partial \boldsymbol{v}}{\partial \mathbf{f}}\right) \cdot \mathrm{d}\dot{\boldsymbol{p}} = \mathbf{e} \tag{10}$$

as the unreduced form of Kane's equations for a particle system.

*Remark*. Practitioners of Kane's methodology typically write (10) as

$$\mathbf{e} + \mathbf{e}^* = \mathbf{0}\,, \tag{11}$$

where the elements of the $\mathbf{e}^*$ column matrix are called "generalized inertia forces", defined as

$$\mathbf{e}^* \equiv -\int \left(\frac{\partial \boldsymbol{v}}{\partial \mathbf{f}}\right) \cdot \mathrm{d}\dot{\boldsymbol{p}}\,. \tag{12}$$

Equation (11) is an homage to D'Alembert [4].

https://doi.org/10.3311/ECCOMASMBD2021-171

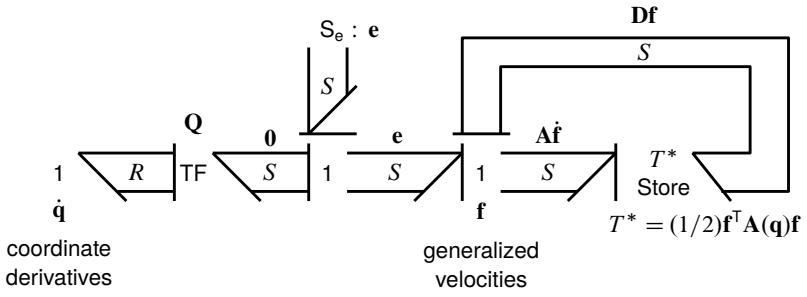


**Figure 2**. Multibond graph of reduced Kane's equations, velocity form

### 3.3 Bond Graph Representation of the Unreduced Equations

Figure 1 displays a multibond graph [14, 15] of Kane's equations in unreduced form. Here we have converted from a Stieltjes integral representation of differential particle masses to a large but finite sum of $N$ mass particles with inertial velocities $\boldsymbol{v}_n$ and masses $m_n$. There are three 1-junctions (common flow, effort summing) on the bond graph, with associated flow matrices $\dot{\mathbf{q}}$, $\mathbf{f}$, and $\{\boldsymbol{v}_n\}$ from left to right. There are two transformer (TF) elements connecting the three 1-junctions; one to represent the transformation of the $\mathbf{Q}$ matrix, and the other to represent the transformation of the partial velocity vectors.

The constitutive equations for the multibond TF element with modulus given by the partial velocity vectors are written below it. They imply perfect power conservation by this TF element (all bond graph TF elements have this property). Essentially the principle of virtual power represents the constraint forces in such a way that, in combination with the partial velocity vectors, they form an ideal machine, represented by the TF element.

The inertial subsystem on the right for the free particles is in so-called derivative causality, as indicated by the position of the causal stroke on the multibond, and its associated efforts are transferred across the TF element to the left side of the $\mathbf{f}$ 1-junction as $\mathbf{e}^*$. Similarly the impressed forces transfer to the same location as $\mathbf{e}$. Meanwhile there is a zero matrix on the right side of that 1-junction, because there are no effort sources to the left of that 1-junction. The sum of efforts on the left side of the $\mathbf{f}$ 1-junction yields the unreduced form of Kane's equations as expressed in (11). This could be considered a bond-graphic derivation of Kane's equations, because the bond-graph representation of the system as an ideal machine is evidently equivalent to the principle of virtual power.

### 3.4 Reduced Velocity Form and System Matrices

To find the reduced velocity form of Kane's equations, we return to the representation of the system as an infinite collection of particles, each having an associated differential mass and momentum. Using the partial velocity expansion for $\boldsymbol{v}$ from (3), we may write the derivative of the momentum vector for a particle as

$$\mathrm{d}\dot{\boldsymbol{p}} = \left[\left(\frac{\partial \boldsymbol{v}}{\partial \mathbf{f}^{\mathsf{T}}}\right)\,\mathrm{d}m\right]\dot{\mathbf{f}} + \left[\frac{\mathrm{d}}{\mathrm{d}t}\left(\frac{\partial \boldsymbol{v}}{\partial \mathbf{f}^{\mathsf{T}}}\right)\,\mathrm{d}m\right]\mathbf{f}\,. \tag{13}$$

Substituting this into the Stieltjes integral in (10), we find

$$\mathbf{A}\dot{\mathbf{f}} + \bar{\mathbf{D}}\mathbf{f} = \mathbf{e}\,, \tag{14}$$

where $\mathbf{A}$ is the system mass matrix given by

$$\mathbf{A} \equiv \int \left(\frac{\partial \boldsymbol{v}}{\partial \mathbf{f}}\right) \cdot \left(\frac{\partial \boldsymbol{v}}{\partial \mathbf{f}^{\mathsf{T}}}\right)\,\mathrm{d}m\,, \tag{15}$$

https://doi.org/10.3311/ECCOMASMBD2021-171

and $\bar{\mathbf{D}}$ is the system gyrator matrix given by

$$\bar{\mathbf{D}} \equiv \int \left( \frac{\partial \boldsymbol{v}}{\partial \mathbf{f}} \right) \cdot \frac{\mathrm{d}}{\mathrm{d}t} \left( \frac{\partial \boldsymbol{v}}{\partial \mathbf{f}^{\mathsf{T}}} \right) \mathrm{d}m \, ; \tag{16}$$

"gyrator" is standard bond-graph terminology for a matrix $\bar{\mathbf{D}}$ which maps a column matrix of input flows $\mathbf{f}$ to a column matrix of output efforts $\bar{\mathbf{D}}\mathbf{f}$.

$\mathbf{A}$ is a function only of $\mathbf{q}$, and by differentiation of (15), we find the identity

$$\dot{\mathbf{A}} = \bar{\mathbf{D}} + \bar{\mathbf{D}}^{\mathsf{T}} \, . \tag{17}$$

We will make use of this fact below. Although (16) provides a unique definition for $\bar{\mathbf{D}}$, any matrix $\mathbf{D}$ that satisfies (17) and for which $\mathbf{D}\mathbf{f} = \bar{\mathbf{D}}\mathbf{f}$ will serve for $\bar{\mathbf{D}}$ in (14). These two properties also guarantee that $\mathbf{D}^{\mathsf{T}}\mathbf{f} = \bar{\mathbf{D}}^{\mathsf{T}}\mathbf{f}$. Equation (14) (with $\bar{\mathbf{D}}$ replaced by $\mathbf{D}$) is what we consider the standard reduced velocity form of Kane's equations, for scleronomic systems. It is applicable to systems composed of point masses, rigid bodies, and flexible bodies modeled with a finite number of degrees of freedom.

*Remark.* Flexible bodies will not be considered here, but in Sec. 4 we provide the formulas to compute $\mathbf{A}$ and $\mathbf{D}$ from rigid body mass properties and velocities. Clearly it is $\mathbf{D}\mathbf{f}$ rather than $\mathbf{D}$ that is actually required in (14), and in Sec. 3.7 below we also develop an alternative approach to computing $\mathbf{D}\mathbf{f}$ as a whole rather than $\mathbf{D}$ separately from $\mathbf{f}$ . One must be cautious in the interpretation of the $\mathbf{D}\mathbf{f}$ term, because due to differentiation of the partial velocity vectors in (16), $\mathbf{D}$ is itself already linear in $\mathbf{f}$, so that the term as a whole is quadratic rather than linear in $\mathbf{f}$.

To develop a bond graph for the reduced velocity form of Kane's equations, we first consider the total kinetic co-energy function $T^*(\mathbf{q}, \mathbf{f})$ for the particle system, which can be written in terms of the mass matrix $\mathbf{A}$ as

$$T^*(\mathbf{q}, \mathbf{f}) \equiv (1/2)\mathbf{f}^{\mathsf{T}}\mathbf{A}(\mathbf{q})\mathbf{f}. \tag{18}$$

The total rate of change of kinetic energy is then given as

$$\begin{aligned} \frac{\mathrm{d}T^*}{\mathrm{d}t} &= \frac{\partial T^*}{\partial \mathbf{f}^{\mathsf{T}}}\dot{\mathbf{f}} + \frac{\partial T^*}{\partial \mathbf{q}^{\mathsf{T}}}\dot{\mathbf{q}} \\ &= \mathbf{f}^{\mathsf{T}}\mathbf{A}\dot{\mathbf{f}} + (1/2)\mathbf{f}^{\mathsf{T}}\dot{\mathbf{A}}\mathbf{f} \\ &= \mathbf{f}^{\mathsf{T}}(\mathbf{A}\dot{\mathbf{f}}) + \mathbf{f}^{\mathsf{T}}(\mathbf{D}\mathbf{f}). \end{aligned} \tag{19}$$

This suggests that a system kinetic co-energy store may be represented as having two multibond ports: one with effort $\mathbf{A}\dot{\mathbf{f}}$, and one with effort $\mathbf{D}\mathbf{f}$. A full multibond graph of the reduced form of the equations, using a two-port kinetic co-energy ($T^*$) store, is shown in Fig. 2, where Eq. (14) is represented at the $\mathbf{f}$ 1-junction to the left of the $T^*$ store. The left (I) port of the store, with effort $\mathbf{A}\dot{\mathbf{f}}$, has flow causality, while the right (C) port of the store, with effort $\mathbf{D}\mathbf{f}$, has effort causality.

### 3.5 Generalized Momentum Form and Generalized Gyration Forces

Now consider the generalized momentum matrix $\mathbf{p}$, which we initially define as

$$\mathbf{p} \equiv \int \left( \frac{\partial \boldsymbol{v}}{\partial \mathbf{f}} \right) \cdot d\boldsymbol{p} \, . \tag{20}$$

Using the definition of the mass matrix in (15), we can also write this as

$$\mathbf{p} = \mathbf{A}\mathbf{f} \, . \tag{21}$$

Regarding $\mathbf{p}$ in (21) as a function $\hat{\mathbf{p}}(\mathbf{q}, \mathbf{f})$, we see that we could compute the mass matrix from the partial derivative of $\hat{\mathbf{p}}$ with respect to $\mathbf{f}$:

$$\hat{\mathbf{p}}(\mathbf{q}, \mathbf{f}) \equiv \mathbf{A}(\mathbf{q})\mathbf{f} \, , \tag{22}$$

https://doi.org/10.3311/ECCOMASMBD2021-171

and therefore $\mathbf{A}$ is given by

$$\mathbf{A} = \frac{\partial \hat{\mathbf{p}}}{\partial \mathbf{f}^{\mathsf{T}}}\,. \tag{23}$$

To find a differential equation for $\mathbf{p}$, differentiate (21) with respect to time, yielding

$$\dot{\mathbf{p}} = \mathbf{A}\dot{\mathbf{f}} + \dot{\mathbf{A}}\mathbf{f}\,. \tag{24}$$

Using Eq. (17) for $\dot{\mathbf{A}}$, and the velocity form (14) to eliminate $\mathbf{A}\dot{\mathbf{f}}$, we find the differential equation for $\mathbf{p}$ as:

$$\dot{\mathbf{p}} = \mathbf{e} + \mathbf{D}^{\mathsf{T}}\mathbf{f}\,. \tag{25}$$

This we regard as one of a pair of equations of motion. In order to integrate these equations for $\mathbf{p}$, we have to solve simultaneously for $\mathbf{f}$ from $\mathbf{p}$. Using (21), we find the second of the pair as

$$\mathbf{f} = \mathbf{A}^{-1}\mathbf{p}. \tag{26}$$

Equations (25) and (26), taken as a pair, we consider to be Kane's momentum equations of motion for a scleronomic system.

The transpose of the gyrator matrix $\mathbf{D}$ is evidently itself a gyrator matrix, mapping the flow matrix $\mathbf{f}$ to an effort matrix $\mathbf{D}^{\mathsf{T}}\mathbf{f}$. Again, we should treat this product with care, because it is quadratic rather than linear in the generalized velocities $\mathbf{f}$. We name the output effort matrix $\hat{\mathbf{e}}$, and call it generalized gyration force:

$$\hat{\mathbf{e}} \equiv \mathbf{D}^{\mathsf{T}}\mathbf{f}\,, \tag{27}$$

which allows us to write (25) as

$$\dot{\mathbf{p}} = \mathbf{e} + \hat{\mathbf{e}}\,. \tag{28}$$

The product $\mathbf{D}^{\mathsf{T}}\mathbf{f} = \bar{\mathbf{D}}^{\mathsf{T}}\mathbf{f}$ has a straightforward per-particle interpretation. Using the definition of $\bar{\mathbf{D}}$ from (16), we find

$$\hat{\mathbf{e}} = \int \frac{\mathrm{d}}{\mathrm{d}t}\left(\frac{\partial \boldsymbol{v}}{\partial \mathbf{f}}\right) \cdot \mathrm{d}\boldsymbol{p}, \tag{29}$$

which allows us to define the differential generalized gyration force contributed by each particle as

$$\mathrm{d}\hat{\mathbf{e}} = \frac{\mathrm{d}}{\mathrm{d}t}\left(\frac{\partial \boldsymbol{v}}{\partial \mathbf{f}}\right) \cdot \mathrm{d}\boldsymbol{p}. \tag{30}$$

Note the parallelism between the definitions of $\mathbf{p}$ and $\hat{\mathbf{e}}$ in (20) and (29), respectively.

### 3.6 Hamiltonian Properties and Bond Graphs for Momentum Equations

Continuing with the momentum form of the equations, let us first assume the system is holonomic, so that $\mathbf{f} = \dot{\mathbf{q}}$. In this case the derivative of a partial velocity vector can be written as

$$\frac{\mathrm{d}}{\mathrm{d}t}\left(\frac{\partial \boldsymbol{v}}{\partial \dot{\mathbf{q}}}\right) = \left(\frac{\partial \boldsymbol{v}}{\partial \mathbf{q}}\right), \tag{31}$$

which is the well-known "cancellation of dots" identity. Therefore the generalized gyration force in (29) reduces to

$$\hat{\mathbf{e}} = \int \left(\frac{\partial \boldsymbol{v}}{\partial \mathbf{q}}\right) \cdot \mathrm{d}\boldsymbol{p} = \int \left(\frac{\partial \boldsymbol{v}}{\partial \mathbf{q}}\right) \cdot \boldsymbol{v}\mathrm{d}m = \frac{\partial T^*}{\partial \mathbf{q}}, \tag{32}$$

where $T^*$ is the kinetic co-energy function defined in (18). To get this into Hamiltonian form, we need to convert the kinetic co-energy function $T^*$ to the kinetic energy function $T$. Using (26) with $\mathbf{f} = \dot{\mathbf{q}}$, we find

$$T^*(\mathbf{q}, \dot{\mathbf{q}}) = T(\mathbf{q}, \mathbf{p}) \equiv (1/2)\mathbf{p}^{\mathsf{T}}\mathbf{A}^{-1}\mathbf{p}\,. \tag{33}$$

https://doi.org/10.3311/ECCOMASMBD2021-171

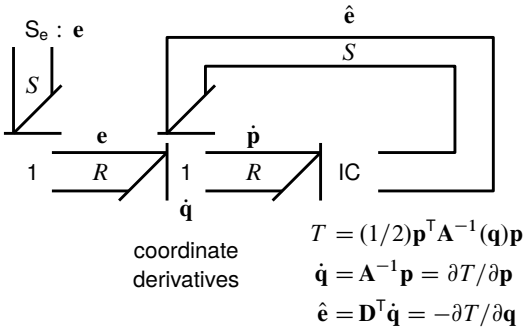


**Figure 3**. Multibond graph of reduced Kane's equations, holonomic momentum form

Making use of the identity

$$\frac{\partial \mathbf{A}^{-1}}{\partial q_r} = -\mathbf{A}^{-1}\frac{\partial \mathbf{A}}{\partial q_r}\mathbf{A}^{-1},$$

we find we may write the generalized gyration forces as

$$\hat{\mathbf{e}} = -\frac{\partial T}{\partial \mathbf{q}}\,. \tag{34}$$

By partial differentiation of $T$ with respect to $\mathbf{p}$, we also find

$$\frac{\partial T}{\partial \mathbf{p}} = \mathbf{A}^{-1}\mathbf{p} = \dot{\mathbf{q}}\,, \tag{35}$$

so that the holonomic momentum equations may be expressed as the Hamiltonian pair

$$\dot{\mathbf{p}} = \mathbf{e} - \frac{\partial T}{\partial \mathbf{q}}\,, \quad \dot{\mathbf{q}} = \frac{\partial T}{\partial \mathbf{p}}. \tag{36}$$

We regard the holonomic momentum equations as fully Hamiltonian, because the right side of both equations is *generated* by partial differentiations of the kinetic energy function $T$ (we are ignoring the generalized impressed force $\mathbf{e}$ here, as is conventional). In this case we say that the kinetic energy function $T$ is *monogenic* [16, p. 30].

To develop a bond graph for the holonomic momentum form, we differentiate (33):

$$\begin{aligned}\frac{\mathrm{d}T}{\mathrm{d}t} &= \frac{\partial T}{\partial \mathbf{p}^{\mathsf{T}}}\dot{\mathbf{p}} + \frac{\partial T}{\partial \mathbf{q}^{\mathsf{T}}}\dot{\mathbf{q}} \\ &= \mathbf{p}^{\mathsf{T}}\mathbf{A}^{-1}\dot{\mathbf{p}} - (1/2)\mathbf{p}^{\mathsf{T}}\mathbf{A}^{-1}\dot{\mathbf{A}}\mathbf{A}^{-1}\mathbf{p} \\ &= \dot{\mathbf{q}}^{\mathsf{T}}(\dot{\mathbf{p}}) - \dot{\mathbf{q}}^{\mathsf{T}}\left(\mathbf{D}^{\mathsf{T}}\dot{\mathbf{q}}\right)\,,\end{aligned} \tag{37}$$

which again suggests a two-port kinetic energy store, with effort $\dot{\mathbf{p}}$ on one port, and effort $\mathbf{D}^{\mathsf{T}}\dot{\mathbf{q}}$ on the other. The resulting bond graph of the holonomic momentum form of Kane's equations in shown in Fig. 3. In this case, the required kinetic energy ($T$) store is identified as the standard multibond IC element, first used (as a field rather than a multibond element) specifically for this purpose by Karnopp in [17]. The multibond IC element is defined in such a way that it requires the monogenic property of $T$ to hold, i.e. the flow on the (left) I-port and the effort on the (right) C-port are given by the Hamiltonian differentiation operations on $T$ defined above, and shown in the figure.

Now for the nonholonomic case, we can still differentiate $T$ with respect to $\mathbf{p}$, and get the valid equation $\mathbf{f} = \partial T/\partial \mathbf{p} = \mathbf{A}^{-1}\mathbf{p}$. However, $\hat{\mathbf{e}}$ is no longer generated by $\partial T/\partial \mathbf{q}$, so that the right side of only one of the pair is generated by $T$:

$$\dot{\mathbf{p}} = \mathbf{e} + \hat{\mathbf{e}},\ \mathbf{f} = \frac{\partial T}{\partial \mathbf{p}}\,. \tag{38}$$

https://doi.org/10.3311/ECCOMASMBD2021-171

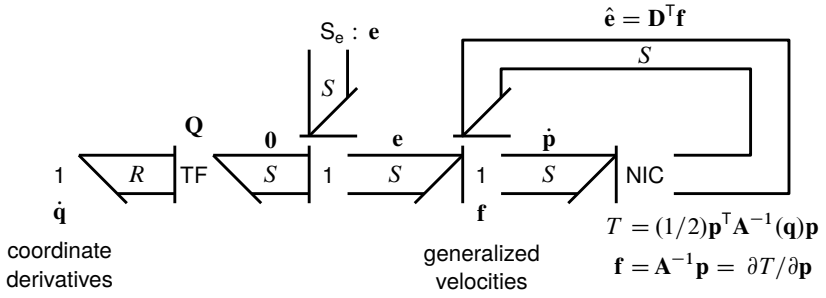


**Figure 4**. Multibond graph of reduced Kane's equations, nonholonomic momentum form

Thus, in the nonholonomic case, the kinetic energy function $T$ is not monogenic, because it doesn't generate the right sides of both equations in the pair. We may however regard the nonholonomic momentum equations as being partially Hamiltonian, because the kinetic energy function generates one of the pair. A bond graph for this case is shown in Fig. 4; in this case we show the required $T$ store as a newly defined bond-graph element, the nonholonomic IC, or NIC element. This energy store has the partially Hamiltonian property defined above, which generates the flow $\mathbf{f}$ on the left (I) port from $\partial T/\partial \mathbf{p}$, but requires the $\mathbf{D}^\mathsf{T}$matrix to generate the effort $\hat{\mathbf{e}}$ on the right (C) port. Importantly, when the system being described is actually holonomic, the NIC element reduces to the standard IC element defined above.

### 3.7 Lagrangian Form and Bond Graphs for Velocity Equations

An alternative form of the velocity equations in Sec. 3.4 can be developed from the momentum form developed in Secs. 3.5–3.6, which is partially Lagrangian in the nonholonomic case, and fully Lagrangian in the holonomic case. Starting from the generalized momentum function $\hat{\mathbf{p}}(\mathbf{q}, \mathbf{f})$ defined above in Eq. (22), we take the total derivative of $\hat{\mathbf{p}}(\mathbf{q}, \mathbf{f})$ symbolically, finding

$$\dot{\hat{\mathbf{p}}} = \left(\frac{\partial \hat{\mathbf{p}}}{\partial \mathbf{f}^\mathsf{T}}\right)\dot{\mathbf{f}} + \left(\frac{\partial \hat{\mathbf{p}}}{\partial \mathbf{q}^\mathsf{T}}\right)\dot{\mathbf{q}}\,. \tag{39}$$

Then using the definition of $\hat{\mathbf{p}}$ in (22), we see that $\partial\hat{\mathbf{p}}/\partial\mathbf{f}^\mathsf{T}$is equal to $\mathbf{A}$, so we have

$$\dot{\hat{\mathbf{p}}} = \mathbf{A}\dot{\mathbf{f}} + \left(\frac{\partial \hat{\mathbf{p}}}{\partial \mathbf{q}^\mathsf{T}}\right)\dot{\mathbf{q}}. \tag{40}$$

Substituting this into the momentum equation of motion (28), we have

$$\mathbf{A}\dot{\mathbf{f}} + \left(\frac{\partial \hat{\mathbf{p}}}{\partial \mathbf{q}^\mathsf{T}}\right)\dot{\mathbf{q}} = \mathbf{e} + \hat{\mathbf{e}}. \tag{41}$$

This form of the nonholonomic velocity equations is believed to be a new result, which is useful in several ways. We call it the partially Lagrangian form of the velocity equations.

First, it has a partially Lagrangian property, as we shall explain. The left side of (41) is generated by the left side of (40), which in turn is generated by differentiation of the kinetic co-energy function, i.e.

$$\dot{\hat{\mathbf{p}}} = \frac{\mathrm{d}}{\mathrm{d}t}\left(\frac{\partial T^*}{\partial \mathbf{f}}\right),$$

where $T^*$ is the nonholonomic kinetic co-energy function defined in (18). Therefore we can write (41) in the form

$$\frac{\mathrm{d}}{\mathrm{d}t}\left(\frac{\partial T^*}{\partial \mathbf{f}}\right) = \mathbf{e} + \hat{\mathbf{e}}\,. \tag{42}$$

https://doi.org/10.3311/ECCOMASMBD2021-171

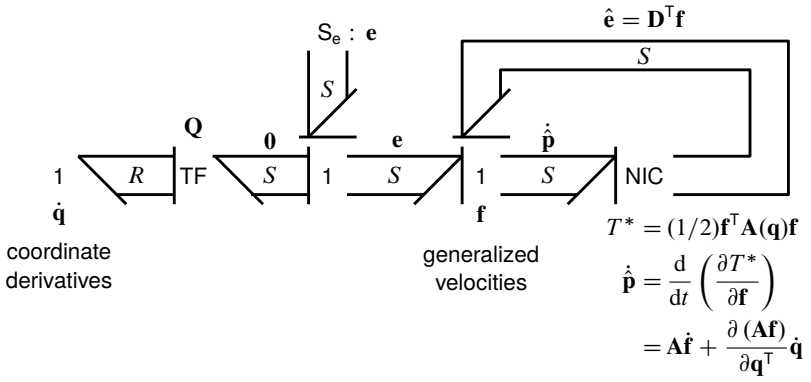


**Figure 5**. Multibond graph of reduced Kane's equations, nonholonomic partially Lagrangian velocity form

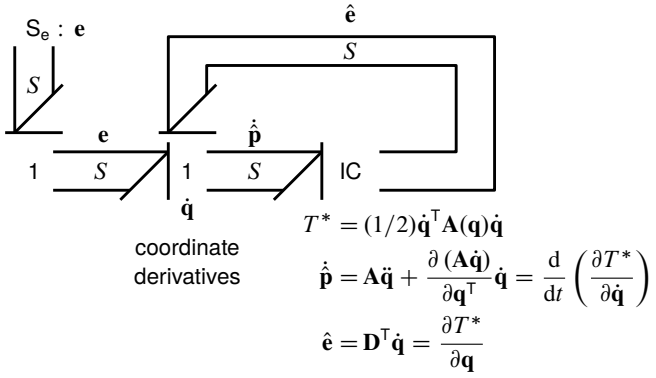


**Figure 6**. Multibond graph of reduced Kane's equations, holonomic Lagrangian form

Figure 5 displays a multibond graph of the partially Lagrangian form of the velocity equations, using the NIC multibond-graph element defined in Sec. 3.6. As in the momentum case, the energy function $T^*$ associated with the NIC element generates the column matrix of efforts on the left (I) side of the element ($\dot{\hat{\mathbf{p}}}$), but not the column matrix of efforts $\hat{\mathbf{e}}$ on the right (C) side of the element.

If the system were fully holonomic, the left side of Eq. (42) would be $\mathrm{d}\left(\partial T^*/\partial\dot{\mathbf{q}}\right)/\mathrm{d}t$, while, using (32), the right side would be $e + \partial T^*/\partial\mathbf{q}$. Clearly, these are are Lagrange's equations. Therefore Eq. (42) demonstrates a partially Lagrangian property, which becomes completely Lagrangian in case that the system is holonomic. From another point of view, in the holonomic case, the kinetic co-energy function $T^*$ is seen to be monogenic, in that it generates both sides of the equation (setting **e** aside), while in the nonholonomic case, it generates only one side of the equation. Thus, as in the momentum equations, the associated energy function is or is not monogenic according as the system is or is not holonomic. Figure 6 displays a multibond graph of the velocity equations in the fully Lagrangian form, using again the standard multibond-graph IC element.

Besides having the partially Lagrangian property, Eq. (41) provides a useful alternative implementation for the computing the product **Df**. Comparing (41) to (14), we find

$$\mathbf{Df} = \frac{\partial\hat{\mathbf{p}}}{\partial\mathbf{q}^\mathsf{T}}\dot{\mathbf{q}} - \hat{\mathbf{e}}\,. \tag{43}$$

The expression on the right side of (43) may be simpler to compute by analysis than the one on the left side, particularly if one or more of the coordinates **q** does not appear in the expression for $\hat{\mathbf{p}}$. A

https://doi.org/10.3311/ECCOMASMBD2021-171

generalized coordinate $q_r$ is defined as ignorable if it does not appear explicitly in the momentum function $\hat{\mathbf{p}}$ (or equivalently the mass matrix $\mathbf{A}$). If all generalized coordinates are ignorable, then

$$\mathbf{Df} = -\hat{\mathbf{e}} = -\mathbf{D}^{\mathsf{T}}\mathbf{f}. \qquad \text{(all coordinates ignorable)} \tag{44}$$

This could also be derived directly from Eq. 17.

### 3.8 Extension to Rheonomic Systems, Including Generalized Constraint Forces.

Now, in the final stage of our analysis, we complete the method of constraint relaxation, by enforcing the previously relaxed $S_c$ rheonomic flow constraints, thereby removing the limitation of the analysis to scleronomic systems, and allowing the determination of the reactions associated with the rheonomic constraints. Therefore in addition to partitioning the flow matrix $\mathbf{f}$ according to (2), we must partition the effort matrix $\mathbf{e}$ as

$$\mathbf{e} = \begin{bmatrix} {}^{\mathrm{u}}\mathbf{e} \\ {}^{\mathrm{c}}\mathbf{e} \end{bmatrix}, \tag{45}$$

where ${}^{\mathrm{u}}\mathbf{e}$ is the column vector of impressed efforts corresponding to ${}^{\mathrm{u}}\mathbf{f}$, and ${}^{\mathrm{c}}\mathbf{e}$ is the column matrix of constraint reactions to be found, corresponding to the directly known flow constraints ${}^{\mathrm{c}}\mathbf{f}$.

Equation (14), the reduced velocity form of the equations of motion, when partitioned according to this scheme, becomes

$$\begin{bmatrix} {}^{\mathrm{u}}\mathbf{e} \\ {}^{\mathrm{c}}\mathbf{e} \end{bmatrix} = \begin{bmatrix} {}^{\mathrm{uu}}\mathbf{A} & {}^{\mathrm{uc}}\mathbf{A} \\ {}^{\mathrm{cu}}\mathbf{A} & {}^{\mathrm{cc}}\mathbf{A} \end{bmatrix} \begin{bmatrix} {}^{\mathrm{u}}\dot{\mathbf{f}} \\ {}^{\mathrm{c}}\dot{\mathbf{f}} \end{bmatrix} + \begin{bmatrix} {}^{\mathrm{u}}\mathbf{D} \\ {}^{\mathrm{c}}\mathbf{D} \end{bmatrix} \mathbf{f}, \tag{46}$$

where we are partitioning $\mathbf{A}$ according to its rows and columns, but we are partitioning $\mathbf{D}$ only according to its rows. The first row of (46) gives a solution for ${}^{\mathrm{u}}\dot{\mathbf{f}}$ as

$${}^{\mathrm{u}}\dot{\mathbf{f}} = \left[{}^{\mathrm{uu}}\mathbf{A}\right]^{-1} \left[{}^{\mathrm{u}}\mathbf{e} - {}^{\mathrm{uc}}\mathbf{A}\,{}^{\mathrm{c}}\dot{\mathbf{f}} - {}^{\mathrm{u}}\mathbf{Df}\right], \tag{47}$$

while the second row directly gives the solution for the constraint reactions as

$${}^{\mathrm{c}}\mathbf{e} = {}^{\mathrm{cu}}\mathbf{A}\,{}^{\mathrm{u}}\dot{\mathbf{f}} + {}^{\mathrm{cc}}\mathbf{A}\,{}^{\mathrm{c}}\dot{\mathbf{f}} + {}^{\mathrm{c}}\mathbf{Df}; \tag{48}$$

in order to implement these computationally (47) must be evaluated before (48).

To work with the reduced momentum form of the equations of motion, we may proceed similarly. The first row of the partitioned form of (25) gives an equation for ${}^{\mathrm{u}}\dot{\mathbf{p}}$, as

$${}^{\mathrm{u}}\dot{\mathbf{p}} = {}^{\mathrm{u}}\mathbf{e} + {}^{\mathrm{u}}\left[\mathbf{D}^{\mathsf{T}}\right]\mathbf{f}, \tag{49}$$

while the first row of the partitioned form of (21) yields the solution for ${}^{\mathrm{u}}\mathbf{f}$ as

$${}^{\mathrm{u}}\mathbf{f} = \left[{}^{\mathrm{uu}}\mathbf{A}\right]^{-1} \left[{}^{\mathrm{u}}\mathbf{p} - {}^{\mathrm{uc}}\mathbf{A}\,{}^{\mathrm{c}}\mathbf{f}\right]. \tag{50}$$

The momentum formulation for the unconstrained flows, (49, 50), shows a clear computational advantage over the velocity formulation (47, 48) in that the known constrained flows do not have to be differentiated to find ${}^{\mathrm{u}}\mathbf{f}$ in the momentum formulation, whereas they do in the velocity formulation. However, it is not possible to avoid differentiating the constrained flows in order to find the constraint reactions ${}^{\mathrm{c}}\mathbf{e}$. Although a momentum formulation for the constraint reactions can be developed [18], it offers no computational advantages over the velocity formulation, and therefore the velocity formulation for the constraint reactions, (48), is recommended for use in all cases.

https://doi.org/10.3311/ECCOMASMBD2021-171

## 4 RIGID-BODY FORMS OF THE SYSTEM MATRICES

We consider now a system of $N$ rigid bodies indexed by $n$, with body $n$ having angular velocity $\boldsymbol{\omega}_n$ in the inertial frame, and its center of mass having linear velocity $\boldsymbol{v}_n$ in the same frame. Body $n$ will have total mass $m_n$, and rotational inertia tensor $\mathbf{I}_n$. The velocity vectors for each body can be written as

$$\boldsymbol{\omega}_n = \left(\frac{\partial \boldsymbol{\omega}_n}{\partial \mathbf{f}^{\mathsf{T}}}\right)\mathbf{f}, \quad \boldsymbol{v}_n = \left(\frac{\partial \boldsymbol{v}_n}{\partial \mathbf{f}^{\mathsf{T}}}\right)\mathbf{f}. \tag{51}$$

Euler defined the linear and angular momentum vectors as

$$\boldsymbol{p}_n = m_n \boldsymbol{v}_n, \quad \boldsymbol{h}_n = \mathbf{I}_n \cdot \boldsymbol{\omega}_n, \tag{52}$$

respectively. We assume that the total impressed force acting through the center of mass is $\boldsymbol{F}_n$, and the total impressed moment acting about the center of mass is $\boldsymbol{M}_n$.

By Stieltjes integration of the particle contributions over each body, we may show the following system relationships, which are listed without proof (using the summation convention over $n$):

$$\mathbf{e} = \left(\frac{\partial \boldsymbol{v}_n}{\partial \mathbf{f}}\right) \cdot \boldsymbol{F}_n + \left(\frac{\partial \boldsymbol{\omega}_n}{\partial \mathbf{f}}\right) \cdot \boldsymbol{M}_n \tag{53}$$

$$\mathbf{p} = \hat{\mathbf{p}}\,(\mathbf{q}, \mathbf{f}) = \left(\frac{\partial \boldsymbol{v}_n}{\partial \mathbf{f}}\right) \cdot \boldsymbol{p}_n + \left(\frac{\partial \boldsymbol{\omega}_n}{\partial \mathbf{f}}\right) \cdot \boldsymbol{h}_n \tag{54}$$

$$\mathbf{A} = \frac{\partial \hat{\mathbf{p}}}{\partial \mathbf{f}^{\mathsf{T}}} = m_n \left(\frac{\partial \boldsymbol{v}_n}{\partial \mathbf{f}}\right) \cdot \left(\frac{\partial \boldsymbol{v}_n}{\partial \mathbf{f}^{\mathsf{T}}}\right) + \left(\frac{\partial \boldsymbol{\omega}_n}{\partial \mathbf{f}}\right) \cdot \mathbf{I}_n \cdot \left(\frac{\partial \boldsymbol{\omega}_n}{\partial \mathbf{f}^{\mathsf{T}}}\right) \tag{55}$$

$$\mathbf{D} = m_n \left(\frac{\partial \boldsymbol{v}_n}{\partial \mathbf{f}}\right) \cdot \frac{\mathrm{d}}{\mathrm{d}t}\left(\frac{\partial \boldsymbol{v}_n}{\partial \mathbf{f}^{\mathsf{T}}}\right) + \left(\frac{\partial \boldsymbol{\omega}_n}{\partial \mathbf{f}}\right) \cdot \mathbf{I}_n \cdot \frac{\mathrm{d}}{\mathrm{d}t}\left(\frac{\partial \boldsymbol{\omega}_n}{\partial \mathbf{f}^{\mathsf{T}}}\right) + \left(\frac{\partial \boldsymbol{\omega}_n}{\partial \mathbf{f}}\right) \cdot \left(\boldsymbol{\omega}_n \times \frac{\partial \boldsymbol{h}_n}{\partial \mathbf{f}^{\mathsf{T}}}\right) \tag{56}$$

$$\hat{\mathbf{e}} = \mathbf{D}^{\mathsf{T}}\mathbf{f} = \frac{\mathrm{d}}{\mathrm{d}t}\left(\frac{\partial \boldsymbol{v}_n}{\partial \mathbf{f}}\right) \cdot \boldsymbol{p}_n + \frac{\mathrm{d}}{\mathrm{d}t}\left(\frac{\partial \boldsymbol{\omega}_n}{\partial \mathbf{f}}\right) \cdot \boldsymbol{h}_n\,. \tag{57}$$

All the reduced form equations derived above for particle systems apply equally well for rigid-body systems, when these results for the system matrices are used in the equations.

For holonomic systems, we can use the previously mentioned "cancellation of dots" identity for the linear velocity vectors, as well as an additional identity for the angular velocity vectors, which is

$$\frac{\mathrm{d}}{\mathrm{d}t}\left(\frac{\partial \boldsymbol{\omega}_n}{\partial \dot{\mathbf{q}}}\right) = \left(\frac{\partial \boldsymbol{\omega}_n}{\partial \mathbf{q}}\right) + \boldsymbol{\omega}_n \times \left(\frac{\partial \boldsymbol{\omega}_n}{\partial \dot{\mathbf{q}}}\right). \tag{58}$$

Under these circumstances, we have the following simplifications:

$$\mathbf{D} = m_n \left(\frac{\partial \boldsymbol{v}_n}{\partial \dot{\mathbf{q}}}\right) \cdot \left(\frac{\partial \boldsymbol{v}_n}{\partial \mathbf{q}^{\mathsf{T}}}\right) + \left(\frac{\partial \boldsymbol{\omega}_n}{\partial \dot{\mathbf{q}}}\right) \cdot \mathbf{I}_n \cdot \left(\frac{\partial \boldsymbol{\omega}_n}{\partial \mathbf{q}^{\mathsf{T}}}\right), \tag{59}$$

$$\hat{\mathbf{e}} = \mathbf{D}^{\mathsf{T}}\dot{\mathbf{q}} = \left(\frac{\partial \boldsymbol{v}_n}{\partial \mathbf{q}}\right) \cdot \boldsymbol{p}_n + \left(\frac{\partial \boldsymbol{\omega}_n}{\partial \mathbf{q}}\right) \cdot \boldsymbol{h}_n\,. \tag{60}$$

### 4.1 Relationship to Previous Results

In the authors' previously published paper [3], which covers only the scleronomic momentum form for rigid-body systems, we define the $\mathbf{C}$ matrix as

$$\mathbf{C} = m_n \frac{\mathrm{d}}{\mathrm{d}t}\left(\frac{\partial \boldsymbol{v}_n}{\partial \mathbf{f}}\right) \cdot \left(\frac{\partial \boldsymbol{v}_n}{\partial \mathbf{f}^{\mathsf{T}}}\right) + \frac{\mathrm{d}}{\mathrm{d}t}\left(\frac{\partial \boldsymbol{\omega}_n}{\partial \mathbf{f}}\right) \cdot \mathbf{I}_n \cdot \left(\frac{\partial \boldsymbol{\omega}_n}{\partial \mathbf{f}^{\mathsf{T}}}\right), \tag{61}$$

from which it is clear that $\mathbf{D}$ and $\mathbf{C}$ are related according to

$$\mathbf{D} = \mathbf{C}^{\mathsf{T}} + \left(\frac{\partial \boldsymbol{\omega}_n}{\partial \mathbf{f}}\right) \cdot \left(\boldsymbol{\omega}_n \times \frac{\partial \boldsymbol{h}_n}{\partial \mathbf{f}^{\mathsf{T}}}\right). \tag{62}$$

The $\mathbf{A}$ and $\mathbf{C}$ matrices are sufficient to define the momentum forms, without requiring the $\mathbf{D}$ matrix.

https://doi.org/10.3311/ECCOMASMBD2021-171

## REFERENCES


[1] Paynter, H.: Analysis and design of engineering systems; class notes for MIT course 2.751 (1961)

[2] Karnopp, D., Margolis, D., Rosenberg, R.: System Dynamics. Third edn. Wiley (2000)

[3] Phillips, J.R., Amirouche, F.: A momentum form of Kane's equations for scleronomic systems. Mathematical and Computer Modelling of Dynamical Systems **24**(2) (2018) 143–169

[4] Kane, T.R.: Dynamics of nonholonomic systems. J. Appl. Mech. **28**(4) (1961) 574–578

[5] Kane, T.R., Wang, C.F.: On the derivation of equations of motion. J. Soc. Indust. Appl. Math. **13**(2) (1965) 487–492

[6] Kane, T.R., Levinson, D.A.: Dynamics: Theory and Applications. McGraw-Hill (1985)

[7] Amirouche, F.: Fundamentals of multibody dynamics: theory and applications. Springer Science & Business Media (2007)

[8] Kane, T., Banerjee, A.: A conservation theorem for simple nonholonomic systems. Journal of Applied Mechanics **50**(3) (1983) 647–651

[9] Banerjee, A.K.: Order-n formulation of equations of motion with efficient choices of motion variables. Guidance, Navigation, and Control and Co-located Conferences. American Institute of Aeronautics and Astronautics (August 1994)

[10] Mitiguy, P.C., Kane, T.R.: Motion variables leading to efficient equations of motion. The International Journal of Robotics Research **15**(5) (1996) 522–532

[11] Roithmayr, C.M., Hodges, D.H.: Dynamics: Theory and Application of Kane's Method. Cambridge University Press (2016)

[12] Papastavridis, J.G.: Analytical Mechanics. World Scientific Publishing Co Pte Ltd, Singapore (2014)

[13] Wang, L., Pao, Y.: Jourdain's variational equation and Appell's equation of motion for nonholonomic dynamical systems. Am. J. Phys **71**(1) (January 2003)

[14] Breedveld, P.: Multibond graph elements in physical systems theory. J. Franklin Inst. **319**(1/2) (1985) 1–36

[15] Fahrenthold, E., Wargo, J.: Vector and tensor based bond graphs for physical systems modeling. Journal of the Franklin Institute **328**(5-6) (1991) 833–853

[16] Lanczos, C.: The variational principles of mechanics. University of Toronto press (1970)

[17] Karnopp, D.: An approach to derivative causality in bond graph models of mechanical systems. J. Franklin Inst. **329**(1) (1992) 65–75

[18] Phillips, J.R., Amirouche, F.: Corrigendum: a momentum form of Kane's equations for scleronomic systems. Mathematical and Computer Modelling of Dynamical Systems (2018) 1–4

https://doi.org/10.3311/ECCOMASMBD2021-172

ECCOMAS Thematic Conference on Multibody Dynamics
December 12 - 15, 2021, Budapest, Hungary

# Assessment of variable step-size integration of multibody systems

**Maurizio Ruggiu**[1], **Francisco González**[2]

[1] Dipartimento di Ingegneria Meccanica, Chimica e dei Materiali
Università di Cagliari
Via Marengo, 2, 09123 Cagliari, Italy
maurizio.ruggiu@dimcm.unica.it

[2] Laboratorio de Ingeniería Mecánica
University of A Coruña
Mendizábal s/n, 15403 Ferrol, Spain
f.gonzalez@udc.es

## ABSTRACT

When performing the numerical integration of multibody systems (MBS) dynamics, the analyst can choose from a wide variety of methods and implementations. Selecting the most appropriate option for a particular application is not a straightforward task; as a consequence, several benchmark examples have been formulated by the MBS research community with the intent to assess the accuracy and performance of different solution methods when applied to certain kinds of mechanical problems. This paper introduces a variation of the slider-crank mechanism, already employed as benchmark problem in the MBS literature, intended to evaluate the performance of variable-step MBS algorithms. Three cases, featuring singular configurations and variable-frequency external actions, were defined. The example is used to illustrate some necessary elements in the definition of a benchmark problem and in the process of comparing different solution methods, as well as difficulties that can arise during this task. The proposed example was used to evaluate the behaviour of a variable-step index-3 augmented Lagrangian algorithm with velocity and acceleration projections, as well as other well-known solution methods.

**Keywords:** Benchmark problems, Numerical integration, Efficient Methods, Singular configurations.

## 1 INTRODUCTION

A considerable number of methods and algorithms for the simulation and analysis of Multibody System (MBS) Dynamics have been proposed since the early developments in this area were first published [1, 2]. The performance of each approach depends on the characteristics of the problems to which it is applied, and so methods that are effective in the simulation of a certain type of mechanical system may be inefficient when applied to mechanisms with a different topology or subjected to other kinds of physical phenomena. Fully recursive methods [3], for instance, may become ineffective in the solution of heavily constrained multibody systems; mechanisms that feature redundant constraints or singular configurations pose a problem for solution algorithms that expect the Jacobian matrix of the constraints to have a full row rank throughout the motion [4, 5]. Moreover, implementation techniques, third-party software libraries, e.g., for the linear algebra routines required by most MBS codes, and the hardware platform used to execute the code, as well as the interaction between them, have a critical impact on the time elapsed in computations [6, 7]. For these reasons, selecting an appropriate MBS formalism for its application to a particular problem may prove challenging in some cases, particularly when efficiency constraints are imposed as a requirement.

Benchmark problems represent a useful tool to evaluate the accuracy and efficiency of MBS codes, as well as their ability to handle particular kinds of problems. Ideally, benchmarks should be simple enough to enable their exact reproduction by any researcher or team interested in using them. At the same time, they must be nontrivial problems that provide interesting information about some aspect of the behaviour of the solution method [8]. In recent years, several initiatives have been put

https://doi.org/10.3311/ECCOMASMBD2021-172

forward by MBS researchers to propose meaningful test problems that can be generally accepted as benchmarks by the community. The IFToMM Library of Computational Benchmark Problems [9] is a well-known collection of such examples, which includes test problems for forward- and inverse-dynamics, as well as linearization. These examples illustrate the performance of MBS formulations and implementations when dealing with complex issues such as redundant constraints, singular configurations, stiff problems, and contacts, to mention just a few. Another instance of collection of benchmark problems can be found in [10], which puts forward a series of cases for the validation of flexible multibody dynamics algorithms. Benchmark problems for contact dynamics were introduced in [11]. In the case of MBS dynamics, benchmarking is not limited to the algorithms for the integration of the equations of motion, but has also been extended to applications in which the multibody part is a necessary component, like estimators based on Kalman filters [12]. Benchmark problems for particular applications of MBS dynamics can be found in the areas of railway vehicles [13] and co-simulation [14].

Variable step-size integration methods are frequently used in MBS dynamics applications. These algorithms adapt the step-size of the integration formula to the time-scale of the dynamics of the problem under study with the goal of reducing the time elapsed in computations. In some cases, the step-size control solution is combined with the MBS formulation used to handle the equations of motion, e.g., [15]. This paper introduces a variation of the well-known slider-crank benchmark problem particularly geared towards the assessment of variable step-size integration methods. Two new versions of the linkage were defined, with and without singular configurations. Both were subjected to the action of a force that varied over time, to prevent a periodic system motion.

A particular goal of the present paper is to assess the ability of the variable-step index-3 augmented Lagrangian algorithm with velocity and acceleration projections, introduced in [15], to take advantage of step-size adjustment during motion to deliver more accurate and efficient simulation results. Other formulations and integration formulas were used as well to evaluate the ability of the proposed example to be used in the assessment of variable-step integrators. Results showed that the combination of singular configurations and externally applied forces with variable frequency made the proposed example a challenging problem for most solution methods.

## 2 METHODS

There exist three components that should always be present in the definition of a benchmark problem for MBS dynamics algorithms:

- A definition of the problem to be solved. This must include the specification of the properties and initial state of the mechanical system, as well as information about the manoeuvre to be simulated, such as duration in time and input forces and torques.
- A reference solution which, for the purposes of benchmarking, can be considered correct. This reference solution may be obtained from experimental results, an analytical solution of the problem at hand, or upon convergence of several simulation processes.
- Appropriate error metrics and comparison criteria. These enable the assessment of the solutions obtained with different simulation methods [16].

Moreover, other optional components can be added too, such as reference implementations of the simulation code or data structures to enable the efficient collection and processing of simulation results.

In order to be useful, benchmark examples should be clearly defined problems that are easy to replicate. They should also represent nontrivial scenarios, which are meaningful or challenging in at least one respect. Ideally, they should also be representative of a wider class of systems. For instance, a slider-crank that undergoes singular configurations can be defined in a straightforward way with a reduced set of kinematic and kinetic parameters. In spite of being a relatively

simple mechanical system, it poses a problem for simulation algorithms that cannot deal with rank-deficient Jacobian matrices; even some solution methods that can handle them need to be carefully adjusted to deliver correct results [5], as is the case of augmented Lagrangian algorithms. Results obtained with this linkage can then be used to assess the general ability of solution methods to carry out the simulation of systems with singularities.

In some cases, it is possible to find an analytical solution for the motion of simple mechanical systems. Generally, this is not the case. In benchmark problems that do not represent a physical system, for which experimental results are not available, physical magnitudes can be used as indicators instead. For instance, the variation of the mechanical energy can be used to quantify the accuracy of a given simulation method if the benchmark problem represents a conservative system. These indicators should be used with precaution, as a precise energy conservation does not necessarily guarantee the correctness of the obtained results. Arriving at a reference solution through the convergence of several simulation methods is advisable when analytical and experimental solutions are not available.

Error metrics and criteria are also an important component of a benchmark problem. First, it is necessary to select the variables that will be selected to evaluate the accuracy of a solution. These may include kinematic variables, such as positions, velocities, and accelerations, or kinetic magnitudes like forces or energies. Usually $n$ variables of interest can be selected and will suffice to measure the precision of the results. It is also necessary to specify at what points in time these variables will be evaluated. When using fixed-step integrators this is relatively simple, as data can be gathered regularly during the simulation. With variable-step simulators usually interpolation methods have to be used. Second, a metric to quantify the deviation of the results obtained with a particular method with respect to the reference solution is necessary. The local error at time point $t_i$ for variable $y_j$ can be evaluated as

$$\varepsilon_j(t_i) = y_j(t_i) - y_j^{\text{ref}}(t_i) \tag{1}$$

where $y_j^{\text{ref}}$ denotes the value that corresponds to the reference solution. Relative definitions of the error can be used too [16]. Absolute errors, however, show a better behaviour when the variables of interest approach zero. The total error of a simulation can be calculated as

$$\varepsilon_{\text{T}} = \sqrt{\frac{1}{n}\sum_{j=1}^{n}\frac{w_j}{m}\sum_{i=1}^{m}\left(\varepsilon_j(t_i)\right)^2} \tag{2}$$

where $m$ is the total number of time points collected during the simulation and $w_j$ is a weight factor that represents the contribution of variable $j$ to the total error. Factor $w_j$ can also be used to make errors dimensionless, so that variables with different units can be added together in a single error indicator. Besides the total error in (2), it is also possible to select other indicators, such as the maximum or minimum absolute error for a single variable or group of variables.

The existence of a metric like the one in (2) makes it possible to establish a validity criterion that determines whether a simulation is accurate enough or not. A criterion like this is particularly important if the benchmark problem is to be used to compare several solution approaches in terms of efficiency, because that comparison should be carried out requesting the same accuracy level from every method.

Finally, comparison criteria can be defined to quantify the differences between the different solution methods. The elapsed time in computations is a commonly used criterion to rank algorithms and implementations, but other metrics, such as energy balances and satisfaction of kinematic constraints can be used too [17].

### 2.1 Problem description

The benchmark problem used in this paper is a variation of the well-known slider-crank linkage, already included in the IFToMM benchmark library [9] and shown in Fig. 1. This planar mechan-

https://doi.org/10.3311/ECCOMASMBD2021-172

ical system is composed of two rods, links 1 and 2, with uniformly distributed mass $m_1$ and $m_2$ and length $L_1$ and $L_2$, respectively. The slider, link 3, has mass $m_3$ and moves without friction along the $x$ axis. The mechanism moves under gravity effects with $g = 9.81$ m/s$^2$ acting along the negative $y$ axis. The system has one degree of freedom; at time $t = 0$, rod 1 is at an angle $\theta_{1,0}$ with respect to the $x$ axis and the velocity of point Q is $\dot{x}_{Q,0}$. A horizontal external force $f$ acts on point Q during motion.

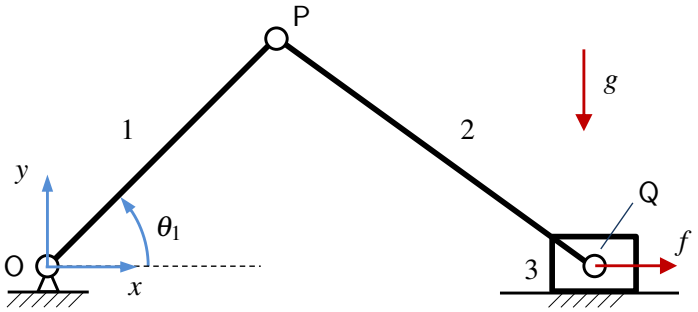


**Figure 1**. Slider-crank mechanism used as benchmark problem.

Three simulation cases are considered as shown in Table 1, which details the values of the physical parameters of the system, its initial state, and the externally applied actions.

**Table 1**. Simulation cases

| **Case** | $L_1$ (m) | $L_2$ (m) | $m_1$ (kg) | $m_2$ (kg) | $m_3$ (kg) | $I_{G,1}$ (kgm$^2$) | $I_{G,2}$ (kgm$^2$) | $\theta_{1,0}$ (rad) | $\dot{x}_{Q,0}$ (m/s) | $f$ (N) |
|---|---|---|---|---|---|---|---|---|---|---|
| **1** | 1 | 1 | 1 | 1 | 0 | 1/12 | 1/12 | $\pi/4$ | -4 | 0 |
| **2** | 3 | 6 | 1.5 | 3 | 0.25 | 9/8 | 9 | 0 | 0 | $100\sin(\pi t)$ |
| **3** | 1 | 1 | 1 | 1 | 0 | 1/12 | 1/12 | $\pi/4$ | 0 | $100\sin(\pi t)$ |

Case 1 corresponds to the slider-crank benchmark problem in [9]. In this case, rods 1 and 2 have the same length ($L_1 = L_2$) and this causes the linkage to pass through a singular configuration when $\theta_1 = \pm\pi/2$, i.e., when both rods are aligned on the $y$ axis. From here the linkage can continue its motion either as a slider-crank mechanism or as a pendulum with point Q motionless at the location of point O. The slider is massless and the externally applied force $f$ in this case is zero during motion.

In case 2, rods 1 and 2 have different lengths and so the linkage motion is not affected by singular configurations. The externally applied force follows now a sinusoidal expression whose frequency increases with time, $f = 100\sin(\pi t)$. The introduction of this force gives rise to numerical difficulties in the solution of the problem. The system ceases to be conservative and its motion is no longer periodic. Moreover, the extreme positions of the motion, reached when both rods are aligned on the $x$ axis and, thus, with the external force $f$, become challenging from the point of view of numerical simulation. There, depending on the value of the force $f$ and the accuracy of the integration process, the motion can continue following one of two possible branches, namely those that correspond to $\dot{\theta}_1 > 0$ and to $\dot{\theta}_1 < 0$.

Case 3 uses the same physical parameters as case 1, but the externally applied force $f$ now follows the sinusoidal expression from case 2. The resulting problem is subjected to both singular configurations and numerical difficulties at the extreme points of the motion.

### 2.1.1 Variables of interest and metrics

The mechanical system under study has one degree of freedom and a single variable should be enough to keep track of its motion. However, in cases 1 and 3 singular configurations exist and these give rise to the existence of two branches of motion. For this reason, two variables will be monitored and used to evaluate the error in Eq. (2): angle $\theta_1$ between link 1 and the $x$ axis, and the $x$ coordinate of point Q on the slider.

The sampling interval for error evaluation was set to 10 ms; a total simulation length of 10 s was used in cases 1 and 2, whereas this duration was reduced to 5 s for case 3. The total errors associated with variables $\theta_1$ and $x_Q$ were aggregated into a single error indicator using Eq. (2) using weights $w_\theta = 1\ \text{rad}^{-2}$ and $w_{x_Q} = 1\ \text{m}^{-2}$, intended to make the final metric dimensionless. Case 1 is a conservative system, and so the total mechanical energy was used there as additional metric.

When using variable step-size integrators, the variables of interest are usually not evaluated exactly at the sampling points. This also happens when constant integration steps are used, but they are not exact dividers of the sampling interval. In these cases, data need to be interpolated; a linear polynomial interpolation has been used here to determine the necessary values.

Two levels of accuracy have been established for the defined cases. In case 1, a high-precision simulation corresponds to a maximum admissible total error $\varepsilon_T = 2 \cdot 10^{-4}$. This is roughly equivalent to the energy criterion set in the IFToMM benchmark, which accepted simulations with maximum energy errors below 0.001 J. The admissibility threshold for low-precision simulation in this case was increased up to $\varepsilon_T = 2 \cdot 10^{-3}$. However, different precision requirements can be specified for the three cases; the selected thresholds are shown in Table 2.

**Table 2**. Maximum admissible errors for each simulation case

| **Case** | High-precision $\varepsilon_T$ | Low-precision $\varepsilon_T$ |
|---|---|---|
| **1** | $2 \cdot 10^{-4}$ | $2 \cdot 10^{-3}$ |
| **2** | $5 \cdot 10^{-3}$ | $5 \cdot 10^{-2}$ |
| **3** | $1 \cdot 10^{-2}$ | $1 \cdot 10^{-1}$ |

The selection of the threshold depends on factors like the time scale of the dynamics and the difficulty of the problem.

## 2.2 Solution methods

Several solution methods were used to carry out the forward-dynamics simulation of the benchmark example. Their main characteristics are summarized on Table 3. Unless otherwise specified, MATLAB implementations were used to perform the simulation.

The first method (AL) uses the index-1 augmented Lagrangian algorithm with position and velocity projections presented in [18], integrated with the trapezoidal rule (TR) in fixed-point iteration form. Method ALi3p stands for the index-3 augmented Lagrangian algorithm with projections of velocities and accelerations [19, 20]. Algorithm ALi3pvs is the variable-step version of ALi3p introduced in [15]. These three methods described the benchmark problem using a set of 18 natural coordinates [1] subjected to 18 redundant kinematic constraints. Besides, methods mAL and mNS were also assessed, in which MATLAB ode45 integration formula is used. The first one uses a stabilized augmented Lagrangian algorithm, while the second adopts a null-space formulation similar to the one in [21]. These methods described the system with Cartesian variables, namely the $x$ and $y$ coordinates of the centre of mass of each body, and impose on them 11 independent constraint equations. In cases 1 and 3, the Jacobian matrix of these constraints loses rank and, as

https://doi.org/10.3311/ECCOMASMBD2021-172

**Table 3**. Summary of the methods employed to solve the slider-crank benchmark problem

| Method | Coordinates | Constraints | Integrator | Step-size |
|---|---|---|---|---|
| **AL** | 18 natural, 3D | 18 redundant | TR | fixed |
| **ALi3p** | 18 natural, 3D | 18 redundant | TR | fixed |
| **ALi3pvs** | 18 natural, 3D | 18 redundant | TR | variable |
| **mAL** | 12 Cartesian, 2D | 11 independent | ode45 | variable |
| **mNS** | 12 Cartesian, 2D | 11 independent | ode45 | variable |
| **mAL-ode4** | 12 Cartesian, 2D | 11 independent | ode4 | fixed |
| **mNS-ode4** | 12 Cartesian, 2D | 11 independent | ode4 | fixed |

expected, the mNS method was unable to successfully complete the simulation. For the purpose of comparing fixed- and variable-step integrators, methods mAL and mNS were also combined with a fourth order, fixed-step Runge-Kutta integration formula, denoted in the text as ode4.

### 2.3 Reference solution

Reference solutions for each case were obtained by convergence of the different methods summarized in Section 2.2. An additional simulation with a Simscape model of the mechanism was also included in this process, intended to confirm the results obtained by the authors by means of third-party software. Figures 2 and 3 show the slider displacement $x_Q$ that correspond to the reference solutions of cases 1 and 2. Upon convergence, the differences in the monitored variables across the solutions delivered by the methods remained below $2.5 \cdot 10^{-4}$ m for $x_Q$ and $2 \cdot 10^{-4}$ rad for $\theta_1$ at every sampling point. For case 1, the error in mechanical energy of the reference solution was lower than $2 \cdot 10^{-6}$ J.

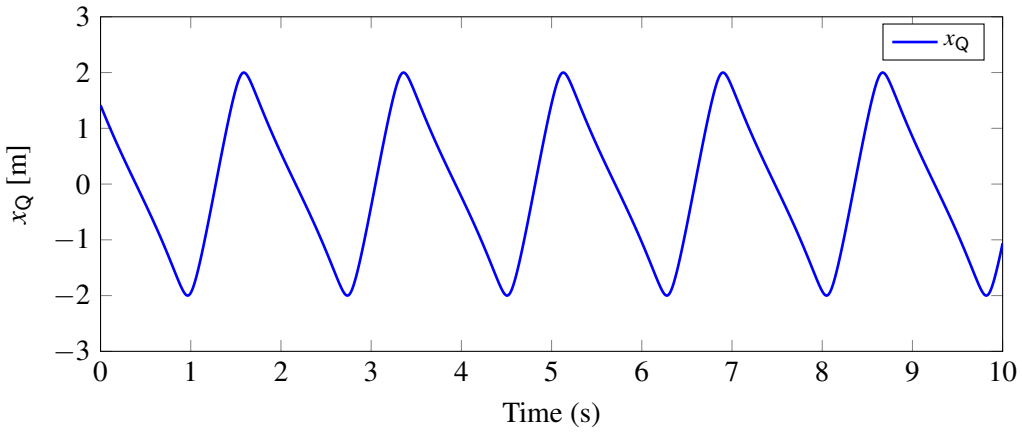


**Figure 2**. Reference solution: displacement $x_Q$ of the slider in case 1.

Obtaining a reference solution in case 3 became more complicated. Figure 4 displays the slider displacement delivered by different solution methods in this case; these results show that it was not possible to achieve convergence during the last seconds of the motion, even with very stringent simulation conditions. The system dynamics becomes chaotic due to the combination of singular configurations and the applied force $f$. Under these circumstances, using a 10 s-simulation as benchmark would not convey interesting information regarding the capability of the methods to deliver accurate solutions. For these reasons, the total duration of this numerical experiment was

https://doi.org/10.3311/ECCOMASMBD2021-172

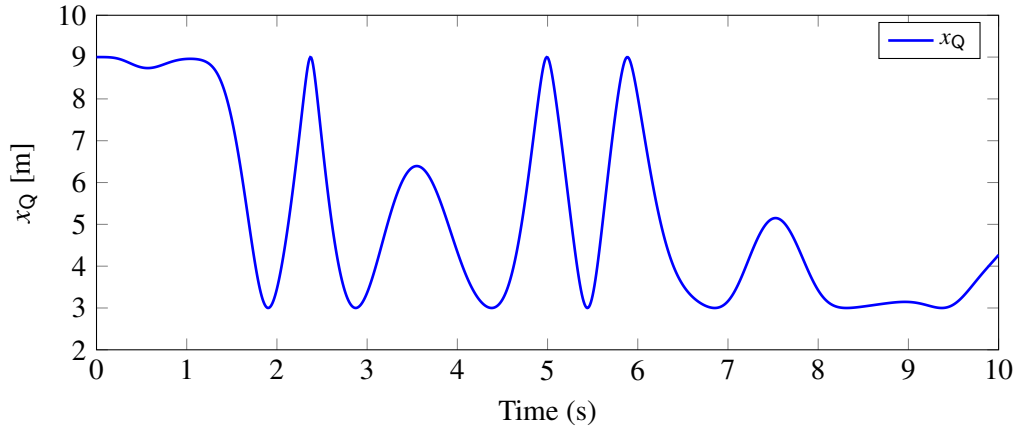


**Figure 3**. Reference solution: displacement $x_Q$ of the slider in case 2.

shortened to 5 s. Even with this reduced duration, it was not possible to decrease the maximum differences between solutions at convergence below $7 \cdot 10^{-3}$ m for $x_Q$ and $10^{-2}$ rad for $\theta_1$.

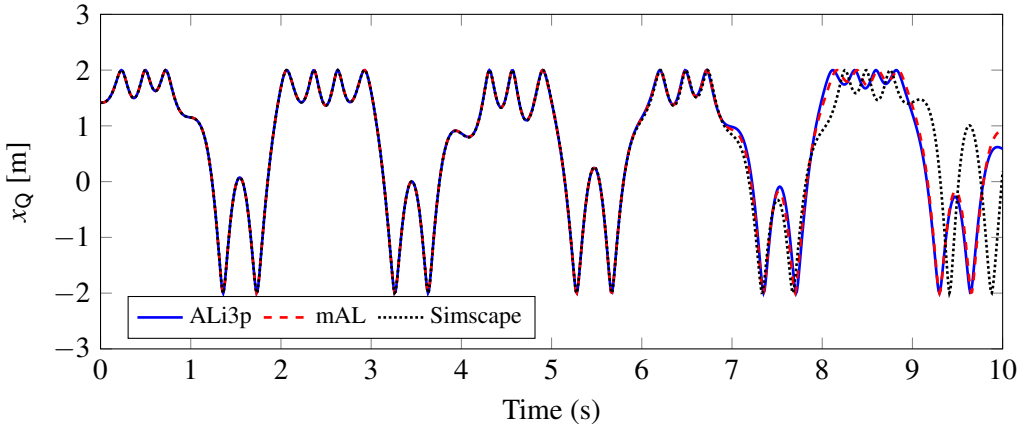


**Figure 4**. Displacement $x_Q$ of the slider in case 3 obtained with different solution methods.

## 3 RESULTS

The benchmark scenarios defined in Section 2 were used to evaluate and compare the performance of the simulation solutions in Table 3. The computations were performed on an Intel Core i7-7700HQ at 2.80 GHz with 16 GB of RAM, running Windows 64-bit and Matlab R2020b.

In the case of the constant-step AL and ALi3p formulations, the integration step-size $h$ was found to be the parameter that had the greatest impact on the efficiency and accuracy of the simulation. Both were able to deal with singular configurations in cases 1 and 3. For the low precision case, both methods delivered comparable results in terms of efficiency. For high precision, the ALi3p method was clearly superior; in case 2 the AL solver was unable to meet the required error threshold. It must be noted that the formulation parameters were the same in all simulation cases, with the notable exception that case 3 required the use of a higher penalty factor in the ALi3p solution ($\alpha = 10^{15}$ instead of $\alpha = 10^{12}$ used in the other two cases). The results delivered by ALi3p were used next for comparison with those delivered by its variable-step counterpart. A summary of the results of the most efficient simulations for high and low precision levels is shown in Table 4. The elapsed time corresponds to the average of three runs of each scenario.

For the variable-step ALi3pVS method, attaining the levels of accuracy specified in Table 2 de-

https://doi.org/10.3311/ECCOMASMBD2021-172

**Table 4**. Best results obtained with the ALi3p solver

| | High precision | | | Low precision | | |
|---|---|---|---|---|---|---|
| | $\varepsilon_T$ | Elapsed (s) | $h$ (ms) | $\varepsilon_T$ | Elapsed (s) | $h$ (ms) |
| **Case 1** | $1.6 \cdot 10^{-4}$ | 11.07 | 1.5 | $1.9 \cdot 10^{-3}$ | 4.82 | 3.5 |
| **Case 2** | $3.6 \cdot 10^{-3}$ | 17.83 | 0.75 | $4.8 \cdot 10^{-2}$ | 5.31 | 3 |
| **Case 3** | $5.4 \cdot 10^{-3}$ | 24.83 | 0.25 | $8.7 \cdot 10^{-2}$ | 3.95 | 2.25 |

pended on a number of factors. The user must specify the upper and lower limits within which the integration step $h$ has to remain, $h_{\max}$ and $h_{\min}$. Besides these, the criteria used to stop the Newton-Raphson iteration, namely the number of iterations $\gamma$ and the norm of the maximum admissible increment of the variables upon convergence, $\varphi_{\max}$, were found to be the most relevant. Tuning these parameters was not a straightforward process, because the impact of a given selection on the simulation performance is highly nonlinear. Moreover, because the algorithm adjusts the step-size based on its previously used value, the initially used step-size $h_0$ must also be considered a parameter of the simulation. In the reported simulations, these parameters were varied in the following ranges: $h_{\max} \in [0.5, 10]$ ms, $h_{\min} \in [0.05, 1]$ ms, $\gamma \in [1, 10]$, $\varphi_{\max} \in [10^{-5}, 10^{-15}]$. Table 5 shows the parameter combinations that delivered the most efficient simulation for the high-precision requirement in every case. In case 3 it was not possible to achieve an improvement over the constant-step ALi3p method.

**Table 5**. Best results obtained with the ALi3pvs solver, high precision

| | $\varepsilon_T$ | Elapsed (s) | $h_{\max}$ (ms) | $h_{\min}$ (ms) | $h_0$ (ms) | $\gamma$ | $\varphi_{\max}$ |
|---|---|---|---|---|---|---|---|
| **Case 1** | $9.1 \cdot 10^{-5}$ | 9.2 | 10 | 0.05 | 0.5 | 10 | $10^{-7}$ |
| **Case 2** | $2.8 \cdot 10^{-3}$ | 17.7 | 5 | 0.05 | 1 | 2 | $10^{-11}$ |
| **Case 3** | Same as ALi3p | | - | - | - | - | - |

Table 6 shows the results delivered by the step-size adjustment method for the low-precision case.

**Table 6**. Best results obtained with the ALi3pvs solver, low precision

| | $\varepsilon_T$ | Elapsed (s) | $h_{\max}$ (ms) | $h_{\min}$ (ms) | $h_0$ (ms) | $\gamma$ | $\varphi_{\max}$ |
|---|---|---|---|---|---|---|---|
| **Case 1** | $1.7 \cdot 10^{-3}$ | 3.3 | 3.5 | 0.05 | 2 | 2 | $10^{-6}$ |
| **Case 2** | $1.1 \cdot 10^{-2}$ | 3.7 | 10 | 0.05 | 1 | 2 | $10^{-7}$ |
| **Case 3** | $9.9 \cdot 10^{-2}$ | 3.68 | 2 | 0.05 | 1 | 2 | $5 \cdot 10^{-8}$ |

It is difficult to provide general recommendations on the selection of the ALi3pvs parameters. For low-precision simulations, it seems advisable to decrease the limit of admissible iterations per step $\gamma$ and regulate the error of the simulation by tuning the convergence criterion $\varphi_{\max}$.

The mAL and mNS solvers completed the simulation of the example in shorter times than the AL, ALi3p, and ALi3pvs methods. This is explained by the different modelling used, which led to a smaller problem size, and also by the fact that the code was specifically implemented to deal with this example, while the former methods employed a library that took care of the automatic generation of the equations of motion. The purpose of this Section, however, is not comparing

the different methods, but verifying the effect of using variable-step integration to perform the simulation.

As mentioned, the mNS solver was unable to deal with the singular configurations in cases 1 and 3. In case 2, nonetheless, it delivered the most efficient solution. The results obtained in this case with mNS were compared to a fixed-step counterpart of the method that used a fourth order Runge-Kutta formula with a constant step-size (ode4). This comparison is shown in Fig. 5; data from mAL are included as well. These results show that variable-step solvers were able to increase the precision of the computations while keeping the required computational load lower than their fixed-step counterparts.

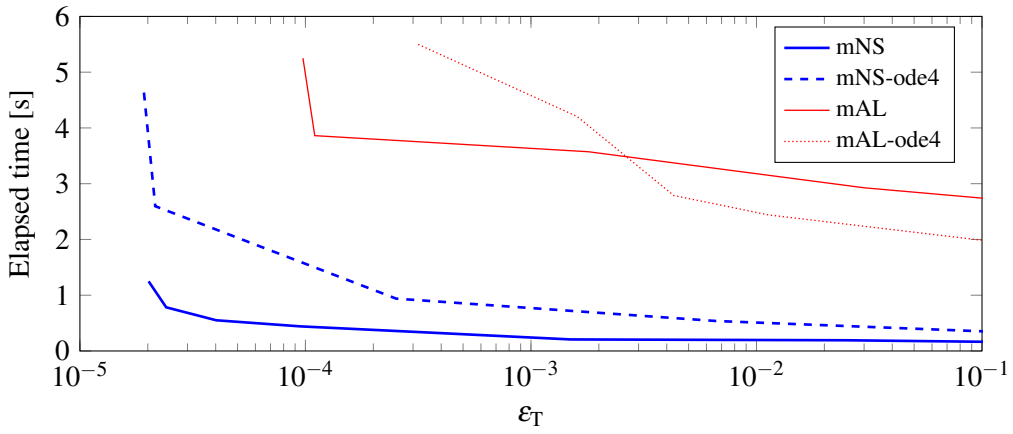


**Figure 5**. Elapsed time in the solution of case 2 as a function of the precision $\varepsilon_T$ delivered by each method.

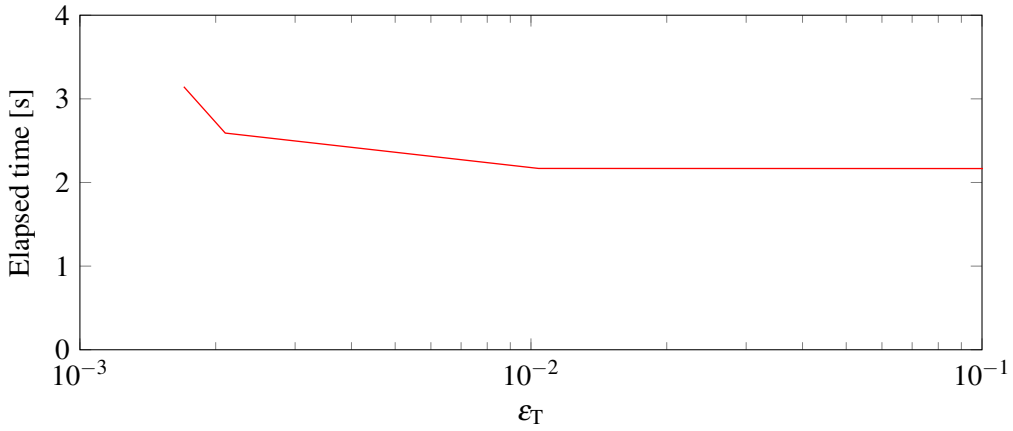


**Figure 6**. Elapsed time in the solution of case 3 as a function of the precision $\varepsilon_T$ delivered by method mAL.

The results in case 1 for methods mAL and mAL-ode4 followed similar trends to those shown in Fig. 5: when higher precision was required, variable-step integration showed a comparative advantage with respect to the fixed-step method. In case 3 the mAL-ode4 integration only managed to converge to the reference solution with step-sizes below 1.5 ms; moreover, decreasing the integration step-size did not improve the accuracy of the results. In this case, the variable-step method delivered better results for all precision levels; these are summarized in Fig. 6.

https://doi.org/10.3311/ECCOMASMBD2021-172

## 4 CONCLUSIONS

In this work, a benchmark example for the evaluation of variable-step multibody dynamics formulations has been introduced. The selected example consists in three variations of a planar slider-crank linkage, with different physical parameters and applied external forces with variable frequency. The combination of these forces with the existence of singular configurations in the mechanism resulted in a challenging problem for variable-step integration methods. A common approach used by these methods is the reduction of the step-size when it is necessary to deal with fast dynamics; this poses a problem if the mechanism is moving near a singular configuration, because the step-size reduction often leads to numerical problems in these positions.

The slider-crank linkage example also served to highlight relevant aspects of the definition of benchmark problems, such as the availability of a reference solution and the necessity of suitable metrics to compare the performance of different solution methods.

The three proposed cases of this benchmark problem were used to assess the ability of variable-step integration methods for multibody system dynamics to improve the efficiency delivered by their fixed-step counterparts. Results showed that the performance of each approach depends on the precision requirements and the characteristics of the problem being solved and confirmed the usefulness of the proposed example for benchmarking applications.

## ACKNOWLEDGMENTS

F. González acknowledges the support of the Ministry of Economy of Spain through the Ramón y Cajal programme, contract RYC-2016-20222.

## REFERENCES

[1] García de Jalón, J., Bayo, E.: Kinematic and Dynamic Simulation of Multibody Systems: The Real-Time Challenge. Springer-Verlag, New York (NY), USA (1994) ISBN:3-540-94096-0.

[2] Bauchau, O.A.: Flexible Multibody Dynamics. Springer, Dordrecht, The Netherlands (2011) ISBN:978-94-007-0334-6.

[3] Featherstone, R.: Robot dynamics algorithms. Springer, New York (NY), USA (1987) ISBN:978-1-4757-6437-6.

[4] García de Jalón, J., Gutiérrez-López, M.D.: Multibody dynamics with redundant constraints and singular mass matrix: existence, uniqueness, and determination of solutions for accelerations and constraint forces. Multibody System Dynamics **30**(3) (2013) 311–341

[5] González, F., Dopico, D., Pastorino, R., Cuadrado, J.: Behaviour of augmented Lagrangian and Hamiltonian methods for multibody dynamics in the proximity of singular configurations. Nonlinear Dynamics **85**(3) (2016) 1491–1508

[6] González, M., González, F., Dopico, D., Luaces, A.: On the effect of linear algebra implementations in real-time multibody system dynamics. Computational Mechanics **41**(4) (2008) 607–615

[7] Torres-Moreno, J.L., Blanco-Claraco, J.L., López-Martínez, J., Giménez-Fernández, A.: A comparison of algorithms for sparse matrix factoring and variable reordering aimed at real-time multibody dynamic simulation. In: Proceedings of the ECCOMAS Thematic Conference on Multibody Dynamics, Zagreb, Croatia (2013)

[8] González, M., González, F., Luaces, A., Cuadrado, J.: A collaborative benchmarking framework for multibody system dynamics. Engineering with Computers **26**(1) (2010) 1–9

[9] IFToMM Technical Committee for Multibody Dynamics: Library of computational benchmark problems (2021) URL:https://www.iftomm-multibody.org/benchmark/.

[10] Bauchau, O.A., Betsch, P., Cardona, A., Gerstmayr, J., Jonker, B., Masarati, P., Sonneville, V.: Validation of flexible multibody dynamics beam formulations using benchmark problems. Multibody System Dynamics **37**(1) (2016) 29–48

[11] Masoudi, R., Flores, P., McPhee, J.: Benchmark problems for contact dynamics in multibody systems. In: The 3rd International Conference on Multibody System Dynamics (IMSD), Busan, South Korea (2014)

[12] Sanjurjo, E., Naya, M.Á., Blanco-Claraco, J.L., Torres-Moreno, J.L., Giménez-Fernández, A.: Accuracy and efficiency comparison of various nonlinear Kalman filters applied to multibody models. Nonlinear Dynamics **88**(3) (2017) 1935–1951

[13] Bezin, Y., Pålsson, B.A.: Multibody simulation benchmark for dynamic vehicle-track interaction in switches and crossings: modelling description and simulation tasks. Vehicle System Dynamics (2021) 1–16

[14] Zar, A., González, F., Rodríguez, B., Luaces, A., Naya, M.A., Cuadrado, J.: Benchmark problems for co-simulation methods. In: COSIM 2021: International Symposium on Co-Simulation and Solver Coupling in Dynamics, Ferrol, Spain (2021)

[15] Dopico, D., Sanjurjo, E., Cuadrado, J., Luaces., A.: A variable time-step and variable penalty method for the index-3 augmented Lagrangian formulation with velocity and acceleration projections. In: Proceedings of the ECCOMAS Thematic Conference on Multibody Dynamics, Prague, Czech Republic (2017)

[16] González, M., Dopico, D., Lugrís, U., Cuadrado, J.: A benchmarking system for MBS simulation software: Problem standardization and performance measurement. Multibody System Dynamics **16**(2) (2006) 179–190

[17] Marques, F., Souto, A.P., Flores, P.: On the constraints violation in forward dynamics of multibody systems. Multibody System Dynamics **39**(4) (2016) 385–419

[18] Bayo, E., Ledesma, R.: Augmented Lagrangian and mass-orthogonal projection methods for constrained multibody dynamics. Nonlinear Dynamics **9**(1-2) (1996) 113–130

[19] Cuadrado, J., Cardenal, J., Morer, P., Bayo, E.: Intelligent simulation of multibody dynamics: space-state and descriptor methods in sequential and parallel computing environments. Multibody System Dynamics **4**(1) (2000) 55–73

[20] Dopico, D., González, F., Cuadrado, J., Kövecses, J.: Determination of holonomic and nonholonomic constraint reactions in an index-3 augmented Lagrangian formulation with velocity and acceleration projections. Journal of Computational and Nonlinear Dynamics **9**(4) (2014)

[21] Shabana, A.A.: Computational Dynamics. Second edn. Wiley, Hoboken, NJ, USA (2001) ISBN:978-0-471-05326-2.

https://doi.org/10.3311/ECCOMASMBD2021-112

ECCOMAS Thematic Conference on Multibody Dynamics
December 12 - 15, 2021, Budapest, Hungary

# Influence of Generalized Coordinates on System Dynamics

**Altay Zhakatayev**[1,2], **Yuriy Rogovchenko**[1], **Matthias Pätzold**[2]

[1] Dept. of Mathematics
University of Agder
4604 Kristiansand, Norway
altay.zhakatayev@uia.no, yuriy.rogovchenko@uia.no

[2] Department of ICT
University of Agder
4879 Grimstad, Norway
matthias.paetzold@uia.no

## ABSTRACT

We investigate the effect of the choice of a set of generalized coordinates (GCs) on the simulation of the behavior of the dynamical system using the single-link spherical pendulum as an example. Specifically, we focus our attention on numerical errors and the simulation time necessary to simulate system dynamics. The Lagrangian method is applied to obtain the equations of motion. The generalized Euler angles are used as GCs. The GCs depend on the direction of the axes along which they are defined. Therefore, by parameterizing the directions of these two axes, different sets of GCs with the corresponding system of nonlinear differential equations are obtained. For a spherical pendulum, we demonstrate that the optimal sets of GCs leading to the minimum simulation time are orthogonal sets. However, contrary to our expectations, orthogonal sets do not result in the minimum simulation error. Additionally, the intrinsic generalized Euler angles lead to faster simulations than the extrinsic ones. Therefore, different choices of GCs are not equivalent from a numerical point of view and further research is needed to develop a strategy for selecting an optimal set of GCs.

**Keywords:** Generalized Coordinates, Davenport Angles, Lagrangian Dynamics, Optimal Generalized Coordinates, Multibody Systems Dynamics.

## 1 INTRODUCTION

Dynamic equations describing the evolution of systems can be derived using the Newton-Euler, Lagrangian, Hamiltonian method, or other formalisms [1]. The Newton-Euler formalism employs Cartesian coordinates for the position vector. In contrast, Lagrangian and Hamiltonian mechanics utilize *generalized coordinates* (GCs), which can be any set of variables suitable to fully describe the configuration of a system, e.g., Cartesian coordinates, relative and absolute angles, linear and angular momentum, and energy [2]. The number of variables is often chosen to be equal to the number of degrees of freedom (DOF) of the system, but it may also contain more variables than necessary. From a theoretical point of view, all possible sets of GCs are equally valid for describing system dynamics [3]. However, from a numerical or computational point of view, there can be differences. For simple systems with a few DOF, it is expected that there will be no discernible computational differences with regard to the choice of a set of GCs and efficiency is not an issue. However, for complex multi-body systems with a large number of DOF, the efficiency and computational time required to perform the analysis can vary greatly depending on the selected set of GCs.

A methodology of switching between different sets of GCs for multi-DOF planar mechanical systems was considered in [4]. The authors were primarily concerned with the development of a mathematical description for deriving control equations in a direct and transparent manner. Using Cartesian coordinates and the full row rank property of the constraint Jacobian matrix formed by independent constraints, Wehage and Haug [5] proposed a numerical criterion to obtain the minimum set of GCs. The method was extended for nonholonomic systems in [6]. Later work in this direction can be found in [7, 8]. Efficient formulation of dynamic equations was the topic

https://doi.org/10.3311/ECCOMASMBD2021-112

in [9–12]. Still, these works did not compare the effect of different sets of GCs on the solution of dynamic equations. In addition, there is a gap in the literature regarding the choice of optimal sets of GCs that lead to the numerical solution of differential equations with minimal error within the shortest simulation time. To the best of the authors' knowledge, there are no qualitative rules for selecting the optimal set of GCs [13]. As a result, there is a need in modern engineering for deeper investigations of the choice of GCs for describing the system dynamics.

In this work, our main motivation is to contribute to the investigation of the influence of a choice of GCs on the numerical solution of dynamic equations. The main objective of this paper is to understand the dependence of simulation error and time on the selected set of GCs. Another objective is to find the optimal set of GCs for a single-link spherical pendulum, which is considered as a test system. It is widely accepted that the problem-solving-experience is necessary to select the optimal set of GCs [13] and the search for a procedure which helps to identify the optimal set of GCs for a given system still continues.

The main novelty of this paper is the analysis of the dependence of the overall simulation error and computation time on the selected set of GCs based on the parameterized Davenport angles [14]. The main contributions of our work are to show that there are optimal sets of GCs for the spherical pendulum, and that choice of a GCs set has an impact on the simulations. Our principal results are the following. First, the choice of GCs strongly affects the simulation time and accuracy. Second, the optimal sets of GCs that minimize the simulation time do not coincide with those that minimize the gross simulation error. Third, the intrinsic Davenport angles appear to be more optimal for the spherical pendulum than extrinsic ones.

The paper is organized as follows. Sect. 2 gives a brief description of dynamic equations of motion. The kinematics of the spherical pendulum used as a test bed system is discussed in Sect. 3, where four types of sets of GCs are considered. Sect. 4 describes the simulations settings, and the simulations results are presented in Sect. 5. Finally, Sect. 6 presents the conclusions.

## 2 DYNAMIC EQUATIONS OF MOTION

In this paper, we develop dynamic equations of motion using the Lagrangian formalism. Let us define a set of GCs as $\mathbf{q} \in \mathbb{R}^n$, where $n$ is the number of DOF of a mechanical system under consideration, and $\mathbf{q} = [q_1,\ q_2, \ldots, q_n]^T$ is a column vector. Here, the transpose operator is denoted as $[\cdot]^T$. The corresponding set of *generalized velocities* (GVs) $\dot{\mathbf{q}} \in \mathbb{R}^n$ is defined as the time derivative of the GCs, i.e., $\dot{\mathbf{q}} = [\dot{q}_1,\ \dot{q}_2, \ldots, \dot{q}_n]^T$, where the overdot denotes the time differentiation operator. Equations of motion of a mechanical system can often be written in the form

$$M(\mathbf{q})\ddot{\mathbf{q}} + \mathbf{C}(\mathbf{q}, \dot{\mathbf{q}}) + \mathbf{G}(\mathbf{q}) = \mathbf{Q} \tag{1}$$

where $M(\mathbf{q}) \in \mathbb{R}^{n \times n}$ is the symmetric inertia matrix, $\mathbf{C}(\mathbf{q}, \dot{\mathbf{q}}) \in \mathbb{R}^n$ is the vector of Coriolis and normal inertial forces, and the vector $\mathbf{G}(\mathbf{q}) \in \mathbb{R}^n$ describes the effect of gravity. The vector of generalized forces is $\mathbf{Q} = [Q_1,\ Q_2, \ldots, Q_n]^T$. The dynamic equation (1) comprises a set of $n$ second-order differential equations.

To solve these equations with numeric solvers or to tackle a control problem of a mechanical system, it is desirable to have a system of $2n$ first-order differential equations instead. As a result, Eq. (1) is further modified to the so-called state-space form

$$\dot{\mathbf{x}} = \mathbf{f}(\mathbf{x}, \mathbf{Q}) \tag{2}$$

where $\mathbf{x} = [\mathbf{q}^T,\ \dot{\mathbf{q}}^T]^T \in \mathbb{R}^{2n}$ is the state vector, and $\mathbf{Q}$ serves as the control input vector. The nonlinear state function $\mathbf{f}$ can be written as

$$\mathbf{f}(\mathbf{x}, \mathbf{Q}) = \begin{bmatrix} \dot{\mathbf{q}} \\ -M^{-1}\left(\mathbf{C}(\mathbf{q}, \dot{\mathbf{q}}) + \mathbf{G}(\mathbf{q}) - \mathbf{Q}\right) \end{bmatrix}. \tag{3}$$

https://doi.org/10.3311/ECCOMASMBD2021-112

Our task now is to select a mechanical system and different sets of GCs that describe its kinematics. Then, for the selected sets of GCs, we formulate and solve the dynamic equations in Eq. (2), where **f** is defined by (3).

## 3 KINEMATICS OF A SPHERICAL PENDULUM

As our test system, we consider a single-link spherical pendulum which is symmetric with respect to the rotation about its axis, as shown in Fig. 1a. We intentionally chose the spherical pendulum because its motion is three-dimensional, while the motion of a simple pendulum is only two-dimensional. Although in reality the spherical pendulum still has a limited range of angular motion, we can assume that there are no restrictions on the range of its motion. Three angles are required to correctly orient a three-dimensional object in the three-dimensional space. However, due to rotational symmetry around its own symmetry axis, only two angles are used to fully specify the configuration (orientation) of the pendulum in our model. This pair of angles will be denoted as $q_1$ and $q_2$. The Euler angles were generalized to rotations with respect to non-orthogonal axes in [14], also called Davenport angles [15, 16]. In this work, Davenport angles are used as GCs. The mass, inertia matrix about the center of mass, length, and the length up to the center of mass of the pendulum will be designated by $m$, $I$, $L$, and $L_c$, respectively.

In the following, the Denavit-Hartenberg (DH) convention will be utilized to derive the kinematics of the pendulum [17, 18]. The fixed global axes $X$, $Y$, $Z$ (Fig. 1) are used later to visualize the simulation results. The local axes $x_i$, $y_i$, $z_i$, $i = 0, 1, 2$, define a frame $i$. These frames are used to derive the kinematics with the DH convention. To simplify the visualization, the local $y_i$ axes are not shown in Fig. 1. The local axes $x_0$, $y_0$, $z_0$ are also fixed. Even if they might seem redundant due to the presence of $X$, $Y$, $Z$, their introduction facilitates the derivation. The counterclockwise rotation angles of $q_1$ and $q_2$ are determined by the right-hand rule. The origin of the local coordinate system 2 can be located either at the end of the link or at its center of mass. In the derivations, the latter is chosen, but in Fig. 1, the former is used for the presentation clarity. In what follows, we will consider four cases with different sets of GCs.

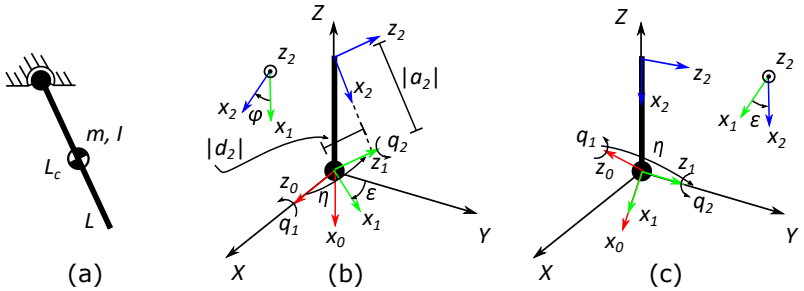


Figure 1: Schematic diagrams of the spherical pendulum (a), its kinematics with coordinate frames, angular parameters, and GCs for Cases I, III (b) and Cases II, IV (c).

### 3.1 Case I

In the first case, we assume that the axis of the first GC $q_1$ is aligned along the global axis $X$, while the axis of the second GC has an arbitrary initial direction with respect to the global axes (see Fig. 1b). The rotations are assumed to be intrinsic. Due to the rotation around the local axis, the direction of $q_2$ is affected by $q_1$. There are three angular parameters for this system: $\eta$ – the angle between $z_0$ and $z_1$ with respect to the axis $x_1$, $\varepsilon$ – the angle between $x_1$ and $Y$ with respect to the axis $X$, and $\varphi$ – the angle between $x_1$ and $x_2$ with respect to the axis $z_2$. We note that the unit vector $x_1$ is in the $YZ$ plane. Additionally, there are two spatial parameters $d_2$ and $a_2$, which are used in

https://doi.org/10.3311/ECCOMASMBD2021-112

the DH derivations. The geometry results in the following identities for the system parameters

$$d_2 = L_c s(\eta) c(\varepsilon), \tag{4a}$$

$$a_2 = -L_c \sqrt{1 - (s(\eta)c(\varepsilon))^2}, \tag{4b}$$

$$\varphi = \text{atan2}\left( -\frac{c(\eta)c(\varepsilon)}{\sqrt{1-(s(\eta)c(\varepsilon))^2}}; \frac{s(\varepsilon)}{\sqrt{1-(s(\eta)c(\varepsilon))^2}} \right), \tag{4c}$$

where $s(\eta)$ and $c(\eta)$ are short notations for $\sin\eta$ and $\cos\eta$ functions, and similarly for the $\varepsilon$. Given $x$ and $y$, the output of the function $\text{atan2}(y;x)$ is the angle in the range $(-\pi, \pi]$. It can be observed from Eq. (4) that $\varphi$, $d_2$ and $a_2$ depend only on the other two parameters: $\eta$ and $\varepsilon$. The link and joint parameters for a spherical pendulum are summarized in Tab. 1, where $\theta_i$, $d_i$, $a_i$, and $\alpha_i$ denote the corresponding DH parameters.

### 3.2 Case II

In the second case, it is assumed that the axis of the first GC $q_1$ is tilted with respect to the global frame, while the second GC $q_2$ has its initial direction aligned with respect to the global axis $Y$, as shown in Fig. 1c. Again, intrinsic rotations are assumed, so that the direction of the axis $q_2$ is influenced by the rotation $q_1$. There are two parameters in this system: $\eta$ – the angle between $z_0$ and $z_1$ with respect to the axis $x_1$, and $\varepsilon$ – the angle between $x_1$ and $x_2$ with respect to the axis $z_2$. We note that $x_1$ is in the $XZ$ plane. Similarly to Case I, the link and joint parameters for the spherical pendulum are listed in Tab. 1.

The homogeneous transformation matrices [19] for the Cases I and II are obtained by substituting the DH parameters into the homogeneous transformation matrix ${}^{i-1}A_i \in \mathbb{R}^{4\times4}$ from the local frame $i$ to the frame $i$-1 defined by

$${}^{i-1}A_i = \begin{bmatrix} c(\theta_i) & -c(\alpha_i)s(\theta_i) & s(\alpha_i)s(\theta_i) & a_i c(\theta_i) \\ s(\theta_i) & c(\alpha_i)c(\theta_i) & -s(\alpha_i)c(\theta_i) & a_i s(\theta_i) \\ 0 & s(\alpha_i) & c(\alpha_i) & d_i \\ 0 & 0 & 0 & 1 \end{bmatrix} \tag{5}$$

and including both translation and rotation. The position of the center of mass in the local body-fixed frame 2 is ${}^2\mathbf{r}_2 = [0,\ 0,\ 0,\ 1]^T$, because the origin coincides with the center of mass. With respect to the global frame 0, the center of mass of the link is $\mathbf{r}_2 = T_2\, {}^2\mathbf{r}_2$, where $T_2 = {}^0A_1\, {}^1A_2$ is the combined homogeneous transformation matrix from the frame 2 to frame 0. The potential energy of the link is $V = -m\mathbf{g}^T\mathbf{r}_2$, where $\mathbf{g} = [g_x,\ g_y,\ g_z,\ 0]^T$ and $g_x$, $g_y$, $g_z$ are the components of the gravitational constant 9.81 m/s$^2$ in the frame 0. For instance, in Case I, $\mathbf{g} = 9.81[1,\ 0,\ 0,\ 0]^T$, while in Case II, $\mathbf{g} = 9.81[c(\varepsilon),\ c(\eta)s(\varepsilon),\ \text{-}s(\eta)s(\varepsilon),\ 0]^T$.

The linear velocity of the center of mass in the global frame 0 can be obtained as $\mathbf{v}_2 = \dot{\mathbf{r}}_2 = \dot{T}_2\, {}^2\mathbf{r}_2$. The translational kinetic energy is $K_t = 1/2 m\mathbf{v}_2^2$. The angular velocity of the link around its center of mass in the body-fixed frame 2 is ${}^2\boldsymbol{\omega}_2 = T_2^T\mathbf{q}_1 + {}^1A_2^T\mathbf{q}_2$, where $\mathbf{q}_i = [0,\ 0,\ \dot{q}_i,\ 0]^T$ for $i = 1, 2$. Then, the rotational kinetic energy is $K_r = {}^2\omega_2^T\, {}^2J_2\, {}^2\omega_2/2$, where ${}^2J_2 \in \mathbb{R}^{4\times4}$ is the inertia matrix in the body-fixed frame 2. This matrix can be written as

$${}^2J_2 = \begin{bmatrix} I_{xx} & I_{xy} & I_{xz} & 0 \\ I_{yx} & I_{yy} & I_{yz} & 0 \\ I_{zx} & I_{zy} & I_{zz} & 0 \\ 0 & 0 & 0 & 0 \end{bmatrix} = \begin{bmatrix} {}^2I_2 & \mathbf{0} \\ {}_{3\times3} & {}_{3\times1} \\ \mathbf{0} & 0 \\ {}_{1\times3} & \end{bmatrix}. \tag{6}$$

The total kinetic energy is $K = K_t + K_r$. Both $K$ and $V$ are the functions of GCs $q_1$, $q_2$, and the parameters $\eta$, $\varepsilon$.

https://doi.org/10.3311/ECCOMASMBD2021-112

| Case I | | | | | Case II | | | | |
|---|---|---|---|---|---|---|---|---|---|
| Joint, $i$ | $\theta_i$ | $d_i$ | $a_i$ | $\alpha_i$ | Joint, $i$ | $\theta_i$ | $d_i$ | $a_i$ | $\alpha_i$ |
| 1 | $\frac{\pi}{2}-\varepsilon+q_1$ | 0 | 0 | $-\eta$ | 1 | $q_1$ | 0 | 0 | $-\eta$ |
| 2 | $\phi+q_2$ | $d_2$ | $a_2$ | 0 | 2 | $\varepsilon+q_2$ | 0 | $-L_c$ | 0 |

Table 1: DH parameters and variables for a spherical pendulum.

### 3.3 Case III

Geometrically, this case is similar to Case I, but the rotations $q_1$ and $q_2$ are assumed to be extrinsic. In other words, the axes of the rotation of $q_1$ and $q_2$ are fixed with respect to the global frame X-Y-Z. Therefore, the rotation $q_1$ does not affect the axis of rotation of $q_2$. Since the DH convention is only applicable to intrinsic rotations, in this subsection we use simple rotation matrices $R \in \mathbb{R}^{3\times3}$ to describe the kinematics.

The rotation matrix for $q_1$ will be a simple rotation matrix relative to the $z$-axis. From Fig. 1b, it can be observed that in the global frame 0 the unit vector $z_1 = [-s(\eta)c(\varepsilon),\ s(\eta)s(\varepsilon),\ c(\eta)]^T$. Thus, both $z_1$ and $q_2$ define the principal rotation axis and the angle by which the rotation matrix ${}^1R_2$ can be found

$$ {}^1R_2 = \begin{bmatrix} k_1 s^2(\eta)c^2(\varepsilon)+c(q_2) & -k_1 s^2(\eta)s(\varepsilon)c(\varepsilon)-c(\eta)s(q_2) & -s(\eta)(k_1 c(\eta)c(\varepsilon)-s(\varepsilon)s(q_2)) \\ -k_1 s^2(\eta)s(\varepsilon)c(\varepsilon)+c(\eta)s(q_2) & k_1 s^2(\eta)s^2(\varepsilon)+c(q_2) & s(\eta)(k_1 c(\eta)s(\varepsilon)+c(\varepsilon)s(q_2)) \\ -s(\eta)(k_1 c(\eta)c(\varepsilon)+s(\varepsilon)s(q_2)) & s(\eta)(k_1 c(\eta)s(\varepsilon)-c(\varepsilon)s(q_2)) & k_1 c^2(\eta)+c(q_2) \end{bmatrix}. \tag{7} $$

where $k_1 = 1-c(q_2)$.

### 3.4 Case IV

This case is similar to Case II, but this time with the extrinsic angles $q_1$ and $q_2$. Similarly to Case III, $q_1$ does not influence the rotation axis of $q_2$. The rotation matrix for $q_1$ is obtained from the unit vector $z_0 = [\text{-}s(\eta)s(\varepsilon),\ c(\eta),\ s(\eta)c(\varepsilon)]^T$ (see Fig. 1) which specifies the principal axis. Thus, the rotation matrix is

$$ {}^0R_1 = \begin{bmatrix} k_2 s^2(\eta)s^2(\varepsilon)+c(q_1) & -s(\eta)(k_2 c(\eta)s(\varepsilon)+c(\varepsilon)s(q_1)) & -k_2 s^2(\eta)s(\varepsilon)c(\varepsilon)+c(\eta)s(q_1) \\ -s(\eta)(k_2 c(\eta)s(\varepsilon)-c(\varepsilon)s(q_1)) & k_2 c^2(\eta)+c(q_1) & s(\eta)(k_2 c(\eta)c(\varepsilon)+s(\varepsilon)s(q_1)) \\ -k_2 s^2(\eta)s(\varepsilon)c(\varepsilon)-c(\eta)s(q_1) & s(\eta)(k_2 c(\eta)c(\varepsilon)-s(\varepsilon)s(q_1)) & k_2 s^2(\eta)c^2(\varepsilon)+c(q_1) \end{bmatrix}, \tag{8} $$

where $k_2 = 1-c(q_1)$. The rotation matrix for $q_2$ is a simple rotation matrix about the $y$-axis.

For Cases III and IV the overall rotation matrix is found as $R_2 = {}^1R_2\,{}^0R_1$ (in reverse order), due to the rotation sequence with respect to the global axes (extrinsic rotations). The position of the center of mass in the initial configuration is ${}^2\mathbf{r}_2 = [\text{-}L_c,\ 0,\ 0]^T$. The same radius vector after the rotations becomes $\mathbf{r}_2 = R_2\,{}^2\mathbf{r}_2$ (expressed in the frame 0). By redefining $\mathbf{g} = [9.81,\ 0,\ 0]^T$, the potential energy of the link equals $V = -m\mathbf{g}^T\mathbf{r}_2$. By using the linear velocity of the link center of mass $\mathbf{v}_2 = \dot{\mathbf{r}}_2 = \dot{R}_2\,{}^2\mathbf{r}_2$, the translational kinetic energy is found as $K_t = 1/2 m\mathbf{v}_2^2$. The angular velocities in the global frame are $\omega_2 = [\text{-}s(\eta)c(\varepsilon)\dot{q}_2,\ s(\eta)s(\varepsilon)\dot{q}_2,\ \dot{q}_1+c(\eta)\dot{q}_2]^T$ for the Case III and $\omega_2 = [\text{-}s(\eta)s(\varepsilon)\dot{q}_1,\ c(\eta)\dot{q}_1+\dot{q}_2,\ s(\eta)c(\varepsilon)\dot{q}_1]^T$ for the Case IV. The corresponding rotational kinetic energy in the global frame can be expressed as $K_r = 1/2\omega_2^T I_2\omega_2$. The inertia matrix in the global frame is $I_2 = R_2\,{}^2I_2R_2^T \in \mathbb{R}^{3\times3}$, where ${}^2I_2 \in \mathbb{R}^{3\times3}$ is the inertia matrix in the body-fixed frame (upper-left submatrix of ${}^2J_2$ in Eq. 6). As in Cases I and II, both the total kinetic energy $K = K_t + K_r$ and the potential energy depend on the GCs $q_1$, $q_2$, and the parameters $\eta$, $\varepsilon$.

The Lagrangian is found as $L = K - V$. By using the Lagrangian in the Lagrange-Euler equations of motion, a system of two coupled second-order differential equations is obtained for the link motion in terms of the GCs $q_1$ and $q_2$. These equations contain the parameters $\eta$ and $\varepsilon$ and can be written in the form of Eq. (1) by defining the vector of the GCs as $\mathbf{q} = [q_1,\ q_2]^T$ and the vector of the GVs as $\dot{\mathbf{q}} = [\dot{q}_1,\ \dot{q}_2]^T$.

https://doi.org/10.3311/ECCOMASMBD2021-112

## 4 SIMULATIONS

Simulations were performed to investigate the influence of a set of GCs on the dynamic behavior. For selected values of parameters $\eta$ and $\varepsilon$, the dynamic equations of motion were automatically generated using the Lagrangian formalism and the Symbolic Math Toolbox™ of MATLAB. The obtained nonlinear differential equations were transformed to the form of Eq. (2) suitable for numerical integration. For all four cases, there are singularities at $\eta = 0$ and $\eta = \pi$, where the axes of $q_1$ and $q_2$ coincide. Therefore, by specifying the number of intervals $N \in \mathbb{N}$ and the angular step size $\Delta = \pi/N$, the range of variation for $\eta$ is chosen as $\eta = i\Delta$, $i = 1, 2, \ldots, N-1 \in \mathbb{N}$. Similarly, the range for $\varepsilon$ is $\varepsilon = i\Delta$, $i = -N, -N+1, \ldots, N-1 \in \mathbb{Z}$. The physical parameters were assumed to have the values $m = 1$, $L = 1$, $L_c = 1$, $I = 0_{3\times3}$ corresponding to a simple mass-point spherical pendulum.

The analytical description of a mass-point spherical pendulum oscillation expressed in the spherical coordinate frame was also obtained as

$$\ddot{q}_1 = sq_1 cq_1 \dot{q}_2 - \frac{g}{L_c} sq_1, \quad \ddot{q}_2 = -2\frac{sq_1 cq_1}{sq_1^2}\dot{q}_1\dot{q}_2. \tag{9}$$

Here, $q_1$ and $q_2$ are denoting the polar and azimuthal angles, respectively. The solution of Eq. (9) serves as a baseline case. The root-mean-square (RMS) error $Er$ was computed as $Er = \sqrt{\sum_{i=1}^{N_\tau}[(X_i - X_{i,r})^2 + (Y_i - Y_{i,r})^2 + (Z_i - Z_{i,r})^2]/N_\tau}$ where $X_i$ and $X_{i,r}$ are the $x$ components of the center of mass of the pendulum in the global $XYZ$ frame obtained from a set of GCs and from the baseline model, respectively. The number of time samples is $N_\tau$. Each solution of the dynamic equation corresponding to a specific set of GCs was compared to the baseline case through $Er$. Additionally, the simulation time $\tau$ was recorded for each combination of the parameters $\eta$ and $\varepsilon$.

Two different initial conditions (ICs) were considered. The first IC (denoted by IC1) corresponds to the situation where the initial values of GCs are nonzero, i.e., $q_1 \neq 0$, $q_2 \neq 0$, while the initial values of the GVs are zero, i.e., $\dot{q}_1 = \dot{q}_2 = 0$. The second IC (denoted by IC2), assumes that the initial values of the GCs are zero $q_1 = q_2 = 0$, while the initial values of the GVs are nonzero. The numerical values of the ICs depend on the selected values of the parameters $\eta$ and $\varepsilon$. Therefore, the correct initial values must be computed for each simulation. For a given initial link position $\mathbf{r}_{2i}$ and velocity $\mathbf{v}_{2i}$ in the global reference frame, the corresponding ICs at arbitrary values of $\eta$ and $\varepsilon$ can be found by solving the nonlinear algebraic equations $\mathbf{r}_2(q_1, q_2) - \mathbf{r}_{2i} = \mathbf{0}$ and $\mathbf{v}_2(q_1, q_2) - \mathbf{v}_{2i} = \mathbf{0}$ for $q_1$ and $q_2$. The obtained initial values for the GCs are denoted as $q_{1,i}$ and $q_{2,i}$. This task was accomplished using the nonlinear system solver `fsolve` of MATLAB with the default settings, except that the maximum number of allowed iterations was set to $10^3$.

Using the appropriate ICs, the MATLAB function `ode45` was utilized to solve nonstiff differential equations and to simulate the system behavior for each combination of $\eta$ and $\varepsilon$. The number of steps used to vary the parameters was chosen to be $N = 20$. The duration of the simulation time was set to 20 s, with a sampling interval of 1 ms, i.e., $N_\tau = 20000$. The relative and absolute tolerance levels were set to $10^{-4}$. The simulations were performed on a ThinkPad notebook with an Intel Core i5-10310U CPU processor and 16 GB RAM.

## 5 RESULTS

From the numerical simulation point of view, the most important factors are the actual simulation time $\tau$ and the accuracy of the simulation results, evaluated by $Er$. The RMS simulation error for the Cases I-IV and two different ICs are shown in Fig. 2. Each sub-figure displays the RMS error $Er$ as a function of the parameters $\eta$ and $\varepsilon$. The gray dots indicate the parameter values for which the ICs were found for a given set of GCs. The colored dots indicate the RMS error value for those parameter values where the dynamic equations were integrated. In regions without colored dots (white background) the ICs allowing the integration were not found. This behavior is expected because the initial link position might not be attainable for some sets of GCs. The set of GCs for which dynamic equations were integrated is a subset of a set of GCs for which ICs

https://doi.org/10.3311/ECCOMASMBD2021-112

were found, which in turn is a subset of a set of all possible GC variations. For many sets of GCs with admissible ICs, the corresponding dynamic equations of motion were not integrated due to the divergence of the integration process at a certain simulation instant. The fact the ICs were not found for all combinations of $\eta$ and $\varepsilon$, and that the equations of motion were not integrated for all cases with the correct ICs, shows that a set of GCs influences the system dynamics.

An orthogonal set of GCs does not necessarily result in the smallest $Er$. For instance, for Case I with both IC1 and IC2, $Er$ has smaller values (by a factor of two to four) for the set of non-orthogonal GCs in comparison with the simulations for the set of orthogonal GCs corresponding to $\eta = \pi/2$ and $\varepsilon = \pm\pi/2$. This might be explained by different degrees of coupling and interplay of simulation errors in the dynamic equations of motion. For Cases I and III, “clusters" of integrable sets of GCs are grouped around $\eta = \pi/2$ and $\varepsilon = \pm\pi/2$ (valid for both ICs). On the other hand, for $\varepsilon = 0$ or $\pi$ the dynamic equations were not integrated, which makes sense because for these parameter values the axis of $q_2$ coincides with the initial vertical link position and thus becomes a redundant DOF. A similar conclusion can be drawn for the integrable “clusters" for Cases II and IV around $\eta = \pi/2$ and $\varepsilon = 0$ or $\pi$. In these cases, at $\varepsilon = \pm\pi/2$ dynamic equations were not integrated due to the aforementioned reason. Thus, the obtained results suggest that there is no clear strategy for the selection of the optimal set of GCs that would minimize the RMS error $Er$. However, by choosing an orthogonal set of GCs we ensure that the obtained model is integrable.

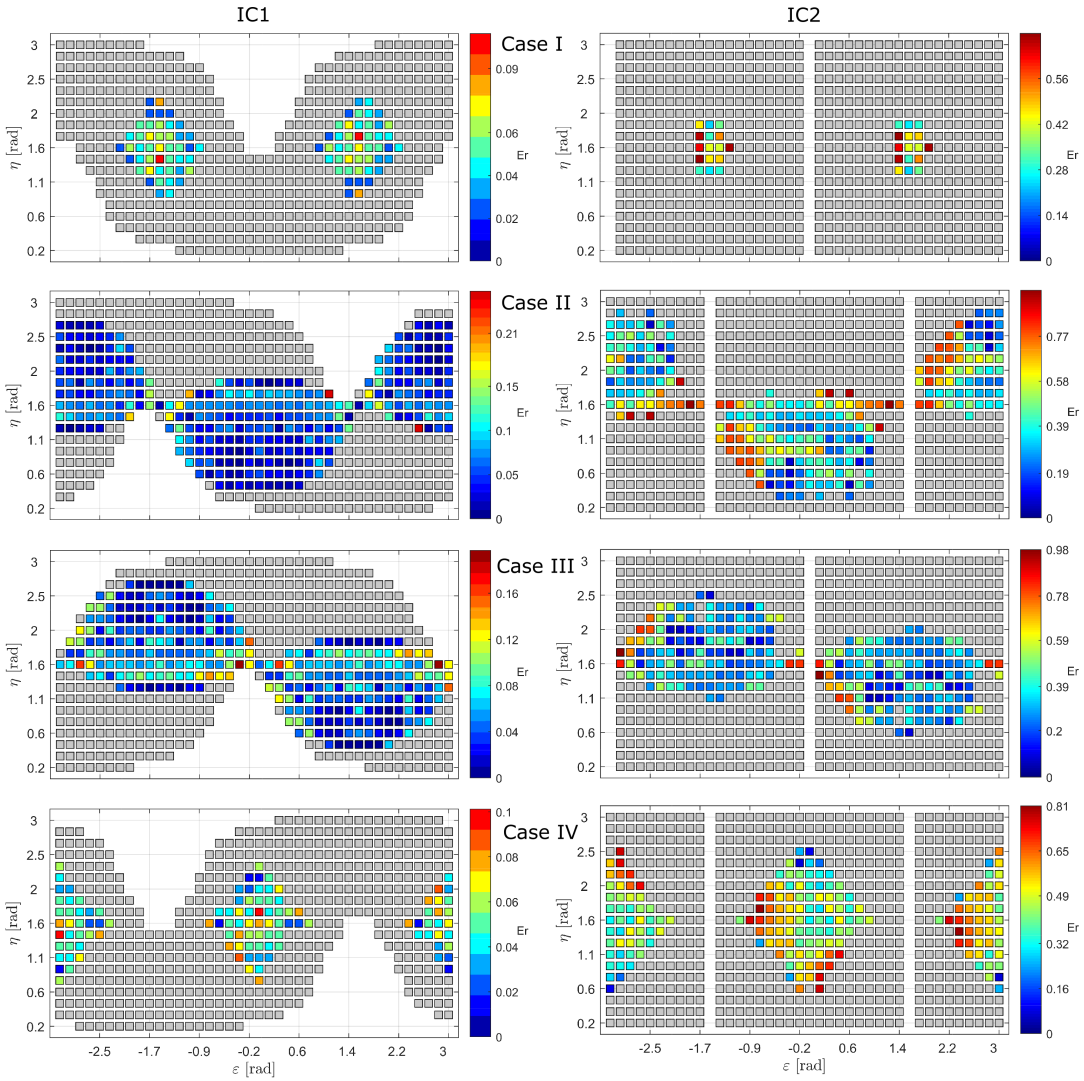


Figure 2: The RMS $Er$ for Cases I-IV with two different ICs. Note that the color bars have different scaling for each subplot.

https://doi.org/10.3311/ECCOMASMBD2021-112

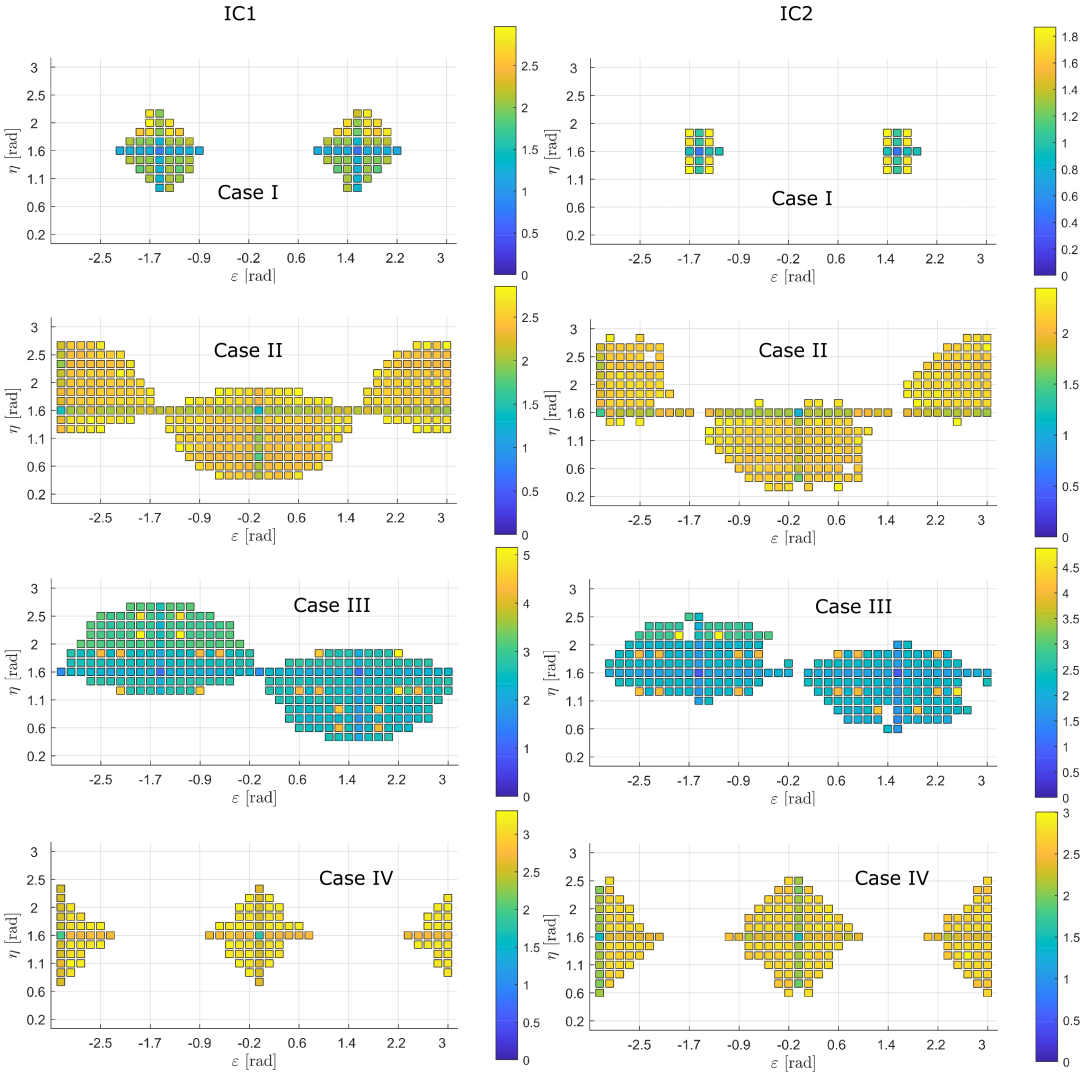


Figure 3: Simulation time ($\log_{10}(\tau/\tau_r)$) for Cases I-IV with two different ICs. The color bars have different scaling for each subplot.

Simulation times are shown in Fig. 3 on a logarithmic scale $\log_{10}(\tau/\tau_r)$. Here we can clearly see that the choice of the orthogonal set of GCs leads to a faster simulation. This observation is valid for four cases and for both ICs. For example, simulations with a non-orthogonal set of GCs can require two to five orders of magnitude longer simulation time compared to that with orthogonal counterparts. As a result, the orthogonal sets of GCs ($\eta = \pi/2$ and $\varepsilon = \pm\pi/2$ for Cases I and III, $\eta = \pi/2$ and $\varepsilon = 0$ (or $\varepsilon = \pi$) for Case II and IV) lead to more efficient simulations. In fact, for the Cases I-IV, the minimum values of the real simulation time are equal to 0.17, 0.77, 0.46, 2.12 s (IC1) and 0.15, 0.63, 0.36, 1.48 s (IC2), respectively. Thus, using the local Davenport angles defined for intrinsic rotations leads to faster simulations (by a factor of two to three) compared to the global Davenport angles defined for extrinsic rotations. Finally, it can be observed that using the first GC with an arbitrary rotation axis direction (Cases II and IV) results in slower simulations than using the set of GCs with an arbitrary direction of the second rotation axis (Cases I and III).

In summary, we conclude that a set of GCs affects the description of the system dynamics, simulation error and simulation time. The optimal set of GCs that minimizes the RMS error does not simultaneously minimize the simulation time and vice versa.

## 6 Conclusions

Different sets of GCs (generalized Euler angles) have been considered from the accuracy point of view and the computation time. It has been shown that there exists a set of orthogonal GCs that allows a fast integration of the equations of motion. However, the use of orthogonal Davenport angles does not necessarily result in the minimum gross simulation error. In certain cases, non-orthogonal Davenport angles yield the minimum gross simulation error. Additionally, it has been observed that the use of intrinsic Davenport angles as GCs leads to more efficient simulations compared to extrinsic Davenport angles.

## REFERENCES

[1] Baruh, H.: Analytical Dynamics. McGraw-Hill (1999)

[2] Goldstein, H.: Classical Mechanics. Addison-Wesley (1980)

[3] Lanczos, C.: The Variational Principles of Mechanics. 4th edn. University of Toronto Press (1970)

[4] Freeman, R.A., Tesar, D.: The generalized coordinate selection for the dynamics of complex planar mechanical systems. Journal of Mechanical Design **104**(1) (01 1982) 206–217

[5] Wehage, R.A., Haug, E.J.: Generalized coordinate partitioning for dimension reduction in analysis of constrained dynamic systems. ASME. J. Mech. Des. **104**(1) (01 1982) 247–255

[6] Nikravesh, P.E., Haug, E.J.: Generalized coordinate partitioning for analysis of mechanical systems with nonholonomic constraints. ASME. J. Mech., Trans., and Autom. **105**(3) (1983) 379–384

[7] Terze, Z., Naudet, J.: Structure of optimized generalized coordinates partitioned vectors for holonomic and non-holonomic systems. Multibody System Dynamics **24**(2) (2010) 203–218

[8] Wehage, K.T., Wehage, R.A., Ravani, B.: Generalized coordinate partitioning for complex mechanisms based on kinematic substructuring. Mechanism and Machine Theory **92** (2015) 464 – 483

[9] Reungwetwattana, A., Toyama, S.: An efficient dynamic formulation for multibody systems. Multibody System Dynamics **6**(3) (2001) 267–289

[10] González, F., Dopico, D., Pastorino, R., Cuadrado, J.: Behaviour of augmented Lagrangian and Hamiltonian methods for multibody dynamics in the proximity of singular configurations. Nonlinear Dynamics **85**(3) (2016) 1491–1508

[11] Yang, L., Yao, W., Li, Z.: UK method for solving multi-body system dynamics with singular problems. Advances in Mechanical Engineering **10**(4) (2018) 1–13

[12] Impelluso, T.J.: The moving frame method in dynamics: reforming a curriculum and assessment. International Journal of Mechanical Engineering Education **46**(2) (2018) 158–191

[13] Stephen T. Thornton, J.B.M.: Classical Dynamics of Particles and Systems. 5th edn. Thomson Brooks/Cole (2004)

[14] Davenport, P.B.: Rotations about nonorthogonal axes. AIAA Journal **11**(6) (1973) 853–857

[15] Shuster, M.D., Markley, F.L.: Generalization of the Euler angles. J. Astronaut. Sci. **51**(2) (2003) 123–132

[16] Wittenburg, J., Lilov, L.: Decomposition of a finite rotation into three rotations about given axes. Multibody System Dynamics **9**(4) (2003) 353–375

[17] Craig, J.J.: Introduction to Robotics, Mechanics and Control. Pearson Prentice Hall (2005)

[18] Abdel-Malek, K.A., Arora, J.S.: Human Motion Simulation, Predictive Dynamics. Elsevier (2013)

[19] Fu, K.S., Gonzalez, R.C., Lee, C.S.G.: Robotics: Control, Sensing, Vision and Intelligence. 5th edn. McGraw-Hill Book Company (1987)

# Section
# MECHATRONICS, ROBOTICS AND CONTROL

https://doi.org/10.3311/ECCOMASMBD2021-164

ECCOMAS Thematic Conference on Multibody Dynamics
December 12 - 15, 2021, Budapest, Hungary

# A compliant and redundantly actuated 2-DOF 3RRR PKM: Less is more

**Dustin Berendsen, Aditya Sridhar, Ronald Aarts**

Faculty of Engineering Technology, Applied Mechanics & Data Analysis,
University of Twente, P.O. Box 217, 7500 AE Enschede, The Netherlands
berendsendustin@gmail.com, adityaganesh1994@gmail.com, r.g.k.m.aarts@utwente.nl

## ABSTRACT

The development of a compliant (or flexure-based) manipulator with redundant actuation has been considered before, showing that the redundancy can be exploited to increase the support stiffness and reduce actuator loads. In this previous design the manipulator's workspace has been defined to encompass all kinematically accessible end effector positions. In this paper we reconsider the design philosophy. It appears that limiting the workspace ("less") ultimately results in a better performance in a larger area ("more") as before.

The dynamic performance of the manipulator is evaluated with a flexible multibody model. The links are assumed to be rigid. The SPACAR software is used as its flexible beam element can describe the non-linear behaviour of the flexure joints well at rather large deflections. This numerically efficient model is well-suited for design optimisation which aims at the largest workspace area while assuring a minimal parasitic natural frequency and limiting the local stresses throughout the full workspace. Furthermore, the simulations show that preloading of the flexures results in smaller required actuator torques.

An optimised design has been build. A control system has been synthesised that handles the actuator redundancy by minimising the 2-norm of the driving torques. It is demonstrated that the setup's behaviour is similar to the model and that in particular the preloading significantly lowers the required actuator torques.

**Keywords:** Flexure-based mechanisms, Redundantly actuated parallel kinematic manipulator (PKM), Non-linear beam elements, Experimental system identification, Actuator torque balancing

## 1 INTRODUCTION

In [1] a compliant and redundantly actuated 2-DOF 3RRR parallel kinematic manipulator (PKM) (Figure 1(a)) has been introduced as "best of both worlds" for precision applications. Being a compliant mechanism, or more precisely a flexure-based mechanism, deterministic behaviour can be realised because of the low level of friction, hysteresis and backlash [2, 3]. Being also a redundantly actuated PKM, it combines the advantages of PKM, i.e. the high stiffness, low inertia and large accelerations, with an improved handling of singularities and optimised actuator loading made possible by the redundancy [4, 5]. Simulations indeed demonstrated advantages of combining both concepts. The flexure hinges in compliant manipulators inherently show a reduced support stiffness for large joint angles. In a PKM with a redundant link this reduction can be limited. Furthermore, the redundant actuation offers a possibility to combine load balancing techniques with preloading of the compliant joints to reduce the actuator efforts needed to keep the end effector (EE) stationary at any position different from the equilibrium position [1].

A PKM with "classical" joints can be operated throughout the complete kinematically admissible range [6]. Mimicking this behaviour with flexure joints is a challenge as the required joint angles are quite large even for advanced joint concepts that emerged in recent years [7]. Hence

https://doi.org/10.3311/ECCOMASMBD2021-164

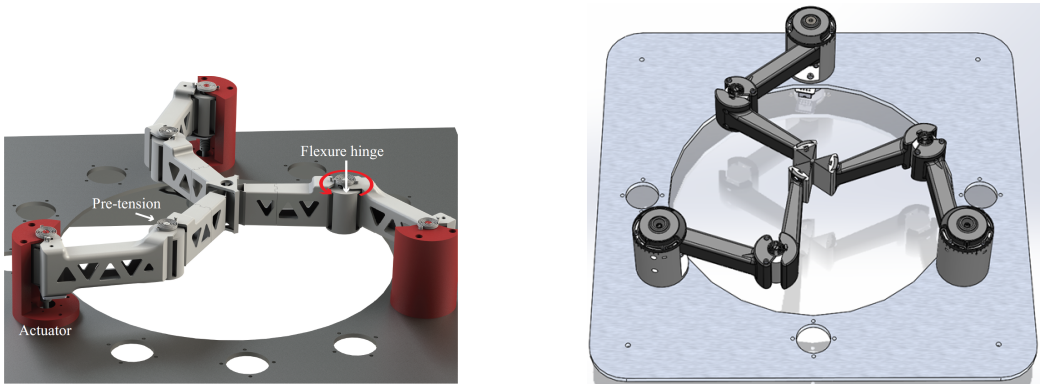


(a) Original version of [1]. (b) Redesign with optimized workspace (this paper).

**Figure 1**. Designs of planar 2-DOF 3RRR PKM with compliant joints.

we investigate in this paper how a similar performance can be obtained throughout the same or larger workspace area as before ("more") when the joint angles are limited ("less"). This can be accomplished by using longer links, which come with the drawback of an increased mass, but can still be beneficial if this is compensated by an increased support stiffness due to less required joint rotations. The optimisation of this trade-off is presented in this paper as well the experimental validation with an implementation of a control scheme.

## 2 DESIGN OPTIMISATION

In this section, the steps involved in the mechatronic design of the manipulator are addressed. The system to be manufactured should be a proof-of-concept that demonstrates its main characteristics. High accuracy and high performance are not the main targets in order to limit the costs. E.g. metal flexures are expected to show most ideal behaviour. However, 3D printing is used to realize the mechanical components. Some larger parts are printed in PLA with the FDM process which is relatively cheap. The flexure hinges require a higher accuracy for the thin leaf springs and are printed in Nylon with the SLS process. Rotational motors are used to actuate the system, although the bearings in these motors to some extent sacrifice the compliant behaviour of the manipulator.

### 2.1 Kinematic analysis and definitions of the workspace

The three arms of the 3RRR PKM are assumed to be similar and the actuators are located at the corners of an equilateral triangle, see Figure 1. At first a simplified kinematic model is used to determine the reachable workspace and the required joint rotations. The rigid links are connected with ideal rotational joints. Two important geometrical parameters are the total length $L$ of each arm and the distance $R$ of each actuator to the centre of the triangle. The workspace reachable by the EE is bounded by three circular arcs with radii $L$ of which an example is shown in red and labelled "Def$^n$ 1" in Figure 2. This is the workspace that has been considered in [1]. The worst case dynamic performance is found in the corners of this area where two arms are fully

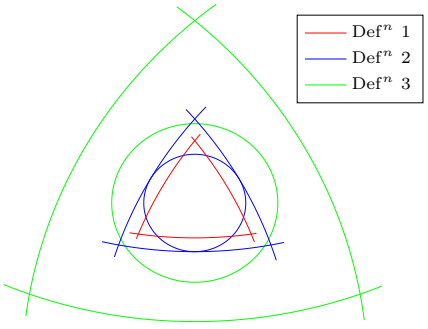


**Figure 2**. Workspace definitions.

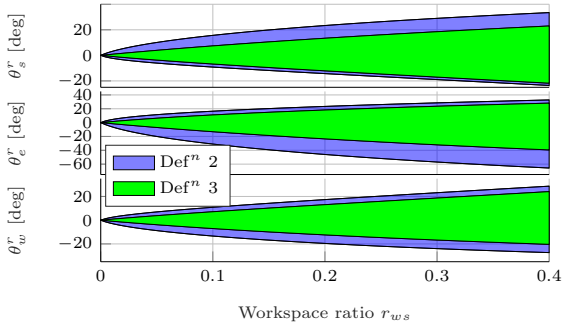


**Figure 3**. Rotation ranges of the joints.

https://doi.org/10.3311/ECCOMASMBD2021-164

stretched. In these locations the support stiffness will be lowest as several joints are at or close to their extreme rotation angles.

The blue curves, labelled "Def$^n$ 2", in Figure 2 present a first alternative workspace definition. Instead of trying to move to all reachable locations, the corners are cut off e.g. by limiting the workspace to the enclosed circle. It can be shown that using longer arms, i.e. larger $L$, and restricting the joint rotations, a larger workspace area can be reached with the same ratio between mass and support stiffness as before [8]. Although this is an improvement, it appeared that for controlled EE motion still difficulties arose from singular behaviour near the three locations on the enclosed circle where one of the arms is fully stretched.

Hence a third definition of the workspace is presented with the green curves, labelled "Def$^n$ 3", in Figure 2. This workspace is a circle which is some fixed offset radius $R_o$ smaller than the maximum enclosed circle such that the (near) singularities are avoided. This results in even more reduced ranges of the rotations for the joints as presented in Figure 3. The joint angles in this figure are computed for a manipulator where the total arm length $L$ is split into equal halves for the upper and lower arm respectively. The required rotational ranges are presented as functions of the so-called (linear) workspace ratio, which is defined as

$$r_{\text{ws}} = \sqrt{A_{\text{ws}}/A_{\text{fp}}} \tag{1}$$

where $A_{\text{ws}}$ is the workspace area and $A_{\text{fp}}$ is the triangular area of the manipulator's footprint. It can be seen that the third definition of the workspace requires smaller joint angles to reach the same area. A drawback is that the arm length increases even more compared to "Def$^n$ 2" which could result in less support stiffness as will be examined next in a dynamic analysis.

### 2.2 Parametric model

A more detailed flexible multibody model of the manipulator is used to obtain an optimal design of the system to be manufactured with 3D printing. First the joint concepts are detailed. Next relevant dimensional parameters are defined that are optimized.

In the previous design [1], the shoulder and elbow joint are butterfly joints [9]. This joint type is used at the shoulder location for its small pivot shift compared to many other flexure joints. This is also favourable in the current design as at the shoulder the rotation is driven by a motor with a fixed rotational axis. For the elbow joint it is essential that the flexure can handle rather rotations as can be seen in Figure 3. Although other, more complex joint types [7] may offer a larger range of motion, the butterfly hinge will also be adequate for the present concept.

In the previous design, the basic working principle of the butterfly hinge was also used in the wrist joint to connect the three arms. A disadvantage is the need of an intermediate body that can give rise to additional rotational DOF at the EE, which can result in unwanted parasitic vibrations or

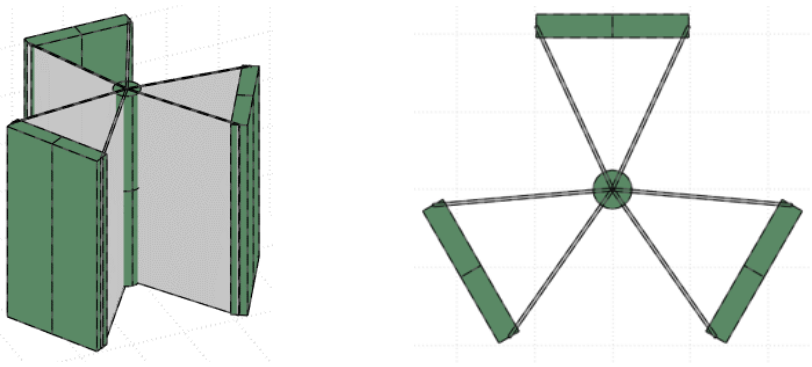

(a) Overview (b) Top view

**Figure 4**. Schematic representation of the Tri-Cartwheel joint.

https://doi.org/10.3311/ECCOMASMBD2021-164

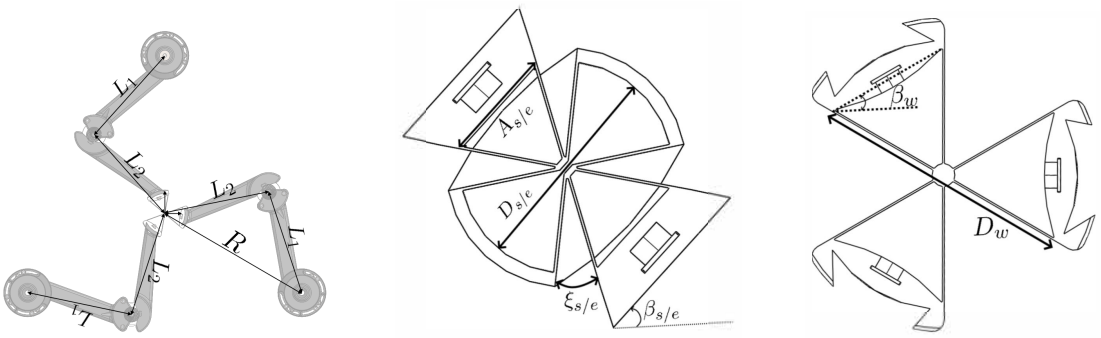


(a) Manipulator level. (b) Elbow and shoulder. (c) Wrist.

**Figure 5**. Design parameters.

even loss of the redundancy. Hence a so-called Tri-Cartwheel joint, see Figure 4 is proposed for this connection. This hinge shows a larger pivot shift and more stresses will appear in the deformed leaf springs, but for the considered range of motion this appears to be acceptable.

For design optimization the overall model of the manipulator with the joints is expressed in a set of parameters, see Figure 5. To limit the computer time needed for the optimization, the number of parameters is limited to a reasonable number as will be explained next. Some parameters are fixed by design or it is know beforehand that some extreme value is the most likely outcome, see Table 1(a). Table 1(b) lists the varying parameters with lower and upper bounds.

**Table 1**. Design parameters of the 3RRR RA-PKM as defined Figure 5.

(a) Fixed parameters

| Parameter | Value | Unit |
|---|---|---|
| $\xi_s$ | 22.5 | deg |
| $\xi_e$ | 30 | deg |
| $R$ | 230.5 | mm |
| $t$ | 0.4 | mm |
| $h_{s/e}$ | 40 | mm |
| $h_w$ | 50 | mm |

(b) Variable parameters with upper bound (ub), lower bound (lb) and optimal value (opt, Section 2.6).

| Parameter | ub | lb | opt | Unit |
|---|---|---|---|---|
| $A_s$ | 9 | 20 | 12.0 | mm |
| $D_s$ | 10 | 60 | 16.9 | mm |
| $A_e$ | 9 | 20 | 15.9 | mm |
| $D_e$ | 10 | 60 | 30.5 | mm |
| $D_w$ | 10 | 60 | 56.4 | mm |
| $L_r$ | 1.1 | 1.8 | 1.34 | |
| $\beta_s$ | $-90$ | 0 | $-0.1$ | deg |
| $\beta_e$ | $-90$ | 0 | $-71.3$ | deg |
| $\beta_w$ | $-30$ | 30 | 20.0 | deg |
| $R_o$ | 0 | 50 | 25.9 | mm |

At manipulator level, the link lengths and the location of the actuators strongly affect the workspace ratio as defined in Eq. (1). The radius $R$ at which the actuators are positioned, see Figure 5(a), is fixed to the value used in [1]. The link lengths $L_1$ and $L_2$ of upper and lower arm, respectively, are taken identical and are described by a single design variable, the length ratio $L_r$ defined as

$$L_r = \frac{L}{R} = \frac{L_1 + L_2}{R} = \frac{2L_1}{R} = \frac{2L_2}{R}. \tag{2}$$

A final parameter that affects the (effective) workspace is the offset radius $R_o$ that was introduced to exclude singularities from the workspace labelled "Def$^n$ 3" in Figure 2.

At hinge level, the leaf springs are characterized by their length, width $h$ and thickness $t$. The latter two dimensions are fixed for all joints. It is known that the thickness $t$ of the leaf springs tends to be minimized as it reduces stress build-up without affecting the support stiffness too much. Hence $t = 0.4$ mm which is close the minimal required thickness for the used SLS process.

For the optimal performance of the Butterfly hinges, it has been found that the clearance angles $\xi_s$

https://doi.org/10.3311/ECCOMASMBD2021-164

and $\xi_e$ as indicated in Figure 5(b) need to be minimized [10]. Hence these angles are fixed to the minimal estimated required clearance angle for the expected range of motion.

Finally, the stiffness properties of the joints depend on the other dimensions listed in Table 1(b) as well as the hinge orientation angles $\beta_s$, $\beta_e$ and $\beta_w$. These angles describe the respective hinge orientations from a global point of view, see Figures 5(b) and (c).

### 2.3 2-DOF dynamic model

A low order 2-DOF model is derived first. It should capture the main low frequent dynamic behaviour and will be used for the control synthesis. The low order model can be obtained relatively straightforwardly e.g. using the Euler-Lagrange equation for the kinematic model of Section 2.1 supplemented with (link) mass and (joint) stiffness properties. The result can be expressed in the usual way as

$$\bar{\mathbf{M}}(\mathbf{q})\ddot{\mathbf{q}} + \mathbf{C}(\mathbf{q},\dot{\mathbf{q}})\dot{\mathbf{q}} + \mathbf{Q}(\mathbf{q}) = \mathbf{A}^T(\mathbf{q})\boldsymbol{\tau}, \tag{3}$$

where $\mathbf{q}$ are the two independent coordinates for which it is convenient to take the EE coordinates $x_{EE}$ and $y_{EE}$. Matrix $\bar{\mathbf{M}}$ is the configuration dependent (reduced) mass matrix; $\mathbf{C}$ accounts for the Coriolis terms; $\mathbf{Q}$ represents the (non-linear) stiffness contribution and the transpose of the Jacobian matrix $\mathbf{A}$ transforms the three actuator torques $\boldsymbol{\tau}$ into effective forces on the EE.

### 2.4 Stiffness balancing with preloaded joints

The term $\mathbf{Q}$ in Eq. (3) is directly linked to the finite stiffness of the flexure joints for rotation in the compliant direction. In the neutral configuration of the manipulator with the EE in the centre, this term is zero. To position the EE at locations near the extremity of the workspace, this term can be quite large and even result in actuator saturation making these locations unreachable. Lowering the stiffness is mostly not possible, but as shown in [1] preloading of the joints can result in lower required actuator torques. Although preloading isn't possible for the Nylon flexures, metal clock springs can be installed at the hinges to realize preloading.

A quick way to evaluate the effectiveness of these springs makes use of an analysis of the stored potential energy. Knowing the kinematic configuration of the manipulator, Section 2.1, the potential energy stored in all flexure joints can be computed as a function of the EE position, see Figure 6(a). With zero potential energy in the neutral configuration, the energy stored increases towards the boundary of the workspace.

Similarly, the energy stored in the preloaded clock springs can be evaluated. It appears that this energy can decrease when moving towards the boundary with adequate settings for preload and

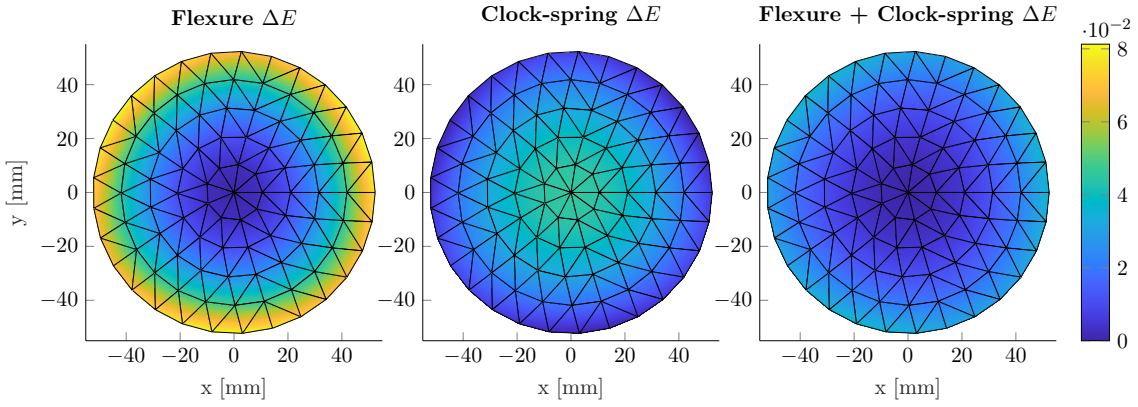


(a) Flexure joints. (b) Balancing clock springs. (c) Combined.

**Figure 6**. Potential energy stored in the flexure joints (left), balancing clock springs (middle) and combined (right).

https://doi.org/10.3311/ECCOMASMBD2021-164

stiffness. Figure 6(b) shows an example where the minimum energy level in the workspace is arbitrarily set to zero. Combining these plots give Figure 6(c) which illustrates that for the manipulator with these balancing clock springs still some positive stiffness is observed, but less compared to the unbalanced case. In this way it will be easier to reach the full workspace with limited actuator torques.

### 2.5 Controller synthesis

Reconsidering the equation of motion (3), it can be seen that any specific motion can be accomplished by applying the effective force on the EE as follows from the right-hand side of this equation. In other words, the actuator torques should be such that the term $\mathbf{A}^T(\mathbf{q})\boldsymbol{\tau}$ equals the left-hand side of this equation. Because of the redundant actuation there is no unique solution. Let's consider e.g. the stationary positioning of the manipulator in which case only the stiffness has to be handled, i.e.

$$\mathbf{A}^T(\mathbf{q})\boldsymbol{\tau} = \mathbf{Q}(\mathbf{q}), \tag{4}$$

from which it can be seen that with one valid solution for $\boldsymbol{\tau}$, all other solutions can be found by adding any vector from the null space of the Jacobian matrix $\mathbf{A}^T$. A common procedure is to select the set of torques $\boldsymbol{\tau}$ that minimize a specific norm. Considering the 2-norm, the solution equals

$$\boldsymbol{\tau} = (\mathbf{A}^T(\mathbf{q}))^\dagger \mathbf{Q}(\mathbf{q}), \tag{5}$$

where $()^\dagger$ indicates the (Moore-Penrose) pseudo-inverse of the matrix.

It can be noted that in view of possible actuator saturation, the use of the $\infty$-norm is more adequate as this minimizes the largest required actuator torque. However, it was found that the benefit from this norm was relatively small and hence the simpler computation of the 2-norm will be implemented in the set-up.

For controlled motion, the required effective EE force is generated by a control system, where feedback and feedforward control can be combined. Feedforward makes use of system knowledge as the equation of motion (3) is evaluated in real-time for a prescribed trajectory $(\mathbf{q}, \dot{\mathbf{q}}, \ddot{\mathbf{q}})$. Relevant parameters of the manipulator need to be estimated. In this paper only relatively slow motions are considered and hence only stiffness feedforward will be applied, i.e. Eq. (4).

In addition feedback control is used to account for model inaccuracies in the feedforward control and disturbances. PID-control will be implemented following the approach of [11].

### 2.6 Design optimization

The workspace for the test-setup is optimized for the parametric model outlined in Section 2.2. Ten design parameters have been defined in Table 1(b). Material properties are given in Table 2 for the materials introduced at the beginning of this Section 2.

To assure the optimization doesn't result in deteriorated dynamic performance, constraints are imposed that require the parasitic natural frequencies to be at least as high as in the previous design [1]. Table 3 lists all constraints, which also impose that the stresses are below the maximum allowable stress, Table 2, with a safety factor of 1.5. Furthermore, the actuator limits have to be taken into account. The upper arms are actuated with Maxon EC45 Flat 70W motors that offer a maximum nominal torque of 0.128 Nm.

The MATLAB script `fminsearchcon` is used for the optimization, which implements a direct search method where non-linear inequality constraints are included by means of a penalty function [12]. As the goal is to obtain the maximum workspace, the inverse of the workspace ratio $r_{ws}$ of Eq. (1) is minimized. As the constraints include natural frequencies and stresses these are evaluated in the neutral configuration as well as in two critical EE locations on the border of the workspace. For this purpose a flexible multibody model of the manipulator has been defined in the SPACAR software package [13]. All leaf springs are modelled with non-linear flexible beam

https://doi.org/10.3311/ECCOMASMBD2021-164

**Table 2**. Material properties of the test setup.

| Material | Property | Value | Unit |
|---|---|---|---|
| PolyLactic Acid (PLA) | Tensile strength | 45 | MPa |
| | Young's modulus | 3.5 | GPa |
| | Density | 1250 | kg/m$^3$ |
| Nylon (PA2200) | Tensile strength | 45 | MPa |
| | Young's modulus | 1.7 | GPa |
| | Density | 930 | kg/m$^3$ |

**Table 3**. Non-linear inequality constraints.

| Property | Value | Unit |
|---|---|---|
| Maximum stress | $\leq 30$ | MPa |
| First parasitic eigenfrequency | $\geq 45$ | Hz |
| Second parasitic eigenfrequency | $\geq 50$ | Hz |
| Balanced driving torque | $\leq 0.1$ | Nm |
| Non-balanced driving torque | $\leq 0.4$ | Nm |

elements as this has been proven to be an accurate and efficient approach [1, 7, 10]. The obtained optimal values for the parameters are included in Table 1 and a CAD model of the manipulator is shown in Figure 1(b). Figure 7(a) illustrates the first natural frequency throughout the workspace. Clearly it satisfies the constraint and it can be verified that the other constraints are not violated either. The parasitic natural frequency doesn't vary much which shows that the support stiffness remains rather constant. The accompanying vibration mode in the neutral configuration is presented in Figure 7(b) from which it is clear that this is an out-of-plane vibration.

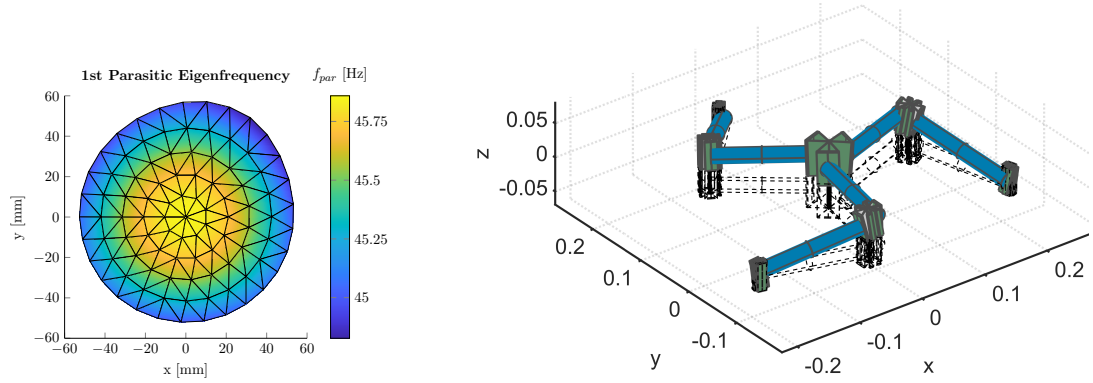


(a) First parasitic frequency (in Hz). (b) First parasitic vibration mode.

**Figure 7**. First parasitic vibration.

Evaluating the optimized design, it appears that it results in a further increase of the workspace area while the first simulated parasitic natural frequency is kept above 45 Hz. More specifically, the workspace ratios as shown in Figure 2 are respectively $r_{ws} = 0.1922$ in the original "Def$^n$ 1" (red) [1], $r_{ws} = 0.2167$ for "Def$^n$ 2" (blue) [8], but can now be increased to $r_{ws} = 0.3532$ (green).

## 3 EXPERIMENTAL RESULTS

### 3.1 System identification

The dynamic behaviour of the actual manipulator has been characterized with system identification where a multi-sine excitation is used to estimate the frequency response of Figure 8. In agreement with the equation of motion (3), the redundant actuation and the sensing are transformed to two degrees of freedom being both in-plane forces $F_x$, $F_y$ and translations $x_{ee}$, $y_{ee}$ of the EE. This experiment is performed at 14 locations in the workspace (red curves). The blue curves indicate averages of these measurements.

In the theoretical equation of motion, the translations in $x$ and $y$ directions of the EE near the neutral configuration can be modelled as decoupled motions. In the FRF plots this is confirmed as the diagonal terms are larger than the off-diagonal cross-coupling terms.

The first parasitic natural frequency appears to be about 500 rad/s or 80 Hz. This frequency is

https://doi.org/10.3311/ECCOMASMBD2021-164

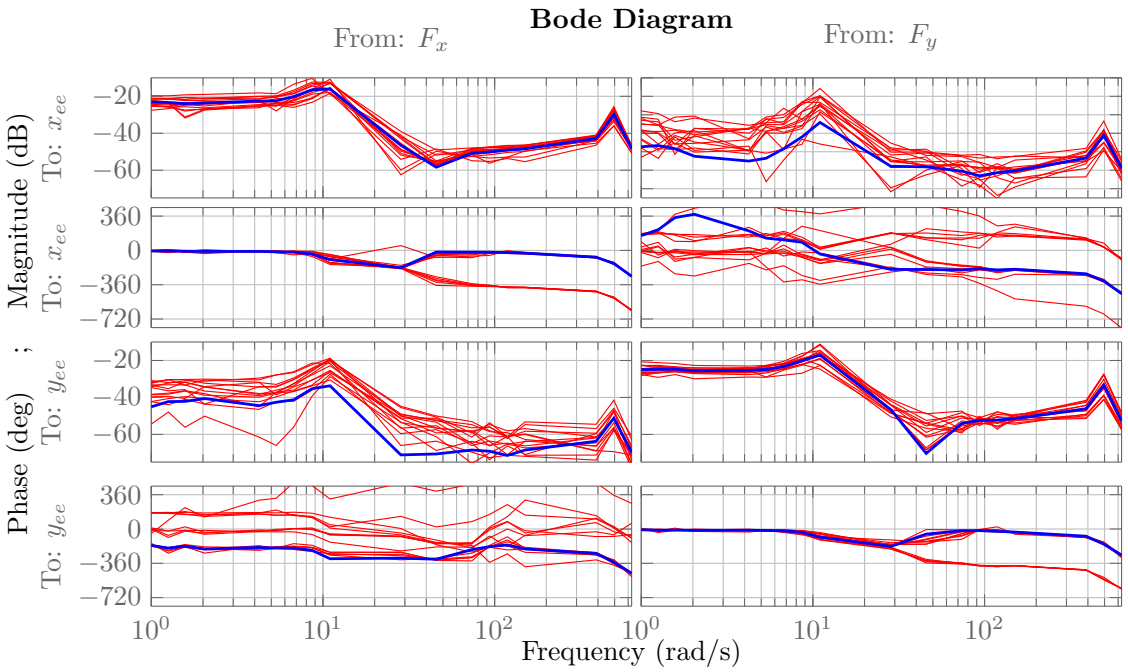


**Figure 8**. Identified frequency response functions (FRF) in 14 different EE locations (red) and average (blue).

higher than expected in Section 2.6. A possible cause could be a larger stiffness, which to some extent can be explained as the model doesn't account for flexible shaft couplings that are installed between the actuators and upper arms. This higher natural frequency could be beneficial for the controller stability. Unfortunately however, the FRF plots also show an anti-resonance (or zero pair in the transfer function) near 30 rad/s or 5 Hz. Even worse, in some of the FRF curves this zero pair is combined with a phase lag of $-180°$ instead of the usual phase lead of $180°$, which indicates these are non-minimum phase zeros. Such zeros will make it hard or impossible to achieve a high control bandwidth. Although these anti-resonances and accompanying zeros can be simulated in the SPACAR models, their existence was not included in the design optimization.

### 3.2 Controller tuning

The observation in the previous section of a mainly diagonal plant can be used to apply a diagonal controller as well. In this way the settings of the PID-controller are found quite straightforwardly [11]. However, to handle the destabilizing effects from the anti-resonances described in the previous section, the PID-controller is supplemented with a notch filter. Setting the filter frequency at about 495 rad/s or 79 Hz, a stable closed-loop system could be obtained with a open-loop crossover frequency of about 18 rad/s or 3 Hz.

### 3.3 Reference tracking

To demonstrate the controlled motion of the EE a circular reference trajectory is defined close to the boundary of the workspace, see Figure 9(a). An initial linear segment is added to move the EE from the neutral configuration to the circle. The actual motion is included in the plot. It shows reasonable tracking accuracy with some occasional small spikes. These may be caused by cogging effects of the (direct-drive) motors or other disturbances which are only weakly suppressed as the controller bandwidth is rather limited. Also noticeable is an increased noise level in the lower right corner of the circle. This is due to quantisation noise of the digital encoders that measure the rotation with a resolution of 512 lines per revolution, so 2048 counts per revolution. In this experiment only two encoders were used, which results in an output singularity in this region. This can be avoided by exploiting the redundant sensing. Figure 9(b) presents the actuator torques during the motion, which will be discussed in more detail next.

https://doi.org/10.3311/ECCOMASMBD2021-164

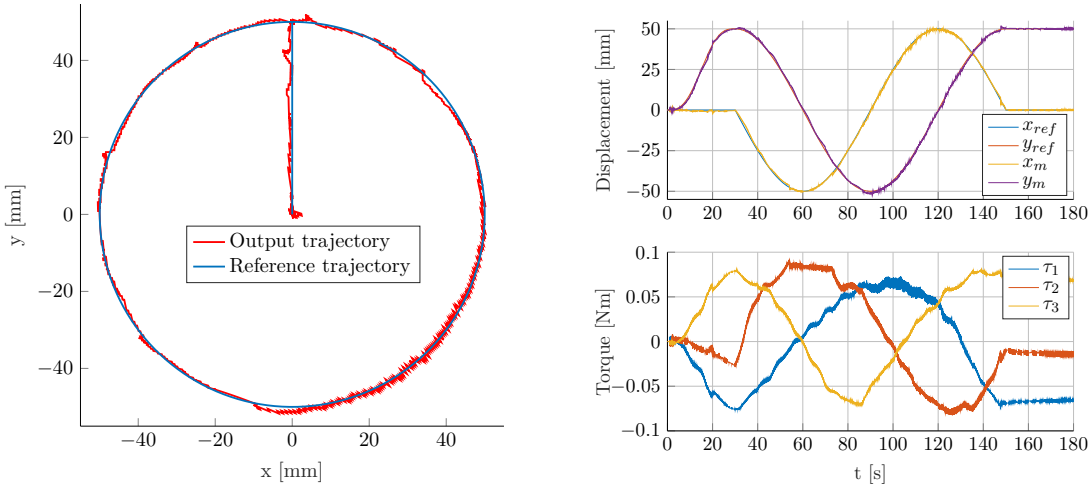


(a) Output trajectory vs. reference trajectory. (b) Required actuator torques.

**Figure 9**. Tracking of a circular reference path.

### 3.4 Stiffness balancing

As outlined in Section 2.4 the preloading of the flexure joints plays an important role in reducing the actuator torques needed to cope with the stiffness of the joints. The balancing of the actuator torques is investigated by positioning the EE throughout the workspace with and without preloading of elbow and shoulder joints. Figure 10(b) shows that with preloading the maximum torques of all actuators stay well within the imposed limit. Without this preloading it can be seen in Figure 10(a) that the torque limits are already exceeded before the edges of the workspace are reached. Hence only a smaller area is shown.

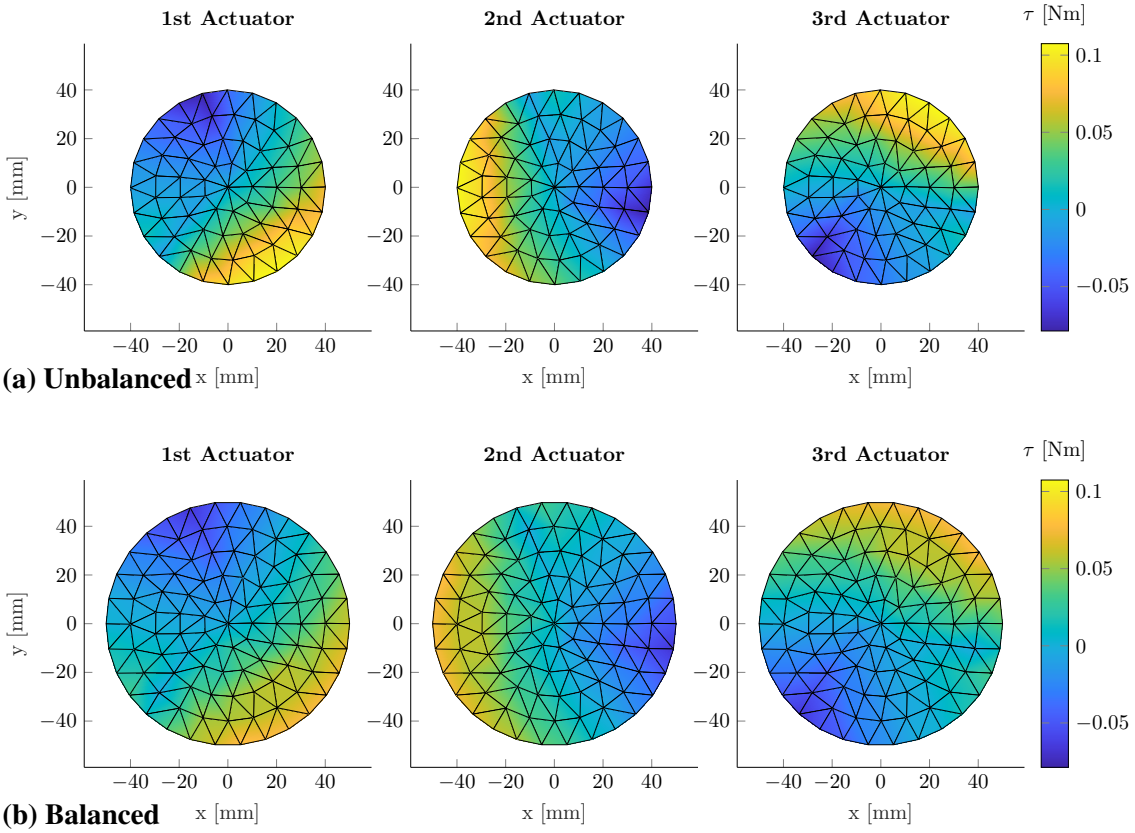


**(a) Unbalanced**

**(b) Balanced**

**Figure 10**. Experimentally determined actuator torques for the unbalanced (a/top) and balanced (b/bottom) manipulator.

## 4 CONCLUSION

This paper shows a new design approach for a planar 2-DOF 3RRR parallel manipulator with redundant actuation and compliant joints, i.e. flexure joints. The goal was to maximize the workspace area in which a similar or better performance could be realized as before [1] in terms of the first parasitic natural frequency. It turned out to be beneficial to limit the workspace to a circle that avoids (near) singular manipulator configurations. In this way the ranges for the joint rotations are restricted such that the joint support stiffnesses of the deformed flexures are reduced less. This allows for the use of longer link lengths which in the end results in a significant increase of the workspace area. In addition a new concept is proposed for the wrist joint connecting the three arms in the end effector. A flexible multibody model has been built where the leaf springs in the flexure joints are modelled with the non-linear beam elements of the SPACAR software. The parameters in this model have been optimized to obtain the largest workspace area while satisfying constraints regarding the parasitic natural frequencies, local stresses and actuator limits.

A hardware implementation of this manipulator has been realized. Although the mechanical parts of this setup have been manufactured with relatively low-cost 3D printing, it demonstrates some of the main features like the sufficiently high parasitic natural frequency. However, it also appeared that the closed-loop performance is considerably limited by the existence of anti-resonances or transfer function zeros that could have been predicted by the SPACAR flexible multibody models, but were not taken into account during the design. A further increase of the workspace area could result from applying a more advanced joint type for the elbow joints allowing larger rotations. For true high performance the flexure hinges should be manufactured from different material like e.g. metal. Also the use of frictionless actuators like pure torque motors should be considered. Attention should be paid to using sufficiently accurate sensors and taking advantage of the sensor redundancy. Finally, in order to handle higher velocities the stiffness or position dependent feedforward control should be supplemented with the acceleration, velocity and position dependent inertia effects of the equation of motion (3).

The setup in particular proved that preloading of the shoulder and elbow joints results in a significant reduction of the required actuator torques in agreement with the modelled prediction.

## REFERENCES

[1] Cornelissen, R., Müller, A., Aarts, R.: A compliant and redundantly actuated 2-DOF 3RRR PKM: Best of both worlds? In Kecskeméthy, A., Geu Flores, F., eds.: Multibody Dynamics 2019. Springer International Publishing, Cham (2020) 163–171 doi:10.1007/978-3-030-23132-3_20.

[2] Soemers, H.: Design principles for precision mechanisms. T-Point Print VoF (2011) ISBN:978-90-365-3103-0.

[3] Howell, L.L., Magleby, S.P., Olsen, B.M.: Handbook of Compliant Mechanisms. John Wiley & Sons Ltd. (2013) ISBN:978-1-119-95345-6.

[4] Kock, S., Schumacher, W.: A parallel x-y manipulator with actuation redundancy for high-speed and active-stiffness applications. In: Proceedings of the 1998 IEEE International Conference on Robotics and Automation. Volume 3., Leuven, Belgium (1998) 2295–2300 doi=10.1109/ROBOT.1998.680665.

[5] Müller, A., Hufnagel, T.: Model-based control of redundantly actuated parallel manipulators in redundant coordinates. Robotics and Autonomous Systems **60**(4) (2012) 563–571 doi:10.1016/j.robot.2011.11.014.

[6] Krajoski, K., Müller, A., Gattringer, H., Jörgl, M.: Design, modeling and control of an experimental redundantly actuated parallel platform. In Niel, K., Roth, P., eds.: Proceedings

of the OAGM&ARW Joint Workshop 2016 “Computer Vision and Robotics”, University of Applied Sciences Upper Austria, Wels Campus (2016) 209–216 doi:10.3217/978-3-85125-528-7-29.

[7] Naves, M., Brouwer, D., Aarts, R.: Building block-based spatial topology synthesis method for large-stroke flexure hinges. J. Mechanisms Robotics **9**(4) (2017) 041006 (9 pages) doi:10.1115/1.4036223.

[8] Sridhar, A.: Workspace optimisation and motion control of a redundant flexural 2-DoF 3RRR parallel kinematic manipulator. Master’s thesis, University of Twente, Enschede, The Netherlands (2020)

[9] Henein, S.: Short communication: Flexure delicacies. Mechanical Sciences **3**(1) (2012) 1–4 doi:10.5194/ms-3-1-2012.

[10] Wiersma, D.H., Boer, S.E., Aarts, R.G.K.M., Brouwer, D.M.: Design and Performance Optimization of Large Stroke Spatial Flexures. Journal of Computational and Nonlinear Dynamics **9**(1) (11 2013) 011016 (10 pages) doi:10.1115/1.4025669.

[11] Dijk, J., Aarts, R.: Analytical one parameter method for PID motion controller settings. IFAC Proceedings Volumes **45**(3) (2012) 223–228 doi:10.3182/20120328-3-IT-3014.00038.

[12] D’Errico, J.: fminsearchbnd, fminsearchcon – on MATLAB Central File Exchange. https://www.mathworks.com/matlabcentral/fileexchange/8277-fminsearchbnd-fminsearchcon (2006) Accessed September 2020.

[13] Jonker, J.B., Meijaard, J.P.: SPACAR — Computer program for dynamic analysis of flexible spatial mechanisms and manipulators. In Schiehlen, W., ed.: Multibody Systems Handbook. Springer, Berlin, Heidelberg (1990) 123–143 doi:10.1007/978-3-642-50995-7_9.

https://doi.org/10.3311/ECCOMASMBD2021-192

ECCOMAS Thematic Conference on Multibody Dynamics
December 12 - December 15, 2021, Budapest, Hungary

# Simulation of the Dynamics of the 3-CRS Parallel Robot with a Bond Graph Approach

**Benjamin Boudon[1], Pierre Malafosse[1], Louis Guigon[1], Rebecca Margetts[2], Chedli Bouzgarrou[1], Thu Thuy Dang[1], Nicolas Bouton[1]**

[1] Université Clermont Auvergne, CNRS,
SIGMA Clermont, Institut Pascal,
F-63000 Clermont-Ferrand, France.
[benjamin.boudon, pierre.malafosse,
louis.guigon, chedli.bouzgarrou,
thu-thuy.dang, nicolas.bouton]
@sigma-clermont.fr

[2] Nottingham Trent University
Digital Innovation Research Group
Department of Engineering
Clifton, Nottingham. NG11 8NS. UK
rebecca.margetts@ntu.ac.uk

## ABSTRACT

This paper presents a bond graph model of the 3-CRS parallel robot and the associated simulations. The structural and modular approach proposed with bond graph permits the systematic modeling of mechatronic multibody systems. From a library of elements, the model is built as an assembly of components or modules (rigid bodies and kinematic joints) by following the structure of the actual system.

The bond graph model of the robot consists of a multibody system (MBS) augmented with electrical actuators and controllers. Simulations have been conducted to test several kinematic configurations, dynamics scenarios and to evaluate robot performance.

**Keywords:** Bond Graph, Parallel Robot, Mechatronics, Dynamics, Control.

## 1 INTRODUCTION

**Context description** For many applications in robotics (namely a quick robot for pick and place [1, 2] or robots dedicated to machining [3]), it is crucial to take into account all the physical phenomena: of course mechanics but also electrical and thermal. To do so, a mechatronic approach is needed so as to gather, in the same model, different physics. Moreover, during the designing of new parallel robots, different topologies of robot are tested. Having a tool which permits the user to easily obtain the kinematics and dynamics for different topologies can reduce modeling time and errors with regards to ad hoc methods. The bond graph (BG) offers this multi-physics approach in the modeling, control and analysis of parallel robots. Computer science and software dedicated to BGs have progressed considerably in the last two decades and give new insights on older research works made in multibody modeling with bond graphs. [4, 5, 6].

**Problem description** The overall objective of this ongoing research work is to analyze the BG approach in the modeling, simulation and control of parallel robots, as opposed to a classic approach. Different lines of work can be considered: a modular modeling approach thanks to its **graphical, structural and object oriented features**, the possibility of model inversion–based control with the bi-causal bond graph [7, 8, 9, 10, 11](**causality feature**), the model reduction [12, 13, 14, 15] and the power flow analysis due to its intrinsic **energetic** properties. In this paper, the aim is to develop a modeling framework of mechatronic robots with a systematic, structural and modular approach. This work is an extension of the work done in [16, 17] by the use of a more formalized and flexible library.

**Case study** In this paper, the study is focused on an original parallel robot: the 3-CRS, a parallel reconfigurable robot proposed by C.Bouzgarrou [18, 19, 20].

https://doi.org/10.3311/ECCOMASMBD2021-192

**Outline** The remainder of the paper is organized as follows. Section 2 describes the kinematic structure and the operation of the 3-CRS robot. The modeling and simulation framework is detailed in section 3. Then, the full BG model of the robot will be presented in section 4. Finally, before concluding, simulation results will be presented in section 5.

## 2 THE 3-CRS ROBOT

### 2.1 Description of the system

The first studies in this frame have been conducted on the 3-CRS [19]. This robot is an original parallel mechanism having 6 degrees of freedom (DOFs) with only 3 limbs (Figure 1). This mechanism uses two motorized joints per limb: the prismatic joint and the first revolute joint. These two form an equivalent of one actuated cylindrical joint (C). The rest of the arm is composed of four passive revolute joints equivalent to a revolute (R) and a spherical joint (S). This topology has led to the name "3-CRS".

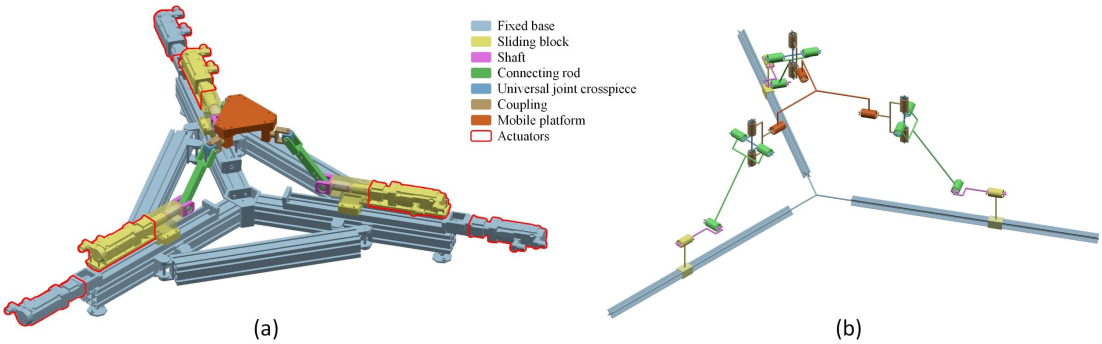


Figure 1: CAD visualization (a) and kinematics scheme (b) of the 3-CRS robot

### 2.2 Benefits of such a parallel structure

This new paradigm of actuation opens up research fields on new families of robots, which should particularly interest the parallel robotics community. According to its dimensional synthesis, this mechanism can have remarkable kinematic properties in its category such as a large orientation workspace [18] or reconfiguration capabilities [20].

## 3 MODELING OF THE PHYSICAL SYSTEM

### 3.1 Modeling robots with BG

The bond graph was invented by H. Paynter [21] in 1959 and quickly developed in the mechanical field by R. Rosenberg, D. Karnopp and D. Margolis [22] at MIT Boston, USA. Multibody systems methods have been reviewed in [23]. Practical modeling guidelines for multibody systems with bond graph have been formalized in [17]. In the past, few complex robots were simulated because the equations had to be manually derived from bond graph. Over the last 20 years, software environments have evolved to allow the user to fully take advantage of the graphical aspect of BG. Moreover, equations are automatically generated and solved with classical ODE or DAE schemes.

### 3.2 A modular approach using a BG Multibody Models Library

The modeling of the robot has been conducted with a modular approach. It was derived from the Tiernego and Bos [24] method for modeling multibody systems (MBS) with bond graph, which consists of writing the Newton-Euler equations used with the absolute coordinate. Rigid bodies and kinematic joints can be modeled beforehand as objects and form a library. The BG models of the rigid bodies and the kinematic joints are detailed in [17]. This library can then be used to model complex MBS by assembling the models of bodies and kinematic joints.

https://doi.org/10.3311/ECCOMASMBD2021-192

The concept of this library presented in [17] has been broadened and consolidated by using 20-sim's software features. Every model contains different versions of itself which can be switched using the "implementation" feature in 20-sim. These versions can allow the user to block the joint's DOFs using modular effort sources (MSe) or damping and friction elements (R, C). Similarly, it is possible to change the rigid body's angle definition from Cardan angles to a quaternion-based transformation.

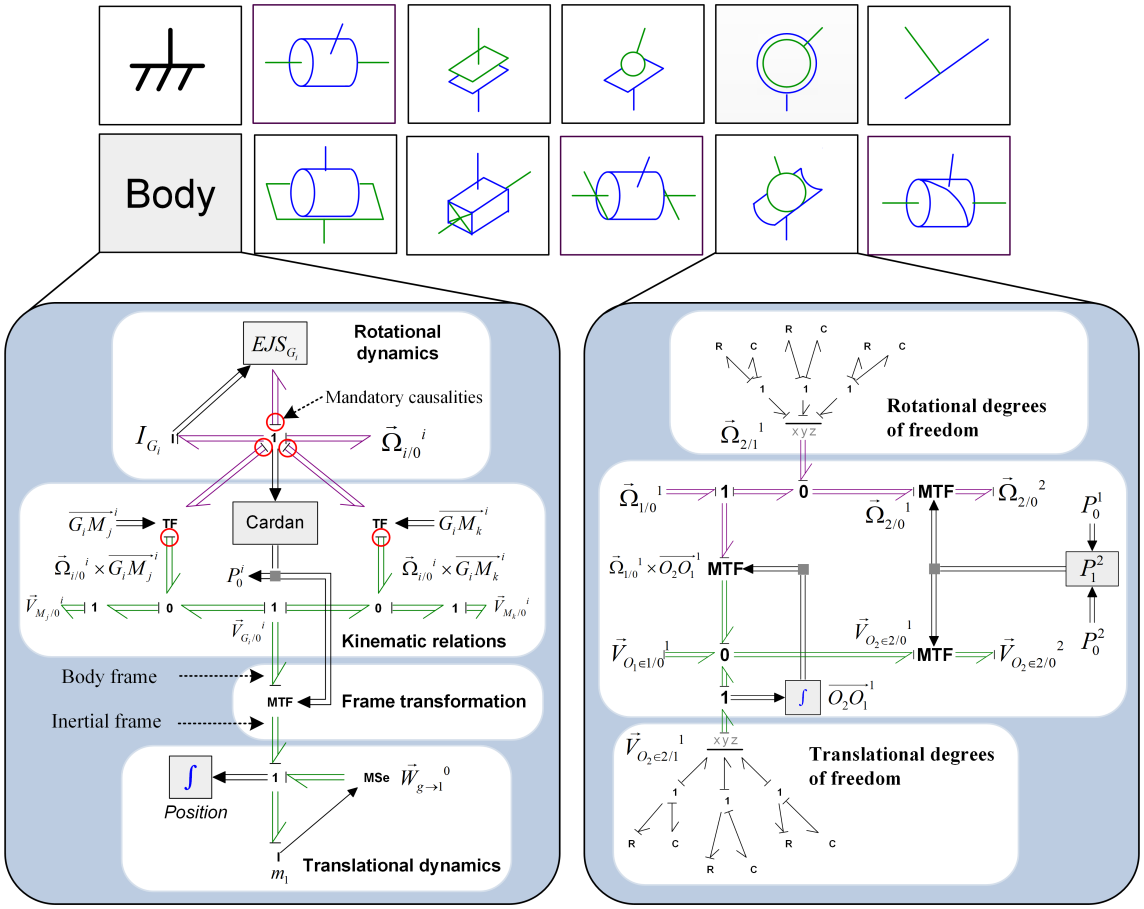


Figure 2: Overview of the Multibody Models Library

### 3.3 The robot's physical model

#### 3.3.1 modeling of the robot's structure

Once the BG library for MBS has been completed, the physical model of the 3-CRS can be built from an assembly of BG rigid bodies and kinematic joints.

R-C elements are used to suppress the DOFs of the joints. These R-C elements can represent a small deformation of the kinematic joints. The orientations are expressed using Cardan angles. Each body is defined by a center of mass and two anchor points which are placed relatively to it. Therefore, the dimensions of each body is set by defining the anchor points' local coordinates. Finally, the center of mass (COM) is expressed in global coordinates to locate the part.

The initial configuration of the robot needs to be initialized on the 20-sim model. Indeed, the COM coordinates and orientations of each part of the robot are required. To recover this information relative to a specific pose of the robot, the motion transformations of all the kinematic chains have been fully determined using the joint parameters which have been computed by the inverse geometric model of the 3-CRS from a given end-effector pose. This data can then be automatically incorporated into the model by running an external script. If the initial pose of the robot is not modified, the 20-sim model does not require these script to run a simulation.

https://doi.org/10.3311/ECCOMASMBD2021-192

### 3.3.2 Modeling of the actuators

The 3CRS robot requires 6 brushless AC synchronous motors to be mounted on the joints. The motors and their associated power electronics and controller systems are provided by Parker Hannifin (the manufacturer). The motors are from the Parvex NX310EAK family capable of delivering up to 1kW mechanical power at the shaft. For a rapid robotic system, brushless AC synchronous motors are good candidates because of their very high torque-to-mass ratio which yields high dynamic performance (commonly 4 to 5 times higher than the brushed DC motor counterpart). In the literature, BG modelling of AC synchronous motors are well established [25, 26, 27]. However, in this study, we will consider in the first approach that the electrical dynamics of the motors is infinitely higher than the mechanical dynamics. This assumption enables us to propose a very simple model of the actuators where input current is converted onto torque by a simple gain corresponding to a constant motor's torque sensitivity Kt.

The mechanical part of the motor is then modeled using a bond graph as shown on Figure 3. It is coupled with a reductor and a ball-screw transmission.

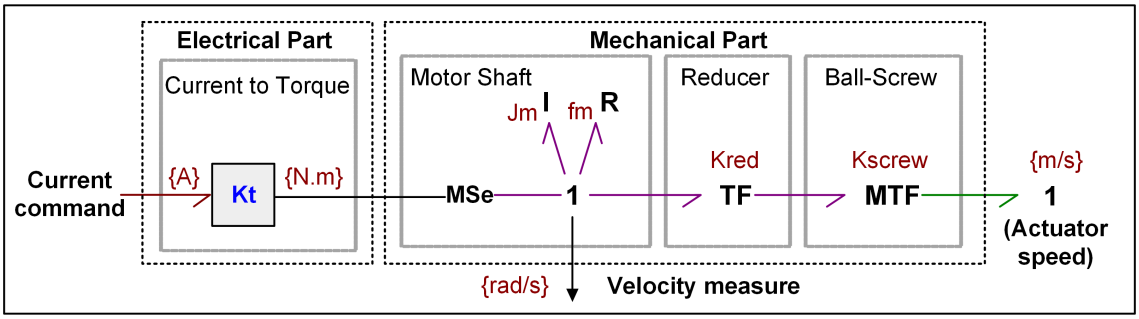


Figure 3: BG model of an actuator

### 3.4 Full bond graph physical model

The full BG physical model of the 3-CRS can be seen on Figure 4.

The six actuators are connected to the three prismatic joints and the three revolute joints. As the actuators are modeled using scalar bond graph, the output of these blocks imposes a flow on the joint's actuated degree of freedom. Therefore, three rotational speeds and three translation speeds are imposed on the system.

https://doi.org/10.3311/ECCOMASMBD2021-192

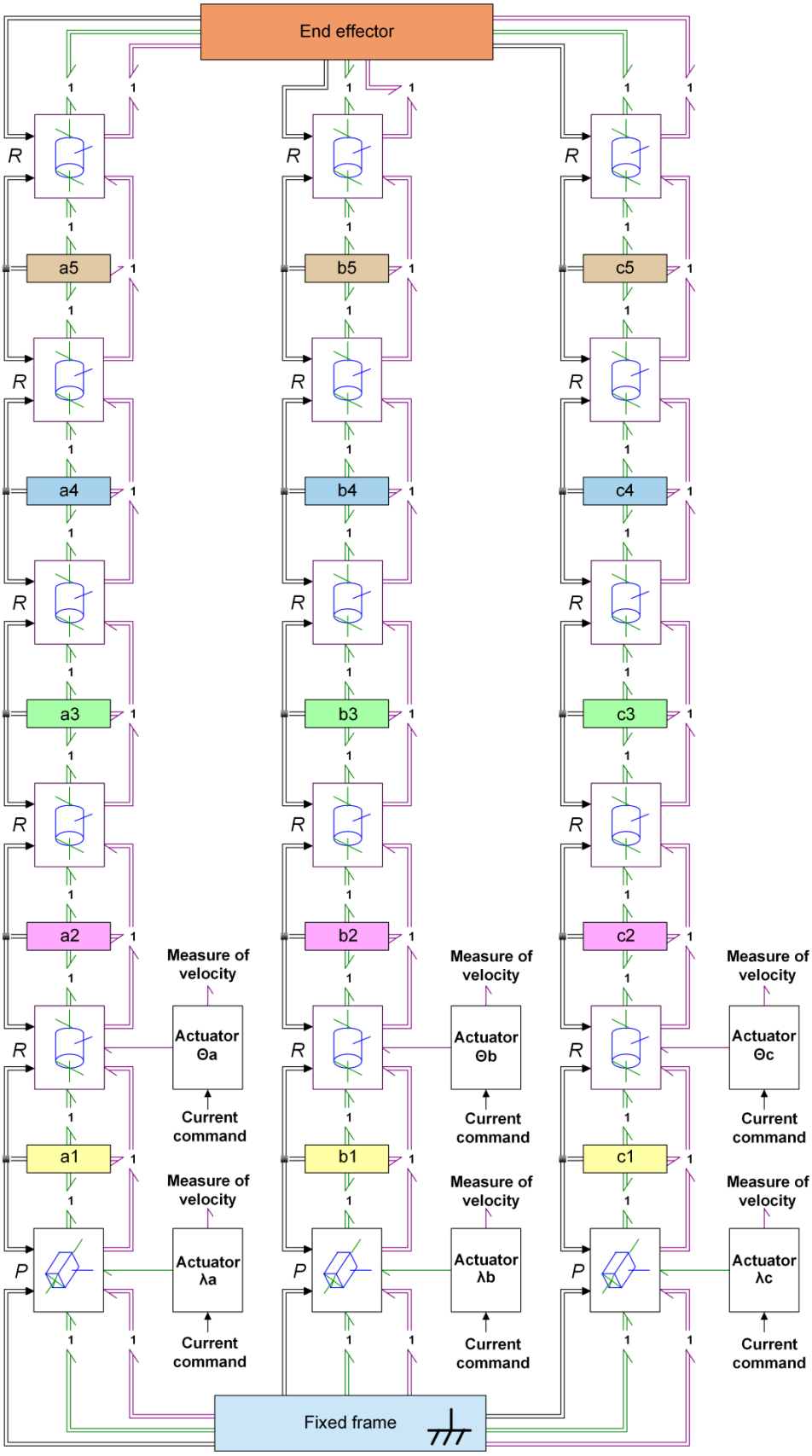


Figure 4: Full physical model of the 3-CRS

https://doi.org/10.3311/ECCOMASMBD2021-192

## 4 CONTROL PRINCIPLE OF THE 3-CRS ROBOT

The control principle of the 3-CRS is described in the red box of Figure 5 and it is composed of two main sections:

– A trajectory generation (strategy control) computing the end effector's coordinate setpoints (X, Y, Z, $\alpha$, $\beta$, $\gamma$) and a following Inverse Geometric Model (IGM) to compute the corresponding joint parameters ($\lambda$a, $\theta$a, $\lambda$b, $\theta$b, $\lambda$c, $\theta$c).

- A robot controller (axis regulation loop) that computes each motor current so as to move the end-effector of the robot to the desired pose (position and orientation).

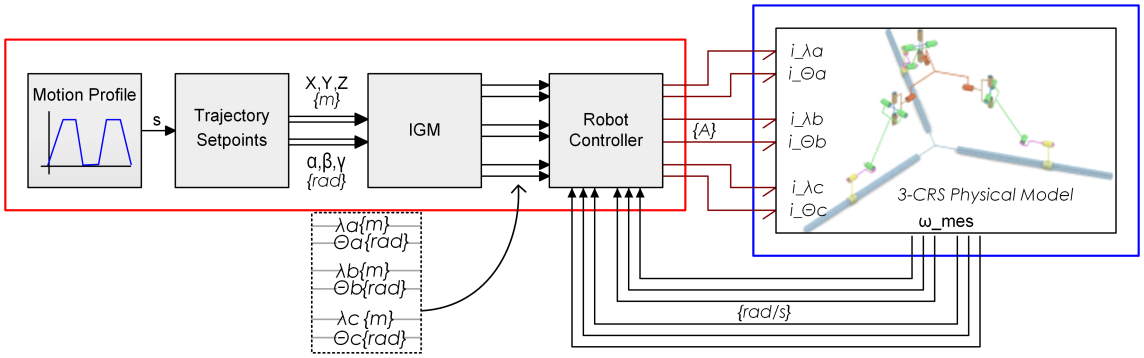


Figure 5: Full model of the 3-CRS

### 4.1 Trajectory generation

**Linear interpolation** The "Motion Profile" block on the left-hand side of Figure 5 has only one output named $s$. This is a coefficient evolving from 0 to 1 along a predefined curve. This coefficient defines how fast the robot should go from its initial position $p_i$ to its final position $p_f$.

The spacial trajectory generation is computed by the block "Trajectory Setpoints". This block uses the path primitive method and generates a rectilinear path to the setpoint. Therefore, as a function of the coefficient $s$, the pose $p$ of the end-effector, and hence both the position and the orientation can be written as:

$$p(s) = p_i + \frac{s}{||p_f - p_i||}(p_f - p_i) \tag{1}$$

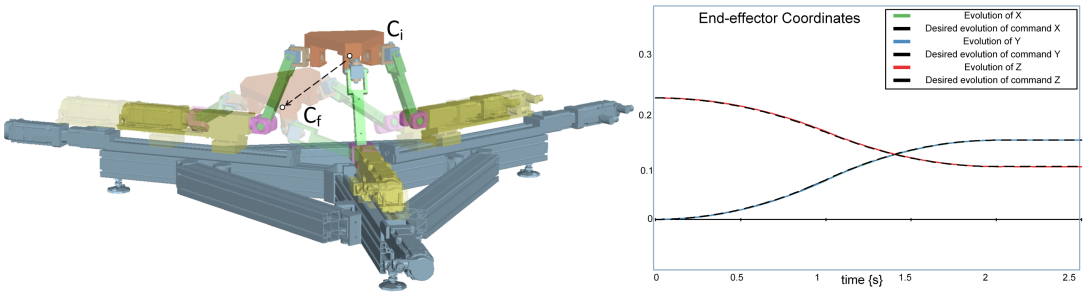


Figure 6: Evolution of the coordinates of the end-effector's COM

**Inverse Geometric Model (IGM)** The "IGM" block converts the end-effector pose given as an input into the six actuated joints parameters (3 positions and 3 angles). Through an analytical study and using transformation matrices, the IGM of the robot is explicitly solved (not presented here for the sake of conciseness). For one position of the effector, there are four possible configurations on each arm leading to 64 sets of solutions for the robot. This block ensures to select one of them and outputs their numerical value. These six joint parameters are finally used to determine the joint setpoints used in the "Robot Controller" block. The theory behind the inverse geometric model has first been presented by Bouzgarrou [20] and will be detailed further in an upcoming paper.

https://doi.org/10.3311/ECCOMASMBD2021-192

### 4.2 Axis regulation loop

For each actuated joint, the axis regulation loop is composed of two control law: A proportional control law regulates the position and a proportional-integral (PI) control law is dedicated to speed regulation. There are two axis regulation loops per arm : the first one controls the prismatic joint's linear position $\lambda$ $(m)$ and speed $\dot{\lambda}$ $(m.s^{-1})$ and the second one controls the rotational joint's angular position $\theta$ $(rad)$ and speed $\dot{\theta}$ $(rad.s^{-1})$. An example of prismatic joint controller is displayed on Figure 7.

The first objective of the axis regulation loops is to get a response with zero static error. In terms of dynamic performance, the goal is to give the fastest response with no overshoot. The value of settings of the controllers have been determined analytically. The "Robot controller" block contains three identical prismatic joint controllers (Figure 7) as well as three revolute joint controllers.

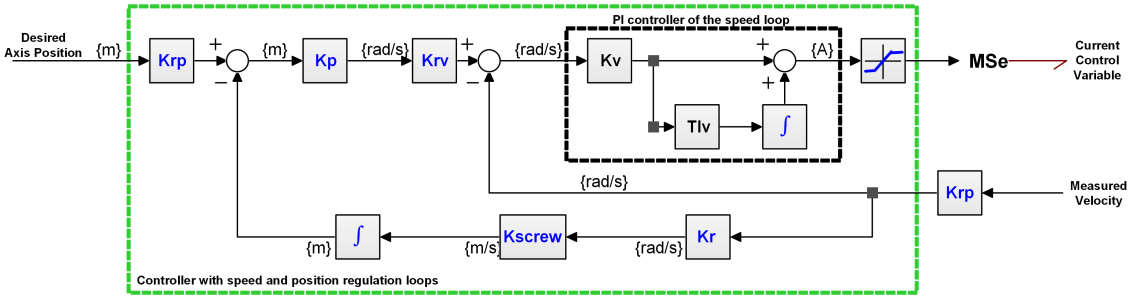


Figure 7: Axis regulation loop of an actuator

## 5 SIMULATION RESULTS

### 5.1 Minimum response time of the 3-CRS

For the sake of simplicity, the three prismatic joint's actuators will be referred to as "$\lambda$-actuators". Following the same principle, the rotational joint's actuators will called "$\theta$-actuators".

Even though the controllers have been set to give the fastest response with no overshoot, there will be a threshold called minimal reconfiguration time $\Delta t$ of the robot under which the behavior of the robot will be unreliable. Such a limit is expected to be due to inertia effects and to the motor's torque overload.

On Figure 8, the value of $\Delta t$ is slowly decreased until a significant overshoot appears on the system's response on either actuator. From there, the behaviour of the robot can be considered as unreliable and the threshold can be quantified. For values of $\Delta t$ superior to 0.4 seconds, the maximum overshoot can be found on the $\lambda$-actuators and does not exceed 0.5 millimeters, equivalent to a 0.2% error. However, when setting the response time to 0.3 seconds, the overshoot on this actuator skyrockets to 4 millimeters, approaching 2% of error.
Therefore, the minimum response time of the model can be set to 0.4 seconds.

Even with such a value of $\Delta t$, Figure 8(a) shows that the motors have not yet reached their maximum speed as the response still follows the command faithfully. This observation confirms that the threshold of 0.4 seconds is due to inertia and torque overload. Ignoring the fact that the robot will not follow the desired position, it is possible to decrease even more the response time to find the joints' maximum speed and acceleration.

https://doi.org/10.3311/ECCOMASMBD2021-192

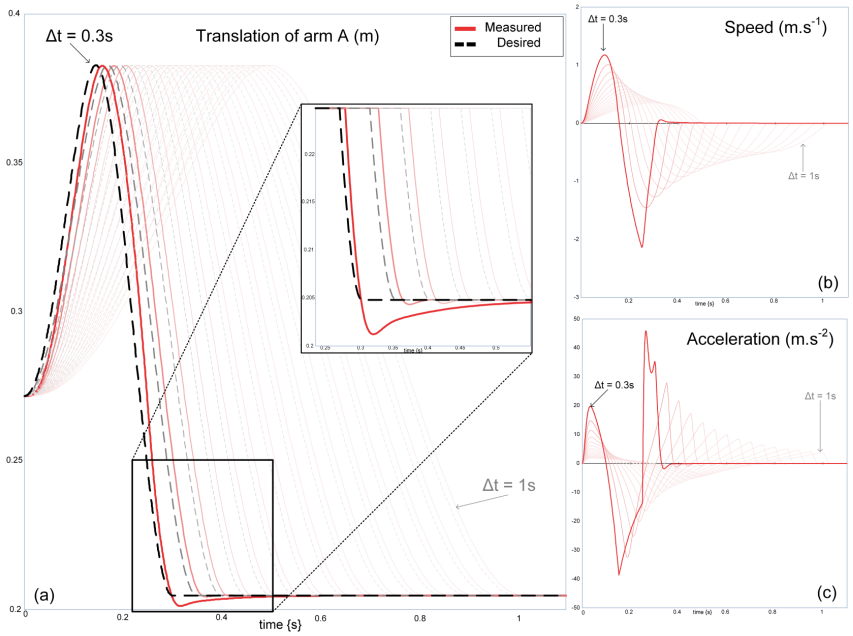


Figure 8: Behaviour of a $\lambda$-actuator for $\Delta t$ between 1s and 0.3s

### 5.2 Torque developed by the motors

This section will be dedicated to complete the study of the response time of the 3-CRS. In Section 5.1 the authors have stated that the position overshoot seen in Figure 8 for $\Delta t$ under 0.4 seconds was due to the motor's torque overload. Figure 9 confirms that statement. Indeed, this figure shows that a torque saturation appears on the motor's $\lambda$-actuators at 7.99 $N.m$ for $\Delta t$ equal to 0.3 seconds. The same figure could be drawn for the $\theta$-actuators but in this range, the torque saturation has not appeared yet.

This torque limit value of 7.99 $Nm$ comes from the modeling of the motors. As the AC synchronous motors' electrical part has been modeled by a simple gain $K_t$ corresponding to the motor's torque sensitivity, the motors' torque is proportional to the phase RMS input current. Figure 7 shows that a current limitation has been built in the controller. Therefore, the torque reaches a limit whenever the current is at its maximum. The values of peak current and torque sensitivity have been determined thanks to the motor's data sheet. This behaviour unveils the limits of this simple AC motor model. Assuming that the electrical part of the motor is perfect, it leads to a model that has better performances than the real motor. This difference is visible in the data sheet which displays a 6.6 $Nm$ torque peak. For this reason, a more advanced model of the AC synchronous motors is already being developed.

Finally, this torque analysis challenges the accuracy of the 0.4 seconds threshold defined in the previous section. But, further analysis have shown that the real torque limit of 6.6 $Nm$ was not reached until $\Delta t$ was decreased to 0.38 seconds. Therefore, not only does the torque analysis confirms the previously defined value, but its also improves its accuracy. The response time threshold can therefore be fixed to 0.39 seconds.

https://doi.org/10.3311/ECCOMASMBD2021-192

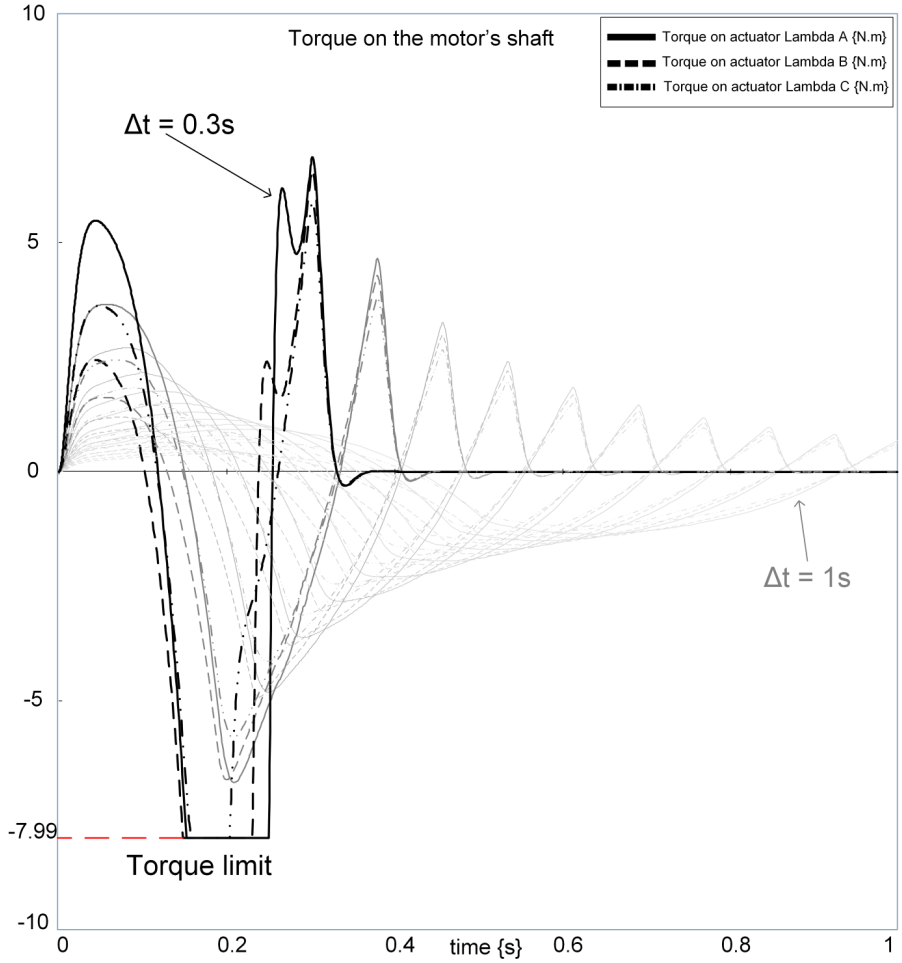


Figure 9: Torque developed by the motors on the $\lambda$-actuators.

## 6 CONCLUSIONS

The different steps to model the complex 3-CRS parallel robot in BG with a modular approach have been presented.

Thanks to its graphical and oriented object features, the BG allows a modular modeling approach which can be efficient in the context of designing new parallel robots with different topologies. The BG is also a well adapted tool for modeling mechatronic systems. Complete AC electrical actuators could be integrated in the same model.

Dynamic simulations have been presented and used to analyze different robotic issues (minimum response time of the 3-CRS and torques developed by the motors).

## REFERENCES

[1] Adrien Koessler, Nicolas Bouton, Sébastien Briot, Belhassan Chedli Bouzgarrou, and Youcef Mezouar. Linear adaptive computed torque control for singularity crossing of parallel robots. In *ROMANSY 22–Robot Design, Dynamics and Control*, pages 222–229. Springer, 2019.

[2] Adrien Koessler, Alexandre Goldsztejn, Sébastien Briot, and Nicolas Bouton. Dynamics-based algorithm for reliable assembly mode tracking in parallel robots. *IEEE Transactions on Robotics*, 36(3):937–950, 2020.

[3] Asia Maamar, Belhassen Chedli Bouzgarrou, Vincent Gagnol, and Raouf Fathallah. Time

domain stability analysis for machining processes. In *Advances in Acoustics and Vibration*, pages 77–88. Springer, 2017.

[4] Ashaf Zeid and Chih-Hung Chung. Bond graph modeling of multibody systems: a library of three-dimensional joints. *Journal of the Franklin Institute*, 329(4):605–636, 1992.

[5] Ashaf Zeid and James L. Overholt. Singularly perturbed formulation : explicit modeling of multibody systems. *Journal of The Franklin Institute*, 332(1):21–45, 1995.

[6] Wilfrid Marquis-Favre and Serge Scavarda. Bond graph representation of multibody systems with kinematic loops. *Journal of the Franklin Institute*, 335B(4):643–660, 1998.

[7] P.J. Gawthrop. Bicausal bond graphs. In *ICBGM*, GAW95.

[8] P.J. Gawthrop. Physical interpretation of inverse dynamics using bi-causal bond graphs. *Journal of Franklin Institute*, pages 743–769, 2000.

[9] Roger Ngwompo. Bond graph methodology for the design of an actuating system : application to a two-link manipulator. *IEEE*, 1997.

[10] Roger Ngwompo, Serge Scavarda, and Daniel Thomasset. Physical model-based inversion in control systems design using bg representation - theory. *Proceedings of the Institution of Mechanical Engineers, Part I: Journal of Systems and Control Engineering*, 215(2):95–103, 2000.

[11] Roger Ngwompo, Serge Scavarda, and Daniel Thomasset. Physical model-based inversion in control systems design using bond graph representation - application. *Proceedings of the Institution of Mechanical Engineers, Part I: Journal of Systems and Control Engineering*, 2000.

[12] Tulga Ersal. *Realization-preserving simplification and reduction of dynamic system models at the graph level*. Thèse de doctorat, 2007.

[13] Ersal Tulga. Structural simplification of modular bg models based on junction inactivity. *Elsevier Simulation Modelling Practice and Theory*, pages 175–196, 2009.

[14] T. Ersal, H. Fathy, and J. L. Stein. Realization-preserving structure and order reduction of nonlinear energetic system models using energy trajectory correlations. *Journal of Dynamic Systems, Measurement and Control*, 2009.

[15] L. S. Louca, D. G. Rideout, T. Ersal, and J. L. Stein. *Energy based bond graph reduction*. Springer, 2011.

[16] Benjamin Boudon, François Malburet, and Jean-Claude Carmona. Simulation of a helicopter's main gearbox semiactive suspension with bond graphs. *Multibody System Dynamics*, 40(4):375–405, 2017.

[17] Benjamin Boudon, Thu Thuy Dang, Rebecca Margetts, Wolfgang Borutzky, and François Malburet. Simulation methods of rigid holonomic multibody systems with bond graphs. *Advances in Mechanical Engineering*, 11(3):1687814019834153, 2019.

[18] Khaled Assad Arrouk, Belhassen Chedli Bouzgarrou, and Grigore Gogu. Cad based techniques for workspace analysis and representation of the 3crs parallel manipulator. In *19th International Workshop on Robotics in Alpe-Adria-Danube Region (RAAD 2010)*, pages 155–160. IEEE, 2010.

[19] Anh Vu Nguyen, Belhassen Chedli Bouzgarrou, Karine Charlet, and Alexis Béakou. Static and dynamic characterization of the 6-dofs parallel robot 3crs. *Mechanism and machine theory*, 93:65–82, 2015.

[20] Chedli Bouzgarrou, Adrien Koessler, and Nicolas Bouton. Singularity analysis and reconfiguration mode of the 3-crs parallel manipulator. In *2020 IEEE International Conference on Robotics and Automation (ICRA)*, pages 10384–10390. IEEE, 2020.

[21] H. M. Paynter. *Analysis and Design of Engineering systems*. MIT Press, Cambridge, 1961.

[22] D. C. Karnopp, D. L. Margolis, and R. C. Rosemberg. *System Dynamics - Modeling and Simulation of Mechatronics Systems*. John wiley sons edition, 2000.

[23] Wolfgang Borutzky. *Bond Graph Methodology - Development and Analysis of Multidisciplinary Dynamic System Models*. Springer-Verlag, London, springer edition, 2010.

[24] M.J.L. Tiernego and A.M. Bos. Modelling the dynamics and kinematics of mechanical systems with multibond graphs. *Journal of the Franklin Institute*, 319:37–50, 1985.

[25] Sergio JUNCO, Gonzalo DIEGUEZ, and Facundo RAMIREZ. Une librairie 20sim pour la simulation basée bond graphs de systèmes de commande de machines électriques. In *Conférence Internationale Francophone d'Automatique (CIFA)*, JUN08.

[26] Li Teng, Liu Yanjie, and Sun Lining. Bond graph model of permanent magnet linear synchronous motor. In *2010 2nd International Conference on Industrial and Information Systems*, volume 2, pages 128–131. IEEE, 2010.

[27] Matías A Nacusse and Sergio J Junco. Switchable structured bond: A bond graph device for modeling power coupling/decoupling of physical systems. *Journal of Computational Science*, 5(3):450–462, 2014.

https://doi.org/10.3311/ECCOMASMBD2021-168



# Desensitized motion planning for underactuated multibody systems

Paolo Boscariol, Dario Richiedei

Dipartimento di Tecnica e Gestione dei Sistemi Industriali
Università degli Studi di Padova
Stradella S. Nicola 3, 36100 Vicenza, Italy
paolo.boscariol@unipd.it
dario.richiedei@unipd.it

**FULL PAPER**

## 1 Abstract

Model-plant mismatches can severely limit the effectiveness of conventional model-based motion design methods. To solve this issue, a method for robust trajectory planning that can reduce the effects of parametric uncertainties is presented in this work. The method is based on an indirect variational formulation, which is translated into a Two-Point Boundary Value Problem (TPBVP) and then solved numerically. Robustness is obtained by incorporating into the problem the sensitivity functions of the plant, and imposing some additional constraints on the initial and final points of the trajectory. A formulation aimed at reducing both the residual and the transient oscillations, as well as keeping small the control effort, is also proposed. The work presents a numerical verification of the effectiveness of the method for an underactuated system, such as a double-pendulum crane, by showing its effectiveness and robustness when performing fast rest-to-rest motions.

## 2 Introduction

High-speed and precise motion of underactuated multibody systems is challenging since this kind of mechatronic systems requires suitable trajectory profiles for limiting the vibrations that can incur both during the motion and after motion completion. The problem has been dealt with in countless works, facing it either as a control design problem or as a motion design problem. The latter approach might be convenient in all applications in which the use of a sophisticated control technique is limited by the unavailability of high-bandwidth sensors [1]. A common classification of the vast literature on motion design marks the distinction between model-free and model-based approaches. The first ones are mainly based on the use of properly interpolated time laws to define either the motion in the joint space or in the operational space. Vibration reduction and precise tracking are enforced by minimizing kinematic quantities, such as the jerk, or mixed performance indexes, thus enhancing the smoothness of the motion profile [2, 3]. Such methods are often of convenient application due to their rather simple implementation and for being suitable to a wide range of applications.

Model-based planning methods, in contrast, rely on the exploitation of the dynamic model of the manipulator for which the reference inputs are planned. Among model-based methods, it is common to cast motion design problem as an optimal control one, thus allowing to employ the results of an extensive and mature literature [4]. The motion design methods rooted in optimal control can further be split between direct and indirect methods.

Direct methods use a proper discretized description of the kinematic quantities of the multibody system to translate an optimal control problem into a parameter optimization one [5]. The resulting finite-dimensional problem is therefore solvable using one of the many parametric optimization algorithms.

Indirect methods are instead based on calculus of variations, which is used to set-up and solve the motion design problem as a Two-Point Boundary Value Problem (TPBVP). Successful applications of this methods are found, among others, for flexible link robots [6], flexible joint robots [7], mobile robots [8], lumped spring-mass systems with nonlinear springs [9], and for cable-driven robots [10], [11], [12] . Indirect control methods are generally chosen for their accuracy [4], however their field of application is often limited to small scale problems by the difficulty of finding a numerical solution of the problem under investigation. This limitation is commonly referred to as the 'curse of dimensionality' [13]. Additionally, most of the indirect methods proposed so far have limited robustness to mismatches between the description of the plant used for planning and the actual system dynamics. This problem has been extensively dealt with in the field of closed-loop control, while it has received less attention in the field of motion planning. Among the few works that, to the best of authors' knowledge, focus explicitly on robust motion design, one is [14], in which the optimization problem is mode robust by introducing in the cost function a Gaussian cumulative noise term. Another relevant work is [15], in which the authors take into account the effects of a varying payload on the motion design through the modification of bounds on the joint torques.

A different approach to model-based motion planning is the well-known input shaping technique. Input shaping motion planning techniques work by convolving a reference signal, either a position reference or a force reference, with a baseline of impulses to ensure reduced residual vibrations. The popularity of shaping filters is motivated by their very straightforward implementation and for being suitable to a wide range of applications, such as in the movement of suspended loads [16], [17]. Shaping techniques can be, however, unsuitable in some applications, such as the ones in which the time delay required by the shaping action is close

to the specified motion time dictated by the application. The issue of robustness of input shaping has been also widely discussed, leading to several robust versions such as the ZVD shaper [18]. Increasing robustness however exacerbates the aforementioned problem of the delayed response.

This work proposes an indirect approach to robust motion planning in underactuated multibody systems. By exploiting the mathematical frame proposed in [19] for inverse dynamics, and then extended in [20], the method computes the optimal reference trajectory for rest-to-rest motion of an underactuated multibody system to accomplish several design tasks. First, it should ensure reduced transient load oscillation, both in term of peak and average value, even in the execution of fast motions. Secondly, reduced control effort is required, in term of reduced amplitude and harmonic content of the required accelerations for the actuated coordinates. Finally, robustness with respect to an uncertain critical parameter should be granted. The numerical results obtained provide a clear evidence of the improved capability of the proposed method over similar input shaping methods when dealing with fast motion applications.

## 3 System model formulation

Let $n$ be the number of degrees of freedom of the system under investigation and given a proper choice of a vector of $n$ independent coordinates $\mathbf{q}$, a set of $n$ nonlinear ordinary differential equations is used to describe its dynamics:

$$\mathbf{M}(\mathbf{q})\ddot{\mathbf{q}}(t) = \mathbf{K}(\mathbf{q}) + \mathbf{G}(\mathbf{q},\dot{\mathbf{q}}) + \mathbf{B}(\mathbf{q})\mathbf{F}(t) \tag{1}$$

$\mathbf{M} \in \Re^{n\times n}$ is the mass matrix, $\mathbf{K} \in \Re^{n}$ is the vector of position-dependent forces while vector $\mathbf{G} \in \Re^{n}$ collects gyroscopic and centrifugal forces as well as the damping forces. The vector of the external actuation and control forces $\mathbf{F} \in \Re^{m}$ is input into the system dynamics through the force distribution matrix $\mathbf{B} \in \Re^{n\times m}$. Since $m < n$, the system is underactuated. The dynamic model in (1) can be rewritten by partitioning $\mathbf{q}$ into the vector of $m$ actuated generalized coordinates, and the vector $\mathbf{q}_u$ of the $n-m$ unuactuated ones [21]:

$$\begin{bmatrix} \mathbf{M}_{aa} & \mathbf{M}_{au} \\ \mathbf{M}_{au}^T & \mathbf{M}_{uu} \end{bmatrix} \begin{bmatrix} \ddot{\mathbf{q}}_a \\ \ddot{\mathbf{q}}_u \end{bmatrix} = \begin{bmatrix} \mathbf{K}_a(\mathbf{q}) \\ \mathbf{K}_u(\mathbf{q}) \end{bmatrix} + \begin{bmatrix} \mathbf{G}_a(\mathbf{q},\dot{\mathbf{q}}) \\ \mathbf{G}_u(\mathbf{q},\dot{\mathbf{q}}) \end{bmatrix} + \begin{bmatrix} \mathbf{B}_a \\ 0 \end{bmatrix} \mathbf{F} \tag{2}$$

This reformulation highlights that the motion of the unactuated coordinates is excited by the motion of the actuated ones, while is not directly affected by the external forces $\mathbf{F}$:

$$\ddot{\mathbf{q}}_u = \mathbf{M}_{uu}^{-1}(\mathbf{K}_u + \mathbf{G}_u) - \mathbf{M}_{uu}^{-1}\mathbf{M}_{au}^T\ddot{\mathbf{q}}_a \tag{3}$$

As far as the motion of the actuated coordinates is concerned, it is excited and controlled by the $m$ actuation forces collected in $\mathbf{F}$, and can be perturbed by the motion of the unactuated coordinates. However, the use of effective controllers in the actuators, that ensure high bandwidth and effective disturbance rejection (such as high gain controllers, feedforward or load observer schemes), allows the actuators to get rid of the elastic dynamics of the unactuated degrees of freedom. A similar result is obtained in the case of small inertia ratios, i.e. whenever the reflected load inertia is smaller than those of the actuators. Hence, the motion the actuated coordinates can be interpreted as the external and independent input for the dynamics of the unactuated ones. One one hand, it can excite the oscillating dynamics of the unactuated subsystem; on the other one, a proper design of such a motion can lead to reduced undesired vibrations. Under these hypotheses, the problem of optimal motion planning for load vibration control can just rely on the subsystem model in (3) in lieu of the full system model (1).

A simplified model of the actuators dynamics is instead included in the model adopted for motion planning, to account for their finite bandwidths that do not allow tracking high frequency components of the reference trajectory. The actual acceleration of the actuated coordinates is therefore written as a function of the reference acceleration $\ddot{\mathbf{q}}_a^{ref}(t)$:

$$\ddot{\mathbf{q}}_a(t) = \mathbf{h}(\ddot{\mathbf{q}}_a^{ref}(t)) \tag{4}$$

The overall dynamic model adopted for the trajectory synthesis is therefore the following one, where the exogenous input is $\ddot{\mathbf{q}}_a^{ref}(t)$:

$$\begin{bmatrix} \ddot{\mathbf{q}}_u \\ \ddot{\mathbf{q}}_a \end{bmatrix} = \begin{bmatrix} \mathbf{M}_{uu}^{-1}(\mathbf{K}_u(\mathbf{q}) + \mathbf{G}_u(\mathbf{q},\dot{\mathbf{q}})) \\ 0 \end{bmatrix} + \begin{bmatrix} -\mathbf{M}_{uu}^{-1}\mathbf{M}_{au}^T \\ \mathbf{I} \end{bmatrix} \mathbf{h}(\ddot{\mathbf{q}}_a) \tag{5}$$

The re-formulation proposed in (5) is suitable to compute, as the output of the design algorithm, the reference profile $\mathbf{q}_{ref}$ for commanding each actuator. This approach has three paramount advantages over the use of the full dynamic model. First of all,

it reduces the number of uncertain parameters and does not need precise models of friction forces on the actuated coordinates, which are instead required if optimal motion planning is aimed at computing the optimal control force (i.e. an inverse dynamics problem) to ensure no steady-state errors. The computation of the control forces to be exerted by the actuators is here demanded to the axis control of each actuator (e.g. to its native controller). The second advantage is that smaller models are more reliable under a computational point of view, being usually better conditioned. Finally, the optimal reference for the actuated coordinates can be used as the position reference of the actuators even if the native position and speed controllers are adopted. Indeed, these 'closed' proprietary control schemes cannot be usually modified in industrial mechatronic systems and they are often designed to accept a position reference signal as the only exogenous input.

A simple and effective way to model $\mathbf{h}$ in (5) is to approximate it through its dominant poles. This is one of the few, if not the only, available options when the manufacturers' data sheet provide little or no information on the actuation and control implementation. If the closed-loop system is nearly critically damped, the closed-loop bandwidth value can be incorporated just through the time constant $\tau$ of the first-order linear model:

$$\dddot{\mathbf{q}}_a(t) = -\frac{1}{\tau}\ddot{\mathbf{q}}_a(t) + \frac{1}{\tau}\ddot{\mathbf{q}}_a^{ref}(t) \tag{6}$$

In practice, $\tau$ behaves also as a smoothing parameter that can be also wisely tuned to reduce the harmonic content of the reference trajectory. The inclusion of (6) into (5) requires augmenting the state vector with $\ddot{\mathbf{q}}_a$ as follows:

$$\begin{bmatrix} \dddot{\mathbf{q}}_u \\ \ddot{\mathbf{q}}_a \end{bmatrix} = \begin{bmatrix} \mathbf{M}_{uu}^{-1}\left(\mathbf{K}_u(\mathbf{q}) + \mathbf{G}_u(\mathbf{q},\dot{\mathbf{q}})\right) - \mathbf{M}_{uu}^{-1}\mathbf{A}_{au}^T\ddot{\mathbf{q}}_a \\ -\dfrac{\ddot{\mathbf{q}}_a}{\tau} \end{bmatrix} + \begin{bmatrix} 0 \\ \dfrac{1}{\tau} \end{bmatrix} \ddot{\mathbf{q}}_a^{ref} \tag{7}$$

This model formulation can be finally cast to fit the classical form of a set of first-order ordinary differential equations, as required for solving the trajectory optimization problem, with $\mathbf{u}$ the control vector and $\mathbf{x}$ the state vector:

$$\mathbf{u} = \ddot{\mathbf{q}}_a^{ref}; \qquad \mathbf{x} = [\dot{\mathbf{q}}_u, \ddot{\mathbf{q}}_a, \dot{\mathbf{q}}_a, \mathbf{q}_u, \mathbf{q}_a]^T; \qquad \dot{\mathbf{x}} = \mathbf{f}(\mathbf{x}, t, \mathbf{u}); \tag{8}$$

## 4 Variational formulation of robust trajectory planning

The formulation of the proposed robust trajectory problem applies to point-to-point motion, for which the initial and the final configurations of the system are the obvious choice as the 'left' and 'right' boundary conditions [4]. Since the state trajectory is free between the two boundary points, and hence an infinite number of trajectories connecting them can be defined, the proposed approach aims at finding the one that minimizes a suitable cost function $J$:

$$J = \int_{t_0}^{t_f} g\,(\mathbf{x}, t, u)\,dt \tag{9}$$

The scalar function $g$ can be chosen arbitrarily to fulfill the required goals of the trajectory design. By combining the cost function with the two boundary conditions on $\mathbf{x}(t)$ and treating the system model as a constraint, the following optimization problem is defined:

$$\begin{cases} \min J(\mathbf{x}(t), t, \mathbf{u}) = \min \displaystyle\int_{t_0}^{t_f} g(\mathbf{x}, t, \mathbf{u})dt \\ \\ subject\ to: \\ \mathbf{x}(t_0) = \mathbf{x}_0; \qquad \mathbf{x}(t_f) = \mathbf{x}_f; \\ \dot{\mathbf{x}}(t) = \mathbf{f}(\mathbf{x}, t, \mathbf{u}); \end{cases} \tag{10}$$

The most common way to solve such problem is to use the calculus of variations, such as the Pontryagin's Minimum Principle (PMP) [22]. To improve the optimization problem in (10) with robustness specifications, it can be augmented with some sensitivity functions, as suggested in the previous work of one of the Authors [19].

Let us assume that the dynamic model of the system is affected by the uncertain scalar parameter $\mu$, and therefore eq. (8) can be written as:

$$\dot{\mathbf{x}}(t) = \mathbf{f}\,(\mathbf{x}, t, \mathbf{u}, \mu) \tag{11}$$

If $\mathbf{f}$ is continuous in $(\mathbf{x}, t, \mu)$ and is continuously differentiable with respect to $\mathbf{x}$ and $\mu$ for any value of $(\mathbf{x}, t, \mu)$ in the interval $[t_0, t]$, then the system response $\mathbf{x}(t, \mu)$ can be evaluated as:

$$\mathbf{x}(t, \mu) = \mathbf{x}(t_0) + \int_{t_0}^{t} \mathbf{f}(s, \mathbf{x}(s), \mu)ds \tag{12}$$

https://doi.org/10.3311/ECCOMASMBD2021-168

Since the latter is differentiable, the partial derivative of the state with reference to the uncertain parameter $\mu$, denoted as $\mathbf{S}(t)$, can be computed as:

$$\mathbf{S}(t) = \frac{\partial \mathbf{x}(t)}{\partial \mu} = \int_{t_0}^{t} \left[ \frac{\partial \mathbf{f}(s, \mathbf{x}(s,\mu), \mu)}{\partial \mathbf{x}} \frac{\partial \mathbf{x}(s,\mu)}{\partial \mu} + \frac{\partial \mathbf{f}(s, \mathbf{x}(s,\mu), \mu)}{\partial \mu} \right] ds \tag{13}$$

$\mathbf{S}(t)$ describes how the system response is affected by the deviation of $\mu$ from its nominal value $\mu_0$. One way to obtain small sensitivity is to enforce its amplitude at the "critical" time instants of the motion, such as the initial and final ones $t_0$ and $t_f$. To do so, the motion design problem (10) should be re-cast by augmenting the dynamic model and the state vector:

$$\dot{\mathbf{x}}^r(t) = \mathbf{f}^r(\mathbf{x}, \mathbf{S}, t, \mathbf{u}, \mu) = \left[ \begin{array}{c} \mathbf{f}(\mathbf{x}, t, \mathbf{u}, \mu) \\ \dfrac{\partial \mathbf{f}(\mathbf{x}, t, \mathbf{u}, \mu)}{\partial \mu} \end{array} \right]_{\mu=\mu_0} \tag{14}$$

$$\mathbf{x}^r(t) := \left[ \begin{array}{c} \mathbf{x}(t) \\ \mathbf{S}(t) \end{array} \right] \tag{15}$$

The 'robustification' (or 'desensitization') procedure through the inclusion of sensitivity functions therefore leads to the definition of the robust optimization problem of eq. (16):

$$\left\{ \begin{array}{l} \min J^r(\mathbf{x}^r, t, \mathbf{u}) = \min \displaystyle\int_{t_0}^{t_f} g^r(\mathbf{x}^r, t, \mathbf{u}, \mu) dt \\ subject\ to: \\ \mathbf{x}(t_0) = \mathbf{x}_0; \quad \mathbf{x}(t_f) = \mathbf{x}_f; \\ \mathbf{S}(t_0) = 0; \quad \mathbf{S}(t_f) = 0; \\ \dot{\mathbf{x}}(t) = \mathbf{f}(\mathbf{x}(t), t, \mathbf{u}, \mu); \quad \dot{\mathbf{S}}(t) = \dfrac{\partial \mathbf{f}(\mathbf{x}(t), t, \mathbf{u})}{\partial \mu}; \end{array} \right. \tag{16}$$

The optimization problem in eq. (16) can be solved using the Pontryagin's Minimum Principle (PMP), which exploits the Hamiltonian of the system:

$$\mathscr{H} = g^r + \boldsymbol{\lambda}^T \mathbf{f}^r(\mathbf{x}^r, t, \mathbf{u}) \tag{17}$$

The Hamiltonian function includes the vector of Lagrangian multipliers $\boldsymbol{\lambda} \in R^N$ to constrain the solution to the system dynamics. The three conditions imposed by the PMP are then:

$$\dot{\mathbf{x}} = \frac{\partial \mathscr{H}}{\partial \boldsymbol{\lambda}}; \qquad \dot{\boldsymbol{\lambda}} = -\frac{\partial \mathscr{H}}{\partial \mathbf{x}}; \qquad \frac{\partial \mathscr{H}}{\partial \mathbf{u}} = 0; \tag{18}$$

This problem is usually solved numerically through collocation [23] or shooting techniques [24]. Analytic solutions are usually practical only for simple problems.

## 5 Model of the application example

The underactuated multibody system under investigation consists of two masses ($m_1$ and $m_2$) suspended to a translating cart through two ropes, whose lengths are $L_1$ and $L_2$. The following values have been assumed: $m_1 = 0.192$ kg, $m_2 = 0.201$ kg, $L_1 = 0.470$ m, $L_2 = 0.391$ m, $\tau = 0.1$ s. The motion to be performed is, for all tests, a rest-to-rest displacement with 0.3 m amplitude to be completed in 3 s. According to Fig. 1, the cart position is denoted $y_{cart}$, while the angular displacement of the two masses are defined through angles $\theta_1$ and $\theta_2$. Using $u(t) = \ddot{y}_{cart}^{ref}$ as the input of the dynamic model of the subsystem representing the load, the dynamic model can be specified, according to the notation of (7), by the following matrices:

$$\mathbf{B}_a = 1; \quad \mathbf{K}_a = 0; \quad \mathbf{G}_a = 0; \tag{19}$$

$$\mathbf{M}_{au} = \left[ \begin{array}{cc} L_1(m_1 + m_2(1 + L_2\cos(\theta_2))) & m_2 L_2 \cos(\theta_2) \\ L_1\cos(\theta_2) + L_2 & L_2 \end{array} \right] \tag{20}$$

$$\mathbf{K}_u = \left[ \begin{array}{c} -g(m_1+m_2)\sin(\theta_1) + \ddot{y}_{cart}(m_1+m_2)\cos(\theta_1) \\ -g\sin(\theta_1+\theta_2) + \ddot{y}_{cart}\cos(\theta_1+\theta_2) \end{array} \right] \tag{21}$$

https://doi.org/10.3311/ECCOMASMBD2021-168

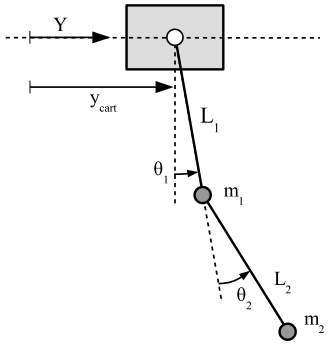


Figure 1: Kinematic model of the double-pendulum crane

$$\mathbf{G}_u = \begin{bmatrix} m_2 L_2(\dot{\theta}_1^2 + \dot{\theta}_2^2)\sin(\theta_2) \\ -L_1^2\dot{\theta}_1^2\sin(\theta_2) \end{bmatrix} \tag{22}$$

The first-order model required for trajectory planning is based on the following state vector:

$$\mathbf{x}(t) = \left[\ddot{y}_{cart}, \dot{\theta}_1, \dot{\theta}_2, \dot{y}_{cart}, \theta_1, \theta_2, y_{cart}\right]^T \tag{23}$$

The 'robustification' is made with respect to $L_1$, which significantly affects both natural frequencies $\omega_1$ and $\omega_2$ [16]. The augmented state vector is therefore:

$$\mathbf{x}^r(t) = \left[\ddot{y}_{cart}, \dot{\theta}_1, \dot{\theta}_2, \dot{y}_{cart}, \theta_1, \theta_2, y_{cart}, \dot{s}_1, \dot{s}_2, s_1, s_2\right]^T \tag{24}$$

which includes the sensitivity functions:

$$\begin{aligned} s_1(t) &= \frac{\partial \theta_1(t)}{\partial L_1}; \qquad & s_2(t) &= \frac{\partial \theta_2(t)}{\partial L_1}; \\ \dot{s}_1(t) &= \frac{\partial \dot{\theta}_1(t)}{\partial L_1}; \qquad & \dot{s}_2(t) &= \frac{\partial \dot{\theta}_2(t)}{\partial L_1}; \end{aligned} \tag{25}$$

The sensitivity functions are evaluated analytically using (14) and (15). It should also be pointed out that the sensitivity function $\partial y_{cart}/\partial L_1$ and its time derivatives are not included in the model since they are always zero, being $y_{cart}(t)$ independent form $L_1$ in the model of the subsystem assumed here.

## 6 Load sway reduction: numerical results and comparison with input shapers

The performance evaluation of the proposed method is conducted through numerical simulation and the comparison with two benchmark input shaping methods: the Negative Zero Vibration (NZV) shaper [25], and the Zero Vibration Derivative (ZVD) shaper [26]. The goal of the motion planning is to design a motion profile for rest-to-rest motion with negligible residual and transient oscillations, as well as with enhanced robustness. The requirement of zero residual vibrations for the nominal case is obtained by imposing, in the optimization problem, null values for $\theta_1$, $\theta_2$ and for their time derivatives at final time $t_f$. As for the transient behaviour, it is required to reduce both the 'average' and the peak values of the relative displacement between the cart and the end-point mass, while ensuring reasonably small accelerations. To satisfy these requirements, function $g$ has been defined as follows:

$$g = \frac{1}{2}u^2 + \beta \exp\left(\left(\gamma(L_1\sin(\theta_1) + L_2\sin(\theta_1+\theta_2))\right)^2\right) \tag{26}$$

Such a definition of $g$ trades off between the reduction of the acceleration reference signal $u(t)$, i.e. the control effort, and the load oscillation, which is weighed by the positive scalar weight $\beta$ and by the scaling factor $\gamma$. The use of the exponential emphasizes the peaks of the oscillation in the cost function, thus keeping them small. In practice it roughly approximates a kind of *minmax* optimization problem within the frame of the classical optimal control, thus allowing for a straightforward numerical solution. The possibility of defining different objective functions to accomplish various secondary goals, besides the usual requirement of zero residual vibration, is an important advantage of the variational approach over input shaping. Indeed, input shaping motion planning techniques work by convolving an arbitrary reference signal with a sequence of impulses whose number, amplitudes and times of application depend on the natural frequency and damping of the vibrational modes to control, and on the desired robustness. Other control objectives, such as reduction of the transient oscillations and of the control effort, should be obtained by a clever selection of the original reference signal to be convolved with the shaper. The problem of reducing transient oscillations and control effort is exacerbated in three cases: if the desired motion time is comparable with the period of natural oscillation,

https://doi.org/10.3311/ECCOMASMBD2021-168

Table 1: Performance measurements

| Test | $\ddot{y}_{max}$ $[m/s^2]$ | $\ddot{y}_{RMS}$ $[m/s^2]$ | $\dddot{y}_{max}$ $[m/s^3]$ | $\dddot{y}_{RMS}$ $[m/s^3]$ |
|---|---|---|---|---|
| NZV | 0.2141 | 0.1299 | 1.6982 | 0.7381 |
| ZVD | 0.7067 | 0.3727 | 20.5333 | 6.0468 |
| TPBVP, $\beta = 0$ | 0.3337 | 0.1840 | 3.7308 | 10.0657 |
| TPBVP, $\beta = 20$ | 0.5571 | 0.2283 | 19.2325 | 3.6195 |
| TPBVP, $\beta = 50$ | 0.7030 | 0.2835 | 25.5660 | 4.2066 |

if the desired robustness increases, and in the presence of more vibrational modes to control. Indeed, the convolution of the unshaped reference with the shaper impulses introduces delays that are higher as the natural frequency decreases. The number of such impulses is higher for robust shapers and for multi-mode shapers. The latter, indeed, are obtained by cascading two or more shaping filters. Hence, the only way to retain the original motion time is to pre-compensate the delay by reducing the time duration of the reference signal prior to shaping. This feature can be a limiting factor when the overall time delay is comparable with the required motion time, since the unshaped motion profiles have very high accelerations that cause high transient oscillations.

In the proposed test case, both the shapers have been fed with a displacement reference profile described by a fifth-degree polynomial function, to ensure continuous accelerations, whose duration is set to compensate for the delay introduced by the shapers. Since $\omega_1 = 3.640\ rad/s$ and $\omega_2 = 9.017\ rad/s$ in the nominal model (null damping is assumed), the NZV shaper introduces a delay equal to 0.808 s, while the ZVD shaper delay is equal to 1.789 s. Hence, the total times for the unshaped motions should be set to 2.192 s and 1.211 s, respectively. Two sample values of $\beta$, i.e. $\beta = 0$ and $\beta = 50$, have been chosen to solve the TPVBP problem, to show how it affects the amplitude of the transient load oscillation. The scaling factor $\gamma$ is set to 50 for all tests, which has proved to produce a proper weighting factor for the sway angles $\theta_1$ and $\theta_2$. Moreover, it has been observed that using two variable weighting factor do not provide significant performance improvements. All the reference speed and acceleration profiles for cart are shown in Fig. 2. Figure 2 and 3 show that, for the test-case under consideration, the ZVD shaper requires higher actuator effort than the other two methods, given that it requires the highest RMS cart acceleration ($0.3727\ m/s^2$). The lowest actuator effort is required by the NZV shaper, which requires a RMS acceleration as low as $0.1299\ m/s^2$. However, it does not share the robustness sported by the two other methods, which can be judged by measuring the residual vibrations in 5. It should be also pointed out that jerk continuity is obtained only by the proposed method: obtaining jerk continuity with input shaping techniques requires polynomials with higher degree, and hence even higher accelerations. The load oscillations for the three motion profiles are reported in Fig. 4 and 5. Figure 4 refers to the nominal conditions: the NZV shaper, the ZVD shaper and the variational solution with $\beta = 0$ have similar transient load oscillation and null residual ones. In contrast, a sensible peak load oscillation is obtained by setting $\beta = 50$, as expected, at the cost of a small increase of the cart accelerations. Figure 5 simulates a mismatch between the actual system and the model adopted for the synthesis, in which the length of the first cable, $L_1$, is increased by 20%. In this case, the residual load oscillation is rather small for all three robust methods, while the only non-robust one, i.e. the NZV shaper, produces a residual peak load oscillation that is roughly one third of the transient one. The proposed method with $\beta = 0$ and the ZVD shaper lead to very similar results, while setting $\beta = 50$ can reduce even further the amplitude of residual vibrations. Tables 1 and 2 summarize all these results.

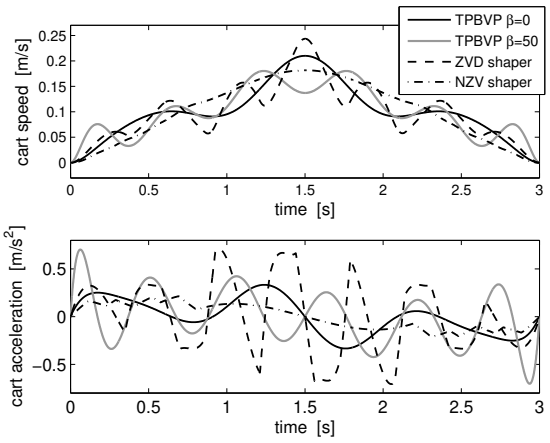


Figure 2: Planned cart speed and acceleration: proposed method with $\beta = 0$ and $\beta = 50$, NZV and ZVD shaper

https://doi.org/10.3311/ECCOMASMBD2021-168

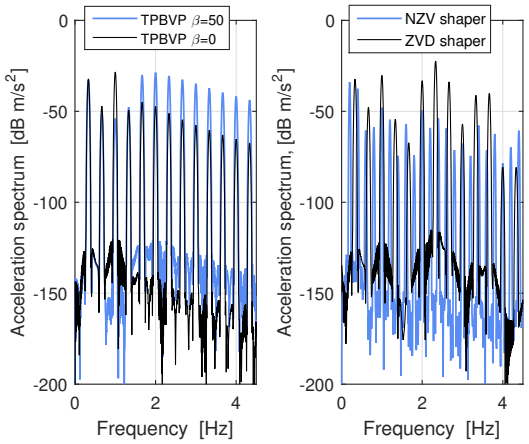


Figure 3: Spectrum of planned cart acceleration: proposed method with $\beta = 0$ and $\beta = 50$, NZV and ZVD shaper

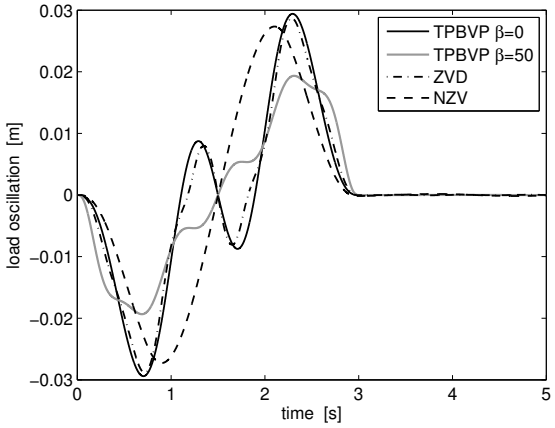


Figure 4: Load oscillation with unperturbed plant

Table 2: Performance measurements: peak ans RMS load oscillation, measured in $[mm]$

| Test | transient peak | transient RMS | residual peak | residual peak, $\Delta L_1 = 20\%$ |
|---|---|---|---|---|
| NZV | 27.347 | 17.037 | 0.169 | 8.850 |
| ZVD | 28.807 | 14.917 | 0.042 | 1.622 |
| TPBVP $\beta = 0$ | 29.404 | 15.817 | 0.000 | 1.774 |
| TPBVP $\beta = 20$ | 21.984 | 12.943 | 0.001 | 1.470 |
| TPBVP $\beta = 50$ | 19.646 | 12.374 | 0.001 | 1.465 |

## 7 Conclusion

In this work a method for the robust design of motion profiles for underactuated multibody systems has been presented. The method is based on the definition of a robust optimization problem constrained to the plant dynamics, which is set-up with the aid of parametric sensitivity functions and by exploiting the Pontryagin's Minimum Principle. The performances are assessed by comparison with the application of NZV and ZVD shapers, showing that, for the case under consideration, the proposed method has similar robustness properties of the widely adopted ZVD shaper, while requiring lower actuator effort and bandwidth. Additionally, a suitable definition of the cost function adopted for the synthesis of the motion profile, allows significantly reducing the peak transient oscillation at the cost of a minor increase of the control effort.

## References

[1] A. Gasparetto, P. Boscariol, A. Lanzutti, R. Vidoni. Trajectory planning in robotics. Mathematics in Computer Science, 1–11, 2012.

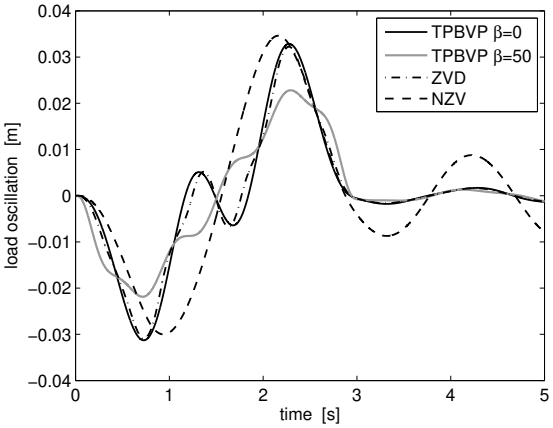


Figure 5: Load oscillation with perturbed plant ($\Delta L_1 = +20\%$)

[2] P. Barre, R. Bearee, P. Borne, E. Dumetz. Influence of a jerk controlled movement law on the vibratory behaviour of high-dynamics systems. Journal of Intelligent & Robotic Systems, 42(3):275–293, 2005.

[3] A. Gasparetto, V. Zanotto. A technique for time-jerk optimal planning of robot trajectories. Robotics and Computer-Integrated Manufacturing, 24(3):415–426, 2008.

[4] D. Kirk. Optimal control theory: an introduction. Dover Pubns, 2004.

[5] J. T. Betts. Survey of numerical methods for trajectory optimization. Journal of guidance, control, and dynamics, 21(2):193–207, 1998.

[6] O. Dahl. Path constrained motion optimization for rigid and flexible joint robots. In International Conference on Robotics and Automation, volume 2, 223–229. IEEE, 1993.

[7] P. Boscariol, A. Gasparetto. Model-based trajectory planning for flexible-link mechanisms with bounded jerk. Robotics and Computer-Integrated Manufacturing, 29(4):90–99, 2013.

[8] D. Balkcom, M. Mason. Time optimal trajectories for bounded velocity differential drive vehicles. The International Journal of Robotics Research, 21(3):199–217, 2002.

[9] C. M. Pappalardo, D. Guida. Adjoint-based optimization procedure for active vibration control of nonlinear mechanical systems. Journal of Dynamic Systems, Measurement, and Control, 139(8):081010, 2017.

[10] M. Bamdad. Time-energy optimal trajectory planning of cable-suspended manipulators. In Cable-Driven Parallel Robots, 41–51. Springer, 2013.

[11] A. Idà, Edoardo andBerti, T. Bruckmann, M. Carricato. Rest-to-rest trajectory planning for planar underactuated cable-driven parallel robots. Cable-Driven Parallel Robots, Mechanisms and Machine Science, vol 53.:207–218, 2018.

[12] E. Idà, T. Bruckmann, M. Carricato. Robust point-to-point trajectory planning for nonlinear underactuated systems: Theory and experimental assessment. IEEE Transactions on Robotics, 35:1338–1351, 2019.

[13] R. Bellman, et al. The theory of dynamic programming. Bulletin of the American Mathematical Society, 60(6):503–515, 1954.

[14] D. Gallardo, O. Colomina, F. Flórez, R. Rizo. A genetic algorithm for robust motion planning. In International Conference on Industrial, Engineering and Other Applications of Applied Intelligent Systems, 115–121. Springer, 1998.

[15] K. Shin, N. McKay. Robust trajectory planning for robotic manipulators under payload uncertainties. IEEE transactions on Automatic Control, 32(12):1044–1054, 1987.

[16] W. Singhose, D. Kim, M. Kenison. Input shaping control of double-pendulum bridge crane oscillations. Journal of Dynamic Systems, Measurement, and Control, 130(3):034504, 2008.

[17] T. Singh. Optimal reference shaping for dynamical systems: theory and applications. CRC Press, 2009.

[18] N. C. Singer, W. P. Seering, et al. Preshaping command inputs to reduce system vibration. Massachusetts Institute of Technology, Artificial Intelligence Laboratory, 1988.

[19] P. Boscariol, A. Gasparetto. Robust model-based trajectory planning for nonlinear systems. Journal of Vibration and Control, 22(18):3904–3915, 2016.

[20] P. Boscariol, D. Richiedei. Rest-to-rest trajectory planning for underactuated cable-driven parallel robots. Robotics and Computer-Integrated Manufacturing, 50:256–265, 2018.

[21] R. Belotti, D. Richiedei, I. Tamellin, A. Trevisani. Response optimization of underactuated vibration generators through dynamic structural modification and shaping of the excitation forces. The International Journal of Advanced Manufacturing Technology, 112:505–524, 2021.

[22] L. Pontriagin, R. Gamkrelidze. The mathematical theory of optimal processes, volume 4. CRC, 1986.

[23] L. Shampine, I. Gladwell, S. Thompson. Solving ODEs with MATLAB. Cambridge Univ Pr, 2003.

[24] R. W. Holsapple. A modified simple shooting method for solving two-point boundary value problems. Ph.D. thesis, Texas Tech University, 2003.

[25] W. Singhose, W. Seering, N. C. Singer. Time-optimal negative input shapers. Journal of Dynamic Systems, Measurement, and Control, 119(2):198–205, 1997.

[26] W. Singhose. Command shaping for flexible systems: A review of the first 50 years. International Journal of Precision Engineering and Manufacturing, 10(4):153–168, 2009.

https://doi.org/10.3311/ECCOMASMBD2021-199



# Synthesis of an Extended Kalman Filter for Cable-Driven Parallel Robots

**Giovanni Boschetti**[1], **Francisco González**[2], **Giulio Piva**[1], **Dario Richiedei**[1], **Borja R. Frade**[2], **Alberto Trevisani**[1]

[1] Department of Management and Engineering
University of Padua
Stradella S. Nicola 3, 36100,
Vicenza, Italy
[giovanni.boschetti, dario.richiedei, alberto.trevisani]@unipd.it,
giulio.piva@phd.unipd.it

[2] Laboratorio de Ingeniería Mecánica
University of A Coruña
Rúa Mendizábal s/n, 15403,
Ferrol, Spain
[f.gonzalez, borja.rfrade]@udc.es

## ABSTRACT

Cable-driven parallel robots are light-weight parallel robots where cables replace rigid actuators to move an end-effector. As a consequence, they can be characterized by very large workspaces, high-dynamic handlings, ease of reconfigurability and/or low-cost architecture. Since the driving links are flexible, the state variables of the robot cannot be always directly measured, thus the development of state observers is essential. In this work a general approach to develop a nonlinear state observer based on an Extended Kalman Filter is proposed and validated numerically by referring to a cable-suspended parallel robot. The state observer is based on a system model obtained converting a set of Differential Algebraic Equations into Ordinary Differential Equations through two different methods: the penalty formulation and the Udwadia-Kalaba formulation.

**Keywords:** State estimation, Extended Kalman Filter, Cable-Driven Parallel Robots, Penalty Formulation, Udwadia-Kalaba.

## 1. INTRODUCTION AND MOTIVATION

Parallel robots (e.g., the Stewart-Gough platform) typically actuate the end-effector by driving rigid links, in Cable-Driven Parallel Robots (CDPRs), conversely, the end-effector is actuated by flexible cables. Parallel robots can be designed to achieve high stiffness at the end-effector and payload capacity, but the weight of the actuators and their fixed minimum and maximum lengths may limit considerably the feasible velocity and the workspace. Alternatively, parallel robots can be designed to achieve high velocity at the expenses of payload capacity, but the workspace limitations cannot be overcome (e.g., Delta robots). In CDPRs, instead, each cable is wound around a winch connected to a motor. The winch can easily provide several meters of cable not only enabling large workspaces, but also assuring minimal inertias, lightweight structures, easy reconfigurability and modularity of the system.

Despite these advantages, the current deployment of CDPRs seems hampered mainly by the fact that cables are unilateral elements: they can only exert pulling forces. If they become slack, the end-effector cannot be made follow a prescribed trajectory or exert the required wrench to perform a task: in manufacturing or heavy handling, this can obviously introduce relevant performance and safety issues since the control of the end-effector may be lost [1]. The use of CDPRs has, however, already been suggested in several different operation fields, such as heavy handling, medical rehabilitation, rescue and home assistance, industrial manufacturing, or sport shooting (see for example [2] and the references therein). In the future, a wide use of CDPRs can be foreseen thanks to their lightweight structure (which makes them energy efficient), modularity and reconfigurability (which makes them flexible and easy to transport) and finally, the potentially high dynamics and payload capacity (which makes them effective in a wide range of industrial applications). The presence of flexible elements can however introduce accuracy issues as a

consequence of cable elasticity and sagging. Additionally, the upper and lower bounds on admissible cable tensions impose implementing complex planning and motion control strategies. These problems clearly demand developing and using accurate dynamic models for CDPRs.

There is no single classification universally recognized for CDPRs, not even the terminology adopted is unified. CDPRs topologies can however be very dissimilar, and every topology presents advantages and drawbacks that must be considered at the design stage and when developing planning and control algorithms. To try to simplify the analysis the main categories shown in Table 1 can be used to classify CDPRs.

**Table 1.** Classifications of CDPRs

| Workspace | Actuation | Constraints | Exit-points |
|---|---|---|---|
| Planar | Under-actuated | Under-constrained | Fixed |
| Spatial | Fully-actuated | Fully-constrained | Reconfigurable |
| | Over-actuated | Redundant | |

As for the workspace, a CDPR can obviously operate in a three-dimensional space or into a bi-dimensional (planar) space.

As for the actuation, if the end-effector of a CDPR is driven by $n_{ac}$ active cables, depending on the number of degrees of freedom, $n_{dof}$, of the end-effector, the CDPR can be:

- Under-actuated if $n_{ac} < n_{dof}$ [3]
- Fully-actuated, if $n_{ac} = n_{dof}$ [4];
- Over-actuated, if $n_{ac} > n_{dof}$ [5].

Another critical feature of a CDPR is the capability of cables to react to external forces acting on the end-effector. Different cases can be recognized:

- Under-constrained: there exist some directions along which cables cannot exert equilibrating reactions to external wrenches applied to the end-effector [6];
- Fully-constrained: the end-effector can maintain equilibrium against every external wrench (under the assumption of infinite maximum cable tension) [7];
- Redundant: the number of cables is greater than the minimum one making the robot fully-constrained [8].

Finally, CDPRs can also present reconfiguration capabilities for their exit points (i.e., the points on the opposite side of the cable with respect to the points connected to the end-effector). Typically, the exit points are fixed, but more in general, they can follow the motion of, for example, drones [9], motors moving along a fixed frame [10] or even other manipulators. These robots are called Reconfigurable Cable-Driven Parallel Robots (RCDPRs) and are expected to have interesting applications also in the rescue and home assistance fields.

A critical issue in the field of cable robotics is ensuring that cable tensions are positive. Therefore, proper motion planning and control should be performed by adopting advanced techniques. In the case of feedback control, advanced control schemes often require the knowledge of the full state of the system (see e.g. [11,12]), that is in contrast usually not available. To overcome this issue, state observers can be designed and implemented [13,14]**.**

In this paper, an Extended Kalman Filter (EKF) is adopted to estimate the state variables of a CDPR. The dynamics of a CDPR is highly nonlinear and imposes the development of nonlinear state observer, such as EKFs, which are widely used in state estimation of nonlinear systems starting from a complete model formulated through first-order Ordinary Differential Equations (ODEs). A widespread approach in the literature of CDPRs is writing the Newton-Euler equations of motion for the end-effector under the hypothesis that cables are stiff, massless and straight, and often the contribution of the motor inertial properties to the overall system dynamics is neglected, or just considered through approximations or through non-systematic approaches. On the other hand, redundant coordinates are never used in dynamic models, although this choice has several

https://doi.org/10.3311/ECCOMASMBD2021-199

benefits in modelling this CDPRs (e.g. to simulate cable failures or bouncing motions), and also make easier the development of models including both the motors and the end-effector. The latter is therefore the approach investigated in this work for the design of state observers.

Since the models implemented in the state observer need to be in ODEs representation, the conversion of DAEs into ODEs must be performed. This step can be carried out taking advantage of different formulations. In this work, two well established formulations are investigated: the penalty formulation [15] and the Udwadia-Kalaba formulation [16], since both the approaches are well suited for handling multibody systems with redundant constraints [15,17], as often occurs in CDPRs.

## 2. DYNAMIC MODELING OF A CABLE-DRIVEN PARALLEL ROBOT

### 2.1. Differential-Algebraic Equations (DAEs) modeling technique

Let us collect the coordinates of a CDPR into the vector of dependent coordinates $\mathbf{q} \in \mathbb{R}^p$. The following set of DAEs, of index 3, is obtained to model the system dynamics [18]:

$$\begin{cases} \mathbf{M}\ddot{\mathbf{q}} + \mathbf{J}^T\boldsymbol{\lambda} = \mathbf{f} \\ \boldsymbol{\Phi}(\mathbf{q}) = \mathbf{0} \end{cases} \tag{1}$$

where $\boldsymbol{\Phi}(\mathbf{q})$ is the set of *n* kinematic constraint equations, $\mathbf{M} \in \mathbb{R}^{p\times p}$ is the mass matrix, $\mathbf{f} \in \mathbb{R}^p$ is the vector of the external forces, $\boldsymbol{\lambda} \in \mathbb{R}^n$ is the vector of the Lagrange multiplier and $\mathbf{J} \in \mathbb{R}^{n\times p}$ is the Jacobian of the constraint equations, $\mathbf{J} = \left[\frac{\partial \boldsymbol{\Phi}}{\partial \mathbf{q}}\right]$.

The CSPR studied in this work, as sketched in Figure 1**,** is a cable-suspended robot: a three-DOF suspended end-effector (modeled as a lumped mass $m$) is driven by four cables winding on winches and actuated by motors (whose equivalent moments of inertia reflected to the motor shaft are $J_{m,1}, J_{m,2}, J_{m,3}, J_{m,4}$). The system is therefore overactuated, as often happens in CDPRs, since this configuration increases the static equilibrium workspace [19]. Vector $\mathbf{q} = \begin{bmatrix}\mathbf{p}^T & \boldsymbol{\theta}^T\end{bmatrix}^T$ includes the absolute Cartesian positions of the end-effector $\mathbf{p} = \begin{bmatrix}x_p & y_p & z_p\end{bmatrix}^T$ and the angular positions of the motors $\boldsymbol{\theta} = \begin{bmatrix}\theta_1 & \theta_2 & \theta_3 & \theta_4\end{bmatrix}^T$. Under the assumption that cables are perfectly stiff and taut, and hence behave as holonomic, ideal kinematic constraints, the *i-th* constraint (*i*=1,..,4) that relates the end-effector coordinates and the angular positions of the motors is $\mathbf{l}_i = \mathbf{p} - \mathbf{a}_\mathbf{i}$ (with $\mathbf{a}_\mathbf{i}$ the absolute position of the exit-point of cable *i*), where $\|\mathbf{l}_\mathbf{i}\| = l_{0,i} + r_i\theta_i$ is the *i-th* cable length ($l_{0,i}$ is the *i-th* cable length corresponding to $\theta_i$=0 and $r_i$ is the radius of the *i-th* winch).

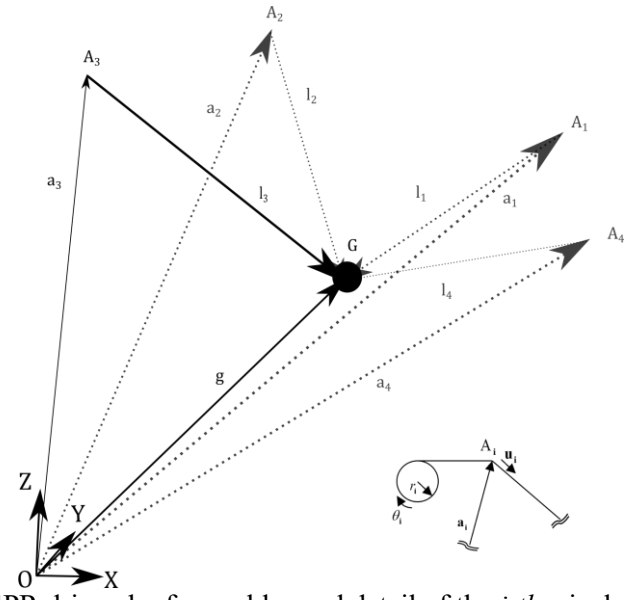


**Figure 1.** CSPR driven by four cables and detail of the *i-th* winch and exit point.

https://doi.org/10.3311/ECCOMASMBD2021-199

The *i-th* position constraint can therefore be expressed in the following form:

$$\Phi_i = \mathbf{p}^T\mathbf{p} - 2\mathbf{p}^T\mathbf{a_i} + \mathbf{a_i}^T\mathbf{a_i} - {l_{0,i}}^2 - 2l_{0,i}r\theta_i - r^2\theta_i^2 = 0 \tag{2}$$

The conversion of the set of DAEs to a set of nonlinear ODEs, both for simulating the system and for designing the state observer, can be done through different approaches. Three different approaches are here considered, as briefly discussed in Sections 2.2, 2.3 and 2.4.

### 2.2.DAE to ODE conversion: projection matrix

A usual way to convert a DAE model into a minimal set of ODE is using the "projection matrix method", by means of the matrix (here denoted as $\mathbf{R} \in \mathbb{R}^{(p-n_{dof})\times p}$) that relates the dependent (redundant) velocities, $\dot{\mathbf{q}}$, and the independent (minimal) ones, $\dot{\mathbf{z}}$:

$$\dot{\mathbf{q}} = \mathbf{R}(\mathbf{q})\dot{\mathbf{z}} \tag{3}$$

taking the time-derivative of Eq. (3), $\ddot{\mathbf{q}} = \mathbf{R}(\mathbf{q})\ddot{\mathbf{z}} + \dot{\mathbf{R}}(\mathbf{q},\dot{\mathbf{q}})\dot{\mathbf{z}}$, leads to the minimal set of ODEs

$$\mathbf{R}(\mathbf{q})^T\,\mathbf{M}\mathbf{R}(\mathbf{q})\ddot{\mathbf{z}} = \mathbf{R}(\mathbf{q})^T\left(\mathbf{f} - \mathbf{M}\dot{\mathbf{R}}(\mathbf{q},\dot{\mathbf{q}})\dot{\mathbf{z}}\right) \tag{4}$$

Eq. (4) can be expressed in the following compact form, with the obvious meaning of the symbols:

$$\bar{\bar{\mathbf{M}}}\ddot{\mathbf{z}} = \bar{\bar{\mathbf{f}}} \tag{5}$$

### 2.3. DAE to ODE conversion: Penalty Formulation

To retain all the redundant coordinates in the multibody model, a formulation often used to convert the DAEs model to an ODEs system is using the "Penalty Formulation", which allows directly simulating the time evolution of all the dependent coordinates [18]. The penalty formulation assumes that the Lagrange multipliers are proportional to the constraint violation at the configuration, velocity, and acceleration levels. In its simplest form, the following definition is assumed, by means of the three scalar tuning parameters $\alpha$, $\xi$ and $\omega$.

$$\boldsymbol{\lambda} = \alpha\left(\ddot{\boldsymbol{\Phi}} + 2\xi\omega\dot{\boldsymbol{\Phi}} + \omega^2\boldsymbol{\Phi}\right) \tag{6}$$

The choice of their values has been carried out by following the advices proposed in the literature (see e.g. [15]); if the model is used in the design of a state observer, they can be treated as two tuning parameters. Since the constrains of the system under investigation are scleronomic, the time-derivative of the position constraints can be expressed as

$$\begin{aligned}\dot{\boldsymbol{\Phi}}(\mathbf{q}) &= \mathbf{J}\dot{\mathbf{q}} \\ \ddot{\boldsymbol{\Phi}}(\mathbf{q}) &= \mathbf{J}\ddot{\mathbf{q}} + \dot{\mathbf{J}}\dot{\mathbf{q}}\end{aligned} \tag{7}$$

and therefore, the following set of *p* ODEs is obtained to model the dynamics of the CDPR:

$$\left(\mathbf{M} + \mathbf{J}^T\alpha\mathbf{J}\right)\ddot{\mathbf{q}} + \mathbf{J}^T\alpha\left(\dot{\mathbf{J}} + 2\xi\omega\mathbf{J}\right)\dot{\mathbf{q}} + \mathbf{J}^T\alpha\omega^2\boldsymbol{\Phi} = \mathbf{f} \tag{8}$$

again, Eq. (8) can be written in the following compact form

$$\bar{\mathbf{M}}(\mathbf{q})\ddot{\mathbf{q}} + \bar{\mathbf{C}}(\mathbf{q})\dot{\mathbf{q}} + \bar{\mathbf{K}}(\mathbf{q}) = \mathbf{f} \tag{9}$$

### 2.4. DAE to ODE conversion: Udwadia-Kalaba formulation

A different approach to convert the DAEs into a set of ODEs retaining all the *p* dependent coordinates is through the methods exploiting the exact evaluation of the Lagrange multipliers, most of which are related to the Gauss' principle of least constraint. The most famous of these methods is, probably, the Udwadia-Kalaba formulation [20], that holds for systems with non-

https://doi.org/10.3311/ECCOMASMBD2021-199

singular mass matrix. The acceleration of the $p$ dependent coordinates of the constrained system, $\ddot{\mathbf{q}}$, is obtained as the sum of the free-body (unconstrained) accelerations $\ddot{\mathbf{q}}_f$,

$$\ddot{\mathbf{q}}_f = \mathbf{M}^{-1}\mathbf{f} \tag{10}$$

and a perturbation due to the kinematic constraints, $\ddot{\mathbf{q}}_c$, that can be computed as follows:

$$\ddot{\mathbf{q}}_c = \mathbf{M}^{-\frac{1}{2}}\mathbf{B}^{\dagger}\left(\mathbf{\Gamma} - \mathbf{J}\ddot{\mathbf{q}}_f\right) \tag{11}$$

matrix $\mathbf{B}^{\dagger}$ is the pseudoinverse of **B**, with

$$\mathbf{B} = \mathbf{J}\mathbf{M}^{-\frac{1}{2}}, \tag{12}$$

while $\mathbf{\Gamma}$ is due to the acceleration constraint equations:

$$\mathbf{\Gamma} = -\frac{\partial\left(\mathbf{J}\dot{\mathbf{q}}\right)}{\partial\mathbf{q}}\dot{\mathbf{q}} - 2\dot{\mathbf{J}}\dot{\mathbf{q}} - \ddot{\mathbf{\Phi}} \tag{13}$$

since this formulation arises from a DAE system of index 1, position and speed constraints usually are not satisfied after numerical integration of the equation of motions. Therefore, the Baumgarte stabilization [21] is usually introduced, by leading to the following set of ODEs to be integrated:

$$\ddot{\mathbf{q}} = \mathbf{M}^{-1}\mathbf{f} + \mathbf{M}^{-\frac{1}{2}}\mathbf{B}^{\dagger}\left(\mathbf{\Gamma} - 2\chi\dot{\mathbf{\Phi}} - \varphi^2\mathbf{\Phi} - \mathbf{J}\ddot{\mathbf{q}}_f\right) \tag{14}$$

where $\chi$ and $\varphi$ are Baumgarte stabilization parameters that are tuned with a trial-and-error procedure. If the model is used in the design of a state observer, they could be treated as two tuning parameters.
Whenever **M** is singular, the extension of this formulation provided in [22] could be exploited.

## 3. DEVELOPMENT OF THE EXTENDED KALMAN FILTER (EKF)

Extended Kalman Filters (EKFs) are widely used as nonlinear state observers to estimate unmeasured variables in multibody systems [14]. An EKF provides optimal estimates $\hat{\mathbf{x}}(t)$ of the actual state $\mathbf{x}(t) = \begin{bmatrix}\dot{\mathbf{q}}^T & \mathbf{q}^T\end{bmatrix}^T$ of a first-order system representation, by merging the prediction of a nominal model $\dot{\mathbf{x}}(t) = \boldsymbol{f}_c(\mathbf{x}(t),\mathbf{u}(t))$ ($\mathbf{u}(t)$ is the input vector), with a closed-loop correction inferred through the measurements retrieved from a proper set of sensors $\mathbf{y}(t) = g(\mathbf{x}(t),\mathbf{u}(t))$ ensuring observability. The resulting closed-loop estimation is based on a prediction-correction scheme, that in the continuous time leads to the following form

$$\dot{\hat{\mathbf{x}}}(t) = \boldsymbol{f}_c(\mathbf{x}(t),\mathbf{u}(t)) + \mathbf{L}(\mathbf{y}(t) - \hat{\mathbf{y}}(t)) \tag{15}$$

where **L** is the filter gain and $\mathbf{y}(t) - \hat{\mathbf{y}}(t)$ is the output-estimation error ($\hat{\mathbf{y}}(t)$ is the estimated output), usually denoted as the innovation. In practice, the EKF is implemented in discrete-time and the vectors through the discretized form of the function $f_c$, here denoted as $f$:

$$\begin{cases}\mathbf{x}_k = \boldsymbol{f}\left(\mathbf{x}_{k-1},\mathbf{u}_{k-1}\right)\\ \mathbf{y}_k = \boldsymbol{g}\left(\mathbf{x}_k,\mathbf{u}_k\right)\end{cases} \tag{16}$$

where $k$ denotes the simulation step.

The discrete-time model $\boldsymbol{f}$ and the noisy input measurements $\mathbf{u}_k$ are adopted for computing the prediction (or a-priori estimation) $\hat{\mathbf{x}}_{k|k-1} = \boldsymbol{f}\left(\hat{\mathbf{x}}_{k-1|k-1},\mathbf{u}_k\right)$, that is then corrected through the output estimation error $\left(\mathbf{y}_k - \hat{\mathbf{y}}_{k|k-1}\right)$, with $\hat{\mathbf{y}}_{k|k-1} = \boldsymbol{g}\left(\hat{\mathbf{x}}_{k|k-1},\mathbf{u}_k\right)$, weighed through the time-varying filter gain $\mathbf{L}_{k|k}$, leading to the following recursive scheme:

$$\hat{\mathbf{x}}_{k|k} = \hat{\mathbf{x}}_{k|k-1} + \mathbf{L}_{k|k}\left(\mathbf{y}_k - \hat{\mathbf{y}}_{k|k-1}\right) \tag{17}$$

The term $\mathbf{L}_{k|k}\left(\mathbf{y}_k - \hat{\mathbf{y}}_{k|k-1}\right)$ is a closed-loop correction, in the control theory sense, forcing the

estimation to track sensor measurements by compensating for noise and model uncertainty. To compute $\mathbf{L}_{k|k}$ at each time step**,** the EFK algorithm replaces the nonlinear model with its Jacobian matrices computed about the estimated state trajectory and uses them in the propagation of the noise covariance matrices [14].

As an example, the EKF developed with the penalty formulation is based on Eq. (9), which allows expressing the accelerations in the following form:

$$\ddot{\mathbf{q}} = \bar{\mathbf{M}}(\mathbf{q})^{-1}\mathbf{f} - \bar{\mathbf{M}}(\mathbf{q})^{-1}\bar{\mathbf{K}}(\mathbf{q}) - \bar{\mathbf{M}}(\mathbf{q})^{-1}\bar{\mathbf{C}}(\mathbf{q})\dot{\mathbf{q}} \tag{18}$$

the following first-order representation of the system is obtained:

$$\begin{bmatrix}\ddot{\mathbf{q}}\\ \dot{\mathbf{q}}\end{bmatrix} = \begin{bmatrix}-\bar{\mathbf{M}}^{-1}\bar{\mathbf{C}} & \mathbf{0}\\ \mathbf{I} & \mathbf{0}\end{bmatrix}\begin{bmatrix}\dot{\mathbf{q}}\\ \mathbf{q}\end{bmatrix} + \begin{bmatrix}-\bar{\mathbf{M}}^{-1} & \mathbf{0}\\ \mathbf{0} & \mathbf{0}\end{bmatrix}\begin{bmatrix}\bar{\mathbf{f}}\\ \mathbf{0}\end{bmatrix} \tag{19}$$

where the equivalent external forces vector $\bar{\mathbf{f}}$ is:

$$\bar{\mathbf{f}} = \mathbf{f} - \bar{\mathbf{K}}(\mathbf{q}) \tag{20}$$

Several discretization schemes can be adopted, with different accuracy, stability and computational effort [14,18]. In this paper, with the goal of simplify the computational for boosting real time estimation and aware of the positive effect of the filter correction that can compensate for energy losses due to the numerical integration scheme, discretization is performed with a simplified method based on an approximation of the forward Euler scheme (with time-step $\mathrm{d}t$ ), as often done in control theory. The following state-dependent matrices are defined, due to the dependence of some submatrices on $\mathbf{q}$ and $\dot{\mathbf{q}}$ (that is omitted for clarity of representation):

$$\begin{aligned}\mathbf{A}_{d,k} &\approx \mathbf{I} + \begin{bmatrix}-\bar{\mathbf{M}}^{-1}\bar{\mathbf{C}} & \mathbf{0}\\ \mathbf{I} & \mathbf{0}\end{bmatrix}_k \mathrm{d}t\\ \mathbf{B}_{d,k} &\approx \begin{bmatrix}-\bar{\mathbf{M}}^{-1} & \mathbf{0}\\ \mathbf{0} & \mathbf{0}\end{bmatrix}_k \mathrm{d}t\end{aligned} \tag{21}$$

where $\mathbf{A}_{d,k}$ and $\mathbf{B}_{d,k}$ represent the discrete counterpart of the continuous-time matrices of Eq. (19). Then, the discrete-time model $\mathbf{x}_{k+1} = \boldsymbol{f}\left(\mathbf{x}_k, \mathbf{u}_k\right)$ of Eq. (18) is cast as follows:

$$\begin{bmatrix}\dot{\mathbf{q}}\\ \mathbf{q}\end{bmatrix}_k = \mathbf{A}_{d,k-1}\begin{bmatrix}\dot{\mathbf{q}}\\ \mathbf{q}\end{bmatrix}_{k-1} + \mathbf{B}_{d,k-1}\begin{bmatrix}\bar{\mathbf{f}}\\ \mathbf{0}\end{bmatrix}_{k-1} \tag{22}$$

and in the following compact form (that apparently resembles the one of a linear system):

$$\mathbf{x}_k = \mathbf{A}_{d,k-1}\mathbf{x}_{k-1} + \mathbf{B}_{d,k-1}\mathbf{u}_{k-1} \tag{23}$$

with the obvious definitions of the state and input vectors:

$$\mathbf{x}_k = \begin{bmatrix}\dot{\mathbf{q}}\\ \mathbf{q}\end{bmatrix}_k \qquad \mathbf{u}_k = \begin{bmatrix}\bar{\mathbf{f}}\\ \mathbf{0}\end{bmatrix}_k \tag{24}$$

By following the recursive scheme of the EKF, the covariance propagation is computed as:

$$\hat{\mathbf{P}}_{k|k-1} = \mathbf{A}_{d,k-1}\mathbf{P}_{k-1}\mathbf{A}_{d,k-1}^T + \mathbf{Q} \tag{25}$$

where $\mathbf{Q}$ is the covariance matrix of the of the model noise, that is in practice a tuning parameter that represents in an abstract way the amount of model uncertainty. Then, the filter gain is computed as

$$\mathbf{L}_{k|k} = \hat{\mathbf{P}}_{k|k-1}\mathbf{H}^T\left(\mathbf{H}\hat{\mathbf{P}}_{k|k-1}\mathbf{H}^T + \mathbf{R}\right)^{-1} \tag{26}$$

where $\mathbf{R}$ denotes the covariance matrix of measurement noise that can be treated as a tuning parameter, and H is the Jacobian of $\boldsymbol{g}$ . Finally, the covariance propagation matrix is updated by setting

https://doi.org/10.3311/ECCOMASMBD2021-199

$$\mathbf{P}_k = \left(\mathbf{I}\text{-}\mathbf{L}_{k|k}\mathbf{H}\right)\hat{\mathbf{P}}_{k|k-1} \tag{27}$$

## 4. NUMERICAL RESULTS

### 4.1. Description of the test case

The system under investigation is a Cable-Suspended Parallel Robot (CSPR), which is a particular CDPR where all the cables are connected to the end-effector from the top of the frame, and therefore the possibility to get positive tensions in the cables is just provided by gravity. The CSPR analysed as the test case is sketched in Figure 2: it is made by 4 motors that actuate the end-effector, modeled as a point mass $m = 3[\text{kg}]$. The frame dimensions are $1.69 \times 1.775 \times 1.89$ [m] ($\text{w} \times \text{l} \times \text{h}$, in Figure 2). Therefore, it can be classified as a spatial, over-actuated, under-constrained CDPR with fixed exit-points. The exit points are assumed to coincide with the upper the vertices $A_i$ of the frame ($i$=1,..,4). The actuators have equal rotational moments of inertia $J_{m,i} = 5.12e-4[\text{kgm}^2]$ ($i$=1,..,4) (including both the motor rotor and the winch). Rigid and taut cables are assumed, as is often reasonable if low-frequency motions are considered.

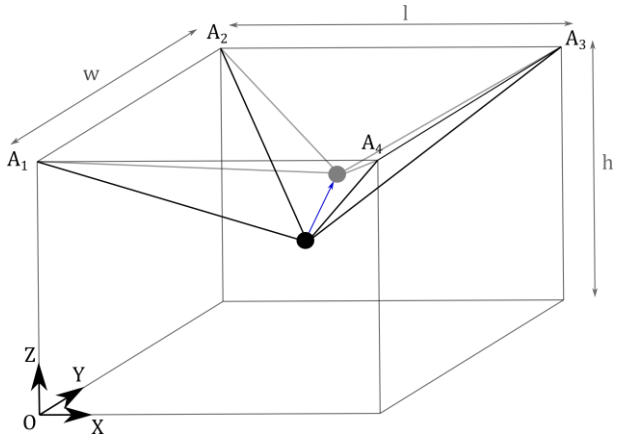


**Figure 2**. Basic scheme of the CSPR

The actuators are supposed to be equipped by low resolution encoder measuring $\boldsymbol{\theta}$, with just 150 pulses per revolution and operating in 4x resolution; such a choice ensures observability. The torques exerted by each motor is available as well, as usually supplied by commercial drivers and as required by the state observer. The simulator adopted to represent the "real system", i.e. the system that produces the "actual" values of the state vector to be estimated by the state observer, has been implemented through the projection matrix method, which uses a minimal coordinate representation, and does not require any tuning parameter in the conversion of the DAEs to ODEs, as in contrast is required by both the Penalty and the Udwadia-Kalaba formulations. The "actual" values of $\boldsymbol{\theta}$ that are fed to the state observer are corrupted by quantization noise. Additionally, some errors in the mass matrices of the models employed in the observer will be considered in Section 4.4, to assess the observer capability of getting rid of such uncertainties by merging the model and the closed loop correction. Two different EKFs are tested, by adopting the Penalty and the Udwadia-Kalaba formulations for the model-based filter prediction. In this way, the impact of different multibody formulations on the estimate accuracy is evaluated.
Besides comparing the observer outcomes with the actual state, the estimates of the end-effector position and velocities are made through the forward kinematics and the noisy measurements provided by the encoders. As for the estimation of the motor shaft speeds, it is obtained by numerical derivation and by low pass filtering through a first-order filter with a 15 Hz bandwidth. Increasing the bandwidth does not allow properly removing high frequency noise introduced by derivation of the encoder signal corrupted by the coarse quantization. On the other hand, such a filter creates a phase lag in the estimated speeds and therefore further reducing the bandwidth would decrease the stability margin if such estimates are used in feedback control loops.

https://doi.org/10.3311/ECCOMASMBD2021-199

The simulated test consists of a rest-to-rest motion from point $P_i = \{0.8875 \quad 0.8425 \quad 0.9450\}$ [m] to point $P_f = \{1.0 \quad 1.0 \quad 1.5\}$ [m] through a linear path, as shown in Figure 2, by means of a 5th-degree polynomial law of motion.

### 4.2. State observer based on penalty formulation: EKF-P

The Cartesian coordinates of the end-effector positions ( $x_p$ , $y_p$ and $z_p$ ) and velocities ( $\dot{x}_p$ , $\dot{y}_p$ and $\dot{z}_p$ ) are shown from Figures from 3 through 5. In each figure, a comparison is shown among the "real system" coordinates, the estimates of the EKF based on penalty formulation (hereafter denoted as EKF-P) and the estimations obtained through forward kinematics. The inspection of the velocity estimates reveals that the use of the EKF remarkably reduces the effect of the quantization noise on the derivatives, compared to the kinematics estimation, without introducing visible delay.

A closer look on the result can be inferred from the error plots shown in Figures 6 and 7, that are also summarized in Table 2 through the RMS (root mean square) values.

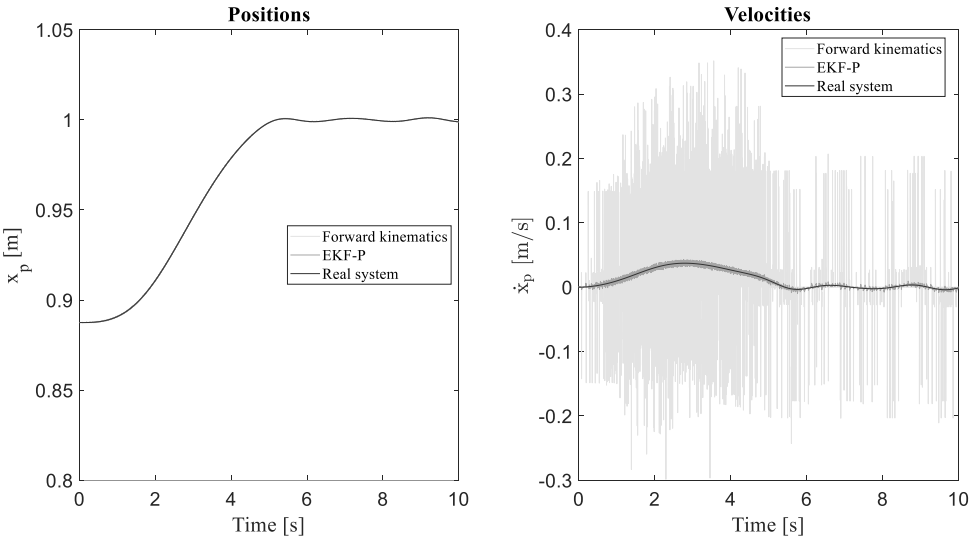


**Figure 3.** Comparison of actual and estimated $x_p$ and $\dot{x}_p$

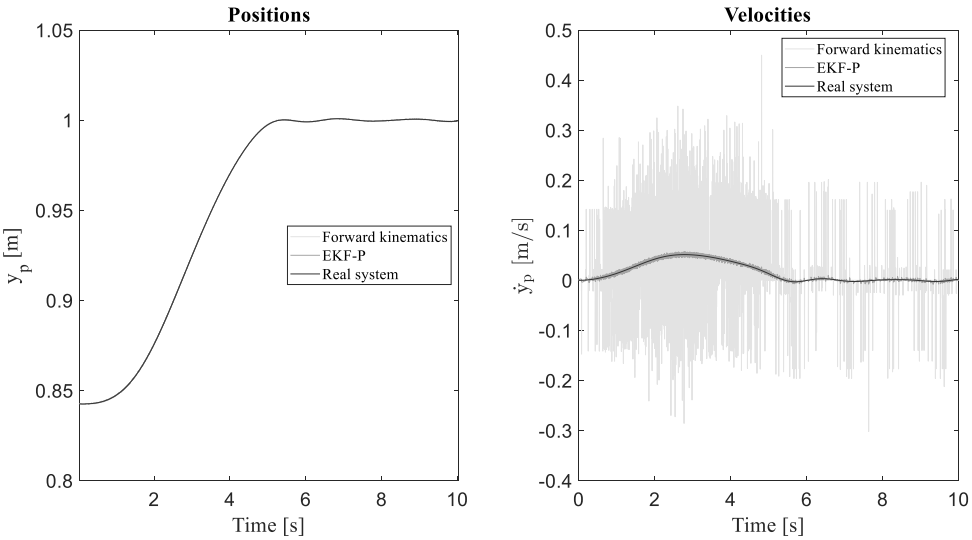


**Figure 4.** Comparison of actual and estimated $y_p$ and $\dot{y}_p$

https://doi.org/10.3311/ECCOMASMBD2021-199

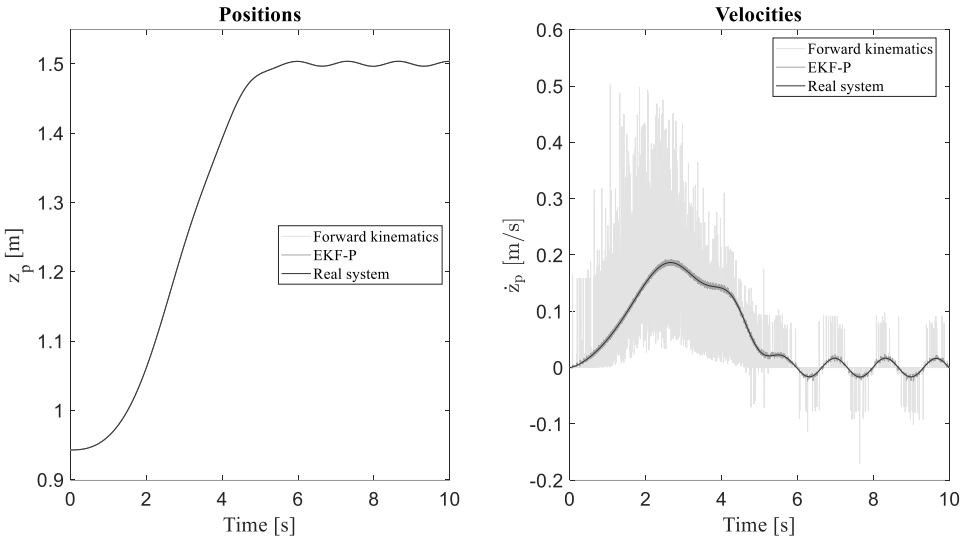


**Figure 5.** Comparison of actual and estimated $z_p$ and $\dot{z}_p$

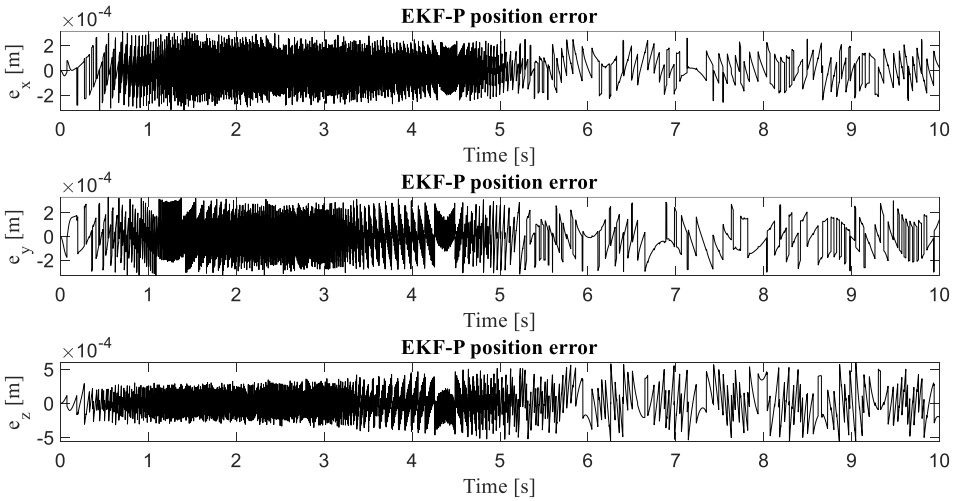


**Figure 6.** Time-history of position estimation errors of the EKF-P

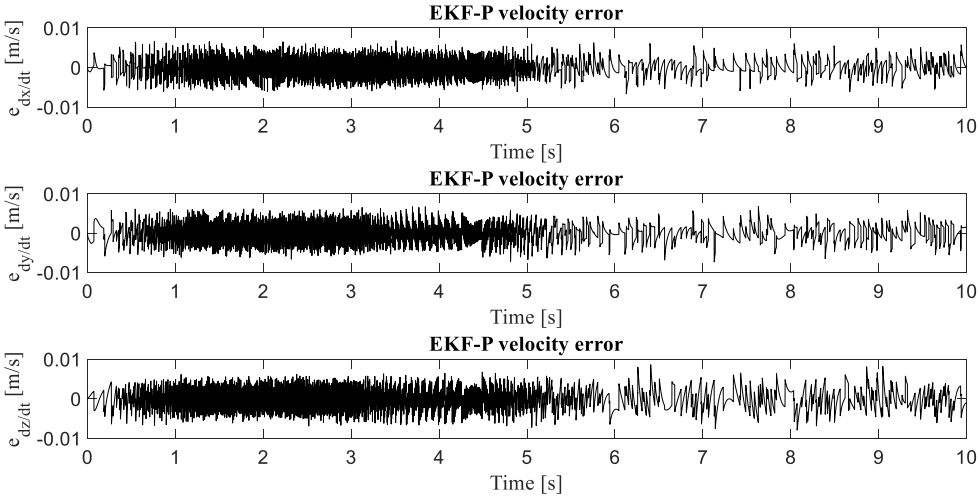


**Figure 7.** Time-history of velocity estimation errors of the EKF-P

https://doi.org/10.3311/ECCOMASMBD2021-199

### 4.3.State observer based on Udwadia-Kalaba formulation: EKF-UK

The Udwadia-Kalaba formulation has been implemented as well, leading to the observer hereafter denoted as EKF-UK. The results of the simulation are compared with the actual values, and the estimation errors are plotted in Figures 8 and 9. The results are very similar with those provided by the EKF-P, and an effective speed noise rejection is, again, obtained.

Table 2 allows comparing the three different estimation approaches. While similar errors are obtained in term of position, the use of both the EKFs drastically reduces the speed RMS estimation error.

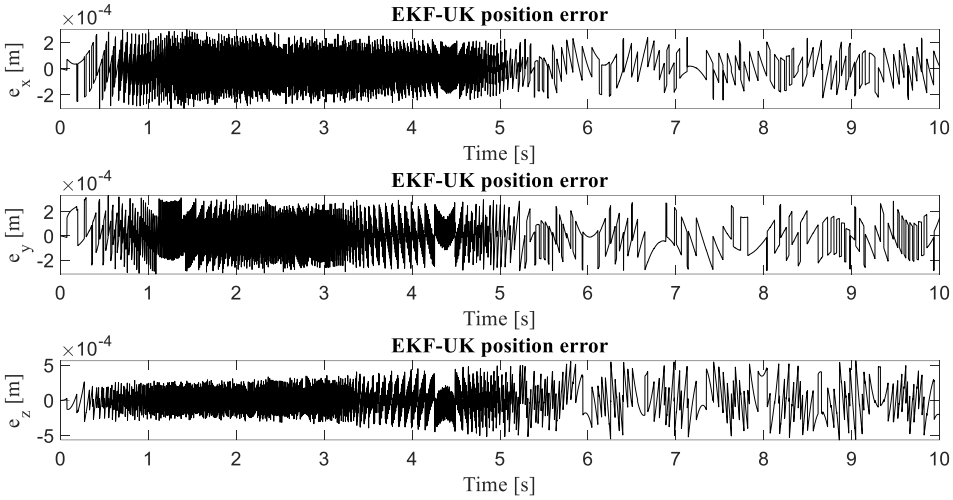


**Figure 8.** Time-history of position estimation errors of the EKF-UK

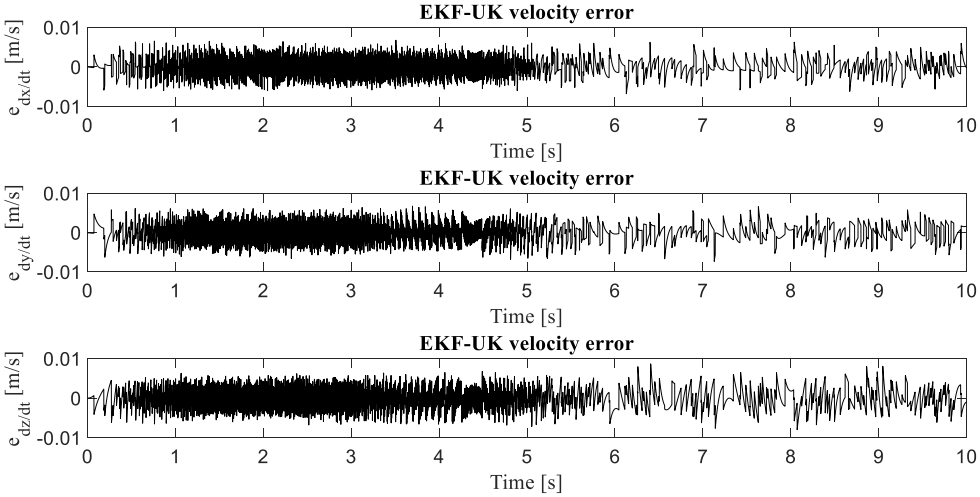


**Figure 9.** Time-history of velocity estimation errors of the EKF-UK

**Table 2.** RMS errors of position and velocity estimates against "real system"

| | EKF-P | EKF-UK | Forward kinematics | | EKF-P | EKF-UK | Forward kinematics |
|---|---|---|---|---|---|---|---|
| $e_x^{RMS}$ [m] | 1.13e-4 | 1.08e-4 | 1.20e-4 | $e_{dx/dt}^{RMS}$ [m/s] | 2.13e-3 | 2.18e-3 | 0.064 |
| $e_y^{RMS}$ [m] | 1.32e-4 | 1.28e-4 | 1.26e-4 | $e_{dy/dt}^{RMS}$ [m/s] | 2.24e-3 | 2.29e-3 | 0.059 |
| $e_z^{RMS}$ [m] | 2.04e-4 | 1.99e-4 | 2.43e-4 | $e_{dz/dt}^{RMS}$ [m/s] | 2.53e-3 | 2.55e-3 | 0.055 |

https://doi.org/10.3311/ECCOMASMBD2021-199

### 4.4. Estimation in the presence of model uncertainty

A sensitivity analysis on the two EKFs has also been carried out by assuming random bounded perturbations of **M** (ranging in the interval [0, +10%]). Despite the relevant mismatch between the actual system model and the ones used in the state observer, a negligible increase of the estimation error is obtained, as shown in Table 3.

**Table 3.** RMS errors of position and velocity with model mismatch

| | **EKF-P** | **EKF-UK** | | **EKF-P** | **EKF-UK** |
|---|---|---|---|---|---|
| $e_x^{RMS}$ [m] | 1.13e-4 | 1.08e-4 | $e_{dx/dt}^{RMS}$ [m/s] | 2.16e-3 | 2.21e-3 |
| $e_y^{RMS}$ [m] | 1.30e-4 | 1.27e-4 | $e_{dy/dt}^{RMS}$ [m/s] | 2.23e-3 | 2.28e-3 |
| $e_z^{RMS}$ [m] | 2.04e-4 | 1.99e-4 | $e_{dz/dt}^{RMS}$ [m/s] | 2.58e-3 | 2.60e-3 |

## 5. CONCLUSIONS

This work discusses the synthesis of two formulations of EKFs for the state estimations in Cable-Driven Parallel Robot by means of some different multibody formulations. The approach is general and can be applied to several configurations Cable-Driven Parallel Robot. Among the two formulations presented to obtain ODEs from DAEs of the multibody model, the Udwadia-Kalaba formulation has shown some advantages due to a lower number of parameters to be tuned by the designer compared to the penalty formulation, that has led to a faster and simple tuning of the model adopted for the filter design. Overall, the performances of EKF-P and EKF-UK are comparable, and in both cases the computational effort wase small enough to allow for real time computation.

## ACKNOWLEDGMENTS

The authors acknowledge the financial support by the Italian Ministry of University and Research through the research grant “SISTEMA - Dipartimenti di Eccellenza”.

## REFERENCES

[1] Boschetti, G., Minto, R. and Trevisani, A.: Improving a cable robot recovery strategy by actuator dynamics. Applied Sciences (Switzerland) (2020) **10** 1–19

[2] Trevisani, A.: Planning of dynamically feasible trajectories for translational, planar, and underconstrained cable-driven robots. Journal of Systems Science and Complexity (2013) **26** 695–717

[3] Idà, E., Briot, S. and Carricato, M.: Robust Trajectory Planning of Under-Actuated Cable-Driven Parallel Robot with 3 Cables. Springer Proceedings in Advanced Robotics (2021) 15 pp 65–72

[4] Albus, J., Bostelman, R. and Dagalakis, N.: The NIST robocrane. Journal of Robotic Systems (1993) **10** 709–24

[5] Rosati, G., Zanotto, D. and Agrawal, S. K.: On the Design of Adaptive Cable-Driven Systems. Journal of Mechanisms and Robotics (2011) **3**

[6] Ida, E., Marian, D. and Carricato, M.: A Deployable Cable-Driven Parallel Robot with Large Rotational Capabilities for Laser-Scanning Applications. IEEE Robotics and Automation Letters (2020) **5** 4140–7

[7] Sun, C., Gao, H., Liu, Z., Xiang, S., Yu, H., Li, N. and Deng, Z.: Design and optimization of three-degree-of-freedom planar adaptive cable-driven parallel robots using the cable wrapping phenomenon. Mechanism and Machine Theory (2021) **166** 104475

[8] Lamaury, J. and Gouttefarde, M.: Control of a large redundantly actuated cable-suspended parallel robot. Proceedings - IEEE International Conference on Robotics and Automation (2013) 4659–64

[9] Jiang, Q. and Kumar, V.: The inverse kinematics of cooperative transport with multiple aerial robots. IEEE Transactions on Robotics (2013) **29** 136–45

[10] Gagliardini, L., Caro, S., Gouttefarde, M. and Girin, A.: Discrete reconfiguration planning for Cable-

Driven Parallel Robots. Mechanism and Machine Theory (2016) **100** 313–37

[11] Belotti, R., Richiedei, D., Tamellin, I. and Trevisani, A.: Pole assignment for active vibration control of linear vibrating systems through Linear Matrix Inequalities. Applied Sciences (Switzerland) (2020) **10**

[12] Richiedei, D. and Tamellin, I.: Active control of linear vibrating systems for antiresonance assignment with regional pole placement. Journal of Sound and Vibration (2021) **494** 115858

[13] Palomba, I., Richiedei, D. and Trevisani, A.: Kinematic state estimation for rigid-link multibody systems by means of nonlinear constraint equations. Multibody System Dynamics (2017) **40** 1–22

[14] Pastorino, R., Richiedei, D., Cuadrado, J. and Trevisani, A.: State estimation using multibody models and non-linear Kalman filters. International Journal of Non-Linear Mechanics (2013) **53** 83–90

[15] González, F. and Kövecses, J.: Use of penalty formulations in dynamic simulation and analysis of redundantly constrained multibody systems. Multibody System Dynamics (2013) **29** 57–76

[16] Udwadia, F. E., Kalaba, R. E. and Phohomsiri, P.: Mechanical systems with nonideal constraints: Explicit equations without the use of generalized inverses. Journal of Applied Mechanics, Transactions ASME (2004) **71** 615–21

[17] Yang, L., Xue, S. and Yao, W.: Application of Gauss principle of least constraint in multibody systems with redundant constraints. Proceedings of the Institution of Mechanical Engineers, Part K: Journal of Multi-body Dynamics (2020) **235** 150–63

[18] Jalon, J. G. de. and Bayo, E.: Kinematic and Dynamic Simulation of Multibody Systems. Springer-Verlag, New York, NY (1994) ISBN:3-540-94096-0

[19] Riechel, A. T. and Ebert-Uphoff, I.: Force-Feasible Workspace analysis for underconstrained, point-mass cable robots. Proceedings - IEEE International Conference on Robotics and Automation (2004) vol 2004 pp 4956–62

[20] Falco, D. De, Pennestrì, E. and Vita, L.: The udwadia-kalaba formulation: A report on its numerical efficiency in multibody dynamics simulations and on its teaching effectiveness. Multibody Dynamics, ECCOMAS Thematic Conference (2005) 21–4

[21] Baumgarte, J.: Stabilization of constraints and integrals of motion in dynamical systems. Computer Methods in Applied Mechanics and Engineering (1972) **1** 1–16

[22] Udwadia, F. E. and Phohomsiri, P.: Explicit equations of motion for constrained mechanical systems with singular mass matrices and applications to multi-body dynamics. Proceedings of the Royal Society A: Mathematical, Physical and Engineering Sciences (2006) **462** 2097–117

https://doi.org/10.3311/ECCOMASMBD2021-201



# Path Tracking in Cable Suspended Parallel Robots through Position-Dependent Model Predictive Control with Embedded Integrator

**Jason Bettega**[1], **Dario Richiedei**[1], **Alberto Trevisani**[1]

[1] Department of Management and Engineering
Università degli Studi di Padova
Stradella S. Nicola 3, 36100 Vicenza, Italy
jason.bettega@phd.unipd.it
[dario.richiedei, alberto.trevisani]@unipd.it

## ABSTRACT

This work proposes a novel Model Predictive Control (MPC) algorithm for Cable-Driven Robots (CDRs), with a suspended configuration, to achieve good performances in terms of trajectory tracking of the end-effector as well as ensuring the positiveness of cable tensions. A two-stage controller is exploited to handle model nonlinearities. Firstly, a position-dependent MPC algorithm with embedded integrator is designed to evaluate the optimal cable tensions that are required to track trajectory, while considering constraints on the feasible tensions. Secondly, the related motor torques are evaluated taking into account the dynamics of the electric motor themselves, through a dedicated feedforward approach. With the goal to assess the proposed control algorithm, a 3-dof cable suspended spatial robot is considered and different trajectory tracking tasks are performed: firstly, an unfeasible reference is tested in order to assess the control algorithm in the worst-case scenario and, secondly, two feasible and common trajectories are considered as reference laws of motion. Simulative outcomes are displayed and contour errors are reported to numerically evaluate the controller performances.

**Keywords:** Model Predictive Control, embedded integrator, Cable-Driven Robots, Trajectory tracking, Tension control.

## 1. INTRODUCTION

Precise path tracking control in Cable Suspended Parallel Robots (CSPRs) is a challenging topic in the field of control of multibody systems, due to the positivity constraints on cable tensions, and for this reason it is attracting even more attention in the literature. On the one hand, from the open-loop point of view, trajectory planning strategies have been suggested to a-priori ensure positive and bounded cable tensions along given paths (e.g. [1], [2]). On the other hand, from the closed-loop perspective, some standard industrial controllers, such as PID controllers, have been often applied to this kind of robotic systems in the last decades, showing adequate results ([3], [4]). However, advanced control techniques have to be considered to get even better performances. Additionally, standard techniques do not embed the positiveness constraints on the cable tensions, as well as bounds on the feasible maximum tensions: since control must complies with these requirements, a-posteriori verification or control saturation are therefore usually adopted.

In this paper, precise path tracking control in a CSPR is solved by exploiting and extending the idea of Model Predictive Control (MPC). Indeed, among the model-based control techniques, MPC has several features that make it very attractive for Cable-Driven Robots (CDRs) in general. The basic idea of MPC is to solve an optimal control problem defined by a cost function over a receding horizon and constrained by the system dynamics and by bounds on

https://doi.org/10.3311/ECCOMASMBD2021-201

some variables; these features make it attractive for motion control of multibody systems (see e.g. [5], [6], [7]). The optimization problem over the future control variables is solved at each time step by predicting the future system states and outputs. Hence, MPC provides an optimal sequence of the control input, in accordance with some metrics. The great advantage that makes MPC particularly suitable for CDRs is represented by its capability to embed constraints on input and output variables without requiring a-posteriori saturations.

In the very last years, attention has been spent by a few researchers in the field of CDRs to apply the concepts of MPC ([8], [9], [10], [11], [12]), also showing promising results. Different MPC architectures are proposed by these papers, with reference of fully constrained CDRs, and different approaches are proposed to deal with the nonlinear dynamic behavior of the system. The idea of MPC has been also adopted to plan dynamic transition trajectories for a fully-actuated three-degree-of-freedom cable suspended robot in [13].

In this work, the proposed MPC scheme is based on a two-step strategy that splits the system into two subsystems and uses them in a sequential approach. First, feedback MPC is designed for the subsystem made by the suspended mass by computing the positive tensions. In this way, the dynamic matrix of the state-space model is constant, while just the input matrix depends on the system pose. Nonlinearities is handled by updating the model at each time step of the control loop, and then assuming the input matrix as constant along the prediction interval used for the MPC design, thus reducing the computational burden, and allowing for real-time calculation. Then, a model-based approach is used to compute the reference motor torques, by exploiting the dynamic model of the motors, the optimal tensions computed by the MPC and the commanded speed and acceleration. The control assumes feedback of position and speed of the suspended mass and rigid cables. No tension feedback is instead adopted. To ensure effective tracking, an embedded integrator is here adopted in the MPC formulation (MPC-EI) by formulating the model through the difference variables, that easily allows including the requirement of small variations of the cable tensions to get smooth control actions.

Numerical assessment of the control performances is made through a fully-actuated three-degree-of-freedom cable-suspended robot (i.e. with a lumped end-effector), controlled by three cables.

## 2. SYSTEM MODEL

The studied system is depicted in Figure 1. The subsystem made by the lumped mass suspended through three cables is modeled through three ordinary differential equations (ODEs):

$$m\ddot{\mathbf{p}} = m\mathbf{g} + \sum_{i=1}^{3}\left(-T_i \frac{\mathbf{p}-\mathbf{A}_i}{\|\mathbf{p}-\mathbf{A}_i\|}\right). \tag{1}$$

$\mathbf{p} = [x \quad y \quad z]^T \in \mathbb{R}^3$ is the absolute position of the end-effector, whose mass is m; $\mathbf{A}_i \in \mathbb{R}^3$ denotes the absolute position of the fixed output points of the spools $(i = 1,2,3)$; $\mathbf{g} = [0 \quad 0 \quad -g]^T \in \mathbb{R}^3$ is the vector of gravity acceleration; $T_i$ is the tension of the $i^{th}$ cable.

The dynamic model of the $i^{th}$ motor is described by the following ODE:

$$J_i\ddot{\theta}_i(t) + f_{v,i}\dot{\theta}_i(t) = C_{m,i}(t) - T_i(t)r_i\ , \tag{2}$$

where $\theta_i$ is the motor shaft absolute rotation, $J_i$ indicates the moment of inertia of rotor, drum and idle pulleys, $f_{v,i}$ is the viscous friction coefficient, $C_{m,i}$ is the motor torque and $r_i$ represents the drum radius.

The kinematic constraint equation relating the rotation of the $i^{th}$ motor and the length of the $i^{th}$ cable, under the assumption that cables are not slack and therefore behave as holonomic ideal constraints, is:

https://doi.org/10.3311/ECCOMASMBD2021-201

$$\rho_i = \rho_{i0} - r_i \theta_i \ , \tag{3}$$

where $\rho_i$ is the $i^{th}$ cable length ($\rho_i = \|\mathbf{p} - \mathbf{A}_i\|$) and $\rho_{i0}$ is the cable length corresponding to $\theta_i = 0$.

Denoting with $\boldsymbol{\theta} = \begin{bmatrix} \theta_1 & \theta_2 & \theta_3 \end{bmatrix}^T \in \mathbb{R}^3$ the vector containing the absolute motor rotations, the resulting dynamic model, in terms of non-minimal coordinates, is defined as follows:

$$\mathbf{M}\ddot{\mathbf{q}} + \mathbf{J}^{\mathbf{T}}\boldsymbol{\lambda} = \mathbf{Q} \ , \tag{4}$$

where $\mathbf{M} = diag\{J_1, J_2, J_3, m, m, m\} \in \mathbb{R}^{6\times 6}$ is the mass matrix, $\mathbf{q} = \begin{bmatrix} \mathbf{p}^T & \boldsymbol{\theta}^T \end{bmatrix}^T \in \mathbb{R}^6$ is a set of six dependent coordinates containing both the absolute cartesian position of the end-effector $\mathbf{p}$ and the absolute motor rotations $\boldsymbol{\theta}$, $\mathbf{J} \in \mathbb{R}^{6\times 3}$ is the Jacobian of the position constraints, $\boldsymbol{\lambda} \in \mathbb{R}^{3\times 1}$ is the vector of the Lagrange multipliers and $\mathbf{Q} \in \mathbb{R}^{6\times 1}$ contains the external forces (gravity forces, friction, motor torques).

To meet the formalism of control theory, the set of DAEs obtained is converted into a minimal set of ODEs. By exploiting a matrix $\mathbf{R} \in \mathbb{R}^{6\times 3}$ such that

$$\dot{\mathbf{q}} = \mathbf{R}\dot{\mathbf{p}} \ , \tag{5}$$

then the usual form of a multibody system dynamic model is obtained:

$$\left(\mathbf{R}^{\mathbf{T}}\mathbf{M}\mathbf{R}\right)\ddot{\mathbf{p}} + \left(\mathbf{R}^{\mathbf{T}}\mathbf{M}\dot{\mathbf{R}}\right)\dot{\mathbf{p}} = \mathbf{R}^{\mathbf{T}}\mathbf{Q} \ . \tag{6}$$

Since Eq. (6) directly relates the input torques of the electric motors (contained in vector **Q**) with the end-effector cartesian position, such a model is exploited to simulate the real system in a Matlab-Simulink environment, also including simplified models of the sensors and the actuators.

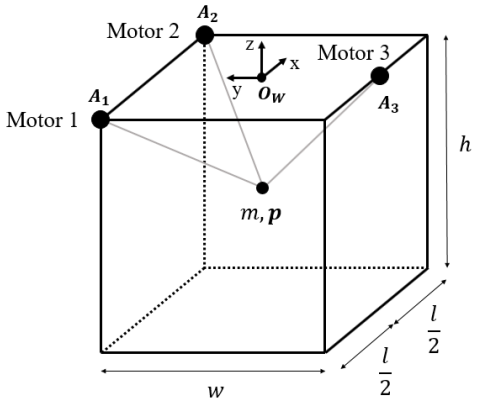


**Figure 1.** Scheme of the CSPR under investigation.

## 3. DESIGN OF THE CONTROL SCHEME

The dynamic model in Eq. (6) is nonlinear, due to the dependence of $\mathbf{R}$ on positions. To simplify the control design, the synthesis of the proposed MPC scheme is based on a two-step strategy that splits the system into two subsystems and uses them in a sequential approach. First, feedback MPC is designed for the subsystem made by the suspended mass by computing the positive tensions to track the desired spatial path. Then, the model in Eq. (2) is adopted to compute the reference motor torques. Further feedforward terms compensating for gravity forces and inertial terms of the suspended mass could be adopted to improve; however, in this work they are not included in order to emphasize the effectiveness of the feedback action.

### 3.1. Synthesis of MPC

https://doi.org/10.3311/ECCOMASMBD2021-201

**State-Space model.** The ODEs in Eq. (1) can be transformed into a first-order model through state vector $\boldsymbol{\chi}_\mathbf{c} = \begin{bmatrix} \dot{\mathbf{p}}^T & \mathbf{p}^T \end{bmatrix}^T \in \mathbb{R}^6$, obtaining the following nonlinear continuous-time state-space system:

$$\begin{cases} \dot{\boldsymbol{\chi}}_\mathbf{c}(t) = \mathbf{A}_\mathbf{c}\,\boldsymbol{\chi}_\mathbf{c}(t) + \mathbf{B}_\mathbf{c}(\mathbf{p})\mathbf{T}(t) + \mathbf{B}_\mathbf{gc}\,\mathbf{g} \\ \mathbf{y}_\mathbf{c}(t) = \mathbf{C}_\mathbf{c}\,\boldsymbol{\chi}_\mathbf{c}(t) \end{cases}, \tag{7}$$

where $\mathbf{A}_\mathbf{c} \in \mathbb{R}^{6\times 6}$ is the constant dynamic matrix, $\mathbf{B}_\mathbf{c}(\mathbf{p}) \in \mathbb{R}^{6\times 3}$ is the pose-dependent input matrix, $\mathbf{B}_\mathbf{gc} \in \mathbb{R}^{6\times 3}$ is the matrix that describe the relationship between the vector of gravity acceleration and the state vector, $\mathbf{C}_\mathbf{c} \in \mathbb{R}^{3\times 6}$ is the output matrix, and are defined as follows ($\mathbf{V}(\mathbf{p}) \in \mathbb{R}^{3\times 3}$ is the matrix containing the unitary vectors of the cables, $\mathbf{I}_3 \in \mathbb{R}^{3\times 3}$ is the identity matrix and $\mathbf{0}_3 \in \mathbb{R}^{3\times 3}$ is the null matrix):

$$\mathbf{A}_\mathbf{c} = \begin{bmatrix} \mathbf{0}_3 & \mathbf{0}_3 \\ \mathbf{I}_3 & \mathbf{0}_3 \end{bmatrix}, \quad \mathbf{B}_\mathbf{c}(\mathbf{p}) = \begin{bmatrix} -\frac{1}{m}\mathbf{V}(\mathbf{p}) \\ \mathbf{0}_3 \end{bmatrix}, \quad \mathbf{B}_\mathbf{gc} = \begin{bmatrix} \mathbf{I}_3 \\ \mathbf{0}_3 \end{bmatrix}, \quad \mathbf{C}_\mathbf{c} = \begin{bmatrix} \mathbf{0}_3 & \mathbf{I}_3 \end{bmatrix}. \tag{8}$$

The cable tensions are included in the input vector $\mathbf{T} = \begin{bmatrix} T_1 & T_2 & T_3 \end{bmatrix}^T \in \mathbb{R}^3$, and $\mathbf{y}_\mathbf{c} \in \mathbb{R}^3$ is the system output.

By discretizing the continuous-time state-space model in Eq. (7) with a sampling time $T_s$, the following set of difference equations is obtained:

$$\begin{cases} \boldsymbol{\chi}_\mathbf{d}(k+1) = \mathbf{A}_\mathbf{d}\,\boldsymbol{\chi}_\mathbf{d}(k) + \mathbf{B}_\mathbf{d}(\mathbf{p})\mathbf{T}(k) + \mathbf{B}_\mathbf{gd}\,\mathbf{g} \\ \mathbf{y}_\mathbf{d}(k) = \mathbf{C}_\mathbf{d}\,\boldsymbol{\chi}_\mathbf{d}(k) \end{cases}, \tag{9}$$

where $k$ denotes the generic time instant, $\boldsymbol{\chi}_\mathbf{d}$ and $\mathbf{y}_\mathbf{d}$ are, respectively, the discrete state and output vectors, while $\mathbf{A}_\mathbf{d} \in \mathbb{R}^{6\times 6}$, $\mathbf{B}_\mathbf{d}(\mathbf{p}) \in \mathbb{R}^{6\times 3}$, $\mathbf{B}_\mathbf{gd} \in \mathbb{R}^{6\times 3}$, $\mathbf{C}_\mathbf{d} \in \mathbb{R}^{3\times 6}$ are the matrices of the discrete-time model. In this paper, to simplify the computation, discretization is performed through through the following approximation of the Euler method, altough other approaches can be adopted:

$$\mathbf{A}_\mathbf{d} = \mathbf{I} + T_s\mathbf{A}_\mathbf{c}, \quad \mathbf{B}_\mathbf{d}(\mathbf{p}) = T_s\mathbf{B}_\mathbf{c}(\mathbf{p}), \quad \mathbf{B}_\mathbf{gd} = T_s\mathbf{B}_\mathbf{gc}, \quad \mathbf{C}_\mathbf{d} = \mathbf{C}_\mathbf{c}. \tag{10}$$

As stated in the Introduction, to provide effective tracking of the spatial path, the formulation of MPC-EI is adopted. Therefore, by introducing the difference variables as follows:

$$\Delta\boldsymbol{\chi}_\mathbf{d}(k) = \boldsymbol{\chi}_\mathbf{d}(k) - \boldsymbol{\chi}_\mathbf{d}(k-1), \tag{11}$$

$$\Delta\mathbf{T}(k) = \mathbf{T}(k) - \mathbf{T}(k-1), \tag{12}$$

and the augmented state vector $\boldsymbol{\chi} \in \mathbb{R}^9$,

$$\boldsymbol{\chi}(k) = \begin{bmatrix} \Delta\boldsymbol{\chi}_\mathbf{d}(k) \\ \mathbf{y}_\mathbf{d}(k) \end{bmatrix}, \tag{13}$$

then the following augmented state-space model is obtained:

$$\begin{cases} \boldsymbol{\chi}(k+1) = \mathbf{A}\,\boldsymbol{\chi}(k) + \mathbf{B}(\mathbf{p})\Delta\mathbf{T}(k) \\ \mathbf{y}(k) = \mathbf{C}\,\boldsymbol{\chi}(k) \end{cases}, \tag{14}$$

where the matrices $\mathbf{A} \in \mathbb{R}^{9\times 9}$, $\mathbf{B}(\mathbf{p}) \in \mathbb{R}^{9\times 3}$, $\mathbf{C} \in \mathbb{R}^{3\times 9}$ assume the following meaning:

$$\mathbf{A} = \begin{bmatrix} \mathbf{A}_\mathbf{d} & \mathbf{0}_{6\times 3} \\ \mathbf{C}_\mathbf{d}\mathbf{A}_\mathbf{d} & \mathbf{I}_3 \end{bmatrix}, \quad \mathbf{B}(\mathbf{p}) = \begin{bmatrix} \mathbf{B}_\mathbf{d}(\mathbf{p}) \\ \mathbf{C}_\mathbf{d}\mathbf{B}_\mathbf{d}(\mathbf{p}) \end{bmatrix}, \quad \mathbf{C} = \begin{bmatrix} \mathbf{0}_{3\times 6} & \mathbf{I}_3 \end{bmatrix}. \tag{15}$$

While $\mathbf{A}$ and $\mathbf{C}$ are constant, matrix $\mathbf{B}(\mathbf{p})$ is position dependent.

https://doi.org/10.3311/ECCOMASMBD2021-201

**Evaluation of the prediction matrices.** MPC exploits the output prediction over a selected prediction horizon $N_p$. Nonlinearities is handled in this work by updating matrix $\mathbf{B_d}(\mathbf{p})$ at each time step, based on the system configuration. Such a matrix is then assumed constant over the prediction horizon for control design.

The predicted output $\mathbf{Y} \in \mathbb{R}^{3N_p}$ in vectorial form is described as:

$$\mathbf{Y} = \mathbf{F}\mathbf{x}(k_i) + \mathbf{\Phi}(\mathbf{p})\mathbf{\Delta T}_{\mathbf{N_c}} \,, \tag{16}$$

where the matrices $\mathbf{F} \in \mathbb{R}^{3N_p \times 9}$ and $\mathbf{\Phi}(\mathbf{p}) \in \mathbb{R}^{3N_p \times 3N_c}$ assume the following expression:

$$\mathbf{F} = \begin{bmatrix} \mathbf{CA} \\ \mathbf{CA}^2 \\ \vdots \\ \mathbf{CA}^{N_p} \end{bmatrix}, \quad \mathbf{\Phi}(\mathbf{p}) = \begin{bmatrix} \mathbf{CB}(\mathbf{p}) & \mathbf{0} & \cdots & \mathbf{0} \\ \mathbf{CAB}(\mathbf{p}) & \mathbf{CB}(\mathbf{p}) & \cdots & \mathbf{0} \\ \vdots & \vdots & \vdots & \vdots \\ \mathbf{CA}^{N_p-1}\mathbf{B}(\mathbf{p}) & \mathbf{CA}^{N_p-2}\mathbf{B}(\mathbf{p}) & \cdots & \mathbf{CA}^{N_p-N_c}\mathbf{B}(\mathbf{p}) \end{bmatrix}. \tag{17}$$

Once the value of the state at a generic time instant $k_i$ is known, together with the control action along the control horizon, these matrices allow to achieve the value of the outputs along all the prediction horizon, hence describing the future system response.

**Constrained optimization problem.** The following cost function $J$ is defined and minimized to solve the trajectory tracking problem:

$$J = (\mathbf{Y^{des}} - \mathbf{Y})^T \mathbf{R_Y} (\mathbf{Y^{des}} - \mathbf{Y}) + \mathbf{\Delta T}_{\mathbf{N_c}}{}^T \mathbf{R_{\Delta T}} \mathbf{\Delta T}_{\mathbf{N_c}} \,, \tag{18}$$

where $\mathbf{R_Y} \in \mathbb{R}^{3N_p \times 3N_p}$ and $\mathbf{R_{\Delta T}} \in \mathbb{R}^{3N_c \times 3N_c}$ are weighting matrices, $\mathbf{\Delta T}_{\mathbf{N_c}} \in \mathbb{R}^{3N_c}$ contains the future control actions and $\mathbf{Y^{des}} \in \mathbb{R}^{3N_p}$ is the vector of the reference trajectories along the prediction horizon, described as:

$$\mathbf{Y^{des}} = \begin{bmatrix} \mathbf{I}_3 & \mathbf{I}_3 & \cdots & \mathbf{I}_3 \end{bmatrix}^T \mathbf{r}(k_i) = \mathbf{F^{des}} \mathbf{r}(k_i) \,, \tag{19}$$

where $\mathbf{F^{des}} \in \mathbb{R}^{3N_p \times 3}$ and $\mathbf{r}(k_i) \in \mathbb{R}^3$ is the vector of reference trajectories at time step $k_i$. It should be noted that the proposed formulation of MPC with embedded integrator includes in the cost function the variation of the cable tensions through $\mathbf{\Delta T}_{\mathbf{N_c}}$, rather than the value of the tensions. This aspect is particularly useful in real case scenarios, as discussed in [12], because large variations of cable tensions are not physically feasible.

Constraints on the magnitude of the cable tensions are embedded in the control synthesis through lower ($\mathbf{T_{min}} = T_{\min} \begin{bmatrix} 1 & 1 & 1 \end{bmatrix}^T$) and upper bounds ($\mathbf{T_{max}} = T_{\max} \begin{bmatrix} 1 & 1 & 1 \end{bmatrix}^T$) on the feasible control input $\mathbf{T}(k)$ defined through the following element-wise inequalities, related to the minimum and the maximum allowable cable tensions $T_{\min}$ and $T_{\max}$:

$$\mathbf{T_{min}} \leq \mathbf{T}(k) \leq \mathbf{T_{max}} \,. \tag{20}$$

Lower bounds define the positiveness tension requirements; upper bounds are related to the maximum admissible load. Constraints are then properly translated into bounds on the difference control signal $\mathbf{\Delta T}(k)$ and hence on $\mathbf{\Delta T}_{\mathbf{N_c}}$. Since $J$ is quadratic and the constraints are described through linear inequalities, a standard quadratic programming problem is adopted to control design. In this paper, the Hildreth's method is exploited because of its good numerical conditioning.

Since the input of the MPC formulation with embedded integrator is defined by the difference variable $\mathbf{\Delta T}(k)$, the predicted optimal inputs are written in a vectorial form as follows:

https://doi.org/10.3311/ECCOMASMBD2021-201

$$\mathbf{\Delta T}_{\mathbf{N_c}} = \left[\mathbf{\Delta T}(k_i) \quad \mathbf{\Delta T}(k_i+1) \quad \cdots \quad \mathbf{\Delta T}(k_i+N_c-1)\right]^T , \tag{21}$$

where $N_c$ is the control horizon and it indicates the number of samples that are considered in order to apply the optimal control action. Among all the values contained in the optimal solution $\mathbf{\Delta T}_{\mathbf{N_c}}$, only the first 3 terms (which represent the entries of $\mathbf{\Delta T}(k_i)$ in Eq. (21)) are considered while the remaining ones are discarded, in accordance with the Receding Horizon Principle and therefore making the MPC algorithm a closed-loop controller.

### 3.2. Computation of the motor torques

Once the optimal tensions $T_i^{MPC}$ are computed by the proposed MPC, the motor torques $C_{m,i}$ are achieved through a feedforward approach by exploiting the inverse-dynamic model of each actuator (see Eq. (2)), with nominal inertia ($\hat{J}_i$) and viscous friction coefficients ($\hat{f}_{v,i}$), and considering acceleration and speed references $\ddot{\theta}_i^{ref}(t)$ and $\dot{\theta}_i^{ref}(t)$ (obtained through inverse kinematics of the load reference trajectory). Therefore, considering the $i^{th}$ electric motor, its commanded torque is evaluated as follows:

$$C_{m,i} = \hat{J}_i \ddot{\theta}_i^{ref}(t) + \hat{f}_{v,i}\dot{\theta}_i^{ref}(t) + r_i T_i^{MPC}(t) \tag{22}$$

## 4. NUMERICAL RESULTS

### 4.1. System description

The parameters of the studied system are reported in Table 1. In the practical implementation, since MPC is a model-based control technique, it is assumed that accurate tuning of the model parameters is available, by exploiting any of the well-established techniques for model identification in multibody systems (see e.g. [14]), or specifically developed for cable robots (see e.g. [15]). Three motion references have been simulated to highlight the paramount features of the proposed control scheme. A simulation environment has been developed through Matlab-Simulink.

**Table 1.** System parameters

| Parameter | Description | Value |
|---|---|---|
| $J_{m,1}, J_{m,2}, J_{m,3}$ | Motor inertias | $2.6\times10^{-5}$ $\left[\text{kgm}^2\right]$ |
| $f_{v,1}, f_{v,2}, f_{v,3}$ | Motor viscous friction coefficients | $5\times10^{-3}$ $\left[\text{Nms/rad}\right]$ |
| $r_1, r_2, r_3$ | Radius of the pulleys | 0.036 $\left[\text{m}\right]$ |
| $m$ | Mass of the suspended load | 2.94 $\left[\text{kg}\right]$ |
| $T_{\min}$ ; $T_{\max}$ | Minimum and maximum tensions | 5 ; 100 $\left[\text{N}\right]$ |
| $T_s$ | Sampling time | $2\times10^{-3}$ $\left[\text{s}\right]$ |
| $N_c$ ; $N_p$ | Control and prediction horizons | 1 ; 60 |
| $\mathbf{R_Y}$ ; $\mathbf{R_{\Delta T}}$ | Weighting matrices | $\mathbf{I}_{180}$ ; $1\times10^{-3}\,\mathbf{I}_3$ |

### 4.2. Test cases

#### 4.2.1. Test 1: point-to-point motion with an unfeasible trajectory.

The first trajectory is made by a descending step reference for the z-axis, while keeping the references on x-axis and y-axis equal to the initial conditions. This trajectory is unfeasible be-

https://doi.org/10.3311/ECCOMASMBD2021-201

cause it would require negative infinite acceleration along the z-axis as well as negative tensions and hence would lead to slack cables. The presence of constraints on the feasible tensions in the control synthesis allows tracking the reference as fast as possible, while ensuring feasible tensions. The temporal tracking response in the z-axis is displayed in Figure 2, while Figure 3 shows the commanded cable tensions and corroborate the correctness of the proposed approach in handling constraints.

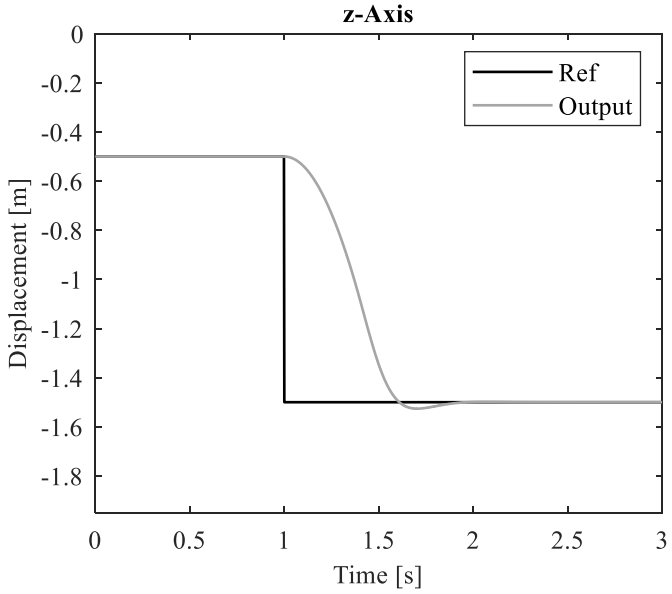


**Figure 2.** Temporal tracking response with step reference.

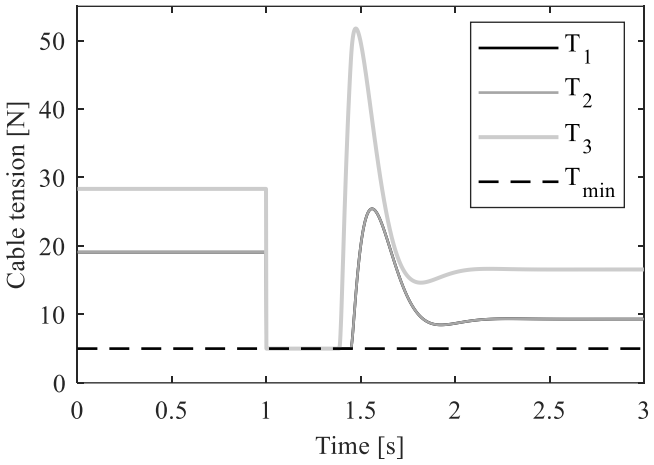


**Figure 3.** Cable tensions with step reference.

### 4.2.2. Test 2: point-to-point motion with a feasible trajectory.

To verify the control performance in the presence of a feasible trajectory, a $5^{th}$-degree polynomial motion law has been designed for a rest-to-rest motion lasting 3 seconds, to track a spatial straight line. Additional interval times of 1 second are also considered both at the beginning and at the end, in order to evaluate the controller in steady-state conditions. The spatial path tracking response is reported in Figure 4, together with its contour error in order to assess the performance of the proposed control algorithm. The control effectiveness is clearly proven, as the RMS value of the contour error is just $5.6\times10^{-5}\left[\mathrm{m}\right]$. The error could be further reduced through finer tuning of the controller, which is however beyond the paper goals. The optimal cable tensions computed by the MPC are reported in Figure 5.

https://doi.org/10.3311/ECCOMASMBD2021-201

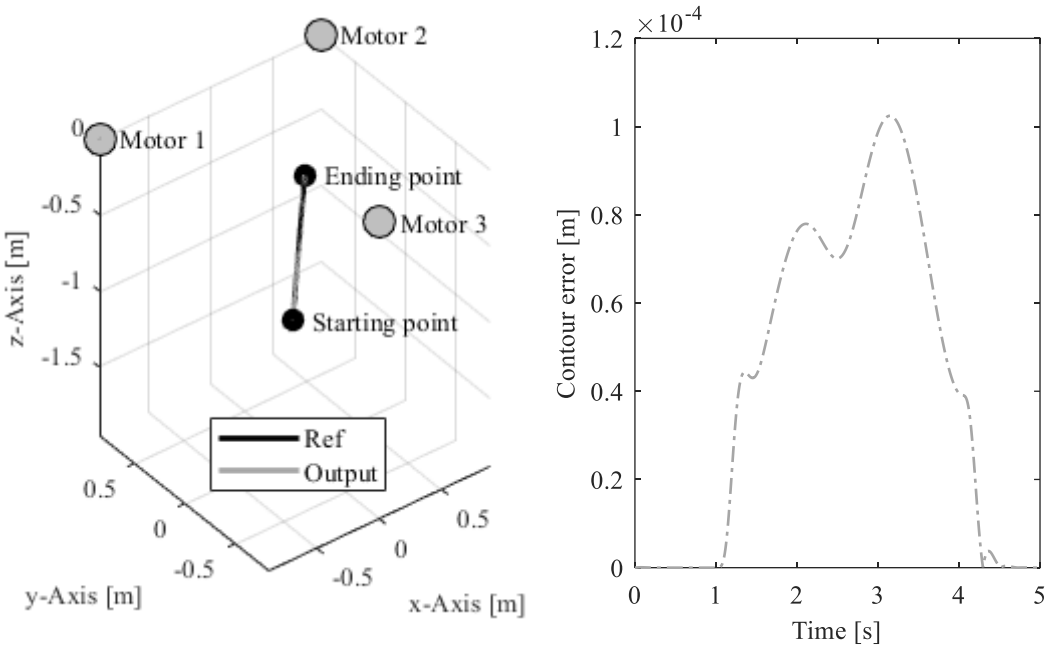


**Figure 4.** 3D-cartesian trajectory tracking response with 5th-degree polynomial reference (on the left) and its contour error (on the right).

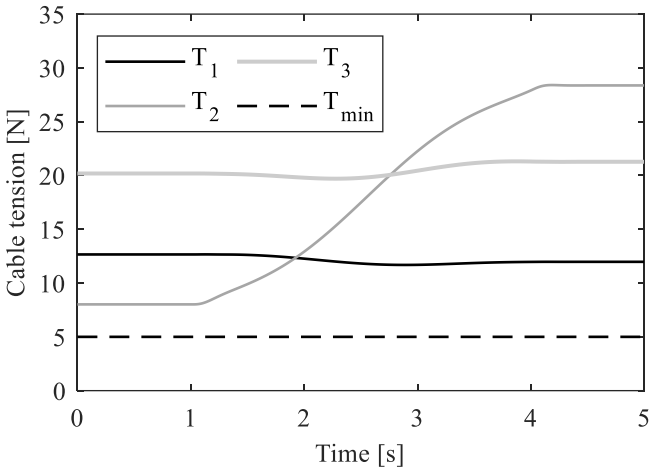


**Figure 5.** Cable tensions with 5th-degree polynomial reference.

### 4.2.3. Test 3: circular path.

The last test consists of a circular planar reference path to be tracked by the end-effector, considering an overall time interval of 5 seconds. The timing law adopted to parametrize the path is a 5th-degree polynomial, and the reference path goes outside the static workspace, which is a condition rarely considered in the literature, that makes the test case severe. In this test case a classical MPC formulation, without embedded integrator, is also tested (which is an easier and more common algorithm) in order to compare it with the MPC-EI; the same design parameters of Table 1 are used for both controllers, with the focus to make a fair comparison. Only the parameter $\mathbf{R}_{\Delta\mathbf{T}}$ is assumed with a different value; indeed, to avoid the instability of the classical MPC algorithm while keeping the same prediction and control horizons, its value is set one hundred times smaller and therefore equals to $1\times10^{-5}\,\mathbf{I}_3$. The planar tracking responses are displayed in Figure 6 for both controllers, together with their contour errors to have a clearer image of the performances. It should be noted that the classical MPC formulation, without embedded integrator, leads to a worse path tracking characterized by a huge contour error and a non-zero steady-state error. More precisely, the MPC algorithm without embedded integrator

https://doi.org/10.3311/ECCOMASMBD2021-201

has an RMS contour error equals to $10.1\times10^{-3}\left[\mathrm{m}\right]$, while the MPC-EI formulation provides a contour error whose RMS value is equal to $8.3\times10^{-4}\left[\mathrm{m}\right]$. Since the contour error results to be lowered by one order of magnitude, these results corroborates the effectiveness of the presented controller. Finally, the optimal cable tensions commanded by the MPC-EI are shown in Figure 7, underlying that this controller is capable to increase the overall performance in terms of path tracking, ensuring at the same time that the boundaries on cable tensions are verified.

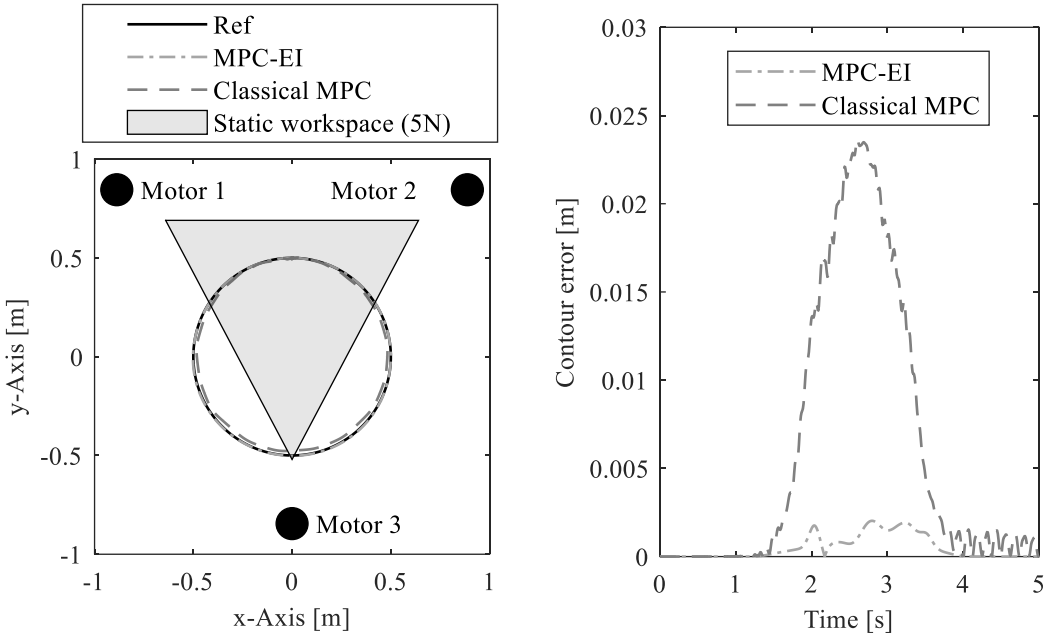


**Figure 6.** Comparison between Classical MPC and MPC-EI: 2D-cartesian trajectory tracking responses with circular reference (on the left) and relative contour errors (on the right).

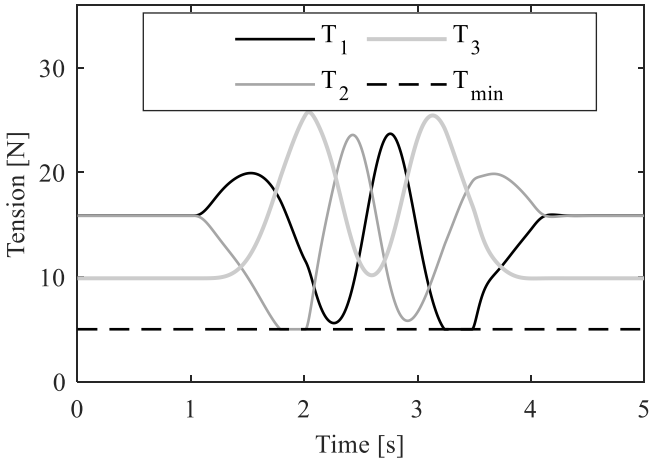


**Figure 7.** MPC-EI cable tensions with circular reference.

## 5. CONCLUSIONS

This paper proposes the preliminary results on a new Model Predictive Control algorithm tailored for path tracking control in Cable-Driven Robots. Control is performed by two sequential actions, that have been conceived to handle the highly nonlinear differential equations form the motor torque to the end-effector position. The first one is responsible for the evaluation of the optimal cable tensions while the second one consists in computing the required motor torques.By means of the implementation of a constrained time-varying MPC, the first step computes positive and bounded cable tensions, while minimizing a proper performance

index that includes the tracking error and the tension variation. The use of an embedded integrator has been proposed to ensure accurate path tracking, in particular at steady-state conditions. The second action of the control scheme, on the other hand, permits to evaluate the necessary motor torques through a feedforward approach.

Three numerical test-cases have been proposed through a three-cable spatial robot, showing good performances in path tracking tasks and ensuring the positiveness of the cable tensions. To better understand the advantages coming from the MPC-EI, this latter has been also compared with a classical MPC formulation, without embedded integrator, which represents an easier and more common algorithm. By looking at the contour error, it has been noticed that MPC-EI has been capable to reduce it by one order of magnitude, ensuring at the same time the verification of the boundaries on all cable tensions and, therefore, confirming its supremacy.

## REFERENCES

[1] Trevisani, A.: Underconstrained planar cable-direct-driven robots: A trajectory planning method ensuring positive and bounded cable tensions. Mechatronics 20 (2010) 113–27 doi:10.1016/j.mechatronics.2009.09.011

[2] Idà, E., Bruckmann, T., Carricato, M.: Rest-to-Rest Trajectory Planning for Underactuated Cable-Driven Parallel Robots. IEEE Trans. Robot. 35 (2019) 1338–51 doi:10.1109/TRO.2019.2931483

[3] Korayem, M. H., Tourajizadeh, H., Bamdad, M.: Dynamic load carrying capacity of flexible cable suspended robot: Robust feedback linearization control approach. J. Intell. Robot. Syst. Theory Appl. 60 (2010) 341–63 doi:10.1007/s10846-010-9423-x

[4] Khosravi, M. A., Taghirad, H. D.: Robust PID control of fully-constrained cable driven parallel robots. Mechatronics 24 (2014) 87–97 doi:10.1016/j.mechatronics.2013.12.001

[5] Boscariol, P., Gasparetto, A., Zanotto, V.: Active position and vibration control of a flexible links mechanism using model-based predictive control. J. Dyn. Syst. Meas. Control. Trans. ASME 132 (2010) 1–4 doi:10.1115/1.4000658

[6] Boscariol, P., Gasparetto, A., Zanotto, V.: Simultaneous position and vibration control system for flexible link mechanisms. Meccanica 46 (2011) 723–37 doi:10.1007/s11012-010-9333-9

[7] Boscariol, P., Zanotto, V.: Design of a controller for trajectory tracking for compliant mechanisms with effective vibration suppression. Robotica 30 (2012) 15–29 doi:10.1017/S0263574711000415

[8] Vermillion, C., Sun, J., Butts, K.: Model predictive control allocation for overactuated systems - Stability and performance. In: IEEE Conference on Decision and Control, New Orleans, LA, USA (2007) 1251–6 doi:10.1109/CDC.2007.4434722

[9] Katliar, M., Fischer, J., Frison, G., Diehl, M., Teufel, H., Bülthoff, H. H.: Nonlinear Model Predictive Control of a Cable-Robot-Based Motion Simulator. IFAC-PapersOnLine 50 (2017) 9833–9 doi:10.1016/j.ifacol.2017.08.901

[10] Qi, R., Rushton, M., Khajepour, A., Melek, W. W.: Decoupled modeling and model predictive control of a hybrid cable-driven robot (HCDR). Rob. Auton. Syst. 118 (2019) 1–12 doi:10.1016/j.robot.2019.04.013

[11] Santos, J. C., Chemori, A., Gouttefarde, M.: Model predictive control of large-dimension cable-driven parallel robots. Mech. Mach. Sci. 74 (2019) 221–32 doi:10.1007/978-3-030-20751-9_19

[12] Santos, J. C., Chemori, A., Gouttefarde, M.: Redundancy Resolution Integrated Model Predictive Control of CDPRs: Concept, Implementation and Experiments. In: IEEE International Conference on Robotics and Automation (ICRA), Paris, France (2020) 3889–95 doi:10.1109/ICRA40945.2020.9197271

[13] Xiang, S., Gao, H., Liu, Z., Gosselin, C.: Dynamic transition trajectory planning of three-DOF cable-suspended parallel robots via linear time-varying MPC. Mech. Mach. Theory 146 (2020) 103715 doi:10.1016/j.mechmachtheory.2019.103715

[14] Richiedei, D., Tamellin, I., Trevisani, A.: A homotopy transformation method for interval-based model updating of uncertain vibrating systems. Mech. Mach. Theory 160 (2021) 104288 doi:10.1016/j.mechmachtheory.2021.104288

[15] Idà, E., Briot, S., Carricato, M.: Identification of the inertial parameters of underactuated Cable-Driven Parallel Robots. Mech. Mach. Theory 167 (2022) 104504 doi:10.1016/j.mechmachtheory.2021.104504

https://doi.org/10.3311/ECCOMASMBD2021-138

ECCOMAS Thematic Conference on Multibody Dynamics
December 12 - 15, 2021, Budapest, Hungary

# A Heuristic Sequencing Method for Time Optimal Tracking of Open and Closed Paths

**Christian Zauner**[1], **Hubert Gattringer**[1], **Andreas Müller**[1], **Matthias Jörgl**[2]

[1] Institute of Robotics
Johannes Kepler University Linz
Altenbergerstraße 69, 4040 Linz, Austria
[christian.zauner, hubert.gattringer, a.mueller]@jku.at

[2] Trotec Laser GmbH
Freilingerstraße 99, 4614 Marchtrenk, Austria
matthias.joergl@troteclaser.com

## ABSTRACT

Tracking sequences of predefined open and closed paths is of crucial interest for applications like laser cutting and similar production processes. These distinct paths are connected by non-productive, four times continuously differentiable trajectories, which also account for the overall process time. Heuristic methods are applied in order to find a proper sequencing of the open and closed path and thereby minimize the overall process time subject to constraints given by the system limits. To this end the exact traversing times of the non-productive linking trajectories are computed, which also have to be time optimal subject to the system limits. Finally two heuristic algorithms are presented and compared with respect to solution quality and calculation time using randomly generated problems.

**Keywords:** Path Planning, Heuristic Scheduling, Traveling Salesman Problem, Laser Cutting Machine.

## 1 INTRODUCTION

For laser cutting applications a cutting job consists of predefined open and closed paths. Since theses paths are often not connected the question arises, how these paths should be sorted in order to minimize overall process time. Numerous contributions, concerning this topic, can be found in the literature, as indicated by the review paper [1], where 72 contributions are collected and compared with respect to the used methods and algorithms.

Although a more general approach would be conceivable, this work focuses on paths on the 2D plane and gantry like robotic systems as shown in figure 1. These systems are subject to restrictions like maximum velocity, acceleration and jerk for each axis respectively. Furthermore there are process specific constraints. In case of the laser cutting process the maximum velocity tangentially to the path depends on the material which has to be cut and in order to ensure a clean cut the velocity at the beginning and at the end of each path has to be zero. Subject to these constraints a time optimal path tracking solution for each path can be found and the optimal partial solutions can be connected by time optimal trajectories along straight lines. With an increasing number of paths to track the impact of the non-productive traversing time introduced by these links on the overall process time is getting dominant if the sequencing is not handled properly. To this end two heuristic approaches are provided, tested and compared with respect to an integer linear programming algorithm. The optimal traversing time of the non-productive linking trajectories depends non-linearly either on the end points as well as the system limits. In contrast to e.g. [2], where a piecewise linear function is introduce approximating this non-linear behaviour, in this work analytic, non-linear expressions are derived and used for the optimal traversing time.

https://doi.org/10.3311/ECCOMASMBD2021-138

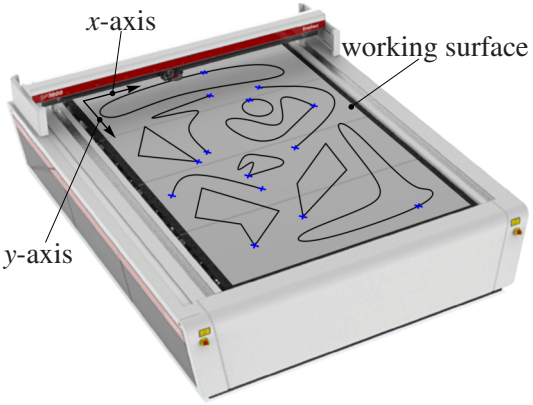


**Figure 1**. Gantry laser cutting machine

## 2 PROBLEM DEFINITION AND COMBINATORIAL BACKGROUND

Before setting up the problem definition some graph theoretical terminology should be introduced, which is used through out the following sections. An undirected graph is defined by a set of nodes $\mathfrak{N} = \{n_i \mid 0 \leq i < N\}$, where $N$ denotes the number of nodes, and a set of edges $\mathfrak{E} \subseteq \{e_{i,j} \mid 0 \leq i < N, i < j < N\}$ connecting some or all of these nodes, where edge $e_{i,j}$ is equivalent to $e_{j,i}$. An undirected graph can be

- weighted, if each edge $e_{i,j}$ is associated with a weight $w_{i,j}$.
- simple, if each edge $e_{i,j}$ is unique in $\mathfrak{E}$.
- an undirected multigraph, if edges are allowed to be not unique in $\mathfrak{E}$.
- connected, if each pair of nodes can be connected by a sequence of edges in $\mathfrak{E}$
- complete, if each pair of nodes is connected by exactly one edge.

A cycle in the graph is a sequence of edges, which starts and ends at the same node. Special cycles are Eulerian cycles, which contain every edge of a graph once, and Hamilton cycles, which start and end at the same node and traverse every other node of the graph exactly once. A Hamilton cycle is also called a tour of the graph.

A spanning tree of a connected graph is a subset of edges, which does not contain cycles and contains all nodes. Consequently the minimum spanning tree of a connected, weighted graph is the spanning tree with the minimum total edge weight.

Finding the tour with the minimum total edge weight in a complete, undirected, weighted graph is equivalent to solving the corresponding symmetric traveling salesman problem. This very well know NP-hard combinatorial problem is assumed to be not solvable in polynomial time. The number of all tours in such a graph can be stated by $N_T = \frac{(N-1)!}{2}$, which grows extremely fast by an increasing number of nodes. Therefore a brute force approach can only be suitable for a very low number of nodes. Although there exist many exact algorithms to solve a traveling salesman problem, like branch-and-cut or branch-and-bound, an exact solution is getting more and more impractical with an increasing number of nodes. Actually for most applications a good approximation of the optimal solution would suffice. This can be achieved efficiently by heuristic algorithms.

A cutting job, which has to be processed by the laser cutting machine, consists of several cutting paths, denoted $c_i$, with $1 \leq i \leq N_c$. Each of these paths $c_i$ is defined by two points in the 2D plane, a start point $\mathbf{r}_{s,i}$ and an end point $\mathbf{r}_{e,i}$. These two points are connected by a path, for which it is assumed, that a time optimal trajectory, with respect to the machine and process constraints,

https://doi.org/10.3311/ECCOMASMBD2021-138

is known. Additionally a job should start and end at a defined idle position given by $\mathbf{r}_0$. Since the trajectories for each cutting path are already assumed to be optimal, the overall processing time can be reduced by finding a processing sequence of these paths, which minimizes the total non-productive traversing time between the consecutive paths. To this end a complete, undirected, weighted graph of the start and end points of the cutting paths is constructed with edge weights according the traversing time between these points. The optimal solution of the problem corresponds then to the solution of the symmetric traveling salesman problem given by this graph.

The cutting paths $c_i$ can be closed, i.e. $\mathbf{r}_{s,i} = \mathbf{r}_{e,i}$, or open, i.e. $\mathbf{r}_{s,i} \neq \mathbf{r}_{e,i}$. Without loss of generality it is assumed, that the first $N_{cc}$ paths are closed and the remaining $N_{co}$ paths are open, which means that the conditions

$$\mathbf{r}_{s,i} = \mathbf{r}_{e,i} \quad \text{for} \quad 1 \leq i \leq N_{cc} \tag{1}$$

$$\mathbf{r}_{s,i} \neq \mathbf{r}_{e,i} \quad \text{for} \quad N_{cc} < i \leq N_c = N_{cc} + N_{co} \tag{2}$$

are fulfilled. This can be always obtained by reordering indices. Since the start and end point coincide, closed paths can be represented by a single node in the graph. Based on this, the $N = N_{cc} + 2N_{co} + 1$ nodes of the graph can be associated with the start (and end) points of the cutting paths as well as the idle position according to the mapping

$$\mathbf{r}_n(n_i) = \begin{cases} \mathbf{r}_0 & & & \text{for} & i = 0 \\ \mathbf{r}_{s,i} & & & \text{for} & 1 \leq i \leq N_{cc} \\ \mathbf{r}_{s,j} & \text{with} & j = N_{cc} + (i - N_{cc} + 1)/2 & \text{for} & N_{cc} < i < N \wedge (i - N_{cc}) \text{ is odd} \\ \mathbf{r}_{e,j} & \text{with} & j = N_{cc} + (i - N_{cc})/2 & \text{for} & N_{cc} < i < N \wedge (i - N_{cc}) \text{ is even} \end{cases} . \tag{3}$$

With the definition of the edge weights, provided in the following section, the graph is fully defined and the traveling salesman problem can be solved. But if open cutting paths are present, i.e. $N_{co} > 0$, each algorithm used has to enforce, that these paths are actually traversed in the solution.

## 3 OBJECTIVE FUNCTION

Regardless of whether the problem is solved by an exact algorithm or by a heuristic, the objective is to find the tour with the minimum total edge weight. In order to compute the edge weights, a special metric is introduced. Since the overall goal is to achieve a time optimal solution all the considered links connecting two points on the 2D plane have to be time optimal on their own. Therefore the distance between two arbitrary points can be expressed by the minimum time needed to traverse a straight line between these two points satisfying the constraints of the robotic system. The resulting distance measure satisfies the triangle inequality as well as the remaining requirements of a metric.

The transition from one point in the 2D plane $\mathbf{r}_n(n_i) = \mathbf{r}_i = \begin{bmatrix} x_i & y_i \end{bmatrix}^\mathsf{T}$ to another point $\mathbf{r}_n(n_j) = \mathbf{r}_j = \begin{bmatrix} x_j & y_j \end{bmatrix}^\mathsf{T}$, corresponding to the nodes $n_i$ and $n_j$ respectively, is performed according to a time optimal $\sin^2$-jerk trajectory. This trajectory has the property, that it is continuously differentiable until the fourth derivative, which is beneficial, since the excitation of vibrations is reduced. Another advantage of this trajectory is, that the minimum traversing time between two points can be calculated analytically with respect to maximum velocity, acceleration and jerk. These maximum values can be defined for the each axis individually by $v_{\max,k}$, $a_{\max,k}$ and $j_{\max,k}$ with $k \in \{x, y\}$. Additionally the maximum tangential velocity, acceleration and jerk can be constrained by $v_{\max,t}$, $a_{\max,t}$ and $j_{\max,t}$ respectively. In order to calculate the minimum traversing time the distances $\Delta x_{i,j} = x_j - x_i$ and $\Delta y_{i,j} = y_j - y_i$ along each axis are needed, which can be used to calculate the Euclidean distance

$$\Delta d_{i,j} = \sqrt{{\Delta x_{i,j}}^2 + {\Delta y_{i,j}}^2} \tag{4}$$

https://doi.org/10.3311/ECCOMASMBD2021-138

between the two points. With these distance measures the actual maximum values for a straight path between the points $\mathbf{r}_i$ and $\mathbf{r}_j$ can be stated by

$$v_{\max,i,j} = \min\left( v_{\max,x}\frac{\Delta d_{i,j}}{|\Delta x_{i,j}|}, v_{\max,y}\frac{\Delta d_{i,j}}{|\Delta y_{i,j}|}, v_{\max,t} \right), \tag{5}$$

$$a_{\max,i,j} = \min\left( a_{\max,x}\frac{\Delta d_{i,j}}{|\Delta x_{i,j}|}, a_{\max,y}\frac{\Delta d_{i,j}}{|\Delta y_{i,j}|}, a_{\max,t} \right), \tag{6}$$

$$j_{\max,i,j} = \min\left( j_{\max,x}\frac{\Delta d_{i,j}}{|\Delta x_{i,j}|}, j_{\max,y}\frac{\Delta d_{i,j}}{|\Delta y_{i,j}|}, j_{\max,t} \right). \tag{7}$$

The trajectory over time $t$ can then be defined by

$$\mathbf{r}_{i,j}(t) = \mathbf{r}_i + \frac{\mathbf{r}_j - \mathbf{r}_i}{\Delta d_{i,j}}\xi(t, \Delta d_{i,j}, v_{\max,i,j}, a_{\max,i,j}, j_{\max,i,j}) \tag{8}$$

with the function $\xi(t, \Delta d, v_{\max}, a_{\max}, j_{\max})$ satisfying the properties

$$\xi(0, \Delta d, v_{\max}, a_{\max}, j_{\max}) = 0, \tag{9}$$

$$\xi(t_E, \Delta d, v_{\max}, a_{\max}, j_{\max}) = \Delta d, \tag{10}$$

$$0 \leq \dot{\xi}(t, \Delta d, v_{\max}, a_{\max}, j_{\max}) \leq v_{\max}, \tag{11}$$

$$|\ddot{\xi}(t, \Delta d, v_{\max}, a_{\max}, j_{\max})| \leq a_{\max}, \tag{12}$$

$$|\dddot{\xi}(t, \Delta d, v_{\max}, a_{\max}, j_{\max})| \leq j_{\max}. \tag{13}$$

By partitioning the traversing time $t_E$ in 7 phases by interleaving 4 jerk phases of length $t_j$ with 3 jerk free phases of lengths $t_a$, $t_v$ and $t_a$ corresponding to phases of constant acceleration respectively velocity, $\xi(t)$ and its derivatives (omitting the last arguments for brevity) can be stated by

$$\dddot{\xi}(t) = \begin{cases} 0 & t < 0 \\ j_{\max}\sin\left(\frac{\pi t}{t_j}\right)^2 & 0 \leq t < t_j \\ 0 & t_j \leq t < t_j + t_a \\ -j_{\max}\sin\left(\frac{\pi(t-t_j-t_a)}{t_j}\right)^2 & t_j + t_a \leq t < 2t_j + t_a \\ 0 & 2t_j + t_a \leq t \leq \frac{t_E}{2} \\ \dddot{\xi}(t_E - t) & \frac{t_E}{2} < t \end{cases}, \tag{14}$$

$$\ddot{\xi}(t) = \int_0^t \dddot{\xi}(\tau)\mathrm{d}\tau, \qquad \dot{\xi}(t) = \int_0^t \ddot{\xi}(\tau)\mathrm{d}\tau, \qquad \xi(t) = \int_0^t \dot{\xi}(\tau)\mathrm{d}\tau \tag{15}$$

with $t_E = 4t_j + 2t_a + t_v$, $t_j = 0$ if $\Delta d = 0$, $t_j > 0$ if $\Delta d > 0$, $t_a \geq 0$ and $t_v \geq 0$. The maximum values of $\ddot{\xi}(t)$ and $\dot{\xi}(t)$ as well as the final value $\xi(t_E)$ can be expressed in terms of

$$\max_t(|\ddot{\xi}(t)|) = \ddot{\xi}(t_j) = \frac{j_{\max}t_j}{2} = \hat{a} \leq a_{\max}, \tag{16}$$

$$\max_t(|\dot{\xi}(t)|) = \dot{\xi}(2t_j + t_a) = \hat{a}t_a + \frac{2\hat{a}^2}{j_{\max}} = \hat{v} \leq v_{\max}, \tag{17}$$

$$\xi(t_E) = \hat{a}{t_a}^2 + \frac{6\hat{a}^2 t_a}{j_{\max}} + \hat{v}t_v + \frac{8\hat{a}^3}{{j_{\max}}^2} = \Delta d. \tag{18}$$

In order to get a time optimal trajectory, four cases have to be distinguished, which have the following solutions:

https://doi.org/10.3311/ECCOMASMBD2021-138

- $t_a = 0 \wedge \hat{a} \leq a_{\max} \wedge t_v = 0 \wedge \hat{v} \leq v_{\max}$

$$\hat{a} = \frac{1}{2}\sqrt[3]{{j_{\max}}^2 \Delta d} \qquad \hat{v} = \frac{1}{2}\sqrt[3]{j_{\max} \Delta d^2} \qquad t_j = \sqrt[3]{\frac{\Delta d}{j_{\max}}} \tag{19}$$

$$\Delta d \leq \sqrt{\frac{8{v_{\max}}^3}{j_{\max}}} \wedge v_{\max} \leq \frac{2{a_{\max}}^2}{j_{\max}} \vee \Delta d \leq \frac{8{a_{\max}}^3}{{j_{\max}}^2} \wedge v_{\max} > \frac{2{a_{\max}}^2}{j_{\max}} \tag{20}$$

- $t_a = 0 \wedge \hat{a} \leq a_{\max} \wedge t_v > 0 \wedge \hat{v} = v_{\max}$

$$\hat{a} = \sqrt{\frac{j_{\max} v_{\max}}{2}} \qquad t_v = \frac{\Delta d}{v_{\max}} - \sqrt{\frac{8 v_{\max}}{j_{\max}}} \qquad t_j = \sqrt{\frac{2 v_{\max}}{j_{\max}}} \tag{21}$$

$$\Delta d > \sqrt{\frac{8{v_{\max}}^3}{j_{\max}}} \wedge v_{\max} \leq \frac{2{a_{\max}}^2}{j_{\max}} \tag{22}$$

- $t_a > 0 \wedge \hat{a} = a_{\max} \wedge t_v = 0 \wedge \hat{v} \leq v_{\max}$

$$\hat{v} = \sqrt{\frac{{a_{\max}}^4}{{j_{\max}}^2} + a_{\max} \Delta d} - \frac{{a_{\max}}^2}{j_{\max}} \qquad t_a = \sqrt{\frac{{a_{\max}}^2}{{j_{\max}}^2} + \frac{\Delta d}{a_{\max}}} - \frac{3 a_{\max}}{j_{\max}} \qquad t_j = \frac{2 a_{\max}}{j_{\max}} \tag{23}$$

$$\frac{8{a_{\max}}^3}{{j_{\max}}^2} < \Delta d \leq \frac{2 v_{\max} a_{\max}}{j_{\max}} + \frac{{v_{\max}}^2}{a_{\max}} \implies v_{\max} > \frac{2{a_{\max}}^2}{j_{\max}} \tag{24}$$

- $t_a > 0 \wedge \hat{a} = a_{\max} \wedge t_v > 0 \wedge \hat{v} = v_{\max}$

$$t_a = \frac{v_{\max}}{a_{\max}} - \frac{2 a_{\max}}{j_{\max}} \qquad t_v = \frac{\Delta d}{v_{\max}} - \frac{v_{\max}}{a_{\max}} - \frac{2 a_{\max}}{j_{\max}} \qquad t_j = \frac{2 a_{\max}}{j_{\max}} \tag{25}$$

$$\Delta d > \frac{2 v_{\max} a_{\max}}{j_{\max}} + \frac{{v_{\max}}^2}{a_{\max}} \wedge v_{\max} > \frac{2{a_{\max}}^2}{j_{\max}} \tag{26}$$

The terminal time of $\xi(t, \Delta d, v_{\max}, a_{\max}, j_{\max})$ can then be stated by

$$t_E(\Delta d, v_{\max}, a_{\max}, j_{\max}) = \begin{cases} 4\sqrt[3]{\frac{\Delta d}{j_{\max}}} & \Delta d \leq \sqrt{\frac{8{v_{\max}}^3}{j_{\max}}} \wedge \Delta d \leq \frac{8{a_{\max}}^3}{{j_{\max}}^2} \\ \sqrt{\frac{8 v_{\max}}{j_{\max}}} + \frac{\Delta d}{v_{\max}} & \Delta d > \sqrt{\frac{8{v_{\max}}^3}{j_{\max}}} \wedge v_{\max} \leq \frac{2{a_{\max}}^2}{j_{\max}} \\ 2\left(\frac{a_{\max}}{j_{\max}} + \sqrt{\frac{{a_{\max}}^2}{{j_{\max}}^2} + \frac{\Delta d}{a_{\max}}}\right) & \frac{8{a_{\max}}^3}{{j_{\max}}^2} < \Delta d \leq \frac{2 v_{\max} a_{\max}}{j_{\max}} + \frac{{v_{\max}}^2}{a_{\max}} \\ \frac{2 a_{\max}}{j_{\max}} + \frac{v_{\max}}{a_{\max}} + \frac{\Delta d}{v_{\max}} & \Delta d > \frac{2 v_{\max} a_{\max}}{j_{\max}} + \frac{{v_{\max}}^2}{a_{\max}} \wedge v_{\max} > \frac{2{a_{\max}}^2}{j_{\max}} \end{cases}. \tag{27}$$

Finally the minimum traversing time between the points $\mathbf{r}_i$ and $\mathbf{r}_j$, which defines the edge weight $w_{i,j}$ between the nodes $n_i$ and $n_j$, is

$$w_{i,j} = t_E(\Delta d_{i,j}, v_{\max,i,j}, a_{\max,i,j}, j_{\max,i,j}). \tag{28}$$

## 4 CHRISTOFIDES ALGORITHM

The Christofides algorithm [3] is a construction heuristic based on the minimum spanning tree of the complete, undirected, weighted graph. The main steps of the algorithm are as follows:

- Build the minimum spanning tree

https://doi.org/10.3311/ECCOMASMBD2021-138

- Select all nodes of the minimum spanning tree with an odd degree
- Find a minimum-weight perfect matching of the complete subgraph of these nodes
- Combine the edges from the perfect matching with the minimum spanning tree
- Form an Eulerian cycle on the result
- Convert the Eulerian cycle to a Hamiltonian circle (tour) by skipping all repeating nodes

The total sum of the edge weights (tour length) of the so gained tour over all nodes of the graph is guaranteed to be within 1 and 1.5 times the length of the optimal tour, if the edge weights satisfy the triangle inequality.

As shown in [4] this algorithm can also be used to obtain a near optimal solution for problems with $N_{co} > 0$, i.e. open paths are present. In order to guarantee that an open path $c_j$ with $j > N_{cc}$ with the corresponding nodes $n_i$ and $n_{i+1}$, according to start and end point thereof, is traversed, the weight $w_{i,i+1}$ has to be modified according to

$$w_{i,i+1} = \min(\min\{w_{i,k} \mid k > i+1\}, \min\{w_{k,i+1} \mid k < i\}). \tag{29}$$

This ensures, that the edge corresponding to an open cutting path is selected, when building the minimum spanning tree. Additionally it has to be ensured, that these edges are not skipped when converting the Eulerian cycle to the Hamilton cycle. As stated in [4] this procedure leads to the downside that the triangle inequality is no longer satisfied and the major benefit, which is the upper bound of 1.5 times of the optimal tour length, does no longer apply.

The algorithm used for solving the examples is implemented in Python based on the packages numpy and networkx. In order to speed up the calculation time of the minimum-weight perfect matching a heuristic approach is chosen for problems with $N \geq 1000$. Therefore the minimum-weight perfect matching is not performed on the complete subgraph of the odd degree nodes, but on a minimum-weight sparse subgraph thereof, with a minimum degree of the occurring nodes of five.

## 5 LIN-KERNIGHAN-HELSGAUN (LKH) ALGORITHM FOR PROBLEMS WITH OPEN AND CLOSED PATH

In contrast to the Christofides algorithm, which terminates once a feasible solution is found, the Lin-Kernighan-Helsgaun algorithm [5], which is based on the algorithm of Lin-Kernighan [6], is an iteratively improving heuristic. After a preprocessing phase, essentially based on an extended minimum spanning tree, a suboptimal initial solution is generated with any suitable and fast construction heuristic. This initial solution is then improved by so called $k$-opt exchanges, which means that in every iteration step, $k$ edges of the current tour are replaced by $k$ other edges, in order to improve the tour. Special heuristic rules are applied to decide which edges should be removed and which edges should be used instead. This drastically reduces the according search spaces and consequently also the calculation time. To decrease the calculation time even further the $k$-opt exchanges are constructed sequentially from $k = 2$ to $k = 5$. Once an improvement is found the exchange is applied immediately and the algorithm proceeds with the next iteration step. The algorithm terminates when no further improvement of the tour length with respect to $k \leq 5$ and the applied heuristic rules can be found.

This algorithm can be applied straightforwardly to a problem with solely closed paths, i.e. problems with $N_{cc} > 0$ and $N_{co} = 0$. In order to use this algorithm with open and closed paths, i.e. problems with $N_{cc} \geq 0$ and $N_{co} > 0$, some modifications in the problem setup and the algorithm are necessary.

In the preprocessing phase of the algorithm constructive sets are associated to each node, which are used to decide which edge should be added in the iteration phase. With open cutting paths

present, it has to be ensured, that the according edges are part of these sets. Additionally when constructing the initial tour, it has to be ensured, that these edges are part of the initial tour. In the iterative improving phase two modifications of the algorithm are applied, in order to ensure the validity of the solution tour and to reduce the calculation time. Firstly edges according to the open cutting paths are never removed from the current solution. Secondly each time an edge $e_{i,j}$ is considered to be added to the current solution, it is determined whether the start or end node $n_i$ or $n_j$ of this edge is either start or end node of an open cutting path. If so, it is checked whether flipping the sequential order of the two end points of the affected open path may further improve the current solution. Figure 2 shows the edges (dashed lines), which are taken into account, when any edge connecting the two open paths in the figure is considered to be added to the current solution, and the edges (fully drawn lines), which are actually chosen. The algorithm used for solving the examples is implemented in C++17 based on the standard library.

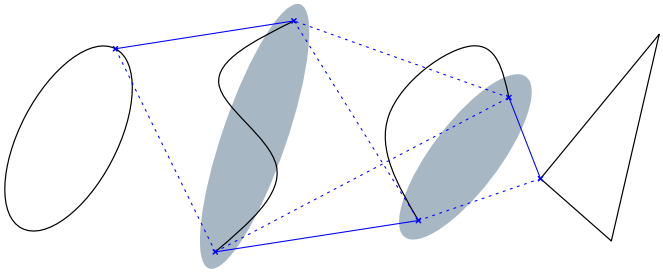

**Figure 2**. Selection of actually added edges in case of open paths

## 6 INTEGER LINEAR PROGRAMMING

In order to solve the traveling salesman problem by integer linear programming each edge $e_{i,j}$ is associated with a boolean variable $\hat{e}_{i,j} \in \{0,1\}$, which indicates whether the respective edge is part of the solution tour or not. According to the work of [7] the optimization problem can be stated by

$$\min_{\hat{e}_{i,j}} \sum_{i=0}^{N-1} \sum_{j=i+1}^{N-1} \hat{e}_{i,j} w_{i,j} \tag{30}$$

$$\text{s.t.} \sum_{j=i+1}^{N-1} \hat{e}_{i,j} + \sum_{j=i+1}^{N-1} \hat{e}_{j,i} = 2 \qquad 0 \leq i < N \tag{31}$$

$$\hat{e}_{i,i+1} = 1 \qquad i \in \{N_{cc}+1, N_{cc}+3, \ldots, N-2\} \tag{32}$$

By the first constraint it is enforced, that each node is part of the solution and has a degree of two, which means it has one incoming and one outgoing edge. The second constraint (32) ensures, that the edges associated with the open cutting paths are part of the solution edges. Solving this problem does not necessarily result in a valid tour, since also a number of cycles containing all nodes fulfil the constraints. Therefore additional constraints, which eliminate cycles have to be added. The number of this constraints grows exponentially with an increasing number of nodes. Therefore the optimization problem is solved iteratively and in every iteration constraints

$$\sum_{(i,j)\in\mathfrak{C}_k} \hat{e}_{i,j} \leq |\mathfrak{C}_k| - 1 \tag{33}$$

for each occurring cycle $\mathfrak{C}_k = \{(i_1,j_1),(i_2,j_2),\ldots,(i_{N_k},j_{N_k})\}$ are added with $N_k = |\mathfrak{C}_k|$ according to the set of $N_k$ edges $\{e_{i_1,j_1}, e_{i_2,j_2}, \ldots, e_{i_{N_k},j_{N_k}}\}$ forming the cycle. The algorithm used for solving the examples is implemented in Matlab based on `intlinprog(...)`.

## 7 EXAMPLES

The examples shown in this section are created randomly based on the Voronoi cells of randomly distributed points in the 2D plane. Each problem consist of $N_{cc}$ closed and $N_{co}$ open cutting

paths. The constraining maximum values use for calculating the edge weights are stated in table 1. Table 2 compares the total edge weight of the solution tours, excluded the weights of the edges according to the open cutting paths, acquired by the different algorithms. Since all the provided algorithms are implemented in different frameworks, comparing the actual calculation time is not really meaningful. Nonetheless the approximate calculation times are stated in table 3 for reference purpose. For the problem sizes of $N > 101$ the integer linear programming approach did not terminate in a reasonable time span, which is noted by a $-$ in the tables. Graphical representations are provided for the problems of sizes $N \leq 101$, as can be seen in the figures 3 to 10. The figures for the problems with a higher number of nodes are omitted, since the graphical representation is getting less and less expressive.

As can be seen in table 3 the Christofides heuristic and LKH heuristic perform equally well for small problem sizes, regarding solution quality as well as calculation time. But with an increasing number of nodes the LKH outperforms the Christofides heuristic in both criteria, especially regarding the calculation time. Additionally it has to be noted, that for the Christofides heuristic and problems with $N \geq 1000$, a heuristic approach has to be used for the minimum-weight perfect matching, in order to get a result in reasonable time. Remarkable is the fact, that for all the examples, for which an optimal solution has been found by the integer linear programming algorithm, the LKH heuristic leads to the exact same solution.

**Table 1**. Examples: Used maximum values according to the system limits

| | $v_{\max}$ | $a_{\max}$ | $j_{\max}$ |
|---|---|---|---|
| | $\mathrm{m\,s^{-1}}$ | $\mathrm{m\,s^{-2}}$ | $\mathrm{m\,s^{-3}}$ |
| $x$-axis | 1 | 5 | 50 |
| $y$-axis | 1 | 5 | 50 |
| tangentially | 1.2 | $\infty$ | $\infty$ |

**Table 2**. Examples: Total edge weight of solution tour for different algorithms

| Problem sizes | | | Total edge weight of solution tour in s | | | |
|---|---|---|---|---|---|---|
| $N$ | $N_{cc}$ | $N_{co}$ | Unsorted | LKH | Christofides | ILP |
| 31 | 25 | 5 | 62.470 | 23.931 | 24.282 | 23.931 |
| 101 | 70 | 30 | 163.539 | 58.215 | 60.881 | 58.215 |
| 301 | 250 | 50 | 506.788 | 145.305 | 151.549 | – |
| 1001 | 700 | 300 | 1675.920 | 378.299 | 399.266 | – |
| 3001 | 2500 | 500 | 4975.530 | 976.974 | 1020.000 | – |

**Table 3**. Examples: Approximate calculation time for different algorithms

| Problem sizes | | | Approximate calculation time in s | | | |
|---|---|---|---|---|---|---|
| $N$ | $N_{cc}$ | $N_{co}$ | Edge Weights | LKH | Christofides | ILP |
| 31 | 25 | 5 | $3.5 \times 10^{-2}$ | $3.8 \times 10^{-1}$ | $4.1 \times 10^{-1}$ | 2.9 |
| 101 | 70 | 30 | $4.3 \times 10^{-2}$ | 1.9 | 2.3 | 11.2 |
| 301 | 250 | 50 | $1.0 \times 10^{-1}$ | 3.6 | 27.6 | – |
| 1001 | 700 | 300 | $4.8 \times 10^{-1}$ | 11.7 | 28.5 | – |
| 3001 | 2500 | 500 | 1.0 | 19.9 | 213 | – |

https://doi.org/10.3311/ECCOMASMBD2021-138

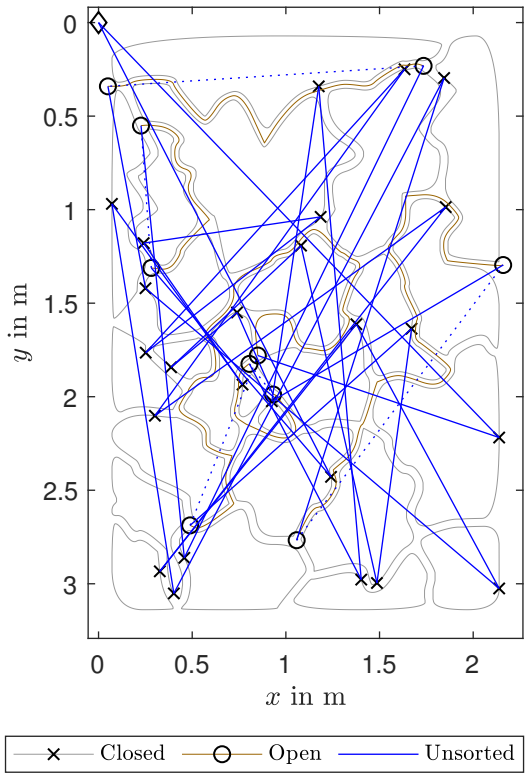


**Figure 3**. Example $N = 31$: Random Tour

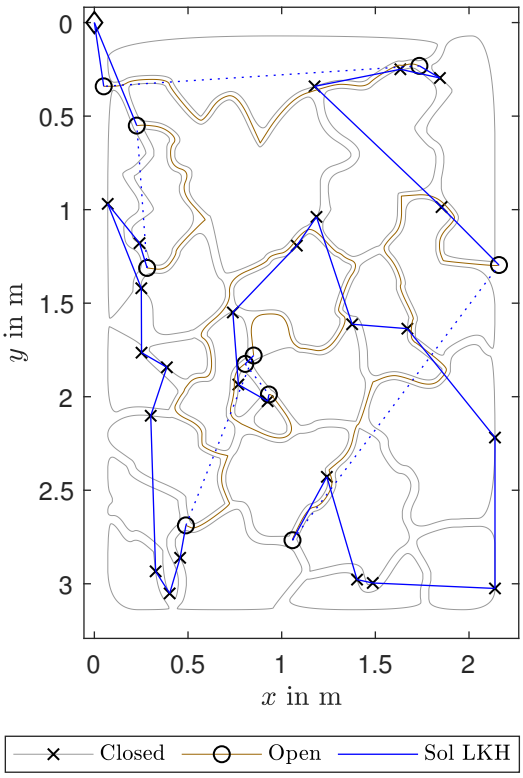


**Figure 4**. Example $N = 31$: Solution LKH

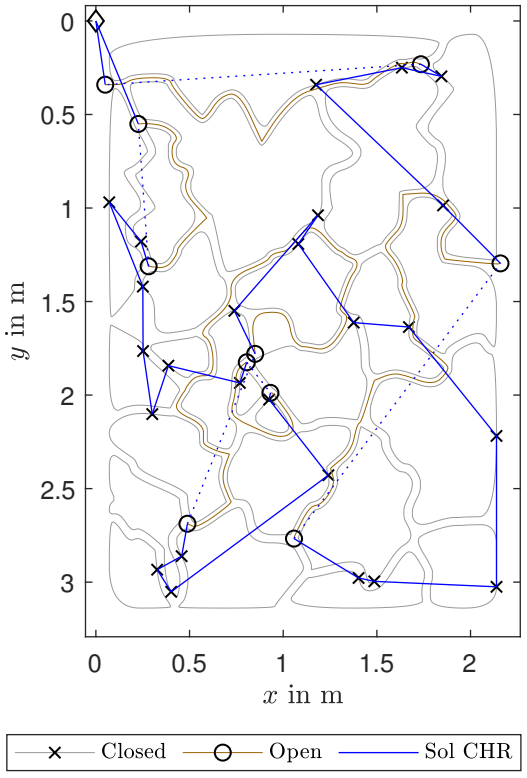


**Figure 5**. Example $N = 31$: Solution Christofides

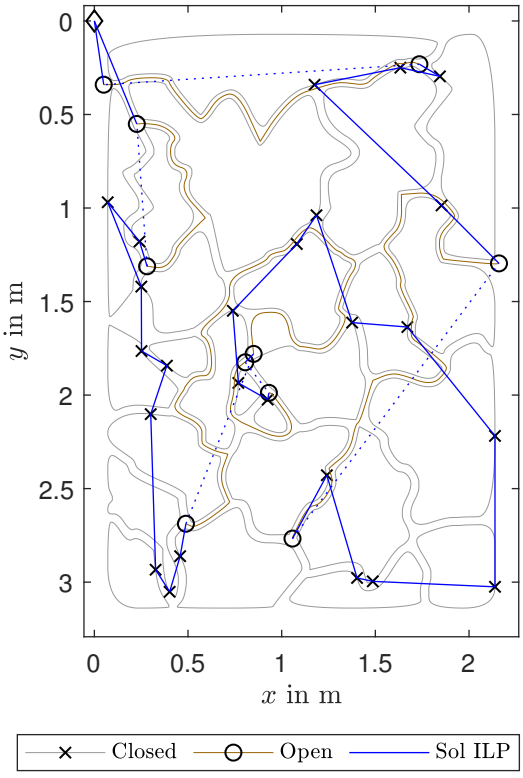


**Figure 6**. Example $N = 31$: Solution ILP

https://doi.org/10.3311/ECCOMASMBD2021-138

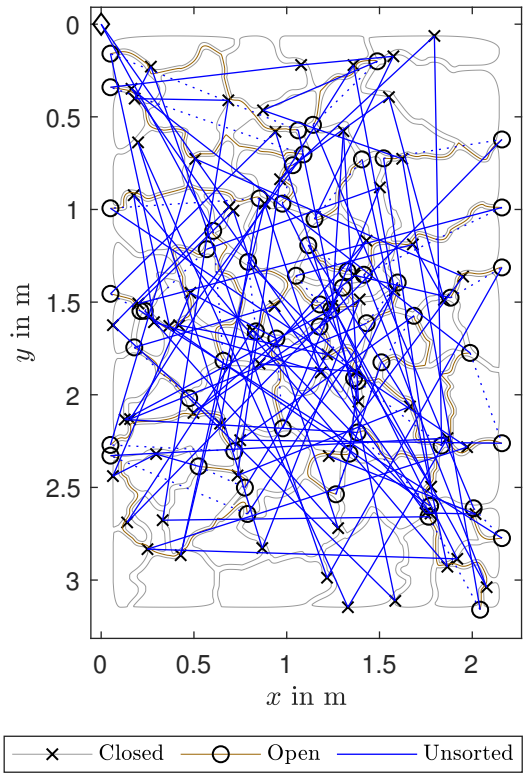


**Figure 7**. Example $N = 101$: Random Tour

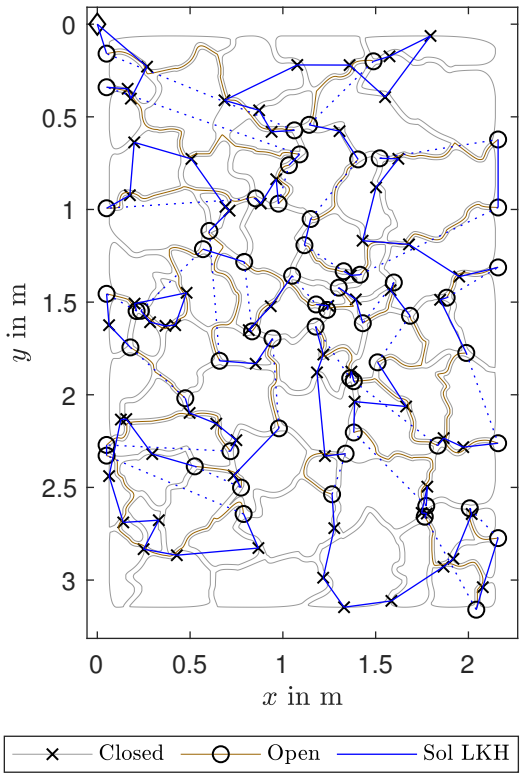


**Figure 8**. Example $N = 101$: Solution LKH

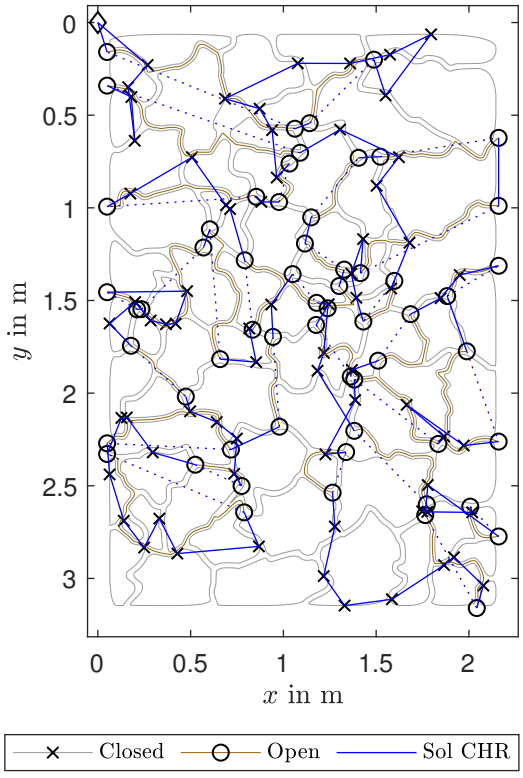


**Figure 9**. Example $N = 101$: Solution Christofides

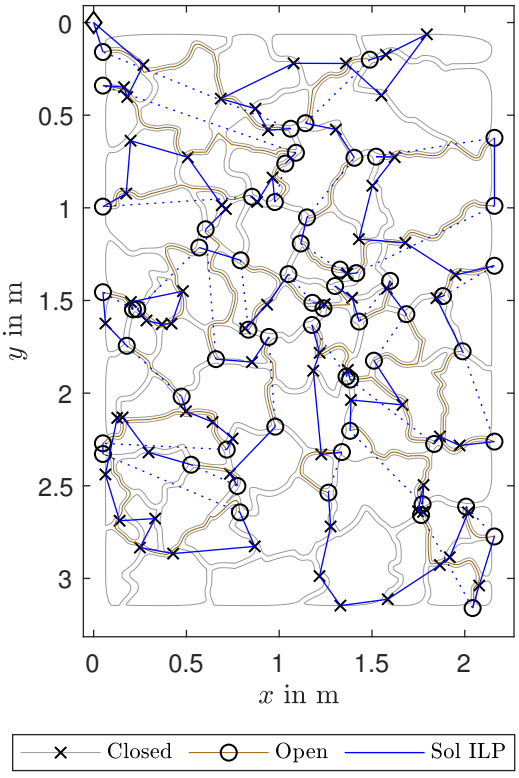


**Figure 10**. Example $N = 101$: Solution ILP

https://doi.org/10.3311/ECCOMASMBD2021-138

## 8 CONCLUSION

It has been shown, that the Christofides heuristic as well as the LKH heuristic can be applied for sequencing open and closed cutting paths, while minimizing the overall traversing time of the non-productive trajectories, connecting these paths. This has been achieved by minor extensions on the respective algorithms and by introducing a special metric for calculating the edge weights, which models the traversing time of an time optimal $\sin^2$-jerk trajectory along a straight path in the 2D plane.

Finally the Christofides heuristic, the LKH heuristic and an integer linear programming algorithm are compared, regarding solution quality and calculation time using random generated examples of different problem sizes. The results of these examples indicate that both the Christofides and the LKH heuristic are capable of finding good approximations of the optimal tour for small problem sizes and that the LKH heuristic performs better, especially regarding calculation time, for problems with a higher number of nodes.

## ACKNOWLEDGMENTS

Supported by the "LCM - K2 Center for Symbiotic Mechatronics" within the framework of the Austrian COMET-K2 program.

## REFERENCES

[1] Dewil, R., Vansteenwegen, P., Cattrysse, D.: A review of cutting path algorithms for laser cutters. The International Journal of Advanced Manufacturing Technology **87**(5) (2016) 1865–1884

[2] Dewil, R.: On generating tool paths for laser cutters. (2014)

[3] Christofides, N.: Worst-case analysis of a new heuristic for the travelling salesman problem. Technical report, Carnegie-Mellon Univ Pittsburgh Pa Management Sciences Research Group (1976)

[4] Jörgl, M., Gattringer, H., Müller, A.: An Almost Time Optimal Route Planning Method for Complex Manufacturing Topologies. In: Computer Aided Systems Theory – EUROCAST 2015, Springer International Publishing (2015) 673–680

[5] Helsgaun, K.: An effective implementation of the Lin–Kernighan traveling salesman heuristic. European Journal of Operational Research **126**(1) (2000) 106–130

[6] Lin, S., Kernighan, B.W.: An effective heuristic algorithm for the traveling-salesman problem. Operations research **21**(2) (1973) 498–516

[7] Dantzig, G., Fulkerson, R., Johnson, S.: Solution of a large-scale traveling-salesman problem. Journal of the operations research society of America **2**(4) (1954) 393–410

https://doi.org/10.3311/ECCOMASMBD2021-233



# Motion Capture Based Model Identification of the Humanoid Robot REEM-C Using Static Poses

**Felix Aller**[1], **Monika Harant**[2] **and Katja Mombaur**[3]

[1] Institute of Computer Engineering
Heidelberg University
Berliner Str. 45, 69120 Heidelberg, Germany
felix.aller@ziti.uni-heidelberg.de

[2] Department of Mathematics for the Digital Factory
Fraunhofer Institute for Industrial Mathematics
Fraunhofer-Platz 1, 67663 Kaiserslautern, Germany
monika.harant@itwm.fraunhofer.de

[3] CERC Human-Centred Robotics and Machine Intelligence
University of Waterloo
200 University Avenue West, Waterloo, Canada, N2L 3G1
katja.mombaur@uwaterloo.ca

**ABSTRACT**

In this paper, we describe an approach for the model identification of the humanoid robot REEM-C. In contrast to previous work, we do not attempt to determine all dynamic parameters simultaneously. It is not clear whether such approaches can lead to redundancies in the optimization problem. We deliberately restrict ourselves to a very precise determination of the center-of-mass (COM) and the mass of the individual rigid bodies. As a result, we do not use Persistent Exciting (PE) trajectories and perform the identification based on motion capture and force plate measurements of 172 static poses. This results in more accurate experimental data and allows a more precise update of static parameters by means of an optimization problem. The inertial parameters are not updated and have to be adjusted using classical approaches, but based on the already improved static parameters. We report the performance of optimization by comparing the distance of the ground-projected-center-of-mass (GCOM) against the measured GCOM from the model information of the original and optimized model for each static pose. The improvement of the optimized model is furthermore reflected by means of a recorded dynamic squat motion and by analyzing the residual torques and forces acting at the floating base of the robot.

**Keywords:** multibody dynamics, humanoid robot, inertial parameters, model identification.

## 1 INTRODUCTION

Humanoid robots are on the advance with capabilities that make them suitable for use outside of laboratory environments. Their application in collaboration with humans or for tasks that are too dangerous or monotonous for humans is thus within reach [1, 2, 3]. Due to their anthropomorphic structure, they have advantages in a complex working environment made by humans for humans [4] and their bipedal locomotion makes it possible to master more challenging terrain [5]. This advantage comes at a cost, as an upright posture and locomotion is not statically stable for most configurations, as is the case for multi-legged robots. Thus, many motion sequences push the robot to its limits in order to perform complex tasks while maintaining static and dynamic stability [6].

There are many different approaches to generating motion sequences for humanoids, and those that reach a robot's limits exploit the full dynamic properties described in the robot's model [7].

https://doi.org/10.3311/ECCOMASMBD2021-233

For the challenging task of developing whole-body motions on complex multibody systems such as humanoid robots, knowledge of the exact dynamic properties of the mechanical system are required. This is further complicated by inaccuracies in the dynamic model parameters for which we can distinguish between four different categories:

1. The geometry or kinematic structure of the robot, which is usually generated from the underlying CAD files and is very precise.
2. The mass and centers-of-masses of all rigid bodies involved, which is also exported from CAD, but often only reflects a fraction of the individual (electrical) components within the rigid body.
3. The moments of inertia, which are also derived from the CAD. A uniform density distribution within the individual rigid bodies is often assumed. For this reason, the moments of inertia are also only an approximation of the body with individual components of different unknown densities.
4. Limitations of the robot in terms of joint angles, torques or velocity. These can be determined fairly accurately based on the motor specification.

As category 2 and 3 are mostly mere, flawed approximations of the actual parameters, much attention is paid to model identification using multibody dynamics, initially for manipulators in the 1980's [8, 9, 10]. This method was extended to be applicable to humans [11] and humanoid robots [12, 13]. Subsequent work further extends this method by also including joint torque information of the actuated joints [14]. Each method requires a set of trajectories, also called Persistent Exciting (PE) trajectories with the aim to excite all the dynamics of the system [15, 16]. The two methods differ in the way that the former requires the torques to be calculated from external contact forces using inverse dynamics, whereas the latter method obtains the torques directly from the robot's force torque sensors in each joint. Both methods have already been compared by applying them to a state-of-the-art humanoid [17].

A general disadvantage of dynamic model identification based on PE-trajectories lies in the fact that acceleration data is approximated, which can lead to errors in the parameter estimation. Furthermore, most robots, such as the one used in this work, are not equipped with sensors to measure joint torques leading to errors due to the estimation of torque from contact forces. It has also not yet been investigated to what extent the simultaneous optimization of all dynamic parameters can lead to redundancies in the optimization problem.

In this work, we carry out a model identification procedure on the humanoid robot REEM-C by PAL Robotics for parameters of category 2. We focus on identifying and update center of mass locations and masses so that the model best fits the experimental data, which consists of a large set of static poses. The approach of splitting the simultaneous identification of static and dynamic parameters of categories 2. and 3. respectively and the use of static poses allows a more accurate approximation of 2. to reality. This approximation can subsequently serve as a basis for the more precise identification of the dynamic parameters. The level of model improvement is evaluated by means of a dynamic reference motion.

This paper is organized as follows. In Section 2, we describe the humanoid robot REEM-C and the kinematic and dynamic modeling of an anthropomorphic system. In Section 3, we present the carried out method for model identification. The results of the updated parameter sets are described in Section 4. The results are discussed in Section 5. Section 6 ends the paper with a conclusion and perspectives for future research.

https://doi.org/10.3311/ECCOMASMBD2021-233

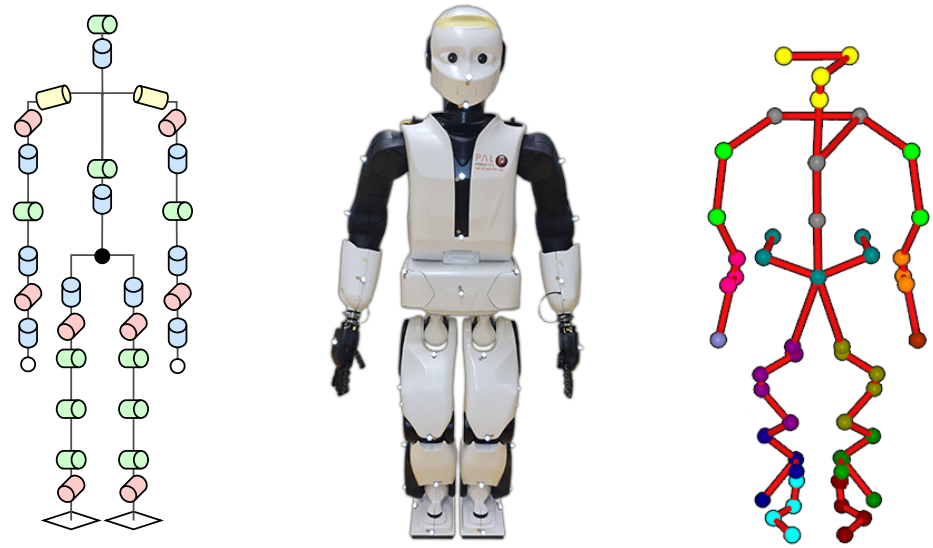

**Figure 1**. Kinematic structure of REEM-C with 30 (actual) DOF without hands (2 head, 7 each arm, 2 waist, 6 each leg, 19 each hand) [18], the real robot with applied marker set [18], and the actual marker set consisting of 51 optical markers.

## 2 ANTHROPOMORPHIC DESCRIPTION

### 2.1 Humanoid robot REEM-C

REEM-C is a humanoid robot developed by PAL Robotics. With its 1.64 m size the robot is considered an adult sized robot (Fig. 1 center). It features 30 DOF (Fig. 1 left) not considering each hand with 19 additional DOF. This is roughly the same amount as the number of DOF of comparable robots such as ARMAR-4 (41), WALK-MAN (31), HRP-2 (30), Talos (30) or DRC-HUBO+ (28) again, not considering the varying DOF of each of the robots' hands. All joints of REEM-C are revolute and powered by high gain driving brushed DC motors except for the underactuated hands. Each motor encoder can track the position and velocity of the motion characteristic, as external perturbations are rejected by the position controlled motors. REEM-C is equipped with multiple sensors such as an IR-camera, force torque sensors in the ankles and wrists and an IMU located in the waist, which is also hosting the batteries of the robot and is the heaviest rigid body in the system. The robotic feet are rubber coated with a sole size of 21.0 cm $\times$ 14.0 cm. However, the actual support polygon of REEM-C while standing on one leg is estimated to be 15.5 cm $\times$ 10.6 cm, which is a significantly smaller area. The total weight of the robot was measured and amounts to 77.6 kg, whereas the robotic model only accounts for 67.55 kg.

Even if this weight difference seems large, it can easily be justified. PAL Robotics is always adapting newer versions of the robot to different requirements. In this regard, REEM-C has been equipped with more powerful knee motors in the current version 4. In addition, the classic generation of the initial model from the available CAD files does not take electrical wiring into account. Furthermore, a homogeneous battery and a homogeneous computer are assumed. The paint and the lubricant of the motors are not considered. There are also different manufacturing tolerances and the same material is not always used for the robot's casing, although the different materials used are considered to be identical.

The joint configuration of REEM-C does not contain any closed loop and is therefore modeled using a kinematic tree structure. The origin of the whole system is called the floating base, the freeflyer or the base link. The floating base determines the global position and orientation of the robot with respect to the inertial frame. This state is achieved by adding an additional 6-DOF joint

https://doi.org/10.3311/ECCOMASMBD2021-233

connecting the floating base to the inertial frame. This results in a system consisting of

$$q = [q_b \quad q_j]^T, \tag{1}$$

where

$$q_J = [q_0 \quad \dots \quad q_n]^T. \tag{2}$$

The number of actual joints is represented by $n \in \mathbb{N}$. The configuration of the virtual joints to achieve the global state in terms of translation and rotation of the floating base is indicated by $q_b \in \mathbb{R}^6$. The joint configurations of the actuated joints is represented by $q_j \in \mathbb{R}^n$. This gives a total number of DOF of $n+6$ where only $n$ joints are actually actuated so the resulting system is always underactuated, regardless of the size of $n$. We therefore obtain a maximum number of 74 DOF for REEM-C.

### 2.2 Dynamic Modeling

The development of dynamic models is an important part of the implementation of motion trajectories for robots. Especially in model-based trajectory generation, the quality of the resulting motion depends on the individual model parameters. Target trajectories generated on the basis of models naturally vary in complexity. Accordingly, simpler motion sequences such as the typical zero-moment-point based walking of a humanoid are more forgiving of model inaccuracies. With more complex motion sequences, model inaccuracies become increasingly severe, such as when crossing obstacles [19]. If additional velocity requirements are added to a challenging trajectory for highly dynamic and impulsive motion sequences, even the smallest model inaccuracies make execution on a real robot impossible. The latter category includes movements that shift the pelvis of the multibody system system along the vertical axis, such as sit-to-stand transitions. Therefore, the description of the robotic system must correspond as closely as possible to reality.

A rigid body system can be described using the equation of motion which can be written in the following form as a set of ODEs:

$$H(q,p)\ddot{q} + N(q,\dot{q},p) + C(q,\dot{q},p) = F(q,\dot{q},p,\tau)\,, \tag{3}$$

where $q$, $\dot{q}$ and $\ddot{q}$ are vectors of the joint coordinates of position, velocity and acceleration, respectively. The generalized inertia matrix which is dependent on $q$ and $p$ is written as $H(q,p)$. Likewise, the acting gravity which depends on $q$ and $\dot{q}$ is denoted as $C(q,\dot{q})$. The produced torque by the actuation system is written as $F(q,\dot{q},p,\tau)$, which also includes external forces.

The generalized inertia matrix of the robot and its corresponding motors can be further described as

$$H(q,p) = \sum_{b=1}^{n} (J_b^x)^T\, m_b J_b^x + (J_b^\omega)^T I_b J_b^\omega\,. \tag{4}$$

The nonlinear effects $N(q,\dot{q},p)$ are described as:

$$N(q,\dot{q},p) = \sum_{b=1}^{n} (J_b^x)^T m_b \dot{J}_b^x + (J_b^\omega)^T I_b \dot{J}_b^\omega - \left((J_b^\omega)^T I_b J_b^\omega \dot{q}\right) J_b^\omega\,, \tag{5}$$

where $J_b^x$ and $J_b^\omega$ are the Jacobians containing the translatory and rotatory information of each rigid body $b$. The inertia tensor of $b$ in the global frame is denoted as $I_b$.

The parameter set which contains the model parameters from categories 1 – 4 (see Section 1) is denoted as $p$. As mentioned earlier we focus on the identification of the static parameters $p_s \subset p$: the rigid body masses $m_b$ and the center-of-mass (COM) locations of $b$ with respect to the local

https://doi.org/10.3311/ECCOMASMBD2021-233

body frame, $c_b \in \mathbb{R}^3$. Using $m_b$ and $c_b$ we can describe the mean location of a distribution of mass in space, i.e. the distribution which has the property that the weighted position vectors relative to this point are zero and denote it as $r(q) = (x, y, z)$ with

$$r(q) = \frac{1}{M} \sum_{b=1}^{n} m_b r_b(q, p_s) \,, \tag{6}$$

where $M$ is the total mass of the system. The global position of $c_b$ is obtained by $r_b$ based on the current configuration $q$ of the robot. The ground-projected-center-of-mass (GCOM) is defined as $G := (x, y, h_G)$, with $h_G$ being the floor height.

## 3 APPLIED METHOD FOR MODEL IDENTIFICATION

While previous work has attempted to determine all dynamic parameters simultaneously, our decision to focus on $p_s$ allows a identification based on static poses. Therefore no PE trajectories are needed. This benefits the data quality and accuracy of model improvement. Additionally, we do not rely on the internal sensor values of the robot, as we aim for the highest possible precision of the measured values. In the case of REEM-C, the motor encoders do not take into account gear backlash and an overall mechanical system tilt was observed when the GCOM reached the edge of the support polygon. Therefore, we utilize measurement systems from a state-of-the-art motion capture lab. This method is particularly suitable for robots that do not have the necessary sensors or measuring accuracy to determine the external contact forces and position information of the rigid bodies. This makes this method completely robot-independent and applicable to all kinds of different multi-body systems. Subsequently, the inertia matrices are to be estimated, but on the basis of the optimized, already determined static parameters.

### 3.1 Static poses

Static poses offer the advantage of taking a measurement at a stage when the robot is almost at rest and the measurements are nearly free of noise. One disadvantage, however, is that a large amount of poses are required. A combination of systematic and randomly generated poses was used. We distinguish 6 categories of poses (Fig. 2 left to right):

1. Double-legged – feet 2 cm apart on one force plate, focus on right arm,
2. Single-legged – standing on the left leg, focus on right leg,
3. Single-legged – standing on the right leg, focus on left leg,
4. Double-legged – feet 2 cm apart on one force plate, focus on torso joints (Fig. 3(a)),
5. Double-legged – feet 2 cm apart on one force plate, crouching,
6. Double-legged – feet 20 cm apart with both feet on one force plate (Fig. 3(b)) and both feet on one force plate each (Fig. 3(c)),

A total of 172 static poses was generated. Each pose is a static joint configuration, i.e. the GCOM resides within the convex hull of the support polygon. For each configuration, the individual degrees of freedom were systematically set to less than 10% and more than 90% of their minimum and maximum joint range. In addition, at least 10 random poses were generated for the double-legged categories.

The kinematic data were collected using a passive motion capture system at 150 Hz (Qualisys, Gothenburg, Sweden) and two ground-embedded force plates at 900 Hz (Bertec, Columbus, OH, USA). We applied a custom marker set on REEM-C with 51 motion capture markers (14 mm)

https://doi.org/10.3311/ECCOMASMBD2021-233

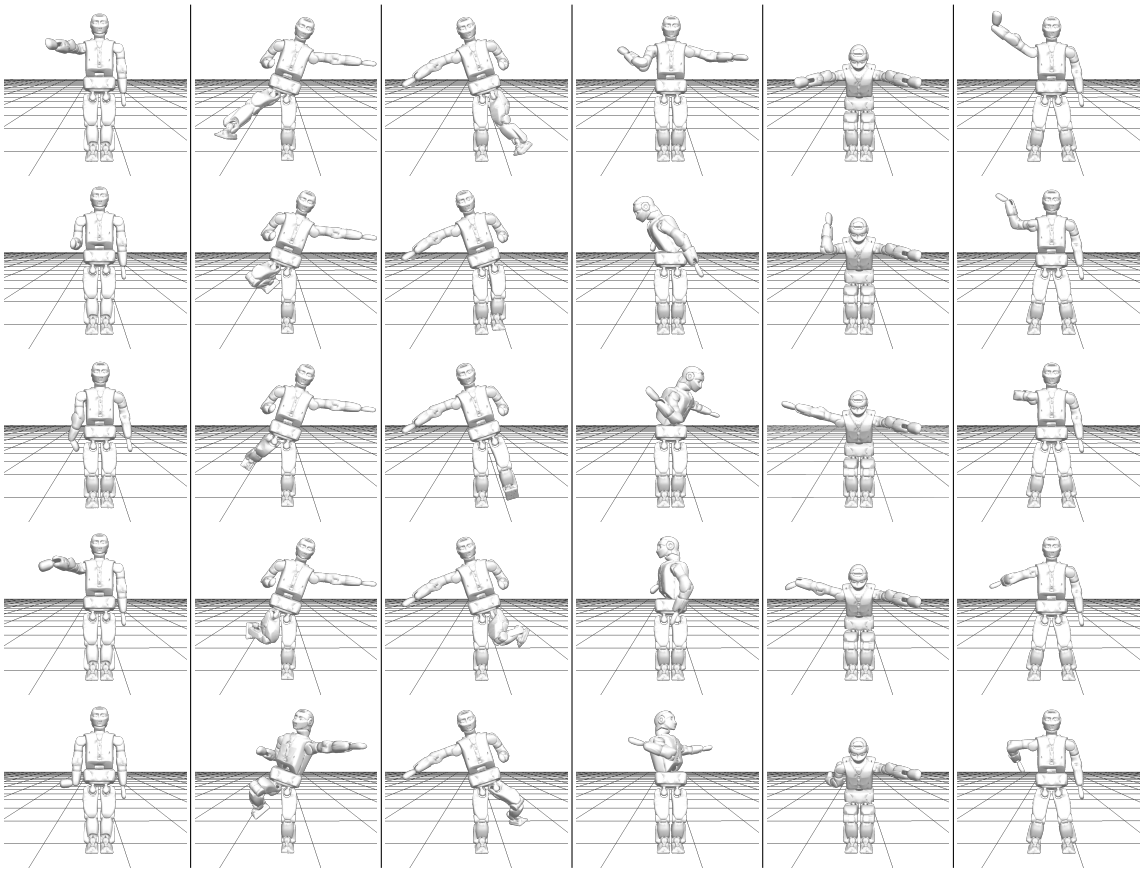

**Figure 2**. Examples from the applied static poses. From left to right: (1.) On both feet, (2.) On left foot, (3.) On right foot, (4.) Torso rotation, (5.) Crouching, (6.) Both feet (wide).

(Fig. 1 right). The marker and force data were filtered with a bi-directional Butterworth filter with a cut-off frequency of 10 Hz.

For each of the static poses, we use the ground-embedded force plates to measure the corresponding center-of-pressure (COP). The COP is a dynamic point described by the forces exerted by two rigid bodies in contact. Generally, we consider the rigid body of one or more feet of the robotic system and the ground surface on which the robot is standing. Let us consider the simplified case of a humanoid with one foot in contact with the ground. The contact force is always positive because the foot cannot penetrate the ground. The COP describes a point at which the sum of all compressive forces perpendicular to the sole of the foot is equivalent to a single force acting at a point where the resulting moment is exactly zero. We distinguish two cases: the contact of a single foot, where the COP must always lie within the convex hull spanned by the flat contact of the foot with the ground, and the contact of both feet, where the convex hull is spanned by both foot contact surfaces. In the latter case, the COP can lie between both feet and outside the actual contact area of one foot. In static poses, i.e. a situation in which no other forces act apart from the gravitational forces, the COP corresponds to the GCOM.

### 3.2 Kinematic Fitting of the Experimental Data

For the parameter optimization it is vital to be able to calculate the GCOM for different poses and model parameters and compare it to the measured COP. As mentioned earlier, markers were attached to all segments of the robot and recorded as well to be able to obtain the position of the robot as accurate as possible. The joint positions recorded by the robot itself can not measure a global tilt of the system induced by the gear backlash.

https://doi.org/10.3311/ECCOMASMBD2021-233

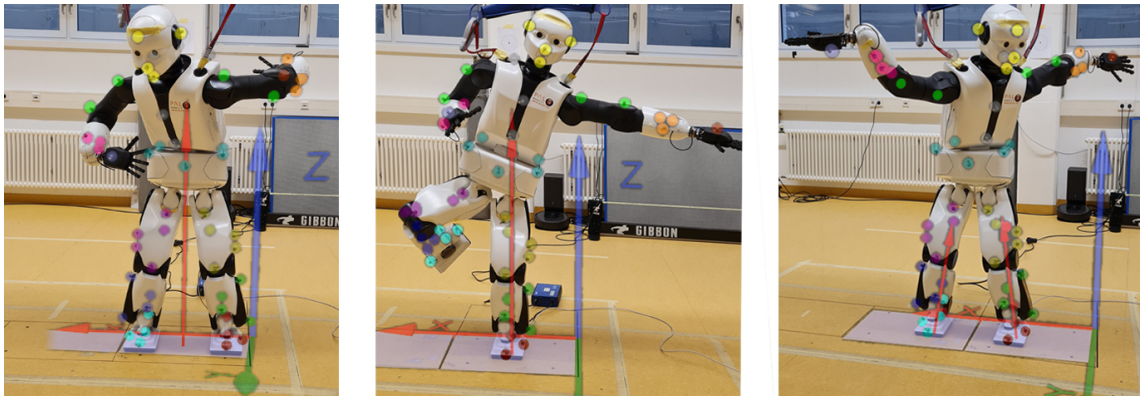

**Figure 3**. Three different types of static poses of the humanoid REEM-C with applied marker set (highlighted) on force plates (highlighted) with indicated force vector: (a) standing on both feet on one force plate, (b) standing on one foot, (c) standing on both feet on two force plates.

For fitting the marker positions onto the model of REEM-C, virtual markers were included in the model description and their position with respect to the segment they are attached to were determined via measurements as well as a calibration trial with the robot standing in a neutral pose. The joint positions of the trials are obtained by minimizing the distance between virtual-markers and motion capture markers for each frame:

$$\min_{q} \sum_{m=1}^{N_m} ||r_m^V(q) - r_m^C||_2^2 \tag{7}$$

with joint angles $q$, the positions of the virtual markers and of the corresponding motion capture markers are denoted by $r_m^V$ and $r_m^C$, $m = 1,\ldots,N_m$, respectively, with $N_m$ being the total amount of markers used. Note that $q$ are the joint positions of one frame or time instance and also include the position and orientation of the floating base in space.

The optimization problem is solved using the Levenberg-Marquardt method [20] provided by the open source Rigid Body Dynamics Library – RBDL [21]. This iterative method starts at an initial guess and is refining it until a termination criterion is met. It is quite robust with respect to different starting values. However, if the orientation of the model specified by the initial guess is far away from the orientation specified by the motion capture markers, the calculated solution can contain joint angles of over 360 degrees and more, exceeding the range of motion of the robot. In order to avoid this effect, the orientation of the pelvis segment is estimated first using the position of the corresponding motion capture markers, and included in the initial guess of the first frame. The start values of the remaining frames are taken from the previous one.

### 3.3 Experimental Parameter Identification

The recorded marker data are fitted to the model using inverse kinematics. For each static pose, the GCOM obtained by the dynamic properties of the model is compared to the COP obtained through force plate measurements. As described in Section 3.1, the measured COP corresponds to the GCOM during a static pose, and is therefore denoted as $GCOM^{REF}$. Their deviation is minimized by solving a least squares problem by updating a set of static model parameters $p_s$:

$$\min_{p_s} \sum_{n=1}^{N} \|g_{GCOM}(q_n, p_s) - GCOM_n^{REF}\|^2 \tag{8}$$

$$s.t. \quad g_{mass}(p_s) = M \tag{9}$$

https://doi.org/10.3311/ECCOMASMBD2021-233

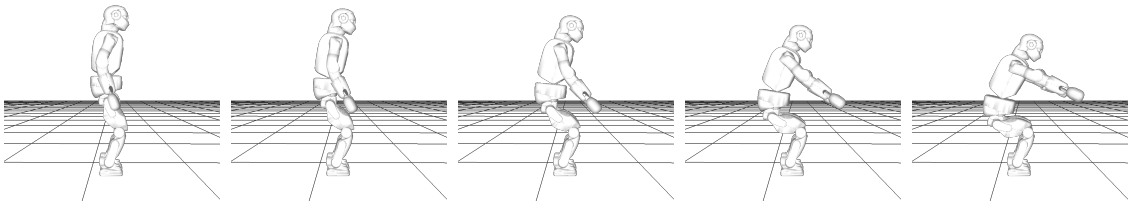

**Figure 4**. Validation motion for model identification which is comparable to the human squat exercise. The robot shifts the pelvis along the vertical axis and maintains static stability by shifting the arms and upper body within a period of 5 seconds.

with $N$ the number of poses considered and $GCOM_m^{REF}$ the recorded GCOM of pose $m$. The functions $g_{GCOM}$ and $g_{mass}$ calculate the GCOM of pose $m$ specified by the recorded joint positions $q_m$ and the total mass of the robot model based on the current static parameters $p_s$. The measured total mass of the robot is denoted by $M$. The parameters consist of the mass and COM location of the main segments of the robot: shank, thigh, pelvis, trunk, upper arm, forearm and hand. Segments consisting of only a motor and a cover could not be considered during the optimization and were fixed at the values given in the original model, as the change in the measured GCOM would be too small and lead to redundancies in the problem formulation. The same applies to the head and foot segments. The optimization problem is solved with the SQP method using Gauss-Newton Hessian and a Levenberg-Marquardt regularization term using the optimal control software package MUSCOD II [22].

### 3.4 Validation of model identification

For validation of the model identification a reference motion was recorded using the same experimental setup. The chosen motion is similar to the human squat exercise, in which the COM is moved along the vertical plane and at the same time static stability is maintained by shifting the arms and upper body (Fig. 4). The data obtained was not used during the optimization process. The marker data was fitted to the robot model and the torques were calculated using inverse dynamics. To assess the quality of the model, we evaluated the joint torques and forces acting at the floating base. These calculated residual forces should be practically very small compared to the external and internal forces in the equilibrium case for underactuated degrees of freedom. Therefore, they are considered as the actual error of the numerical solution and can be used as a benchmark for the quality of model optimization.

## 4 RESULTS

### 4.1 Comparison of static poses

We evaluate the improved accuracy of the optimization problem by analyzing the distance of the recorded $GCOM^{REF}$ and the GCOM obtained by the model parameters for both, the original and the optimized model (Fig. 5). The optimization problem was able to reduce the deviations for all 172 poses to varying degrees. An overall distance correction from (avg. 9.2 mm, std. 2.3 mm) to (avg. 0.6 mm, std. 0.4 mm) is reported. However, the optimization does not decrease the distances to the same extent for all static poses.

### 4.2 Residual forces and torques

The quality of the model identification is evaluated by the analysis of the residual forces and torques against a reference trajectory. We report the residual forces and torques acting at the floating base during the squat motion along all axis and compare the original model against the optimized model after the identification procedure (Fig. 6). For all plots we identify an oscillation

https://doi.org/10.3311/ECCOMASMBD2021-233

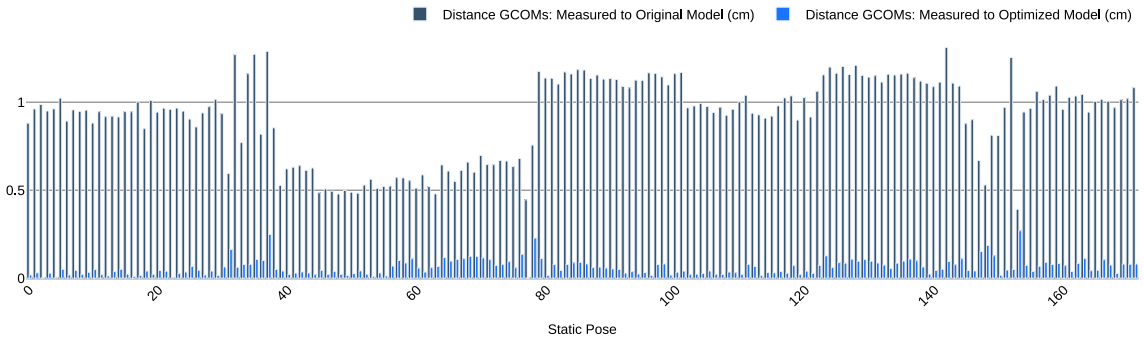


**Figure 5**. Distance of GCOM to $GCOM^{REF}$ for all 172 static poses for the original model (dark-blue) and the optimized model (light-blue) obtained by model identification.

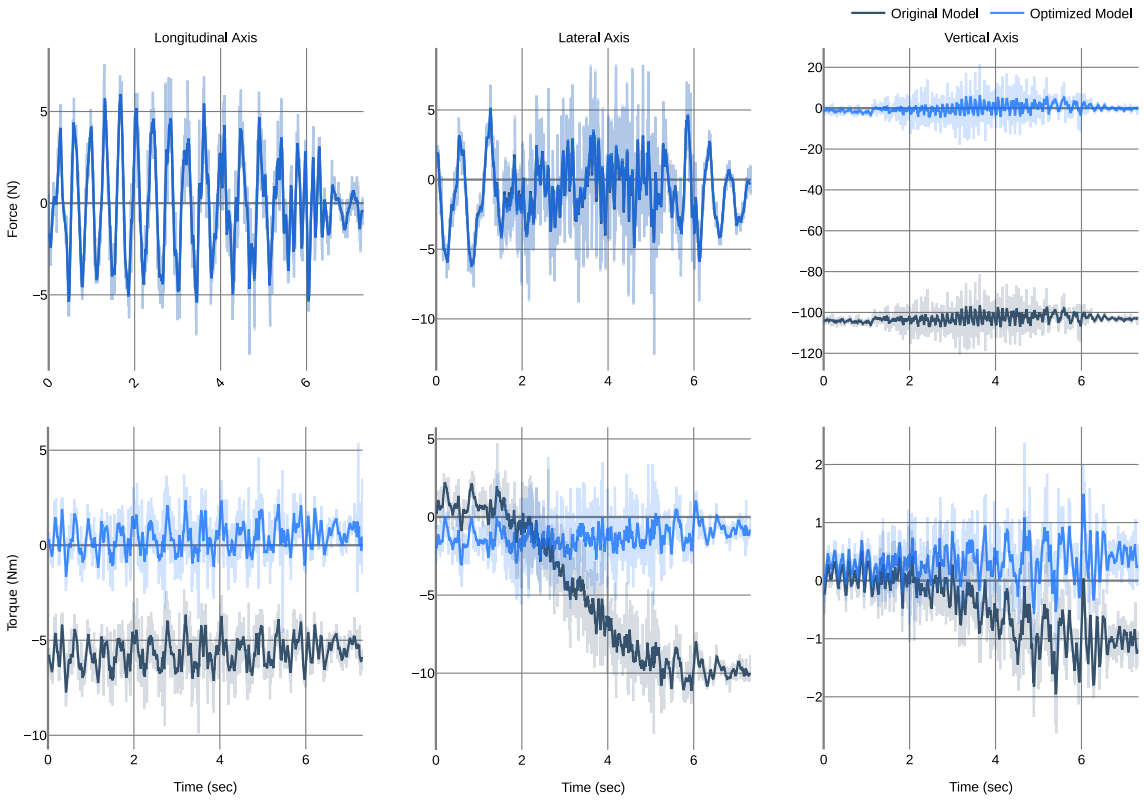


**Figure 6**. Residual forces (top) and torques (bottom) along all axis of the validating squat-motion. The actual motion takes place between seconds 1 and 6. We compare the residual forces with the original model (dark-blue) and the optimized model (light-blue) obtained by model identification. We applied a moving mean with a centralized window of 7 frames to reduce the oscillations induced by the COM-stabilizer of the underlying control architecture of the robot. The original data are semi-transparent in the background.

https://doi.org/10.3311/ECCOMASMBD2021-233

**Table 1**. Avg. [std] of the absolute values of residual torques and forces of the base link obtained by inverse dynamics of the squat-motion.

| *Model* | $T_x$ [$Nm$] | $T_y$ [$Nm$] | $T_z$ [$Nm$] | $F_x$ [$N$] | $F_y$ [$N$] | $F_z$ [$N$] |
|---|---|---|---|---|---|---|
| Original Model | 5.66 [0.98] | 5.98 [4.07] | 0.68 [0.48] | 1.86 [1.66] | 2.28 [1.72] | 103.02 [4.03] |
| Optimized Model | 0.87 [0.69] | 1.35 [1.01] | 0.41 [0.30] | 1.86 [1.66] | 2.29 [1.73] | 2.68 [3.04] |

of the original data. Therefore, a moving mean with a centralized window of seven frames was applied to the data.

For the acting residual forces about the longitudinal and lateral axis we can not observe any change or improvement (Fig. 6 top). For the acting residual forces about the vertical axis a shift of the force trajectory can be observed, leading to a correction of the absolute values of $F_z$ (Tab. 1). The acting residual torques show different signatures about all axis for both models (Fig. 6 bottom). Along the longitudinal axis, a clear offset of the original model of less than -5 Nm can be observed. This offset is no longer recognizable for the optimized model and an oscillation of almost around zero is shown. For $T_x$ the residual torques are smaller for the optimized model (Tab. 1). Along the lateral axis, the original model diverged further into the negative the longer the movement lasted. This trend is no longer visible in the optimized model and for $T_y$ smaller residual torques are present (Tab. 1). However, there is a minimal offset to an oscillation around zero again. Similar to $T_y$, the residual moments acting around the vertical axis $T_z$ diverge further into the negative, even if not to the same extent. This trend was corrected for the optimized model, despite a slightly higher offset to zero than for $T_y$. For $T_z$ there was only a slight improvement apart from the trend adjustment, as the deviation was already small at the beginning (Tab. 1).

## 5 DISCUSSION

The results show an overall improvement of the model optimized by the model identification procedure. The decrease in distances (Fig. 5), demonstrates that the optimization problem was able to approach a deviation of almost zero by updating the static model parameters. However, this does not represent the quality of the model obtained, but evaluates the process of overall optimization. The fact that the optimization could not minimize all distances to the same extent can be explained by possible over-fitting of certain poses. When generating the poses, as already discussed, all degrees of freedom were systematically covered and supplemented with additional random poses. It appears, however, that some poses are preferred during the optimization. The differences between the individual minimization can possibly be approximated by applying a weighting of the individual poses. Altogether, a minimization in line with expectations was achieved.

The oscillation of residual forces and torques (Fig. 6) is explained by the control architecture of REEM-C which performs COM stabilization in order to prevent a loss of balance. This is particularly evident along the longitudinal and lateral axes, where the robot tries to keep its GCOM close to the center of its support polygon by making minimal compensating movements. For the acting residual forces about the vertical axis a distribution of the unaccounted mass of $\sim$10.5 kg to the respective segments can be identified, reducing the absolute vertical force $F_z$. For the forces acting on the longitudinal and lateral axes, no significant changes are observed. This is due to the fact that the translatory forces acting in the horizontal plane are applied here. These are mainly influenced by the inertial parameters of the segments and the acceleration acting on these segments. Since we have not updated the inertial matrices and the motion is also slow, no change was expected. By analyzing the residual torques along all axes, we can observe two things: the overall quality of the original model and the quality of this mass distribution. The optimization could not only improve the residual torques, but also achieve the improvement while simultaneously incorporating the

substantial missing masses. The small offset in the residual torques can be explained by a slight over-fitting of the experimental data, minor errors in the marker fitting and small measurement inaccuracies of the force plate and the motion capture system.

## 6 CONCLUSION

Our results show a significant improvement of the model by updating the segment masses and COM locations. We are confident that the mass distributions in this case also correspond to reality. This assumption is partly based on the fact that highly dynamic sit-to-stand movements were possible using this model, which could not be realized with the original model, of course, under the assumption that the inertia matrices already had sufficient quality based on the CAD exports at the beginning. The remaining residual forces and torques are probably also a result of the not yet perfect inertia matrices, although our identification already represents an enormous improvement. This is the next step in this 2-phase approach to iterative model improvement: Based on these values, the inertia parameters can now be estimated on basis of the equation of motion, as in previous work [12, 13, 14]. Of course, for a large number of robots this involves torque estimation, error-prone data due to finite differences, or noisy data due to possible control architecture. However, a very accurate approximation of the static parameters of the dynamic model has already been realized. The absence of possible redundancies in the optimization problem due to simultaneous determination of all dynamic parameters is also ensured. The further improvement of the model and also the use of the proposed model and its further analysis on the basis of highly dynamic sit-to-stand transitions will be part of a future publication.

## ACKNOWLEDGMENTS

This work was supported by the project EUROBENCH funded by H2020 Topic ICT 27-2017 under grantagreement number 779963. We thank PAL Robotics for the opportunity to work with the REEM-C robot within the EUROBENCH project.

## REFERENCES

[1] Kheddar, A., Caron, S., Gergondet, P., Comport, A., Tanguy, A., Ott, C., Henze, B., Mesesan, G., Englsberger, J., Roa, M.A., et al.: Humanoid robots in aircraft manufacturing: The airbus use cases. IEEE Robotics & Automation Magazine **26**(4) (2019) 30–45

[2] Jung, T., Lim, J., Bae, H., Lee, K.K., Joe, H.M., Oh, J.H.: Development of the humanoid disaster response platform DRC-HUBO+. IEEE Transactions on Robotics **34**(1) (2018) 1–17

[3] Asfour, T., Waechter, M., Kaul, L., Rader, S., Weiner, P., Ottenhaus, S., Grimm, R., Zhou, Y., Grotz, M., Paus, F.: ARMAR-6: A high-performance humanoid for human-robot collaboration in real-world scenarios. IEEE Robotics & Automation Magazine **26**(4) (2019) 108–121

[4] Al-Shuka, H.F., Allmendinger, F., Corves, B., Zhu, W.H.: Modeling, stability and walking pattern generators of biped robots: a review. Robotica **32**(6) (2014) 907–934

[5] Goswami, A.: Postural stability of biped robots and the foot-rotation indicator (FRI) point. The International Journal of Robotics Research **18**(6) (1999) 523–533

[6] Griffin, R.J., Wiedebach, G., Bertrand, S., Leonessa, A., Pratt, J.: Walking stabilization using step timing and location adjustment on the humanoid robot, atlas. In: 2017 IEEE/RSJ International Conference on Intelligent Robots and Systems (IROS), IEEE (2017) 667–673

[7] Kashiri, N., Abate, A., Abram, S.J., Albu-Schaffer, A., Clary, P.J., Daley, M., Faraji, S., Furnemont, R., Garabini, M., Geyer, H., et al.: An overview on principles for energy efficient robot locomotion. Frontiers in Robotics and AI **5** (2018) 129

[8] Atkeson, C.G., An, C.H., Hollerbach, J.M.: Estimation of inertial parameters of manipulator loads and links. The International Journal of Robotics Research **5**(3) (1986) 101–119

[9] Armstrong, B., Khatib, O., Burdick, J.: The explicit dynamic model and inertial parameters of the PUMA 560 arm. In: Proceedings. 1986 IEEE international conference on robotics and automation. Volume 3., IEEE (1986) 510–518

[10] Sujan, V.A., Dubowsky, S.: An optimal information method for mobile manipulator dynamic parameter identification. IEEE/ASME transactions on mechatronics **8**(2) (2003) 215–225

[11] Venture, G., Ayusawa, K., Nakamura, Y.: Motion capture based identification of the human body inertial parameters. In: 2008 30th Annual International Conference of the IEEE Engineering in Medicine and Biology Society, IEEE (2008) 4575–4578

[12] Ayusawa, K., Venture, G., Nakamura, Y.: Identification of the inertial parameters of a humanoid robot using unactuated dynamics of the base link. In: Humanoids 2008-8th IEEE-RAS International Conference on Humanoid Robots, IEEE (2008) 1–7

[13] Ayusawa, K., Venture, G., Nakamura, Y.: Identification of humanoid robots dynamics using floating-base motion dynamics. In: 2008 IEEE/RSJ International Conference on Intelligent Robots and Systems, IEEE (2008) 2854–2859

[14] Mistry, M., Schaal, S., Yamane, K.: Inertial parameter estimation of floating base humanoid systems using partial force sensing. In: 2009 9th IEEE-RAS International Conference on Humanoid Robots, IEEE (2009) 492–497

[15] Gautier, M., Khalil, W.: Exciting trajectories for the identification of base inertial parameters of robots. The International journal of robotics research **11**(4) (1992) 362–375

[16] Swevers, J., Ganseman, C., Tukel, D.B., De Schutter, J., Van Brussel, H.: Optimal robot excitation and identification. IEEE transactions on robotics and automation **13**(5) (1997) 730–740

[17] Ogawa, Y., Venture, G., Ott, C.: Dynamic parameters identification of a humanoid robot using joint torque sensors and/or contact forces. In: 2014 IEEE-RAS International Conference on Humanoid Robots, IEEE (2014) 457–462

[18] Aller, F., Harant, M., Sontag, S., Millard, M., Mombaur, K.: I3SA: The Increased Step Size Stability Assessment Benchmark and its Application to the Humanoid Robot REEM-C. In: 2021 IEEE/RSJ International Conference on Intelligent Robots and Systems (IROS), submitted and accepted, IEEE (2021)

[19] Koch, K.H., Mombaur, K., Stasse, O., Soueres, P.: Optimization based exploitation of the ankle elasticity of HRP-2 for overstepping large obstacles. In: 2014 IEEE-RAS International Conference on Humanoid Robots, IEEE (2014) 733–740

[20] Marquard, D.W.: An Algorithm for Least-Squares Estimation of Nonlinear Parameters. Journal of the Society for Industrial and Applied Mathematics **11**(2) (1963) 431–441

[21] Felis, M.L.: RBDL: an efficient rigid-body dynamics library using recursive algorithms. Autonomous Robots **41**(2) (2017) 495–511

[22] Leineweber, D., Schäfer, A., Bock, H., Schlöder, J.: An efficient multiple shooting based reduced SQP strategy for large-scale dynamic process optimization: Part II: Software aspects and applications. Computers & Chemical Engineering **27**(2) (2003) 167–174

https://doi.org/10.3311/ECCOMASMBD2021-152



# Mathematical Model and Control Simulation of Hexapod Robot Locomotion in Tripod Gait

**Krešimir Osman**[1], **Trpimir Alajbeg**[2]

[1] Zagreb University of Applied Sciences
Department of Electrical Engineering
Konavoska 2, 10000 Zagreb, Croatia
kresimir.osman@tvz.hr

[2] Zagreb University of Applied Sciences
Department of Electrical Engineering
Konavoska 2, 10000 Zagreb, Croatia
trpimir.alajbeg@tvz.hr

## ABSTRACT

This paper presents the research of a hexapod robot as it movement along a defined path. Firstly, the performance of the robot product architecture is presented and a mathematical kinematic model of the robot is derived according to it, i.e. its legs using the Denavit-Hartenberg method and homogeneous transformations. The purpose of this was to obtain the equations of inverse kinematics. A simplified robot product architecture based on rectangular robot design was used to perform the mathematical model. It is shown by a simplified kinematic scheme. In addition, a control algorithm was performed using a PID controller in each ankle. The controller's parameters are adjusted on one leg of the robot, and after that, this is used to adjust the control on the other legs in this way. The simulation of the controlled motion of the robot was performed using the computer program MATLAB Simulink and the Simscape Multibody environment. In doing so, only the robot's movement on flat terrain was observed. The tripod gait was chosen for the motion model due to the simplicity of creating the model and performing the simulation, as well as the speed of movement.

**Keywords:** hexapod robot, tripod gait, rectangular robot design, PID control

## 1. INTRODUCTION

The application of behavioural simulations (kinematic and dynamic model) in robotics have been quite popular in recent years. One of the important reasons is that it allows developers and researchers to predict, test and validate robotic performance before prototyping and production [1]. It also allows faster and easier improvement of management strategies, focused on safety and more cost-effectiveness.

Using knowledge from nature, i.e. by studying and investigating the locomotion of animals helped researchers develop different types of so-called bio-inspired robot [2]. Among these, the most convenient is the researching of arthropods that have six legs and thus simply maintain their stability (insects, centipedes, symphylans, millipedes etc.). They show quite a robustness of the system in case of damage to the legs. One of the typical examples of the development of robots from this group is the hexapod robot based on the anatomy and locomotion of insects.

Hence, researchers encounter the problem of operating such robotic systems, which are quite complex and have an increased number of degrees of freedom (DOF) of motion due to the performance of the legs of robots from multiple ankles (links) [2]. In practice, many commercial six-legged robots have already been carried out, which have found their application in many areas such as [3]: research in remote and inaccessible places (space, seabed, volcanoes, etc.), dangerous environments (like military operations), construction work, transport operations, etc.

Therefore, in hexapod robots, two typical systems at architectures and locomotions originating from spider insects (hexagonal hexapod) and cockroaches (rectangular hexapod) can be found in

the literature [4]. In this paper, a robot configuration based on a rectangular hexapod system architecture is described. The hexapod robot is a type of mobile robot that achieves its locomotion using six legs (three on each side of chassis), of which at least three or more legs must be on the ground to achieve their stable condition.

When moving in nature, insects can use different types of gait. Inspired by this [5], the most common types of gait they can perform (4 typical walks) of hexapod robots are wave gait, tetrapod gait, transition gait and tripod gait. In this paper, a model of behaviour based on tripod gait is presented. The reason that tripod gait is the most interesting because of movement speed. It is the fastest gait of insects when they maintain their body in dynamic balance [6].

Figure 1 shows the simplified product architecture of a hexapod robot, while figure 2 shows model of one hexapod robot (observed) leg with all the joints and ankles. On this basis, kinematic analysis was done to obtain a mathematical model of the robot. The Denavit-Hartenberg (D-H) method [7]was used to establish the joint coordinate system of a hexapod robot for it's one leg. Individual parameters on each joint and variables on joints (1 - root, 2- hip and 3 - knee joint) are defined, and the equation of motion for the leg is obtained. On each ankle of the open kinematic chain, right-wing orthonormal coordinate systems are systematically joined. As the final equation, a matrix equation is obtained, and the position of the top of the robot's leg relative to the coordinates of the robot's body. Solving the problem of inverse kinematics gives the values of the angles of rotation for each of the joints, i.e., the servo motors on them, for a given point in space at the observed robot leg.

When planning the trajectory of the movement of hexapod robots, the movement of the robot's leg in its stance (supporting) phase and swing (suspending) phase, and the transfer phase should be considered throughout the moving cycle. When performing the behaviour of the robot, the simulation was made for flat terrain. The simulation was performed using a combination of MATLAB Simulink tool and Simscape Multibody environment. The last one is very acceptable for block diagram modelling because it allows a block view of all sensors, bodies, system elements, joints and constraints using block components from the Simscape™ family. It also provides the possibility of 3D displaying the animation of the dynamics of the observed robot system. The control algorithm is derived using a PID controller on one robot leg (in each joint). The controller's parameters are adjusted on one leg of the robot, and after that, this is used to adjust the control on the other legs in this way. In joints 1 and 2 PID algorithm is based on position control [8]while in joint 3 is based on force control [8].

Below is a brief description of how this work is organized by its units. After this introduction, the next section briefly addresses some earlier research by the authors which this research is an extension of, while Section 3 describes the authors' motivation for conducting this research. Section 4 describes the hexapod robot product architecture, while Section 5 describes kinematic analysis with mathematical model of the hexapod robot. Section 6 presents control algorithm used and the next section presents conducted simulation, while Section 8 presents the obtained results with discussion. As the final section of the paper, Section 9 provides a conclusion for the research presented, as well as the possible directions of future research.

## 2. LITERATURE REVIEW

In this chapter, the authors give a brief overview of works in the field of creation, modelling and control of hexapod robots. We want to point out the work of authors Stoian and Vlado [9], who showed so-called two-tier (multi-hierarchical) governance structure. Namely, the control algorithm that is used in case of insufficient walking is presented in such way that it analyses the working space and gives commands to the robot joints. Its goal is to minimize robot movements in such way that the position is secured in an acceptable proximity to the desired position. There are also papers with an adaptive approach of robot motion control, like a paper of Quyang et al. [10]. The development of algorithms is based on the observed knowledge from nature, where a three-dimensional two-layer network of an artificial central sample generator (CPG) was created to generate the robot trajectory. The first layer of the generator generates several basic patterns of

movement, while the second controls the behavior of the robot's legs, in such way that it adapts to changes in the environment in a particular pattern of movement. A motion simulation was performed, as well as an experiment. Some of the papers also show certain applications of robots for particular purposes, such as work of Gökrem and Can [11], which gives a comparison of two regulators PID and Fuzzy Logic, and would be applied to greenhouses, and for operations of searching of missing persons. and rescuing. The paper presents the structure of robots and based on that cognition, control algorithms are developed. There also can be found a presentation of some ready-made solutions such as the development of hexapod robots type RHex, by Saranli et al. [12] with six degrees of freedom of movement, where a robot simulation and an experiment in walking, running and turning a robot are shown. Like in this paper, there are many papers that conduct their simulation using the Simscape tool. One of such papers is the one of author Urrea et. al. [13] showing the application of MATLAB simulink tools, Simscape Multibody plugin and VRML language. A three-dimensional model of the robot is shown in the VRML language, while a PID controller is used for control to obtain a predetermined robot displacement. The work of Deng et al. [14] is interesting because it gives an overview of robot movement in rolling gait mode and trajectory planning. The idea is to constantly change the gait according to the different environment in which the robot moves, as well as the state of its stability. The CPG network is also used in the work of the author Campos [15], where the movement of hexapod robots on different types of terrain is shown, and the control is solved multi-hierarchically for three levels using a central sample generator. The work of the author Tedeschi and Carbone [16] provides an overview of robot movement planning with the aim of improving stability speed, navigation autonomy and energy efficiency. In addition, a classification of hexapod robots with their description is given.

## 3. MOTIVATION

With this paper, the authors wanted to present the beginning of their research on the internal project „KO006-2020/1 - Establishment and equipping of laboratory for the course „Systems and Control Algorithms in Robotics" and „Mobile Robotics" at the Polytechnic Graduate Professional Study of Electrical engineering" supported by Zagreb University of Applied Sciences, Zagreb, Croatia., which is currently in active phase. It is planned that part of the developed and presented algorithms for the movement of hexapod robots will be used as part of laboratory exercises in these courses. Also, by researching this area, authors wanted to expand their knowledge in the field of mobile robotics, and they wanted to share it with other young scientists who can also use it, as they are just like them at the beginning of their research.

## 4. HEXAPOD ROBOT PRODUCT ARCHITECTURE

When creating the architecture of the hexapod robot, the authors were guided by already known findings from published papers. Here we primarily mean studies of the movement of animals in nature and their natural forms [17]-[18]. As it is well known, many arthropods (such as insects and crustaceans) have six legs for the purpose of maintaining static stability and dynamic stability, and a certain robustness of their architecture during their movement. It is interesting that their body is made as segmented, which is covered with a connected outer skeleton. As one of the examples of hexapod motion in nature, we can give the example of a cockroach and the robot architecture derived from it, shown in Figure 1.

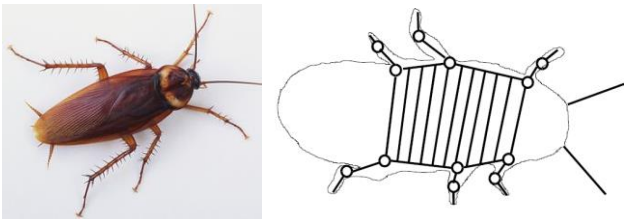

**Figure 1.** Example of anatomy of an insect from nature (cockroach) and based on that derived architecture of a hexapd robot shown by a simplified kinematic scheme

https://doi.org/10.3311/ECCOMASMBD2021-152

A typical example of a robot developed on the abovementioned knowledge of insect anatomy and their movement is the hexapod robot [2]. What has been developed in them are already known modes of movement, one of which will be a tripod gait that will be considered during the control of this robot. The biggest problem is degrees of freedom of movement on the legs [4], and we can say that it is quite a complex problem to solve the control, ie to create a control algorithm. In hexapod robot architecture, we can find two main subgroups in the literature, namely rectangular and hexagonal robot architecture [17]. Both architectures are inspired by the appearance of insects, where the difference between them is in the symmetry of the position of all 6 legs along the body. In the rectangular design, this is done symmetrically, while in the hexagonal design, the legs are placed asymmetrically along the robot body. It is important to say that in the literature there is another division according to the type of legs of hexapod robots [19], where this type of robot is classified in the group of robots with bio-inspired legs in which are mammals, arachnids and reptiles.

In our work, we used the simplified architecture of the hexapod robot, which is shown in Figure 2 with all the legs, their ankles, and joints. It should be noted that each robot joint has a servo motor, which is controlled. Each leg is numbered and all the considered coordinate systems are placed on the diagram. According to the given scheme, the performed kinematic analysis of the robot will be presented in the next chapter of this paper.

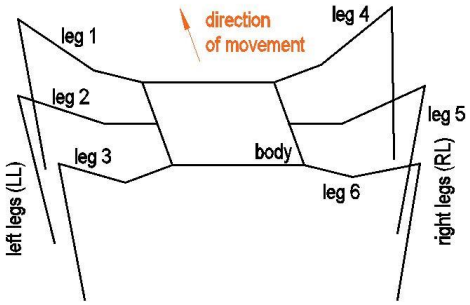


**Figure 2.** Representation of the considered hexapod robot, shown by a simplified kinematic scheme

## 5. KINEMATIC AND DYNAMIC ANALYSIS WITH MATHEMATICAL MODEL

In the previous chapter, we briefly described the architecture of the hexapod robot. Also, we showed its simplified configuration shown in the kinematic scheme in Figure 2. That is important to be to explained before conducting the kinematic analysis for the reason that we can predict all the effects of individual robot motion performance. Considering the symmetrical rectangular structure of the legs of the hexapod robot, it can be seen that we have 3 legs which are located on both sides, where each leg has 3 degrees of freedom of movement (3 DOF). In order to be able to perform an inverse kinematic model of a robot on this basis, we need to define coordinate systems for legs and body in the diagram, which later will be used to create all the different phases during the tripod gait movement of the robot. Coordinate systems were selected as follows (Figure 3):

$R_0(O_0, X_0, Y_0, Z_0)$ – global coordinate system

$R_b(O_b, X_b, Y_b, Z_b)$ – coordinate system of robot body

$R_{li}$ $(O_{li}, X_{li}, Y_{li}, Z_{li})$ – coordinate system of robotic leg ($i$ = 1, 2,…6 – number of robot leg)

Figure 3 already shows and observes the robot leg (leg no. 5, marked in purple, is selected here). It was created in such way that it has three degrees of freedom of movement, because it has already been shown that the minimum number of joints of a robot's leg is needed to ensure its mobility and movement in different types of gait. Thanks to the symmetrical configuration of the robot, it is enough to perform the analysis on only one leg of the robot.

https://doi.org/10.3311/ECCOMASMBD2021-152

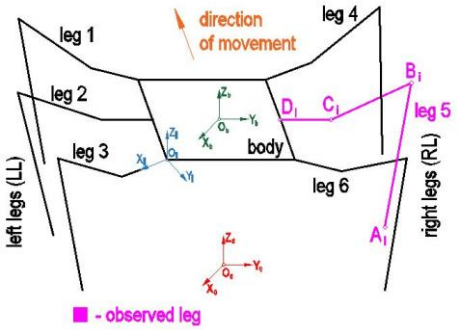


**Figure 3.** Simplified kinematic scheme of robots with defined oordinate systems

Individual parameters on each joint and variables on joints (1 – root joint, 2- hip joint and 3 - knee joint) are defined, and the equation of motion for the leg is obtained in next chapter. On each link of the presented open kinematic chain, right-wing orthonormal coordinate systems are systematically joined.

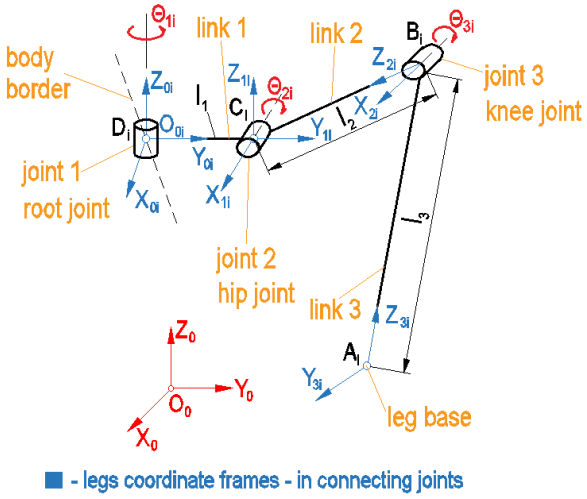


**Figure 4.** Simplified kinematic scheme of the observed leg of robot no. 5 with defined coordinate systems shown

When deriving the equations of motion of the hexapod robot, we use Denavit-Hartenberg's algorithm [7], which we will apply to the shown observation leg of the robot in Figure 4. In most literature [5]-[6] we will find the names denoting the marked points in the diagram in Figure 4. Thus joint 1 is called "thorax", link 1 is called "coxa", link 2 is called "femur", and link 3 is called "tibia". Mentioned algorithm is based on the systematic association of right-handed orthonormal coordinate systems to each open kinematic chain member. Since we have a more complex kinematic structure (3 DOF) here, the mathematical model of direct kinematics [7] is solved by relative or homogeneous coordinate transformations e.g. Denavit - Hartenberg parameters for the observed robot leg with 3 DOF have already been derived in the paper by the author Mănoiu-Olar [20], we present them here in tabular form (Table 1).

**Table 1.** Denavit - Hartenberg parameters for the observed robot leg (3 DOF)

| Link | $a_i$ | $\alpha_i$ | $d_i$ | $\Theta_i$ |
|---|---|---|---|---|
| 1 | $l_1$ | 90° | $d_1$ | $\Theta_1$ |
| 2 | $l_2$ | 0° | 0 | $\Theta_2$ |
| 3 | $l_3$ | 180° | 0 | $\Theta_3$ |

A matrix of homogeneous transformation ${}^{i-1}A_i$ can also be found in [19, 20], which connects the link *i-1* with the link *i*. Based on it, a total transformation is performed later by multiplying the matrices ${}^{0}A_1$, ${}^{1}A_2$ i ${}^{2}A_3$ in order to obtain the resultant matrix representing the relationship

between the global coordinate system and the coordinate system at the base of the robot leg ${}^{0}A_3$. The solution of the mentioned system gives the equations of the direct kinematics of the tool, ie the base of the robot leg (tool configuration space) (5.1) - (5.3):

$$p_x = cos\theta_1(l_1 + l_2 \cdot cos\theta_2 + l_3 \cdot \cos(\theta_2 - \theta_3)) \quad (5.1)$$

$$p_y = sin\theta_1(l_1 + l_2 \cdot cos\theta_2 + l_3 \cdot \cos(\theta_2 - \theta_3)) \quad (5.2)$$

$$p_z = d_1 + l_2 \cdot sin\theta_2 + l_3 \cdot \sin(\theta_2 - \theta_3)) \quad (5.3)$$

The next step in kinematic analysis is to determine the angles in a particular joint depending on the coordinates of that same joint in the coordinate system (joint space). Abovementioned variables will enable us when controlling the robot, and as a starting point we will use the equations of direct kinematics already defined. This problem has already been solved in the available literature [21], so here we list the obtained formulas (5.4) - (5.6):

$$\Theta_1 = artg(\frac{y_1}{x_1}) \quad (5.4)$$

$$\Theta_2 = arcos\left(\frac{l_2^2 + x_3^2 + y_3^2 - l_3^2}{2 \cdot l_2 \cdot \sqrt{x_3^2 + y_3^2}}\right) + artg(\frac{y_3}{x_3}) \quad (5.5)$$

$$\Theta_3 = \Pi - \arccos(\frac{l_2^2 + l_3^2 - (x_3^2 + y_3^2)}{2 \cdot l_2 \cdot l_3}) \quad (5.6)$$

where are:

$l_1, l_2, l_3$ [m] - lengths of links 1, 2 and 3,

$\theta_1$ [°] - angle closed by the robot body with link 1,

$\theta_2$ [°] - angle closed by link 1 with link 2,

$\theta_3$ [°] - angle closed by link 2 with link 3.

In dynamic analysis, the purpose is to obtain the dynamic equations of motion of robot legs. For this purpose, it is necessary to consider all the necessary mass and geometry of the legs (length and thickness of the legs), and the geometry of the servo motor in order to obtain the most realistic dynamic model. The parameters used will calculate all the required volumes and the axial and centrifugal dynamic moments of inertia of the links and servo motors required to perform this analysis. Regarding this is an analysis of a multi-ankle leg, a much more applied model was chosen for this purpose, and that is the Lagrange-Euler model, which is needed due to the possibility of controlling the force of touch by a link 3 of the robotic leg. The model is based on the application of generalized coordinates and a combination of the following equations [8]: Lagrange equations of the second kind with Lagrange function $L(q, \dot{q})$, kinetic energy of the manipulator $T$ (includes the effects of translational and rotational motions), and potential energies $U$. Similar derived dynamic model for a robotic leg with 3 DOF can already be found in the literature [13, 22]. Due to the fact that all actuators (servo motors) in the joints are of the same mass, it is marked for all 3 servo motors with the same symbol $m_{SM}$. It should be emphasized that the masses of cables, associated electronics and other connecting elements were not considered in this analysis. The vector equation representing the dynamic model of the robotic arm [8] is written in the form:

$$\boldsymbol{D(q)\ddot{q} + c(q, \ddot{q}) + h(q) + b(\dot{q}) = M_t} \quad (5.7)$$

where are:

$\boldsymbol{D(q)}$ - manipulator inertia tensor - symmetric matrix of dimensions n x n,

$\boldsymbol{c(q, \ddot{q})}$ - connection vector of the i - th joint product of joint velocities and connection matrix of velocities C - matrix of dimensions n x n - represents centrifugal and Coriolis forces,

$\boldsymbol{h(q)}$ - vector of gravitational action - vector of dimensions n x 1 - describes the influence of gravity on the manipulator

$\boldsymbol{b(\dot{q})}$ - represents the friction that opposes the movement of the robotic arm.

https://doi.org/10.3311/ECCOMASMBD2021-152

$\boldsymbol{q}$ - vector of joint variables.

Below are the equations of actuator moments (5.8) - (5.10) obtained on the basis of the described approach:

$$M_{t1} = \ddot{\theta}_1 \cdot (I_{m1} + I_{l1} + m_{SM} \cdot (l_1^2 + r_{SM}) + m_2 \cdot (r_1^2 + r_2^2)) \quad (5.8)$$

$$M_{t2} = \ddot{\theta}_2 \cdot (I_{m2} + I_{l2} + m_{SM} \cdot l_2^2 + m_3 \cdot r_3^2) - g \cdot (l_3 \cdot \cos(\theta_2 + \theta_3) \cdot \left(3m_{SM} + m_1 + \frac{3m_2}{2}\right) + l_2 \cdot cos\theta_2 \left(2m_{SM} + m_1 + \frac{m_2}{2}\right)) \quad (5.9)$$

$$M_{t3} = \ddot{\theta}_3 \cdot (I_{m3} + I_{l3}) - g \cdot l_3 \cdot \cos(\theta_2 + \theta_3) \cdot (3m_{SM} + m_1 + \frac{3m_2}{2}) \quad (5.10)$$

where are:

$M_{t1}, M_{t2}, M_{t3}$ [Nm] - actuator moment (servo motors) in joints 1, 2 and 3,

$I_{m1}, I_{m2}, I_{m3}$ [kg·m$^2$] - dynamic moment of inertia of servo motor in joints 1, 2 and 3,

$I_{l1}, I_{l2}, I_{l3}$ [kg·m$^2$] - dynamic moment of inertia of robotic leg joints 1, 2 and 3,

$m_{SM}$ [kg] - mass of servo motor in joints 1, 2 and 3,

$m_1, m_2, m_3$ [kg] - mass of linksof the robot leg 1, 2 and 3,

$r_{SM}$ [m] - radius of rotation of servo motor in joints 1, 2 and 3,

$r_1, r_2, r_3$ [m]- radius of rotation of the center of mass in the links of the robot leg 1, 2 and 3,

$\ddot{\theta}_1, \ddot{\theta}_2, \ddot{\theta}_3$ [m/s$^2$] - angular accelerations in joints 1, 2 and 3.

The generalized contact force acting on the robotic manipulator [8] is calculated according to equation (5.11):

$$\boldsymbol{F} = \boldsymbol{M_t} - \boldsymbol{b}(\dot{\boldsymbol{q}}) \quad (5.11)$$

## 6. DESCRIPTION OF USED ALGORITHM FOR HEXAPOD ROBOT CONTROL

A PID controller has been selected to control the robot's ankle joint, i.e. the servo motor built into it. It is primarily chosen due to its derivational characteristic, thus improving the stability of the regulatory system. It is possible to increase the gain constant *K*, and at the same time reduce the integration constant $T_i$, which contributes to increasing the ability to more accurately monitor the reference quantity [23]. Today, this type of regulator is still the most common type of industrial regulators. The reason for this lies in the experience of the staff involved in their setup and commissioning, but also in their simplicity and comprehensibility of the control algorithm.

When developing a control algorithm, the simplest example of robot's usage locomotion on flat terrain is taken here.

The control signal of the PID controller can be written with the following expression [24]

$$u(t) = K[e(t) + \frac{1}{T_i}\int_0^t e(\tau)d\tau + T_d \frac{de(t)}{dt}] \quad (6.1),$$

or in the another form

$$u(t) = Ke(t) + K_i \int_0^t e(\tau)d\tau + K_d \frac{de(t)}{dt} \quad (6.2),$$

where are:

*K* - proportional gain constant of the regulator,

$K_i = K / T_i$ - gain constant (reset) of the integration part of the regulator,

$K_d = K \cdot T_d$ - gain constant of the derivation part of the regulator.

Usually, it takes a long time to set the parameters of the PID controller. On the one hand, it makes it easier for us to train the staff to do it (manual adjustment). On the other hand, the procedures for this purpose have already been developed. In this paper, the setting option in program MATLAB Simulink was used using the PID tuner window, correcting the values using the *slider*

https://doi.org/10.3311/ECCOMASMBD2021-152

*for response time* and *transient phenomena* options.

The control structure for two joints 1 and 2 of one robot leg shown in Figure 5, where we can observe that there are two parts of the system: the part with the regulator and the part of the system that concerns the robot. The control of these two joints was performed by position (joint rotation angle). The mathematical model of robots and the problem of Inverse kinematics has already been described in more detail in the previous chapter of this article.

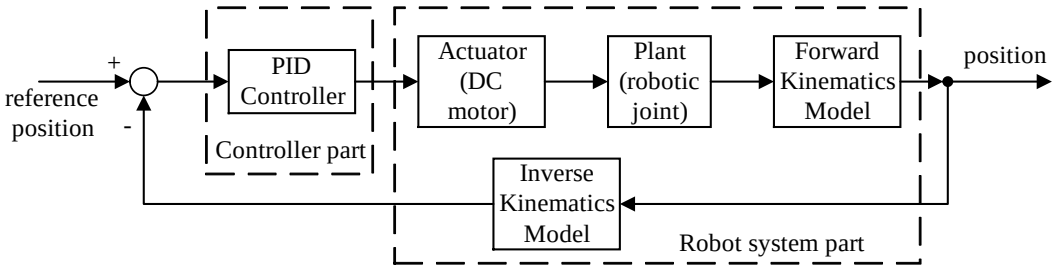


**Figure 5.** Display of the concept of control system for robotic joints 1 and 2

When used the contact force control on which the control of link 3 is based (because it has contact with the environment (ground)), it is necessary to install a contact force sensor that compares the measured force with the given once. In this case, the presentation of the management concept is shown in Figure 6.

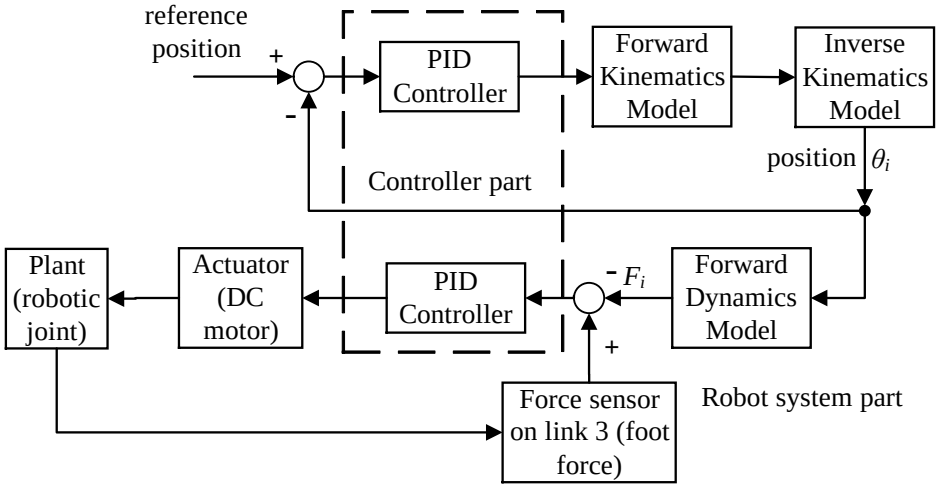


**Figure 6.** Display of the concept of control system for robotic joint 3

## 7. SIMULATION

Before creating the block model, it is necessary to calculate the parameters we need to create that model. For this purpose, Table 2 shows the values of the parameters that we used when calculating the dynamic moments of inertia [8] of the robot body and legs, as well as their masses (Note: for the dimensions of the robot body and legs, the overall dimensions were taken). When calculating the dynamic moments of inertia, we assumed that due to the symmetrical structure of the components the center of mass coincides with the center of gravity of the body. It is also assumed that the material of each component has homogeneous properties, i.e. that the material behaves the same in all directions of the component.

A combination of MATLAB Simulink and Simscape Multibody was used to create the simulation model. The use of the Simscape Multibody environment was very helpful because the hexapod robot has 6 legs, and each of them has 3 degrees of freedom of movement. This is the model itself, and it makes the behavior simulation quite complex. This environment has the advantage that it already created blocks for a certain type of joints, as well as the ankles of the legs. Each block already has the ability to individually adjust its parameters (geometry, mass, center of mass and moments of inertia).

Table 2. Parameters needed to calculate the masses and dynamic moments of inertia of individual robot components

| Robot geometry | |
|---|---|
| Dimensions of robot body ($L$ x $W$ x $H$) [mm] | 150 x 70 x 4 |
| Dimensions of link 1 ($l_1$ x $w_1$ x $h_1$) [mm] | 36 x 13 x 8 |
| Dimensions of link 2 ($l_2$ x $w_2$ x $h_2$) [mm] | 52 x 10 x 3 |
| Dimensions of link 3 ($l_3$ x $w_3$ x $h_3$) [mm] | 75 x 15 x 3 |
| Dimensions of servo motor ($\Phi D_{SM}$ x $l_{SM}$) [mm] | Φ12 x 28 |
| Material for robot body and legs and their density | |
| duralumin | $\rho$ = 2500 kg/m$^3$ |

The PID block in the MATLAB Simulink tool was used for control in block model in MATLAB SImulink. It has already been said that the setting option within the MATLAB Simulink using the PID *tuner* window was used to set the parameters of the PID controller. When creating a motion trajectory, a rectilinear motion was used as a function of the direction given to the function in the block. When planning the trajectory of the movement of hexapod robots, the movement of the robot's leg in its stance (supporting) phase and swing (suspending) phase, and the transfer phase should be considered throughout the moving cycle.

Each leg has three joints, each joint contains a servo motor. In the starting position, angle in the joint A is set to value 0°, in the joint B to 45°and in joint C to value 30°. During robot moving, it is first planned to move legs 1, 3 and 5 (marked in Figure 1). After these legs touch the ground, the same movement is achieved by legs 2, 4 and 6 with the same amplitude and frequency of movement. In the presented simulation, the robot walk along a straight path of a certain distance was performed, and therefore the robot movement analysis was performed.

## 8. DISCUSSION ON OBTAINED RESULTS

Figures 7 and 8 show the obtained responses of the moments in the joints 2 and 3 of the observed robotic leg after the performed simulation. It should be noted that the changes in the angles in the joints are set to vary in the range from -45 ° to 45 ° for the joint 2, and in the range from -30 ° to 30 ° for the joint 3. What should be mentioned is that when modeling the kinematic and the dynamic model of the robot, individual phases during the rotation of the legs were not considered. Namely, the movement of the robot's leg in its stance (supporting) phase, swing (suspending) phase, and the transfer phase should be considered throughout the moving cycle. Some models have already been derived on this topic, as shown in [25].

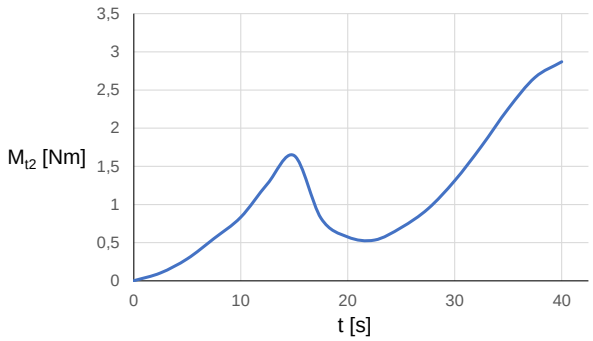


**Figure 7.** Display of the change of moment in the joint 2 of observed robotic leg

https://doi.org/10.3311/ECCOMASMBD2021-152

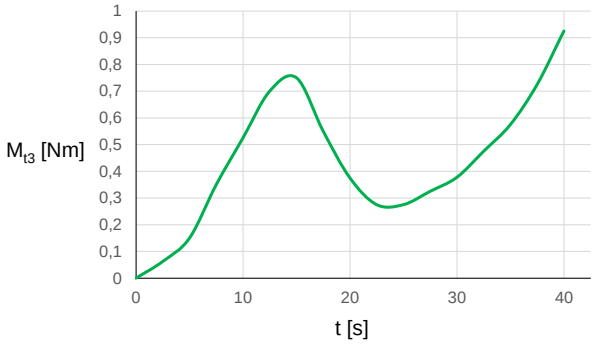


**Figure 8.** Display of the change of moment in the joint 3 of observed robotic leg

## 9. CONCLUSION AND SOME POSSIBLE WAYS OF FUTURE RESEARCH

In this paper, a development of mathematical model and the control algorithm of a hexapod robot during tripod gait locomotion is described. The kinematic analysis was done to obtain a mathematical model of the robot. It was done using the Denavit-Hartenberg (D-H) method and homogenous transformations to establish the joint coordinate system of a hexapod robot for its one leg. Solving the problem of inverse kinematics gives the values of the angles of rotation for each of the joints, for a given point in space at the observed robot leg. During hexapod robot trajectory planning, the movement of the robot's leg in its stance (supporting) phase and swing (suspending) phase, and the transfer phase should be considered throughout the moving cycle. Simulation is performed using combination of computer tool MATLAB Simulink and Simscape Multibody environment. The intention is to take advantage of that, so that could be used in teaching laboratory exercises in one of the courses at the graduate study on Zagreb University of Applied Sciences. The mathematical model presented is derived according to a model based on rectangular hexapod design configuration, using PID controllers in each leg joint. During the conduct of the research it has been proven that a major drawback is use of a PID controller which is quite difficult to set their controller parameters. When developing a control algorithm, the simplest example of robot's usage locomotion on flat terrain is taken here.

The development and application of another regulator based on adaptive control, as well as, its application for these robots on uneven terrains, has been presented as several directions for future research. The intention is to develop algorithms for other standard types of gait hexapod robots, and compare them with each other. It would also be good to make a prototype of the described robot, and conduct experimental results in order to confirm the simulation results.

## ACKNOWLEDGMENTS

The research presented in this paper is part of internal project „KO006-2020/1 - Establishment and equipping of laboratory for the course „Systems and Control Algorithms in Robotics" and „Mobile Robotics" at the Graduate Study of Electrical Engineering at Zagreb University of Applied Sciences, Zagreb, Croatia**.**

## REFERENCES

[1] M. Shahriari. Design, Implementation and Control of a Hexapod Robot using Reinforcement Learning Approach", M.Sc. Thesis, Kish Island, Iran, 2013.

[2] S. Mănoiu-Olaru and M. Niţulescu. Matlab Simulator for Gravitational Stability Analysis of a Hexapod Robot. The Romanian Review Precision Mechanics, Optics & Mechatronics, No. 39, 2011.

[3] J. A. Tenreiro Machado and M. F. Silva. An Overview of Legged Robots. MME 2006 – International Symposium on Mathematical Methods in Engineering, Ankara, Turkey, 2006.

[4] G. Carbone and M. Ceccarelli. Legged Robotic Systems", In: Cutting Edge Robotics ARS Scientific Book, Wien, pp. 553-576, 2005.

[5] R. Campos, V. Matos, Cristina Santos. Hexapod locomotion: A nonlinear dynamical systems approach. IECON 2010 - 36th Annual Conference on IEEE Industrial Electronics Society

[6] X. Duan, W. Chen, S. Yu and J. Liu. Tripod gaits Planning and Kinematics Analysis of a Hexapod Robot. 2009 IEEE International Conference on Control and Automation, Chistchurch, New Zealand, pp. 1850-1855, 2009.

[7] R.P. Paul. Robot Manipulators: Mathematics, Programming and Control, The Computer Control of Robot Manipulators. The MIT Press, Cambridge Massachusetts and London, England, 1981.

[8] Z. Kovačić, S. Bogdan, V. Krajči. Osnove robotike. Graphis, Zagreb, Croatia, 2002.

[9] V. Stoian, I. C. Vladu. A Control Algorithm for Hexapod Mobile Robot Gait in Fault Conditions, 20th International Conference on System Theory, Control and Computing (ICSTCC), Sinaia, Romania, pp. 349-354, 2016.

[10] W. Ouyang, H. Chi, J. Pang, W. Liang and Q. Ren. Adaptive Locomotion Control of a Hexapod Robot via Bio-Inspired Learning, Frontiers in Neurorobotics, open acess, doi: 10.3389/fnbot.2021.627157

[11] L. Gökrem and M. Serhat Can. Hexapod Robot Design and Performance Comparison of Fuzzy and PID Control Methods, Balkan Journal of Electrical and Computer Engineering, Vol. 8, No. 1, pp. 88-97, 2020.

[12] U. Saranli, M. Buehler and D. E. Koditschek. Design, Modeling and Preliminary Control of a Compliant Hexapod Robot, IEEE International Conference on Robotics and Automation, Vol. 3, ICRA 2000, pages 2589-2596, 2000.

[13] C. Urrea, L. Valenzuela and J. Kern. Design, Simulation, and Control of a Hexapod Robot in Simscape Multibody, InTech Open, open science, Applications from Engineering with MATLAB Concepts, chapter 5, pp. 125-137, 2016.

[14] H. Deng, G. Xin, G. Zhong and M. Mistry. Gait and trajectory rolling planning and control of hexapod robots for disaster rescue applications, Robotics and Autonomous Systems, 95, pp. 13-24, 2017.

[15] R. D. Costa Campos. Hexapod Locomotion: a Nonlinear Dynamical Systems Approach. MSc thesis, Universidade do Minho Escola de Engenharia, Portugal. 2009.

[16] F. Tedeschi and G. Carbone. Hexapod Walking Robot Locomotion, Motion and Operation Planning of Robotic Systems, Mechanisms and Machine Science, 29, pp. 439-468, 2015.

[17] X. Ding, Z. Wang, A. Rovetta and J.M. Zhu. Locomotion analysis of hexapod robot, in book: Climbing and Walking Robots, Behnam Miripour (Ed.), InTech, Vienna, Austria, pp. 291-310., 2010.

[18] S. Mănoiu-Olaru, M. Nițulescu. Stability Analysis Software Platform Dedicated for a Hexapod Robot, in book: Advances in Intelligent Control Systems and Computer Science, vol. 187, Loan Dumitrache (Ed.), Springer Nature Switzerland AG, pp. 143-156, 2019.

[19] R. Shirpurkar. Investigation of Effects of Changing Length Scales of Uniformly Structured Rough Terrain on Hexapedal Locomotion using Simulation, M.Sc. thesis, University of California, San Diego, USA, 2'19.

[20] S. Mănoiu-Olaru. Hexapod robot. Mathematical support for modeling and control. In: System Theory, Control, and Computing (ICSTCC), 2011 15th International Conference, Sinaia. IEEE; pp. 1‑6., 2011.

[21] R.K. Barai, P. Saha, and A. Mandal. SMART-HexBot: Simulation, Modeling, Analysis and Research Tool for Hexapod Robot in Virtual Reality and Simulin. In: AIR '13 Proceedings of Conference on Advances in Robotics, Pune, India, 2013.

[22] M. Nitulescu, M. Ivanescu, V. D. Hai Nguyen and S. Manoiu – Olaru. Designing the Legs of a Hexapod Robot, In: 2016 20th International Conference on System Theory, Control and Computing (ICSTCC), Sinaia, Romania, pp. 119-124, 2016.

[23] Z. Vukić, Lj. Kuljača. Automatsko upravljanje – analiza linearnih sustava, Kigen, Zagreb, Hrvatska, 2005.

[24] K.J. Astrom, T. Hagglund. PID Controllers: Theory, Design, and Tuning, second edition, International Society for Measurement and Control, Research Triangle Park, NC, USA, 1995.

[25] E. H. Hasnaa, B. Mohammed. Planning tripod gait of an hexapod robot, In: 14th International Multi-Conference on Systems, Signals & Devices (SSD), pp. 163-168, 2017.

https://doi.org/10.3311/ECCOMASMBD2021-257

ECCOMAS Thematic Conference on Multibody Dynamics
December 12 - 15, 2021, Budapest, Hungary

# A recursive dynamics algorithm for soft robotic manipulators made of viscoelastic material

**Makoto Iwamura**[1], **Kento Hirata**[1], **Yoshiki Maeda**[1], **Kyuji Oto**[1]

[1] Department of Mechanical Engineering
Fukuoka University
8-19-1 Nanakuma, Jonan, 814-0180 Fukuoka, Japan
iwamura@fukuoka-u.ac.jp

## ABSTRACT

In recent years, research and development of robots that exist in the same space as humans and can collaborate with humans have been actively carried out. If the body of a robot is made of a hard material, it may cause injury. Therefore, attempts have been made to make a robot with a soft body using rubber or resin. In order to accelerate such research on soft robotics, it is necessary to establish fast and stable simulation algorithm for robots containing viscoelastic bodies such as rubber and resin. Therefore, in this study, we consider to approximate viscoelastic bodies with finite rigid body segments and connect them with joints and linear viscoelastic elements such as Voigt model and Maxwell model to approximate viscoelastic properties. The recursive dynamics algorithm is used to speed up the calculation, and the generalization-$\alpha$ method is used to stabilize the numerical integration. In particular, we propose a new method on how to incorporate the Maxwell model into recursive dynamics algorithm and generalization-$\alpha$ method. The effectiveness of the proposed method is confirmed by some numerical examples.

**Keywords:** Soft robotics, Recursive algorithm, Viscoelastic material, Maxwell model.

## 1 INTRODUCTION

In the past, industrial robots had to be fenced for safety and completely separate the working range of humans and robots. However, due to the relaxation of the law, robots that meet certain conditions can now exist and collaborate in the same space as humans without being surrounded by fences. Furthermore, in recent years, many robots for long-term care and home use have been developed, and robots are deeply entering the living space of human beings. If the body of a robot that collaborates with a person is made of a hard material, it may cause serious injury when it comes into contact with a person. Therefore, attempts have been made to give the robot a soft body using rubber or resin. In order to accelerate the research and development of such soft robotics [1], it is necessary to establish a high-speed and stable dynamical simulation technology for robot systems including viscoelastic bodies such as rubber and resin. So far, research has been conducted to describe viscoelastic bodies by the nonlinear finite element method and incorporate them into multibody dynamics analysis [2, 3], however there is a problem that the theory is difficult and the calculation time is enormous.

Therefore, in this study, we consider to approximate viscoelastic bodies with finite rigid body segments and connect them with joints and linear viscoelastic elements such as Voigt model and Maxwell model to express viscoelastic properties. The recursive dynamics algorithm [4] is used to speed up the calculation, and the generalized-$\alpha$ method [5] is used to stabilize the numerical integration. In this paper, we examine how to incorporate the Maxwell model into the recursive dynamics algorithm and the generalized $\alpha$ method, and propose a new method. We perform a dynamical simulation of a 2-link manipulator composed of rubber links to confirm the effectiveness of the proposed method.

https://doi.org/10.3311/ECCOMASMBD2021-257

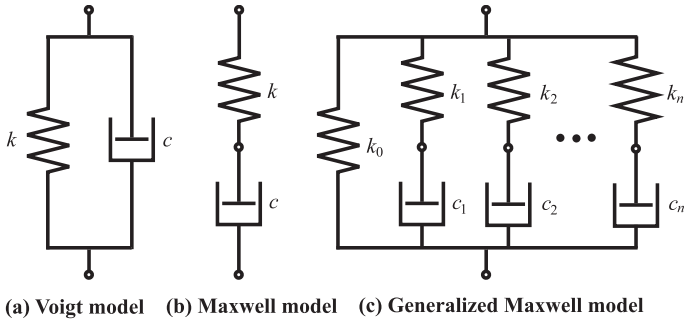


**Figure 1**. Linear viscoelastic model

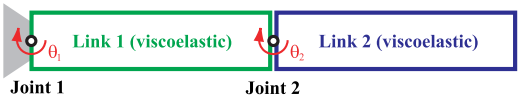


**Figure 2**. 2-link manipulator made of silicone rubber

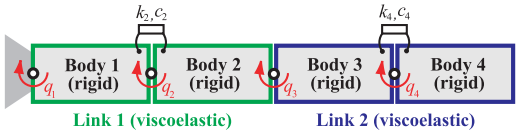


**Figure 3**. Finite segment approximation

## 2 MODEL OF SOFT ROBOT SYSTEM INCLUDING VISCOELASTIC BODY

The nonlinear finite element method is sometimes used to model a viscoelastic body, but it is not suitable for real-time simulation due to the large amount of calculation. On the other hand, a method of approximately expressing viscoelasticity by using the Voigt model, Maxwell model, generalized Maxwell model, etc., which combine the spring element and damper element as shown in Fig. 1, is also used. In this study, individual viscoelastic bodies included in a robot system are approximated by multiple rigid body elements connected by rotational joints or prismatic joints, and viscoelastic properties are expressed by adding spring elements and damper elements to the joints.

As an example, consider a 2-link manipulator composed of rubber links as shown in Fig. 2. Here, one link is approximated by two rigid body segments, and it is assumed that the axial deformation is negligible, and the bending deformation is expressed by connecting with a rotating joint. Then, by adding an appropriate rotary spring and rotary damper to the joint, the viscoelastic property of the link is approximately expressed. As a result, the system in Fig. 2 can be modeled as in Fig. 3. In the following, the relative angular displacement of the joint $i$ is $q_i$, the spring constant of the spring added to the joint $i$ is $k_i$, and the viscous damping coefficient of the damper is $c_i$. The length of the body $i$ is $l_i$, the mass is $m_i$, and the moment of inertia around the center of gravity is $I_i$.

In this study, as a stepping stone for the construction of a general calculation method, we formulate an algorithm that can perform high-speed and stable calculations for the system that was modeled as an open-loop rigid multibody system as shown in Fig. 4 and the Voigt model or Maxwell model as shown in Fig. 5 was added to the joints. When a soft robot system containing a viscoelastic body is modeled as a rigid multibody system as shown in Fig. 4, a high-speed recursive algorithm can be applied to dynamic calculations. In addition, the generalized-$\alpha$ method, which has excellent stability and allows a large time step size, is used for numerical integration.

## 3 RECURSIVE DYNAMICS ALGORITHM

In this section, the recursive dynamics algorithm [4] is extended to a rigid multibody system in which rigid bodies are connected in series by rotating joints as shown in Fig. 4 and a Voigt model or Maxwell model is added to the joints as shown in Fig. 5. It is assumed that the total number of bodies is $N$, including the rigid body elements introduced to approximate the viscoelastic body. Here, the body $i$ coordinate system $\Sigma_i$ is defined so as to match the joint $i$ on the root side. Let

https://doi.org/10.3311/ECCOMASMBD2021-257

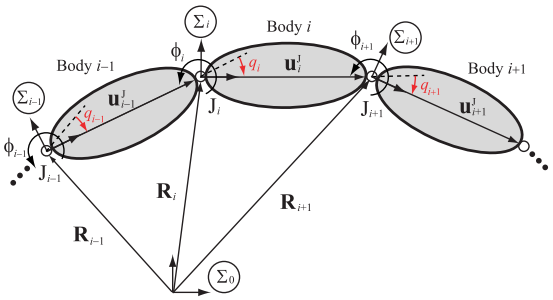


**Figure 4**. Relationship between neighboring bodies

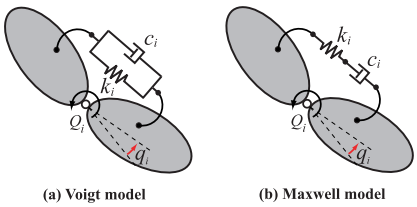


**Figure 5**. Viscoelastic model added to joints

the vector from the origin of the absolute coordinate system $\Sigma_0$ to the origin of $\Sigma_i$ be $\boldsymbol{R}_i$, and the angle of $\Sigma_i$ with respect to $\Sigma_0$ be $\phi_i$. Then, the velocity relationship and acceleration relationship between the adjacent body $i$ and body $i-1$ can be expressed by the following equations.

$$\boldsymbol{v}_i = \boldsymbol{D}_i \boldsymbol{v}_{i-1} + \boldsymbol{J}_i \dot{q}_i \tag{1}$$

$$\boldsymbol{a}_i = \boldsymbol{D}_i \boldsymbol{a}_{i-1} + \boldsymbol{J}_i \ddot{q}_i + \boldsymbol{\beta}_i \tag{2}$$

where $\boldsymbol{v}_i = [\dot{\boldsymbol{R}}_i^T \ \dot{\phi}_i]^T$, $\boldsymbol{a}_i = [\ddot{\boldsymbol{R}}_i^T \ \ddot{\phi}_i]^T$, $\boldsymbol{J}_i$ is the Jacobian matrix which represents the effect of joint velocity $\dot{q}_i$ on generalized velocity $\boldsymbol{v}_i$, $\boldsymbol{D}_i = \mathrm{diag.}[\boldsymbol{A}_i, 1]$, $\boldsymbol{A}_i$ is the rotation matrix from $\Sigma_i$ to $\Sigma_{i-1}$, and $\boldsymbol{\beta}_i = \dot{\boldsymbol{D}}_i \boldsymbol{v}_{i-1} + \dot{\boldsymbol{J}}_i \dot{q}_i$.

On the other hand, the equations of motion of the body $i$ can be expressed as follows.

$$\boldsymbol{M}_i \boldsymbol{a}_i + \boldsymbol{h}_i = \boldsymbol{Q}_i \tag{3}$$

where $\boldsymbol{M}_i$ is the generalized mass matrix, $\boldsymbol{h}_i$ is the quadratic velocity vector, $\boldsymbol{Q}_i$ is the generalized force vector. The generalized force $\boldsymbol{Q}_i$ acting on the body $i$ is divided into three forces, that is, the generalized force $\boldsymbol{Q}_i^J$ received from the body $i-1$ via the joint $i$, the reaction force of the generalized force $\boldsymbol{Q}_{i+1}^J$ exerted by the body $i$ on the body $i+1$ via the joint $i+1$, and the other generalized forces $\boldsymbol{Q}_i^O$. Therefore, it can be expressed as $\boldsymbol{Q}_i = \boldsymbol{Q}_i^J + \boldsymbol{Q}_i^O - \boldsymbol{D}_{i+1}^T \boldsymbol{Q}_{i+1}^J$. By substituting this into Eq. (3), solving for $\boldsymbol{Q}_i^J$, and taking the inner product with $\boldsymbol{J}_i$, then the joint driving torque $\tau_i$ can be obtained.

$$\boldsymbol{Q}_i^J = \boldsymbol{M}_i \boldsymbol{a}_i + \boldsymbol{h}_i - \boldsymbol{Q}_i^O + \boldsymbol{D}_{i+1}^T \boldsymbol{Q}_{i+1}^J \tag{4}$$

$$\tau_i = \boldsymbol{J}_i^T \boldsymbol{Q}_i^J + \overline{Q}_i \tag{5}$$

where $\overline{Q}_i$ is the reaction torque of $Q_i$ applied by the Voigt model or Maxwell model added to the joint $i$.

Inverse dynamics calculation can be executed by calculating the equations (1) and (2) from the root $i = 1$ to the tip $i = N$, and then calculating the equations (4) and (5) from the tip $i = N$ to the root $i = 1$. By repeatedly using this inverse dynamics calculation, the mass matrix $\boldsymbol{M}$, and the centrifugal, Coriolis and gravitational force $\boldsymbol{h}$ of the following equations of motion in minimal form can be calculated efficiently.

$$\boldsymbol{M}(\boldsymbol{q})\ddot{\boldsymbol{q}} + \boldsymbol{h}(\boldsymbol{q}, \dot{\boldsymbol{q}}) = \boldsymbol{\tau} \tag{6}$$

## 4 NUMERICAL INTEGRATION METHOD

Numerical integration methods are roughly divided into explicit methods and implicit methods. Since a system containing a viscoelastic body is generally a stiff system, it is necessary to make the time step $h$ extremely small when using the explicit method in which the stable range is limited, which requires a huge amount of calculation time. On the other hand, the implicit method is

https://doi.org/10.3311/ECCOMASMBD2021-257

excellent in stability, and since the time step $h$ can be taken large, the solution can be obtained in a short calculation time. Here, we use the generalized-$\alpha$ method [5], which is a single-step implicit method. The implicit method requires iterative calculations at each step, and at that time the Jacobian matrix must be calculated. Hence, we propose a method for calculating the Jacobian matrix strictly and at high speed using the recursive dynamics algorithm formulated in section 3 to shorten the calculation time.

### 4.1 Generalized-$\alpha$ method

Let us divide the interval $t \in [0, t_f]$ for the solution into $0 = t_0 < t_1 < \cdots < t_{p-1} < t_p = t_f$ and express the value of $\boldsymbol{q}(t)$ at time $t_n$ as $\boldsymbol{q}_n$. We also introduce an auxiliary variable vector $\boldsymbol{a}_n$ of the same dimension as the acceleration that defined by the following recurrence formula.

$$(1-\alpha_m)\boldsymbol{a}_{n+1} + \alpha_m \boldsymbol{a}_n = (1-\alpha_f)\ddot{\boldsymbol{q}}_{n+1} + \alpha_f \ddot{\boldsymbol{q}}_n,\ \boldsymbol{a}_0 = \ddot{\boldsymbol{q}}_0 \tag{7}$$

Then, we use the following formula in which $\ddot{\boldsymbol{q}}_n$ and $\ddot{\boldsymbol{q}}_{n+1}$ in Newmark's integral formula are replaced with $\boldsymbol{a}_n$ and $\boldsymbol{a}_{n+1}$, respectively.

$$\dot{\boldsymbol{q}}_{n+1} = \dot{\boldsymbol{q}}_n + h(1-\gamma)\boldsymbol{a}_n + h\gamma \boldsymbol{a}_{n+1} \tag{8}$$

$$\boldsymbol{q}_{n+1} = \boldsymbol{q}_n + h\dot{\boldsymbol{q}}_n + h^2\left(\frac{1}{2} - \beta\right)\boldsymbol{a}_n + h^2\beta \boldsymbol{a}_{n+1} \tag{9}$$

From equations (7) to (9), the following relationship can be obtained.

$$\dot{\boldsymbol{q}}_{n+1} = \frac{\gamma}{h\beta}(\boldsymbol{q}_{n+1} - \boldsymbol{q}_n) + \left(1 - \frac{\gamma}{\beta}\right)\dot{\boldsymbol{q}}_n + h\left(1 - \frac{\gamma}{2\beta}\right)\boldsymbol{a}_n \tag{10}$$

$$\ddot{\boldsymbol{q}}_{n+1} = \frac{1-\alpha_m}{h^2\beta(1-\alpha_f)}\left\{\boldsymbol{q}_{n+1} - \boldsymbol{q}_n - h\dot{\boldsymbol{q}}_n - h^2\left(\frac{1}{2} - \beta\right)\boldsymbol{a}_n\right\} + \frac{\alpha_m \boldsymbol{a}_n - \alpha_f \ddot{\boldsymbol{q}}_n}{1-\alpha_f} \tag{11}$$

From equations (10) and (11), it can be seen that $\dot{\boldsymbol{q}}_{n+1}$ and $\ddot{\boldsymbol{q}}_{n+1}$ are only functions of $\boldsymbol{q}_{n+1}$, if $\boldsymbol{q}_n$, $\dot{\boldsymbol{q}}_n$, $\ddot{\boldsymbol{q}}_n$ and $\boldsymbol{a}_n$ at time $t$ are known. If the above equations are partially differentiated with respect to $\boldsymbol{q}_{n+1}$, the following relationships can be obtained.

$$\frac{\partial \dot{\boldsymbol{q}}_{n+1}}{\partial \boldsymbol{q}_{n+1}} = \gamma' \boldsymbol{E},\ \frac{\partial \ddot{\boldsymbol{q}}_{n+1}}{\partial \boldsymbol{q}_{n+1}} = \beta' \boldsymbol{E} \tag{12}$$

where $\gamma' \equiv \gamma/(h\beta),\ \beta' \equiv (1-\alpha_m)/\{h^2\beta(1-\alpha_f)\}$.

The residual of the equations of motion in minimal form (6) at time $t = t_{n+1}$ is written by explicitly expressing $\dot{\boldsymbol{q}}_{n+1}$ and $\ddot{\boldsymbol{q}}_{n+1}$ are functions of $\boldsymbol{q}_{n+1}$ as follows.

$$\boldsymbol{e}(\boldsymbol{q}_{n+1}) \equiv \boldsymbol{M}(\boldsymbol{q}_{n+1})\ddot{\boldsymbol{q}}_{n+1}(\boldsymbol{q}_{n+1}) + \boldsymbol{h}(\boldsymbol{q}_{n+1}, \dot{\boldsymbol{q}}_{n+1}(\boldsymbol{q}_{n+1})) - \boldsymbol{\tau}_{n+1} \tag{13}$$

From the above equation, the Jacobian matrix obtained by differentiating $\boldsymbol{e}$ with respect to $\boldsymbol{q}_{n+1}$ can be calculated as follows.

$$\begin{aligned}\frac{\partial \boldsymbol{e}}{\partial \boldsymbol{q}_{n+1}} &= \frac{\partial \boldsymbol{M}(\boldsymbol{q}_{n+1})}{\partial \boldsymbol{q}_{n+1}}\ddot{\boldsymbol{q}}_{n+1}(\boldsymbol{q}_{n+1}) + \boldsymbol{M}(\boldsymbol{q}_{n+1})\frac{\partial \ddot{\boldsymbol{q}}_{n+1}}{\partial \boldsymbol{q}_{n+1}} \\ &\quad + \frac{\partial \boldsymbol{h}(\boldsymbol{q}_{n+1}, \dot{\boldsymbol{q}}_{n+1}(\boldsymbol{q}_{n+1}))}{\partial \boldsymbol{q}_{n+1}} + \frac{\partial \boldsymbol{h}(\boldsymbol{q}_{n+1}, \dot{\boldsymbol{q}}_{n+1}(\boldsymbol{q}_{n+1}))}{\partial \dot{\boldsymbol{q}}_{n+1}}\frac{\partial \dot{\boldsymbol{q}}_{n+1}}{\partial \boldsymbol{q}_{n+1}} \\ &= \beta' \boldsymbol{M}(\boldsymbol{q}_{n+1}) + \gamma' \boldsymbol{D}^t(\boldsymbol{q}_{n+1}) + \boldsymbol{K}^t(\boldsymbol{q}_{n+1}) \equiv \boldsymbol{S}(\boldsymbol{q}_{n+1})\end{aligned} \tag{14}$$

where $\boldsymbol{K}^t$ and $\boldsymbol{D}^t$ are matrices defined as follows.

$$\boldsymbol{K}^t(\boldsymbol{q}_{n+1}) \equiv \frac{\partial \boldsymbol{M}(\boldsymbol{q}_{n+1})}{\partial \boldsymbol{q}_{n+1}}\ddot{\boldsymbol{q}}_{n+1}(\boldsymbol{q}_{n+1}) + \frac{\partial \boldsymbol{h}(\boldsymbol{q}_{n+1}, \dot{\boldsymbol{q}}_{n+1}(\boldsymbol{q}_{n+1}))}{\partial \boldsymbol{q}_{n+1}},\ \boldsymbol{D}^t(\boldsymbol{q}_{n+1}) \equiv \frac{\partial \boldsymbol{h}(\boldsymbol{q}_{n+1}, \dot{\boldsymbol{q}}_{n+1}(\boldsymbol{q}_{n+1}))}{\partial \dot{\boldsymbol{q}}_{n+1}} \tag{15}$$

If $\boldsymbol{S}(\boldsymbol{q}_{n+1})$ can be calculated, $\boldsymbol{q}_{n+1}$, $\dot{\boldsymbol{q}}_{n+1}$ and $\ddot{\boldsymbol{q}}_{n+1}$ at time $t = t_{n+1}$ can be obtained by repeating the following calculation until $\boldsymbol{e}(\boldsymbol{q}_{n+1}) = \boldsymbol{0}$ is satisfied within the margin of error.

$$\boldsymbol{S}(\boldsymbol{q}_{n+1}^{(k)})\Delta \boldsymbol{q}_{n+1}^{(k)} = -\boldsymbol{e}^{(k)},\ \boldsymbol{q}_{n+1}^{(k+1)} = \boldsymbol{q}_{n+1}^{(k)} + \Delta \boldsymbol{q}_{n+1}^{(k)},\ \dot{\boldsymbol{q}}_{n+1}^{(k+1)} = \dot{\boldsymbol{q}}_{n+1}^{(k)} + \gamma' \Delta \boldsymbol{q}_{n+1}^{(k)},\ \ddot{\boldsymbol{q}}_{n+1}^{(k+1)} = \ddot{\boldsymbol{q}}_{n+1}^{(k)} + \beta' \Delta \boldsymbol{q}_{n+1}^{(k)} \tag{16}$$

https://doi.org/10.3311/ECCOMASMBD2021-257

### 4.2 Acceleration of generalized-$\alpha$ method by recursive algorithm

In this study, we propose a Jacobian matrix calculation method with high calculation efficiency that takes advantage of the characteristics of the recursive algorithm, and introduce it into the generalized-$\alpha$ method to speed up the calculation. From Eq. (14), it can be seen that $\boldsymbol{K}^t$ and $\boldsymbol{D}^t$ can be expressed as follows.

$$\boldsymbol{K}^t(\boldsymbol{q}_{n+1}) = \frac{\partial}{\partial \boldsymbol{q}}\{\boldsymbol{M}(\boldsymbol{q})\ddot{\boldsymbol{q}} + \boldsymbol{h}(\boldsymbol{q},\dot{\boldsymbol{q}})\}\bigg|_{t=t_{n+1}} = \frac{\partial \boldsymbol{\tau}}{\partial \boldsymbol{q}}\bigg|_{t=t_{n+1}}, \boldsymbol{D}^t(\boldsymbol{q}_{n+1}) = \frac{\partial}{\partial \dot{\boldsymbol{q}}}\{\boldsymbol{M}(\boldsymbol{q})\ddot{\boldsymbol{q}} + \boldsymbol{h}(\boldsymbol{q},\dot{\boldsymbol{q}})\}\bigg|_{t=t_{n+1}} = \frac{\partial \boldsymbol{\tau}}{\partial \dot{\boldsymbol{q}}}\bigg|_{t=t_{n+1}} \tag{17}$$

Since the matrix $\boldsymbol{K}^t$ is the partial derivative of the inverse dynamics relationship with respect to $\boldsymbol{q}$, it can be obtained by the following calculation.

1) Perform the following calculations from $i = 1$ to $N$ and $k = 1$ to $N$.

$$\frac{\partial \boldsymbol{v}_i}{\partial q_k} = \boldsymbol{D}_i \frac{\partial \boldsymbol{v}_{i-1}}{\partial q_k} + \frac{\partial \boldsymbol{D}_i}{\partial q_k}\boldsymbol{v}_{i-1} \tag{18}$$

$$\frac{\partial \boldsymbol{a}_i}{\partial q_k} = \boldsymbol{D}_i \frac{\partial \boldsymbol{a}_{i-1}}{\partial q_k} + \frac{\partial \boldsymbol{D}_i}{\partial q_k}\boldsymbol{a}_{i-1} + \frac{\partial \boldsymbol{\beta}_i}{\partial q_k} \tag{19}$$

2) Perform the following calculations from $i = N$ to 1 and $k = 1$ to $N$.

$$\frac{\partial \boldsymbol{Q}_i^J}{\partial q_k} = \boldsymbol{M}_i \frac{\partial \boldsymbol{a}_i}{\partial q_k} + \frac{\partial \boldsymbol{h}_i}{\partial q_k} - \frac{\partial \boldsymbol{Q}_i^O}{\partial q_k} + \boldsymbol{D}_{i+1}^T \frac{\partial \boldsymbol{Q}_{i+1}^J}{\partial q_k} + \frac{\partial \boldsymbol{D}_{i+1}^T}{\partial q_k}\boldsymbol{Q}_{i+1}^J \tag{20}$$

$$\frac{\partial \tau_i}{\partial q_k} = \boldsymbol{J}_i^T \frac{\partial \boldsymbol{Q}_i^J}{\partial q_k} + \frac{\partial \overline{Q}_i}{\partial q_k} \tag{21}$$

These recurrence formulas are obtained by partially differentiating Eqs. (1), (2) and Eqs. (4), (5) with respect to $q_k$. Since $\partial \boldsymbol{D}_i/\partial q_k$, $\partial \boldsymbol{\beta}_i/\partial q_k$ and $\partial \boldsymbol{h}_i/\partial q_k$ appearing in the equation can be calculated in advance, by starting from a known initial value and solving the above recurrence formula in sequence, $\partial \boldsymbol{\tau}/\partial \boldsymbol{q} = \boldsymbol{K}^t$ can be obtained without any differential calculation.

Similarly, the matrix $\boldsymbol{D}^t = \partial \boldsymbol{\tau}/\partial \dot{\boldsymbol{q}}$ can be calculated as follows.

1) Perform the following calculations from $i = 1$ to $N$ and $k = 1$ to $N$.

$$\frac{\partial \boldsymbol{v}_i}{\partial \dot{q}_k} = \boldsymbol{D}_i \frac{\partial \boldsymbol{v}_{i-1}}{\partial \dot{q}_k} \tag{22}$$

$$\frac{\partial \boldsymbol{a}_i}{\partial \dot{q}_k} = \boldsymbol{D}_i \frac{\partial \boldsymbol{a}_{i-1}}{\partial \dot{q}_k} + \frac{\partial \boldsymbol{\beta}_i}{\partial \dot{q}_k} \tag{23}$$

2) Perform the following calculations from $i = N$ to 1 and $k = 1$ to $N$.

$$\frac{\partial \boldsymbol{Q}_i^J}{\partial \dot{q}_k} = \boldsymbol{M}_i \frac{\partial \boldsymbol{a}_i}{\partial \dot{q}_k} + \frac{\partial \boldsymbol{h}_i}{\partial \dot{q}_k} - \frac{\partial \boldsymbol{Q}_i^O}{\partial \dot{q}_k} + \boldsymbol{D}_{i+1}^T \frac{\partial \boldsymbol{Q}_{i+1}^J}{\partial \dot{q}_k} \tag{24}$$

$$\frac{\partial \tau_i}{\partial \dot{q}_k} = \boldsymbol{J}_i^T \frac{\partial \boldsymbol{Q}_i^J}{\partial \dot{q}_k} + \frac{\partial \overline{Q}_i}{\partial \dot{q}_k} \tag{25}$$

These recurrence formulas are obtained by partially differentiating Eqs. (1), (2) and Eqs. (4), (5) with respect to $\dot{q}_k$. Since $\partial \boldsymbol{\beta}_i/\partial \dot{q}_k$ and $\partial \boldsymbol{h}_i/\partial \dot{q}_k$ appearing in the equation can be calculated in advance, by starting from a known initial value and solving the above recurrence formula in sequence, $\partial \boldsymbol{\tau}/\partial \dot{\boldsymbol{q}} = \boldsymbol{D}^t$ can be obtained without any differential calculation.

Since $\boldsymbol{M}(\boldsymbol{q}_{n+1})$ can be calculated efficiently by the method explained in section 3, the Jacobian matrix $\boldsymbol{S}(\boldsymbol{q}_{n+1})$ in Eq. (14) can be calculated quickly and accurately if $\boldsymbol{K}^t(\boldsymbol{q}_{n+1})$ and $\boldsymbol{D}^t(\boldsymbol{q}_{n+1})$ are obtained by the above calculation procedure. However, in order to perform dynamics computations, it is necessary to calculate $\overline{Q}_i$ in Eq. (5), and in order to calculate the Jacobian matrix, it is

https://doi.org/10.3311/ECCOMASMBD2021-257

necessary to obtain $\partial\overline{Q}_i/\partial q_k$ in Eq. (21) and $\partial\overline{Q}_i/\partial\dot{q}_k$ in Eq. (25). In the following, the calculation methods of $\overline{Q}_i$, $\partial\overline{Q}_i/\partial q_k$ and $\partial\overline{Q}_i/\partial\dot{q}_k$ in the case of the Voigt model are summarized in section 5. On the other hand, the Maxwell model is not easy, so in section 6, we first examine the analysis method of the Maxwell model for a simple 1DOF system. Then, using the results, we propose the calculation methods of $\overline{Q}_i$, $\partial\overline{Q}_i/\partial q_k$ and $\partial\overline{Q}_i/\partial\dot{q}_k$ in the case of the Maxwell model in section 7.

## 5 CALCULATION METHOD FOR VOIGT MODEL

The Voigt model can express creep, which is one of the viscoelastic properties. In this chapter, we explain the calculation methods of $\overline{Q}_i$, $\partial\overline{Q}_i/\partial q_k$ and $\partial\overline{Q}_i/\partial\dot{q}_k$ in the case of the Voigt model, and confirm the effectiveness of the proposed method by numerical simulation.

### 5.1 Method for computiong $\overline{Q}_i$, $\partial\overline{Q}_i/\partial q_k$ and $\partial\overline{Q}_i/\partial\dot{q}_k$

In the case of the Voigt model shown in Fig. 5 (a), the reaction torque $\overline{Q}_i$ of the torque $Q_i$ applied to the joint $i$ can be expressed by the following equation.

$$\overline{Q}_i = k_i(q_i - q_i^0) + c_i\dot{q}_i \tag{26}$$

where $q_i^0$ is the angle at which the spring has a natural length. From the above equation, it can be seen that $\partial\overline{Q}_i/\partial q_k$ and $\partial\overline{Q}_i/\partial\dot{q}_k$ can be calculated as follows.

$$\frac{\partial\overline{Q}_i}{\partial q_k} = \begin{cases} k_i & (k=i) \\ 0 & (k\neq i) \end{cases}, \quad \frac{\partial\overline{Q}_i}{\partial\dot{q}_k} = \begin{cases} c_i & (k=i) \\ 0 & (k\neq i) \end{cases} \tag{27}$$

### 5.2 Verification by numerical simulation

Here, we consider the case where a 2-link manipulator composed of rubber links as shown in Fig. 2 is modeled as shown in Fig. 3 and a Voigt model is added to the joint. The following reference trajectories are given to the 2-link manipulator shown in Fig. 2.

$$\begin{cases} \theta_1(t) &= -\dfrac{\pi}{4}\cos(\dfrac{\pi}{t_f}t) + \dfrac{\pi}{4} \\ \theta_2(t) &= \dfrac{\pi}{4}\cos(\dfrac{\pi}{t_f}t) - \dfrac{\pi}{4} \end{cases} \quad (0 \le t \le t_f) \tag{28}$$

where $t_f$ is the operating time. First, assuming that the two links are rigid bodies, inverse dynamics calculation is performed to obtain the joint driving torques. Then, those driving torques are applied to the 1st and 3rd joints of the model shown in Fig. 3, forward dynamics calculations are conducted, and dynamics simulations that take viscoelasticity into consideration are performed. We set $l_1 = l_2 = l_3 = l_4 = 0.1$m, $m_1 = m_2 = m_3 = m_4 = 0.01840$kg, $I_1 = I_2 = I_3 = I_4 = 1.54866 \times 10^{-5}$ kgm$^2$, $k_1 = k_3 = 0.0001$Nm/rad, $k_2 = k_4 = 8000.0$Nm/rad, $c_1 = c_3 = 0.0$, $c_2 = c_4 = 0.2$Nms/rad and $t_f = 2$s in the simulation.

Let us consider the solution that computed by the Runge-Kutta method with the sufficiently small time step $h = 6.66667 \times 10^{-5}$ as the true solution of this problem. Figure 6 shows the errors of the proposed method and the Runge-Kutta method with respect to the reference solution. The Runge-Kutta method has high accuracy, but since it is an explicit method, it is easily destabilized and diverged when $h > 1.0 \times 10^{-4}$. On the other hand, the proposed method is based on the generalized-$\alpha$ method which is an implicit method that has excellent stability, it was possible to obtain a solution without divergence even if $h$ is increased.

Figure 7 shows the calculation time required to simulate a physical phenomenon for 2 seconds using the Runge-Kutta method and the proposed method (CPU: Intel (R) Core (TM) i7-7700 CPU @ 3.60GHz, Compiler: Visual C ++). From the figure, the calculation time is also significantly shortened, and it can be confirmed that the calculation time is faster than the Runge-Kutta method when compared with the same $h$. Furthermore, even if the time step $h$ is large, it does not become

https://doi.org/10.3311/ECCOMASMBD2021-257

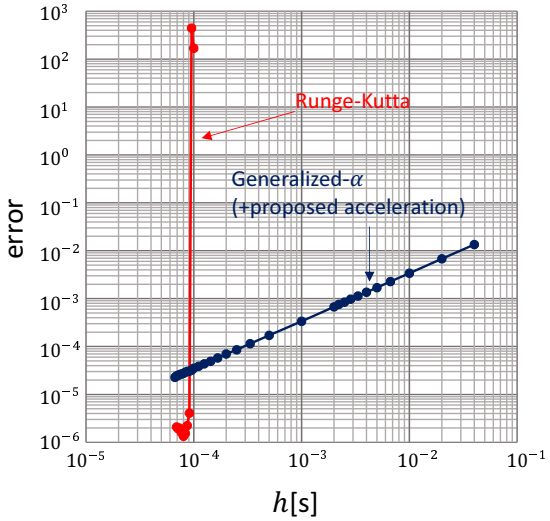


**Figure 6**. Comparison of integration error (Voigt model)

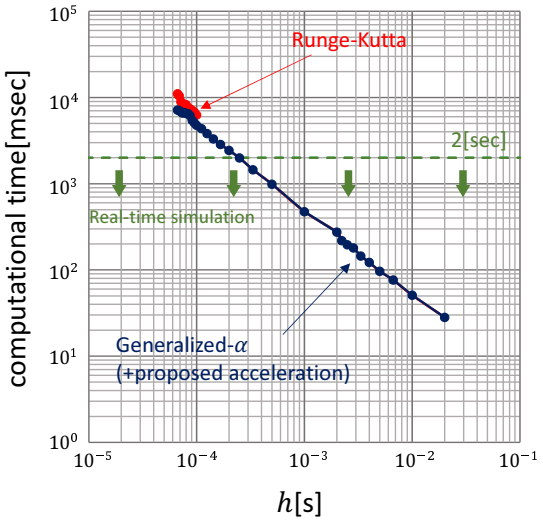


**Figure 7**. Comparison of computational time (Voigt model)

unstable, so the calculation can be speeded up within the range that satisfies the required accuracy. In this problem, when $h > 2.5 \times 10^{-4}$, the calculation time is less than 2 seconds, and real-time calculation can be achieved.

From the above, it was confirmed that when the Voigt model is added to the joint, high-speed and stable dynamics simulation is possible by the proposed method.

## 6 EXAMINATION OF ANALYSIS METHOD OF MAXWELL MODEL

The Voigt model can express creep, which is one of the important properties of viscoelastic bodies, but it is necessary to be able to handle the Maxwell model in order to express stress relaxation, which is another important property. However, in the Maxwell model, it is not easy to calculate $\overline{Q}_i$, and the calculation method of its partial derivative has not been established. So far, when calculating the Maxwell model, the equation of motion was often converted into a state equation and the numerical integration method developed for the first-order differential equation was applied. However, in order to introduce the Maxwell model into the calculation methods proposed in sections 3 and 4, it is necessary to be able to apply the generalized-$\alpha$ method in the form of the equations of motion. Therefore, in this section, the calculation method is first developed for a simple 1DOF system. Then, in section 7, the calculation method is extended to the multibody system.

### 6.1 Conventional method based on state equations

First, the commonly used calculation method will be explained. Let us denote the mass is $M$, the displacement is $q(t)$, and the external force is $Q(t)$ for the 1DOF Maxwell model shown in Fig. 8, then the equation of motion can be written by

$$M\ddot{q}(t) = Q(t) \tag{29}$$

If the displacement of the spring and damper alone is denoted by $q_k(t)$ and $q_c(t)$ respectively, then the following relationship holds.

$$q(t) = q_k(t) + q_c(t) \tag{30}$$

https://doi.org/10.3311/ECCOMASMBD2021-257

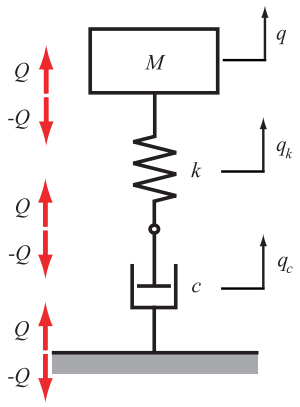


**Figure 8**. 1-DOF Maxwell model

On the other hand, if the spring constant is $k$ and the damping coefficient is $c$, the external force $Q(t)$ can be expressed in the following two ways.

$$Q(t) = -kq_k(t) \tag{31}$$
$$Q(t) = -c\dot{q}_c(t) \tag{32}$$

From Eqs. (29), (31) and (32), the following relationship can be obtained.

$$\dot{q}_k(t) = -\frac{M}{k}\dddot{q}(t) \tag{33}$$
$$\dot{q}_c(t) = -\frac{M}{c}\ddot{q}(t) \tag{34}$$

By differentiating Eq. (30) with respect $t$ and substituting Eqs. (33) and (34) leads to

$$\dot{q}(t) = \dot{q}_k(t) + \dot{q}_c(t) = -\frac{M}{k}\dddot{q}(t) - \frac{M}{c}\ddot{q}(t) \tag{35}$$

That is, the following relationship is obtained.

$$\dddot{q}(t) = -\frac{k}{M}\dot{q}(t) - \frac{k}{c}\ddot{q} \tag{36}$$

Define the state variables as $x_1(t) = q(t)$, $x_2(t) = \dot{q}(t)$, $x_3(t) = \ddot{q}(t)$, then the following state equations can be obtained.

$$\dot{x}_1(t) = x_2(t) \tag{37}$$
$$\dot{x}_2(t) = x_3(t) \tag{38}$$
$$\dot{x}_3(t) = -\frac{k}{M}x_2(t) - \frac{k}{c}x_3(t) \tag{39}$$

By applying the numerical integration method developed for the first-order differential equations such as the Runge-Kutta method to the state equations, the time response $q(t)$ can be calculated.

### 6.2 Proposed method based on equations of motion

In order to introduce the Maxwell model into the calculation methods proposed in sections 3 and 4, it is necessary to enable numerical integration by the generalized-$\alpha$ method in the form of the equations of motion without converting it to the state equations.

By differentiating Eq. (30) with respect $t$ and substituting Eqs. (31) and (32) leads to

$$\dot{q}(t) = \dot{q}_k(t) + \dot{q}_c(t) = -\frac{1}{k}\dot{Q}(t) - \frac{1}{c}Q(t) \tag{40}$$

https://doi.org/10.3311/ECCOMASMBD2021-257

That is, the following differential equation is obtained.

$$\dot{Q}(t)+\frac{k}{c}Q(t)=-k\dot{q}(t) \tag{41}$$

Define the initial value of $Q(t)$ is $Q_0$, then the solution of this differential equation is derived as

$$Q(t)=-e^{-\frac{k}{c}t}\left\{\int_0^t e^{\frac{k}{c}\tau}k\dot{q}(\tau)d\tau-Q_0\right\} \tag{42}$$

When the equation of motion (29) and the external force of Eq. (42) are discretized by the time step $h$, it can be expressed as the following equation at $t=t_{n+1}$.

$$\begin{aligned} M\ddot{q}_{n+1} &= Q_{n+1} && (43)\\ Q_{n+1} &= -e^{-\frac{k}{c}\{(n+1)h\}}\left\{\sum_{j=0}^{n+1}e^{\frac{k}{c}(jh)}k\dot{q}_j h-Q_0\right\} && (44)\end{aligned}$$

Furthermore, by arranging the Eq. (44), the following recurrence formula can be obtained.

$$\begin{aligned} Q_{n+1} &= -e^{-\frac{k}{c}\{(n+1)h\}}\left\{\sum_{j=0}^{n}e^{\frac{k}{c}(jh)}k\dot{q}_j h-Q_0+e^{\frac{k}{c}\{(n+1)h\}}k\dot{q}_{n+1}h\right\}\\ &= -k\dot{q}_{n+1}h+e^{-\frac{k}{c}h}\left[-e^{-\frac{k}{c}(nh)}\left\{\sum_{j=0}^{n}e^{\frac{k}{c}(jh)}k\dot{q}_j h-Q_0\right\}\right]\\ &= -k\dot{q}_{n+1}h+e^{-\frac{k}{c}h}Q_n && (45)\end{aligned}$$

On the other hand, Newmark's integral formula is expressed as follows.

$$\begin{aligned} \dot{q}_{n+1} &= \dot{q}_n+h(1-\gamma)\ddot{q}_n+h\gamma\ddot{q}_{n+1} && (46)\\ q_{n+1} &= q_n+h\dot{q}_n+h^2\left(\frac{1}{2}-\beta\right)\ddot{q}_n+h^2\beta\ddot{q}_{n+1} && (47)\end{aligned}$$

Here, if we define $\Delta q=q_{n+1}-q_n$, the following relationship can be obtained.

$$\begin{aligned} q_{n+1} &= q_n+\Delta q && (48)\\ \dot{q}_{n+1} &= \left(1-\frac{\gamma}{2\beta}\right)h\ddot{q}_n+\frac{\gamma}{\beta h}\Delta q && (49)\\ \ddot{q}_{n+1} &= \left(1-\frac{1}{2\beta}\right)\ddot{q}_n-\frac{1}{\beta h}\dot{q}_n+\frac{1}{\beta h^2}\Delta q && (50)\end{aligned}$$

In the generalized-$\alpha$ method, the equation of motion is modified as follows in order to improve the numerical damping characteristics.

$$\begin{aligned} M\ddot{q}^* &= Q^* && (51)\\ \ddot{q}^* &= (1-\alpha_m)\ddot{q}_{n+1}+\alpha_m\ddot{q}_n && (52)\\ Q^* &= (1-\alpha_f)Q_{n+1}+\alpha Q_n && (53)\end{aligned}$$

Substituting Eqs. (52), (53) and Eqs. (48) to (50) into Eq. (51), we can obtain the following equation.

$$\begin{aligned} \left\{\frac{1-\alpha_m}{h^2\beta(1-\alpha_f)}M+\frac{\gamma}{\beta}k\right\}\Delta q &= \left[\left(e^{-\frac{k}{c}h}+\frac{\alpha_f}{1-\alpha_f}\right)Q_n-\frac{1-\alpha_m}{1-\alpha_f}M\left\{\left(1-\frac{1}{2\beta}\right)\ddot{q}_n-\frac{1}{\beta h}\dot{q}_n\right\}\right.\\ &\quad\left.-\frac{\alpha_m}{1-\alpha_f}M\ddot{q}_n-k\left\{\left(1-\frac{\gamma}{2\beta}\right)h^2\ddot{q}_n+\left(1-\frac{\gamma}{\beta}\right)h\dot{q}_n\right\}\right] && (54)\end{aligned}$$

Since the coefficient of $\Delta q$ and right hand side in the above equation are known, $\Delta q$ can be calculated. Then, by substituting $\Delta q$ into Eqs (48) to (50), $q_{n+1}$, $\dot{q}_{n+1}$ and $\ddot{q}_{n+1}$ can be calculated. Furthermore, by substituting $\dot{q}_{n+1}$ into Eq. (45), $Q_{n+1}$ can be obtained. By repeating the above procedure, the time response $q(t)$ can be calculated.

https://doi.org/10.3311/ECCOMASMBD2021-257

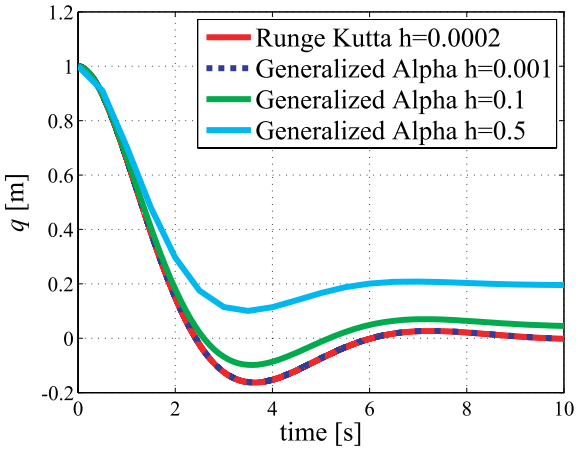


**Figure 9**. Comparison of time response

### 6.3 Verification by numerical simulation

Here, we compare the proposed method explained in Section 6.2 with the conventional method explained in Section 6.1. As an example, the dynamics simulation was performed with the parameters set to $M = 1\text{kg}$, $D = 1\text{Ns/m}$, $K = 1\text{N/m}$, $Q_0 = -1.0\text{N}$, $q(0) = 1.0\text{m}$, $\dot{q}(0) = 0\text{m/s}$ and $\ddot{q}(0) = Q_0/M = -1.0\text{m/s}^2$. The red line in Fig. 9 shows the result of solving by applying the conventional method and the Runge-Kutta method. Since the time step $h$ is set sufficiently small as $h = 0.0002$, it is considered that a solution close to the true one is obtained. Therefore, the validity of the proposed method is verified using this solution as a reference solution. The result of the calculation with $h = 0.001$ by the proposed method is shown by the blue dashed line in Fig. 9. From the figure, it can be confirmed that the blue dashed line overlaps with the red line and the calculation can be performed accurately. Since the proposed method uses the generalized-$\alpha$ method, which is an implicit numerical integration method, it did not diverge even if it was increased to $h = 0.1, 0.5$. From the above, the validity of the proposed calculation method was confirmed.

## 7 CALCULATION METHOD FOR MAXWELL MODEL

In this section, the analysis method of the Maxwell model developed for 1DOF system in section 6 is extended to multibody systems. We formulate the calculation methods of $\overline{Q}_i$, $\partial\overline{Q}_i/\partial q_k$ and $\partial\overline{Q}_i/\partial\dot{q}_k$ required when using the methods proposed in sections 3 and 4 for the Maxwell model.

### 7.1 Method for computiong $\overline{Q}_i$, $\partial\overline{Q}_i/\partial q_k$ and $\partial\overline{Q}_i/\partial\dot{q}_k$

In the case of the Maxwell model shown in Fig. 5 (b), the torque $Q_i(t)$ applied to the joint $i$ can be calculated from Equation (42) as follows.

$$Q_i(t) = -e^{-\frac{k_i}{c_i}t}\left\{\int_0^t e^{\frac{k_i}{c_i}\tau} k_i\dot{q}_i(\tau)d\tau - Q_i^0\right\} \tag{55}$$

where $Q_i^0$ is the initial value of $Q_i(t)$. Then, the Eq. (5) can be expressed as follows.

$$\tau_i = \boldsymbol{J}_i^T\boldsymbol{Q}_i^J + \overline{Q}_i(t),\ \overline{Q}_i(t) = -Q_i(t) = e^{-\frac{k_i}{c_i}}\left\{\int_0^t e^{\frac{k_i}{c_i}\tau} k_i\dot{q}_i(\tau)d\tau - Q_i^0\right\} \tag{56}$$

From Eq. (45), it is understood that $Q_i(t)$ can be expressed by the following recurrence formula, if it is discretized by the time step $h$ at $t = t_n$.

$$Q_i(t_n) = -k_i\dot{q}_i(t_n)h + e^{-\frac{k_i}{c_i}h}Q_i(t_{n-1}) \tag{57}$$

https://doi.org/10.3311/ECCOMASMBD2021-257

Therefore, $\overline{Q}_i(t)$ in Eq. (56) can be calculated by the following recurrence formula.

$$\overline{Q}_i(t_n) = k_i\dot{q}_i(t_n)h + e^{-\frac{k_i}{c_i}h}\overline{Q}_i(t_{n-1}) \tag{58}$$

Next, let us consider the calculation methods of $\partial\overline{Q}_i/\partial q_k$ and $\partial\overline{Q}_i/\partial\dot{q}_k$ that required when calculating the Jacobian matrix. By shifting the subscript of Eq. (58) by one and rewriting it for $t = t_{n+1}$, the following equation is obtained.

$$\overline{Q}_i(t_{n+1}) = k_i\dot{q}_i(t_{n+1})h + e^{-\frac{k_i}{c_i}h}\overline{Q}_i(t_n) \tag{59}$$

By partially differentiating the above equation, the following relationship can be obtained.

$$\left.\frac{\partial\overline{Q}_i}{\partial q_i}\right|_{t=t_{n+1}} = \frac{\partial\overline{Q}_i(t_{n+1})}{\partial q_i(t_{n+1})} = 0, \quad \left.\frac{\partial\overline{Q}_i}{\partial\dot{q}_i}\right|_{t=t_{n+1}} = \frac{\partial\overline{Q}_i(t_{n+1})}{\partial\dot{q}_i(t_{n+1})} = k_i h \tag{60}$$

That is, $\partial\overline{Q}_i/\partial q_k$ and $\partial\overline{Q}_i/\partial\dot{q}_k$ can be calculated as follows.

$$\frac{\partial\overline{Q}_i}{\partial q_k} = 0, \quad \frac{\partial\overline{Q}_i}{\partial\dot{q}_k} = \begin{cases} k_i h & (k = i) \\ 0 & (k \neq i) \end{cases} \tag{61}$$

From the above, the calculation method proposed in sections 3 and 4 can be extended to the multibody system in which the Maxwell model is added to the joint.

### 7.2 Verification by numerical simulation

Here, we consider the case where a 2-link manipulator composed of rubber links as shown in Fig. 2 is modeled as shown in Fig. 3 and a Maxwell model is added to the joints. As in section 5.2, the desired trajectory represented by Eq. (28) is given to the 2-link manipulator in Fig. 2, and the inverse dynamics calculation is performed by assuming that the two links are rigid bodies. Then, the obtained joint driving torques are applied to the 1st and 3rd joints of the model shown in Fig. 3 to perform a dynamic simulation considering viscoelasticity. The parameters are set to $l_1 = l_2 = l_3 = l_4 = 0.1$m, $m_1 = m_2 = m_3 = m_4 = 0.01840$kg, $I_1 = I_2 = I_3 = I_4 = 1.54866 \times 10^{-5}$kgm$^2$, $k_1 = k_3 = 0.0001$Nm/rad, $k_2 = 5000.0$Nm/rad, $k_4 = 7000.0$Nm/rad, $c_1 = c_3 = 0.0001$Nms/rad, $c_2 = 0.2$Nms/rad, $c_4 = 0.3$Nms/rad and $t_f = 2$s.

Let us consider the solution that computed by the Runge-Kutta method with the sufficiently small time step $h = 6.66667 \times 10^{-5}$ as the true solution of this problem. Figure 10 shows the errors of the proposed method and the Runge-Kutta method with respect to the reference solution. The Runge-Kutta method has high accuracy, but since it is an explicit method, it is easily destabilized and diverged when $h > 9.52 \times 10^{-5}$. On the other hand, the proposed method is based on the generalized-$\alpha$ method which is an implicit method that has excellent stability, it was possible to obtain a solution without divergence even if $h$ is increased.

Figure 11 shows the calculation time required to simulate a physical phenomenon for 2 seconds using the Runge-Kutta method and the proposed method (CPU: Intel (R) Core (TM) i7-7700 CPU@3.60GHz, Compiler: Visual C ++). From the figure, the calculation time is also significantly shortened, and it can be confirmed that the calculation time is faster than the Runge-Kutta method when compared with the same $h$. Furthermore, even if the time step $h$ is large, it does not become unstable, so the calculation can be speeded up within the range that satisfies the required accuracy. In this problem, when $h > 2.5 \times 10^{-4}$, the calculation time is less than 2 seconds, and real-time calculation can be achieved.

From the above, it was confirmed that high-speed and stable dynamical simulation is possible by the proposed method even when the Maxwell model is added to the joint.

https://doi.org/10.3311/ECCOMASMBD2021-257

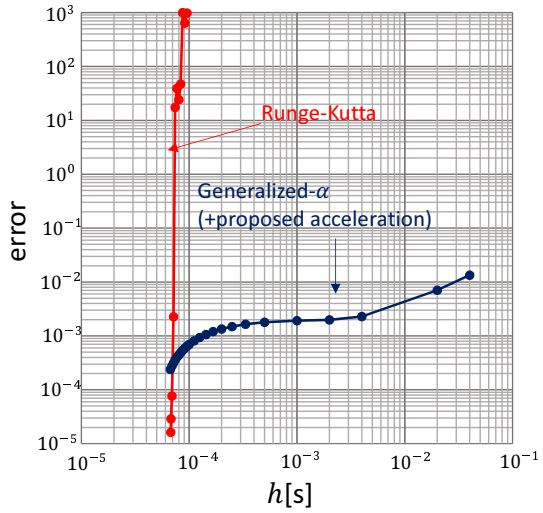


**Figure 10**. Comparison of integration error (Maxwell model)

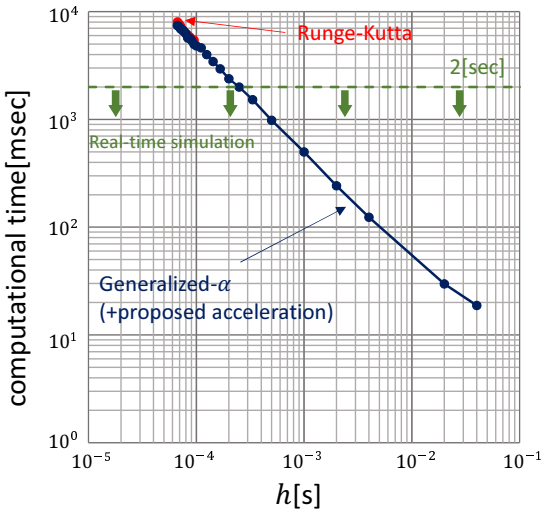


**Figure 11**. Comparison of computational time (Maxwell model)

## 8 CONCLUSIONS

In this study, we investigated a high-speed and stable dynamic calculation method for soft robot systems containing viscoelastic bodies such as rubber and resin. The viscoelastic bodies were approximated by finite rigid body segments, and they were connected by joints and linear viscoelastic elements such as the Voigt model and Maxwell model to express the viscoelastic properties. Then, the recursive dynamics algorithm was used to speed up the calculation, and the generalized-$\alpha$ method was used to stabilize the numerical integration. In this paper, we examined how to incorporate the Maxwell model into recursive dynamics algorithm and the generalized-$\alpha$ method, and proposed a new method. We applied the proposed method to a 2-link manipulator composed of rubber links and confirmed the effectiveness of the proposed method. In our future work, we will extend the proposed method to the generalized Maxwell model as shown in Fig. 1 (c) in order to reproduce the actual behavior of the viscoelastic body more accurately.

## REFERENCES

[1] Laschi, C., eds.: Soft Robotics, Trends, Applications and Challenges, Proceedings of the Soft Robotics Week, Springer (2016).

[2] Zhang, Y., Tian, Q., Chen, L., Yang, J.: Simulation of a viscoelastic flexible multibody system using absolute nodal coordinate and fractional derivative method, Multibody System Dynamics, **21** (2009) 281-303.

[3] Mohamed, A.A., and Shabana, A.A.: A nonlinear visco-elastic constitutive model for large rotation finite element formulations, Multibody System Dynamics, **26** (2011) 57-79.

[4] Iwamura, M, Sugiyama, H., Sato, K.: Recursive inverse and forward dynamics algorithms for flexible manipulators. Proceedings of the 6th Asian Conference on Multibody Dynamics, USB 9 pages, 2012.

[5] Arnold, M., and Bruls, O.: Convergence of the generalized-$\alpha$ scheme for constrained mechanical systems, Multibody System Dynamics, **18** (2007) 185-202.

https://doi.org/10.3311/ECCOMASMBD2021-130

ECCOMAS Thematic Conference on Multibody Dynamics
December 12 - 15, 2021, Budapest, Hungary

# On the Dynamics and Optimal Control of Constrained Mechanical Systems

**Simeon Schneider, Peter Betsch**

Institute of Mechanics
Karlsruhe Institute of Technology (KIT)
Otto-Ammann-Platz 9, 76131 Karlsruhe, Germany
simeon.schneider@kit.edu, peter.betsch@kit.edu

## ABSTRACT

The focus of this work is on optimal control in redundant coordinates with a special attention to the boundary constraints that arise in this context. Due to the similarity of the optimization problem of optimal control to the Lagrangian formalism of classical mechanics, this is considered first. Once the mechanical problem of the boundary conditions in redundant coordinates has been discussed, the knowledge gained is transferred to the optimal control problem in order to solve the problem in redundant coordinates. Finally, for each section the equivalence of the problem in minimal coordinates and redundant coordinates is shown by numerical results.

**Keywords:** Optimal control, boundary value problems, multibody dynamics

## 1 INTRODUCTION

Optimal control contains a large field of applications, from the optimal control of economical or chemical processes to the optimal control of robots or satellites. The latter ones can be summarized to mechanical systems and represent the focus of attention within this work.
There are several methods to describe the behaviour of the systems, the two most frequently chosen being the description of the complete system in minimal or redundant coordinates. However, depending on the choice of the description of the system, different types of mathematical systems of equations arise. As is well known, the description of the system in minimal coordinates yields a system of ordinary differential equations (ODEs), whereas the description of the system in redundant coordinates yields a system of differential algebraic equations (DAEs) for the equations of motion. Of course, both systems of equations describe the same motion of the mechanical system. Since the equations of motion are the constraints in the optimal control problem of the mechanical system, their description plays an essential role in the formulation of the optimal control problem. While the analytical and numerical solution of the optimal control problem in minimal coordinates can be considered as already well researched, this is not yet true for the description in redundant coordinates. However, since finding minimal coordinates can be difficult and in the worst case impossible, the focus of the present work lies on using DAEs as state equations in the optimal control problem. Due to the parallels between the Lagrangian formalism of classical mechanics and the optimization problem of optimal control, the Lagrangian formalism will be considered first. Subsequently, the obtained knowledge is applied to the optimal control problem, with special attention to the boundary constraints to be defined.
To keep it short and simple, the general approach will be illustrated with the example of a physical pendulum on a slide depicted in Figure 1.

## 2 CONSTRAINED MECHANICS AND THE LAGRANGIAN FORMALISM

In this section the boundary value problem (BVP) of the Lagrangian formalism will be considered with a special attention to the boundary conditions arising in redundant coordinates. Before starting with the description of the BVP in redundant coordinates, however, we will briefly discuss

https://doi.org/10.3311/ECCOMASMBD2021-130

the BVP in minimal coordinates. Once the procedure is known, the BVP is derived in redundant coordinates and the problems which arise are discussed. Thereupon, a simple but promising way to solve the mechanical BVP in redundant coordinates is described. The equivalence of both boundary value problems under consideration is illustrated with a numerical example.

### 2.1 The mechanical BVP in minimal coordinates

Let $I \in [t_0,\, t_f]$ be a time interval, $q : I \to \mathscr{M}$ be the minimal coordinates on the configuration manifold $\mathscr{M} := \{q \in \mathbb{R}^2 \,|\, q_1 = x_1, q_2 = x_6\}$ of the system at hand (Fig. 1), and $\mathscr{TM}$ be the tangent bundle, see for example [2]. Then the Lagrangian $L : \mathscr{TM} \to \mathbb{R}$ is defined by

$$L(q) = T(q,\dot{q}) - V(q) = \frac{1}{2}\dot{q}^a g_{ab} \dot{q}^b - V(q)$$

with $T : \mathscr{TM} \to \mathbb{R}$ being the kinetic energy, $V : \mathscr{M} \to \mathbb{R}$ being the potential energy and $g_{ab}$ being the metric tensor, better known as mass matrix. Finally let $\mathbb{P} \in \mathscr{M} \times \mathscr{T}^*\mathscr{M}$ be the phase space of the mechanical system. Then using Hamilton's principle, the mechanical BVP is described by the optimization problem

**Problem 1.** ***Mechanical BVP in minimal coordinates (MBVPM)***
*Find the extremal curve $\gamma : I \to \mathbb{P}$ given by the action integral*

$$S^M(q) = \int_{t_0}^{t_f} L(q,\dot{q})\, \mathrm{d}t \tag{1}$$

Using Livens principle, see [3], [4], one may also set the equivalent problem to (1) by

**Problem 2.** ***Extended mechanical BVP in minimal coordinates (MBVPML)***
*Find the extremal curve $\gamma : I \to \mathbb{P}$ given by the action integral*

$$S^M(q,v,p) = \int_{t_0}^{t_f} L(q,v) - p_a(v^a - \dot{q}^a)\, \mathrm{d}t \tag{2}$$

with $v \in \mathscr{TM}$ and and $p \in \mathscr{T}^*\mathscr{M}$.

Taking the variation of (2) yields

$$\delta S^M(q,v,p) = \int_{t_0}^{t_f} (\frac{\partial L(q,v)}{\partial v^a} - p_a)\delta v^a + (\frac{\partial L(q,v)}{\partial q^a})\delta q^a + (\dot{q}^a - v^a)\delta p_a + p_a \delta \dot{q}^a \,\mathrm{d}t \tag{3}$$

Applying the integration by parts

$$\int_{t_0}^{t_f} p_a \delta \dot{q}^a \,\mathrm{d}t = [p_a \delta q^a]_{t_0}^{t_f} - \int_{t_0}^{t_f} \dot{p}_a \delta q^a \,\mathrm{d}t \tag{4}$$

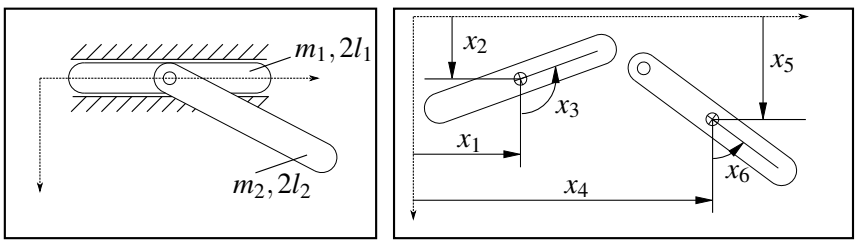


**Figure 1**. Multibody system of a physical pendulum on a moving slide taken from [1].

https://doi.org/10.3311/ECCOMASMBD2021-130

and inserting the Legendre transformation resulting from the variation $\delta v^a$, which yield the Legendre transformed function $H^M : \mathscr{T}^*M \to \mathbb{R}$ of the Lagrangian,

$$H^M = \frac{1}{2} p_a g^{ab} p_b + V(q) \tag{5}$$

finally yields

$$\delta S^M(q,p) = \int_{t_0}^{t_f} (-\dot{p}_a - \frac{\partial H^M(q,p)}{\partial q^a}) \delta q^a + (\dot{q}^a - \frac{\partial H^M(q,p)}{\partial p_a}) \delta p_a \, \mathrm{d}t + [p_a \delta q^a]_{t_0}^{t_f} \tag{6}$$

Now, imposing the stationary condition $\delta S^M(q,p) = 0$, one obtains the necessary optimality conditions

$$\begin{aligned} \dot{q}^a &= \frac{\partial H^M(q,p)}{\partial p_a} \\ \dot{p}_a &= -\frac{\partial H^M(q,p)}{\partial q^a} \end{aligned} \tag{7}$$

along with the boundary conditions

$$0 = [p_a \delta q^a]_{t_0}^{t_f} \tag{8}$$

Note that, at this stage, we do not impose the common end-point conditions on $\delta q^a$, but rather keep the boundary conditions leading to a BVP comprised of (7) and (8).

### 2.2 The mechanical BVP in redundant coordinates

Let $x : I \to \mathscr{M}$ be the description of the mechanical system in redundant coordinates and thus $\mathscr{M} := \{x \in \mathbb{R}^6 | g^r(x) = 0\}$. Then the Lagrangian in redundant coordinates may be defined by

$$\hat{L}(x,y) = T(x,\dot{x}) - V(x) - y_r g^r(x) = \frac{1}{2} \dot{x}^i \hat{g}_{ia} \dot{x}^j - V(x) - y_r g^r(x) \tag{9}$$

In analogy to the last section we obtain

**Problem 3.** ***Extended mechanical BVP in redundant coordinates (MBVPRL)***
*Find the extremal curve $\gamma : I \to \mathbb{P}$ given by the action integral*

$$S^M(x,\hat{v},\hat{p},y) = \int_{t_0}^{t_f} \hat{L}(x,\hat{v},y) - \hat{p}_i(\hat{v}^i - \dot{x}^i) \, \mathrm{d}t \tag{10}$$

Following the steps which led to (3) - (6), we obtain

$$\delta S^M(x,\hat{p},y) = \int_{t_0}^{t_f} (\frac{\partial \hat{H}(x,\hat{p},y)}{\partial x^i} - \dot{\hat{p}}_i) \delta x^i + (\dot{x}^i - \frac{\partial \hat{H}(x,\hat{p},y)}{\partial \hat{p}_i}) \delta \hat{p}_i + g^r(x) \delta y_r \, \mathrm{d}t + \left[\hat{p}_i \delta x^i\right]_{t_0}^{t_f} \tag{11}$$

where the Hamiltonian $\hat{H}^M$ in redundant coordinates is given by

$$\hat{H}^M(x,\hat{p},y) = \hat{p}_i \hat{g}^{ij} \hat{p}_j + V(x) + y_r g^r(x) \tag{12}$$

Thus, the mechanical BVP in redundant coordinates is described by the necessary optimality conditions

$$\begin{aligned} \dot{x}^i &= \frac{\partial \hat{H}^M(x,\hat{p},y)}{\partial p_i} \\ \dot{\hat{p}}_i &= -\frac{\partial \hat{H}^M(x,\hat{p},y)}{\partial x^i} \\ 0 &= \frac{\partial \hat{H}^M(x,\hat{p},y)}{\partial y_r} \end{aligned} \tag{13}$$

https://doi.org/10.3311/ECCOMASMBD2021-130

along with the boundary conditions

$$0 = \left[\hat{p}_i \delta x^i\right]_{t_0}^{t_f} \tag{14}$$

However, due to the constraints $g^r(x) = 0$ associated with $(13)_3$, the variations $\delta x$ are not independent and shall be further investigated with respect to the boundary conditions. Since (13) gives rise to index-3 DAEs, see [5], it is well known, that the implicit definition of $y_r$ is given by

$$\frac{\mathrm{d}^2}{\mathrm{d}t^2}(g^r(x)) = G^r(x,p,y) \tag{15}$$

However, since either $x^i$ or $p_i$ is properly defined on the boundary, $y_r$ is in general unknown on the boundaries, until the solution is known. Thus $g^r(x(t)) = 0$ holds on the boundaries, which reduces the independent redundant coordinates to $a$ and thus only $a$ boundary conditions may be defined with respect to the variation of $x$ on the boundaries. To answer the question of properly set admissible boundaries, it is helpful to decompose the redundant coordinates into their normal and tangential parts. This is to happen in the following section.

### 2.2.1 Decomposed vector spaces

Let $\mathscr{B}_{\hat{V}_p}$ and $\mathscr{B}_{\hat{V}_p^*}$ be the bases of the local vector spaces $\hat{V}_p$ and $\hat{V}_p^*$ at point $p$ on $\mathscr{M}$ in redundant coordinates. Let further $\mathscr{B}_{\mathscr{T}_p\mathscr{M}}$ and $\mathscr{B}_{\mathscr{T}_p^*\mathscr{M}}$ be the bases of the tangential spaces $\mathscr{T}_p\mathscr{M}$ and $\mathscr{T}_p^*\mathscr{M}$, and $\mathscr{B}_{\mathscr{N}_p\mathscr{M}}$ and $\mathscr{B}_{\mathscr{N}_p^*\mathscr{M}}$ be the bases of the normal spaces $\mathscr{N}_p\mathscr{M}$ and $\mathscr{N}_p^*\mathscr{M}$ at $p$. Now let's assume, the mapping $n^r(x) = \text{const.}$ exists and thus $g^r(n^s(x)) = 0$ holds. Since the constraints $g^r(x)$ are known in redundant coordinates, following [1] , see also [6], [7] and [8], a straight forward calculation yields the metric tensors associated with the normal and tangential spaces, $(\hat{g}_{rs}, \hat{g}^{rs})$, and $(g_{ab}, g^{ab})$, respectively, along with the Jacobians

$$\frac{\partial x^i}{\partial n^r} : \hat{V}_p \to \mathscr{N}_p\mathscr{M}, \quad \frac{\partial n^r}{\partial x^i} : \hat{V}_p^* \to \mathscr{N} *_p \mathscr{M}, \tag{16}$$

$$\frac{\partial x^i}{\partial q^a} : \hat{V}_p \to \mathscr{T}_p\mathscr{M}, \quad \frac{\partial q^a}{\partial x^i} : \hat{V}_p^* \to \mathscr{T} *_p \mathscr{M}, \tag{17}$$

Now let the bases of the decomposed local vector space $V_p := \mathscr{N}_p\mathscr{M} \cup \mathscr{T}_p\mathscr{M}$ and its dual space $V_p^* := \mathscr{N} *_p \mathscr{M} \cup \mathscr{T} *_p \mathscr{M}$ be defined by $\mathscr{B}_{V_p}$ and $\mathscr{B}_{V_p^*}$, whereat by definition

$$\mathscr{B}_{\mathscr{T}_p\mathscr{M}} \perp \mathscr{B}_{\mathscr{N}_p\mathscr{M}}, \qquad \mathscr{B}_{\mathscr{T}_p^*\mathscr{M}} \perp \mathscr{B}_{\mathscr{N}_p^*\mathscr{M}} \tag{18}$$

holds. This leads to the mappings

$$\frac{\partial x^j}{\partial z^i} : \hat{V}_p \to \mathscr{N}_p\mathscr{M} \cup \mathscr{T}_p\mathscr{M} \tag{19}$$

$$\frac{\partial z^j}{\partial x^i} : \hat{V}_p^* \to \mathscr{N} *_p \mathscr{M} \cup \mathscr{T} *_p \mathscr{M} \tag{20}$$

where the coordinates $z^i = \{n^r, q^a\}$ and momenta $p_i = \{p_r, p_a\}$ have been introduced.

**Remark.** ***Velocity components in normal directions***
*Since*

$$\frac{\mathrm{d}g^r(x)}{\mathrm{d}t} = \frac{\partial g^r(x)}{\partial n^s}\dot{n}^s = 0 \tag{21}$$

*and* $\frac{\partial g^r(x)}{\partial n^s} \neq 0$ *in general, it can be seen that* $\dot{n}^s = 0$ *holds.*

https://doi.org/10.3311/ECCOMASMBD2021-130

### 2.2.2 The boundary conditions in redundant coordinates

Using the relationships

$$\delta x^i = \frac{\partial x^i}{\partial z^j}\delta z^j = \frac{\partial x^i}{\partial n^r}\delta n^r + \frac{\partial x^i}{\partial q^a}\delta q^a \tag{22}$$

$$\hat{p}_i = \frac{\partial z^j}{\partial x^i}p_j = \frac{\partial n^r}{\partial x^i}p_r + \frac{\partial q^a}{\partial x^i}p_a \tag{23}$$

inserting them into (11) and making use of $\dot{n}^r = p_r = 0$ leads to the necessary optimality conditions in decomposed coordinates given by

$$\dot{q}^a = \frac{\partial H^M(q,n,p)}{\partial p_a} \tag{24a}$$

$$0 = -\frac{1}{2}p_a\frac{\partial g^{ab}}{\partial n^r}p_b - \frac{\partial V}{\partial n^r} - y_r \tag{24b}$$

$$\dot{p}_a = -\frac{\partial H^M(q,n,p)}{\partial q^a} \tag{24c}$$

$$0 = g^r(x) \tag{24d}$$

with the Hamiltonian being defined by (5). For the boundary conditions follow

$$\begin{aligned} 0 &= \left[p_i\frac{\partial x^i}{\partial n^r}\delta n^r\right]_{t_0}^{t_f} + \left[p_i\frac{\partial x^i}{\partial q^a}\delta q^a\right]_{t_0}^{t_f} \\ &= [p_r\delta n^r]_{t_0}^{t_f} + [p_a\delta q^a]_{t_0}^{t_f} \\ &= [p_a\delta q^a]_{t_0}^{t_f} \end{aligned} \tag{25}$$

since $p_r = 0$ everywhere.

**Remark.** ***The implicit definitions of*** $y_r$
*It can be seen from* (24b) *that r ODEs in redundant coordinates correspond to the implicit definition of* $y_r$.

**Remark.** ***The duality of the derivative of the constraints and the variation for*** $\delta n^r$
*A straight forward calculation yields*

$$\frac{\mathrm{d}^2}{\mathrm{d}t^2}(g^r(x)) = G^r(x,\hat{p},y) = g^{rs}G_s(q,n,p,y) \tag{26}$$

*with*

$$G_r(q,n,p,y) = -\frac{1}{2}p_a\frac{\partial g^{ab}}{\partial n^r}p_b - \frac{\partial V}{\partial n^r} - y_r \tag{27}$$

Writing (25) in terms of redundant coordinates finally yields the proper BVP in redundant coordinates, defined by the necessary optimality conditions (13) and the boundary conditions

$$0 = \left[\hat{p}_i\frac{\partial x^i}{\partial q^a}\delta q^a\right]_{t_0}^{t_f} \tag{28}$$

**Remark.** ***Setting boundary conditions by using Lagrangian multipliers***
*The natural boundary conditions* (28) *may also be augmented with suitable end-point conditions by using Lagrangian multipliers in the action integral. For example, this leads to*

$$S^M(\cdot) = \int_{t_0}^{t_f} L(q,\dot{q})\,\mathrm{d}t + \mu_a^0(q^a(t_0) - \bar{q}_0^a) + \mu_a^N(q^a(t_f) - \bar{q}_N^a) \tag{29}$$

*and*

$$S^M(\cdot) = \int_{t_0}^{t_f} L(x,\dot{x},y)\,\mathrm{d}t + \mu_a^0\frac{\partial q^a}{\partial x^i}(x^i(t_0) - \bar{x}_0^i) + \mu_a^N\frac{\partial q^a}{\partial x^i}(x^i(t_f) - \bar{x}_N^i) \tag{30}$$

*where* $\bar{q}_0^a, \bar{q}_N^a$ *and* $\bar{x}_0^i, \bar{x}_N^i$*, respectively, are prescribed coordinates.*

https://doi.org/10.3311/ECCOMASMBD2021-130

### 2.3 Numerical example of the mechanical BVP

In the following, the BVP of the mechanical system depicted in Fig. 1 is solved in minimal coordinates and redundant coordinates to show the equivalence of the BVPs numerically. As can be observed from Fig. 1, the constraints are specified by

$$g^1(x) = x^2 \tag{31a}$$
$$g^2(x) = x^3 \tag{31b}$$
$$g^3(x) = x^1 - x^4 + l_2 \sin(x^6) \tag{31c}$$
$$g^4(x) = x^2 - x^5 + l_2 \cos(x^6) \tag{31d}$$

Let the potential energy in redundant and minimal coordinates be defined by

$$V(x) = -m_1 g x^2 - m_2 g x^5, \qquad V(q) = -m_2 g l_2 \cos(q^2) \tag{32}$$

with $g$ being the gravitational constant. Let further the kinetic energy be given by

$$T(x,p) = \frac{1}{2} p^i \hat{g}_{ij} p^j, \qquad T(q,n,p) = \frac{1}{2} p^a g_{ab} p^b \tag{33}$$

with the metric tensors

$$\hat{g}_{ij} = \hat{\mathbf{M}} = \begin{bmatrix} m_1 & 0 & 0 & 0 & 0 & 0 \\ 0 & m_1 & 0 & 0 & 0 & 0 \\ 0 & 0 & \frac{m_1(2l_1)^2}{12} & 0 & 0 & 0 \\ 0 & 0 & 0 & m_2 & 0 & 0 \\ 0 & 0 & 0 & 0 & m_2 & 0 \\ 0 & 0 & 0 & 0 & 0 & \frac{m_2(2l_2)^2}{12} \end{bmatrix} \tag{34}$$

and

$$g_{ab} = \mathbf{M} = \begin{bmatrix} m_1 + m_2 & m_2 l_2 \cos(q^2) \\ m_2 l_2 \cos(q^2) & \frac{4}{3} m_2 l_2^2 \end{bmatrix} \tag{35}$$

Applying the midpoint rule to the differential part, with step size $h = t_{n+1} - t_n$, finally yields the discrete necessary optimality conditions in redundant coordinates as

$$\begin{aligned} x_{n+1}^i - x_n^i &= h \frac{\partial H^M}{\partial \hat{p}_i^{n+\frac{1}{2}}}; & n &= \{0,1,...,N-1\} \\ \hat{p}_i^{n+1} - \hat{p}_i^n &= -h \frac{\partial H^M}{\partial x^i_{n+\frac{1}{2}}}; & n &= \{0,1,...,N-1\} \\ 0 &= g^r(x_n); & n &= \{0,1,...,N\} \end{aligned} \tag{36}$$

along with the boundary conditions

$$\begin{aligned} \tfrac{\partial q_0^a}{\partial x_0^i}(x_0^i - \bar{x}_0^i)\delta\mu_a^0 &= 0; & \tfrac{\partial q_N^a}{\partial x_N^i}(x_N^i - \bar{x}_N^i)\delta\mu_a^N &= 0 \\ (\tfrac{\partial x_0^i}{\partial q_0^a}\hat{p}_i^0 - \mu_a^0)\delta q_0^a &= 0; & (\tfrac{\partial x_N^i}{\partial q_N^a}\hat{p}_i^N - \mu_a^N)\delta q_N^a &= 0 \end{aligned} \tag{37}$$

Since the implicit definition of $y_r$ can't be done properly on the boundary by the discrete system of ODEs, the implicit definitions are enforced by making use of (15). Thus, the additional boundary conditions

$$G^r(x_0, \hat{p}_0, y_0) = 0; \qquad G^r(x_N, \hat{p}_N, y_N) = 0 \tag{38}$$

https://doi.org/10.3311/ECCOMASMBD2021-130

| | | |
|---|---|---|
| $\bar{x}(t_0)$ | = | $[0,\ 0,\ 0,\ 1,\ 0,\ \frac{\pi}{2}]^T$ |
| $\bar{x}(t_f)$ | = | $[0,\ 0,\ 0,\ -1,\ 0,\ -\frac{\pi}{2}]^T$ |
| $(m_1, m_2)$ | = | $(1,1)$ |
| $(l_1, l_2)$ | = | $(1,1)$ |
| $T$ | = | 1.8 |
| $N$ | = | 100 |

**Table 1**. Specified boundary conditions as well as physical and geometric parameters of the mechanical system.

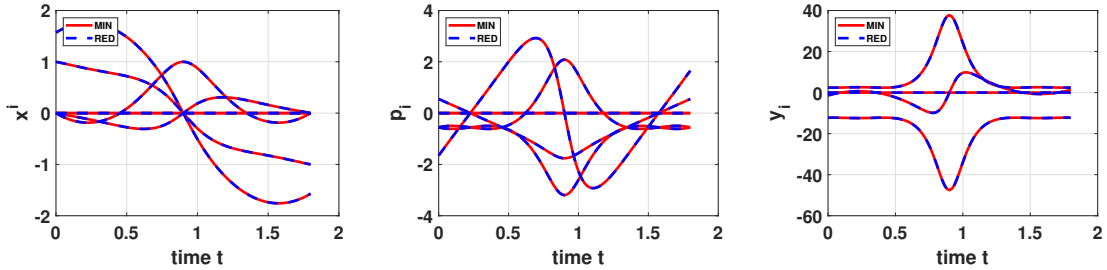


**Figure 2**. Solutions of the mechanical boundary value problem defined by Table 1. Here the positions (left) and momenta (center) are shown in redundant coordinates. The dual quantities $y_r$ in minimal coordinates are calculated by making use of (24b)

are enforced which ensure the definition of $y_r$ on the boundaries.

For the discrete necessary optimality conditions in minimal coordinates follows

$$\begin{aligned} q_{n+1}^a - q_n^a &= h \frac{\partial H^M}{\partial p_a^{n+\frac{1}{2}}}; & n &= \{0,1,...,N-1\} \\ p_a^{n+1} - p_a^n &= -h \frac{\partial H^M}{\partial q_{n+\frac{1}{2}}^a}; & n &= \{0,1,...,N-1\} \end{aligned} \tag{39}$$

along with the boundary conditions

$$\begin{aligned} (q_0^a - \bar{q}_0^a)\delta\mu_a^0 &= 0; & (q_N^a - \bar{q}_N^a)\delta\mu_a^N &= 0 \\ (p_a^0 - \mu_a^0)\delta q_0^a &= 0; & (p_a^N - \mu_a^N)\delta q_N^a &= 0 \end{aligned} \tag{40}$$

The boundary conditions chosen for the example, the length and mass of the slide and the pendulum as well as the length of the time interval $I \in [0,\ T]$ and the number of discrete time intervals, $N$, is shown in Table 1

Comparing the solutions depicted in Fig. 2, it can be seen that the BVPs are indeed equivalent.

Fig. 3 also shows a sequence of the solution of the mechanical boundary value problem.

## 3 OPTIMAL CONTROL OF CONSTRAINED MECHANICAL SYSTEMS USING REDUNDANT COORDINATES

In this section the BVP arising from the optimal control problem shall be treated by using redundant coordinates. Therefore, the well known optimal control problem in minimal coordinates will be discussed briefly to show the close connection between the Lagrange formalism in the mechanical BVP and the optimal control problem. Afterwards the necessary optimality conditions for the optimal control problem in redundant coordinates proofed in [9] shall be viewed. The boundary

https://doi.org/10.3311/ECCOMASMBD2021-130

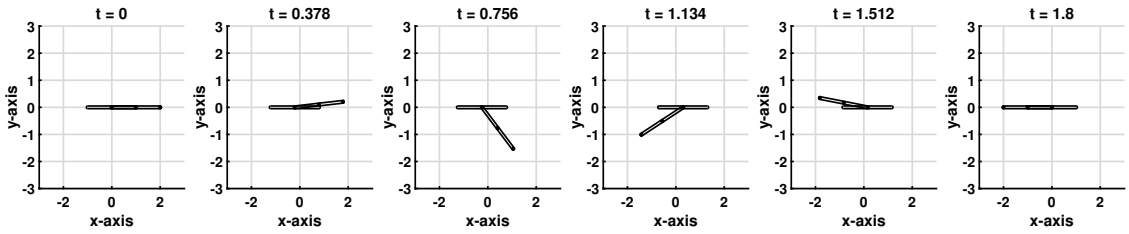


**Figure 3**. Snapshots of the motion resulting from the BVP with data given in Table 1.

conditions for the redundant coordinates will be described and finally the equivalence between the BVPs in terms of redundant and minimal coordinates will be shown with a numerical example.

### 3.1 The optimal control BVP in minimal coordinates

Let the controlled equations of motion be defined by (7) together with the control forces $u : I \to \mathbb{R}^2$ and thus

$$\dot{q}^i = \frac{\partial H^M}{\partial p_a}, \qquad \dot{p}_a = -\frac{\partial H^M}{\partial q^a} + u_a \tag{41}$$

Then the standard optimal control problem reads

**Problem 4.** ***Optimal control problem in minimal coordinates (OCBVPM)***
*Minimize*

$$\mathbb{S}^{OC}(q,p,u) = \int_{t_0}^{t_f} C(q,p,u)\,\mathrm{d}t \tag{42}$$

*subject to*

$$\begin{aligned} \dot{q}^a &= \frac{\partial H^M}{\partial p_a} \\ \dot{p}_a &= -\frac{\partial H^M}{\partial q^a} + u_a \end{aligned} \tag{43}$$

Augmenting the objective function of the optimization problem with the dynamic constraints (43) yields

**Problem 5.** ***Augmented optimization problem in minimal coordinates (OCBVPML)***
*Extremize*

$$\mathbb{S}^{OC}(q,p,u,\lambda^q,\lambda_p) = \int_{t_0}^{t_f} C(q,p,u) + \lambda_a^q \left(\dot{q}^a - \frac{\partial H^M}{\partial p_a}\right) + \lambda_p^a \left(\dot{p}_a - (-\frac{\partial H^M}{\partial q^a} + u_a)\right)\,\mathrm{d}t \tag{44}$$

$$= \int_{t_0}^{t_f} \lambda_a^q \dot{q}^a + \lambda_p^a \dot{p}_a - \mathbb{H}^{OC}(\cdot)\,\mathrm{d}t \tag{45}$$

Here, the Hamiltonian of the optimal control problem

$$\mathbb{H}^{OC}(q,p,u,\lambda^q,\lambda_p) = \lambda_a^q \frac{\partial H^M}{\partial p_a} + \lambda_p^a(-\frac{\partial H^M}{\partial q^a} + u_a) - C(q,p,u) \tag{46}$$

https://doi.org/10.3311/ECCOMASMBD2021-130

hast been introduced, see e.g. [8], [10] , [11]. Following the Lagrangian formalism by taking the variation and then applying integration by parts for the terms $\lambda_i^q \delta \dot{x}^i$ and $\lambda_p^a \delta \dot{p}_a$ finally yields

$$\begin{aligned}\delta \mathbb{S}^{OC}(q,p,u,\lambda^q,\lambda_p) = \int_{t_0}^{t_f} & \delta\lambda_a^q \left( \dot{q}^a - \frac{\partial \mathbb{H}^{OC}(\cdot)}{\partial \lambda_a^q} \right) + \delta\lambda_p^a \left( \dot{p}_a - \frac{\partial \mathbb{H}^{OC}(\cdot)}{\partial \lambda_p^a} \right) \\ & + \delta q^a (-\dot{\lambda}_a^q - \frac{\partial \mathbb{H}^{OC}(\cdot)}{\partial q^a}) + \delta p_a (-\dot{\lambda}_p^a - \frac{\partial \mathbb{H}^{OC}(\cdot)}{\partial p_a}) + \delta u_a \frac{\partial \mathbb{H}^{OC}(\cdot)}{\partial u_a} \, \mathrm{d}t \\ & + [\lambda_a^q \delta q^a]_{t_0}^{t_f} + \left[\lambda_p^a \delta p_a\right]_{t_0}^{t_f}\end{aligned} \tag{47}$$

Thus, the necessary optimality conditions using minimal coordinates yield

$$\begin{aligned} \dot{q}^a &= \frac{\partial \mathbb{H}^{OC}(\cdot)}{\partial \lambda_a^q}, & \dot{\lambda}_a^q &= -\frac{\partial \mathbb{H}^{OC}(\cdot)}{\partial q^a} \\ \dot{p}_a &= \frac{\partial \mathbb{H}^{OC}(\cdot)}{\partial \lambda_p^a}, & \dot{\lambda}_p^a &= -\frac{\partial \mathbb{H}^{OC}(\cdot)}{\partial p_a} \\ 0 &= \frac{\partial \mathbb{H}^{OC}(\cdot)}{\partial u_a} \end{aligned} \tag{48}$$

along with the boundary conditions

$$0 = [\lambda_a^q \delta q^a]_{t_0}^{t_f}, \qquad 0 = \left[\lambda_p^a \delta p_a\right]_{t_0}^{t_f} \tag{49}$$

### 3.2 The necessary optimality conditions in redundant coordinates

Using redundant coordinates for the controlled equations of motion, the optimal control problem under investigation is given by

**Problem 6.** ***Optimal control problem in redundant coordinates (OCBVPR)***
*Minimize*

$$\hat{\mathbb{S}}^{OC}(x,\hat{p},y,\hat{u}) = \int_{t_0}^{t_f} C(x,\hat{p},y,\hat{u}) \, \mathrm{d}t \tag{50}$$

*subject to*

$$\begin{aligned} \dot{x}^i &= \frac{\partial \hat{H}^M}{\partial \hat{p}_i} \\ \dot{\hat{p}}_i &= -\frac{\partial \hat{H}^M}{\partial x^i} + \hat{u}_i \\ 0 &= g^r(x) \end{aligned} \tag{51}$$

with $\hat{u} : I \to \mathbb{R}^6$. Again augmenting the objective function with the dynamic constraints (51) yields

$$\begin{aligned} \bar{\mathbb{S}}^{OC}(x,\hat{p},y,\hat{u},\hat{\lambda}^q,\hat{\lambda}_p,\eta) &= \int_{t_0}^{t_f} C(x,\hat{p},y,u) + \hat{\lambda}_i^q (\dot{x}^i - \frac{\partial \hat{H}^M}{\partial \hat{p}_i}) + \hat{\lambda}_p^i (\dot{\hat{p}}_i - (-\frac{\partial \hat{H}^M}{\partial x^i} + \hat{u}_i)) + \eta_r g^r(x) \, \mathrm{d}t \\ &= \int_{t_0}^{t_f} \hat{\lambda}_i^q \dot{q}^i + \hat{\lambda}_q^i \dot{\hat{p}}_i - \bar{\mathbb{H}}^{OC}(x,\hat{p},y,\hat{u},\hat{\lambda}^q,\hat{\lambda}_p,\eta) \, \mathrm{d}t \end{aligned} \tag{52}$$

with

$$\bar{\mathbb{H}}^{OC}(x,\hat{p},y,\hat{u},\hat{\lambda}^q,\hat{\lambda}_p,\eta) = \hat{\lambda}_i^q \frac{\partial \hat{H}^M}{\partial \hat{p}_i} + \hat{\lambda}_p^i (-\frac{\partial \hat{H}^M}{\partial x^i} + \hat{u}_i) - \eta_r g^r(x) - C(x,\hat{p},y,u) \tag{53}$$

https://doi.org/10.3311/ECCOMASMBD2021-130

One might now again demand

$$\delta\bar{\mathbb{S}}^{OC}(x,\hat{p},y,\hat{u},\hat{\lambda}^q,\hat{\lambda}_p,\eta)=0$$

to get the necessary optimality conditions. However, it is proofed in [9] (see also [10]), that this approach is not feasible. Instead, following [9], the proper necessary optimality conditions for the optimal control problem in redundant coordinates are given by

$$\begin{aligned}
\dot{x}^i &= \frac{\partial\hat{\mathbb{H}}^{OC}(\cdot)}{\partial\hat{\lambda}_i^q}, & \dot{\hat{\lambda}}_i^q &= -\frac{\partial\hat{\mathbb{H}}^{OC}(\cdot)}{\partial x^i}\\
\dot{\hat{p}}_i &= \frac{\partial\hat{\mathbb{H}}^{OC}(\cdot)}{\partial\hat{\lambda}_p^i}, & \dot{\hat{\lambda}}_p^i &= -\frac{\partial\hat{\mathbb{H}}^{OC}(\cdot)}{\partial\hat{p}_i}\\
0 &= g^r(x), & 0 &= \frac{\partial\hat{\mathbb{H}}^{OC}(\cdot)}{\partial y_r}\\
0 &= \frac{\partial\hat{\mathbb{H}}^{OC}(\cdot)}{\partial\hat{u}_i}
\end{aligned} \tag{54}$$

with the Hamiltonian being

$$\hat{\mathbb{H}}^{OC}(x,\hat{p},y,\hat{u},\hat{\lambda}^q,\hat{\lambda}_p,\eta)=\hat{\lambda}_i^q\frac{\partial H^M}{\partial\hat{p}_i}+\hat{\lambda}_p^i(-\frac{\partial H^M}{\partial x^i}+\hat{u}_i)-\eta_r G^r(x,\hat{p},y,\hat{u})-C(x,\hat{p},y,\hat{u}) \tag{55}$$

whereat $G^r(x,\hat{p},y,\hat{u})$ corresponds to the implicit definition of the dual normal quantity $y_r$. For index-3 DAEs one has

$$G^r(x,\hat{p},y,\hat{u})=\frac{\mathrm{d}^2 g^r(x)}{\mathrm{d}t^2} \tag{56}$$

### 3.3 The optimal control problem in redundant coordinates

Even though the proper necessary optimality conditions in redundant coordinates are given by [9] (see also [10]), the treatment of the boundary conditions for (OCBVPR) still demands further elaboration. Comparing (53) and (55), it can be seen that the natural boundary conditions nevertheless arise from integration by parts:

$$\int_{t_0}^{t_f}\hat{\lambda}_i^q\delta\dot{x}^i\,\mathrm{d}t=\left[\hat{\lambda}_i^q\delta x^i\right]_{t_0}^{t_f}-\int_{t_0}^{t_f}\dot{\hat{\lambda}}_i^q\delta x^i\,\mathrm{d}t \tag{57}$$

$$\int_{t_0}^{t_f}\hat{\lambda}_p^i\delta\dot{\hat{p}}_i\,\mathrm{d}t=\left[\hat{\lambda}_p^i\delta p_i\right]_{t_0}^{t_f}-\int_{t_0}^{t_f}\dot{\hat{\lambda}}_p^i\delta\hat{p}_i\,\mathrm{d}t \tag{58}$$

and thus the proper optimal control BVP is initially given by the necessary optimalty conditions (54) along with the boundary conditions

$$\left[\hat{\lambda}_i^q\delta x^i\right]_{t_0}^{t_f}=0 \qquad\qquad \left[\hat{\lambda}_p^i\delta\hat{p}_i\right]_{t_0}^{t_f}=0 \tag{59}$$

However, since $p_r=0$ and $n^r(x)=\text{const.}$ has to hold everywhere and especially on the boundaries, the corresponding variations have to vanish. Making use of (19) and (20), the boundary conditions in redundant coordinates reduce to

$$0=\left[\hat{\lambda}_i^q(\frac{\partial x^i}{\partial n^r}\delta n^r+\frac{\partial x^i}{\partial q^a}\delta q^a)\right]_{t_0}^{t_f}=[\lambda_r^q\delta n^r+\lambda_a^q\delta q^a]_{t_0}^{t_f}=[\lambda_a^q\delta q^a]_{t_0}^{t_f} \tag{60}$$

$$0=\left[\hat{\lambda}_p^i(\frac{\partial n^r}{\partial x^i}\delta p_r+\frac{\partial q^a}{\partial x^i}\delta p_a)\right]_{t_0}^{t_f}=\left[\lambda_p^r\delta p_r+\lambda_p^a\delta p_a\right]_{t_0}^{t_f}=\left[\lambda_p^a\delta p_a\right]_{t_0}^{t_f} \tag{61}$$

Accordingly, the proposed form of the optimal control BVP in redundant coordinates is given by the necessary optimality conditions (54) together with the boundary conditions

$$0=\left[\hat{\lambda}_i^q\frac{\partial x^i}{\partial q^a}\delta q^a\right]_{t_0}^{t_f} \qquad\qquad 0=\left[\lambda_p^i\frac{\partial q^a}{\partial x^i}\delta p_a\right]_{t_0}^{t_f} \tag{62}$$

https://doi.org/10.3311/ECCOMASMBD2021-130

### 3.4 Numerical example of the optimal control BVP

Let the cost functionals be defined by

$$C(x,\hat{p},y,\hat{u}) = \frac{1}{2}\hat{u}_i\hat{g}^{ij}\hat{u}_j, \qquad C(q,p,u) = \frac{1}{2}u_a g^{ij}u_a$$

with the metric tensors given by

$$\hat{g}^{ij} = \hat{\mathbf{M}}^{-1}, \qquad g^{ab} = \mathbf{M}^{-1}$$

Using once more the midpoint rule for the discretization of the differential equations in the necessary optimality conditions in term of redundant coordinates yields

$$\begin{array}{rcll}
x^i_{n+1} - x^i_n & = & h\frac{\partial \hat{\mathbb{H}}^{OC}}{\partial \hat{\lambda}_i^{q,n+\frac{1}{2}}}; & n = \{0,1,...,N-1\} \\
p_i^{n+1} - p_i^n & = & h\frac{\partial \hat{\mathbb{H}}^{OC}}{\partial \hat{\lambda}^i_{p,n+\frac{1}{2}}}; & n = \{0,1,...,N-1\} \\
\hat{\lambda}_i^{q,n+1} - \hat{\lambda}_i^{q,n} & = & h(-\frac{\partial \hat{\mathbb{H}}^{OC}}{\partial x^i_{n+\frac{1}{2}}}); & n = \{0,1,...,N-1\} \\
\hat{\lambda}^{\,i}_{p,n+1} - \hat{\lambda}^{\,i}_{p,n} & = & h(-\frac{\partial \hat{\mathbb{H}}^{OC}}{\partial \hat{p}_i^{\,n+\frac{1}{2}}}); & n = \{0,1,...,N-1\} \\
0 & = & g^r(x^i_n); & n = \{0,1,...,N\} \\
0 & = & \frac{\partial \hat{\mathbb{H}}^{OC}(\cdot)}{\partial y^n_r}; & n = \{0,1,...,N\} \\
0 & = & \frac{\partial \hat{\mathbb{H}}^{OC}(\cdot)}{\partial \hat{u}^n_i}; & n = \{0,1,...,N\}
\end{array} \tag{63}$$

As already done in the context of the mechanical BVP, the boundary conditions may also be enforced by Lagranian multipliers. Consequently, we get

$$\begin{array}{rclrcl}
\frac{\partial q^a_0}{\partial x^i_0}(x^i_0 - \bar{x}^i_0)\delta\mu^0_a & = & 0; & \frac{\partial q^a_N}{\partial x^i_N}(x^i_N - \bar{x}^i_N)\delta\mu^N_a & = & 0 \\
\frac{\partial x^i_0}{\partial q^a_0}(p^0_i - \bar{p}^0_i)\delta\nu^a_0 & = & 0; & \frac{\partial x^i_N}{\partial q^a_N}(p^N_i - \bar{p}^N_i)\delta\nu^a_N & = & 0 \\
(\frac{\partial x^i_0}{\partial q^a_0}\lambda^{q,0}_i - \mu^0_a)\delta q^a_0 & = & 0; & (\frac{\partial x^i_N}{\partial q^a_N}\lambda^{q,N}_i - \mu^N_a)\delta q^a_N & = & 0 \\
(\frac{\partial q^a_0}{\partial x^i_0}\lambda^i_{p,0} - \nu^a_0)\delta p^0_a & = & 0; & (\frac{\partial q^a_N}{\partial x^i_N}\lambda^i_{p,N} - \nu^a_N)\delta p^N_a & = & 0
\end{array} \tag{64}$$

together with the implicit definition of the dual quantities $y_r$ on the boundaries already known from the mechanical BVP given by (56).

In minimal coordinates, the discrete necessary optimality condition simplify to

$$\begin{array}{rcll}
q^a_{n+1} - q^a_n & = & h\frac{\partial \mathbb{H}^{OC}}{\partial \lambda_a^{q,n+\frac{1}{2}}}; & n = \{0,1,...,N-1\} \\
p_a^{n+1} - p_a^n & = & h\frac{\partial \mathbb{H}^{OC}}{\partial \lambda^a_{p,n+\frac{1}{2}}}; & n = \{0,1,...,N-1\} \\
\lambda_a^{q,n+1} - \lambda_a^{q,n} & = & h(-\frac{\partial \mathbb{H}^{OC}(\cdot)}{\partial q^a_{n+\frac{1}{2}}}); & n = \{0,1,...,N-1\} \\
\lambda^i_{p,n+1} - \lambda^i_{p,n} & = & h(-\frac{\partial \mathbb{H}^{OC}(\cdot)}{\partial p_i^{\,n+\frac{1}{2}}}); & n = \{0,1,...,N-1\} \\
0 & = & \frac{\partial \mathbb{H}^{OC}(\cdot)}{\partial u^n_a}; & n = \{0,1,...,N\}
\end{array} \tag{65}$$

along with the boundary conditions

$$\begin{array}{rclrcl}
(q^a_0 - \bar{q}^a_0)\delta\mu^0_a & = & 0; & (q^a_N - \bar{q}^a_N)\delta\mu^N_a & = & 0; \\
(p^0_a - \bar{p}^0_a)\delta\nu^a_0 & = & 0; & (p^N_a - \bar{p}^N_a)\delta\nu^a_N & = & 0; \\
(\lambda^{q,0}_a - \mu^0_a)\delta q^a_0 & = & 0; & (\lambda^{q,N}_a - \mu^N_a)\delta q^a_N & = & 0; \\
(\lambda^a_{p,0} - \nu^a_0)\delta p^0_a & = & 0; & (\lambda^a_{p,N} - \nu^a_N)\delta p^N_a & = & 0;
\end{array} \tag{66}$$

https://doi.org/10.3311/ECCOMASMBD2021-130

| | | |
|---|---|---|
| $\bar{x}(t_0)$ | $=$ | $[0,\ 0,\ 0,\ 0,\ 1,\ 0]^T$ |
| $\bar{p}(t_0)$ | $=$ | $[0,\ 0,\ 0,\ 0,\ 0,\ 0]^T$ |
| $\bar{x}(t_f)$ | $=$ | $[0,\ 0,\ 0,\ 0.7071,\ 0.7071,\ \frac{\pi}{4}]^T$ |
| $\bar{p}(t_f)$ | $=$ | $[0,\ 0,\ 0,\ 0,\ 0,\ 0]^T$ |
| $(m_1, m_2)$ | $=$ | $(1, 1)$ |
| $(l_1, l_2)$ | $=$ | $(1, 1)$ |
| $T$ | $=$ | $5$ |
| $N$ | $=$ | $100$ |

**Table 2**. Specified boundary conditions as well as physical and geometric parameters of the mechanical system in the optimal control problem

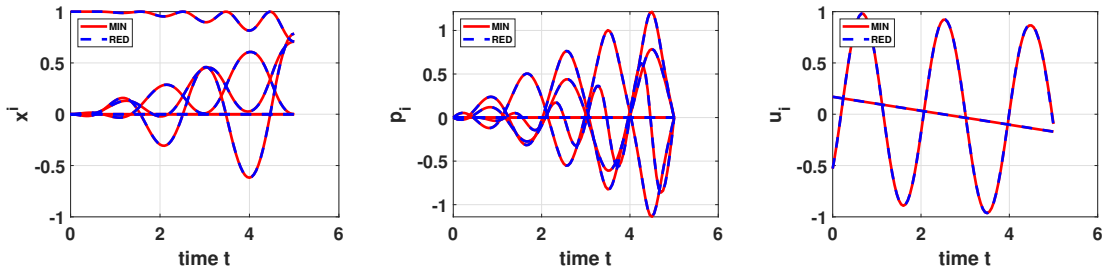


**Figure 4**. Solutions of the optimal control problem boundary value problem defined by Table 2. Here the positions (left) and momenta (center) are shown in redundant coordinates while the redundant controls (right) are shown in minimal coordinates.

The boundary conditions chosen for the optimal control example, the length and mass of the slide and the pendulum as well as the length of the time interval $I \in [0,\ T]$ and the number of discrete time intervals, $N$, is shown in Table 2.

Comparing the solutions depicted in Fig. 4, it can be seen that the two BVP under consideration are indeed equivalent.

Fig. 5 also shows a sequence of the solution of the optimal control boundary value problem.

## 4 CONCLUSION

In this paper, the boundary value problem of the optimal control problem in redundant coordinates was considered in more detail. Due to the mathematical similarity of the Lagrange formalism of classical mechanics and the optimal control problem, the first step was to consider the boundary

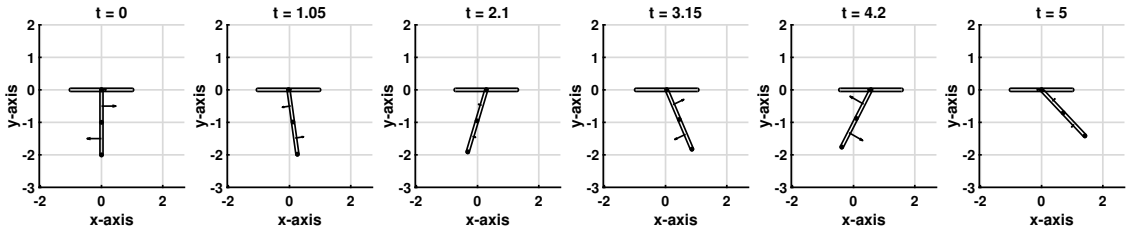


**Figure 5**. Sequence of the motion of the controlled mechanical system defined by the optimal control BVP with the data given in Table 2.

value problem in redundant coordinates in the simplified framework of classical mechanics. After the requirements on the variations on the boundary, which occur due to the algebraic constraints imposed on the redundant coordinates, were discussed on the mechanical level, the knowledge gained from this was transferred to the optimal control problem. Here, the challenging optimal control problem in redundant coordinates was first discussed and the correct necessary optimality conditions were referred to. Subsequently, with the help of the clear separation of the coordinates into normal and tangential parts, which was already known from the mechanical boundary value problem, the optimal control problem was formulated in redundant coordinates. Finally, it was verified by means of a numerical example that the optimal control problem formulated in both redundant and minimal coordinates leads to equivalent numerical results.

## ACKNOWLEDGEMENTS

This work was funded by the Deutsche Forschungsgemeinschaft (DFG, German Research Foundation) – project number 442997215. This support is gratefully acknowledged.

## REFERENCES

[1] Blajer, W.: An orthonormal tangent space method for constrained multibody systems. Comput. Methods Appl. Mech. Engrg. **121** (1995) 45–57

[2] Arnol'd, V.: Mathematical Methods of Classical Mechanics. Springer (1989) doi: 10.1007/978-1-4757-2063-1.

[3] Livens, G.: On Hamilton's principle and the modified function in analytical dynamics. Proceedings of the Royal Society Edinburgh **39(IX)** (1919) 113–119 doi: 10.1017/S0370164600018617.

[4] Bou-Rabee, N.: Hamilton-Pontryagin integrators on Lie groups. PhD thesis, California Insitute of Technology (2007)

[5] Gear, C.W. Leimkuhler, B., Gupta, G.: Automatic integration of Euler-Lagrange equations with constraints. Journal of Computational and Applied Mathematics **12-13** (1985) 77–90

[6] Betsch, P.: The discrete null space method for the energy consistent integration of constrained mechanical systems part I: Holonomic constraints. Comput. Methods Appl. Mech. Engrg. **194** (2005) 5159–5190

[7] Betsch, P., Leyendecker, S.: The discrete null space method for the energy consistent integration of constrained mechanical systems. part II: Multibody dynamics. Int. J. Numer. Meth. Engng **67** (2006) 499–552 doi: 10.1002/nme.1639.

[8] Ober-Blöbaum, S.: Discrete Mechanics and Optimal Control. PhD thesis, Paderborn (2008)

[9] Roubíček, T., Valášek, M.: Optimal control of causal differential–algebraic systems. J. Math. Anal. Appl. **269** (2002) 616–641

[10] Gerdts, M.: Optimal Control of ODEs and DAEs. De Gruyter, Berlin, Boston (2011) ISBN 978-3-11-024995-8.

[11] Betsch, P., Becker, C.: Conservation of generalized momentum maps in mechanical optimal control problems with symmetry. Int. J. Numer. Meth. Engng **111**(2) (2017) 144–175 doi: 10.1002/nme.5459.

# Section
# SLENDER STRUCTURES

https://doi.org/10.3311/ECCOMASMBD2021-226

ECCOMAS Thematic Conference on Multibody Dynamics
December 12 - 15, 2021, Budapest, Hungary

# One-Dimensional Modelling of Developable Elastic Strips by Geometric Constraints and their Link to Surface Isometry

**Benjamin Bauer**[1,2], **Michael Roller**[1], **Joachim Linn**[1], **Bernd Simeon**[2]

[1] Mathematics for the Digital Factory
Fraunhofer Institute for Industrial Mathematics (ITWM)
Fraunhofer Platz 1, 67663 Kaiserslautern, Germany
[benjamin.bauer, michael.roller, joachim.linn]@itwm.fraunhofer.de

[2] Felix-Klein-Zentrum for Mathematics
TU Kaiserslautern
Erwin-Schrödinger-Straße 52, 67663 Kaiserslautern, Germany
simeon@mathematik.uni-kl.de

## ABSTRACT

The goal of this paper is to introduce a kinematical reduction for the structural model of Kirchhoff-Love shells with developable base surfaces. The dimensional reduction to a curve and a vector field along it decreases the involved number of degrees of freedom. Local coordinates in form of a relatively parallel frame allow us to simplify the geometric constraints occurring in the model and prevent instabilities caused by points or segments of zero curvature. The core of this work is to prove equivalence of these requirements and the isometry of the transformation. Subsequently, we derive the one-dimensional bending energy functional for rectangular strips. In order to compute the equilibrium state of a static shell, we minimise a penalised version of this functional over the finitely many degrees of freedom stemming from an isogeometric discretisation. Several example strips clamped at both ends illustrate the feasibility of this approach.

**Keywords:** developable surfaces, Bishop frame, Kirchhoff-Love shells, isogeometric discretization, energy method.

## 1 INTRODUCTION

Thin-walled structural parts, denoted as shell structures in Computational Mechanics, frequently appear in engineering designs due to their special mechanical properties (cf. [1, sec. 1.1]). These are mainly determined by their geometric characteristics: Two parts, manufactured from the same material and subject to the same external loads, can be designed geometrically to react either very stiff or easily deformable.

Classical shell theories [2] aim at reducing both involved degrees of freedom and numerical costs by modelling sheet-like objects via their centre surface. Developable shell structures may be flattened by bending deformations, without any changes in the surface metric that imply high membrane stresses. Therefore, such surface geometries are good candidates for applications which demand highly flexible parts.

Flexible flat cables (FFCs) are prototypical examples of such structures and important components in computer hardware or consumer electronics products. Large spatial deformations of FFCs occur e.g. during the (dis-)assembly of such products. Their simulation is an essential part of a digitalized product development, as well as digital product lifecycle management.

Within the last century, several approaches to specialise Kirchhoff-Love type shell models for developable surfaces occurred [3]. Sadowsky [4] and Wunderlich [5] studied the bending energy of a narrow Kirchhoff-Love strip and integrated it along the direction of zero curvature, thereby

https://doi.org/10.3311/ECCOMASMBD2021-226

reducing it to the length dimension only. Starostin and van der Heijden [6], as well as Dias and Audoly [7] recently proposed one-dimensional models for ribbons.

In our work we take first steps to investigate the suitability of specialized ruled surface shell models of this type as computational models for applications as sketched above for FFC. In section 2, we consider the geometry of developable surfaces and justify geometric constraints that model isometric deformations. This generalises the approach proposed in [6] to base curves that possess arbitrary geodesic curvature and may exhibit points or segments of vanishing total curvature. Furthermore, we inspect surface singularities occurring from self-penetration of matter closer. A relatively parallel frame [8] (in literature also rotation minimising frame, parallel transported frame or Bishop frame) allows to decompose the director of the developable and thereby ruled surface. Section 3 proves the equivalence of our geometric model and vanishing of the surface membrane energy. Thus, the stored energy function of the transformations inspected consists only of the bending energy. We analytically integrate this energy over the second surface parameter and end up with a result similar to [5] in section 4. Section 5 explains the numerical treatment of the optimisation process: we address the non-linear constraints by a penalty method and employ an interior point method [9] to compute the stable equilibrium state. Finally, we display and discuss our results in section 6.

## 2 GEOMETRIC MODEL

Every developable surface is ruled, that means it can be represented by a regular base curve (also called directrix) $\boldsymbol{\gamma}$ and a director vector field $\mathbf{d}$ in the form

$$\boldsymbol{\phi} : (u,v) \mapsto \boldsymbol{\gamma}(u) + v\mathbf{d}(u). \tag{1}$$

This representation scheme is illustrated in Figure 1. Conversely, a ruled surface is developable if and only if the determinant of curve tangent $\mathbf{t}$, director and director derivative $\det[\mathbf{t},\mathbf{d},\dot{\mathbf{d}}]$ vanishes everywhere along the base curve [10, chap. 5.5]. The dotted derivative stresses that $u$ is not necessarily an arc-length parameter, following the convention of [10], whereas a prime as in $\boldsymbol{\gamma}'$ shall always denote derivatives with respect to the arc-length parameter $s$ of $\boldsymbol{\gamma}$.

We regard strips that possess dedicated (local) length, width and thickness dimensions. This means, we may assume $\boldsymbol{\gamma}$ to match the centre-line of $\boldsymbol{\phi}$ such that the width, defined as cross section in the normal plane to $\mathbf{t}$, is constantly $2w$. Similarly, we define the thickness normal to $\boldsymbol{\phi}$ and assume it to constantly be $2t$. The capital letter $L$ shall denote the length of $\boldsymbol{\gamma}$ and emphasize the geometric characteristics $L \gg w \gg t$ of the strip.

Developable surfaces may exhibit singularities in form of neighboured rulings intersecting each other as depicted in Figure 2, which may be seen as a violation of the impenetrability of matter. All these intersection points form an (in general not continuous) curve, called edge of regression (cf. [10, chap. 5.1]). Characteristically, the surface normal vanishes in these singular points $(u^*,v^*)$ such that

$$\det \mathbf{A}(u^*,v^*) = \|\partial_u\boldsymbol{\phi}(u^*,v^*) \times \partial_v\boldsymbol{\phi}(u^*,v^*)\|^2 = 0, \tag{2}$$

where $\boldsymbol{A} : (u,v) \mapsto \left[\partial_\alpha\boldsymbol{\phi}(u,v)\cdot\partial_\beta\boldsymbol{\phi}(u,v)\right]_{\alpha,\beta\in\{u,v\}}$ is the metric tensor and $\partial_u\boldsymbol{\phi}$, $\partial_v\boldsymbol{\phi}$ denote the tangent vectors of the surface in $\phi(u,v)$ along the isoparametric lines (constant $v$ or $u$, respectively).

Note that if director and curve tangent are parallel, the surface normal reads $v(\dot{\mathbf{d}}\times\mathbf{d})$. Hence, then there is a singularity lying on $\boldsymbol{\gamma}$. Thus, for regular surfaces, $\mathbf{t}$ and $\mathbf{d}$ need to be linearly independent. Furthermore, without loss of generality, we may scale $\mathbf{d}$ such that its component normal to $\boldsymbol{\gamma}$ is of unit length, i.e. $\|\mathbf{d}-(\mathbf{d}\cdot\mathbf{t})\mathbf{t}\| \equiv 1$. The symbol $\equiv$ means pointwise equality for all parameters $u$. With this, the parameter domain of $\boldsymbol{\phi}$ becomes rectangular and we may write $\boldsymbol{\phi} : [0,L]\times[-w,w] \to \mathbb{R}^3$.

https://doi.org/10.3311/ECCOMASMBD2021-226

### 2.1 Local Frame Coordinates

In order to rigorously define the curvature terms in the subsequent paragraphs, we will assume the necessary smoothness $\boldsymbol{\gamma} \in \mathscr{C}^2$ and $\mathbf{d} \in \mathscr{C}^1$ throughout the whole paper, where $\mathscr{C}^k$ denotes the space of k-times continuously differentiable functions. This provides existence [11] of a relatively parallel frame $(\mathbf{t}, \mathbf{m}_1, \mathbf{m}_2)$ along $\boldsymbol{\gamma}$ with generalised Frenet equations

$$\frac{\mathrm{d}}{\mathrm{d}u}\begin{bmatrix}\mathbf{t}\\ \mathbf{m}_1\\ \mathbf{m}_2\end{bmatrix} \equiv \begin{bmatrix} & k_1 & k_2\\ -k_1 & & \\ -k_2 & & \end{bmatrix}\begin{bmatrix}\mathbf{t}\\ \mathbf{m}_1\\ \mathbf{m}_2\end{bmatrix}$$

and enables us to decompose the director as

$$\mathbf{d} \equiv d_0\mathbf{t} + d_1\mathbf{m}_1 + d_2\mathbf{m}_2 \tag{3}$$

with coordinate functions $d_0, d_1, d_2$ with respect to the relatively parallel frame.

Using the curvature components $k_1, k_2$ of the frame, we may write

$$\det[\mathbf{t}, \mathbf{d}, \dot{\mathbf{d}}] \equiv d_1 \underbrace{\left(\dot{d}_2 + d_0 k_2 \|\dot{\boldsymbol{\gamma}}\|\right)}_{\equiv:\pi_G^{(2)}} - d_2 \underbrace{\left(\dot{d}_1 + d_0 k_1 \|\dot{\boldsymbol{\gamma}}\|\right)}_{\equiv:\pi_G^{(1)}}. \tag{4}$$

As $\det[\mathbf{t}, \mathbf{d}, \dot{\mathbf{d}}] \equiv 0$, the tangent plane of $\boldsymbol{\phi}$ is spanned by $\mathbf{t}$ and $\mathbf{d}$. Then the unit normal vector of $\boldsymbol{\phi}$ reads $\boldsymbol{\eta}(\cdot, v) \equiv \mathbf{t} \times \mathbf{d} \equiv -d_2\mathbf{m}_1 + d_1\mathbf{m}_2$ independently of $v \in [-w, w]$.

### 2.2 Rectangular Strips and Rectifying Developables

In the special case of rectangular strips, the surface $\boldsymbol{\phi}$ matches the rectifying developable (RD) of its centre-line $\boldsymbol{\gamma}$, which is the envelope of planes spanned by tangent and Frenet binormal $\mathbf{b}$. The model of [6] exploits this representation such that the director reads $\mathbf{d} \equiv \frac{\tau}{\kappa}\mathbf{t} + \mathbf{b}$, where $\kappa$ and $\tau$ denote the Frenet curvature and torsion, respectively.

Since the definition of the RD requires an existing Frenet frame, we generalise this concept to curves which are twice continuously differentiable. For this, we utilise three characteristic properties of the RD: $\boldsymbol{\phi}$ is developable, $\boldsymbol{\gamma}$ is a geodesic on $\boldsymbol{\phi}$ and the curve tangent and director are pointwise linear independent [12, Proposition 4.1]. Note that we already treated the third condition above regarding regularity and that a geodesic line is characterised by having zero geodesic curvature

$$\kappa_g \equiv \frac{\det[\dot{\boldsymbol{\gamma}}, \ddot{\boldsymbol{\gamma}}, \boldsymbol{\eta}]}{\|\dot{\boldsymbol{\gamma}}\|^3} \equiv k_1 d_1 + k_2 d_2$$

everywhere [13].

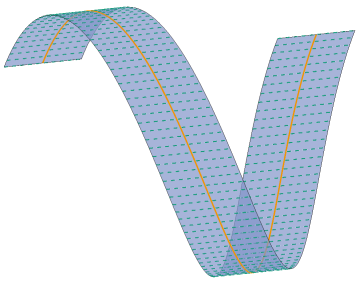

Figure 1: Representation of a helicoidal strip as ruled surface with orange base curve and greenly dashed rulings.

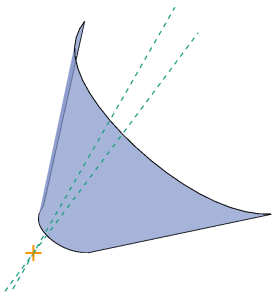

Figure 2: Intersection of a pair of neighboured rulings in an orange point outside of the strip.

https://doi.org/10.3311/ECCOMASMBD2021-226

Thus, we get a system of geometric constraints

$$\det[\mathbf{t},\mathbf{d},\dot{\mathbf{d}}] \equiv 0, \qquad \kappa_g \equiv 0, \qquad \|\mathbf{d}-(\mathbf{d}\cdot\mathbf{t})\mathbf{t}\| \equiv 1. \tag{5}$$

If a ruled surface $\boldsymbol{\phi}$ satisfies these conditions, we call it generalised rectifying developable (GRD). Furthermore, the edge of regression restricts the surface width via the regularity condition (2) to the well-known [6, sec. 2.1]

$$w < \min_{s\in[0,L]} |v^*(s)| = \frac{1}{\max_{s\in[0,L]} |\dot{d}_0(s)|}, \tag{6}$$

or vice versa $|\dot{d}_0| < \frac{1}{w}$ globally on $[0,L]$.

### 2.3 Generalisation to Curved Bands

Next, we follow the spirit of [7] and admit a priori curved directrix in the reference configuration. This means, we relax the requirement of $\boldsymbol{\gamma}$ being a geodesic and simply require the base curve to maintain its geodesic curvature. Note that this is obviously necessary concerning isometric transformations.

Consider the partial derivatives of $\boldsymbol{\phi}$ which define a unique normal vector if and only if their cross-product

$$\|\boldsymbol{\phi}_u \times \boldsymbol{\phi}_v\| \equiv \|\dot{\boldsymbol{\gamma}}\| + v\dot{d}_0 - v\kappa_g\|\dot{\boldsymbol{\gamma}}\| - d_0\kappa_g\|\dot{\boldsymbol{\gamma}}\|$$

does not vanish. This yields for the critical value $v^*$

$$v^* \equiv \frac{\|\dot{\boldsymbol{\gamma}}\|}{\dot{d}_0 - \kappa_g\|\dot{\boldsymbol{\gamma}}\|(1+d_0^2)} \in \mathbb{R}\cup\{\infty\}.$$

The regularity condition (6) generalises to

$$\left|\dot{d}_0 - \kappa_g\|\dot{\boldsymbol{\gamma}}\|(1+d_0^2)\right| < \frac{\|\dot{\boldsymbol{\gamma}}\|}{w}. \tag{7}$$

## 3 Isometry of the Model

In the previous section, we justify several geometric conditions for our model that ensure the isometric deformation of a strip. Now we aim at rigorously proving equivalence between these constraints and isometry. In order to differentiate between initial and deformed state, we indicate belongingness to the initial configuration with a superset $^\circ$ for all variables. For simplicity, we assume that the initial state is planar here and generalise this statement later.

**Proposition 3.1.** *Let $\boldsymbol{\phi}^\circ$ be a planar surface described in the form* (1)*, such that the director satisfies the regularity condition* (7) *and the scaling condition $\|\mathbf{d}^\circ - (\mathbf{d}^\circ\cdot\mathbf{t}^\circ)\mathbf{t}^\circ\| \equiv 1$.*

*Then $\boldsymbol{\phi}$ is an isometrically deformed state of $\boldsymbol{\phi}^\circ$ if and only if $\boldsymbol{\phi}$ is ruled and satisfies the following properties:*

- *(a) The deformed state $\boldsymbol{\phi}$ is developable, i.e.* $\det[\mathbf{t},\mathbf{d},\dot{\mathbf{d}}] \equiv 0$.
- *(b) The geodesic curvature of the directrix is preserved, i.e. $\kappa_g \equiv \kappa_g^\circ$.*
- *(c) There is no change in the width of the strip, i.e. $d_1^2 + d_2^2 \equiv 1$.*
- *(d) There is no tensile strain along $\boldsymbol{\gamma}$, i.e. $\|\dot{\boldsymbol{\gamma}}\| \equiv \|\dot{\boldsymbol{\gamma}}^\circ\|$.*
- *(e) There is no penetration of matter, i.e. $d_0$ satisfies* (7)*.*

https://doi.org/10.3311/ECCOMASMBD2021-226

The subsequent proof establishes equivalence on the global level instead of proving necessity and sufficiency separately. Only for two minor claims, we treat both sides consecutively (indicated by "$\Leftarrow$" or "$\Rightarrow$").

*Proof.* For the start, remember the Gaussian Theorema Egregium [14] after which Gaussian curvature is preserved under isometric deformations. As $\boldsymbol{\phi}^\circ$ is planar, $\boldsymbol{\phi}$ must be developable and therewith ruled if it is an isometrically deformed state. Therefore, $\boldsymbol{\phi}$ may be parametrised in the form (1) with decomposed director (3) for both sides of the claim.

As we regard a flat reference configuration, $\boldsymbol{\gamma}^\circ$ is a plane curve. We may construct a frame $(\mathbf{t}^\circ, \mathbf{m}_1^\circ, \mathbf{m}_2^\circ)$ from the curve tangent $\mathbf{t}^\circ$ and the constant plane normal $\mathbf{m}_2^\circ$. Note that this frame is a relatively parallel frame, but has only one non-zero curvature component $k_1^\circ \equiv: \kappa_g^\circ$, which is the (geodesic) curvature of $\boldsymbol{\gamma}^\circ$. This yields the representation

$$\boldsymbol{\phi}^\circ \equiv \boldsymbol{\gamma}^\circ + v\mathbf{d}^\circ, \qquad \mathbf{d}^\circ \equiv d_0^\circ \mathbf{t}^\circ + \mathbf{m}_1^\circ.$$

We compute the expressions for the symmetric metric tensors $\mathbf{A}, \mathbf{A}^\circ$ and subtract them from each other. The entries of the resulting difference tensor $\Delta\mathbf{A} := \mathbf{A} - \mathbf{A}^\circ$ may be written as polynomials in $v$ with coefficients $x_{11}, y_{1\alpha}, z_{\alpha\beta} : [0,L] \to \mathbb{R}$ for $\alpha, \beta \in \{1,2\}$ defined via

$$\Delta\mathbf{A}(u,v) =: \begin{bmatrix} x_{11}(u)\, v^2 + y_{11}(u)\, v + z_{11}(u) & y_{12}(u)\, v + z_{12}(u) \\ y_{12}(u)\, v + z_{12}(u) & z_{22}(u) \end{bmatrix}.$$

The deformation from $\boldsymbol{\phi}^\circ$ to $\boldsymbol{\phi}$ is isometric if and only if this difference tensor vanishes globally on $[0,L] \times [-w,w]$, especially for each $v \in [-w,w]$. This happens if and only if the six coefficient functions $x_{11}, y_{1\alpha}, z_{\alpha\beta}$ are constantly zero. We consider one entry after the other in order to link them to the properties $(a) - (e)$ and immediately simplify the remaining coefficients.

"*(d)*" First consider $z_{11} \equiv \|\dot{\boldsymbol{\gamma}}\|^2 - \|\dot{\boldsymbol{\gamma}}^\circ\|^2$, which vanishes if and only if the curves $\boldsymbol{\gamma}, \boldsymbol{\gamma}^\circ$ have the same derivative norm.

"*(e)*" With this we compute $z_{12} \equiv (d_0 - d_0^\circ)\|\dot{\boldsymbol{\gamma}}\|$, which vanishes if and only if $d_0 \equiv d_0^\circ$. At first glance this might confuse, as the angle between rulings and tangent are supposed to change during arbitrary deformations. However, this indicates that a pair of coordinates $(u,v)$ describes different material points in reference and deformed configuration, respectively, if and only if the angles change.

Nevertheless, there is a valid parametrisation of the reference configuration for every $d_0^\circ$ that satisfies the edge-of-regression-condition. "$\Leftarrow$" If property *(e)* holds, we may choose $d_0^\circ$ matching $d_0$ in order to describe both configurations with the same parameter set. "$\Rightarrow$" Otherwise, there would be a self-penetration of matter which cannot occur during an isometric deformation.

"*(c)*" We simplify $z_{22} \equiv d_1^2 + d_2^2 - 1$ which enforces unit length of the projection of the director to the normal plane in deformed state if and only if the coefficient vanishes.

"*(b)*" The preservation of the geodesic curvature of the directrix is equivalent to

$$y_{11} \equiv 2\|\dot{\boldsymbol{\gamma}}\| \left(\kappa_g^\circ - k_1 d_1 - k_2 d_2\right) \equiv 2\|\dot{\boldsymbol{\gamma}}\| \left(\kappa_g^\circ - \kappa_g\right) \equiv 0.$$

"*(a)*" We end up with two remaining coefficients

$$x_{11} \equiv {\pi_G^{(1)}}^2 + {\pi_G^{(2)}}^2 - \|\dot{\boldsymbol{\gamma}}\|^2 d_0^2 {\kappa_g}^2, \qquad y_{12} \equiv d_1 \pi_G^{(1)} + d_2 \pi_G^{(2)} - \|\dot{\boldsymbol{\gamma}}\| d_0 \kappa_g.$$

"$\Rightarrow$" Assume that both $x_{11}$ and $y_{12}$ vanish completely (i.e. the deformation is isometric). Then we may solve the latter for $\|\dot{\boldsymbol{\gamma}}\| d_0 \kappa_g^\circ$ and insert it in the former, which gives

$$x_{11} \equiv (1 - d_1^2){\pi_G^{(1)}}^2 + (1 - d_2^2){\pi_G^{(2)}}^2 - 2 d_1 d_2 \pi_G^{(1)} \pi_G^{(2)}.$$

https://doi.org/10.3311/ECCOMASMBD2021-226

We insert *(c)* and eventually get

$$x_{11} \equiv d_2^2 {\pi_G^{(1)}}^2 + d_1^2 {\pi_G^{(2)}}^2 - 2d_1 d_2 \pi_G^{(1)} \pi_G^{(2)} \equiv \left( d_1 \pi_G^{(2)} - d_2 \pi_G^{(1)} \right)^2 \equiv \det[\mathbf{t}, \mathbf{d}, \dot{\mathbf{d}}]^2 \equiv -\kappa_G. \quad (8)$$

Hence, $x_{11}$ vanishes only if the deformed configuration is developable.

"$\Leftarrow$" Now assume vice versa that $\boldsymbol{\phi}$ is developable and thus

$$\det[\mathbf{t}, \mathbf{d}, \dot{\mathbf{d}}] \equiv d_1 \pi_G^{(2)} - d_2 \pi_G^{(1)} \equiv 0. \quad (9)$$

Since *(c)*, for each $u_0 \in [0, L]$ we have $d_1(u_0) \neq 0$ or $d_2(u_0) \neq 0$ - without loss of generality let the former be true. Then we may solve

$$0 \equiv \frac{\mathrm{d}}{\mathrm{d}u}(1) \equiv \frac{\mathrm{d}}{\mathrm{d}u}(d_1^2 + d_2^2) \equiv d_1 \dot{d}_1 + d_2 \dot{d}_2$$

for $\dot{d}_1(u_0)$ and insert the result in (9). For clarity we omit the dependency in $u_0$, but use $=$ to indicate that the following statements hold in a single point:

$$0 = d_1 \pi_G^{(2)} - d_2 \pi_G^{(1)} = d_1 \dot{d}_2 + \frac{d_2^2}{d_1} \dot{d}_2 + d_0 \|\dot{\boldsymbol{\gamma}}\| \left( d_1 k_2 - d_2 k_1 \right).$$

We conclude that $d_1 + \frac{d_2^2}{d_1} = \frac{1}{d_1}$ and solve for

$$\dot{d}_2 = -d_1 d_0 \|\dot{\boldsymbol{\gamma}}\| \left( d_1 k_2 - d_2 k_1 \right).$$

We plug this and the corresponding term for $\dot{d}_1$ into $y_{12}$ and get

$$y_{12} \equiv \underbrace{d_1 \dot{d}_1 + d_2 \dot{d}_2}_{\equiv 0} + \underbrace{d_0 \|\dot{\boldsymbol{\gamma}}\| (d_1 k_1 + d_2 k_2) - d_0 \|\dot{\boldsymbol{\gamma}}\| \kappa_g}_{\equiv 0} \equiv 0,$$

which holds globally due to the arbitrary choice of $u_0$. As we established $y_{12} \equiv 0$, we may use (8) for $x_{11}$ which vanishes by assumption. □

For generalisation, consider the case of a non-planar but still developable reference configuration $\boldsymbol{\phi}^\circ$. By the definition of developability, there exists a planar state $\boldsymbol{\phi}^p$ that is an isometric deformation of $\boldsymbol{\phi}^\circ$. The planar state is obviously developable and needs to fulfil

$$1 \equiv \det \mathbf{A}^\circ(\cdot, 0) \equiv \det \mathbf{A}^p(\cdot, 0) \equiv {d_1^p}^2 + {d_2^p}^2.$$

Hence, we may interchange the roles of $\boldsymbol{\phi}^\circ$ and $\boldsymbol{\phi}^p$ and apply Proposition 3.1 on them and, then again, we may employ Proposition 3.1 for the transformation between $\boldsymbol{\phi}^p$ and $\boldsymbol{\phi}$.

**Corollary 3.2.** *Let $\boldsymbol{\phi}^\circ$ be a developable surface described in the form* (1)*, such that the director satisfies the regularity condition* (7) *and the scaling condition $\|\mathbf{d}^\circ - (\mathbf{d}^\circ \cdot \mathbf{t}^\circ)\mathbf{t}^\circ\| \equiv 1$.*

*Then $\boldsymbol{\phi}$ is an isometrically deformed state of $\boldsymbol{\phi}^\circ$ if and only if $\boldsymbol{\phi}$ is ruled and satisfies the following properties:*

- *(a) The deformed state $\boldsymbol{\phi}$ is developable, i.e.* $\det[\mathbf{t}, \mathbf{d}, \dot{\mathbf{d}}] \equiv 0$.
- *(b) The geodesic curvature of the directrix is preserved, i.e. $\kappa_g \equiv \kappa_g^\circ$.*
- *(c) There is no change in the width of the strip, i.e. $d_1^2 + d_2^2 \equiv 1$.*
- *(d) There is no tensile stress along $\boldsymbol{\gamma}$, i.e. $\|\dot{\boldsymbol{\gamma}}\| \equiv \|\dot{\boldsymbol{\gamma}}^\circ\|$.*
- *(e) There is no penetration of matter, i.e. $d_0$ satisfies* (7)*.*

https://doi.org/10.3311/ECCOMASMBD2021-226

## 4 Energy Functional

As we established in the previous section, the conditions in Corollary 3.2 yield geometric constraints for isometric deformations of developable bands. Thus, we may compute the static equilibrium state of a strip under these requirements and given boundary conditions by minimising the stored energy. As we already outlined, there is no membrane deformation present such that this energy functional only consists of the bending part.

For the sake of simplicity, we consider a rectangular strip with geodesic base line $\boldsymbol{\gamma}$ parametrised by arc-length, and a flat reference configuration. We compute the mean curvature $H$ of a ruled surface (1) and simplify the resulting expression via (5). This results in

$$H(\cdot, v) \equiv \frac{(d_1 k_2 - d_2 k_1)(d_0^2 + 1)}{1 + v d_0'}.$$

Note that the denominator of $H$ matches exactly the transformation factor for the area element $\mathrm{d}A = (1 + v d_0')\,\mathrm{d}s\mathrm{d}v$. Hence, the bending energy of a uniformly isotropic reads

$$\begin{aligned} \Xi(\boldsymbol{\phi}) = \frac{D}{2} \iint_{\boldsymbol{\phi}} H^2 \mathrm{d}A &= \frac{D}{2} \int_0^L (d_1 k_2 - d_2 k_1)^2 \left(d_0^2 + 1\right)^2 \int_{-w}^{w} \frac{1}{1 + v d_0'} \,\mathrm{d}v\,\mathrm{d}s \\ &= Dw \int_0^L (d_1 k_2 - d_2 k_1)^2 \left(d_0^2 + 1\right)^2 V(w d_0')\,\mathrm{d}s, \end{aligned} \tag{10}$$

where, $D = \frac{2t^3 E}{3(1-\nu^2)}$ denotes the flexural rigidity of the material with Young's modulus $E$ and Poisson ration $\nu$ and

$$V(w d_0') = \frac{1}{w d_0'} \log\left(\frac{1 + w d_0'}{1 - w d_0'}\right) = 1 + \mathscr{O}((w d_0')^2)$$

gives the small width approximation term which may be neglected under linearisation about an infinitely narrow band [5]. Note that non-rectangular strips yield the same energy functional (10) with an additional additive term in the argument of $V$.

## 5 Numerical Model and Implementation

In order to compute the stable static equilibrium of a rectangular strip under specified boundary conditions, we minimise the energy functional (10) regarding the geometric constraints 3.2(a)-(d) and the simplified regularity condition 6. The base curve $\boldsymbol{\gamma}$ and the director field $\mathbf{d}$ constitute the degrees of freedom, where latter is represented by the coefficient functions $d_i$.

Requiring 3.2(c) introduces an angle $\sigma$ such that $d_1 \equiv -\sin\sigma$ and $d_2 \equiv \cos\sigma$. This angle also occurs as polar coordinate of the curvatures $(k_1, k_2) : [0, L] \to \mathbb{R}^2$ and between relatively parallel and Frenet frame, wherever latter exists. Thereby, 3.2(c) is taken into account explicitly.

A penalty approach addresses the remaining constraints

$$\min_{\boldsymbol{\gamma}, d_0, \sigma} \quad \Xi + c_1 \Psi + c_2 \Theta + c_3 \Omega \tag{11}$$

$$\Psi = \int_0^L \det[\dot{\boldsymbol{\gamma}}, \mathbf{d}, \dot{\mathbf{d}}]^2 \mathrm{d}u, \tag{11a}$$

$$\Theta = \int_0^L \kappa_g^2 \mathrm{d}u, \tag{11b}$$

$$\Omega = \int_0^L \left(\|\dot{\boldsymbol{\gamma}}\| - 1\right)^2 \mathrm{d}u \tag{11d}$$

with penalty weights $c_i > 0$. In this formulation, $c_1 \to \infty$ ensures developability, $c_2 \to \infty$ maintains the geodesic property of $\boldsymbol{\gamma}$ and $c_3 \to \infty$ enforces the inextensibility of the base curve.

https://doi.org/10.3311/ECCOMASMBD2021-226

As this model requires at least $\mathscr{C}^2$-smoothness (almost everywhere), isogeometric curves are predestinated candidates for discretisation of $\boldsymbol{\gamma}$, $d_0$ and $\sigma$. Given a polynomial degree $p$ and the number of desired control points $n+1$, a clamped knot vector $U = [u_0, \dots, u_{n+p+1}]$ with

$$0 = u_0 = \dots u_p < u_{p+1} \leq \dots \leq u_n < u_{n+1} = \dots = u_{n+p+1} = L$$

defines the family of B-Spline basis functions $\{N_{i,p} : [0,L] \to [0,1] \mid i = 0, \dots, n\}$. These are constructed recursively by

$$N_{i,0}(u) = \begin{cases} 1 & \text{, if } u \in [u_i, u_i + 1] \\ 0 & \text{, otherwise} \end{cases},$$
$$N_{i,p}(u) = \frac{u - u_i}{u_{i+p} - u_i} N_{i,p-1}(u) + \frac{u_{i+p+1} - u}{u_{i+p+1} - u_{i+1}} N_{i+1,p-1}.$$

A B-Spline curve $\boldsymbol{\beta}$ in $q$ dimensions then reads

$$\boldsymbol{\beta} : [0,L] \to \mathbb{R}^q,\ u \mapsto \sum_{i=0}^{n} N_{i,p}(u) \mathbf{p}_i,$$

where $\mathbf{p}_i \in \mathbb{R}^q$ are the control points, which become the degrees of freedom for our approach. For details on the properties of B-Spline basis functions, NURBS, and related curves confer [15].

For minimisation, we utilise the interior point optimiser IPopt [9] on the functional 11, where the boundary conditions are treated as constraints. The automatic differentiation library autodiff [16] computes the derivatives for gradients and Hessian matrices. Theoretical background may be looked up in [17].

## 6 Results and Conclusion

We choose three benchmarks to apply the model described in the previous section on. For each case, the boundary conditions and a flat reference geometry pose the input such that length and width of the plane strip coincide with the x- and y-axis, respectively.

For the first example, the start ($u = 0$) remains completely fixed, whereas the end ($u = L$) is dragged towards the start and the tangent direction in the end point is flipped upwards by $\frac{\pi}{4}$. Under these boundary conditions, the problem reduces to two dimensions where the director is transported parallelly along the plane curve. Figure 3 illustrates the equilibrium state.

The boundary conditions of the second use depicted in 4 case enforce a spatial base curve. As before, the start is kept fixed whereas the second end is translated in both negative x- and positive y-direction and the tangent remains fixed. Additionally, we specify a boundary condition for the director at the second end.

The third example displayed in Figure 5 illustrates the extension to curved reference directrices. Instead of a purely rectangular reference state, we choose a quarter of a two-dimensional torus with radius 4. Hence, the (geodesic) curvature of the base curve is constantly $\kappa_g^\circ \equiv \frac{1}{4}$ and needs to be preserved in the deformed state. Therefore, the penalty term $\Theta$ in (11b) is updated to yield preservation of curvature as $\int_0^L (\kappa_g - \kappa_g^\circ)^2 \mathrm{d}u$. We then drag the second end ($u = L$) both upward and in opposite tangent direction.

Although all example benchmarks compute suiting equilibrium configurations, the computations involve high iteration numbers with small steps that indicate susceptibility to slow convergence. The condition numbers of the Hessian matrix within the last iteration for the three examples read $9.5 \cdot 10^{17}$, $1.1 \cdot 10^{18}$, $1.5 \cdot 10^{17}$ respectively. Hence, the solution process requires numerical improvement in order to achieve real time applicability.

Furthermore, an ordinary differential equation related to the relatively parallel transport of normal vectors may substitute automatic differentiation. In order to properly model FFCs, the bending energy of section 4 requires incorporation of an anisotropic material law.

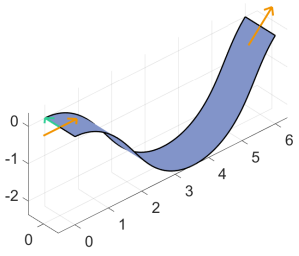

Figure 3: Equilibrium configuration under planar boundary conditions.

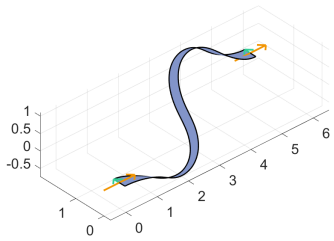

Figure 4: Example with non-planar base curve.

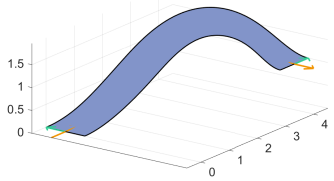

Figure 5: Example with curved reference directrix.

## REFERENCES


[1] Chapelle, D., Bathe, K.J.: The Finite Element Analysis of Shells - Fundamentals: Fundamentals. Computational Fluid and Solid Mechanics. Springer-Verlag Berlin Heidelberg, Berlin, Heidelberg (2011) ISBN: 978-3-642-16408-8.

[2] Bischoff, M., Bletzinger, K.U., Wall, W.A., Ramm, E.: Models and finite elements for thin-walled structures. In: Encyclopedia of computational mechanics. Volume 172. Wiley, Chichester (2004) ISBN:0470846992.

[3] Fosdick, R., Fried, E., eds.: The Mechanics of Ribbons and Möbius Bands. 1st edn. Springer Netherlands, Dordrecht and s.l. (2016) ISBN:978-94-017-7300-3.

[4] Sadowsky, M.: Ein elementarer Beweis für die Existenz eines abwickelbaren Möbiusschen Bandes und Zurückführung des geometrischen Problems auf ein Variationsproblem. Sitzungsberichte der Preussischen Akademie der Wissenschaften (1930)

[5] Wunderlich, W.: Über ein abwickelbares Möbiusband. Monatshefte für Mathematik **66**(3) (1962) 276–289 doi:10.1007/BF01299052.

[6] Starostin, E.L., van der Heijden, G.H.M.: Equilibrium shapes with stress localisation for inextensible elastic möbius and other strips. Journal of Elasticity **119**(1) (2015) 67–112 doi:10.1007/s10659-014-9495-0.

[7] Dias, M.A., Audoly, B.: "Wunderlich, meet Kirchhoff": A general and unified description of elastic ribbons and thin rods. Journal of Elasticity **119**(1-2) (2015) 49–66 doi:10.1007/s10659-014-9487-0.

[8] Bishop, R.L.: There is more than one way to frame a curve. The American Mathematical Monthly **82**(3) (1975) 246–251 doi:10.2307/2319846.

[9] Wächter, A., Biegler, L.T.: On the implementation of an interior-point filter line-search algorithm for large-scale nonlinear programming. Mathematical Programming **106**(1) (2006) 25–57 doi:10.1007/s10107-004-0559-y.

[10] Struik, D.J.: Lectures on classical differential geometry. 2nd edn. Dover Publications, Mineola, NY, USA (1988) ISBN:0486656098.

[11] Krejčiřík, D., Šediváková, H.: The effective hamiltonian in curved quantum waveguides under mild regularity assumptions. Reviews in Mathematical Physics **24**(07) (2012) doi:10.1142/S0129055X12500183.

[12] Izumiya, S., Takeuchi, N.: New special curves and developable surfaces. Turkish Journal of Mathematics **28** (2004) 153–163 doi: 10.14943/83700.

[13] do Carmo, M.P.: Differential geometry of curves and surfaces. Prentice-Hall, Englewood Cliffs, New Jersey, USA (1976) ISBN:0132125897.

[14] Gauss, C.F.: Allgemeine Flächentheorie (disquisitiones generales circa superficies curvas). Engelmann, Leipzig, Germany (1889) doi:10.24355/DBBS.084-201303011402-0.

[15] Piegl, L., Tiller, W.: The NURBS Book. Springer, Berlin, Heidelberg (1995) ISBN:978-3-642-97387-1.

[16] Leal, A.: Autodiff, a modern, fast and expressive C++ library for automatic differentiation. (2018) url: https://autodiff.github.io.

[17] Griewank, A., Walther, A.: Evaluating derivatives: Principles and techniques of algorithmic differentiation. 2nd edn. Society for Industrial and Applied Mathematics, Philadelphia, USA (2008) ISBN:978-0-89871-659-7.

https://doi.org/10.3311/ECCOMASMBD2021-144

ECCOMAS Thematic Conference on Multibody Dynamics
December 12 - 15, 2021, Budapest, Hungary

# Effective Inelastic Bending Behavior of Multi-Wire Cables Using Finite Elements Accounting for Wire Contact

**Muhannad Hawwash**[1,2], **Vanessa Dörlich**[1], **Joachim Linn**[1], **Ralf Müller**[2], **Roger Keller**[3]

[1]Department Mathematics for the Digital Factory
Fraunhofer Institute for Industrial Mathematics ITWM
Fraunhofer Platz 1, 67663 Kaiserslautern, Germany
[muhannad.hawwash, vanessa.doerlich, joachim.linn]@itwm.fraunhofer.de

[2]Chair of Applied Mechanics
Technical University of Kaiserslautern
Gottlieb-Daimler-Straße, 67653 Kaiserslautern, Germany
[hawwash, ram]@rhrk.uni-kl.de

[3]Burckhardt Compression AG
Franz Burckhardt Strasse 5, 8404 Winterthur Switzerland
roger.keller@burckhardtcompression.com

## ABSTRACT

This contribution focuses on the investigation of inelastic structural effects occurring during the bending deformation of cables using detailed finite element models of helix wire strands. Due to the complex structure of cables usually consisting of concentric layers of intertwined wires, shields and the outer jacket, inelastic deformation behaviour has to be expected. In this work, we model simplified cables as strands of helix wires discretised with quadratic beam elements to investigate the influence of geometric parameters such as the helix angle of the wires and the interactions of the wires by means of frictionless or frictional contact models. Starting at low model complexity, we use double wire and seven wire models to simulate pure bending of intertwined strands omitting material inelasticity to avoid superposition of structural and material effects. Different variations of contact states in the undeformed configuration of the seven wire strand are taken into account allowing for the direct observation of the influence of active contacts on the strand's bending response. First steps towards modelling the interactions between wires and objects relevant in cable bundle assembly, e.g. cable ties or clips, are presented for the double wire model. The presented models yield a valuable toolbox for the investigation of specific structural parameters affecting the deformation behaviour of cables.

**Keywords:** Cable simulation, nonlinear beam, frictional wire contact, multi-wire strand, bending experiment.

## 1 INTRODUCTION

In the development and manufacturing process of modern cars, cables and hoses are important system components, see Fig. 1 left. In automotive industry, virtual assembly planning and digital validation of system layouts require fast and physically correct simulations of the mechanical behaviour of cables and hoses. Section 6 of [1] and section 4 of [2] summarise application examples from vehicle industry and [3] describes virtual product realisation processes using one-dimensional deformable objects from the design phase to production and assembly planning.

In this work, we present a modelling approach using a detailed finite element (FE) model [4] for composite cables which can be used to investigate the effective inelastic constitutive behavior of abstract cables resulting from structural effects. We follow approaches for detailed wire strand models using finite element models as described in [5, 6, 7, 8, 9, 10] for the investigation of wire

https://doi.org/10.3311/ECCOMASMBD2021-144

strands under load. However, while these contributions use finite volume elements, we use finite beam elements to model the individual wires. Following the method given in [11], we approximate the centreline of each wire with a helix and discretise it with quadratic shape functions. This allows for a comparatively easy implementation of the boundary and loading conditions as well as relatively short computation times.

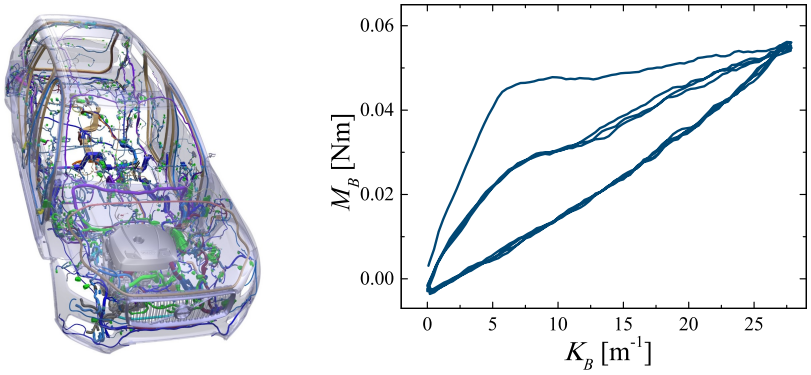


**Figure 1**. Left: Overview of the system of cables and hoses in a car. *Courtesy of Volvo Cars and Fraunhofer-Chalmers Research Centre, Gothenburg.* Right: Experimental result of the pure bending of a cable specimen given as bending moment $M_B$ vs. bending curvature $K_B$ diagram [12].

Cyclic pure bending experiments on a simple cable specimen show that the effective mechanical response of cables is usually strongly nonlinear and inelastic [12, 13], see Fig. 1 right. Presumably, material plasticity, damage and structural effects on the level of individual constituents such as contact and friction between wires occur in such experiments due to the structural complexity of cables. In real experiments, material and structural effects can hardly be investigated separately with acceptable experimental effort. Previous work of the authors focused on modelling the inelastic bending behaviour of a simple cable using standard constitutive laws for elasto-plasticity and damage in the framework of geometrically exact rod models [14]. While it was possible to simulate the bending response of the cable on the level of the sectional quantities of the geometrically exact rod, this approach only yields an inelastic model for one class of cables and the modelling parameters for one specific cable type. It does not allow for the investigation of the underlying inelastic effects which is necessary to enable a more universal estimation of the deformation behaviour of any cable based on its structure in the future.

We therefore investigate these effects and their interplay separately with cable models using finite elements on the level of wires in this work. A commercial FEM tool [15] is used to model the pure bending of a cable. We model the cable as an abstract strand of intertwined wires starting at low model complexity. In this first step, the wires are modelled as materially elastic in order to avoid a superposition of material and structural inelasticity.

This modelling approach can furthermore be used to investigate the influence of different helix angles of the wires on the effective behaviour of the abstract cable model. Therefore, the pure bending simulation is performed using models with different wire helix angles as initial stress-free configuration. The modelling approach presented in this work allows for versatile and detailed investigations of the effective mechanical response of wire strands as abstract cable models. We will show that it is useful for specific simulation experiments on cable-like structures to get a better understanding of the different material and structural inelastic effects which occur in real experiments performed on cables. While it is not simply possible to switch friction on and off in real experiments and measure the influence of friction on the effective behaviour, we can perform such investigations using the presented model.

https://doi.org/10.3311/ECCOMASMBD2021-144

## 2 Cable model using finite elements

Cables undergo large spatial deformations in applications. Therefore, we discretise the wires in our abstract cable model using finite beam elements with quadratic shape functions [4]. The beam element is a one-dimensional line element in space and is defined by three nodes having six degrees of freedom per node: translations in $x$, $y$ and $z$ directions and rotations about the $x$, $y$ and $z$ axes [15]. In order to avoid superposition of structural and material inelastic effects, we model the wires using a linear elastic material model with standard parameters for a copper alloy ($E = 1.1 \cdot 10^5$ MPa, $\nu = 0.34$). We thereby deliberately omit material inelasticity which certainly occurs during the deformation of the wires in real experiments.

### 2.1 Wire strand geometry

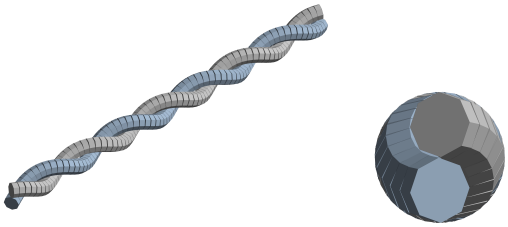

**Figure 2**. 3D FE model of the double wire strand with a wire helix angle of $\alpha_c = 36°$.

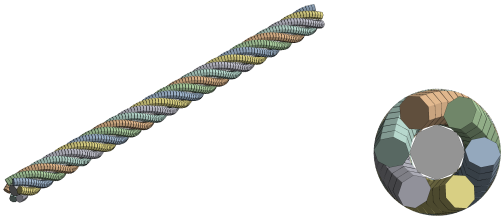

**Figure 3**. 3D FE model of the seven wire strand with a wire helix angle of $\alpha_c = 36°$.

The first model we investigate is a double wire strand consisting of two intertwined helices, see Fig. 2. The second simplified cable is modelled using seven wires with one straight wire as core and six helices in the outer layer, see Fig. 3. The intertwined wires are modelled as stress-free helices [11], one helix resembling one metallic wire. While the definition of the geometric parameters of the double wire strand is straightforward, the choice of the geometric parameters of the stress-free configuration of the seven wire strand determines the contact state in the undeformed cross section. The necessary parameters for the double helix structure are the helix radius $r$ and the wire radius, where both wires have the same radius $R$. In the seven wire strand, the outer wires' cross sections have an elliptic shape in the plane orthogonal to the $z$-axis of the structure. The radius of the ellipse depends on the helix angle $\alpha$ of the wire and essentially determines if neighbouring wires are in contact, see Fig. 4. Here, the core wire radius $R_c$ and outer wire radius $R_w$ can differ resulting in different contact states in the undeformed cross sections. We distinguish three cases [11, 16]. In the first case, the outer wires and the core wire have the same radius resulting in a cross section where the outer wires are only in contact with their neighbouring wires in the outer layer, see Fig. 5 left. The condition

$$R\sqrt{1+\frac{\tan^2\left(\frac{\pi}{2}-\frac{\pi}{m}\right)}{\sin^2\alpha}} = r, \tag{1}$$

with the number of outer wires $m$, has to be fulfilled. In the second case, core and outer wire radii are different and fulfil the condition

$$R_w\sqrt{1+\frac{\tan^2\left(\frac{\pi}{2}-\frac{\pi}{m}\right)}{\sin^2\alpha}} < R_c + R_w. \tag{2}$$

This results in a cross section as shown in Fig. 5 middle, where the outer wires are only in contact with the core wire in the undeformed configuration. In order to generate a cross section, where

https://doi.org/10.3311/ECCOMASMBD2021-144

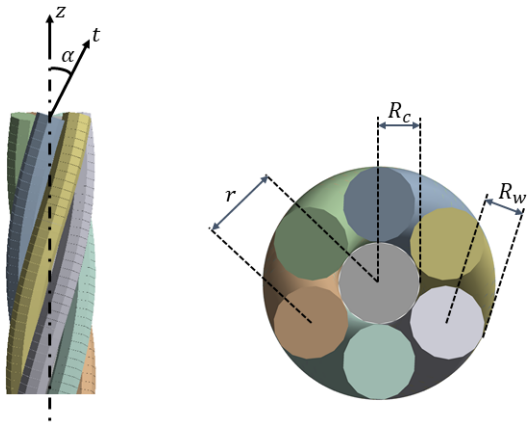


**Figure 4**. Definition of the parameters of a seven wire strand according to [16].

all neighbouring wires are in contact in the initial configuration, see Fig. 5 right, the radii have to fulfil

$$R_w \sqrt{1 + \frac{\tan^2(\frac{\pi}{2} - \frac{\pi}{m})}{\sin^2 \alpha}} = R_c + R_w. \tag{3}$$

To ensure comparable results and boundary conditions in the virtual experiments, we aimed at a resulting strand radius of approximately 8 mm and a specimen length of 220 mm for all models. For all seven wire strand models, a helix radius $r = R_c + R_w = 5.33\,\text{mm}$ was used. Model variants with different helix angles were set up for the double helix and the seven wire model to investigate the influence of this geometric parameter. The parameters for the seven wire strand models are summarised in table 1.

**Table 1**. Geometric modelling parameters for the seven wire strand models. Wire radii are given in mm.

| contact case | $\alpha_a = 9°$ | $\alpha_b = 18°$ | $\alpha_c = 36°$ |
|---|---|---|---|
| *I* | $R_c = R_w = 2.642$ | $R_c = R_w = 2.567$ | $R_c = R_w = 2.257$ |
| *II* | $R_c = 3.233, \quad R_w = 2.1$ | | |
| *III* | $R_c = 2.691, R_w = 2.642$ | $R_c = 2.766, R_w = 2.567$ | $R_c = 3.076, R_w = 2.257$ |

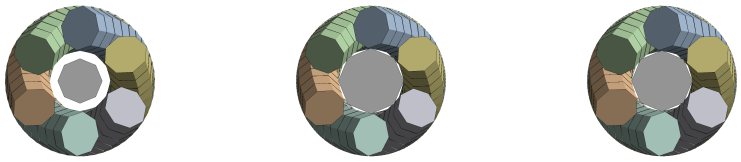

**Figure 5**. Cross sections of seven wire strand models with different wire radii in undeformed state. Left: Only outer wires are in contact, with $R_c = R_w$. Middle: Outer wires are only in contact with core wire, $R_c \neq R_w$. Right: Each wire is in contact with its neighbours, $R_c \neq R_w$.

## 2.2 Contact modelling

During mechanical loading, contact between wires occurs and must be taken into account. We use the Coulomb friction model provided in ANSYS to model contact between wires [15]. The

pure penalty contact formulation was chosen to model wire-to-wire contact in this work. In order to investigate the influence of friction on the effective bending response of the cable, simulations without and with friction have been performed. A Coulomb friction model with varying isotropic friction coefficients was used for that purpose.

The presented wire strand models were further enhanced in order to investigate the influence of additional objects on the wire interactions, especially the friction behaviour. Those first steps include the introduction of rings resembling objects such as cable ties, clamps or clips, see Fig 6. We investigated double wire strand models with one central ring and two equally distanced rings with an inner diameter of $D_i = 16.5$ mm, outer diameter $D_o = 17$ mm and the width $w = 5$ mm. The bonded contact formulation, which connects the degrees of freedom of both contact objects in the relevant region, was used to model the interaction between the rings and the wires in order to emulate clamping or tight rings.

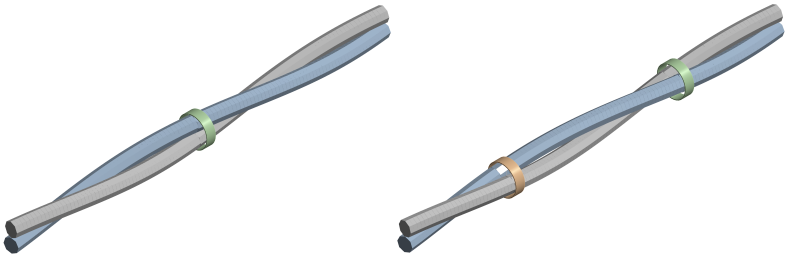

**Figure 6**. Double helix models with helix angle $\alpha_a$ and additional rings modelled as rigid bodies.

## 3 Virtual pure bending experiments

### 3.1 Boundary conditions

The boundary conditions of a planar pure bending experiment yield a deformation state where a constant bending moment acts on the specimen. In an ideal setup, neither lateral or normal forces nor torsional moments occur. Thus, a homogeneous specimen will reach a configuration in the static equilibrium with a constant bending curvature along the specimen. In this work, the pure bending boundary conditions were defined using a homogeneous beam model and later applied to the composite structures described in the previous section. Fig. 7 shows the implementation of the boundary conditions using a hinged support on the left, and a simple movable support on the right end. Bending was induced by applying the bending angle $\theta_B$ on both ends up to a maximum of 90°. In all virtual experiments, one full load cycle including loading and unloading to $\theta_B = 0°$ was simulated.

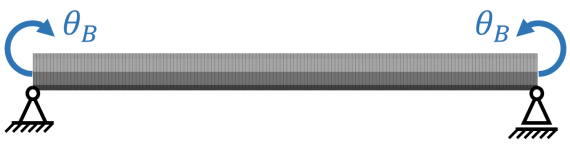


**Figure 7**. Boundary conditions for pure bending of a homogeneous beam.

The boundary conditions were applied to the composite wire strand structures using remote points which control the degrees of freedom of the nodes in the cross sections on the strand ends. Fig. 8 shows the deformed configurations of the double and seven wire strand models at $\theta_B = 90°$ with a constant global curvature of the structure, resulting in a semi-circular shape of the specimen.

https://doi.org/10.3311/ECCOMASMBD2021-144

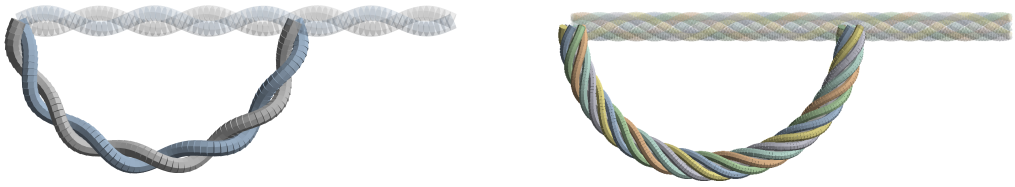

**Figure 8**. Deformed configurations of FE models of the composite structures. Left: Double wire strand with a helix angle of $\alpha_c = 36°$. Right: Seven wire strand with a helix angle of $\alpha_c = 36°$.

### 3.2 Analytical solution for pure bending of a wire strand

The results of the simulation experiments will be examined by analysing the bending moment $M_B$ as a function of the bending curvature $k$. Costello derives in [16] an analytical expression for the bending moment of an $m$ wire strand consisting of one core wire and $m_2$ outer wires with helix angle $\alpha$ under bending,

$$M_B = \frac{\pi E}{4}\left[\frac{2m_2 \sin\alpha}{(2+\nu\cos^2\alpha)}R_w^4 + R_c^4\right]\frac{1}{\rho}, \tag{4}$$

with the wires' Young's modulus $E$, their Poisson ratio $\nu$ and the bending radius $\rho$ of the strand, i.e. the inverse of the bending curvature,

$$k = \frac{1}{\rho}. \tag{5}$$

This expression has been derived neglecting friction and under the assumption that the outer wires are only in contact with the core wire, but not their neighbouring outer wires to minimise wire interactions. Thus, the analytical solution for $m_2 = 6$ is comparable to our virtual simulations using the seven wire model with contact case *II* given by equation (2).

### 3.3 Results

The following section summarises a choice of simulation results using the presented FE models to demonstrate their capabilities.

We compare our numerical results derived with a seven wire strand model with contact case *II*, see eq. (2), with the analytical solution introduced in the previous section. Fig. 9 shows the analytical and numerical results for the three investigated helix angles $\alpha$. The analytical and numerical results show good agreement for all helix angles and thus validate our FE model. A minor deviation can be observed for the largest helix angle $\alpha_c$, where the FE solution exceeds the analytical solution at higher curvatures. Here, contact between the outer wires occurs in the FE model, which is not considered in the analytical solution, resulting in stiffer behaviour.

Fig. 10 shows the influence of the helix angle on the effective bending behaviour for the double (left) and seven wire strand models (right). Both figures show that the strand's stiffness decreases with an increasing helix angle. The analytical solution shown in Fig. 9 gives the same tendency. This result is caused by the fact that the bending behaviour of helix wires with a smaller helix angle tends towards the behaviour of straight wires, resulting in higher local material strain. The behaviour of wires with a higher helix angle, however, resembles the behaviour of a spring with smaller local strains in bending.

The presented model takes into account different contact states in the cross section, as defined in section 2.1. Fig. 11 allows for the comparison of the bending behaviour of the different models

https://doi.org/10.3311/ECCOMASMBD2021-144

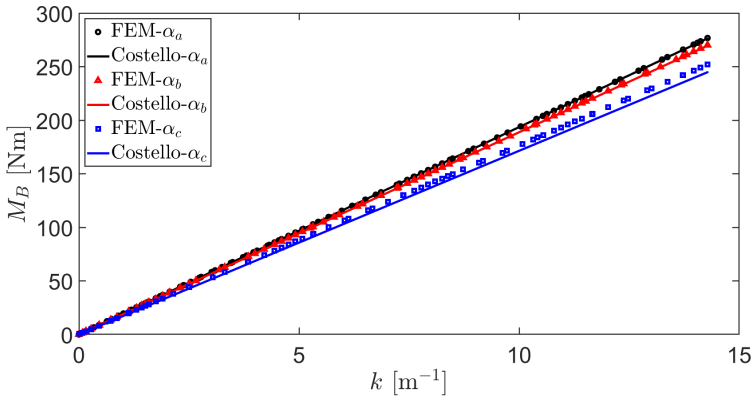


**Figure 9**. Comparison of analytical results derived using Costello's solution [16] with numerical results for seven wire strands with contact case II and helix angles $\alpha_a = 9°$, $\alpha_b = 18°$ and $\alpha_c = 36°$.

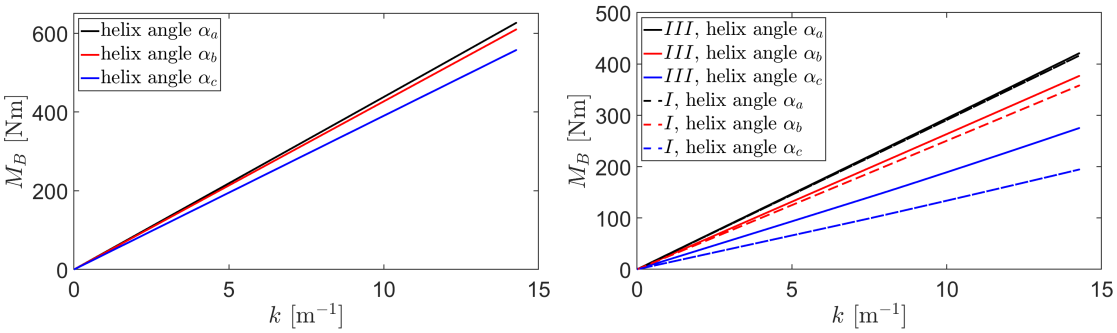


**Figure 10**. Influence of the helix angle used to model the wire strands on the effective bending behaviour. Left: Double helix model. Right: Seven wire strand models with contact cases I and III.

with helix angle $\alpha_b = 18°$. The results show that contact cases *I* and *III* yield similar results while contact case *II* shows significantly less stiff behaviour. In case *II*, the core wire is only in contact with the outer wires. In case *I* , the outer wires are in contact with each other and in case *III*, the outer wires are additionally in contact with the core wire. This means that for models with helix angle $\alpha_b = 18°$, the contacts between core and outer wires contribute less to the composite stiffness than contacts between outer wires. Similar behaviour can be observed for the smaller helix angle $\alpha_a = 9°$. For models with a higher helix angle $\alpha_c = 36°$, however, the model with contact state *I* shows the least stiff behaviour, see Fig. 12 while contact states *II* and *III* yield bending moments in a similar range. This implies that for this higher helix angle, the contacts between neighbouring outer wires contribute less to the effective stiffness of the composite structure.

Figures 11 and 12 additionally show the results for each model with frictional contact. For both helix angles, using frictional instead of frictionless contact results in hysteresis cycles. The smallest hysteresis cycle occurs for the model with contact state *II* and $\alpha_b$ and the largest for contact state *III* and $\alpha_c$. This coincides with the number of elements in contact in the respective models, which is lowest for contact state *II* and $\alpha_b$ and highest for contact state *III* and $\alpha_c$. The result for contact case *I* in Fig. 12 allows for the study of the curvature dependence of the frictional effects. Here, the hysteresis loop only opens after a curvature of approximately 8 m$^{-1}$ has been reached. The observation of the beam elements in contact yielded that this curvature marks the

https://doi.org/10.3311/ECCOMASMBD2021-144

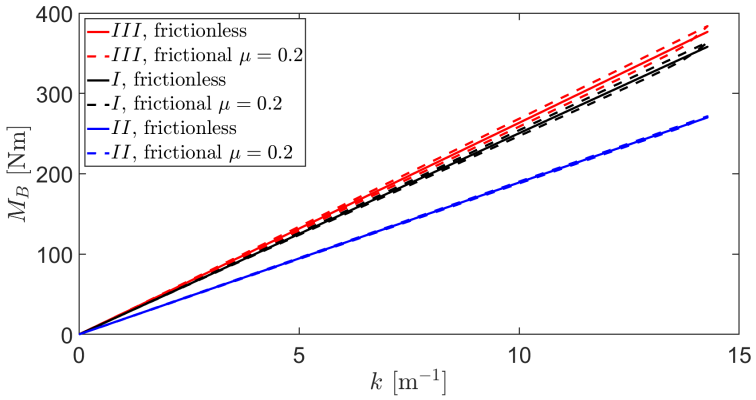


**Figure 11**. Simulation results for pure bending of seven wire models with helix angle $\alpha_b$ and different contact states *I, II* and *III*. For each model, results of frictionless and frictional contact are given.

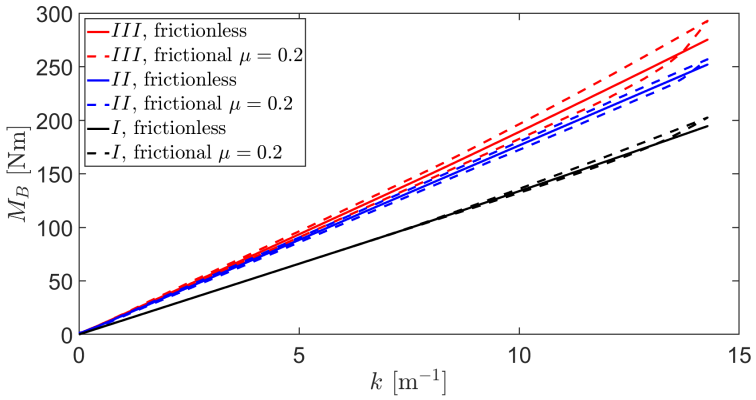


**Figure 12**. Simulation results for pure bending of seven wire models with helix angle $\alpha_c$ and different contact states *I, II* and *III*. For each model, results of frictionless and frictional contact are given.

onset of sliding between elements in contact leading to frictional behaviour. Below this curvature, the beam elements do not slide on each other and the frictional model does not contribute to the bending moment.

We will now take a closer look at simulation results obtained with double wire strand models. Fig. 13 shows the pure bending results using a frictionless and frictional contact model for the strand model with helix angle $\alpha_a$. It shows that the use of frictional contact has no influence on the bending moment of the double wire strand. Closer investigations showed, that almost no sliding between beam elements occurs in this structural model under pure bending. Consequently, the choice of frictional contact cannot influence the response of the composite model. This is also the case for larger helix angles.

In order to enforce sliding between the beam elements in the double wire strand, additional restrictions on the wire movement were introduced by adding rigid body rings with bonded contact, as described in section 2.2. Fig. 14 shows the resulting bending moments for frictionless and frictional contact for these models. One additional rigid body ring in the middle of the strand increases the stiffness of the composite model more than two rings. Furthermore, the hysteresis opens at a smaller bending curvature and the hysteresis cycle is bigger. This coincides with the fact that a

https://doi.org/10.3311/ECCOMASMBD2021-144

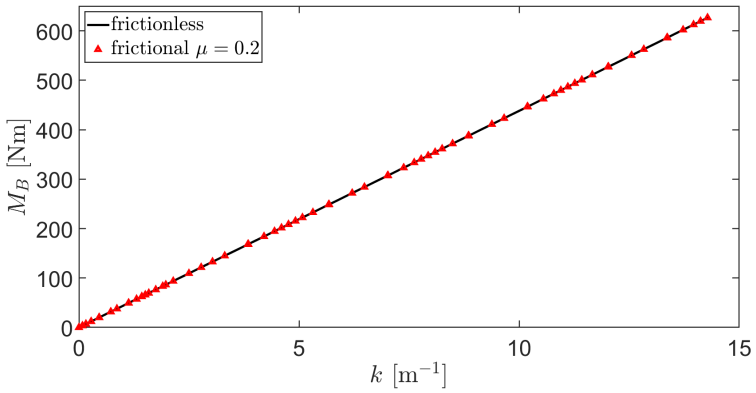


**Figure 13**. Influence of friction on the double wire strand model with helix angle $\alpha_a$.

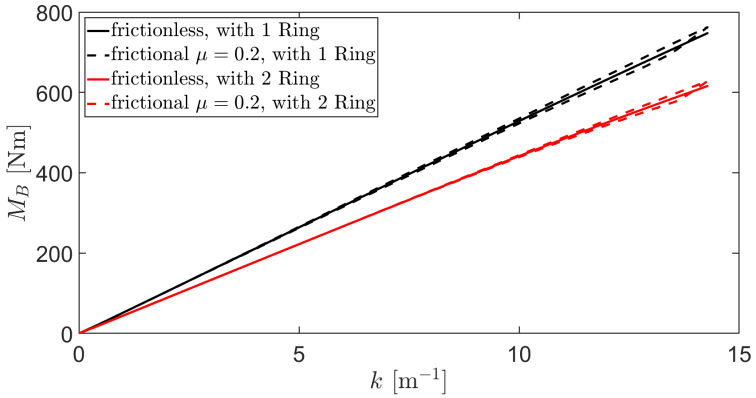


**Figure 14**. Influence of friction on the double wire models with helix angle $\alpha_a$ with one (black) or two (red) additional rigid body rings.

higher number of elements is in sliding contact during loading for the model with one ring, even though the percentage of elements in contact is higher in the original model without any rings.

## 4 CONCLUSIONS

In this work, we presented an approach to model the effective mechanical response of helix wire strands for the investigation of cable behaviour under mechanical load. A commercial finite element tool was used to generate structural models for double and seven wire strands. The wires were modelled as stress-free helices in the straight initial configuration accounting for different helix angles in different models. Frictionless and frictional contact models were used to investigate the influence of friction on the effective behaviour of the presented composite structures. The wires were modelled as materially linear elastic in order to avoid a superposition of material and structural inelastic effects. The FE models of the wire strands were used for virtual pure bending experiments.

We have shown that the presented modelling approach is useful to improve the understanding of the influence of structural effects on the composite behaviour. The results show that structural parameters such as the helix angle of the wires, already has an influence on the resulting behaviour, even for frictionless contact. Furthermore, the results showed that special attention has to be paid to correct modelling of the cross section and definition of the contacts within the cross section of the composite structure as the number of contacts strongly affects the deformation behaviour. The

influence of friction on the results depends on the specific structural model and can be impacted by objects in the environment. In this work we took first steps to simulate objects relevant for cable bundle assembly by adding rigid body rings to the double helix structure.

While this work shows the capabilities and usefulness of the FE wire strand models for the investigation of structural effects occurring under bending load, the model does not suffice to represent the complex inelastic behaviour of a real cable as shown in Fig. 1 right. Thus, a comparison of simulation results with experimental results is not possible, yet. In order to approach the inelastic behaviour of a real cable specimen, the material model of the wires has to be extended to an elasto-plastic model and the viscoplastic polymer jacket has to be added. It has been shown in previous work [14], that the qualitatively different behaviour in the first and following cycles is a result of initial damage during the first load cycle, e.g. detachment of the jacket from wires. Consequently, a proper approach to model the interactions between wires and the polymer layer has to be used. Another option is the generation of experimental data for simplified cable strands using elastic wires to approach the wire strand models presented here.

## REFERENCES

[1] Linn, J., Dreßler, K.: Discrete Cosserat Rod Models Based on the Difference Geometry of Framed Curves for Interactive Simulation of Flexible Cables. Mathematics in Industry, vol 27. Springer, Cham. (2017)

[2] Linn, J., Hermansson, T., Andersson, F., Schneider, F.: Kinetic Aspects of Discrete Cosserat Rods. In: Proceedings of the 8th ECCOMAS Thematic Conference on Multibody Dynamics, Prague (2017)

[3] Hermansson, T.: Computational Methods for Deformable 1D Objects in Virtual Product Realization. PhD thesis, Chalmers Tekniska Hogskola (Sweden) (2017)

[4] Zienkiewicz, O.C., Taylor, R.L., Zhu, J.Z.: The finite element method: its basis and fundamentals. Elsevier (2005)

[5] Chiang, Y.J.: Characterizing simple-stranden wire cables under axial loading. Robust Engineering Company, MI, USA (1996)

[6] Nawrocki, A., Labrosse, M.: A finite element model for simple straight wire rope strands. Department of Mechanical Engineering, Department of Biomedical Engineering, The University of Akron, Akron, OH 44325-0302, USA (1999)

[7] Sun, J.F., Wang, G.L., Zhang, H.O.: Elasto-plastic contact problem of laying wire rope using FE analysis. Springer-Verlag London Limited (2005)

[8] Ghoreishi, S.R., Messager, T., Cartraud, P., Davies, P.: Validity and limitations of linear analytical models for steel wire strands under axial loading, using a 3D FE model. International Journal of Mechanical Sciences, Volume 49, Issue 11 (2007)

[9] Stanova, E., Fedorko, G., Fabian, G.M., Kmet, S.: Computer modelling of wire strands and ropes Part II: finite element-based applications. Advances in Engineering Software,Volume 42, Issue 6 (2011)

[10] Foti, F., de Luca di Roseto, A.: Analytical and finite element modelling of the elastic–plastic behaviour of metallic strands under axial–torsional loads. International Journal of Mechanical Sciences, Volumes 115–116 (2016)

[11] Stanova, E., Fedorko, G., Fabian, G.M., Kmet, S.: Computer modelling of wire strands and ropes Part I: Theory and computer implementation. Advances in Engineering Software,Volume 42, Issue 6 (2011)

[12] Dörlich, V., Linn, J., Diebels, S.: Flexible beam-like structures - experimental investigation and modeling of cables. In: Advances in Mechanics of Materials and Structural Analysis. Springer (2018) 27–46

[13] Dörlich, V., Linn, J., Diebels, S.: Bending of Viscoplatic Cables. Proceedings in Applied Mathematics and Mechanics (2017)

[14] Dörlich, V., Cesarek, P., Linn, J., Diebels, S.: Experimental investigation and numerical modeling of resultant-based bending plasticity in cables. In: Proceedings of the 8th ECCOMAS Thematic Conference on Multibody Dynamics, Prague (2017)

[15] ANSYS: Mechanical User's Guide (2020 R2). `https://ansyshelp.ansys.com` (September 24, 2021)

[16] Costello, G.A.: Mechanical Engineering Series-Theory of Wire Rope, 2nd ed. Springer, New York (1997)

https://doi.org/10.3311/ECCOMASMBD2021-156

ECCOMAS Thematic Conference on Multibody Dynamics
December 12 - 15, 2021, Budapest, Hungary

# First Steps in Data Based Constitutive Modelling of Inelastic Effects in Composite Cables Using Preisach Hysteresis Operators

**Davide Manfredo**[1,2], **Vanessa Dörlich**[1], **Joachim Linn**[1], **Martin Arnold**[2]

[1] Fraunhofer ITWM
Fraunhofer Platz 1, 67663 Kaiserslautern, Germany
[davide.manfredo,vanessa.doerlich,joachim.linn]@itwm.fraunhofer.de
[2] Institute of Mathematics
Martin Luther University Halle-Wittenberg
Theodor-Lieser-Str. 5, 06120 Halle (Saale), Germany
martin.arnold@mathematik.uni-halle.de

## ABSTRACT

The present contribution aims at describing hysteresis behaviour arising from cyclic bending experiments on cables by means of the Preisach operator. As shown in pure bending experiments, slender structures such as electric cables behave inelastically and open hysteresis loops arise, with noticeable difference between the first load cycle and the following ones. The Preisach operator plays an important role in describing the input-output relation in hysteresis behaviours and it can be expressed as a superposition of relay operators. The definition of the Preisach plane occurs naturally from the definition of Preisach operator and hysteresis loops can be computed by integrating a suitable kernel function over a domain included in the Preisach plane. A mathematical formulation of the problem is introduced and a first attempt is made to mathematically determine the hysteresis behaviour that describes the relation between curvature and bending moment. Therefore, a suitable kernel function is identified in a way that its integration over the Preisach plane results in the bending moment of the specimen, and a comparison between different kernel functions is performed.

**Keywords:** Cable simulation, Cosserat rods, inelastic cable properties, data based constitutive modelling, Preisach hysteresis operators.

## 1 INTRODUCTION

Electric cables, as those shown in Fig. 1(a), are complex objects due to their multi-material composition and their geometric properties [1, 2]. Consequently, different internal interaction effects occur and lead to an observed effective inelastic deformation behaviour of such cables. Cyclic bending experiments show open hysteresis loops with noticeable difference between the first load cycle and the following ones, as shown in Fig. 1(c). In this regard, efforts have been made to develop inelastic constitutive models in the framework of geometrically exact Cosserat rods [3]. Fig. 1(b) describes the setup of the pure bending experiment as introduced in [2], which enables direct access to the bending moment and bending curvature. By applying only a bending moment on the specimen, a deformation state of pure bending is achieved. The configuration of the experiment ensures that no normal or shear forces act on the specimen during the experiment. The centerline of the specimen is bent into a circular arc with constant bending curvature and consequently constant bending moment along the specimen during the test.
In the framework of continuum mechanics, such deformation effects are modelled using suitable constitutive equations for specific material behaviour [4, 5]. In the presented work, we aim at modelling the observed behaviour on an abstract level using hysteresis operators. The choice of this mathematical framework has been motivated by the ability of such operators to describe hysteresis phenomena with enough generality and without the need of a priori assumptions on the material behaviour.

https://doi.org/10.3311/ECCOMASMBD2021-156

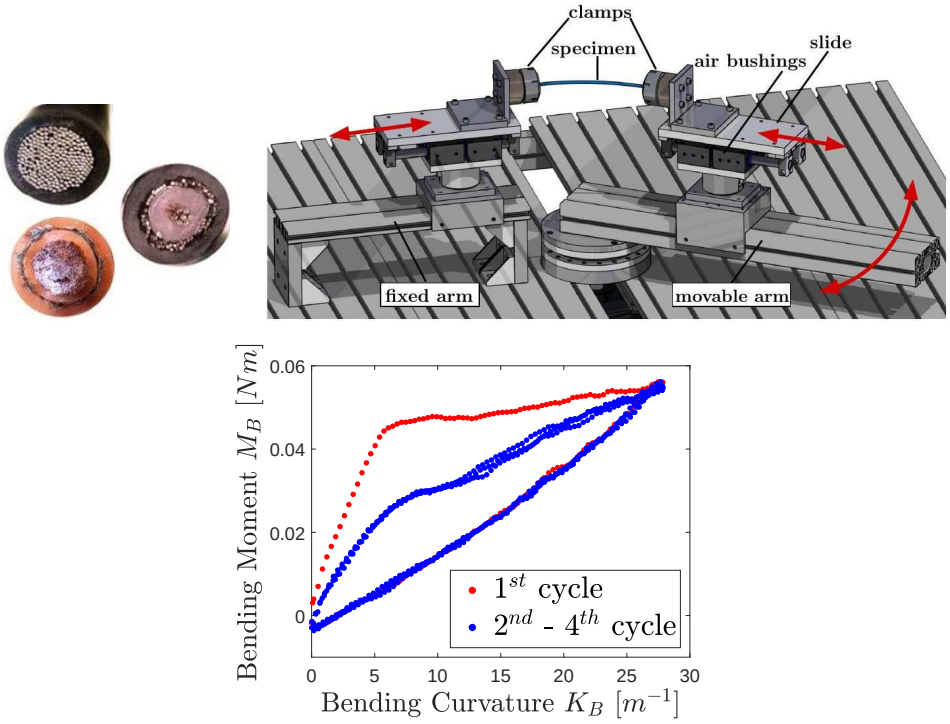


**Figure 1**. (a) Cross sections of different electric cables. (b) Pure bending test rig. (c) Bending moment vs. bending curvature diagram measured in a pure bending experiment.

## 2 HYSTERESIS OPERATORS

With hysteresis, we refer to a relation between two scalar time dependent quantities that cannot be expressed in terms of a single-valued function [6], and this relationship describes a rate independent memory effect [7], i.e. the output is invariant with respect to changes of the time scale, and at each time $t$ it may depend not only on the value of the input at time $t$, but also on its previous evolution. As shown in [6, 7, 8], hysteresis and hysteresis operators are a well-studied topic with a variety of applications, mainly hysteresis effects arising from electric and magnetic phenomena. The Preisach operator $\mathscr{P}$ plays a major role in modelling the input-output relation in hysteresis behaviours and can be expressed as a superposition of relay operators $\mathscr{R}$.
In this section, we will denote by $v(t)$ any input function and by $w(t)$ any output function, even when talking about specific cases (e.g. bending curvature and bending moment), whereas in the next section the notation will become more specific.

### 2.1 Relay operator

Given any couple $(a_1, a_2) \in \mathbb{R}^2$ with $a_1 < a_2$, we introduce the relay operator $\mathscr{R}_{a_1,a_2}$. For any continuous input function $v \in \mathscr{C}([0,t_{end}])$, starting from an initial value $\xi \in \{\pm 1\}$, the output

$$w = \mathscr{R}_{a_1,a_2}[v,\xi] : [0,t_{end}] \to \{\pm 1\} \tag{1}$$

will be equal to $-1$ if the input function $v(t)$ crosses the threshold value $a_1$ from above, and will be equal to $+1$ if $v(t)$ crosses the threshold value $a_2$ from below.
Formally, this can be expressed as

$$w(0) := \begin{cases} -1, & v(0) \le a_1 \\ \xi, & a_1 < v(0) < a_2 \\ 1 & v(0) \ge a_2 \end{cases} \tag{2}$$

https://doi.org/10.3311/ECCOMASMBD2021-156

and for any $t \in ]0, t_{end}]$, setting $X_t = \{\tau \in ]0,t] : v(\tau) = a_1 \text{ or } v(\tau) = a_2\}$,

$$w(t) := \begin{cases} w(0), & X_t = \emptyset \\ -1, & X_t \neq \emptyset \text{ and } v(\max(X_t)) = a_1, \\ 1 & X_t \neq \emptyset \text{ and } v(\max(X_t)) = a_2. \end{cases} \tag{3}$$

The relay operator can be interpreted as a switch operator between the values $-1$ and $+1$, with switching interval of width $a_2 - a_1$ and centered in $\frac{a_2+a_1}{2}$. A graphical representation of the relay operator is given in Fig. 2.

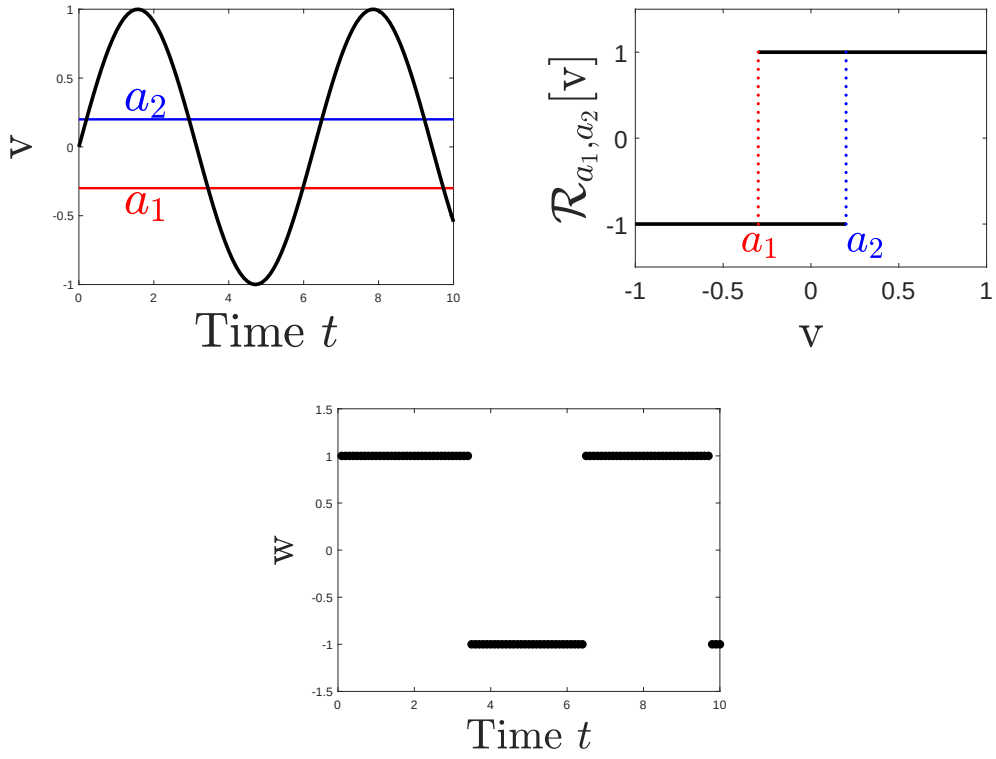


**Figure 2**. (a) Input function $v(t) = \sin(t)$, with $t \in [0, 10]$. (b) Diagram of the relay operator with $a_1 = -0.3$ and $a_2 = 0.2$. (c) Output function $w(t) = \mathscr{R}_{a_1,a_2}[v, \xi](t)$, with initial value $\xi = 1$.

From the next subsection, for simplicity of notation, we will omit the initial value $\xi$ when writing the relay operator $\mathscr{R}_{a_1,a_2}[v](t)$. This choice is justified by the fact that one could assume $\xi = -1$ or $\xi = 1$ without loss of generality.

### 2.2 Preisach operator

In the early 1930s, Preisach investigated whether the magnetisation in ferromagnetic materials adjusts without inertia to the applied magnetic field. Performing switching experiments allowed him to affirm the question, and he postulated that the magnetisation depends on the magnetic field through a linear superposition of relay operators. Hence, the previously described relay operator is the "building block" of the Preisach operator, which is in fact defined as a superposition of relay operators multiplied by a suitable kernel function $\omega(r,s)$, assumed to vanish for large values of $|s|$ and $r$,

$$w(t) = \mathscr{P}[v](t) = \int_0^{+\infty} \int_{-\infty}^{+\infty} \omega(r,s) \mathscr{R}_{s-r,s+r}[v](t) ds dr. \tag{4}$$

https://doi.org/10.3311/ECCOMASMBD2021-156

Here, $v(t)$ and $w(t)$ are respectively the input (Fig. 3(a)) and the output function, $s$ and $r$ are the coordinates of the Preisach plane, and $\mathscr{R}_{s-r,s+r}[v](t) \in \{\pm 1\}$ is the relay operator with switching interval of width $2r$ and centered in $s$. Preisach provided a simple geometrical interpretation for the operator $\mathscr{P}$, which turns out to be very useful from an operative point of view. If we consider an input function $v(t)$, for every time $t$ we determine the sets

$$A_{\pm}(t) = \{(r,s) \in \mathbb{R}_+ \times \mathbb{R} : \mathscr{R}_{s-r,s+r}[v](t) = \pm 1\}. \tag{5}$$

The union of such sets corresponds to the so-called Preisach plane.
Let $v : [0,t_E] \to \mathbb{R}$ be a piecewise monotone function, with monotonicity partition $0 = t_0 < t_1 < \cdots < t_N = t_E$. One can verify (see [6])that the dividing line

$$B(t) = \partial A_+(t) \cap \partial A_-(t), \tag{6}$$

also called memory curve, at each time $t$ is the graph of a function which can be defined recursively by

$$\begin{aligned} &\psi(0) = \max\{g^-(v(0)), \min\{g^+(v(0)), 0\}\} \\ &\psi(t) = \max\{g^-(v(t)), \min\{g^+(v(t)), \psi(t_i)\}\} \quad \text{for } t_i < t \le t_{i+1}, \quad 0 \le i \le N-1. \end{aligned} \tag{7}$$

Here, $g^-(v)$ denotes the straight line with slope $-1$ through the point $(0,v)$ and $g^+(v)$ denotes the straight line with slope $+1$ through the point $(0,v)$. Note that $B(t)$ carries the total memory information present in the system at time $t$ (see [6]).
In Fig. 3, starting from a specific input function (Fig. 3(a)) two examples of memory curves are deduced and depicted in Fig. 3(b). Fig. 3(b) depicts also one specific choice of subset of Preisach plane, i.e. the triangle $\{(r,s) | r \in [0,28], -28 + r \le s \le 28 - r\}$. If we consider the blue line to be the memory curve $B(t_\alpha)$ for some $t_\alpha$, the sets $A_+(t_\alpha)$ and $A_-(t_\alpha)$ will be the parts of the Preisach plane respectively below and above the blue line. Analogously, assuming the red line to be the memory curve $B(t_\beta)$ for some $t_\beta$, $A_+(t_\beta)$ and $A_-(t_\beta)$ are the subsets of the Preisach plane respectively below and above the red line.
One can observe how the description of the Preisach plane depends on the specific input that is being considered as it will be explained more rigorously in the next section. In fact, in Fig. 3(b), the set $\{(r,s) | r \in [0,28], -28 + r \le s \le 28 - r\}$ is determined by

$$\max_{t \in [0,t_{end}]} v(t) = 28 \text{ and } \min_{t \in [0,t_{end}]} v(t) = 0 \tag{8}$$

where $v : [0,t_{end}] \to \mathbb{R}$ is the input function depicted in Fig. 3(a).
From this, one can already understand that the choice of a suitable subset of the Preisach plane could be modified depending on the features of the input function, as well as other specifics of the studied problem. For example, the most common choice is to work over a triangular subset of the Preisach plane, but one could also choose a rectangular subset (see [6]).
Using $\mathscr{R}_{s-r,s+r}[v](t) \in \{\pm 1\}$ and the definition of $A_{\pm}(t)$, (1) can be rewritten as

$$w(t) = \int_{A_+(t)} \omega(r,s) ds dr - \int_{A_-(t)} \omega(r,s) ds dr. \tag{9}$$

It should be noted that Preisach hysteresis operators provide a model for causal response (see [7]), such that the output value $w(t)$ at time $t$ depends only on inputs $v(t')$ at past times $t' \le t$. Thus, hysteresis loops can be computed by integrating a suitable kernel function $\omega(r,s)$ over a domain included in the Preisach plane.

https://doi.org/10.3311/ECCOMASMBD2021-156

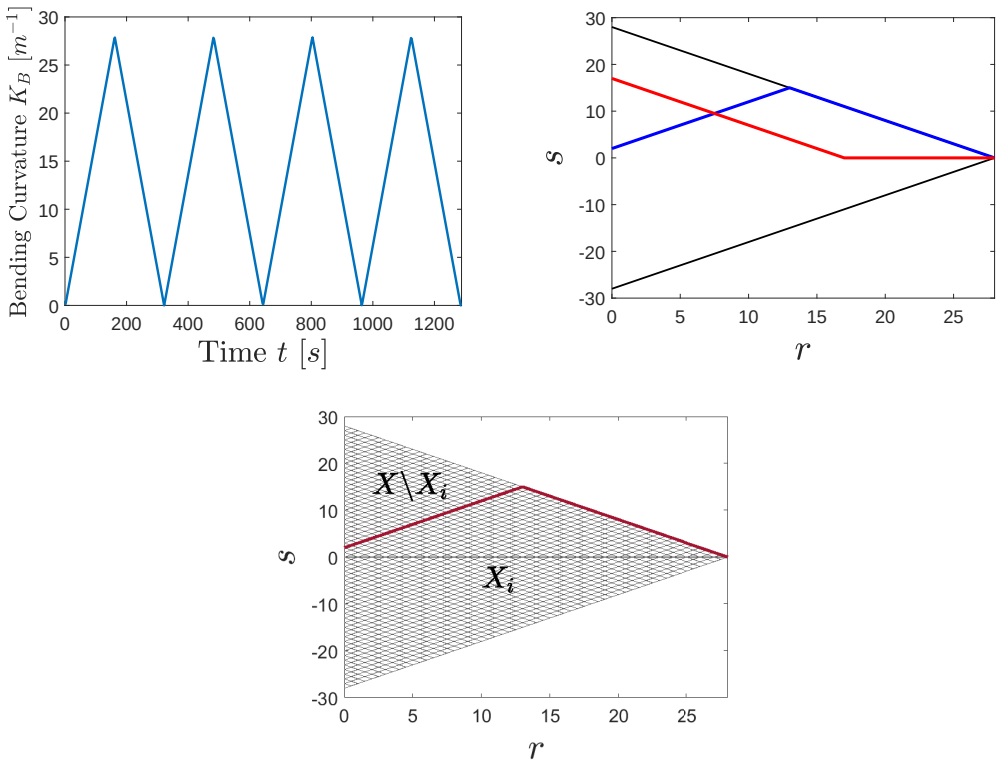


**Figure 3**. (a) Input given as curvature vs. time. (b) Domain (black triangle) included in the Preisach plane with two examples of memory curve. (c) Domain included in the Preisach plane with an example of triangulation and a memory curve.

## 3 PROBLEM

As previously mentioned, we would like to describe the relation input - output (bending curvature - bending moment), by means of the Preisach operator, utilising data coming from a pure bending cyclic experiment. This translates into finding a suitable kernel function $\omega(r,s)$ such that its integral over the Preisach plane results in a good approximation of the measured output. This topic has been of interest in the past decades, and several approaches have been presented, such as approximations techniques based on a finite number of optimally chosen experiments [9], approximation by means of neural networks [10, 11] and approximation by means of least square methods [12, 13, 14]. In this work, we utilise the latter.

### 3.1 Problem formulation

As shown in Fig. 1(c), we deal with measurements of bending moment values with respect to bending curvature value during 4 consecutive load cycles. The dataset that we will consider consists of $\{t_i\}_{i=1}^T$, bending curvature $\{K_{B_i}\}_{i=1}^T$ and bending moment $\{M_{B_i}\}_{i=1}^T$. Note that the values of time and bending curvature are prescribed by the experimental procedure, while the values of bending moment are measured. Moreover, it is relevant to underline that here the time represents rather an order parameter, than a time variable as it is normally considered. Since we are dealing with a rate independent process, the time data could be rescaled and shifted, without causing any change in our approach.

Starting from the input function, for each time step $t_i$, we recursively define the Preisach plane, i.e. the sets $A_{\pm}(t_i)$ and the memory curve $B(t_i)$ from (7). Thus, our goal is to find $\omega(r,s)$ such that the

https://doi.org/10.3311/ECCOMASMBD2021-156

following expression is minimised

$$\frac{1}{T}\sum_{i=1}^{T}\frac{1}{2}\left(M_{B_i}-\int\int_{A_+(t)}\omega(r,s)dsdr+\int\int_{A_-(t)}\omega(r,s)dsdr\right)^2. \tag{10}$$

To this end, we will take into account only a subset of the Preisach plane, in particular a subset of $\mathbb{R}_{\geq 0}\times\mathbb{R}$ spanned by the memory curve $B(t)$. More specifically, calling $K_B:[0,t_{end}]\to\mathbb{R}$ the bending curvature function (Fig. 3(a)), setting $m=\max\left(\left|\min_{t\in[0,t_{end}]}K_B(t)\right|,\left|\max_{t\in[0,t_{end}]}K_B(t)\right|\right)$ we consider the triangle

$$\{(r,s)|r\in[0,m],-m+r\leq s\leq m-r\}. \tag{11}$$

As shown in [13, 14], we choose a tolerance $d$ to round the input values and we divide the part of the Preisach plane crossed by the memory curve $B(t)$ in $n$ elements, such that at each time step, $B(t_i)$ lays on their edges (see Fig. 3(c)). We denote by $\{e^m\}_{m=1}^n$ the elements of the triangulation, $X\subset\mathbb{N}_+$ the set of indices given to the elements of the triangulation, and we define the following sets:

$$\begin{aligned}&X_i=\{m\in X|e^m \text{ below the memory curve at time } t_i\},\\&X\backslash X_i=\{m\in X|e^m \text{ above the memory curve at time } t_i\}.\end{aligned} \tag{12}$$

We observe that $\bigcup_{m\in X_i}\{e^m\}$ and $\bigcup_{m\in X\backslash X_i}\{e^m\}$ are the discrete corresponding sets of $A_+(t_i)$ and $A_-(t_i)$ respectively.

We assume that the kernel function $\omega(r,s)$ is piecewise constant over each element of the mesh, and we want to approximate the output as

$$M_{B_i}\approx\sum_{m\in X_i}\int\int_{e^m}\omega(r,s)dsdr-\sum_{m\in X\backslash X_i}\int\int_{e^m}\omega(r,s)dsdr\quad i=1,...,T. \tag{13}$$

Now, for each time step, we define the row vector $\boldsymbol{\Delta}_i=[\delta_i^1,...,\delta_i^n]$, where

$$\delta_i^m=\begin{cases}1 & \text{if } m\in X_i\\-1 & \text{if } m\in X\backslash X_i\end{cases}. \tag{14}$$

Calling $x^m=\int\int_{e^m}\omega(r,s)dsdr$, we have

$$\Delta=\begin{bmatrix}\boldsymbol{\Delta}_1\\\vdots\\\boldsymbol{\Delta}_T\end{bmatrix}\in\mathbb{R}^{T\times n},\quad \boldsymbol{X}=\begin{bmatrix}x^1\\\vdots\\x^n\end{bmatrix}\in\mathbb{R}^n,\quad \boldsymbol{Y}\in\begin{bmatrix}M_{B_1}\\\vdots\\M_{B_T}\end{bmatrix}\in\mathbb{R}^T. \tag{15}$$

Hence, the function to be minimised is $f(\boldsymbol{X})=\frac{1}{2}\|\Delta\cdot\boldsymbol{X}-\boldsymbol{Y}\|^2$.

In our case, we deal with insufficient experimental data (more unknowns than observations), hence the rank of the matrix $\Delta$ is $\text{rank}(\Delta)=q<\min\{T,n\}$. We then need to perform a singular value decomposition of the matrix $\Delta^T\Delta=USV^T$, where $S$ is a diagonal matrix, with $\text{rank}(S)=q$.

We extract $\hat{S},\hat{U},\hat{V}$ from $S,U,V$, respectively, by eliminating the rows and the columns of $S$ that are zero, and the corresponding columns of $U$ and $V$. Setting $\boldsymbol{X}=\hat{V}\boldsymbol{Z}$, the expression to be minimised becomes

$$g(\boldsymbol{Z})=\boldsymbol{Z}^T\hat{S}\boldsymbol{Z}-\boldsymbol{Y}^T\Delta\cdot\hat{V}\boldsymbol{Y}. \tag{16}$$

It is easily verified, that once a minimiser $\boldsymbol{Z}^*$ of $g$ is found, then $\boldsymbol{X}^*=\hat{V}\boldsymbol{Z}^*$ minimises $f$.

### 3.2 Kernel function and approximated data

A minimiser $\boldsymbol{Z}^*$ of $g$ can be found using the Matlab function *quadprog*. In Fig. 4(a), an approximation of the kernel function $\omega(r,s)$ is shown, and the integral of such kernel function over the domain included in the Preisach plane results in the diagram shown in Fig. 4(c). Comparing the experimental data in Fig. 1(c) with the diagram in Fig. 4(c), one can see that this approach describes the relation input - output (i.e. bending curvature - bending moment) observed during the experiments quite well. One should note that the step-like behaviour of the diagram in Fig. 4(c) is due to the tolerance value $d$. However, the approximated kernel function shows a highly nonlinear behaviour.

https://doi.org/10.3311/ECCOMASMBD2021-156

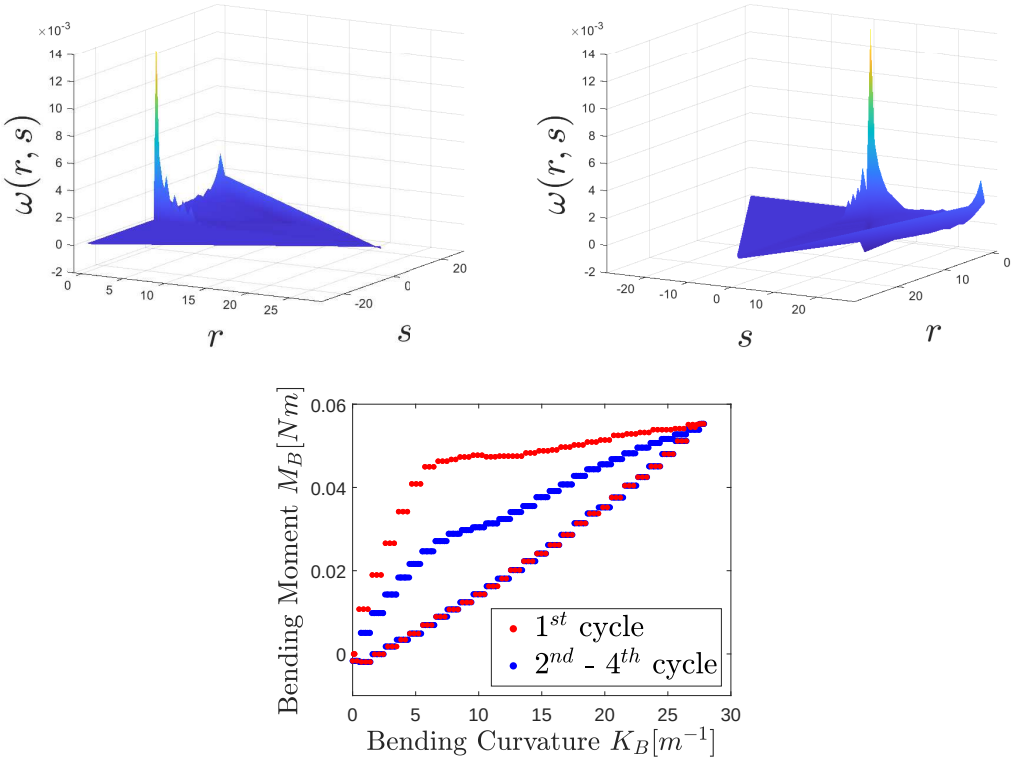


**Figure 4**. (a,b) Kernel function obtained by minimising 16, observed by different angles. (c) Estimated plot of bending moment vs. curvature obtained by means of the hysteresis operator.

## 4 COMPARISON OF DIFFERENT KERNEL FUNCTIONS

In this section we apply the described procedure to pure bending data coming from a similar yet different pure bending experiment, using the same cable type as in Fig. 1(c). As shown in Fig. 5, the experiment consists of a higher number of load cycles with increasing maximum bending curvature. For each maximum bending curvature $\{K_B^k\}_{k=1}^9$, three cycles are performed. Afterwards, the curvature is increased until the next maximum bending curvature and three cycles are executed on this level. This procedure is continued until a maximum bending curvature of $31.4\text{m}^{-1}$ is reached. This yields a total of 27 load cycles.

From these data, we extract those concerning loading cycles $10-12$ (purple) with maximal bending curvature $K_B^4 = 6.9\text{m}^{-1}$, cycles $16-18$ (yellow) with $K_B^6 = 10.4\text{m}^{-1}$, cycles $19-21$ (orange) $K_B^7 = 17.45\text{m}^{-1}$ and cycles $25-27$ (blue) with $K_B^9 = 31.4\text{m}^{-1}$. We treat these data as separate data sets and approximate separate kernel functions for each data set.

In Figs. 6, 7, 8, 9, we show on top the estimated kernel function seen from two different angles, on bottom left the measured values of the bending moment w.r.t bending curvature and on bottom right the estimated hysteresis diagram evaluated by means of the kernel function integrated over the suitable subset of the Preisach plane. One can notice that with this experiment, the difference in the hysteresis diagrams between the first cycle and the following ones is less visible, probably due to the fact that the cable is bent many times on one bending curvature, adding damage incrementally from one curvature level to the next. In the experiment shown in Fig. 1(c), the whole damage accumulation occurs during the first load cycle.

At first, one can notice how the Preisach operator is able to reproduce very different hysteresis behaviours, either with noticeable difference between first and following loading cycles (Fig. 4, 6, 7, 8) and with static hysteresis (Fig. 9). Observations can be made by comparing Fig. 4 and 9. Both

https://doi.org/10.3311/ECCOMASMBD2021-156

cases deal with similar maximal values of bending curvature as input. In Fig. 4, the bending moment in the first cycle differs from the following ones and the identified kernel function is non-smooth. In Fig. 9, however, the bending moment shows a static hysteresis as there is no difference between the cycles and the kernel function appears smoother.

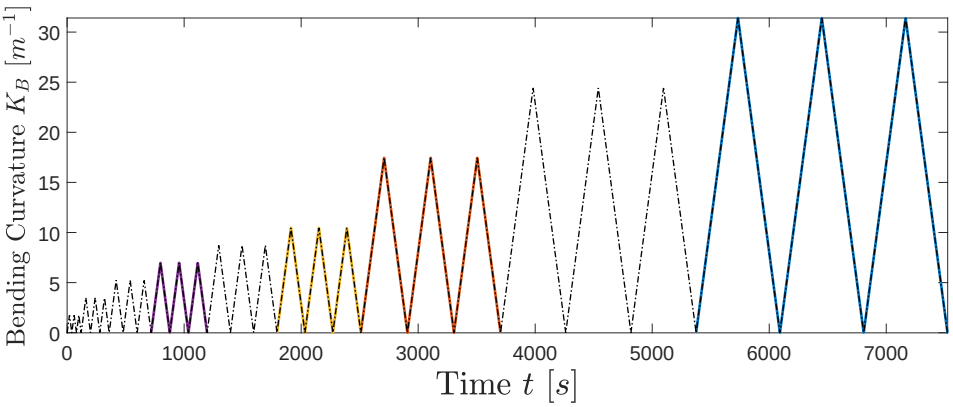


**Figure 5**. Input given as bending curvature vs. time. The purple, yellow, orange and blue parts are the input of Figs. 6, 7, 8, 9 respectively.

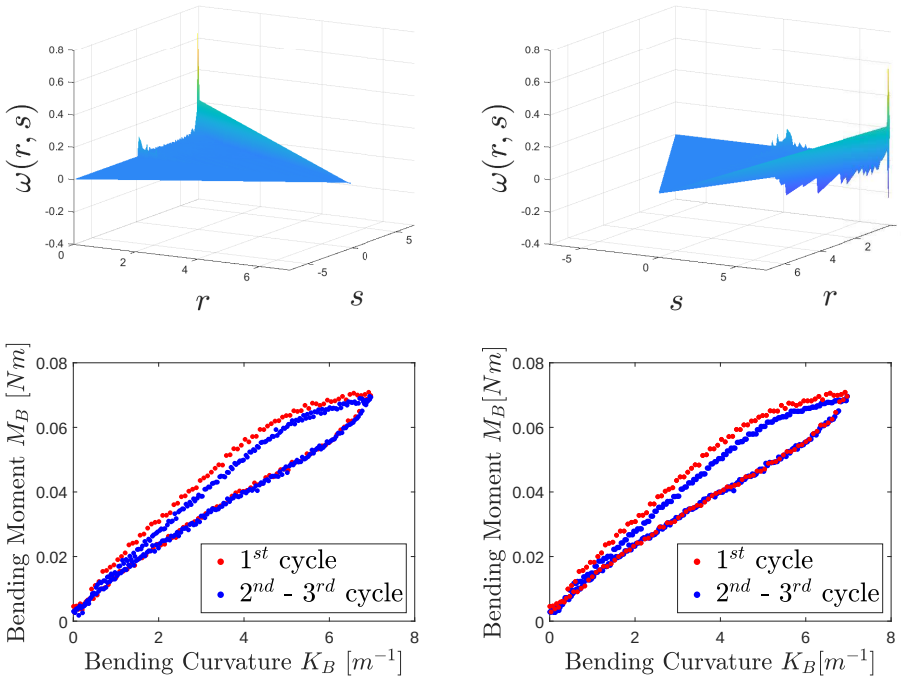


**Figure 6**. Results for cycles 10 - 12. (a), (b) Estimated kernel function seen from two different angles. (c) Measured bending moment vs. bending curvature, starting from a piecewise linear input (bending curvature). (d) Estimated plot of bending moment vs. curvature.

https://doi.org/10.3311/ECCOMASMBD2021-156

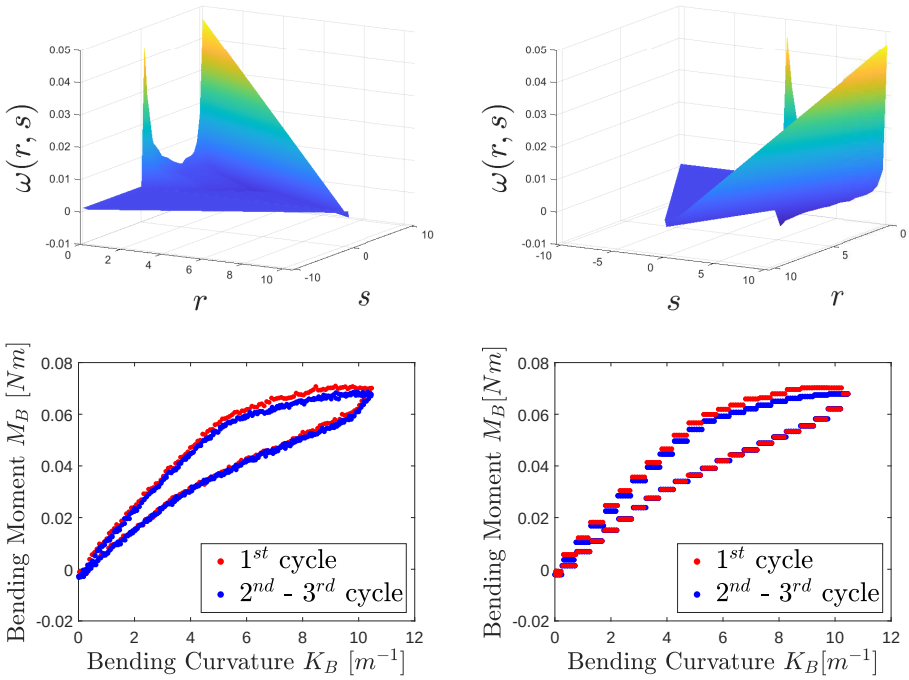


**Figure 7**. Results for cycles 16 - 18. (a), (b) Estimated kernel function seen from two different angles. (c) Measured bending moment vs. bending curvature, starting from a piecewise linear input (bending curvature). (d) Estimated plot of bending moment vs. curvature.

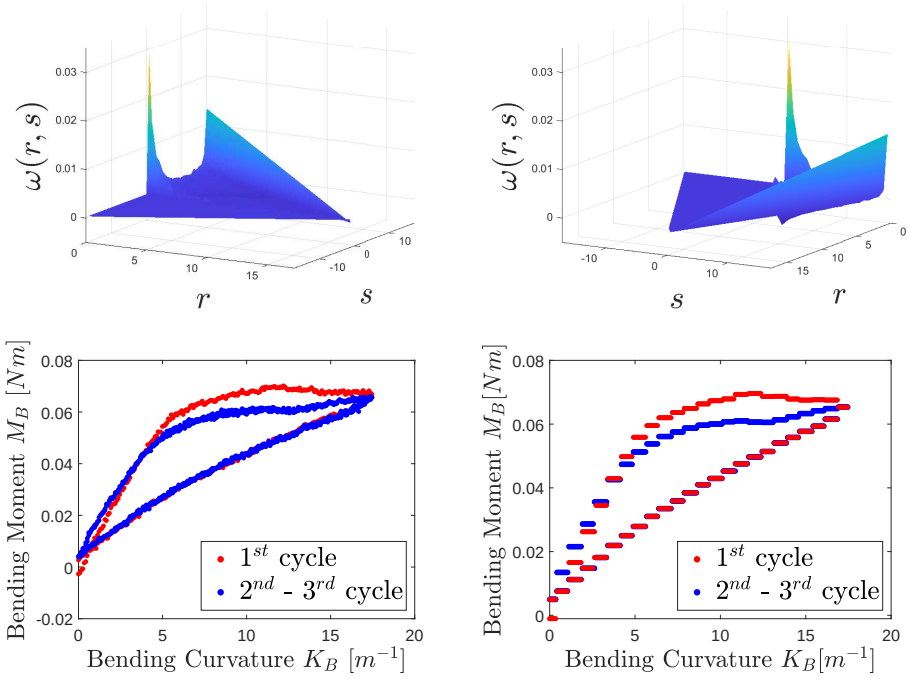


**Figure 8**. Results for cycles 19 - 21. (a), (b) Estimated kernel function seen from two different angles. (c) Measured bending moment vs. bending curvature, starting from a piecewise linear input (bending curvature). (d) Estimated plot of bending moment vs. curvature.

https://doi.org/10.3311/ECCOMASMBD2021-156

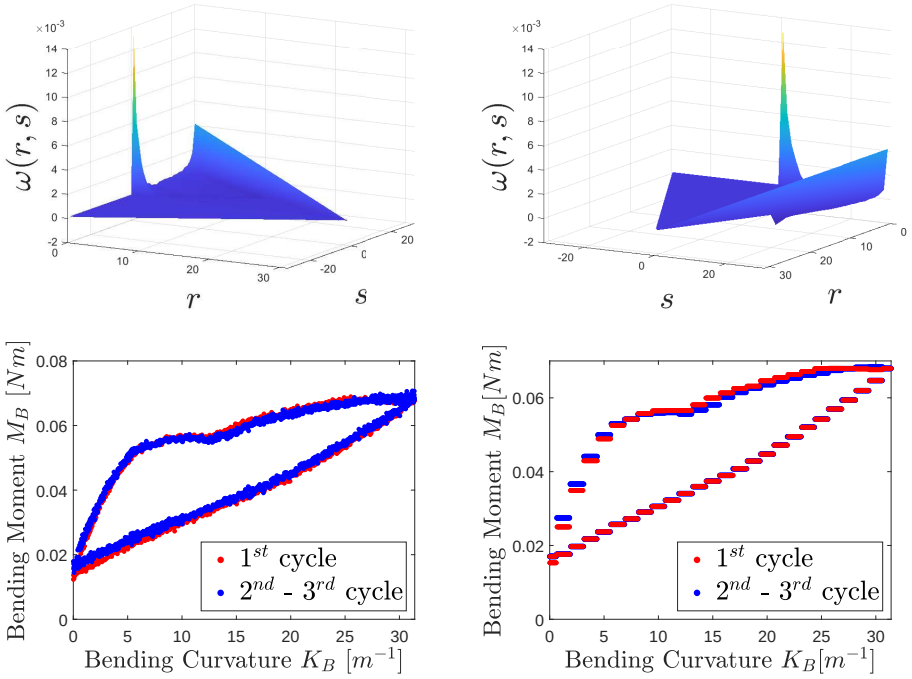


**Figure 9**. Results for cycles 25 - 27. (a), (b) Estimated kernel function seen from two different angles. (a) Measured bending moment vs. bending curvature, starting from a piecewise linear input (bending curvature). (d) Estimated plot of bending moment vs. curvature.

## 5 CONCLUSION

The Preisach operator seems to be a very powerful and versatile tool to describe inelastic deformation behaviours of electric cables and the consequent open hysteresis loops arising from bending experiments. Moreover, such mathematical tool captures the different hysteresis cycles very well and is relatively easy to implement. However, the interpretation and the comparison of kernel functions in different cases appear non-trivial, even when observing similar phenomena. The possible correlation between the properties of the kernel function and the physical phenomenon should be topic of further investigation.

## ACKNOWLEDGMENTS

This project has received funding from the European Union's Horizon 2020 research and innovation programme under the Marie Skłodowska-Curie grant agreement No 860124.

## REFERENCES

[1] Dörlich, V., Linn, J., Diebels, S.: Flexible beam-like structures - experimental investigation and modeling of cables. In: Advances in Mechanics of Materials and Structural Analysis. Advanced Structured Materials 80. (2018) 27 – 46 Springer International Publishing.

[2] Dörlich, V., Linn, J., Diebels, S.: Bending of viscoplastic cables. In: PAMM. Proceedings in Applied Mathematics and Mechanics 17. (2017) 293 – 294

[3] Dörlich, V., Češarek, P., Linn, J., Diebels, S.: Experimental investigation and numerical modeling of resultant-based bending plasticity in cables. In: ECCOMAS Thematic Conference on Multibody Dynamics, Prague, Czech Republic (June 2017) 37 – 46

[4] Podio-Guidugli, P.: A Primer in Elasticity. Springer Netherlands (2000) ISBN:978-94-017-0594-3.

[5] Haupt, P.: Continuum Mechanics and Theory of Materials. Springer-Verlag Berlin Heidelberg (2001) ISBN:978-3-662-04775-0.

[6] Brokate, M., Sprekels, J.: Hysteresis and Phase Transitions. Springer-Verlag, New York, NY (1996) ISBN:978-1-4612-4048-8.

[7] Visintin, A.: Differential Models of Hysteresis. Springer-Verlag, Berlin Heidelberg (1994) ISBN:978-3-662-11557-2.

[8] Mayergoyz, I.: Mathematical Models of Hysteresis. Springer-Verlag New York (1991) ISBN:978-1-4612-3028-1.

[9] Hoffmann, K., Sprekels, J., Visintin, A.: Identification of hysteresis loops. Journal of Computational Physics **78**(1) (1988) 215 – 230 doi:10.1016/0021-9991(88)90045-9.

[10] Cirrincione, M., Miceli, R., Ricco Galluzzo, G., Trapanese, M.: Preisach function identification by neural networks. In: IEEE Transactions on Magnetics. (September 2002) 2421 – 2423 Vol 38.

[11] Zakerzadeh, M., Firouzi, M., Sayyaadi, H., Shouraki, S.: Hysteresis nonlinearity identification using new Preisach model-based artificial neural network approach. Journal of Applied Mathematics **2011**(SI1) (2011) 1 – 22 doi:10.1155/2011/458768.

[12] Hoffmann, K., Meyer, G.: A least squares method for finding the Preisach hysteresis operator from measurements. Numerische Mathematik **55**(6) (1989) 695 – 710 doi:10.1007/BF01389337.

[13] Shirley, M., Venkataraman, R.: On the identification of Preisach measures. In: Smart Structures and Materials 2003: Modeling, Signal Processing, and Control, San Diego, California, United States (2003) 326 – 336 Volume 5049.

[14] Joseph, D.: Parameter Identification for the Preisach Model of Hysteresis. Virginia Polytechnic Institute and State University, Blacksburg, Virginia, United States (2001) Ph. D. Thesis.

https://doi.org/10.3311/ECCOMASMBD2021-207



# Realistic parameters for dynamic simulation of composite cables using a damped Cosserat rod model

**Dominik Jungkenn[1], Fabio Schneider-Jung[1], Fredrik Andersson[2] and Joachim Linn[1]**

[1] Fraunhofer Institute for Industrial Mathematics ITWM
Department Mathematics for the Digital Factory (MDF)
Fraunhofer Platz 1, 67663 Kaiserslautern, Germany
(dominik.jungkenn, fabio.julian.schneider-jung, joachim.linn)@itwm.fraunhofer.de
[2] Fraunhofer Chalmers Research Centre for Industrial Mathematics FCC
Department Geometry and Motion Planning
Chalmers Science Park, 41288 Gothenburg, Sweden
fredrik.andersson@fcc.chalmers.se

## ABSTRACT

Digital prototyping presents one of today's biggest chances in boosting efficiency of product development in automotive industry. Handling flexible parts, such as cables and hoses, is a big challenge in this context. The software IPS Cable Simulation addresses this topic and solves the problem for a wide field of applications. To obtain reliable simulation results, a basic set of parameters describing the effective mechanical properties of the flexible parts is an essential part of the model. The development of the MeSOMICS measurement machine represents a practical solution to this need for experimental data. Additional challenges are related to dynamic simulations of vehicles in operation mode. To solve these, we introduced the durability and dynamics module as an extension to the established software. This leads to an extended set of required parameters. In order to obtain these dynamic parameters, two different experimental setups have been realized. The experiments investigate damped torsional and bending oscillations, and yield parameters that can conveniently be treated as effective viscous properties within the framework of our software.

**Keywords:** cable simulation, dynamics, Cosserat rods, damping parameters, measurements.

## 1 MOTIVATION AND STATE OF THE ART

In today's automotive industry, digital validation at an early stage has become a standard procedure in product development. This includes the validation of flexible parts such as cables and hoses. The variety of electronics used in modern vehicles has made the cable system one of the central parts when it comes to safety and function of the product. So far the simulation based validation of cables and hoses using the IPS software family has focused on the basic functionality of the vehicles, namely the proper design of moving parts (such as doors, lids or the suspension linkage and steering) as well as the validation of production processes (assembly and disassembly by human workers as well as robotic applications). We aim to extend the field of application for our software by simulations of products in more dynamical operation, where inertial and damping effects need to be considered, and generalize our models and simulation methods correspondingly.

### 1.1 Classical linear viscoelasticity

Extending the range of applications from static or sequentially performed quasistatic equilibrium computations to fully dynamic simulations driven by transient structural excitations, we need to include viscoelastic constitutive properties in our structural model to account for internal damping effects, besides elastic structural response and inertia. Very common are one-dimensional rheological models for this purpose, as have been described e.g. in [1], and more recently by [2] with

https://doi.org/10.3311/ECCOMASMBD2021-207

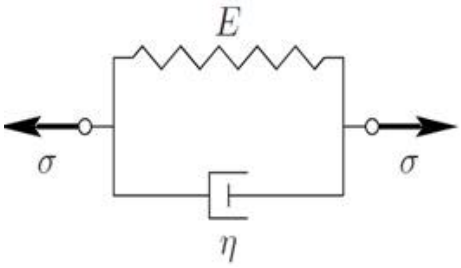


Figure 1: Schematic visualisation of a Kelvin-Voigt damping model

a focus on flexible multibody systems. These models usually consist of serial or parallel combinations of linear or nonlinear springs and dashpots, forming models of varying complexity. The Kelvin-Voigt (KV) type damping model, which we introduced in our previous work [3], is on the more simple part of the scale. It consists of an elastic spring-type and a viscous damper-type element connected in parallel (see Fig. 1). We refer to the conference paper [4] for basic numerical experiments exploring Cosserat rod dynamics with Kelvin-Voigt type viscous damping.

In the one dimensional case, the stress strain relation of the Kelvin-Voigt model reads:

$$\sigma = E\varepsilon + \eta\dot{\varepsilon} \tag{1}$$

Eqn. (1) with elastic modulus E and viscous damping $\eta$ results as an approximation of a more general rheological model of Generalized Maxwell (GM) type in the low frequency range, as briefly discussed in section 4.4 of [5]. In 3D solid mechanics, a similar constitutive model can be stated in tensorial form [6] following [7], as has been shown in [5] and more recently discussed by Bauchau and Nemani [2]. The latter paper focuses on Maxwell-type damping behavior of beams with rectangular cross-sections and non-negligible cross-sectional warping and is the most recent publication related to our research. The presented numerical experiments conclude in a general dissuasion against Kelvin-Voigt type modeling of viscoelastic beams. However, the use-cases presented by Bauchau and Nemani differ to a large extent from our field of application.

It turns out that in our application case the benefits of this simpler model outweigh the potential drawbacks of the model. In the so called Standard Linear Solid (SLS) model — this is defined [1] as a GM model with only one viscous Maxwell element, consisting of an elastic spring and a viscous damper in row, parallel to the elastic spring, equivalent to a one term Prony series — as well as in GM models of more complex type, stiffness and damping parameters are inevitably coupled as real and imaginary parts of a complex response function (see [14] Ch. XII §123). While this reflects the built-in causality of the material response, which is certainly a not only desired, but mandatory property for a proper material model, the hard wired coupling of elastic stiffness and viscous damping makes parameter identification for GM models a tedious task. Differently, the two parameters of the KV model can be adjusted independently, which turns out to be a favourable feature if one tries to match the effective, cross sectional response of a complicated composite structure as a cable (see Fig. 2). Trying to achieve the same with the 3 parameters of SLS model,

Figure 2: A collection of composite cables with complex cross sectional structure

our experience shows that one encounters substantial difficulties.

Therefore we still regard the KV approach to low frequency viscoelastic response of composite cable structures as the prefered choice. This paper aims to further substantiate that claim by applying physical experiments.

https://doi.org/10.3311/ECCOMASMBD2021-207

### 1.2 Viscoelastic rods

Most works on rods with viscoelastic properties deal with *linear* Euler–Bernoulli or Timoshenko beam models. In contrast, viscous damping models for *geometrically nonlinear* beams or rods are rarely found in literature. Notably, Antman [8] introduced a damping model of the form

$$\boldsymbol{F} = \hat{\mathbb{C}}_F \cdot (\boldsymbol{\Gamma} - \boldsymbol{\Gamma}_0) + \hat{\mathbb{V}}_F \cdot \dot{\boldsymbol{\Gamma}}, \qquad \boldsymbol{M} = \hat{\mathbb{C}}_M \cdot (\boldsymbol{K} - \boldsymbol{K}_0) + \hat{\mathbb{V}}_M \cdot \dot{\boldsymbol{K}} \tag{2}$$

with the cross section integrated viscous response given in the effective constitutive equations (2) for the material sectional forces and moments characterized by the diagonal matrices

$$\hat{\mathbb{V}}_F = diag(\gamma_{S1}, \gamma_{S2}, \gamma_E), \qquad \hat{\mathbb{V}}_M = diag(\gamma_{B1}, \gamma_{B2}, \gamma_T)\ , \tag{3}$$

with positive, but otherwise undetermined parameters. Antman's approach was primarily motivated as an artificial, regularizing viscous modeling element introduced to suppress the formation of shock waves in the hyperbolic dynamics of elastic Cosserat rods. For a brief review of other related work, we refer to [5], as well as to the more recent work of Bauchau et al. [2].

## 2 SHORT OVERVIEW OF THE VISCOELASTIC COSSERAT ROD MODEL

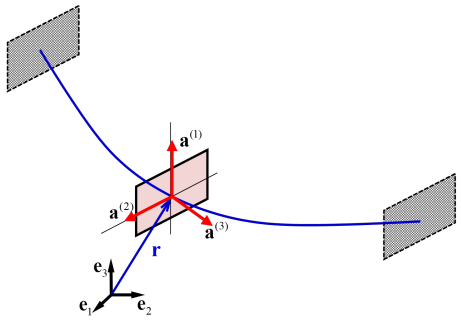


Figure 3: Schematic sketch of the centerline curve and moving frame defining a Cosserat rod.

The geometrically exact theory of Cosserat rods has been introduced by [9] and [10]. Following their work, our Cosserat rod is defined by its *centerline* curve $\boldsymbol{r}(s,t) = r_k(s,t)\boldsymbol{e}_k$, with cartesian component functions $r_k(s,t)$ w.r.t. the fixed global orthonormal frame $\{\boldsymbol{e}_1, \boldsymbol{e}_2, \boldsymbol{e}_3\}$ of Euclidian space, and the *"moving frame"* $\hat{\boldsymbol{R}}(s,t) = \boldsymbol{a}^{(k)}(s,t) \otimes \boldsymbol{e}_k \in SO(3)$ of orthonormal directors, booth smooth functions of the curve parameter $s$ and the time $t$. The local cross sections with normals $\boldsymbol{a}^{(3)}$ along the rod are spanned by the pair of directors $\{\boldsymbol{a}^{(1)}, \boldsymbol{a}^{(2)}\}$, as sketched in Fig. 3.

### 2.1 Material strain measures

The material strain measures associated to the configuration variables are given by the components $\Gamma_k = \boldsymbol{a}^{(k)} \cdot \partial_s \boldsymbol{r}$ of the tangent vector in the local frame (i.e.: $\boldsymbol{\Gamma} = \hat{\boldsymbol{R}}^T \cdot \partial_s \boldsymbol{r} = \Gamma_k \boldsymbol{e}_k$), with $\Gamma_1$, $\Gamma_2$ measuring *transverse shear deformation* and $\Gamma_3$ measuring *extensional dilatation*, and the *material Darboux vector* $\boldsymbol{K} = \hat{\boldsymbol{R}}^T \cdot \boldsymbol{\kappa} = K_k \boldsymbol{e}_k$, obtained from its spatial counterpart $\boldsymbol{\kappa} = K_k \boldsymbol{a}^{(k)}$ governing the Frénet equations $\partial_s \boldsymbol{a}^{(k)} = \boldsymbol{\kappa} \times \boldsymbol{a}^{(k)}$ of the frame directors, with $K_1$, $K_2$ measuring *bending curvature* w.r.t. the director axes $\{\boldsymbol{a}^{(1)}, \boldsymbol{a}^{(2)}\}$, and $K_3$ measuring *torsional twist* around the cross section normal. In general, the *reference configuration* of the rod, given by its centerline $\boldsymbol{r}_0(s)$ and frame $\hat{\boldsymbol{R}}_0(s) = \boldsymbol{a}_0^{(k)}(s) \otimes \boldsymbol{e}_k$, may have non-zero curvature and twist (i.e.: $\boldsymbol{K}_0 \neq 0$). However we may assume zero initial shear ($\Gamma_{01} = \Gamma_{02} = 0$), such that all cross sections of the reference configuration are orthogonal to the centerline tangent vector, which coincides with the cross section normal (i.e.: $\partial_s \boldsymbol{r}_0 = \boldsymbol{a}_0^{(3)} \Rightarrow \Gamma_{03} = 1$) if we choose the *arc–length* $s$ of the reference centerline as curve parameter.

https://doi.org/10.3311/ECCOMASMBD2021-207

### 2.2 Dynamic equilibrium equations

The constitutive equations (2) – or more general ones of viscoelastic type (see Ch. 8.2 in [11]) – are required to close the system of dynamic equilibrium equations

$$\partial_s \boldsymbol{f} + \boldsymbol{f}_{ext} = (\rho_0 A)\partial_t^2 \boldsymbol{r} \tag{4}$$

$$\partial_s \boldsymbol{m} + \partial_s \boldsymbol{r} \times \boldsymbol{f} + \boldsymbol{m}_{ext} = \partial_t(\rho_0 \hat{\boldsymbol{J}} \cdot \boldsymbol{\omega}) \tag{5}$$

which has to be satisfied by the *spatial* stress resultants $\boldsymbol{f} = \hat{\boldsymbol{R}} \cdot \boldsymbol{F}$ and stress couples $\boldsymbol{m} = \hat{\boldsymbol{R}} \cdot \boldsymbol{M}$ with appropriate boundary conditions (see [10]). The *inertial terms* appearing on the r.h.s. of the equations of the *balance of forces* (linear momentum) Eqn. (4) and the *balance of moments* (angular momentum) Eqn. (5) depend parametrically on the local *mass density* $\rho_0(s)$ along the rod as well as on geometrical parameters of the local cross section (i.e.: area $A(s)$ and area moment tensor $\hat{\boldsymbol{J}}(s,t) = \hat{\boldsymbol{R}} \cdot \hat{\boldsymbol{J}}_0(s) \cdot \hat{\boldsymbol{R}}^T$) and contain the accelerations of the centerline positions $\partial_t^2 \boldsymbol{r}(s,t)$ as well as the *angular velocity* vector $\boldsymbol{\omega}(s,t)$, which is implicitely defined by the the temporal evolution equations $\partial_t \boldsymbol{a}^{(k)} = \boldsymbol{\omega} \times \boldsymbol{a}^{(k)}$ of the frame in close analogy to the Darboux vector, and its time derivative $\partial_t \boldsymbol{\omega}(s,t)$ as dynamical variables (see [10], [11] and [3] for details).

### 2.3 Identification of minimal set of parameters for experimental work

For slow motions like opening or closing doors and lids a quasistatic approach yields the best trade-of between accuracy and speed. In this approach we utilize a geometrically non-linear Cosserat rod model and combine it with a linear constitutive model [12] and [5]. When searching for a solution of the non-linear balance equations, we use the minimization of potential energy, which (besides gravity and frictionless contact interaction) is determined by the elastic potential energy

$$\mathscr{V} = \frac{1}{2} \int_0^L \boldsymbol{\Gamma}^T \hat{\mathbb{C}}_\Gamma \boldsymbol{\Gamma} + \boldsymbol{K}^T \hat{\mathbb{C}}_K \boldsymbol{K} ds \tag{6}$$

with $\hat{\mathbb{C}}_\Gamma = diag(GA_1, GA_2, EA)$ and $\hat{\mathbb{C}}_K = diag(EI_1, EI_2, GJ_T)$. Here, the material strain and curvature measures are denoted as $\boldsymbol{\Gamma}$ and $\boldsymbol{K}$, respectively and the *effective stiffness parameters* of the cables

$$[GA_1], [GA_2], [EA], [EI_1], [EI_2] \text{ and } [GJ_T] \tag{7}$$

need to be determined for practical applications in cable simulation. For cables and hoses, we determine these parameters using the MeSOMICS test rig, a highly automated measurement setup that has been developed at ITWM [13] specially for cable simulation applications.

The kinematics of suspension linkage will, for instance, undergo substantially faster motions in dynamic operation scenarios in the frequency range up to 50 Hz. As a consequence, inertial and damping effects play a considerable role in the motion of cables and hoses that are attached to these parts of the vehicle. In order to simulate these kinds of scenarios, we have to move from the quasistatic to a transient simulation approach. Here we assume a Kelvin-Voigt-type material to take damping effects into account [3], as the considered frequency range is still on the slow side, compared to much faster internal relaxation effects of the involved materials. Therefore, we additionally consider dissipative effects modeled by the so called *dissipation function* [14][1]

$$\mathscr{D} = \int_0^L \dot{\boldsymbol{\Gamma}}^T \hat{\mathbb{V}}_\Gamma \dot{\boldsymbol{\Gamma}} + \dot{\boldsymbol{K}}^T \hat{\mathbb{V}}_K \dot{\boldsymbol{K}} ds \,, \tag{8}$$

with $\hat{\mathbb{V}}_\Gamma = diag(\eta_G A_1, \eta_G A_2, \eta_E A)$ and $\hat{\mathbb{V}}_K = diag(\eta_E I_1, \eta_E I_1, \eta_G J_T)$, and driven by the strain and curvature rates $\dot{\boldsymbol{\Gamma}}$ and $\dot{\boldsymbol{K}}$. In addition to the above mentioned effective stiffness parameters we need to obtain the *effective viscous parameters*:

$$[\eta_G A_1], [\eta_G A_2], [\eta_E A], [\eta_E I_1], [\eta_E I_2] \text{ and } [\eta_G J_T] \,. \tag{9}$$

[1] Eqn. (8) is deduced from the volumetric continuum version of the dissipation function of a *Kelvin-Voigt solid*, as discussed in [6] Ch. V §34 and [7], adapted to our Cosserat rod in [3]. For details, see also [5].

https://doi.org/10.3311/ECCOMASMBD2021-207

The number of parameters that need to be determined experimentally can be further reduced by utilizing theoretically deduced critical damping values for tensile, torsional and transverse shear vibrations [4]. In particular for tensile and shearing excitations, this is a reasonable simplification, since these have been shown to have negligible effects on the overall deformation behavior of the rod due to their high frequency and low amplitude characteristic.

According to the results of a linearized structural vibration analysis [4], effective critical damping values for extensional, torsional and transverse shear vibration modes are given by

$$[\eta_E A]_{cr} = \frac{4L}{\pi}\sqrt{\rho_L [EA]}\,, \quad [\eta_G J_T]_{cr} = \frac{4L}{\pi}\sqrt{[\rho_0 J_T][GJ_T]}\,, \quad [\eta_G A]_{cr} = 2\sqrt{[\rho_0 I][GA]}\,, \tag{10}$$

where $\rho_L = \rho_0 A$ is mass per length, and $[\rho_0 I] = \rho_L (I/A)$ and $[\rho_0 J_T] = 2[\rho_0 I]$ denote the rotational inertia parameters of the circular cross section, with $I_{1,2} \equiv I$ and $J_T = 2I$. While $[\eta_E A]_{cr}$ and $[\eta_G J_T]_{cr}$ scale proportional to the rod length $L$, $[\eta_G A]_{cr}$ scales proportional to the *radius of gyration* $\sqrt{I/A}$ of the cross section, independent of $L$.

For composite cables, neither $[GA]$ nor $[\eta_G A]$ are practically measurable quantities. Similarily, quasistatic and dynamic uniaxial tension experiments to determine $[EA]$ and $[\eta_E A]$ are plagued by systematic problems induced by often not well defined clamping of the cables at the boundaries. Although the approximation $[EA] \approx (A/I)[EI]$ typically underestimates tensional stiffness, it yields reasonable values for practical applications, as $[GA] \approx [EA]/3$ does. Eqn. (10) may then be used to calibrate effective damping parameters $[\eta_E A]$ and $[\eta_G A]$ w.r.t. their critical values.

Differently, effective torsional damping is directly accessible via a simple experimental setup. Also bending oscillations of cables can be investigated experimentally, as demonstrated in [15].

## 3 EXPERIMENT

Two experimental prototypes (similar to the stiffness measurements) have been set up and are being tested at ITWM. One is a dynamic bending test (see Figs. 4 and 5), the other setup is a dynamic torsion test, following the standard torsional pendulum test for measuring the torsional stiffness of plastics [16] (see Fig. 6, 7 and 8). In both tests the specimens are fixed on one end. The free end is deflected mechanically. After releasing, the decaying free oscillation is recorded using a high speed camera.

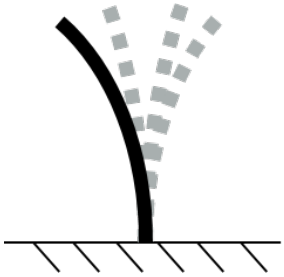

Figure 4: Schematic sketch of the experimental setup for bending oscillation measurements.

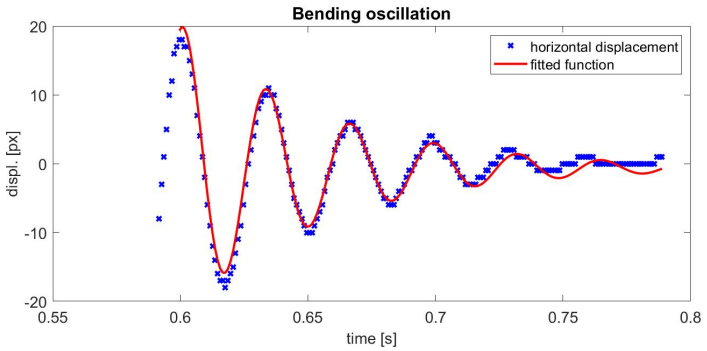


Figure 5: Data from an example measurement.

### 3.1 Dynamic bending test

The evaluation of the recorded data uses the *lsqnonlin*-function built-in in MATLAB to estimate the damped Eigenfrequency $\Omega$ and decay constant $\delta$ from the recorded data. Related dynamic bending stiffness and effective damping constant are computed based on Euler-Bernoulli beam theory

$$[EI]_{dyn} = \omega^2 C_{bc}\,, \qquad [\eta_E I] = 2\delta C_{bc}\,, \tag{11}$$

with $\omega = \sqrt{\Omega^2 + \delta^2}$ and constant $C_{bc} = \rho A \left(\frac{L}{\mu_0}\right)^4$ determined by boundary conditions.

https://doi.org/10.3311/ECCOMASMBD2021-207

### 3.2 Dynamic torsion test

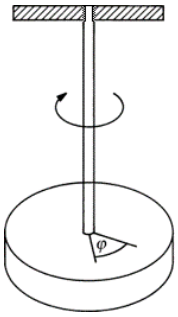


Figure 6: Measurement scheme for torsional oscillations.

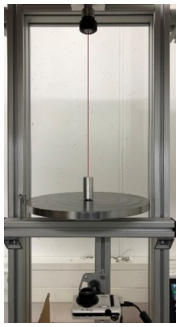

Figure 7: Experimental setup for torsion oscillations.

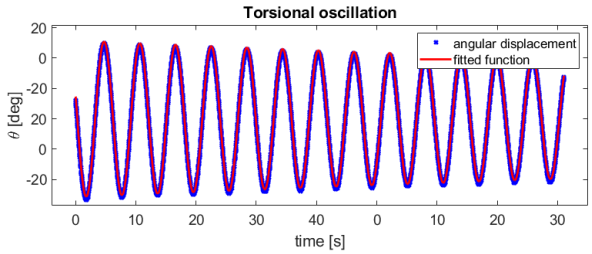


Figure 8: Extracted data from an example measurement.

The setup for measuring torsional oscillations (see Figs. 6, 7) resembles the well-known torsional pendulum, where the sample is fixed on one end, while the other end is attached to a heavy disc. After a manually induced initial torsional deflection, the experimental data displayed in Fig. 8 show that the disc rotates in a damped harmonic rotational oscillation.

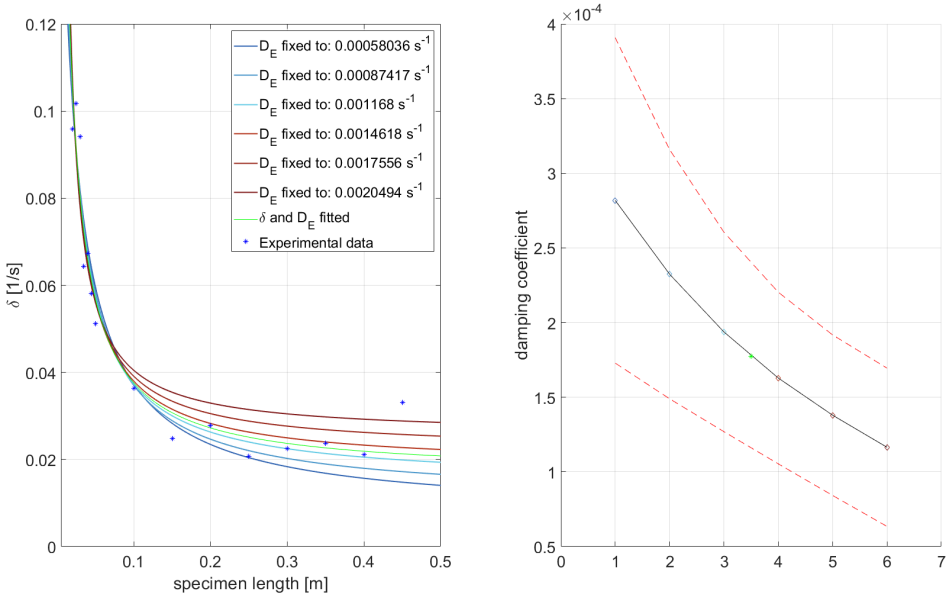


Figure 9: Torsional damping behavior for different specimen lengths. Left graph shows the 95% confidence interval for the fitting parameter related to $D_E$, depicted in six steps. Right graph shows the resulting uncertainty in $\delta$ for fixed values of $D_E$, based on the 95% confidence intervals of each individual fit with fixed values for $D_E$.

The recorded trajectories are fitted with a circular function to obtain the torsion angle $\varphi$ over time. The extracted data is then fitted analogous to the bending damping evaluation. With $J_{Disc}$ the inertial moment of the disc on the torsional pendulum and the cable mass neglected it holds

$$[GJ]_{dyn} = \omega^2 L J_{Disc} \ , \qquad [\eta_G J] \approx 2\delta L J_{Disc} - L D_E \ , \tag{12}$$

with $\omega = \sqrt{\Omega^2 + \delta^2}$ and $D_E$ summarizing damping effects occurring at the fixation of the specimen. In order to determine $D_E$ we need to increase sample length as much as possible, since the

term for the effective damping constant in (12) translates to

$$\delta \approx \frac{\frac{[\eta_G J]}{L} + D_E}{2J_{Disc}} \Rightarrow \delta \overset{L\to\infty}{\longrightarrow} \frac{D_E}{2J_{Disc}} \,. \tag{13}$$

However, since space in our setup is limited and recorded data shows significant variance (see Fig. 9), the estimation of $D_E$ is still under investigation. Upon variation of the specimen length we expect a behavior of $\delta$ that follows a $\frac{1}{L}$-trajectory, see Eqn. (13). At the moment, the uncertainty of $D_E$ based on the 95 % confidence interval in the fit considering $[\eta_G J]$ and $D_E$ as a parameter leads to a combined uncertainty range of about 184 % for $[\eta_G J]$, spanning from $0.635 \times 10^{-4} s^{-1}$ (lowest point of the lower red dashed line depicted in the right graph of Fig. 9) to $3.908 \times 10^{-4} s^{-1}$(highest point of the upper red dashed line depicted in the right graph of Fig. 9). This leads to a temporary loss of reliability for the results for $[\eta_G J]$. For further reading on the torsional damping measurement setup, see [17].

## 4 APPLICATION IN SIMULATION

We performed simulations of a cable of fixed length (200 mm) clamped to a rigid body that undergoes a sweep motion excitation (See Fig. 10).

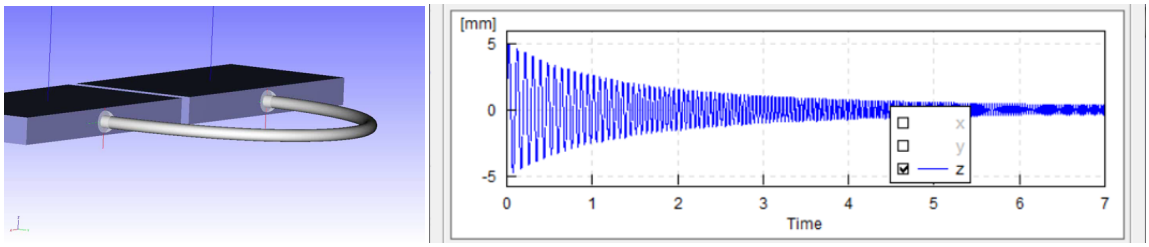


Figure 10: Setup of the virtual experiment (left) and applied sweep motion from 10 Hz to 38 Hz (right).

The resulting movement of the simulated cable is read out at the apex of the arch. In order to get a grasp of the sensitivity of a realistic use case against deviations in the measured damping value, we performed the simulation with varying values for $[\eta_E I]$. Reasonable boundaries for measured parameters are $\pm 50\%$ of the measured value as an already conservative estimation. The results for this interval is shown in Fig. 11. It appears, that with decreasing damping, the size of the amplitude envelope increases as expected (from left to right in the graphics row).

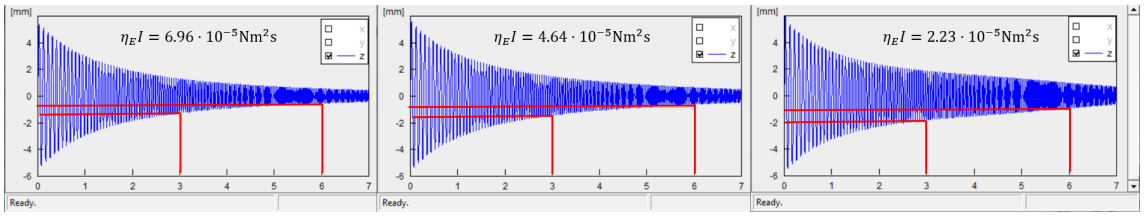


Figure 11: Resulting cable motion with values of 1.5 times the measured value, measured value and 0.5 times the measured value applied.

However, the changes in resulting motion are relatively small compared to the change in damping value. As a reference we compare the amplitudes at 3 s and 6 s of the sweep motion excitation, which refers to excitation frequencies of 22 Hz and 34 Hz, respectively (see red lines in Fig. 11). The amplitudes at these points differ only within $\pm 1$ mm from each other. In our field of application this represents a satisfying precision.

https://doi.org/10.3311/ECCOMASMBD2021-207

However, since the behavior does not change its characteristic within these boundaries, we decreased the applied damping value further to 1/5th and 1/10th of the measured value respectively. The results are shown in Fig. 12, which starts with the measured value applied and shows the effect of decreasing damping value from left to right. This simulation shows a clear appearance of a resonance at 5.5 s, which translates to 32 Hz in the sweep motion.

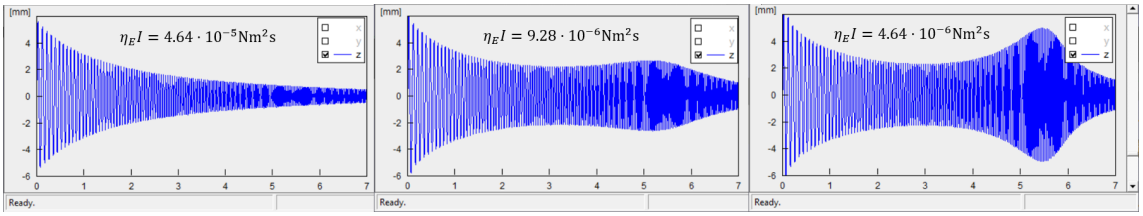


Figure 12: Resulting cable motion with values of measured value, 1/5th of the measured value and 1/10th of the measured value applied.

## 5 CONCLUSION

Our preliminary results are promising and indicate that the Kelvin-Voigt-type material model is suited to simulate dynamic behavior of cables and hoses within the considered time scale of low oscillation frequencies. Fitting the extracted motion data yields a damping value $[\eta_E I]$ (or $[\eta_G J]$) as well as a dynamic stiffness parameter $[EI]_{dyn}$ (or $[GJ]_{dyn}$). The obtained parameters can be used as effective mechanical properties within the framework of our simulation software.
While the results for bending oscillations have shown to be sufficiently robust, the interpretation of torsional oscillations is subject of ongoing research.

## 6 OUTLOOK

The simulation study shown in section 4 provides a lot of insight to the realistic use-case behavior. However, an additional validation experiment is subject of ongoing research in our department (see Fig. 13). This will yield further insight in terms of parametrization and applicability of the Kelvin-Voigt damping behavior.

Figure 13: Experimental setup for validation of simulation results.

https://doi.org/10.3311/ECCOMASMBD2021-207

## REFERENCES


[1] R.M. Christensen, Theory of Viscoelasticity, p. 1–34, 1982.

[2] Olivier A. Bauchau and Nishant Nemani, Modeling viscoelastic behavior in flexible multibody systems, *Multibody System Dynamics*, 51(2), p. 159–194, 2020.

[3] H. Lang, J. Linn and M. Arnold, Multibody dynamics simulation of geometrically exact Cosserat rods, *Multibody System Dynamics*, 25(3), p. 285–312, 2011.

[4] H. Lang, S. Leyendecker and J. Linn, Numerical experiments for viscoelastic Cosserat rods with Kelvin-Voigt damping, *Proceedings of ECCOMAS Thematic Conference on Multibody Dynamics*, p. 453–462, Zagreb, Croatia, 2013.

[5] Linn, J. and Lang, H. and Tuganov, A., Geometrically exact Cosserat rods with Kelvin–Voigt type viscous damping, *Mechanical Sciences*, 4(1), p. 79–96, 2013.

[6] L. D. Landau and J. M. Lifshitz , Theory of Elasticity, 1986.

[7] Jean Lemaitre and Jean-Louis Chaboche, Mechanics of Solid Materials, 1990.

[8] Stuart S. Antman, Invariant Dissipative Mechanisms for the Spatial Motion of Rods Suggested by Artificial Viscosity, *Journal of Elasticity*, 70(1-3), p. 55–64, 2003.

[9] E. Reissner, On One-Dimensional Large-Displacement Finite-Strain Beam Theory, *Studies in Applied Mathematics*, 52(2), p. 87–95, 1973.

[10] J.C. Simo, A finite strain beam formulation. The three-dimensional dynamic problem. Part I, *Computer Methods in Applied Mechanics and Engineering*, 49(1), p. 55–70, 1985.

[11] Stuart S. Antman, Elasticity, *Nonlinear Problems of Elasticity*, p. 457–530, 1995.

[12] J. Linn, T. Hermannsson, F. Andersson and F. Schneider, Kinetic aspects of discrete Cosserat rods based on the difference geometry of framed curves, *Proceedings of ECCOMAS Thematic Conference on Multibody Dynamics*, p. 163–176, Prague, Czech Republic, 2017.

[13] MeSOMICS Homepage: www.mesomics.eu.

[14] L. D. Landau and J. M. Lifshitz, Statistical Physics - Part I, 1980.

[15] F. Schneider, Y. Kunz, J. Linn, V. Dörlich and F. Andersson, Kelvin-Voigt Damping Parameters for cosserat rod dynamics, *ECCOMAS Multibody Dynamics Conference*, Duisburg, Germany, 2019.

[16] Kunststoffe - Bestimmung dynamisch-mechanischer Eigenschaften - Teil 2: Torsionspendel-Verfahren, *DIN EN ISO 6721-2:2019-09*.

[17] Philipp Knaus, Bestimmung der Torsionsdämpfung von Stäben und Kabeln, *Bachelor's thesis*, 2021, Technical University Kaiserslautern.

# Section
# VEHICLE DYNAMICS AND AEROSPACE APPLICATIONS

https://doi.org/10.3311/ECCOMASMBD2021-251



# Handling Evaluation of Tractor-semitrailer with Split Fifth Wheel Coupling Undergoing an ISO Double Lane Change Manoeuvre

**A. Jogi**[1], **S. Chandramohan**[1], **S. Dash**[2]

[1] Department of Mechanical Engineering
Indian Institute of Technology Madras
Chennai, India -600036
ajithjogi@gmail.com, sujatha@iitm.ac.in

[2] Department of Mechanical Engineering
National Institute of Technology Tiruchirappalli
Trichy, India -620015
sabyadash21@gmail.com

## ABSTRACT

Tractor-semitrailers face the issue of off-tracking which restricts their movement through congested areas. One of the innovative and passive methods to reduce off-tracking in tractor-semitrailers is to implement a Split fifth wheel coupling (SFWC). Studies show that off-tracking is reduced by up to 21% for a circular turning manoeuvre. The handling performance of the tractor-semitrailer with SFWC is not evaluated yet and hence needs to be ad-dressed. In the present work, in order to assess the handling performance of the vehicle with SFWC, simulations are carried out for ISO double lane change manoeuvre at various speeds. The results are compared with those of the Conventional fifth wheel coupling (CFWC) model to understand the relative performance of the tractor-semitrailer with SFWC. The results show that the performance of tractor-semitrailers with SFWC is on par with that of vehicles with CFWC at lower speeds; in fact, for speeds below 40 kmph, the lateral acceleration experienced by the semitrailer of SFWC vehicle is less compared to that of CFWC vehicle. However, it becomes a little unstable at higher speeds. With the development of stability control systems like Electronic stability control (ESC), optimized for tractor-semitrailers with SFWC, their performance would improve.

**Keywords:** Split fifth wheel coupling, Off-tracking, Hitch, Tractor-Semitrailer, DLC, Handling

## 1. INTRODUCTION

Tractor-semitrailers are articulated freight carrying vehicles, where a portion of the trailer's load is supported by the tractor. Usually, these are lengthy vehicles making them difficult to manoeuvre in congested roads, since the space required to take the turn increases with wheelbase. Off-tracking is a metric to measure this turning space, which is defined as the radial distance between the trajectory of the front and rearmost axles of a vehicle during the turning manoeuvre. Many researchers, including Jindra [1], Pretty [2] and Choi et al. [3] have worked on the modelling of off-tracking. Steering the semitrailer axle is one of the effective methods for reduction of off-tracking; however, it includes a complex system to control the steering, which makes it expensive. Jogi and Chandramohan [4] have developed a new hitch mechanism, termed Split fifth wheel coupling (SFWC) which reduces the maximum off-tracking by a significant margin. SFWC is a passive mechanism without the inclusion of complex systems.

It is necessary to evaluate the handling performance of the tractor-semitrailer with SFWC to ensure its safe operation. Double lane change (DLC) manoeuvre is one of the handling evaluation methods, wherein the vehicle swiftly changes its lane and comes back to its original lane to avoid an obstacle. There are various kinds of DLC specifications which have been compared with each other by Peng and Yang [5]. ISO DLC is one of the standards for such tests. ADAMS /Car tool is capable of performing the simulations of closed-loop ISO DLC test and provides good results [6].

https://doi.org/10.3311/ECCOMASMBD2021-251

### 1.1. SFWC

The Conventional fifth wheel coupling (CFWC) consists of a turntable fixed to the chassis of the tractor. It receives the kingpin of the semitrailer, forming a joint which serves not only as an articulation point, but also as the point of vertical load transfer from the semitrailer to the tractor. Figure 1 (a) shows the conceptual model of the tractor-semitrailer with CFWC. On the other hand, SFWC being a novel off-racking reduction mechanism, the articulation point and the point of vertical load transfer have been separated by a certain distance. It consists of two sub-units: cylindrical joint and roller mechanism, as shown in Figure 1 (b). The former takes care of articulation, whereas the latter allows the vertical load transfer from the semitrailer to the tractor even when the vehicle is articulating. Studies have shown that the SFWC, when equipped on the conventional tractor-semitrailer, reduces maximum off-racking by up to 21% for a circular manoeuvre [4]. When analysed for 90º and 180º turning manoeuvre, it was found to reduce the maximum off-racking by up to 13.9% and 14.7% respectively [7].

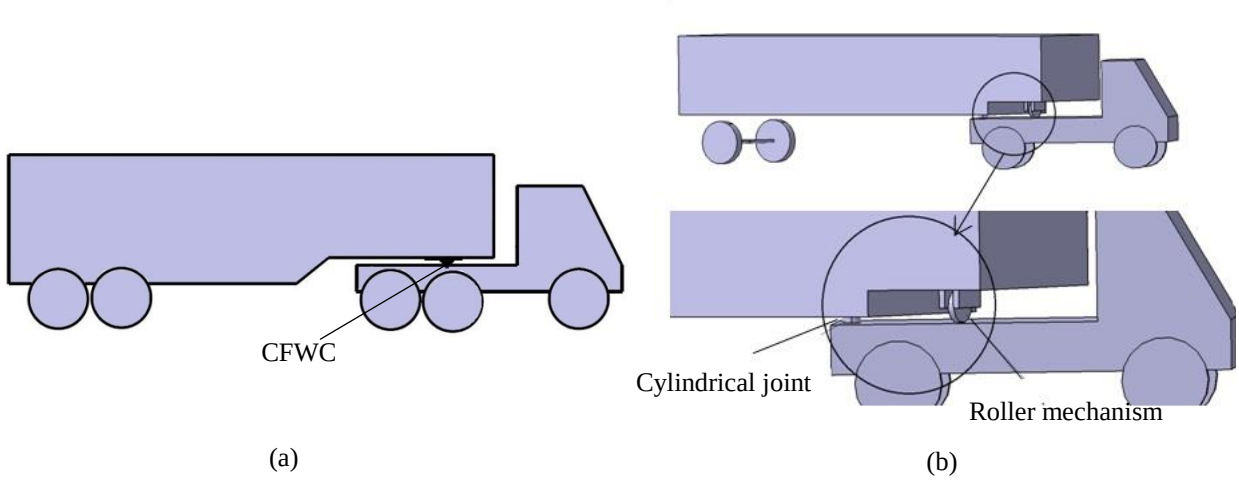


**Figure 1.** Conceptual model of the tractor-semitrailer with (a) CFWC (b) SFWC (Courtesy: Jogi and Chandramohan [7]).

## 2. METHODOLOGY

In the present work, a multi-body virtual prototype is built using the ADAMS Car tool. Initially, the CFWC model is built as per the specifications of AASHTO Standard Design Interstate Tractor-Trailer WB-62, specifications of which are mentioned in Appendix 1. Using the template builder option, CFWC model is modified into SFWC, by adding a roller mechanism and curved track. The kingpin offset chosen for the SFWC model is 812.8 mm. To evaluate the handling performance of the vehicle with SFWC, it is simulated for closed-loop ISO double lane change (DLC) manoeuvre, the specifications of which are mentioned in Figure 2. Five speeds are chosen for the study: 20 kmph to 60 kmph with an interval of 10 kmph.

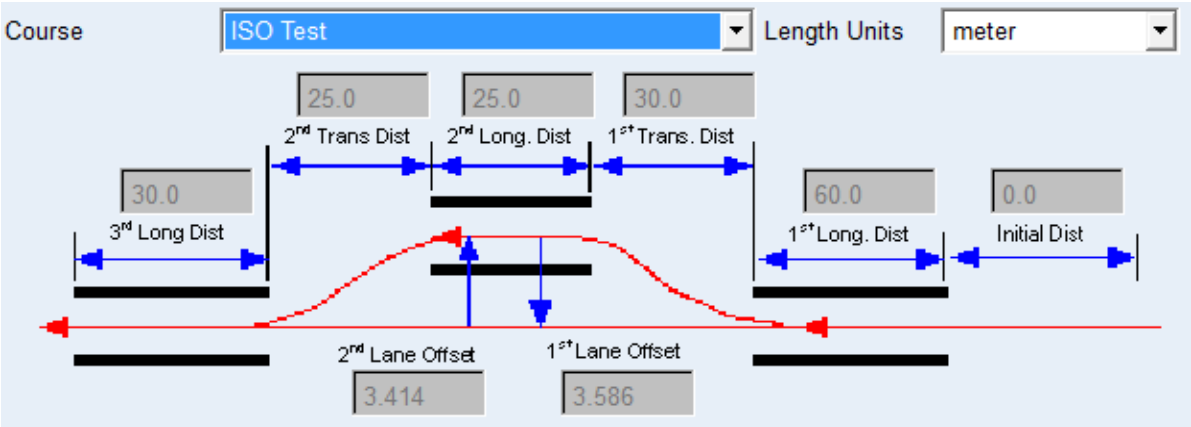


**Figure 2.** Specifications of ISO DLC course for heavy vehicles (Courtesy: MSC Software Corporation [8])

https://doi.org/10.3311/ECCOMASMBD2021-251

As shown in Figure 2, the actual length of the ISO DLC course is 170 m; however, to study the behaviour of the vehicle after finishing the course, the vehicle is run for an additional distance of about 130 m. The turn direction is chosen to be right for all simulation runs. The default value for the caster, camber and toe angles are chosen as 0º. Gear position is selected as suggested by the tool for the engine speed to be in the range between stall speed and max revolutions per minute limit. The default 2D flat road and default controller are used for all simulation runs. The simulation data are used to plot the trajectory, yaw rate response, lateral acceleration response and articulation angle response of both the vehicle models. To understand the relative performance of the tractor-semitrailer with SFWC, the results of both models are compared with each other and useful conclusions are drawn.

## 3. RESULTS AND DISCUSSION

The comparison of trajectories of the two vehicles at different velocities with respect to the target path is carried out. This gives insight into the ability of the vehicle to follow the ISO DLC path at various speeds. Figure 3 shows the trajectory of the tractor and semitrailer units of both SFWC and CFWC models at speeds varying from 20 kmph to 60 kmph with a step size of 10 kmph. One can observe that both the models trace the ISO double lane change path pretty well. The path traced by the units of tractor-semitrailer with SFWC matches that of the respective units of the CFWC model for speeds below 40 kmph. At 50 kmph speed, both vehicles show some instability after exiting the last turn of the DLC course. At 60 kmph the SFWC model tends to oscillate more than the CFWC model; however, both models complete the test without the lift-off of any of their wheels. Since the behaviour of both vehicles is similar at speeds below 40 kmph, the trajectory of the tractor unit of SFWC model exactly matches that of CFWC. However, at 40 kmph speed one can observe that the semitrailer unit of SFWC traces comparatively an inner path. Since its path is slightly closer to that of its tractor, one can understand that the off-tracking posed by SFWC model is less.

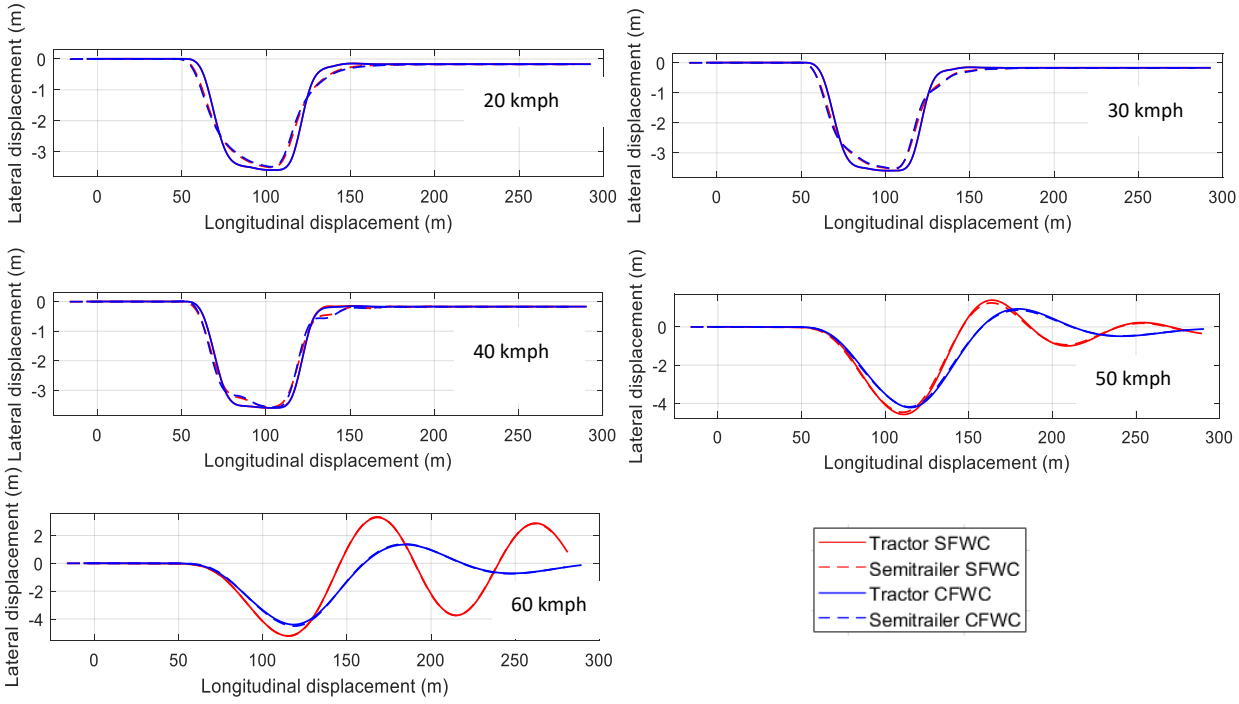


**Figure 3.** Trajectory of the tractor-semitrailer with SFWC and CFWC at various speeds

Figure 4 shows the yaw rate response of the vehicles at different speeds. The yaw rate response of both SFWC and CFWC models match each other at 20 kmph, however, at 30 kmph there is a noticeable difference during the last turn of the DLC course. This difference is even more pronounced at 40 kmph, the yaw rate of the SFWC model being higher during the turns. The trend of the yaw rate response is similar for speeds 20, 30 and 40 kmph. At 50 and 60 kmph speeds, the trend is quite different from the rest because of the instabilities arising due to the high-speed cornering.

https://doi.org/10.3311/ECCOMASMBD2021-251

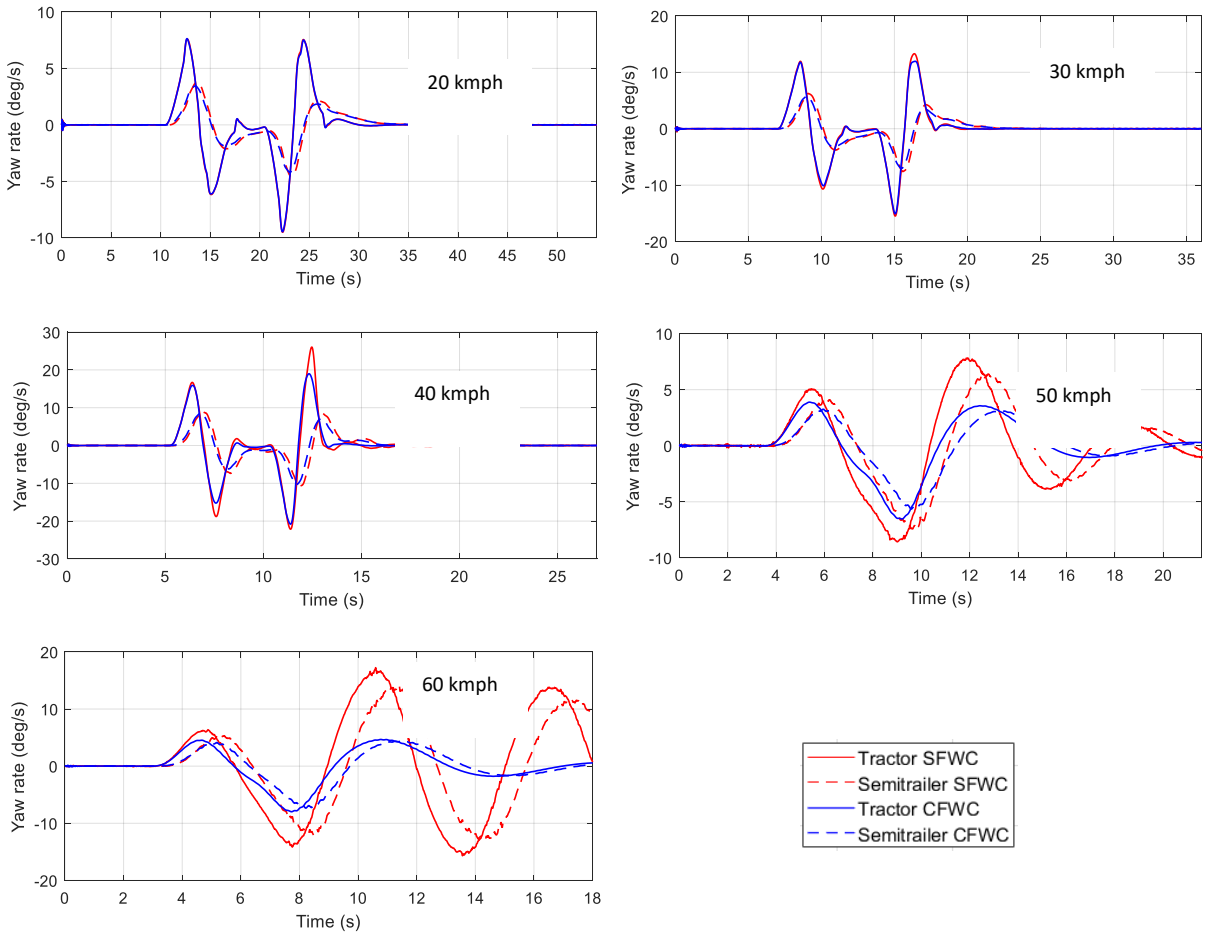


**Figure 4.** Yaw rate response of the tractor-semitrailer with SFWC and CFWC at various speeds

The study of the lateral acceleration experienced by the vehicle plays an important role. Figure 5 shows the lateral acceleration response of the vehicle tractor and semitrailer at different speeds. There is a noise in the lateral acceleration data during the beginning of the simulation run and can be ignored. Again, the trend followed by the lateral acceleration response at speeds 50 and 60 kmph is different from that of 20, 30 and 40 kmph for both the vehicle models. One can observe that the peak lateral accelerations experienced by the vehicle units occur during the turns. Also, the semitrailer units experience less lateral acceleration when compared to their respective tractors, due to the fact that, their path is comparatively a smoothened curve, which is evident from the trajectory plots. Interestingly, the lateral acceleration experienced by the semitrailer of SFWC vehicle is less when compared to that of CFWC vehicle for speeds below 40 kmph. Due to high speeds, the vehicles are not able to take sharp turns, which is evident from the yaw rate response for 50 and 60 kmph. Hence, corresponding lateral acceleration values also decrease when compared to those of 40 kmph. The actual curves for lateral acceleration for both units of SFWC at speeds 50 and 60 kmph contain a large amount of noise and hence are smoothened (smoothing parameter p = 0.999) for better representation. The actual plots and curve-fitting data can be found in Appendix 2.

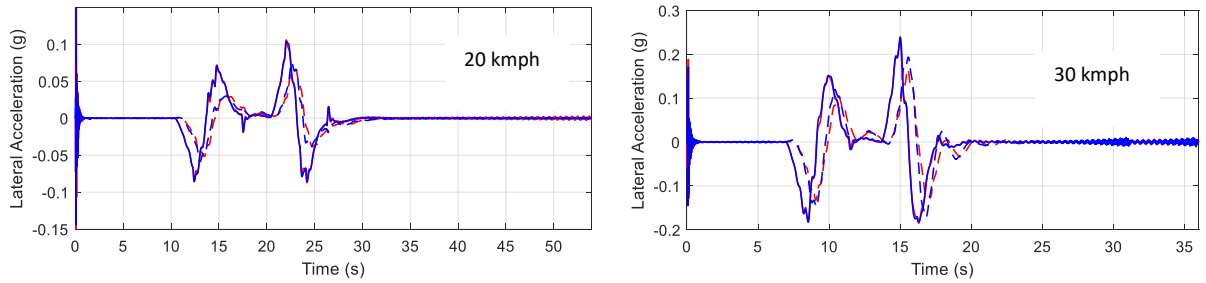

https://doi.org/10.3311/ECCOMASMBD2021-251

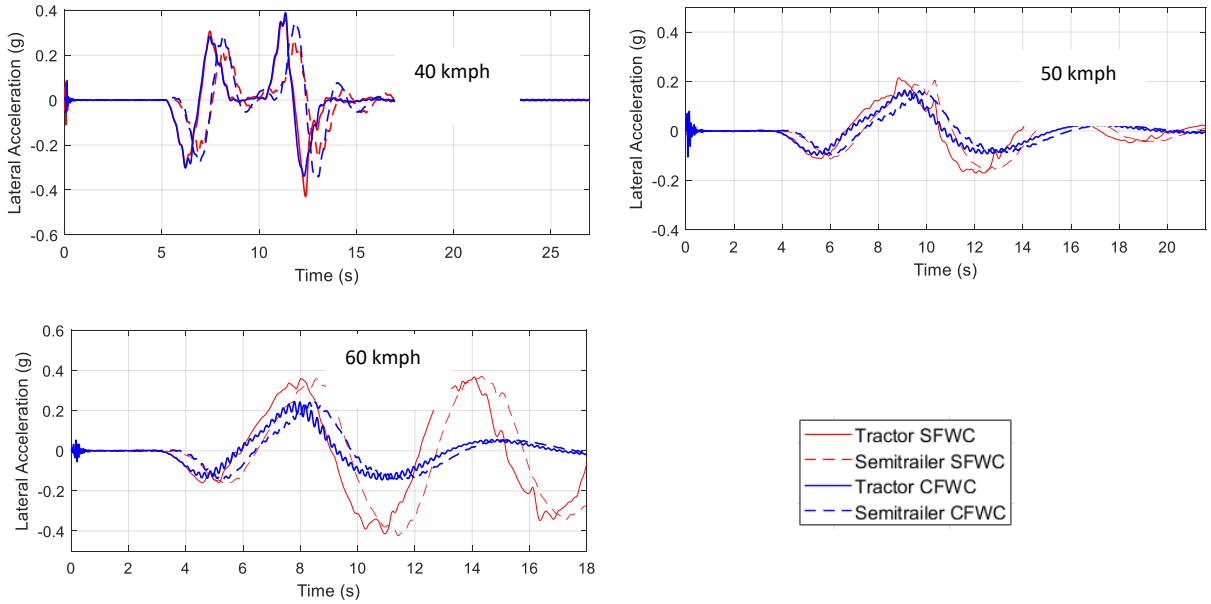


**Figure 5.** Lateral acceleration response of the tractor-semitrailer with SFWC and CFWC at various speeds

Figure 6 shows the articulation angles of the tractor and semitrailer units of both SFWC and CFWC models at speeds varying from 20 kmph to 60 kmph at intervals of 10 kmph. Again, the trend of the articulation angle curve for speeds between 20 and 40 kmph are similar to each other and different from the rest of the speeds. The articulation angle of SFWC vehicle is comparatively higher at all the speeds, owing to the fact that the effective wheelbase of the semitrailer of the SFWC vehicle is smaller, the overall length being the same.

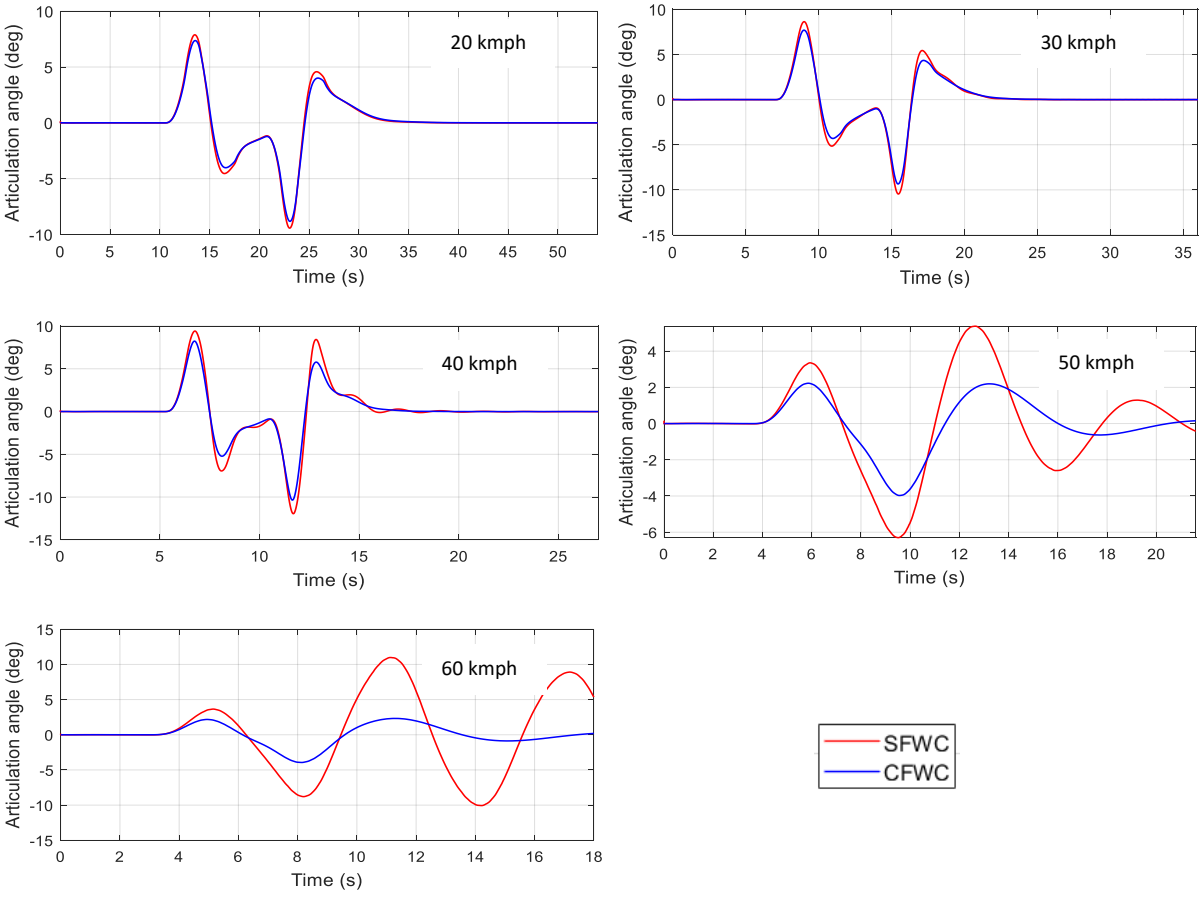


**Figure 6.** Articulation angle curves of the tractor-semitrailer with SFWC and CFWC at various speeds

## 4. SUMMARY AND CONCLUSION

To study the handling characteristics of the tractor-semitrailer with SFWC in comparison with the conventional vehicle, the DLC test is carried out, which is an obstacle avoidance manoeuvre. The virtual prototypes of both the vehicle types have been subjected to ISO DLC using the ADAMS/ Car tool at different speeds ranging from 20 kmph to 60 kmph with a step size of 10 kmph. The SFWC model traces the target path pretty well at lower speeds; however, it is a little unstable at higher speeds when compared to the CFWC model. The behaviour of both vehicles changes significantly between from 40 to 50 kmph. The lateral acceleration response explains that the DLC is a very dynamic manoeuvre and can generate rapid rates of change of lateral acceleration. Interestingly, for speeds below 40 kmph, the lateral acceleration experienced by the semitrailer of SFWC vehicle is less compared to that of CFWC vehicle. One should note that the DLC manoeuvre is highly dependent on the driver's steering input. The default driver model present in ADAMS/ Car tool is optimized for the tractor-semitrailer with CFWC. Hence, the actual steering input to be given to SFWC vehicles may vary. In the present study, the performance of the tractor-semitrailer with SFWC is on par with that of CFWC at speeds below 50 kmph. The vehicle's inability to trace the ISO DLC path is more pronounced at higher speeds. With the development of stability control systems like ESC, optimized for tractor-semitrailers with SFWC, their performance would improve.

## REFERENCES

[1] F. Jindra, Off-tracking of Tractor-trailer Combinations. J. Automob. Eng. 96–101, 1963.

[2] R.L. Pretty, On the off-tracking of semi-trailers. ARRB Proceedings, vol. 2, Part 1, 1964.

[3] J. Choi, J. Baek, S. Lee, W. Kang, Offtracking model on horizontal curve sections. Eastern Asia Society for Transportation Studies, vol. 3, No. 1, 2001.

[4] A. Jogi, S. Chandramohan, Kinematic analysis of tractor-semitrailer with split fifth wheel coupling during low speed turning maneuvers, SAE Int. J. Commer. Veh. 10(2): 2017, doi:10.4271/2017-01-1554, 2017.

[5] Y. Peng, X. Yang, Comparison of various double lane change manoeuvre specifications, Vehicle System Dynamics, 50:7, 1157-1171, DOI: 10.1080/00423114.2012.659741, 2012.

[6] N. Khettou, D. Trifkovic, S. Muzdeka, Using modelling and simulation to predict dynamics of converted ground vehicle, Defence Science Journal, Vol. 66, No. 5, pp. 509-516, DOI : 10.14429/dsj.66.9783, 2016.

[7] A. Jogi, S. Chandramohan, Zero-speed off-tracking analysis of tractor-semitrailer with split fifth wheel coupling for 90° and 180° turning manoeuvres, Biswal B., Sarkar B., Mahanta P. (eds) Advances in Mechanical Engineering, Lecture Notes in Mechanical Engineering. Springer, Singapore, 2020.

[8] MSC ADAMS Car 2019.2 help document (MSC.Software\Adams\2019\help \adams_car\dialogboxes\dbox_ana_ful_ilc_sub.html)

https://doi.org/10.3311/ECCOMASMBD2021-251

## APPENDIX 1

### Specifications of reference tractor-semitrailer: Interstate Tractor-Trailer WB-62

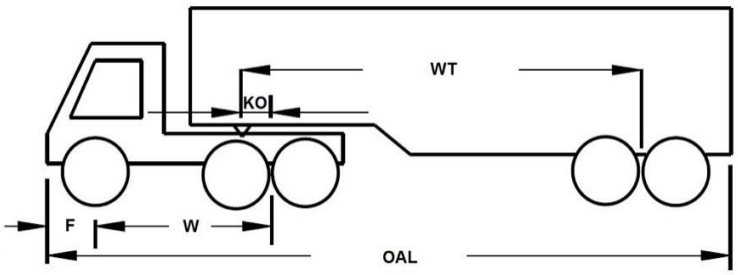


| | |
|---|---|
| Tractor wheelbase (W) | 6.10 m |
| Front overhang (F) | 0.91 m |
| Semitrailer wheelbase (WT) | 12.80 m |
| Kingpin offset (KO) | 0.30 m |
| Overall length (OAL) | 21.03 m |

**Figure A1.** Specifications of reference tractor-semitrailer Interstate Tractor-Trailer WB-62

## APPENDIX 2

### The lateral acceleration response (with noise) and curve-fitting data

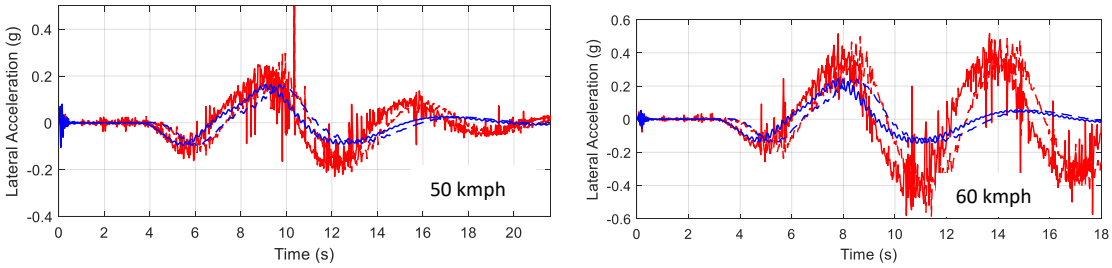


**Figure A2.** Lateral acceleration response of the tractor-semitrailer with SFWC and CFWC at 50 and 60 kmph speed without smoothing of the curves

Curve fitting data for SFWC lateral acceleration response:

- Smoothing spline: f(x) = piecewise polynomial computed from p
- Smoothing parameter: p = 0.999

**Table A2.** Goodness parameters of the fit

| | SFWC Tractor | SFWC Trailer |
|---|---|---|
| **SSE** | 1.907 | 0.871 |
| **R-square** | 0.7993 | 0.8946 |
| **Adjusted R-square** | 0.7769 | 0.8828 |
| **RMSE** | 0.04296 | 0.02903 |

https://doi.org/10.3311/ECCOMASMBD2021-223

ECCOMAS Thematic Conference on Multibody Dynamics
December 12 - 15, 2021, Budapest, Hungary

# Development of Steering Laws to Assist the Driving of a Independent Front and Rear Steering Vehicle

**Louis DAMBACHER[1], Benjamin BOUDON[1], Nicolas BOUTON[1], Roberto LOT[2], Nicolas LALANDE[3], Roland LENAIN[4]**

[1] Université Clermont Auvergne,CNRS
SIGMA Clermont, Institut Pascal
63000 Clermont-Ferrand, France
[louis.dambacher, benjamin.boudon,
nicolas.bouton]@sigma-clermont.fr

[2] Departement of industrial Engineering
University of Padova
35131 Padova,Italy
roberto.lot@unipd.it

[3] Airbus Helicopters
Aéroport de Marseille Provence
13700 Marignane, France
nicolas.lalande.as@gmail.com

[4] French National Institute
for Agriculture, Food,
and Environment (INRAE)
63170 Aubière, France
roland.lenain@inrae.fr

**ABSTRACT**

This paper proposes a control strategy to control the yaw rate of a 2-independent-steering-gears vehicle operated by a driver. The approach is based on adaptive techniques to account the slip effects. An extended kinematic model is used which takes into account slipping effects through side-slip angles. A 3-steps state observer is proposed to estimate a characteristic parameter defining the tyre-ground contact. This state observer use only the value of control variables and the yaw rate measurement of the vehicle. Thanks to the proposed approach the driver can safely steer the 2-steering-gears off-road vehicle using one steering actuator without losing control at high speeds as will be the case with two independent steering actuators.

**Keywords:** 2-steering-gears vehicle, Vehicle dynamics, Yaw rate control, Adaptive control, State observer.

## 1 INTRODUCTION

The purpose of this paper is in the field of assisted ground vehicle dynamics, and more specifically in the development of steering systems for two-steering-gears vehicles. This sector is in regain of interest with the improvement of the on-board electronics. This improvement is highlighted in the automotive field by the optimisation of comfort, agility and driving safety. On-board electronics allows, when the vehicle is equipped, to handle 2 steering gears on one vehicle. Vehicles with two steering gears offer many opportunities to improve the driver's driving comfort:

- Vehicle dynamics are improved, especially on slippery ground.
- Complex manoeuvres that would be impossible to perform with a traditional single-steer vehicle are now possible. Vehicle agility is improved.
- Behaviours that could endanger the driver can be avoided by the intervention of a second steering gear. The stability of the vehicle is improved.
- From an energy point of view, the presence of two steering gears makes it possible to "distribute" the wear of the front and rear tyres. The life of the tyres is therefore increased.

In short, the presence of two independent steering gears allows the driver to have better control of the vehicle, and human/vehicle interaction is therefore optimised.

https://doi.org/10.3311/ECCOMASMBD2021-223

However, despite all these advantages, the use of a vehicle with two independent steering gears can also be very dangerous for the driver. Indeed, without assistance, a vehicle of this type id difficult to handle, especially at high speed. It is to answer this problem that it was chosen to develop the two following contributions in this paper:

- The development of a control law that allows the driver to drive a 2-steering-gears vehicle in off-road conditions without putting himself in danger.
- The development of a state observer reflecting the behaviour of the tyre-ground contact, which is essential for the implementation of an efficient control law. The constraint of this observation is that it must be done at the lowest cost and therefore use the fewest possible sensors.

For this purpose, it was chosen to use a model adapted to the control, but still sufficiently sophisticated to take into account the main phenomena associated to the dynamics of the vehicle and the interactions of the tyres with the ground. Indeed, in previous works, very advanced dynamic representations can be found [1]. But the large number of parameters makes them difficult to use for control. In the opposite case, simple kinematic models have been developed for control purposes [2]. However, these models are not representative of various phenomena, in particular: the lack of grip, the vehicle inertia, or the load transfer phenomenon. In this paper a hybrid approach is used allowing the use of simplified models adapted in real time by observers [3], [4]. These observers are based on a simplified model of tyre/ground contact extending the traditional definition [5] of the cornering phenomenon.

## 2 Vehicle modelling for control purposes

The vehicle model used to test the various control laws developed is a very simplified model of the vehicle. The vehicle is reduced to a bicycle shape (figure 1) where the front (and the rear axle) is considered as a single wheel. Nevertheless this modelling takes into account the phenomena of slipping, by introducing the presence of side-slip angle, at the front, at the rear and at the G point of the model. This model is called "Extended Kinematic Model" [6],[7].

https://doi.org/10.3311/ECCOMASMBD2021-223

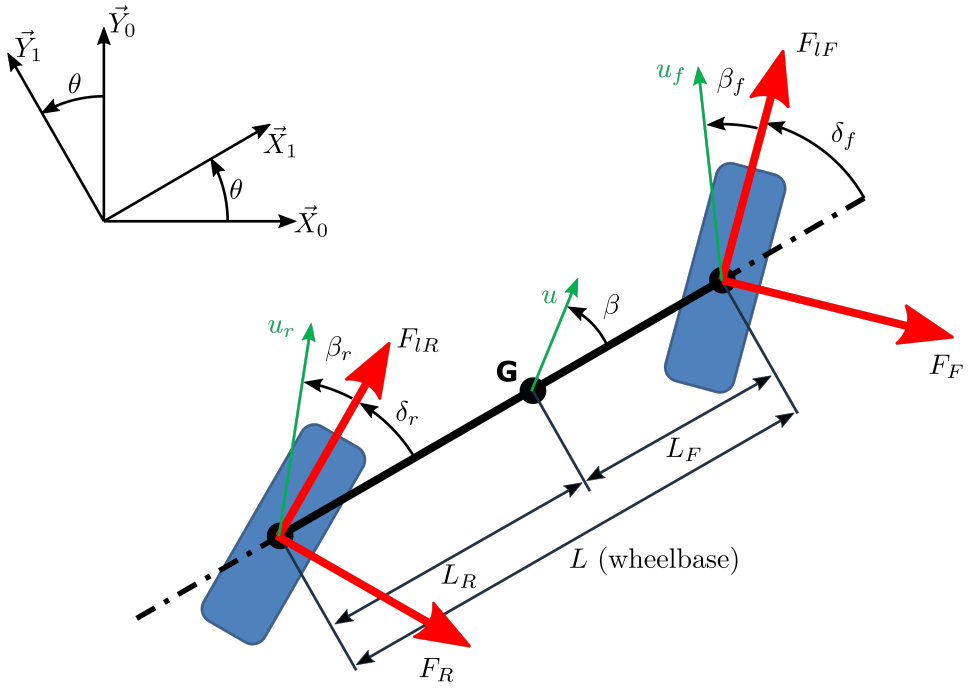


**Figure 1**. 4WS extended kinematic model

The notations used are as follows:

$\theta$ : Yaw angle

$\delta_r$ : Rear steering angle
$\delta_f$ : Front steering angle

$u_r$ : Speed at the center of the rear gear
$u_f$ : Speed at the center of the front gear
$u$ : Speed at vehicle G-point

$\beta_r$ : Rear slip angle
$\beta_f$ : Front slip angle
$\beta$ : Global slip angle at G-point

$F_{lR}$ : Rear longitudinal contact force
$F_{lF}$ : Front longitudinal contact force
$F_R$ : Rear lateral contact force
$F_F$ : Front lateral contact force

$L$ : Wheelbase of the vehicle

### 2.1 Kinematic equations

A first kinematic analysis allows us to establish the link between the speed of the rear axle $u_r$ and the speed at the G point $u$ as well as the link between the rear side-slip angle $\beta_r$ and the global side-slip angle $\beta$.
The chassis is considered as a rigid body. The kinematic relation (1) inside the body can be written:

https://doi.org/10.3311/ECCOMASMBD2021-223

$$\vec{u}_r = \vec{u} + (L_R\vec{X}_1) \wedge \dot{\theta}\vec{Z}_1 \tag{1}$$

$$= \vec{u} - L_R\dot{\theta}\vec{Y}_1 \tag{2}$$

$$\Rightarrow \begin{pmatrix} u_r\cos(\delta_r+\beta_r) \\ u_r\sin(\delta_r+\beta_r) \\ 0 \end{pmatrix}_1 = \begin{pmatrix} u\cos(\beta) \\ u\sin(\beta) \\ 0 \end{pmatrix}_1 - \begin{pmatrix} 0 \\ L_r\dot{\theta} \\ 0 \end{pmatrix}_1 \tag{3}$$

The projections on the axis $\vec{X}_1$ and $\vec{Y}_1$ enable to obtain 2 scalar equations :

$$\Leftrightarrow \begin{cases} u_r\cos(\delta_r+\beta_r) = u\cos(\beta) \\ u_r\sin(\delta_r+\beta_r) = u\sin(\beta) - L_R\dot{\theta} \end{cases} \tag{4}$$

$$\Rightarrow \begin{cases} u = \frac{u_r\cos(\delta_r+\beta_r)}{\cos(\beta)} \\ \tan(\delta_r+\beta_r) = \tan(\beta) - \frac{L_R\dot{\theta}}{u\cos(\beta)} \end{cases} \tag{5}$$

$$\boxed{\Rightarrow \begin{cases} u = \frac{u_r\cos(\delta_r+\beta_r)}{\cos(\beta)} \\ \beta_r = \arctan(\tan(\beta) - \frac{L_R\dot{\theta}}{u\cos(\beta)}) - \delta_r \end{cases}} \tag{6}$$

The equations linking the speed of the front gear $u_f$ and the speed at the G point $u$ as well as the relation between the front side-slip angle $\beta_f$ and the global side-slip angle $\beta$ are obtained in the same way. The relations are as follows:

$$\boxed{\Rightarrow \begin{cases} u = \frac{u_f\cos(\delta_f+\beta_f)}{\cos(\beta)} \\ \beta_f = \arctan(\tan(\beta) + \frac{L_F\dot{\theta}}{u\cos(\beta)}) - \delta_f \end{cases}} \tag{7}$$

### 2.2 Tyre force model

Due to the application of a lateral force on the wheel, during its own rotation, the tyre/ground contact area moves from the position $C_0$ to a position $C$. The angle $\beta$ formed by the straight line $(C_0C)$ and the longitudinal axis in the main wheel plane is called the side-slip angle.
The most well-known way of modelling tyre-ground contact is Pacejka's so-called Magic Formula [8]. This formula links, among other things, the lateral force Y and the side-slip angle $\beta$. However, this model is not suitable for an off-road application. Moreover, because of the numerous parameters involved in this formula, it is not adapted to the control. It is chosen here to model the tyre-ground contact using an adaptable cornering stiffness $C_e$ as follows:

$$Y = C_e\beta \tag{8}$$

The adaptability of the value of the cornering stiffness $C_e$ is done thanks to the "Observer" block detailed in the paragraph 4. The general principle is illustrated in the figure 2

https://doi.org/10.3311/ECCOMASMBD2021-223

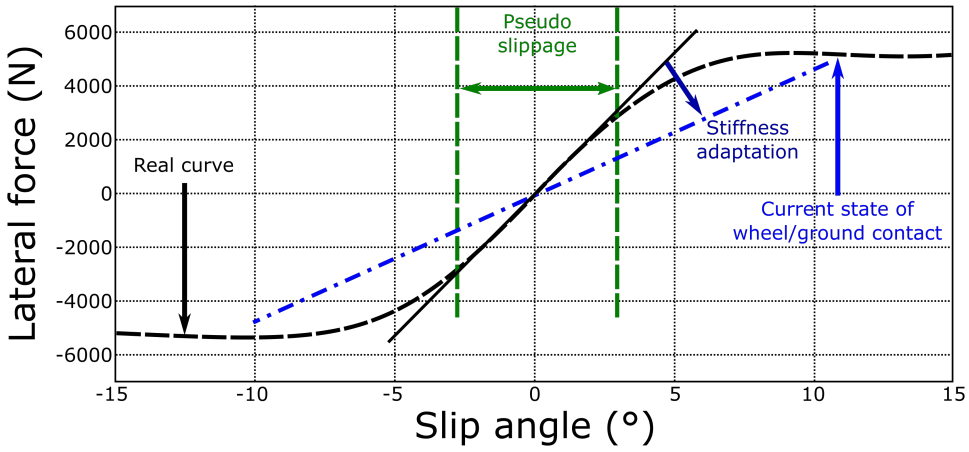


**Figure 2**. Principe of cornering stiffness $C_e$ adaptability

As shown in the figure 2, a linear relation (black line) with $C_e$ constant is valid only for small side-slip angles. To describe the real curve (black dashed line) for higher side-slip angles the slope of the line, which is $C_e$, is modified in real time, this is the adaptation of the cornering stiffness (blue dashed line).

### 2.3 Dynamic equations

The Physical phenomena and the modelling assumptions are as follows :

- The wheel/ground contact forces are modelled as explained in subsection 2.2 .
- Only one rigid solid is considered here, that of the vehicle's chassis.
- Only one inertia is taken into account, that of the chassis in the yaw plane. The other inertia, such as those of the wheels for example, are neglected.

From Newton's second law, it is possible to determine the system of equations (9) :

$$\begin{cases} \dot{\beta} = \frac{1}{um}[F_{lf}sin(\delta_f - \beta) + F_{lr}sin(\delta_r - \beta) - C_f\beta_f cos(\delta_f - \beta) - C_r\beta_r cos(\delta_r - \beta)] - \dot{\theta} \\ \ddot{\theta} = \frac{1}{I_z}[L_rC_r\beta_r cos(\delta_r) - F_{lr}L_r sin(\delta_r) - L_fC_f\beta_f cos(\delta_f) + F_{lf}L_f sin(\delta_f)] \end{cases} \tag{9}$$

This is a system of ordinary differential equations (ODEs) with two inputs : $\delta_f$ and $\delta_r$ describing the evolution of the global side-slip angle $\beta$ and the evolution of the yaw rate of the vehicle $\dot{\theta}$.
To fully describe the behaviour of the vehicle in the yaw plane, three kinematic equations must be added to the equations of system (9). This is the system of equations (10) :

$$\begin{cases} \dot{\beta} = \frac{1}{um}[F_{lf}sin(\delta_f - \beta) + F_{lr}sin(\delta_r - \beta) - C_f\beta_f cos(\delta_f - \beta) - C_r\beta_r cos(\delta_r - \beta)] - \dot{\theta} \\ \ddot{\theta} = \frac{1}{I_z}[L_rC_r\beta_r cos(\delta_r) - F_{lr}L_r sin(\delta_r) - L_fC_f\beta_f cos(\delta_f) + F_{lf}L_f sin(\delta_f)] \\ u = \frac{u_r cos(\beta_r + \delta_r)}{cos(\beta)} \\ \beta_r = arctan(tan(\beta) - \frac{L_r\dot{\theta}}{ucos(\beta)}) - \delta_r \\ \beta_f = arctan(tan(\beta) + \frac{L_f\dot{\theta}}{ucos(\beta)}) - \delta_f \end{cases} \tag{10}$$

It is the equation linking the speed of the rear axle $u_r$ and the speed at the G point $u$ that is implemented, as it is the rear wheels that are driven.

https://doi.org/10.3311/ECCOMASMBD2021-223

## 3 Steering law

The steering law developed is designed to assist the driver in driving the two-steering-gears vehicle at high speed. This steering law controls the rear axle while the front axle is steered by the driver. The main objective of this steering law is to limit the effects of slippery ground on the driver's driving and to make the driver feel as if he or she is driving a traditional vehicle with one steering gear while driving on difficult ground in a vehicle with two steering gears.
As can be seen on the figure 3, the control architecture is composed of two main blocks: the control loop and the observer, which will be detailed in the section 4. From measurements made at the output of the vehicle model, the observer aims to reconstruct variables that feed the control law.

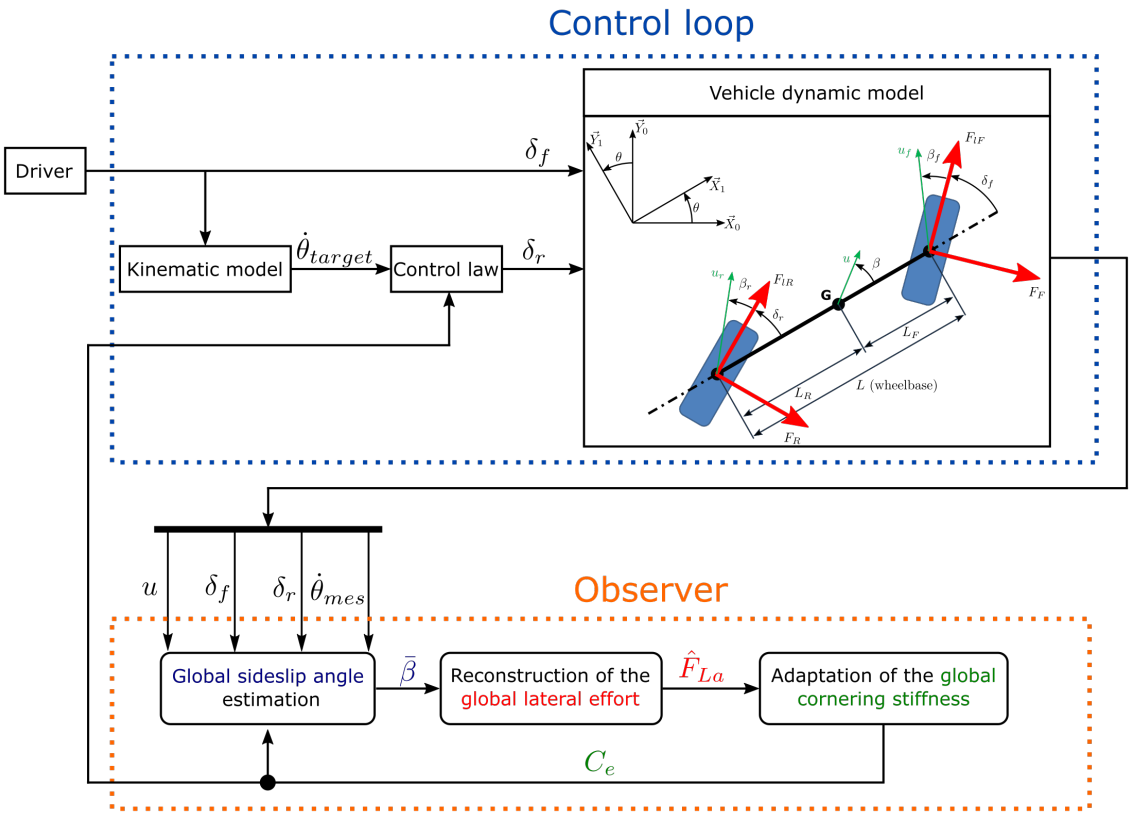


**Figure 3**. Global architecture of the control system

### 3.1 Principle of Yaw Rate Control

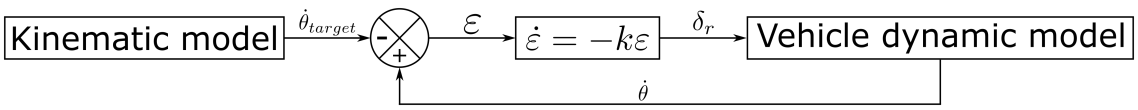


**Figure 4**. Yaw rate control

The target yaw rate $\dot{\theta}_{target}$ is obtained from a kinematic model of a bicycle shape vehicle (like in figure 1) modelled without slippage. More precisely, the contact between the wheels and the ground is considered as a rolling without slipping (RWS) contact. A purely geometrical analysis allows to define the result of equation (11), defining the yaw rate of the vehicle in rolling without slipping conditions. For a vehicle, steered by the front gear, the target yaw rate can be obtained with the following relation :

$$\dot{\theta}_{target} = \frac{u_r \tan(\delta_f)}{L} \tag{11}$$

https://doi.org/10.3311/ECCOMASMBD2021-223

### 3.2 Implementation of the control law

The error $\varepsilon$ is defined as follows:

$$\varepsilon = \dot{\theta} - \dot{\theta}_{target} \tag{12}$$

The control law is based on an exponential decrease of the error to 0. This translates mathematically into the differential equation (13):

$$\dot{\varepsilon} = -k\varepsilon \text{ with } k > 0 \tag{13}$$

$$\Leftrightarrow \ddot{\theta} = k(\dot{\theta}_{target} - \dot{\theta}) \tag{14}$$

From (9) and neglecting the longitudinal forces, the following equation can be written :

$$\ddot{\theta} = \frac{1}{I_z}[\overbrace{L_r C_r}^{A_r}\beta_r \cos(\hat{\delta}_r) - \overbrace{L_f C_f}^{A_f}\beta_f \cos(\delta_f)] \tag{15}$$

The aim is to isolate the rear steering angle $\delta_r$ variable. Since $\beta_r$ depends on $\delta_r$, it is not possible to isolate it easily. A back-stepping strategy is used here, using the intermediate control variable $u_{\beta_r}$, the target value for $\beta_r$ . This is illustrated in Figure 5.

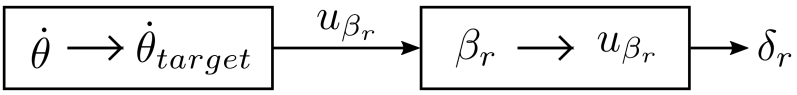


**Figure 5**. Back-stepping Strategy

By replacing the expression (15) of $\ddot{\theta}$ in (14), it is possible to easily isolate $\beta_r$ and thus determine the value $u_{\beta_r}$ :

$$u_{\beta_r} = \frac{1}{A_r \cos(\hat{\delta}_r)}\left[I_z k(\dot{\theta}_{target} - \dot{\theta}) + A_f \beta_f \cos(\delta_f)\right] \tag{16}$$

$\beta_r$ and $\delta_r$ are kinematically related according to equation (17):

$$\beta_r = \overbrace{\arctan(\tan(\beta) - \frac{L_f \dot{\theta}}{u\cos(\beta)})}^{B_r} - \delta_r \tag{17}$$

And finally the the expression for $\delta_r$ can be determined :

$$\boxed{\delta_r = B_r - u_{\beta_r}} \tag{18}$$

## 4 Cornering Stiffness observer

### 4.1 State observer

The purpose of an observer is to estimate an unmeasurable state $\hat{X}$, from measurable variables $Y$ and control variables $v$ in order to be able to use them in the control law. Figure 6 illustrates how a state observer is used in control.

https://doi.org/10.3311/ECCOMASMBD2021-223

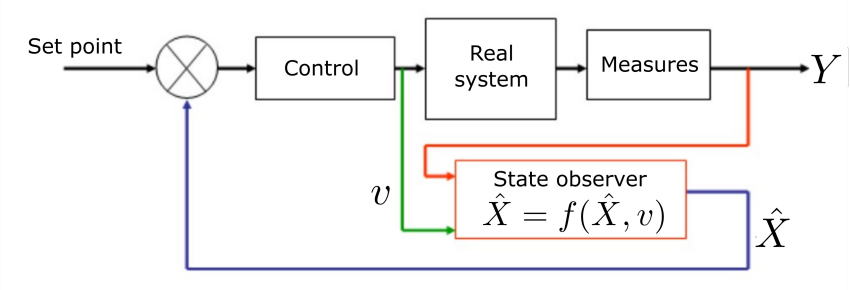


**Figure 6**. State observer

### 4.2 Cornering stiffness observation

As mentioned in paragraph 2.2, the contact between the tyres and the ground is modelled using a linear relation between the lateral force $Y$ and the side-slip angle $\beta$. The relation is in fact non-linear, so it was chosen to adapt this coefficient $C_e$ from this relation. The coefficient $C_e$ is called the cornering stiffness, so this is the cornering stiffness adaptation strategy. This strategy, shown in Figure 7, is composed of 3 steps detailed below. The last step is of course the estimation of the cornering stiffness, which is then fed back into the operations of the first step. The cornering stiffness is therefore regulated.

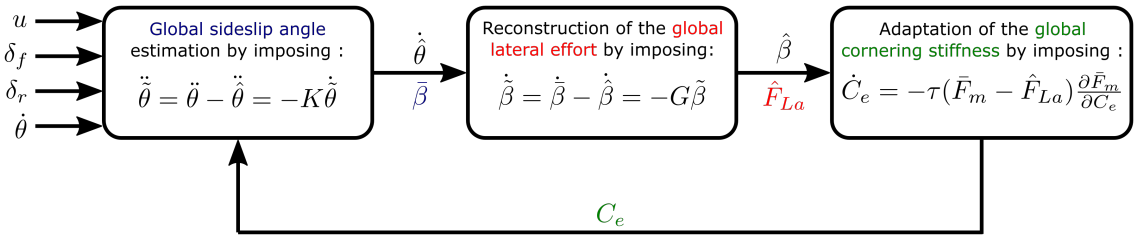


**Figure 7**. Cornering stiffness observer

The notations used are as follows:

$\hat{X}$ : Estimated variable
$\bar{X}$ : Measured variable or reconstruction of a measurement
$\tilde{X} = \bar{X} - \hat{X}$

*Step 1* :
Here, the aim is to reconstruct the global side-slip angle $\bar{\beta}$ from the measurement (by sensor) of the yaw rate $\dot{\theta}$. The strategy adopted here is to make converge an estimation $\dot{\hat{\theta}}$ of the yaw rate to the yaw rate $\dot{\theta}$ measured by sensor, using $\bar{\beta}$ considered here as a control variable. The method for convergence from $\dot{\hat{\theta}}$ to $\dot{\theta}$ is to impose an exponential decrease of the error, as in paragraph 3.1:

$$\ddot{\tilde{\theta}} = -k\dot{\tilde{\theta}} \Leftrightarrow \ddot{\theta} - \ddot{\hat{\theta}} = -k(\dot{\theta} - \dot{\hat{\theta}}) \text{ with } k > 0 \tag{19}$$

The side-slip angle $\bar{\beta}$ appears in the expression of $\ddot{\hat{\theta}}$ thanks to the the second equation of (9). However, due to the non-linearity of the last two equations of the system (10), it is very difficult to extract $\bar{\beta}$. It was therefore decided to linearise these equations and not to take into account the longitudinal forces. The simplified expression of $\ddot{\theta}$ is as follows:

$$\ddot{\hat{\theta}} = a_{11}\dot{\hat{\theta}} + a_{12}\bar{\beta} + b_{11}\delta_f + b_{12}\delta_r \tag{20}$$

With :

$$a_{11} = -\frac{C_e(L_f^2 cos(\delta_f) + L_r^2 cos(\delta_r))}{uI_z} \qquad a_{12} = \frac{C_e(L_r cos(\delta_r) - L_f cos(\delta_f))}{I_z}$$
$$b_{11} = \frac{C_e L_f cos(\delta_f)}{I_z} \qquad b_{12} = -\frac{C_e L_r cos(\delta_r)}{I_z}$$

https://doi.org/10.3311/ECCOMASMBD2021-223

By replacing this in equation (19) :

$$\ddot{\theta} - \ddot{\hat{\theta}} = -k\dot{\tilde{\theta}} \tag{21}$$

$$\ddot{\theta} - a_{11}\dot{\hat{\theta}} - a_{12}\bar{\beta} - b_{11}\delta_f - b_{12}\delta_r = -k\dot{\tilde{\theta}} \tag{22}$$

Finally :

$$\boxed{\bar{\beta} = \frac{\ddot{\theta} - a_{11}\dot{\hat{\theta}} - b_{11}\delta_f - b_{12}\delta_r + k\dot{\tilde{\theta}}}{a_{12}}} \tag{23}$$

*Step 2* :
Here, the aim is to reconstruct the global lateral force $\hat{F}_{La}$ from $\bar{\beta}$. The strategy adopted here is to make converge an estimation $\hat{\beta}$ of side-slip angle to $\bar{\beta}$ , using $\hat{F}_{La}$ considered here as a control variable. The method for convergence from $\hat{\beta}$ to $\bar{\beta}$ is to impose an exponential decrease of the error, as in paragraph 3.1 and as the precedent step :

$$\dot{\tilde{\beta}} = -k\tilde{\beta} \Leftrightarrow \dot{\bar{\beta}} - \dot{\hat{\beta}} = -k(\bar{\beta} - \hat{\beta}) \text{ with } k > 0 \tag{24}$$

The global lateral force is defined as follows:

$$\bar{F}_{La} = C_e(\beta_f cos(\delta_f - \bar{\beta}) + \beta_r cos(\delta_r - \bar{\beta})) \tag{25}$$

From (9) and neglecting the longitudinal forces, the following equation can be written :

$$\dot{\hat{\beta}} = -\frac{1}{um}\hat{F}_{La} - \dot{\hat{\theta}} \tag{26}$$

By replacing this in equation (24) :

$$\dot{\bar{\beta}} - \dot{\hat{\beta}} = -k\tilde{\beta} \tag{27}$$

$$\dot{\bar{\beta}} + \frac{1}{um}\hat{F}_{La} + \dot{\hat{\theta}} = -k\tilde{\beta} \tag{28}$$

Finally :

$$\boxed{\hat{F}_{La} = -um(\dot{\hat{\theta}} + \dot{\bar{\beta}} + k\tilde{\beta})} \tag{29}$$

*Step 3* :
Here, the aim is to reconstruct the global cornering stiffness $C_e$. The strategy adopted here is the MIT Rule [9] to make converge $\hat{F}_{La}$ to $\bar{F}_{La}$ by adapting the value of $C_e$.
The MIT Rule is formulated as follows:

$$\dot{C}_e = -\tau e\frac{\partial e}{\partial C_e} \tag{30}$$

With :

$$\begin{cases} e = \bar{F}_{La} - \hat{F}_{La} \\ \bar{F}_{La} = C_e(\beta_f cos(\delta_f - \bar{\beta}) + \beta_r cos(\delta_r - \bar{\beta})) \\ \hat{F}_{La} = -um(\dot{\hat{\theta}} + \dot{\bar{\beta}} + k\tilde{\beta}) \end{cases} \tag{31}$$

Finally by replacing this in equation (30), the following equation can be written :

$$\boxed{\dot{C}_e = -\tau(\bar{F}_{La} - \hat{F}_{La})(\beta_f cos(\delta_f - \bar{\beta}) + \beta_r cos(\delta_r - \bar{\beta}))} \tag{32}$$

## 5 Simulation results

### 5.1 Presentation of the global model

The Simulink model shown in Figure 8 is designed to simulate the behaviour of the 2-steering-gear vehicle under different simulation scenarios. If tests of different control laws with different vehicle models are to be done, the general architecture of the simulator would be maintained.

https://doi.org/10.3311/ECCOMASMBD2021-223

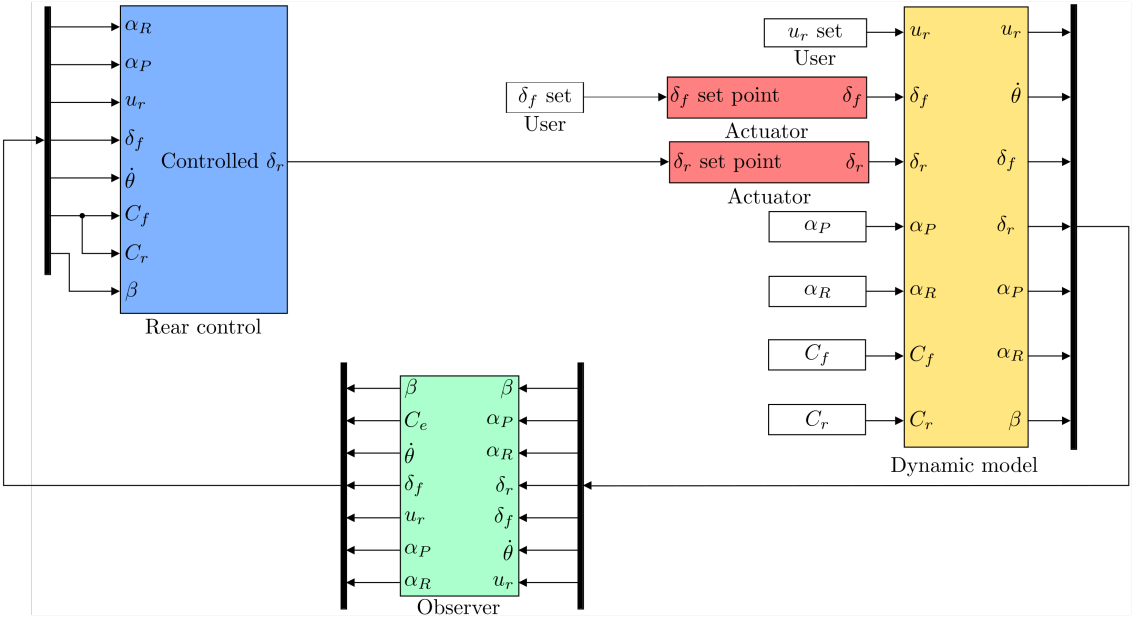


**Figure 8**. Global simulator scheme

This simulator is composed of different blocks:

- "Actuator" block : In order to represent the actuators as non-ideal, they are considered as second order systems with a 5%response time of 0.24 seconds.
- "Dynamic model" block : The evolution equations of the dynamic model are implemented here.
- "Rear control" block : The steering law acting on the steering (rear, in this case) gear is implemented here.
- "Observer" block: The cornering stiffness (parameter defining the tyre-ground slip) is reconstructed in this block.

### 5.2 Simulation conditions

Simulations were conducted to test the developed control law and the observer. The vehicle's forward speed is 50 km/h and the driver imposes (from 0.5 seconds) a front steering angle of 15 degrees. A sudden change from grippy to slippery ground is simulated at 2.5 seconds (see blue curve in figure 9).

### 5.3 Cornering observation results

The cornering stiffness observation results (in red) presented in Figure 9 are quite good (0.25 seconds delay) since the only measurement made to reconstruct the drift stiffness is the yaw rate measurement.

https://doi.org/10.3311/ECCOMASMBD2021-223

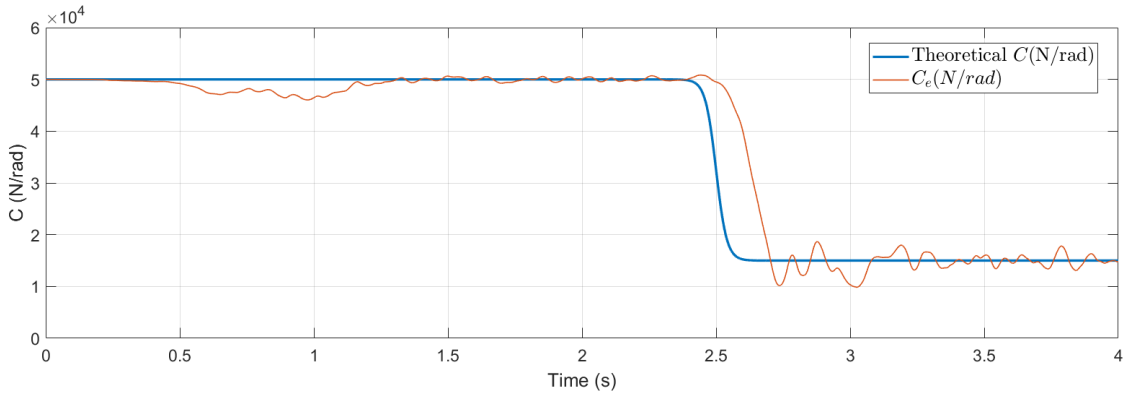


**Figure 9**. Results of the cornering stiffness observation

### 5.4 Steering law results

As explained in paragraph 5.2, the steering law is tested in a turn, with a sudden change of ground during the turn. According to figure 10, without rear wheel control, the vehicle has an under-steer behaviour: The yaw rate is lower than desired. This under-steer behaviour is accentuated after 2.5 seconds on slippery ground.

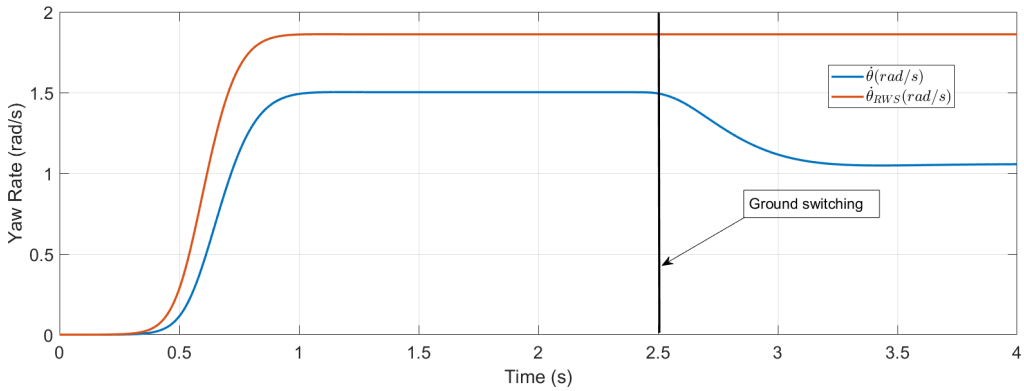


**Figure 10**. Yaw rate of the vehicle during test

It can be seen on Figure 11 that the control law does exactly what it is asked to do on grippy ground. At 2.5 seconds, the sudden change of ground disrupts the system, but here again the control law make converge the vehicle's yaw rate to its set point.

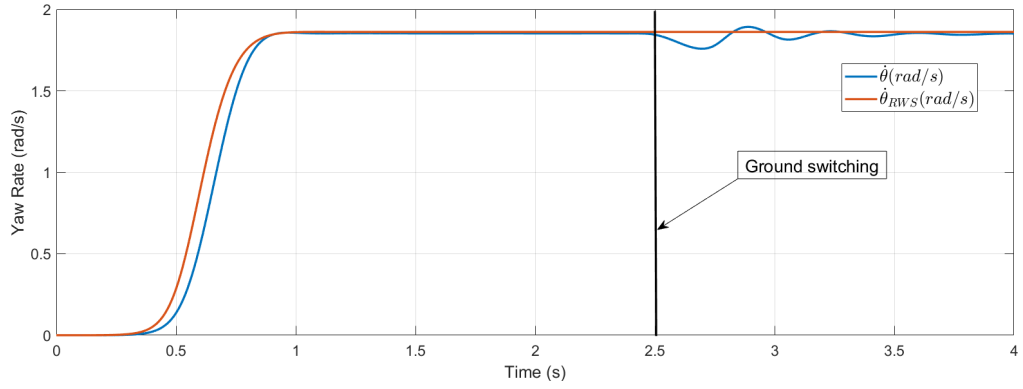


**Figure 11**. Yaw rate of the vehicle during test

## 6 Conclusion and futur works

The method presented in this paper fulfils the objective of providing the driver with a driving assistance system that allows him to drive on slippery ground more easily than a vehicle with one steering gear. This objective was achieved by using a control law that ensures the convergence of the vehicle's yaw rate towards a target yaw rate set by the driver. This control law works in parallel with a state observer which, based on an adaptive linear model, reflects the lateral behaviour of the tyre/ground contact.
This has been tested in simulation, with encouraging results for experimental validation on autonomous mobile robots and then on a prototype off-road vehicle (buggy type) with 2 steering gears.
In this paper, only the issue of maintaining a yaw rate has been treated and, more importantly, the control law acts only on one steering gear. By adopting a configuration where the driver does not act directly on one of the steering gears and by allowing the control law to act on both the front and rear gears, the field of possibilities is greatly expanded. Future works will focus on yaw and roll stability issues. This will require new control strategies, in particular optimal and predictive control.

## ACKNOWLEDGMENTS

This work was sponsored by a public grant overseen by the French National Research Agency as part of the "Investissements d'Avenir" through the IMobS3 Laboratory of Excellence (ANR-10-LABX-0016) and the IDEX-ISITE initiative CAP 20-25 (ANR-16-IDEX-0001).

## REFERENCES

[1] N. Dal Bianco, R. Lot, and M. Gadola, "Minimum time optimal control simulation of a GP2 race car," *Proceedings of the Institution of Mechanical Engineers, Part D: Journal of Automobile Engineering*, vol. 232, no. 9, pp. 1180–1195, 2018.

[2] C. Samson, "Control of Chained Systems Application to Path Following and Time-Varying Point-Stabilization of Mobile Robots," *IEEE Transactions on Automatic Control*, vol. 40, no. 1, pp. 64–77, 1995.

[3] N. Bouton, *Stabilité dynamique des véhicules légers tout-terrain*. PhD thesis, 2009.

[4] D. Denis, "Contribution à la modélisation et à la commande de robots mobiles reconfigurables en milieu tout-terrain : application à la stabilité dynamique d'engins agricoles," 2015.

[5] J.-P. Brossard, *Dynamique du véhicule Modélisation des systèmes complexes*. Presse Polytechniques Romandes, 2013.

[6] R. Lenain, B. Thuilot, C. Cariou, and P. Martinet, "Adaptive and predictive path tracking control for off-road mobile robots," *European Journal of Control*, vol. 13, no. 4, pp. 419–439, 2007.

[7] C. Cariou, R. Lenain, B. Thuilot, and M. Berducat, "Automatic Guidance of a Four-Wheel-Steering Mobile Robot for Accurate Field Operations," *Journal of Field Robotics*, vol. 26, no. 6-7, p. 15, 2009.

[8] E. Bakker, L. Nyborg, and H. B. Pacejka, "Tyre Modelling for Use In Vehicle Dynamics Studies," *SAE Technical Papers*, vol. 1, 1987.

[9] K. Astrom and B. Wittenmark, *Adaptive Control Second Edition*. New-York: Addison-Wesley, 1994.

https://doi.org/10.3311/ECCOMASMBD2021-161

ECCOMAS Thematic Conference on Multibody Dynamics
December 12 - 15, 2021, Budapest, Hungary

# Modeling and Simulation of a High-speed Maglev Vehicle on an Infinite Elastic Guideway

**Georg Schneider**[1], **Patrick Schmid**[1], **Florian Dignath**[2], **Peter Eberhard**[1]

[1] Institute of Engineering and Computational Mechanics
University of Stuttgart
Pfaffenwaldring 9, 70569 Stuttgart, Germany
[georg.schneider, patrick.schmid, peter.eberhard]@itm.uni-stuttgart.de

[2]thyssenkrupp Transrapid GmbH
Moosacher Str. 58, 80809 Munich, Germany
florian.dignath@thyssenkrupp.com

## ABSTRACT

For magnetic levitation transport systems with pillared tracks, detailed simulation models of the coupled system of vehicle and guideway offer a valuable contribution to find a tradeoff between stiff/heavy guideway elements, required to keep disturbances small for the controller, and low material consumption. This work provides a novel model of a detailed rigid multibody Transrapid maglev vehicle with three sections moving along an infinite periodically pillared elastic guideway mapping the two-dimensional heave-pitch motion of the vehicle and the elastic bending of the guideway elements. The infinite guideway is realized by moving system boundaries, i.e., the same few Euler-Bernoulli beams representing the current track segment are used repeatedly to form an infinite sequence of guideway elements. The equations of motion of the elastic beams and the rigid multibody vehicle are obtained from the multibody modeling and simulation toolbox Neweul-M$^2$. A detailed magnet model in combination with a model predictive control scheme are used for the first time in a large maglev vehicle model in this contribution. All model components are combined and coupled in a Simulink model. Simulation results show more severe overshoots and oscillations of the guideway deflection below the vehicle the faster the vehicle passes, which is resulting in bigger control errors and magnet motions at the rear end of the vehicle compared to the vehicle mid and front. Therefore, in contrast to previous presumptions, the most critical situations are to be expected at the rear end magnet, not at the front end.

**Keywords:** High-speed Maglev, Transrapid, Flexible Multibody System, Infinite Elastic Guideway, Moving System Boundaries.

## 1 INTRODUCTION

To this day, the only commercial high-speed magnetic levitation (maglev) train is implemented at the Shanghai Maglev Transportation line between Pudong International Airport and Longyang Road Station. It is based on the electromagnetic suspension (EMS) technology and runs with a maximum speed of 430 km/h during rush hour. Currently, a new high-speed maglev train with a maximum speed of more than 600 km/h is under development at the Chinese rolling stock manufacturer CRRC Qingdao Sifang Co., Ltd. [1]. A prototype of the future vehicle has already been presented to the public. The new high-speed maglev train aims to close the gap between current high-speed railway technology with top speeds of 300 to 350 km/h and aircrafts traveling with speeds around 900 km/h. Therefore, the new maglev train offers a notable alternative for short to medium-haul flights regarding economic and ecologic aspects. For safety and ride comfort aspects, a perfectly rigid guideway would be desirable. However, with increasing stiffness requirements,

https://doi.org/10.3311/ECCOMASMBD2021-161

production costs and material consumption for the guideway girders are also increasing. For finding a tradeoff, simulations and analyses with suitable models taking into account the dynamical behavior of the coupled system of guideway, vehicle, magnet, and controller provide valuable insights.

The dynamic interaction of maglev vehicles and their pillared track is investigated in numerous previous publications focusing on different aspects. Some publications focus on the bending of an elastic beam representing the guideway but simplify the vehicle by a point mass or single constant force [2, 3, 4]. Others exploit a detailed vehicle model, but the guideway is modeled by rigid elements [5, 6]. In [7, 8, 9], these approaches are combined by a rigid multibody vehicle crossing either a short series of elastic guideway elements or a single one, respectively. The simulation results from [9] show that for high speeds the elastic deformation of the guideway element causes a disturbance that influences the vehicle dynamics for several seconds after the vehicle has left the elastic guideway element. Thus, to predict the coupled system dynamics during a ride on a periodically pillared track, a model is required that allows the vehicle to travel a longer distance, including passing multiple elastic guideway elements. The idea of a guideway of infinite length represented by a finite number of guideway elements is already discussed in [10] but not elaborated in detail. Furthermore, as pointed out in [11], a more detailed vehicle model as, for example, described in [5, 6] is desirable to obtain accurate results.

The novel aspect of this contribution is the infinite elastic guideway formed by a repeating sequence of a few guideway elements combined with a detailed model of a complete Transrapid maglev vehicle consisting of three sections. Furthermore, this is the first complete vehicle model making use of the detailed magnet model from [12] and a model predictive control (MPC) scheme from [13], proving the usability of such kind of magnet models in combination with an MPC approach for the simulation of large maglev vehicle models. This novel model allows to investigate the differences in dynamics at the magnets at the front and rear end of the vehicle compared to the magnets in the middle. To the best of the authors' knowledge, such a detailed coupled system has not been modeled, investigated, and published before.

The subsequent sections are structured as follows. Section 2 describes the simulation model implemented and used in this contribution. It comprises the mechanical models of vehicle and guideway, magnet models and controllers, as well as the Simulink model of the coupled system. Interesting simulation results obtained from this model regarding the guideway dynamics, control accuracy, and the influence of guideway stiffness are presented and discussed in Sec. 3. Finally, a conclusion follows in Sec. 4.

## 2 SIMULATION MODEL

In this contribution, the multibody system approach is used to set up a two-dimensional model of a maglev vehicle moving along an infinite elastic guideway, mapping the heave-pitch motion and vertical guideway bending. Figure 1 visualizes the complete mechanical system in an undeformed state. In the following, the model components are explained in detail, especially the mechanical models of vehicle and guideway as well as the coupled system.

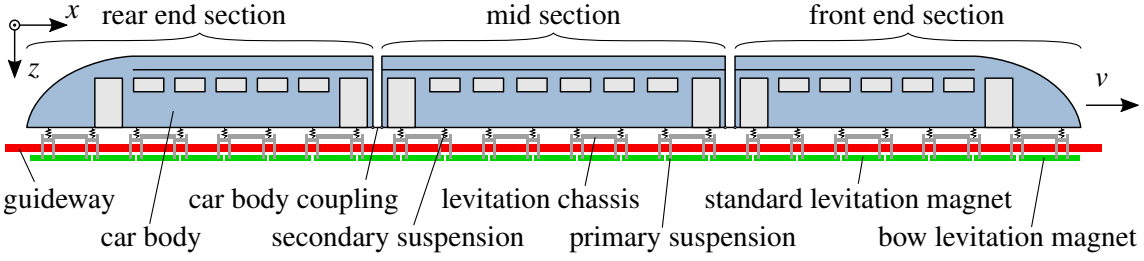


**Figure 1**. Components of the complete vehicle model on the guideway.

https://doi.org/10.3311/ECCOMASMBD2021-161

### 2.1 Mechanical Guideway Model

Based on the model from [9], where the guideway is modeled as single elastic Euler-Bernoulli beam preceded and followed by a rigid track, in this contribution the track model is extended to represent a regularly pillared elastic guideway of infinite length. For efficiency reasons, the number of system states is kept small by using just a few guideway elements and applying the concept of moving system boundaries as described in [10]. The basic idea of this concept is to consider only as many guideway elements as coupled by the vehicle and use them repeatedly. To obtain the few required guideway elements, a single guideway element is copied multiple times, thus all guideway elements are identical.

#### 2.1.1 Single Guideway Element

The basic unit for the guideway model, a single guideway element, is modeled as simply supported single-span Euler-Bernoulli beam with a length of 24.768 m discretized by 24 finite beam elements and reduced to its first three eigenmodes. For a description of the beam representing a single guideway element please refer to [9], where detailed explanations are provided about how moving magnet forces are applied to the beam by means of equivalent nodal forces and torques at its nodes, and how nodal coordinates are interpolated to get the deflections at arbitrary positions between the nodes using Hermite interpolation polynomials.

#### 2.1.2 Moving System Boundaries

The complete infinite track is represented by a small number of identical guideway elements described above, which are used repeatedly. The minimum number of required guideway elements depends on the number of elements coupled by the moving vehicle. In general, the maximum number of guideway elements covered – at least partially – by the vehicle is

$$n_{\text{covered}} = \lceil l_{\text{vehicle}}/l_{\text{beam}} \rceil + 1 \tag{1}$$

with the overall vehicle length $l_{\text{vehicle}}$, single beam length $l_{\text{beam}}$, and the ceiling function $\lceil x \rceil$, mapping $x$ to the least integer greater than or equal to $x$. Taking into account only the guideway elements which are coupled by the vehicle is sufficient, because the guideway elements are decoupled from each other. Therefore, there is no guideway dynamics ahead of the foremost covered beam, and the vibrating beams behind the rearmost covered one do not have any influence on the vehicle. Nevertheless, the implementation of the coupled model in Simulink requires two more guideway elements. First, to allow for simulations with non-constant velocity, the times when guideway elements must be shifted to be reused is determined based on the vehicle position and not by the simulation time. That is, as soon as the vehicle front leaves a beam there must be the next one already available in front of it. Due to the block execution order in Simulink and also due to graphical representation reasons, the next beam shall be in its position already before the vehicle enters it. Therefore, an additional guideway element has to be available in front of the foremost covered one to avoid the vehicle "falling off" the track. Second, the states of a guideway element must be reset to their nominal values to reuse it after it has been passed by the vehicle. Resetting the system states in Simulink requires the subsystem of the respective guideway element to be disabled for at least one time step, which reduces the number of available guideway elements during that time. For implementation efficiency reasons, it is advantageous to keep the number of enabled guideway elements constant at all times. Therefore, the passed guideway element remains disabled not just for one time step, but for the complete time it takes for the vehicle front to cross a beam, and an additional guideway element is added to compensate for the disabled one. Thus, the number of required guideway elements for the simulation model is

$$n_{\text{required}} = n_{\text{covered}} + 2\,. \tag{2}$$

In Fig. 2, the concept is visualized with an example. Here, the maximum number of guideway elements covered by the vehicle is $n_{\text{covered}} = 7$ as shown in the first configuration at time $t_1$. An

https://doi.org/10.3311/ECCOMASMBD2021-161

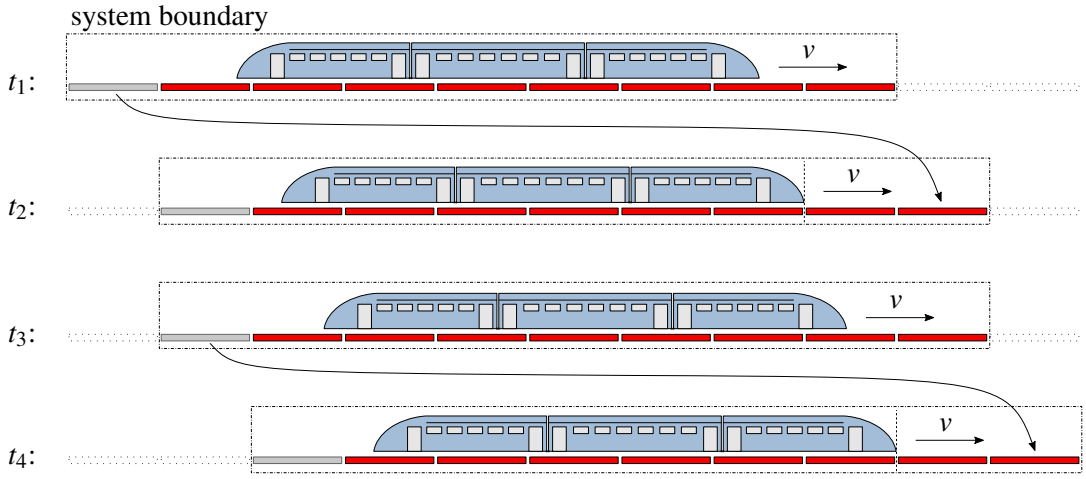


**Figure 2**. Concept of moving system boundaries: A small number of guideway elements is used repeatedly to realize an infinitely long elastic guideway and keep the number of system states small at the same time.

eighth guideway element is already in position in front of the vehicle, still uncovered but ready to be entered. These eight guideway elements colored red are enabled in the Simulink model. A ninth guideway element, colored gray, is located behind the rearmost enabled one and is disabled in Simulink. These nine guideway elements together with the vehicle define the system boundary. As soon as the vehicle enters the so far foremost beam, the disabled guideway element from the rear is re-enabled, its states are reset, and it is shifted from behind the vehicle to the very front, as shown in the second configuration at time $t_2$. The new rearmost, now uncovered guideway element is getting disabled. As long as the vehicle front does not reach the next beam, the guideway element positions and thus the system boundaries remain unchanged, see the configuration at time $t_3$. When the vehicle enters the next beam at time $t_4$, the shifting process is repeated. So the model boundaries, given by the rear and front end of the currently considered track segment, are shifted along the track together with the moving vehicle and an infinitely long elastic guideway is realized while the number of system states is kept small. If guideway vibrations should be analyzed in detail, an arbitrary number of additional guideway elements may be added behind the vehicle to observe the decay in guideway oscillations after a vehicle has passed. For the analysis of the vehicle dynamics, additional guideway elements behind the vehicle are not necessary.

### 2.2 Mechanical Vehicle Model

The vehicle model is based on the descriptions in [5, 6], representing a detailed two-dimensional rigid multibody model of the maglev vehicle Transrapid mapping the heave-pitch motion in the $x$-$z$-plane. Left and right side ($y$-direction) of the system are summed up. Figure 1 gives an overview of the mechanical vehicle components.

#### 2.2.1 Kinematics

The model consists of three sections: a rear end section, a mid section, and a front end section. Each section consists of rigid bodies for a car body, four levitation chassis, and seven or eight levitation magnets, respectively. Each section has the length of eight standard levitation magnets, but the magnets are arranged in such a way that the neighboring levitation chassis of two sections are connected by a magnet. At the front and rear end of the vehicle, bow levitation magnets are installed that are longer and have more poles. Thus, they have a shifted center of gravity (COG) and higher mass and inertia compared to a standard levitation magnet. The levitation chassis at the

https://doi.org/10.3311/ECCOMASMBD2021-161

rear and front end of the vehicle also differ from the others, since they have a cladding mounted resulting in a shifted COG as well as higher mass and inertia. In addition, the rear and front end section car bodies have shifted COGs and less mass and inertia compared to the mid section due to different geometries.

The car bodies' kinematics are defined with respect to an inertial system. The kinematics of the levitation chassis and levitation magnets are defined with respect to their respective car body. The levitation magnets connecting two sections belong to the respective rearward section, i.e., the levitation magnet between rear end section and mid section is defined with respect to the rear end car body, and the levitation magnet between mid section and front end section is defined with respect to the mid car body.

Each of the rigid bodies has two degrees of freedom (DOF): a translational one in $z$-direction and a rotational one about the $y$-axis. For three car bodies, twelve levitation chassis, and 23 levitation magnets this results in $(3+12+23)\cdot 2 = 76$ DOF for the complete vehicle.

### 2.2.2 Force Elements

The bodies are coupled by force elements. Elastomer element couplings, represented by linear spring-damper combinations in the model, connect the car bodies. The car bodies are supported on the levitation chassis by the soft secondary suspension, which is realized by air spring rockers at the real vehicle, see [6], for example. Their purpose is the decoupling of the car body dynamics from the higher frequency vibrations of magnets and chassis. In the model, the mass and inertia of the rockers is neglected, but their leverage is taken into account for the computation of the stiffness of the air springs that are modeled as linear spring-damper elements. The levitation chassis are supported on the magnets by very stiff elastomer elements, also modeled as linear spring-damper combinations. Finally, the magnets are coupled to the guideway by the magnet forces that attract the magnets to the guideway from below. The magnet forces are computed by the magnet model described in the subsequent section and they are implemented as inputs to the mechanical model. As the used magnet model computes one concentrated force per half magnet, two force elements per standard levitation magnet are implemented. The bow levitation magnets are simplified by three half magnets and thus three magnet forces are applied there.

## 2.3 Magnet Model

The electromagnet dynamics of the levitation magnets is considered by means of the magnet model presented in [12], including the effects of magnetic reluctances, fringing and leakage flux, magnetic saturation, and eddy currents. Two models are available: a detailed one of a complete magnet computing forces at each of the twelve magnet poles, and a simplified one of a half magnet summing up the forces in a single concentrated substitute force per half magnet. The detailed model is described by a set of differential-algebraic equations (DAEs) formulated in terms of the magnetic flux. Solving a set of DAEs is computationally intensive and, therefore, unsuitable for simulating large vehicle models with numerous magnets involved. The simplified model, however, is described by a single ordinary differential equation (ODE), or two ODEs for a complete magnet, respectively. The simplified model is derived from the detailed model in a numerical model reduction procedure yielding characteristic diagrams for the inductance, its derivative, and the force that are exploited by the simplified model. Both model variants have nearly the same input-output structure and almost the identical static and dynamic behavior, but the simplified one allows a tremendous speedup of two orders of magnitude compared to the detailed one. This makes it usable for the model in this contribution with 21 standard levitation magnets and two bow levitation magnets, equivalent to 48 half magnets in total. The magnet model is validated for a Transrapid's levitation magnet, i.e., the simulation results obtained with it in [12] match measurements very well nearly across the whole operation range of the magnet.

https://doi.org/10.3311/ECCOMASMBD2021-161

### 2.4 Controller

Maglev systems based on the EMS system, i.e., working with attractive magnet forces, are inherently unstable due to the reciprocal relation of magnet force and air gap. The electromagnets must be actively controlled to keep the air gap in a safe range to avoid physical contact between the vehicle and the guideway. Each half magnet has its own gap measurement unit (GMU) and is controlled individually by its own magnet control unit, which provides the voltage for the magnet based on the gap, acceleration, and current measurements.

A promising approach to control high-speed maglev vehicles is nonlinear MPC as stated in [14], because system constraints and the nonlinear nature of the magnet control system can be considered actively in the control design. However, different quasi-static loads for the individual magnet parts or just plant-model mismatch require the use of an offset-free MPC scheme. In this contribution, the integral error approach from [13] is used, which is found suitable for application for a Transrapid vehicle. See [13] for a detailed discussion and comparison to other offset-free MPC approaches for the magnet control system. By varying the cost functional's weighting matrices of the underlying optimal control problem being solved at each time step to determine the control input, the speed of the closed-loop system can be adapted in an intuitive manner. In this paper, one parameterization of the weighting matrices and the desired gap is used for all vehicle velocities.

### 2.5 Coupled System

The mechanical models of the vehicle and the guideway, respectively, are set up with the Matlab-based multibody modeling and simulation toolbox Neweul-M$^2$ [15]. With Neweul-M$^2$, the equations of motion are computed in symbolic form and written to Matlab files for numerical evaluation. Furthermore, the equations of motion are exported to C code and compiled as mex files, allowing to include them as S-functions in Simulink. The magnet and controller models are created with Matlab/Simulink as well. Therefore, all system components, i.e., the mechanics, the magnets, and the controllers, are coupled in Simulink. The Simulink model topology is shown in Fig. 3 and the variables used there are described in Tab. 1.

The equations of motion for the vehicle and guideway mechanics (yellow blocks) are included by means of the S-functions that are exported automatically by Neweul-M$^2$. From the outputs of the mechanical models, various air gaps and air gap velocities are computed by interpolating the nodal coordinates and velocities of the guideway $\boldsymbol{w}$, $\boldsymbol{\varphi}$, $\dot{\boldsymbol{w}}$, and $\dot{\boldsymbol{\varphi}}$ using Hermite polynomials as described in [9] and subtracting the results from the corresponding $z$-positions and velocities of the magnet at the concentrated substitute magnet forces and GMUs $\boldsymbol{z}_{\mathrm{MF}}$, $\dot{\boldsymbol{z}}_{\mathrm{MF}}$, and $\boldsymbol{z}_{\mathrm{GMU}}$. The vector of air gaps at the GMUs $\boldsymbol{s}_{\mathrm{GMU}}$, vector of accelerations at the GMUs $\ddot{\boldsymbol{z}}_{\mathrm{GMU}}$, and vector of currents $\boldsymbol{I}$, provided by the magnet models (summed up in the green block), are the inputs for the individual controllers (summed up in the blue block). The controllers, in return, provide the vector of magnet voltages $\boldsymbol{U}$ serving as input for the magnet models together with the vectors of air gaps and air gap velocities at the concentrated substitute magnet forces $\boldsymbol{s}_{\mathrm{MF}}$ and $\dot{\boldsymbol{s}}_{\mathrm{MF}}$. In addition to the vector of magnet currents $\boldsymbol{I}$, the magnets primarily provide the vector of concentrated substitute magnet forces $\boldsymbol{F}_{\mathrm{MF}}$ coupling the vehicle and guideway subsystems. This signal is used directly as input to the vehicle mechanics. For application of the magnet forces to the guideway, $\boldsymbol{F}_{\mathrm{MF}}$ has to be replaced by a vector of nodal forces and torques $\boldsymbol{F}_{\mathrm{nodal}}$. This is realized by a decomposition with the aid of Hermite polynomials distributing the concentrated substitute magnet forces to equivalent nodal forces and torques acting at neighboring beam nodes as described in [9]. The $x$-position of the front end car body over time $\boldsymbol{x}_{\mathrm{CB}}$ is provided by a workspace variable and serves as input to the vehicle mechanics block. Finally, the $x$-positions of the concentrated substitute magnet forces $\boldsymbol{x}_{\mathrm{MF}}$ are passed to the guideway block. From these positions, quantities like the position of the vehicle front or the overall length of already passed guideway elements are computed, which are required for the correct arrangement of the few available guideway elements to form the track segment within the current system boundaries.

https://doi.org/10.3311/ECCOMASMBD2021-161

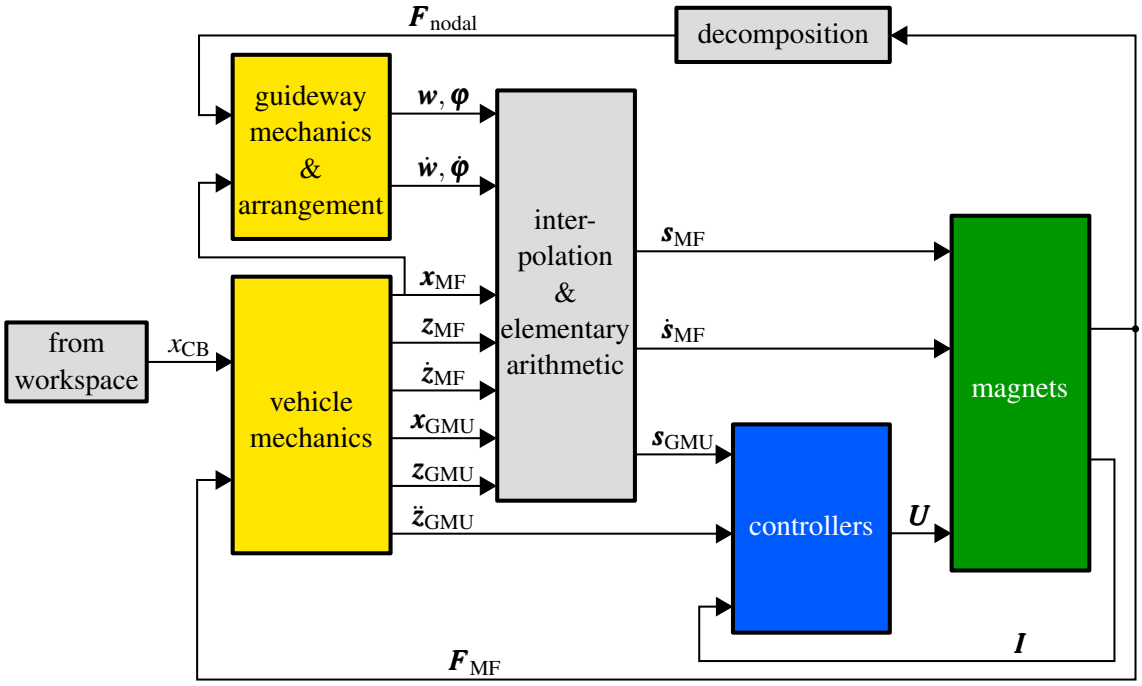


**Figure 3**. Schematic setup of the coupled model in Simulink. Descriptions of all variables used are given in Tab. 1.

**Table 1**. List of variables used in Fig. 3.

| variable | description |
|---|---|
| $x_{CB}$ | $x$-position of front end car body |
| $\boldsymbol{x}_{MF}$ | vector of $x$-positions of concentrated substitute magnet forces |
| $\boldsymbol{z}_{MF}$ | vector of $z$-positions of magnets at concentrated substitute magnet forces |
| $\dot{\boldsymbol{z}}_{MF}$ | vector of $z$-velocities of magnets at concentrated substitute magnet forces |
| $\boldsymbol{x}_{GMU}$ | vector of $x$-positions of gap measurement units |
| $\boldsymbol{z}_{GMU}$ | vector of $z$-positions of magnets at gap measurement units |
| $\ddot{\boldsymbol{z}}_{GMU}$ | vector of $z$-accelerations of magnets at gap measurement units |
| $\boldsymbol{w}, \boldsymbol{\varphi}$ | vectors of nodal coordinates (translational and rotational) of beams |
| $\dot{\boldsymbol{w}}, \dot{\boldsymbol{\varphi}}$ | vectors of nodal velocities (translational and rotational) of beams |
| $\boldsymbol{s}_{MF}$ | vector of air gaps at concentrated substitute magnet forces |
| $\dot{\boldsymbol{s}}_{MF}$ | vector of air gap velocities at concentrated substitute magnet forces |
| $\boldsymbol{s}_{GMU}$ | vector of air gaps at gap measurement units |
| $\boldsymbol{U}$ | vector of magnet voltages |
| $\boldsymbol{I}$ | vector of magnet currents |
| $\boldsymbol{F}_{MF}$ | vector of concentrated substitute magnet forces |
| $\boldsymbol{F}_{nodal}$ | vector of nodal forces and torques |

https://doi.org/10.3311/ECCOMASMBD2021-161

## 3 SIMULATION RESULTS

For the simulations in this contribution, the mechanical vehicle model and the magnet model described in Sec. 2 are parameterized according to the so-called TR08, the Transrapid vehicle which is the predecessor of the vehicle running at the Shanghai Maglev Transportation line. The MPC scheme uses the such parameterized models for its internal controller model. The guideway beams are parameterized with data from the first generation of concrete guideway at the 30 km test facility in northern Germany (TVE) as provided by [11]. No pre-buckling of the beams is modeled, but they are undeflected in the unloaded state when their own weight is the only applied force acting on them.

In the following, the presented model is used to simulate a Transrapid vehicle with three sections moving along a periodically pillared infinite elastic guideway with various velocities. Different model characteristics are examined such as the guideway dynamics below a passing vehicle as well as the air gap's control accuracy and the magnet motion at different positions along the vehicle. Moreover, the influence of different guideway stiffness values on the mechanical magnet dynamics is analyzed.

### 3.1 Guideway Dynamics

Figure 4 shows the deflection of a single guideway element at mid span $w_{\text{mid}}$ versus the position of the foremost magnet force $x_{\text{MF,front}}$, while the vehicle is passing with different velocities. At $x_{\text{MF,front}} = 0$, the foremost magnet force enters the beam and leaves it again at the first dashed vertical line. Thus, the complete beam is covered by the vehicle until the rearmost magnet force enters the beam at the second dashed vertical line. Finally, at the last dashed vertical line the rearmost magnet force leaves the beam, which is then uncovered and can oscillate freely.

In contrast to the corresponding but preliminary study in [9], the guideway element is now completely covered by subsequent vehicle sections for some time, which allows the analysis of its dynamic behavior under the load of the passing vehicle. In the quasi-static case, here represented by a vehicle speed of 18 km/h, the deflection smoothly increases with increasing overlap of vehicle and beam, reaching a value of nearly 6 mm when the beam is covered completely, and decreases again to zero when the vehicle leaves. The higher the velocity of the passing vehicle, the more severe overshoots and oscillations are visible, meaning more challenging disturbances for the controllers at the mid and rear vehicle sections to deal with.

The dynamics of the deflections in Fig. 4 can be explained as follows. The bending of an Euler-Bernoulli beam is described by a partial differential equation of second order in time, see [10], for example. For constant vehicle velocity, the excitation of the beam caused by the increasing load of the entering vehicle adopts the shape of a ramp signal. The same holds for the unloading

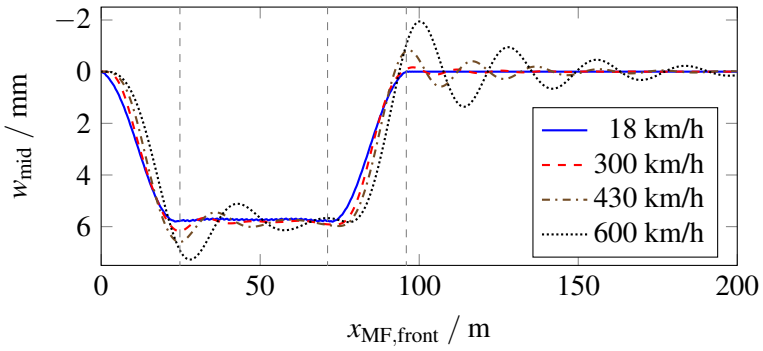


**Figure 4**. Deflection of a single guideway element at mid span versus position of the foremost magnet force for various velocities.

process with a decreasing load when the vehicle leaves the beam. The ramp shape of the excitation approximates more and more a step shape the faster the vehicle is running. Thus, the overshoot and oscillations visible in the beam deflection for high velocities approximately represent a step response of a second order system. A higher velocity, i.e., a more step-like excitation, results in a stronger overshoot and oscillations of the beam with its eigenfrequency, which in turn induce vibrations to the vehicle.

Based on these results, for such high velocities a higher guideway stiffness is strongly recommended to reduce the guideway deflections and thus make the control task easier. However, this increases the production effort for the guideway, which highlights the necessity of finding a trade-off between acceptable effort and girder elasticity manageable by the magnet controller.

### 3.2 Air Gap Control Accuracy and Magnet Motion Along the Vehicle

This section investigates the control accuracy and the magnet motion at different positions along the vehicle and for different vehicle velocities. From a control design perspective, there must be a compromise to keep the air gap within a safe range and simultaneously reduce the magnet motion to improve the ride comfort. The relative air gap control error $\Delta s/s_{\mathrm{des}} = (s_{\mathrm{meas}} - s_{\mathrm{des}})/s_{\mathrm{des}}$, i.e., the relative deviation of the measured air gap $s_{\mathrm{meas}}$ from the desired air gap $s_{\mathrm{des}}$ measured at the GMUs of magnets located at the very rear end, in the middle, and at the very front end of the vehicle, respectively, are plotted in the upper row of Fig. 5. The second row of Fig. 5 shows the normalized absolute magnet motion $z/z_{\mathrm{nom}}$ with the nominal magnet $z$-position $z_{\mathrm{nom}}$ being at $s_{\mathrm{des}}$ below the undeformed beam.

At all three considered positions along the vehicle, the air gap control error grows with increasing vehicle speed. This comes along with an increasing phase shift of the magnet motion with respect to the guideway deflection with increasing velocity. The faster the vehicle passes, the farther behind the point where two guideway elements adjoin is the point where the magnet reaches its highest position. One reason for these effects is more oscillating guideway dynamics, see Fig. 4.

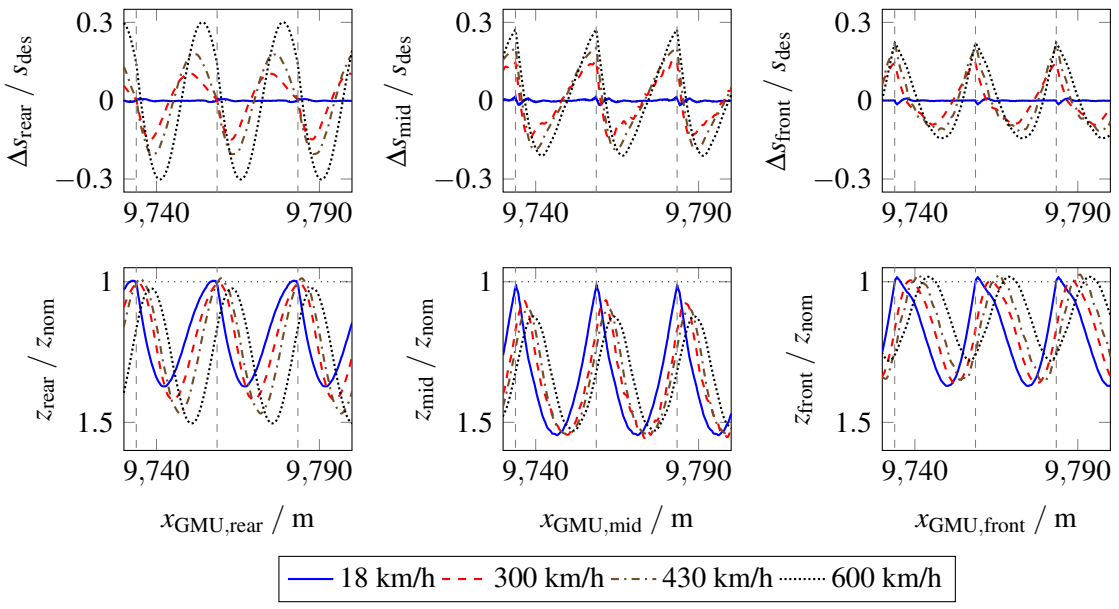


**Figure 5**. Relative air gap control error and normalized absolute magnet $z$-positions at GMUs of magnets at the very rear end, in the middle, and at the very front end of the vehicle, respectively. Vertical dashed lines mark the positions where one guideway element ends and the next one begins.

https://doi.org/10.3311/ECCOMASMBD2021-161

Moreover, the controller has to deal with a higher frequency of disturbances, but magnetic inductance and inertia forces regarding the mechanics are limiting factors for how fast the magnet suspension system can respond to changing air gaps.

Especially for high velocities, the biggest air gap control errors occur at the rear end of the vehicle, while the best control accuracy is achieved at the vehicle front. The magnet's $z$-motion is relatively small at the front compared to the mid and rear end positions as well. An explanation for this observation is that the vehicle front always enters a resting, undeflected guideway element, while magnets in the middle and rear part enter an already deformed and possibly oscillating beam. Therefore, the kink in the bending line at the positions where two guideway elements adjoin is less severe for the magnets in the front area of the vehicle than in the middle part. Furthermore, the guideway deflections for the controller to deal with at the vehicle front are smaller than at the middle and rear end magnets, since the girder is initially unloaded and thus the bending is still increasing while the vehicle front passes. This is also the reason for the effect revealed by the plots in the second row of Fig. 5, that the magnet motion depends on the vehicle speed, but differently for rear end, middle, and front end positions. While the amplitude of the oscillations increases with velocity at the rear end, it decreases slightly in the middle and at the front end. However, the smaller amplitudes for the vertical magnet motion at the middle and front end at higher velocities come along with higher air gap amplitudes because of the limited performance of the magnet suspension system. The vehicle rear end, where the biggest deviations from the desired air gap occur, seems to be the most critical part regarding a contact between vehicle and guideway. However, in the simulations for this contribution the air gaps are in a non-critical range even for high velocities highlighting the performance of the MPC approach used for the magnet controllers.

### 3.3 Influence of Guideway Stiffness

In this section, the influence of the guideway stiffness on the air gap control error and vertical magnet motion is analyzed by varying the elasticity of the modeled Euler-Bernoulli beam. Young's modulus $E$ takes the values 75 %, 100 %, 125 %, and 150 % of the value $E_0$ representing the first generation of concrete guideway at the TVE used for the studies investigated above. The upper row of Fig. 6 shows the maximum relative air gap control error $\max(|\Delta s|)/s_{\mathrm{des}}$ from Fig. 5 for the different stiffness values plotted over the vehicle speed at the rear end, middle, and front end of the vehicle for different velocities. In analogy, the amplitude of magnet motion $\Delta z = z_{\max} - z_{\min}$ normalized with $z_{\mathrm{nom}}$ is plotted in the second row of Fig. 6. The values $z_{\max}$ and $z_{\min}$ are the maximum and minimum, respectively, of the magnet $z$-position as shown in the second row of Fig. 5. For $v = 600$ km/h and $E/E_0 = 75\,\%$, the simulation becomes unstable quickly at the beginning, thus no values are contained in the plots for this parameter combination.

In general, both the maximum air gap control error and the amplitude of magnet motion decrease with increasing guideway stiffness, because the maximal guideway deflection decreases as well. Looking at different velocities, at the rear end the effect of elasticity variation on the magnet motion is stronger for higher velocities, whereas at the middle and especially at the front end it is nearly equal for all analyzed velocities except for 600 km/h, for which it is even smaller. This is caused by the more severe guideway oscillations that the rear end magnet has to deal with while it leaves the beam. The quite sudden unbending of the beam for high vehicle speeds leads to an overshoot, see Fig. 4, meaning that the beam is bent upwards while the rear end magnet is still under it. The small influence of elasticity variation at the front end for 600 km/h is also clearly visible in the maximum air gap control error.

https://doi.org/10.3311/ECCOMASMBD2021-161

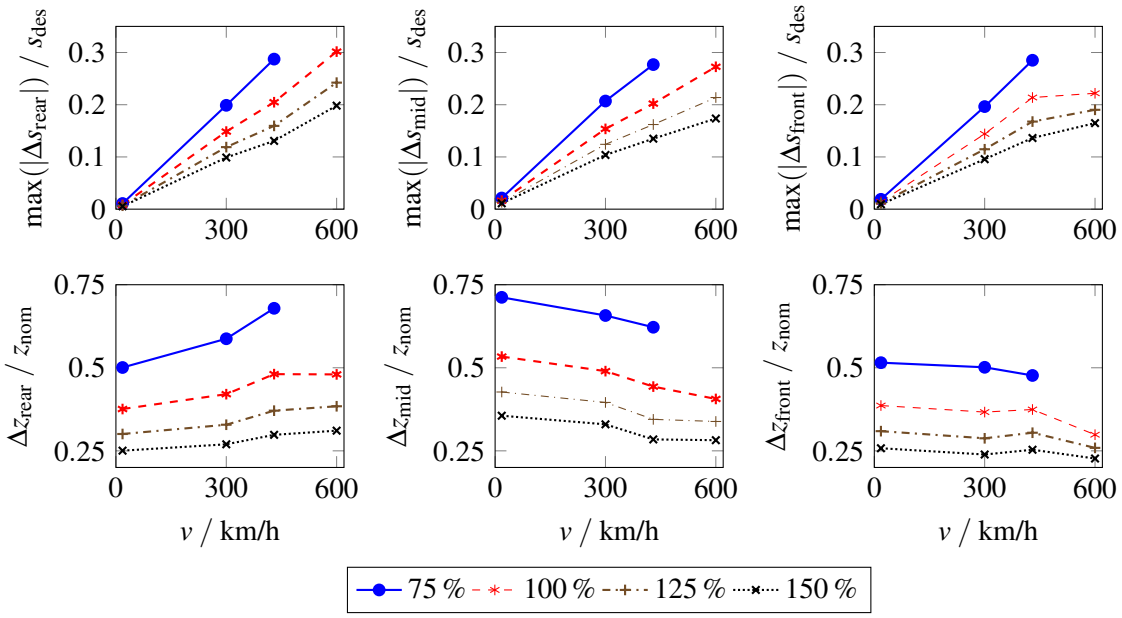


**Figure 6**. Maximum air gap control error and amplitude of vertical magnet motion at the very rear end, in the middle, and at the very front end of the vehicle, respectively, for different guideway elasticity values $E/E_0$ plotted over different velocities.

## 4 CONCLUSIONS

The requirements for the guideway of a high-speed maglev system are contradictory. For the vehicle's magnet suspension system, girders would be preferable that are as stiff as possible to keep the disturbances due to bending small. On the other hand, this goes along with intensive material consumption and expensive production costs, but economic viability is essential for competitiveness with other transportation systems. This publication makes a contribution towards finding a tradeoff between these opposing requirements using a detailed model of a Transrapid vehicle with three sections traveling on an infinite elastic guideway mapping the two-dimensional heave-pitch motion of the vehicle. The system dimension is kept small due to system boundaries moving along with the vehicle allowing to reuse the same few guideway elements for the guideway again and again. The faster the vehicle moves, the more severe are overshoot and oscillations of the guideway deflection below the passing vehicle resulting in bigger magnet motions and air gap control errors at the middle and rear end of the vehicle compared to the vehicle front end. A remarkable new result is that controlling the vehicle rear magnets seems to be the most critical part at high speeds due to relatively intense guideway dynamics at the rear end. The situation at the vehicle front is even less critical than at the middle of the vehicle, where the difference between the slopes of the two adjacent bending lines is largest because both beams are maximally deflected at this moment. The same tendency holds also for the influence of the guideway elasticity on the magnet motion. It is smaller at the vehicle front than at the middle and rear parts, but at all locations a higher stiffness is advantageous due to smaller guideway deflections.

For further investigations with this model, additional guideway disturbances like offsets at adjoining girders and at adjoining stator packs could be taken into account. However, the disturbance due to guideway deflection is dominating. Another scenario that can be investigated with this model is the failure of one or several levitation magnets, to investigate if neighboring magnets are able to take over the additional load. Furthermore, analyzing the relation between span-crossing frequency, beam eigenfrequency, and speed of the magnet control closed-loop system are planned to analyze potential resonance effects and favorable parameters regarding the ride comfort.

https://doi.org/10.3311/ECCOMASMBD2021-161

## REFERENCES


[1] Lin, G., Sheng, X.: Application and further development of maglev transportation in China. Transportation Systems and Technology **4**(3) (2018) 36–43

[2] Popp, K., Schiehlen, W.: Dynamics of magnetically levitated vehicles on flexible guideways. In Pacejka, H.B., ed.: Proceedings of IUTAM Symposium on the Dynamics of Vehicles on Roads and Railway Tracks. Amsterdam, Swets and Zeitlinger (1976) 479–503

[3] Meisinger, R.: Simulation of maglev vehicles riding over single and double span guideways. Mathematics and Computers in Simulation **21**(2) (1979) 197–206

[4] Meisinger, R.: Simulation of a single and double-span guideway under action of moving MAGLEV vehicles with constant force and constant gap. Sonderdruck Schriftenreihe der Georg-Simon-Ohm-Fachhochschule Nürnberg **14** (2002)

[5] Hägele, N., Dignath, F.: Vertical dynamics of the maglev vehicle transrapid. Multibody System Dynamics **21**(3) (2009) 213–231

[6] Dellnitz, M., Dignath, F., Flaßkamp, K., Hessel-von Molo, M., Krüger, M., Timmermann, R., Zheng, Q.: Modelling and analysis of the nonlinear dynamics of the Transrapid and its guideway. In: Progress in Industrial Mathematics at ECMI 2010. Volume 17. Heidelberg, Springer (2012) 113–123

[7] Han, J.B., Han, H.S., Lee, J.M., Kim, S.S.: Dynamic modeling and simulation of ems maglev vehicle to evaluate the levitation stability and operational safety over an elastic segmented switch track. Journal of Mechanical Science and Technology **32**(7) (2018) 2987–2998

[8] Wang, Z., Xu, Y., Li, G., Yang, Y., Chen, S., Zhang, X.: Modelling and validation of coupled high-speed maglev train-and-viaduct systems considering support flexibility. Vehicle System Dynamics **57**(2) (2019) 161–191

[9] Schneider, G., Liang, X., Dignath, F., Eberhard, P.: Simulation of the maglev train transrapid traveling on a flexible guideway using the multibody systems approach. In Kecskeméthy, A., Geu Flores, F., eds.: Multibody Dynamics 2019. ECCOMAS 2019. Computational Methods in Applied Sciences. Volume 53. Cham, Springer (2020) 503–510

[10] Popp, K., Schiehlen, W.: Ground Vehicle Dynamics. Springer, Berlin (2010)

[11] Ren, S., Romeijn, A., Klap, K.: Dynamic simulation of the maglev vehicle/guideway system. Journal of Bridge Engineering **15**(3) (2010) 269–278

[12] Schmid, P., Schneider, G., Dignath, F., Liang, X., Eberhard, P.: Static and dynamic modeling of the electromagnets of the maglev vehicle transrapid. IEEE Transactions on Magnetics **57**(2) (2021) 1–15

[13] Schmid, P., Eberhard, P.: Offset-free nonlinear model predictive control by the example of maglev vehicles. In: Proceedings of 7th IFAC Conference on Nonlinear Model Predictive Control. Bratislava (July 2021)

[14] Schmid, P., Eberhard, P., Dignath, F.: Nonlinear model predictive control for a maglev vehicle regarding magnetic saturation and guideway irregularities. IFAC-PapersOnLine **52**(15) (2019) 145–150

[15] Kurz, T., Eberhard, P., Henninger, C., Schiehlen, W.: From Neweul to Neweul-M$^2$: Symbolical equations of motion for multibody system analysis and synthesis. Multibody System Dynamics **24**(1) (2010) 25–41

https://doi.org/10.3311/ECCOMASMBD2021-121

ECCOMAS Thematic Conference on Multibody Dynamics
December 12 - 15, 2021, Budapest, Hungary

# Model Order Reduction for Elastic Multibody Systems with Fast Rotating Flexible Bodies

**Lennart Frie**[1] , **Oliver Dieterich**[2] , **Peter Eberhard**[1]

[1] Institute of Engineering and Computational Mechanics, University of Stuttgart
Pfaffenwaldring 9, 70569 Stuttgart, Germany
lennart.frie@itm.uni-stuttgart.de
peter.eberhard@itm.uni-stuttgart.de

[2] Airbus Helicopters Germany GmbH
Dynamics and Vibrations
Industriestr. 4, 86607 Donauwörth, Germany
oliver.dieterich@airbus.com

## ABSTRACT

The dynamical behavior of Elastic Multibody Systems (EMBS) is often analyzed using virtual prototypes described by high-dimensional systems of differential equations. Model Order Reduction (MOR) is a key step to permit efficient system evaluations by approximating the full system with a reduced order surrogate model. It is one challenge in MOR of EMBS, to describe the dynamics induced through the coupling of bodies in the reduced system. In this contribution, a workflow for the reduction of EMBS with fast rotating bodies is presented. The rotation causes a change of dynamical behavior due to inertia forces and, therefore, cannot be neglected. In the scope of this work a linear description of rotating bodies with constant angular velocity is given. Different projection-based MOR techniques are compared and applied to an industrial model of a helicopter with rotating rotor. For this purpose, a short introduction on modeling of EMBS and MOR is given. Substructured reduction is then contrasted to the reduction of the coupled system for modal reduction techniques, moment matching based on Krylov subspaces, and Proper Orthogonal Decomposition. The approximation errors of the reduced systems are compared in frequency domain. It is shown that rotation-dependent terms are essential to describe the dynamic behavior of the system correctly. Reduced models with low approximation errors and large speed-up are obtained with substructured Proper Orthogonal Decomposition and outperform the standard techniques modal truncation and Craig-Bampton reduction.

**Keywords:** Elastic Multibody System, Rotating Body, Model Order Reduction, Rotor Dynamics.

## 1 INTRODUCTION

Elastic Multibody Systems (EMBS) are often simulated to study the dynamical behavior of complex mechanical systems. High complexity of the underlying models and increasing demands on details make the use of Model Order Reduction (MOR) inevitable. MOR aims at generating reduced models that allow numerically efficient system evaluations with a small approximation error in the mathematically defined space of interest. Classical reduction approaches in the field of EMBS, e.g., the Craig-Bampton-Method (CBM) [1], reduce the different bodies separately with modal MOR techniques and then build the reduced system by assembling the reduced bodies. However, these standard methods can not always account correctly for the interaction between the different bodies. Nevertheless, modal approaches are still state of the art. Input-output based MOR techniques, instead, are often better suited for coupled systems [2]. This contribution extends existing MOR methods for usage for EMBS with fast rotating bodies where additional, rotation-dependent terms have to be added to the equations of motion. Furthermore, the applicability to an industrial use case, here a helicopter model with non-rotating flexible airframe and rotating main rotor, is demonstrated and the reduced order systems are compared. The novelty of the contribution is the application of existing MOR methods to EMBS with fast rotating bodies in a workflow that is applicable to large scale systems.

https://doi.org/10.3311/ECCOMASMBD2021-121

## 2 THEORETICAL BACKGROUND

### 2.1 Elastic Multibody Systems with Rotating Bodies

In computational mechanics, EMBS are often described with the floating frame of reference approach, see e.g. [3]. The idea is to separate the motion of the system into large nonlinear described rigid body motion and small linear described elastic deformations with respect to a moving reference frame that is rigidly attached to the body. The equations of motion of an EMBS can then be written as

$$\underbrace{\begin{bmatrix} \boldsymbol{M}_\mathrm{r} & \boldsymbol{M}_\mathrm{re} \\ \boldsymbol{M}_\mathrm{er} & \boldsymbol{M}_\mathrm{e} \end{bmatrix}}_{=:\boldsymbol{M}} \begin{bmatrix} \ddot{\boldsymbol{q}}_\mathrm{r} \\ \ddot{\boldsymbol{q}}_\mathrm{e} \end{bmatrix} = \boldsymbol{h}, \tag{1}$$

where the mass matrix $\boldsymbol{M}$ is separated into a submatrix $\boldsymbol{M}_\mathrm{r}$ which describes the rigid body dynamics, a submatrix $\boldsymbol{M}_\mathrm{e}$ which is a block-diagonal matrix containing all element mass matrices of the elastic bodies, and the coupling matrices $\boldsymbol{M}_\mathrm{re}$ and $\boldsymbol{M}_\mathrm{er}$ with $\boldsymbol{M}_\mathrm{re} = \boldsymbol{M}_\mathrm{er}^\mathrm{T}$. The vectors $\boldsymbol{q}_\mathrm{r}$ and $\boldsymbol{q}_\mathrm{e}$ are the rigid body coordinates and the elastic coordinates, respectively. In this work only rotational rigid body motion is considered. The force vector $\boldsymbol{h}$ summarizes Coriolis, constraint, centrifugal, inner and external forces.

A tool often used to describe small elastic deformations of a single body $k$ of the system is the linear Finite Element Method (FEM). The equations of motion of the free body $k$ then read

$$\boldsymbol{M}_\mathrm{e}^\mathrm{k}\ddot{\boldsymbol{q}}_\mathrm{e}^\mathrm{k} + \boldsymbol{K}_\mathrm{e}^\mathrm{k}\boldsymbol{q}_\mathrm{e}^\mathrm{k} = \boldsymbol{f}^\mathrm{k} \tag{2}$$

with external forces $\boldsymbol{f}^\mathrm{k}$ and the linear material stiffness matrix $\boldsymbol{K}_\mathrm{e}^\mathrm{k}$ that describes the linear part of inner forces $\boldsymbol{k}_\mathrm{e}^\mathrm{k}$ of the body resulting from virtual work of inner forces

$$\boldsymbol{k}_\mathrm{e}^\mathrm{k}\boldsymbol{\delta q}_\mathrm{e}^\mathrm{k} = \int\limits_{V_0^\mathrm{k}} \boldsymbol{\delta\dot{\varepsilon}}^{\mathrm{k}^\mathrm{T}}\boldsymbol{\sigma}^\mathrm{k}\mathrm{dV}. \tag{3}$$

The distortion velocities $\dot{\boldsymbol{\varepsilon}}^\mathrm{k}$ and the stress $\boldsymbol{\sigma}^\mathrm{k}$ in Equation (3) can be expressed with the distortion matrices $\boldsymbol{B}_\mathrm{L}^\mathrm{k}$, $\boldsymbol{B}_\mathrm{N}^\mathrm{k}$ and material matrix $\boldsymbol{H}^\mathrm{k}$ by

$$\boldsymbol{\delta\dot{\varepsilon}}^\mathrm{k} = \left(\boldsymbol{B}_\mathrm{L}^\mathrm{k} + \boldsymbol{B}_\mathrm{N}^\mathrm{k}\right)\boldsymbol{\delta\dot{q}}^\mathrm{k}, \qquad \boldsymbol{\sigma}^\mathrm{k} = \boldsymbol{\sigma}_0^\mathrm{k} + \boldsymbol{H}^\mathrm{k}\left(\boldsymbol{B}_\mathrm{L}^\mathrm{k} + \frac{1}{2}\boldsymbol{B}_\mathrm{N}^\mathrm{k}\right), \tag{4}$$

see e.g. [4]. Here, $\boldsymbol{\sigma}_0^\mathrm{k}$ are pre-stresses in the body and subscripts '$L$' and '$N$' denote linear and nonlinear parts of $\boldsymbol{B}^\mathrm{k}$, respectively. For a stress-free reference configuration, $\boldsymbol{\sigma}_0^\mathrm{k} = \boldsymbol{0}$, the inner forces of the body $k$ can be written as

$$\boldsymbol{k}_\mathrm{e}^\mathrm{k} = \underbrace{\int\limits_{V_0^\mathrm{k}} \boldsymbol{B}_\mathrm{L}^{\mathrm{k}^\mathrm{T}}\boldsymbol{H}^\mathrm{k}\boldsymbol{B}_\mathrm{L}^\mathrm{k}\mathrm{dV}}_{=\boldsymbol{K}_\mathrm{e}^\mathrm{k}\boldsymbol{q}_\mathrm{e}^\mathrm{k}} + \underbrace{\int\limits_{V_0^\mathrm{k}} \boldsymbol{B}_\mathrm{N}^{\mathrm{k}^\mathrm{T}}\boldsymbol{H}^\mathrm{k}\boldsymbol{B}_\mathrm{L}^\mathrm{k}\mathrm{dV}}_{\text{II}} + \underbrace{\frac{1}{2}\int\limits_{V_0^\mathrm{k}} \left(\boldsymbol{B}_\mathrm{L}^\mathrm{k} + \boldsymbol{B}_\mathrm{N}^\mathrm{k}\right)^\mathrm{T}\boldsymbol{H}^\mathrm{k}\boldsymbol{B}_\mathrm{N}^\mathrm{k}\mathrm{dV}}_{\text{III}}. \tag{5}$$

With the assumption that $\boldsymbol{q}_\mathrm{e}, \dot{\boldsymbol{q}}_\mathrm{e}$ and $\ddot{\boldsymbol{q}}_\mathrm{e}$ are small, the nonlinear parts (II) and (III) in Equation (5) are neglected in linear FEM and only the first integral is kept in Equation (2).

However, the situation for fast rotating bodies is more complicated and usual linear FEM is not sufficient. If the body $k$ underlies fast rotations, it is loaded with large inertia forces

$$\boldsymbol{h}_{\omega_\mathrm{e}}^\mathrm{k} = \underbrace{-2\int\limits_{V_0^\mathrm{k}} \boldsymbol{N}^{\mathrm{k}^\mathrm{T}}\tilde{\boldsymbol{\omega}}^\mathrm{k}\boldsymbol{N}^\mathrm{k}\dot{\boldsymbol{q}}_\mathrm{e}^\mathrm{k}\mathrm{dm}}_{=:\boldsymbol{G}_\mathrm{e}^\mathrm{k}\dot{\boldsymbol{q}}_\mathrm{e}^\mathrm{k}} \underbrace{-\int\limits_{V_0^\mathrm{k}} \boldsymbol{N}^{\mathrm{k}^\mathrm{T}}\tilde{\boldsymbol{\omega}}^\mathrm{k}\tilde{\boldsymbol{\omega}}^\mathrm{k}\left(\boldsymbol{R} + \boldsymbol{N}^\mathrm{k}\boldsymbol{q}_\mathrm{e}^\mathrm{k}\right)\mathrm{dm}}_{=:\boldsymbol{K}_\mathrm{s}^\mathrm{k}\boldsymbol{q}_\mathrm{e}^\mathrm{k}} \tag{6}$$

https://doi.org/10.3311/ECCOMASMBD2021-121

which add to $\boldsymbol{f}^{\mathrm{k}}$ on the right side of Equation (2). Here, $\boldsymbol{N}^{\mathrm{k}}$ are the finite element ansatz functions, $\boldsymbol{R}$ is the position of a point of the undeformed body described in the reference frame, $\tilde{\boldsymbol{\omega}}^{\mathrm{k}}$ is a skew-symmetric matrix with

$$\tilde{\boldsymbol{\omega}}^{\mathrm{k}} = \begin{bmatrix} 0 & -\omega_3^{\mathrm{k}} & \omega_2^{\mathrm{k}} \\ \omega_3^{\mathrm{k}} & 0 & -\omega_1^{\mathrm{k}} \\ -\omega_2^{\mathrm{k}} & \omega_1^{\mathrm{k}} & 0 \end{bmatrix} \tag{7}$$

and $\boldsymbol{\omega}^{\mathrm{k}} = [\omega_1^{\mathrm{k}}, \omega_2^{\mathrm{k}}, \omega_3^{\mathrm{k}}]^{\mathrm{T}}$ are the angular velocities of the body $k$. The matrices $\boldsymbol{G}_{\mathrm{e}}^{\mathrm{k}}$ and $\boldsymbol{K}_{\mathrm{s}}^{\mathrm{k}}$, defined in Equation (6), both depend on $\boldsymbol{\omega}^{\mathrm{k}}$ and are called gyroscopic matrix and spin softening matrix of the body $k$, see e.g. [5].

If the assumption of small deformations should be still justified, the large inertia forces must not result in large deformations, but only in large stress in the body. The stress is in linear approximation described by $\boldsymbol{\sigma}^{\mathrm{k}} = \boldsymbol{H}^{\mathrm{k}}\boldsymbol{B}_{\mathrm{L}}^{\mathrm{k}}$ and, thus, the integral (II) in Equation (5) is not small anymore. For this reason, an additional stiffness has to be considered in directions of large inertia forces. This so-called geometric stiffness depends on the stress in the body and, therefore, on the rotational velocity of the body. It can be added to the linear equation of motion of the body by expanding the integral (II) to a Taylor series at $\boldsymbol{q}_{\mathrm{e}}^{\mathrm{k}} = \boldsymbol{0}$ and just considering the terms linear in $\boldsymbol{q}_{\mathrm{e}}^{\mathrm{k}}$. This leads to the approximation

$$\boldsymbol{K}_{\mathrm{geo}}^{\mathrm{k}}\boldsymbol{q}_{\mathrm{e}}^{\mathrm{k}} \approx \int_{V_0^{\mathrm{k}}} \boldsymbol{B}_{\mathrm{N}}^{\mathrm{k}\mathrm{T}}\boldsymbol{H}^{\mathrm{k}}\boldsymbol{B}_{\mathrm{L}}^{\mathrm{k}}\mathrm{dV}, \tag{8}$$

where the matrix $\boldsymbol{K}_{\mathrm{geo}}^{\mathrm{k}}$ is called geometric stiffness matrix. The linear approximation is only valid for a given nominal stress in the body and, thus, for a given nominal angular velocity. For this specific velocity, the updated equations of motion of a rotating body then read

$$\boldsymbol{M}_{\mathrm{e}}^{\mathrm{k}}\ddot{\boldsymbol{q}}_{\mathrm{e}}^{\mathrm{k}} + \boldsymbol{G}_{\mathrm{e}}^{\mathrm{k}}\dot{\boldsymbol{q}}_{\mathrm{e}}^{\mathrm{k}} + \underbrace{\left(\boldsymbol{K}_{\mathrm{e}}^{\mathrm{k}} + \boldsymbol{K}_{\mathrm{geo}}^{\mathrm{k}} + \boldsymbol{K}_{\mathrm{s}}^{\mathrm{k}}\right)}_{=:\,\hat{\boldsymbol{K}}_{\mathrm{e}}^{\mathrm{k}}}\boldsymbol{q}_{\mathrm{e}}^{\mathrm{k}} = \boldsymbol{f}_{\mathrm{e}}^{\mathrm{k}} \tag{9}$$

with $\boldsymbol{G}_{\mathrm{e}}^{\mathrm{k}}$ and $\boldsymbol{K}_{\mathrm{s}}^{\mathrm{k}}$ from Equation (6), $\boldsymbol{K}_{\mathrm{geo}}^{\mathrm{k}}$ from Equation (8), and the updated stiffness matrix $\hat{\boldsymbol{K}}_{\mathrm{e}}^{\mathrm{k}}$. For a detailed explanation see [4].

With the description of the separate bodies the equations of motion of the coupled system can now be set up. A suitable description of a coupled EMBS is the formulation in minimal coordinates $\boldsymbol{q} \in \mathbb{R}^N$ with

$$\begin{bmatrix} \boldsymbol{q}_{\mathrm{r}} \\ \boldsymbol{q}_{\mathrm{e}} \end{bmatrix} = \boldsymbol{J}\boldsymbol{q}, \tag{10}$$

where $\boldsymbol{J}$ is the global Jacobian matrix of the system, see e.g. [6]. The coupled EMBS is then described by

$$\boldsymbol{J}^{\mathrm{T}}\boldsymbol{M}\boldsymbol{J}\ddot{\boldsymbol{q}} + \boldsymbol{J}^{\mathrm{T}}\begin{bmatrix} \boldsymbol{0} & \boldsymbol{0} \\ \boldsymbol{0} & \boldsymbol{G}_{\mathrm{e}} \end{bmatrix}\boldsymbol{J}\dot{\boldsymbol{q}} + \boldsymbol{J}^{\mathrm{T}}\begin{bmatrix} \boldsymbol{0} & \boldsymbol{0} \\ \boldsymbol{0} & \hat{\boldsymbol{K}}_{\mathrm{e}} \end{bmatrix}\boldsymbol{J}\boldsymbol{q} = \boldsymbol{J}^{\mathrm{T}}\begin{bmatrix} \boldsymbol{h}_{\mathrm{r}} \\ \boldsymbol{f}_{\mathrm{e}} \end{bmatrix}, \tag{11}$$

where $\boldsymbol{M}_{\mathrm{e}}$ in $\boldsymbol{M}$, $\boldsymbol{G}_{\mathrm{e}}$ and $\hat{\boldsymbol{K}}_{\mathrm{e}}$ are block-diagonal matrices containing the corresponding matrices of the different bodies, $\boldsymbol{h}_{\mathrm{r}}$ are the rigid body forces, and $\boldsymbol{f}_{\mathrm{e}}$ are the external forces applied to the nodes of the elastic bodies.

The matrix $\boldsymbol{J}$ depends on the orientation of the reference systems of the bodies and, therefore, Equation (11) is nonlinear. For small rotations around a reference orientation, it can be linearized with small-angle approximation and neglect of terms nonlinear in $\boldsymbol{q}$. The linearized equation of motion of the system then reads

$$\boldsymbol{M}_{\mathrm{L}}\ddot{\boldsymbol{q}} + \boldsymbol{G}_{\mathrm{L}}\dot{\boldsymbol{q}} + \boldsymbol{K}_{\mathrm{L}}\boldsymbol{q} = \boldsymbol{f}_{\mathrm{L}}, \tag{12}$$

https://doi.org/10.3311/ECCOMASMBD2021-121

but includes certain terms due to fast rotations. The index 'L' is omitted in the following but we always refer to the linearized system from here on. It can be interpreted as second order system

$$\begin{aligned} \boldsymbol{M}\ddot{\boldsymbol{q}} + \boldsymbol{G}\dot{\boldsymbol{q}} + \boldsymbol{K}\boldsymbol{q} &= \boldsymbol{B}\boldsymbol{u}, \\ \boldsymbol{y} &= \boldsymbol{C}\boldsymbol{q} \end{aligned} \tag{13}$$

with system matrices $\boldsymbol{M}, \boldsymbol{G}, \boldsymbol{K} \in \mathbb{R}^{N\times N}, \boldsymbol{B} \in \mathbb{R}^{N\times b}, \boldsymbol{C} \in \mathbb{R}^{c\times N}$ inputs $\boldsymbol{u} \in \mathbb{R}^b$ and outputs $\boldsymbol{y} \in \mathbb{R}^c$.

### 2.2 Projection-Based Model Order Reduction

The dimension $N$ of the system in Equation (13) is usually high and system evaluations are numerically expensive. It is the goal of MOR, to approximate the full order system with a low order system while simultaneously ensuring a low approximation error. In projection-based MOR this is done by the projection of the state vector

$$\boldsymbol{q} \approx \boldsymbol{V}\tilde{\boldsymbol{q}}, \qquad \dim(\boldsymbol{q}) = N \gg \dim(\tilde{\boldsymbol{q}}) = n \tag{14}$$

into a low dimensional subspace $\mathscr{V} = \operatorname{span}\{\boldsymbol{V}\}$ with the projection matrix $\boldsymbol{V} \in \mathbb{R}^{N\times n}$. Plugging this into Equation (13) and left-multiplying with $\boldsymbol{V}^{\mathrm{T}}$ yields the reduced order model

$$\begin{aligned} \underbrace{\boldsymbol{V}^{\mathrm{T}}\boldsymbol{M}\boldsymbol{V}}_{=:\tilde{\boldsymbol{M}}}\ddot{\tilde{\boldsymbol{q}}} + \underbrace{\boldsymbol{V}^{\mathrm{T}}\boldsymbol{G}\boldsymbol{V}}_{=:\tilde{\boldsymbol{G}}}\dot{\tilde{\boldsymbol{q}}} + \underbrace{\boldsymbol{V}^{\mathrm{T}}\boldsymbol{K}\boldsymbol{V}}_{=:\tilde{\boldsymbol{K}}}\tilde{\boldsymbol{q}} &= \underbrace{\boldsymbol{V}^{\mathrm{T}}\boldsymbol{B}}_{=:\tilde{\boldsymbol{B}}}\boldsymbol{u}, \\ \tilde{\boldsymbol{y}} &= \underbrace{\boldsymbol{C}\boldsymbol{V}}_{=:\tilde{\boldsymbol{C}}}\tilde{\boldsymbol{q}}. \end{aligned} \tag{15}$$

The choice of $\boldsymbol{V}$ is the key challenge here, since there are two contrary requirements, i.e. that the reduced system dimension shall be small, $n \ll N$, and the approximation error is requested to be low. Classical modal approaches propose finding $\boldsymbol{V}$ by taking selected dominant eigenmodes $\boldsymbol{V} = [\boldsymbol{\phi}_1, \ldots, \boldsymbol{\phi}_n]$ of the system as its columns.

A second approach is to approximate the input-output behavior of the system. Therefore, in Krylov reduction the transfer function $\boldsymbol{H}(s)$ of Equation (13) is written as a power series where $s$ is the Laplace variable. Now, the terms of the power series of the reduced system, that are also called moments, are matched up to a defined order $J_l$ around shifts in frequency domain $s = \sigma_l$ with those of the full system. The moments are not calculated explicitly, but are implicitly matched by the use of Krylov subspaces. A numerically stable algorithm to produce such subspaces is the second order Arnoldi (SOAR) algorithm, explained in [7] and [8]. Choosing the projection matrix for $J_l = 1$ with

$$\operatorname{span}(\boldsymbol{V}) = \operatorname{span}[\ (\sigma_1^2\boldsymbol{M} + \sigma_1\boldsymbol{G} + \boldsymbol{K})^{-1}\boldsymbol{B}, \quad \ldots, \quad (\sigma_\nu^2\boldsymbol{M} + \sigma_\nu\boldsymbol{G} + \boldsymbol{K})^{-1}\boldsymbol{B}\ ] \tag{16}$$

for $l = 1, \ldots, \nu$ ensures

$$\boldsymbol{H}(\sigma_l) = \tilde{\boldsymbol{H}}(\sigma_l) \tag{17}$$

and if $\boldsymbol{C} = \boldsymbol{B}^{\mathrm{T}}$,

$$\frac{\partial \boldsymbol{H}(\sigma_l)}{\partial s} = \frac{\partial \tilde{\boldsymbol{H}}(\sigma_l)}{\partial s}, \tag{18}$$

as [9] shows. In this basic form, the order of the reduced model is always a multiple of the number of inputs $b = \dim(\boldsymbol{u})$.

A third approach on generating $\boldsymbol{V}$ is based on balanced truncation, see e.g. [10]. It aims at retaining just those states in the reduced system that are easy to reach and easy to observe, i.e., those that require little energy to be reached and yield large observation signals when excited. The computation of the Gramian matrices that are required to detect those states is numerically

https://doi.org/10.3311/ECCOMASMBD2021-121

expensive and, therefore, not practicable for large-scale systems. However, the Gramian matrix of controllability

$$\boldsymbol{P} = \frac{1}{\pi} \int_{s_{\min}}^{s_{\max}} \hat{\boldsymbol{F}}(s) \hat{\boldsymbol{F}}(s)^{\mathrm{T}} \mathrm{ds} \tag{19}$$

with

$$\hat{\boldsymbol{F}}(s) := \left[\mathrm{Re}\left(\boldsymbol{F}(s)\right), \mathrm{Im}\left(\boldsymbol{F}(s)\right)\right] \in \mathbb{R}^{\mathrm{N}\times 2\mathrm{b}}, \quad \boldsymbol{F}(s) = \left(s^2\boldsymbol{M} + s\boldsymbol{G} + \boldsymbol{K}\right)^{-1} \boldsymbol{B} \in \mathbb{C}^{\mathrm{N}\times \mathrm{b}} \tag{20}$$

can be approximated with Proper Orthogonal Decomposition (POD). Therefore, $\nu$ different snapshots $\hat{\boldsymbol{F}}(\sigma_l)$ are computed at frequencies $s = \sigma_l$ for $l = 1, ..., \nu$ and these snapshots are combined to

$$\boldsymbol{Z} = \left[\hat{\boldsymbol{F}}(\sigma_1), \hat{\boldsymbol{F}}(\sigma_2), \ldots, \hat{\boldsymbol{F}}(\sigma_\nu)\right] \in \mathbb{R}^{N\times 2\nu b}. \tag{21}$$

The projection matrix is then build with the first $n$ eigenvectors $\boldsymbol{v}_{\mathrm{i}} \in \mathbb{R}^{\mathrm{N}}, i = 1, 2, ..., n$ from the eigenvalue problem

$$\frac{1}{2\nu b} \boldsymbol{Z}\boldsymbol{Z}^{\mathrm{T}} \boldsymbol{v}_{\mathrm{i}} = \lambda_{\mathrm{i}} \boldsymbol{v}_{\mathrm{i}} \tag{22}$$

and reads $\boldsymbol{V} = [\boldsymbol{v}_1, \boldsymbol{v}_2, \ldots, \boldsymbol{v}_n]$. For further details on Gramian matrices and POD, see [10] and [11].

## 3 REDUCTION OF ELASTIC MULTIBODY SYSTEMS WITH ROTATING BODIES

A workflow for the reduction of EMBS is outlined in Figure 1. We start with discretized flexible bodies $k = 1, \ldots, \kappa$ as used in FEM in the upper box. For the sake of simplicity, just two bodies are illustrated here, but the procedure is also applicable for an EMBS with $\kappa > 2$ bodies. The equations of motion of the free bodies are formulated with linear FEM. The marked points are the coupling points that have to be defined.

If a body $k$ underlies fast rotations, additional terms in the linear equation of motion have to be considered. Therefore, the inertia forces are computed for a given constant rotational velocity vector $\boldsymbol{\omega}_{\mathrm{c}}^{\mathrm{k}}$. In this work the multibody simulation tool Neweul-M$^2$ [12] is used for the computation of the inertia forces. The assumption of a constant rotational velocity is valid for many use cases and necessary in order to obtain a linear description that represents the nonlinear rotation-dependent effects so that this linear description can be used for linear MOR. With the constant inertia forces, also the gyroscopic matrix $\boldsymbol{G}_{\mathrm{e}}^{\mathrm{k}}$ and the spin softening matrix $\boldsymbol{K}_{\mathrm{s}}^{\mathrm{k}}$ are obtained.

With the constant inertia forces $\boldsymbol{h}_{\omega_{\mathrm{e}}}^{\mathrm{k}}(\boldsymbol{\omega}_{\mathrm{c}}^{\mathrm{k}})$, the geometric stiffness matrix $\boldsymbol{K}_{\mathrm{geo}}^{\mathrm{k}}$ can be computed iteratively from the equilibrium $\boldsymbol{h}_{\omega_{\mathrm{e}}}^{\mathrm{k}}(\boldsymbol{\omega}_{\mathrm{c}}^{\mathrm{k}}) = \boldsymbol{k}_{\mathrm{e}}^{\mathrm{k}}$ with a nonlinear static finite-element solver, here MSC Nastran [13]. If the EMBS contains different rotating bodies, this procedure is carried out for each of them and Equation (9) is obtained for each body. Up to here all elastic bodies are treated separately.

The reduced model of the EMBS can now be calculated with two different strategies introduced in [14]. One, illustrated on the left side of Figure 1, is to first couple the system and thereafter reduce the coupled system with one of the methods proposed in Subsection 2.2. This workflow is in the following referred to as block structure preserving reduction (BSPR). However, another procedure that is often beneficial for the reduction of multibody systems is to divide the system into substructures, e.g. the individual bodies of a system with $\kappa$ bodies, first and then build reduced bases separately for these bodies. The reduced bodies are afterwards coupled to obtain the reduced coupled system. This approach is in the following called separate bases reduction (SBR) and visualized with the right path in Figure 1. The reduced bodies are graphically indicated by sparser grids. Reduced separate substructure models have various advantages. They are often easier to validate [15] and provide the possibility of independent component optimization. In addition, substructured models are useful in modern product development where different departments work on different components [14] because substructures can be changed without having to reduce the

https://doi.org/10.3311/ECCOMASMBD2021-121

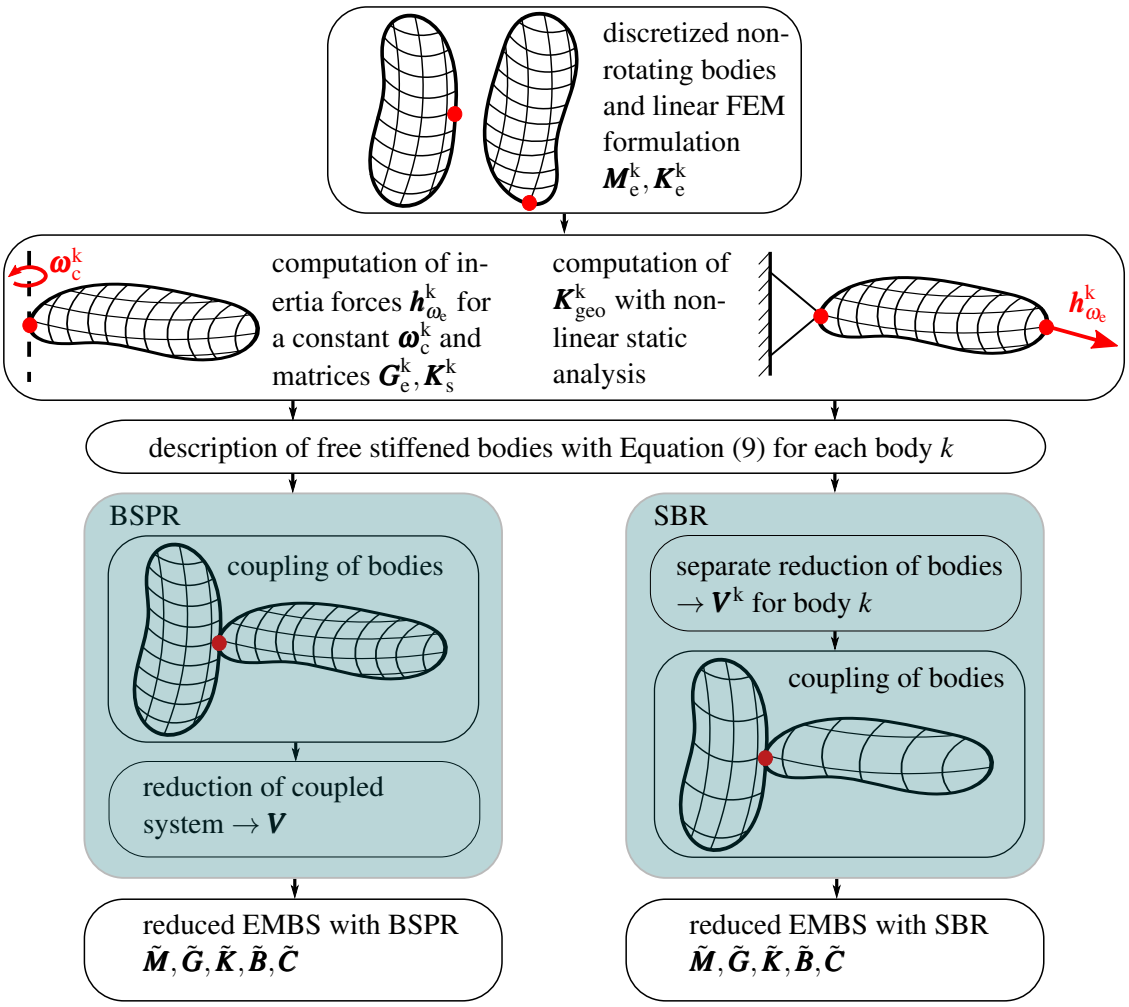


Figure 1: Workflow for the reduction of EMBS with rotating bodies

whole system again. One of the most frequently used SBR methods is the CBM introduced in [1]. The CBM is an extension of simple modal truncation and combines eigenmodes of the body with static constraint modes that define displacements due to unit forces at boundary nodes where the bodies are connected.

## 4 NUMERICAL EXAMPLE

The workflow presented in Section 3 is now applied to an industrial helicopter model as shown in Figure 2. The model of the airframe and the model of the rotor result from discretization for FEM and have 281 992 and 3 726 degrees of freedom (dof), respectively. A typical problem here is the approximation of the airframe with a low-rank model which can account for interactions with a coupled rotor. This is needed, e.g., for multi-domain simulations with aerodynamic rotor simulation tools. A basic modal truncation of the airframe model without considering the rotor leads to a reduced model that neglects important modes, e.g., shaft-bending modes. To counteract this, it is the state of the art approach to attach a surrogate mass that replaces the rotor inertia as explained in [16]. The loaded model is then reduced with modal truncation and the added surrogate mass is removed later by the use of negative boundary conditions in the coupling process. It is a problem with this procedure to find an adequately set up surrogate mass to approximate the inertia of a rotating rotor.

During operation, the rotor rotates with a constant velocity. This allows the application of the

https://doi.org/10.3311/ECCOMASMBD2021-121

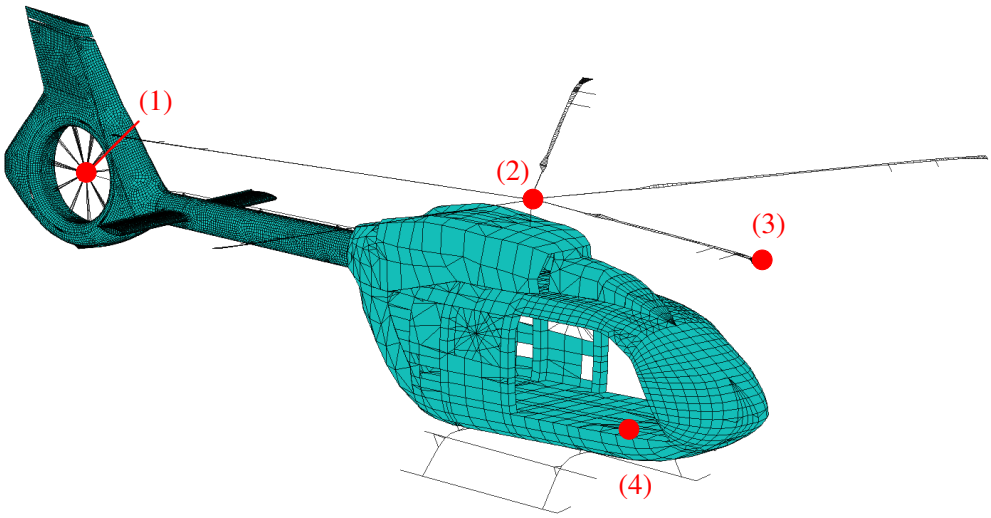


Figure 2: Model of a helicopter airframe with coupled rotor and marked inputs and outputs (model provided by Airbus Helicopters)

procedure described in Section 3 to obtain an appropriate linear model. The difference between the rotor modeled with linear FEM alone and with the additional rotation-dependent terms introduced in Subsection 2.1 is shown in Figure 3.

The Campbell Diagram in Figure 3a illustrates the change of blade eigenfrequencies over increasing angular velocities. Here, the first 9 eigenfrequencies are shown over the angular velocity subjected to the nominal operational velocity. The linear equation of motion of a rotating body is only valid for a constant rotational velocity. Thus, the Campbell Diagram results from computation of the rotation dependent terms at 50 linearly spaced frequencies in the interval $[0, 140]\,\% \cdot f_{\mathrm{op}}$ with nominal operation frequency $f_{\mathrm{op}}$. Some eigenfrequencies are strongly shifted, e.g., the first eigenfrequency from 1.14 Hz in the non-rotating case to 6.69 Hz for rotation with $f_{\mathrm{op}}$ or the third eigenfrequency from 6.23 Hz to 17.42 Hz. Especially the blade flapping eigenfrequencies marked with $1, 3, 4, 6$ and 9 rise strongly due to geometric stiffening. The dependency of the eigenfrequen-

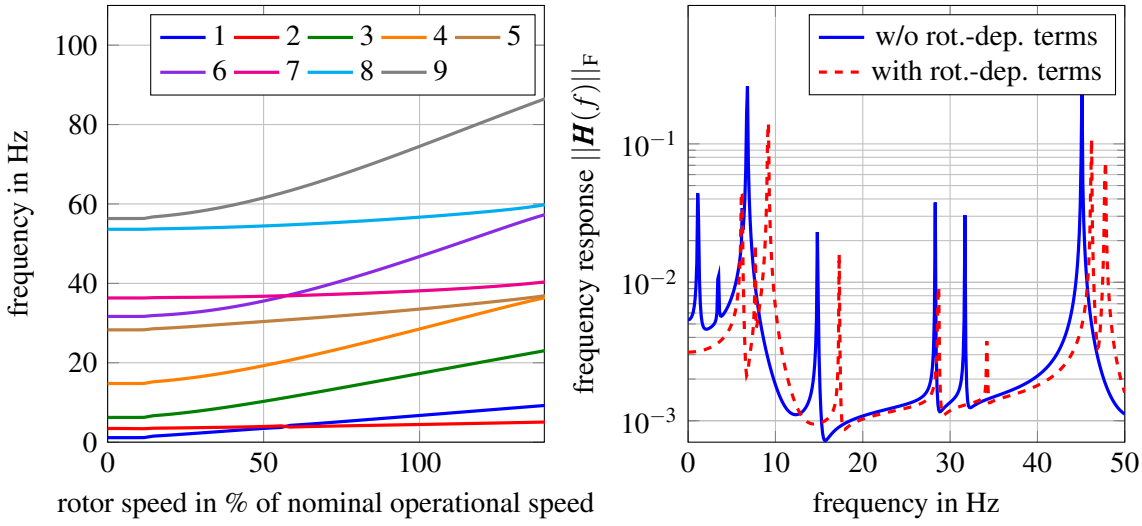


(a) Campbell Diagram

(b) Frobenius norm of the transfer function

Figure 3: Change of the dynamical behavior of a clamped rotor blade due to rotation (model provided by Airbus Helicopters)

https://doi.org/10.3311/ECCOMASMBD2021-121

cies on the rotational velocity shows insistently that the dynamical behavior of the blade is strongly dependent on its rotation and, therefore, that the equations of motion are nonlinear in general.

In Figure 3b the transfer function of two different models is compared. One is obtained from linear FEM, alone where the rotational dependence is ignored. The other model is also linear but contains the additional rotation-dependent terms at operational angular velocity. Input and output for the transfer function are both set at the tip of the blade, marked with (3) in Figure 2. It can be seen that both models behave very different. For a static load the rotating blade deforms less than the non-rotating blade which indicates the increase of stiffness due to geometric stiffening. With the rotation-dependent terms, the eigenfrequencies of the model change. Hereby, the amplitudes of the transfer function shift as well. Furthermore all amplitudes of the frequency response are lower for the stiffened rotating blade.

Both plots in Figure 3 demonstrate that the dynamical behavior of the blade is strongly dependent on its rotation and thus, that the rotation dependent terms have to be included in the equation of motion of the EMBS. For the reduction of the rotor and the study of the system input-output behavior it is thus not adequate to just use the non-rotating model obtained from linear FEM. Instead, the geometric stiffness matrix and other rotation-dependent terms from Equation (9) have to be included in the equations of motion of the rotating blade. In the following, 4 characteristic nodes are depicted for the study of the dynamical behavior as marked in Figure 2. They display the deformations at the fenestron hub (1), at the coupling point of rotor and airframe which is the main rotor hub (2), near the blade tip (3), and at the pilot's feet (4).

## 5 RESULTS

In this section different reduction approaches are compared for the helicopter model. Therefore, the relative transfer function error of the reduced system in Frobenius norm

$$\varepsilon = \frac{||\boldsymbol{H}(s) - \tilde{\boldsymbol{H}}(s)||_F}{||\boldsymbol{H}(s)||_F} \tag{23}$$

is calculated in the frequency band from 1 to 50 Hz with the Frobenius norm

$$||\boldsymbol{H}(s)||_F = \sqrt{\text{trace}\left(\boldsymbol{H}(s)\boldsymbol{H}^H(s)\right)}. \tag{24}$$

### 5.1 Reduction of Free Bodies

At first the different reduction methods are compared for the free bodies rotor and airframe separately. An adequately reduced model of the separate bodies is a prerequisite for the combination in the coupled system. In Figure 4 the airframe and the rotor are reduced separately to orders around 100. The order of the reduced models is given in the legend in each case. Four different models are compared for the airframe and three models are compared for the rotor. The models are generated with the reduction techniques introduced in Subsection 2.2, model truncation (mod), moment matching with Krylov subspaces (Krylov) and POD. In addition to that, a reduction with an added surrogate mass is implemented for the airframe (mod am). This is done by generating the projection matrix with a model that contains an additional surrogate mass to represent the rotor that will be attached later. The model without surrogate mass is than reduced with the obtained projection matrix.

The modal truncation shows the poorest results with an error in the range of $10^{-3}$ to more than $10^{0}$. As described in [10], this is because a large number of eigenmodes is needed to account for local forces and, therefore, to describe the input-output behavior correctly. For the defined inputs and outputs the reduced airframe model generated with an added point mass reveals a smaller approximation error because the surrogate mass attached to the rotor shaft ensures to keep relevant shaft-bending modes in the reduced basis.

https://doi.org/10.3311/ECCOMASMBD2021-121

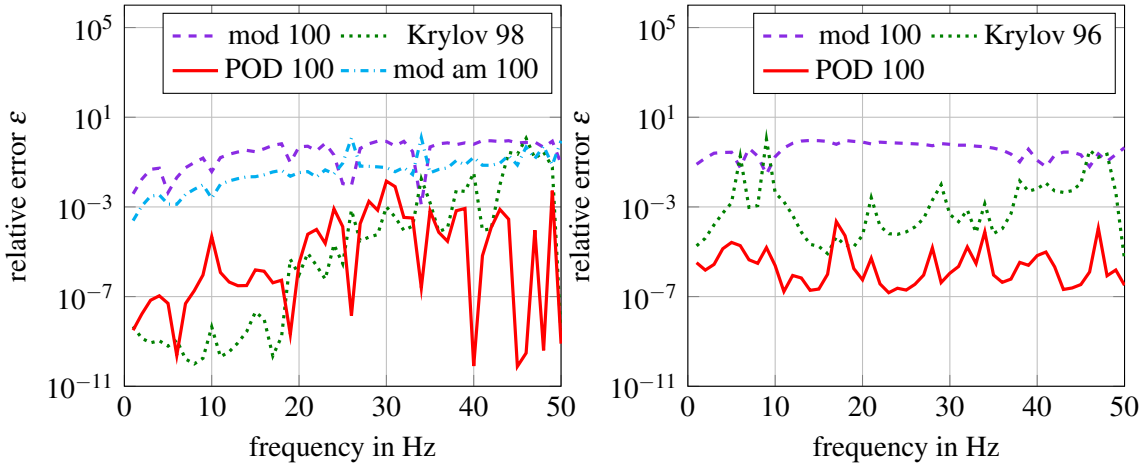


(a) airframe (b) rotor

Figure 4: Relative error for reduced bodies

The error for moment matching depends highly on the chosen shifts $\sigma_k$. They are here set linearly spaced between 0 and 50 Hz. For a reduction order of about 100, moment-matching displays a smaller error than the modal methods. The POD allows a small approximation error for both bodies and here never exceeds $10^{-2}$. The snapshots for POD are in this work linearly distributed in the range from 1 to 50 Hz with steps of 1 Hz. According to the BSPR workflow, the reduced airframe and rotor can now be coupled to obtain the reduced system.

### 5.2 Reduction of Coupled Elastic Multibody Systems

Figure 5 shows the reduction errors for BSPR and SBR. With the exception of modal truncation, the comparison of both plots exhibits that the reduction errors for SBR are at least similarly small as those of BSPR. Modal truncation with added mass and CBM are techniques developed especially for SBR and, therefore, are not applicable in the BSPR framework and only included in the comparison of SBR. For both approaches the POD displays the smallest error.

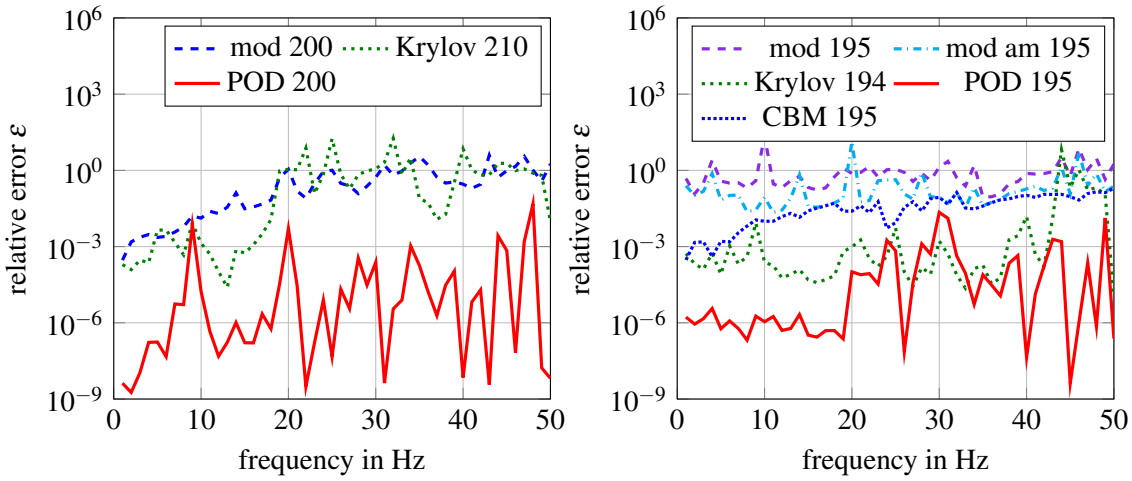


(a) BSPR (b) SBR

Figure 5: Relative error for reduced system

For the SBR, simple modal truncation reveals large errors. This is because the reduction of the bodies already induces a relatively large error as was shown in Subsection 5.1. In addition to that, modal truncation can neither account for the interaction between the different bodies and the dynamics induced by the coupling nor is it able to regard arbitrary dissipative forces, i.e., if $\boldsymbol{G}$ is not proportional to $\boldsymbol{M}$ and $\boldsymbol{K}$, which is the case if $\boldsymbol{G} \neq \boldsymbol{0}$, the eigenmodes may become complex. The approach outlined in Section 4, were a surrogate mass is attached to generate the reduced basis for the airfame is also presented in Figure 5b. The reduced model of the airframe with added mass is coupled to a reduced rotor obtained from modal truncation. The error for the resulting reduced coupled system is smaller than for the model generated with simple modal truncation but still relatively large. The modal truncation is also improved with the CBM by adding constraint modes which leads to a small error especially for low frequencies. Hence, both state of the art methods CBM and modal truncation with added mass can both improve the simple modal truncation. Nevertheless, the input-output based techniques, moment matching and POD, lead to even smaller approximation errors for the same reduction order. Especially the POD exhibits a good approximation to the full order transfer function. For the reduction order of 195, the maximal relative error for POD is $10^{-2}$ in contrast to $10^{-1}$ for CBM and $10^{1}$ for modal truncation with added mass.

It is another advantage of POD is that the reduction error scales down fast with increasing reduced orders. Figure 6 shows the relative errors for POD with SBR with reduced orders 95, 195 and 295. While the reduced model of order 95 exhibits a relatively large approximation error between $10^{-3}$ and $10^{0}$, the previously used model with 195 dof has a much smaller error especially for low frequencies. The approximation can be further improved by increasing the reduced order to 295 with the result that the error never exceeds $10^{-4}$. This offers the possibility to choose a model that is reduced to the respective requirements in terms of numerical efficiency and approximation quality. If one wishes for a smaller approximation error for the POD in Figure 5b, this can be reached by increasing the reduction order.

The reduction of the system from 285 713 dof to only 195 dof enables much more efficient evaluations. The calculation of the transfer function at a single frequency point takes 56.4 CPU seconds for the full system and only 0.05 seconds for the reduced one which is less than 0.1% and means an enormous speed-up.

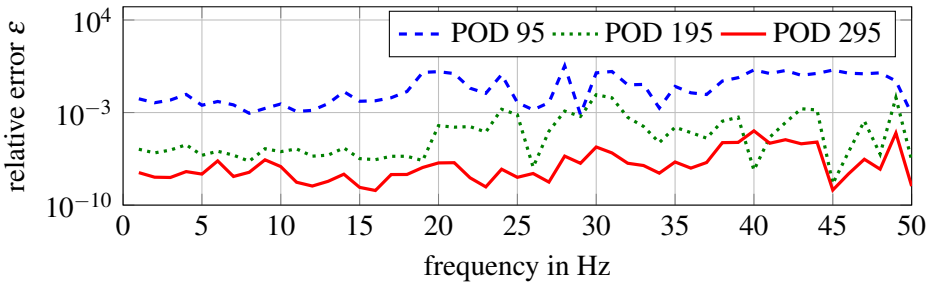


Figure 6: Relative error of POD with SBR for different reduction orders

### 5.3 Comparison of Modeling Error and Reduction Error

Two different possible errors were presented in Section 4 and Subsection 5.2. One arises from neglecting the rotation-dependent terms when formulating the equations of motion of a rotating body and is referred to here as modeling error. This error is prevented by adding these additional terms for a given constant angular velocity. The other error is the approximation error from reduction and is inevitable since a reduced model is necessary to enable efficient system evaluations. In this section both errors are contrasted. Therefore, the system is excited at the blade tip in vertical direction and the deformations at the output nodes (1), (2), (3) and (4) are computed.

https://doi.org/10.3311/ECCOMASMBD2021-121

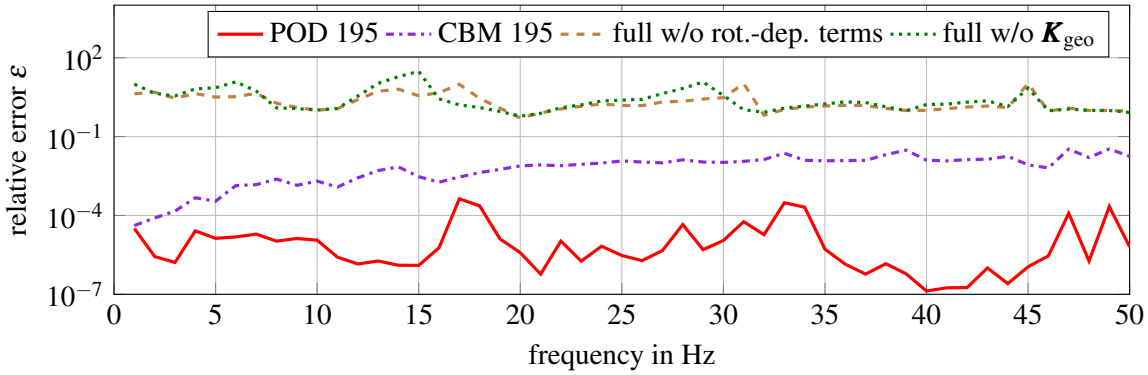


Figure 7: Influence of rotation dependent terms on vibration behavior

Figure 7 visualizes the relative error of the transfer functions for the different models related to the transfer function of the full-order model with rotation-dependent terms at nominal angular velocity. The errors of the reduced systems obtained from POD and CBM in the framework of SBR are confronted with the errors of two full-order models. One, called 'full w/o rot.-dep terms', neglects all rotation dependent terms and the other one, called 'full w/o $\boldsymbol{K}_{\text{geo}}$' is a model where geometric stiffness is neglected but all other rotation-dependent terms from Equation (9) are contained.

The error made when using the full non-rotating rotor model or a model without geometric stiffness is notable larger than the error of both reduced models on the presented frequency interval. Thus, all reduced models derived from the non-rotating model cannot serve as adequate reduced order model for the EMBS with fast rotating rotor. It can be seen, that especially the geometric stiffening of the body has large impact on the dynamical behavior. The reduced model generated with CBM with 195 dof approximates the full-order system better than both full-order models and exhibits low approximation errors i.e. for low frequencies. The POD again approximates the system with rotating rotor even better and has the smallest error over the whole frequency range. It reveals an maximal approximation error that is smaller in 4 orders of magnitude in comparison to the models without rotation-dependent terms.

## 6 CONCLUSION

This contribution presented a workflow for the reduction of Elastic Multibody Systems with rotating bodies. The obtained results improve the results from standard techniques highly. It was demonstrated that rotation dependent terms, i.e. geometric stiffness, have to be considered when modeling systems with fast rotating elastic bodies. Based on the linear description of a constantly rotating body with small deviations from reference configuration, projection based linear model order reduction could be applied. Especially the reduction of the bodies separately with proper orthogonal decomposition followed by a coupling of the reduced bodies allowed reduced models with low approximation errors. This was shown by consideration of the transfer function error of an industrial helicopter model. With the generated reduced, model the time needed to calculate the transfer function of the system, could be reduced by a factor greater than 1000.

**Acknowledgments**

This research is done within the framework of the EVOLVE research project (FKZ 20A1902C) funded by the German Federal Ministry of Economics and Energy.

Gefördert durch:

Bundesministerium für Wirtschaft und Energie

aufgrund eines Beschlusses des Deutschen Bundestages

https://doi.org/10.3311/ECCOMASMBD2021-121

## REFERENCES


[1] Craig, R.; Bampton, M.: Coupling of Substructures for Dynamic Analyses. AIAA Journal, Vol. 6, No. 7, pp. 1313–1319, 1968.

[2] Holzwarth, P.; Eberhard, P.: Input-Output Based Model Reduction for Interconnected Systems. In Oñate, E.; Oliver, J.; Huerta, A. (Eds.): Proceedings of the 5th European Conference of Computational Mechanics, Barcelona, 2014.

[3] Shabana, A.: Flexible Multibody Dynamics: Review of Past and Recent Developments. Multibody System Dynamics, Vol. 1, pp. 189–222, 1997.

[4] Schwertassek, R.; Wallrapp, O.: Dynamik flexibler Mehrkörpersysteme (in German). Braunschweig: Vieweg, 1999.

[5] Kirchgäßner, B.: Finite Elements in Rotordynamics. Procedia Engineering, Vol. 144, pp. 736–750, 2016.

[6] Nowakowski, C.: Zur Modellierung und Reduktion elastischer Bauteile unter verteilten Lasten für die Mehrkörpersimulation (in German). Dissertation, Schriften aus dem Institut für Technische und Numerische Mechanik der Universität Stuttgart, Vol. 35. Aachen: Shaker Verlag, 2014.

[7] Salimbahrami, S.B.: Structure Preserving Order Reduction of Large Scale Second Order Models. Dissertation, Technische Universität München. München, 2005.

[8] Fehr, J.: Automated and Error-Controlled Model Reduction in Elastic Multibody Systems. Dissertation, Schriften aus dem Institut für Technische und Numerische Mechanik der Universität Stuttgart, Vol. 21. Aachen: Shaker Verlag, 2011.

[9] Baur, U.; Beattie, C.; Benner, P.; Gugercin, S.: Interpolatory Projection Methods for Parameterized Model Reduction. SIAM Journal for Scientific Computing, Vol. 33, No. 5, pp. 2489–2518, 2011.

[10] Lehner, M.: Modellreduktion in elastischen Mehrkörpersystemen (in German). Dissertation, Schriften aus dem Institut für Technische und Numerische Mechanik der Universität Stuttgart, Vol. 10. Aachen: Shaker Verlag, 2007.

[11] Antoulas, A.: Approximation of Large-Scale Dynamical Systems. Philadelphia: SIAM, 2005.

[12] Kurz, T.; Eberhard, P.; Henninger, C.; Schiehlen, W.: From Neweul to Neweul-M$^2$: Symbolical Equations of Motion for Multibody System Analysis and Synthesis. Multibody System Dynamics, Vol. 24, No. 1, pp. 25–41, 2010.

[13] MSCSoftware: MSC Nastran 2012 – Quick Reference Guide, 2011.

[14] Holzwarth, P.: Modellordnungsreduktion für substrukturierte mechanische Systeme (in German). Dissertation, Schriften aus dem Institut für Technische und Numerische Mechanik der Universität Stuttgart, Vol. 51. Aachen: Shaker Verlag, 2017.

[15] Bestle, P.; Eberhard, P.; Hanss, M.: Musical Instruments - Sound Synthesis of Virtual Idiophones. Journal of Sound Vibration, Vol. 395, pp. 187–200, 2017.

[16] Hasbun, M.; Saberi, H.; Blumenstein, R.: Modal Elastic Component Enhancements for RCAS. VFS International 76th Annual Forum & Technology Display, 2020.

https://doi.org/10.3311/ECCOMASMBD2021-170



# Analysis of the Dynamic Behavior of a Counterbalance Forklift Truck through Multibody Modelling and Simulation

**Marco Pinelli**[1,2], **Monica Giovannucci**[2], **Alberto Martini**[3]

[1] School of Engineering
University of Bologna
V.le del Risorgimento 2
40136 Bologna, Italy
marco.pinelli5@studio.unibo.it

[2] Toyota Material Handling
Manufacturing Italy SpA
Via Persicetana Vecchia 10,
40132 Bologna, Italy
monica.giovannucci@toyota-industries.eu

[3] DIN – Dept. of Industrial Engineering
University of Bologna
V.le del Risorgimento 2,
40136 Bologna, Italy
alberto.martini6@unibo.it

## ABSTRACT

This work deals with the analysis of the dynamic response of a counterbalance forklift truck prototype when performing standard verification maneuvers, defined by the manufacturer's testing protocols. The research aims at developing numerical tools based on multibody models to predict accurately the dynamic loads acting on the forklift in the conditions of interest. In particular, this study focuses on a specific test condition, namely the passage on a steel plate obstacle at constant speed, which is one of the most severe maneuvers of the reference cycle in terms of dynamic loads. A model of the complete forklift is developed inside a commercial multibody environment. It takes into account the ground/tire interactions, by means of a simplified nonlinear contanct model, and the load handling assembly dynamics. An experimental campaign is designed and conducted to asses the vehicle behavior when running on the obstacle, by measuring the vibrations of the chassis and of the mast, as well as the forces generated by the mast tilting actuators. The measured data are exploited for model update and validation. The numerical results provided by the updated model show a satisfactory accuracy.

**Keywords:** Virtual Testing, Vehicle Dynamics, Tire-ground Interaction, Experimental Validation, Force Transducers.

## 1. INTRODUCTION

Counterbalance forklift trucks (FLTs) represent a very common equipment for material handling in industrial applications [1]. Usually, the vertical compliance of their suspension systems is mainly provided by tires, since they are not equipped with elastic elements and/or shock absorbers, with the vehicle being supported at three points (namely, the two front wheels and the pivot of the rear axle, which determine the stability triangle). In addition, solid rubber tires or cushion tires are adopted for most applications. These features cause the behavior of FLTs during motion to be significantly affected by ground irregularities, hence safety issues and high dynamic loads possibly being experienced [2-5]. Accordingly, new FLT prototypes manufactured by Toyota Material Handling Manufacturing Italy S.p.A. (Bologna, Italy), which promoted this research, must be verified with rigorous experimental campaigns to assess the actual vehicle response and measure the dynamic stresses that its main components may undergo during operation. Such tests are costly and time consuming, also because numerous transducers (typically strain gauges rosettes) are needed to monitor complex components properly.

https://doi.org/10.3311/ECCOMASMBD2021-170

This study aims at developing a multibody model to predict the dynamic loads experienced by a FLT that hits a steel plate obstacle when running in straight line at constant high speed, which is one of the most critical testing conditions in the manufacturer's verification protocols. In particular, the final objective is implementing reliable numerical tools to achieve an accurate estimate of the dynamic stresses acting on the FLT main components (in particular, the chassis), hence possibly reducing the need for experimental tests. To the Authors' best knowledge, most of the studies on FLT dynamics available in the literature dealt with the topic of vehicle stability [2, 6-11] or operator's safety [12-15], whereas only few works aimed at developing predictive models to help the structural and durability design of FLT components [16, 17].

A preliminary model had been developed in [5] to assess the possibility of simulating accurately the dynamic response of the chassis assembly, while neglecting the behavior of the load handling assembly, for the FLT operating unloaded. The results therein reported have been exploited to develop a more refined model that takes into account also the load handling assembly dynamics. It allows to estimate the forces acting between the mast and the chassis, as well as to assess both the unloaded and loaded operating conditions. The new model, implemented by using a commercial multibody software package, is here presented.

## 2. DESCRIPTION OF THE INVESTIGATED FORKLIFT

The studied vehicle is an electric FLT characterized by a total mass of about 6 tons and a load capacity of 2.5 tons. The front axle is driven by an electric motor, whereas the steering mechanism is located in the rear axle. The FLT is equipped with two couples of wheels, with a bigger radius for the front axle tires (Fig. 1 – some portions of the image are concealed due to NDA).

The load handling assembly (forks, fork positioner and mast) includes two actuation systems:

- two hydraulic cylinders (referred to as tilt cylinders) act symmetrically between the chassis and the mast (one on each side) and control the mast tilting angle (backward or forward, with respect to the vertical position);
- one further hydraulic cylinder controls the fork positioner lifting (and the mast extension) through a transmission chain.


**Figure 1.** Side view of the studied FLT during tests.

## 3. EXPERIMENTAL TESTS

### 3.1. Sensor setup and measurements

Experiments were performed to characterize the behavior of the studied FLT in both static and dynamic operating conditions. To this purpose, the FLT was equipped with six accelerometers and two load cells.

- Two piezoelectric accelerometers were placed on the left and right sides of the chassis, near the wheel hubs of the front axle, with vertical measuring axis.

- One piezoelectric accelerometer was placed on the rear part of the chassis, lying on the vehicle vertical-longitudinal plane of symmetry and close to the rear axle pivot, for measuring vertical acceleration as well.
- One triaxial MEMS accelerometer was placed on the chassis under the operator seat, for monitoring the accelerations along the longitudinal, vertical and lateral directions, respectively.
- Two piezoelectric accelerometers were installed on the left and right sides of the mast, above each tilt cylinder joint.
- The two load cells were placed in the mast/tilt cylinders connections, replacing the joint pivots and measuring the axial forces exerted by the tilt cylinders (referred to as tilt forces).

Acceleration and force signals were acquired with a sampling frequency of 5 kHz and 1 kHz, respectively. A low-pass filter (cutting frequency 50 Hz) has been applied in the post processing to all the signals, since no relevant frequency content was observed above 20 Hz.

Two loading conditions were tested, namely the unloaded FLT (referred to as NL condition) and the FLT loaded at about 80% of its capacity (WL).

Three different tests were conducted. In the first test, the static tire vertical loads and tilt forces were measured for both the NL and WL conditions, in order to assess the vehicle mass properties and distribution. The ground/tires normal loads were determined by means of vehicle weighing scales lying on a horizontal plane, with the mast in vertical position.

In the second test, the FLT was kept still on the ground and a steel block of 500 kg was lifted and then rapidly released (Fig. 1). This test was meant to excite primarily the resonance associated with the hydraulic circuit of the tilt cylinders, hence possibly permitting to estimate the corresponding stiffness and damping parameters. The mast was kept tilted by 8° backwards. Indeed, in this configuration the tilt cylinders are almost orthogonal to the mast, thus making straightforward to determine their equivalent stiffness.

The third test consisted of five passages on the obstacle carried out at constant velocity, for each loading condition. The mast was kept tilted by 8° backwards (consistently with the test mentioned above), with the forks close to the ground.

### 3.2. Experimental results

The static test showed that the actual mass distribution of the FLT closely matches the nominal one, without significant discrepancies. In particular, the centers of mass of both the load handling assembly and of the chassis assembly lie on the vertical-longitudinal plane of symmetry of the vehicle.

The second experiment appeared successful in exciting the vibration mode involving the oscillations of the mast around its hinges. Figure 2 shows the measured tilt force acting on the right tilt cylinder during the test. Due to NDA, the values are normalized in this chart and in the ones reported hereafter. The oscillations exhibit an exponentially decaying trend, hence being clearly ascribable to a free vibration response. The corresponding damped natural frequency (about 2.5 Hz) can be easily determined by computing the Power Spectral Density (PSD) of the signal, while the damping factor can be estimated by using the logarithmic decrement method. These values can be exploited to estimate the equivalent stiffness of the tilt cylinders, by considering the vibrations of a simplified 1-DOF system with known inertia and natural frequency. The estimated stiffness and damping values are used to initialize the numerical model before the updating process.

As for the third test, the measurements exhibited satisfactory repeatability, for each loading condition. Out-of-plane phenomena appear negligible, as the signals measured by the homologous sensors (i.e., on the left and right sides of the FLT) are basically coincident. In particular, the accelerations of the left-front axle (LFA) and the right-front axle (RFA) confirm

that the front wheels hit the obstacle almost simultaneously, since the maximum delay between the signals is 0.0006 s (namely, 3 samples).

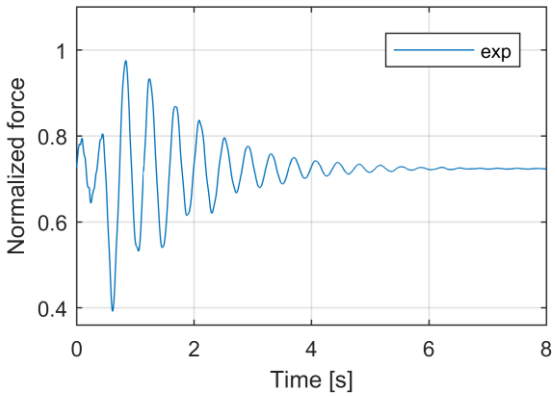


**Figure 2.** Tilt force measured (exp) on the right tilt cylinder.

Figure 3 shows the analysis in frequency domain of the LFA acceleration signal for the NL loading condition. A major frequency peak at about 5 Hz that can be observed. By applying a narrow bandpass filter centered on such peak, the front and the rear axle appear in phase. Hence, the frequency is reasonably related to the bounce mode of the vehicle.

Consistently with preliminary investigations [5], the signals measured by the accelerometers on the front axle (particularly the LFA) appear more reliable and with less noise than the others. Therefore, the LFA acceleration is chosen as the reference acceleration signal to be compared with the numerical model.

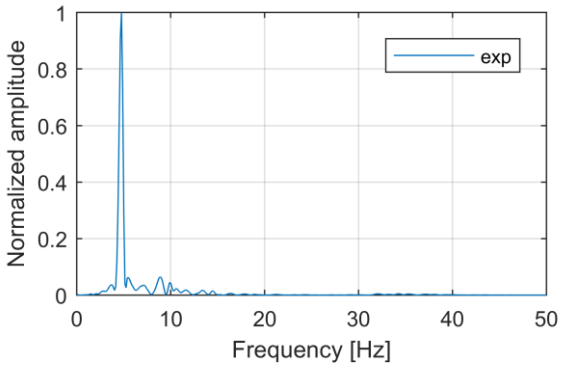


**Figure 3.** Normalized PSD of the measured (exp) LFA acceleration.

## 4. NUMERICAL MODEL AND SIMULATIONS

### 4.1. Model implementation

A numerical model of the complete FLT (Fig. 4) is implemented by using the multibody software RecurDyn (FunctionBay, Seongnam, South Korea). All the FLT parts are modelled as rigid bodies. Their mass properties are assigned based on both CAD geometries and experimental measurements.

Contact ground-to-surface functions between ground and wheels are set. However, the actual tire compliance is modeled by using a nonlinear lumped-stiffness parameter acting between each wheel and the corresponding axle, estimated from the static load-deflection curve provided by the tire manufacturer.

As for the load handling assembly, the lifting actuator is modeled with as a nonlinear spring that generates a null force when the fork positioner assembly rebounds. The tilt cylinders are modeled with a single linear spring acting on the FLT vertical-longitudinal plane of symmetry: the corresponding initial stiffness and damping values have been estimated as described in

Section 3.2. The load in the WL condition is a rigid block supported by the forks through contact functions.

All the other joints are modelled by using ideal constraints.

The static vertical loads on the four wheels and the static tilt forces computed with the model closely match the measured ones for both the NL and the WL loading conditions (error below 1.5 %).

Simulations of the vehicle dynamics are performed by prescribing the motion of the driving wheels, through velocity functions.

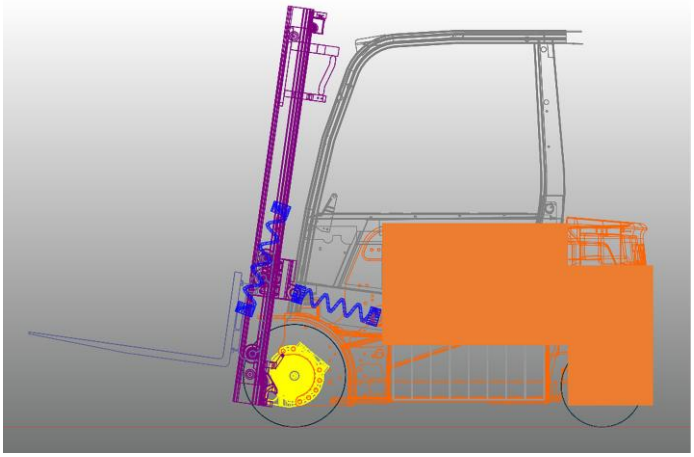

**Figure 4.** Numerical model implemented with RecurDyn.

### 4.2. Model updating and validation

A preliminary sensitivity analysis permitted to identify the subset of parameters that affect the dynamic response of the FLT most significantly. Such subset was adopted to run the model updating process on the basis of a fully factorial design.

The model accuracy was evaluated in terms of its capability to correctly predict the two measured quantities that are deemed essential for assessing properly the FLT dynamics, according to the manufacturer's knowhow, namely:

- vertical acceleration of the front axle, in terms of amplitude and location of the highest peak (generated by the impact with the obstacle), and of frequency content;
- tilt force, in terms of amplitude and location of the highest peaks, and of frequency content.

Model updating was performed by focusing on the NL case. Indeed, such loading condition is the most critical in terms of accelerations experienced by the FLT, hence possibly causing higher overall stresses.

Figure 5 shows the comparison between the measured data and the numerical results (normalized with respect to the measured maximum value) concerning the NL case, for the LFA acceleration and the tilt force provided by the updated model. It is worth noting that the measured tilt force reported in the graph is the sum of the signals of both load cells, since the tilt cylinders are modelled with a single element. Both quantities are matched satisfactorily by the updated model, in terms of amplitude, main resonance and general damping. The LFA acceleration and tilt force peaks occurring during the obstacle/tires impact phase (at about 0.5 s) are slightly overestimated by the simulations. These discrepancies may be reasonably related to local nonlinear deformations of the tires, which are not taken into account by the implemented contact model. Nonetheless the numerical results are deemed sufficiently accurate.

The set of optimal parameters obtained for the NL case were then adopted to simulate also the behavior exhibited by the FLT in the WL case. The comparison between the measured data and

the numerical results for the WL loading condition, in terms of the LFA acceleration and the tilt force, is reported in Fig. 6. The first peak of both monitored quantities appears largely overestimated. Moreover, some relevant high-frequency oscillations observed in the LFA signal are missed. However, the trend of the tilt force is replicated with sufficient precision. Hence, the accuracy of the model is still considered acceptable, although further improvements may be required.

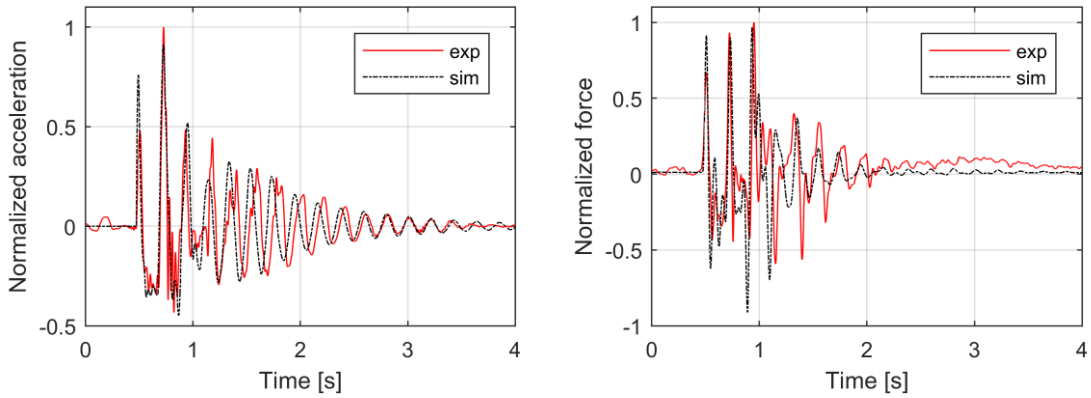


**Figure 5.** Experimental (exp) vs. numerical (sim) results, NL condition, LFA acceleration (left) and tilt force (right).

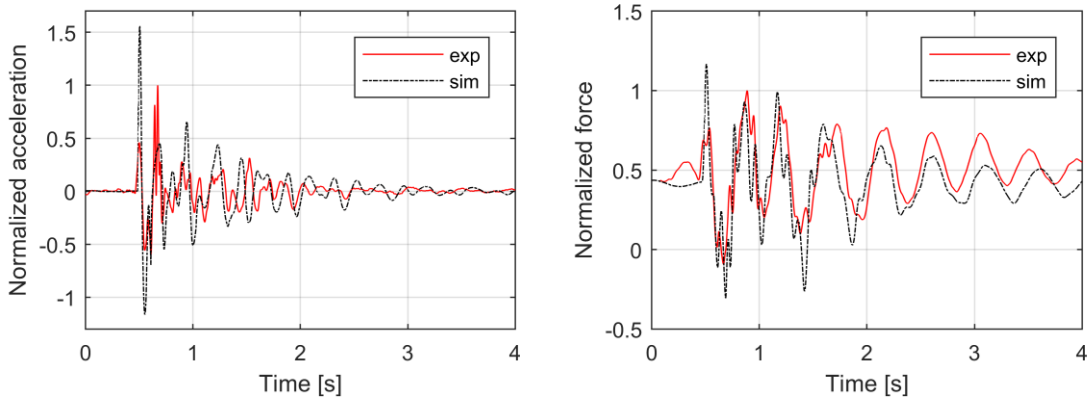


**Figure 6.** Experimental (exp) vs. numerical (sim) results, WL condition, LFA acceleration (left) and tilt force (right).

## 5. CONCLUSIONS

The presented work investigated the dynamic response of a counterbalance forklift truck executing a reference operating cycle, according to the manufacturer's testing protocols. The study focused on the implementations of numerical tools to predict reliably the forklift behavior in terms of accelerations and forces acting on the chassis, in order to help the structural design process during the development of new products.

An experimental campaign was conducted to characterize the vehicle response when running on a steel plate obstacle at constant velocity with two different loading condition, as well as to estimate the main stiffness and damping properties of the system.

A multibody model of the full vehicle was developed by using a commercial software package. The model takes into account the nonlinear road/wheels interaction and the load handling assembly dynamics. It was updated and validated by exploiting the data gathered from the experiments.

The updated model proven effective in replicating the main dynamic phenomena experienced by the vehicle after impacting the obstacle. In particular, the accelerations and tilt forces exhibited by the unloaded forklift can be closely matched. The numerical results appear acceptable also for the loaded condition, although some discrepancies can be observed for acceleration and tilt

force peaks related to the impact phase.

The future steps will aim at refining the tire/ground contact model, in order to further improve the model accuracy during the impact phase.

## ACKNOWLEDGMENTS

EnginSoft (Trento, Italy) is gratefully acknowledged for operative cooperation and support.

## REFERENCES

[1] Industrial Truck Association: Lifting America – The Economic Impact of Industrial Truck Manufacturers, Distributors and Dealers, report. Oxford Economics, New York, NY, USA (2017) Available online: https://www.oxfordeconomics.com/recent-releases/lifting-america (accessed on 24th September 2021).

[2] Rebelle, J., Mistrot, P., Poirot, R.: Development and validation of a numerical model for predicting forklift truck tip-over. Vehicle System Dynamics 47(7) (2009) 771–804.

[3] Larsson, T.J., Oldertz, C.: Hazardous exposures and injury types associated with the use of industrial lift trucks in Sweden 2005-2007. Safety Science Monitor 15(3) (2011).

[4] Saric, S., Bab-Hadiashar, A., Hoseinnezhad, R., Hocking, I.: Analysis of forklift accident trends within Victorian industry (Australia). Safety Science 60 (2013) 176–184.

[5] Martini A., Bonelli, G.P., Rivola, A.: Virtual Testing of Counterbalance Forklift Trucks: Implementation and Experimental Validation of a Numerical Multibody Model. Machines 8(2):26 (2020). doi: 10.3390/machines8020026

[6] Strandberg, L.: Danger, rear wheel steering. Journal of Occupational Accidents 5 (1983) 39–58.

[7] Frazer-Nash Consultancy Limited: Fork lift truck validation and trials, Health and Safety Executive Research Report 456. HSE Books, Sudbury, UK (2006) Available online: http://www.hse.gov.uk/research/rrhtm/rr456.htm (accessed on 24th September 2021).

[8] Popescu, S., Nastase, S., Csatlos, C.: Contributions to theoretical and experimental study of the dynamic stability of the forklift trucks. Journal of Engineering Studies and Research 18(3) (2012) 115–121.

[9] Milanowicz, M., Budziszewski, P., Kedzior, K.: Numerical analysis of passive safety systems in forklift trucks. Safety Science 101 (2018) 98–107.

[10] Gardella M., Martini A.: Multibody Models and Simulations to Assess the Stability of Counterbalance Forklift Trucks. In Multibody Dynamics 2019 – ECCOMAS 2019. Computational Methods in Applied Sciences 53 (2020) 526–533. Kecskeméthy, A., Geu Flores, F., Eds.; Springer, Cham, Switzerland. doi: 10.1007/978-3-030-23132-3_63

[11] Larsson, T.J., Lambert, J., Wilde, M., Tully, G., Askew, H., Skinner, W., Carter, B., Martin, T., Kenningham, L.: Industrial forklift trucks - dynamic stability and the design of safe logistics. Safety Science Monitor, *7*(1) (2003).

[12] Yang, M., Xu, G., Dong, Q., Han, X.: Vibration Study of Fork-lift Truck Based on the Virtual Prototype Technology. Sensors & Transducers, 170(5) (2014) 177–183.

[13] Malchaire, J., Piette, A., Mullier, I.: Vibration exposure on fork-lift trucks. Annals of Occupational Hygiene 40(1) (1996) 79–91.

[14] Lemerle, P., Mistrot, P.: A New Tire Model to Predict Vibration Emission of Counterbalance Trucks. Tire Science and Technology 28(2) (2000) 119–137.

[15] De Man, P., Lemerle, P., Mistrot, P., Verschueren, J.-Ph., Preumont, A.: An investigation of a semi-active suspension for a forklift truck. Vehicle System Dynamics 43(2) (2005) 107–119.

[16] Doçi, I., Bajraktari, M., Imeri, V.: Studying dynamic effects on warehouse forklift during forward movement with full loading. In: 16th International Research/Expert Conference Trends in the Development of Machinery and Associated Technology - TMT 2012, Dubai, UAE (2012) 551–554.

[17] Doçi, I., Imeri, V.: Dynamic Analysis of Forklift during Load Lifting using Modeling and Simulations. International Journal of Current Engineering and Technology 3(2) (2013) 342–347.

## Author index


MŰEGYETEM 1782


MAGYAR TUDOMÁNYOS AKADÉMIA
1825


Academia Europaea
19 88
The Academy of Europe
Budapest Knowledge Hub


Budapest, 2021